ADVANCES IN INTELLIGENT SYSTEMS AND COMPUTING 194

Sukhan Lee
Hyungsuck Cho
Kwang-Joon Yoon
Jangmyung Lee (Eds.)

Intelligent Autonomous Systems 12

Springer

Advances in Intelligent Systems and Computing 194

Editor-in-Chief

Prof. Janusz Kacprzyk
Systems Research Institute
Polish Academy of Sciences
ul. Newelska 6
01-447 Warsaw
Poland
E-mail: kacprzyk@ibspan.waw.pl

For further volumes:
http://www.springer.com/series/11156

Sukhan Lee, Hyungsuck Cho, Kwang-Joon Yoon, and Jangmyung Lee (Eds.)

Intelligent Autonomous Systems 12

Volume 2: Proceedings of the 12th International Conference IAS-12, Held June 26–29, 2012 Jeju Island, Korea

Springer

Editors
Sukhan Lee
College of Information and
Communication Engineering
Sungkyunkwan University
Gyeonggi-Do
Korea

Hyungsuck Cho
Daegu Gyeongbuk Institute of Science
and Technology
Daegu
Korea

Kwang-Joon Yoon
Konkuk University
Seoul
Korea

Jangmyung Lee
Department of Electronics Engineering
Pusan National University
Pusan
Korea

ISSN 2194-5357 e-ISSN 2194-5365
ISBN 978-3-642-33931-8 e-ISBN 978-3-642-33932-5
DOI 10.1007/978-3-642-33932-5
Springer Heidelberg New York Dordrecht London

Library of Congress Control Number: 2012948092

Printed on acid-free paper

Springer is part of Springer Science+Business Media (www.springer.com)

Preface

Intelligent autonomous systems are emerged as a key enabler for the creation of a new paradigm of services to humankind, as seen by the recent advancement of autonomous cars licensed for driving in our streets, of unmanned aerial and underwater vehicles carrying out hazardous tasks on-site, and of space robots engaged in scientific as well as operational missions, to list only a few. In the foreseeable future, the services intelligent autonomous systems provide us with are expected to spread into every fabric of our society, beyond the aforementioned transportation, security and space exploration, to include manufacturing, healthcare, environment and energy, and, ultimately, personal/domestic assistance for our daily lives. This edition aims at serving the researchers and practitioners in related fields with a timely dissemination of the recent progress on intelligent autonomous systems, based on a collection of papers presented at the 12^{th} International Conference on Intelligent Autonomous Systems, held in Jeju, Korea, June 26–29, 2012. With the theme of "Intelligence and Autonomy for the Service to Humankind", the conference has covered such diverse areas as autonomous ground, aerial, and underwater vehicles, intelligent transportation systems, personal/domestic service robots, professional service robots for surgery/rehabilitation, rescue/security and space applications, and intelligent autonomous systems for manufacturing and healthcare. The papers presented at the conference are not only rich in their technical contents, including autonomous navigation, SLAM, machine vision/perception, cognitive systems, human-robot interaction, biomimetic systems, decision-support systems, web-based and networked robotics, mobiligence, life engineering, and micro/nano robots for intelligent autonomous systems. But, they are in high quality as more than 50% of the papers presented were from the 24 special invited sessions. For better readability, this edition has the total 168 papers grouped into 4 chapters: Chapter I: Autonomous Ground Vehicles and Mobile Manipulators, Chapter II: Unmanned Aerial and Underwater Vehicles and Bio-inspired Robotics, Chapter III: Service Robotics and Human-Robot Interaction, Chapter IV: Autonomous Multi-Agent Systems and Life Engineering, where individual chapters, edited respectively by Sukhan Lee, Kwang Joon Yoon, Jangmyoung Lee and Hyungsuk Cho, begin with a brief introduction written by the respective chapter editors. I do hope that readers find Intelligent Autonomous System 12 stimulating and enjoyable.

Sukhan Lee
General Chair, IAS-12

Contents

III: Service Robotics and Human-Robot Interaction

by Jangmyung Lee

Interactions between the human and robots play a key role for service robots such as medical and personal robots. The teleoperation with haptic interface can be classified as an example of the human-robot interaction and it is a very useful tool for medical robots as well as personal service robots. In the haptic interface, the stability of the system needs to be analyzed since the local slave system becomes unstable with the increase of the time delay. Also not only the haptic interface but also the visual feedback to the human from the robot are very critical for the successful tele-services over the communication channels such as Internet.

Firstly, there are also eighteen papers on medical and personal service robots including surgical navigation and safety issues in this chapter. They are listed as follows:

1. Design of Master Console Haptic Handle for Robot Assisted Laparoscopy
2. A New Concept for "Vaginal Hysterectomy" Robot
3. Mechanism of a Learning Robot Manipulator for Laparoscopic Surgical Training
4. Fusion of Inertial Measurements and Vision Feedback for Microsurgery
5. An Orbital Velocity-Based Obstacle Avoidance Algorithm for Surgical Robots
6. HOG-Based Person Following and Autonomous Returning Using Generated Map by Mobile Robot Equipped with Camera and Laser Range Finder
7. Fast Range Image Segmentation and Smoothing using Approximate Surface Reconstruction and Region Growing
8. Resilient Navigation through Probabilistic Modality Reconfiguration
9. Scaling Vector Field SLAM to Large Environments
10. Observation planning for object search by a mobile robot with uncertain recognition
11. Effects of a Frequency-Dependent Dissipative Element in Haptic Interaction
12. A Case Study of Safety in the Design of Surgical Robots : The ARAKNES platform
13. Classification of Modeling for Versatile Simulation Goals in Robotic Surgery
14. Role of Holographic Displays and Stereovision Displays in Patient Safety and Robotic Surgery
15. A methodological framework for the definition of patient safety measures in robotic surgery. The experience of SAFROS project
16. System concept for collision-free robot assisted surgery using real-time sensing
17. The Autonomous Photovoltaic MarXbot
18. Automatic Segmentation and Decision Making of Carotid Artery Ultrasound Images.

The following four papers are handling haptic teleoperation issues for the robots and they are listed as follows:

19. Bilateral Tele-manipulation with a Humanoid Robot Hand/Arm between USA and Japan
20. Stable Rate-Mode Bilateral Teleoperation Based on Time Domain Passivity Approach
21. Backstepping Control of Quadrotor-Type UAVs and its Application to Tele-operation over the Internet
22. Experiments on Intercontinental Haptic Control of Multiple UAVs

There are eighteen papers discussing about various kinds of interactions between human and robots including measurement and recognition for the effective interactions and they are listed as follows:

23. Textual Affect Detection in Human Computer Interaction
24. Face Alignment Based on 3D Face Shape Model and Markov Random Field
25. Spontaneous Facial Expression Recognition by Fusing Visible and Thermal Infrared Images
26. A Wearable Plantar Pressure Measurement System: Design Specifications and First Experiments with An Amputee
27. Human-Robot Interaction-based Intention Sharing of Assistant Robot for Elderly People
28. Human Tracking Using Improved SJPDAF
29. Research on the Personalized Interaction Model Driven by User Behavior
30. A Novel Closed-loop Feedback Frame for Data Processing
31. Facial Expression Recognition from Infrared Thermal Videos
32. Motion Planning of a Dual Manipulator System for Table Tennis
33. Integrated Balance Control on Uneven Terrain
34. Towards Meta-reasoning for Human-Robot Interaction
35. Learning probabilistic decision making by a service robot with generalization of user demonstrations and interactive refinement
36. A topic recognition system for real world human-robot conversations
37. Semi-Autonomous Car Control Using Brain Computer Interfaces
38. Perceptual Social Dimensions of Human-Humanoid Robot Interaction
39. Complex Emotional Regulation Process in Active Field State Space
40. A Development of Art Robot System for Representation of Brightness of Image

Through this chapter, it is noticed that the service robotics are coming near to our daily lives and the technologies are ready to be used for the service robots. However, the safety and reliability must be checked seriously with some standards to make the robots affordable, sustainable, dependable and also compatible to other peripheral devices. Keywords of this chapter are listed as follows:

Medical Robotics and Surgical Navigation
Medical robotics
Personal/Domestic Service Robots, and
Safety and Standards in Robotic Surgery
Haptic Teleoperation
Human-Robot Interaction.

Design of Master Console Haptic Handle for Robot Assisted Laparoscopy*

Chi Yen Kim[1], Byeong Ho Kang[2], Min Cheol Lee[3], and Sung Min Yoon[2]

[1] Division of Mechanical Engineering Technology
Yeungnam College of Science & Technology
Daegu, South Korea
chiykim@ync.ac.kr
[2] School of Mechanical Engineering
Pusan National University
Busan, South Korea
kbh8548@nate.com
Tactics1019@gmail.com
[3] Department of Mechanical Engineering
Pusan National University
Busan, South Korea
mclee@pusan.ac.kr

Abstract. Now robot assisted laparoscopy has some problem to depend only on image of the surgical field. However, there is a research result which shows that it is possible to measure the operation force on commercialized instrument inside patient without sensors [1]. By using measured information, haptic technique can be implemented into surgical robot system. Therefore, this paper proposes the design of master console handle to put haptic function into laparoscopy surgical robot system. The design is centered on the implementation particularly. Therefore this paper suggests the design of master console handle whose structure can match with the joint and DOF of instrument to and the adoption of cable-conduit mechanism to make light structure t to perform a delicate haptic function. Cable-conduit mechanism removes the weight and inertia of link caused by haptic actuator and encoder which is separated from handle link.

Keywords: Haptic, Surgical robot, Robot assisted Laparoscopy.

1 Introduction

Robot assisted laparoscopy is better than standard laparoscopy as easier instrument manipulation, limited mobility of straight laparoscopic instruments and ergonomic

* This research was supported by Basic Science Research Program through the National Research Foundation of Korea (NRF) funded by the Ministry of Education, Science and Technology (2011-0014915)

S. Lee et al. (Eds.): Intelligent Autonomous Systems 12, AISC 194, pp. 3–10.
springerlink.com

position for the surgeon [2]. In robot assisted laparoscopy, while the surgeon's hands and fingers direct the surgery using master console handle, the movements are translated by the computer to precise movement of the microsurgical instruments on the robotic arms inside the patient's body. As the surgeon is separated from patient, he cannot feel the touch of organ and so has to depend only on image of the surgical field, which occur some problems [3].

To improve laparoscopy surgical robot system to supplying to surgeon with the surgical field sensing information, several researches have attempted to put haptic function into surgical robot system[4][5][6]. However, these studies has mainly focused on haptic mechanism and stayed in research step before becoming commercialized. And commercialized laparoscopic surgical robot, Da Vinci, adopts better redundant DOF master handle then DOF of slave robot to perform comport driving to reduce fatigue. To realize haptic function on existed surgical robot system, each link of master handle has to contain encoder to measure the movement of surgeon’s motion and haptic actuator to generate haptic force. Therefore, increasing weight and inertia makes difficult to perform a delicate haptic function as surgical sense.

This study proposes light master handle design which can be used in already commercialized surgical robot system to apply haptic function. To facilitate application of haptic system into commercialized system application, this paper suggests very similar structure with the end-effect part of instrument used in slave robot arm. To prune the weight and inertia of handle so that it can generate minute force which can be felt by human, cable-conduit structure is adopted.

2 Design of Master Handle

2.1 Design of Master Console Handle

As explained at introduction, commercialized laparoscopy surgical robot systems use a redundant DOF master handle to perform comport driving for surgeon. However, the redundant DOF master console handle will meet the difficulties when haptic function is applied into the system in that added links increase the weight and inertia as well as complex haptic force calculation is required to generate the force. Actually, the reason why commercialized surgical robot didn’t consider the haptic system is the difficulties to measure the operating force on instrument. However, in previous research shows the possibility of sensing the force without sensors [1].Thus, this paper designs the handle with considering haptic system.

Generally human has habitude to orient himself to implement easily in spite of constrained shape. Particularly, if shape of handle is same as ocular one of instrument, adoptive habitude is much better in visual servoing system like as laparoscopy. Therefore, this paper proposes the design of master console handle whose structure can match with the joint and DOF of instrument as possible as it can.

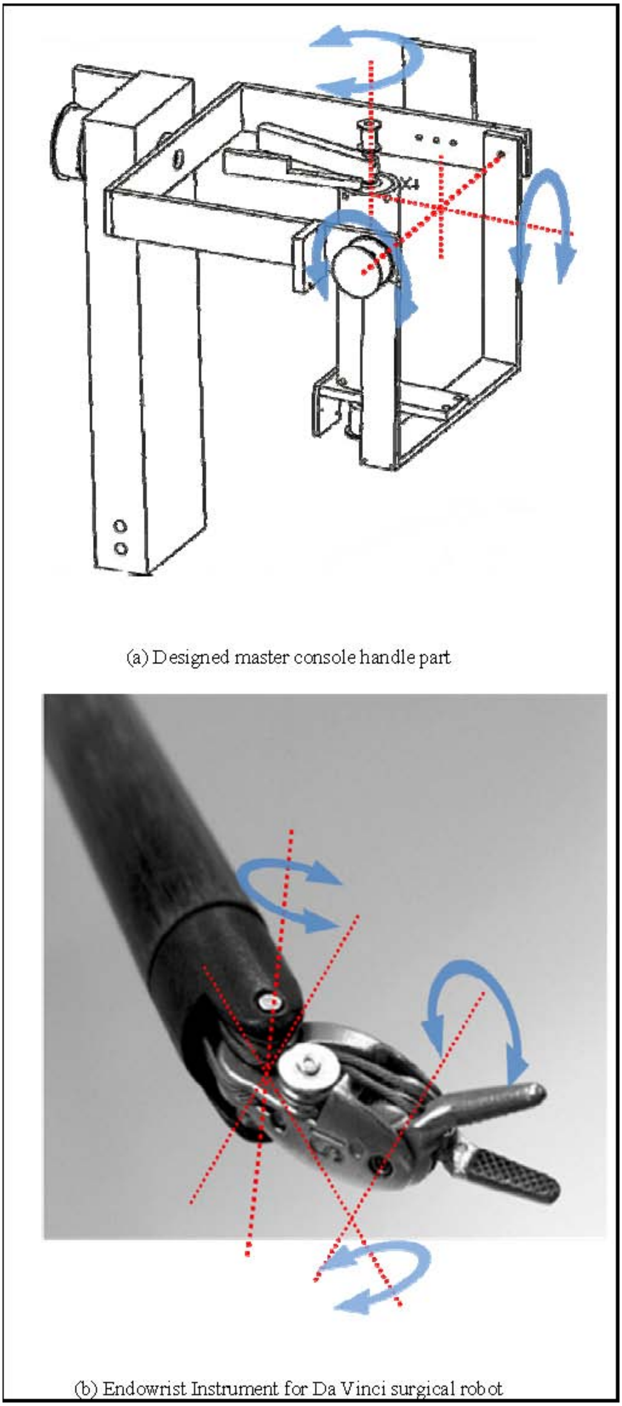

(a) Designed master console handle part

(b) Endowrist Instrument for Da Vinci surgical robot

Fig. 1. Designed scheme compared with Endowrist instrument tip

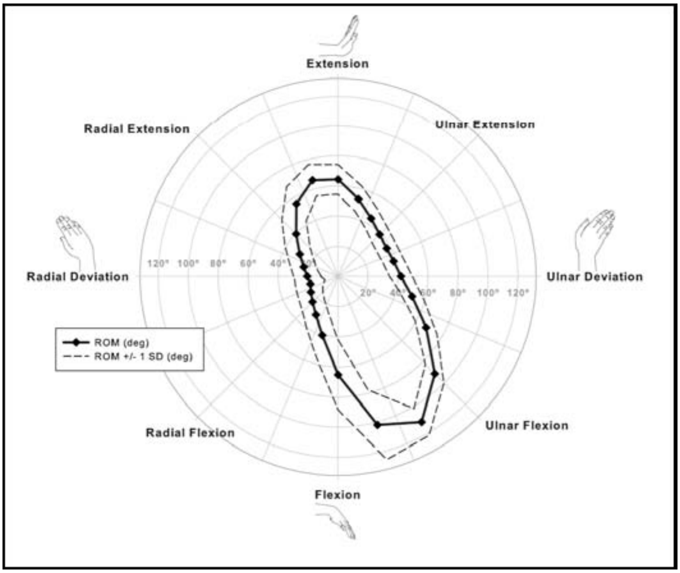

Fig. 2. Mean range of motion [7]

Fig. 1 shows the handle design scheme proposed by this paper. To make similar shape and structure with the tips of instrument, gripping axis is deviated from the union axis origin. The roll and pitch axis of handle are concentrated on one point same as the instrument. And the number of DOF, joints of handle is equal to one of instrument. During designing the shape, the size and workable space is decided after considering the size of hands and range of motion value as shown in Fig 2 stated in Joseph's paper [7].

2.2 Adopt of Cable Conduit Structure

The major contribution of this paper is the weight reduction design to embody the haptic function in robot assisted laparoscopy. To make light structure, this paper suggests the adoption of cable-conduit power transmission mechanism to measure the motion of surgeon's handling and generate the haptic force in master handle. Cable-conduit mechanism can be simply explained as cable displacement transmission caused by cable sliding on conduit and fixation during the rigid state of conduit. However, as a conduit shows flexible feature and motion, it looks like transferring the motion and force freely in the space. Therefore, inner motion of free space object like as the handle in the master console of the robot assisted laparoscope seems to be transferable after using cable conduit method. Again, the force seems to be able to be transmitted as the force of cable system is transferred by the tension of cable displacement.

The dynamic of cable-conduit mechanism is analyzed by Agrawal and et at [8]. As the paper said in details, the force and motion is transmitted by relative movement between cable and conduit. For the reason, the friction between them affects much on the force and movement as following government equation.

$$u''(x,t) - \frac{\mu}{R(x)} u'(x,t) sign(\dot{u}(x,t)) = 0 \quad (1)$$

Where, $u(x,t)$ denote its axial displacement in x at time t, the partial derivative of a function $u(x,t)$ to the spatial variable x is denoted by $u'(x,t)$ and the partial derivative with respect to the time variable t by $\dot{u}(x,t)$, μ is the coefficient of friction, $R(x)$ is the radius at x as shown in fig .3

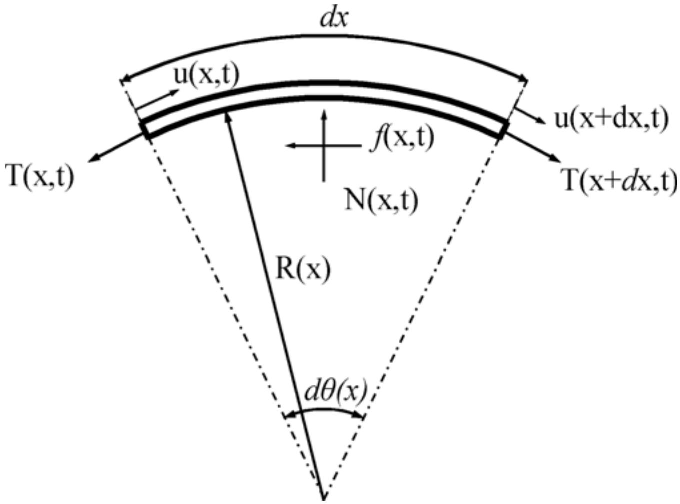

Fig. 3. Forces balance diagram of cable element [8]

In fact, the cable-conduit system has a merit which transmits the force and displacement freely in space. However the force is affected by shape of conduit, as R(x) in eq. 1. The shape seems to be friction in force transmission. The shape friction brings on slacking phenomenon which occasion time delay caused by cable propagation and remaining backlash during reverse direction changing as analyzed at[8].

From the viewpoint of applying cable conduit into master consol haptic handle, slacking effect will occur time delayed measurement at the first movement of surgeon's motion and wrong measurement at the moment of changing direction. Therefore, to prevent the problem, low friction cable-conduit material has to be chosen. And curvature length of cable-conduit could be linearised straightly as possible as it can in the implementation of constructing master console handle for haptic system.

3 Realization and Experimental Test

The proposed design of this paper in Fig. 1 is exemplified by producing model made up by aluminum and PVC pipe as shown in fig 4. Whole weight of exemplified model is less than 0.8 Kg except standing object which is installed in right side in fig 4.Therefore the proposed design and realization satisfies the light 4 DOF structure enable to make up precise haptic system available to master console handle for robot assisted laparoscope system. Still under constructing, the feeling of driving is experimented and felt as natural and non-constraint movement within wrist moving range as in Fig. 2.

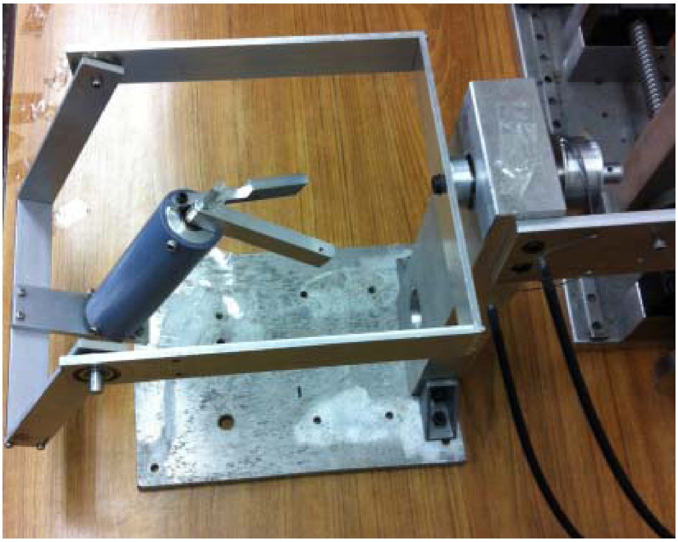

Fig. 4. Exemplified handle model

To make up complete handle, pulley for each joint should be attached on. But the whole weight of 4 DOF will be not over 1.2 kg. Comparing with 5 DOF existing handle which contains encoder and sometimes motor to compensate weight, proposed system is much lighter structure below the weight of motor and encoder and so could be less burden to surgeon.

The final aim of this study is constructing complete 4 DOF haptic handle using cable-conduit which is able to make user fill the force generated for haptic signal as well as measure the motion of user movement. However it is in process study, this paper tries to cover up to making structure and showing the possibility of adopting cable-conduit. To prove the possibility of adopting cable-conduit mechanism in handle for surgical robot master consol, this paper examined the cable conduit system for 1 DOF as shown in Fig. 5. The experimental test system is constructed to generate movement and measure it in other side. Also the pretension can be adjustable by using sliding plate and screw.

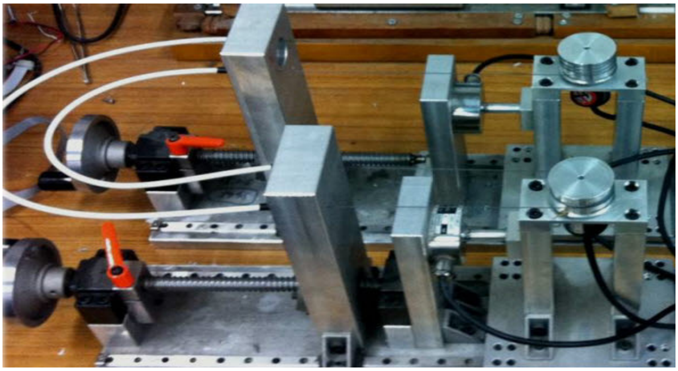

Fig. 5. Experimental system of cable conduit system

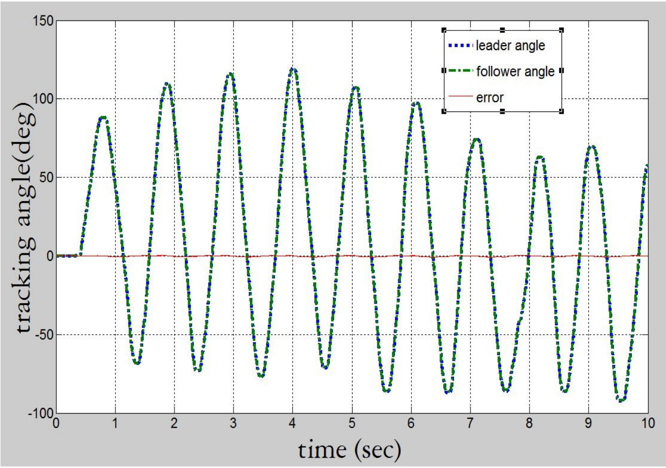

Fig. 6. Experimental test result of cable conduit system

The experimental test was performed by generating periodic and repetitive trajectory on driving pulley and measuring the following pulley connected cable-pulley system as shown in Fig. 5. In the experiment, this paper used conduit for bicycle break system which is a little high stiffness and lubricated. From the experimental test result shown in Fig. 6 it is found that there is not much effect of slacking which considered in chapter 2. Therefore, it is possible to adopt cable-conduit system in master console haptic handle for robot assisted laparoscope.

4 Conclusion

This paper studied to make light master handle design which can be used in already commercialized surgical robot system to apply haptic function. To facilitate application of haptic system into commercialized system application, this paper suggests very similar structure with the end-effect part of instrument used in slave robot arm. Also, to prune the weight and inertia of handle so that it can generate minute force which can be felt by human, cable-conduit structure is adopted. Cable-conduit system can bring slacking phenomenon which can occur time delay and mis-measurement in master console handle system, this paper examined the performance using experimental test system. From the test result, it is proven that lubricated and a little stiffness conduit is adoptable to make up haptic handle. Although this study is in process, this paper proved the possibility of proposed method.

Acknowledgment. This research was supported by Basic Science Research Program through the National Research Foundation of Korea (NRF) funded by the Ministry of Education, Science and Technology (2011-0014915).

References

[1] Lee, M.C., Kim, C.Y., Yao, B., Penie, W.J., Song, Y.E.: Reaction Force Estimation of Surgical Robot Instrument Using Perturbation Observer with SMCSPO Algorithm. In: Proceedings of AIM 2010, Montreal, Canada, pp. 181–186 (July 2010)
[2] Corcione, F., Esposito, C., Cuccurullo, D., Settembre, A., Miranda, N., Amato, F., Pirozzi, F., Caizzo, P.: Advantages and limits of robot-assisted laparoscopic surgery. Surgical Endoscopy 19(1), 117–119 (2002)
[3] Giulianotti, P., Coratti, A., Angelini, M., Sbrana, F., Cecconi, S., Balestracci, T., Caravaglios, G.: Robotics in General Surgery- Personal Experience in a Large Community Hospital. Archives of Surgery (238), 777–784 (2003)
[4] Vlachos, K., Papadopoulos, E., Mitropoulos, D.N.: Design and Implementation of a Haptic Device for Training in Urological Operations. IEEE Transactions on Robotics and Automation 19, 801–809 (2003)
[5] Payandeh, S., Li, T.: Towards new designs of haptic devices for minimally invasive surgery. International Congress Series, pp. 775–781 (2003)
[6] Hayward, V., Gregorio, P., Astley, O., Greenish, S., Doyon, M.: Freedom-7: A High Fidelity Seven Axis Haptic Deviec With Application to Surgical Training. In: Experimental Robotics Vi, pp. 445–456 (1998)
[7] Crisco, J.J., Heard, W.M.R., Rich, R.R., Paller, D.J., Wolfe, S.W.: The mechanical Axes of the Wrist Are Oriented Obliquely to the Anatomical Axes. The Journal of Bone & Joint Surgery 93, 169–177 (2011)
[8] Agrawal, V., Penine, W.J., Yao, B.: Modeling of Transmission Characteristics Across a Cable-Conduit System. IEEE Trans. on Robotics 36(5), 914–924 (2010)
[9] Jacobs, I.S., Bean, C.P.: Fine particles, thin films and exchange anisotropy. In: Rado, G.T., Suhl, H. (eds.) Magnetism, vol. III, pp. 271–350. Academic, New York (1963)
[10] Elissa, K.: Title of paper if known (unpublished)
[11] Nicole, R.: Title of paper with only first word capitalized. J. Name Stand. Abbrev. (in press)
[12] Yorozu, Y., Hirano, M., Oka, K., Tagawa, Y.: Electron spectroscopy studies on magneto-optical media and plastic substrate interface. IEEE Transl. J. Magn. Japan 2, 740–741 (1987); [Digests 9th Annual Conf. Magnetics Japan, p. 301 (1982)]
[13] Young, M.: The Technical Writer's Handbook. University Science, Mill Valley (1989)

A New Concept for a “Vaginal Hysterectomy” Robot

Kovit Khampitak[1], Wathanyu Neadsanga[2],
Sirivit Taechajedcadarung-Sri[1], and Thantakorn Pongpimon[1]

[1] Khon Kaen University,
[2] Rajamangala University of Technology Isan,
Khon Kaen 40002 Thailand
kovit@kku.ac.th

Abstract. The design concept of a novel vaginal hysterectomy robot which is composed of three compound robots is discussed. The results of *in vitro* mechanical evaluation of the first two prototypes are reported and ideas for future development discussed.

Keywords: Surgical robot, Medical robot, Hysterectomy robot.

1 Introduction

Nowadays, the Da Vinci surgical system, approved by the FDA in September 2001, is the state-of-the-art surgical technology [1]. Its disadvantages are its higher costs and longer operating room times [2]. In addition, none of the existing robotic systems are equipped to provide high quality feedback; this is of major concern as errors can have potentially devastating consequences [3].

Many different types of small task specific medical robots are currently being developed in many institutes. For example, a robot that provides assisted motion for knee and shoulder joints is gaining wide acceptance [4]. A robot-controlled fluid system was introduced to detect ex *vivo* breast cancer chemotherapy sensitivity [5].

In surgery, the SpineAssist robot has shown a high level of accuracy *in vivo* for the implantation of lumbar pedicle screws [6]. A dexterous miniature robot for natural orifice transluminal endoscopic surgery has been tested in multiple animal model studies [7] and also been performed successfully in humans, including appendectomy and cholecystectomy [8-10].

Hysterectomy is the most common non-pregnancy-related surgery, with approximately 600,000 procedures performed annually in the USA [11]. Vaginal hysterectomy, a natural orifice procedure, has been reported as a standard hysterectomy which the advantage of less pain and rapid recovery [12]. However, before performing this procedure a new surgeon needs a period of learning from an expert. In order to simplify this procedure we have designed a prototype of a compound multiple simultaneous vaginal hysterectomy robot and subjected it to mechanical tests. Once perfected, we hope this robot could help the young gynecologists to perform vaginal hysterectomies with the same speed and success rate achieved by an expert.

S. Lee et al. (Eds.): Intelligent Autonomous Systems 12, AISC 194, pp. 11–16.
springerlink.com

2 Design Concept and Procedure

The compound vaginal hysterectomy robot is composed of three small robots working simultaneously; ligaments and vessels cutting, uterine bisecting and vaginal cuff sealing robots. The mechanical joints were located in a common body with motions controlled by external moving slings.

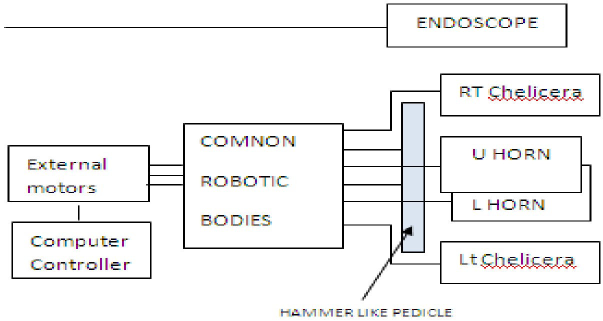

Fig. 1. Diagram showed a compound vaginal hysterectomy robot

2.1 Ligaments and Vessels Cutting Robot

In the first scorpion-like robot, the right and left chelicerae could move with two DOFs diving by two sling sheaths. The robot was able to grip and manipulate the uterine suspensory ligaments and vessels at the parametrium to free the uterus from human cavity.

Fig. 2. The right and left chelicerae of the scorpion- like robot were able to grip and manipulate the ligaments and vessels at parametrium. (black arrow)

2.2 Uterine Bisecting Robot

A Dynastes Hercules-like robot was designed to manipulate the uterus, working simultaneously with the first robot. It could move its upper and lower horns (two DOFs) by opening and closing their joint.

During the large uterine operation this robot could bisect the large uterus with a cutting saw. Each horn was composed of an inner longitudinal groove containing a movable saw. The saw is moved by a power sling and sheath from an external motor. It saws the uterus into two smaller pieces which can then be easily removed though the vaginal canal.

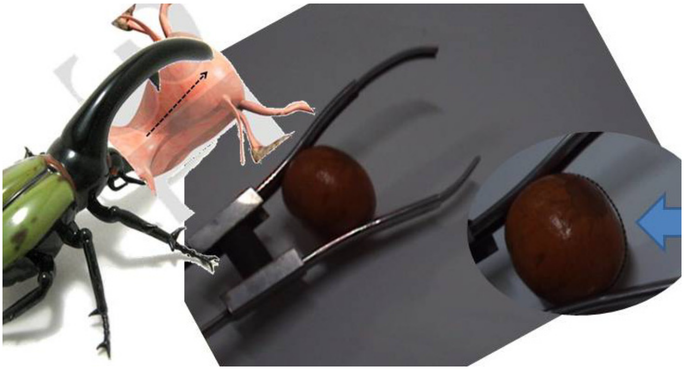

Fig. 3. A Dynastes Hercules-like robot was designed to manipulate and cut the uterus simultaneously with the work of the first robot. During the large uterine operation this robot can bisect the uterus using a cutting saw inside the sulcus. (arrow)

2.3 Vaginal Cuff Sealing Robot

This is a robot with two hammer-like pedicles, containing suture material. It could work automatically after the start of the process. We plan to produce a first prototype in the near future.

Fig. 4. Vaginal cuff sealing robot

3 Experiments

The tests occurred in October 2011 in Khon Kaen University, Thailand. The purpose was to test the mechanical movement of the first prototypes of the ligaments and vessels cutting and uterine bisecting robots.

3.1 The Mechanical Test of the Ligaments and Vessels Cutting Robot

Ten pieces of fresh raw meat size 5x5x0.5 cm^3 were used in this experiment. A 3 minute gripping test was performed to compare between the robotic chelicerae and traditional Heaney clamps. The depths of tissue collapse were recorded by visual ruler and the results subject to statistical analysis. Table 1 shows that there were no statistically significant differences between the results achieved with the two devices.

Table 1. The gripping test compared between the robotic chelicerae and traditional Heaney clamps

Experiment	**Gripping test of tissue collapse(mm)**		
	The robotic chelicerae	***Traditional Heaney clamps***	***p.***
1	2	3	> .o5
2	3	3	
3	3	3	
4	3	2	
5	2	2	
6	3	3	
7	3	3	
8	3	3	
9	2	3	
10	2	2	

No statistical difference by Wilcoxon Signed Rank test*

3.2 The Mechanical Test of the Uterine Bisecting Robot

The mechanical bisecting experiment was performed using apple fruit as the specimens. In three experiments, one achieved complete bisection of the fruit while the other two trials resulted only in partial bisections of the apples. The problems were caused by instability of the sling motion and the lack of stability of the specimens during the cutting process.

4 Discussion

Nowadays, the new technology using robotic surgery and other automated devices, is gradually penetrating our practice. The steps of development of the surgical robots could be divided into three essential stages.

The first stage is "Robot assisted human surgeries". The DaVinci Model is already on the market and shows many benefits in assisting surgeries. The next models, which are now being developed in many laboratories around the world will be quite small in size and have a quick set-up time. However, these robots still need human to operate in the external console, their operators require considerable training to use them, and they are still expensive.

The second stage is "Human assisted robotic surgery". The surgical procedures for the robots need to be simplified so that the robot could easily operate under human guidance. The vaginal hysterectomy robot being developed in our laboratory is small sized and designed specifically for this type of operation. The surgeon should be able to control the robot simply by giving permission for each of operating steps. After it is completely developed, the robot could help young gynecologists to operate as if they are experienced experts. In addition, they might do the vaginal hysterectomy in less than 30 minutes.

The last stage will be "Real robotic surgery". The robots will be able to perform the operation with limited or even no human control. In this stage the major development trends will be; 1) miniaturization and augmented reality [13, 14], 2) automation [15] and 3) no theatre operation or remote controlled telesurgery.

5 Future Work

In further work, the prototype of the third robot will be produced. Then, the first and second robots will be combined with it to investigate the compound device's functioning and control system. Finally, we hope to develop the vaginal hysterectomy robot so as to miniaturize it. We also hope to give it augmented reality and create a semiautomatic robot.

6 Conclusion

In this paper, we reported our tests of two prototypes of a vaginal hysterectomy robot which are designed to perform the procedures of the traditional vaginal hysterectomy. The experiments showed no different in gripping power between traditional method and robotic power. However, the bisection processes need to be revised and re-evaluated.

Acknowledgements. This research was performed at Khon Kaen University (KKU) with financial support from the KKU research fund. The authors wish to thank the Head of the Department of Obstetrics and Gynecology, Faculty of Medicine for giving permission to conduct this study and Prof. Dr.Terry Rambo for English correction.

References

1. Ayav, A., Bresler, L., Brunaud, L., et al.: Early results of one-year robotic surgery using the Da Vinci system to perform advanced laparoscopic procedures. J. Gastrointest Surg. 8(6), 720–726 (2004)
2. Turchetti, G., Palla, I., Pierotti, F., et al.: Economic evaluation of da Vinci-assisted robotic surgery: a systematic review. Surg. Endosc. 26(3), 598–606 (2012)
3. Tavakoli, M., Aziminejad, A., Patel, R.V., et al.: Methods and mechanisms for contact feedback in a robot-assisted minimally invasive environment. Surg. Endosc. 20(10), 1570–1579 (2006)
4. Wilkening, A., Baiden, D., Ivlev, O.: Assistive control of motion therapy devices based on pneumatic soft-actuators with rotary elastic chambers. IEEE Int. Conf. Rehabil. Robot 2011, 1–6 (2012)
5. Kleinhans, R., Brischwein, M., Wang, P., et al.: Sensor-based cell and tissue screening for personalized cancer chemotherapy. Med. Biol. Eng. Comput. 50, 117–126 (2012)
6. Sukovich, W., Brink-Danan, S., Hardenbrook, M.: Miniature robotic guidance for pedicle screw placement in posterior spinal fusion: early clinical experience with the Spine Assist. Int. J. Med. Robot 2(2), 114–122 (2006)
7. Lehman, A.C., Wood, N.A., Farritor, S., et al.: Dexterous miniature robot for advanced minimally invasive surgery. Surg. Endosc. 25(1), 119–123 (2012)
8. Kalloo, A.N., Singh, V.K., Jagannath, S.B., et al.: Flexible transgastric peritoneoscopy: a novel approach to diagnostic and therapeutic interventions in the peritoneal cavity. Gastrointest Endosc. 60(1), 114–117 (2004)
9. Lima, E., Henriques-Coelho, T., Rolanda, C., et al.: Transvesical thoracoscopy: a natural orifice translumenal endoscopic approach for thoracic surgery. Surg. Endosc. 21(6), 854–858 (2007)
10. Raman, J.D., Bergs, R.A., Fernandez, R., et al.: Complete transvaginal NOTES nephrectomy using magnetically anchored instrumentation. J. Endourol. 23(3), 367–371 (2009)
11. Wu, J.M., Wechter, M.E., Geller, E.J., et al.: Hysterectomy rates in the United States, 2003. Obstet. Gynecol. 110(5), 1091–1095 (2007)
12. Jahan, S., Das, T.R., Mahmud, N., et al.: A comparative study among laparoscopically assisted vaginal hysterectomy, vaginal hysterectomy and abdominal hysterectomy: experience in a tertiary care hospital in Bangladesh. J. Obstet. Gynaecol. 31(3), 254–257 (2012)
13. Marescaux, J., Solerc, L.: Image-guided robotic surgery. Semin. Laparosc. Surg. 11(2), 113–122 (2004)
14. Nishihara, S., Sugano, N., Nishii, T., et al.: Clinical accuracy evaluation of femoral canal preparation using the ROBODOC system. J. Orthop. Sci. 9(5), 452–461 (2004)
15. Menciassi, A., Quirini, M., Dario, P.: Microrobotics for future gastrointestinal endoscopy. Minim. Invasive Ther. Allied Technol. 16(2), 91–100 (2007)

Mechanism of a Learning Robot Manipulator for Laparoscopic Surgical Training

Tao Yang[1], Jiang Liu[1], Weimin Huang[1], Yi Su[2], Liangjing Yang[3], Chee Kong Chui[3], Marcelo H. Ang Jr.[3], and Stephen K.Y. Chang[4]

[1] Dept. of Computer Graphics and Interface,
Dept. of Computer Vision and Image Understanding
Institute for Infocomm Research, Singapore
{tyang,jliu,wmhuang}@i2r.a-star.edu.sg
[2] Dept. of Computing Science, Institute of High Performance Computing, Singapore
suyi@ihpc.a-star.edu.sg
[3] Dept. of Mechanical Engineering, National University of Singapore, Singapore
{mpeyl,mpecck,mpeangh}@nus.edu.sg
[4] Dept. of Surgery National University Hospital, Singapore
cfscky@nus.edu

Abstract. This paper presents a robot manipulator for hand-over-hand guidance training of laparoscopic surgery. Details of the mechanical design, kinematic analysis and control mechanism of the robot are presented. The robot records motion of surgical tool manipulated by master surgeon, and provides physical guidance to the trainee based on the recorded motion. The robotic manipulator can accurately reproduce the five degree of freedom manipulation of laparoscopic instrument during surgery. A hybrid spherical mechanism is applied for decoupling and reproducing the motion of surgical tool to facilitate implementation of control mechanism. The manipulators for left and right hands are capable of precise execution of a recorded trajectory with observed maximum error of 2.12 mm and 2 mm respectively during an experiment on user interaction.

Keywords: Laparoscopy, Surgical training, Robot manipulator.

1 Introduction

Laparoscopic surgery with small incisions on the patient as the main treatment approach has become a preference for many types of surgeries. Ninety five percent of cholecystectomy is performed laparoscopically as reported in [1]. Laparoscopic surgery imposes high visual and physical constrains. Surgeons are subjected to demanding visual and physical constrains due to the nature of laparoscopic surgery [2]. Training is crucial for surgeons to obtain the necessary level of proficiency in performing laparoscopic surgeries safely and effectively [3]. Current laparoscopic training equipments range from physical box trainers to virtual simulators [4, 5]. While there are different advantages associated with each of the training methods,

S. Lee et al. (Eds.): Intelligent Autonomous Systems 12, AISC 194, pp. 17–26.
springerlink.com

none of them mimic the conventional ‘hand-over-hand’ guidance that surgeons use to teach the novice surgeons by holding and guiding novice surgeon’s hands to perform certain tasks or corrections in order to train the motor skills. Researchers have explored the application of robotic assistance in teaching calligraphy and trajectories guidance [6, 7] to train motor skills. However, robotic assistance for the honing of laparoscopic motor skill, to our knowledge, has not been attempted.

In this paper, we propose a robotic platform to deliver robotic assisted laparoscopic skill training. The focus is on the design and development of the robot apparatus capable of active guidance and interactive surgical training. Its mode of operation and training methods are described in Section 2. In Section 3, the design and development of the robotic apparatus are discussed. Kinematics and control implementation are discussed in Section 4. Subsequently, Section 5 discusses the performance of the robotic platform through experimental validation. The paper concludes in Section 6 with a summary of the contributions of this work and our future direction.

2 Overview of Training Method

‘Master–apprentice’ and ‘hand-over-hand’ guidance training strategies are reliable and effective techniques in laparoscopic surgical training, especially for difficult surgical scenarios. The proposed platform is designed to facilitate training with the learning methods to achieve similar outcome as that of ‘hand over hand’ training model. Our developed robotic platform mimics traditional ‘hand over hand’ training strategy to provide physical guidance to the novices during training. This laparoscopic training robot has five degree of freedom on each manipulator that can control the orientation and position of its associated laparoscopic instrument.

In the proposed training model, the master operates on a 3D virtual patient model which is reconstructed from patient CT images, and has his hand motions learned and recorded in the training system. There are two guiding approaches. These approaches include complete guidance which is implemented through supervised control scheme, and haptic cue guidance from shared control and human-robot collaborative control scheme.

In complete guidance, the novice is experiencing the tool manipulative motion of a master surgeon kinesthetically by holding onto the surgical instrument that follows the recorded tool manipulative trajectory of the master surgeon. This provides a deeper appreciation to the master surgeon’s motion than mere visual and didactic guidance. In haptic cue guidance, the novice is allowed to operate on the patient specific anatomical model with some degree of motion guidance from the robotic device based on his own knowledge. Haptic is implied through the robot manipulator if the novice’s operation deviates from master surgeon’s operation. It is advantageous that the novice can be trained via ‘hand over hand’ method without the master being physically present. Although there has not been any conclusive evidence of benefits to laparoscopic training through kinesthetic guidance from recorded motion, subjects appear to perform tasks better after going through it as suggested in [8].

3 Design and Development

Laparoscopic instruments are long and slender tools. Its applicator is driven by lever mechanism through a handle. Generally, the mobility of a laparoscopic tool constrained at the insertion point (trocar) includes four degree of freedom namely roll, pitch, yaw and translation. The control of the handle's grasping motion is another degree of freedom though not contributive to its kinematic configuration. Figure 1 illustrates the mobility of one surgical instrument during the surgical process. The robot apparatus which consists of two manipulators representing the surgical instruments is designed with five degree of freedom to fulfill the required mobility. Details of the kinematics of the mechanism are presented in Section 4.

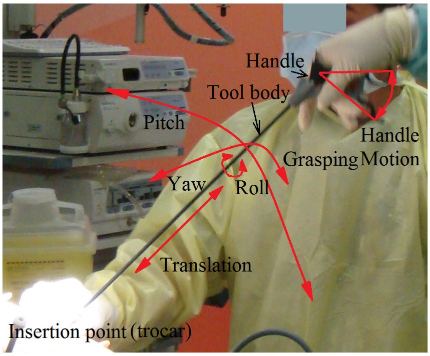

Fig. 1. Motion of surgical instrument in laparoscopy procedure

The mechanism, as shown in Figure 2(a), is designed to mimic the kinematic motion of laparoscopic instruments. Spherical mechanism, rack and pinion system, and modified instrument handle, which are highlighted in Figure 3, have been used. The mobility of the mechanism is designed as an exact mimic of the kinematics of laparoscopic procedure. Since the task space of laparoscopic procedure can be readily expressed in spherical coordinates, an ideal mechanism design will be one with axes of control corresponding to the spherical coordinates. The orientation joints should coincident at a point for optimal geometric workspace efficiency [9]. Hence, the hybrid spherical mechanism as shown in Figure 3 is adopted. This hybrid mechanism possesses the advantages of both serial and parallel manipulator as explained in [9]. Similarly, this spherical mechanism is advantageous for both hardware and software performance. Unlike most general manipulators, the spherical mechanism is highly decoupled with each of the actuated axes of control corresponding to task-oriented space coordinates. This direct mapping of joint space to task-oriented space allows high frequency control and enables fast data updating from the actuation and sensory unit to the graphic and haptic rendering module without being burdened by space domain transformation.

In laparoscopic surgery, the instrument is manipulated at substantial moment arm about the insertion point (trocar). This requires high operational torque range for the pitch and yaw axis of control. Although closed-chain mechanism generally provides structural stability, the structural redundancy is workspace inefficient and collision prone with at least two manipulators simulating the laparoscopic instruments. The argument for parallel mechanism to improve manipulator stiffness is therefore ineffective as it either increases structural link length index or reduces workspace [10]. This may also raise safety concern in user interaction due the high manipulator stiffness associated with parallel linkage configuration. The proposed structure enables a more even and appropriate sizing of actuators for the range of operation configurations.

Apart from kinematic requirements, user centric design attributes like ergonomics and usability are considered. The modified handle is the only physical user interface in the user workspace. All other actuation and control mechanisms are concealed underneath the insertion point (trocar). This user centric configuration produces a more realistic operating environment during training.

The range of forces for haptic feedback on each axis is designed for general laparoscopic simulation. Existing literature has shown that the maximum pulling forces along the translation direction, grasping and cutting force are about 17 N, 16 N [11] and 14 N [12] respectively. The actuators are specified base on these guidelines to permit wide range of haptic feedback.

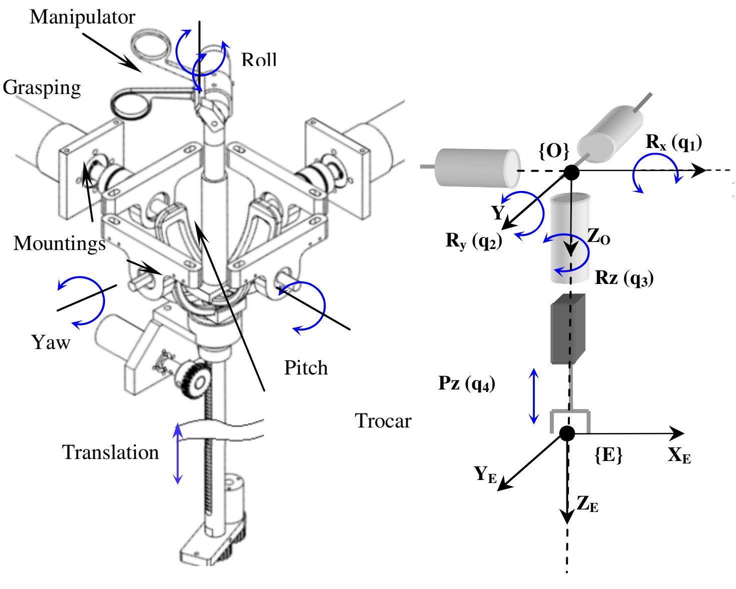

Fig. 2. (a) Mechanical mobility of the robot. The travelling limit for pitch, yaw, roll, translation, handle grasping motion are 120º, 120 º,360 º, 350mm and 60 º respectively. (b) Kinematic model of surgical instrument.

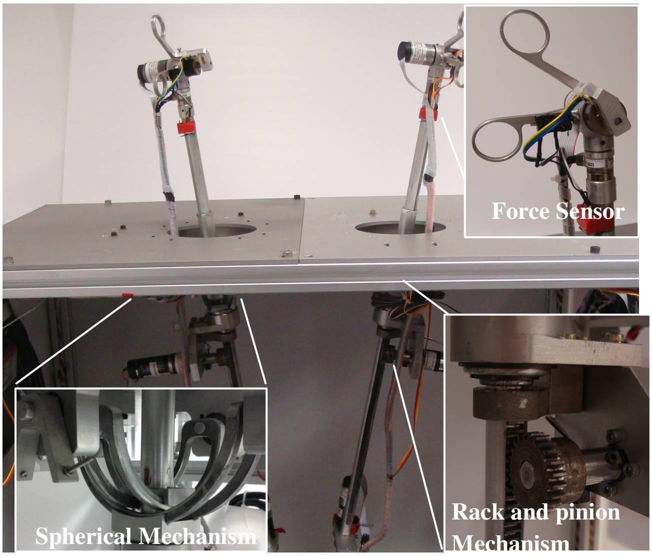

Fig. 3. Details of robotic laparoscopic training device

4 Robotic Mechanism

4.1 Kinematic Analysis

In laparoscopic procedures where the surgical instrument is constrained along the insertion point (trocar) in its axial direction, the task space configuration can be defined with four degree of freedom through Euler angles, roll, pitch, yaw and translation $(\alpha,\beta,\gamma,\rho)$. Figure 2(b) illustrates the frame assignment of the multibody system for kinematic analysis. Actuators are mounted such that their axes of control are aligned to the respective axis of transformation. Hence joint variables (q_1, q_2, q_3, q_4) correspond to the Euler angle and translation $(\alpha,\beta,\gamma,\rho)$.

Homogenous transformation matrix (1) expresses the forward kinematics of Frame E in Cartesian coordinates,

$$^{0}\mathrm{T_E} = \begin{bmatrix} \hat{X}_x & \hat{Y}_x & \hat{Z}_x & E_x \\ \hat{X}_y & \hat{Y}_y & \hat{Z}_y & E_y \\ \hat{X}_z & \hat{Y}_z & \hat{Z}_z & E_z \\ 0 & 0 & 0 & 1 \end{bmatrix} = \begin{bmatrix} s_1 s_2 s_3 + c_2 c_3 & s_1 s_2 c_3 - c_2 s_3 & c_1 s_2 & q_4(c_1 s_2) \\ c_1 s_3 & c_1 c_3 & -s_1 & -q_4 s_1 \\ s_1 c_2 s_3 - s_2 c_3 & s_1 c_2 c_3 + s_2 s_3 & c_1 c_2 & q_4(c_1 c_2) \\ 0 & 0 & 0 & 1 \end{bmatrix} \quad (1)$$

where $s_i\ c_i, i = 1,2,3$ denote $\sin(q_i)$ and $\cos(q_i)$ respectively.

Jacobian matrix to map the joint space (q_1, q_2, q_3, q_4) into task space is formulated as shown in eq. (2).

$$
\mathrm{J_E} = \begin{bmatrix} -q_4(s_1 s_2) & q_4(c_1 c_2) & 0 & c_1 s_2 \\ -q_4 c_1 & 0 & 0 & -s_1 \\ -q_4(s_1 c_2) & -q_4(c_1 s_2) & 0 & c_1 c_2 \\ 1 & 0 & 0 & 0 \\ 0 & 1 & 0 & 0 \\ 0 & 0 & 1 & 0 \end{bmatrix}. \tag{2}
$$

With a given homogeneous matrix acquired from the sensory unit ${}^{0}\mathrm{T_E}$, the inverse kinematics is as follows:

$$
\begin{aligned}
q_1 &= \arctan 2\left(-E_y, E_z / \cos q_2\right), \\
q_2 &= \arctan 2\left(E_x, E_z\right), \\
q_3 &= \arctan 2\left(\hat{X}_y, \hat{Y}_y\right), \\
q_4 &= E_x / (\cos q_1 \cdot \sin q_2) \ .
\end{aligned} \tag{3}
$$

4.2 Control Scheme

Figure 4 illustrates the force compensation control scheme implemented on the system. In addition to force feedback mechanism, a dynamic model can be incorporated to compensate undesirable disturbance. The control implementation facilitates the execution of feedback at a rate of 20 kHz to ensure determinism and maintain fidelity. Hence a feedback mechanism is sufficient for the force compensation application.

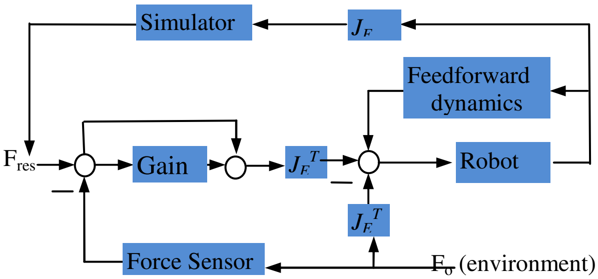

Fig. 4. Impedance control with force feedback

When the mechanism is driven by user as a passive device, parasitic forces are compensated through force control scheme. The interactive force between user and HMI is acquired by a 6 DOF force sensor installed underneath the handle, as shown in Figure 3. The parasitic force due to the system environment, F_O, measured by the force sensor in Cartesian coordinates was converted into torque on each joint with Jacobian matrix (2). Each actuator is commanded with appropriate current to move in corresponding direction according to the direction and magnitude of the torque, and hence reduces parasitic forces measured by the force sensing units.

Current control is implemented to generate the desired force output F_{des} for the user. The force reference, F_{res}, as shown in Figure 4 is set as F_{des}- F_O . The current set point, i_{ref} is computed by equation (4) as shown below:

$$i_{ref} = K_{\phi}^{-1} J_E^{\ T} F_{res} \tag{4}$$

where K_{ϕ} is a 4 by 4 diagonal matrix representing the torque constant of each actuated axis of control,

J_E is the 6 by 4 task space Jacobian matrix,
F_{res} is the desired force/torque vector output in Cartesian coordinates.

In the case of parasitic force compensation without tool- tissue interaction, F_{des} is equal to zero. Hence, any force reading due to the interaction between user and robot is converted into corresponding current command to drive the actuators to minimize the force reading. Similar method is applied to generate haptic feedback during tool-tissue interaction in the virtual environment with F_{des} being the required haptic force to output. The computation and actual rendering methodology of the tool-tissue interactive force, F_{des} is an interesting research topic [13]. It is however beyond the scope of this paper.

For complete guidance, a PID position control is implemented to reproduce the master surgeon's trajectory. All actuators for joints (q_1, q_2, q_3, q_4) and handle grapping joint are commanded to move as per the desired trajectory and velocity which acquired from the master surgeon's operation. A position control is appropriate as there is no need for variation in intensity of guidance.

For haptic cue guidance, shared controls of the manipulators are required. Both the user and the predetermined trajectory work as the inputs to the robot to achieve the varying intensity of motion guidance. The force sensor measures the forces F_{des} that the user experiences, and compensates the parasitic force. At the same time, the current position of the manipulator T_n is compared with the predetermined trajectory T_m which acquired from the master surgeon's operation. If the difference is greater than a prescribed value, haptic cue force is provided based on the difference of the two trajectories as follow

$$F_g = K(T_m - T_n) \tag{5}$$

where K is the coefficient to adjust the force magnitude with respect to trajectory differences.

4.3 Control Hardware

The control hardware platform consists of NI CompactRIO with Xilinx Virtex-5 LX110 reconfigurable I/O FPGA core and real-time embedded controller with 400 MHz processor, 128 MB DRAM memory. Each robotic arm is equipped with six degree of freedom high precision force sensing unit, ATI Nano17, calibrated at a force resolution of 0.0125 N and torque resolution 0.0625 Nmm.

This hardware configuration allows high speed control loop execution, and ensures task determinism for managing communication flow crucial to haptic fidelity and human-machine interface applications in laparoscopic surgical training robot system. The FPGA-based real-time hardware platform is effective in the implementation of reliable controls including force feedback signal processing. The parallelism nature of the FPGA operation mechanism facilitated fast and robust coordination amongst axes simplifying the issue of joint synchronization.

Control operation and computational task were mostly hard programmed in FPGA. This allows minimal delay in the compensation of the parasitic forces. Control of the manipulator is implemented with FPGA at a rate of 20 kHz to ensure determinism and maintain fidelity.

5 Experimental Results

The kinematics and dynamics profiles were acquired and analyzed for a given path execution in a specified operational workspace. To evaluate the efficacy of the control mechanism, a recorded trajectory was executed by the robot under condition with and without user interaction. Kinematic trajectories were acquired through the encoder with joint control scheme at frequency of 100 samples/second and subsequently transformed to 3D Cartesian coordinates for analysis. As this computational task is independent of the control loop mechanism, it does not create any bottleneck in the control mechanism. The force profile was acquired by the 6-DOF force sensor through FPGA-based DAQ module.

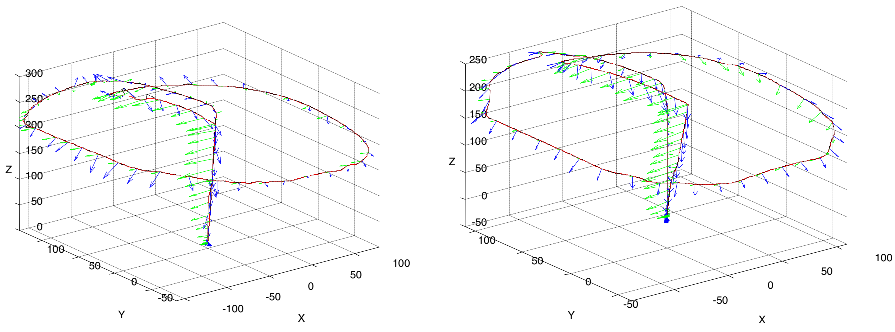

(a) (b)

Fig. 5. (a) execution and force on handle of left manipulator, (b) execution and force on handle of right manipulator. Red line is the recorded trajectory, black line is the execution results, blue arrow indicates the force vector on handle, and green arrow indicates the moment vector on handles

The robot was tested when it was working under complete guidance in the presence of user-system interaction. When there was no interaction with the user, the maximum errors of execution on the left and right manipulators were 2.12 mm and 1.55 mm respectively. The robot was also tested by guiding a user to perform the recorded path. In order to minimize the effect of visual guidance, the trajectory was neither displayed nor known to the user prior to the test. Figure 5 depicts the 3D trajectory and the force profile in Cartesian coordinates when the robot was interacting with a user. The mechanical components and motion control mechanism are capable of precise and accurate execution. The maximum errors of execution on both right and left manipulators are 1.87 mm and 2 mm respectively. The maximum errors of each joint in the left and right manipulators are tabulated in Table 1.This trajectory spanned an approximated (0.2 x 0.2 x 0.2) m^3 workspace and was subjected to a maximum interaction force range of 3.6 N and torque of 73.7 Nmm.

Table 1. maximum error of each joint

Joint	Manipulator	
	Left	Right
Pitch (Q_1)	0.230°	0.425°
Yaw (Q_2)	0.241 °	0.313 °
Roll (Q_3)	1.66 °	1.67 °
Translation (Q_4)	0.524 mm	1.35 mm

6 Conclusion

The contribution of this work is on the introduction of a new robot apparatus for hand-over-hand guidance in laparoscopic surgical training. The active robot manipulator designed with appropriate specifications implements an interactive platform that can adequately meet the training needs of laparoscopic surgeries.

The robot is developed with the provision of complete guidance method capable of guiding the novice according to a recorded trajectory. This complete guidance method could provide the novice with deeper appreciation of how an experienced surgeon deals with specified surgical scenarios. Concurrently, we are developing the haptic cue guidance method which allows varying degree of guidance. This will be integrated to the system to facilitate a variant of the hand-over-hand training method.

Acknowledgements. This work is partially supported by research grant SERC 092-148-0072 and 102-148-0009 from the Agency for Science, Technology and Research, Singapore.

References

1. Voyles, C.R., et al.: A practical approach to laparoscopic cholecystectomy. Am J. Surg. 161(3), 365–370 (1991)
2. Alberich-Bayarri, A., et al.: Volume Mesh Generation and Finite Element Analysis of Trabecular Bone Magnetic Resonance Images. In: 29th Annual International Conference of the IEEE Engineering in Medicine and Biology Society, EMBS 2007 (2007)
3. Derossis, A.M., Fried, G.M., et al.: Development of a model for training and evaluation of laparoscopic skills (0002-9610 (Print))

4. Derossis, A.M., et al.: The effect of practice on performance in a laparoscopic simulator. Surg. Endosc. 12(9), 1117–1120 (1998)
5. Woodrum, D.T., et al.: Construct validity of the LapSim laparoscopic surgical simulator. The American Journal of Surgery 191(1), 28–32 (2006)
6. Teo, C.L., Burdet, E., Lim, H.P.: A robotic teacher of Chinese handwriting. In: Proceedings. 10th Symposium on Haptic Interfaces for Virtual Environment and Teleoperator Systems, HAPTICS 2002(2002)
7. Bluteau, J., et al.: Haptic guidance improves the visuo-manual tracking of trajectories. PLoS One 3(3), e1775 (2008)
8. Lee, C.-S., et al.: Designing an Active Motor Skill Learning Platform with a Robot-Assisted Laparoscopic Trainer. In: 33rd Annual International Conference of the IEEE Engineering in Medicine and Biology Society, Boston (2011)
9. Vijaykumar, R., Tsai, M., Waldron, K.: Geometric optimization of manipulator structures for working volume and dexterity. In: Proceedings of 1985 IEEE International Conference on Robotics and Automation (1985)
10. Piccin, O., et al.: Kinematic modeling of a 5-DOF parallel mechanism for semi-spherical workspace. Mechanism and Machine Theory 44(8), 1485–1496 (2009)
11. Rosen, J., et al.: Surgeon-tool force/torque signatures–evaluation of surgical skills in minimally invasive surgery. Stud. Health Technol. Inform. 62, 290–296 (1999)
12. Yang, T., et al.: Modeling cutting force of laparoscopic scissors. In: 2010 3rd International Conference on Biomedical Engineering and Informatics, BMEI (2010)
13. Misra, S., Ramesh, K.T., Okamura, A.M.: Modeling of tool-tissue interactions for computer-based surgical simulation: A literature review. Presence-Teleoperators and Virtual Environments 17(5), 463–491 (2008)

Fusion of Inertial Measurements and Vision Feedback for Microsurgery

Yan Naing Aye, Su Zhao, Cheng Yap Shee, and Wei Tech Ang

School of Mechanical and Aerospace Engineering
Nanyang Technological University
Singapore
yanna@ntu.edu.sg

Abstract. A microsurgery system that achieves real-time enhanced micrometer scale positioning accuracy by fusing visual information from a high speed monovision camera mounted on an optical surgical microscope and acceleration measurements from an intelligent handheld instrument, *ITrem2*, is presented. The high speed camera captures images of the tool tip of *ITrem2* to track its position in real-time. The focus value of the tool tip in the acquired image is used to locate the tool tip along the principal axis of the objective lens of the microscope and edge based geometric template matching gives the position in pixel coordinates. *ITrem2* utilizes four dual-axis miniature digital MEMS accelerometers to sense and update the motion information. The system has a first in, first out (FIFO) queue to track the recent history of the slow non-drifting position estimation from the vision system and acceleration readings from the inertial sensors together with their respective time stamps. In the proposed method, real-time visual servoing of micrometer scale motion is achieved by taking into account the dynamic behavior of the vision feedback and incorporating synchronized fusion of these complementary sensors.

Keywords: sensor fusion, visual servoing, microsurgery.

1 Introduction

Fusion of vision and inertial sensors has been used in many systems, especially in augmented reality applications. An important aspect of the fusion is to relate acquired information from multiple sensors which have different sampling rates. Redbinder [1] presented a method to fuse low bandwidth visual observations and high bandwidth rate gyro measurements to estimate the camera orientation. The system introduced a fixed time delay to the inertial measurements before performing sensor integration. With assumed periodic measurements, jitter was not considered. Armesto [2] presented a generic multi-rate sampling data system using size-varying input and output equations. Measurements need not be synchronous and periodic. The real-time issues were not taken into account. Jeroen *et al.* [3] described a tightly coupled

S. Lee et al. (Eds.): Intelligent Autonomous Systems 12, AISC 194, pp. 27–35.
springerlink.com

real-time camera pose estimation supporting multi-rate signals synchronized by using one central clock. While this method provides real-time performance, it is not suitable for loosely coupled systems where the camera cannot be mounted on the moving object.

To reduce the amount of information that needs to be extracted from the vision system, Huster [4] described a method that generated useful vehicle trajectories to achieve more robust sensing. As a further step, to limit the error for a short period of missing vision measurements, Parnian [5] presented tool motion modeling. It tracked an industrial tool using vision and inertial sensors fusion. The tool motion modeling was proposed to bind the error in the acceptable range for a short period of missing data. These methods are appropriate for the applications where the nature of the movement of the object being tracked is deterministic. In the context of micromanipulation in microsurgery, physiological tremor is a well-studied hand movement. Several techniques for online modeling and estimation of tremor have been implemented [6,7,8].

The use of visual servo control is common in sensor fusion applications. Karras [9] demonstrated the fusion of a laser vision system and inertial measurement units. A visual servoing method was developed to control an underwater robotic vehicle. Sensor fusion for micromanipulation tasks was presented by Zhou [10]. In that paper, force and vision feedback were integrated for sensor-based microassembly. They discussed the implementation of an optical beam deflection sensor in a force controlled micropositioning systems. In contrast to other systems, it used force sensor as an alternative complementary sensor.

The approach described in this paper deals with the real-timeliness of a high performance visual servo control system that is to be used in the computer vision aided intelligent handheld instrument, *ITrem2*, to enhance human manual positioning accuracy at the micrometer scale in microsurgery. Vision measurements from a high speed monovision camera mounted on an optical surgical microscope and inertial information from *ITrem2* is combined and exploited to compensate the error caused by physiological hand tremor of a surgeon while nullifying common types of erroneous motion such as drift. *ITrem2* not only requires micrometer scale accuracy but also hard real-time prerequisite. The proposed method emphasizes on improving the feedback sensing by utilizing accurate time stamps of the vision and inertial measurements that are provided by the real-time computer. Time aware fusion of the inertial measurements provides micrometer accuracy even with significant delay and jitter in the vision measurements.

2 Methodology

The structure of the *ITrem2* system is shown schematically in Fig. 1.

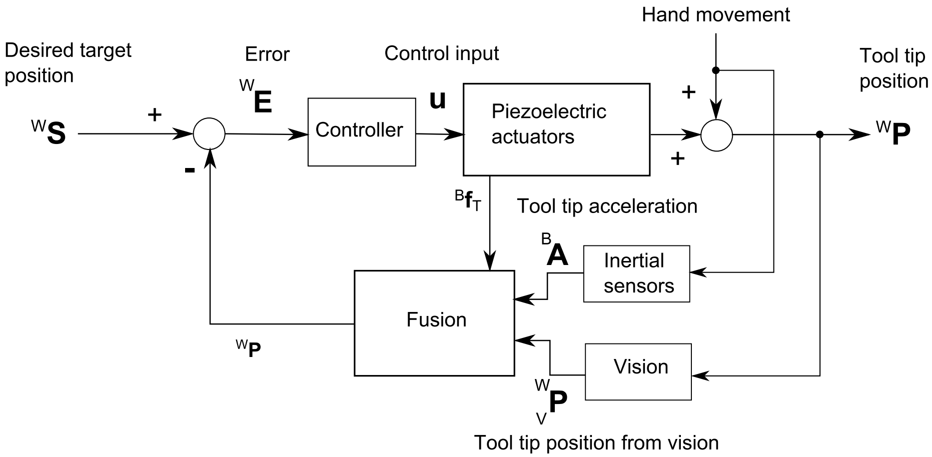

Fig. 1. Position-based visual servo with fusion of inertial sensing

2.1 Vision System

The vision system of *ITrem2* constantly extracts the tool tip feature in each acquired image using edge based geometric template matching. The geometric matching gives the coordinate positions of the tool tip in sub-pixel accuracy.

There are several focusing algorithms to estimate the distance of the tool tip from the center of the objective lens based on the blurriness of an image [11]. Among them, Normalized Variance method is mentioned to provide the best overall performance. After calibration, the value of ${}^{W}Z$ in the world coordinate frame can be solved on-line from focus value calculation of the tool tip using parabola-fitting approximation [12].

2.2 Inertial Measurement Unit

The rotation matrix, ${}^{W}\mathbf{R}_{B}$, is used to transform the tool tip acceleration from the body coordinate frame to the world coordinate frame as shown in (1). It is updated at each sample point using *Euler Angle Sequence*.

$$ {}^{W}\mathbf{A} = {}^{W}\mathbf{R}_{B}\,{}^{B}\mathbf{A} \tag{1} $$

$$ {}^{W}\mathbf{A} = {}^{W}\mathbf{f}_{B}({}^{B}\mathbf{A}) \tag{2} $$

where ${}^{W}\mathbf{f}_{B}$ represents the function that performs coordinate transformation. Tilt sensing method using nonlinear regression model of low-g MEMS accelerometer described by Ang [13] is used to calculate the tilt and roll angles of *ITrem2*. Pan angle rotation is obtained from orientation of the tool tip image in the pixel frame.

2.3 Visual Servo Control

ITrem2 uses position based visual servo control integrated with inertial sensing to fulfill the need for hard real-timeliness in microsurgery. The micromanipulator in

ITrem2 is a piezo actuated parallel flexural mechanism that generates the 3D motion so that erroneous hand motion can be compensated. For a point-to-point positioning task in which the tool tip at ${}^{W}\mathbf{P}$ is to be brought to a desired target location, ${}^{W}\mathbf{S}$, in the world coordinate frame, the error function may be defined as

$$ {}^{T}\mathbf{E}\,({}^{T}\mathbf{f}_B) = {}^{T}\mathbf{f}_B\;({}^{B}\mathbf{f}_W(\,{}^{W}\mathbf{P} - {}^{W}\mathbf{S}\,)) \tag{3} $$

where the coordinate transformation from the tool tip frame to the body frame, ${}^{T}\mathbf{f}_B$, is the value to be controlled. The control input to be computed is the desired micromanipulator translational movement, $\mathbf{u}$, as shown in (4)

$$ \mathbf{u} = -K\,{}^{T}\mathbf{E}({}^{T}\mathbf{f}_B), \tag{4} $$

where K is a proportional feedback gain. The proportional control law will drive the tool tip so that the value of the error function is zero.

2.4 Fusion Algorithm

Each time an image is acquired, the vision system stores the time stamp of the image with an accuracy of one microsecond. When the image processing and pose estimation are completed, the estimated world coordinate of the tool tip from vision, ${}^{W}_{V}\mathbf{P}$, the controlled value, ${}^{T}\mathbf{f}_B$, and the associated time stamp are sent to the fusion unit. The fusion unit has a first in, first out (FIFO) queue that stores the latest measurements from the accelerometers and associated estimated tool tip position, ${}^{W}\mathbf{P}$. Since the sampling rate of the vision system is much slower than that of the inertial measurement, without assuming periodicity, the fusion unit checks the availability of the vision information at each inertial measurement cycle. If new image information is available, the fusion unit performs the following steps to estimate the current position.

1) The position estimation of the tool tip from vision, ${}^{W}_{V}\mathbf{P}$, is associated with the corresponding acceleration measurement in the queue by calculating the delay time of the image and using the inertial sampling period ${}_{A}T$. Due to the considerable jitter in the sampling period of the vision system, the delay time is not constant and the exact value is calculated from the time stamp associated with the image.

2) If the piezoelectric actuators are turned off, the tool tip of the *ITrem2* will be at a neutral position. Using ${}^{W}_{V}\mathbf{P}$ and ${}^{T}\mathbf{f}_B$, the neutral position of the tool tip of *ITrem2* in the world coordinate frame, ${}^{W}_{V}\mathbf{P}'$, is calculated.

3) The tool tip velocity of *ITrem2* is calculated using the last two positions obtained from vision measurements, which are illustrated in the Fig. 2.

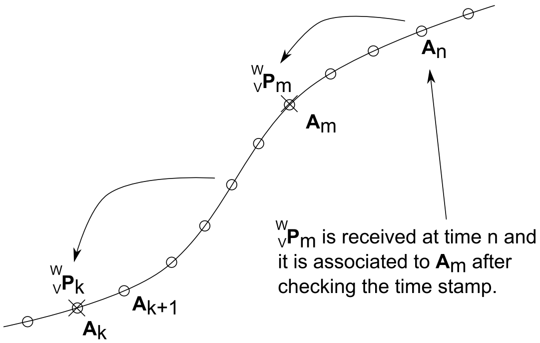

Fig. 2. Illustration of acceleration measurements and vision information

Initially, $\Delta\mathbf{P}_k$ and $\Delta\mathbf{V}_k$ are set to zero. Then, $\Delta\mathbf{P}_m$ and $\Delta\mathbf{V}_m$ are calculated iteratively from $k+1$ to m using

$$\Delta\mathbf{P}_i = \Delta\mathbf{P}_{i-1} + {}_AT\ {}^W\mathbf{V}_{i-1} + \frac{1}{2}{}_AT^2\ {}^W\mathbf{A}_{i-1}, \tag{5}$$

$$\Delta\mathbf{V}_i = \Delta\mathbf{V}_{i-1} + {}_AT\ {}^W\mathbf{A}_{i-1}, \quad i = k+1, \ldots, m. \tag{6}$$

Thereafter, the tool tip velocity at time m is obtained from the following equation.

$$V_m = \frac{1}{(m-k)_AT}({}^W_V\mathbf{P}'_m - {}^W_V\mathbf{P}'_k - \Delta\mathbf{P}_m) + \Delta\mathbf{V}_m \tag{7}$$

4) The measured tool tip position, ${}^W_V\mathbf{P}'_m$, and the predicted tool tip position in the queue, ${}^W\mathbf{P}_m$, are fused with the Kalman filter.

5) The tool tip position at time n is estimated iteratively from the new ${}^W\mathbf{P}_m$, $\mathbf{V}_m$, and $\mathbf{A}_m$ as follows.

$$^W\mathbf{P}_i = {}^W\mathbf{P}_{i-1} + {}_AT\ {}^W\mathbf{V}_{i-1} + \frac{1}{2}{}_AT^2\ {}^W\mathbf{A}_{i-1}, \tag{8}$$

$$^W\mathbf{V}_i = {}^W\mathbf{V}_{i-1} + {}_AT\ {}^W\mathbf{A}_{i-1}, \quad i = m+1, \ldots, n. \tag{9}$$

If there is no new vision information, the fusion unit simply updates the pose estimation for the current acceleration sample value using (8) and (9).

3 Experiment

3.1 Setup

The experimental setup of *ITrem2* is shown in Fig. 3. The experiment is conducted to track the tremor like movement produced by a piezoelectric motion generator (Physik

Instrumente GmbH & Co.KG, Germany) comprising an E-712-3CDA digital controller and a P-561.3CD piezo-nanopositioning system. It can generate three DOF (degree-of-freedom) linear motion of up to 150µm peak to peak in each axis. It also provides analog output lines to monitor the position of each axis and these are used as the ground truth for the experiment. *ITrem2* is mounted on the motion generator with its inertial sensing axes aligned with the corresponding axes of the motion generator.

The vision system consists of an optical surgical microscope (M651 MSD, Mikrosysteme Vertrieb GmbH, Germany) with a built-in coaxial illuminator and retrofitted with a monovision camera (piA640 -210gm/gc camera from Basler AG, Germany). The microscope is equipped with a beamsplitter and a stereo attachment for a second observer. Therefore the workspace can be viewed simultaneously by the camera, a surgeon, and an assistant. The monovision camera provides the workspace view of 5mm x 3.7 mm and its sampling rate is 50Hz. Image processing is performed in real-time using the NI PXIe-8130 real-time embedded computer running on LabVIEW real-time operating system connected to the camera via a Gigabit ethernet interface. IMAQ Vision for LabVIEW is used to implement the edge based geometric template matching.

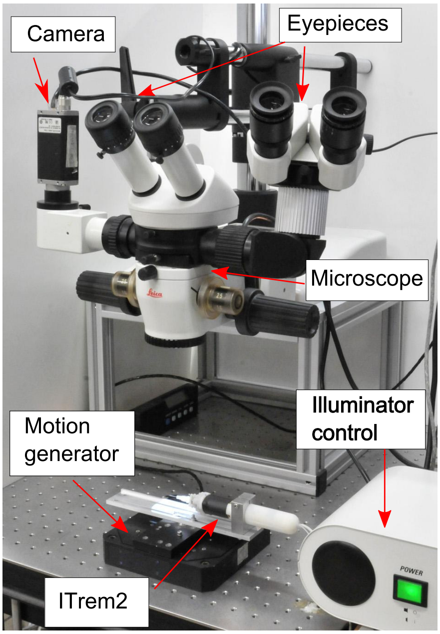

Fig. 3. Experiment setup of microscope, camera and motion generator

There are four dual-axis miniature digital MEMS accelerometers (ADIS16003, Analog Devices, USA) inside *ITrem2*. They sense three DOF motion of the instrument tip using the method similar to its predecessor [14]. After performing a moving average filtering, the embedded microcontroller (AT89C51CC03, Atmel, USA) inside *ITrem2* sends the acceleration data to the real-time computer at 333 samples per second. The CAN (Controller-area network) interface with a bandwidth of 500kbps is used to achieve robust and real-time communication between the embedded microcontroller and the real-time computer. Three DOF motion of the micromanipulator in *ITrem2* is generated by the piezo actuated parallel flexural mechanism. Maximum movement of the micromanipulator along X-axis and Y-axis is 150μm and that of Z-axis is 28μm.

3.2 Results

To assess the performance of the fusion algorithm, the experiment was carried out using constant ${}^{T}\mathbf{f}_B$ i.e. K=0. Therefore, the error in (3) is uncorrected and the output of the vision feedback can be compared with the ground truth position of the motion generator. The sensing experiment is conducted using a sinusoidal movement of 51μm peak-to-peak at 10Hz along the X-axis of the world coordinate frame.

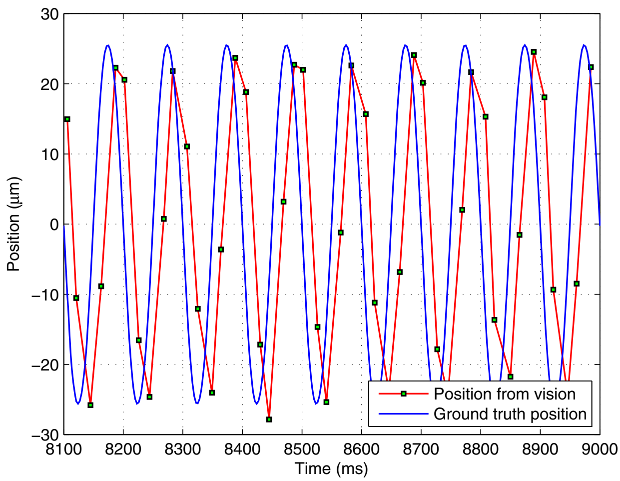

Fig. 4. Position information using vision only

There is an obvious delay in position information from the vision system compared to the ground truth positions from motion generator as shown in Fig. 4. The estimated positions from the fusion unit versus the ground truth positions are shown in Fig. 5.

To measure the accuracy of the fusion algorithm under different frequencies, the experiment was also performed with various sinusoidal movements from 2Hz to 8Hz at intervals of 2Hz. The RMSE of the vision measurements is smaller at the lower frequencies. Probable causes are larger phase lag and greater motion blur of the tool tip image at the higher frequencies. On the other hand, the signal-to-noise ratio of the acceleration measurements is better at the higher frequencies. The results shown in Table I confirm that the fusion of these complementary sensors provides lower RMSE at various frequencies from 2Hz to 10Hz.

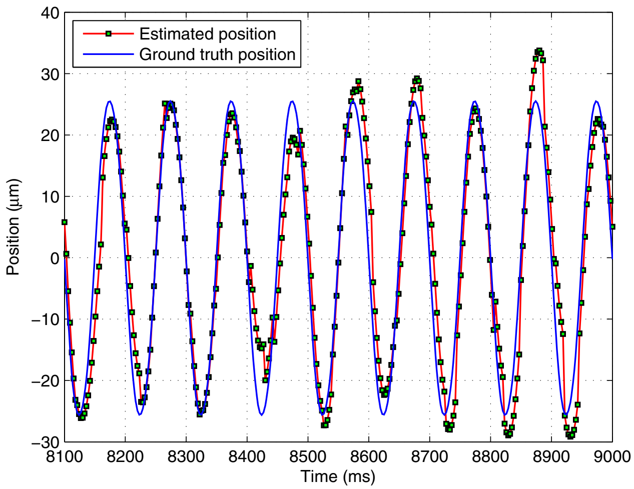

Fig. 5. Estimated positions using the fusion algorithm

Table 1. Accuracy at different frequencies

Frequency (Hz)	Peak-to-peak displacement (µm)	RMSE using vision only (µm)	RMSE using Fusion (µm)	Error reduction (%)
10	51	19.12	6.09	68.12
8	56	17.19	5.90	65.68
6	60	13.98	5.30	62.08
4	63	9.97	5.23	47.54
2	64	5.25	4.95	5.71

4 Conclusion

This paper presents an algorithm for real-time fusion of visual and inertial sensors. With the modified feedback in the visual servo control to take into account delay and jitter of the vision system, the system substantially improves sensing speed and accuracy for microscopic applications. It is intended to cancel rapid erroneous hand movement caused by tremor and, at the same time, to provide absolute position for automatic micromanipulation tasks.

Acknowledgements. Vision-Aided Active Handheld Instrument for Microsurgery project is funded by Agency for Science, Technology & Research (A*STAR) and the College of Engineering, Nanyang Technological University. The authors thank them for the financial support of this work.

References

1. Rehbinder, H., Ghosh, B.K.: Multi-rate fusion of visual and inertial data. In: International Conference on Multisensor Fusion and Integration for Intelligent Systems, MFI 2001, pp. 97–102 (2001)
2. Armesto, L., Chroust, S., Vincze, M., Tornero, J.: Multi-rate fusion with vision and inertial sensors. In: Robotics and Automation, Proceedings of ICRA 2004, April 26 - May 1, vol. 1, pp. 193–199 (2004)
3. Hol, J.D.: Robust real-time tracking by fusing measurements from inertial and vision sensors. Journal of Real-Time Image Processing 2, 149–160 (2007)
4. Huster, A., Frew, E.W., Rock, S.M.: Relative position estimation for AUVs by fusing bearing and inertial rate sensor measurements. In: OCEANS 2002 MTS/IEEE, October 29-31, vol. 3, pp. 1863–1870 (2002)
5. Parnian, N., Golnaraghi, M.F.: Integration of vision and inertial sensors for industrial tools tracking. Sensor Review 27(2), 132–141 (2007)
6. Tan, U.-X., Veluvolu, K., Latt, W.T., Shee, C.Y., Riviere, C., Ang, W.T.: Estimating displacement of periodic motion with inertial sensors. IEEE Sensors Journal 8, 1385–1388 (2008)
7. Veluvolu, K.C., Ang, W.T.: Estimation of physiological tremor from accelerometers for real-time applications. Sensors 11(3), 3020–3036 (2011)
8. Latt, W.T., Veluvolu, K.C., Ang, W.T.: Drift-free position estimation of periodic or quasi-periodic motion using inertial sensors. Sensors 11(6), 5931–5951 (2011)
9. Karras, G.C., Loizou, S.G., Kyriakopoulos, K.J.: A visual-servoing scheme for semi-autonomous operation of an underwater robotic vehicle using an IMU and a Laser Vision System. In: Robotics and Automation, ICRA 2010, May 3-7, pp. 5262–5267 (2010)
10. Zhou, Y., Nelson, B.J., Vikramaditya, B.: Fusing force and vision feedback for micromanipulation. In: Proceedings of 1998 IEEE International Conference on Robotics and Automation, May 16-20, vol. 2, pp. 1220–1225 (1998)
11. Yu Sun, S., Duthaler, S., Nelson, B.J.: Autofocusing Algorithm Selection in Computer Microscopy. In: IEEE/RSJ International Conference on Intelligent Robots and Systems, August 2-6, pp. 70–76 (2005)
12. Wu, Q., Merchant, F.A., Castleman, K.R.: Microscope Image Processing. Academic Press (2008)
13. Ang, W.T., Riviere, C.N., Khosla, P.K.: Nonlinear regression model of a low-g MEMS accelerometer. IEEE Sensors J. 7(1&2), 81–88 (2007)
14. Latt, W.T., Tan, U.-X., Shee, C.Y., Riviere, C.N., Ang, W.T.: Compact Sensing Design of a Hand-held Active Tremor Compensation Instrument. IEEE Sensors Journal 9, 1864–1871 (2009)

An Orbital Velocity-Based Obstacle Avoidance Algorithm for Surgical Robots

Jung-Min Han and Byung-Ju Yi

Department of Electronic Systems Engineering
Hanyang University, Ansan, Korea
mister_eight@naver.com, bj@hanyang.ac.kr

Abstract. This paper introduces an obstacle avoidance methodology of autonomous assistant robot for surgery. Currently employed master-slave surgical robots just copy movements that a surgeon creates. This kind of behavior causes unexpected collision on a vulnerable surface of an organ and makes possibility of danger which causes serious injury. Many of diagnostic technology with navigation systems are used to make up for these disadvantages and an obstacle avoidance algorithm in this research also contribute to raise safety of surgery. We present 4 states of two instruments in terms of shortest distance as a measure of collision. Then, the autonomous motion of a robotic instrument is generated by a motion planning algorithm which incorporates an orbital velocity component into attractive potential function. As a result, the robotic instrument exhibits a natural maneuver movement around obstacles. A hardware-in the-loop approach is employed to control the motion of the two instruments and the effectiveness of the proposed motion planning algorithm was verified through several simulation examples.

Keywords: Obstacle Avoidance, Autonomous movement, Trajectory planning, Medical robot.

1 Introduction

The Laparotomy is an operation method that a surgeon opens the patient's belly and puts into hands to treat symptoms of illness. This procedure has a fatal weakness causing so many risks such as scars, a long time to recovery, a severe pain, and an infection during an open procedure. So MIS (Minimally Invasive Surgery) was devised to overcome these concerns.

Minimally Invasive Surgery (MIS) is a method to treat an affected part with various thin instruments putting through a small hole on the patient's abdominal surface. It has been called "Laparoscopic surgery".

Because MIS deals with tiny and sensitive organs in the body, the robotic surgery that has high accuracy and is able to do minimal invasion is needed. In most of developed robotic surgery systems, a surgeon handles a slave device with several kinds of tool at its distal end. An advanced robotic solution is the most well-known da

S. Lee et al. (Eds.): Intelligent Autonomous Systems 12, AISC 194, pp. 37–50.
springerlink.com

Vinch system [1], which consists of a master control part and several slave robot arms, the end of which have surgical instruments.

But accurate devices still have problems which come from the lack of information for example real-time location of organ.

So Navigation system or imaging system has developed to overcome these problems and autonomous movement technology for the surgical robot also is needed [2-4]. In mobile and industrial area, there are many well-developed systems for robots [5-9].

This work proposes an orbital velocity-based obstacle avoidance algorithm for a surgical task of laparoscopic surgery. In experiment, the surgical tools performed maneuvering motions with respect to relative location. And, we show that an autonomous tool is able to avoid possible collision successfully between tools in real time by this suggested algorithm.

2 Principle of Algorithm

2.1 Environment

In Fig. 1, several surgical tools are inserted through a hole on the abdominal surface. The position of the hole is named "Remote Center of Motion (RCM)" or "fulcrum" point and we assume that it is a fixed point in the robot coordinate during the surgical procedure.

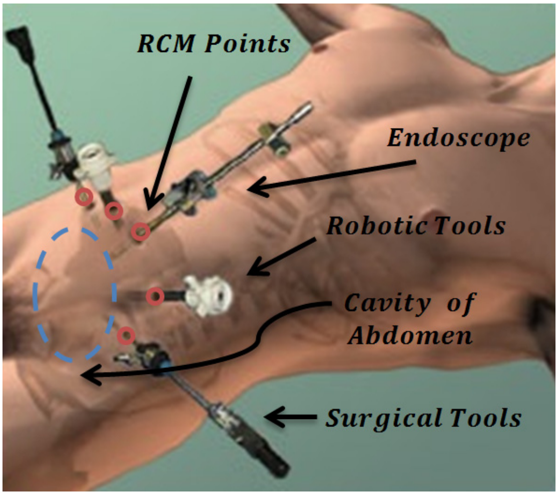

Fig. 1. Minimally invasive surgery with multiple holes

Also, positions of three fulcrum points and end points of tools are known by sensor information. The workspace of tools can be a corn shape whose top points are three fulcrum points. Two tools are manually manipulated by a surgeon and the other tool is controlled by a robot performing autonomous movement to assist other tools.

2.2 Definition of State

Once the positions of the fulcrum points and the end points of the three tools are known, the state between tools can be defined. Four states are required to define the relationship between positions of tools. We give it name as Point to Point, Point to Line, Line to Point, Line to Line. The procedure to distinguish each state is as follows.

Firstly, se suppose that tools are lines connecting the fulcrum point and the end point. To define the positional relationship, shortest distance between lines (or tools) or between point and line have to be derived (Fig. 2).

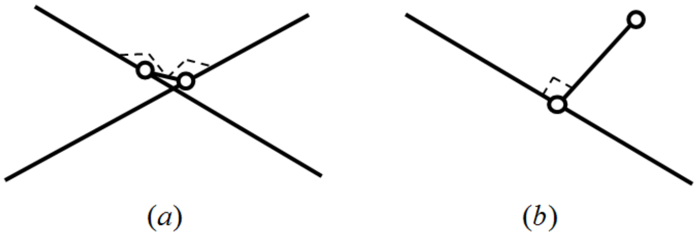

Fig. 2. (a) Shortest distance between two lines (b) Shortest distance between line and point

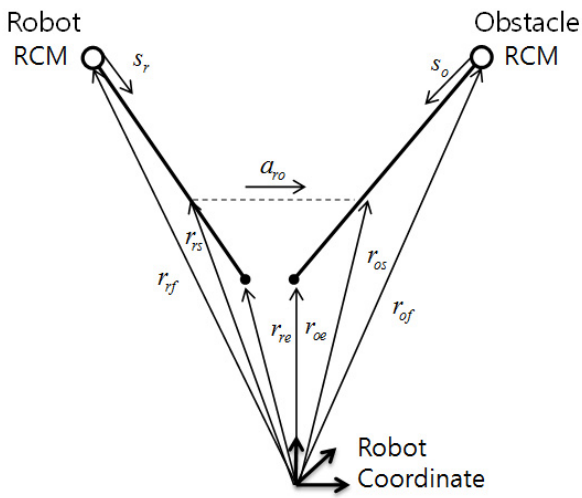

Fig. 3. Two tools and shortest distance

It is noted that a line connecting two lines in a shortest distance is perpendicular to both lines. In Fig. 3, two unit vectors along each instrument can be defined as

$$\underline{s}_r = \frac{\underline{r}_{re} - \underline{r}_{rf}}{\left|\underline{r}_{re} - \underline{r}_{rf}\right|} \tag{1}$$

and

$$\underline{s}_o = \frac{\underline{r}_{oe} - \underline{r}_{of}}{\left|\underline{r}_{oe} - \underline{r}_{of}\right|}. \tag{2}$$

Moment of each unit vector with respect to the global frame is given by

$$\underline{s}_{rm} = \underline{r}_{rf} \times \underline{s}_r \tag{3}$$

and

$$\underline{s}_{om} = \underline{r}_{of} \times \underline{s}_o. \tag{4}$$

And the mutual moment of the two unit vectors is defined as

$$\underline{a}_{ro} = \underline{s}_r \times \underline{s}_o. \tag{5}$$

Then, the moment of a_{ro} with respect to the global frame is

$$\underline{a}_{rom} = \underline{r}_{rf} \times \underline{a}_{ro} = \underline{r}_{of} \times \underline{a}_{ro} \tag{6}$$

Since $(\underline{a}_{ro}; \underline{a}_{rom})$ is orthogonal both to $(\underline{s}_r; \underline{s}_{rm})$ and $(\underline{s}_o; \underline{s}_{om})$, mutual moments between two screws are

$$MM = \underline{s}_r \circ \underline{a}_{rom} + \underline{a}_{ro} \circ \underline{s}_{rm} = 0 \tag{7}$$

and

$$MM = \underline{s}_o \circ \underline{a}_{rom} + \underline{a}_{ro} \circ \underline{s}_{om} = 0. \tag{8}$$

From (5) and (6), we have

$$\underline{a}_{ro} \circ \underline{a}_{rom} = 0. \tag{9}$$

Combining three constraint equations (7), (8), and (9) yields

$$\begin{bmatrix} \underline{s}_r^T \\ \underline{s}_o^T \\ \underline{a}_{ro}^T \end{bmatrix} \underline{a}_{rom} = \begin{bmatrix} -\underline{a}_{ro} \circ \underline{s}_{rm} \\ -\underline{a}_{ro} \circ \underline{s}_{om} \\ 0 \end{bmatrix}. \tag{10}$$

Inverting (10) gives

$$\underline{a}_{rom} = \begin{bmatrix} \underline{s}_r^T \\ \underline{s}_o^T \\ \underline{a}_{ro}^T \end{bmatrix}^{-1} \begin{bmatrix} -\underline{a}_{ro} \circ \underline{s}_{rm} \\ -\underline{a}_{ro} \circ \underline{s}_{om} \\ 0 \end{bmatrix}. \tag{11}$$

Finally, the vectors that connect the two points on the shortest distance are obtained, respectively, as

$$\underline{r}_{rc} = \frac{\underline{s}_{rm} \times \underline{a}_{rom}}{\underline{s}_{rm} \circ \underline{a}_{ro}} \tag{12}$$

and

$$\underline{r}_{oc} = \frac{\underline{s}_{om} \times \underline{a}_{rom}}{\underline{s}_{om} \circ \underline{a}_{ro}}. \tag{13}$$

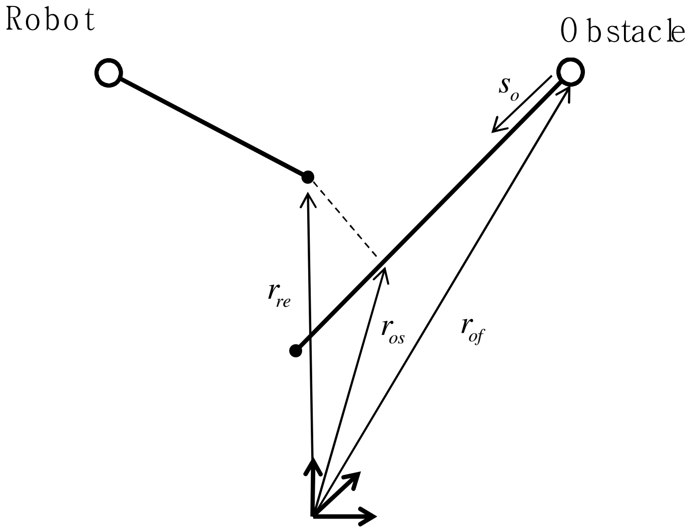

Fig. 4. Two tools and shortest distance

Now, we are looking for a shortest distance between a point and a line as shown in Fig. 4. The vector to the shortest point from the coordinate origin is denoted as

$$\underline{r}_{os} = \underline{r}_{of} + L \times \underline{s}_o. \tag{14}$$

here

$$L = s_o \circ (r_{re} - r_{of}) \tag{15}$$

According to that information, state between tools can be defined. In Fig. 5, a and b denote the distance from each fulcrum point to the end of each instrument. a' and b' denote the extended lines of which ends a shortest line between the two lines is connected. Then, there are four different cases as shown in Fig. 5. Classification of those four cases is useful when we develop an obstacle avoidance algorithm between tools.

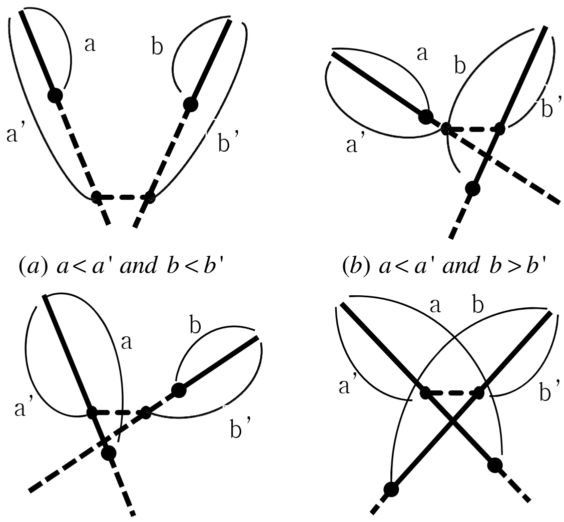

$(a)\ a < a'\ and\ b < b'$ $(b)\ a < a'\ and\ b > b'$

$(c)\ a > a'\ and\ b < b'$ $(d)\ a > a'\ and\ b > b'$

Fig. 5. (a) Point to Point ; Shortest distance between two lines (b) Point to Line ; Shortest distance between a point and a line (c) Line to Point ; Shortest distance between a line and a point (d) Line to Line ; Shortest distance between two lines.

2.3 Direction Generation

After the states are defined, several unit vectors defined in Fig. 6 will be used to generate direction and also orbital velocity centered by a closest point at each state. We consider three instruments that play the role of goal, obstacle, and robot.

${}^{rf}\underline{P}_{re}$: Unit vector along the robot instrument

${}^{re}\underline{P}_{ge}$: Unit vector from the robot end to the end of the goal instrument

${}^{re}\underline{P}_{oe}$: Unit vector from the robot end to the obstacle end

${}^{of}\underline{P}_{oe}$: Unit vector along the obstacle instrument

${}^{oe}\underline{P}_{ge}$: Unit vector from the obstacle end to the end of the goal instrument

${}^{gf}\underline{P}_{ge}$: Unit vector along the goal instrument.

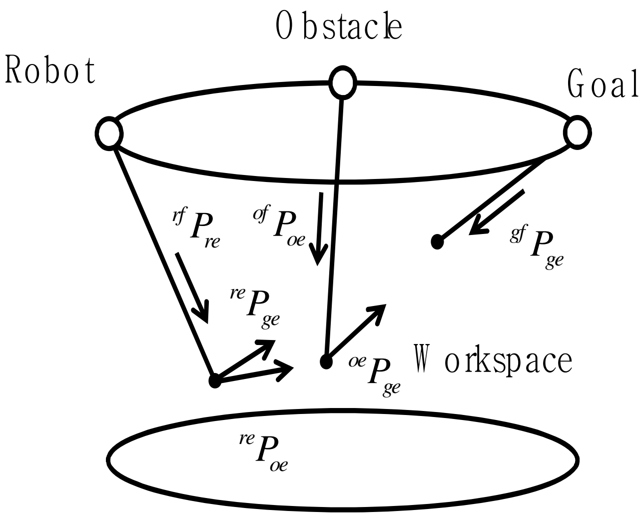

Fig. 6. Modeled environment of surgical situation

2.4 Potential Function

Typically, potential functions have been employed to deal with obstacle avoidance. There are two kinds of potential functions. For obstacle avoidance, a repulsive potential is used and for goal tracking purpose, an attractive potential is used [10].

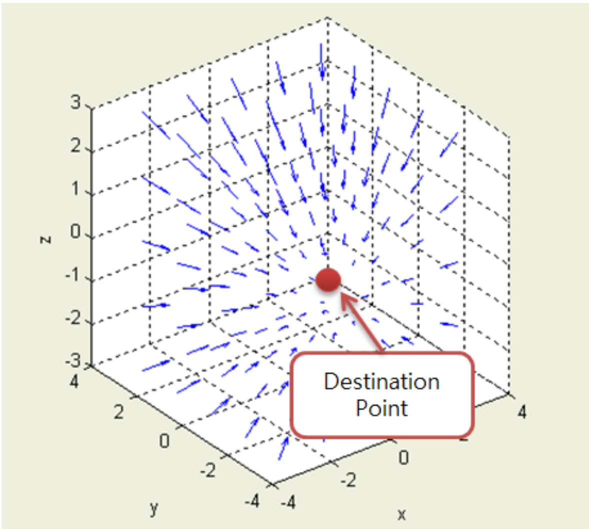

Fig. 7. Potential Field for tracking purpose

When the position vector of the goal and the robot are denoted as $\underline{r}_g = \left(x_g \quad y_g \quad z_g\right)^T$ and $\underline{r}_r = \left(x_r \quad y_r \quad z_r\right)^T$, we define the attractive potential as follows

$$P_{attr} = 2\eta_{attr}\left({}^{r}\underline{P}_g\right)^2, \tag{16}$$

where η_{attr} is a scaling factor. Differentiating (16) with respect to the ${}^{r}\underline{P}_g = \left(\underline{r}_g - \underline{r}_r\right)$ gives the attractive force $\underline{F}_{attr}$ toward the goal position

$$\underline{F}_{attr} = 2\eta_{attr}\,{}^{r}\underline{P}_g. \tag{17}$$

Fig. 7 shows an example of such potential function that generates an attractive force toward the goal position.

Similarly to the attractive potential, the repulsive potential can be defined [2] as $\underline{r}_{obs}$

$$P_{repul} = 2\eta_{attr}\left(\underline{r}_{obs} - \underline{r}_r\right)^2, \tag{18}$$

where $\underline{r}_{obs}$ denotes the position vector of the obstacle.

2.5 Velocity Generation

Now, we design the velocity vector of a robot tool such that it arrives at the goal position without collision to the obstacle. First of all, the velocity vector approaching to the goal position is designed by adapting the attractive force of Eq. (17) as

$$\underline{V}_{attr} = 2\eta_{attr}\,{}^{r}\underline{P}_g\left|1 - e^{-t^2}\right|, \tag{19}$$

where the attraction force is designed to have an exponential term, which devotes to prevent the initial excessive velocity.

Similarly, the velocity vector that avoids the obstacle is designed by adapting the repulsive force of Eq. (19) as

$$\underline{V}_{repul} = -2\eta_{repul}\,{}^{r}\underline{P}_o\left|1 - e^{-t^2}\right|. \tag{20}$$

Usually the velocity vector of the robot is designed by combining Eq. (19) and Eq. (20). The typical velocity vector according to this approach is defined as

$$\underline{v}_r = \underline{V}_{repul} + \underline{V}_{attr}. \tag{21}$$

However, when using the repulsive function, the resulting force gets larger as the robot approaches the obstacle. Thus, the behavior of the robot is sometimes not smooth or unstable. To avoid this behavior, a maximum velocity should be defined and used as a measure of safety.

In this work, a modified obstacle avoidance scheme is proposed without relying on the repulsive potential. A prime idea of this approach is generation of an orbit velocity.

2.6 Orbital Velocity-Based Vector Generation

With various unit vectors defined in the previous section, an orbital velocity helps to avoid obstacle effectively and thus prevent collision by generating a spherical trajectory around the obstacle. An orbit velocity is simply added to current velocity vector of the tool tip to modify its direction.

Policy of generating the orbit velocity varies with respect to the obstacle and the goal. For the obstacle, the robot only needs to avoid, but for the goal, the robot has to approach to the end of the tool. Often these two cases can be combined.

To generate an orbital velocity, we employ the operation of the cross product between unit vectors and an angular velocity vector about the axis of rotation, which is expressed in Fig. 8 as

$$\underline{v}_{orbit} = \underline{\omega} \times \underline{P}_{radius}, \tag{22}$$

where $\underline{P}_{radius}$ as shown in Fig. 8 is the vector along the shortest distance between the robot instrument and the obstacle instrument in the four cases of Fig. 5 and $\underline{\omega}$ denotes the angular velocity of the vector $\underline{P}_{radius}$.

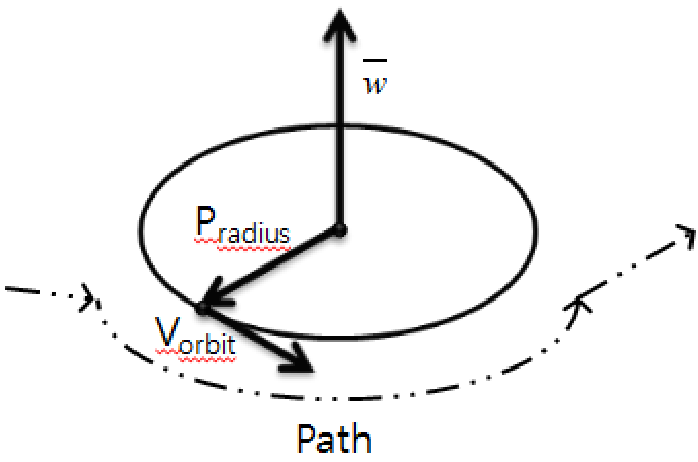

Fig. 8. Orbital velocity

Table 1. Orbital velocity vectors

Status	***Pivot Vector***	***Orbital Vector***
Point to Point	$\underline{w} = {}^{re}\underline{P}_{ge} \times {}^{re}\underline{P}_{oe}$	$\underline{v}_{orbit} = \underline{w} \times (-{}^{re}\underline{P}_{oe})$
Point to Line	$\underline{w} = {}^{re}\underline{P}_{ge} \times {}^{re}\underline{P}_{oc}$	$\underline{v}_{orbit} = \underline{w} \times (-{}^{re}\underline{P}_{oc})$
Line to Point	$\underline{w} = {}^{rc}\underline{P}_{oe} \times {}^{rf}\underline{P}_{re}$	$\underline{v}_{orbit} = \underline{w} \times {}^{rf}\underline{P}_{re}$
Line to Line	$\underline{w} = {}^{rc}\underline{P}_{oc} \times {}^{rf}\underline{P}_{re}$	$\underline{v}_{orbit} = \underline{w} \times {}^{rf}\underline{P}_{re}$

The key is the decision of a proper rotational axis for $\underline{\omega}$ to avoid collision. It depends on the choice of appropriate unit vectors defined in Section II. Table I shows that for each status the direction of $\underline{\omega}$ is decided by the cross product of two unit vectors which are directed to the goal and the obstacle. Accordingly, the direction of the orbit velocity is decided as shown in Fig. 9 such that the motion of the robot tip is tangential to the circular orbit around the obstacle tool to avoid collision with the obstacle.

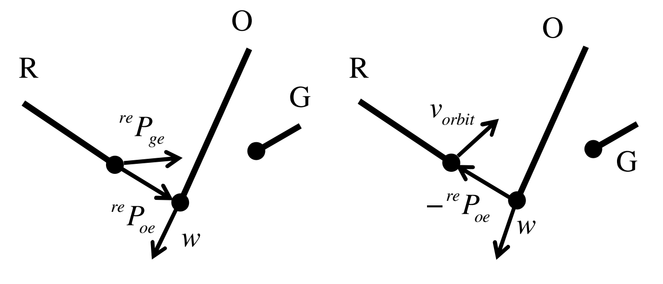

(a)

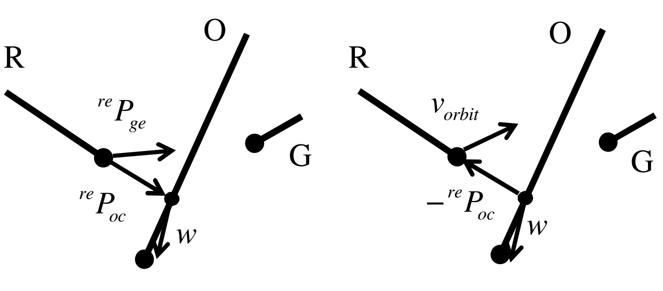

(b)

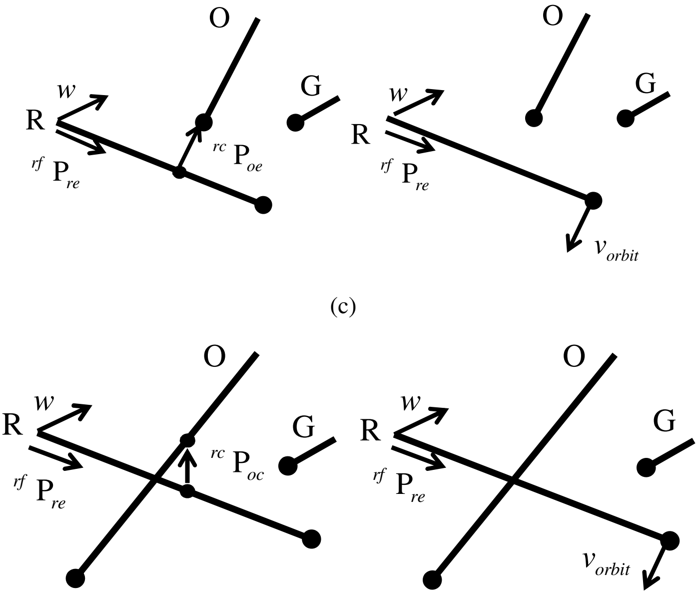

Fig. 9. Orbit velocity generation
(a) Point to Point (b) Point to Line (c) Line to Point (d) Line to Line

By using this methodology, we come up with a direction vector which takes care of the goal direction, the obstacle, and the orbital behavior.

$$\underline{v}_{dir} = \underline{v}_r + \underline{v}_{orbit} \tag{23}$$

This composed vector is a unit vector that the robotic tool is heading instantaneously. Lastly, multiplying the scaled magnitude (Eq. (19)) of the attractive force to the direction vector given in Eq. (23), the total velocity vector of the robot tool can be generated as

$$\underline{v} = 2\eta_{attr} \left| {}^{r}\underline{P}_g \right| \left| 1 - e^{-t^2} \right| \underline{v}_{dir} \tag{24}$$

In the simulation section, we will show the effectiveness of the orbit velocity component as compared to not using such component in Eq. (23).

3 Simulation Result

In the simulation, we consider a test environment which is operated by two manually controlled instruments by surgeons and one robot instrument. The number of surgeon can be one or two and the role of the robot is delivery of water or suction or gauze to the operation area. In order to show such behavior, this simulation will present that a robot moves to the goal position (i.e., the end position of the goal instrument) while avoiding the obstacle instrument.

3.1 Trajectory

Initially, we consider the trajectory of the end of robotic tools. Fig. 10 shows the simulation result and the line denotes the trace of the robot end point. If a robotic tool encounters an obstacle on the way to the goal, it tries to maneuver the obstacle centered at the closest point between tools. The robot avoids the obstacle with distance adjusting the velocity by using suggested algorithm so that it smoothly avoids collision with the obstacle.

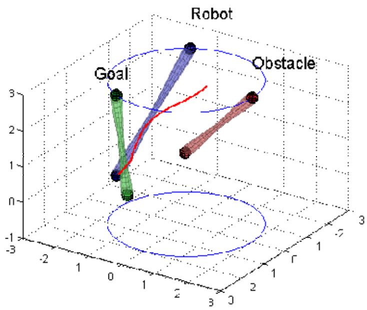

(a)

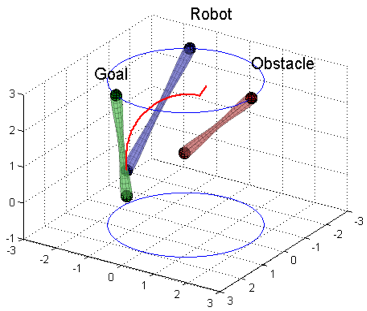

(b)

Fig. 10. Trajectories of tools and velocity of the robot tool (a) orbit method applied (b) orbit method not applied

3.2 Distance

The velocity profile shows that the direction velocity vector taking care of goal and obstacle keeps relatively appropriate distance without rapid variation of velocity including the orbit component as compared to the other case (Fig. 11(b)) which does not include the orbit component.

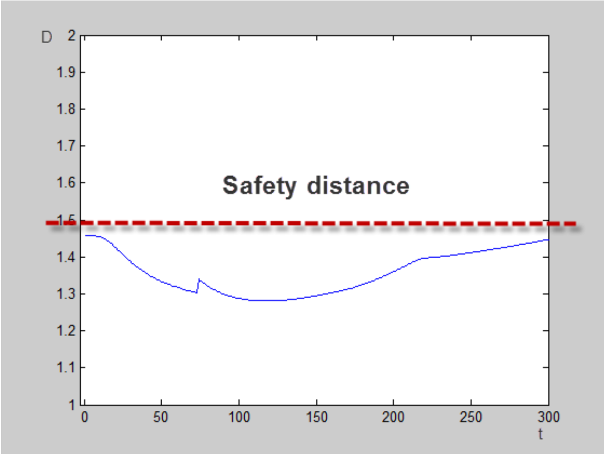

(a)

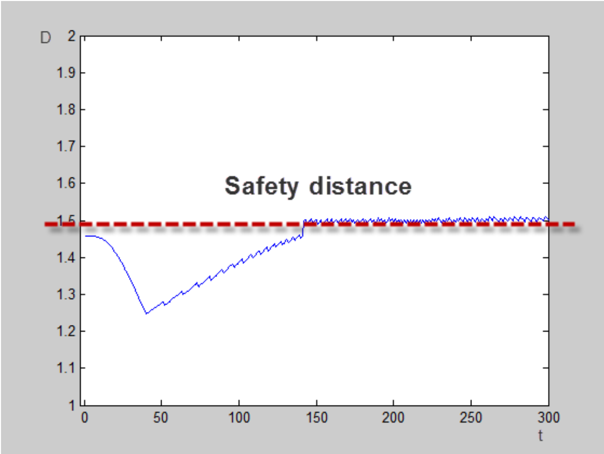

(b)

Fig. 11. Distance variation graph
(a) orbit method applied (b) orbit method not applied

This graphs of Fig. 11 (a) shows variation of distance between the robot tool when the orbit method is applied and the graphs of Fig. 11 (b) shows variation of distance between the robot tool when the orbit method is not applied, respectively. Safety distance has set 2 in this simulation. Comparing these graphs, in Fig. 11 (a), the change of distance moves smoothly and continueoulsy. But, Fig. 11 (b) shows unstable change of distance respectively. This result shows that robotic tool can perform better motion behavior when orbital velocity is applied to the artificial potential method.

4 Conclusion

This work deals with a maneuver algorithm as a first step of minimally invasive surgery before the clinical implementation. Firstly, four states are defined. Next, using the four states, the direction and velocity of the robot tool are derived. Different from artificial potential method which is based on the attractive and repulsive force vectors, we proposed a vector approach combined with an orbit velocity, which is the main contribution of this research work. As a result, this method shows smooth goal tracking and obstacle avoiding behavior in the surgical space. The further study will be implementation of the proposed motion planning algorithm to real Laparoscopic surgery using a robotic tool.

References

1. Niemeyer, G., Swarup, N., Guthanrt, G., Toth, G., Younge, R., Nowlin, W.: Camera Referenced Control in a Minimally Invasive Surgical Apparatus. World patent WO0060521
2. Inoue, S., Toyoda, K., Kobayashi, Y., Fujie, M.G.: Autonomous Avoidance based on Motion Delay of Master-Slave Surgical Robot. In: International Conference of the IEEE EMBS (September 2009)
3. Kang, H., Wen, J.T.: Robotic Assistants aid Surgeons During Minimally Invasive Procedures. IEEE Engineering in Medicine and Biology Magazine 20(1) (2001)
4. Dumpert, J., Lehman, A.C., Wood, N.A., Oleyniko, D., Farritor, S.M.: Semi-Autonomous Surgical Tasks Using a Miniature in Vivo Surgical Robot. In: Proc. of IEEE Int. Conf. on Engineering in Medicine and Biology Society, EMBC (2009)
5. Khatib, O.: Real-time Obstacle Avoidance for Manipulators and Mobile Robots. In: Proc. of IEEE Int. Conf. on Robotics and Automation, pp. 500–505 (1985)
6. Brock, O., Khatib, O.: Real-Time Replanning in High-Dimensional Configuration Spaces Using Sets of Homotopic Paths. In: Proc. of Int. Conf. on Robotics and Automation, pp. 550–555 (2000)
7. Cen, Y., Wang, L., Zhang, H.: Real-time Obstacle Avoidance Strategy for Mobile Robot Based On Improved Coordinating Potential Field with Genetic Algorithm. In: Proc. of IEEE Int. Conf. on Control Applications, pp. 415–419 (2007)
8. Chancharoen, R., Sangveraphunsiri, V., Sanguanpiyapan, K., Chatchaisucha, P., Dharachantra, P., Nattarorn, S., Pongparit, S.: Collision Avoidance Technique for Uncalibrated Visual Servoing for Industrial Robots. In: Proc. of IEEE Int. Conf. on Industrial Technology, pp. 594–599 (2002)
9. Kumar, R., Jensen, P., Taylor, R.: Experiments with a Steady Hand Robot in Constrained Compliant Motion and Path Following. In: Proc. of IEEE International Workshop on Robot and Human Interaction (1999)
10. Iraji, R., Manzuri-Shalmanit, M.T.: A New Fuzzy-Based Spatial Modelfor Robot Navigation among Dynamic Obstacles. In: Proc. of IEEE International Conference on Control and Automation (2007)

HOG-Based Person Following and Autonomous Returning Using Generated Map by Mobile Robot Equipped with Camera and Laser Range Finder

Masashi Awai[1], Takahito Shimizu[1], Toru Kaneko[1],
Atsushi Yamashita[2], and Hajime Asama[2]

[1] Department of Mechanical Engineering, Shizuoka University
3-5-1 Johoku, Naka-ku, Hamamatsu-shi, Shizuoka 432-8561, Japan
{f0130004,f0030029,tmtkane}@ipc.shizuoka.ac.jp
[2] Department of Precision Engineering, The University of Tokyo
7-3-1 Hongo, Bunkyo-ku, Tokyo 113-8656, Japan
{yamashita,asama}@robot.t.u-tokyo.ac.jp

Abstract. In this paper, we propose a mobile robot system which has functions of person following and autonomous returning. The robot realizes these functions by analyzing information obtained with camera and laser range finder. Person following is performed by using HOG features, color information, and shape of range data. Along with person following, a map of the ambient environment is generated from the range data. Autonomous returning to the starting point is performed by applying a potential method to the generated map. We verified the validity of the proposed method by experiment using a wheel mobile robot in an indoor environment.

Keywords: Mobile Robot, Laser Range Finder, Camera, Person Following.

1 Introduction

In recent years, introduction of autonomous mobile robots to environments close to us is expected. Examples include shopping cart robots returning automatically to the shopping cart shed after shopping, and guide robots directing the way from the current location to the starting point in unknown environments. A robot which accomplishes these purposes needs functions of person following and autonomously returning to the starting point functions [1]-[3]. In this paper, we propose a mobile robot system that has functions of human following and returning to the starting point autonomously while avoiding obstacles.

The proposed mobile robot follows a person by using shape of range data, HOG (Histograms of Oriented Gradients) features, and color information, in parallel with generating a map by LRF data on the outward way from the starting point to the goal. On the return way, the mobile robot returns to the starting point autonomously while avoiding obstacles by using the generated map.

S. Lee et al. (Eds.): Intelligent Autonomous Systems 12, AISC 194, pp. 51–60.
springerlink.com

2 Outline

In this paper, we verify the validity of the system using the mobile robot equipped with the Laser Range Finder (LRF) and the camera. The mobile robot acquires two-dimensional (2-D) range data of 180 degrees forward by the LRF. The mobile robot also acquires the image in the front direction by the camera.

The operating environment of the mobile robot is a flat and static environment, and the mobile robot moves in 2-D space.

The mobile robot detects and follows a person by using the LRF and the camera when moving on the outward way. At the same time, the mobile robot generates a map with range data measured by the LRF.

The mobile robot generates a potential field from the generated map by an artificial potential method. Then, it moves on the return way along gradient directions of the generated potential field. At the same time, the mobile robot avoids obstacles not recorded in the map by reconstruction of the potential field.

3 Person Following on Outward Way

The mobile robot performs person following and map generation on the outward way. In this paper, the mobile robot follows the person by using person detection.

Person detection is performed by evaluating a value of person likelihood. The value of person likelihood is evaluated on the shape of range data and the HOG features in acquired images. However, this evaluation is ineffective to follow the person in environment where more than one person exist. Because, the shape of LRF data and HOG features are not specific to the person to be followed but common to all persons. Therefore, color information is added to the shape of range data and HOG features.

We use a particle filter for person following. In particle filter algorithm, a particle is assigned a weight at each particle position. However, calculation of weight at each particle position is computationally expensive. Thus, assigning the weight to the particle is performed as follows. First, the robot acquires range data (Fig. 1(a)). Next, values of person likelihood are evaluated only at the range data positions (Fig. 1(b), (c)). In the particle filter algorithm, particles near to range data positions are assigned a weight as evaluated values.

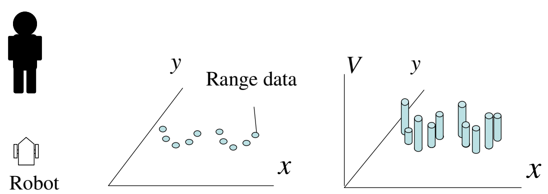

(a) Measurement. (b) Range data. (c) Evaluation.

Fig. 1. Data evaluation

3.1 Evaluation on shape of Range Data

Evaluation on the shape of range data uses template matching proposed in [4].

The 2-D map image is generated from the range data measured at each angle for the template matching. In the 2-D map image, the region beyond the detected range is in black and the other region is in white. Fig. 3 shows leg template for matching in the 2-D map image.

While following the person, matching scores are obtained by performing the matching at each range data position in the 2-D map image. Matching score R is obtained by SAD (Sum of Absolute Difference).

$$R = \sum_{j=0}^{M} \sum_{i=0}^{M} \left| I(i, j) - T(i, j) \right|, \tag{1}$$

where $T(i, j)$ is a pixel value on the template image ($M \times M$). (i, j) is position on the image, and $I(i, j)$ is a pixel value on the 2-D map image.

Equation (2) shows person likelihood score $P_L(\theta)$ of the range data position whose angle is θ.

$$P_L(\theta) = 1 - aR(\theta), \tag{2}$$

where $R(\theta)$ is a matching score of the range data position whose angle is θ, and a is a parameter for normalizing value of $R(\theta)$.

Finally, Equation (3) shows the evaluated value on shape of range data $V_L(\theta)$.

$$V_L(\theta) = \frac{P_L(\theta)}{\sum_{\theta=0}^{N} P_L(\theta)}, \tag{3}$$

where N is number of range data.

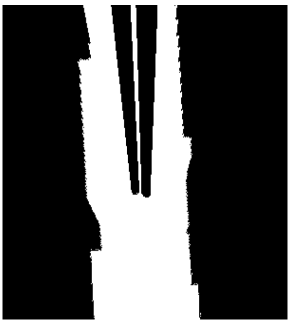

Fig. 2. Range data

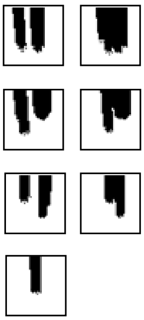

Fig. 3. Leg templates

3.2 Evaluation on HOG Features

Person detection in acquired images is performed by using the Real Adaboost algorithm with HOG features. The validity of HOG features for person detection is verified in [5].

For person detection on HOG features, image regions to perform person detection are selected in acquired image. By setting the size of person, the size and position of the image region are determined according to each range data position (angle and distance). Person likelihood score $P_H(\theta)$ is calculated by performing person detection on each selected image region in the acquired image while following the person.

$$P_H(\theta) = bH(\theta) + c, \tag{4}$$

where $H(\theta)$ is the final classifier value of Real Adaboost on the selected image region according to range data position whose angle is θ. b and c are parameters for normalizing value of $H(\theta)$. Equation (5) shows the evaluated value on HOG features $V_H(\theta)$.

$$V_H(\theta) = \frac{P_H(\theta)}{\sum_{\theta=0}^{N} P_H(\theta)}, \tag{5}$$

3.3 Evaluation on Color Histogram

Detecting the person to be followed is performed by using color histogram. To be robust to the change in brightness, the color histogram of hue h and saturation s is made by using pixel values converted into HSV. The mobile robot acquires color information on the person who is to be followed by the mobile robot before the person following begins.

While the mobile robot follows the person, the color information is acquired from the image region which is selected according to each position of acquired range data. Then, the color histogram is made and the degree of similarity with the color histogram made before the person following begins is calculated.

The Bhattacharyya coefficient [6] is used for calculating the degree of similarity with the histograms. Equation (6) shows Bhattacharyya coefficient $L(\theta)$ of range data position whose angle is θ.

$$L(\theta) = \sum_{h}^{h_n} \sum_{s}^{s_n} \sqrt{H_t(h,s) \times H(h,s,\theta)}, \tag{6}$$

where $H_t(h, s)$ is the frequency of each bin of the color histogram of the person that is acquired before the mobile robot begins person following. $H(h, s, \theta)$ is the frequency of each bin of the color histogram acquired in image for angular θ direction while the mobile robot follows the person. h_n is the number of bins of hue h, and s_n is the number of bins of saturation s.

Finally, Equation (7) shows the evaluated value on color information $V_C(\theta)$.

$$V_C(\theta) = \frac{L(\theta)}{\sum_{\theta=0}^{N} L(\theta)}, \tag{7}$$

3.4 Integration of Evaluated Values

The integrated value of person likelihood $V(\theta)$ is determined by $V_L(\theta)$, $V_H(\theta)$ and $V_C(\theta)$.

$$V(\theta) = \alpha V_L(\theta) + \beta V_H(\theta) + (1 - \alpha - \beta) V_C(\theta), \tag{8}$$

where $\alpha(\geq 0)$, $\beta(\geq 0)$ are weight coefficients.

3.5 Tracking by Particle Filter

Person following is performed by using a particle filter with value of $V(\theta)$. Particle filter is performed as follows.

(i) Initial particles are distributed around the person with random noise
(ii) Particles are moved based on the system model given by Equation

$$\mathbf{x}_{t|t-1} = \mathbf{x}_{t-1} + \mathbf{v}_{t-1} T, \tag{9}$$

where $\mathbf{x}_t$ is position in time t, $\mathbf{v}_t$ is velocity in time t, and T is updating cycle.
(iii) Each particle is assigned a weight as $V(\theta)$ of near range data position.
(iv) New particles are generated depending on the weight as resampling process.

First, process (i) is performed. Next, processes (ii), (iii) and (iv) are performed. After that, processes (ii), (iii) and (iv) are performed repeatedly.

4 Map Generation on Outward Way

The mobile robot generates the map of ambient environment while it moves on the outward way. The LRF is used to measure the ambient environment during the mobile robot movement, and the ambient environment map is generated by integrating each measurement data. Measurement data integration needs an accurate self-location estimation of the mobile robot. In this study, the estimation is made by dead reckoning. However, dead reckoning has a problem of error accumulation caused by wheel slipping. In order to decrease this error accumulation, the robot aligns each measurement data by the ICP algorithm [7].

Moving objects do not exist in the same place. Therefore, it is necessary to remove moving objects from the map. The mobile robot removes moving objects by a method in [8].

5 Motion on Return Way

The mobile robot moves on the return way according to the Laplace potential method [9]. The robot generates the potential field in the map obtained on the outward way. Then the robot moves on the return way along a gradient direction of the generated potential field.

For the robot to avoid obstacles not recorded in the map, the LRF measures an ambient environment while the robot moves on the return way and the robot reconstructs a potential field. This makes the movement of the robot safe on the return way.

6 Experiment

6.1 Experiment Device

We used the mobile robot ”Pioneer3” of MobileRobots, Inc (Fig. 4). The robot has 2 drive wheels and 1 caster. Its maximum speed is 400mm/sec. It turns with the velocity differential of right and left wheels. The LRF is model LMS200-30106 by SICK. It is equipped at a height of 30cm above the ground. The sensing range is 180 degrees in one plane and the resolution is 0.5 degrees.

The camera is equipped at a height of 80cm above the ground. As the specs on computers, CPU is Intel Core 2Duo T9300 2.5GHz, and memory is 3.5GB.

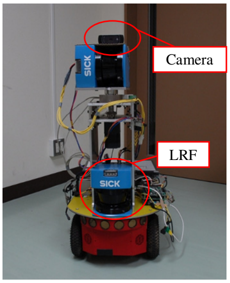

Fig. 4. Mobile robot

Fig. 5. Environment

6.2 Experiment Environment

We conducted experiment in which the mobile robot follows a person to the goal and then returns to the starting point. Experiment environment is a corridor with a flat floor. Figure 5 shows the experiment environment. There are some pedestrians in experiment environment.

6.3 Experimental Result

On the outward way, the mobile robot followed the person.

Figure 6 shows acquired data when the static obstacle is exists.

Figure 6(a) shows an image acquired with the camera while the robot followed the person. In Fig. 6(a), the person existing on the left is the person to be followed by the mobile robot.

Figure 6(b) shows a 2-D map image generated by range data acquired with the LRF. Particles are shown as red points in Fig. 6(b).

Figure 6(c) shows evaluation value on shape of range data $V_L(\theta)$. The horizontal axis in Fig. 6(c) indicates the view angle from the robot (the positive and negative values correspond to the right and left angle, respectively). In Fig. 6(c), it is shown that high values appear in the vicinity of the angle where the person and static obstacle exist.

Figure 6(d) and (e) show evaluation value on HOG features $V_H(\theta)$ and evaluation value on color information $V_C(\theta)$. It is shown that high values appear in the vicinity of the angle where the person exists.

Finally, Fig. 6(f) shows the integrated value of person likelihood $V(\theta)$. It is shown that the highest values appear in the vicinity of the angle where the person to be followed exists. It shows that using $V(\theta)$ is better than only using $V_L(\theta)$ for following person in this situation.

(a) Acquired image.

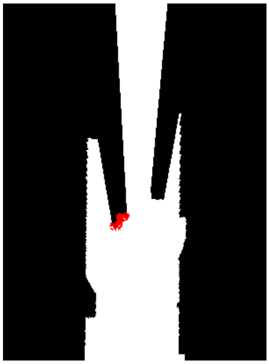

(b) Range data and particle

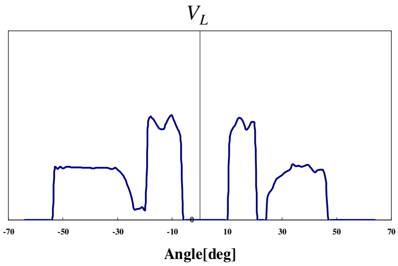

(c) Evalustion value of LRF $V_L(\theta)$.

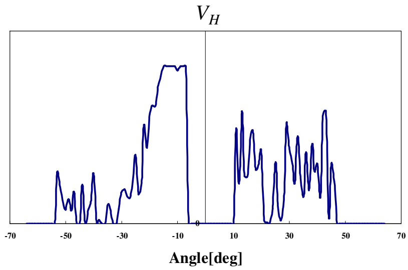

(d) Evalustion value of HOG $V_H(\theta)$.

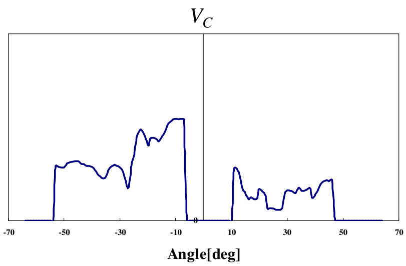

(e) Evalustion value of color V_c (θ).

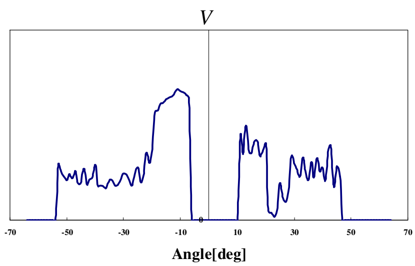

(f) Integrated evaluation value $V(\theta)$.

Fig. 6. Acquired data when the static obstacle is exists

Figure 7 shows acquired data when the pedestrian is exists.

Figure 7(a) and (b) show acquired image and range data as with Fig. 6. The right person is the person who should be followed by the mobile robot.

Figure 7(c) and (d) show $V_L(\theta)$ and $V_H(\theta)$. High values appear in the vicinity of the angle where the persons exist.

Figure 7(e) shows $V_C(\theta)$. High values appear in the vicinity of the angle where the person to be followed exists.

Finally, Fig. 7(f) shows $V(\theta)$. High values appear in the vicinity of the angle where the person to be followed exists.

(a) Acquired image.

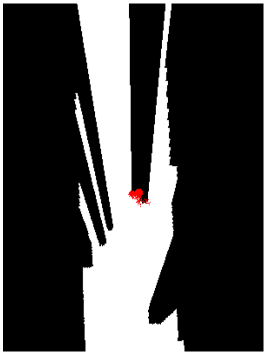

(b) Range data and particle

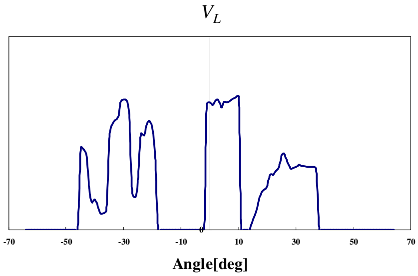

(c) Evalustion value of LRF $V_L(\theta)$.

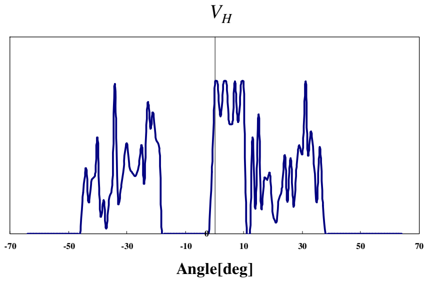

(d) Evalustion value of HOG $V_H(\theta)$.

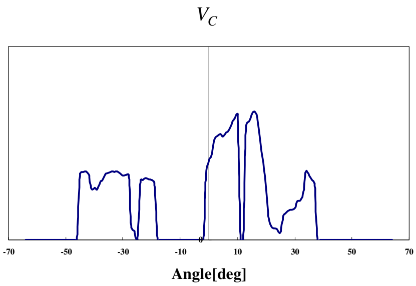

(e) Evalustion value of color $V_c(\theta)$.

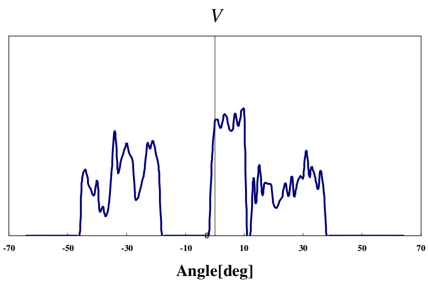

(f) Integrated evaluation value $V(\theta)$.

Fig. 7. Acquired data when the pedestrians exist

It is shown that using $V(\theta)$ is better than using $V_H(\theta)$, $V_L(\theta)$ for person following in this situation, and robust following can be performed even if high values in one evaluation appear in the vicinity of the angle where the person to be followed does not exist.

The mobile robot followed the person by using the particle filter in which particles are assigned the weight based on $V(\theta)$ in experimental environment.

Figure 8(a) shows the generated map and the robot trajectory on the outward way. It is shown that stationary object map was generated by moving object removal. The robot moved on the return way by using the map which had been generated on the outward way. On the return way, the new obstacle that did not exist on the outward way existed.

Figure 8(b) shows the trajectory of the robot on the return way. It is shown that the robot returned to the starting position while avoiding the new obstacle.

These results show that the mobile robot can detect and follow the person by the proposed method in the experimental environment and can return to the starting point while avoiding obstacles.

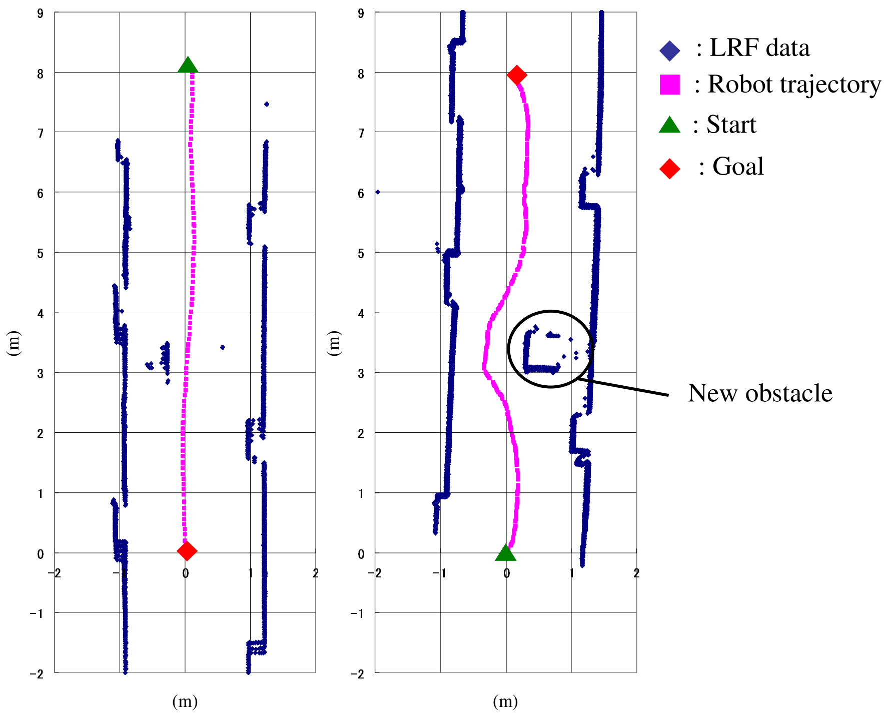

(a) Outward way (b) Return way

Fig. 8. Generated map and trajectory of mobile robot

7 Conclusion

In this paper, we construct the mobile robot system that has functions of person following and returning to the starting point autonomously while avoiding obstacles.

Person following is achieved by using shape of range data, HOG features and color information. Map generation is achieved by the ICP algorithm and the moving object detection. The robot returns to the starting point according to the Laplace potential method with generated map, and a path of avoiding obstacle is generated by reconstructing a potential field.

Acknowledgements. This work was in part supported by MEXT KAKENHI, Grant-in-Aid for Young Scientist (A), 22680017.

References

1. Misawa, M., Yoshida, T., Yuta, S.: A Smart Handcart with Autonomous Returning Function. Journal of Robotics Society of Japan 25(8), 1199–1206 (2007) (in Japanese)
2. Lixin, T., Yuta, S.: Mobile Robot Playback Navigation Based on Robot Pose Calculation Using Memorized Ominidirectional Images. Journal of Robotics and Mechatronics 14(4), 366–374 (2002)
3. Tsuda, N., Harimoto, S., Saitoh, T., Konishi, R.: Mobile Robot with Following and Returning Mode. In: Proceedigs of the 18th IEEE International Symposium on Robot and Human Interactive Communication (RO-MAN 2009), ThB1.3, pp. 933–938 (2009)
4. Okusako, S., Sakane, S.: Human Tracking with a Mobile Robot using a Laser Range-Finder. Journal of Robotics Society of Japan 24(5), 605–613 (2006) (in Japanese)
5. Dalal, N., Triggs, B.: Histgrams of Oriented Gradients for Human Detection. In: Proceedings of the 2005 IEEE Computer Society Conference on Computer Vision and Pattern Recognition, pp. 886–893 (2005)
6. Kailath, T.: The Divergence and Bhattacharyya Distance Measures in Signal Selection. IEEE Transactions on Communication Technology COM-15(1), 52–60 (1967)
7. Besl, P.J., Mckay, N.D.: A Method for Registration of 3-D Shapes. IEEE Transaction on Pattern Analysis and Machine Intelligence 14(2), 239–256 (1992)
8. Iwashina, S., Yamashita, A., Kaneko, T.: 3-D Map Building in Dynamic Environments by a Mobile Robot Equipped with Two Laser Range Finders. In: Proceedings of the 3rd Asia International Symposium on Mechatronics, vol. TP1-3(1), pp. 1–5 (2008)
9. Sato, K.: Deadlock-free Motion Planning Using the Laplace Potential Field. In: Proceedings of the Joint International Conference on Mathematical Methods and Supercomputing in Nuclear Applications, pp. 449–461 (1994)

Fast Range Image Segmentation and Smoothing Using Approximate Surface Reconstruction and Region Growing*

Dirk Holz and Sven Behnke

Autonomous Intelligent Systems Group, University of Bonn, Germany
{holz,behnke}@ais.uni-bonn.de

Abstract. Decomposing sensory measurements into relevant parts is a fundamental prerequisite for solving complex tasks, e.g., in the field of mobile manipulation in domestic environments. In this paper, we present a fast approach to surface reconstruction in range images by means of approximate polygonal meshing. The obtained local surface information and neighborhoods are then used to 1) smooth the underlying measurements, and 2) segment the image into planar regions and other geometric primitives. An evaluation using publicly available data sets shows that our approach does not rank behind state-of-the-art algorithms while allowing to process range images at high frame rates.

1 Introduction

As robots and autonomous systems move away from laboratory setups towards complex real-world scenarios, both the perception capabilities of these systems and their abilities to acquire and model semantic information must become more powerful. A key issue is the extraction of semantic information from sensory data and its decomposition into parts of interest that are relevant for the tasks of the robot. For mobile manipulation in domestic environments, for example, the perception of objects and their surroundings is a key prerequisite. A common approach [1] in 3D perception is to

1. detect horizontal support planes,
2. extract and cluster points on top of these planes, and
3. perform further processing, e.g., recognizing, classifying or tracking of the found clusters.

Here, one of the fundamental problems is to segment the 3D data into planes and other geometric primitives—or regions of local surface continuity in general.

In this paper, we address the problem of segmenting range images and organized point clouds in real-time on domestic service robots. The central idea of our approach is to approximately reconstruct the surface and segment the range image by growing regions using the resulting local mesh neighborhoods. By means of easily exchangeable components, our generalized region growing approach allows for different region

* This research has been partially funded by the FP7 ICT-2007.2.2 project ECHORD (grant agreement 231143) experiment ActReMa.

S. Lee et al. (Eds.): Intelligent Autonomous Systems 12, AISC 194, pp. 61–73.
springerlink.com

models (e.g. planes) that are segmented in the data. We present models for segmenting planes, regions of local surface continuity, and simple geometric primitives at high frame rates (see Fig. 1).

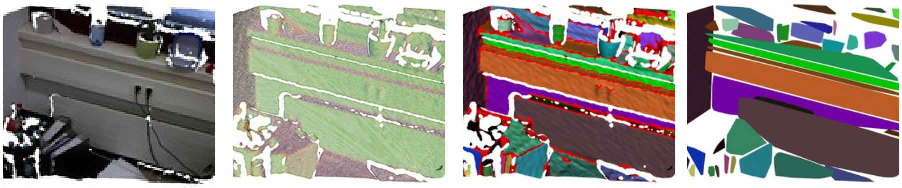

(a) Input cloud (b) Triangle mesh (c) Segmentation (d) Polygonalization

Fig. 1. Example of surface reconstruction and (plane) segmentation on a RGB-D point cloud: (a) input cloud; (b) constructed mesh; (c) result of segmenting planes in the mesh (red points are assigned to multiple planes); (d) polygonalization as a collection of alpha shapes. Using the Microsoft Kinect camera at a resolution of 160×120, we can compute full polygonalizations with roughly 30 Hz on a standard dual-core notebook.

Furthermore, we use the same mesh neighborhoods to 1) efficiently compute local surface normals and curvature estimates, as well as 2) smooth both the 3D measurements and the computed normals using a bilateral filter.

This paper is organized as follows: After giving a brief overview on related work in range image and 3D plane segmentation in Section 2, we present our approach in Section 3 and discuss how to detect geometric primitives using initial segmentations. We use multiple data sets for evaluating the efficiency and robustness of our approach and summarize the results in Section 4.

2 Related Work

Research on computer and robot vision produced a wide variety of approaches to range image segmentation—and plane segmentation in particular. Hoover et al. [2] compiled a survey and performed an evaluation of early work. Three different types of approaches can be distinguished according to the underlying working principle: methods using random sample consensus (RANSAC), 3D Hough transforms, and region growing. In the context of segmenting 3D laser range scans, another popular approach is to first detect lines in planar cuts, and to merge neighboring lines into local plane patches (see Vosselman et al. [3] for an overview).

2.1 Segmentation Based on Sample Consensus

RANSAC-based approaches try to find models for geometric primitives that best explain a set of points and the set of inliers supporting it. For segmenting a complete range image, Lee et al. [4] sequentially remove inliers from the original data set, and continue the segmentation with the residual points. Silva et al. [5] first identify connected regions and apply RANSAC region-wise. Gotardo et al. [6] compute an edge map for pre-segmentation and use a variant based on the M-estimator sample consensus (MSAC) to fit model parameters.

Another efficient solution to segmenting even unorganized point clouds and detecting simple geometric primitives such as planes, cylinders and spheres has been proposed by Schnabel et al. [7]. They decompose unorganized point clouds using an octree subdivision and apply RANSAC only to subsets of the original point cloud.

In previous work [8], we adapted the perception scheme from Section 1 as well as the techniques from [1] and [7], and made them applicable to the measurements of time-of-fight (ToF) cameras. We presented techniques to cope with the specific error sources of the cameras, and to speed up processing by exploiting the image-like data organization. After detecting the most dominant plane, we applied the octree-based primitive detection of Schnabel et al. [7] only to already extracted and segmented points above that plane. In [9], we further speeded up the segmentation process by using integral images for computing local surface normals more efficiently, and using the index neighborhood underlying the 3D data to extract and track segments of points and object candidates, respectively. The overall approach is applicable in real time on a Microsoft Kinect camera and has been used for real-time object tracking and grasp planning [10].

2.2 Hough-Based Plane Segmentation

The Hough transform is the de-facto standard for finding lines and circles in 2D images. Various extensions to 3D exist that try to find, respectively, planes and maxima in histograms over the possible space of plane orientations and distances. For an overview, and an evaluation for Hough-based segmentation approaches, we refer to the works of Vosselman et al. [3] and Borrmann et al. [11].

RANSAC- and Hough-based segmentation share a common disadvantage. Points belonging to the same segment do not necessarily lie on connected components. Both approaches will merge plane segments if they share a common orientation and distance to the origin. In addition, Hough-based segmentation may suffer from discretization effects.

In [9], we present a fast plane segmentation approach that uses a similar parameter space as the Hough transform. We pre-cluster points and segment planes first in normal space and then, for each cluster, in distance space to obtain individual planes. We compensate for discretization effects by conducting a post-processing step in which neighboring segments are merged if their parameters do not considerably deviate. Still, unconnected planar patches may get merged into the same cluster.

2.3 Segmentation Using Region Growing

The idea of region growing-based segmentation is to exploit the image-like data structure. Hähnel et al. [12] connect neighboring points in 3D laser range scans to a mesh-like structure. The scans are then segmented recursively by merging connected patches that are likely to lie on the same planar surface. Poppinga et al. [13] apply the same approach to Time-of-Flight cameras and re-formulate the algorithm in an incremental fashion. They grow planar regions by adding neighboring points whose distance to the plane lies below a threshold. Centroid and covariance matrix for estimating the plane parameters are thereby incrementally updated.

Here, we follow a similar approach. Instead of incrementally computing the covariance matrix, however, we compute the normals for all points beforehand and simply average local surface normals to obtain an estimate of the plane's normal. That is, we only store and incrementally update the centroids in both Cartesian and normal space.

Other popular region growing-approaches to range image segmentation make use of local surface curvature. Regions are grown until points with a considerably larger curvature are reached. Just like Gotardo et al. [6] for RANSAC-based segmentation, Harati et al. [14], first compute an edge map to find connected regions of local surface continuity. Rabbani et al. [15] approximate local surface curvature by first fitting planar segments to local point neighborhoods and then computing, for each point, the distance to that plane. Recently, Cupec et al. [16] followed a similar approach. They first apply 2.5D Delaunay triangulation on a range image to obtain an initial triangular mesh and then use the maximum distance of an examined point to all triangles in a region to determine whether or not the point is added.

Here, we deduce a surface reconstruction directly from the image-like data structure, and use the local ring neighborhood around vertices to 1) efficiently compute local surface normals and curvature estimates, and 2) efficiently smooth the depth measurements using a bilateral filter. Our framework allows for using different types of models for region growing, including the approaches of Poppinga et al. [13], Harati et al. [14], Rabbani et al. [15] and Cupec et al. [16], as well as our fast approximation (see Section 3).

3 Fast Mesh Construction and Segmentation

In this section, we describe our approaches to approximate surface reconstruction and segmentation based on region growing. The overall processing pipeline is composed of the following components:

1. Deduce approximate mesh from image neighborhood.
2. Use mesh neighborhood to compute approximate local surface normals and curvature estimates.
3. Bilateral filtering to smooth both points and normals.
4. Segmentation based on region growing.

All components described in the above list use the same fixed neighborhoods. These neighborhoods come either directly from the mesh structure or can be pre-computed using a variety of search trees, if the input data is unstructured.

3.1 Exploiting Structure for Fast Approximate Meshing

The central idea of our surface reconstruction approximation is to deduce the desired mesh structure directly from the image-like organization of measurements. In fact, the algorithms presented in the following could easily be applied on local index neighborhoods in range images. However, an approximate mesh allows for 1) applying a wide variety of sophisticated algorithms from the field of computer graphics, as well as for storing certain edge weights, e.g., the difference vectors for integral image-based normal computation from our previous work [9].

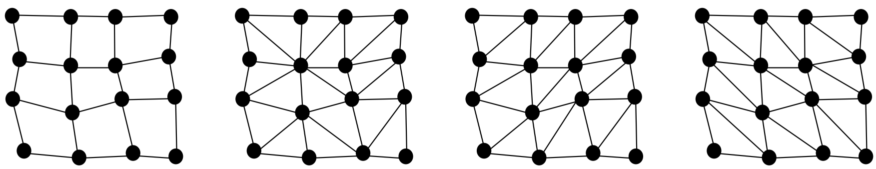

(a) Quad (b) Adaptive (c) Left cut (d) Right cut

Fig. 2. Fast approximate meshing using a quad mesh (a) and different triangulations (b-d). Compared to the adaptive approach (b), triangulations using only left cuts (c) or only right cuts (d) can be obtained slightly faster.

We traverse a given range image R once and check for every point $\mathbf{p}_i = R(u,v)$:

- if $R(u,v)$ and its neighbors $R(u,v+1)$, $R(u+1,v+1)$, and $R(u+1,v)$ (in the next row and the next column) are valid depth measurements, as well as
- if all edges between $R(u,v)$ and these three neighbors are not occluded.

The first check is necessary because of the structure in the sensory data that we exploit. If the sensor cannot acquire a valid depth measurement for a certain pixel, it has to store an invalid one, in order to keep the structure organized.

The latter occlusion checks can be easily done by examining the difference vectors between $\mathbf{p}_i$ and its three neighbors. If it falls into a common line of sight with the viewpoint from where the measurements have been taken, one of the underlying surfaces occludes the other. The condition for the validity of an edge between point $\mathbf{p}_i$ and its neighbor $\mathbf{p}_j$ can be formulated as

$$valid = \left(\left(\left| \mathbf{p}_i \cdot \mathbf{p}_j \right| \leq \cos \varepsilon_\theta \right) \wedge \left(\| \mathbf{p}_i - \mathbf{p_j} \|^2 \leq \varepsilon_d^2 \right) \right), \tag{1}$$

where ε_θ and ε_d denote maximum angular and length tolerances, respectively.

If all checks are passed, $R(u,v)$ and its neighbors are used to extend the so far built mesh. Otherwise, holes arise. Referring to Fig. 2, we distinguish four types of meshes:

1. Quad meshes are formed by connecting pixel $R(u,v)$ to $R(u,v+1)$, $R(u+1,v+1)$, and $R(u+1,v)$.
2. Fixed left and right cut meshes are formed by cutting quads either from top right to bottom left (left cut) or from top left to bottom right (right cut).
3. Adaptive triangulation cuts the quad along the diagonal that has a smaller length.

For triangulations, a single invalid neighbor causes that only one triangle is added. After construction, we simplify the resulting mesh by removing all vertices that are not used in any polygon. An example triangulation is shown in Fig. 3(b).

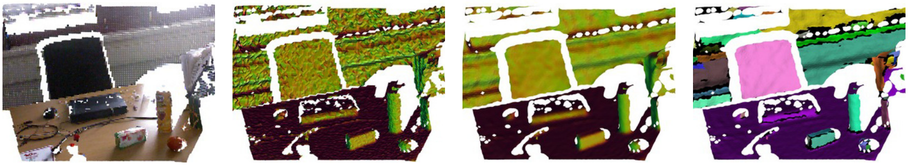

(a) Input cloud (b) Initial mesh (c) Filtered mesh (d) Segmented mesh

Fig. 3. Approximate surface reconstruction, bilateral filtering and segmentation on an example point cloud (a). The filtered mesh (c) is considerably smoother than the initially approximated mesh (b) and allows for cleanly segmenting regions of local surface continuity (d). The meshes in (b) and (c) are colored w.r.t. the vertices' normal orientation (mapped to RGB space, object-space normal map). In (d) segments are colored randomly.

3.2 Fast Computation of Surface Normals and Curvature

We compute the local surface normal $\mathbf{n}_i$ for point $\mathbf{p}_i$ as the weighted average of the plane normals of the faces surrounding $\mathbf{p}_i$. Using the cross product between the difference vectors of the bounding vertices to compute the face normals, and choosing the weights to be proportional to the area of triangles, removes the need of normalizing the face normals beforehand. Thus, we can obtain $\mathbf{n}_i$ as:

$$\mathbf{n}_i = \frac{\sum_{j=0}^{N_T} (\mathbf{p}_{j,a} - \mathbf{p}_{j,b}) \times (\mathbf{p}_{j,a} - \mathbf{p}_{j,c})}{\| \sum_{j=0}^{N_i} (\mathbf{p}_{j,a} - \mathbf{p}_{j,b}) \times (\mathbf{p}_{j,a} - \mathbf{p}_{j,c}) \|}, \tag{2}$$

where $\mathbf{p}_{j,a}$, $\mathbf{p}_{j,b}$ and $\mathbf{p}_{j,c}$ form triangle j. In the actual implementation, we simply iterate over the faces, compute the difference vectors and their cross product, and add them to the normals of the involved points. Finally, we normalize all point normals at once. An example for computed local surface normals (color coded) can be seen in Fig. 3(b).

3.3 Bilateral Filtering

Naturally, sensor measurements are affected by noise. Since this noise can hinder further processing like segmentation, we apply a bilateral filter for smoothing both the points and their normals while preserving edges in the sensed geometric structures. Again, instead of searching, we directly extract a point's neighborhood from the mesh. That is, we filter both a point $\mathbf{p}_i$ and its normal $\mathbf{n}_i$ over its 1-ring-neighborhood N_i, i.e., all points that are directly connected to $\mathbf{p}_i$ by an edge in the mesh:

$$\mathbf{p}_i = \sum_{j \in N_i} w_{ij} \mathbf{p_i} / \sum_{j \in N_i} w_{ij}, \qquad \mathbf{n}_i = \sum_{j \in N_i} w_{ij} \mathbf{n_i} / \sum_{j \in N_i} w_{ij}, \tag{3}$$

$$w_{ij} = \underbrace{e^{\|\mathbf{p}_i - \mathbf{p_j}\|}}_{\text{distance term}} \underbrace{e^{\|\mathbf{n}_i - \mathbf{n}_j\|_1}}_{\text{normal term}} \underbrace{e^{(I_i - I_j)/c_I}}_{\text{intensity term}}, \tag{4}$$

where the optional intensity term is only evaluated for colored point clouds and range images where also an intensity image is available. The normalization constant c_I is used to scale the intensity differences to lie in the interval $[0,1]$. An example of filtering an input mesh can be seen in Fig. 3(c).

3.4 Region Growing-Based Segmentation

Despite the generalization over different neighborhood searches and region models, the implementation of our segmentation algorithm does not considerably deviate from other region growing algorithms in the literature. Given a set of seed points (and a priority queue of seeds),

Outer loop, until all points are processed:
1. we iteratively select the next seed point,
2. initialize the region model of interest, and
3. put the seed point onto the empty processing queue.

Inner loop, while the processing queue is not empty:
4) We take the next point from the processing queue,
5) check its compatibility with the region model,
6) and add it in case of compatibility.
7) We add the point's neighbors to the processing queue (again, only if they're compatible).

3.5 Different Region Models for Segmentation

We have encapsulated the processing steps (2) initialization, (5) point compatibility, (6) model update, and (7) neighbor compatibility in exchangeable region models allowing to configure and control the behavior of the segmentation.

We have implemented several region models for approximate plane segmentation using local surface normals, as well as for segmenting regions of local surface continuity as a pre-segmentation for further processing. Both are detailed in the following. In addition, we added models that reproduce the behavior of segmentation algorithms found in the literature.

Approximate Plane Segmentation. For plane segmentation, we initialize the centroid and the normal of the region model using the seed point and its normal (instead of computing them using an initial set of points as in the approach of Poppinga et al. [13]). In order to determine the compatibility of a point $\mathbf{p}_i$ to the model, we simply check the angle between its normal $\mathbf{n_i}$ and the normal in the plane model, as well as $\mathbf{p}_i$'s distance to the plane. For updating the model w.r.t. $\mathbf{p}_i$, we incrementally update the plane's centroid, but instead of incrementally updating a covariance matrix to derive a plane normal from it, we incrementally update its centroid in normal space. That is, by pre-computing the surface normals on the mesh neighborhood, and approximating the plane normal by averaging over point normals, we can reduce the number of computations considerably.

In order to obtain full polygonalizations as the one shown in Fig. 1(d), we 1) compute the convex or concave hulls (using alpha shapes) for all planar patches, and, if a triangulation is required, 2) decompose them again using ear clipping.

Extracting Locally Smooth Surfaces. For detecting geometric primitives, we need a rough pre-segmentation of the scene. This can easily be accomplished within the neighbor compatibility check of the models by, e.g., examining changes in the local surface curvature or comparing a point's surface normal with either the region's mean surface normal or the surface normal of the seed point. A typical result of applying a segmentation using the latter model is shown in Fig. 3(d). Points on the same physical (locally smooth) surface end up in the same segment.

3.6 Detecting Geometric Primitives

For every locally smooth segment, we try to find the geometric primitive that best explains the underlying point set. Whereas we can directly compute a least squares plane fit to all the points in a segment, we use RANSAC to find the best sphere and cylinder model. Here, the computational efficiency of our approach comes from applying RANSAC only if the computed planar model does not fully explain the segment. Typical results of applying the rough pre-segmentation and primitive detection are shown in Fig. 4.

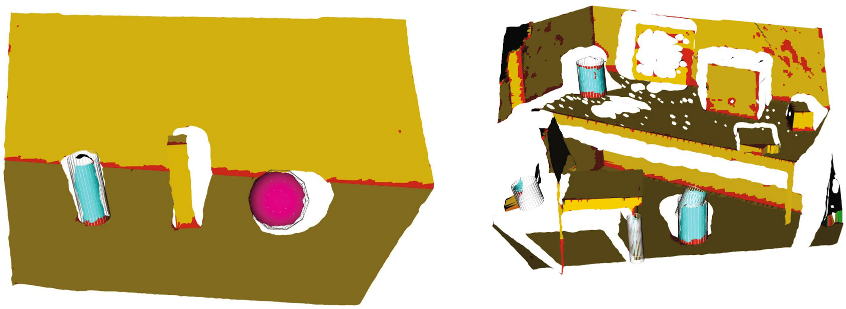

(a) Example 1 (b) Example 2

Fig. 4. Examples of detecting planes (yellow), cylinders (cyan) and spheres (magenta). Points and polygons belonging to multiple segments are colored red. All points are projected onto the found models.

Since we still stick to the RANSAC-based primitive detection for spheres and cylinders, we focus the experimental evaluation to plane segments directly obtainable from region segmentation and extracted using our approximate model.

4 Experiments and Results

We evaluate the correctness and efficiency of our approach using two publicly available data sets for which ground truth plane segmentations are available: the SegComp data set from Hoover et al. [2], and the recently published Kinect data set by Oehler et al. [17]. For the evaluation, we follow (and refer to) the scheme of [2]. Measured runtimes of the individual processing steps show that our approach can process range images at high frame rates—at a resolution of 160×120 in real-time with 30 Hz (see

Table 1). Compared the approach of Oehler et al. [17], we obtain better segmentation results (see Table 2) while being a faster by a factor of 4 (they need >100 ms for 160×120, and > 2 s for 640×480).

4.1 Estimating a Simple Isotropic Noise Model

For all the aforementioned region models, parameters like, for instance, the distance to the model and the deviation between surface normals play an important role. Whereas the latter can be neglected after applying the bilateral filter, the distance to the model is a parameter that is crucial for the quality of the segmentation. It resembles the amount of noise hindering a measurement to lie on the ideal model.

In order to obtain a rough estimate of the amount of noise at a given point, we use a simple isotropic noise model. As suggested in [18], we assume Gaussian noise $\mathcal{N}(0, \sigma^2)$ and use a simple quadratic polynomial of distance to determine σ, since noise in range sensors usually increases quadratically with the measured distance. Since the primary sensor used in our work is a Microsoft Kinect camera, we have computed a simple error model for this sensor. In 10 different scenes (ranging from scenes with only close range measurements to views of wide open space), we have collected 100 range images each. For each of the locations, we compute the mean and standard deviation per pixel and perform a least squares fit to find appropriate coefficients for the quadratic model; resulting in:

$$\sigma(d) = 0.00263d^2 - 0.00518d + 0.00752. \tag{5}$$

For the range images in the SegComp data set, that are slightly more affected by noise, we simply set $2\sigma(d)$ as the maximally allowed deviation of a point to its region model.

4.2 Plane Segmentation Using the SegComp Data Sets

Typical results of applying the presented approximate plane segmentation on range images and organized point clouds can be seen in Figures 5 and 6. Considering our goal of obtaining a fast decomposition into dominant planes and other objects of interest, the obtained results are more than satisfying. Moreover, as can be seen in the detailed comparison in Table 2, the proposed method does not considerably rank behind state-of-the-art range image segmentation approaches, while providing very efficient means to compute—within milliseconds—rough scene segmentations.

On the ABW data set [2], our approximate plane segmentation approach tends to over-segment the range image. This is caused by a special characteristic of the used camera that is not explicitly handled here resulting in inconsistent normal orientations. Besides over-segmented planar patches, our approach correctly detects 80% of the planes.

In the PERCEPTRON data set, no special sensor characteristics cause errors and our approach yields similar results as the work by Gotardo et al. [6]. Referring to Table 2, over-segmentations are rare for our approach. Instead, a considerable amount of ground truth planes is not perceived. These planes are formed by only a small number of points and are neglected here due a minimum region cardinality that we use to eliminate very small planar patches.

We also evaluated our approach using the recently published Kinect data set by Oehler et al. [17]. This data set comprises two different sets of point clouds with corresponding ground truth segmentations – one for plane segmentation and one for cylinder segmentation. Naturally, we obtain a larger amount of over-segmentations here, since larger cylinders in the planes data set are labeled as noise while unconnected regions

Table 1. Measured runtimes* for the individual processing steps

Resolution	160×120	320×240	640×480
Mesh Construction	11 ms	45 ms	188 ms
Computing Normals	2 ms	7 ms	33 ms
Smoothing/Filtering	10 ms	38 ms	155 ms
(Plane) Segmentation	6 ms	30 ms	126 ms
Overall Frequency	$\approx$ 35 Hz	$\approx$ 8 Hz	$\approx$ 2 Hz

*Measured over 1000 runs on an Intel Core 2 DUO 2.26 GHz (no parallelization), using approximate plane segmentation (Sec. 3.5) of a mesh constructed using adaptive triangulation (Sec. 3.1).

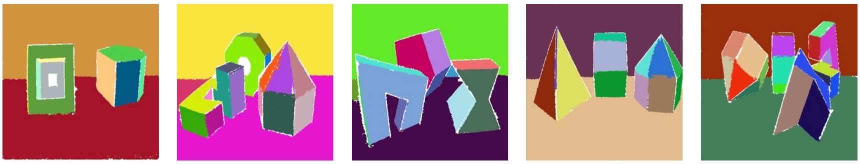

(a) 10 / 14, 4 misses (b) 18 / 24, 6 misses (c) 10 / 13, 2 over, 1 miss (d) 12 / 13, 1 over (e) 22 / 22

Fig. 5. Plane segmentation using the SegComp PERCEPTRON training data set (segments randomly colored). In total, 109 of 126 planes were correctly segmented (approx. 86.5%). Not correctly found are very small plane segments, e.g., the inner parts of the objects in (a) and (b). In addition, some planes are oversegmented due to noise, e.g., the support plane in (c). The estimated plane normals deviate from ground truth by roughly $(2.5 \pm 1.6)^\circ$.

(a) 10 / 11 (b) 9 / 10 (c) 9 / 9 (d) 5 / 8, 3 over (e) 5 / 9, 2 over, 2 miss

Fig. 6. Approximate plane segmentation using (a-c) the SegComp ABW data set [2], and (d-e) the data set by Oehler et al. [17]. ABW: On average, 12.2 planes out of 15.2 planes are correctly segmented, while roughly two planes per image are oversegmented. Kinect: for the data set from [17] over-segmentations are primarily caused by detecting planes on the surface of cylinders or in small regions not marked as beloning to planes in ground truth. Overall, roughly 58 % of planes are correctly segmented (80% pixel overlap), while Oehler et al. only achieve 54.9 % (at 51 % pixel overalp, see [17]).

Table 2. Detailed benchmarking results on the SegComp data sets for plane segmentation

Approach	correctly detected	orientation deviation	over-segmented	under-segmented	missed / not detected	noise / non-existent
SegComp ABW data set (30 test images) from [2], (80 % pixel overlap as in [6])						
USF[6]	12.7 (83.5%)	1.6°	0.2	0.1	2.1	1.2
WSU [6]	9.7 (63.8%)	1.6°	0.5	0.2	4.5	2.2
UB [6]	12.8 (84.2%)	1.3°	0.5	0.1	1.7	2.1
UE [6]	13.4 (88.1%)	1.6°	0.4	0.2	1.1	0.8
OU [6]	9.8 (64.4%)	–	0.2	0.4	4.4	3.2
PPU [6]	6.8 (44.7%)	–	0.1	2.1	3.4	2.0
UA [6]	4.9 (32.2%)	–	0.3	2.2	3.6	3.2
UFPR [6]	13.0 (85.5%)	1.5°	0.5	0.1	1.6	1.4
Oehler et al. [17]	11.1 (73.0%)	1.4°	0.2	0.7	2.2	0.8
Ours	12.2 (80.1%)	1.9°	1.8	0.1	0.9	1.3
SegComp PERCEPTRON data set (30 test images) from [2], (80 % pixel overlap as in [6])						
USF [6]	8.9 (60.9%)	2.7	0.4	0.0	5.3	3.6
WSU [6]	5.9 (40.4%)	3.3	0.5	0.6	6.7	4.8
UB [6]	9.6 (65.7%)	3.1	0.6	0.1	4.2	2.8
UE [6]	10.0 (68.4%)	2.6	0.2	0.3	3.8	2.1
UFPR [6]	11.0 (75.3%)	2.5	0.3	0.1	3.0	2.5
Oehler et al. [17]	7.4 (50.1%)	5.2	0.3	0.4	6.2	3.9
Ours	11.0 (75.3%)	2.6	0.4	0.2	2.7	0.3

belonging to a single plane are labeled as one segment. However, visually inspecting the segmentation results reveals that all dominant planes are reliably segmented.

5 Conclusions and Future Work

We have presented a simple, yet efficient approach to segmenting range images and organized point clouds. Using an approximate polygonal reconstruction directly deduced from the image-like structure, we are able to efficiently compute point features such as local surface normals, and to smooth the measured data using a bilateral filter.

Experimental evaluation has shown that our approach does not considerably rank behind state-of-the-art range image segmentation techniques. However, regarding its computational complexity, it exploits several simplifications and approximations finally making the overall segmentation (and primitive detection) algorithm run within milliseconds on point clouds acquired by typical RGB-D cameras.

It remains a matter of future work to exploit the extracted information about segmented planar patches (and geometric primitives) in further processing steps like registration.

Implementations of all components presented in this paper are (or are going to be) publicly available within the open source Point Cloud Library PCL[1].

[1] The latest stable release of the Point Cloud Library PCL is available at `http://pointclouds.org`

References

1. Rusu, R.B., Blodow, N., Marton, Z.C., Beetz, M.: Close-range scene segmentation and reconstruction of 3D point cloud maps for mobile manipulation in human environments. In: Proc. of the IEEE/RSJ International Conference on Intelligent Robots and Systems (IROS), St. Louis, MO, USA, pp. 1–6 (2009)
2. Hoover, A., Jean-Baptiste, G., Jiang, X., Flynn, P.J., Bunke, H., Goldgof, D.B., Bowyer, K., Eggert, D.W., Fitzgibbon, A., Fisher, R.B.: An experimental comparison of range image segmentation algorithms. IEEE Transactions on Pattern Analysis and Machine Intelligence 18, 673–689 (1996)
3. Vosselman, G., Gorte, B.G.H., Sithole, G., Rabbani, T.: Recognising structure in laser scanner point clouds. Information Sciences 46(8), 1–6 (2004)
4. Lee, K.-M., Meer, P., Park, R.-H.: Robust adaptive segmentation of range images. IEEE Transactions on Pattern Analysis and Machine Intelligence 20, 200–205 (1998)
5. Silva, L., Bellon, O., Gotardo, P.: A global-to-local approach for robust range image segmentation. In: Proc. of the Int. Conference on Image Processing (ICIP), Rochester, NY, USA, pp. 773–776 (2002)
6. Gotardo, P., Bellon, O., Silva, L.: Range image segmentation by surface extraction using an improved robust estimator. In: Proc. of the IEEE Conference on Computer Vision and Pattern Recognition (CVPR), Madison, WI, USA, pp. 33–38 (2003)
7. Schnabel, R., Wahl, R., Klein, R.: Efficient RANSAC for point-cloud shape detection. Computer Graphics Forum 26(2), 214–226 (2007)
8. Holz, D., Schnabel, R., Droeschel, D., Stückler, J., Behnke, S.: Towards semantic scene analysis with time-of-flight cameras. In: Proc. of the 14th RoboCup International Symposium, Singapore, (2010)
9. Holz, D., Holzer, S., Rusu, R.B., Behnke, S.: Real-Time Plane Segmentation Using RGB-D Cameras. In: Röfer, T., Mayer, N.M., Savage, J., Saranlı, U. (eds.) RoboCup 2011. LNCS, vol. 7416, pp. 306–317. Springer, Heidelberg (2012)
10. Stückler, J., Steffens, R., Holz, D., Behnke, S.: Real-time 3D perception and efficient grasp planning for everyday manipulation tasks. In: Proc. of the European Conference on Mobile Robots (ECMR), Örebro, Sweden, pp. 177–182 (2011)
11. Borrmann, D., Elseberg, J., Lingemann, K., Nuechter, A.: The 3D Hough transform for plane detection in point clouds: A review and a new accumulator design. 3D Research 2, 1–13 (2011)
12. Hähnel, D., Burgard, W., Thrun, S.: Learning compact 3D models of indoor and outdoor environments with a mobile robot. Robotics and Autonomous Systems 44(1), 15–27 (2003)
13. Poppinga, J., Vaskevicius, N., Birk, A., Pathak, K.: Fast plane detection and polygonalization in noisy 3D range images. In: Proc. of the IEEE/RSJ International Conference on Intelligent Robots and Systems (IROS), Nice, France, pp. 3378–3383 (2008)
14. Harati, A., Gächter, S., Siegwart, R.: Fast range image segmentation for indoor 3D-SLAM. In: Proc. of the IFAC Symposium on Intelligent Autonomous Vehicles (IAV), Toulouse, France (2006)
15. Rabbani, T., van den Heuvel, F., Vosselman, G.: Segmentation of point clouds using smoothness constraint. International Archives of the Photogrammetry, Remote Sensing and Spatial Information Sciences 36, 248–253 (2006)
16. Cupec, R., Nyarko, E.K., Filko, D.: Fast 2.5D mesh segmentation to approximately convex surfaces. In: Proc. of the European Conference on Mobile Robots (ECMR), Örebro, Sweden, pp. 49–54 (2011)

17. Oehler, B., Stueckler, J., Welle, J., Schulz, D., Behnke, S.: Efficient Multi-resolution Plane Segmentation of 3D Point Clouds. In: Jeschke, S., Liu, H., Schilberg, D. (eds.) ICIRA 2011, Part II. LNCS, vol. 7102, pp. 145–156. Springer, Heidelberg (2011)
18. Anderson, D., Herman, H., Kelly, A.: Experimental characterization of commercial flash ladar devices. In: International Conference of Sensing and Technology, Palmerston North, New Zealand (2005)

Resilient Navigation through Probabilistic Modality Reconfiguration

Thierry Peynot[1], Robert Fitch[1], Rowan McAllister[1], and Alen Alempijevic[2]

[1] Australian Centre for Field Robotics, The University of Sydney, NSW 2006, Australia
{tpeynot,rfitch,r.mcallister}@acfr.usyd.edu.au
[2] Mechatronics and Intelligent Systems Group, University of Technology Sydney, NSW 2007, Australia
Alen.Alempijevic@uts.edu.au

Abstract. This paper proposes an approach to achieve resilient navigation for indoor mobile robots. Resilient navigation seeks to mitigate the impact of control, localisation, or map errors on the safety of the platform while enforcing the robot's ability to achieve its goal. We show that resilience to *unpredictable* errors can be achieved by combining the benefits of independent and complementary algorithmic approaches to navigation, or *modalities*, each tuned to a particular type of environment or situation. In this paper, the modalities comprise a path planning method and a reactive motion strategy. While the robot navigates, a Hidden Markov Model continually estimates the most appropriate modality based on two types of information: context (information known *a priori*) and monitoring (evaluating unpredictable aspects of the current situation). The robot then uses the recommended modality, switching between one and another dynamically. Experimental validation with a SegwayRMP-based platform in an office environment shows that our approach enables failure mitigation while maintaining the safety of the platform. The robot is shown to reach its goal in the presence of: 1) unpredicted control errors, 2) unexpected map errors and 3) a large injected localisation fault.

1 Introduction

Motion planning and control of a mobile robot necessarily involves multiple sources of uncertain information such as control uncertainty, localisation uncertainty, and mapping errors. Current research seeks to address these sources of uncertainty by modelling them in the context of the planning problem [1,5]. However, problems arising during execution of a plan are not always predictable (and hence able to be modelled). For example, it is difficult to predict localisation errors ahead of time, or to anticipate which map locations actually contain large errors. We are interested in mitigating the impact of such unpredictable errors on robot performance and safety. We introduce the term *resilience* to refer to this goal. Resilient navigation seeks to mitigate the impact of control, localisation, and map errors on the safety of the platform while enforcing the robot's ability to achieve its goal.

In this paper, we study resilient navigation in the context of indoor mobile robots. We believe resilience is best achieved by combining the benefits of multiple independent

S. Lee et al. (Eds.): Intelligent Autonomous Systems 12, AISC 194, pp. 75–88.
springerlink.com

algorithmic approaches, or *modalities*, each tuned to a particular type of environment or situation. The idea is to develop a set of modalities that covers the range of possible situations, and then to reconfigure the system dynamically in response to unpredicted errors. The key challenges are: 1) how to choose a suitable set of modalities, 2) how to represent information that describes the robot's context, and 3) how to decide which modality is most appropriate at any given time. Because we are dealing with uncertain information, these challenges require solutions in probabilistic form.

Our approach in choosing a set of modalities is to include a motion planning strategy that requires global information, and a reactive strategy that requires only local information. These two modalities are complementary. If the navigation goal is within the field of view (FOV) of the robot, a reactive obstacle avoidance approach (e.g. [8, 10]) can be feasible. However, reactive approaches have known limitations. They can become trapped in dead-ends or U-shape obstacles, and it is difficult to obtain smooth trajectories. If the goal is located outside of the robot's FOV, the recommended strategy is to use a motion planning algorithm that reasons more globally, especially if some prior knowledge of the environment is available. In addition, smoother and more efficient paths can be obtained (see Fig. 1). However, in cluttered environments, such a strategy can only be effective if sufficiently accurate map and global localisation are available. In addition, the control of the platform needs to be robust and precise enough to follow the planned trajectory.

An alternative is to combine the two strategies to obtain a *hybrid* system [4]. Typically, a motion planning algorithm computes a global plan, generating a list of way-points along the computed trajectory which are passed to a reactive motion method. A drawback of these hybrid techniques is that even if the motion planner can produce smooth trajectories (or trajectories respecting some pre-defined constraints), the execution of such types of trajectories cannot be enforced. Another inconvenience is that events that provoke failure of one of the components will often provoke failure of the combination, whereas this can be mitigated by using the appropriate method at the right time. A comparison of the different strategies discussed in this paper is shown in Table 1.

Table 1. Comparison of navigation strategies

Strategy:	**Planning**	**Reactive**	**Hybrid**	**Our approach**
Robust to dead-ends	√	×	√	√
Robust to dynamic obstacles	×	√	√	√
Robust to errors in localisation or map	×	√	√	√
Optimised paths (when possible)	√	×	×	√

Instead, we propose a modality-switching algorithm based on a *hidden-markov model* (HMM) that considers *context* and *monitoring* information. If the system is aware that path execution cannot safely handle a difficult situation such as a narrow doorway, it is appropriate to switch to a reactive strategy. This situation can be evaluated using the localisation of the robot in a map, and detecting the presence of this narrow passage. However, reasoning only on this context information will not be sufficient to handle situations where the error/uncertainty of global localisation is high, where elements of the map have moved, or where a dynamic obstacle has appeared. Fast local replanning integrating map updates can partially address this problem but is computationally expensive and can lead to instabilities in control. Therefore, we propose to choose a modality based on context information *and* monitoring information (such as proximity to obstacles observed from laser data).

We evaluate our approach through hardware experiments with an indoor mobile robot in an office environment. We show that failures can be mitigated in challenging situations while maintaining the safety and liveness of the platform. The situations we consider include: control errors, localisation errors, map errors (unexpected obstacles), and presence of an "aggressive" human dynamic obstacle.

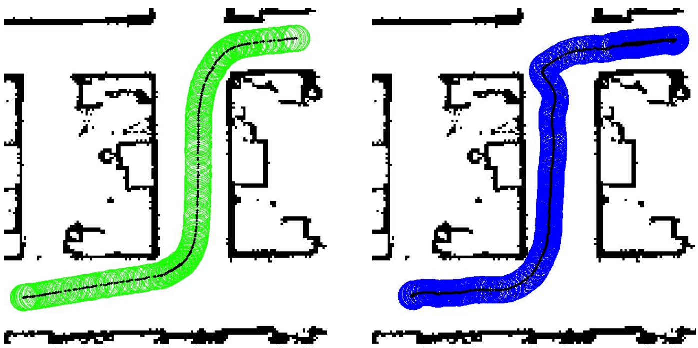

(a) *PLAN* (b) *REACT* (Hybrid)

Fig. 1. Trajectory obtained using a planner (a) and a *hybrid* approach (b). Obstacles in the map are in black. Circles represent the radius of the robot. Approximate size of the area shown: $6.5m \times 7.5m$.

2 Related Work

Previous work has considered multi-modal systems for the navigation of an indoor mobile robot. [11] proposed the Robel system: a robot controller that learns different ways of combining sensory-motor functions to achieve a navigation task. Robel uses a Markov decision process (MDP) to provide a policy. However, MDPs are generally computationally expensive and policies often have to be computed off-line or at low frequencies. Our system was designed to be efficient enough for the robot to be reactive: modality switching can happen quickly when needed. Besides, an MDP requires the states to be fully observable. [15] proposed a system based on a partially observable MDP (POMDP) that can be used to detect, diagnose and recover from faults. However, the policy is computed off-line and the robot does not have a real alternative navigation modality when the path planning strategy fails. Our approach does not require explicit detection and identification of specific faults such as a localisation error; it focuses on mitigating failures that could occur in consequence, finding alternatives to obtain robustness while maintaining safety.

Motion planning and obstacle avoidance are well-studied problems in the literature. See [6] for a comprehensive review up to 2005. More recently, researchers have sought to address motion planning under uncertainty in control [1], localisation [5] or sensing and environment map [9]. However, these studies typically require the ability to *predict* possible errors, as they need to model the uncertainty in the context of the planning problem. In this paper, we are interested in mitigating the impact of *unpredictable* errors.

3 Probabilistic Modality Reconfiguration

The approach we propose is a probabilistic framework for an indoor robot endowed with two main navigation modalities: 1) a global planner (*PLAN*), and 2) a reactive motion approach (*REACT*). In addition, a *STOP* modality is included for emergency and safety. This method builds on our previous work for an outdoor mobile robot with modalities appropriate to flat terrain and rough terrain [13].

Our approach is to estimate the likelihood of each modality being most suitable using an HMM. The HMM is appropriate since states are not directly observable and it provides a time integration that prevents jitter (too frequent modality changes, see Fig. 5). Crucially, the probabilistic approach allows the system to handle uncertainty in the different sources of information.

The goal of the HMM is to provide a *modality recommendation*. The HMM is constructed such that the number of states is equal to the number of available modalities. Fig. 2 provides a graphical representation of our three-state HMM, where each state x_k corresponds to the proposition: "modality m_k is the appropriate modality to apply at this point in time."

Two categories of information are input to the HMM: 1) *context* information is global environmental knowledge known *a priori*, and 2) *monitoring* information is online execution knowledge of the observed immediate situation. The framework is designed as a Markov *conditional estimation* system [2]. It estimates the conditional state $x_{k,t}$ at time t, knowing context observation until time t, $O_{1:t}$, and online monitoring information $M_{1:t}$. If the robot is endowed with N different modalities, the probability that m_k is the appropriate modality to apply at time t can be written, $\forall k \in [\![1,N]\!]$,

$$P(x_{k,t}|O_{1:t},M_{1:t}) \propto P(O_t|x_{k,t}) \sum_{i=1}^{N} P(x_{k,t}|x_{i,t-1},M_t) P(x_{i,t-1}|O_{1:t-1},M_{1:t-1}) \qquad (1)$$

where $P(O_t|x_{k,t})$ is an observation probability (computed using the *context* information), and $P(x_{k,t}|x_{i,t-1},M_t)$ is the conditional probability of transition from state x_i to state x_k, knowing the *monitoring* data M_t at time t. The following sub-sections describe more specifically the different modalities of the robot used in this paper and the nature of the context and monitoring information.

3.1 Context

The context information relates to the distance d from the robot boundaries to the closest obstacles as seen on an *a priori* global map. This information is used to predict the

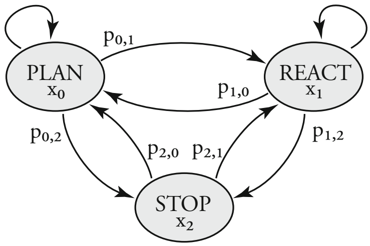

Fig. 2. Graphical representation of the 3-state HMM

likely modality at a given map location. We determined experimentally that the *PLAN* modality is likely to fail in situations where the robot is too close to obstacles, i.e. closer than a *security distance* $d_s = 0.15m$, equal to half the radius of the robot. Therefore, intuitively, the *a priori* recommendation based on context information is to use *PLAN* in areas sufficiently clear from obstacles ($d > d_s$), *REACT* in areas that are close to an obstacle on the global map ($d \leq d_s$), and *STOP* in places immediately proximal to obstacles ($d < d_c$, *critical distance*).

d (the observation O_t) is calculated online using the current localisation of the robot in the map. To integrate this observation in the system (HMM), probability density functions (pdf) are used to take into account uncertainties. The main sources of uncertainties are the (x, y) localisation of the robot in the map and the location of the obstacles in the map itself. The map is an occupancy grid that was built using the laser of the robot assuming perfect localisation. Therefore, the map uncertainty can be expressed as $\sigma_{map} = \sigma_{laser}$, the standard deviation of the range measurements of the laser scanner. $\sigma_{laser} = 0.03\ m$ for the Hokuyo laser on our robot.

The uncertainty in the *a priori* map is independent of the uncertainty of the current localisation, as the map was built beforehand, using a different localisation. Therefore, the standard deviation on the observation of d can be expressed as the sum of the uncertainties: $\sigma = \sigma_{map} + \sigma_{loc}$, where σ_{loc} represents the localisation uncertainty provided by the algorithm mentioned in Sec. 4.

3.1.1 Modality STOP

We define the distribution of $p(O_t|x_2)$, or $p(d|STOP)$, as an inverse sigmoid centred on the critical distance d_c (see Fig. 3 in red):

$$P(d|STOP) = 1 - \frac{1-\alpha}{1 + e^{-(d-d_c)/\sigma}} \tag{2}$$

where σ partly defines the curvature of the sigmoid. σ (similar to the standard deviation of a Gaussian) corresponds to the uncertainty in d, and $d_c = 0$ is the critical distance.

The distribution $p(d|STOP)$ represents the likelihood that observation d is made, knowing that the robot should stop. The inverse sigmoid accounts for the uncertainty in the observation and in the knowledge of this threshold value. The limit of this sigmoid, when d tends to infinity, is superior to zero (see Fig. 3). This accounts for the fact that the map does not capture all information in the world, in particular dynamic obstacles.

The value of this limit represents the chance of having to stop the robot while infinitely away from map obstacles, i.e. the chance of having a dynamic object appearing withing less than d_c of the robot, α. It is crucial to account for the possibility of this event sufficiently so that the system maintains a chance of capturing it [7]. Thus, this value is set to a value higher than the actual probability of occurrence as would be determined statistically. In our implementation we set $\alpha = 0.05$.

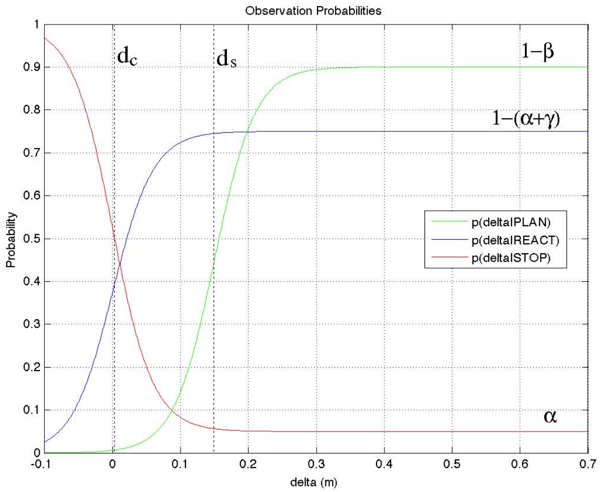

Fig. 3. Probability density functions for the context information (shown before normalisation, with $\sigma_{loc} = 0$). These are functions of d, representing the distance to the closest obstacles to the robot, as seen in the map.

3.1.2 Modality REACT

The distribution of $p(O_t|x_1)$, or $p(d|REACT)$, is defined as a sigmoid centred on d_c (see Fig. 3 in blue):

$$P(d|REACT) = \frac{1-(\alpha+\gamma)}{1+e^{-(d-d_c)/\sigma}} \tag{3}$$

where $\sigma = \sigma_{map} + \sigma_{loc}$, as defined earlier. To guarantee safety, the main restriction for this modality is that it cannot be used too close to obstacles ($d < d_c$), hence the sigmoid.

There are two secondary restrictions. One consideration is the chance of a dynamic object appearing within a distance d_c to the robot, i.e. $\alpha = 0.05$. The other is the *a priori* chance of failure of *REACT* in general, even in an open map (recall that this modality is subject to local minima). This chance of failure highly depends on the environment, which we capture with the probability: $\gamma = 0.20$. Considering the events represented by α and γ as independent, the limit of the sigmoid $p(d|REACT)$ when d tends to infinity is set to $1-(\alpha+\gamma) = 0.75$.

3.1.3 Modality PLAN

The distribution of $p(O_t|x_0)$, or $p(d|PLAN)$, is also defined as a sigmoid, centred on the security distance d_s (see Fig. 3 in green):

$$P(d|PLAN) = \frac{1-\beta}{1+e^{-(d-d_s)/\sigma}} \tag{4}$$

Note that once again the limit of the sigmoid $p(O_t|m_0)$ when d tends to infinity is lower than 1. This accounts for the chance of having dynamic objects appearing within d_s of the robot bounds. We consider the prior probability of this event to be $\beta = 0.10$ ($\beta > \alpha$), therefore the limit of the sigmoid distribution is $1-\beta = 0.9$. For high values of d it is important to set the chance of success of *PLAN* higher than *REACT* (if the goal is far, it is known that *PLAN* is more likely to succeed), i.e. $\beta < \alpha + \gamma$. Finally, note that these distributions need to be normalised before integration in the HMM.

3.2 Monitoring

Contrary to context information, the purpose of monitoring information is to check the actual "appropriateness" of the current situation, with regard to the possible modalities, using data only observable during execution. The online monitoring uses δ, the distance from the robot bounds to the closest obstacle detected in laser measurements. Recall that the online monitoring contributes to the computation of the transition probabilities of the HMM. If the robot gets too close to obstacles seen in current laser scans while operating in *PLAN*, it should switch to *REACT*. In this way, if global localisation is temporarily inaccurate, or if obstacle points are in a different location than on the (static) global map, this situation can be handled by *REACT*, contrary to *PLAN*.

More specifically, the intuitive rules of transitions (given here without uncertainty, for convenience) are the following. The corresponding transition probabilities used in the HMM are given in parenthesis, in both full (e.g. $P(x_2|x_1,\delta)$) and equivalent reduced form (e.g. $p_{1,2}$). First, let us consider the output transitions of x_0 (i.e. *PLAN*).

- The transition $P(x_1|x_0,\delta) = p_{0,1}$ (*PLAN* to *REACT*) is likely if $d_c < \delta < d_s$, i.e. an obstacle is detected by the laser in the *intermediate* proximity of the robot.
- The transition $P(x_2|x_0,\delta) = p_{0,2}$ (*PLAN* to *STOP*) is likely if $\delta < d_c$, i.e. an obstacle is detected by the laser in the *immediate* proximity of the robot.
- $P(x_0|x_0,\delta) = p_{0,0}$ (*PLAN* to *PLAN*) is likely if $\delta > d_s$, i.e. the robot is clear from obstacles.

The other transitions can be defined similarly, using the same short notations as above: $p_{1,0} = p_{2,0} = p_{0,0}$, $p_{1,1} = p_{2,1} = p_{0,1}$, $p_{1,2} = p_{2,2} = p_{0,2}$.

Because of the uncertainty in δ (the laser measurements), these rules are defined probabilistically using sigmoid distributions similar to those defined in Sec. 3.1 and shown in Fig. 3. In this case the main source of uncertainty is the relative inaccuracy of the laser measurements, therefore the σ of the sigmoids is: $\sigma = \sigma_{laser}$. The output transition probabilities from each state are normalised, as their sum must equal 1.

4 Implementation

Our experimental platform consists of the Segway RMP100 base with onboard PCs and various sensors, including a Hokuyo UTM-30LX laser range-finder and encoders in the mobile base for odometry [12]. Localisation is computed using the Monte Carlo Localisation (MCL) algorithm [14]. The robot's belief is represented by a set of weighted hypotheses which approximate the posterior under a common Bayesian formulation of the localisation problem. We update this distribution using data from odometry, the laser range-finder, and a predefined map of the environment.

The test area is an office environment occupied by over 25 people and consisting mainly of student workstations and fixed and movable furniture. This area is thus well-suited for evaluating real-world applicability.

4.1 Available Modalities

Modality m_0 is *PLAN*. We implemented the well-known Latombe Grid-Search algorithm [3] for nonholonomic planning, customised to find paths with minimum change in curvature. Although the name may seem to imply a discrete search space, the algorithm does use continuous coordinates. A detailed summary can be found in [6]. The planner is complete with respect to the resolution of its given proximity grid and time interval of the path set [3]. Because this proof is not constructive, we do not have a method for determining parameter values analytically. We hand-tuned them empirically and found a reasonable grid resolution of $0.2m \times 0.2m \times \frac{\pi}{8} rad$ and path set time intervals of 2 or 4 seconds. Our path set has angular velocities chosen from $\{-\frac{\pi}{4}, -\frac{\pi}{8}, -\frac{\pi}{16}, -\frac{\pi}{32}, 0, \frac{\pi}{32}, \frac{\pi}{16}, \frac{\pi}{8}, \frac{\pi}{4}\}$ and linear velocities from $\{0.2m/s, 0.1m/s\}$. Our priority queue uses a cost function that combines minimum distance to goal with minimum change in curvature.

Modality m_1 is *REACT*. This is a reactive collision avoidance method that avoids sensed obstacles. We implemented a potential field method derived from a model of human navigation [8]. This method directly controls angular acceleration and produces smooth paths. We chose this method because the robot operates in an office-like environment amenable to human-like paths. Because the laser cannot scan all 360° around the robot, the perception data that *REACT* uses is a local fusion of laser scans. Odometry is used for localisation in order to avoid the influence of errors in global localisation.

Modality m_2 is *STOP*. This is the safety modality; it applies when the robot has come too close to an obstacle and the only reasonable option is to halt. If *STOP* was provoked by monitoring information, the robot can only resume when the obstacle responsible for the stop is dynamic and has moved away. To account for this, our system continues to evaluate the HMM recommendation even though the robot is stationary.

4.2 Modality Switching

PLAN is the default starting modality, as it has the highest prior probability. When switching from *PLAN* to *REACT*, a goal waypoint must be chosen. We initially choose the next waypoint on the last path computed by *PLAN*. However, because of localisation or map errors, this waypoint may intersect an obstacle. In this case, the next waypoint of the plan that is confirmed as clear from obstacles becomes the new goal for *REACT*. It is then preferable to switch back to *PLAN* quickly to avoid the risk of *REACT* falling into local minima.

5 Experiments

The experimental validation in this section illustrates the resilience of our probabilistic reconfiguration approach, which allows the mitigation of unpredictable failures. Examples of causes of such failures are: errors of the controller while executing a planned path, errors in the map (i.e. presence of objects that could not be integrated in the map early enough) and large localisation uncertainty or error. We also compare our method to simple threshold rules for modality switching. Results were obtained using the platform described in Sec. 4.

The illustrations show the estimated robot trajectory during each test, using coloured points to represent the modality used at the time. The selected modality corresponds to the highest output probability $P(x_{k,t}|O_{1:t}, M_{1:t})$ at each time step t. The HMM and the modality selection were updated at $10Hz$.

5.1 Modality Reconfiguration in Static Environment

5.1.1 Unpredicted Control Error

The experiment in Fig. 4(a) illustrates how our framework allowed the system to maintain the robot's safety in the presence of unpredicted errors of the controller during execution of the planned trajectory. The robot started executing a planned path similar to the one in Fig. 1(a), which was successful using *PLAN* only. However, at the (expected) end of the turn around the first corner, the controller "overshot", risking the safety of the platform. This event was detected by our system, which switched to *REACT* to recover. When safe, the robot returned to the *PLAN* modality to complete its mission.

5.1.2 Going through a Narrow Doorway

We also tested the robot's ability to follow a corridor and then pass through a $0.85m$-wide doorway (the robot's diameter is $0.6m$). As the corridor is reasonably large (about $1.7m$ in average), the robot first used *PLAN* and only switched to *REACT* to negotiate the doorway passage.

5.2 Unexpected Map Error and Comparison to Simple Threshold Rules

Fig. 4(b) shows another example of modality switching to negotiate an unexpected situation safely: an unpredictable large error in the map. This situation is caused by the presence of an unexpected obstacle. This simulates a map error. In order to avoid the box, the robot switches to *REACT*, then returns to *PLAN* once the situation is safe and the map is more consistent with the current observation. A likely collision was thus avoided.

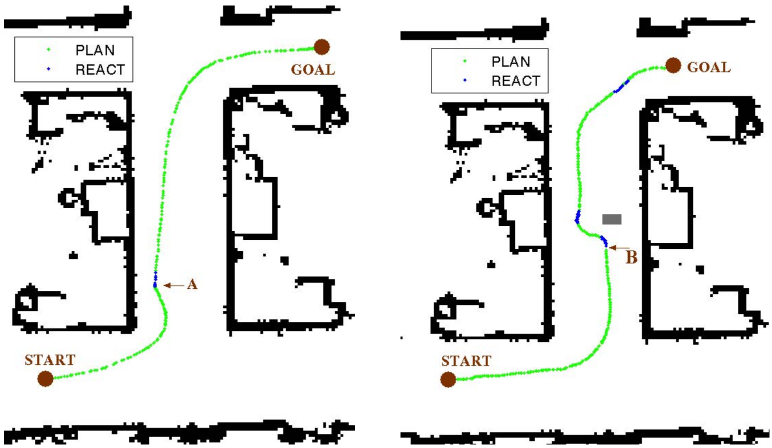

(a) Control error

(b) Error in map: unexpected obstacle (grey box)

Fig. 4. Examples of robot trajectory executed with modality switching. Known obstacles in the map are shown in black, while the colour points show the (estimated) positions of the centre of the robot. Green means the recommended modality is *PLAN*, while blue means the recommended modality is *REACT*. Approximate size of the area shown: $6.5m \times 7.5m$.

Fig. 5 illustrates a similar test using a recommendation based on simple logical rules comparing d and δ to "hard" thresholds equal to d_c and d_s. It can be seen that such strategy can provoke frequent undesirable modality switches, contrary to the HMM of our approach.

5.3 Presence of Dynamic Obstacles

We validated that the robot is resilient to the presence of highly dynamic obstacles. In the test shown in Fig. 6(a), a pedestrian coming from the top left of the scene walked quickly towards the robot. On approach, the robot first switched to *REACT* and then tried to evade (event C). Once the human had left the vicinity, the robot could resume its mission. A similar situation occurred again later in the test, with an even more sudden appearance of the human in the FOV of the robot. This event was again safely handled by the robot. This test shows that, although the robot can nominally execute optimised trajectories, it can also safely react to dynamic obstacles, comparably to a pure reactive motion strategy.

5.4 Injected Localisation Fault

In this experiment, a significant localisation fault was artificially created by introducing a sudden and unexpected offset of $1m$ to the output of the localisation estimator. Fig. 6(b) shows the clear offset to the right between the estimated position and the reality. However, the robot was still able to safely achieve its mission by switching to *REACT* when appropriate.

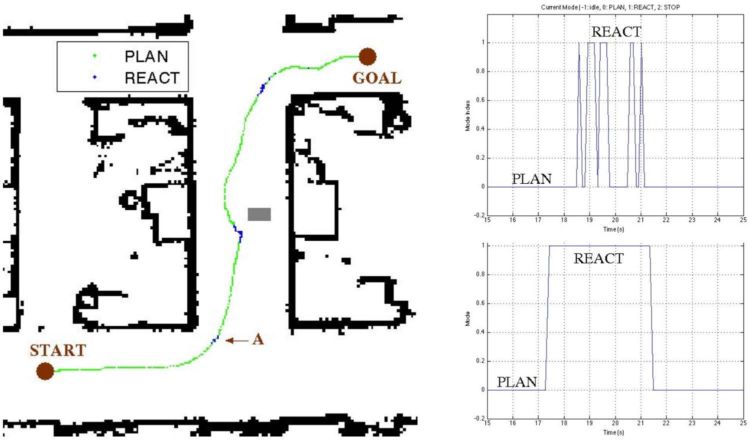

(a) Map error: unexpected obstacle

(b) Modality recommendation: 0=*PLAN*, 1=*REACT*

Fig. 5. Comparison with a simple threshold strategy. The robot encounters an unexpected obstacle in (a). (b) shows the chosen modality over time for the 10s surrounding event A in (a). Modality switching with fixed thresholds results in unacceptable oscillation (top) compared to our method (bottom).

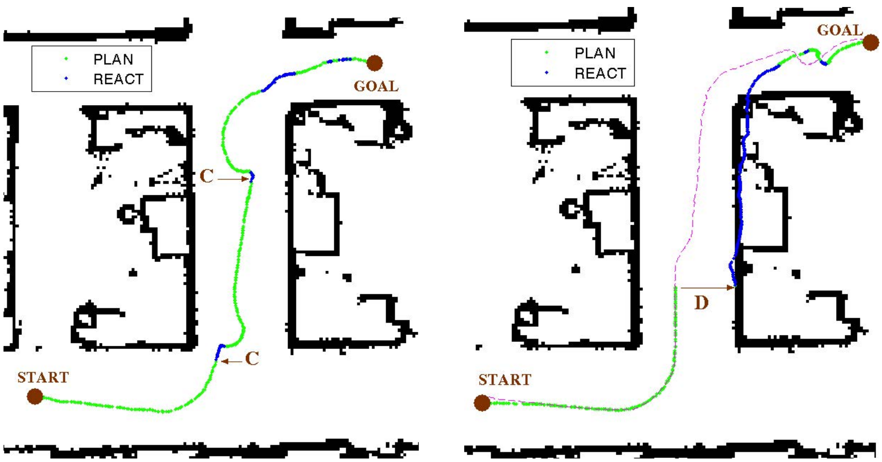

(a) Dynamic obstacle

(b) Localisation fault

Fig. 6. (a): Presence of highly dynamic obstacles (events C). (b): Modality switching with injected localisation fault (sudden offset to the right of 1m, see D). As a result, the estimated positions of the robot appear to be *on* the right wall (blue line). The magenta dashed line shows the reference localisation.

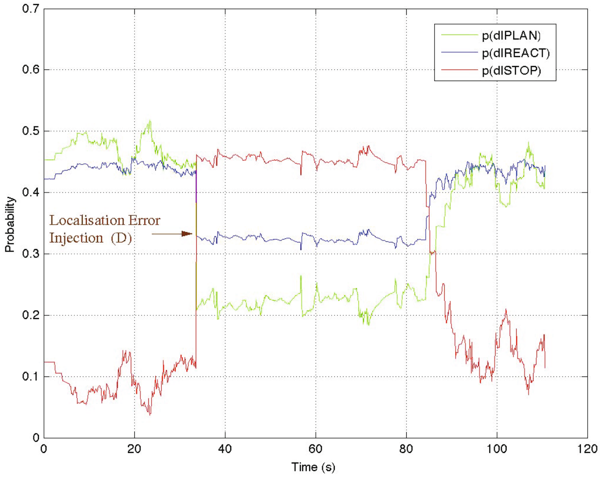

Fig. 7. Partial probabilities for context information, corresponding to the test in Fig. 6(b)

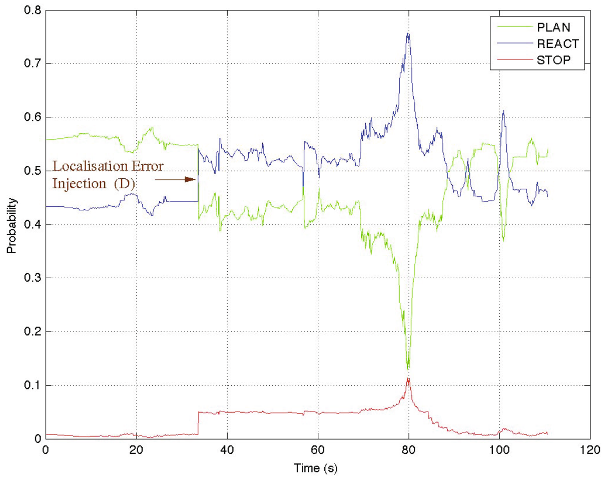

Fig. 8. Partial probabilities for all three states (i.e. modality recommendation), corresponding to the test in Fig. 6(b)

The context information is shown in Fig. 7 and the corresponding partial probabilities of modality recommendation are shown in Fig. 8. The moment of the localisation fault injection is clearly visible at $t = 35s$ (event D) on both figures. Fig. 7 indicates that with context information alone the robot should definitely *STOP*. If the robot could rely only on its current global localisation estimate and map, it would not have been safe to continue, since according to its estimated position the robot appears to be *on* the location of known obstacles in the map (see Fig. 6(b)). However, our system recommended a better alternative: a prudent switch to *REACT*. The localisation algorithm then progressively corrected its estimation up to a point when the situation became comfortable enough again to use *PLAN* to finish the mission. This shows our system to be resilient to large unpredicted localisation or map errors.

6 Conclusion

We have shown that a multiple modality strategy for resilient navigation, based on a probabilistic framework, can be applied to an indoor mobile robot to combine the advantages of navigation modalities while maintaining the safety of the platform. In our implementation, the robot is able to plan and execute smooth paths (minimising change in curvature) when possible, while being very reactive when needed. The system was applied online and shown to be reliable and robust in the presence of map errors and large localisation uncertainties or offsets. The concept is demonstrated with one choice of planning and reactive modality, however, these planning and reactive methods are easily interchangeable.

Future work will exploit the monitoring and context information for diagnosis and recovery of particular components of the system. Currently, both types of information are only exploited to compute a modality recommendation. However, we saw in Sec. 5.4 that the discrepancy between context and monitoring indicates a likely error in the map or global localisation. This could be used to actively repair these components, while the robot uses a reactive modality.

Acknowledgments. This work was supported in part by the Australian Centre for Field Robotics (ACFR) and the NSW State Government. This material is based on research sponsored by the Air Force Research Laboratory, under agreement number FA2386-10-1-4153. The U.S. Government is authorized to reproduce and distribute reprints for Governmental purposes notwithstanding any copyright notation thereon.

References

1. Alterovitz, R., Simeon, T., Goldberg, K.: The stochastic motion roadmap: A sampling framework for planning with markov motion uncertainty. In: Robotics: Science and Systems II (2007)
2. Arnaud, E., Memin, E., Cernuschi-Frias, B.: Conditional filters for image sequence based tracking - application to point tracking. IEEE Transactions on Image Processing 14(1), 63–79 (2005)
3. Barraquand, J., Latombe, J.: Nonholonomic multibody mobile robots: Controllability and motion planning in the presence of obstacles. Algorithmica 10, 121–155 (1993)
4. Brock, O., Khatib, O.: High-speed navigation using the global dynamic window approach. In: Proc. of IEEE International Conference on Robotics and Automation (1999)
5. Bryand, A., Roy, N.: Rapidly-exploring random belief trees for motion planning under uncertainty. In: Proc. of IEEE International Conference on Robotics and Automation (2011)
6. Choset, H., Lynch, K.M., Hutchinson, S., Kantor, G.A., Burgard, W., Kavraki, L.E., Thrun, S.: Principles of Robot Motion: Theory, Algorithms, and Implementations. MIT Press, Cambridge (2005)

7. Dearden, R., Clancy, D.: Particle filters for real-time fault detection in planetary rovers. In: 12th International Workshop on Principles of Diagnosis (2002)
8. Huang, W.H., Fajen, B.R., Fink, J.R., Warren, W.H.: Visual navigation and obstacle avoidance using a steering potential function. Robotics and Autonomous Systems 54(4), 288–299 (2006)
9. Kurniawati, H., Bandyopadhyay, T., Patrikalakis, N.M.: Global motion planning under uncertain motion, sensing, and environment map. In: Robotics: Science and Systems VII (2011)
10. Minguez, J., Montano, L.: Nearness diagram navigation (ND): Collision avoidance in troublesome scenarios. IEEE Transactions on Robotics and Automation 20(1), 45–59 (2004)
11. Morisset, B., Ghallab, M.: Learning how to combine sensory-motor functions into a robust behavior. Artificial Intelligence 172, 392–412 (2008)
12. al., N.K.e.: RobotAssist - a Platform for Human Robot Interaction Research. In: Proc. of ARAA Australasian Conference on Robotics and Automation (2010)
13. Peynot, T., Lacroix, S.: Selection and monitoring of navigation modes for an autonomous rover. In: Khatib, O., Kumar, V., Rus, D. (eds.) The 10th International Symposium on Experimental Robotics, vol. 39, pp. 121–130. Springer, Berlin (2008)
14. Thrun, S., Fox, D., Burgard, W., Dellaert, F.: Robust monte carlo localization for mobile robots. Artificial Intelligence 128(1-2), 99–141 (2000)
15. Fernandez, V.V.R.S.J.: Probabilistic models for monitoring and fault diagnosis. In: 2nd IARP and IEEE/RAS Joint Workshop on Technical Challenges for Dependable Robots in Human (2002)

Scaling Vector Field SLAM to Large Environments

Jens-Steffen Ralf Gutmann, Dhiraj Goel, and Mario E. Munich

Evolution Robotics, 1055 E. Colorado Blvd., Suite 340, Pasadena, CA 91106, USA
{steffen,dhiraj,mario}@evolution.com

Abstract. Vector field SLAM is a framework for localizing a mobile robot in an unknown environment by learning the spatial distribution of continuous signals such as those emitted by WiFi or active beacons. In our previous work we showed that this approach is capable of keeping a robot localized in small to medium sized areas, e.g. in a living room, where four continuous signals of an active beacon are measured. In this paper we extend the method to larger environments up to the size of a complete home by deploying more signal sources for covering the expanded area. We first analyze the complexity of vector field SLAM with respect to area size and number of signals and then describe an approximation that divides the localization map into decoupled sub-maps to keep memory and run-time requirements low. Experimental results from running the system in houses of up to 125 m^2 demonstrate the performance of our approach. The presented methods are suitable for commercial low-cost products including robots for autonomous and systematic floor cleaning.

1 Introduction

Localization for mobile robots in indoor environments is, to a large extent, a solved problem. By choosing a platform, appropriate sensors, computing hardware, algorithms, and a process for setup, a mobile robot can be created for autonomous navigation in almost any indoor space [16].

The question from a consumer perspective then becomes, how inexpensive a system can be designed, and how simple the setup process be made. In the context of autonomous floor cleaning, the hardware costs should be as small as possible (within a few tens of dollars) and the setup be minimal, e.g. the often suggested approach of first fully mapping an environment for the purpose of localization afterwards [4] will not be accepted by many end consumers.

In this respect, approaches using vision or small laser range finders have become very successful within the last few years. Samsung's Hauzen is arguably the first effective autonomous vacuum cleaner showing systematic navigation. A camera pointing towards the ceiling is used for tracking the pose of the robot [11]. The same sensor configuration is used nowadays on many other robot vacuums, including those of Yujin Robotics, Philips and LG Electronics. In addition to the up-facing camera, LG's Roboking also uses an optical sensor observing the floor surface. A different sensing technology is employed in Neato's XV-11 vacuum robot: a miniature laser range finder [12]. Navigation using this sensor has been a research topic for more than two decades [13].

S. Lee et al. (Eds.): Intelligent Autonomous Systems 12, AISC 194, pp. 89–100.
springerlink.com

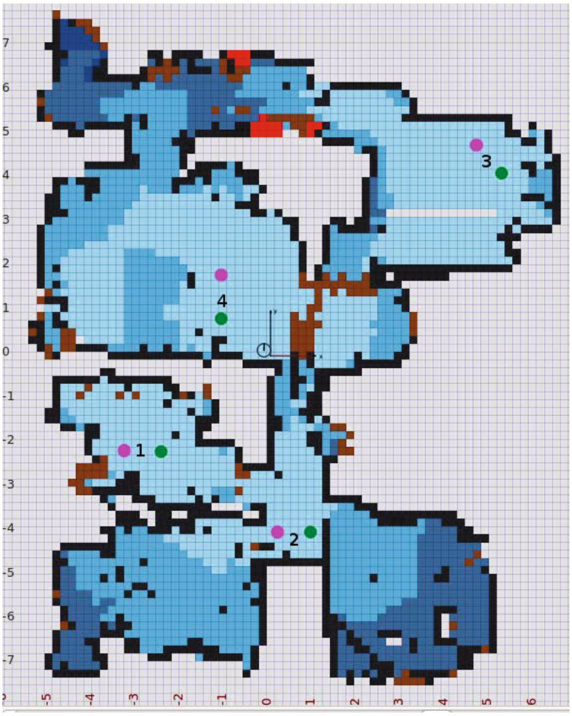

Fig. 1. Map generated using the localization results of our extensions to vector field SLAM when cleaning a large 3-bedroom home environment (108 m^2) with four Northstar beacons. The Northstar spots projected onto the ceiling are indicated by green and cyan discs. Shades of blue mark open space the robot was traversing, where the lighter the blue the more visibility there is to a beacon. Obstacles are drawn in black, floor level changes in brown, and areas where the robot got stuck in red. Units are in meters.

Our approach to low-cost indoor navigation employs active beacons in the form of *Northstar* navigation cubes that can be placed freely into the environment to be cleaned. Each cube projects two patterns onto the ceiling which are observed by a sensor on the robot (see Fig. 1 and Fig. 4). It can be argued that placing beacons is a modification to the environment. However, other systems also require changes before a robot can operate, e.g. turning on lights for a vision system, installing virtual walls for defining the area the robot is allowed to navigate in, or, in general, opening doors and clearing of obstacles. We envision our system to eventually work with existing infrastructure already present in a home, e.g. WiFi signals. In the following, we formulate our approach independent of the signals employed.

The advantages of our system compared to vision or range finders are low memory foot print and frugal computational requirements. The necessary data structures fit into tens of kilobytes and are updated several times a second on low-cost computational hardware, like an ARM 7 processor. This reduces the cost of components which can make the difference between success and failure of a consumer product.

Localization using active beacons looks trivial at first sight as the pose of the robot could be triangulated from the known beacon positions [2]. However, usually the beacon positions are not known *a priori* and the beacon signals become distorted by reflections off walls and furniture causing *multi-path* effects. The latter is also a well-known problem with other similar signals, like GPS in urban canyons [5], or the mobile positioning in wireless networks [8].

Instead of modeling or filtering multi-path signals, recent approaches compute a signal map over the environment, sometimes also referred to as *location fingerprinting* [17]. The signal map can be learnt by Expectation-Maximization [15] or Gaussian Process Latent Variable Models [7]. In our approach we learn the signal map using a simultaneous localization and mapping (SLAM) approach.

Since the signal map consists of signal vectors over space we refer to this method as *vector field SLAM*. Our previous work demonstrates how this method keeps a robot localized in small- to medium-sized environments where four continuous signals of a single Northstar beacon are measured [9,10].

When applying our method to larger environments, one needs to deploy more signal sources in order to cover the expanded area. However, the straight-forward approach of extending the dimension of the signal vector to hold all signals is costly. In this paper we show that memory scales quadratically and run-time cubically in the signal dimension. In order to avoid this drastic increase, we describe an approximation that divides the localization map into decoupled sub-maps each associated with only part of the signal sources. This keeps the algorithmic complexity similar to when using a single Northstar beacon at the cost of a sub-optimal solution.

Since the area that can be covered by beacons is limited, it is important to also have accurate relative position estimation. We equip our robot with both wheel-odometry and a gyroscope. The use of a gyroscope improves motion estimation significantly allowing the robot to move out of areas covered by beacons for extended periods of time. Furthermore, in large environments the robot usually has a higher risk of getting stuck somewhere, and often, the user might want to pause or kidnap the robot, e.g. for maintenance. After such events, the system must be able to resume cleaning. To this end we formulate a tracking approach that allows the robot to re-localize itself in a previously mapped area when resumed.

We evaluate our extensions to vector field SLAM in large home environments with sizes ranging from 35 to 125 m^2 and with up to four beacons. As an example, Fig. 1 shows a typical home environment containing four navigation cubes that has been fully explored by our robot. As the experiments will demonstrate, our approach is capable of keeping a robot localized in such environments.

This paper is organized as follows. The next section summarizes our method of vector field SLAM. Section 3 describes our extensions for allowing the method to work in large environments without increasing the algorithmic complexity. Experimental results are in Section 4 followed by our conclusions in Section 5.

2 Vector Field SLAM

In vector field SLAM the spatial variation of continuous signals are learnt and simultaneously used for localization. Examples of signals are the received signal strengths of

WiFi base stations or the signals measured from active beacons. The particular physical characteristics of the signals do not matter as long as signals can be uniquely identified, are stationary over time and change continuously over space. In our experiments in Section 4 we use the coordinates of two spots projected onto the ceiling as our signals.

A vector field is represented as a regular grid with fixed node positions $\mathbf{b}_i$, $i = 1 \ldots N$, where each node $\mathbf{m}_i \in \mathbb{R}^M$ holds a vector of expected signal values when placing the robot at position $\mathbf{b}_i$ and pointing in a fixed orientation θ_0. Without loss of generality, let $\theta_0 = 0$. Vector field and robot pose are then estimated through the application of simultaneous localization and mapping (SLAM).

Let the robot path be a time series of poses $\mathbf{x}_0 \ldots \mathbf{x}_T$, $\mathbf{x}_t \in \mathrm{SE}(2)$, i.e. the set of rigid transformation in the 2-dimensional horizontal plane. Without loss of generality, let $\mathbf{x}_0 = (0,0,0)^T$. At each time step $t = 1 \ldots T$ the robot receives a motion input $\mathbf{u}_t$ with covariance $\mathbf{R}_t$ and a measurement $\mathbf{z}_t$ of the continuous signals with covariance $\mathbf{Q}_t$. We consider that the measurements are also affected by calibration parameters $\mathbf{c}$ of the sensor. These parameters can reflect for example a rotational sensitivity in an antenna measuring WiFi signal strengths. For our active beacon system, calibration $\mathbf{c}$ encodes a coordinate offset caused by a small error in the ideal horizontal plane of the sensor.

A motion model defined by a function g describes the motion of the robot since the previous time step:

$$\mathbf{x}_t = g(\mathbf{x}_{t-1}, \mathbf{u}_t) + \mathbf{e}_u \tag{1}$$

where $\mathbf{e}_u$ is a zero mean error with covariance $\mathbf{R}_t$.

Furthermore, a sensor model defined by function h predicts an observation given current robot pose, sensor calibration and vector field:

$$\mathbf{z}_t = h(\mathbf{x}_t, \mathbf{c}, \mathbf{m}_1 \ldots \mathbf{m}_N) + \mathbf{e}_z \tag{2}$$

where $\mathbf{e}_z$ is a zero mean error with covariance $\mathbf{Q}_t$.

Our particular sensor model is composed of a rotational and a translational part:

$$h(\mathbf{x}_t, \mathbf{c}, \mathbf{m}_1 \ldots \mathbf{m}_N) = h_R(h_0(x, y, \mathbf{m}_1 \ldots \mathbf{m}_N), \theta, \mathbf{c}) \tag{3}$$

where $\mathbf{x}_t = (x, y, \theta)$ is the robot pose at time t, h_R is a continuous function that rotates the expected signal values according to robot orientation θ and applies a correction based on the sensor calibration $\mathbf{c}$ (for details, see [9]), and h_0 is a bilinear interpolation of the expected signal values from the four nodes of the cell containing the robot (see Fig. 2):

$$h_0(x, y, \mathbf{m}_1 \ldots \mathbf{m}_N) = \sum_{j=0}^{3} w_j \mathbf{m}_{i_j} \tag{4}$$

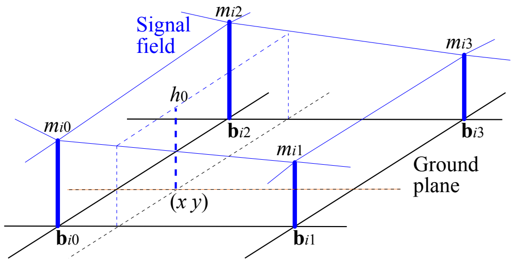

Fig. 2. Bilinear interpolation from cell nodes. Illustrated is a 1-dimensional vector field, i.e. a signal field. For dimensions of 2 and higher, bilinear interpolation is analogous according to Eq. (4).

with

$$w_0 = \frac{(b_{i_1,x} - x)(b_{i_2,y} - y)}{(b_{i_1,x} - b_{i_0,x})(b_{i_2,y} - b_{i_0,y})} \tag{5}$$

$$w_1 = \frac{(x - b_{i_0,x})(b_{i_2,y} - y)}{(b_{i_1,x} - b_{i_0,x})(b_{i_2,y} - b_{i_0,y})} \tag{6}$$

$$w_2 = \frac{(b_{i_1,x} - x)(y - b_{i_0,y})}{(b_{i_1,x} - b_{i_0,x})(b_{i_2,y} - b_{i_0,y})} \tag{7}$$

$$w_3 = \frac{(x - b_{i_0,x})(y - b_{i_0,y})}{(b_{i_1,x} - b_{i_0,x})(b_{i_2,y} - b_{i_0,y})}. \tag{8}$$

By choosing a standard motion model [16] and a suitable initialization, the robot trajectory, the sensor calibration and the vector field can be estimated. In our previous work we presented different implementations of this model including an off-line non-linear optimization through GraphSLAM, an extended Kalman filter (EKF-SLAM) [9] and an exactly sparse extended information filter (ESEIF-SLAM) [10]. All methods show the ability to keep a robot localized in an environment of the size of a living room where a single Northstar beacon has been placed.

For running the method on an embedded platform, the ESEIF-SLAM variant is particularly interesting. The method is constant time, and space grows linearly with the size of the area explored. These properties allow us to run the method on a low-end ARM 7 processor clocked at 44 MHz with only 64 kByte of RAM.

3 Extensions to Large Environments

In order to extent vector field SLAM to large environments, several additions are integrated into the algorithm.

3.1 Space and Run-Time Complexity of ESEIF-SLAM

We first take a closer look at the space and run-time complexities. Fig. 3 shows a sample grid consisting of 8 cells that models a vector field over an environment.

As long as the robot stays within a cell, our ESEIF-SLAM approach updates robot pose, sensor calibration and the four cell nodes by integrating motion and sensor information. This results in information links between all involved variables, i.e. entries in the information matrix that correspond to robot pose, calibration, the four cell nodes, and the cross information between all of them are, in general, non-zero. In other words, the information matrix of a vector field consisting of a single cell is fully dense.

When moving into a neighboring cell, the ESEIF approach performs a *sparsification* step [18]. First, we marginalize over robot pose and sensor calibration. This removes them from the state vector and leaves the information matrix with only the node's information and their cross entries. Next we relocate robot and sensor calibration using a sensor measurement in the new cell. For details, see [10].

The effect of this approach is that each node shares information with at most eight neighboring ones as the links in Fig. 3 indicate. The nodes can be classified by the number of other nodes they link to. Only inner ones (nodes 6, 7 and 10) have eight connections. Nodes at the border have either 7 (node 11), 5 (nodes 2, 3, 5, 8, 9 and 14) or only 3 links (nodes 1, 4, 12, 13 and 15). In practice we found that the average connectivity per node is about 6. Of course this depends on the layout of the environment, e.g. in an open room the factor is larger as there are more inner nodes.

The space requirements for N nodes with signal dimension M can now be estimated. In the following we ignore for a moment the robot and calibration variables as they only add a constant term. The ESEIF stores an information vector (size NM), an estimate of the mean (also size NM) and the sparse information matrix. The latter holds N information matrices of all nodes which, due to symmetry, each require a size of $\frac{1}{2}M(M+1)$. The cross information can be stored in about $\frac{1}{2} \cdot 6M^2$ where the factor $\frac{1}{2}$ accounts for the fact that each link is shared between two nodes. In total the space requirements for vector field SLAM using the ESEIF are

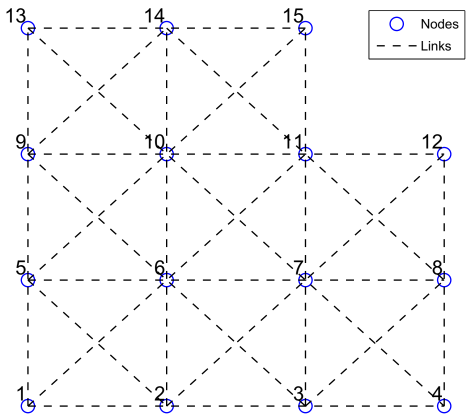

Fig. 3. Sample grid in vector field SLAM with information links between nodes as they appear in our ESEIF-SLAM implementation

$$Space_{\text{ESEIF}} \approx N(\frac{7}{2}M^2 + \frac{5}{2}M) + const. \quad (9)$$

As for run-time, ESEIF-SLAM is constant time, i.e. does not depend on N [10]. The most expensive operation is the recovery of a part of the estimated mean. In our formulation, we update robot pose, sensor calibration and the four cell nodes. This involves solving a linear equation system in these variables with a symmetric and positive definite system matrix. We use Cholesky decomposition which takes time cubic in the number of variables. If we ignore constant terms and factors, our time complexity therefore is

$$Time_{\text{ESEIF}} = O(M^3). \quad (10)$$

3.2 Dividing Localization Map into Decoupled Sub-Maps

In order to cover a larger area, more beacons are installed in the environment. In the most general situation, the signals of all beacons might be visible at some location. If this were modeled without loss of information then the signal dimension M needs to be expanded to hold signal values of all beacons. However, increasing M has a drastic effect on the space and run-time of our ESEIF formulation. When doubling the number of signals, the space increases by a factor of four (Eq. 9) and run-time by a factor of 8 (Eq. 10).

Fortunately most home environments consist of rooms separating the space into areas where at most one beacon is visible. In situations where the areas covered by beacons overlap, we can choose to ignore information from all but one beacon, e.g. using the beacon that provides the highest signal certainty.

The natural choice of representing this structure is by using multiple localization sub-maps, one for each area around a beacon. Whenever the robot moves out of the area of the current beacon, which is detected by measuring the signal strengths, and into the area of another one, a new sub-map for the signals of this beacon is started, or, if the robot has already visited the area before, it re-localizes in the corresponding sub-map. The sub-maps are decoupled as they do not share signals between them.

There are different approaches for maintaining the relations between sub-maps. For example, in the atlas framework [3] the maps are linked by uncertain rigid-body transformations, i.e. they can rotate and translate slightly with respect to each other. A different approach is decoupled stochastic mapping as proposed by Leonard and Feder [14]. Each map is anchored at a fixed global pose. When switching from one sub-map to another one, special care has to be taken about the cross information between robot and map features.

Due to its lean requirements, we use decoupled stochastic mapping. In our approach we maintain the relative pose uncertainty, computed from odometry and the gyroscope, from when the robot left a map until it re-entered it. In practice we limit this uncertainty to a certain maximum covariance. The uncertainty is then added to the pose uncertainty of the robot in our relocation step of the ESEIF [10]. This, of course, can introduce larger changes in the robot pose and works well only as long as the error when closing loops stays small.

The advantage of this approach is that signal dimension M stays the same as for a single beacon. Only the number N of nodes increases for storing additional maps.

3.3 Re-localization for Resuming Navigation

In large environments there is an increased risk of the robot becoming stuck in tight areas or in situations with many obstacles. Furthermore, for a cleaning robot it is desirable for the user to have an option for pausing and resuming the robot, e.g. for emptying the dust bin or changing the cleaning pad. Once resumed, the robot should quickly find its position in the area already explored and continue cleaning.

We use the following procedure for re-localizing the robot. Using a measurement $\mathbf{z}_t$ of signals emitted from one beacon, we find the cell and location that most likely corresponds to the measurement. In case there are multiple possibilities, we discard the hypothesis and retry after traveling some distance.

Once a unique location has been determined we start a localization filter based on an EKF that tracks the robot pose from the found location. In this tracking method we ignore the uncertainties associated with the nodes in the vector field and increase the uncertainties $\mathbf{Q}_t$ of measurements to compensate for this modeling error. If the filter is able to successfully track the robot pose for a certain number of measurements and over a certain distance, we stop the tracking filter and insert the robot back to the corresponding localization map by using the relocation procedure of the ESEIF with the found pose and a large pose covariance.

4 Results

We have implemented vector field SLAM and our extensions for large environments on a developer version of our Mint Cleaner robot [6]. The robot is equipped with a sensor observing infrared light spots projected onto the ceiling by a Northstar beacon (see Fig. 4). Details of the Northstar system have been presented earlier [19]. Each projected pattern carries a different frequency encoded in the signal to ease the data association on the robot. Different Northstar beacons also provide different frequencies. The sensor on the robot detects these patterns and measures the direction to both spots on the ceiling. The sensor then reports the coordinates of both direction vectors projected onto the sensor plane, thus the signal dimension is $M = 4$.

Under ideal circumstances the reported spot coordinates change linearly with the robot position. However, infrared light reaches the sensor not only on a direct line but also over multiple paths by reflecting off walls and other objects, so the spot coordinates change in a non-linear way as the robot approaches an obstructed area.

The computations on the robot are performed by an ARM 7 processor clocked at 44 MHz with 64 kByte of RAM. We set the number of nodes to $N = 96$ which results in a memory size for the localization maps of about 26 kBytes. This is roughly the maximum size we could afford for localization under the tight memory constraints. The processing time for integrating a motion and a sensor measurement is about 50 ms. Localization updates are performed while other control routines are also running on the CPU.

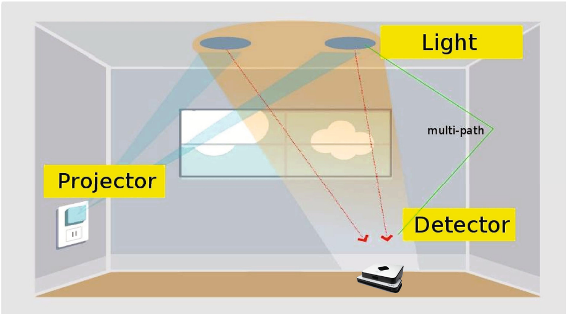

Fig. 4. The Northstar system. An optical sensor on the robot measures the bearing to two spots on the ceiling projected by an infrared beacon. The beacon is also available as a battery-powered device that can be placed more freely in the room, e.g. on top of furniture or on counter tops.

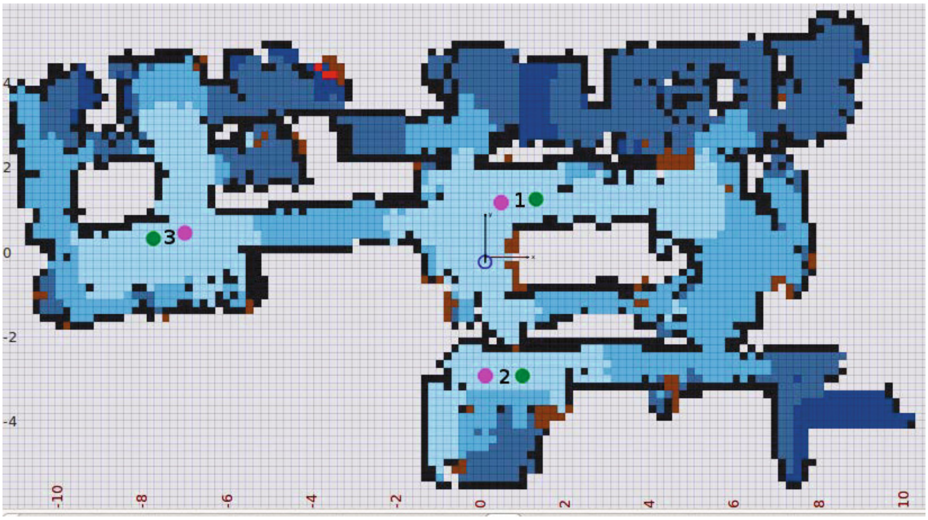

Fig. 5. Cleaning run in a different large home environment with a size of 125 m^2 covered by three Northstar beacons. Units are in meters.

We tested our extensions in three different home environments with one to four Northstar beacons. Maps obtained by the robot in two of them are shown in Fig. 1 and Fig. 5. The robot navigated in these homes by following a cleaning strategy based on systematically covering sectors of the environment. As long as at least one beacon is visible to the robot, the strategy moves the robot onto a neighboring region until no space is left to clean. At the end the robot follows along the perimeter of detected obstacles for a thorough cleaning around walls and furniture.

Table 1. Statistics of occupancy and visibility in environments

	Mean	Std	Min	Max
Occupied (%)	21.13	4.25	16.56	28.78
NS visible (%)	55.64	10.27	42.51	74.33
NS not visible (%)	23.21	9.71	6.63	37.83

As the robot moves through the environment it creates an occupancy grid map using the position information from localization. This is an instance of mapping with known poses [16]. Each visited cell is classified into one of the following categories:

- obstacles (drawn in black) the robot bumped into,
- floor changes (drawn in brown) detected by two sensors in the front of the robot,
- hazards (drawn in red) where the robot got stuck or had driving problems, and
- free space (drawn in shades of blue) that the robot explored.

We also encode the visibility to beacons in the free-space cells. The lighter the blue a cell is drawn, the better the visibility to a projected spot on the ceiling is.

We carried out a total of 25 runs in the three environments and we varied the number of beacons. Table 1 shows the statistics of the environments with respect to occupancy and visibility to beacons. On average about 21 % of an environment is occupied by obstacles, floor changes or hazards. From roughly 56 % of visited places at least one beacon was visible (2 brightest levels of blue). The cleaning program continued to navigate in areas not covered by Northstar in about 23 % of the total environment explored.

As we do not have ground truth information of the robot poses during the runs, we use the following two metrics for evaluating the navigation performance:

- Double walls: if the localization of the robot were perfect, the map obtained by the robot would show obstacles and walls exactly once at the correct places. While we do not know the exact positions of walls, we can still verify that each of them is mapped exactly once. Thus by measuring the percentage of walls mapped more than once, we obtain an indication of how well the robot was localized.
- Maximum angular error: similarly as we usually know the global orientation of walls, we can measure the angle of the wall in the map showing the largest deviation from the nominal one.

Table 2 shows our findings for the 25 runs. On average we obtain about 4 % of wrongly placed walls. In some cases there are none (e.g. Fig. 5), while in others there can be as much as 10 % of additional obstacles. The robot was paused and resumed during some runs as well, because either the user wanted to change the cleaning cloth or the robot got stuck (in some cases as many as 7 times, as indicated by the red cells in Fig. 1). In either case, the robot was not necessarily started near the location where it was paused.

The angular error is, on average, about $9.5°$ with outliers going as large as $23°$. While this seems significant, it does not always lead to a catastrophic failure. Often the map of the environment is bent along its main direction. The robot is still able to successfully navigate from one side of the environment to the other one by changing its orientation

Table 2. Localization statistics of runs

	Mean	Std	Min	Max
Double walls (%)	4.15	3.12	0	10.17
Max angular error (deg)	9.48	5.23	1.91	23.19
Number of pause/resume	0.55	1.65	0	7

Fig. 6. Area covered as a function of number of beacons. Error bars indicate the 1σ interval of the standard deviation.

along the path according to the learned localization map. Only when trying to close a loop over a longer trajectory with a larger error in rotation, the method is likely to fail.

We also evaluated how much of the environment our cleaning algorithm will explore when varying the number of beacons in the environment of Fig. 5. Recall that the cleaning strategy only moves on as long as any of the beacons stays visible. Fig. 6 shows the area covered as a function of the number of beacons used.

As expected, the more beacons there are, the larger the area the robot explores. Note that when placing four beacons in the environment the robot hits the physical boundaries of the home. If the environment were larger then the robot would likely have moved on and covered more space.

5 Conclusions

We have presented extensions to vector field SLAM for scaling the localization approach to large environments. Our results demonstrate that a robot is able to navigate in home environments of up to 125 m^2 and keep its absolute position with an accuracy that allows it to clean systematically.

A limitation of our extensions is the requirement of additional sensors for accurate relative motion estimation. On our robot we use, besides odometry, a gyroscope which keeps the rotational uncertainty of the robot pose small. In general, this is beneficial for the consistency in on-line SLAM [1].

For future work, the reduction of the localization map is important. In order to further reduce memory requirements, nodes of the vector field in areas that are no longer needed could be removed. Similarly, nodes having a significantly small uncertainty could be replaced by fixed values.

References

1. Bailey, T., Nieto, J., Guivant, J., Stevens, M., Nebot, E.: Consistency of the EKF-SLAM algorithm. In: Int. Conference on Intelligent Robots and Systems, IROS (2006)
2. Borenstein, J., Everett, H.R., Feng, L.: Navigating Mobile Robots: Systems and Techniques. A.K. Peters, Ltd., Wellesley (1996)
3. Bosse, M., Newman, P., Leonard, J., Teller, S.: SLAM in Large-scale Cyclic Environments using the Atlas Framework.. Int. Journal of Robotics Research 23 (12), 1113–1139 (2004)
4. Burgard, W., Cremers, A., Fox, D., Lakemeyer, G., Hähnel, D., Schulz, D., Steiner, W., Thrun, S.: The interactive museum tour-guide robot. In: National Conference on Artificial Intelligence, AAAI (1998)
5. Cui, Y., Ge, S.: Autonomous vehicle positioning with GPS in urban canyon environments. Transactions on Robotics and Automation 19(1) (2003)
6. Evolution Robotics Inc.: Introducing Mint – the evolution of floor care (2011), http://www.mint-cleaner.com
7. Ferris, B., Fox, D., Lawrence, N.: WiFi-SLAM using Gaussian process latent variable models. In: Int. Joint Conference on Artificial Intelligence, IJCAI (2007)
8. Gustafsson, F., Gunnarsson, F.: Mobile positioning using wireless networks. IEEE Signal Processing Magazine, 41–53 (2005)
9. Gutmann, J.S., Brisson, G., Eade, E., Fong, P., Munich, M.: Vector Field SLAM. In: Int. Conference on Robotics and Automation (ICRA), Anchorage (2010)
10. Gutmann, J.S., Eade, E., Fong, P., Munich, M.: A constant-time algorithm for Vector Field SLAM using an exactly sparse extended information filter. In: Robotics: Science and Systems (RSS), Zaragoza, Spain (2010)
11. Jeong, W., Lee, K.: CV-SLAM: A new ceiling vision-based SLAM technique. In: Int. Conference on Intelligent Robots and Systems, IROS (2005)
12. Konolige, K., Augenbraun, J., Donaldson, N., Fiebig, C., Shah, P.: A low-cost laser distance sensor. In: Int. Conference on Robotics and Automation, ICRA (2008)
13. Konolige, K., Grisetti, G., Kummerle, R., Burgard, W., Limketkai, B., Vincent, R.: Sparse pose adjustment for 2D mapping. In: Int. Conf. on Intelligent Robots and Systems (2010)
14. Leonard, J., Feder, H.: Decoupled Stochastic Mapping. Journal of Oceanic Engineering 26 (4), 561–571 (2001)
15. Ocaña, M., Bergasa, L., Sotelo, M., Flores, R., Llorca, D., Schleicher, D.: Automatic training method applied to WiFi+ultrasound POMDP navigation system. Robotica 27 (2009)
16. Thrun, S., Burgard, W., Fox, D.: Probabilistic Robotics. MIT Press, Cambridge (2005)
17. Varshavsky, A., de Lara, E., Hightower, J., LaMarca, A., Otsason, V.: GSM indoor localization. Pervasive and Mobile Computing 3, 698–720 (2007)
18. Walter, M.R., Eustice, R.M., Leonard, J.J.: Exactly sparse extended information filters for feature-based SLAM. Int. Journal of Robotics Research 26(4), 335–359 (2007)
19. Yamamoto, Y., Prijanian, P., Brown, J., Munich, M., Bernardo, E.D., Goncalves, L., Ostrowski, J., Karlsson, N.: Optical sensing for robot perception and localization. In: Workshop on Advanced Robotics and its Social Impacts, ARSO (2005)

Observation Planning for Object Search by a Mobile Robot with Uncertain Recognition

Matthieu Boussard and Jun Miura

Active Intelligent Systems Laboratory, Department of Computer Science and Engineering, Toyohashi University of Technology, Toyohashi, Japan

Abstract. In order to handle complex tasks in an unknown environment, a robot has to build a map with both free space information and objects type and location. We present an active vision system which first detects candidate objects using global detection mechanism, and later identifies them by moving the robot closer and by using a local recognition mechanism. Having multiple candidates and uncertain algorithm outcomes, we cast the problem as a Markov Decision Process. We exhibit the modelization process, the capability of online solver to quickly find a good action, and finally the implementation on a real robot. This implementation consists of a set of Robot Technology Components (RT components) implementing each part of our method.

1 Introduction

In order to perform more complex tasks, robots have to get a better understanding of their environment. We are considering an indoor environment where a robot can interact with humans. One of its most important tasks is to preserve its integrity, and thus has to know where it may move safely. This has led to many SLAM algorithms (Simultaneous Localization and Mapping)[12]. To fulfil complex tasks, the free space map is not sufficient anymore. Instead, the robot has to know what kind of objects are in its environment and should be able to locate them. For a task like serving coffee, the robot has to know what a "coffee cup" is and where it can be found. The problem of searching and locating those objects on the map is called the object search problem.

In this paper we recognize the objects by using computer vision algorithms. To recognize an object with a very high accuracy, the robot needs a high resolution image of it. This can be obtained by either being close to the object or by zooming in on it. This process will be extremely slow if exhaustively applied to a whole room. We thus introduce a two-step object recognition process. In the first step, the robot detects candidate objects using a fast and non robust algorithm where many false positive can remain but with as few false negative as possible. Then the robot will identify them by coming closer and applying a recognition method. Since the computer vision algorithms are uncertain, this leads to a planning problem under uncertainty.

2 Observation Planning

The observation planning is an active vision process where a robot has to build a sequence of actions in order to increase its knowledge about the environment. The nature

S. Lee et al. (Eds.): Intelligent Autonomous Systems 12, AISC 194, pp. 101–110.
springerlink.com

and the effects of those actions depend on the capabilities of the robot. For instance the robot can move, turn, use different kind of sensors, take high definition pictures, etc. It can also has various goals, like SLAM, object recognition, exploration. Our goal is to recognize and locate objects with high accuracy on a freespace map. From only one viewpoint[1], because of its pose, occlusion, lighting, or distance, the recognition may fail. Therefore the robot has to define a set of different viewpoints. To be efficient, the robot should select carefully the viewpoints and we should make an observation policy upon them, which will define the order and the location of every observation action. Many work have been done in observation planning, each having their own assumption. So, we will present existing solutions, then describe more formally our problem and show the associated MDP, and finally detail the implementation on a real robot.

2.1 Related Works

Sjöö et al. [11] present an attention mechanism and methods for depth computation, used to control the zoom level in order to perform a SIFT matching at an accurate distance measure. Here the map is provided before the object search phase, so the robot can compute a navigation graph. The observation plan is based on several greedy methods which may lead to non optimal behaviour. The object detection is made online using two kinds of algorithms, one for adapting the zoom level, and one to recognize objects once a final window is defined.

We are interested here in an unknown environment, where only the boundaries of the exploration are is given. In [8], Meger et al. present *Curious George*, a combination between an attention system and a SLAM algorithm. This attention system allows the robot to take high definition pictures of potentially interesting areas, which are used offline to perform the object detection. When the robot finishes to observe an area, it uses a frontier-based exploration to select the best next viewpoint, goes there to perform a new observation step. This process is repeated until the whole room is explored. The principle of alternatively performing move and observation action is used by Shubina and Tsotsos in [10], where they compute a probability of objects presence and probability of object detection using a certain type of recognition algorithm. They later use the function to compute a utility value, the actions being selected in a best-first manner according to it. Experiments show how they can tune this utility function in order to get a desirable behaviour.

Some authors tried not to use greedy approaches to improve the quality of the result. To obtain a long term plan, Aydemir et al. [2] are using a high level planner to select low level strategies to find a target object. Masuzawa and Miura [7] present an online object recognition in an unknown room. The algorithm first detects candidates objects and computes also frontier for exploration. Then, instead of directly selecting the best next viewpoint, their method computes a long term policy. The main issue here is that the authors rely on an ad-hoc world modelization in order to speed up their planning algorithm, but still, since they are performing an exhaustive search, the algorithm is too slow to be solved for larger problem online.

[1] We define a viewpoint as the robot pose from where it can observe a particular candidate object.

In this paper, we aim at using a general MDP modelization to find a good observation policy. MDPs have been widely studied [9]. They offer a strong theoretical background for action planning under uncertainty, optimality proofs, and many specialized algorithms dealing with planning in large state space problems where the classical algorithms cannot be used. The details of the model and the solver are not fixed and can be changed according to any assumption or improvement, so are the object detection and recognition algorithm.

2.2 Problem Statement

The robot has to make a map of an unknown room, and to locate objects on this map, see Fig.1. We make the same assumptions as in [7] : the only information provided is the object's models, defined by a (or a set of) picture and the object dimension. Their location and their occurrences are unknown (one object may not even be present in the room). The movement of the robot are assumed certain, i.e. given the current location and the goal location, the probability of reaching the goal is 1, the associated cost is also constant. This is a strong assumption since the actual robot effectors are not perfect, and the computed map can also have some errors.

We use two kinds of object recognition algorithms, one for candidate objects detection (*Detect*), and the other for object recognition (*Ident*). The candidates detection is a color histogram-based detection algorithm. It is fast and can detect object from a far distance, but it is not very robust, can return false positive, and cannot make the difference between objects of the same color. The other algorithm is a SIFT matching algorithm [6]. It can recognize very accurately the objects, but it is more time consuming, and needs a good image of the candidate to be matched. Nevertheless, several parameters can impact the detection, like the distance to the object, the object's pose, lighting, occlusions. We assume that we can compute, for every object recognition algorithm, a probability of recognizing one object according to given parameters, like the distance and priors information.

Fig.2 shows the formal description of an environment where the robot has to find objects. The object search process uses a 2-steps approach. Let l_r be the current robot pose. It first uses *Detect*, that returns a set C of candidates objects. Each candidate $c \in C$

(a) Objects (b) Simplified room

Fig. 1. Mapping situation

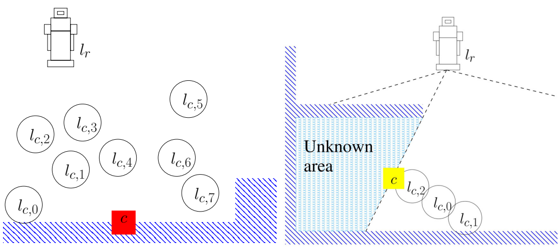

(a) Candidate object c and a set of viewpoints $\{l_{c,i}\}$ (b) Frontier-based candidate detection

Fig. 2. Representation of the environment

has a set $L_c = \{l_{c,i}\}_{i=0...n_c}$ of n_c viewpoints, $l_{c,i} \in \mathbb{R}^2$, from where it can be identified ,see Fig.2(a). The second step uses $Ident$ on candidate c, and $Ident(l_{c,i}) \rightarrow \{F,T\}$ returns the result of the identification. Since this process is uncertain, we note the probability of successful identification by $P_{Ident}(l_{c,i})$. Finally we would like the robot to minimize the overall mission time.

We use an approach similar to frontier-based ones to find candidates in an unobserved area, see Fig.2(b). When updating the model, the frontier between known and unknown environment is computed, and a set of viewpoints to detect objects in this unknown environment is computed. This set behaves exactly like any $\{l_{c,i}\}_{i=0...n_c}$ with two differences : $Detect$ is used instead of $Ident$ and $Detect$ always succeed, $P_{Detect}(l_{c,i}) = 1$

3 Observation Planning Problem as a Markov Decision Processes

Markov Decision Process [9] formalizes a sequential decision problem under uncertainty. This process is supposed to be fully observable, i.e. the observed state is the actual state of the system. An MDP is a 4-tuple $\langle S, A, P, R \rangle$, where :

- S is the (finite) set of states,
- A is the (finite) set of actions,
- $P : S \times A \times S \rightarrow [0;1]$ is the transition function,
- $R : S \times A \rightarrow \mathbb{R}$ is the reward function.

A policy π is a function $\pi : S \rightarrow A$ that gives for every state $s \in S$, the action $a \in A$ to perform. Following this policy, we can compute the expected reward $E^{\pi}\left[\sum_{t=0}^{\infty} \gamma^t r_t | s_0 = s\right]$ starting from state s and following the policy π. We use the total expected discounted reward, with a discount factor $0 \leq \gamma < 1$ and r_t the reward at step t. For every state $s \in S$, the unique optimal value function is given by the Bellman equation. $\forall s \in S$:

$$V^*(s) = \min_{a \in A} \left(r(s,a) + \gamma \sum_{s' \in S} p(s,a,s') V^*(s') \right) \tag{1}$$

From the optimal value function, we compute one optimal policy, noted π^*. V^* can be classically computed using Value Iteration, but it is not suited neither for large state space nor for online application. In order to use MDP to solve the observation planning problem, we need to define its four components, namely $\langle S, A, T, R \rangle$.

3.1 States Set S

Since the transitions are independent to history (Markov property) the current state has to contain only the information needed to take the decision. Thus a state is composed by :

- the current location $l \in \{l_{c,i}\} \cup l_r$. The decision are taken only on a viewpoint $l_{c,i}$, thus we do not consider any other location in the decision process.

- the set $\{\{l_{0,0}, l_{0,1}, \dots\}, \dots, \{l_{c,0}, l_{c,1}, \dots\}\}$ representing, for every n candidate object, the visited viewpoints from where an identification has been tried. This allows the robot not to observe twice the same object from the same viewpoint. We only consider a limited history for each object, define by *Max_Obs*, thus the maximum size of this set is $\binom{|L_c|}{Max\_Obs}$.
- A set of Boolean I_c representing the information whether the candidate c still needs to be checked.

Hence, a state s is defined by : $s = \langle Id, \{\{l_{0,0}, \dots, l_{0,n_0}\}, \dots, \{l_{c,0}, \dots l_{c,n_c}\}\}, \{I_0, \dots I_c\}\rangle$. The size of the complete state space is given by the Eq.2 :

$$|S| = |\bigcup_{c \in C} L_c| * 2^{|C|} * \prod_{c \in C} \binom{|L_c|}{Max\_Obs} \qquad (2)$$

This set is large and adding an object increases its size exponentially, but it is yet possible to merge some states together. Since a state has to contain all information needed to take the decision, any superfluous information can be forgotten. So, once an object does not need to be checked anymore, only the I_i information is kept. Still, the state space should not be used completely, and the resolution algorithms should only extend the necessary states (see Sec.4).

3.2 Actions Set A

The robot has only one kind of action : a macro action preforming a move action followed by an observation action (*Detect* or *Ident*). The robot selects a viewpoint, goes there and observes the related object. Its outcomes will be described by the transition function. Note that if a viewpoint is not reachable then the robot cannot execute the related macro action. If an object has no viewpoints, it is ignored.

3.3 Transition Function P

We assume that the moves of the robot, made by another piece of software, are deterministic. In this paper, we are not considering any uncertainty on candidate detection. So, after applying *Detect* to an unknown area, this area is considered as known, and no detection should be performed again in that area. Furthermore, in order to limit the expansion of the search tree, we state that the agent can only go on a non-visited viewpoint of a non-recognized object. *Ident* is stochastic and the transition function is defined by $P_{Ident}(l_{c,i})$. For instance, in this work we are using SIFT features to recognize the objects. We can estimate $P_{Ident}(l_{c,i})$ by studying the effect of the distance on the recognition probability. From experiments, we can compute the mean and the standard deviation of the number of SIFT matches according to several distance for various objects. With those information we estimate $P_{Ident}(l_{c,i}), \forall l_{c,i}$. Furthermore, we define a maximum number of observations *Max_Obs* per object. Once this limit is reached, the object shouldn't be checked anymore. Fig.3 shows this process. We consider that the observation succeeds if a candidate is identified as being the object and fails when it cannot decide (Unknown). It is impossible to apply an observation action on an identified object and also for those that have been observed *Max_Obs* times.

3.4 Reward and Cost Function *R*

The cost function is given by the travelling time plus the time of the image processing. As discussed in the conclusion, optimizing the mission time and the number of identified objects is a complex multicriteria optimization problem.

4 Algorithms

The selection of an algorithm to solve the object search problem has been studied in [4]. In this paper, the authors dealt online (less than 1sec) with problems having $|C| = 8, Max\_Obs = 2, |L_c| = 15$ which is reasonably large as an object search problem. The authors conclude that *LRTDP* [3], an heuristic algorithm, is the best suited for solving the MDP for object search with a limited number of objects. The general process of the system in the object search context is shown in the Fig.4. It first gathers information about the environment, updates if needed the related MDP model, then runs a planning algorithm to select the action to perform and finally executes it. Then the process is repeated until the end of the mission, defined by having no more candidate object to identify. The system is thus able to adapt to any change in the environment or with any information gathered on candidates objects before every decision step.

5 System Implementation

The implementation has been done using OpenRTM-AIST [1] as an implementation of RT-middelware. It allows the development of software components (RTC) and provides an interface to dynamically compose and plug a set of components. The complete system is presented Fig.5. The SLAM RTC(2) maintains a freespace map of the explored area. The main control is made by the Planner RTC(7). It can request a up-to-date MDP from the Modelizer RTC(6), solve it, and send the commands to the other components. If it is a move action, the Global pathplanner RTC(5) computes a global route sent to the local Pathplanner RTC(3), which react to unforeseen objects and avoids moving obstacles. If it is an observation action (*Detect* or *Ident*) a request is sent to the Observation controller RTC(4), which will send an image processing request to the related RTC, manage the results and send update to the Modelizer. The rest of the RTCs (1) controls the hardware (Camera, Robot, URG, buffers).

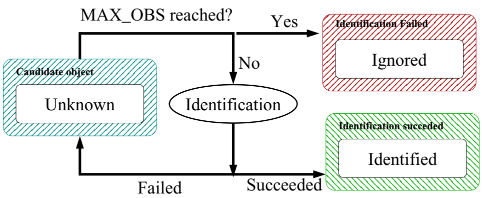

Fig. 3. Observation outcomes

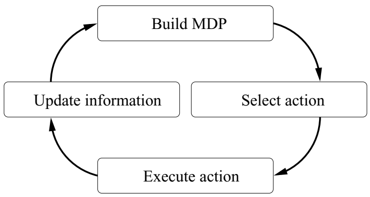

Fig. 4. Global execution loop

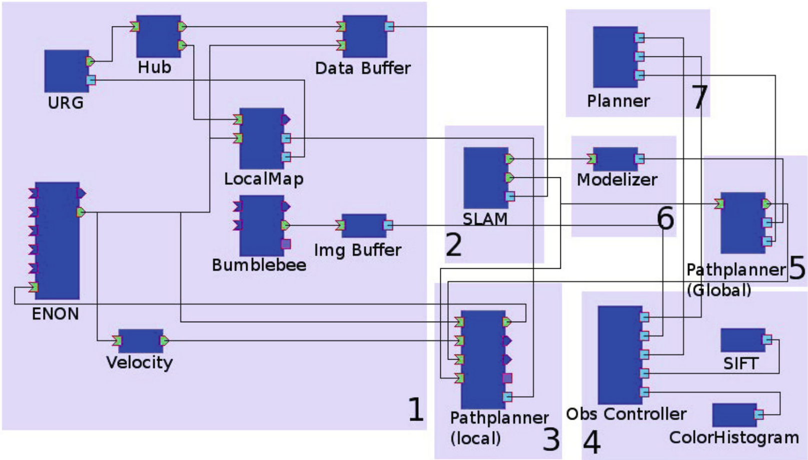

Fig. 5. Global RT components system

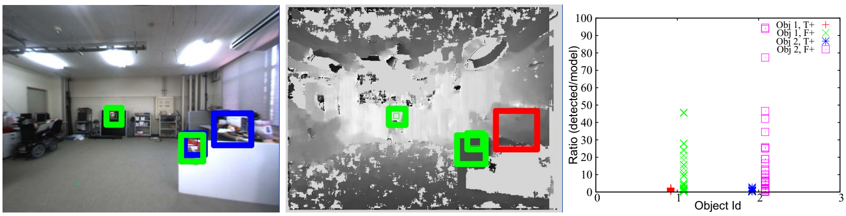

(a) Color detection (b) Verification (c) Surface ratio for true/false positive (T+/F+)

Fig. 6. False positive filter

The candidate detection is the first step of the object search upon which the policy is computed. If this step is not reliable the quality of the computed plan will be poor, even it is optimal. As a *Detect* function we are using a Color Histogram search. Since it is not robust, it will either return many false positive (too sensitive), or miss real candidate objects (not sensitive enough). Since we don't want to miss any real candidate, *Detect* should remain *"sensitive enough"*. Also we get the depth information from the stereo camera, we can follow the method proposed in [5]. When an object is detected, we compute the mean of its depth values. We have its world coordinate x,y,z and its model (previously given), so we can project the model at the detected location x,y,z in the image. We now have a candidate box, and a model box in the image, the algorithm can then compute the ratio between those two areas. Fig.6(c) shows for two different objects this ratio when computed with true positive (T+) and for false positive (F+). To reject incoherent objects, we keep results with a ratio in $[0.2;4]$, where all the true positive ratio value are. Fig.6 shows a false positive elimination where one object (the right-most one) is removed while keeping the true positive[2].

6 Experimental Result

We use a Fujitsu ENON robot with a Point grey bumblebee stereo camera, and a Hokuyo URG laser range finder. We also embed a laptop computer connected to the lab network using a wireless connection. On the LAN we can use desktop computers with standard GPU cards (Geforce 8600GTS).

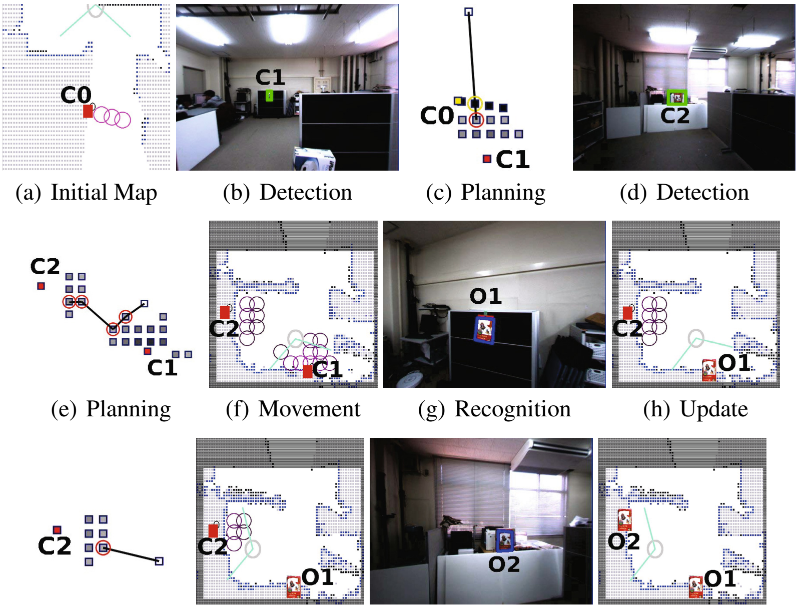

(a) Initial Map (b) Detection (c) Planning (d) Detection

(e) Planning (f) Movement (g) Recognition (h) Update

(i) Planning (j) Movement (k) Recognition (l) Update

Fig. 7. Example of semantic mapping

Fig.7 shows a global mission execution, within given boundaries (the brighter area in Fig.7(f)). The robot is in its starting position. It finds an unknown area from the free space map. The frontier between known an unknown area c_0 and the location from where *Detect* should be performed is computed (a). A *Detect* action is also performed from the starting position, returning one candidate object c_1 (b). With this information the MDP is computed, solved, and the next action is selected (go and detect candidate in the unknown area) (c). The action is performed by the robot by first going to the selected viewpoint. Then, since the candidate is an unknown area, the *Detect* action is performed and returned a new candidate c_2 (d). A new MDP is build and solved (e).

[2] Note that one false positive remains, it will be removed later by SIFT matching.

The robot moves to the selected location (f). The candidate is really a candidate object, *Ident* is applied, returning the pose and the type of the object o_1 (g). This information is used to update the map (h). One candidate remains so the MDP is build, solved (i), the action is executed (j). The object o_2 is identified (k), and the map is updated (l). Finally, no more candidate nor unknown area remains, the mission is over.

7 Conclusion

We show an MDP model of the object search problem using a mobile robot. By computing a policy for candidate detection, object recognition and exploration the robot can efficiently build this map. The MDP model can be solved using *LRTDP*, an online algorithm with a good anytime behaviour. Our model is designed for our specific hardware limitation, nevertheless it can be adapted regarding to new hardware capabilities, like the presence of zooming capabilities or 3D scanner. Furthermore, the planner has been developed as a component using RT-middleware, and thus can later easily be used on different type of hardware. The current candidate detection is made at discrete time decided by the policy computed from MDP. In the future, we would like to continuously integrate candidate detection. Also this paper focused only on optimizing the mission time ; we would like to investigate how to include the number of recognized objects in the decision process leading to a multi-objective optimization problem. As we would like the robot to evolve among humans we cannot consider the environment as static, maintaining an up to date map is also a challenging perspective.

Acknowledgements. This work is supported by NEDO (New Energy and Industrial Technology Development Organization, Japan) Intelligent RT Software Project.

References

1. Ando, N., Suehiro, T., Kotoku, T.: A Software Platform for Component Based RT-System Development: OpenRTM-Aist. In: Carpin, S., Noda, I., Pagello, E., Reggiani, M., von Stryk, O. (eds.) SIMPAR 2008. LNCS (LNAI), vol. 5325, pp. 87–98. Springer, Heidelberg (2008)
2. Aydemir, A., Sjöö, K., Folkesson, J., Pronobis, A., Jensfelt, P.: Search in the real world: Active visual object search based on spatial relations. In: ICRA 2011. IEEE, Shanghai (2011)
3. Bonet, B., Geffner, H.: Labeled RTDP: Improving the convergence of real-time dynamic programming. In: Giunchiglia, E., Muscettola, N., Nau, D.S. (eds.) ICAPS, pp. 12–31. AAAI (2003)
4. Boussard, M., Miura, J.: Observation planning with on-line algorithms and GPU heuristic computation. In: ICAPS 2010 Workshop on Planning and Scheduling Under Uncertainty (2010)
5. Helmer, S., Lowe, D.G.: Using stereo for object recognition. In: ICRA 2010, pp. 3121–3127. IEEE (2010)
6. Lowe, D.G.: Distinctive image features from scale-invariant keypoints. International Journal of Computer Vision 60(2), 91–110 (2004)
7. Masuzawa, H., Miura, J.: Observation planning for environment information summarization with deadlines. In: IROS 2010, Taipei, Taiwan, pp. 30–36 (2010)

8. Meger, D., Muja, M., Helmer, S., Gupta, A., Gamroth, C., Hoffman, T., Baumann, M., Southey, T., Fazli, P., Wohlkinger, W., Viswanathan, P., Little, J.J., Lowe, D.G., Orwell, J.: Curious george: An integrated visual search platform. In: CRV, pp. 107–114. IEEE Computer Society, Washington, DC (2010)
9. Puterman, M.L.: Markov Decision Processes: Discrete Stochastic Dynamic Programming. Wiley (2005)
10. Shubina, K., Tsotsos, J.K.: Visual search for an object in a 3D environment using a mobile robot. Comput. Vis. Image Underst. 114, 535–547 (2010)
11. Sjöö, K., Gálvez-López, D., Paul, C., Jensfelt, P., Kragic, D.: Object search and localization for an indoor mobile robot. Journal of Computing and Information Technology, Special Issue on Advanced Mobile Robotics 17(1) (2009)
12. Thrun, S., Burgard, W., Fox, D.: Probabilistic Robotics (Intelligent Robotics and Autonomous Agents). MIT Press (2005)

Effects of a Frequency-Dependent Dissipative Element in Haptic Interaction

Yo-An Lim[1] and Jeha Ryu[2]

[1] Department of Mechatronics, Gwangju Institute of Science and Technology, (Samsung Advanced Institute of Technology), Mt. 14-1, Nongseo-dong, Giheung-gu, Yongin-si Gyeonggi-do, 446-712, Korea
yoan.lim@samsung.com

[2] Department of Mechatronics, Gwangju Institute of Science and Technology, 1, Oryong-dong, Buk-gu, Gwangju, 500-712, Korea
ryu@gist.ac.kr

Abstract. This paper presents an analytical investigation into effects of a frequency-dependent dissipative element added to a haptic interaction system. A stably displayable impedance range is analyzed by a discrete-time model of a haptic system with a frequency-dependent dissipative element that can reduce the high frequency inputs causing instability in a haptic system. A frequency-dependent dissipative element can, however, reduce the displayable impedance range by generating excessive energy. It is also shown that the generated energy may be reduced by including two linear half-wave rectifiers to a dissipative element, which in turn increases the stably displayable impedance range.

1 Introduction

The human-computer interaction can be made more immersive by using haptic interfaces that provide users with a sense of touch in response to their hand movements in virtual, augmented, or real environments. Haptic interfaces have the potential to function either as input devices similar to computer mice or as output devices that reflect force. Generally, a haptic system is a hybrid system that consists of both a continuous-time and discrete-time system, and it includes a human user, haptic device, controller, and virtual environment as shown in Fig. 1. Ideally, when a haptic interface interacts with virtual objects it should transparently display the impedance of the interaction; infinite impedance for the rigid wall contact and zero impedance for free motion, while guaranteeing stability. In practice, however, transparency and stability, which are primary factors in determining the performance of haptic interaction, can be deteriorated due to several factors. Most notably, displaying virtual objects with very high stiffness by haptic interfaces is still a challenging problem, and many efforts have been made to increase the stably displayable impedance range, such as Colgate et al. [1], Mehling et al. [2], Weir et al. [3], Gosline et al. [4], Niemeyer et al. [5], Diolaiti et al. [6], Ryu et al. [7], and Srikanth et al. [8]. In the meantime, Kim and Ryu [9] presented a passivity-based control framework limiting the energy generation for guaranteeing stability. Adding dissipative elements in a haptic system can stabilize or improve the impedance range and the dissipative elements in previous works can be categorized as:

S. Lee et al. (Eds.): Intelligent Autonomous Systems 12, AISC 194, pp. 111–119.
springerlink.com

(a) viscous damping as in [1,3,4], (b) frequency-dependent damping as in [2,7], and (c) nonlinear damping as in [10,11].

As another research effort to increase the stably displayable impedance range, a nonlinear frequency-dependent dissipative element, referred to the analog input shaper (AIS), was proposed by Lim et al. [12,13]. In this paper, we presents a linear analysis of the frequency-dependent dissipative element using a simplified discrete-time model of a haptic system to see its effects on the stably displayable impedance range. Also, we show that when two linear half-wave rectifiers are added to the frequency-dependent dissipative element the stably displayable impedance range can be significantly improved through reducing the generated energy.

2 Frequency-Dependent Dissipative Element for Haptic Interfaces

In haptic interaction, high-frequency inputs usually occur during collisions with very stiff virtual objects and induce instabilities [2]. Also, it was shown that when the inputs are of high frequency, the output tends to be significantly amplified, and thus the system becomes unstable [12]. Therefore, it can be justified that for a relatively high frequency inputs, adding a frequency-dependent dissipative element, which is basically a low-pass filter, should assist in increasing the stability of a haptic system [12]. However, it should also be considered that the low-pass filter inevitably causes the delay, which is recognized as one of the major causes of instabilities in a haptic system. Therefore, there exists a tradeoff in adding a frequency-dependent dissipative element in a haptic system: the added dissipative element in the high frequency region increases the stability of a haptic system as well as displayable impedance, while low-pass filtering increases the first order time-delay, which in turn decreases the system stability as well as displayable impedance.

In the following, we first present the effects of the frequency-dependent dissipative element on stably displayable impedance range. We then discuss that the addition of two linear half-wave rectifiers to the dissipative element can reduce the energy generated by low-pass filtering, and thus the displayable impedance range can be significantly increased.

2.1 Low-Pass Filtering for Frequency-Dependent Dissipation

Fig. 2 shows a frequency-dependent dissipative element located before a motor current amplifier (i.e. in the signal stage), and the advantages of placing the frequency-

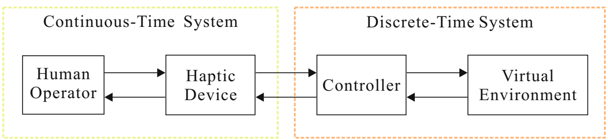

Fig. 1. Basic configuration of a haptic system

dependent dissipative element in a signal stage rather than in a power stage are discussed in [12]. Then, the dynamic equation relating the input voltage (v) to the motor output angle (θ_m) can be written as,

$$\left\{\left(1+\frac{z_1(s)}{z_2(s)}\right)J_m s^2+\left(1+\frac{z_1(s)}{z_2(s)}\right)B_m s\right\}\theta_m = K_t K_i V(s) \tag{1}$$

where z_1 and z_2 are the components of the added low-pass filter element, and J_m, B_m, θ_m, K_t, K_i, and V are rotational inertia, damping, position of a motor, motor torque constant, amplifier current constant, and input to the amplifier, respectively. Therefore, if we select appropriate z_1 and z_2, a frequency-dependent dissipative element (damping) can be obtained. Note that since the frequency of the voluntary motion of human hand is known to be a few Hz, when designing the frequency-dependent dissipative element, it would be reasonable to select its cutoff frequency within a few Hz. In summary, the frequency-dependent dissipative element reduces high frequency force inputs to a haptic device and thus increases the damping in the high frequency region [12].

2.2 Effects of a Low-Pass Filter on Displayable Impedance

Now, the analysis of the effects of the added frequency-dependent dissipative element on the stably displayable impedance range is presented. To this end, a discrete-time model of a haptic system is used as depicted in Fig. 3, and this approach was previously suggested by Hulin et al. [14, 15]. In the figure, the virtual object ($H(z)$) is assumed to have only stiffness, and z^{-1} represents computational delay.

In Fig. 3, the discrete-time transfer function of the haptic device ($G(z)$) can be obtained as,

$$G(z) = \left(1-z^{-1}\right)\frac{1}{B_d}\frac{z\left(1-\mathrm{e}^{-\frac{B_d}{M_d}T}\right)}{(z-1)\left(z-\mathrm{e}^{-\frac{B_d}{M_d}T}\right)} = \frac{1}{B_d}\frac{1-\delta}{z-\delta} \tag{2}$$

where $\delta = e^{-\frac{B_d}{M_d}T}$, and M_d, B_d, and T are inertia, damping of the haptic device, and sampling time, respectively.

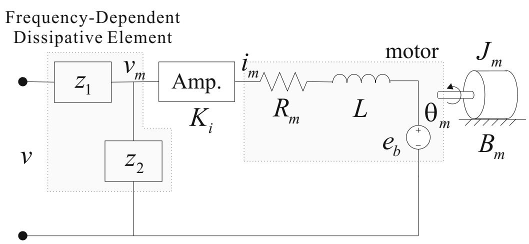

Fig. 2. Frequency-dependent dissipative element in signal stage

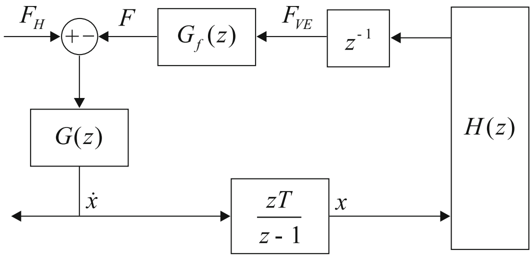

Fig. 3. Simplified discrete-time model of a haptic system

2.2.1 Without a Low-Pass Filter

First, when the dissipative element is not added to the system (i.e., $G_f(z) = 1$), the transfer function between the force from the human operator (F_H) and velocity of the haptic device $(\dot{x})$ can be obtained as,

$$\frac{\dot{x}}{F_H} = \frac{\frac{1}{B_d}(z-1)(1-\delta)}{(z-\delta)(z-1) + \frac{1}{B_d} T K_{VE}(1-\delta)}$$

, and thus the characteristic equation becomes as below.

$$Q(z) = z^2 - (1+\delta)z + \delta + \frac{TK_{VE}(1-\delta)}{B_d} \tag{3}$$

For the stability criterion of the discrete-time system, the Jury's stability test is applied to (3), and the necessary and sufficient conditions for $Q(z)$ to have no root outside or on the unit circle are as follows

Condition (1): $Q(1) = \frac{TK_{VE}(1-\delta)}{B_d} > 0$

Condition (2): $Q(-1) = 2(1+\delta) + \frac{TK_{VE}(1-\delta)}{B_d} > 0$

Condition (3): $\frac{TK_{VE}(1-\delta)}{B_d} + \delta < 1$

Among the above three conditions, Condition (1) and Condition (2) are always satisfied, since $K_{VE} > 0$, $B_d > 0$, $T > 0$, and $0 < \delta < 1$. Therefore, the system is stable if Condition (3) is satisfied, and thus the stably displayable stiffness range can be determined as below:

$$K_{VE} < \frac{B_d}{T} \tag{4}$$

2.2.2 With a Low-Pass Filter

When the dissipative element is a 1st order Butterworth low-pass filter of which cutoff frequency is α rad/sec, its transfer function in Z-domain can be written as,

$$G_f(z) = \frac{C(z+1)}{z+2C-1} \tag{5}$$

where $C = \dfrac{\alpha T}{\alpha T + 2}$, and the transfer function between the force from the human operator and velocity of a haptic device can be written as below.

$$\frac{\dot{x}}{F_H} = \frac{\frac{1}{B_d}(1-\delta)(z+2C-1)(z-1)}{(z+2C-1)(z-1)(z-\delta) + \frac{1}{B_d}TK_{VE}C(z+1)(1-\delta)} \tag{6}$$

Consequently, the characteristic equation becomes as follows,

$$\begin{aligned} Q(z) =& z^3 + (2C-\delta-2)z^2 + (E-2C-2\delta C+2\delta+1)z \\ &+ E + \delta(2C-1) = a_3 z^3 + a_2 z^2 + a_1 z + a_0 \end{aligned} \tag{7}$$

where, $E = \dfrac{TK_{VE}C(1-\delta)}{B_d}$. Therefore, the Jury's stability conditions become:

Condition (1): $Q(1) = 2E > 0$

Condition (2): $Q(-1) = 4(\delta+1)(C-1) < 0$

Condition (3): $K_{VE} < \dfrac{B_d}{TC(1-\delta)}\{1+\delta(1-2C)\}$

Condition (4): $|b_0| > |b_2|$,
where, $b_0 = E^2 + 2\delta(2C-1)E + \delta^2(2C-1)^2 - 1$, and $b_2 = (2C-\delta-3)E + (2\delta C-\delta+1)(2C-\delta-1)$.

Among the above four conditions, Conditions (1) and (2) are always satisfied, since $0 < C < 1$ and $0 < \delta < 1$. Also, if Condition (4) is satisfied, Condition (3) is always satisfied, though the detailed derivation is not shown here. Consequently, the system is stable if Condition (4) is satisfied, and thus the stably displayable stiffness range can be determined as below,

$$K_{VE} < \beta \frac{B_d}{T} \tag{8}$$

where,

$$\begin{aligned} \beta =& \sqrt{(\delta+2C)^2 + 8\delta C - 6\delta - 4C + 9}/2C(1-\delta) \\ &-(4\delta C - \delta - 2C + 3)/2C(1-\delta). \end{aligned}$$

Fig. 4 shows β variations according to the cutoff frequency α when parameters are $M_d = 0.032$ kg, $B_d = 0.02$ Ns/m, and $T = 0.001$ s. The parameters of a haptic device are

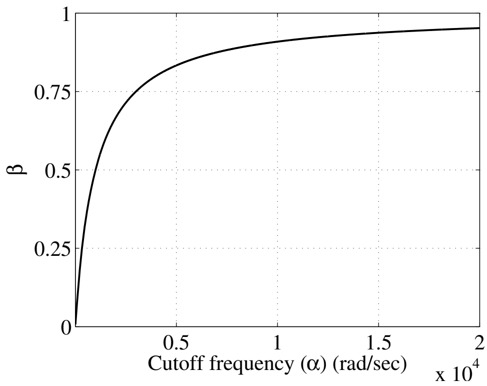

Fig. 4. β variation according to cutoff frequency α

set to those of a commercial haptic device Impulse Engine [16], and the sampling time (T) is typical one in haptic control. By comparing (4) and (8), one can see that the added low-pass filter decreases the stably displayable stiffness range, and the decrease explains that the effect of energy generation by time-delay is larger than that of added damping in the high frequency range. Through simulations the above analysis was confirmed, though the simulation results are not shown here due to the space limitation.

2.3 Linear Half-Wave Rectifiers for Reducing Energy Generation

To reduce the energy generation by the frequency-dependent dissipative element, two linear half-wave rectifiers are added to the low-pass filter as depicted in Fig. 5, which is called "analog input shaper (AIS)". Note that a low-pass filter can be realized by subtracting the output of a high-pass filter from the input. Since the rectifiers are highly nonlinear, the analytical approach is difficult. Thus, how they reduce the generated energy was shown through a simulation example of typical haptic interaction [12]. Since the delay in the haptic system makes a haptic system less passive [1], in the simulation it was shown that the rectifiers could reduce the energy generation, and thus made the haptic system more stable. In the following section, we present simulation results that show the AIS can significantly increase the stably displayable stiffness range.

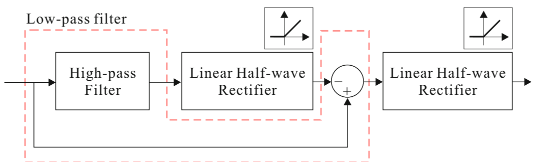

Fig. 5. Low-pass filter with two linear half-wave rectifiers

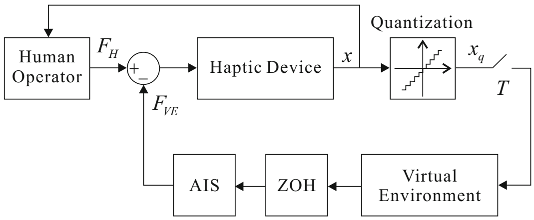

Fig. 6. Haptic system with continuous-time and discrete-time models

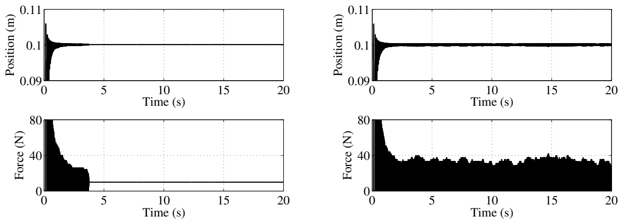

(a) $K = 100$ kN/m (b) $K = 110$ kN/m

Fig. 7. Simulation results without AIS

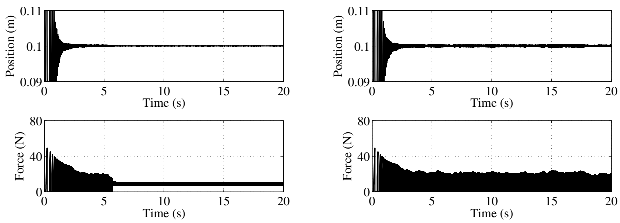

(a) $K = 190$ kN/m (b) $K = 200$ kN/m

Fig. 8. Simulation results with AIS

2.3.1 Simulation

Using a haptic system model in Fig. 6, simulation results that show the AIS can increase the stably displayable stiffness range are discussed in this section. The model in Fig. 6 is a hybrid system that includes both the continuous-time and discrete-time models, and the haptic device is composed of mass, viscous damping, and Coulomb friction as in [16] and can be expressed as follows.

$$M_d\ddot{x} + B_d\dot{x} + C_d\text{sgn}(\dot{x}) = F_H - K_{VE}$$

The parameters are set to $M_d = 0.032$ kg, $B_d = 0.02$ Ns/m, $T = 0.001$ s, and $C_d = 0.5$ N.

Also, the human operator is modeled as a damped mass and can be expressed as

$$M_{ho}\ddot{x} + B_{ho}\dot{x} = F_{ex} - F_H$$

where F_{ex} represents the intentional force of the human operator and is assumed to be constant (10 N), and the parameters are set to $M_{ho} = 0.15$ kg and $B_{ho} = 4.8$ Ns/m as in [16]. In addition, the quantization resolution is 20 μm and the high-pass filter used for the AIS in the simulation is a 1st order Butterworth analog filter.

Simulation results are shown in Figs. 7 and 8. When the AIS is not used, the interaction becomes unstable when the virtual stiffness is between 100 kN/m and 110 kN/m, while when the AIS is used, it becomes unstable when the virtual stiffness is between 190 kN/m and 200 kN/m. Hence, the AIS can increase the stably displayable stiffness range approximately 90 %. However, note that the AIS can reduce the initial contact hardness perceived by a user, since high frequency transient inputs are very helpful to improve the realism of contacting stiff virtual objects [17].

3 Conclusion

Using a simplified discrete-time model of a haptic system, the analysis of a frequency-dependent dissipative element added to a haptic interaction system was presented in this paper. It was shown that when only the frequency-dependent dissipative element was added, the stably displayable impedance range was significantly decreased, since the effect of energy generation by time-delay was larger than that of added damping in the high frequency range. By adding two linear half-wave rectifiers to the dissipative element, however, the generated energy was significantly reduced, which could make significant increase of the stably displayable impedance. For an optimal design of the frequency-dependent dissipative element with the rectifiers, a nonlinear analysis is planned for further research.

Acknowledgement. This work was supported by the Defense Acquisition Program Administration and the Agency for Defense Development under the contract UD100004ID.

References

1. Colgate, J.E., Brown, J.M.: Factors affecting the Z-Width of a haptic display. In: Proceedings of the IEEE 1994 International Conference on Robotics and Automation, San Diego, CA, pp. 3205–3210 (May 1994)
2. Mehling, J.S., Colgate, J.E., Peshkin, M.A.: Increasing the impedance range of a haptic display by adding electrical damping. In: Proceedings of the First Joint Eurohaptics Conference and Symposium on Haptic Interfaces for Virtual Environment and Teleoperator Systems, pp. 257–262 (March 2005)
3. Weir, D.W., Colgate, J.E., Peshkin, M.A.: Expanding haptic display Z-Width using analog electrical damping. In: World Haptics 2007 Second Joint EuroHaptics Conference and Symposium on Haptic Interfaces for Virtual Environment and Teleoperator Systems (Hands-On Demo) (March 2007)

4. Gosline, A.H., Campion, G., Hayward, V.: On the use of eddy current brakes as tunable, fast turn-on viscous dampers for haptic rendering. In: Proceedings of Eurohaptics, pp. 229–234 (2006)
5. Niemeyer, G., Diolaiti, N., Tanner, N.: Wave haptics: Encoderless virtual stiffness. In: Robotics Research, pp. 22–33 (2007)
6. Diolaiti, N., Niemeyer, G.: Wave haptics: Using motor dynamics for stiff coupling to virtual environments. In: Proceedings of the 2006 IEEE International Conference on Robotics and Automation, pp. 3274–3279 (2006)
7. Ryu, D., Song, J.-B., Kang, S., Kim, M.: Frequency domain stability observer and active damping control for stable haptic interaction. IET Control Theory and Applications 2(4), 261–268 (2008)
8. Srikanth, M.B., Vasudevan, H., Muniyandi, M.: DC Motor Damping: A Strategy to Increase Passive Stiffness of Haptic Devices. In: Ferre, M. (ed.) EuroHaptics 2008. LNCS, vol. 5024, pp. 53–62. Springer, Heidelberg (2008)
9. Kim, J.-P., Ryu, J.: Robustly stable haptic interaction control using and energy-bounding algorithm. International Journal of Robotic Research (2009)
10. Ryu, J.-H., Kim, Y.S., Hannaford, B.: Sampled- and continuous-time passivity and stability of virtual environments. IEEE Transactions on Robotics 20(4), 772–776 (2004)
11. Ryu, J.-H., Kwon, D.-S., Hannaford, B.: Stability guaranteed control: Time domain passivity approach. IEEE Transactions on Control Systems Technology 12, 860–968 (2004)
12. Lim, Y.-A., Ahn, H.-S., Ryu, J.: Analogue input shaper for haptic interfaces. IET, Control Theory and Applications 3(12), 1553–1564 (2009)
13. Lim, Y.-A., Ryu, J.: A digital input shaper for stable and transparent haptic interaction. Advanced Robotics 25, 1385–1403 (2011)
14. Hulin, T., Preusche, C., Hirzinger, G.: Stability boundary for haptic rendering: Influence of physical damping. In: Proceedings of the 2006 IEEE/RSJ International Conference on Intelligent Robots and Systems, Beijing, China, pp. 1570–1575 (October 2006)
15. Hulin, T., Preusche, C., Hirzinger, G.: Stability boundary for haptic rendering: Influence of human operator. In: Proceedings of the 2008 IEEE/RSJ International Conference on Intelligent Robots and Systems, Nice, France, pp. 3483–3488 (September 2008)
16. Diolaiti, N., Niemeyer, G., Barbagli, F., Salisbury, J.K.: Stability of haptic rendering: Discretization, quantization, time delay, and coulomb effects. IEEE Transactions on Robotics 22(2), 256–268 (2006)
17. Kuchenbecker, K.J., Fiene, J., Niemeyer, G.: Improving contact realism through event-based haptic feedback. IEEE Transactions on Visualization and Computer Graphics 12(2), 219–230 (2006)

A Case Study of Safety in the Design of Surgical Robots: The ARAKNES Platform

L.A. Sanchez[1], M.Q. Le[1], K. Rabenorosoa[1], C. Liu[1], N. Zemiti[1], P. Poignet[1], E. Dombre[1], A. Menciassi[2], and P. Dario[2]

[1] Dept. of Robotics, LIRMM
French National Center of Scientific Research (CNRS), Montpellier, France
sanchezsec@lirmm.fr, le@lirmm.fr, rabenorosoa@lirmm.fr, liu@lirmm.fr, zemiti@lirmm.fr, poignet@lirmm.fr, dombre@lirmm.fr
[2] BioRobotics Institute, Scuola Superiore Sant'Anna
Pisa, Italy
arianna.menciassi@sssup.it, paolo.dario@sssup.it

Abstract. This work presents a case study of safety in the design of the ARAKNES surgical robotic platform dedicated to single port laparoscopic surgery. The framework for the design of medical robots is shortly described and applied, focusing on safety. Moreover, it is explained how the design process can be placed in the context of the European community directives for medical devices.

Keywords: surgical robots, safety standards, design framework.

1 Introduction

Originally, medical robotics designs were inspired by the success of industrial robotics. However, the specificities of medical applications led to research on original kinematics, actuation mechanisms, compatibility with medical imaging devices, biocompatibility and more, and also to modify the regulations for production of medical devices, comprising surgical robots. After nearly three decades of research in the field, many prototypes have been built and validated technically, some clinically, but just few managed to find their way into operating rooms or medical offices [1].

In general, a medical robot is a complex system that consists of 1) an articulated and motorized mechanical structure, 2) electronic components, 3) a software controller, and 4) a human machine interface (HMI). These components are used to perform interventions in a constrained and not fully structured environment, inside and/or outside of the patient's body, in collaboration with the medical staff. Thus, it is easy to understand that a system failure or dysfunction can be extremely critical. For that reason, safety guidelines should be followed in order to ensure that each component is designed, implemented and integrated to achieve the intended medical tasks in optimal conditions and in compliance with the existing device regulations.

S. Lee et al. (Eds.): Intelligent Autonomous Systems 12, AISC 194, pp. 121–130.
springerlink.com

Hardware safety is the basic requirement for a robot. Prior enhancement methods included sensor redundancy, mechanical limits and default detection [2]. Ng. et al. also presented mechanical safety enhancement methods for a surgical robot [3]. Ergonomics analysis methods have also been used for HMI design [4]. Lewis and Maciejewski put forwards method to analyze joint failures [5] whereas Ikuta et al. used impact force and stress as the safety value for human-care robots [6].

Software safety received more attention with the intensive use of computers, integrated circuits and advanced functionality in robots. Safety approaches which could be used include fault tree analysis [7], [8], even tree analysis [7], fault tolerance algorithm [9] and dependability principles [10]. Recently, Haddadin et al. proposed reactive control strategies that can significantly improve the human safety during physical interaction with environment [11]. The control approach consists of a collision detection method, allowing to reduce contact forces far below any level which is dangerous to humans.

Dombre et al. presented in [1] a generic framework for the design of medical robots taking into account the above mentioned considerations. In this paper, the design process of the ARAKNES platform used for single port laparoscopic surgery is presented [12]. Particular interest is dedicated to system safety. Moreover, it is also described how the design framework can comply with European directives for bringing a surgical robot prototype into the operating room.

This paper is organized as follows. Section 2 introduces the ARAKNES platform and the involved design framework, focusing on the implemented safety features. Section 3 places the design framework in the context of existing European directives for medical devices. Finally, conclusions and perspectives are drawn in section 4.

2 The ARAKNES Platform: From Surgical Gesture Analysis to Robot Design

The ARAKNES platform (Figure 1) is an innovative concept for endoluminal surgery in which the main objective is to locate most of the Degrees of Freedom (DoF) available to the surgeon inside the patient, leading to less invasiveness. Preliminary results concerning the first developed prototypes were presented in [12].

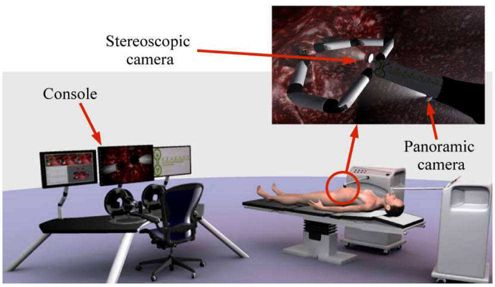

Fig. 1. ARAKNES platform concept for Single Port Laparoscopy [13]

According to [1], the design process can be described by four tasks, which deal with the system specifications, the design methodology, the technological choices, and the system safety. The first three tasks are indirectly related to system safety, while the last one tackles directly the issue. Each task and its corresponding subtasks are shortly described in this section.

2.1 Definition of the Surgical System Specifications

Analysis of the Surgical Gesture

To define the system requirements, the surgical gesture is analyzed by the robotic expert that studies how the medical staff performs a similar procedure. Apart from looking at the state-of-the-art of the concerned intervention, data is measured and recorded (e.g. tool positions, manipulation forces, configuration of the elements inside the operating room). Then, an analysis of all the information will lead to the system specification (i.e. required number of DoF, required speeds, forces, and more).

In the ARAKNES platform for instance, instruments are inserted through a cylindrical access port in the navel, through an incision of about 30–35 mm [14]. The navel is used to gain access to the abdomen in a practically scar-less way. However, it requires a remote-centre-of-motion (RCM) at the level of the umbilicus. Additional information concerning the required forces and speeds can be found in [13]. The ARAKNES system should also offer the surgeon a dexterity and freedom of movement equivalent to the ones of his/her hands.

Kinematic and Dynamic Specifications

The specifications are defined from the data analyzed in the preceding step. For instance, a bimanual robot with six active DoFs plus the gripper is required in order to reproduce the movements of the surgeon's hands. An external manipulator for positioning the miniature arms inside the abdomen should respect the RCM constraint. Refer to [12], [13], [15] for more details on the ARAKNES prototype.

Kinematic Topologies

An appropriate type of kinematics to satisfy the specifications is then selected by the designer [1]. Conventional serial kinematics, for instance, allows achieving a large workspace, high dexterity and good obstacle avoidance capabilities (e.g. "snake" like robots), necessary for completing surgical tasks, while keeping the two miniature robotic manipulators attached to the umbilical access port. Parallel kinematics could offer, on the other hand, a stiff support that complies with the RCM constraint required by the external positioning mechanism holding both the access port and the bi-manual robot [15].

2.2 Design Methodology

Prototypes are the result of a set of design choices, and methodological approaches exist to lead to an implementation of a concept. These approaches depend on whether the starting point is a robot concept (topological synthesis) or parameters optimization of a previously designed concept is carried out (dimensional analysis). In the case of ARAKNES, the starting point is a new concept constrained by the use of the smallest available components, such as electrical actuators and embedded electronic components. The reader can refer to [1] and [3] for more detailed examples of design methodologies.

2.3 Technological Choices

Next, the designer has to make a series of decisions concerning the actuators, sensors and materials which will be used to manufacture the prototypes. For instance, if the system will be used under a MRI or a CT scanner, the compatibility of its components has to be verified. Additionally, certain components must be sterilizable.

2.4 System Safety

Figure 2 shows the bi-manual robot prototype of the ARAKNES platform [12]. The safety features that have been implemented on this prototype are the result of the application of a set of recommendations for risk reduction in medical robots as described in [1]. The recommendations are based on 1) the use of intrinsically safe components, 2) the concept of redundancy, and 3) other additional design constraints, such as joint position and velocity limits and software thresholds on critical signals like contact force. All guidelines in [1] can be applied at the hardware (electromechanical and electrical components), software and operational levels.

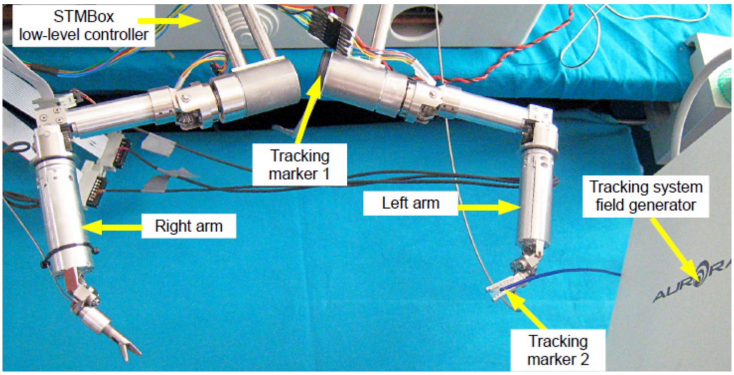

Fig. 2. The bimanual robot prototype for single port laparoscopic surgery

Hardware Safety

The hardware safety is tackled at two levels: the mechanical level and the electrical level.

Concerning the mechanical level, the mechanical design of the bi-manual arms excludes most singularities of the robot's workspace, with the only exception of the wrist singularity which is handled by software [12]. A high reduction ratio limits the speed of the actuators. The robotic arms are designed in such a way that in case of a power failure, the robot is locked due to the gear reduction ratio.

Concerning the electrical level, ST Microelectronics developed custom electronic boards, namely STMBox [12]. These boards could be sterilizable, and include power limitations of the actuator's current in order to avoid overheating or damaging the miniature electrical motors. Moreover, a deadlock watchdog and a communications timeout were integrated in the low-level actuator controller. A watchdog timer is an electronic hardware device that can be used to automatically detect software anomalies and reset the processor, if any occurs. In this case, the system will be restarted or safely stopped as if a human operator had switched off the power.

The global safety sequence performed in case of error is:

1. Engage brakes if available. For instance, the external positioning platform DIONIS [15] has breaks, but the internal bi-manual platform SPRINT does not [13]. On the other hand, it has a reduction ratio that keeps the system in position.
2. Stop motion using the emergency stop ramp time and deceleration.
3. Wait for the axes to be stopped and the brakes to be engaged, as well as limit the time for robot power-off after an error.
4. Disable the power amplifiers.
5. Disable the actuators power, but leaving sensors and encoders powered-on. Thus, joint positions are known at any time, even when motors are uncontrolled.

Software Safety

The software components of the ARAKNES platform involve 1) the surgeon's console interface, 2) the low-level actuator controller and 3) the high-level controller software. In each case, an incremental design through functional blocks of the components has been carried out, allowing to reduce the certification requirements of some components (i.e. the console is considered a Class I medical device while the other two are Class IIb devices as it will be explained in section III).

Software Architecture

As shown in Figure 3, the software architecture was implemented using concurrent processes running in parallel and in separate processing units [12], [16] dedicated to specific tasks: security (Main task), Cartesian control (Left and Right arm tasks), Joint control (STMBox task), Communication with peripheral units and sensors (force sensor and electromagnetic tracker tasks), HMI communication (teleoperation task), and so on.

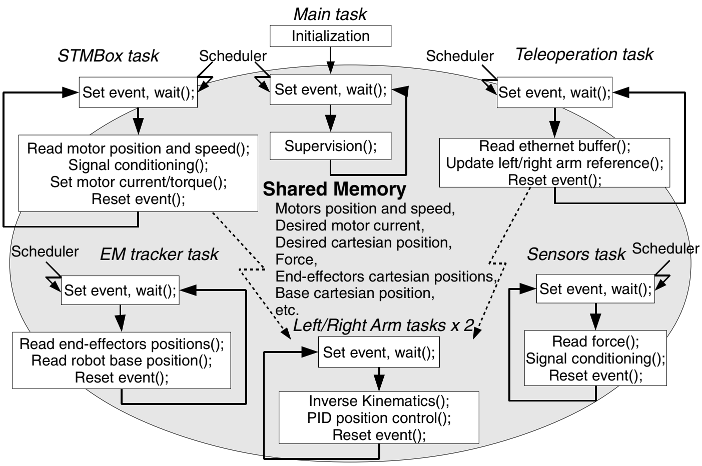

Fig. 3. Modular high-level controller software architecture [12], [16]

Another software safety which was implemented is the supervision task (Figure 4), which uses a software watchdog to verify the correct execution of the other processes at each sampling period in a round-robin manner. It is also possible to check the status of the operating system thanks to the "proc" interface provided in Linux RTAI [12]. If an error is detected an emergency shutdown routine is executed to stop the system in a predictable manner.

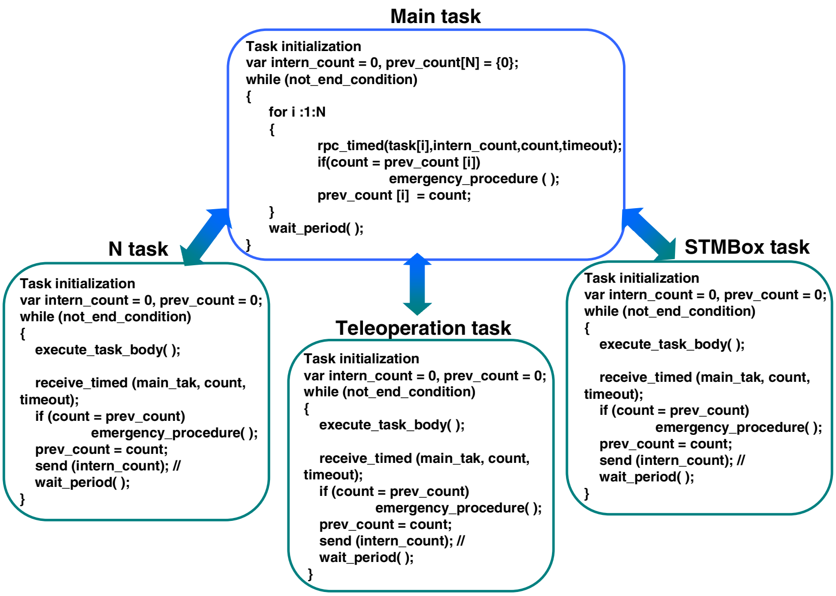

Fig. 4. Dedicated watchdog/supervision process to check task execution in round-robin fashion [12]

Variable time consuming procedures should be avoided to decrease the execution-time of the processes (thus, to increase the sampling frequency for reacting faster in case of emergency). If an overrun is detected, it is taken into account in the control algorithms by using a real elapsed time value.

Kinematic Singularities

The kinematics resolution method takes into account the possibility that the robot is lead through or nearby a singularity configuration by using a damping factor in order to ensure system stability [17]. Most singularities are out of the workspace thanks to the designed mechanical structure, but special care is taken concerning the wrist singularity.

Virtual Fixtures

Virtual fixture joint limits have been implemented. To be effective, these limits must be lower than the mechanical ones. This fictive redundancy allows to increase the lifetime of mechanical components and to guarantee a limit even if the mechanical joint limit is broken. This feature may also be interesting to reduce the workspace according to the operating mode and create forbidden region virtual fixtures.

Concerning the low-level controller software, the custom hardware and software developed by ST Microelectronics allows the use of threshold limits in order to restrict the payload, forces, torques, velocities, and acceleration, which might useful for handling collisions.

Operational Safety

At the operational level, user manuals must be furnished for components such as the high-level and low-level controllers. Software version control and documentation systems were integrated during the implementation phase, as required by most device certification standards. Additionally, other partners of the ARAKNES project [18] are developing advanced functions for the surgeon's console, such as pre-operative planning and training of the surgeon and his team with a simulator.

3 European Community Directives

The European directives 93/42/CEE and 2007/47/CE classify all medical devices into 4 classes:

- Class I: low level of risk
- Class IIa: level of average risk
- Class IIb: high level of risk
- Class III: critical level of risk

The classification depends on criteria such as the duration of use, the level of invasiveness, the active nature – or not – of the device, the concerned organ, etc. According to the previous criteria, each individual component or unit of a surgical robot can take part for any class (e.g. the surgeon's console is Class I as mentioned in Section II). However, if the system is considered globally, a surgical robot could be part of any class between IIa and III. The ARAKNES platform is a Class IIb active surgical device.

Figure 5 shows a diagram of the relationship between the applied medical robot design framework [1] and the European standards for medical devices. The latter define a set of documents and tests required to control the product development, validation and manufacturing processes before the final product release. Readers should refer to these standards to determine the exact requirements for each hardware or software component.

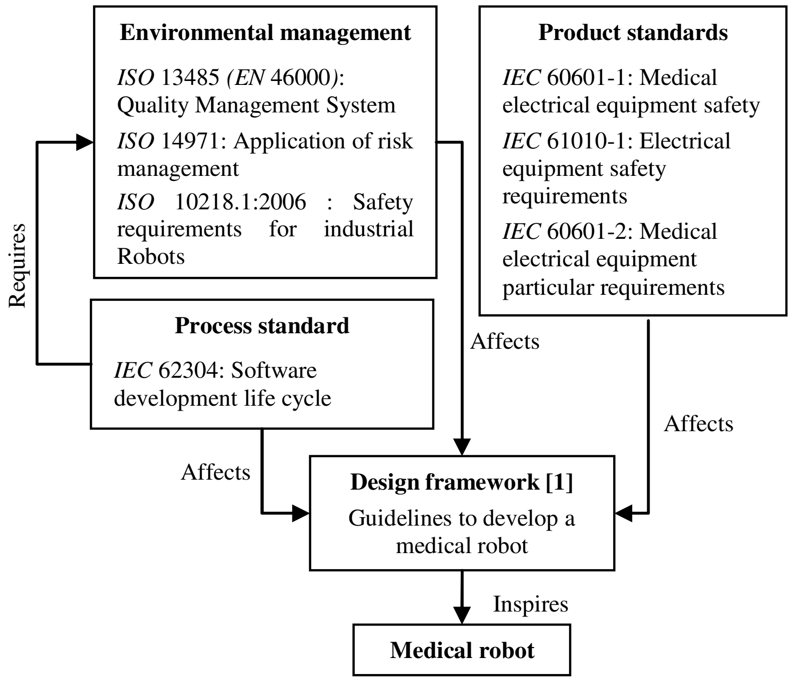

Fig. 5. Relationship between the presented guidelines for medical robot design and the European directives for medical devices

The environmental management is of particular importance in order to obtain the European marking required for taking a robot into the operating room.

Recently, JWG9 (Joint Working Group) has been formed by IEC SC 62A with ISO TC 184/SC2, and it is expected that additional medical robots standards will be introduced [19].

In any case, in the design methodology each subsystem should be identified by the following properties: level of risk, medical device class, and type of component (i.e. electromechanical, electrical, etc.) in order to apply the risk reduction recommendations of [1].

4 Conclusion

In this paper, a case study in the design of surgical robot was provided. A generic framework including system specifications, design methodology, technological choices, etc., has been used for a safety assessment dedicated to the single port laparoscopic surgery. During system integration and evaluation, other remaining issues will be taken into account for providing clear error messages or warning signals (such as lights or sounds) to the surgeon in order to indicate the system's status, errors or unauthorized behaviors. Besides the design criteria for mechanical systems, the one for vision systems will be also considered as one of important research paths to be investigated, as they have indirect impact on patient safety. Finally, another aspect of this study is to improve working conditions within the operation room environment by ensuring not only safety but also comfort and ergonomics of the surgeon during laparoscopic surgery.

Acknowledgements. This work was supported by the European Commission in the framework of ARAKNES FP7 European Project no. 224565.

References

1. Dombre, E., Poignet, P., Pierrot, F.: Design of Medical Robots. In: Troccaz, J. (ed.) Medical Robotics, 1st edn., pp. 141–176. Wiley (2011)
2. Troccaz, J., Lavallee, S., Hellion, E.: A passive arm with dynamic constraints: a solution to safety problems in medical robotics. In: International Conference on Systems, Man and Cybern. Systems Engineering in the Service of Humans, pp. 166–171 (1993)
3. Ng, W.S., Tan, C.K.: On safety enhancements for medical robots. Reliability Engineering & System Safety 54(1), 35–45 (1996)
4. Rau, G., Radermacher, K., Thull, B., Von Pichler, C.: Aspects of Ergonomic System Design Applied to Medical Work Systems. In: Computer-Integrated Surgery: Technology and Clinical Applications, pp. 203–221 (1996)
5. Lewis, C.L., Maciejewski, A.A.: Dexterity optimization of kinematically redundant manipulators in the presence of joint failures. Computers & Electrical Engineering 20(3), 273–288 (1994)
6. Ikuta, K., Nokata, M.: General evaluation method of safety for human-care robots. In: International Conference on Robotics and Automation, vol. 3, pp. 2065–2072 (1999)
7. Khodabandehloo, K.: Analyses of robot systems using fault and event trees: case studies. Reliability Engineering & System Safety 53(3), 247–264 (1996)
8. Connolly, B.: Software safety goal verification using fault tree techniques: a critically ill patient monitor example. In: Conference on Computer Assurance, Systems Integrity, Software Safety and Process Security, pp. 18–21 (1989)
9. Hamilton, D., Visinsky, M., Bennett, J., Cavallaro, J., Walker, I.: Fault tolerant algorithms and architectures for robotics. In: Electrotechnical Conference, pp. 1034–1036 (1994)
10. Dowler, N.J.: Applying software dependability principles to medical robotics. Computing & Control Engineering Journal 6(5), 222–225 (1995)
11. Haddadin, S., Albu-Schaffer, A., De Luca, A., Hirzinger, G.: Collision detection and reaction: A contribution to safe physical human-robot interaction. In: IEEE/RSJ International Conference on Intelligent Robots and Systems, pp. 3356–3363 (2008)

12. Sanchez, A., Petroni, G., Piccigallo, M., Scarfogliero, U., Niccolini, M., Liu, C., Stefanini, C., Zemiti, N., Menciassi, A., Poignet, P., Dario, P.: Real-Time Control and Evaluation of a Teleoperated Miniature Arm for Single Port Laparoscopy. In: International Conference in Medicine and Biology Society, pp. 7049–7053 (2011)
13. Piccigallo, M., Scarfogliero, U., Quaglia, C., Petroni, G., Valdastri, P., Menciassi, A., Dario, P.: Design of a novel bimanual robotic system for single-port laparoscopy. IEEE/ASME Transactions on Mechatronics 15(6), 871–878 (2010)
14. Galvao Neto, M., Ramos, A., Campos, J.: Single port laparoscopic access surgery. Techniques in Gastrointestinal Endoscopy 11(2), 84–93 (2009)
15. Beira, R., Santos-Carreras, L., Rognini, G., Bleuler, H., Clavel, R.: A novel remote-center-of-motion parallel manipulator for minimally invasive surgery. Applied Bionics and Biomechanics, Special issue in Surgical Robotics (2010)
16. Poignet, P., Dombre, E., Merigeaux, O., Pierrot, F., Duchemin, G.: Design and control issues for intrinsically safe medical robots. International Journal on Industrial Robot 30(1), 83–88 (2003)
17. Chiaverini, S., Siciliano, B., Egeland, O.: Review of the damped least-squares inverse kinematics with experiments on an industrial robot manipulator. IEEE Transactions on Control Systems Technology 2(2), 123–134 (1994)
18. ARAKNES Project Website, Internet, http://www.araknes.org, (accessed on January 31, 2012)
19. Doctor Robot, I presume?, International Electrotechnical Commission, http://www.iec.ch/etech/2011/etech_0711/ind-2.htm (accessed on April 24, 2012)

Classification of Modeling for Versatile Simulation Goals in Robotic Surgery

Stefan Jörg, Rainer Konietschke, and Julian Klodmann

Robotics and Mechatronics Center, German Aerospace Center (DLR), Wessling, Germany
stefan.joerg@dlr.de

Abstract. Simulation is common practice for surgeon training in particular for robotic surgery. This paper introduces further relevant applications of simulation that improve patient safety. Therefore, the design of a modular simulator for minimally invasive robotic surgery is presented. The authors introduce a classification of hierarchical levels of modeling details for the three aspects Application, System, and Patient. Furthermore, the principal use case classes Training, Workflow Validation, Workflow Design, Monitoring, and Robot Design of simulation for robotic surgery are introduced. For each class standard simulator setups are presented. The use of the classification is exemplified for Training and Robot Design use cases.

Keywords: surgical robotics, simulation, patient safety.

1 Introduction

It is common practice, to use the method of simulation to train surgeons with the aim to improve patient safety [5] [11] [2]. Training has been recognized as an even more important issue when surgical robotic systems are involved because their use requires new skills [6].

Other than surgical training, there are more useful applications of simulation that increase patient safety in the context of robotic surgery, e.g. preoperative planning or workflow optimization.

The intention of this paper is to introduce the relevant applications of simulation for robotic surgery and to describe their relation to patient safety. In particular, the relevant properties of simulation in robotic surgery are identified and then used to classify the simulation types as use cases which are defined intended applications.

As robotic surgery involves complex technical systems the authors view the simulation thereof from a systems engineering point of view. The System Modeling Language SysML is an industry standard for the specification, analysis, design, verification, and validation of such systems [10]. Following SysML, we define a *use case* as the description of the intended *goal* of a simulation.

To establish a common ground, the definition of a Simulator for Robotic Surgery is given in the following section. Based on this, the main components of

S. Lee et al. (Eds.): Intelligent Autonomous Systems 12, AISC 194, pp. 131–141.
springerlink.com

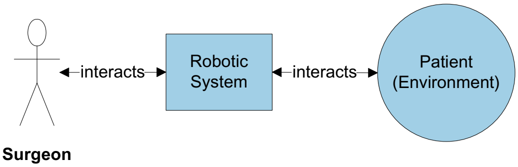

Fig. 1. The Robotic System Simplifies the Interface Between Surgeon and Environment. The Surgeon Only Interacts with the Robotic System.

a simulator for robotic surgery are introduced. Sec. 3 introduces the concept for approximation of the real world with levels of details with the aim to optimize the modeling and simulation effort for a given use case. Sec. 4 introduces the principal use case classes of simulation. Sec. 5 exemplifies the setup of the simulator.

2 A Simulator For Robotic Surgery

In this section the definition of a simulator for robotic surgery is presented. This definition will be later used for the discussion of the relevant use cases and the simulator setups related to that.

There are various definitions of simulation in the literature that reflect the broad application domains of this method [4] [12]. We use the more formal definition of *simulation* as observation or execution of a model over time. A *model* is an approximate representation of a real-world system. A *simulator* implements and executes a model to perform a simulation. *Analysis* is the process to verify and validate the simulation result. Thus, the method of simulation involves the tasks to model, simulate, and analyze.

A simulator interacts with an *entity-under-test*. If the entity is human, the simulation is called *interactive* (human-in-the-loop). Surgeon training is a well-known example of interactive simulation.

Simulation is *real-time* when the simulation time advances with the physical time of the real-world. If the simulator interacts with a real-world system the simulation has to be real-time. Hence, interactive simulation is always real-time.

A model is *discrete-event* or *continuous*. A discrete-event model updates its state upon the occurrence of an event. In general, events occur aperiodically. In contrast to that, a continuous model defines its state as a continuous function of time, e.g. as differential equations. Advanced simulations of real-world systems use a combination of both [4].

Practically, the *implementation* of a simulation approximates the continuous states at periodic steps in simulation time. Similar to that robotic systems are implemented as discrete signal systems. Discrete signal computation means that at certain points in time sensor values are acquired and a control law is executed that generates new motor commands. This similarity can be leveraged to use the same implementation of control laws for the simulation and the real system.

In robotic surgery, the robotic system is usually the main way a surgeon interacts with the patient. Therefore, the focus of this paper is on models where

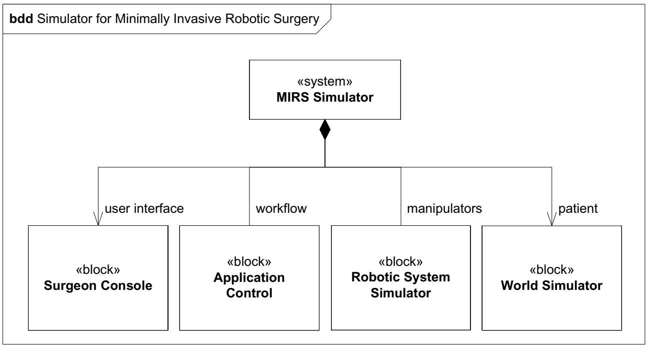

Fig. 2. A Modular Simulator for Minimally Invasive Robotic Surgery (MIRS)

only the robotic system is the intermediate between surgeon and environment (see Fig. 1). This simplifies the user interface. Instead of various surgeon tools only the user console of the robotic system interfaces directly with the surgeon. Especially, for the tele-robotic setups of minimally invasive surgery it is natural to use the same interface for simulation and real-world scenarios [1].

Fig. 2 depicts the main components of a simulator for minimally invasive robotic surgery. The four components Surgeon Console, Application Control, Robotic System Simulator and World Simulator partition the model of the surgical robotic system into corresponding classes: User interface, workflow, manipulators, and patient.

This modularity of the simulator can be used to adapt the simulator to various use cases. The simulator's use case determines the details of each model (its relevant aspects) and the interface between each component (exchange of data between models). Level of detail introduces a classification of aspects of a model's approximation of the real world. The following section discusses the main aspects and introduces corresponding hierarchies of abstraction levels.

3 Level Of Details

A model is an approximation of the real world. Levels of modeling details introduce a classification of this approximation. The main purpose of the introduction of levels of modeling details is the scaling of modeling and computation effort according to the simulation's use case. Hence, a proper classification has to grasp the relevant issues of the simulator's application domain. We refer to these relevant issues as the aspects of the model. For robotic surgery, we identified three relevant aspects of the model:

- The Application Model, which captures the surgical procedure *(Application-Centric)*
- The System Model, which captures the implementation of the robotic system *(System-Centric)*

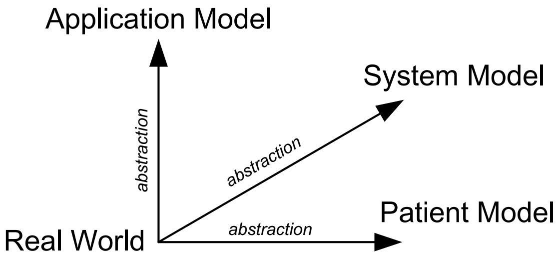

Fig. 3. Three Distinct Aspects of Simulation for Robotic Surgery are Application, System, and Patient

- The Patient Model, which captures the environment with the focus on the patient *(Patient-Centric)*

Together, they span the modeling space for robotic surgery (see Fig. 3). Depending on the simulation's use case, each aspect is of more or less interest, i.e. the approximation needs to be more or less realistic. For each aspect, a hierarchy of abstraction levels further classifies the modeling detail. Starting at the most abstract level each successive level adds a new detail to the model. Finally, Level 0 represents the real-world. These hierarchies for each aspect are the method to easily adapt a simulator setup to the requirements of a distinct use case. In the following, the hierarchies for the three aspects are introduced.

3.1 Application-Centric Modeling Hierarchy

The aspect of application has the focus on how detailed the surgical procedure is modeled.

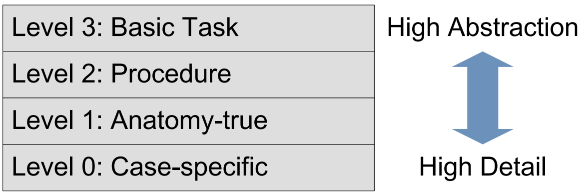

Fig. 4. Application-Centric Levels of Modeling Details

Level 3 Basic Task: On this level, the application model captures only basic tasks, such as suturing or cutting. There is no workflow and no surgical goal.

Level 2 Procedure: The procedure level adds the workflow to the basic tasks. This includes a surgical goal.

Level 1 Anatomy-true: This level adds the details of human anatomy, such as organs and vessels.

Level 0 Case-specific: This level adds the specific data and anatomy parameters of a certain case (patient).

3.2 System-Centric Modeling Hierarchy

The system model has the focus on the modeling details of the implementation of the surgical robotic system. This refers to the main components of a surgical simulator as depicted in Fig. 2. Therefore, for each level the impact on each component is discussed, except the Application Control component which is mainly affected by the Application-Centric aspect.

Level 3 Kinematics: Only the kinematical aspects are modeled on this level, dynamic effects are not considered (e.g. masses, inertia, and forces). **Surgeon Console:** User input is simulated and limited to motion, e.g. playback of prerecorded user input, dedicated test patterns. The **robotic system** is modeled as an ideal positioning device: It follows its desired trajectory instantly. **World:** Manipulation of objects in the environment is limited to motion.

Level 2 Dynamics: This level introduces dynamics, i.e. the effects of masses and forces and torques w.r.t. motion. Relevant dynamic effects of implementation properties are also modeled on this level, e.g. torque ripple, latency, friction. **Surgeon Console:** Simulated user input is augmented by the dynamic properties of input devices. Thus, the effect of input devices on the system, e.g. its control laws, etc., can be investigated. **Robotic System:** The movement of the robot is constrained by its dynamics (e.g. inertia, maximum motor torque, friction, etc.) and by external forces of the environment. An accurate dynamics model of the robotic system is necessary for this [8]. **World:** Interaction of objects (including the robot) in the environment is modeled with forces and torques.

Level 1 Implementation: This level adds the cycle-true computation of discrete signal systems. The cyclic execution at discrete points in time is only an approximation of the continuous physical world. Level 1 models this cyclic execution of the system. Thus, the effects on the system's performance due to this discrete approximation can be incorporated to the simulation. Level 1 is useful to simulate the behavior of implementations of complex systems. Details of the mechatronic implementation are added to the simulation. These include communication errors and delays, computation time, quantization of sensor values. **Surgeon Console:** Mechatronic implementation of input and feedback devices.

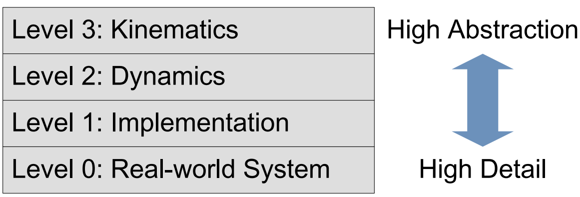

Fig. 5. System-Centric Levels of Modeling Details

Robotic System: Mechatronic implementation of the robotic system. **World:** There are no implementation details of the environment.

Level 0 Real System: This level represents the real-world system, e.g. the robot and its tools, input devices, GUIs, 3D-Displays, the patient, animal models or phantoms.

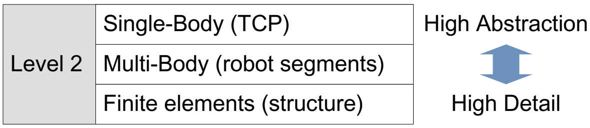

Fig. 6. Reasonable Levels of Modeling Details within Level 2 (Dynamics)

The three levels of kinematics, dynamics and implementation cover the most relevant details of simulation in descending order. It is reasonable to refine this main classification within each level. Especially Level 2, the dynamics, has varying aspects of interest depending on the simulation's use case. Fig. 6 depicts a possible hierarchy within Level 2.

3.3 Patient-Centric Modeling Hierarchy

The patient model regards the details of the environment with the focus on the patient. Basdogan et al. [5] state that versatility in patient modeling, finding the right realism and integrating material properties of organs are all important issues for surgical simulation. The following hierarchy defines three major abstraction steps of the environment model.

Fig. 7. Patient-Centric Levels of Modeling Details

Level 3 Rigid Body: On this level, the environment is modeled as rigid body geometry with stiff object contacts.

Level 2 Soft Tissue: This level adds the detail of material properties to the modeled objects (e.g. soft tissue for organs).

Level 1 Functional: This level adds functions to the tissue, i.e. blood flow, objects are cuttable, tear-able.

Level 0 Real-World: The patient, a phantom or an animal.

4 A Classification Of Principal Use Cases

Starting the classification from a systems engineering point of view the principal use case classes of simulation for robotic surgery are discussed in this section. As robotic surgery involves sophisticated mechatronic systems it is reasonable to derive the categories of application from that domain. Including training from the domain of surgery, the four main categories of goals for simulation in the context of robotic surgery are as follows:

Training - goal of training is to use the method of simulation to improve the skills of involved humans.

Design - goal is to use simulation for the design process of a system. This includes the robotic system, the design of a surgical procedure, etc.

Validation - goal is to identify the proper system or task specifications.

Verification - goal is to use simulation to determine whether a system or procedure works as specified.

In the following, the principal use case classes for simulation of robotic surgery are discussed and related to the four categories. Figures 8-13 show the configuration of the modular simulator, introduced in Section II, for the principal use case classes.

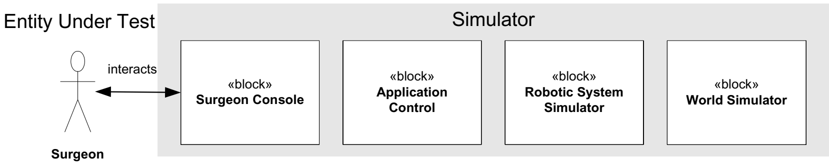

Fig. 8. Simulator Setup for the Class Surgeon Skill Training

Use Case Class Surgeon Skill Training (Category: Training) It is common practice to use simulation to train surgeon skill either on a certain surgical procedure or to operate the robotic system. **Goal:** Improve skills of surgeons. **Typical Setup:** Requires all four components of the simulator (see Fig. 8). The surgeon is the entity-under-test. Hence, the simulation is always interactive. **Patient safety** is immediately affected by surgeon skills. However, a training curriculum is required that proves to enhance surgeon skills [3].

Use Case Class User Interface Design (Category: Design, Validation) **Goal:** Improve and validate the design of the surgeon console. **Typical Setup:** The simulator (see Fig. 8) consists of Application Control, Robotic System and World simulators. The Surgeon Console is the entity-under-test. **Patient Safety:** A validated user interface reduces the risk of mal-operation. An improved user interface puts the surgeon's focus on the surgical procedure. It provides the surgeon with relevant information only and alerts him of impending risks.

Use Case Class Workflow Validation (Category: Validation). Workflow falls into two categories: Surgical Procedure and Technical Workflow. The former

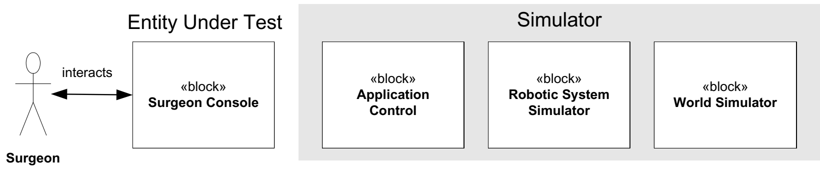

Fig. 9. Simulator Setup for the Class User Interface Designs

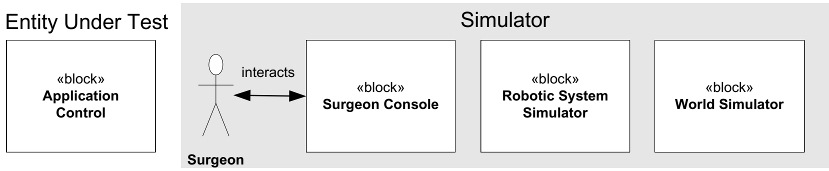

Fig. 10. Simulator Setup for the Class Workflow Validation

has the focus on the surgical goal, the latter on the operation of the robotic system. **Goal:** Validate a given workflow with human-centered (usability) methods. **Typical Setup:** The simulator setup (see Fig. 10) is similar to the class User Interface Design, except that Application Control is the entity-under-test. **Patient safety:** A workflow design that has been validated with the surgeon-in-the-loop reduces the risk for the patient because the workflow has been proven to be more likely performed well by surgeons.

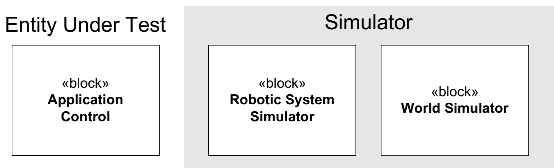

Fig. 11. Simulator Setup for the Class Workflow Design

Use Case Class Workflow Design (Category: Design). **Goal:** Improve the design of a surgical or technical workflow. Pre-operative planning falls into this class. **Typical Setup:** Requires both the robotic system and the world simulators. Application Control is the entity-under-test (see Fig. 11). **Patient safety:** Improved workflow for a certain procedure (e.g. shorter operation time, simplified tasks) reduces the risk for the patient.

Use Case Class Monitoring (Category: Verification). During surgery, the simulator runs in parallel to the real system. A monitor compares the simulation

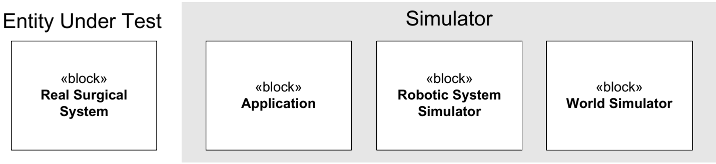

Fig. 12. Simulator Setup for the Class Monitoring

state with the real state. It estimates whether the real system works as intended. A variant of monitoring is predictive simulation, where the future state of the real system is estimated from the current simulation state [7]. **Goal:** Continuously verify real system during operation. **Typical Setup:** The simulator comprises of Application Control, Robotic System Simulator, and World Simulator (see Fig. 12) . The real system is the entity-under-test. **Patient safety:** Monitoring increases patient safety by reducing the risk to deviate from a planned procedure. The comparison of simulated and real state enables to detect system failures, deviations from the planned workflow, and planning errors.

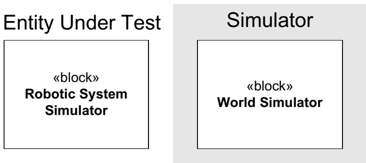

Fig. 13. Simulator Setup for the Class Robot Design

Use Case Class Robot Design (Category: Design, Verification, Validation) **Goal:** Improve the design of the robotic system, e.g. optimize the kinematics for a certain workspace. **Typical Setup:** Requires only the World Simulator (see Fig. 13). The Robotics System Simulator is the entity-under-test. **Patient safety:** A better robotic system that is more suitable for the intended procedure reduces the overall risk for the patient.

5 Simulator Configurations For Use Cases

This Section exemplifies how to setup the simulator regarding its modeling aspects and details for the two principal use case classes Surgeon Skill Training and Robot Design.

5.1 Surgeon Skill Training

The *Surgeon Skill Training* class can be divided into several training goals: (1) **Technical:** training the use of the technical system, i.e. the surgical robotics system, (2) **Procedure:** training a certain surgical procedure and (3) **Patient-specific:** training a patient-specific surgical intervention.

For the **Technical** goal, the mere *basic task* may be sufficient in terms of the *Application*. In case the methods to step through the workspace are part of the training, also the *procedure* needs to be modeled. As concerns the *System*, a simple *kinematics* modeling can usually show most of the relevant system behavior. However, if e.g. the robotic system offers force feedback, also some *dynamics* should be modeled to allow the user to understand this functionality. In the dimension of *Patient*, a *rigid-body* environment is often used; see first training steps in [9]. The force feedback functionality however could be better introduced by using *soft tissue* modeling. If the robotic system uses special instruments (e.g. cautery devices), also a *functional* modeling may be required.

The second goal, **Procedure**, usually involves an *anatomy-true* modeling in *Application*. To allow for interaction between surgical tools and patient, *dynamics* need to be modeled in *System*, and the *Patient* should be modeled either as *soft tissue* or even *functional*.

For the third goal, **Patient-specific**, the *Application* needs to be modeled *case specific*, otherwise it is similar to the second goal Procedure.

5.2 Robot Design

Simulation methods are widely used to optimize a *Robot Design* also in non-medical areas. Usual goals in this class are to find (1) **Kinematics:** the kinematics structure of the robot (e.g. number and sequence of joints, link lengths), (2) **Dynamics:** the dynamics parameters (e.g. masses of the segments, stiffnesses, maximum accelerations, applicable forces and torques), or (3) **Implementation:** the appropriate implementation (e.g. sensor resolution, motor characteristics).

In terms of *Application*, the task needs to be *anatomy-true* in most cases to allow for good comparability with reality. The classification w.r.t. the *System* is straight-forward regarding the goal names. As concerns the *Patient*, a *rigid body* or *soft tissue* modeling can be chosen.

6 Conclusions

The hierarchical levels of modeling details of the three aspects Application, System, and Patient enable the setup of a simulator for versatile goals in robotic surgery. The presented use case classes are only the basis from that the actual use cases are derived further. How this works, is illustrated in the previous section. Moreover, metrics of the impact on patient safety should be developed for each use case. The presented classification is currently used for the implementation of a Robotic System Simulator within the project SAFROS (Patient Safety in Robotic Surgery).

The developed concepts are also applicable to tele-robotics in general, e.g. the operation of robots in hazardous environments such as space or disaster zones, etc. Herein the aspect of Environment of Fig. 3 moves from Patient to the new domain. The levels of modeling details only differ slightly from the proposed ones. Furthermore the described methods enable to combine different simulations (e.g. workflow, monitoring and simulations to design robots), often used separately in various fields of robotics, within one modular simulator. This can be done by merging the modular simulations and their classified use cases with compatible interfaces.

Acknowledgements. The research leading to these results has received funding from the European Union Seventh Framework Programme (FP7/2007-2013) under grant agreement n° 248960. http://www.safros.eu

References

1. da Vinci skills simulator, http://www.intuitivesurgical.com/products/skills_simulator/ (last visited January 30, 2012)
2. Agency for Healthcare Research and Quality: Improving patient saftey through simulation research (2008), http://www.ahrq.gov/qual/simulproj.htm
3. Alimisis, D., Vicentini, M., Fiorini, P.: Towards a problem-based training curriculum for surgical robotics: the SAFROS project. In: Bastiaens, T., Ebner, M. (eds.) Proceedings of World Conference on Educational Multimedia, Hypermedia and Telecommunications, Chesapeake, VA, pp. 297–302 (2011)
4. Banks, J. (ed.): Handbook of Simulation: Principles, Methodology, Advances, Applications, and Practice. Wiley & Sons, New York (1998)
5. Basdogan, C., Sedef, M., Harders, M., Wesarg, S.: VR-based simulators for training in minimally invasive surgery. Computer Graphics and Applications 27(2), 54–66 (2007), doi:10.1109/MCG.2007.51
6. Herron, D., Marohn, M.: A consensus document on robotic surgery. Surgical Endoscopy 22, 313–325 (2008), doi:10.1007/s00464-007-9727-5
7. Hirzinger, G., Brunner, B., Dietrich., J., Heindl, J.: Sensor-based space robotics-ROTEX and its telerobotic features. IEEE Transactions on Robotics and automation 9(5) (1993)
8. Klodmann, J., Konietschke, R., Albu-Schaffer, A., Hirzinger, G.: Static calibration of the DLR medical robot MIRO, a flexible lightweight robot with integrated torque sensors. In: 2011 IEEE/RSJ International Conference on Intelligent Robots and Systems (IROS), pp. 3708–3715. IEEE, San Francisco (2011), doi:10.1109/IROS.2011.6095097
9. Lerner, M., Ayalew, M., Peine, W., Sundaram, C.: Does training on a virtual reality robotic simulator improve performance on the da vinci surgical system? Journal of Endourology 24(3) (2010)
10. Object Managment Group, OMG Systems Modeling Language (OMG SysML), Version 1.2, Document formal/2010-06-01 (2006), http://www.omg.org/spec/SysML/1.2
11. Satava, R.: Historical review of surgical simulation - a personal perspective. World Journal of Surgery 32(2), 141–148 (2008), doi:10.1007/s00268-007-9374-y
12. Sokolowski, J., Banks, C. (eds.): Principles of Modeling and Simulation: A Multidisciplinary Approach. Wiley & Sons, New York (2009)

Role of Holographic Displays and Stereovision Displays in Patient Safety and Robotic Surgery

Ali Sengül[1], Attila Barsi[2], David Ribeiro[1], and Hannes Bleuler[1]

[1] Robotic Systems Laboratory, EPFL
Ecole Polytechnique Fédérale de Lausanne, Switzerland
[2] Holografika Ltd. Budapest, Hungary
ali.sengul@epfl.ch

Abstract. In this study, the role of different 3D vision systems on the patient safety in the context of robotic surgery was studied. Clearly safety is the foremost importance in all surgical procedures. It is well studied in the clinical surgical procedures but the role of different 3D vision system in the context of patient safety is hardly ever mentioned. The assessment of the quality of the 3D images and role of force feedback was studied with two distinct methods (spatial estimation and depth perception) in two different vision systems (holographic and stereovision). The main idea in this study is to investigate quantitatively the role of the vision system in patient safety.

Keywords: Safety in surgical robotics, 3D Display, Depth Perception, Stereovision, Holographic Displays, Force Feedback.

1 Introduction

Current surgical robots are teleoperator devices and in teleoperation systems, operator interface enables the control of the remote surgical tools hence the operator interface must give the surgeon a complete and realistic perception of the surgical site. The operator interface must provide essential visual and haptic information during the surgical procedure.

To increase patient safety during the procedure, 3D visualization can be used to increase the realism of the visual perception. For the construction of 3D images a well-known technique stereoscopy is usually used. The main idea is to create depth illusion to provide the eyes of the viewer with two different images, representing two perspectives of the same object, with a minor deviation similar to the perspectives that both eyes naturally receive in binocular vision. Stereo Vision was introduced in minimal invasive surgery in early 1990s [1]. Stereoscopic vision (SV) is used in surgical robots, as the da Vinci robot (3D for the surgeon, 2D for the assistants) [2]. This system provides the surgeon full SV by using an endoscopic camera with two lenses. The surgeon controls the remote surgical tools under pure 3D vision without any force feedback. The da Vinci robot is capable of generating large forces and has a big danger of not providing force feedback. Patient safety can be improved with the operator interface integrated with force feedback and high quality 3D images.

S. Lee et al. (Eds.): Intelligent Autonomous Systems 12, AISC 194, pp. 143–154.
springerlink.com

The advantage for the use of SV is gain of realism. Numerous research point its advantage in term of speed performance [3, 4] and precision of manipulation [5] but some other research claim that there is no significant benefit [4, 7], they point however that it could be due to the fact that the technology is not advanced enough yet. Some of them show that SV benefits for novice but not for experienced surgeons [8,9]. However, stereovision has also some limitations that should be carefully studied. If we compare a complex real scene viewed binocularly and a computer display of the same scene with all depth cues carefully constructed, the geometric patterns of stimulation striking the two eyes are the same in the two cases. Nevertheless, psychophysical research and experience with virtual reality displays [10] show that the depth in the computer display will appear flattened relative to the real scene from which it is derived. A plausible cause for depth flattening is the fact that computer displays present images on one surface. This means that depth information from focus cues such as; accommodation and the retinal blur gradient are inconsistent with the depicted scene.

Patient safety in a teleoperation system depends on the quality of the presented information in the operator interface. In other words, faithful reproduction of the surgical area in the operator interface is crucial for the patient safety. High quality and realistic rendering of the images and force feedback would increase the patient safety. Studying the interplay of 3D vision and haptics could give some new insights about the future operator interfaces. Therefore, an objective assessment of the quality of the 3D perception with operator interfaces integrated with 3D vision and with haptics is crucial. The operator interfaces can be equipped with haptic devices and advanced 3D visualization displays to increase the perception the surgical area hence the patient safety. New operator interfaces that include holographic displays and force feedback could increase the quality of the representation of the operation room. 3D holographic images can be seen without glasses, without the need for head positioning or eyetracking, since the screen gives a natural ”window-like” 3D vision for multiple viewers.

This research is a part of a larger European project Patient Safety in Robotic Surgery (SAFROS) that is about to increase the safety in surgical robotic. For surgical robotic systems, it is crucial to perceive surgical area accurately and precisely. The visual display must provide an exact replica of surgical area. With the current technology to have an exact replica of the surgical site is not reachable but by knowing the limitation of different displays would help to prevent inappropriate uses of these displays hence it would increase the patient safety [11].

In this study we want to investigate quantitatively (error rates and task completion times) under new operator interfaces with integrated 3D vision and haptics. The assessment of the quality of the 3D will be measured objectively and subjectively. The objective measure is based on distance estimation measures (accuracy and precision) and task completion time; the subjective measures are based on the questionnaire ratings. Furthermore, the assessment will be done with two different vision systems (holographic and stereovision).

Patient safety would be increased by using new surgeon console that includes force feedback and better 3D display with more realistic 3D representation. We assume that using haptic feedback and holographic display would result in a better task performance and presence hence it would increase the patient safety.

This paper is organized as follows. In Section 1 we describe experimental protocols and details of the used hardware and software. In section 2 we present obtained result and in section 3 we discuss our findings concerning depth estimation and spatial assessment.

2 Methods

2.1 Participants

Nine male participants with an average age of 32.5 (ranging from 23 to 59) for the experiment 1 and nine male participants with an average age of 30.6 (ranging from 25 to 42) for the experiment 2 were recruited. They were right-handed participants and had no disorder of vision or touch and had no history of neurological or psychiatric conditions. Each experiment took around 40 minutes per participant. Participants were informed about the general purpose of the research, gave their informed consent and were compensated for participating to the experiment.

2.2 Experimental Protocol and Set up

In this study two different 3D displays (holographic and stereovision) were used. For the stereovision display we will use the display of the MIMIC simulator that is the simulator of the da Vinci Robot [12], see figure 1. For the holographic 3D display, we will use the 3D displays of Holografika, whose HoloVizio technology generates a whole "3D light-field", not only limited number of views, with 3D images that can be seen with unassisted naked eye by multiple viewers simultaneously, see figure 2. With this technology, the 3D display of the surgical area will be visible by all personnel of the operating room, and not only by one single surgeon, as it is customary with the “da Vinci” system [13].

A haptic device (Novint Falcon) was used to track the hand movement and to provide force feedback. CHAI 3D open source platform and set of C++ libraries was used for modeling and simulating the haptics, and for visualization of the virtual world.

Fig. 1. 3D Stereoscopic display of Mimic Simulator with a haptic device

2.2.1 Spatial Estimation Experiment

We conducted a study to evaluate virtual spatial estimation with two different 3D displays. It is assumed that higher level of immersion would increase sense of presence and more realistic display hence it would result a higher patient safety [14]. Immersion is related with the task performance in VR and presence is related with the user's subjective rating.

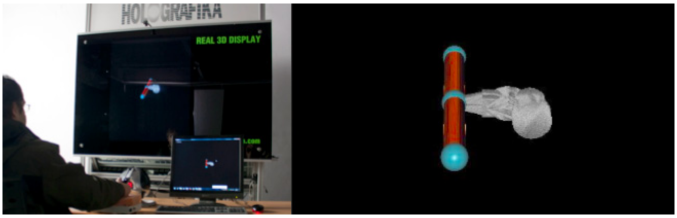

Fig. 2. Holographic 3D display showing spatial estimation experiment VR

The mismatch between accommodation and convergence in stereoscopic displays were shown to cause visual fatigue and discomfort [15]. This would decrease patient safety and using other displays that does not cause visual fatigue and discomfort would be better for patient safety.

For the spatial assessment, we used a technique that is equivalent to the line bisection task. This technique was chosen since it is a common technique to evaluate for spatial processing and it was validated in real world [15]. In this task participants were required to indicate the center of an object (presented in horizontal or vertical) by bisecting the midline [15].

VRs are mainly related with visual channel. Addition of other channels aimed at improving the realism and increased immersion and sense of presence. A significant amount of literature was published to address the visual realism however the contribution of visual and haptic channel in immersion feeling was not well quantified and studied [11]. Therefore in this study we evaluated the immersion and presence of two different displays by using line bisection task and the contribution of haptic feedback.

A virtual environment including a surgical robot and a cylinder was modeled. To indicate the end and the middle of the cylinder, blue spheres were used. A cylindrical tube was shown either horizontally or vertically. Participants were asked to judge the midline of the cylinder moving a virtual model of a robotic tool. They started the movement at the center of the tube and were required the reach rear and front end of the tube and then to judge the center of the tube by pressing a button on the haptic device. During this task their task completion time and their distance to the center was recorded. In order to evaluate the effect of force feedback, for some cases a virtual wall was modeled at the rear and front end of the tube.

The experiment was designed in a 2x2x2 factorial manner. The 3 factors were "direction" of cylindrical tube (horizontal vs. vertical), "force" (with force vs without force), and the type of "display" (stereovision vs holographic). There was a block of practice trial, which was not analyzed. Practice block was followed by 16 experimental blocks of 3 trials each.

2.2.2 Depth Perception Experiment

Depth perception is one of the key issues in 3D displays. In this experiment we evaluated depth perception by using a very simple task. Subjects had to compare the relative depths and relative size of two virtual objects (spheres). Different visual cues are processed by human vision system and combined in human brain to create a 3D perceptual world [16]. Therefore, depth perception is considered as an invisible cognitive state and inaccessible state. To overcome these limitations, researches used allocentric and egocentric distance comparison for the depth perception assessment [11,17,18,19]. In this task observer compares the relative distance between object and a reference point. With this method visual cues involved in depth perception can be accessed directly.

In this study we used the method that was used for depth perception assessment in real word by the works described [11,20,21]. In this experiment, subject answered force choice questions about the size and distance two objects. There were four comparison questions that were composed of two factors (size and/or position), figure 3. These questions are:

1. Both objects are the same size, and at the same depth (apparent sizes are equal),
2. Both objects are the same size, but at different depths (apparent sizes are different),
3. Both objects are different sizes and at the same depth (apparent sizes are different),
4. Both objects are different sizes, but at different depths (such that apparent sizes are equal),

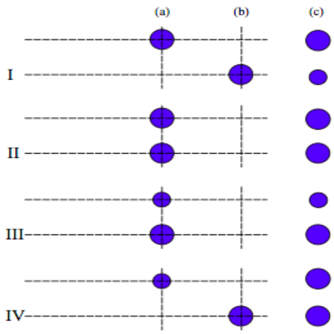

Fig. 3. Four cases of two object (a) and (b) real size and location, (c) retinal size [11]

One might think that using only question 1 and 2 would be sufficient for depth perception evaluation. In this case participants could rely on apparent size rather than the depth that could make it difficult to interpret the result. In order to be sure about the result that is based on perceived and not on the apparent size, two other comparison questions 3 and 4 were added. Furthermore we used spheres as virtual objects to force subjects to rely on stereopsis and convergence, see figure 4 [11].

Fig. 4. Holographic display showing VR of depth perception experiment

The experiment was designed in a 2x2x2 factorial manner. The 3 factors were "size" of the sphere (same vs. different), "depth" (same vs different), and the type of "display" (stereovision vs holographic). A practice trial was performed before the experiment and it was not analyzed. Practice block was followed by 16 experimental blocks of 8 trials each.

2.2.3 Questionnaire

Participants filled out a questionnaire to rate their subjective experiences at the end of the experiment. The questionnaire was adapted from the [22]. The questionnaire was in written form divide into different questions about the presence/immersion, external awareness, quality, enjoyment and ergonomics. Participants were instructed to assign a value ranging from 1 to 7 (1 = strongly disagree to 7 = strongly agree) to 10 statements (see table 1).

2.2.4 Data Analysis

Statistical analysis was made based on the mean of the task completion times and position errors in the spatial estimation experiment and based on the mean of the reaction times and error rates for the depth perception experiment. Data from the all trials were analyzed by repeated-measures ANOVAs on the mean values of task completion times and position errors for spatial estimation experiment and mean values of reaction times and error rates for the depth perception experiment. Individual ANOVA variables were compared with post-hoc tests. Paired t-test was used for the comparison of the questionnaire ratings. All numerical values were presented the mean and between-subjects standard error. A significant effect was reported for $p \leq 0.05$.

Table 1. Questionnaire about the virtual reality experience

Dimension	Questions
Presence/ Immersion	- The depth impression was realistic - I had a 3D impression of the displayed environment and objects.
External awarness	-I was not aware of the real world—the laboratory
Quality	-I could estimate the distance of the objects well. -I had the feeling that I could reach into the virtual world and touch the objects. -I could see the virtual world clearly
Enjoyment	-The quality of the graphical presentation was fascinating.
Ergonomics	-After the experiment I had muscle pain in the neck. -The display was comfortable and not tiring for the eyes -After the experiment I had muscle pain in the arm.

3 Results

3.1 Spatial Estimation Experiment

To compare the spatial assessment performance in both holographic and stereovision display, distance to the center point and task completion time means with standard deviations were shown in fig 5 and fig 6.

ANOVA tests on task completion time rates revealed a main effect of display ($F_{(1, 8)} = 13.9$, $p = 0.005$). Other significant factors are Force ($F_{(1, 8)} = 59.7$, $p < 0.001$) confirming that task completion time was significantly less when force feedback was applied and a significant interaction between Direction and Force. ($F_{(1, 8)} = 16.7$, $p = 0.003$). Post-hoc comparison reveals a significant difference between conditions 1 No Force Horizontal (NFHor) and 2 Force Horizontal (FFHor) ($p = 0.014$), 1 and 4 Force Vertical (FFVer) ($p = 0.03$), 2 No Force Vertical (NFVer) and 3 ($p = 0.01$), 3 and 4 ($p = 0.026$) 3 and 4 ($p = 0.02$) for stereoscopic display and significant difference between conditions 1 (NFHor) and 2 (FFHor) ($p < 0.001$), 1 and 3 (NFVer) ($p = 0.002$), 2 (NFVer) and 3 ($p = 0.003$), 3 and 4 ($p = 0.02$) for holographic display.

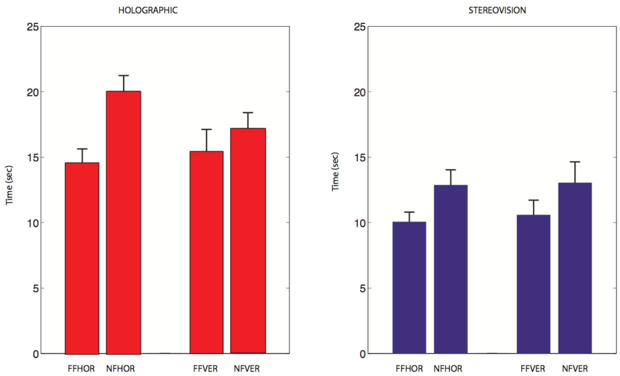

Fig. 5. Task completion time and role of force feedback

ANOVA tests on distance to the center revealed an interaction between Display and Dir ($F_{(1, 8)} = 5.9$, $p = 0.04$). Post-hoc comparison did not reveal any significant difference between conditions for stereoscopic display but it revealed significant difference between conditions 1 (NFHor) and 3 (NFVer) ($p = 0.005$), 2 (FFHor) and 3 (NFVer) ($p = 0.005$), 3 and 4 (FFVer) ($p = 0.02$) for holographic display.

3.2 Depth Perception Experiment

To compare the depth perception performance in both holographic and stereovision display, error rate and response time means with standard deviations were shown in fig 7 and fig 8. For holographic display subjects showed better accuracy but slower response times.

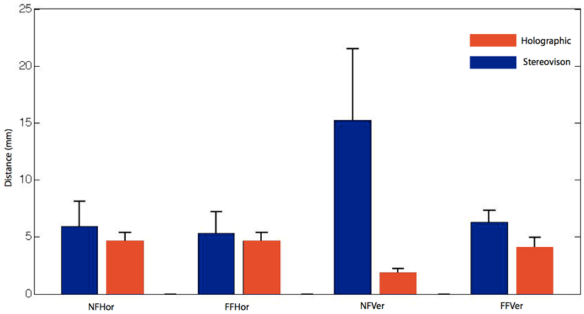

Fig. 6. Distance to center of cylindrical tube

ANOVA tests on error rates revealed a main effect of display ($F_{(1, 8)} = 28.9$, $p < 0.001$), conforming that holographic display has lower error rate compared to stereoscopic display. Other significant factors are Size ($F_{(1, 8)} = 11.7$, $p = 0.009$) and a significant interaction between Display, Size and Depth. ($F_{(1, 8)} = 6.57$, $p = 0.03$).

Post-hoc comparison reveals that for the SV system, different conditions reveals no significant difference between four comparisons but it reveals a significant difference between conditions 1 Same Size Same Position (SSSP) and 3 Different Size Same Position (DSSP)($p = 0.016$), 1 and 4 Different Size Different Position (DSDP) ($p < 0.001$), 2 Same Size Different Position (SSDP) and 3 ($p = 0.037$), 2 and 4 ($p < 0.001$) 3 and 4 ($p = 0.02$) for the holographic display.

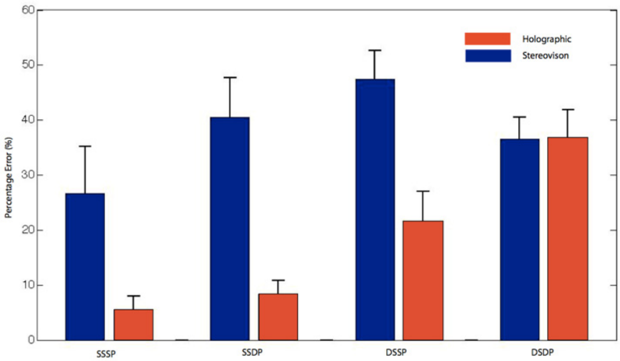

Fig. 7. Percentage error: Holographic display has lower % error

ANOVA tests on reaction time revealed a main effect of display $F_{(1, 8)} = 40.5$, $p < 0.001$), conforming that holographic display has larger response time compared stereoscopic display. Other significant factors are size ($F_{(1, 8)} = 22.2$, $p = 0.002$) and a significant interaction between Display and Size. ($F_{(1, 8)} = 12.83$, $p = 0.007$). Post-hoc comparison reveals that for the SV system, different conditions reveals no significant difference between four comparisons but it reveals a significant difference between conditions 2 and 3 ($p = 0.007$), 2 and 4 ($p=0.01$) for the holographic display.

3.3 Questionnaire

Concerning questionnaire scores, we found that ratings in question Q4 about the effect of force feedback ("I had the feeling that I could reach into the virtual world and touch the objects.") was significantly larger in the force feedback condition (Q4: $p < 0.0413$ for SV and $p = 0.0402$ for holographic vision). No significant difference between force feedback and no feedback condition for the other questions.

Then we performed 2-tailed paired t-test for the average question rating for stereoscopic display and holographic display. In this case we found Q8 (After the experiment I had muscle pain in the neck) significantly higher ratings for the stereoscopic display ($p = 0.003$) and Q9 (The display was comfortable and not tiring for the eyes) significantly higher rating for holographic display ($p < 0.001$).

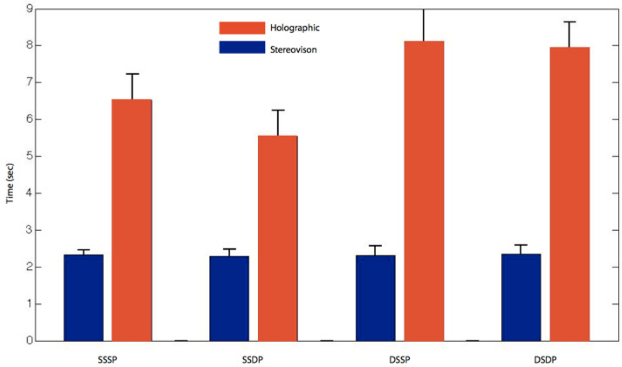

Fig. 8. Reaction time: Holographic display has higher reaction time

4 Discussion

VEs can be viewed using different 3D vision system that can influence the perception of the environment. Role of different 3D virtual reality platform and vision system on the patient safety in the context of robotic surgery was studied. The assessment of the quality of the 3D images and role of force feedback was studied with two distinct methods in two different vision systems (holographic and stereovision). The idea behind this approach was to investigate quantitatively the role of the vision system in patient safety.

We found some difference in task completion time in the spatial estimation experiment. The result of the spatial estimation experiment showed the importance of force feedback. As it is seen in figure 5, participants were able to complete the task faster in the case of force feedback. Providing force feedback at the end front and rear end of the tube enabled them complete the task faster. This could be explained that participants used the visual cues and haptic cue to access the boundaries of the tube. The integration of visual and haptic cues could have increased their performance. Furthermore, movements were less precise for the stereovision display and midline assessment accuracy was lower for the stereovision display. As it is seen in figure 6, the distance to the midline of the tube was lower for the holographic display.

One of the main goals of this study was to determine whether participants' performance in depth perception task changes when different 3D display was used. The ANOVA result on the percentage error of the depth perception experiment revealed a difference. This effect was achieved for most the conditions for the holographic display and this was not the case for the stereovision display. In other words, participants showed a better performance in holographic display compared to the stereovision display. As it is seen in figure 7, participants had significantly lower error rate for the holographic display, except in the ambiguous comparison condition (condition 4: DSDP). Furthermore, ANOVA result on the response time of the depth perception experiment also revealed a difference. The response time for the holographic display was significantly higher then the stereovision display for all the conditions, see fig 8. One might interpret the competing result on accuracy and response time as speed-accuracy problem. However this should not be the case for this experiment because participants were asked to respond when they are sure about the answer. Hence the difference in the error rates could not be due to the speed accuracy tradeoff. In the holographic display participants took more time by looking at different angles, therefore their response times are longer and they have higher accuracy rate.

Subjective ratings on presence/immersion, external awareness, quality and enjoyment were satisfying for both of the 3D displays. However, subjective rating on the ergonomics was not satisfying for the stereovision display. Participants report muscle pain in the neck and discomfort due to the tiring for the eyes for the stereovision display. On the other hand, subjective rating on the ergonomics for the holographic display was satisfying.

5 Conclusion

This study focused on the assessment of surgeon's accuracy and action/perception limit under different surgical operator interface with different 3D vision systems and how different vision system and haptic could increase patient safety. A statistical comparison was done on the quantitative measures of the two distinct displays. A comparison of 3D SV system of the da Vinci simulator and holographic visual system was performed. As expected our result showed that using haptic feedback and holographic display resulted in better task performance and presence hence it would increase the patient safety.

Acknowledgements. This research project is supported by European Project FP-7 SAFROS www.safros.eu

References

1. Cuschieri, A.: Minimal access surgery and the future of interventional laparoscopy. Am. J. Surg. 161, 404–407 (1991)
2. Da Vinci Surgery, Intuitive Surgical (2012), `http://www.intuitivesurgical.com/index.aspx`
3. Vasilyev, V., Novotny, M., Martinez, F., Loyola, H., Salgo, I., Howe, R., Nido, J.: Stereoscopic vision display technology in real-time three-dimensional echocardiography-guided intracardiac beating-heart surgery. J. Thorac. Cardiovasc. Surg. 135, 1334–1341 (2008)
4. Taffinder, N., Smith, S., Huber, J., Russell, R., Darzi, A.: The effect of a second-generation 3D endoscope on the laparoscopic precision of novices and experienced surgeons. Surg. Endosc. 13, 1087–1092 (1999)
5. Mueller-Richter, U., Limberger, A., Weber, P., Ruprecht, K., Spitzer, W., Schilling, M.: Possibilities and limitations of current stereo-endoscopy. Surg. Endosc. 18, 942–947 (2004)

6. Hofmeister, J., Frank, T., Cuschieri, A., Wade, N.: Perceptual aspects of two-dimensional and stereoscopic display techniques in endoscopic surgery: review and current problems. Semin. Laparosc. Surg. 8, 12–24 (2001)
7. Peitgen, K., Walz, M., Holtmann, G., Eigler, F.: A prospective randomized experimental evaluation of three-dimensional imaging in laparoscopy. Gastrointest Endosc. 44, 262–267 (1996)
8. Bergen, P., Kunert, W., Bessell, J., Buess, G.: Comparative study of two-dimensional and three-dimensional vision systems for minimally invasive surgery. Surg. Endosc. 12, 948–954 (1998)
9. Suematsu, Y., Martinez, J., Wolf, B., Marx, G., Stoll, J., DuPont, P.: Three-dimensional echo-guided beating heart surgery without cardiopulmonary bypass: atrial septal defect closure in a swine model. J. Thorac. Cardiovasc. Surg. 130, 1348–1357 (2005)
10. Watt, S., Akeley, K., Ernst, M., Banks, S.: Focus cues affect perceived depth. Journal of Vision, 834–862 (2005)
11. Naceri, A., Chellali, R., Dionne, F., Toma, S.: Depth Perception Within Virtual Environments: Comparison Between two Display Technologies. International Journ. on Advances in Intelligent Systems 3(1&2) (2010)
12. Dv Trainer. Mimics (2012), `http://www.mimic.ws/`
13. Holovizio, Holografika (2012), `http://www.holografika.com/`
14. Beck, L., Wolter, M., Mungard, N., Vohn, R., Staedtgen, M., Kuhlen, T., Sturm, W.: Evaluation of Spatial Processing in Virtual Reality Using Functional Magnetic Resonance Imaging (fMRI). Cyberpsychology Behavior and Social Networking 13 (2010)
15. Hoffman, D., Girshick, A., Akeley, K.: Vergence-accommodation conflicts hinder visual performance and cause visual fatigue. Journal of Vision 8, 1–30 (2008)
16. Swan, J., Jones, A., Kolstad, E., Livingston, M., Smallman, H.: Egocentric depth judgments in optical, see through augmented reality. IEEE Trans. Vis. Comput. Graph 13(3), 429–442 (2007)
17. Loomis, J.M., Da Silva, J.A., Philbeck, J.W., Fukusima, S.S.: Visual perception of location and distance. Current Directions in Psychological Science 5, 72–77 (1996)
18. Loomis, J.M., Knapp, J.M.: Visual perception of egocentric distance in real and virtual environments. In: Hettinger, L.J., Haas, M.W. (eds.) Virtual and Adaptive Environments, pp. 21–46 (2003)
19. Aznar-Casanova, J.A., Matsushima, E.H., Silva, J.A.D., Ribeiro-Filho, N.P.: Can exocentric direction be dissociated from its exocentric distance in virtual environments? Percept Psychophys. 70(3), 541–550 (2008)
20. Gruber, H.E.: The relation of perceived size to perceived distance. The American Journal of Psychology 67, 411–426 (1954)
21. Berryhill, M.E., Fendrich, R., Olson, I.R.: Impaired distance perception and size constancy following bilateral occipitoparietal damage. Exp. Brain Res. 194(3), 381–393 (2009)
22. Armbruster, C., Wolter, M., Kuhlen, T., Spijkers, W., Fimm, B.: Depth Perception in Virtual Reality: Distance Estimantions in Peri- and Extrapersonal Space. Cyber Psychology & Behavior 11 (2008)

A Methodological Framework for the Definition of Patient Safety Measures in Robotic Surgery: The Experience of SAFROS Project

Angelica Morandi[1], Monica Verga[1], Elettra Oleari[1], Lorenza Gasperotti[2], and Paolo Fiorini[2]

[1] e-Services for Life & Health, Fondazione Centro San Raffaele del Monte Tabor Milan, Italy
surname.name@hsr.it

[2] Altair robotics laboratory, Department of Computer Science, University of Verona
lorenza.gasperotti@metropolis.sci.univr.it, paolo.fiorini@univr.it

Abstract. This paper describes an innovative methodological approach developed within the SAFROS European project (Patient Safety in Robotic Surgery, FP7) that allows to identify a set of metrics for the evaluation of patient safety during the pre- and intra-operative phase of robotic interventions. This methodology enlarges the focus of the evaluation: safety is assessed not only through the analysis of features and limitations of the technological solutions involved in the execution of target surgical interventions (product safety) but also in terms of the effects of their interaction within the surgical scenario (process safety). Moreover potentialities and obstacles emerging from the introduction of such technologies into the operating room and the hospital as systems (organizational safety) are evaluated. The proposed method has been applied to the analysis of one gold standard and two benchmark procedures. The output of the analysis is a complex set of key metrics addressing safety at the above described levels. This paper reports the most relevant and interesting subset of the obtained results. The extendibility of the method to the analysis of other interventions will be verified with suitable experiments in the next future.

Keywords: patient safety, robotic surgery, safety metrics, surgical workflow, SAFROS project.

1 Introduction

Patient safety is defined by the World Health Organization (WHO) as the absence of preventable harm to a patient during the process of health care. The discipline of patient safety is the coordinated effort to prevent harm to patients, caused by the process of health care itself [1]. During the last 10 years the relevance attributed to the prevention and management of errors raised considerably within both the American and European medical community. The publication of [2] [3] by the Institute Of Medicine (IOM) and of [4] by the Quality Interagency Coordination Task Force (QuIC) demonstrated the willingness to face the considerable number of medical errors that negatively affect patient outcomes and the performance of the medical staff in general. The introduction of robotic surgery marked a turning point for the surgical practice in the context of

S. Lee et al. (Eds.): Intelligent Autonomous Systems 12, AISC 194, pp. 155–164.
springerlink.com

patient safety [5]. It enhanced the benefits introduced by minimally invasive technologies (reduction of intra- and post- operative blood loss, shortening of patients recovery time etc) and solved some of their limitations providing the surgeon with high quality stereo vision and 7 degrees of freedom tools, thus enabling them to perform extremely precise and dexterous movements [6]. Despite the ability of surgeons in using surgical robots and the precision of such machinery, no study has looked at all aspects of safety in robotic surgery. As of today, the analysis of the effects due to the introduction of robotic technologies has been conducted by evaluating the requirements for a proper preoperative diagnostic, for the performance of the intervention and for the training of surgeons separately (e.g. in [7]). In addition, the evaluation of the performance quality of these phases does not involve the use of metrics that specifically address patient safety. The SAFROS project (Patient Safety in Robotic Surgery, EU 7th Framework Programme) aims at developing technologies and methods for the enhancements of patient safety in surgical procedures extending the analysis to the whole surgical workflow. The SAFROS project addresses the complete planning-execution loop in surgical robotics, to ensure a seamless data flow and consistent accuracy in all phases of robotic-assisted surgery. The project aims at demonstrating that the introduction of assistive technologies improves patient safety during the performance of surgical intervention with respect to their current way of execution. To this extent the identification of a set of metrics for the objective assessment of patient safety is required.

2 Objective

The aim of this paper is to describe the methodological approach introduced in the context of the SAFROS project to define the metrics that will enable the assessment of patient safety in robotic surgery. The analysis has been extended to the whole surgical workflow, starting from the pre-operative phase to the execution of the operation. Moreover it took into account all the aspects concurring to the complexity of the system and to patient safety, including technological, procedural, environmental and patient related factors. This methodology has been developed to identify a list of metrics related to both technical and medical aspects as indicators for a safe surgical performance. The described method has been applied to the analysis of a standardized robot-assisted procedure such as the Robot-Assisted Radical Prostatectomy (RALP) [10] and of two case studies, namely pancreatic tumor enucleation and the Abdominal Aortic Aneurysm (AAA) repair [8] [9]. Positive results obtained from the application of the method in the selected case will be the base for its wider usage.
The first part of the paper reports the methodological framework as it has been developed within the SAFROS project. The description follows the subdivision of the method into the three levels of the analysis: namely product, process and organizational safety. Then the paper reports the results obtained for the specified surgical procedures. Finally, conclusions are drawn and possible extensions proposed.

3 Methods

The methodological approach applied within the SAFROS project includes three increasingly complex levels of analysis: product safety analysis, process safety analysis, and organizational safety analysis. This allows to assess the safety of the applied technologies considering them first singularly, then analyzing their interaction into a surgical process and finally integrating them into a wider organizational context (Fig. 1). Such a schema makes possible to reengineer the surgical process through the introduction of technological innovations and to extract patient safety indicators to assess the impact of these solutions.

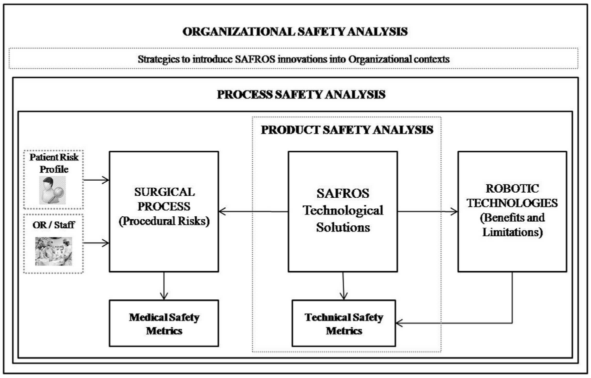

Fig. 1. Schema of the whole methodological approach

Literature researches [7] [11]–[16] and interviews to expert surgical teams and expert robotic surgeons allowed the identification of the most relevant limits affecting commercial surgical robots specifically related to their use in the considered surgical procedures [14] [15]. It has been pointed out that four are the main categories in which robotic features could be grouped (mechanics, imaging, surgical workflow and operating room (OR) environment and patient), each of them bringing benefits and limitations when introduced into a surgical environment. As example, referring to mechanics, the possibility to have accurate tools with scaled movements and extra degrees of freedom represents a great advantage but on the other side robots are cumbersome, with time consuming to set-up.

3.1 Product Safety Analysis

The product safety level aims at evaluating the features of SAFROS technological solutions, some of which are already existing whilst other are being developed within the project. SAFROS products have a potential to increase patient safety, possibly overcoming the current limitations of robotic surgery. The analysis focuses on virtual and synthetic organ models, virtual simulator for training and planning, pre-operative planning technologies, operating room monitoring system and robotic simulator. The specifications of SAFROS technological products were outlined with a set of technical safety metrics to understand their impact on patient safety during surgical interventions and to assess their potentiality. The product safety analysis has been supported by the Goal-Question-Metric (GQM) model [17] [18], a goal-driven measurement system for software development, where each goal triggers the identification of appropriate metrics. We adapted this approach in the context of SAFROS project (see Fig. 2) defining its specific Goal: *"analyze SAFROS products for the purpose to improve the Patient Safety from the view point of medical and robotic experts in the context of robotic surgery"*.

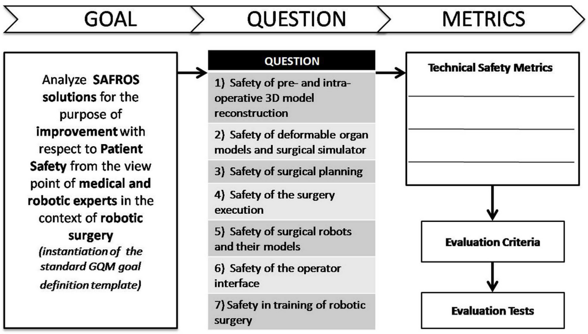

Fig. 2. The GQM approach applied in SAFROS

In order to satisfy the SAFROS objectives, we outlined SAFROS main Questions and the corresponding technical safety metrics. For each solution we pointed out what evaluation criteria have to be investigated and which laboratory evaluation tests we have to perform. As a result, a list of 55 Technical Safety Metrics and related evaluation methods has been obtained. An excerpt of them is provided in the Table 1.

3.2 Process Safety Analysis

The process safety level expands the focus of previous analysis through the application of a systems approach, that evaluates the effects of the interaction of the above mentioned products and their integration into the different phases of surgical procedures. The scope of this research is to identify and select the criticalities in the surgical process in order to design the ways in which SAFROS technologies could reduce them and improve benefits for the patient. At this level the analysis comprises the robotic and the surgical procedures, also including the factors influencing patient safety such as the operating room environment and patient related information. The conclusions of this level of the study conducted to the identification of a list of medical safety metrics related to each element, starting from the study of the risks embedded in the whole surgical scenario.

For this purpose we exploited a simplified version of the Failure Mode and Effects Analysis (FMEA) [19] as risk assessment tool to study the gold standard robot-assisted radical prostatectomy (RALP), and the two SAFROS benchmark procedures (vascular and abdominal). Preliminarily we identified the procedural steps of the pre- and intra-operative phases for each procedure. FMEA helped in identifying all the procedure-related risks, considering also the respective causes and effects. In close collaboration

Table 1. Example of Technical Safety Metrics resulting from the product safety analysis

Technical Safety Metrics	
Products	**Criteria**
Virtual and synthetic organ models	
Realism of physical model dynamic behaviour	Force deviation from actual in dynamic experiments (%, mN)
Mechanical properties	Measured Youngs modulus [Pa], deviation from target [Pa], stress-strain curve acceptability: yes/no
Surgical Planner	
Error between real and reconstructued environment	Linear errors (m), yes/no (task dependant)
Reduction in cognitive load/ time when facing adverse events in simulation	Ratio between trained completion time and untrained completion time %, ratio <1 significantly
Pre-operative planning technologies	
Error between real/registered environment	Linear error (mm), if ¡1cm = yes
Stability of the estimated registration transforms	Variance of the transform parameters, if <5% = yes
Quality of obstacle detection and human tracking	mm, <10cm
Time delay between real world motions and update of the virtual scene	<500ms
Robotic system simulator	
Cartesian positioning accuracy	mm, rad
Accurate torque measurement	N, Nm

with OR personnel (e.g. qualified surgeons, anesthetist, nurses, ...) through site visits and interviews, the risks have been ranked according to a Criticality Index (CI). This parameter is obtained by multiplying the estimated frequency of occurrence (O, from 1 to 4) of the risk by the expected severity (S, from 1 to 5) of the damage caused to the patient in the event the risk converts into reality Fig. 3.

As example, in Table 2 is reported some of the highly ranked risks selection for the most representative procedural steps of the robotic surgical workflow, referring to RALP. From the risk analysis it was possible to deduce a set of medical safety metrics addressing the criticalities of the procedures taken into account. This will enable the qualitative and quantitative assessment of the improvement in patient safety provided by the introduction of SAFROS solutions.

The other determinant factors influencing the safety in surgical theatre are related to patient and the OR environment. Criticalities due to patient-specific clinical and anatomical characteristics, e.g. pathology and comorbidities, outlining the individual risk profile have also been collected by reviewing clinical documentations and informed consents forms and by collecting surgeons opinions. We also encompassed the characteristics of the operating scenario in terms of ergonomics and the role of human factors related to the internal dynamics of the surgical team [20]. The results of the Process

Severity / Occurrence	No damage (1)	Minor damage (2)	Medium damage (3)	Serious damage (4)	Really serious damage (5)
Remote (1)	1	2	3	4	5
Occasional (2)	2	4	6	8	10
Probable (3)	3	6	9	12	15
Frequent (4)	4	8	12	16	20

CI from 1 to 2 = Accettable Risks

CI from 3 to 6 = Low Risks

CI from 7 to 12 = Medium Risks

CI from 13 to 20 = High Risks

Fig. 3. Risk Matrix used to rank the procedural risks

Table 2. Analysis of the risks related to the robot-assisted procedure

Process Step	Related Risks	Causes	Effects
Pre-operative planning	Not adequate evaluation of the surgical strategy	Incomplete/inaccurate evaluation of the pre-operative tests	Prolonged surgery Deviation from planned operation Not prompt reaction of the surgeon to complications
Surgical steps execution: First Surgeon	Partial or missed visualization of the robotic instruments as they are positioned in the pelvis	Technical malfunctions in the optical tool/camera Improper check of the tools (e.g. camera out of focus) Surgeon's inattention	Prolonged surgery Damage to anatomical structure Collisions
Surgical steps execution: First Assistant and the rest of the surgical team	Improper changing of the instruments	First assistants skill (e.g. insufficient confidence with robotic devices) Missed communication between OR staff Lack of knowledge of inserting the robotic instruments	Prolonged surgery Damage of the anatomical structures

safety analysis collected in Fig. 3 are the Medical Safety Metrics obtained from the analysis of the different factors influencing patient safety previously discussed (procedure-related risks, patient-specific data and operative environment).

Table 3. Risk Matrix used to rank the procedural risks

<table>
<tr><th>Procedure-related risks</th><th>Medical Safety Metrics</th></tr>
<tr><td>Robotic-surgical procedure</td><td></td></tr>
<tr><td>- Not adequate evaluation of the surgical strategy (CI=6,93)
- Partial or missed visualization of the robotic instruments as they are positioned in the pelvis (CI=2,83)
- Improper changing of the instruments (CI=2,83)</td><td rowspan="9">- Fidelity of anatomical structures
- Fidelity in feature and spatial relationship of the tumour
- Accuracy in task execution
- Damage to organs/vessels
- Rapid identification of critical situations
- Time to perform specific tasks, e.g. clamping, anastomosis (min)
- Operative time (min)
- Technical set-up of the robotic system
- Adequacy of data for decision making
- Adequacy of patient positioning on surgical table
- Correctness of sterility and shaving procedure
- Standardization of the port placement
- Satisfactory ergonomics of the prime surgeon console
- Adequacy of the internal workspace for the surgeon
- Tool functioning
- Visualization of the working field
- Coordination skills
- Leadership and management skills</td></tr>
<tr><td>AAA repair related-risks</td></tr>
<tr><td>- Serious lumbar bleeding when opening the aneurysm (CI=10,4)
- Bleeding of the suture line (CI=9,4)
- Improper positioning the aortic clamp (CI=8,73)
- Damages to the surrounding structures during the aorta exposition (CI=7,87)
- Needle/suture breaking (CI=6,64)
- Not gradual declamping, respecting the pressure values (CI=6,45)</td></tr>
<tr><td>Pancreatic enucleation related-risks</td></tr>
<tr><td>- Damage to pancreatic duct during enucleation (CI=7,55)
- Damages to pancreatic parenchyma and surrounding anatomic structures during pancreas exposure (CI=7)
- Damage to the spleen and spleen's vessels during pancreas tail resection (CI=6,5)
- Not complete resection of the tumoral mass (CI=4,8)
- Unexpected factors not evaluated during the planning (CI=2,76)</td></tr>
<tr><td>Patient-specific data</td></tr>
<tr><td>- Principal compliant
- Comorbidities
- Body mass index
- Age, gender
- Personal analtomical variability
- Previous interventions</td></tr>
<tr><td>Operative environment</td></tr>
<tr><td>- Noise and light conditions
- Availability of proper instruments
- Distractions/interruptions
- Human factors (teamwork, leadership, pressure...)</td></tr>
</table>

3.3 Organizational Safety Analysis

The organizational safety level addresses the potential impact of the application of new technologies on a higher level environment: the operating room system and the hospital as an institution. It's relevant to evaluate which are the determinants for a successful possible introduction of SAFROS system in this complex organizational environment. In fact, high reliability in healthcare is founded on the context in which care is delivered, called organizational culture, and that has important influences on patient safety [21]. At the day of the publication of this paper the work concerning the Organizational safety analysis is still in progress. It requires considerable efforts and time as it involves different categories of professionals, including lawyers, sociologists, surgeons and members of hospitals management.

4 Results

SAFROS project aims at developing technologies and methods in order to enhance patient safety and proving their effectiveness when introduced in the robotic surgical environment. The analysis conducted to the definition of a set of technical and medical safety metrics for the evaluation of SAFROS solutions applied to pre or intra-operative phases of the robotic-assisted surgical procedure. In Fig. 4 is presented an extract of the result of the entire analysis. SAFROS solutions are reported together with their Technical Safety Metrics. The focus is on the benefits that their introduction imply in the context of patient safety. In the last column are finally referred the Medical Safety Metrics that each solution is addressing to and that will help to evaluate how effectively the patient safety is improved by their introduction.

Table 4. Extract of the SAFROS patient safety analysis results

SAFROS solution	Technical safety metric	Benefits for patient safety	Medical safety metric addressed
Pre-operative patient reconstruction as a reference for intra-operative registration	- Error between real and reconstructed environment - Stability of the estimated registration transforms.	Precise localization of organs, forbidden regions, and target structures	- Fidelity of anatomical structures - Adequacy of data for decision making - Rapid identification of critical situations
Robotic system simulator for pre-operative planning	- Time delay between real world motions and update of virtual scene; - Update rate - Cartesian positioning accuracy	Allow a proper planning of the OR to reduce the risks of wrong localizations. Reduce or avoid "Out of range Motion" due to kinematic limitations	- OR set up time - Rapid identification of critical situations - Instrument collisions
Intra-operative registration	- Error between real and registered environment - Stability of the estimated registration transforms - Target registration error	Matching the real-time US with the pre-operative reconstruction allows better visualization and localization of target structures inside the patient	- Accuracy in task execution - Avoid structures - Overall operative time - Visualization of the working field
Intra-operative supervision system in the shared workspace surgeon/robot	- Quality of obstacle detection and human tracking - Time delay between real world motions and update of virtual scene - Update rate	The supervision system provides an additional safety net for the robot reducing problems at the patient side, through an optical monitoring of workspace of the robot and the surgeon + staff.	- Rapid identification of critical situations: - Instrument collision - Robot/OR staff collisions - Operative time

5 Discussion and Future Perspectives

The application of the proposed method to the considered surgical procedures led to the identification of several metrics for the assessment of patient safety. The complexity of the obtained metrics and their wide focus, embracing not only single components but whole processes and systems, suggests the necessity of a holistic approach for patient safety analysis. Another important outcome of the performed work is the definition of a set of key aspect that should be taken into account for the development of new technological solution for robotic surgery. The application of the proposed protocol to the targeted pancreatic and vascular procedures may be considered as the main limitation of the current work. In fact as for today these interventions are not routinely assisted by robots, since their high complexity of execution has hampered an extensive use of technology. Despite this, their adoption as test-beds for the SAFROS method was grounded on the belief that patient safety, as a systemic notion, could be better addressed in unexplored fields where no consolidated practices exist. The extendibility of the proposed methodological approach to other medical or surgical specialties will be soon analyzed. In fact safety must drive the development of technological solutions in the early design phase and not introduced when already established design constraints can impede further improvements. The correctness of the defined metrics for the assessment of patient safety levels will be verified. Tests on benchmark procedures and selected surgical tasks, e.g. comparing task execution with and without the examined technological solutions, will allow to verify the reliability and consistency of the identified Safety Metrics. Testing activities will be devoted firstly to evaluate if the proposed methodological approach is useful to represent the different aspects of patient safety in robotic surgery. Secondly the experimental phase will validate whether the proposed solutions bring an improvement in patient safety compared to traditional procedures. In addition we will check the results of our analysis comparing them with real data derived from robotic-surgery experience [12]. The definition of the testing protocols and the set-up of the testing activities requires time and resources and will be finalized in the coming period within SAFROS framework. The organizational safety analysis will be completed in the next future, exploring the field of human factors toward the environment of safety culture. The last phase of the study aims at analyzing the existence of possible correlations between the Technical Safety Metrics and the Medical Safety Metrics through execution of test and experiments based on well defined statistical protocols. Confirming the existence of such correlations will demonstrate the proposed method to be suitable for the objective and coherent with the underlying assumptions.

Acknowledgements. The research leading to these results has received funding from the European Union Seventh Framework Programme FP7/2007-2013 under grant agreement n. 248960 (SAFROS). We wish to acknowledge the Vascular Surgery Operative Unit and the Urology Department of Hospital San Raffaele, Milan (Italy), and the General Surgery Department of University Policlinico Borgo Roma, Verona (Italy), for their cooperation within the SAFROS project.

References

1. http://www.who.int/features/factfiles/patient_safety/en/index.html
2. Kohn, L.T., Corrigan, J.M., Donaldson, M.S.: To err is human: building a safer health system. Institute of Medicine Report, National Academy Press, Washington, DC (2000)
3. Edington, M. (ed.): Crossing the Quality Chasm: A New Health System for the 21st Century. Institute of Medicine Report, National Academy Press, Washington, DC (2001)
4. Quality Interagency Coordination Task Force, Doing what counts for patient safety: Federal actions to reduce medical errors and their impact. Agency for Healthcare Research and Quality, Washington, DC (2000)
5. Makary, M.A., Sexton, J.B., Freischlag, J.A., Millman, E.A., Pryor, D., Holzmueller, C., Pronovost, P.J.: Patient safety in surgery. Annals of Surgery 243(5), 628–635 (2006), doi:10.1097/01.sla.0000216410.74062.0f
6. Gutt, C.N., Oniu, T., Mehrabi, A., Kashfi, A., Schemmer, P., Büchler, M.W.: Robot-assisted abdominal surgery. British Journal of Surgery 91(11), 1390–1397 (2004), doi:10.1002/bjs.4700
7. Herron, D.M., Marohn, M.: The SAGES-MIRA Robotic Surgery Consensus Group. A consensus document on robotic surgery. Surgical Endoscopy 22(2), 313–325 (2008), doi:10.1007/s00464-007-9727-5.

8. Nio, D., Diks, J., Bemelman, W.A., Wisselink, W., Legemate, D.A.: Vascular Surgery: A Systematic Review. Eur. J. Vasc. Endovasc. Surg. 33, 263–271 (2007), doi:10.1016/j.ejvs.2006.10.004
9. Martinie, J.B., Smeaton, S.M.: Laparoscopic Approaches to Pancreatic Endocrine Tumors. In: Greene, F.L., Heniford, B.T. (eds.) Minimally Invasive Cancer Management, Part 3, pp. 145–157 (2010)
10. Yuh, B.E., Hussain, A., Chandrasekhar, R., Bienko, M., Piacente, P., Wilding, G., Menon, M., Peabody, J., Guru, K.A.: Comparative analysis of global practice patterns in urologic robot assisted surgery. J. Endourol. 24(10), 1637–1644 (2010), doi:10.1089/end.2010.0024
11. Borden Jr., L.S., Kozlowski, P.M., Porter, C.R., Corman, J.M.: Mechanical failure rate of da Vinci robotic system. Canadian Journal of Urology 14, 3499–3501 (2007)
12. http://www.accessdata.fda.gov/scripts/cdrh/cfdocs/cfRES/res.cfm
13. Murphy, D.G., Bjartell, A., Ficarra, V., Graefen, M., Haese, A., Montironi, R., Montorsi, F., Moul, J.W., Novara, G., Sauter, G., Sulser, T., van der Poel, H.: Downsides of Robot-assisted Laparoscopic Radical Prostatectomy: Limitations and Complications. European Urology 57(5), 735–746 (2010), doi:10.1016/j.eururo.2009.12.021
14. Antoniou, G.A., Riga, C.V., Mayer, E.K., Cheshire, N.J.W., Bicknell, C.D.: Clinical applications of robotic technology in vascular and endovascular surgery. Journal of Vascular Surgery 53(2), 493–499 (2011), doi:10.1016/j.jvs.2010.06.154
15. Zureikat, A.H., Nguyen, K.T., Bartlett, D.L., Zeh, H.J., Moser, A.J.: Robotic-Assisted Major Pancreatic Resection and Reconstruction. Archives of Surgery 146(3), 256–261 (2011), doi:10.1001/archsurg.2010.246
16. Kaushik, D., High, R., Clark, C.J., LaGrange, C.A.: Malfunction of the da Vinci Robotic System During Robot-Assisted Laparoscopic Prostatectomy: An International Survey. Journal of Endourology 24(4), 571–575 (2010), doi: 10.1089=end.2009.0489
17. Basili, V.R., Caldiera, G., Rombach, H.D.: The Goal Question Metric Approach. In: Encyclopedia of Software Engineering, Wiley (1994)
18. Thammarak, K., Intakosum, S.: OPI model: A methodology for development metric based on outcome oriented. In: 8th International Joint Conference on Computer Science and Software Engineering, JCSSE (2011), doi:10.1109/JCSSE.2011.5930144
19. Joint Commission on Accreditation of Healthcare Organizations, Robot-assisted abdominal surgery. Comprehensive Accreditation Manual for Hospitals: The Official Handbook (CAMH) Oakbrook Terrace, IL (2002)
20. Vincent, C., Moorthy, K., Sarker, S.K., Chang, A., Darzi, A.W.: System approaches to surgical quality and safety – From concept to measurements. Annals of Surgery 239(4), 475–482 (2004), doi:10.1097/01.sla.0000118753.22830.41
21. Pronovost, P.J., Berenholtz, S.M., Goeschel, C.A., et al.: High Reliability in Health Care Organizations. Serv. Res. 41(4 Pt 2), 1599–1617 (2006), doi:10.1111/j.1475-6773.2006.00567.x

System Concept for Collision-Free Robot Assisted Surgery Using Real-Time Sensing*

Jörg Raczkowsky, Philip Nicolai, Björn Hein, and Heinz Wörn

Karlsruhe Institute of Technology (KIT)
Institute for Process Control and Robotics, Karlsruhe, Germany
joerg.raczkowsky@kit.edu

Abstract. The introduction of robot assistance into the surgical process yields beside all desired advantages also additional sources of potential risks. This is especially due to the fact that the working space of the robot system is overlapping with the patient and the surgical personnel in a narrow environment around the situs. To enable the usage of partially autonomous robotic system in this field, we propose a novel approach which combines an algorithm for guaranteed collision-free path-planning with a real-time monitoring system of the workspace. This paper details the concept as well as the integration plan, showing first results for both components.

Keywords: robot assistance, monitoring, safety, collision avoidance, trajectory planning, sensing, registration.

1 Introduction

Nowadays, robot assisted surgery is (again) an upcoming technology for the operating room [1]. For comparatively simple surgical treatments, a robot/manipulator system and some manual support are often sufficient. As treatments grow more complex, there is need for support by additional tools. However, the optimal integration of these tools into the OR set up is cumbersome and time consuming. To make the systems more operable, capable and timesaving for the usage in the OR they would benefit from autonomous execution of some of these functions. This approach will in turn help to introduce robotic systems as routinely used assistance systems. For this reason, the Medical Robotics Group of IPR (MeGI) developed a modular platform for robotic surgery called OP:Sense [2] as depicted in Figure 1. This frame is the basis for research on the complete workflow of the different phases of a surgical treatment.

Based on patient data from multiple sources such as imaging and electronic health record (EHR) an individual planning model shall be established. The first phase will be the pre-operative surgical planning which is independent of the tools that will be used during the actual intervention. This plan will then be instantiated and the task

* This research work is partially funded by the European Commission within the FP7 project SAFROS under the contract number 248960. The residual equipment was funded within the large equipment program of the German Science Foundation (DFG).

S. Lee et al. (Eds.): Intelligent Autonomous Systems 12, AISC 194, pp. 165–173.
springerlink.com

planning for the specifically chosen modules can be performed. An especially important part for robotic surgery is the motion planning of the robotic instruments. This contains trajectories to and from the instruments region of interest. In partially autonomous minimally invasive robotic surgery, these could e.g. be used to automatically position the robot instruments near the trocars and then give full manual control to the surgeon.

In order to plan and guarantee safe robotic trajectories, constraints have to be defined that will lead to a safe execution with included exception handling. This will include supervising the scene for detecting obstacles to be included in the trajectory planning. Path planning itself has to take into account all detected obstacles in order to plan a reliable safe trajectory which doesn't pose any threat to either the patient or the medical staff. The combination of both measures as proposed here leads to robotic movements which are both safe and applicable to the live situation in the operation theatre with many different people and devices interacting in a dynamic way.

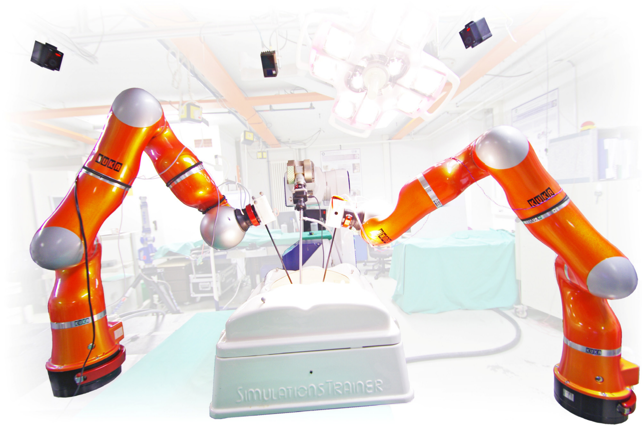

Fig. 1. OP:Sense platform for robot assisted surgery with two light-weight robots and the operation room supervision system (OSS)

2 Planning

2.1 Surgical Planning

In the pre-operative planning of the intervention, several medical decisions have to be made. These include the type of intervention (open surgery vs. minimally invasive surgery) as well as decisions more specific to the patients and their anatomy like the position and size of the incision(s) [3]. The latter have to take into account the properties of the surgical robot system being used such as its workspace, degrees of freedom and joint lengths, resulting in a robot configuration optimized for the actual intervention.

During the intervention, the robots positions at the operation table as well as the patient can be assumed to be static, i.e. both the patient and the robot bases are non-moving. Thus the patient can be regarded as a static obstacle which we propose to initially assess directly before the intervention.

2.2 Intra-operative Planning of Safe Zones

To initially asses the patients geometry and calculate the resulting safe zones in which the robots might work, the sensing system as detailed in III. will be used. After the patient is fully prepared, directly before the intervention itself begins with the first incision, the complete environment is captured by all cameras. This results in a (partially colored) point cloud showing the patient on the OP table which can then be used to build a volumetric model of the scene. Based on the color information the patients surface can be segmented into an interaction zone (that the robot might collide with) and a safe zone which can't be violated. By combining the zone segmentation with the volumetric model, a safe volume can be constructed which will then be used as an obstacle for trajectory planning.

2.3 Trajectory Planning

Based on the information given by the paths defined above, we use an automatic path planning algorithm that combines a deterministic local planning algorithm (A*) with a probabilistic global planning algorithm (PRM) in detail presented in [4]. This combination allows to compute collision-free paths in free wide spaces (e.g. from initial position of the robot to the target position) and is especially suited for cluttered and narrow environments (e.g. near the situs). In this connection we use a collision checking approach based on distance computations which allows detecting collisions reliably. This approach is explained in the following.

2.4 Collision Checking

As stated before, it is crucial for the targeted application to verify that movements/paths of the robot are collision-free. Typically obstacles detection and movement execution are handled in two different spaces:

- Work space (W-space): is the space where the robot and the obstacles exist as 3D geometry model.
- Configuration space (C-space): is the mathematical space spawn by all independent joints (only active joints).

Most approaches concerning collision checking of motion paths of robots rely on spot tests which are calculated at discrete positions along the path in C-space. This requires a pre-calculated step-size depending on the minimum size of the expected obstacles. But even if this size is given or can be calculated discrete collision tests can't guarantee that a robot path is collision free (s. Fig. 2). To overcome this deficiency we use an approach to map W-space distances to C-space areas that are collision free [5] (s. Fig. 2) also efficiently used in path planning algorithms [6]. The proposed method eliminates discretisation and resolution based problems when testing a path for collisions.

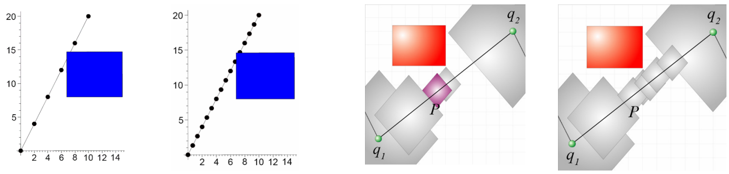

Fig. 2. (left two images) discrete collision checks can fail to detect collisions even if fine sampled, (right two images) our approach transforming W-space distances to C-Space can guarantee that a tested path is collision free

The idea can be summarized in generally determining how much a joint J_i of a robot can be moved before any affected link collides with an obstacles. To exemplify, consider an obstacle and a device with two rotational joints as shown in Fig. 3. Before moving the device, the minimal distance d_{min} between the device and obstacles is computed. The distance consumption table translates d_{min} to a joint value $\Delta\varphi_1$. After the device moves the joint J_1 by $\Delta\varphi_1$, the distance between device and obstacle tends to be 0. Due to the fact that J_1 can be moved by $\Delta\varphi_1$ on both directions, a collision free region of $2\Delta\varphi_1$ along the J_1 axis is set (s. Fig 3 (b), C-space). Similar behaviour is observed if only J_2 is actuated. If J_1 and J_2 are rotated at the same time, the joint values are smaller than the ones calculated when moving only one joint ($\varphi_1 < \Delta\varphi_1$ and $\varphi_2 < \Delta\varphi_2$). All joints movements inside the rhombic region are guaranteed to be collision free [BH1]. Based on that, a parameter-free recursive path test can be implemented that is able to securely detect obstacles of arbitrarily size (s. Fig. 3 (right)).

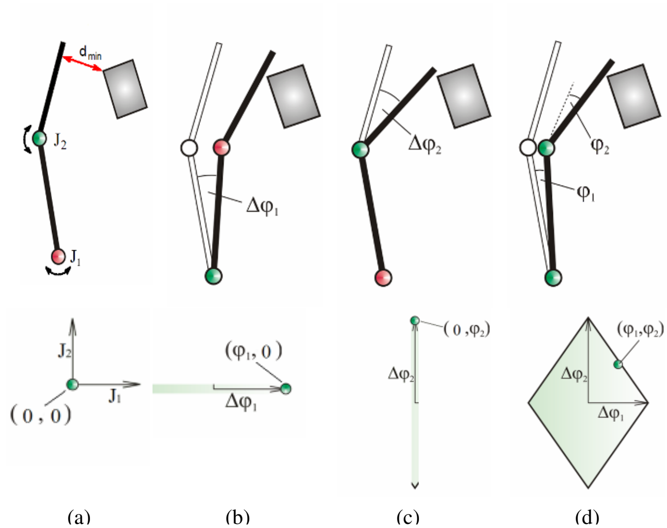

Fig. 3. (a) W-space and C-space of a robot with two rotational joints (J1 and J2). Minimal distance between device and obstacle is computed; (b) only joint J1 is moved on $\Delta\varphi$ just before it collides; (c) same effect moving joint J2; (d) All robot poses inside the rhombus, in C-space, are collision free.

2.5 Collision Prediction and Avoidance

The previous two sections describe how collision-free path-planning and safe collision checking of these paths during execution is done. During manual control this concept has to be operator. So during manual control every **p** cycle of the robot controller (p*4ms–p*12ms), the future position of the robot is estimated based on the input given by the operator and the current velocity and acceleration (s. Fig. 4).

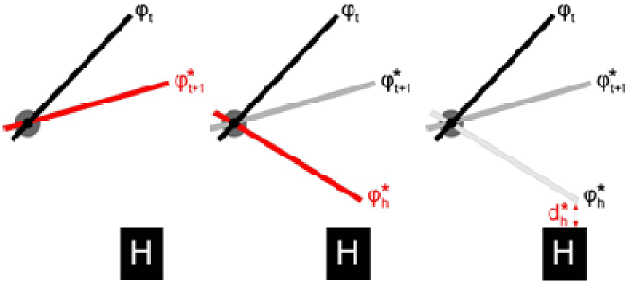

Fig. 4. Left to right: Based on the current input and velocity the future position is estimated at cycle t=t+p; based on the maximum possible deccelaration the estimated stop position is computed; based on the distance at this position, the robot can be freely moved, is slowed down or – if necessary – stopped

Fig. 5. demonstrates this approach with two KUKA-LBR. The predicted positions are shown in transparent. Between the these virtual robots a distance computation is done. Based on the calculated distance, an appropriate strategy is chosen (emergency stop, reduce velocity, change gear ratio of telecontrol, etc.) . The same principle can be used to emulate virtual fixtures (e.g. guiding channels or virtual workspaces, preventing a tool to leave a defined area). In the proposed approach we favor the use of distance calculations over pure collision checking, offering much more flexiblity, even though collision-checking is typically 15 times faster.

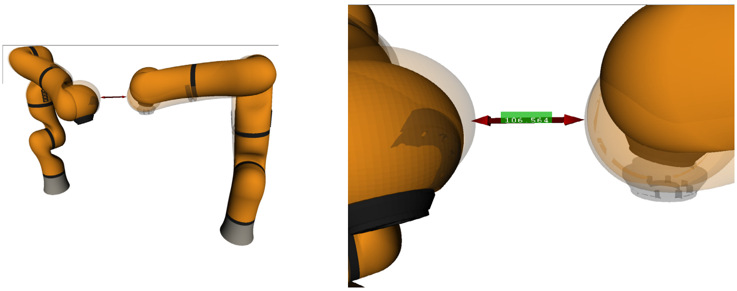

Fig. 5. Example of two LBR tested for collision in real-time with predicted position (transparent robot) using the approach explained in Fig. 4. In this setup the distance calculation takes ~1ms. For comparison: a pure collision test would only take 0.089 ms.

3 Sensing System

3.1 Tasks and Requirements

The task of the operation room sensing system (OSS) is to provide real-time scene information of the surroundings of the robots. As the situation in the operation theatre can be highly dynamic and various people surround the operation table, occlusions are a problem which is encountered very often. In the initial phase of an operation, the 3D surface of a patient has to be detected and segemented to determine safe zones, in which the robot might interact with the patient. For laparotomy, colored 3D information is necessary to detect the safe zone where the incision will be performed based on the parts of the patient that are put under medical cloth. In the case of minimally invasive robotic surgery, the locations of the trocars need to be determined. Independent of the type of operation, this step has to be performed only once and is thus not time-critical. During the intervention, the OSS has to provide real-time information about the current environment of the robots for path-planning with collision avoidance (free W-Space). Also, the robots pose has to be redundantly supervised in order to guarantee the correct execution of the planned trajectories and quickly detect deviations. This, of course, should also run in real-time.

3.2 Configuration

The OP:Sense setup currently integrates 13 cameras monitoring the scene from different angles, alllowing for the supervision of a large working space even with occlusions caused by obstacles and robots. Three different types of cameras are in use to meet the requirements listed above:

- Industrial-standard time-of-flight cameras are used for real-time acquisition of scene information from seven different perspectives. While these offer a high configurability and low latencies, the resulting images only feature a low resolution and no color information.
- A marker-based tracking-system in a six camera configuration provides accurate information for the poses of up to 20 different rigid bodies fitted with spheres. These e.g. include the end-effectors of the robots and other instruments.
- MS Kinect cameras offer high-resolution colored 3D-images (RGB-D) at the cost of a comparatively high latency and a lack of configuration options. Currently, the OSS is expanded to integrate four Kinect cameras into the OP:Sense setup.

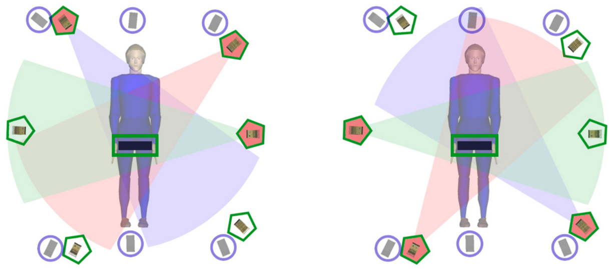

Fig. 6. Configuration of the OSS with six PMD S3 cameras (green pentagons) and six ARTtrack cameras (blue circles) ceiling-mounted around the workspace as well as one PMD CamCube 2.0 directly over the patient (green rectangle); left: S3 group 1 is triggered, right: S3 group 2 is triggered (different beam colors correspond to different frequencies)

While the combination of these sensors offers many advantages and can thus fulfil the requirements listed above, there are also drawbacks to be dealt with. As all systems rely on active IR signals, it has to be guaranteed that no crosstalk between the cameras distorts the measurements. According experiments showed that the simultaneous usage of multiple PMD S3 cameras leads to major distorsions. Thus a shared time- and frequency-multiplexing control mechanism has been developed and implemented. The spatial configuration of the cameras as well as the principle of the multiplexing approach is depicted in Fig. 6.

3.3 Results

Due to the time-multiplexing control for the S3 cameras, not all cameras can be triggered at their nominal speed, resulting in a lower achievable framerate. In practice, two groups of S3 cameras only run at 10 Hz each instead of their maximum refresh rate of 20 Hz. As all information from the cameras are integrated into one central representation of the scene, this model is nevertheless still with a frame rate of 20 Hz. As in each timestep information from different cameras is integrated, we call this an “interlaced” update rate of 20 Hz. Table I shows the detailled results of the current setup.

Table 1. OSS update rate

Sensor / system	**Update rates**	
	Maximum nominal frame rate	***Frame rate achieved in OP:Sense***
PMD S3	20 Hz	10 Hz
PMD CamCube	20 Hz	20 Hz
ARTtrack 2.0	60 Hz	20 Hz
Full scene representation	-	**20 Hz**

In a preliminary step for integration of the collision-free path-planning, a voxel carving algorithm has been applied to the scene model. This results in a free space configuration representation which will serve as the input for the collision-free path-planning algorithm. The prototype implementation is running at 4 Hz in a voxel grid of 40 x 20 x 20 cubes as depicted in Fig. 7.

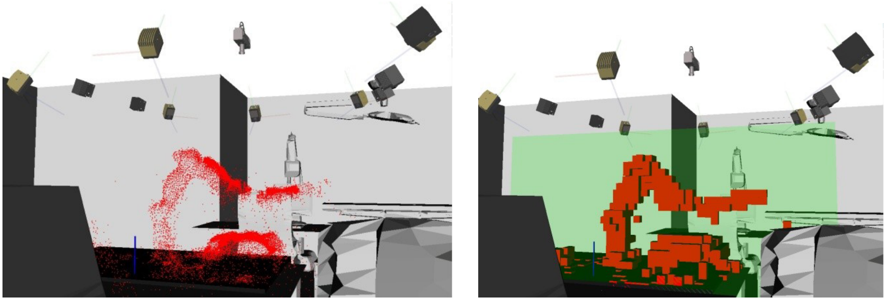

Fig. 7. (left) Registered point cloud, (right) resulting voxel space inside the supervised working volume (green)

4 Integration/Plan Execution

The OP:Sense platform contains currently two KUKA LWR4 light weight robots and one Staeubli RX90 robot. The integration of the robotic systems, sensor systems and other embedded devices is done by a high-level control based on Matlab/SimuLink. This central RAS supervision system consists of several modules that each control one part of the intervention, e.g. the OR workflow or the haptic input devices (s. Fig. 8). It will be expanded based on the concept detailed in this paper by the path-planning module which directly interfaces with the sensing system.

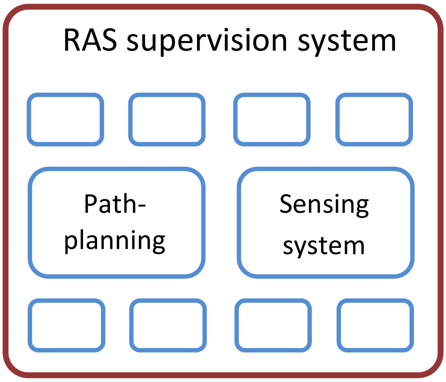

Fig. 8. Schematic view of the RAS supervision system featuring several components including the new path-planning algorithm and the sensing system

5 Summary

The OP:Sense platform offers the opportunity of fast prototyping of surgical robot cells with sensing. Every state during a treatment could be monitored and a decision support is given to the physicians. The paper describes a novel approach for the integration of a path-planning module for collision free trajectories into the platform which is closely coupled to the sensing system, resulting in a reliable and safe human-robot interaction inside the operation room.

Acknowledgements. This research work is partially funded by the European Commission within the FP7 project SAFROS under the contract number 248960. The residual equipment was funded within the large equipment program of the German Science Foundation (DFG). The authors thank the EU Commission and the German Science Foundation (DFG) for the support of the research.

References

1. Taylor, H., Kazanzides, P.: Medical Robotics and Computer-Integrated Interventional Medicine. In: Zelkowitz, M. (ed.) Advances in Computers, vol. 73, pp. 217–258. Elsevier (2008)
2. Nicolai, P., Beyl, T., Moennich, H., Raczkowsky, J., Wörn, H.: OP:Sense – An Integrated Rapid Development Environment in the Context of Robot Assisted Surgery and Operation Room Sensing. In: Proceedings of IEEE International Conference on Robotics and Biomimetics (ROBIO 2011), Phuket, Thailand, December 7-11, pp. 2421–2422 (2011)
3. Schorr, O., Münchenberg, J., Raczkowsky, J., Wörn, H.: KasOp - A Generic System for Pre- and Intraoperative Surgical Assistance and Guidance. In: Proc. of the 15th Int. Congress and Exhibition of Computer Assisted Radiology and Surgery (CARS), Berlin, Germany (2001)
4. Mages, D., Hein, B., Wörn, H.: A Deterministic Hierarchical Local Planner for Probabilistic Roadmap Construction. In: VDI: VDI Berichte, vol. 1956, pp. 29–30 (2006)
5. Mages, D., Hein, B., Wörn, H.: Approximated distance conversion from work space to configuration space of robots based on serial kinematics. In: VDI-Berichte 1841, Robotik (2002)
6. Hein, B., Wörn, H.: Fast Hierarchical A* Path Planning for Industrial Robots Based on Efficient Use of Distance Computations. In: Proc. of 37th International Symposium on Robotics ISR 2006 and 4th German Conference on Robotics Robotik, Munich (2006)

The Autonomous Photovoltaic MarXbot

Florian Vaussard, Philippe Rétornaz, Martin Liniger, and Francesco Mondada

EPFL – STI – LSRO, Station 9, 1015 Lausanne, Switzerland
firstname.lastname@epfl.ch

Abstract. Domestic service robots are currently powered by the mains electricity. The growing multiplication of such devices negatively impacts our environment. In this study, we show the feasibility of harvesting energy from natural light in an indoor environment. The design of the harvester is carefully carried out using an experimental characterisation of several solar panels, while the boost converter is optimised to operate at low-light intensities and the robot is enhanced for low-power operations. The resulting harvester is then thoroughly characterised. Finally, a phototaxis experiment is conducted, proving the feasibility of recharging the robot solely by using this form of energy. The possibility of embedding energy harvesting in indoor mobile robots radically changes the potential impact of this technology in our society.

1 Introduction

Domestic service robots are a rapidly growing market. In 2010, at least 1.45 million units have been sold, mostly vacuum cleaners [1]. This is roughly a 40 % increase compared to the previous year. The total population can be estimated at around seven million units, even if this figure is subject to uncertainty.

All these devices are powered by batteries. In the best case, the robot can recharge itself using the mains electricity and a docking station. In the worst case, primary batteries must be periodically replaced. If these robots are in use only 1 % of the time, given the mentioned population, this equals 600 million hours of activity per year. If we take a reasonable power consumption of 10 W, this represents 6 GW h per year, or 510 *Tonne of Oil Equivalent* (TOE). Our long-term goal is to replace most of this power with renewable energy, for example by harvesting the energy from the surrounding environment.

In a previous study, we considered several types of energy, and showed how some of them are highly promising, such as indoor solar energy or mechanical work produced by humans [14]. The indoor environment is, however, demanding. Compared to outdoors, the house is protected against environmental phenomena, leading to scarce energy resources. In the case of a robot performing periodic tasks at a low duty cycle—like cleaning, watering the plants or patrolling—renewable energies can however account for a fair part of the total energy budget. This is what we want to assess in practice.

In this study, we present the results achieved using a prototype of a photovoltaic robot for indoor use. This energy was chosen for its high potential, especially near windows and other bright places exposed to the sun. A power density of at least 300 W m^{-2} behind a window was assessed during good weather in September using a solarimeter (46° of latitude). This is two orders of magnitude above the indoor lighting.

S. Lee et al. (Eds.): Intelligent Autonomous Systems 12, AISC 194, pp. 175–183.
springerlink.com

There are a number of challenges when scavenging the solar energy directly from a mobile indoor robot. In this study, we address the mechatronics integration, with the main purpose of efficiently moving and orienting the panel, so as to maximise the collected energy. Another problem is the localization of the best spots for being recharged. We show here a simple solution based on phototaxis. More complex situations will be addressed separately.

The key points of our design are first introduced. The prototyped harvester is then validated under well-known conditions. Finally, we prove the feasibility of recharging the robot, using an indoor experiment.

2 Prior Works

A number of outdoor robots are effectively using solar energy, the most notable ones being the three Mars rovers—Sojourner, Spirit, Opportunity—as well as the Antarctic rover ”Cool Robot”. The Mars rovers were fitted with expensive GaAs/Ge and triple-junction solar panels, placed horizontally on top of the robots and providing the necessary power for a few hours per day [12,13]. The operating point of the solar panels is approximated using environmental conditions and a priori knowledge.

“Cool Robot” is designed to operate in Antarctic conditions [7,8]. The power budget has been carefully modelled, including the snow-reflected component, providing a good margin for long-term polar experiments [6]. Such experiments, however, have yet to be conducted.

In the case of indoor robots, there exists only a few rigorous designs. Results are often restricted and inconclusives. Testing conditions are not always well defined, leading to non-reproducible experiments. Worthy designs include the miniature legged inchworm of Hollar [5]. It was able to move forward 3 mm in 30 minutes under the light provided by an optical fiber. The miniature robot “Alice” was also fitted with solar panels, operating under a 3000 ANSI lumens beamer [2]. Power densities of 7.1 and 27.8 $\mathrm{W\,m^{-2}}$ were achieved using crystalline silicon and thin film amorphous silicon cells. The overall power balance is, however, unknown.

The problem of the panel’s orientation is often not considered by researchers, simplified to a horizontal placement. The tracked robot of Hartono is fitted with a fixed-tilt panel and four photodiodes at each corner [4]. These inputs are fed into a neuronal network, which controls the driving motors and switches between several survival strategies. This setup has been tested for 33 hours in uncharacterised outdoor conditions.

In summary, a rigorous design, validated by by a proof a concept experiment, was not yet demonstrated in the literature. We propose to fill in the gap in this study, using a simple approach to locate the energy source.

3 Design

Our design was driven by several key points. First, the system should minimise the consumed energy, while being able to move in an indoor environment. It should also maximise the illumination on the solar panel and efficiently convert the incoming power into usable energy.

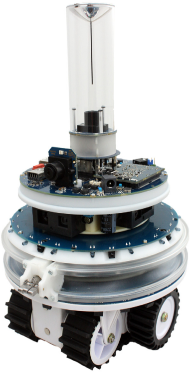

(a)

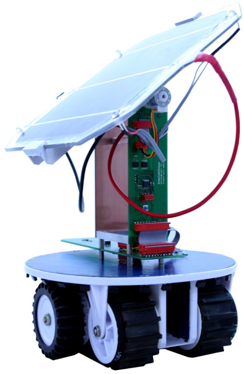

(b)

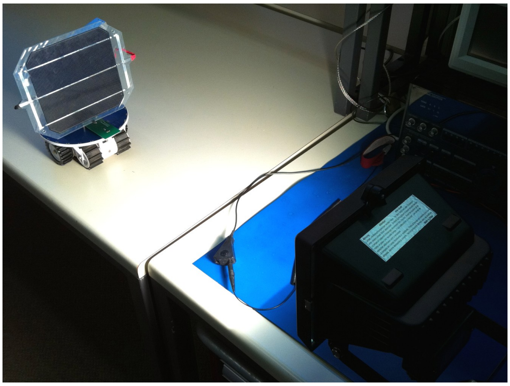

(c)

Fig. 1. The complete marXbot robot (a) and its stripped-down photovoltaic version (b). The photovoltaic marXbot during the efficiency test (c).

Table 1. Experimental cell characterisation

Light Source	**Illumination G** $(\mathrm{W\,m^{-2}})$	**Cell Power** $\mathbf{P}_{\mathrm{cell}}$ (W)	**Area** $\mathbf{A}_{\mathrm{cell}}$ (m^2)	**Efficiency** η_{cell}
Sun[a]	150	0.36	$2.43{\cdot}10^{-2}$	0.099
Artificial[b]	148	0.30	$2.43{\cdot}10^{-2}$	0.083

[a] Behind a window [b] OSRAM 60 W incandescent “daylight” bulb

We are using the small marXbot robot as the mobile platform [3]. It is a highly-modular, low-power mobile robot. Subsystems can be put into sleep when unused, and we are thus able to minimise the wasted energy when recharging. Its rich set of sensors provides the robot with advanced navigation capabilities, like a low-cost range scanner and an embedded ARM-based computer [9] (Fig. 1(a)). For our experiments, we will solely use the mobile base, as pictured in Fig. 1(b).

The characterisation of solar panels is performed by the manufacturers under the Air Mass (AM) 1.5 model, with a standard illumination of $1000\,\mathrm{W\,m^{-2}}$ at sea level. Our conditions are far from this norm: low light intensity and a spectrum filtered by a window can heavily influence the efficiency, as shown by [11]. For our design, we have compared four photovoltaic panels, two made of monocrystalline silicon and two made of thin film amorphous silicon.

During the characterisation process, the I/V curve was recorded using a variable resistive load. We considered two light conditions: the sunlight, as received behind a south-oriented window, and an artificial light. The monocrystalline cell AH508480G (Sunways) outperformed the others. Table 1 shows the efficiency of this cell under the two test conditions.

This single cell is providing a high current (8 A under AM 1.5) at low voltage ($V_{OC} = 0.63\,\mathrm{V}$). Due to space limitations, we were unable to mount several ones in a serial configuration. A boost DC/DC converter has been specially optimised for low-light conditions, based on a model of the prevalent losses at the operating point ($150\,\mathrm{W\,m^{-2}}$). As shown in Sec. 4, the measured efficiency is above 85 % at low light intensity.

To control the photovoltaic subsystem, we are using a two-layer architecture. A low-power 8 bits microcontroller is controlling the DC/DC converter to perform the *Maximum Power Point Tracking* (MPPT). A 16 bits microcontroller is in charge of the high-level control during the experiment, able to put itself and the robot into deep sleep when appropriate. By using the event-based framework Aseba [10], we can easily prototype behaviours and log data.

The alignment of the cell with the light source is crucial to maximise the collected power. While most designs neglect this point, we addressed this issue by adding a rotational *Degree of Freedom* (DOF) to the panel, leading to a total of five DOFs, when taking into account the mobility of the system. Several mechanical solutions have been evaluated, based on the energy required to orient the panel. The efficiency of the mechanical transmission appears to be the limiting factor. The final system is shown in Fig. 1(b). The rotation axis is placed closed to the centre of mass, in order to minimise the gravitational couple on the motor. A stepper motor is in direct drive with the axis.

Four photodiodes were placed at each corner, to allow the localization of the light source using a gradient ascent strategy.

4 Results

An experimental power model of the marXbot was introduced in [3]. For our stripped-down version, the idle consumption is 0.9 W with modules enabled. The total power consumed when moving can be expressed as a quadratic function of the speed.

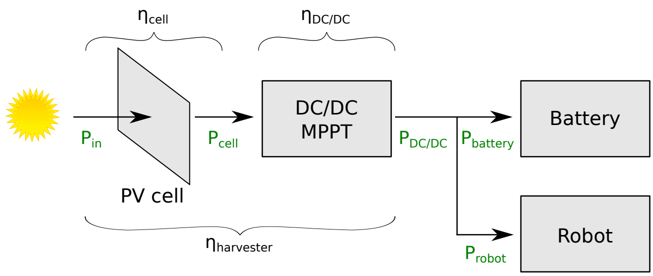

Fig. 2. Simple model of the harvester

The electronics have been further improved during this study to enable a deep sleep state. The power supply of each module can be actively turned off, decreasing the total power consumption to 40 mW.

4.1 Harvester Characterisation

A simple model of the harvester is shown in Fig. 2. The system was characterised using a halogen light of 60 W at a variable distance (Fig. 1(c)). The illumination is measured with a solarimeter at the centre of the cell. The power produced by the cell P_{cell}, as well as the power at the output of the converter $P_{DC/DC}$, are plotted against the illumination G in Fig. 3(a).

P_{cell} appears to be linear (R^2 = 0.9996), as shown by the linear regression

$$P_{cell} = a_{cell} G + b_{cell} = 3.02 \cdot 10^{-3} G + 7.4 \cdot 10^{-3} \,(\mathrm{W}) \ . \tag{1}$$

This implies a constant cell efficiency on the studied range, which equals

$$\eta_{cell} = a_{cell} / A_{cell} = 0.124 \ . \tag{2}$$

On the other side, $P_{DC/DC}$ depends on the efficiency of the DC/DC converter

$$P_{DC/DC} = \eta_{DC/DC} P_{cell} = \eta_{harvester} P_{in} \ . \tag{3}$$

Efficiencies $\eta_{DC/DC}$ and $\eta_{harvester}$ are plotted in Fig. 3(b) and 3(c), respectively.

The achieved efficiency is especially good at low illumination. The harvester's efficiency is above 10 % in the range from 30 to 110 W m^{-2}. At higher illuminations, the high current delivered by the cell increases the Joule losses inside the self and the high-side transistor of the DC/DC converter.

4.2 Phototaxis Experiment

In order to show the viability of our design, a phototaxis experiment was conducted using the setup of Fig. 4(a). A halogen lamp is placed in one corner of the arena, with a fixed tilt angle. The distribution of the light's intensity, as measured by the solarimeter,

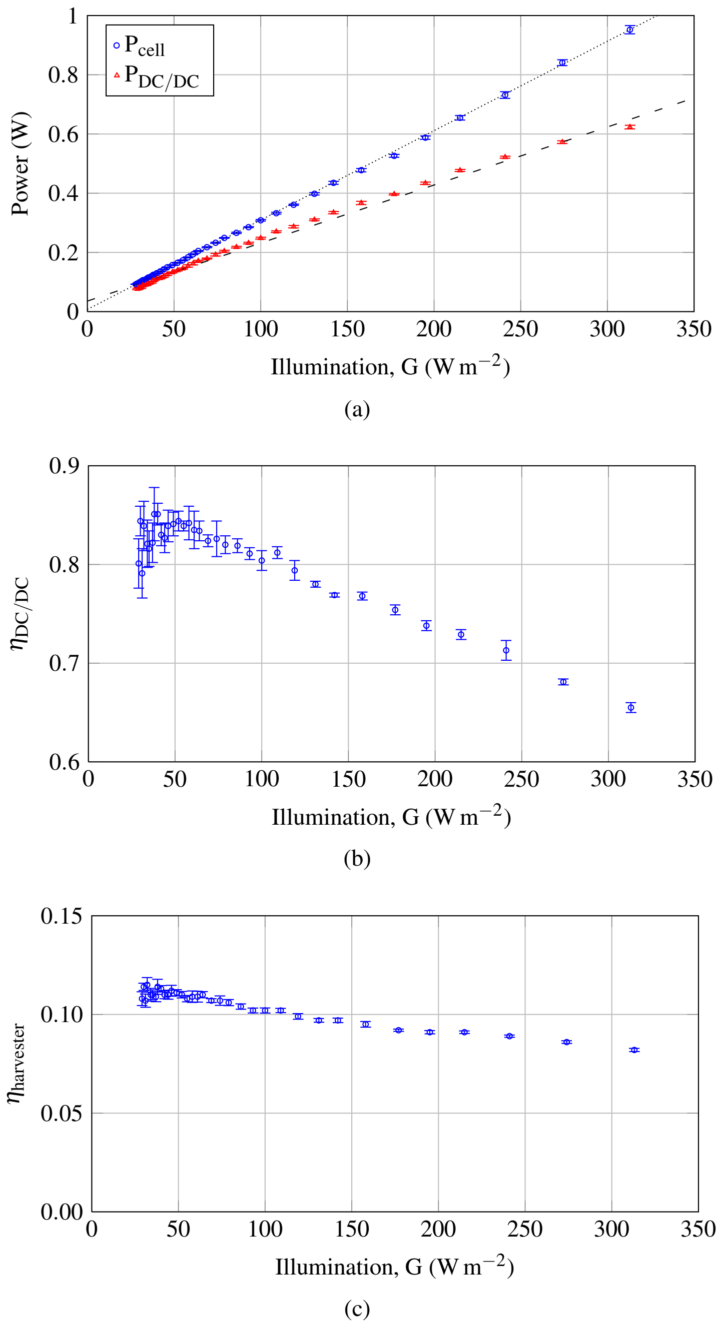

Fig. 3. Experimental results of the solar harvester under halogen illumination

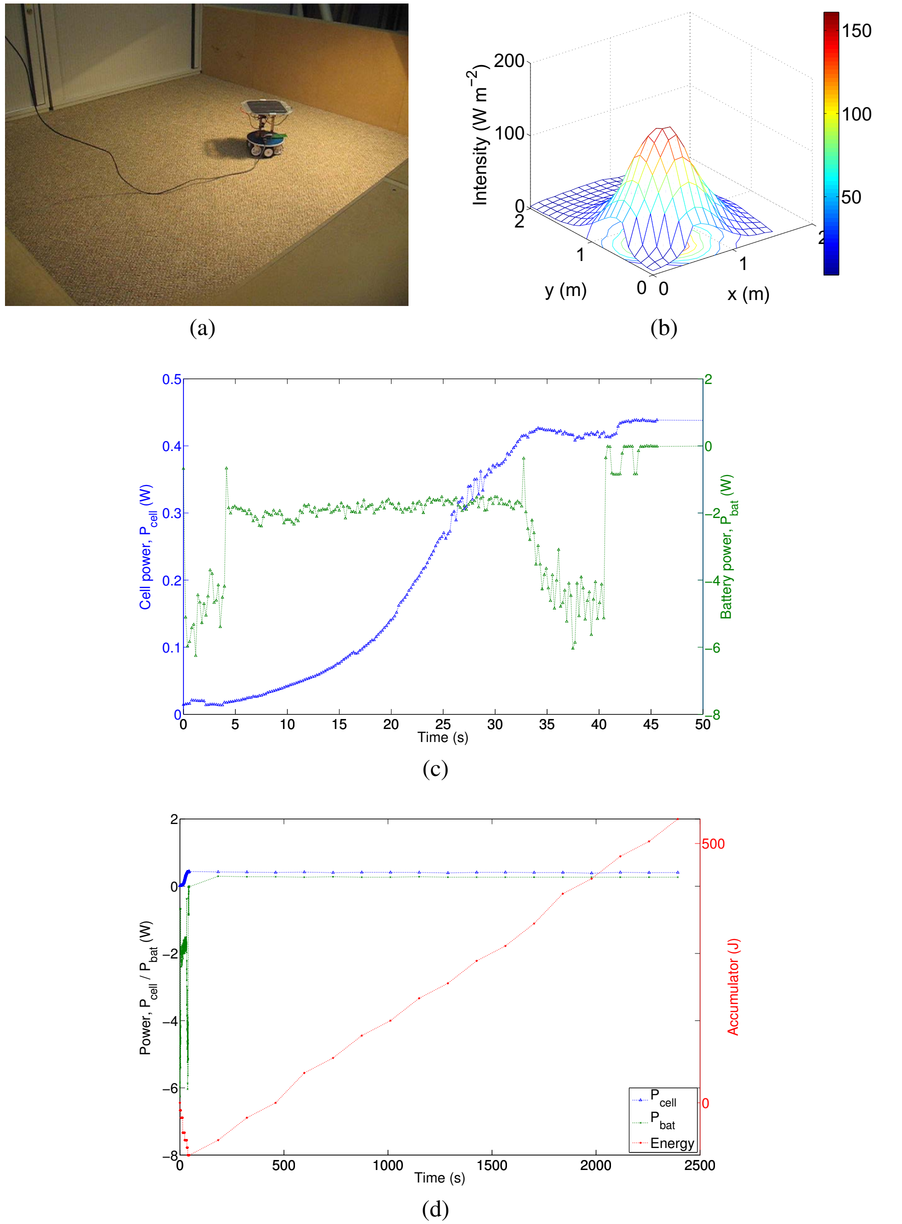

Fig. 4. Phototaxis experiment. (a) Experimental setup. (b) Light intensity distribution. (c) Energy harvesting: maximisation phase. (d) Energy harvesting: recharge phase.

is shown in Fig. 4(b). There is a peak, with a value of 161 W m^{-2}. According to the efficiency of our harvester, we should be able to extract 0.37 W under optimal placement.

A simple P controller was implemented using the photodiodes to control the heading of the robot, while moving autonomously towards the source. When the derivative of the cell's power flattens out, the robot stops its progress and orients the panel towards the light.

The results are shown in Fig. 4(c) and 4(d), using two different time scales. At small scale, the power used to move forward is around 2 W, whereas it uses up to 5 W when turning on spot. This is due to the poor efficiency of the tracked robot when turning on a carpet. The power delivered by the cell increases as the robot is reaching its goal. The power delivered by the DC/DC converter reaches a maximum of 0.297 W after 44 s. This is 80 % of the theoretical maximum.

At a larger time scale, the embedded charge counter first begins to decrease, due to the energy required to move, reaching its minimum at 45 s; 100 J have been used for this part. Then, the battery starts charging. The energy equilibrium is reached after ten minutes. Thereafter, the battery starts gaining energy compared to its initial state. At the end, after 40 minutes of experiment, we have a net gain of 547 J. A total of 130 hours would be needed to recharge the robot, given a battery of 40 W h, for an autonomy of eight hours when moving. Thus, for one hour of autonomy, we need 16 hours of recharge, about one week under reasonable assumptions. This matches our design target of a domestic robot operating a few hours per week. It is close to the theoretical conclusions we draw in [14].

5 Conclusion

We have shown the possibility of autonomously recharging our robot using an indoor experiment and a phototaxis strategy. The chosen light's intensity is what we are expecting from the sun entering the house through windows.

The next step is to test our design in a less synthetic setup, using the real sunlight. In this case, a simple phototaxis strategy might not be enough, and we are planning to integrate the energy-mapping problem inside the *Simultaneous Localization And Mapping* (SLAM) framework.

As pointed out, a tracked robot is rather energy inefficient when moving, especially when turning on spot. An adequate platform is also very important, considering the targeted environment. An efficient locomotion principle has to be adopted when moving indoor. Simple wheels are not a good solution, as they usually get stuck in carpets and other similar obstacles. This will also be a focus of our future researchers.

Acknowledgement. This research was supported by the Swiss National Science Foundation through the National Centre of Competence in Research Robotics.

References

1. International Federation of Robotics: Service Robot Statistics, http://www.ifr.org/service-robots/statistics
2. Boletis, A., Driesen, W., Breguet, J.M., Brunete, A.: Solar cell powering with integrated global positioning system for mm3 size robots. In: IROS, pp. 5528–5533. IEEE (2006)
3. Bonani, M., Longchamp, V., Magnenat, S., Rétornaz, P., Burnier, D., Roulet, G., Vaussard, F., Bleuler, H., Mondada, F.: The marXbot, a miniature mobile robot opening new perspectives for the collective-robotic research. In: IROS, pp. 4187–4193. IEEE (2010)
4. Hartono, P., Tabe, K., Suzuki, K., Hashimoto, S.: Strategy acquirement by survival robots in outdoor environment. In: ICRA, pp. 3571–3575. IEEE (2003)
5. Hollar, S.: A solar-powered, milligram prototype robot from a three-chip process. Ph.D. thesis, University of California (2003)
6. Lever, J., Ray, L.: Revised solar-power budget for cool robot polar science campaigns. Cold Regions Science and Technology 52(2), 177–190 (2008)
7. Lever, J., Ray, L., Streeter, A., Price, A.: Solar power for an antarctic rover. Hydrological Processes 20(4), 629–644 (2006)
8. Lever, J., Streeter, A., Ray, L.: Performance of a solar-powered robot for polar instrument networks. In: Proceedings of IEEE International Conference on Robotics and Automation, ICRA 2006, pp. 4252–4257. IEEE (2006)
9. Magnenat, S., Longchamp, V., Bonani, M., Rétornaz, P., Germano, P., Bleuler, H., Mondada, F.: Affordable slam through the co-design of hardware and methodology. In: 2010 IEEE International Conference on Robotics and Automation (ICRA), pp. 5395–5401. IEEE (2010)
10. Magnenat, S., Rétornaz, P., Bonani, M., Longchamp, V., Mondada, F.: ASEBA: a modular architecture for event-based control of complex robots. IEEE/ASME Transactions on Mechatronics (99), 1–9 (2009)
11. Randall, J., Jacot, J.: Is AM1. 5 applicable in practice? Modelling eight photovoltaic materials with respect to light intensity and two spectra. Renewable Energy 28(12), 1851–1864 (2003)
12. Shirley, D., Matijevic, J.: Mars pathfinder microrover. Autonomous Robots 2(4), 283–289 (1995)
13. Stella, P., Ewell, R., Hoskin, J.: Design and performance of the mer (mars exploration rovers) solar arrays. In: Conference Record of the Thirty-First IEEE Photovoltaic Specialists 2005, pp. 626–630. IEEE (2005)
14. Vaussard, F., Bonani, M., Rétornaz, P., Martinoli, A., Mondada, F.: Towards autonomous energy-wise RObjects. Towards Autonomous Robotic Systems, 311–322 (2011)

Automatic Segmentation and Decision Making of Carotid Artery Ultrasound Images

Asmatullah Chaudhry[1,2], Mehdi Hassan[3], Asifullah Khan[3], Jin Young Kim[2], and Tran Anh Tuan[3]

[1] HRD, PINSTECH, P.O. Nilore 45650, Islamabad, Pakistan
[2] School of Electronics & Computer Engineering, Chonnam National University, Gwangju, S. Korea
[3] Department of Computer & Information Sciences, PIEAS, P.O. Nilore 45650, Islamabad, Pakistan
asmat@jnu.ac.kr, mehdi@pieas.edu.pk, asif@pieas.edu.pk, beyondi@jnu.ac.kr, tuantran2610@yahoo.com

Abstract. Disease diagnostics based on medical imaging is getting popularity day after day. Presence of the arthrosclerosis is one of the causes of narrowing of carotid arteries which may block partially or fully blood flow into the brain. Serious brain strokes may occur due to such types of blockages in blood flow. Early detection of the plaque and taking precautionary steps in this regard may prevent from such type of serious strokes. In this paper, we present automatic image segmentation and decision making technique for carotid artery ultrasound images based on active contour approach. We have successfully applied the automatic segmentation of carotid artery ultrasound images using snake based model. Intima-media thickness (IMT) measurement is used to form a feature vector for classification. Five different features are extracted from IMT measured values. K-nearest neighbors (KNN) classifier is applied for classification of the images. Qualitative comparison of the proposed approach has been made with the manual initialization of snakes for carotid artery image segmentation. Decision is made based on the feature vector obtained from IMT values. Using the proposed approach we have obtained 98.30% classification accuracy. Our proposed approach successfully segment and classify the carotid artery images in an automated way to help radiologists. Obtained results show the effectiveness of the proposed approach.

Keywords: Plaque detection, Snakes model, Image segmentation, IMT measurement, KNN classifier.

1 Introduction

Carotid arteries are main blood supplies to the brain. Narrowing the carotid artery may block the blood flow into the brain and causes a serious brain stroke. Early detection of the plaque in the arteries may prevent from such types of strokes. Non-invasive natures of diagnostic techniques in medical profession are invaluable. Ultrasound imaging is an attractive technique due to its non invasiveness. However, ultrasound images are of the poor quality due to the presence of spackle noise and waves interferences. As a result, carotid artery ultrasound images need considerable

S. Lee et al. (Eds.): Intelligent Autonomous Systems 12, AISC 194, pp. 185–196.
springerlink.com

efforts from radiologists to detect the plaque. Hence, a computer aided diagnostic (CAD) technique for segmentation of carotid artery ultrasound images is highly desirable. It may help the radiologists extract significant information about the plaque and in determining the stage of disease [1, 2].

Most of the CAD techniques require user intervention at certain level. Sometimes inexperienced user intervention may leads toward false results. Snake based method [3]; dynamic programming [4] and combination of both [5] are used for automatic IMT measurement. In [6] authors have proposed a semi-automatic snakes based method for segmentation of carotid artery images. In their approach, a proper seed point is essentially required from the user to segment lumen of the carotid artery. Since, the basic drawback of snake based method is its initialization. Further, inappropriate snakes' initialization may leads toward misleading results. IMT measurement is one of the effective methods for detection of plaque in carotid arteries. In this paper, we have employed automatic initialization of snakes to segment the carotid artery ultrasound images. Five different features are extracted from the IMT measured values. KNN is used for the classification of the segmented images. Obtained results show the effectiveness of the proposed methodology.

Rest of the paper is organized as follows. Section 2 describes the proposed approach; section 3 presents the method of automatic segmentation of ultrasound images. Classification of carotid artery ultrasound images is included in section 4. Section 5 elaborates the experimental results and discussion. Conclusion and future work is described in section 6.

2 The Proposed Method

The proposed scheme of automated carotid artery image segmentation and decision making system consists of the following steps. Its graphical representation is shown in Fig. 1.

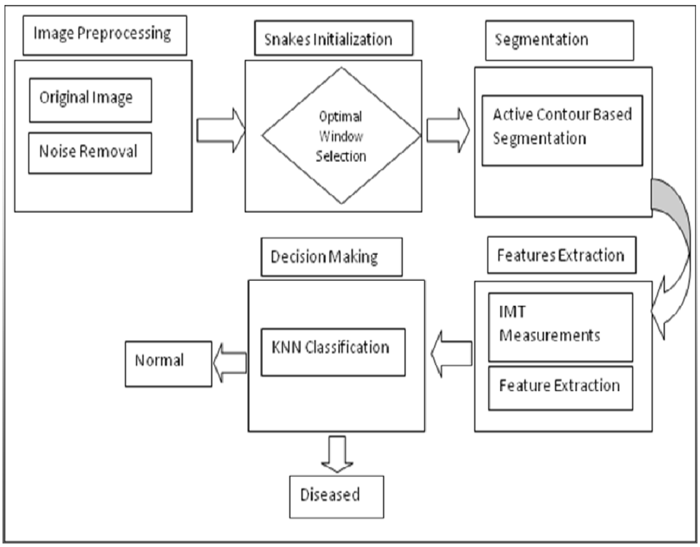

Fig. 1. Flow chart of the proposed approach

2.1 Image Preprocessing

The major drawback of ultrasound images is its poor quality due to the presence of spackle noise and wave interferences [7, 8]. To obtain better segmented image, noise must be removed. For this purpose, we have used median filter for noise removal as image pre-processing step. It is a non linear filter and preserves the image detail in better way.

2.2 Snakes Initialization

The major disadvantage of active contour model is the initialization of snakes [9, 10]. The initial selected window greatly affects on segmentation results. In this paper, snake initialization window is selected in an automatic way to segment the carotid artery ultrasound images. Snakes initialization in an automatic manner is one of the main contributions of this research work. The input to this step is pre-processed image. Automatic window selection methodology is described in detail in the following subsection.

2.3 Object Separation from Background

First of all, we find the objects in the carotid artery ultrasound image. For this purpose, we employ Otsu's method [11] to separate the objects from the background. The Otsu's method is an automatic method of histogram based thresholding. Further, it is a non parametric and unsupervised threshold selection method. The main objective is to separate out the objects from image background considering it as a two class problem (background and the objects). The algorithm calculates the optimal threshold to separate the objects from background so that the intra-class variance becomes minimal by using the following equations.

$$\sigma_{\omega}^{2}(t) = \omega_{1}(t)\sigma_{1}^{2}(t) + \omega_{2}(t)\sigma_{2}^{2}(t) \qquad (1)$$

where, σ_{i}^{2} is the class variance, ω_{i} are the probability of the classes separated by threshold t. Expression (2) is used to maximize the intra-class variance.

$$\sigma_{b}^{2}(t) = \sigma^{2} - \sigma_{\omega}^{2}(t) = \omega_{1}(t)\,\omega_{2}(t)\left[\mu_{1}(t) - \mu_{2}(t)\right]^{2} \qquad (2)$$

The probability of the class $\omega_{1}(t)$ is computed from the histogram as t using expression (3):

$$\omega_{1}(t) = \sum_{0}^{t} p(i) \qquad (3)$$

Whereas, the mean of the class is computed by expression (4):

$$\mu_{1}(t) = \sum_{0}^{t} p(i)x(i) \qquad (4)$$

The objects and the background are separated from the carotid artery ultrasound images. Some isolated and noisy patterns may remain there. These noisy patterns have been removed through morphological opening operation using expression (5). The opening operation is usually used for smoothing the object contours and for elimination of thin protrusions [12].

$$f \circ b = (f \Theta b) \oplus b \tag{5}$$

After the opening morphological operation, the area inside the artery walls needs to be intelligently identified. For this purpose, negative of the Otsu's segmented image is obtained using the expression (6).

$$s = 1 - r \tag{6}$$

where, s is the resultant negative binary image and r is the segmented image by Otsu's approach.

The advantage of image negative is that we are interested to find out the area inside the artery walls. After finding the area inside the artery, the algorithm intelligently decides the location and size of the window for snakes' initialization.

The location of the window may vary from image to image depending upon the objects in the carotid artery ultrasound images. Once the window is determined the active contour method may be applied to segment the carotid artery ultrasound images successfully. The algorithm for automatic snake initialization window is described as below:

Algorithm 1

Begin % this algorithm initializes the snakes for carotid artery.

1. *Input to the algorithm is pre-processed image.*
2. *Object separation from background using Otsu's method.*
3. *Use morphological opening operation for noisy pattern removal.*
4. *Take Negative of Image for finding area inside arterial walls.*
5. *(a) Find the distance between upper and lower arterial wall.*
   (b) Find the length of the carotid artery in ultrasound image.
6. *Place the window for snake initialization between upper and lower arterial wall, keeping in view the fact that the area encompassed is maximum.*

End

3 Ultrasound Carotid Artery Image Segmentation

In our study, we have employed active contour method to segment the carotid artery ultrasound images. Active contour model is proposed by [13] and is being successfully used in computer vision applications. It is based on the energy minimization function. The advantage of using active contour model for segmentation is that the snakes are autonomous and self adapting in search for a minimal energy state and can easily be manipulated. The active contour model can be used to track objects in both spatial and temporal domains.

The governing equation of the snake is based on the internal and external energy components. The expression (7) is used as the governing equation of the active contour model.

$$E(\mathbf{v}) = \underbrace{\int_0^L \alpha(s)\left|\frac{\partial \mathbf{v}}{\partial s}\right|^2 + \beta(s)\left|\frac{\partial \mathbf{v}^2}{\partial s^2}\right|^2 ds}_{S(\mathbf{v})} + P(\mathbf{v}) \tag{7}$$

The parameters α and β are used to control the internal energy $S(\mathbf{v})$, contour stiffness and elasticity. The gradient of image is calculated to find the external energy $P(\mathbf{v})$. The minimum energy is obtained when contour approaches the edge of interests.

To assemble the contours, N piecewise polynomials are used. Each of which is built with a space–independent shape function like B-Spline [14] weighted by the node parameters. The energy function, expression (7) is minimized corresponding to Euler Lagrange partial differential equations (PDE).

$$\mathbf{M}\frac{d^2\mathbf{u}(t)}{dt^2} + \mathbf{C}\frac{d\mathbf{u}(t)}{dt} + \mathbf{Ku}(t) = \mathbf{q}(\mathrm{t}) \tag{8}$$

where **u***(t)* is the vector containing *N* nodes, **M** represents mass matrix, **C** shows the damping matrix, stiffness matrix is described by **K** and external forces are represented by **q** [15].

The motion equations (8) are solved by replacing time derivatives with their discrete approximations. By discretizing time variable *t* results in the following difference matrix equation.

$$\mathbf{Fu}_{\xi} = \mathbf{A}_1\mathbf{u}_{\xi-1} + \mathbf{A}_2\mathbf{u}_{\xi-2} + \mathbf{q}_{\xi-1} \tag{9}$$

where,

$$\mathbf{A}_1 = 2\mathbf{M}/(\Delta t)^2 + \mathbf{C}/(\Delta t), \tag{10}$$

$$\mathbf{A}_2 = -\mathbf{M}/(\Delta t)^2, \tag{11}$$

$$\mathbf{F} = \mathbf{A}_1 + \mathbf{A}_2 + \mathbf{K} \tag{12}$$

The computational cost of expression (9) is very high because of **F** inverse calculation. But an alternative formulation has been proposed by *Weruaga et al.* [16] for translation of the energy function (7) into frequency domain. Matrix inversion is avoided through this procedure because it becomes a point-wise inversion in frequency domain. Initially it is valid for closed contours; however, with the help of hidden extension it can be applied to open contours as well. The following equations are used for the implementation of open active contours in frequency domain:

$$\mathbf{z}_{\xi} = a_1\mathbf{u}_{\xi-1} + a_2\mathbf{u}_{\xi-2} + \eta^{-1}\mathbf{q}_{\xi-1} \tag{13}$$

$$\mathbf{d}_{\xi} = \Gamma\{\mathbf{z}_{\xi}\}, \tag{14}$$

$$[\mathbf{u}_{\xi}\ e] - IDFT\left\{DFT\{[\mathbf{z}_{\xi}\ \mathbf{d}_{\xi}]\}.\hat{\mathbf{h}}\right\} \tag{15}$$

where, $\mathbf{u}_{\xi}$ is N snakes vector, $\mathbf{q}_{\xi-1}$ external forces vector, global mass is represented by η, hidden snake rule is implemented using $\Gamma\{.\}$, $\mathbf{d}_{\xi}$ is the N-node snake extension, e is dummy residual vector, $\hat{\mathbf{h}}$ is the low pass filter of discrete Fourier transform (DFT).

To get the final solution smoother, B-splines are used as a shape function [15], and at each update of the contour some additional calculations are performed. To get better execution time ratio, we use cubic B-splines in this study [17] and interpolate node parameters u using cubic B-splines to achieve active contour v in the image plane.

4 Classifications

Carotid artery disease diagnosis greatly depends upon accurate artery image segmentation. After segmentation the classification step is applied. The images are classified as normal or abnormal. In this study, we have applied KNN classifier for classification of the carotid artery images. Five different features are extracted from the IMT values obtained from carotid artery segmented images to train and test the KNN classifier.

4.1 Features Extraction

Five important features are extracted from the IMT measured values which are being used in classification [18]. Extracted features are scaled down into [0-1] and are given to KNN classifier as an input. Mathematical description of each feature is as under:

$$Average = \frac{1}{n}\sum_{i=1}^{n} x_i \tag{16}$$

$$Var(X) = E\left[(X_i - \mu)^2\right] \tag{17}$$

$$s.d = \sqrt{E\left[(X_i - \mu)^2\right]} \tag{18}$$

$$Skewness = E\left[\left(\frac{X_i - \mu}{\sigma}\right)^3\right] \tag{19}$$

$$Kurtosis = \frac{\sum_{i=1}^{N}\left(Y_i - \bar{Y}\right)^4}{(N-1)\,s^4} \tag{20}$$

4.2 K-Nearest Neighbor Classifier

Nearest Neighbor (NN) is a supervised learning algorithm. It is used to classify the objects on its nearest neighbor training examples. Class is assigned on the basis of minimum Euclidean distance. If K=1 the algorithm becomes simply a nearest neighbor classifier and classify the objects based on its neighbor. For training and testing the KNN classifier, we have used 10-fold cross-validation. The expression (21) is used to find Euclidean distance:

$$S(\mathbf{X}, \mathbf{X_i}) = 1 - \frac{(X.X_i)}{(\|X\|\|X_i\|)} \quad (i = 1, 2, .. N) \tag{21}$$

The minimal Euclidean distance can be calculated by the following expression.

$$S(\mathbf{X}, \mathbf{X}i) = \min\{S(\mathbf{X}, \mathbf{X}_1), S(\mathbf{X}, \mathbf{X}_2), ...S(\mathbf{X}, \mathbf{X}_N)\} \tag{22}$$

where **X** **.X**i represents the dot product of **X** and **X**i vectors and modulus are represented by ||**X**|| and ||**X**i|| respectively. The sample under consideration is assigned the class corresponding to the training sample **X**k.

4.3 Classification Performance Measurements

In statistical prediction, to check the effectiveness of method different types of cross validation techniques are in practice. We have used 10-fold cross validation technique. The class of the test pattern is predicted by the classifier based on the N-1 training samples. The sampling process is repeated for N times and the class of each sample is predicted. The true positive (TP) and true negative (TN) are the number of correctly classified positive and negative classes. The false positive (FP) and false negative (FN) are those images which are incorrectly classified. To evaluate the performance of the classifier the following measures are used.

4.3.1 Accuracy

This measure is used to assess the overall usefulness of the classifier. It can be calculated using the following equation.

$$Accuracy = \frac{TP + TN}{TP + FP + TN + FN} * 100 \tag{23}$$

4.3.2 Matthews Correlation Coefficient

MCC is used as a measure of classification in binary classes and having values from -1 to +1. The value +1 means perfect pattern prediction (classifier never commit a mistake), zero means a random prediction and -1 means that classifier never predict a correct label. It can be obtained using the following equation:

$$MCC = \frac{TP \times TN - FP \times FN}{\sqrt{(TP + FN)(TP + FP)(TN + FN)(TN + FP)}} \tag{24}$$

4.3.3 F-Score

F-score considers precision and recall to measure the accuracy of the test. It is ranging from 0 to 1 is a weighted average of the precision and recall. Whereas 0 shows worst score and 1 shows best score. The F-measure can be calculated by the following formula:

$$precision = \frac{TP}{TP + FP} \tag{25}$$

$$recall = \frac{TP}{TP + FN} \tag{26}$$

$$F.Score = 2 \times \frac{precision \times recall}{precision + recall} \tag{27}$$

5 Results and Discussions

The carotid artery ultrasound images used in this study are obtained from Shifa International Hospital, Islamabad, Pakistan. The Color Doppler ultrasound machine is currently being used for this purpose. We have converted the images into grayscales and further processing has been done on grayscale images. With the help of medical expert, the images are labeled into two classes, i) normal and ii) abnormal. A dataset of 100 images for different patients of different ages has been tested through our proposed approach. All computations have been performed on Intel Core i7 PC with Matlab 7.12.0 (2011a).

Fig. 2 (a) shows one of the original carotid artery ultrasound images. The region of interest (ROI) is selected from the original image. Fig.2 (b) shows the selected ROI. To reduce the spackle noise and wave interferences, median filter is applied on the original image.

A suitable and accurate window has been determined using the procedure described in section 2.2. The selected window for snake initialization is shown in Fig. 2 (c). The carotid artery ultrasound image is segmented using active contour approach is shown in Fig. 2 (d). From Fig. 2 (d), it may be observed that the image is segmented accurately using the active contour method which greatly depends upon the snakes' initialization. If initialization is done well, one can get significant results using active contour technique. As described earlier, manual initialization may lead to false segmented results. Hence, there is need of such a mechanism in which minimum interaction form user is required. In our proposed approach, we have developed a technique for automatic initialization of the snakes for carotid artery ultrasound image segmentation. It segment out the carotid artery ultrasound images in an automatic way and does not require user intervention.

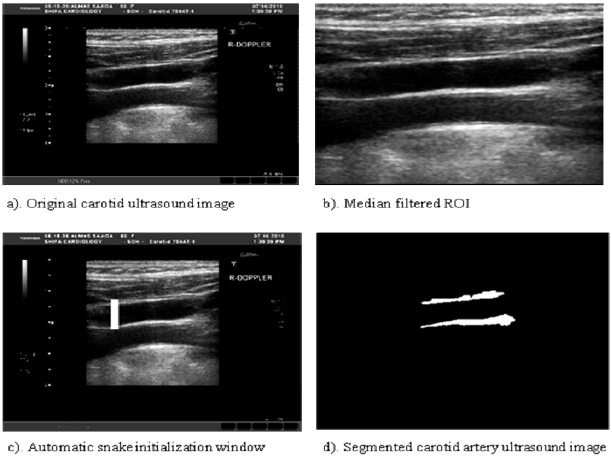

Fig. 2. a). One of the original carotid artery ultrasound image, b) the cropped median filtered ROI, c) the automatically selected window for snake initialization, d) the segmented carotid artery ultrasound image using active contour method

A comparison of manual and our proposed approach of automatic snake initialization have been made for segmentation of carotid artery ultrasound images. The proposed approach shows promising segmentation results for carotid artery ultrasound image segmentation. Fig. 3 (a) shows the carotid artery image of a patient segmented by our proposed approach using automatic initialization of snake window and Fig. 3 (b) shows results through manual snakes initialization. From Fig. 3, it can be observed that image segmented by the proposed approach of automatic initialization and manual initialization approaches do not make any difference, which shows the effectiveness of our proposed approach.

IMT measurement is one of the effective techniques for the detection of the plaque into the carotid artery. One of the normal carotid artery IMT measurements is shown in Fig. 4, which is obtained from the image segmented by our proposed scheme of automatic snake initialization. We have measured the IMT of every normal and abnormal image. Five features, namely, the average, variance, standard deviation, skewness and kurtosis are extracted from measured IMT values. These features are used to train and test the KNN classifier.

Table 1 shows the KNN classification results using five IMT features. It can be observed from Table-I that carotid artery image classification based on the above mentioned features show significant performance.

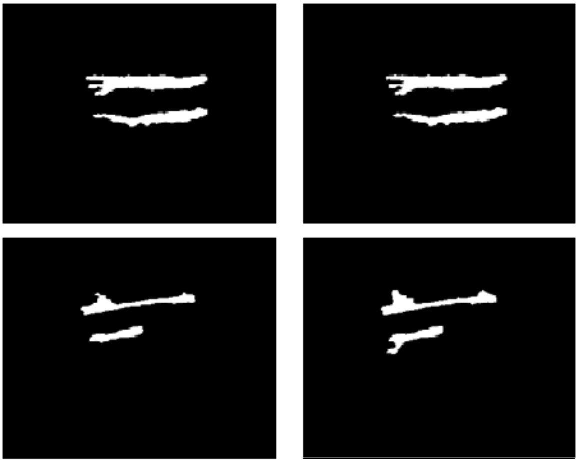

a). Proposed approach b) Manual initialization

Fig. 3. Segmentation results using our proposed approach of automatic snake initialization and manual initialization of snakes

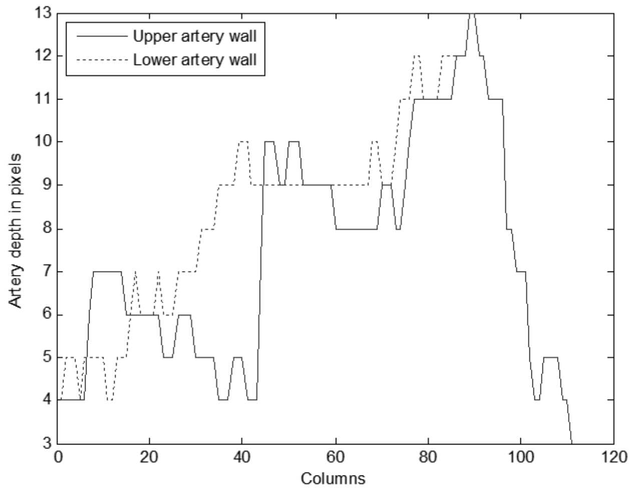

Fig. 4. Graphical representation of IMT measurement of a normal carotid artery ultrasound image

Results obtained through the proposed technique are compared with others based on overall accuracy. Santhiyakumari et al. [19] used MLBPNN for classification and reported a maximum of 96% classification accuracy. In their approach, IMT measurement is used to train the neural networks. Further, they do not mention features extraction strategy and it may be difficult to reproduce the results. While we have used a straight forward approach to classify the segmented carotid artery ultrasound images and obtained the 98.30% classification accuracy. The statistical results show the effectiveness of the proposed approach.

Table 1. Classification Performance Measure of KNN

Classification Validity Measures	Performance
Accuracy	98.30%
MCC	0.9520
F-Score	0.9760

Countries like Pakistan, where there is lack of health facilities to the people living in remote areas. The proposed approach may become helpful to test the possible plaque status in the carotid artery in the absence of a skilled radiologist. Further, the proposed approach can be used as an initial diagnosing tool for the carotid artery diseases and this early detection of plaque in artery may prevent from serious brain strokes.

6 Conclusions

This paper proposes an approach for automated segmentation and classification of carotid artery ultrasound images using active contour model and KNN respectively. The basic problem with the snake model is its initialization. To overcome the problem of manual initialization, we have proposed automatic initialization of snakes for carotid artery images. Carotid artery ultrasound images are segmented by our proposed approach in an automatic way. Performance comparison in terms of window selection is carried out with the manual initialization of snakes. Using manual initialization, window is set empirically and it may be placed at right location. However, if user has less experience and initializes the window at improper place; he may not get accurate segmented results. IMT measurement is used to form a feature vector. Five different features are extracted from IMT values and KNN is used for classification. Based on five different features, we have obtained 98.30% classification accuracy using KNN. While using the proposed approach, the user interaction is minimized and user experience may not affect the results. Segmentation based on minimal user interaction and statistical measures show the usefulness of the proposed approach. In our future work, we intend to extend the feature set and develop an intelligent carotid artery ultrasound image segmentation and classification system.

Acknowledgements. This research work is supported by the Higher Education Commission of Pakistan under the indigenous PhD scholarship program (17-5-4(Ps4-078)/HEC/Sch/2008/) and BK21 Postdoc fellowship program of South Korea.

References

1. Kamel, M., Campilho, A., Abdel-Dayem, A., El-Sakka, M.R.: Fuzzy C-Means Clustering for Segmenting Carotid Artery Ultrasound Images, pp. 935–948. Springer, Berlin (2007)
2. Abdel-Dayem, A.R., El-Sakka, M.R.: Carotid Artery Ultrasound Image Segmentation Using Fuzzy Region Growing. In: Kamel, M.S., Campilho, A.C. (eds.) ICIAR 2005. LNCS, vol. 3656, pp. 869–878. Springer, Heidelberg (2005)
3. Ceccarelli, M., De Luca, N., Morganella, A.: An Active Contour Approach to Automatic Detection of the Intima-Media Thickness. In: IEEE International Conference on Acoustics Speech and Signal Processing, vol. 2, pp. II, 14–19 (2006)
4. Gustavsson, T., Quan, L., Wendelhag, I., Wikstrand, J.: A dynamic programming procedure for automated ultrasonic measurement of the carotid artery. Computers in Cardiology, 297–300 (1994)
5. Rui, R., Lio Aur, C., Jorge, S., Elsa, A., Rosa, S.: Segmentation of the carotid intima-media region in B-mode ultrasound images. Image Vision Computing 28, 614–625 (2010)
6. Moursi, S.G., Sakka, M.R.E.: Semi-automatic snake based segmentation of carotid artery ultrasound images. Communications of the Arab Computer Society (ACS) 2, 1–32 (2009)
7. Hassan, M., Chaudhry, A., Khan, A., Riaz, S.: An Optimized Fuzzy C-Means Clustering with Spatial Information for Carotid Artery Image Segmentation. IBCAST, Islamabad (2011)
8. Chaudhry, A., Hassan, M., Khan, A., Kim, J.Y., Tuan, T.A.: Image Clustering using Improved Spatial Fuzzy C-Means. ACM-ICUMIC, Kula Lumpur (2012)
9. Pham, D.L., Xu, C., Prince, J.L.: A Survey of Current Methods in Medical Image Segmentation. Annual Review of Biomedical Engineering 2, 315–338 (2000)
10. Loizou, C.: Ultrasound image analysis of the carotid artery. PhD Thesis, Kingston University, London, UK (2005)
11. Otsu, N.: A Threshold Selection Method from Gray-Level Histograms. IEEE Transactions on Systems, Man and Cybernetics 9(1), 62–66 (1997)
12. Gonzalez, R.C., Woods, R.E.: Digital Image Processing, 3rd edn. Pearson Prentice Hall (2008)
13. Kass, M., Witkin, A., Terzopoulos, D.: Snakes: Active contour models. International Journal of Computer Vision 1(4), 321–331 (1988)
14. Brigger, P., Hoeg, J., Unser, M.: B-spline snakes: a flexible tool for parametric contour detection. IEEE Transactions on Image Processing 9(9), 1484–1496 (2000)
15. Liang, J., McInerny, T., Terzopoulos, D.: United Snakes [image analysis software]. In: The Proceedings of the Seventh IEEE International Conference on Computer Vision, vol. 2, pp. 933–940 (1999)
16. Weruaga, L., Verdu, R., Morales, J.: Frequency domain formulation of active parametric deformable models. IEEE Transactions on Pattern Analysis and Machine Intelligence 26(12), 1568–1578 (2004)
17. Unser, M.: Splines: A perfect fit for medical imaging. Progress in Biomedical Optics and Imaging, 225–236 (2002)
18. Piao, M., Lee, H.G., Ryu, K.H.: A data mining approach for dyslipidemia disease prediction using carotid arterial feature vectors. In: Int. Conference on Computer Engineering and Technology (ICCET), vol. 2, pp. V2-171–V2-175 (2010)
19. Santhiyakumari, N., Rajendran, P., Madheswaran, M.: Medical Decision-Making system of Ultrasoung carotid artery Intima Media Thickness using Neural Networks. Journal of Digital Imaging 24(6), 1112–1125 (2011)

Bilateral Telemanipulation with a Humanoid Robot Hand/Arm between USA and Japan

Kohei Mima[1], Takanori Miyoshi[1], Masayuki Okabe[2], Makoto Honda[3], Takashi Imamura[1], and Kazuhiko Terashima[1]

[1] Mechanical Engineering
Toyohashi University of Technology, TUT
Toyohashi-shi, Japan
mima@syscon.me.tut.ac.jp, miyoshi@tut.jp,
{ima,terasima}@me.tut.ac.jp
[2] Information and Media Center
Toyohashi University of Technology, TUT
Toyohashi-shi, Japan
okabe@imc.tut.ac.jp
[3] Toyohashi University of Technology, TUT
Chiyoda-ku, Japan

Abstract. This paper presents a tele-control system comprised of a robot hand/arm and an operator. In our system, the angle of the finger of the robot hand is controlled according to the angle of the operator's finger, and the position of the robot arm is controlled according to the position of the operator's arm. Simultaneously, the operator feels the environmental force as detected by the touch sensor attached to the robot hand, resulting in so-called bilateral master/slave control. To date, there have been a few studies of bilateral master/slave systems that use a multi-fingered humanoid robot hand in communication networks with delay caused by physical distance. The purpose of our study was to achieve tele-operation with bilateral master/slave control between the operator's hand/arm and the multi-fingered humanoid robot hand/arm using the Internet with delay caused by distance. For our experiment, the operator was in the USA, and the multi-fingered humanoid robot hand/arm and object were in Japan. Using our system, the operator could successfully grasp and move an object while he felt the reaction force from the object. This technology can applicable to tele-operation such as feeling the hardness and weight of the stone which exist in the moon, on the ground etc.

1 Introduction

The robot with which an operator can operate satisfactorily the object, which exists in a remote place, has been strongly expected, because an operator can work with a robot in a dangerous zone by remote control from a place of safety. Such systems would have a wide field of application such as rescue activities in hazardous environments, the disposal of explosive substances, and the repair of

S. Lee et al. (Eds.): Intelligent Autonomous Systems 12, AISC 194, pp. 197–205.
springerlink.com

nuclear power plants [1,2,3,?] . In addition, a medical specialist can perform an operation on the robot from a remote place, and he can help a patient life at the place in which a doctor is not present[4].

However, in order to realize this function, it is insufficient to operate a robot on a target from a remote place unilaterally. If a robot's vision, hearing, a tactile sense, reaction force from the object, etc. are not fed back to an operator, it leads to a serious accident. Actually, the patient who's organs were pressed by the remote operation robot "Da Vinci" died in Japan[5]. Probably, the accident was able to be prevented, when the reaction force from patient's organs was fed back to the operator, and operator ceased to push it. Thus, bilateral control, in which operator manipulates a robot from a remote place and feels the detected forces of a robot, is very important technology in tele-operation.

The conceptual diagram of the experiment conducted in this paper is shown in Figure 1. The purpose of our study was to achieve an unprecedented bilateral tele-control, in which the multi-fingered humanoid robot hand is operated according to the motion of the operator's hand, and the fingertips of the operator receive the reaction force measured by the sensor at the fingertips of the multi-fingered robot hand via a communication network with a delay because of physical distance. As far as authors get to know, there is no paper in which the object in a remote place is grasped and maneuvered by the robot hand using the commercial Internet, while an operator directly feels the reaction force from the robot as shown in Figure 1.

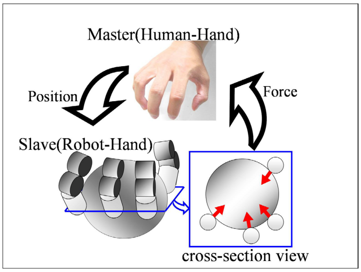

Fig. 1. Conceptual figure of conducted experiment

In this system, we achieved force-position tele-operation, which ensures the accurate positioning in the actual Internet communication with large packet losses. In experiments to test the system, the operator was able to grasp and move the object using a multi-fingered humanoid robot hand/arm by master/slave control feeling fingertip force by tele-operation between the USA and Japan.

2 Bilateral Master/Slave System

A schematic diagram of the master/slave system based on the multi-fingered humanoid robot hand/arm is shown in Figure 2. This system is a bilateral master/slave system using angle and reflected force data. The operator wears a data glove, a haptic-feedback interface, and a 3D tracking system on the right hand.

This data glove is a CyberGlove from CyberGlove Systems Inc. It has 22 sensors to measure each joint angle of the fingers. Additionally, the operator wears a haptic-feedback interface CyberGrasp exoskeleton. This exoskeleton is attached to the back of the hand and guides the force applying tension to the operator's fingertips. The tension in the tendons is controlled by the actuators located in the actuator enclosures. This exoskeleton is able to provide up to approximately 12 [N] force-feedbacks, with the feedback occurring by means of transmitted force data from the robot hand via the Internet. Additionally, the operator wears a FASTRAK 3D tracking system. This FASTRAK is made up of a magnetic field source and a magnetism measurement part, and it measures the relative position between the magnetic source and the measurement part.

The multi-fingered humanoid robot hand is shown in Figure 3. It has 4 fingers with 13 joints. The 1st finger (thumb) has 4 joints, and the 2nd to 4th fingers have 3 joints each. They are arranged like those of the human hand. The thumb is opposable and redundant. The hand is 203.9 [mm] long and 222.2 [mm] wide, which is approximately 1.2 times larger than an adult man's hand. The actuator for the robot hand is a small AC servo motor. Each servo motor provides up to approximately 0.7 [Nm] and has an integrated harmonic gear (1/80) and encoder, directly driving each joint. In the present study, the servo motor was controlled using the torque mode of the servo driver. The input torque τ is calculated by the algorithm in Sec.II.A. Each finger can provide approximately 15 [N] of fingertip force. The fingertip force of the robot hand can be measured by a fingertip type of 6-axis force sensor, covered with an aluminum cap. By using this sensor, we can measure three components of force (Fx, Fy, Fz) and three components of momentum (Tx, Ty, Tz). We use only the force of the X-axis for the CyberGrasp's tension to present force-feedback. The articulated robot arm on the right side of Figure 2 has seven degrees of freedom, the same as a human arm. This robot arm is 1.3 [m] long, and it can carry weight up to about 10 [kg].

In Figure 2, the angular data of fingers and the position data of the hand are transmitted from the master site to the slave site via the Internet. The teleoperator is a multi-fingered humanoid robot hand/arm. It has force sensors and detects the fingertip forces from the environment. The force data are transmitted from the slave site to the master site via the Internet and are presented to the operator. This system is a bilateral master/slave system using angle and reflected force data. However, the control of the robot arm is a unilateral master/slave system because the robot does not have a sensor allowing it to detect environmental force.

2.1 Controlling the Robot Hand

A block diagram illustrating the reference angle of the robot hand is shown in Figure 4, and the layout of the sensors is shown in Figure 5. Although the data glove outputs q_r[rad] of each articular angle, we must reconstruct the suitable

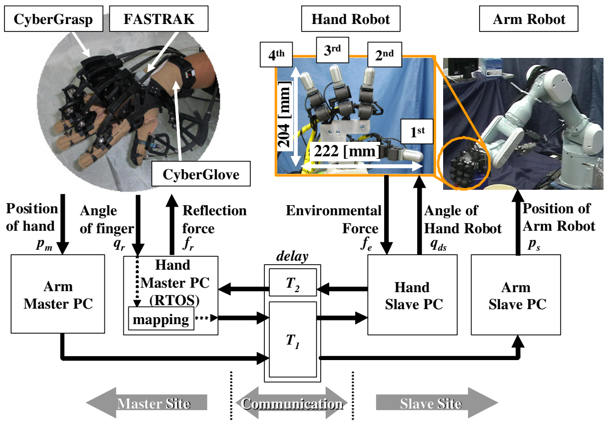

Fig. 2. Bilateral master/slave system with robot hand/arm

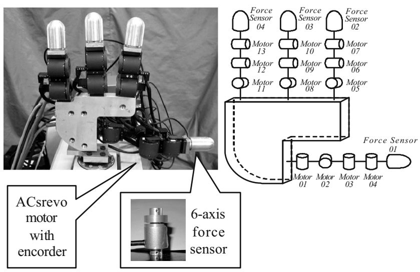

Fig. 3. Multi-fingered humanoid robot hand

angular data, q_m[rad], with data mapping, because of the different structure between the operator's hand and the multi-fingered humanoid robot hand. The data glove detects two data sets, i.e., the angle q_{rIM}[rad] between the index finger and the middle finger, and the angle q_{rMR}[rad] between the middle finger and the ring finger. However, the robot hand has 3 motors arranged at the base of the 2nd (q_{m05}), 3rd (q_{m08}), and 4th fingers (q_{m11}), respectively. Therefore, we must determine 3 reference values for each servo motor from 2 detected values. The equations from the angular data, q_r, to the reference value, q_m, are shown in Eq.(1) and (2), where q_m is a reference value to control the robot hand of the slave site, and suffixes refer to the motor and sensor numbers, respectively.

At the master site, the operator can also feel the reaction force, $f_r(t)$, where $f_r(t) = f_e(t - T_2)$, according to the detected force, f_e, and the communication delay, T_2, from the slave site to the master site, as shown in Figure 2.

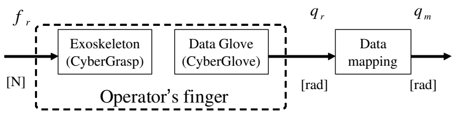

Fig. 4. Control diagram of the master site

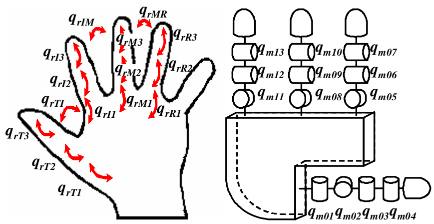

Fig. 5. Sensor layout on the data glove

$$\begin{bmatrix} q_{m01} \\ q_{m02} \\ q_{m03} \\ q_{m04} \end{bmatrix} = \begin{bmatrix} 0 & 1 & 0 & 0 \\ 1 & 0 & 0 & 0 \\ 0 & 0 & 1 & 0 \\ 0 & 0 & 0 & 1 \end{bmatrix} \begin{bmatrix} q_{rTI} \\ q_{rT1} \\ q_{rT2} \\ q_{rT3} \end{bmatrix} \tag{1}$$

$$\begin{bmatrix} q_{m05} \\ q_{m06} \\ q_{m07} \\ q_{m08} \\ q_{m09} \\ q_{m10} \\ q_{m11} \\ q_{m12} \\ q_{m13} \end{bmatrix} = \left[\begin{array}{ccc|ccc|cc} 3/2 & 0 & 0 & -1/2 & 0 & 0 & 0 & 0 \\ 0 & 1 & 0 & 0 & 0 & 0 & 0 & 0 \\ 0 & 0 & 1 & 0 & 0 & 0 & 0 & 0 \\ \hline 1/2 & 0 & 0 & -1/2 & 0 & 0 & 0 & 0 \\ 0 & 0 & 0 & 0 & 1 & 0 & 0 & 0 \\ 0 & 0 & 0 & 0 & 0 & 1 & 0 & 0 \\ \hline -1/2 & 0 & 0 & 3/2 & 0 & 0 & 0 & 0 \\ 0 & 0 & 0 & 0 & 0 & 0 & 1 & 0 \\ 0 & 0 & 0 & 0 & 0 & 0 & 0 & 1 \end{array}\right] \begin{bmatrix} q_{rIM} \\ q_{rI2} \\ q_{rI3} \\ q_{rMR} \\ q_{rM2} \\ q_{rM3} \\ q_{rR2} \\ q_{rR3} \end{bmatrix} \tag{2}$$

The following is the general dynamic equation for each robot finger:

$$\boldsymbol{\tau} = \boldsymbol{M}(\boldsymbol{q_s})\boldsymbol{u_q} + \hat{\boldsymbol{h}}(\boldsymbol{q_s}, \dot{\boldsymbol{q}}_{\boldsymbol{s}}) \tag{3}$$

$$\hat{\boldsymbol{h}}(\boldsymbol{q_s}, \dot{\boldsymbol{q}}_{\boldsymbol{s}}) = \boldsymbol{h}(\boldsymbol{q_s}, \dot{\boldsymbol{q}}_{\boldsymbol{s}}) + \boldsymbol{g}(\boldsymbol{q_s}) + \boldsymbol{f}(\dot{\boldsymbol{q}}_{\boldsymbol{s}}) \tag{4}$$

$$\boldsymbol{u_q} = \ddot{\boldsymbol{q}}_{\boldsymbol{ds}} + \boldsymbol{K_p}\boldsymbol{e} + \boldsymbol{K_d}\dot{\boldsymbol{e}} \tag{5}$$

where q_s is the joint angle of each servo motor and $M(q_s)$ is the inertia matrix. Here, $\hat{h}(q_s, \dot{q}_s)$ refers to the Coriolis, gravity, and centrifugal terms. The PD servo controller is shown in Eq. (5), where q_{ds} is an angular reference and denotes $q_{ds}(t) = q_m(t-T_1)$ according to q_m and communication delay T_1 from the master site to the slave site. In Eq. (5), e denotes the fingertip angular error, $q_{ds} - q_s$ as shown in Figure 6. When robot fingers hit something, i.e., when they encounter the environment, the sensors detect f_e.

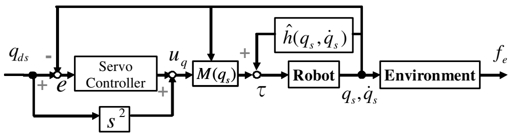

Fig. 6. Control diagram of the robot hand

2.2 Application of a Scattering Matrix

This system applies a scattering matrix. Then, the closed loop can be stabilized by satisfying the following equation from the small gain theorem in Figure 7[6]:

$$||G_{mm}(s)W_m(s)||_\infty ||G_{ss}(s)W_s(s)||_\infty \leq 1 \tag{6}$$

where $G_{mm}(s)$ is the transfer function of the master site from v_m to u_m, $G_{ss}(s)$ is the transfer function of the slave site from u_s to v_s, $W_m(s)$ is a weight function of the master site, and $W_s(s)$ is a weight function of the slave site.

Each finger is controlled by the block diagram in Figure 7. That means our system consists of 4 closed loop system. Although, each closed loop system works independently, they interfere each other through the gripped object. In order to minimize the interference, we chose a soft sponge as the object.

$P_m(s)$ is the dynamic characteristic of the operator's finger, f_r is the tension of wire that acts on a finger, f_h is the fingertip force from the operator's intention, P_s is the dynamic characteristic of the robot hand's finger in Eq. (3)-Eq. (5). Although the identification of $P_m(s)$ is difficult due to its nonlinearity, Eq. (6) is proved by the method described in the next section.

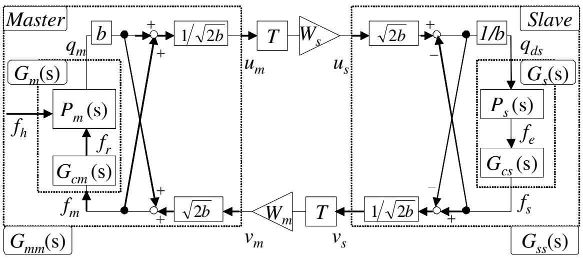

Fig. 7. Block diagram of the master/slave system with a scattering matrix

3 Teleoperation between the USA and Japan

To conduct our experiments, we asked for the cooperation of American CyberGlove Systems Inc. The operator in the USA wore a CyberGlove and used the CyberGrasp interface and a FASTRAK workstation. The operator in Japan operated the humanoid robot hand/arm at Toyohashi University of Technology.

The operator grasped and moved an object in Japan by operating the humanoid robot hand/arm. The staff in Japan gave oral operation instructions to the operator in the USA during the experiment. The operator in the USA manipulated the robot according to the voice instructions.

There is a time difference of eight hours between the USA west coast and Japan. Therefore, we experimented from 2AM to 9AM, Japan standard time, i.e., from 10AM to 5PM, American standard time.

3.1 Experimental Result of Teleoperation

A picture of the tele-operation between the USA and Japan using a humanoid robot hand/arm is shown in Figure 8. In the experiments, the operator grasped an object using a multi-fingered humanoid robot hand/arm by master/slave control, feeling fingertip force by tele-operation between the USA and Japan.

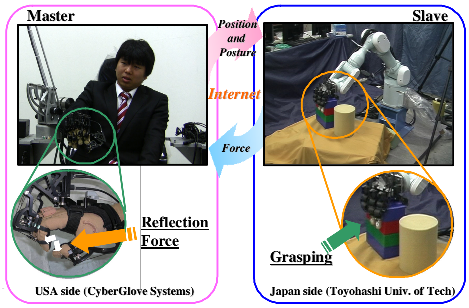

Fig. 8. Experimental situation between Japan and the USA

The round trip time (RTT) during the experiment was about 0.48 [sec], and the establishment of the packet loss was 0.03 [%]. The variation in RTT was small and almost constant.

The experimental result of bilateral master/slave control of the humanoid robot hand is shown in Figure 9, where q_m is a joint angle of the operator's finger, q_{ds} is a reference value of control the robot hand of the slave site, q_s is a joint angle of the robot hand's motor, f_r is the reaction force presented to the operator, and f_e is the fingertip force of the robot hand that was measured by a fingertip type of 6-axis force sensor. As shown in the Figure, the robot hand followed the movement of the finger of the operator. The operator grasped the object from 160 [sec] until 200 [sec], and the fingertip force increased during this period. Then, the operator's finger at the master site presented a reflection force of about 2 [N], corresponding to the value of the fingertip of a 6-axis force sensor.

As shown in the upper part of Figure 9, the motion of the robot appears 0.48 [sec] later than that of the human hand due to the delay of the Internet. The reason for this delay is that all of the data is collected at the master site before it is transmitted, although the actual delay between the master and slave sites is half of RTT. RTT is about 0.48 [sec].

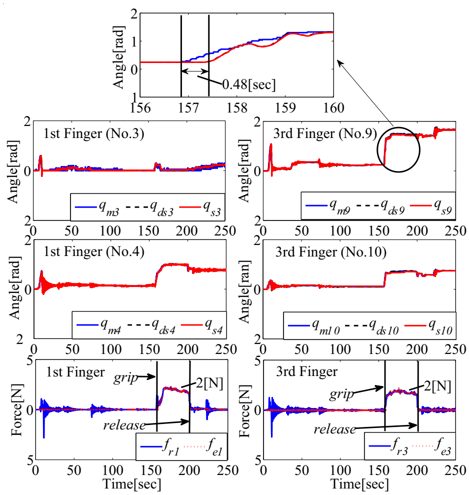

Fig. 9. Experimental results of the robot hand and human hand

The experimental result of unilateral master/slave control of the robot arm is shown in Figure 10, where x_m, y_m, and z_m are the positions of the operator's hand in global coordinates, and x_s, y_s, and z_s are the end point positions calculated from each joint of the robot arm. As shown in Figure 10, the X axis, Y axis, and Z axis coordinates of the robot arm follow the movement of the hand of the operator.

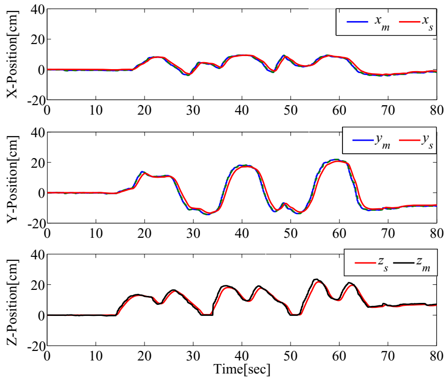

Fig. 10. Experimental result of the robot arm according to human motion

4 Conclusions

In this study, a bilateral master/slave system using a data glove, an exoskeleton, and a humanoid multi-fingered robot hand/arm was studied. First, the stability of the bilateral feedback system was investigated, and we concluded that this system did not satisfy Nyquist stability. Therefore, we installed a scattering matrix and designed wave filters to satisfy the small gain theorem for stabilization. In the experiments, the operator grasped an object using a multi-fingered humanoid robot hand/arm by master/slave control, feeling fingertip force by tele-operation between the USA and Japan. The experimental results showed that this system could grasp and manipulate objects stably, despite the RTT of 0.48 [sec].

Acknowledgments. This work was supported by Professor Goro Obinata and Mr. Shoichiro Kamata of Nagoya University, and the Martin Buss Laboratory of the Technical University Munich.

References

1. Kim, S., Hong, D., Hwang, J.H., Kim, B., Choi, S.W.: Development of an integrated torque sensor-motor module for haptic feedback in teleoperated robot-assisted surgery. In: TePRA 2009, IEEE International Conference on Technologies for Practical Robot Applications (2009)
2. Lovchik, C.S., Diftler, M.A.: The robonaut hand: A dexterous robot hand for space. Proc. IEEE Int. Conf. Rob. Autom. 2, 907–912 (1999)
3. Yamada, H., Muto, T.: Development of a hydraulic tele-operated construction robot using virtual reality (new master-slave control method and an evaluation of a visual feedback system). International Journal of Fluid Power 4(2), 35–42 (2003)
4. Ballantyne, G.H., Moll, F.: The da vinci telerobotic surgical system:the virtual operative field and telepresence surgery. Surg. Clin. North Am. 6, 1293 (2003)
5. http://www.yomidr.yomiuri.co.jp/page.jsp?id=31183
6. Miyoshi, T., Terasima, K., Buss, M.: A design method of wave filter for stabilizing non-passive operating system. In: Proc. of IEEE International Conference on Roobotics and Automation, pp. 1318–1324 (2006)

A Feasibility Study of Rate-Mode Mobile Robot Bilateral Teleoperation with Time Domain Passivity Approach

Ha Van Quang[1], Jee-Hwan Ryu[1], and Youngdo Kwon[2]

[1] School of Mechanical Engineering,
Korea University of Technology and Education,
Cheonan-City, R. of Korea
quang.hut@gmail.com, jhryu@kut.ac.kr
[2] Future IT Research Center,
Samsung Advanced Institute of Technology,
Yongin-city, R. of Korea
ydyd.kwon@samsung.com

Abstract. In this paper, time domain passivity approach is extended for stable rate mode bilateral teleoperation, which often violate closed-loop passivity. Recently proposed energy based framework is implemented to make the closed-loop system passive under variable time-delay. A rate mode teleoperation experiment with mobile robot is conducted to show the feasibility of the proposed idea. Rate mode teleoperation with proposed idea showed much better performance than without case in many aspects.

Keywords: teleoperation, haptic, rate mode, passivity, time domain passivity, mobile robot.

1 Introduction

Teleoperation is one of the oldest research areas in robotics since Ray Goertz has developed the first master/slave manipulator in order to handle radioactive material at Argonne National Laboratory in 1940. However, there are still many issues to solve for making this technology available in real application, such as, time-delay [1], transparency [2], collaboration [3] et al. In teleoperation, human operator controls a slave robot at remote site through a master device. Recently teleoperation is getting more attention due to many interesting application areas such as, surgery [4], satellite maintenance [5], underwater application [6] et al.

Rate mode bilateral teleoperation has been known more difficult to stabilize than the normal mode bilateral teleoperation. In rate mode teleoperation, displacement of the master is mapped into the velocity command of the slave while displacement of the master is mapped into the displacement command of the slave in normal mode. This position based velocity commanding cause intrinsically non-passive closed-loop architecture. Farkhatdinov et al. [7] showed the feasibility of time domain passivity approach for mobile robot teleoperation, and introduced problems and possibilities in rate mode bilateral teleoperation. Park et al. [8] proposed stable rate mode bilateral

S. Lee et al. (Eds.): Intelligent Autonomous Systems 12, AISC 194, pp. 207–215.
springerlink.com

teleoperation for vehicle velocity control using energy bounding approach. Lee and Xu [9] presented feedback γ-passivity to guarantee passivity of master-position/slave-velocity coupled teleoperation system with constant communication delay.

Time Domain Passivity Approach (TDPA) has been proposed by Hannaford and Ryu [10], and it is recently extended by Artigas and Ryu [11] including general delayed network architecture. This paper investigated how architectures with ambiguous causalities, which are hard to have effort and flow power pair, can be modeled with network and how they can be made passive for any communication channel characteristic, such as time-delay and pack-loss.

In this paper, we implement the recently proposed TDPA framework [11] to rate mode bilateral teleoperation system to make the closed-loop system passive. The proposed architecture is tested with a mobile robot. Rate mode bilateral teleoperation with proposed approach allow us to control the speed of mobile robot much easier and smoother without unstable behavior.

2 System Description

The architecture of mobile robot teleoperation is shown in Figure 1. The operator controls the mobile robot by changing the position x_m of master device. In rate mode teleoperation, the position of the master is scaled by gain K and sent to the slave, where it is used as a rate command (v_{sd}). v_{sd} is then become the reference velocity to control the mobile robot moving with the rate v_s.

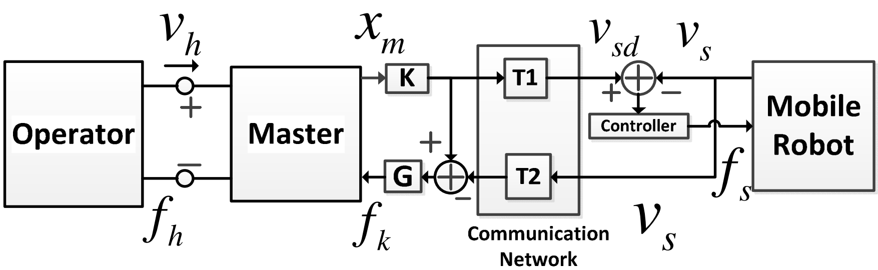

Fig. 1. Mobile robot teleoperation system with rate mode bilateral control architecture

In this research, the haptic feedback which helps the operator feel system will also be considered. Operating in rate mode, the velocity of slave is sensitive with the change of master position. Therefore, neither noise nor small vibration in manipulator device will lead to the bad performance in slave side. In order to minimize the effect of noise in master side to the performance of teleoperation system, we propose the force feedback (denoted by f_k) which is generated base on the mismatch between command and actual velocity of mobile robot. With this type of force feedback, the position of master device will just be able to be changed only when operator apply enough intent force. In order to minimize the time delay of force feedback, mobile robot rate is sent back to the master and used for generating the force f_k which is applied on the master device. The force feedback is generated as the following formula:

$$f_k = G(Kx_m - v_s) \tag{1}$$

Where G is the force feedback gain and K is the scale for velocity command.

3 Stable Rate Mode Teleoperation With TDPA

This Section shows the way how TDPA is implemented to a rate mode mobile robot teleoperation system to make the closed-loop system passive.

3.1 Time Delay Power Network (TDPN)

In [11], Artigas and Ryu proposed a framework to represent any communication channel, even with ambiguous causalities, as 2-port networks characterized by the force and velocity (at each port) conjugate power signals to travel from one terminal to the other, and they defined Time Delay Power Network (TDPN), which separates source and delay by shifting the source to its undelayed location and attaching it to a transport network.

In this paper, TDPN frame work is used to represent above mentioned mobile robot rate mode teleoperation architecture as 2-port network systems with proper causalities. It is essential for applying TDPA since energy flows with proper causalities should be known for formulating TDPA [12].

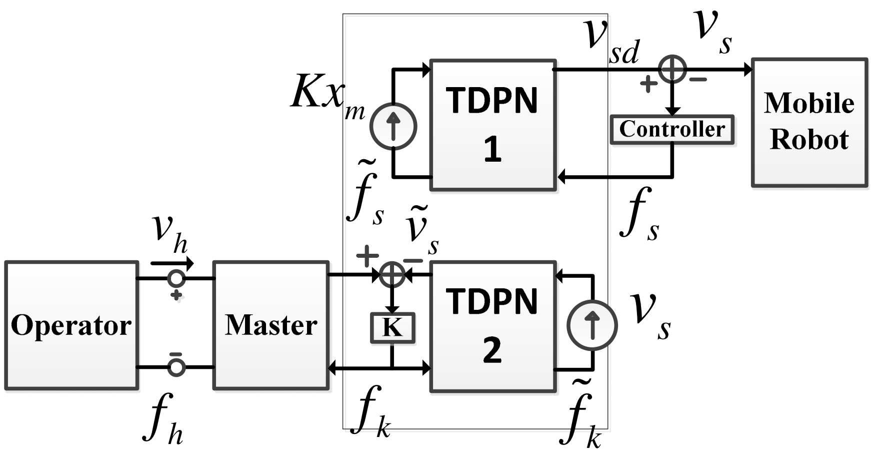

Fig. 2. Augmented TDPN representation of mobile robot teleoperation system with rate mode bilateral control architecture. Delayed signals are defined as: $\tilde{f}_s = f_s(t - T_1)$; $\tilde{v}_s = v_s(t - T_2)$ and $T_1=T_2$.

Fig. 2 shows augmented TDPN representation of mobile robot teleoperation system with rate mode bilateral control architecture. The original architecture can be separated into two TDPNs: velocity command and velocity feedback.

Based on the sign of power in each port, it is also possible to separate input and output energy from observed total energy as follows:

$$E_{obsv}(k) = E_{in}(k) + E_{out}(k) \tag{2}$$

Note that k means the k_{th} step sampling instant (t_k). If the sign of power flow at a port is positive, energy is defined to be flowing into the system and vice versa.

In each channel, it is sufficient to calculate only input energy at the source port and only output energy at the other port since output energy modification at the source port does not make any difference [13].

Input energy in velocity command channel is calculated at the master side (source port) as follows:

$$E_{in}^{M1}(k) = \begin{cases} E_{in}^{M1}(k-1) + \tilde{f}_s \cdot Kx_m \cdot \Delta T & if\ \tilde{f}_s \cdot Kx_m > 0 \\ E_{in}^{M1}(k-1) & if\ \tilde{f}_s \cdot Kx_m \leq 0 \end{cases} \tag{3}$$

While output energy at the slave side is updated as follows:

$$E_{out}^{S1}(k) = \begin{cases} E_{out}^{S1}(k-1) - f_s \cdot v_{sd} \cdot \Delta T & if\ f_s \cdot v_{sd} > 0 \\ E_{out}^{S1}(k-1) & if\ f_s \cdot v_{sd} \leq 0 \end{cases} \tag{4}$$

Note that in equation (4), $v_{sd} = K\tilde{x}_m$.

In contrast to velocity command channel, in velocity feedback channel, the information (velocity) is sent from slave to master, then, slave is considered as source port and input energy is updated in slave side while output energy is from master side:

$$E_{out}^{M2}(k) = \begin{cases} E_{out}^{M2}(k-1) - f_k \cdot \tilde{v}_s \cdot \Delta T & if\ f_k \cdot \tilde{v}_s > 0 \\ E_{out}^{M2}(k-1) & if\ f_k \cdot \tilde{v}_s \leq 0 \end{cases} \tag{5}$$

$$E_{in}^{S2}(k) = \begin{cases} E_{in}^{S2}(k-1) + \tilde{f}_k \cdot v_s \cdot \Delta T & if\ \tilde{f}_k \cdot v_s > 0 \\ E_{in}^{M2}(k-1) & if\ \tilde{f}_k \cdot v_s \leq 0 \end{cases} \tag{6}$$

3.2 Passivity Analysis

The tool used for stability in this paper is TPDA which mentioned that the system is passive only if the energy which flow into the system is always greater than the one flow out of the system. The stability condition of TDPN above can be represented mathematically for each channel as in equation (7), (8).

Velocity command channel:

$$E_{in}^{M1}(k) + E_{out}^{S1}(k) > 0 \tag{7}$$

Velocity feedback channel:

$$E_{out}^{M2}(k) + E_{in}^{S2}(k) > 0 \tag{8}$$

The above equations cannot be used straightforward in delayed network system since energy at both ports is not available at the same time because of the communication time delay. In [13], Ryu et al. proposed a method to make the above conditions become observable. The idea was that, it is sufficient to satisfy non-delayed conditions, (7) (8), if the delayed input energy, calculated at the source port and transmitted to the other port with delay, is greater than the output energy at the other port.

$$E_{obsv}^{1} = E_{in}^{M1}(t - T_1) + E_{out}^{S1}(t) > 0 \tag{9}$$

$$E_{obsv}^{2} = E_{out}^{M2}(t) + E_{in}^{S2}(t - T_2) > 0 \tag{10}$$

3.3 Passivity Controller for Mobile Robot Teleoperation

As mentioned in [10], the Passivity Controller works as a variable damper, which is a function of observed energy flow, that responsible for dissipating the amount of active energy reported by Passivity Observer. Passivity Controller is introduced to dissipate active amount of energy at each delayed network channel.

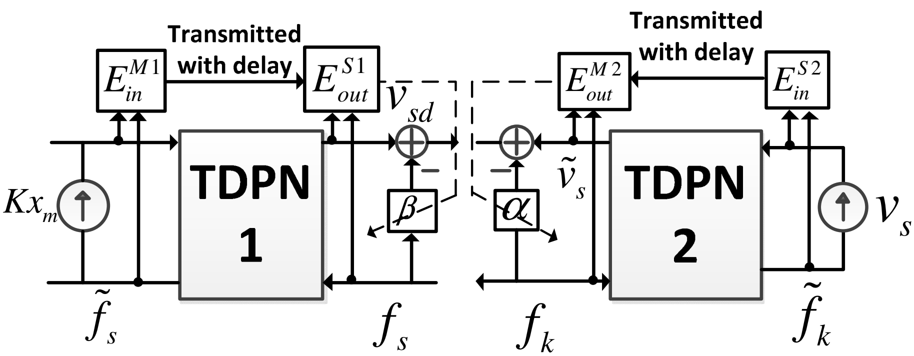

Fig. 3. Passivated TDPN with passivity controllers

Fig. 3 shows passivated TDPNs with passivity controllers. In velocity command channel, the damping element β is adjusted to satisfy (9), which bound the output energy of slave below the delayed input energy from master side.

$$\beta = \begin{cases} \dfrac{-\left(E_{in}^{M1}(k - T_1) + E_{out}^{S_1}(k)\right)}{\Delta T f_s^2} & , E_{obsv}^{1} < 0 \;\&\; f_s \neq 0 \\ 0 & , E_{obsv}^{1} \geq 0 \;\|\; f_s = 0 \end{cases} \tag{11}$$

In velocity feedback channel, the damping element α, is adjusted to make the output energy in master side below the input energy in slave side to satisfy (10) as in equation (12).

$$\alpha = \begin{cases} \dfrac{-\left(E_{in}^{S2}(k - T_2) + E_{out}^{M2}(k)\right)}{\Delta T v_m^2} & , E_{obsv}^{2} < 0 \;\&\; v_m \neq 0 \\ 0 & , E_{obsv}^{2} \geq 0 \;\|\; v_m = 0 \end{cases} \tag{12}$$

4 Experiment

In this Section, the proposed method was experimentally evaluated. Fig. 4 showed the experimental configuration. Mobile robot rate mode bilateral teleoperation experiment was conducted with PHANToM Premium 1.5A as a master and Pioneer P3DX as a slave. All the system is implemented based on Robot Operating System (ROS).

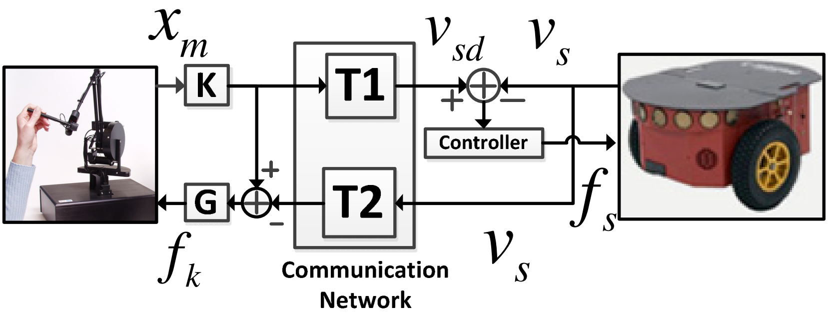

Fig. 4. Experimental Setup

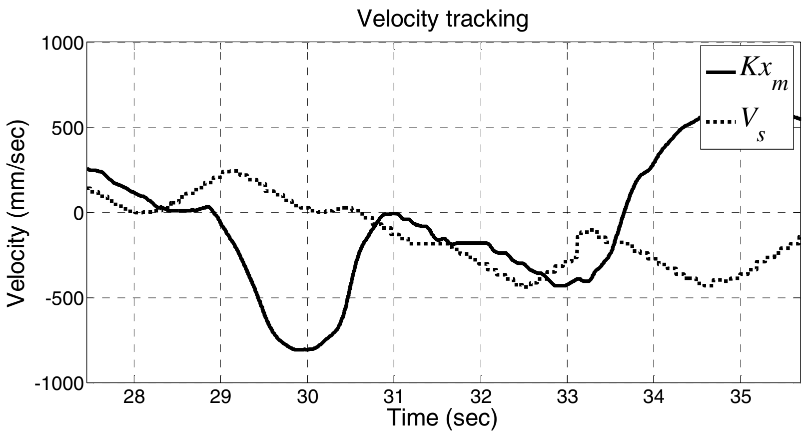

Fig. 5. Velocity tracking without TDPA

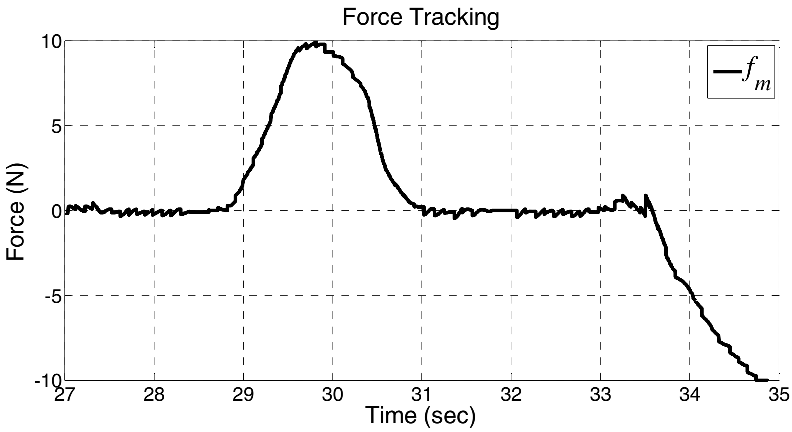

Fig. 6. Force tracking without TDPA

Fig. 5 and 6 showed mobile robot speed and force tracking in case of without TDPA. Around 1.6 sec single trip delays existed including wireless communication lag. In this case, operator felt difficulties to control the speed of mobile robot due to the delayed feedback information. Especially, it was not easy for the operator to stop the motion since the delayed velocity feedback produce delayed force feedback, which keep pushing the operator and it makes the operator confuse. Therefore, the velocity of the mobile robot was oscillating even though the operator was intended to stop the motion.

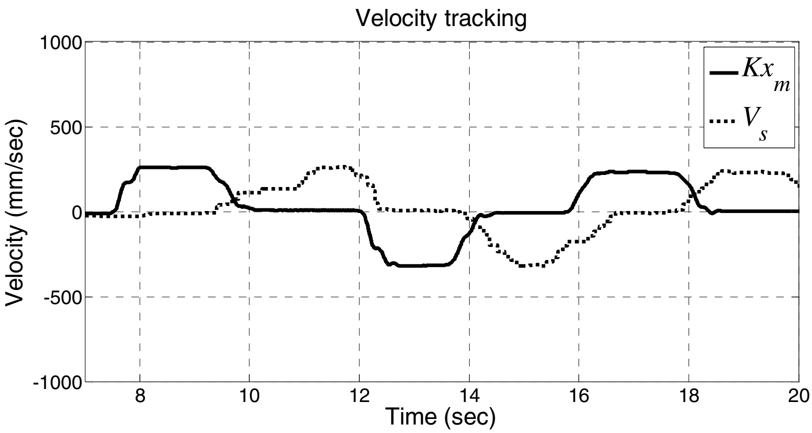

Fig. 7. Velocity tracking without TDPA

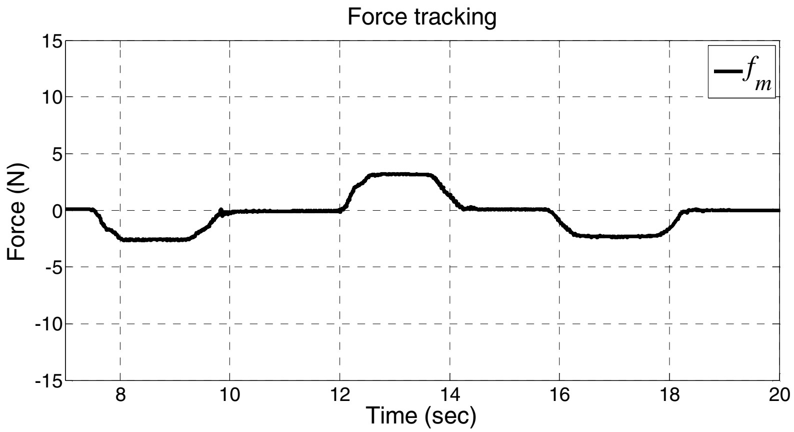

Fig. 8. Force tracking without TDPA

In contrary, thanks to the TDPA (Fig. 7 and 8), the operator can control the speed of the mobile robot with ease. He/she can repeat the stop and go motion without any oscillation.

5 Conclusion

In this paper, recently proposed TDPA framework is implemented to a rate mode mobile robot teleoperation system to make the closed-loop system passive and stable. Experiments with mobile robot were done and showed that the TDPA helps operator easier to control the mobile.

In this preliminary study, we concentrated on the feasibility of applying Time Domain Passivity Approach to stabilize the mobile robot teleoperation system with time delay. Further study on various kind of force feedback and their feasibility will be conducted in the future research. We are also trying to generalize this approach including variable force feedback gain [14] and velocity-position switching teleoperation strategy [15].

Acknowledgements. Authors are grateful of the following supports: Ministry of Knowledge and Economy of Korea grant as part of the Development of a Tele-Service Engine and Tele-Robot Systems with Multi-Lateral Feedback project, and grant from SAMSUNG Electronics CO., LTD.

References

1. Niemeyer, G., Slotine, J.-J.E.: Using Wave Variables in Time Delayed Force Re-flecting Teleoperation, PhD Thesis, Dept of Aeronautics and Astronautics. MIT (September 1996)
2. Lawrence, D.A.: Stability and Transparency in Bilateral Teleoperation. IEEE Transactions on Robotics and Automation 9(5), 624–637 (1993)

3. Fong, T., Thorpe, C., Baur, C.: Multi – Robot Remote Driving with Collaborative Control. IEEE Transactions on Industrial Electronics 50(4), 699–704 (2003)
4. Butner, S.E., Ghodoussi, M.: Transforming a Surgical Robot for Human Telesurgery. IEEE Transactions on Robotics and Automation 19(5), 818–824 (2003)
5. Lew, J.Y., Repperger, D.: Wave Variables Based Teleoperation with Time Delay: Application to Space Based Laser Maintenance. In: IEEE Aerospace Conference Proceedings, vol. 5, pp. 2912–2919 (March 2004)
6. Kwon, D.S., Ryu, J.H., Lee, P.M., Hong, S.W.: Design of a Teleoperation controller for an underwater manipulator. In: Proceedings of the 2000 IEEE International Conference on Robotics and Automation, San Francisco, vol. 04, pp. 3114–3119 (April 2000)
7. Farkhatdinov, I., Ryu, J.H.: A Feasibility Study of Time-Domain Passivity Approach for Bilateral Teleoperation of Mobile Manipulator. In: Proceedings of the International Conference on Control, Automation and Systems (ICCAS 2008), South Korea, pp. 272–277 (2008)
8. Park, S., Seo, C., Kim, J.-P., Ryu, J.: Robustly stable rate – mode bilateral Teleoperation using an energy – bounding approach. Mechatronics 21, 176–184 (2011)
9. Lee, D., Xu, D.: Feedback r-Passivity of Lagrangian Systems for Mobile Robot. In: IEEE International Conference on Robotics and Automation, Shanghai, China, pp. 2118–2123 (May 2011)
10. Hannaford, B., Ryu, J.H.: Time Domain Passivity Control of Haptic Interfaces. IEEE Transaction on Robotics and Automation 18(1), 1–10 (2002)
11. Artigas, J., Ryu, J.H., Preusche, C., Hirzinger, G.: Network Representation and Passivity of Delayed Teleoperation Systems. In: IEEE/RSJ International Conference on Intelligent Robots and Systems, pp. 177–183 (2011)
12. Artigas, J., Ryu, J.H., Preusche, C.: Time Domain Passivity Control for Position – Position Teleoperation Architectures. Presence: Teleoperators and Virtual Environments 19(5), 482–497 (2010)
13. Ryu, J.H., Artigas, J., Preusche, C.: A passive bilateral control scheme for a teleoperator with time – varying communication delay. Elsevier Journal of Mechatronics 20(7), 812–823 (2010)
14. Farkhatdinov, I., Ryu, J.H.: A preliminary experimental study on Haptic teleoperation of mobile robot with variable force feedback gain. In: IEEE Haptics Sympositum, Waltham, Massachusetts, USA, pp. 25–26 (March 2010)
15. Farkhatdinov, I., Ryu, J.H., Poduraev, J.: Control Strategies and Feedback Information in Mobile Robot Teleoperation. In: 17th IFAC World Congress, Seoul, Korea, pp. 14681–14686 (2008)

Backstepping Control of Quadrotor-Type UAVs and Its Application to Teleoperation over the Internet

Dongjun Lee[1], Changsu Ha[1], and Zhiyuan Zuo[2]

[1] School of Mechanical & Aerospace Engineering and IAMD,
Seoul National University, Seoul, 151-744, Korea
{djlee,changsuha}@snu.ac.kr
[2] Department of Mechanical, Aerospace & Biomedical Engineering,
University of Tennessee, Knoxville, TN 37996 USA
zzuo1@utk.edu

Abstract. We propose a novel exponentially-stable backstepping trajectory tracking control law for unmanned aerial vehicles (UAVs), consisting of translational dynamics and attitude kinematics on SE(3), with one thrust force and two angular rates along three orthogonal axes as control inputs. Its application to the recently-proposed UAV Internet teleoperation control architecture [1] is explained, with a new dynamic-extension filter to avoid discontinuity in the control implementation. Experimental results using a real indoor quadrotor-type UAV are also presented to show the efficacy of the proposed theory.

1 Introduction

Unmanned aerial vehicles (UAVs) are promising to achieve many useful applications with the cost associated to the onboard human pilots removed: landscape survey, entertainment and games, suveillance/reconnaissance, remote repair, and precise unmanned attack, to name a few. In particular, quadrotor-type UAVs have recently received much attention, due to its agility, (relative) easiness of control, and availability [2]. Teleoperation of such quadrotor UAVs would even further expand the application horizon of this versatile flying robotic platform [1].

In the first half of this paper, we propose a novel exponentially-stable backstepping trajectory tracking control law for "mixed" quadrotor-type UAVs, which can be modeled as a combination of translational dynamics in E(3) and attitude kinematics in SO(3), with the thrust force $\lambda \in \Re$ and the angular rates $w \in \Re^3$ as the control input. This system is under-actuated (i.e., only 4 control inputs for 6-dimensional SE(3) motion). To address this under-actuation issue, we utilize the backstepping technique on top of the passivity property of the UAV's translation dynamics [3].

Here, we focus on the "mixed" UAVs (i.e., with translation dynamics and attitude kinematics), since many commercially available UAVs, including our laboratory system, Asctec Hummingbird ®, being shipped with a high-performance low-level attitude control-loop already in place, allow us to directly send angular rate command. Due to this, our control law is much simpler (thus, easier to implement) than other backstepping control laws, that are derived for "dynamic" UAVs (i.e., with translation and attitude dynamics [4,5,6]). Our backstepping control also: 1) exploits the geometry of SE(3), thus,

S. Lee et al. (Eds.): Intelligent Autonomous Systems 12, AISC 194, pp. 217–225.
springerlink.com

is free from the singularity due to the SO(3) parameterization (e.g., [7,8]); 2) has transparent control parameters (e.g., damping/spring gains; convergence time constant, etc), thus, can be tuned intuitively (cf. [9,10]); and 3) is flexible in the sense that other kinds of control laws designed for the point mass dynamics would be incorporated into our backstepping framework (e.g. path following, distributed coordination [11]).

We then apply this backstepping trajectory tracking control to the recently proposed UAV Internet teleoperation control architecture of [1]. In particular, we utilize our backstepping control to drive the real quadrotor UAV to follow the trajectory of the (kinematic) Cartesian virtual point (VP), which is teleoperated by a remote human user over the Internet. This UAV-VP coordination problem was only alluded in [1] and, in this paper, we fill that gap. More specifically, 1) we propose a dynamic-extension filter to circumvent the problem of using (potentially discontinuous/unbounded) high-order derivatives of the VP's position in our backstepping trajectory tracking control for the UAV-VP coordination; and 2) provide complete stability/collision-avoidance proof of the combination of the dynamic-extension filter and the VP's kinematic evolution, with the (bounded, yet, arbitrary) master set-position command received from the Internet. Similar to [1], we also apply passive set-position modulation (PSPM [12]) to passify the master side with unreliable/imperfect Internet (with the master position then guaranteed to be bounded), and prove the combination of the master-passivity and slave-stability over the Internet. We also present some pilot experimental results, obtained with Asctec Hummingbird®, VICON Bonita motion capture system®, and Sensable PHANToM Omni®, for the trajectory tracking and the Internet teleoperation.

The rest of this paper is organized as follows. Sec. 2 presents the modeling of the "mixed" quadrotor-type UAV. Our backstepping control is derived and detailed, and its robustness analyzed in Sec. 3. We apply it to UAV teleoperation over the Internet in Sec. 4. Some concluding remarks are given in Sec. 5.

2 Underactuated Quadrotor-Type UAVs

We consider the following quadrotor-type UAV, evolving on SE(3) according to the translation dynamics and attitude kinematics [9]:

$$m\ddot{x} = -\lambda R e_3 + m g e_3 + \delta \quad (1)$$

$$\dot{R} = R S(w) \quad (2)$$

where $m > 0$ is the mass, $x \in \Re^3$ is the Cartesian position w.r.t. the NED (north-east-down) inertial frame with e_3 representing its down-direction, $\lambda \in \Re$ is the thrust along the body-frame down direction, $\delta \in \Re^3$ is the Cartesian disturbance, $R \in SO(3)$ is the rotational matrix describing the body NED frame of UAV w.r.t. the inertial NED frame, $w := [w_1, w_2, w_3] \in \Re^3$ is the angular velocities of the body frame relative to the inertial frame expressed in the body frame, g is the gravitational constant, and $S(\star) : \Re^3 \to so(3)$ is the skew-symmetric operator defined s.t. for $a, b \in \Re^3$, $S(a)b = a \times b$.

The control inputs for (1)-(2) are the thrust force $\lambda \in \Re$ and the angular rates $w \in \Re^3$. This "mixed" UAV (1)-(2) can capture many commercially available UAVs shipped with a manufacturer's low-level attitude control servo-loop implemented (e.g. Asctec

Hummingbird®). These control inputs (λ, w) obtained for (1)-(2) can also be often applied to "dynamic" UVAs as well (i.e., with translation and attitude dynamics). This is because, with the UAVs' attitude dynamics typically fully-actuated and passive, it is straightforward to design angular torque control to track this target angular rate w. Note also that the UAV (1)-(2) is under-actuated, with only 4-DOF control for 6-DOF SE(3) motion.

In the next Sec. 3, we utilize backstepping technique [3] to overcome this under-actuation of (1)-(2) and to drive its Cartesian position $x(t)$ to track a smooth desired trajectory $x_d(t)$. This backstepping trajectory tracking control will then be combined to the teleoperation control framework of [1] and analyzed together in Sec. 4.

3 Backstepping Trajectory Tracking Control of UAVs

Following [11], we first design the desired trajectory tracking control $\nu \in \Re^3$ s.t.

$$\lambda Re_3 = \underbrace{-m\ddot{x}_d + mge_3 + b\dot{e} + ke}_{=:\nu} + \nu_e \tag{3}$$

where $x_d(t) \in \Re^3$ is the smooth desired trajectory with all $\dot{x}_d(t), \ddot{x}_d(t), \dddot{x}_d(t)$ bounded, $e(t) := x(t) - x_d(t)$ is the tracking error, $b, k > 0$ are damping/spring gains, and $\nu_e \in \Re^3$ is the control generation error due to the under-actuation of (1)-(2). In general, $\nu_e \neq 0$, since the last column of R (i.e. Re_3) is not necessarily aligned with the desired control ν. Here, to derive our "nominal" control, let us temporarily assume $\delta = 0$ in (1). Effect of non-zero disturbance δ will be reported in a future publication.

We can then write the closed-loop dynamics

$$m\ddot{e} + b\dot{e} + ke = -\nu_e \tag{4}$$

for which we define

$$V_1 := \frac{1}{2}m\dot{e}^T\dot{e} + m\varepsilon e^T\dot{e} + \frac{1}{2}(k + \varepsilon b)e^T e$$

where $\varepsilon > 0$ is a constant to be chosen below. Differentiating this V_1 with (4), we then have

$$\dot{V}_1 = -(b - m\varepsilon)\dot{e}^T\dot{e} - \varepsilon k e^T e - (\dot{e} + \varepsilon e)^T \nu_e = -\zeta^T Q \zeta - (\dot{e} + \varepsilon e)^T \nu_e \tag{5}$$

where $\zeta := [\dot{e}; e]^T \in \Re^6$ and

$$Q := \begin{bmatrix} b - \varepsilon m & 0 \\ 0 & \varepsilon k \end{bmatrix} \otimes I_3, \ \ P := \begin{bmatrix} m & \varepsilon m \\ \varepsilon m & k + \varepsilon b \end{bmatrix} \otimes I_3$$

with $V_1 = \zeta^T P \zeta / 2$, where $\otimes$ is the Kronecker product and $I_3 \in \Re^{3\times 3}$ is the identity. Both P and Q will then be positive-definite (i.e. $P \succ 0$ and $Q \succ 0$), if we choose $\varepsilon > 0$ s.t.

$$0 < \varepsilon < b/m \tag{6}$$

with the condition for $Q \succ 0$ always implied by that for $P \succ 0$ with $k > 0$.

If $\nu_e = 0$ in (5), we would have $(\dot{e}, e) \to 0$ exponentially. To address the term with ν_e in (5), let us augment V_1 s.t.

$$V_2 = V_1 + \frac{1}{2\gamma}\nu_e^T \nu_e$$

where $\gamma > 0$ is a constant. Differentiating this V_2, we then have

$$\dot{V}_2 = -\frac{b}{2}\dot{e}^T \dot{e} - \varepsilon k e^T e + \frac{1}{\gamma}\nu_e^T(\dot{\nu}_e - \gamma(\dot{e} + \varepsilon e))$$

which suggests the backstepping update law for $\dot{\nu}_e$ s.t.

$$\dot{\nu}_e = \gamma(\dot{e} + \varepsilon e) - \alpha \nu_e \tag{7}$$

so that, with $\alpha > 0$, we can obtain

$$\dot{V}_2 = -\frac{b}{2}\dot{e}^T \dot{e} - \varepsilon k e^T e - \frac{\alpha}{\gamma}\nu_e^T \nu_e$$

implying exponential convergence of $e, \dot{e}$ and ν_e. Here, we assume ε is chosen according to (16), therefore, known.

Control design for (λ, w) is in fact embedded in the update law (7) and needs to be decoded. For this, using (3), we rewrite (7) s.t.

$$[(\dot{\lambda} + \alpha\lambda)R + \lambda R S(w)]e_3 = \dot{\nu} + \alpha\nu + \gamma(\dot{e} + \varepsilon e) =: \bar{\nu} \tag{8}$$

which can be reorganized as

$$\begin{pmatrix} \lambda w_2 \\ -\lambda w_1 \\ \dot{\lambda} + \alpha\lambda \end{pmatrix} = R^T \bar{\nu} \tag{9}$$

where $\bar{\nu}_i \in \Re$ is the i-th element of $\bar{\nu} \in \Re^3$, and $\dot{\nu}$ for $\bar{\nu}$ can be computed by

$$\dot{\nu} = -m\dddot{x}_d - b\ddot{x}_d + k\dot{e} + \frac{b}{m}(-\lambda R e_3 + mg e_3) \tag{10}$$

to avoid the usage of $\ddot{x}$. We can then compute the control inputs (λ, w_1, w_2) from (9): 1) compute w_2, w_1 from the first and second rows of (9) as long as $\lambda \neq 0$; and 2) update λ by solving the differential equation in the last row of (9).

Assuming $\lambda \neq 0$ (to obtain w_1, w_2) is typical for other UAV controls as well (e.g., [4,5,6]), which anyway seems to unlikely happen in practice (e.g., no free fall). Note from (9) that, for the Cartesian position control, we only need λ, w_1 and w_2, not w_3. This is again typical for UAVs control [4,5,6], and we may simply set $w_3 = 0$ or use it for other purpose (e.g., coordinated observation). Since the control parameters b, k, α have clear physical meanings, their tuning can be done intuitively for our control (unlike, e.g., [9]). Due to considering only attitude kinematics, the control decoding equation (9) is also substantially simpler than that in [5,6], which is based on the attitude dynamics. The relation (9) also shows that any (smooth) desired control ν can be incorporated into our backstepping control design, as long as it produces a relation similar to (9) and its computation is implementable similar to $\dot{\nu}$ in (10) here. We now summarize some key properties of our backstepping trajectory tracking control.

Theorem 1. *Consider the UAV (1)-(2) under the backstepping control (8)-(9) with w_3 and $\dot{x}_d, \ddot{x}_d, \dddot{x}_d$ all being bounded. Suppose that $\exists\ \varepsilon_\lambda > 0$ s.t. $\lambda(t) \geq \varepsilon_\lambda\ \forall t \geq 0$. Then, $(\dot{e}, e, \nu_e) \to 0$ exponentially; and $(\ddot{x}, \dot{x}, \lambda, w)$ are bounded.*

4 Application to UAV Teleoperation over the Internet

In this section, we show how the backstepping control, designed/analyzed in Sec. 3, can be used for the UAV Internet teleoperation within the recently proposed framework of [1]. Following [1], consider a (first-order kinematic) Cartesian virtual point (VP), evolving according to

$$\dot{p} = \eta q(k) - \frac{\partial \varphi_o^T}{\partial p}$$

where $p \in \Re^3$ is the VP's position, $q(k) \in \Re^3$ is the master device's position $q(t) \in \Re^3$ received via the Internet at the (slave) reception time t_k^s, $\eta > 0$ is to match different scales between $q(t)$ and $\dot{p}$, and $\varphi_o(||p - p_o||)$ is the obstacle avoidance potential, which produces a repulsive force when p approaches the obstacle at p_o. The command $\eta q(k)$ in (11) enables the user to tele-control the VP's velocity $\dot{p}$ by the master device's position $q(t)$, addressing the problem of master-slave kinematic dissimilarity (i.e. stationary master with bounded workspace; mobile VP with unbounded workspace [13,14]). The kinematic VP is also chosen here as in [1], since it greatly simplifies the stability and collision avoidance analysis as shown below.

The UAV position (1)-(2) then needs to track this VP's position with $(x, \dot{x}) \to (p, \dot{p})$. To apply our backstepping control (9) for this trajectory tracking, as can be seen from (10), we need to compute not only $p, \dot{p}$, but also $\ddot{p}$ and $\dddot{p}$. This requirement of higher-order derivatives of the desired trajectory is in fact true for most of the UAV trajectory tracking control schemes (e.g., [4,5,6,9,10]). Yet, since $q(k)$ switches at each data reception time t_k^s from the (discrete-time) Internet, its time-derivative is not well-defined, and so are $\ddot{p}, \dddot{p}$.

To remedy this problem, we adopt a dynamic-extension filter and use its (continuous-time/smooth) output $\bar{q}(t)$ to control the VP instead of $q(k)$. More specifically, we simulate the VP's position s.t.

$$\dot{p} = \eta \bar{q}(t) - \frac{\partial \varphi_o^T}{\partial p} \tag{11}$$

where $\bar{q}(t)$ is defined from

$$\ddot{\bar{q}}(t) + 2b'\dot{\bar{q}}(t) + k'\bar{q}(t) = k'q(k) \tag{12}$$

with b', k' chosen s.t. the second-order filter is critically damped. Here, note that, if $q(k)$ is bounded, $\ddot{\bar{q}}(t), \dot{\bar{q}}(t), \bar{q}(t)$ are all bounded and well-defined. Then, we can compute $\ddot{p}$ and $\dddot{p}$ s.t., from (11),

$$\ddot{p} = \eta \dot{\bar{q}}(t) - H_{\varphi_o}(p)\dot{p} \tag{13}$$

$$\dddot{p} = \eta \ddot{\bar{q}}(t) - H_{\varphi_o}(p)\ddot{p} - \frac{dH_{\varphi_o}(p)}{dt}\dot{p} \tag{14}$$

where $H_{\varphi_o}(p) := \left[\frac{\partial^2 \varphi_o}{\partial p_i \partial p_j}\right] \in \Re^{3\times 3}$ is the Hessian of φ_o.

Now, to analyze the combined stability and obstacle avoidance of the VP dynamics with the dynamic extension filter (12), define

$$V_p(p,\bar{q},\dot{\bar{q}}) := \varphi_o(p) + \frac{1}{2}||\dot{\bar{q}}||^2 + \bar{\varepsilon}\dot{\bar{q}}^T\bar{q} + \frac{1}{2}(k' + \bar{\varepsilon}b')||\bar{q}||^2$$

where $\bar{\varepsilon} > 0$ is small to make the part of V_p with $\bar{q}$ and $\dot{\bar{q}}$ to be positive-definite. Then, we can show that, from (11) (with $q(k)$ replaced by $\bar{q}(t)$) and (12),

$$\frac{dV_p}{dt} = -\xi^T\bar{Q}\xi - u^T\xi \leq -\underline{\sigma}[\bar{Q}]\cdot||\xi||^2 + ||u||\cdot||\xi|| \tag{15}$$

where $\underline{\sigma}[\bar{Q}]$ is the minimum singular value of $\bar{Q}$, and

$$\bar{Q} := \begin{bmatrix} 1 & -\frac{\eta}{2} & 0 \\ -\frac{\eta}{2} & \bar{\varepsilon}k' & 0 \\ 0 & 0 & b' - \bar{\varepsilon} \end{bmatrix} \otimes I_3$$

with $\xi := \left[\partial\varphi_o^T/\partial p;\, \bar{q};\, \dot{\bar{q}}\right]$, and $u := k'q(k)\cdot\left[0;\, \bar{\varepsilon};\, 1\right]\otimes I_3$.

Thus, if we choose $\bar{\varepsilon} > 0$ to satisfy the following conditions, V_p will be positive-definite w.r.t. $\dot{\bar{q}}, \bar{q}$ and also $Q \succ 0$:

$$\bar{\varepsilon}^2 - b'\bar{\varepsilon} - k' < 0, \;\; \bar{\varepsilon} < b', \;\; \bar{\varepsilon}k' > \eta^2/2$$

which can be further simplified as

$$\eta^2/(2k') < \bar{\varepsilon} < b' \tag{16}$$

since the second condition in the first set of the conditions is implied by (16). The inequality (15) then implies that, similar to the case of ultimate boundedness, if $||\xi|| \geq \frac{||u||}{\underline{\sigma}[\bar{Q}]}$, we will have $\dot{V}_p \leq 0$. Based on this observation, we have the following Prop. 1. For that, we assume that φ_o is constructed s.t. 1) there exists a large enough $\bar{M} > 0$ s.t. $V(t) \leq \bar{M}$ implies no collision with obstacle p_o; and 2) if $\varphi_o(||p - p_o||)$ gets very large, so does $||\partial\varphi_o/\partial p||$.

Proposition 1. *Suppose $q(k)$ is bounded, i.e., $\exists q_{\max} \geq 0$ s.t. $q_{\max} \geq ||q(k)||$, $\forall k \geq 0$. Suppose further that, if $\varphi_o(||p - p_o||) \geq \bar{M}$,*

$$||\frac{\partial\varphi_o}{\partial p}|| \geq \frac{k'q_{\max}\sqrt{1+\bar{\varepsilon}^2}}{\underline{\sigma}[\bar{Q}]}. \tag{17}$$

Then, $\varphi_o \leq \bar{M}$ $\forall t \geq 0$ and $\bar{q}, \dot{\bar{q}}, \ddot{\bar{q}}$ are bounded. Suppose further that $\partial\varphi_o^2/\partial p_i\partial p_i$ and $\partial\varphi_o^3/\partial p_i\partial p_i\partial p_k$ are bounded if $\varphi_o \leq \bar{M}$. Then, $\dot{p}, \ddot{p}, \dddot{p}$ are all bounded.

With $\dot{p}, \ddot{p}, \dddot{p}$ all well-defined, the backstepping control of Sec. 3 can then robustly enable the UAV to track the trajectory of the VP. Here, we assume the obstacle perception potential φ_o is designed s.t. it rapidly increases when the VP p approaches very close to the obstacle p_o to produce high repulsive force to prevent collision; while gradually converge to zero as $||p - p_o|| \to 0$ so that the effect of obstacles can smoothly emerge when they gets close to the VP. An example of such φ_o is

We feedback this obstacle avoidance force along with the UAV's velocity to the human users so that they can perceive the presence of the obstacle over the Internet and/or the state of the UAV. For this, we design the haptic feedback signal $y(t) \in \Re^3$ to be sent to the master, s.t.

$$y(t) := \frac{1}{\eta}\left(\dot{x} + \frac{\partial \varphi_o^T}{\partial p}\right) \tag{18}$$

where the two terms, $\dot{x}/\eta$ and $(1/\eta)\partial\varphi_o^T/\partial p$, are typically complementary, i.e., during the free cruise flying, $\partial\varphi_o^T/\partial p \approx 0$, whereas for the contact with the obstacle, $\dot{x} \approx 0$.

This $y(t)$ is then sent to the master over the Internet. Let us denote by $y(k)$ its reception by the master side over the Internet at the (master) reception time t_k. We incorporate this $y(k)$ into the PD-type teleoperation control τ for the master device s.t.

$$\tau(t) := -B\dot{q} - K_1 q - K(q - \bar{y}(k)) \tag{19}$$

for $t \in [t_k, t_{k+1})$, where $B, K_1, K \succ 0$ are diagonal gain matrices, and $\bar{y}(k)$ is the PSPM-modulation of $y(k)$ (to be defined below). Here, K_1 is included to provide haptic feedback of $y(t)$ (i.e. perception of UAVs velocities or presence of obstacles) while K attempts $||q(t) - \bar{y}(k)|| \to 0$. B is used to avoid oscillatory behavior.

If we use $y(k)$ directly received from the unreliable Internet for (19) instead of $\bar{y}(k)$, the PD-coupling (19) can become unstable. To address this problem, as proposed in [1], we also adopt here passive set-position modulation (PSPM) [12], which is more flexible (e.g., passive feedback of $y(k)$) and less conservative (i.e., selective activation of passifying action only necessary) than conventional time-invariant passivity-enforcing frameworks (e.g., PD-based or wave-based techniques). More precisely, at each t_k, $\bar{y}(k)$ in (19) is computed s.t.

$$\min_{\bar{y}(k)} \; ||y(k) - \bar{y}(k)||$$
$$\text{subj. } E(k) = E(k-1) + D_{\min}(k-1) - \Delta\bar{P}(k) \geq 0$$

where the second line is to enforce passivity, which would likely be violated if we directly utilize (switching) $y(k)$ in (19) without any remedy. Here, $E(k) \geq 0$ is the virtual energy reservoir; $\Delta\bar{P}(k) := ||q(t_k) - \bar{y}(k)||_K^2/2 - ||q(t_k) - \bar{y}(k-1)||_K^2/2$ with $||x||_A^2 := x^T A x$; and $D_{\min}(k) := \frac{1}{t_{k+1}-t_k}\sum_{i=1}^3 b_i(\bar{q}_i(k) - \underline{q}_i(k))^2$, with $b_i > 0$ being the i^{th} diagonal element of B, q_i the i^{th} element of q, and $\bar{q}_i(k)/\underline{q}_i(k)$ the max/min of $q_i(t)$ during $[t_k, t_{k+1})$, $i = 1,2,3$. Note that this PSPM is implemented only for the master side. Also, since the human operator usually keeps injecting energy into the master, $E(k)$ may keep increasing as well. To avoid excessive energy accumulation in $E(k)$, we ceil off $E(k)$, by discarding any energy over a certain threshold $\bar{E}$. See [12] for more details on PSPM.

Theorem 2. *1) The master device with PSPM-modulated control* (19) *is closed-loop passive:* $\exists\, c_1 \in \Re$ *s.t.,* $\int_0^T f^T \dot{q} dt \geq -c_1^2$, $\forall T \geq 0$, *where* $f, \dot{q} \in \Re^3$ *are the human force and velocity. Moreover, if the human user is passive (i.e.* $\exists\, c_2 \in \Re$ *s.t.,* $\int_0^T f^T \dot{q} dt \leq c_2^2$, $\forall T \geq 0$*), the closed-loop VPs teleoperation system is stable, with* $\dot{q}$, q, $q - \bar{y}(k)$, *and* $\dot{p}_i$ *all bounded.*
2) Suppose further that $\ddot{q}, \dot{q} \to 0$, $E(k) > 0\ \forall k \geq 0$, *and* $(x, \dot{x}) = (p, \dot{p})$. *Then, (a) if* $\partial \varphi_o / \partial p = 0$ *(e.g. no obstacles),* $f(t) \to \frac{K_1}{\eta} \dot{x}_i$ *(i.e. UAV velocity perception); or (b) if* $\dot{x} = 0$ *(e.g. stopped by obstacles),* $f(t) \to \frac{K_1}{\eta} \partial \varphi_o / \partial p$ *(i.e. collective obstacle perception).*

Notice the flexibility in designing/using the haptic feedback $y(t)$ (18) provided by PSPM (e.g. other forms of $y(t)$ can be used without jeopardizing passivity). Such a flexibility is usually not achievable by other passivity-based schemes (e.g. wave/PD). The item 1) of Th. 2 and Prop. 1 essentially establishes master-passivity/slave-stability of our closed-loop teleoperation system, which, we believe, is less conservative and more suitable for UAV teleoperation than conventional master-slave (energetic) passivity (e.g., humans need to continuously overcome wind drag or other physical dissipations of UAV - see [15]). Experimental results are shown in Fig. 1, where we can see that: 1) obstacle avoidance is activated and prevents the VP and UAV to collide with the obstacle (4-8 sec.); and 2) the human can haptically perceived the velocity of the UAV (2-4, 8-15 sec.) or the presence of the obstacle (4-8 sec.), with $y(k)$ (18) complementarily switching between these two modes on its own.

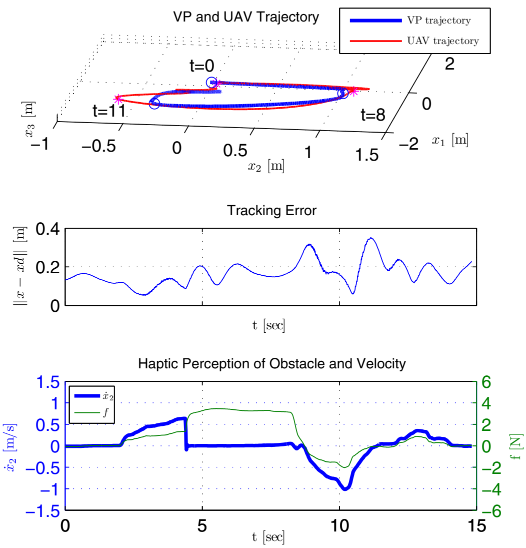

Fig. 1. Teleoperation with haptic perception of obstacle avoidance and flying velocity

5 Conclusions

In this paper, we propose an exponentially-stable backstepping trajectory tracking control law for the quadrotor-type UAV with E(3) dynamics and SO(3) kinematics. Robustness analysis is given. Its application to the UAV Internet teleoperation according to the framework of [1] is explained. Some pilot experiments are performed to validate the theory.

Acknowledgement. Research supported in part by the U.S. NSF grant CMMI-0727480, the Basic Science Program of the NRF of Korea funded by MEST (2012-R1A2A2-A01015797) and the SNU Engineering Research Institute.

References

1. Lee, D.J., Franchi, A., Robuffo Giordano, P., Son, H.-I., Bülthoff, H.H.: Haptic teleoperation of multiple unmanned aerial vehicles over the internet. In: Proc. IEEE Int'l Conference on Robotics & Automation, pp. 1341–1347 (2011)
2. Kumar, V., Michael, N.: Opportunities and challenges with autonomous micro aerial vehicles. In: Proc. of Int'l Symposium on Robotics Research (2011)
3. Sepulchre, R., Jankovic, M., Kokotovic, P.: Constructive nonlinear control. Springer, London (1997)
4. Frazzoli, E., Dahleh, M.A., Feron, E.: Trajectory tracking control design for autonomous helicopters using a backstepping algorithm. In: Proc. American Control Conference, pp. 4102–4107 (2000)
5. Mahony, R., Hamel, T.: Robust trajectory tracking for a scale model autonomous helicopter. International Journal of Robust and Nonlinear Control 14, 1035–1059 (2004)
6. Aguiar, A.P., Hespanha, J.P.: Trajectory-tracking and path-following of underactuated autonomous vehicles with parametric modeling uncertainty. IEEE Transactions on Automatic Control 52(8), 1362–1379 (2007)
7. Castillo, P., Dzul, A., Lozano, R.: Real-time stabilization and tracking of a four-rotor mini rotocraft. IEEE Transactions on Control Systems Technology 12(4), 510–516 (2004)
8. Bouabdallah, S., Siegwart, R.: Backstepping and sliding-mode techniques applied to an indoor micro quadrotor. In: Proc. IEEE Int'l Conf. on Robotics & Automation, pp. 2259–2264 (2005)
9. Hua, M.-D., Hamel, T., Morin, P., Samson, C.: A control approach for thrust-propelled underactuated vehicles and its application to vtol drones. IEEE Transactions on Automatic Control 54(8), 1837–1853 (2009)
10. Roberts, A., Tayebi, A.: Adaptive position tracking of vtol uavs. IEEE Transactions on Robotics 27(1), 129–142 (2011)
11. Lee, D.J.: Distributed backstepping control of multiple thrust-propelled vehicles on balanced graph. In: Proc. IFAC World Congress (2011)
12. Lee, D.J., Huang, K.: Passive-set-position-modulation framework for interactive robotic systems. IEEE Transactions on Robotics 26(2), 354–369 (2010)
13. Lee, D.J., Martinez-Palafox, O., Spong, M.W.: Bilateral teleoperation of a wheeled mobile robot over delayed communication networks. In: Proc. IEEE Int'l Conf. on Robotics & Automation, pp. 3298–3303 (2006)
14. Zuo, Z., Lee, D.J.: Haptic tele-driving of a wheeled mobile robot over the internet: a pspm approach. In: Proc. IEEE Conference on Decision & Control, pp. 3614–3619 (2010)
15. Stramigioli, S., Mahony, R., Corke, P.: A novel approach to haptic tele-operation of aerial robot vehicles. In: Proc. IEEE Int'l Conf. on Robotics & Automation, pp. 5302–5308 (2010)

Experiments on Intercontinental Haptic Control of Multiple UAVs

Martin Riedel[1], Antonio Franchi[1], Paolo Robuffo Giordano[1], Heinrich H. Bülthoff[1,2], and Hyoung Il Son[1]

[1] Max Planck Institute for Biological Cybernetics, Spemannstrasse 38, 72076 Tübingen, Germany
[2] Department of Brain and Cognitive Engineering, Korea University, Seoul, 136-713 Korea
{martin.riedel,antonio.franchi,prg,hhb,hyoungil.son}@tuebingen.mpg.de

Abstract. In this paper we propose and experimentally validate a bilateral teleoperation framework where a group of UAVs are controlled over an unreliable network with typical intercontinental time delays and packet losses. This setting is meant to represent a realistic and challenging situation for the stability the bilateral closed-loop system. In order to increase human telepresence, the system provides the operator with both a video stream coming from the onboard cameras mounted on the UAVs, and with a suitable haptic cue, generated by a force-feedback device, informative of the UAV tracking performance and presence of impediments on the remote site.

In addition to the theoretical background, we describe the hardware and software implementation of this intercontinental teleoperation: this is composed of a semi-autonomous group of multiple quadrotor UAVs, a 3-DOF haptic interface, and a network connection based on a VPN tunnel between Germany and South Korea. The whole software framework is based upon the Robotic Operating System (ROS) communication standard.

1 Introduction

Unmanned Aerial Vehicles (UAVs) represent a promising robotic platform for a large spectrum of current and future applications such as, e.g., indoor and outdoor surveillance, exploration of hazardous areas, search and rescue, and transportation [1]. In recent years, considerable research efforts have been spent towards the use of *multiple* UAVs for addressing some of the aforementioned scenarios. In fact, use of multiple flying robots results in increased flexibility and robustness to single robot failures [2]. However, designing decentralized algorithms for the control of multiple robots with high degree of autonomy is still a challenging task both from the theoretical and actual implementation side, although there have been big achievements from this perspective [3,4].

Especially, a major difficulty is the realization of full autonomy in unstructured/unpredictable environments. The use of bilateral teleoperation (see, e.g., [5]

S. Lee et al. (Eds.): Intelligent Autonomous Systems 12, AISC 194, pp. 227–238.
springerlink.com

for a review) represents in this sense an interesting possibility for improving the performance of a multi-UAV system with the contribution of the human operator's intelligence, i.e., exploiting the human-in-the-loop control. Recently, in this context, there have been several works aimed at developing different bilateral teleoperation algorithms to control multiple robots in an efficient and robust way [6,7,8].

In an intercontinental bilateral teleoperation scenario, very large time delays (usually, in the range of 100 ms) between the operator and slave sides represent one of the major difficulties for both theoretical (i.e., stability) and practical issues (e.g., quality of visual feedback, safety and easiness of maneuvering). The first intercontinental tele-surgical operation (without force feedback) was established between New York, USA, and Strasbourg, France, in 2001 [9]. Recently [10] proposed a protocol to bilaterally teleoperate various haptic devices and slave robots located in different countries.

In long-distance teleoperation, the transmission of visual data is usually more delayed than the transmission of position/force data, because of the large size of video packets. This problem has been investigated in [11] by simulating a visual feedback in the operator site through an intercountry experiment. To the best of our knowledge, however, there was no result in the bilateral teleoperation of multi-robot UAV systems which were truly communicating over an intercontinental Internet connection.

In this paper, we aim at illustrating a software platform and experimental testbed that provides a standardized interface for the bilateral teleoperation of multiple robots (UAVs in our case). The UAVs autonomously keep a desired formation and avoid obstacles while being stably tele-operated by a the remote user. The theoretical framework used in this work, related to the one presented in [7], is then verified through a real intercontinental experiment between Germany and South Korea, thereby stressing in real conditions the robustness of our theoretical claims and software design.

The paper is organized as follows. The haptic teleoperation control framework is reviewed in Sect. 2. In Sect. 3 the proposed software platform is presented with a detailed description of hardware setup for the experiment. Following this, experimental results are reported and discussed in Sect. 4. Finally, the concluding remarks and directions for future research are presented in Sect. 5.

2 Haptic Interaction with Multiple UAVs

In the presented framework the human operator is provided with three kind of interfaces: i) a console used to supervise the group of UAVs (e.g., to switch between different UAV control algorithms/behaviors), ii) a screen providing the video streams of the remote environment from different perspectives (e.g., onboard vs. fixed to the wall), and iii) a haptic device in order to intervene on the overall motion of the group and to receive a force feedback informative of the presence of obstacles and other environmental (e.g., aerodynamical) disturbances.

The haptic device is a generic 3-DOF mechanical system:

$$M(\boldsymbol{x})\ddot{\boldsymbol{x}} + C(\boldsymbol{x}, \dot{\boldsymbol{x}})\dot{\boldsymbol{x}} = \boldsymbol{\tau}^c + \boldsymbol{\tau}^h \tag{1}$$

where $\boldsymbol{x} \in \mathbb{R}^3$ is the configuration vector, $M(\boldsymbol{x}) \in \mathbb{R}^{3\times3}$ the positive-definite and symmetric inertia matrix, $C(\boldsymbol{x}, \dot{\boldsymbol{x}}) \in \mathbb{R}^{3\times3}$ represents Coriolis and centrifugal terms, and $(\boldsymbol{\tau}^c, \boldsymbol{\tau}^h) \in \mathbb{R}^3\times\mathbb{R}^3$, are the control/human forces acting on the device, respectively. We assume, as usually done, that gravity is locally compensated.

The UAVs considered in this work belong to the quadrotor family: these represent a popular choice for a large number of research groups mainly because of their structural simplicity and mechanical robustness. A quadrotor can be conveniently modeled as a 3D rigid body with 3 torques and one force (the thrust) serving as control inputs, with the thrust being always oriented vertically in the body frame. Therefore the quadrotor is an underactuated system since only 4 inputs are available for controlling its 6 DOFs pose. Nevertheless the center of mass of the i-th quadrotor $\boldsymbol{p}_i \in \mathbb{R}^3$ and its yaw angle $\psi_i \in \mathbb{S}^1$ can be shown to be flat outputs [12], i.e., algebraically defining (with their derivatives) the state and the control inputs of the quadrotor [13]. This makes it possible for quadrotor to track any smooth trajectory in the flat output space by using a suitable flight controller, see, e.g., [12,14]. Owing to this property, every quadrotor of the group will be treated as a yaw-orientable 3D point in space $(\boldsymbol{p}_i, \psi_i)$.

In order to let the human interact with the quadrotors while ensuring a safe an cohesive navigation of the UAV group, we assume that $\boldsymbol{p}_i$ can be driven at the kinematic level by the sum of 3 velocity components, $\boldsymbol{u}_i^h$, $\boldsymbol{u}_i^g$, $\boldsymbol{u}_i^e$. These represent the human, group, and environmental control components of the total velocity command, respectively, thus resulting in:

$$\dot{\boldsymbol{p}}_i = \boldsymbol{u}_i^h + \boldsymbol{u}_i^g + \boldsymbol{u}_i^e. \tag{2}$$

The human control is set as $\boldsymbol{u}_i^h = \lambda_h \boldsymbol{x}$ if $i \in M$ and $\boldsymbol{u}_i^h = \boldsymbol{0}$ if $i \notin M$, where $\lambda_h \in \mathbb{R}^+$ is a scaling factor and M is the set of UAVs in communication with the human operator. The group control term $\boldsymbol{u}_i^g$ is chosen in order to enforce the desired UAV formation as much as possible, e.g, by keeping desired inter-distances or relative bearings, and $\boldsymbol{u}_i^e$ has the role of ensuring obstacle avoidance, e.g., by resorting to artificial potential approaches. The term $\boldsymbol{u}_i^e$ can also account for other environmental-related features, such as avoiding dangerous zones or being attracted by promising areas.

Every quadrotor may carry a camera onboard whose optical axis is parallel to the quadrotor frame. In these cases, we assume the yaw angle ψ_i to be autonomously regulated so as to let the camera optical axis match with the horizontal direction of motion, e.g., by using the proportional controller:

$$\dot{\psi}_i = K_\psi \left(\text{atan2}(\dot{\boldsymbol{p}}_{iy}, \dot{\boldsymbol{p}}_{ix}) - \psi_i\right) \tag{3}$$

where K_ψ is a positive gain. This allows to provide the operator with a forward view of the remote environment in case of quasi-horizontal motion.

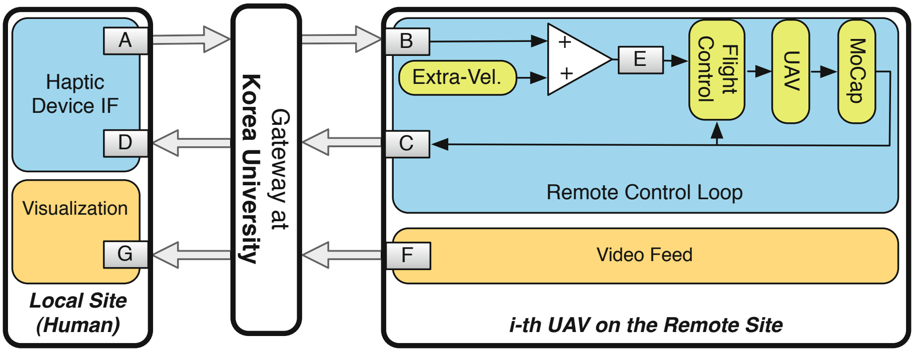

Fig. 1. Signals exchanged in the intercontinental teleoperation system. The relevant signals are labelled as follows: (A) human-commanded velocity at the local site; (B) delayed velocity input received by the i-th UAV at remote site; (C) state of the i-th UAV determined by motion-capture system; (D) delayed states of all UAVs utilized in the calculation of the appropriate haptic force; (E) actual commanded UAV velocity calculated from human-commanded velocity and artificial potential (obstacle avoidance and formation control); (F/G) videos transmitted/received from the remote to the local site.

In order to render to the human operator a haptic perception of the remote environment, we set the control torque as

$$\boldsymbol{\tau}^c = -B\dot{\boldsymbol{x}} + K\left(\frac{1}{|M|}\sum_{i\in M}\dot{\boldsymbol{q}}_i - \lambda_h \boldsymbol{x}\right) \tag{4}$$

where $B, K \in \mathbb{R}^{3\times3}$ are a positive semidefinite damping matrix and a positive gain matrix, respectively, and $\dot{\boldsymbol{q}}_i$ is the velocity of the real i-th quadrotor UAV. Apart from the stabilizing role of the term $B\dot{\boldsymbol{x}}$, the behavior of $\boldsymbol{\tau}^c$ is meant to represent the mismatch between the commanded velocity and the average velocity of the UAVs in M. This way, any external disturbance (e.g., wind gusts) can be perceived by the operator, as well as the presence of any obstacle obstructing the commanded direction of motion.

Several techniques have been proposed in the literature in order to ensure a stable behavior in presence of delays, packet losses, or other non-idealities in the communication channel between the master and slave sides of a bilateral teleoperation channel. In our transcontinental experiments, we made use of a conservative yet simple and effective method, namely, an appropriate tuning of the damping term B in order to dissipate any energy excess. The application of more sophisticated techniques such as [15,16] could provide less average perceptual degradation and their use is left as a future extension of this work.

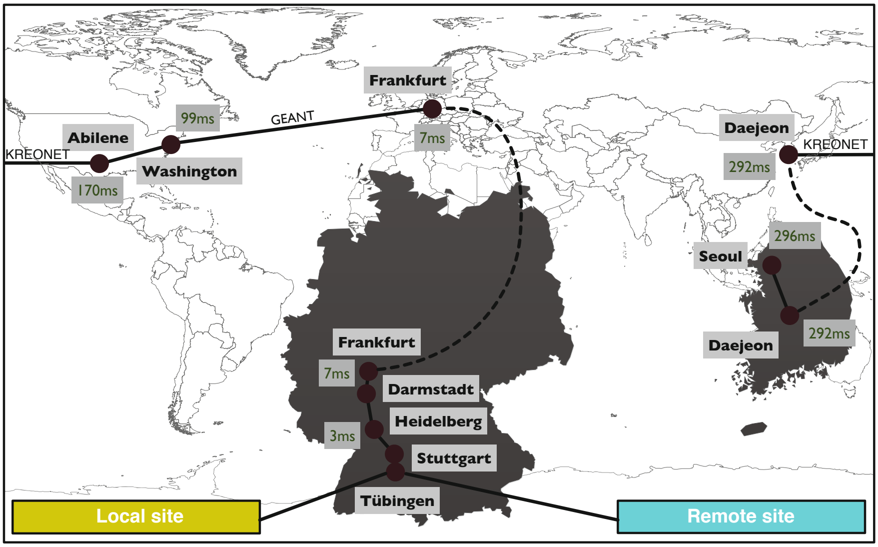

Fig. 2. Representation of the default packet routing and average delays between the MPI of Biological Cybernetics, Tübingen, and Korea University, Seoul. Some local hops were omitted to increase clarity.

3 Experimental Setup

Our experimental setup is made by two environments, namely, the remote (UAV), and the local (human operator) sites, see Fig. 1. These two environments are both located in a building at the Max Planck Institute for Biological Cybernetics, in Tübingen (MPI) but are connected exclusively by means of a real intercontinental Internet channel which passes through a machine located at the Korea University, in Seoul (KU). Tracing packets between both endpoints, revealed a route over the North American continent containing 25 hops resulting in a raw IMCP travel time of about 295 ms, as depicted in Fig. 2. We established a site-to-site OpenVPN[1] connection (dev: tap, proto: udp) between a subnet at the MPI and the machine at KU in order to allow for secure communication, without sacrificing performance (raw single-trip time over the VPN: 305 ms).

On the remote site we use 2 quadrotors[2] as UAVs, for which we developed a custom-made software and hardware setup, see Fig. 3, right. A motion capture system[3] with six cameras monitors the remote-site flight area of $3 \times 4 \times 3$ m and provides position and orientation of each UAV with a frequency of 120 Hz with about 10 ms of delay. Almost all the computation on the remote site is done on a six-core Intel(R) Xeon(R) PC and communication to the UAVs is provided by a

1 openvpn.net
2 mikrokopter.de
3 vicon.com

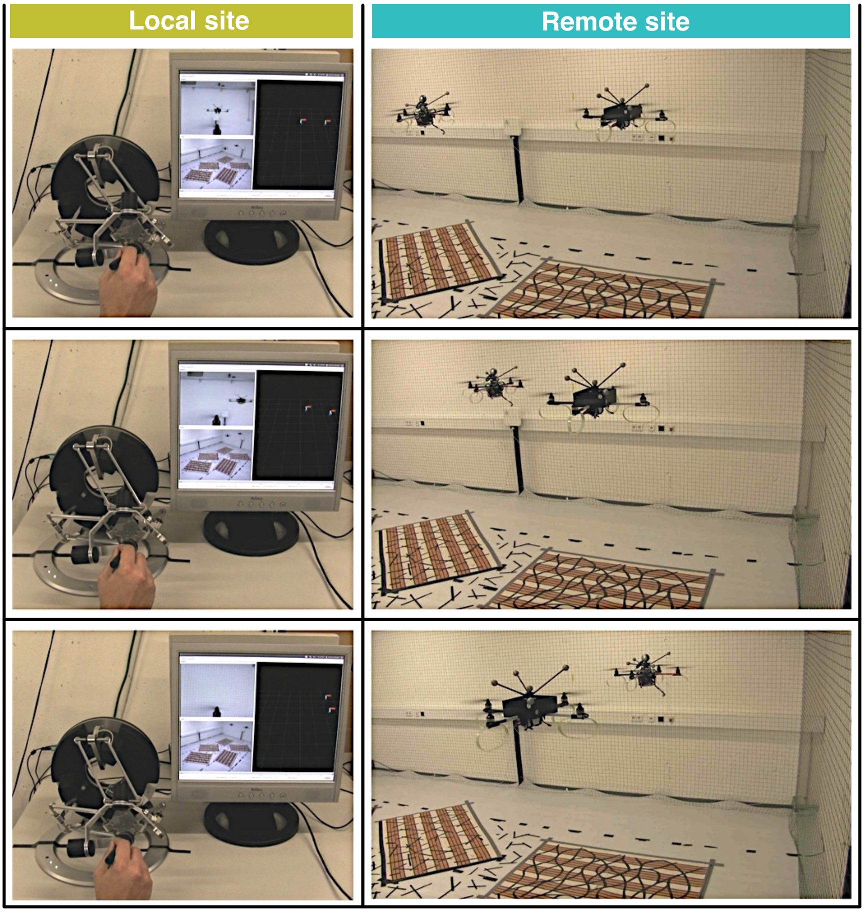

Fig. 3. A representative experiment of intercontinental bilateral teleoperation with 2 quadrotor UAVs. Left column: the local (human operator) site. Right column: the remote (UAV) environment. Each row represents a different time instant. The human operator is provided with a haptic interface in order to control the overall motion of the UAVs and 3 video streams: an onboard view, a global view, and a 3D representation of the UAV states. The two sites are connected through an intercontinental channel implementing a full Germany-South Korea roundtrip.

wireless serial connection XBee-PRO 802.15.4. A separate Intel(R) Pentium(R) 4 gateway PC with 1 Gb optical fiber connection to the Internet and 1 Gb Ethernet to the local network provides routing, firewall and VPN capabilities. One of the UAVs is also equipped with a Q7 board holding an Intel Atom 1.6Ghz CPU to wirelessly transmit image data from an onboard camera, or to run the flight controller without the explicit need of a base station. In addition to the onboard camera we capture the remote site arena also using a wall-mounted fixed camera. Both cameras send a low-resolution MJPEG-encoded video stream (160x120) at

10 fps to the operator site. A standard USB gamepad is used as console in order to control the experimental flow (e.g., liftoff, operate, land, emergency...).

On the local site we use an Omega[4] as haptic device, which provides 3 actuated DOFs. For our remote setup, an Asus WL-500gP with customized TomatoUSB[5] enables us to establish a site-to-site VPN between the router and our local network from any valid IPv4 Internet connection. We are also able to initiate a road-worrier connection directly from a client computer.

We control the 2 quadrotors over the Internet by implementing the approach described in Sec. 2. Both the UAVs keep a formation by following an independent reference trajectory that is a result of the tele-operators input velocity and an artificial potential (providing connectivity preservation and obstacle avoidance), as expressed in (2). UAV State information (position, orientation velocity, and angular velocity) is transmitted over the Internet to the haptic device in order to compute the force feedback (4) which is informative of the remote UAV performance. In addition, we provide the remote operator with a 3D visualization of the quadrotors body-frames in the world frame and two video streams, transmitting an overall view of the flying area and a first-person representation along the axis of one UAV, see Fig. 3, left. By using (3) the optical axis of the camera is able to naturally follow the direction of the user-commanded motion.

We developed a custom framework based on the Robot Operating System[6] (ROS) that simplifies the implementation of multi-robot control algorithms by abstracting all necessary functionality into distinct user-loadable modules. This results in versatile applications, like the intercontinental bilateral control of multiple UAVs. As in ROS, algorithms, drivers and sensors are split into distinct programs, that provide or receive information from and to the rest of the infrastructure.

The software setup is divided into *local* processes, passing from Germany through the gateway in South Korea and back, and *remote* processes that are solely executed in the remote subnet, which are schematized in Fig. 1 from the perspective of the i-th UAV.

Locally, the ROS tool *rviz* provides the video streams and presents a 3D Interface to the human operator. Moreover, the haptic device control process, running at 3 kHz, sends the desired velocity commands at a rate of 100 Hz and receives state information at about 80 Hz from both UAVs to calculate an appropriate haptic feedback (these messages are also used to refresh the 3D Interface).

At the same time, on the remote site, one instance of a custom closed-loop controller for each UAV implements the formation control algorithm and publishes the state information to the other processes at the local site. We interface our quadrotors with a process abstracting the serial communication into the ROS infrastructure. Dedicated applications map the console inputs as well as the video streams into ROS.

---

[4] forcedimension.com

[5] tomatousb.org

[6] ros.org

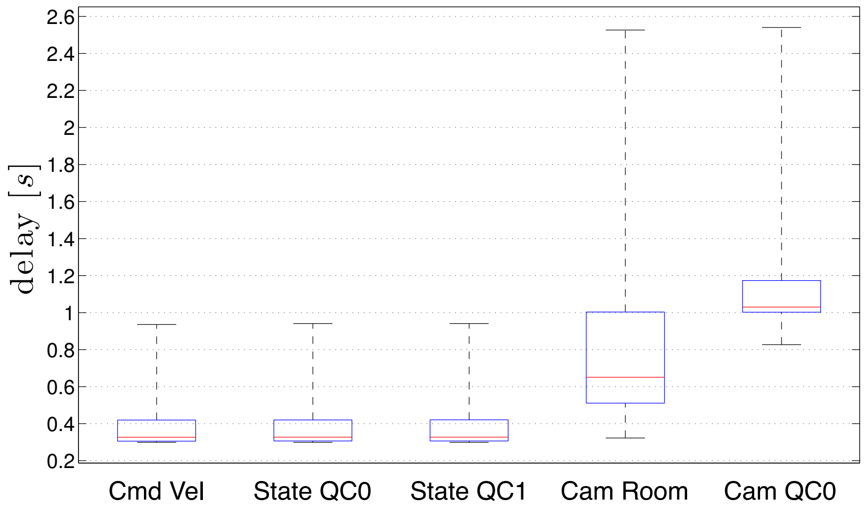

Fig. 4. Boxplots describing the (round-trip) delay times for all messages passing over the gateway at Korea University. Middle bars indicates the median values, while boxes and and whiskers denote the two median quartiles and the maximum-minimum values respectively. Bilateral control-loop messages, i.e., the commanded velocity (Cmd Vel) and the states of both UAVs (State QC0 and State QC1) are transmitted with an average delay of about 350 ms. Video streams are transmitted with the higher average lags of 650 ms and 1 s for the wall-mounted camera (Cam Room) and onboard camera (Cam QC0) respectively. The delay of the onboard camera stream is larger compared to the room video because of the additional wireless link.

4 Results and Discussion

We describe now the results of a representative experiment whose main phases are illustrated in the sequence of Fig. 3. At the beginning of the experiment the UAVs are steered by the human operator toward a wall, the first UAV then immediately stops, thus generating a haptic feedback to the operator. By continuing to apply the desired velocity against that force, the UAVs rearrange and the centroid of the formation is able to move closer to the wall. This event gets fed back to the human by means of a releasing of the set force. A video summary of our intercontinental teleoperation experiment is located at `http://antoniofranchi.com/links/2012-IAS12-InterContTeleOp.html`

As explained in the previous sections, the human operator transmits velocity commands to the remote site by setting the appropriate position on the haptic device. The commands are received by the flight controller of each UAV with varying delay of around 350 ms (see Fig. 4) and added as in (2) in order to calculate the actual UAV velocity reference (see Fig. 1). Fig. 5(a) direclty compares sent and received commands, where the delay is clearly visible. The flight controller then computes the appropriate UAV propeller speeds in order to track that velocity reference with good performances, as shown in the comparison of Fig. 5(b).

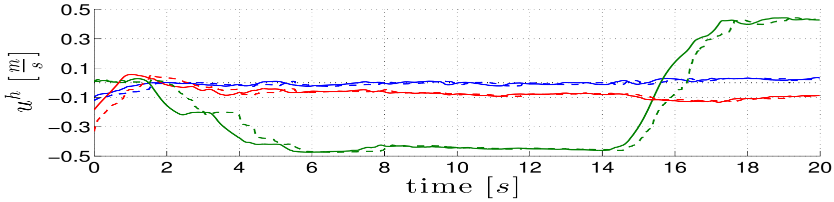

(a)

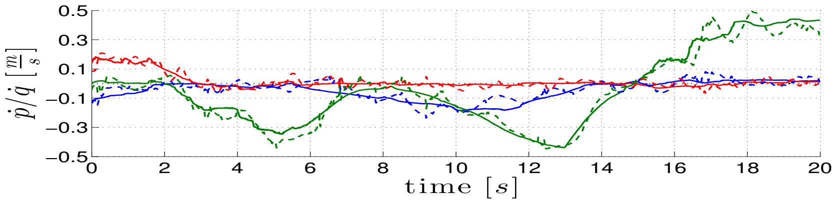

(b)

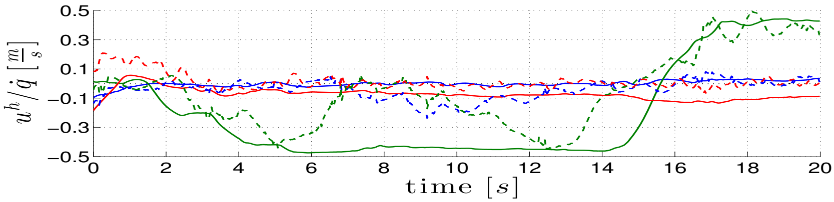

(c)

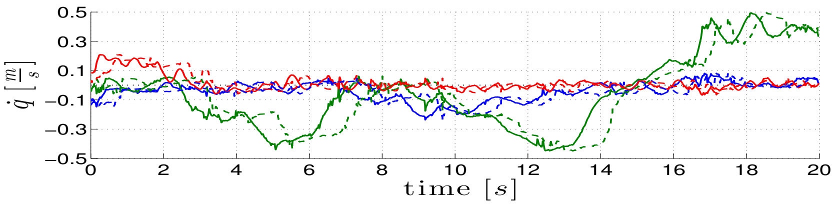

(d)

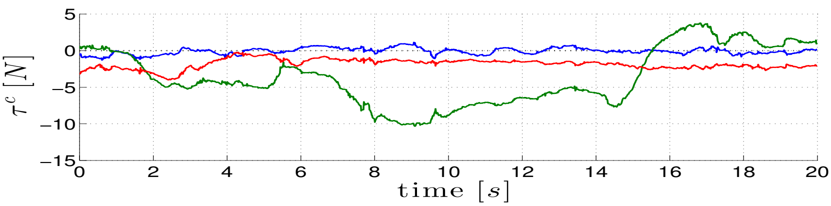

(e)

Fig. 5. A representative experiment of intercontinental bilateral teleoperation with 2 quadrotor UAVs. (a): velocity commanded by the human operator $\boldsymbol{u}^h$, sent (solid) and received (dashed) with delay; (b): desired velocity velocity $\dot{\boldsymbol{p}}$ (solid) versus actual UAV velocity $\dot{\boldsymbol{q}}$ (dashed); (c): commanded velocity $\boldsymbol{u}^h$ (solid) versus actual UAV velocity $\dot{\boldsymbol{q}}$ (dashed); (d) actual UAV velocity $\dot{\boldsymbol{q}}$: sent (solid) and received (dashed) with delay: (e): force feedback $\boldsymbol{\tau}^c$.

On the local site the haptic device is constantly receiving state information of both UAVs at a rate of 80 Hz with still a time-varying delay of 350 ms on average (see Fig. 4 for a statistical analysis of the delay and Fig. 5(d) for a direct comparison between sent and received state signals for one of the two UAVs.). The desired velocity passed to the flight controller $\dot{\boldsymbol{p}}$ is compared to the one commanded by the operator $\boldsymbol{u}^h$ in Fig. 5(c), where it is possible to appreciate the mismatch caused by the influence of the additional contributions given by the formation control and obstacle avoidance terms in (2). That error is used to implement a proportional force feedback, depicted in Fig. 5(e), which therefore has a dual functionality: first it informs the user about the UAV inertia and delay of the communication system, and second it indicates the influence of environmental factors on the UAV dynamics, e.g., presence of obstacles, turbulence, etc.

The transmissions of both video streams suffer of higher latencies compared to the control/haptic-related messages, as clear in Fig. 4. The video stream from the wall-mounted camera has an average delay of 650 ms while the video from the onboard camera experiences an average delay of about 1 s, because of the additional WiFi link. Both video streams have also a much wider variability in the delay when compared with the other signals, with peaks reaching 2.5 s.

In conclusion, the experimental results demonstrate the advantages provided by the use of a haptic feedback beside the visual one in the following way: (1) velocity commands and state messages are transmitted faster and more reliably compared to a video stream and (2) the view angle of 3D environments and camera setups does not always give an accurate representation of distances, which can instead be provided more promptly by the use of suitable haptic cues.

The interested reader can find additional videos concerning the teleoperation of multiple UAVs in different scenarios at `http://www.youtube.com/user/MPIRobotics/videos` .

5 Conclusions and Future Work

In this notes, we presented experiments on the intercontinental bilateral control of a group of UAVs, by relaying packets between Germany and South Korea, forwarding velocity commands to the remote site and sending state information for haptic feedback and visualization purposes back to the local operator. Additionally, we transmitted two video streams to give the operator a complete representation of the remote site. With a average delay of about 350 ms we were able control the UAVs in a stable and reliable manner.

In the future we would like to apply our implementation of intercontinental teleoperation to other teleoperation algorithms and evaluate their performance and robustness in real-world conditions. Our scenario implements a round-trip teleoperation between Europe and Asia, effectively doubling the delay compared to a direct communication channel. We plan to demonstrate our setup with a more standard single-trip delay in a live demo at IAS-12 in South Korea.

Acknowledgments. The authors like to thank Johannes Lächele for creating the simulator and sharing his technical expertise during the creation of the software setup, and the people from Korea University for providing us the access to the relay machine on their campus.

This research was partly supported by WCU (World Class University) program funded by the Ministry of Education, Science and Technology through the National Research Foundation of Korea (R31-10008).

References

1. Valavanis, K.P.: Advances in Unmanned Aerial Vehicles: State of the Art and the Road to Autonomy, vol. 33 (2007)
2. Murray, R.M.: Recent research in cooperative control of multi-vehicle systems 129(5), 571–583 (2007)
3. Michael, N., Fink, J., Kumar, V.: Cooperative manipulation and transportation with aerial robots, Seattle, WA (June 2009)
4. Michael, N., Mellinger, D., Lindsey, Q., Kumar, V.: The GRASP multiple micro-UAV testbed 17(3), 56–65 (2010)
5. Hokayem, P.F., Spong, M.W.: Bilateral teleoperation: An historical survey 42(12), 2035–2057 (2006)
6. Rodríguez-Seda, E.J., Troy, J.J., Erignac, C.A., Murray, P., Stipanović, D.M., Spong, M.W.: Bilateral teleoperation of multiple mobile agents: Coordinated motion and collision avoidance 18(4), 984–992 (2010)
7. Lee, D., Franchi, A., Robuffo Giordano, P., Son, H.I., Bülthoff, H.H.: Haptic teleoperation of multiple unmanned aerial vehicles over the internet, Shanghai, China, pp. 1341–1347 (May 2011)
8. Franchi, A., Secchi, C., Son, H.I., Bülthoff, H.H., Robuffo Giordano, P.: Bilateral teleoperation of groups of mobile robots with time-varying topology (accepted to 2012)
9. Marescaux, J., Leroy, J., Gagner, M., Rubino, F., Mutter, D., Vix, M., Butner, S.E., Smith, M.K.: Transatlantic robot-assisted telesurgery 413, 379–380 (2001)
10. King, H.H., Hannaford, B., Kwok, K.-W., Yang, G.-Z., Griffiths, P., Okamura, A., Farkhatdinov, I., Ryu, J.-H., Sankaranarayanan, G., Arikatla, V., Tadano, K., Kawashima, K., Peer, A., Schauss, T., Buss, M., Miller, L., Glozman, D., Rosen, J., Low, T.: Plugfest 2009: Global interoperability in telerobotics and telemedicine, Anchorage, AK, pp. 1050–4729 (May 2010)
11. Bolopion, A., Stolle, C., Tunnell, R., Haliyo, S., Régnier, S., Fatikow, S.: Remote microscale teleoperation through virtual reality and haptic feedback, San Francisco, CA, pp. 894–900 (September 2011)
12. Mistler, V., Benallegue, A., M'Sirdi, N.K.: Exact linearization and noninteracting control of a 4 rotors helicopter via dynamic feedback, Bordeaux, Paris, France, pp. 586–593 (September 2001)
13. Fliess, M., Lévine, J., Martin, P., Rouchon, P.: Flatness and defect of nonlinear systems: Introductory theory and examples 61(6), 1327–1361 (1995)

14. Lee, T., Leokyand, M., McClamroch, N.H.: Geometric tracking control of a quadrotor UAV on SE(3), Atlanta, GA, pp. 5420–5425 (December 2010)
15. Lee, D.J., Huang, K.: Passive-set-position-modulation framework for interactive robotic systems 26(2), 354–369 (2010)
16. Franken, M., Stramigioli, S., Misra, S., Secchi, C., Macchelli, A.: Bilateral telemanipulation with time delays: A two-layer approach combining passivity and transparency 27(4), 741–756 (2011)

Textual Affect Detection in Human Computer Interaction

Xia Mao, Lin Jiang, and Yuli Xue

The School of Electronic and Information Engineering
Beihang University
Bejing, China
moukyou@buaa.edu.cn, sharley.jl@163.com

Abstract. In this paper we focus on the affect detection of the short text pervasively used in human computer interaction. The research intends to render the interaction more emotionally expressive. In order to estimate the affect in the short text, we construct an affect lexicon firstly. Then a set of extraction rules (ERs) is built to extract the semantic representation of each word. Finally, the affect state of the short text is represented with PAD values and computed through the manually made affect generation rules (AGRs). The evaluation of the results corresponds with the human subjective appraisal.

Keywords: textual affect, semantic, PAD values.

1 Introduction

Short text is an important medium in human computer interaction. In the computer-mediated communication world, people are prone to use short text to maintain their social relationships. Researchers argue that online communication may stimulate rather than inhibit social relations, and chat users find it a medium for rich, intense and interesting experiences [1]. If the computer can sense the underlying emotion in the short text and make corresponding reactions, the interaction would be more intelligent and vivid. Consequently textual affect detection has been a rising research branch integrating natural language processing and affect computation.

Nowadays, natural language processing mainly focuses on the long text and has developed relatively mature techniques. For the long text such as document and essay, machine learning methods have distinct advantages due to the presence of statistical features [2][3]. These approaches, however, fail in processing the short text due to the lack of sufficient features.

We propose a semantic approach to analyze the short text and identify the emotional information. The overview of our approach is as follows. Firstly, we construct an affect lexicon based on a Chinese knowledge system. Then, a rule-based method is employed to extract the semantic representation of each word. Finally, the emotional information can be acquired through a set of emotion rules.

The rest of this paper is organized as follows. Section 2 introduces the related work. In Section 3 the approach is thoroughly illustrated. Section 4 presents the experiments and discussion. Finally, Section 5 gives the conclusion and the future work.

S. Lee et al. (Eds.): Intelligent Autonomous Systems 12, AISC 194, pp. 239–247.
springerlink.com

2 Related Work

Many advanced methodologies for textual affect computation have been developed. Reference [4] developed a real time text-to-emotion engine for expressive internet communications. It employed the keyword spotting techniques and only analyzed the emotional words referring to the person himself/herself and sentences in present continuous or present perfect continuous tense. Reference [5] proposed an approach involving a large-scale real-world commonsense knowledge source: Open Mind Common Sense (OMCS) [6], which enabled the detection more accurate and robust. Reference [7] analyzed the affect of online texts in five steps: symbolic cue analysis, syntactical structure analysis, word-level analysis, phrase-level analysis and sentence-level analysis. The approach took account of the online language features and distinguished the emotion effectively. Reference [8] addressed the problems of emotional expressions extraction and tagging of English blog sentences with emotion tags and intensities. Support Vector Machine based supervised framework was employed using different word and context features.

The existing approaches only address the emotion recognition of English. A psychologist noted that, just as with the rest of commonsense, the recognition of emotion in language depends on traditions and cultures [9]. Nowadays, emotion recognition for Chinese mainly focuses on the polarity recognition and ignores the further analysis of the emotion. So the approach put forward in this paper entails the notion that the accurate recognition of Chinese short text should emphasize the analysis of the short text and Chinese language habits.

Besides, the short text has inherent characteristics: (1) sparse information, (2) lack of rigorous syntax, (3) the present of the injection, onomatopoeia and modal particle. So the approach in this paper principally focuses on the extraction of informative words and does not involve complicate syntax. Also, we try to incorporate the function of some auxiliary words. Moreover, we utilize an on-line Chinese common sense knowledge: HowNet [10] which contains a large number of words and idioms.

Though in this paper, our approach is introduced and implemented in isolation of other approaches, it should be noted that our approach is aimed at Chinese and different languages need to be processed distinctively.

3 Approach

The overall framework of the research is illustrated in figure 1. Firstly, the short text is parsed using the natural language techniques and the redundant words are removed. After the processing, a set of informative words is collected. Then the words are indexed in HowNet to locate the concrete definition. Through the prescribed extraction rules (ERs), each word can find the semantic representation in the Affect Lexicon. Finally, with these information and affect generation rules (AGRs), the affect information in the short text can be estimated.

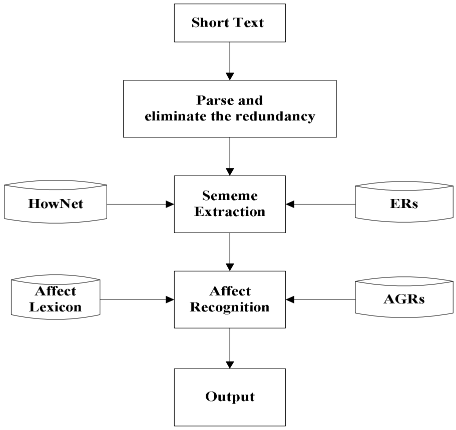

Fig. 1. Framework of the affect computation approach

3.1 The Linguistic Resources

In this paper we use two linguistic resources: HowNet and Affect Lexicon. Here we give a brief introduction to the HowNet and the construction of the Affect Lexicon.

HowNet is an on-line common sense knowledge base unveiling inter-conceptual relations and inter-attribute relations of concepts as connoting in lexicons of the Chinese and their English equivalents. There are two important elements in HowNet: sememe and concept. Generally speaking, a sememe refers to the smallest basic semantic unit that cannot be reduced further. Concept is one kind of description of vocabulary's semantic. Concept is described by the "Knowledge Dictionary Mark-up Language (KDML)", which use sememes as its "vocabulary" [11].In Table 1, we give some examples of KDML. HowNet covers most of the common expressions in Chinese and so in our research we only address the short text which is used in daily life.

Table 1. An example of KDML

Concept	POS	KDML
赌徒|Gamble	N	human,*gamble,undesired,crime
救援|Rescue	V	Help
阴险| insidious	ADJ	aValue,behavior,evil,undesired

There are about 1500 sememes in HowNet (2000 edition). For the construction of the Affect Lexicon, we selected the sememes in the following categories: Event, Entity, Attribute, Attribute Value, Secondary Feature. Besides the sememes, HowNet uses some signs to describe the concept, such as * in Table 1.

To measure the affect information of the sememes, we selected PAD(Pleasure, Arousal, Dominance)[12] model as the emotion model. Three independent annotators familiar with the PAD theory were asked to manually label the sememes with PAD values. The reliability of annotations was measured using Fleiss' Kappa statistics. The calculated Kappa coefficient is 0.96, showing great labeling reliability. Each dimension of PAD values ranges from -1.0 to 1.0 as shown in figure 2.

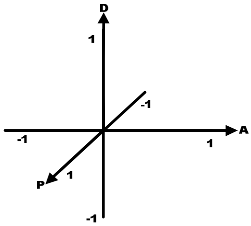

Fig. 2. PAD model

Here we briefly explain the three dimensions of PAD model. Pleasure denotes how pleasant an emotion may be. Arousal represents the level of mental alertness and physical activity. Dominance indicates the controlling and dominant nature of the emotion.

Besides the sememes in HowNet, we also incorporated auxiliary words such as injection, onomatopoeia, modal particle. For each of them, we manually decided which dimension of PAD it belongs to and assigned a degree factor. An example of the Affect Lexicon is shown in Table 2.

Table 2. The example of the affect lexcion

Name	**Category**	**PAD values**
激动|excited	Event	0.6/0.8/0.2
香|scent	Attribute Value	0.5/0.6/0.2
嗜好物| addictive	Entity	-0.6/0.6/-0.5
哇|wow	Modal Particle	<1.5,A>

3.2 Sememe Extraction

From the description of HowNet, we already know that the definition of a word consists of a set of sememes. So the selection of the appropriate sememe implying the affect information needs a thorough analysis of the KDML. We will state the extraction rules from four aspects: noun, adjective, verb, set phrase.

For nouns, we select the sememe with signs: #, %, *, @ due to their high appearing frequencies in HowNet and strong relevance with the affect information. In KDML, their implications are shown in Table 3.

Table 3. The implication of certain signs

Sign	Implication
#	Denote relevant with something
%	Denote being part of something
*	Denote being able to do some actions or used to do some actions
@	Denote being the space or time of some actions

Considering the case of co-occurrence, we set priority for the signs: #> %>*> @.

For most of adjectives in HowNet, they belong to the class of aValue, so we make a general rule for them: selecting the third sememe in the definition.

For the verbs, the event roles&features are significant. Although KDML contains 88 roles&features, only certain of them are relevant with the affect information. The roles and their implication are shown in Table 4.

Table 4. Roles and implication

Roles	Implication
Patient	The object of the action in a sentence
Content	Content of certain thing
Isa	Generic reference
Descriptive	Describe certain action
ResultEvent	Result of certain action
ResultWhole	The final result of certain action
Cause	Cause of certain action
Cost	The cost of certain action
StateFin	Final state of certain action
Manner	Manner of certain action
Degree	Degree of certain action
Purpose	Purpose of certain action
State	The state denoted by certain action

In addition to the event roles&features, we also need to address the negation problems. In HowNet, Unwilling|不愿 and Unable|不能 are two commonly used sememes to signify negation.

Set phrase is a unique phenomenon in Chinese. It can use the fewest words to express abundant information. In HowNet, set phrases are mainly classified to adjectives and verbs, so extraction rules of the above two categories can also be applied to the set phrases.

Also, if none of the mentioned sememes is detected in the definition of a word, the first sememe is the default sememe. But if the first sememe is a sememe category, then the second sememe is selected as the default sememe.

3.3 Affect Computation

The affect computation should consider the characteristics of the short text. We propose that the short text can be divided to two categories according to the property of specific words.

For a short text consisting of only pronoun, noun and adjective, we characterize it as subjective text. In this case we take the PAD values of the adjective word as the affect ground. The whole text's affect can be computed through formula (1).

$$SA = 0.7 \times AA + \frac{0.3}{N} \times (\sum_{i=1}^{N} O_i A) \quad (1)$$

Where SA depicts the PAD values of the short text, AA denotes the PAD values of the adjective, $O_i A$ is the PAD values of the ith word except the adjective, N represents the number of words (except the adjective) in the short text. Here the parameter 0.7 and 0.3 are self-defined and may need optimization and seek more theoretical support in the future work.

If the verb is present in the short text, we refer to it as the appraising text which is a state of certain event. Here we select the verb and noun as the origins of affect information. Firstly, the PAD values of the noun are adjusted with the corresponding adjective. The final values of the noun are the average values of the noun and adjective. For the verb and noun, the affect generation rules are shown in Table 5.

Table 5. Affect generation rules for appraising text

PAD values of Verb	PAD values of Noun	PAD values of Short Text
Positive	Positive	Positive with the average absolute value of the two
Positive	Negative	Negative with the average absolute value of the two
Negative	Positive	Negative with the average absolute value of the two
Negative	Negative	Positive with the average absolute value of the two

After the above processing, each short text's PAD values should be modified according to the auxiliary words' degree factor.

4 Experiments and Discussion

To show our approach's effectiveness, we select three short texts in the actual conversation.

(1)可见其名声之糟糕(shows the reputation is terrible)

(2)我也爱莫能助(I also cannot help it)

(3)我打碎了那个漂亮的花瓶(I broke that beautiful vase)

Here we use the ICTCLAS[13] (2011 Edition) as the parser. To make the examples more clear, we only give sememes in English and ignore the original Chinese.

For the first short text, the parsing result is as follows:

可见(shows)/c 其(the)/rz名声(reputation)/n 之(is)/uzhi糟糕(terrible)/a

Where *c* denotes conjunction, *rz* is demonstrative pronoun, *n* is the noun, *uzhi* refers in particular the 之， *a* means the adjective.

Then the redundant processing is performed to eliminate 可见/c, 其(the)/rz and 之/uzhi.

Indexing in the HowNet, the definitions of the remaining words can be acquired:

名声:attribute, reputation, &human, &organization,
糟糕:aValue, GoodBad, bad, undesired.
According to the ERs, each word has the corresponding sememe:
名声(reputation) -> reputation,
糟糕(terrible)-> bad

The PAD values of each sememe are: reputation:0.3/0.1/0.1， bad: -0.6/-0.3/0.2. According to our rules, they are also the PAD values of名声(reputation) and糟糕(terrible).

According to the AGRs, this short text belongs to the subjective text. Its final values can be computed as follows: 0.3*(reputation)+0.7*(terrible) and the result is -0.33/-0.18/0.17. The PAD values indicate that this short text expresses a negative emotion and the speaker's low mental alertness and low dominant of the environment. The result shows good correspondence with the human judgment.

For the second sentence, the parsing result is as follows:

我(I)/rr也(also)/d 爱莫能助(cannot help it)/vl

Where *rr* refers to the personal pronoun, *vl* means the verb.

The redundant information is也/d. Here爱莫能助 is a set phrase and its definition in HowNet is :

BeUnable, content=help.

So the sememe of it can be represented as follows: - help. "-"indicates the PAD values of help should be reversed. The PAD values of the help are 0.5/0.3/0.6, so the values of the short text are -0.5/-0.3/-0.6. Here the value of D is -0.6 implying low dominance of the environment. It appropriately reflects the underlying meaning of the set phrase.

For the third, the parsing result is as follows:

我(I)/rr 打碎(broke)/v 了/ule 那个(that)/rz 漂亮(beautiful)/a 的/ude1 花瓶(vase)/n

The words了/ule，那个/rz，的/udel are redundant information. And the remaining words' definitions are:

打碎(broke):bump, StateFin=OutOfOrderl,
漂亮(beautiful): aValue， GoodBad, good, desired,

花瓶(vase): tool, cubic, *put, #FlowerGrass.
The sememes of the words are:
打碎(broke)->OutOfOrder,
漂亮(beautiful)-> good,
花瓶(vase)->FlowerGrass.

According to our definitions, the short text is the appraising text, so we can get the final values of花瓶(vase) are 0.6/0.5/0.1. While the values of the word OutOfOrder are -0.6/-0.1/0.2, so the short text's values are -0.6/-0.3/0.15. The final PAD values indicate that the sentence express a negative emotion and the speaker's mental alertness is also negative. According to the meaning of the sentence, the PAD values are reasonable to evaluate the emotion of the sentence.

The PAD values of these short texts reflect the affect information of the speakers. In human computer interaction, we can use the information to make the interaction more vivid and interesting.

Because researchers adopt different evaluation criterion for affect in text, it's a little difficult to compare with other approaches.

5 Conclusion and Future Work

In this paper, we present a semantic approach to compute the affect in the Chinese short text through the extraction of sememe and text classification. To illustrate the approach, we also present a detailed description of the ERs and AGRs. We believe our approach offers a different view in relation to other textual affect computation methods found in the literature. Our approach is feasible and coherent. The computation results conform to the human judgments reasonably.

However, our approach can be further improved in certain aspects. We plan to use the PAD values to drive the lifelike agent to show corresponding expressions and test our approach in other fields to clarify the extent of its application.

Acknowledgements. This work is supported by International Science and Technology Cooperation Program of China and Japan (No.2010DFA11990), National Nature Science Foundation of China (No.61103097).

References

1. Peris, R., Gimeno, M.A., Pinazo, D., Ortet, G., Carrero, V., Sanchiz, M., Ibanez, I.: Online chat rooms: virtual spaces of interaction for socially oriented people. Cyber Psychology and Behavior, 43–51 (2002)
2. Fabrizio, S.: Machine learning in automated text categorization. ACM Computing Surveys 34(1), 1–47 (2002)
3. Ovesdotter, A.C., Roth, D., Sproat, R.: Emotions from text: machine learning for text-based emotion prediction. In: HLT- EMNLP, Canada, pp. 579–586 (2005)

4. Boucouvalas, A.C.: Real Time Text-to-Emotion Engine for Expressive Internet Communications. In: Being There: Concepts, Effects and Measurement of User Presence in Synthetic Environments, pp. 306–318. Ios Press (2003)
5. Liu, H., Lieberman, H., Selker, T.: A Model of Textual Affect Sensing using Real-World Knowledge. In: Proc. the 8th International Conference on Intelligent User Interfaces, pp. 125–132. ACM Press (2003)
6. Singh, P., Lin, T., Mueller, E.T., Lim, G., Perkins, T.: The public acquisition of commonsense knowledge, pp. 1223–1237. Springerlink Press (2002)
7. Neviarouskaya, A., Prendinger, H., Ishizuka, M.: EmoHeart: Automation of Expressive Communication of Emotions in Second Life. In: Proc. International Conference on Online Communities and Social Computing, pp. 584–592. Springerlink Press (2009)
8. Das, D., Bandyopadhyay, S.: Identifying Emotion Expressions, Intensities and Sentence Level Emotion Tags using a Supervised Framwork. In: PACLIC, Japan, pp. 95–105 (2010)
9. James, W.: What is an emotion? In: Calhoun, C., Solomon, R.C. (eds.) Classic Readings in Philosophical Psychology, pp. 127–141. Oxford University Press, NewYork (1984)
10. Dong, Z.D., Dong, Q.: HowNet, http://www.keenage.com
11. Liu, B., Ren, F., Wang, C.: The Building of Chinese Emotion Thesaurus Using How Net Based on the Main Sememe. In: Proc. 4th International Conference on Natural Computation, pp. 91–95. IEEE Press (2008)
12. Mehrabian, A.: Pleasure-arousal-dominance: A general framework for describing and measuring individual differences in temperament. Current Psychology 14, 261–292 (1996)
13. Zhang, H.P., Yu, H.K., Xiong, D.Y., Liu, Q.: HHMM-based Chinese Lexical Analyzer ICTCLAS. In: Proc. 2nd SIGHAN Workshop Affiliated with 41th ACL, pp. 184–187 (2003)

Face Alignment Based on 3D Face Shape Model and Markov Random Field

Rong Xiong*, Junnan Wang, and Jian Chu

State Key Laboratory of Industrial Control Technology,
Zhejiang University, Zheda Road 38, Hangzhou, 310027, China
rxiong@iipc.zju.edu.cn

Abstract. This paper presents a novel method for face alignment under unknown head poses and nonrigid warp, within the framework of markov random field. The proposed method learns a 3D face shape model comprised of 31 facial features and a texture model for each facial feature from a 3D face database. The models are combined to serve as the unary, pairwise and high order constraints of the markov random field. The facial features are located by minimizing the potential function of markov random field, which is solved with dual decomposition. The main contribution of this paper is composed of three aspects. First, Random Project Tree is utilized to learn the manifold structure of the facial feature appearance under different view points. Second, a 3D face shape model is learned to capture the linear part of face shape distribution due to the change of identity and expression, which is served as the high order constraints. Third, Markov random field is introduced to model the non-linear part of the face shape distribution, and also to deal with occlusion of facial features due to head pose variation or ornaments. Experiments was taken on the Texas 3D face database and face images downloaded from the Internet, results shows capability of adapting large head pose variations of the method.

1 Introduction

Face alignment is essentially a kind of image registration problem, which means finding the corresponding facial features in the face image. It is substantially important for many face related tasks like face recognition, video surveillance, human robot interaction, etc.. There are a numbers of methods that have been developed [6] [1]. However, it is still full of difficulties, because of the vast variance of face appearance, related to the illumination, identity, head pose and facial expressions. The main challenge is adapting the alignment algorithm to various conditions.

Roughly, the face alignment methods can be divided into three classes: model based method, holistic method, and feature based method. Model based method, which learns shape and texture models to capture the main pattern of human faces, is considered to be prior to the others. Three most important models

* Corresponding author.

S. Lee et al. (Eds.): Intelligent Autonomous Systems 12, AISC 194, pp. 249–261.
springerlink.com

including Active Shape Mode (ASM) [16] [14], Active Appearance Model(AAM) [15] [4] [7], and 3D morphable model [3] is reviewed briefly below.

ASM is one of the early approaches that attempt to fit the input data with a model which can deform in ways consistent with the training set. ASM works well to the near frontal face image with reasonable initialization. Numerous extensions including multi-view ASM have been proposed [19] [12] to adapt the method to more rigorous conditions, like extreme head poses, etc.. AAM is one of the most important extension of ASM, which learns the texture model of the whole face based on shape free face textures. Multi-view AAM similar to Multi-view ASM is proposed to adapt to appearance changes [13]. Both ASM and AAM learn the shape model and texture model based on PCA, with the hypothesis that both shape and texture is linear distributed in the space respectively, which means they can not adapt to the nonlinearity of 2D face shapes and textures.

Another extensively studied model is 3D morphable model [3], which can thought to be the 3D edition of AAM. Benefited from the 3D face shapes with lower degree of nonlinearity compare to the 2D face shape, the model is well-adapted to head pose variations. However, large computation increases the machine time due to the operation on densely sampled 3D face surface, and *good* initial pose is usually required for practical implementation.

The most related work to our methods is [11], which represents a graphical model including a linear texture model for each facial features based on Geometry blur and a 2D face shape model as the high order constraints. For both texture and shape model are learned on frontal face images, the method can not adapt to severe head pose changes, and occlusion is not handled.

In this paper, we present a model based face alignment method to align the face and locate the facial features even under extreme head poses. First, a 3D face shape model is learned by applying principle component analysis (PCA) to the face shapes from the 3D face database. Second, a texture model for each facial features is learned for each facial features based on random projection tree to catch the manifold structure of each facial feature appearance. Third, markov random field is introduced to represent the linear and nonlinear part of face shape distribution based on pairwise constraints and pattern constraints and deal with occlusion, while the 3D face shape model is served as the high order constraints of face shapes.

The rest of this paper is organized as follows. Section 2 and section 3 explain the 3D face shape model and the texture models of facial features respectively. In section 4, markov random field with occlusion treatment is introduced, together with the algorithm of dual decomposition which minimizes the potential function of markov random filed. Section 5 gives the experimental results with some discussions. Section 6 concludes the paper.

2 3D Face Shape Model

The 3D face shape model is constructed based on the Texas 3D face database [10] [9], which provides 1149 3D face samples and their corresponding color images, as shown in Fig. 1.

Fig. 1. 3D sample faces and the corresponding color faces in Texas 3D face database, the gray ones are the range images, in which brighter mean closer to observer, the color ones are color image. The range image and color image are corresponded pixel to pixel.

Previous work [16] [14] [11] usually adopt tens of facial feature points, including the points locate on the face edge, to represent the face shape. However, the edge points are easily occluded with pose variants, and the texture of them is not discriminative. In this paper, 31 facial features which are mainly located around eyes, eyebrows, nose and mouth are selected to represent the face shape, as shown in Fig. 2.

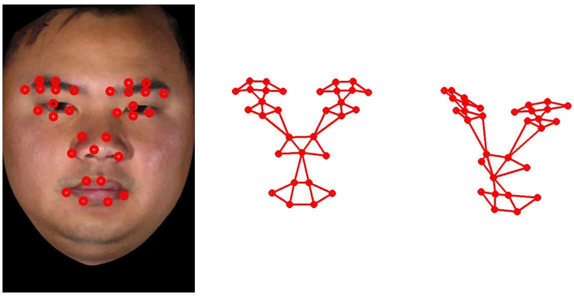

Fig. 2. Facial features and 3D face shape model. (a),Facial features on sample face. (b), Average shape of 3D shape model and the neighborhood. (c), Rotated 3D face shape, yaw=$-20°$,pitch=$-30°$

Let $X_i = \{x_{i1}, y_{i1}, z_{i1}, \cdots, x_{in}, y_{in}, z_{in}\}$ be the $i-th$ 3D face shape in the database, where $\{x_{ij}, y_{ij}, z_{ij} | j = 1 \cdots n\}$is the 3D coordinate of the $j-th$ facial feature in the $i-th$ sample face. Applying PCA to all 3D face shapes, the 3D face shape subspace expanded by k most significant eigenvectors is found. Face shapes lie in the subspace can be expressed as equation (1).

$$X_{3D} = \overline{X_{3D}} + Q_{3D} \times b_{3D} \qquad (1)$$

$\overline{X_{3D}}$ is the mean face shape, Q_{3D} is the matrix comprised of k significant eigenvectors, b_{3D} is the parameter vector with it's component limited in $[-3\sqrt{\lambda_i}, 3\sqrt{\lambda_i}]$ to ensure the synthesized face shape X_{3D} is a "face shape", and λ_i is the eigenvalue corresponding to the $i-th$ eigenvector.

The parameter of the 3D face shape model is estimated based on the 2D coordinates of facial features in face image. Assuming the affine projection camera model, the 3D face features are projected into 2D image according to equation (2).

$$X_{2Di} = P[sR(\overline{X_{3D}} + Q_{3D}b_{3D})|_i + t] \quad (2)$$

where the subscript i means the $i-th$ facial features, X_{2Di} is the projected coordinates of corresponding facial features, P is the affine projection matrix, and $P = \begin{pmatrix} 1\ 0\ 0 \\ 0\ 1\ 0 \end{pmatrix}$ in this paper, s is the scale factor, R is the rotation matrix, and t is the translation vector. By minimizing the projection error Err_{proj} according to equation (3), shape parameter b_{3D}, and transformation parameter including s, R and t can be estimated in an iterative way.

$$Err_{proj} = \sum_{i=1}^{n} \|(X_{2Di} - P[sR(\overline{X_{3D}} + Q_{3D}b_{3D})|_i + t]\|_2 \quad (3)$$

In order to construct the 3D face shape model, the Texas 3D face database is label semiautomatically. First, ASM is applied to color images of frontal face to locate 31 facial features. Second, the error labeled face samples are rejected manually. Third, the 3D coordinates of the labeled facial features are obtained with the corresponding 3D face data. In the experiment, 108 'good' labeled samples are used to construct the 3D face shape model.

3 Texture Models

To represent the distribution of face texture under pose variations, the structure of the distribution should be learned. Some works [17] [8] [5] about face recognition based on manifold learning announced that face texture is a nonlinear low intrinsic dimension manifold which is embedded into the high dimension space. Based on the observation, an affine invariant texture model is established by learning the manifold structure from training set, with the algorithm of random projection tree (RPTree) [18].

Sampling the texture around facial features under different head poses is not an easy job. In this work, we take the advantages brought by the 3D face database to sample the texture automatically. With the 3D face database, the texture around a given facial feature point with variant head poses can be synthesized by rotating the 3D face surface.

As mentioned before, Active Shape Model is efficient to locate facial features on frontal face image. Here, ASM is applied to the frontal face to locate the facial features, and then textures under different head poses are synthesized automatically, as shown in Fig. 3. In this paper, rotations with yaw of $[0°, +60°]$

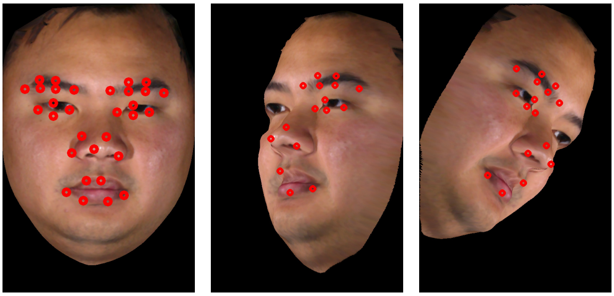

(a) (b) (c)

Fig. 3. Synthesized face image and the corresponding facial features under different head poses. For (b) and (c), only the visible half facial features are displayed. (a), yaw=0°,pitch=0°. (b), yaw=−30°,pitch=15°. (c), yaw=45°,pitch=−30°.

and pitch of $[-45°, +45°]$ with a step of $5°$ are applied to the 3D face data, and considering the symmetry of face, only the left half facial feature textures are extracted. The right half facial feature textures are obtained by mirroring the right ones. The texture is described by geometry blur [2].

For each facial feature, the textures around it under different head poses form a manifold. The manifold is approximated by an RPTree, which is the texture model of the facial feature. After the RPTree is constructed, PCA is applied to the leafs to approximate the linear structure of the subsets.

let T be the set of texture models(the set of RPTrees), $T = \{T_i | i = 1 \cdots n\}$, n is the number of facial features, and the j-th leaf of T_i is described by PCA: $X_{gij} = \overline{X_{gij}} + Q_{gij} b_{gij}$.

Given a texture t, the distance between t and texture model T_i is estimated. First, the corresponding leaf of t is established by search along the RPtree(suppose to be the j-th leaf). Second, the texture parameter b_t is calculated as equation (4).

$$b_t = (Q_{gij}^T Q_{gij})^{-1} Q_{gij}^T (t - \overline{X_{gij}}) \tag{4}$$

then the distance d_{tj} is calculated according to equation (5).

$$d_{tj} = b_t^T \Sigma^{-1} b_t + \gamma \| X_{gij}^* - t \|_2 \tag{5}$$

where $X_{gij}^* = \overline{X_{gij}} + Q_{gij} b_t$, γ is a constant weight, and Σ is a diagonal matrix with the eigenvalues of the j-th leaf as it's diagonal elements. The distance d_{tj} is comprised of 2 parts, the similarity of t to the texture model evaluated by $b_t^T \Sigma^{-1} b_t$, and the distance from t to the subspace of the nearest leaf evaluated by $\gamma \| X_{gij}^* - t \|_2$.

4 Markov Random Field for 2D Face Shape Representation

Markov random field is a kind of undirected graph model which models the neighbor dependence of the nodes. In this paper, the markov random field is used to capture the nonlinear part of face shape by modeling the 2D projection of the 3D face shape, assuming that each facial feature only depends on its neighbors.

Given a markov random field $G(V, E)$. V is the vertex set, and E is the edge set. Let X be the set of random variables of V, and Y be the observation, according to the Hammersley-Clifford theorem, the posterior probability $P(X/Y)$ can be calculated as equation (6).

$$P(X/Y) = \frac{1}{Z} \prod_{c \in C} e^{-\phi_c(x_c)} \tag{6}$$

Z is the normalizing factor, $\phi_c(x_c)$ is the potential function, c is the clique, and C is the set of all cliques. Then maximizing the posterior probability is equivalent to maximizing the potential function $\phi_c(x_c)$.

For face alignment, the nodes of MRF represent the facial feature points, and the random variables of nodes are set to be the offsets of the node position. Face is then aligned by minimizing the potential function $\phi_c(x_c)$.

Given the neighborhood system of face shape, $\phi_c(x_c)$ is calculated according to equation (7).

$$\phi_c(x_c) = \sum_{i=1}^{n} \phi_i x_i + \sum_{e \in E} \phi_e(x_e) \tag{7}$$

where $e \in E$ is the edge, $\phi_i x_i$ is called the unary potential, and $\phi_e(x_e)$ is called the pairwise potential.

4.1 Unary Potential

Unary potential which models the likelihood is calculated as the similarity of textures. Given x_i, and the texture descriptor at corresponding position $f(x_i)$, the unary potential is the distance between $f(x_i)$ and the texture model T_i, as shown in equation (8) according to equation (5).

$$\phi_i(x_i) = b_t^T \Sigma^{-1} b_t + \gamma \| X_{gij}^* - \overline{X_{gij}} \|_2 \tag{8}$$

4.2 Pairwise Potential

The pairwise potential models the smoothness of neighborhood, which means the offset of each node should be similar to its neighbor nodes. The pairwise potential is given in equation 9.

$$\phi_e(x_e) = \beta \times e^{\frac{\|x_i - x_j\|_2}{\varepsilon^2}},\ i, j \in c. \tag{9}$$

β and ε are parameters of the MRF.

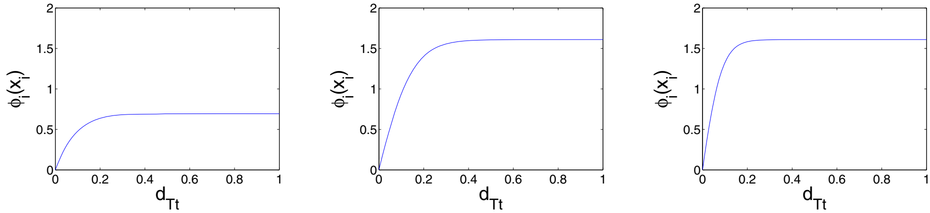

(a) $e = 0.5, \sigma = 0.07$ (b) $e = 0.2, \sigma = 0.07$ (c) $e = 0.2, \sigma = 0.04$

Fig. 4. Unary potential with different parameter values

4.3 Occlusion Handling

Occlusion can be handled easily within the framework of MRF by rewritten the unary potential to be equation (10).

$$\phi_i(x_i) = -\ln((1-e)\exp(-\frac{|d_{tT}|}{\sigma}) + e) \tag{10}$$

where $d_{tT} = b_t^T \Sigma^{-1} b_t + \gamma \| X_{gij}^* - \overline{X_{gij}} \|_2$. Fig. 4 shows the shapes of $\phi_i(x_i)$ with different parameter values.

4.4 Incorporating the MRF with the 3D Face Shape Model

As described above, 3D face shape model and MRF model the linear and nonlinear part of the face shape respectively. For 3D face shape model, it only models the linear part, and can not adapt to the face shape which is not consistent with it. For MRF, it is defined on a 2D graph model, and it does not contain any 3D information to adapt the 3D pose variations, which means, when the 2D face shape differs greatly from the initial 2D shape, the pairwise energy will be resistance to the true facial feature locations.

In order to model the entire face shape variations, 3D face shape model and MRF are incorporated in an iterative way. Given initial location of facial features MRF is applied to estimate the location of features. Then the location of facial features given by MRF is used to estimate the parameters of the 3D face shape model. With the estimated parameters, the 2D coordinates of facial features are calculated and again used as the initial facial features locations of the MRF. Face image is then aligned when the algorithm converges.

5 Experimental Results

To illustrate the performance of the method, the method is applied to align face with variant head poses, to locate the facial features. The Texas 3D face database [10] [9] including 1149 3D face samples and the corresponding color images is used to train model and test the method. Experiments are implemented on a laptop with Intel i5-2410M 2.3 GHz CPU, and 2G RAM, it takes about 3 seconds to align a face image.

5.1 Experiment on Texas 3D Face Database

The face images with different head poses from Texas 3D face database are synthesized for testing. In the experiment, 20 frontal face images are used to synthesize 100 face images with randomly chosen head poses, which are limited to $[-60, 0°]$ of yaw, and $[0, 45°]$ of pitch. The number of correctly aligned face is counted manually, and the average location error of facial features are calculated based on the non-occluded features. The test face images are divided into 2 groups according to the yaw with 60 test images each group, and the result is shown in Table 1.

The average location error is calculated according to equation (11).

$$Err_{loc} = \frac{1}{|V_{no}|}\sqrt{\sum_{i \in V_{no}} \|x_i - x_{ir}\|_2} \tag{11}$$

where V_{no} means the vertex set of non-occluded facial features, $|V_{no}|$ is the size of $|V_{no}|$, x_i is the location of facial feature i, which is estimated with the proposed method, and x_{ir} is the ground truth.

Table 1. Experiment Result of Face Alignment

	N_c [a]		Err_{loc} (pixels)	
Head poses	**Our method**	**ASM**	**Our method**	**ASM**
$-30° < yaw \leq 0°$	54/60	28/60	4.3	4.1 [b]
$-60° \leq yaw \leq -30°$	43/60	0/60	7.6	NA [c]

[a] N_c means number of correct aligned face image

[b] The Err_{loc} of ASM is smaller than the proposed method,for the group $-30° < yaw \leq 0°$ contains 20 frontal face images

[c] ASM failed to align face images with large head pose

Some additional experiments on the synthesized face images, which are aligned with ASM and the proposed method, are shown in Fig. 5. The results shows that the proposed method can locate the facial features more precisely, while the ASM method failed on pose variations, as shown in Fig. 5(e) which failed to converge, and Fig. 5(f), 5(g), which do not locate the feature points precisely.

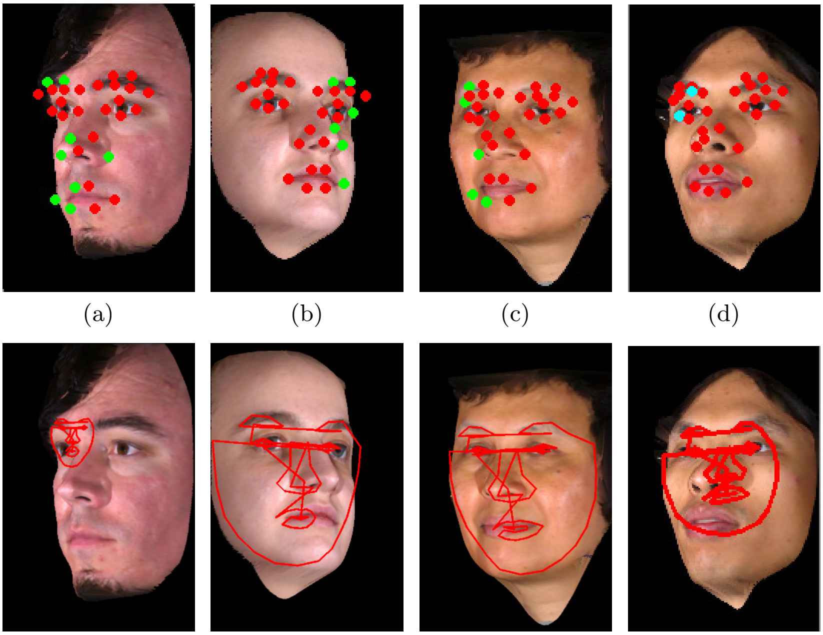

(a) (b) (c) (d)

(e) (f) (g) (h)

Fig. 5. Results of face alignment on Texas 3D face database. First row: results of our method, second raw: results of ASM. Green point means occlusion, while red point means visible feature. (a),(d): $yaw = -30°, pitch = 0$. (b),(e): $yaw = 30°, pitch = 15^{circ}$. (c), (f): $yaw = -15°, pitch = 0°$.

5.2 Experiment on Face Images from the Internet

At last, additional experiments are taken on images downloaded from the Internet, and the result of the proposed method and the ASM is shown in Fig. 6. The results show that the proposed method can handle occlusion caused by hair or glasses as shown in Fig. 6(b), 6(c). Fig. 6(f) means ASM failed to get a result. Further more, the face images are downloaded from the Internet, and they are captured with unconstrained illuminations and are independent with the training set, so the results also shows generalization capability of the models learned from training set.

More experimental results are shown is Fig. 7.

The proposed method is not compared to the multi-view ASM methods for the lack of source code, the comparison should be done in future work.

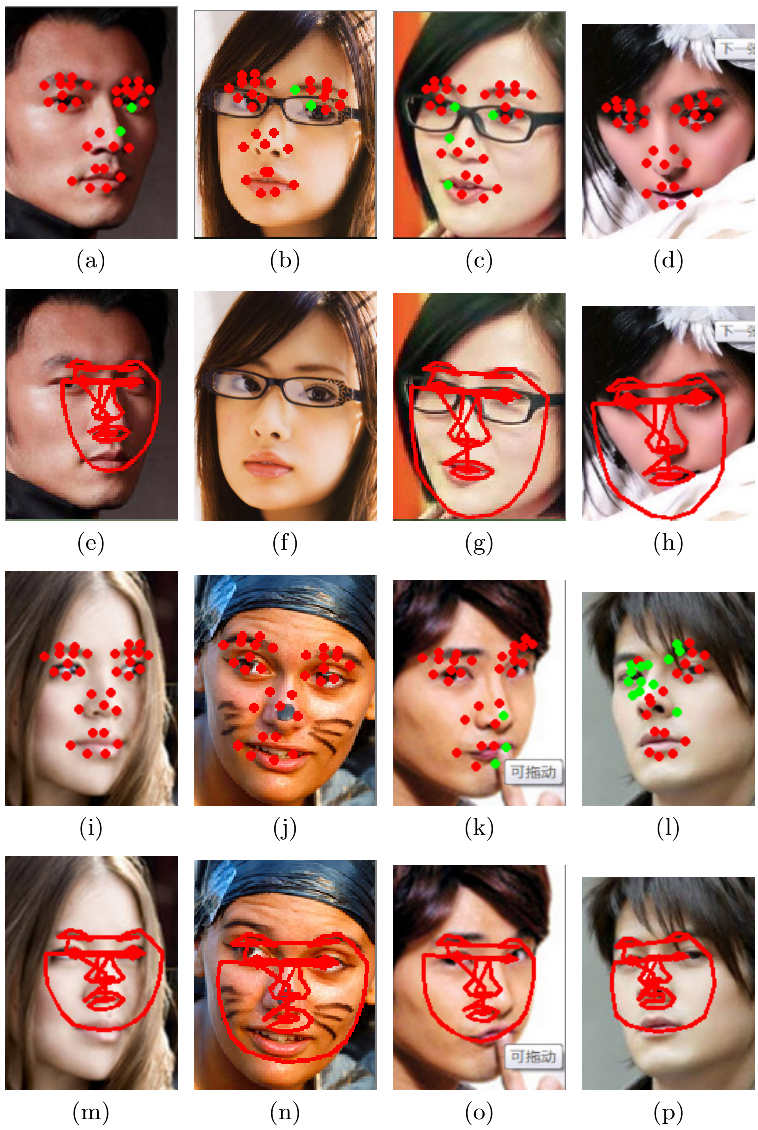

Fig. 6. Results of face alignment: face images downloaded from the Internet.First row: results of our method, second raw: results of ASM. Green point means occlusion, while red point means visible feature. (e) means ASM failed to get a result.

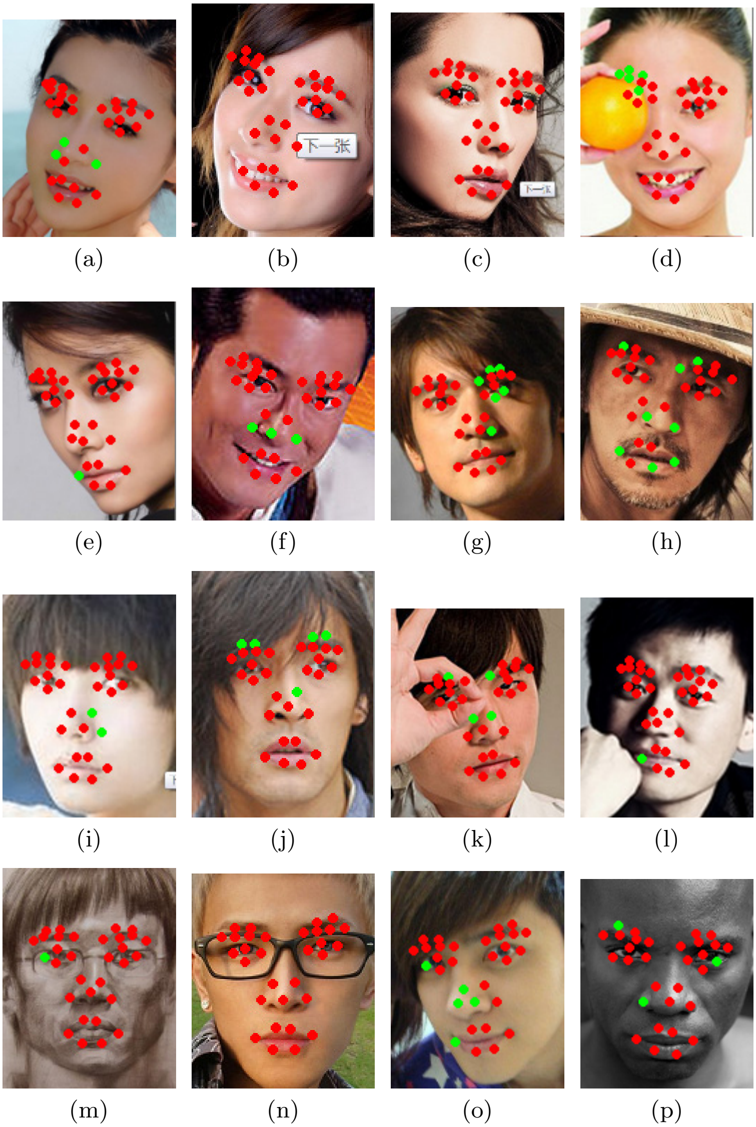

Fig. 7. Some experimental esults of face alignment: face images downloaded from the Internet

6 Conclusion

This paper represents a method for face alignment under pose variations. PCA based models and markov random field are combined to model the linear and nonlinear part of the face shape respectively. The 3D face shape model, which models the pose variation explicitly, reduces the nonlinearity degree of face shape, while the markov random field handles the occlusion and nonlinearity. Further more, a texture model for each facial features is learned with random projection tree. Experiments shows that the method can adapt to pose variations and occlusions robustly.

For future work, the potential facial feature locations should be pre-detected to accelerate the algorithm by reducing the search space of MRF, and the comparison of this method and multi-view ASM methods should be implemented.

References

1. Guidi, G., Vedaldi, A., Soatto, S.: Joint data alignment up to (lossy) transformations. In: CVPR (2008)
2. Berg, A.C., Malik, J.: Geometric blur for template matching. In: CVPR (2001)
3. Blanz, V., Vetter, T.: A morphable model for the synthesis of 3d faces. In: SIGGRAPH (1999)
4. Cootes, T.F., Taylor, C.J.: An algorithm for tuning an active appearance model to new data. In: BMVC (2006)
5. Li, S.Z., Zhang, J., Wang, J.: Nearest manifold approach for face recognition. In: FG (2004)
6. Lucey, S., Cox, M., Sridharan, S., Cohn, J.: Least squares congealing for unsupervised alignment of images. In: CVPR (2008)
7. Matthews, I., Baker, S.: Active appearancemodels revisited. In: IJCV (2004)
8. Fisher, J., Cippola, R., Aranjelovic, O., Shakhnarovich, G., Darrell, T.: Face recognition with image sets using manifold density divergence. In: CVPR (2005)
9. Markey, M.K., Gupta, S., Bovik, A.C.: Anthropometric 3d face recognition. International Journal of Computer Vision (2010)
10. Markey, M.K., Gupta, S., Bovik, A.C.: Texas 3d face recognition database. Image Analysis & Interpretation, SSIAI (2010)
11. Kittler, J., Arashloo, S.R., Christmas, W.J.: Facial feature localization using graph matching with higher order statistical shape priors and global optimization. In: BTAS (2010)
12. Gong, S., Romdhani, S., Psarrou, A.: A multi-view nonlinear active shape model using kernel pca. In: British Machine Vision Conference (1999)
13. Sattar, A., Seguier, R.: Mvaam (multi-view active appearance model) optimized by multi-objective genetic algorithm. Automatic Face & Gesture Recognition (2008)
14. Cooper, D., Cootes, T., Taylor, C., Graham, J.: Active shape models - their training and application. In: Computer Vision and Image Understanding (1995)

15. Cootes, T.F., Edwards, G.J., Taylor, C.J.: Active Appearance Models. In: Burkhardt, H., Neumann, B. (eds.) ECCV 1998. LNCS, vol. 1407, p. 484. Springer, Heidelberg (1998)
16. Cooper, D.H., Cootes, T.F., Taylor, C.J., Graham, J.: Training models of shape from sets of examples. In: BMVC (1992)
17. Hu, Y., Niyogi, P., He, X., Yan, S., Zhang, H.: Face recognition using laplacianfaces. In: PAMI (2005)
18. Kabra, M., Freund, Y., Dasgupta, S., Verma, N.: Learning the structure of manifolds using random projections. In: Neural Information Processing Systems, NIPS (2007)
19. Zhang, L., Ai, H.: Multi-view active shape model with robust parameter estimation. In: ICCV (2006)

Spontaneous Facial Expression Recognition by Fusing Thermal Infrared and Visible Images

Shangfei Wang and Shan He

Key Lab of Computing and Communicating Software of Anhui Province
School of Computer Science and Technology,
University of Science and Technology of China, Hefei, Anhui, P.R. China, 230027
sfwang@ustc.edu.cn, shanhe@mail.ustc.edu.cn

Abstract. In this paper, we propose a method for spontaneous facial expression recognition by fusing features extracted from visible and thermal infrared images. First, the active appearance model parameters and head motion features are extracted from the visible images, and several thermal statistical parameters are extracted from the infrared images. Second, a multiple genetic algorithms-based fusion method is proposed for fusing these two spectrums. We use this proposed fusion method to search for the optimal combination of a similarity measurement and a feature subset. Then, a k-nearest neighbors classifier with the optimal combination is used to classify spontaneous facial expressions. Comparative experiments implemented on the Natural Visible and Infrared Facial Expression database show the effectiveness of the proposed similarity measurement and the feature selection method, and demonstrate the fusion method's advantage over only using visible features.

Keywords: facial expression recognition, thermal infrared, visible, fusion, genetic algorithm.

1 Introduction

Facial expression recognition has attracted more and more attention in recent years. Although, considerable progress has been made in the field of facial expression recognition using visible images [1], it is not robust enough for deployment in uncontrolled environments, such as illumination changes. Furthermore, most existing research has been based on posed expression databases. These artificial poses are usually exaggerated. Spontaneous expressions, on the other hand, may be subtle and differ from posed expressions both in appearance and timing. Therefore, for practical applications, it is important to study natural expression recognition.

Illumination changes can hinder visible expression recognition. However, thermal infrared images, which record the temperature distribution formed by facial vein branches, are not sensitive to illumination conditions. Thus, a few researchers begin to pay attention to thermal expression recognition [2][3][4]. To the best of our knowledge, little attention has been paid to facial expression recognition by fusing images from the visible and infrared spectrums except

S. Lee et al. (Eds.): Intelligent Autonomous Systems 12, AISC 194, pp. 263–272.
springerlink.com

Yoshitomi et al. [5]. Here, we propose spontaneous facial expression recognition by fusing visible and thermal infrared images.

Spontaneous expressions are often accompanied by body gestures and head motions [1]. Only few studies have investigated fusing information from face and head motions to improve recognition performance [6][7][8].Some of these gestures are random and others are performed depending on personal habit. Yet, in either case, meaningful information for affective states can be extracted. For example, nods and shakes can be extracted for recognizing agreement and disagreement. Therefore, we extract both head motion features and facial appearance features from visible images. We define the velocity and rotational speed of head motions as features of head motions. Additionally, the active appearance model (AAM) features are extracted because they capture both facial geometric and appearance information.

Considering the temperature changes of the environment and the temperature drift of thermal infrared cameras, we use differential temperatures between the apex and the onset infrared images instead of their absolute temperatures. Then, we extract several thermal statistical parameters from this differential temperature matrix.

Next, the k-nearest neighbor (KNN) is used as the classifier. A multiple Genetic Algorithms (GAs) is proposed as a feature-level fusion method to search for the optimal combination of a similarity measurement and a feature subset.

We have evaluated the proposed fusion scheme through comparative experiments on the Natural Visible and Infrared Facial Expression (NVIE) database [9]. The experimental results illustrate that fusion improves recognition performance, especially for negative expressions. Head motion features are confirmed to be useful for recognizing spontaneous facial expressions. Moreover, the proposed multiple GAs-based fusion method is verified to be effective at selecting a optimal similarity measurement and a feature subset. This method may provide a general framework for fusing different types of features using similarity measurement-based models.

Compared to the existing literature, our main contributions are the following items:

a. We propose a method for spontaneous facial expression recognition by fusing features from both the visible and infrared spectrums. To our best knowledge, combining head motions, facial appearance, and facial temperatures to recognize spontaneous facial expressions is novel.
b. We propose a feature-level fusion method that uses multiple GAs to search for an optimal combination of a similarity measurement and a feature subset. Although both similarity measurement and feature selection have been deeply and widely researched [10][11], few researchers have made attempts to simultaneously consider similarity measurement selection and feature selection, as a problem of combinatorial optimization [12], and apply it to feature-level fusion.

2 Method

Figure 1 shows the framework of our method. After the visible and thermal infrared expressional images are obtained, visible features and thermal infrared features are extracted. Then, a multiple GAs-based fusion method is adopted on the training set for similarity measurement and feature selection. Last, the KNN classifier with the selected similarity measurement and feature set is evaluated on the test set. Every component of our method is described in detail in this section.

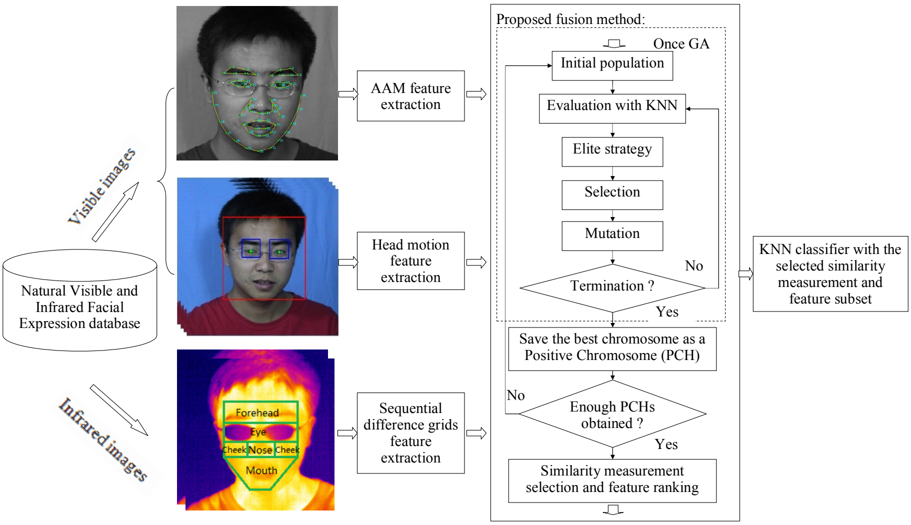

Fig. 1. Framework of the proposed method

2.1 Thermal Infrared Feature Extraction

Four points (the centers of the eyes, the tip of the nose, and tip of the jaw) on the onset and apex infrared expression images are labeled by Ji's methods [13]. Then, the apex and onset infrared images are rotated, resized, and cropped into $M \times N$ images according to these points. Afterwards, the differential temperature matrix, M_s, is obtained by using equation (1).

$$M_s = M_a - M_o, \quad (1)$$

where M_a is the temperature matrixes of the apex infrared image, and M_o is the temperature matrixes of the onset infrared image.

Owing to the opaqueness of infrared light to glass, the area around the eyes is not taken into consideration here. We divide the facial area into four subareas:

the forehead, nose, cheek, and mouth, as shown in Figure 1. Then, each subarea is further divided into several $w \times w$ grids. Afterward, several statistical parameters in each grid of M_s are calculated. These parameters include the minimum, maximum, standard deviation, and mean value of temperature are termed as the sequential difference grid features (SDGFs).

2.2 Visible Feature Extraction

Firstly, the subject's eyes are located in the image sequence using an OpenCV implementation of a Haar-cascade detector and the three parameters proposed in [14]. Then, three features, i.e. the velocity of the head's motion in the x- and y-axis and the rotational speed of the head, are calculated according to the coordinates of the pupils using equations (2), (3), and (4).

$$Velocity_x = \frac{C_x^{apex} - C_x^{onset}}{frame^{apex} - frame^{onset}}, \tag{2}$$

$$Velocity_y = \frac{C_y^{apex} - C_y^{onset}}{frame^{apex} - frame^{onset}}, \tag{3}$$

$$Velocity_r = \frac{\left| arctan(\frac{R_y^{apex} - L_y^{apex}}{R_x^{apex} - L_x^{apex}}) - arctan(\frac{R_y^{onset} - L_y^{onset}}{R_x^{onset} - L_x^{onset}}) \right|}{frame^{apex} - frame^{onset}}, \tag{4}$$

where, (L_x, L_y) represents the coordinates of the left pupil, (R_x, R_y) represents the right pupil, and (C_x, C_y) represents the center of two pupils.

Geometric and appearance features are commonly used in visible facial expression recognition [1]. Because the AAM features capture information about both appearance and shape [15], we use AAM here to extract visible features from the apex expression images. The am_tools [16] are adopted.

2.3 Multiple GAs-Based Fusion

Both sensitive features and similarity measurements are important to classifiers, especially for KNN. KNN performs well in facial expression recognition [17]. Usually, Euclidean distance or a fixed measurement is adopted in KNN. However, the optimal similarity measurement to use with the selected features is uncertain. Thus, we consider similarity measurement selection and feature selection simultaneously as a problem of combinatorial optimization problem and apply GAs. A set of combinations of candidate similarity measurements and feature subsets are used to construct the original evolution space. During the evolution process, the similarity measurement of two patterns is computed using the selected similarity measurement and the feature subset. The classification rate of a KNN classifier on the validation set is used as the fitness value in the GA. At the end of the evolution process, the final surviving chromosome, which contains an encoded similarity measurement and a feature subset, shows the optimal combination.

To avoid local optimal solutions, especially when the dimension of the primitive features is high and the relevant features only account for a small portion of the primitive features [18], multiple GAs are used, as shown in Figure 1. We use GAs to search for the optimal combination of similarity measurement and relevant features multiple times, and the final combination is found by statistically analyzing the nearly optimal solutions from multiple GAs.

Each GA is terminated when the highest fitness achieves the target fitness, or when the number of generations reaches its maximum value. We refer to the best chromosome in the last generation of the GA as a positive chromosome (PCH). This chromosome is saved for subsequent statistical analysis. After a certain number of PCHs have been obtained, the similarity measurement and feature selection are performed based on a statistical analysis of these PCHs. First, the selected frequencies of the candidate similarity measurements among all PCHs are counted. Empirically, a similarity measurement with a higher selected frequency is more suitable for data measurement. After the process of similarity measurement selection is complete, the selected frequencies of all features among the PCHs, for which similarity measurement is equivalent to the previously selected similarity measurement, are counted. The value of the selected frequency of a feature reflects its importance to classification. All features are ranked based on the selected frequencies in descending order. With this method, a feature will not be selected if it is accidently selected once in the course of the GA. These PCHs may not be the best solution. However, the process of feature selection could be made more robust through the use of voting.

Three distance functions, i.e. Euclidean, Manhattan and Chebyshev distance, and two coefficient functions, i.e. cosine and relative coefficient, are investigated as similarity measurements in our experiments. A small distance or a higher coefficient between two samples indicates a higher degree of similarity.

2.4 KNN Classifier

The KNN classifier is implemented to recognize expressions using the selected similarity measurement and the features subset that are obtained from the multiple GAs.

3 Experiments and Analysis

3.1 Experimental Conditions

To evaluate the effectiveness of our method, experiments are implemented on the data chosen from the NVIE database [9]. The NVIE database contains both visible and thermal infrared spontaneous facial expression images of more than 100 subjects. All of the visible expressional sequences were labeled by five students on the intensity of the six basic facial expressions (happiness, sadness, surprise, fear, anger, and disgust) with a three point scale (0, 1, and 2). The expression with the highest average intensity is used as the expression label for the visible and thermal infrared image sequences. For our experiments, a sample was selected under the following criteria. First, the average intensity associated with the labeled expression must be greater than 1. Second, samples with one of three expressions, i.e., happiness, fear, and disgust, were chosen. Third, the data must consist of both visible and thermal infrared image sequences. A total of 535 samples were selected.

The size of the original thermal infrared images was 304×230, and the size of the located facial region was normalized to 84×80 before the SDGFs were extracted. The size of grids was set to 4×4. In total, there were 1120 thermal features: 240 from the forehead, 160 from the nose, 480 from the mouth, and 240 from cheek subarea. In the training phase of the AAM, 61 landmark points were manually marked on each visible apex image, as shown in Figure 1. Half of the samples were used to train the AAM. The left samples were automatically marked with the previously learned AAM. With the automatically marked landmark points, the AAM features of all samples were extracted. In total, there were 33 visible features including 3 head motion features and 30 features extracted via the AAM. After feature extraction, all features were normalized to the interval between 0 and 1 using minimum-maximum normalization.

In the GAs, each chromosome consisted of a code, S, that represented similarity measurement and 30 serial numbers of 30 distinct features selected from the primitive features. The five similarity measurements were selected when the value of S was in the interval [0, 20), [20, 40), [40, 60), [60, 80), and [80, 100). Elite strategy and roulette-wheel selection were adopted. Every surviving chromosome was selected for mutation in the next generation. With a probability of 0.1, its similarity measurement code was added to a random number between 0 and 30 and set to the remainder of the value modulo 100. Between 1 and 5 of its feature codes were randomly replaced by serial numbers of some other unselected features from the primitive features with probabilities of 0.53125, 0.25, 0.125, 0.625, and 0.03125, respectively. The maximum number of generations was 50, and each generation contained 80 chromosomes. For each GA, 100 samples were randomly selected from the training set as validation set to evaluate chromosomes. The target fitness value was set to 0.62. In KNN, the parameter K was set to 7. The GA was independently run 1000 times.

Two comparative experiments were performed to verify the effectiveness of our method. First, a method with the fixed Euclidean distance function was performed to show the effectiveness of the proposed multiple GAs-based fusion method. Second, to analyze the effect of the thermal infrared facial features, we compared the recognition performance of the fusion method to that of only using visible features. All experimental results were yielded using a 5-fold cross-validation.

3.2 Experimental Results and Analysis

Analysis of Similarity Measurement and Feature Selection. The selected frequencies of the five candidate similarity measurements across the 5 folds are shown in Figure 2(a). It is obvious that the orders of the candidate similarity measurements' selected frequencies across the 5 folds are consistent in most cases, which shows the robustness of our method. The Manhattan distance resulted in the highest selected frequency, closely followed by the Euclidean distance. From the experimental design intent, the Manhattan is the most appropriate similarity measurement among those investigated for our data.

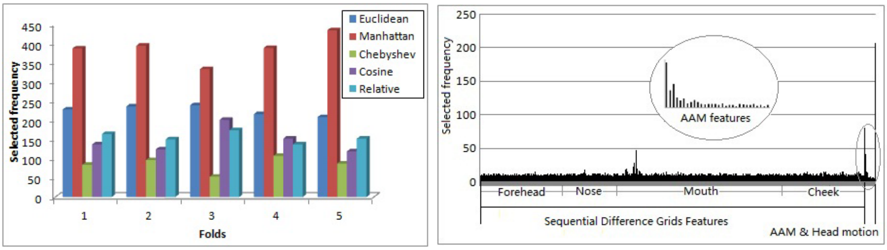

(a) (b)

Fig. 2. (a)Selected frequencies of the candidate similarity measurements;(b)Average selected frequencies of the primitive features.

Figure 2(b) shows the average selected frequencies of the primitive features when the Manhattan distance is selected. A few features' selected frequencies are particularly prominent, illustrating the importance of feature selection. The top 33 selected features consist of three head motion features, several AAM features, and several SDGFs extracted from the mouth and cheek subareas. This set of features verifies the importance of head movement to spontaneous facial expression and the complementary effect of thermal infrared images.

Owing to the AAM features performed by principal component analysis (PCA), features in the front contain more useful information. This reasoning is an explanation for why the selected frequencies of AAM features are gradually declining from front to back, as we can see from Figure 2(b). This also confirms the effectiveness of our feature selection approach.

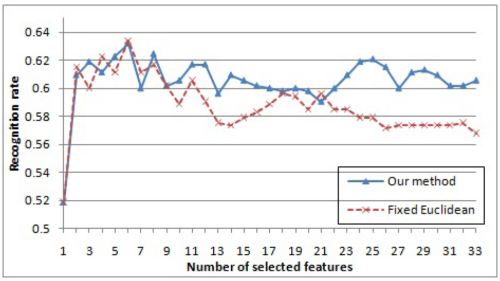

Fig. 3. Recognition rate curves of our method and the fixed Euclidean method

To verify the advantage of the similarity measurement selection, a comparative experiment is performed. We set the similarity measurement to the Euclidean distance, which is the most commonly used distance, to determine whether the selected similarity measurement is most suitable for the data. Figure 3 shows the average recognition rate curves of two classifiers with different similarity measurements using a different number of most optimal features. We find that the proposed method generally outperforms the comparative method. In 28 of the 33 experiments involving different numbers of most optimal features, our methods are at least as good as the methods with the Euclidean distance. The experimental results show that the proposed multiple GAs-based similarity measurement and feature selection method is efficient.

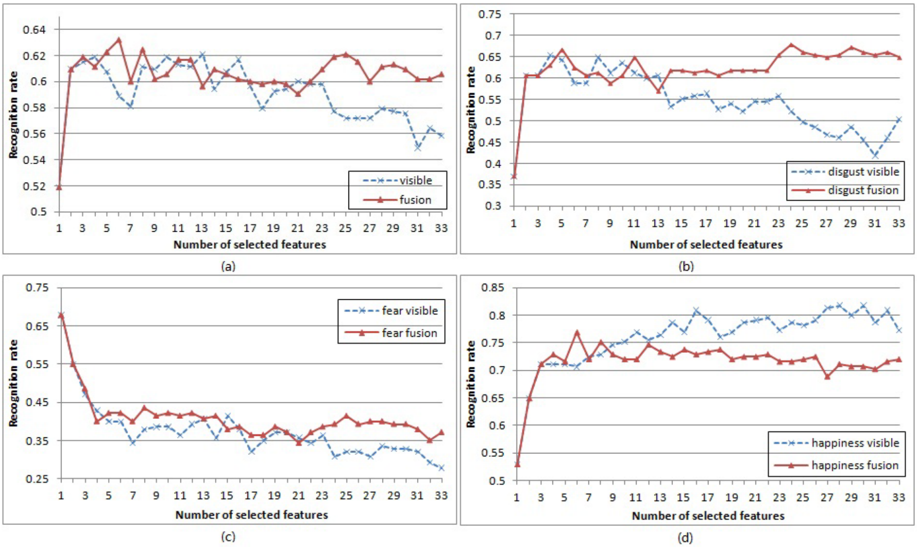

Fig. 4. Recognition rate curves of (a) overall; and of (b) disgust, (c) fear, and (d) happiness

Analysis on Effectiveness of Fusion. To specifically analyze the effect of selected thermal infrared features, we compared results from the fusion method with results from the method using only visible facial features. Here, the Manhattan distance is used as the similarity measurement. The features' selected order that is used for the method using only visible facial features is the same as the order of visible features in the fusion method. The overall recognition rate curves and those of different facial expressions with different numbers of selected features are shown in Figure 5. Apparently, the overall performance is improved by adding the thermal infrared features. The highest overall recognition rate for the fusion method is 63.2%, while it is 62.1% for the visible features-only method.

As the number of selected features increases, the results of fusion method are more robust than those of the method using only visible features method. From the recognition rate curves of different expressions, it is obvious that the recognition rates of negative expressions (disgust and fear) are improved by the fusion method. Although the recognition rate curve of happiness is lower than that of the visible features-only method after some thermal infrared features added, the curve has not declined so much. When only one feature (the velocity of head motion in the y-axis) is selected, the recognition rate of fear is much higher than that of other expressions. However, the recognition rate of fear falls for a larger number of selected features. After carefully checking the experimental samples, it was find that people often have violent head motion when expressing fear. Thus, the velocity of head motion in the y-axis can distinguish fear well, and it becomes relatively important compared to other features. This might be the best explanation for the downgrade of the fear recognition rate curve. Among these top selected features, select SDGFs extracted from the mouth and cheek part are included. These appear to indicate that the temperature variations of the mouth and cheek part are the most reliable sources for spontaneous facial expression recognition compared to other facial regions.

4 Conclusions and Future Work

In this paper, we propose fusing features extracted from visible and thermal infrared images for spontaneous facial expression recognition. First, the AAM features and three head motion features are extracted from visible images, and the proposed SDGFs are extracted from the differential temperature matrix between the apex and the onset thermal infrared images. Then, a multiple GAs-based fusion method is proposed to determine an optimal combination of the similarity measurement and feature subset for the classifier. Experiments on the NVIE database show the effectiveness of the proposed similarity measurement and feature selection method. Experiments also show the fusion method's advantage over only the method using visible features only. By adding thermal infrared features, the overall recognition rates are improved, especially for negative expressions. The information of head motions is confirmed to be useful for spontaneous facial expression, especially for distinguishing fear. The results also seem to indicate that the temperature variations of the mouth and cheek are the more reliable sources of information for spontaneous facial expression recognition relative to other facial regions.

Acknowledgment. This paper is supported by the NSFC (61175037), Special Innovation Project on Speech of Anhui Province (11010202192), project from Anhui Science and Technology Agency and Youth Creative Project of USTC.

References

1. Zeng, Z., Pantic, M., Roisman, G.I., Huang, T.S.: A survey of affect recognition methods: Audio, visual, and spontaneous expressions. IEEE TPAMI 31(1), 39–58 (2009)
2. Hernández, B., Olague, G., Hammoud, R., Trujillo, L., Romero, E.: Visual learning of texture descriptors for facial expression recognition in thermal imagery. CVIU 106(2-3), 258–269 (2007)
3. Khan, M.M.: Cluster-analytic classification of facial expressions using infrared measurements of facial thermal features. Ph.D. Thesis, Department of Computing and Engineering, University of Huddersfield (2008)
4. Jarlier, S., Grandjean, D., Delplanque, S., N'Diaye, K., Cayeux, I., Velazco, M., Sander, D., Vuilleumier, P., Scherer, K.: Thermal analysis of facial muscles contractions. IEEE TAC 2(1), 2–9 (2011)
5. Yoshitomi, Y., Kim, S.I., Kawano, T., Kilazoe, T.: Effect of sensor fusion for recognition of emotional states using voice, face image and thermal image of face. In: Proceedings of the 9th IEEE International Workshop on Robot and Human Interactive Communication, pp. 178–183 (2000)
6. Tong, Y., Chen, J., Ji, Q.: A unified probabilistic framework for spontaneous facial action modeling and understanding. IEEE TPAMI 32(2), 258–273 (2010)
7. Valstar, M.F., Gunes, H., Pantic, M.: How to distinguish posed from spontaneous smiles using geometric features. In: ICMI 2007, pp. 38–45 (November 2007)
8. Gunes, H., Pantic, M.: Dimensional Emotion Prediction from Spontaneous Head Gestures for Interaction with Sensitive Artificial Listeners. In: Allbeck, J., Badler, N., Bickmore, T., Pelachaud, C., Safonova, A. (eds.) IVA 2010. LNCS, vol. 6356, pp. 371–377. Springer, Heidelberg (2010)
9. Wang, S., Liu, Z., Lv, S., Lv, Y., Wu, G., Peng, P., Chen, F., Wang, X.: A natural visible and infrared facial expression database for expression recognition and emotion inference. IEEE TMM 12(7), 682–691 (2010)
10. Yang, L.: An overview of distance metric learning. Technical report, School of Computer Science, Carnegie Mellon University (2007)
11. Dash, M., Liu, H.: Feature selection for classification. Intelligent Data Analysis 1(3), 131–156 (1997)
12. Wang, S., Zhu, H.: Musical perceptual similarity estimation using interactive genetic algorithm. In: IEEE CEC 2010, pp. 1–7 (July 2010)
13. Tong, Y., Wang, Y., Zhu, Z., Ji, Q.: Robust facial feature tracking under varying face pose and facial expression. Pattern Recognition 40(11), 3195–3208 (2007)
14. Lv, Y., Wang, S.: A spontaneous facial expression recognition method using head motion and aam features. In: 2010 Second World Congress on NaBIC, pp. 334–339 (December 2010)
15. Lucey, S., Ashraf, A.B., Cohn, J.: Investigating spontaneous facial action recognition through aam representations of the face. Face Recognition, 275–286 (2007)
16. Tim Cootes, am_tools, http://www.isbe.man.ac.uk/~bim/software/am_tools_doc/.
17. Sebe, N., Lew, M.S., Sun, Y., Cohen, I., Gevers, T., Huang, T.S.: Authentic facial expression analysis. Image and Vision Computing 25(12), 1856–1863 (2007)
18. Li, L., Darden, T.A., Weingberg, C.R., Levine, A.J., Pedersen, L.G.: Gene assessment and sample classification for gene expression data using a genetic algorithm/k-nearest neighbor method. Combinatorial Chemistry and High Throughput Screening 4(8), 727–739 (2001)

A Wearable Plantar Pressure Measurement System: Design Specifications and First Experiments with an Amputee

Xuegang Wang[1], Qining Wang[1], Enhao Zheng[1], Kunlin Wei[2], and Long Wang[1]

[1] Intelligent Control Laboratory, College of Engineering,
Peking University, Beijing 100871, China
qiningwang@pku.edu.cn
[2] Department of Psychology, Peking University, Beijing 100871, China
wei.kunlin@pku.edu.cn

Abstract. In this paper, we present a wearable plantar pressure measurement system for locomotion mode recognition. The proposed system is implemented with four force sensors in each shoe to measure different given position pressure. By phase-dependent pattern recognition, we get reliable classification results of the six investigated modes for a below-knee amputee subject. The satisfactory recognition performances show the prospect of the integration of the proposed system with powered prostheses used for lower-limb amputees.

Keywords: Plantar pressure, locomotion mode recognition, wearable system, below-knee amputee.

1 Introduction

Since the plantar pressure refers to pressure between the plantar surface of the foot and a supporting surface, the distribution of the pressure may reveal important aspects of human gaits, e.g. gait in patients with diabetes. In addition, the plantar pressure differs during different gait phases, which may be used for gait pattern recognition. Thus, increasing studies have been made to measure and analyze the plantar pressure during different locomotion modes.

The existing plantar pressure measurement systems contribute to a variety of application fields [1–3]. As an example, plantar pressure is taking an important role in the studies on prostheses and exoskeletons, e.g. [4–6]. However, plantar pressure device just serves as a footswitch to judge whether the foot is in the phase of stance or swing. Other attempts of utilizing plantar pressure are expected to provide human body with feedback of lower-limb prostheses for dealing with gait asymmetries [7–9].

If plantar pressure is applied in the field of locomotion mode recognition, which few have attempted to do yet, kinds of advantages will appear. Firstly, plantar pressure is a very important variable during locomotion with reasonable physical significance, which makes it easy and traceable to analyze locomotion modes. Secondly, since plantar pressure signals are much stronger than electromyography (EMG), it shows high signal to noise ratio (SNR). It means that more simple processing is requested for than EMG signals do. Thirdly, wearable plantar pressure measurement devices are always installed

S. Lee et al. (Eds.): Intelligent Autonomous Systems 12, AISC 194, pp. 273–281.
springerlink.com

with friendly man-machine interface such as force sensors integrated insole [10] and sole [11] of a shoe. Furthermore, in consideration of the control of lower-limb prostheses, gait phase is important information. Taking example of finite-state control [12], each gait phase means a unique control strategy. Fortunately, plantar pressure [13] is capable of detection of gait phase. This makes it possible to achieve a simple but complete control of lower-limb prosthesis in next research.

In this paper, a wearable plantar pressure measurement system is developed for locomotion mode recognition as well as pilot study of control of powered lower-limb prosthesis. The system consists of sensing subsystem and transmission subsystem. Plantar pressure, measured by force sensors integrated insoles, is employed to classify six tested modes when transferred from measurement insole to a host computer. By phase-dependent pattern recognition, we get reliable classification results of the six investigated modes for a below-knee amputee subject, which shows the prospect of the integration of the proposed system with powered prostheses used for lower-limb amputees.

The rest of this paper is organized as follows. In Section 2, we describe the design specifications of the proposed system. Section 3 presents the classification methods. Experiments with an amputee are shown in Section 4. We conclude in Section 5.

2 Plantar Pressure Measurement System

2.1 Sensing Subsystem

Design concept of a plantar pressure measurement system is measurement of pressure distribution between the plantar surface of the foot and the supporting surface. There are two aspects to consider about. First, force sensors need to be selected in accordance with the system requirements. Second, the amount and positions of sensors need to be resolved. Selection of force sensor should mainly take measurement range, size, thickness and transduction into consideration. Measurement range of a force sensor has to cover the weight of a human and a plus in case of impulse. The size of force sensor is limited by foot. If the size is too large, there will be not enough space to distribute such sensors; On the contrary, if the size is too small, the contact between foot and sensor will be instable during locomotion. Thus, a coin size force sensor may be appropriate. Since contacting sole of foot directly, force sensors are thinner, feeling is better. In addition, simple transduction from force signals to electrical signals will contribute significantly.

Under above consideration, we selected *FlexiForce* A401 (Tekscan, Inc.,). Measurement ranges of 0-1 lb and 0-7000 lb are achievable by utilizing different circuitry. Sensing area is a circle with 1 inch in diameter. The thickness is as thin as 0.208 mm. The sensor is a kind of force sensor resistance (FSR), whose resistance output depends on force.

Sensing unit is implemented in a insole in consideration of generality and convenience. A certain amount of selected force sensors are to distribute in the insole. [14] selected six positions to install the sensors: half at heel and the others at metatarsal areas. One reason why they distributed so much sensors in a area was the small size of the sensors. [15] chose four positions: one at heel and the other three at metatarsal and toe area. Anyway, the three sensors are installed much closely.

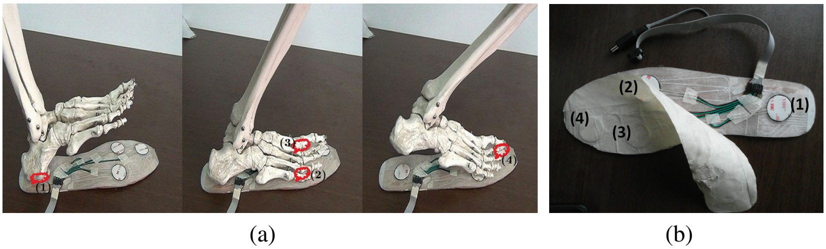

Fig. 1. Positions of sensors research. Locomotion process was illustrated by an artificial foot skeleton to select sensors most reasonable positions. (a) Locomotion process. (b) positions of sensors.

In order to decide the positions, we studied [16] plantar pressure distribution during the phase of stance. We selected four regions of peak force to be the positions to place sensors. To illustrate visually, we utilize an artificial foot skeleton (Fig. 1(a)) to show the selected positions. During locomotion, a foot goes through gait events and phases of heel-contact, stance, toe-off and swing. The selected positions showed maximization of locomotion information and minimization of amount informative. Taking right foot as an example, the regions in Fig. 1(b) distribute: (1) under calcaneus tuberosity; (2) between the fourth and fifth metatarsal bones; (3) under the first metatarsal bone; (4) under hallux toe.

2.2 Transmission Subsystem

The transmission subsystem is developed to collect, process and transmit the plantar pressure sensor signals to host computer. The main subsystem consists of a data acquisition module and a wireless transmission module. The data acquisition module is made up of an operational amplifier (OP), an analog to digital converter (ADC) and a microprogrammed control unit (MCU), as is shown in Fig. 2 The $FlexiForce$ sensor acts as a force sensor resistance in the electrical circuit and its conductance is proportional to the applied force. Thus, when the force sensor is connected to the noninverting interface of OP, the OP outputs an analog voltage proportional to the applied force. A 14-bit ADC then converts the analog voltage to digital signals and sends the signals to the MCU for processing and encoding. The wireless module transmits the digital force signals to PC. It communicates with the MCU via a serial port whose baudrate is programmable. The wireless module operates at a frequency of 434 MHz with a data rate of 250 Kbps. The transmission subsystem is installed on a printed circuit board (PCB), as is shown in Fig. 3(a). The proposed plantar pressure measurement system is implemented as Fig. 3(b). A sensor box containing battery and transmission subsystem is attached to outboard vamp. The other shoe is implemented in the same way.

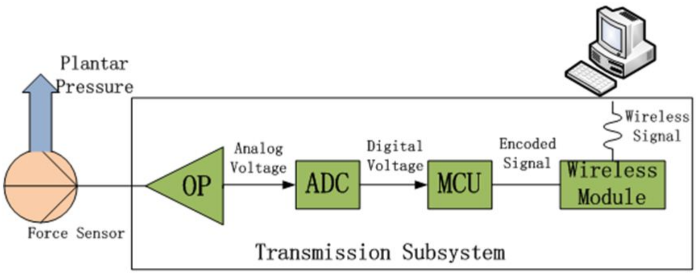

Fig. 2. Structure of transmission subsystem and signal-flow graph

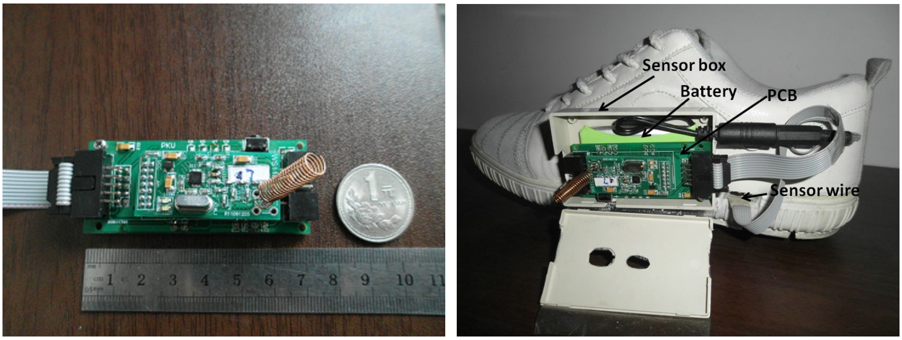

(a) (b)

Fig. 3. Implementation of the proposed plantar pressure measurement system. (a) PCB of transmission subsystem. (b) Sensor box

3 Locomotion Mode Recognition

3.1 Classifier

As we know, human locomotion is a representative rhythmical motion. Movements of feet are alternated rhythmically during locomotion, while plantar pressure varies accordingly periodically. For a certain locomotion mode, obviously, plantar pressure shows similarity at the same phase among different periods. As a consequence, phase-dependent classifier mentioned in [17] is available for the classification. Instead of additional implement named footswitches employed in [17], plantar pressure owns a inherent capacity to detect gait phase [13]. Simply put, the sum of pressure measured by the four force sensors indicates different gait phases. Gait events of foot contact (FC) and foot off (FO) were defined for gait phases. FC was determined when the sum of pressure ascended to a given threshold, while FO occurred when the sum of pressure descended to the threshold. Four event-dependent phase windows were defined: (1) Pre-FO meant the phase prior to FO, (2) Post-FO meant the phase after FO, (3) Pre-FC meant the phase prior to FC and (4) Post-FC meant the phase after FC. The phase windows as classifier analysis windows were 200 ms in width.

3.2 Classification Strategy

Selection of feature set played a significant role in classification. Features were expected to reflect as much information as possible in analysis windows. An analysis window contained eight channels of two feet plantar pressure signals. Firstly, for a channel of signals, the most prominent property was stable curve change. Cubic regression model was made for every independent channel of signals. Four regression coefficients from each channel made up thirty-two features in total. Secondly, it was reasonable to suppose that the correlations between channels of signals were outstanding identification among locomotion modes. The correlations here were expressed simply by inner product of channels of signals vectors. Feature set owned twenty-eight more features. Lastly, when it referred to locomotion modes recognition, sitting and standing were different from the others because of the stillness. We calculated range of every signal channel in an analysis window. The summation was named stillness feature separately.

Selection of classification methods was another significant choice. Decision tree analysis (DTA) with one node was applied to start classification. We utilized the stillness feature as decision parameter to divide modes into two catalogues: sitting and standing modes and the other modes. Then linear discriminant analysis (LDA) was independently used for locomotion recognition in every catalogue.

3.3 Performance Evaluation

Leave-one-out cross-validation (LOOCV) was employed for a convincing evaluation of classification error. The whole feature sets were divided into five sets. Four sets was used to train the classifier, while the rest one was used to evaluate it. Then the procedure was repeated five times to ensure that every sets was used once as testing data. Quantification of classification performance was represented by classification rate (CR) calculated by

$$CR = \frac{N_{cor}}{N_{total}} \times 100\% \tag{1}$$

where N_{cor} was the number of testing data that were classified correctly and N_{total} meant total number of testing data.

To detail classification performance between the certain targeted modes and the estimate results, we defined a confusion matrix by

$$C = \begin{pmatrix} r_{11} & r_{12} & \cdots & r_{1n} \\ r_{21} & r_{22} & \cdots & r_{2n} \\ \cdots & \cdots & \cdots & \cdots \\ r_{n1} & r_{n2} & \cdots & r_{nn} \end{pmatrix} \tag{2}$$

where elements were defined by

$$r_{ij} = \frac{n_{ij}}{n_{i\bullet}} \times 100\%. \tag{3}$$

n_{ij} referred to the number of testing data in mode i estimated as mode j. $n_{i\bullet}$ meant total number of testing data in mode i. r_{ij} indicated the rate of targeted mode i estimated as mode j. Especially when $i = j$, r_{ii} was the accuracy rate of task mode i.

4 Experiments with An Amputee

4.1 Participant and Experiment Protocol

This study was conducted with the informed consent of a below-knee amputee subject, who was free from neurological pathologies. The amputee subject was 45 years of age, 1.70 m in height and 71.0 kg in weight. He usually ambulated without external assistive device except his own prosthesis (a 0.25-m Ottobock 1S90 foot). The prosthetic foot was a kind of solid ankle cushion heel (SACH). Namely, there was no freedom in the ankle. In the experiment, the amputee subject wore a system shoe in the healthy foot, the other in the prosthetic foot. The subject was supposed to practice the tasks several minutes prior to experiment to fit in with the system.

Six locomotion modes were investigated: (1) sitting, (2) standing, (3) normal walking, (4) stepping over obstacles, (5) ascending stairs, (6) descending stairs. For the task of sitting, the amputee subject was instructed to sit on a 65 cm high chair for the convenience of his prosthesis. During standing task, the subject was required to stand still in every trial. For normal walking task, the subject was encouraged to walk straight at his daily walking speed. Obstacles were 40 cm wide, 25 cm deep and 18 cm high for the amputee subject for the sake of safety. The distance between two adjacent obstacles was 70 cm. The subject climbed a obstacle with amputated leg first according to his preference. The other leg followed to climb the same obstacle. A four-stair staircase was used for the task of ascending and descending stairs. The stairs were 75 cm in width, 40 cm in depth and 15 cm in height. Fig. 4 shows the ascending stairs by amputee subject. The subject performed one type of locomotion modes in each trial in the experiment. Each task was repeated. The locomotion mode would not change until 150 complete stride cycles were recorded. Rest periods were allowed between trials.

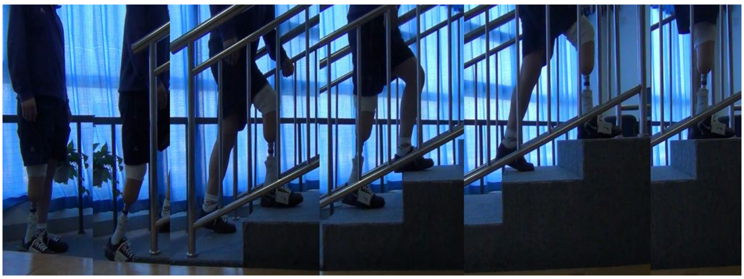

Fig. 4. Ascending stairs. The amputee subject takes the task of ascending stairs on a four-stair staircase.

4.2 Results

Results were achieved in the test processes mentioned above. The accuracy rates of classification in the four phases (Pre-FC, Post-FC, Pre-FO, Post-FO) were 99.05%, 99.01%, 98.64%, 96.82%, respectively. Overall classification results defined by confusion matrixes are shown in Fig. 5. As can be seen from Fig. 5, recognition performances in sitting and standing modes are remarkable to gain a classification accuracy 100%. Among the investigated locomotion modes, sitting and standing obviously differ from the others. As stillness modes, the signals of sitting and standing are time-invariant in a sense compared with the other modes signals. As a consequence, we defined the stillness feature to separate stillness modes from the others using decision tree analysis. It is so identifiable that the recognition performances in the two modes are perfect.

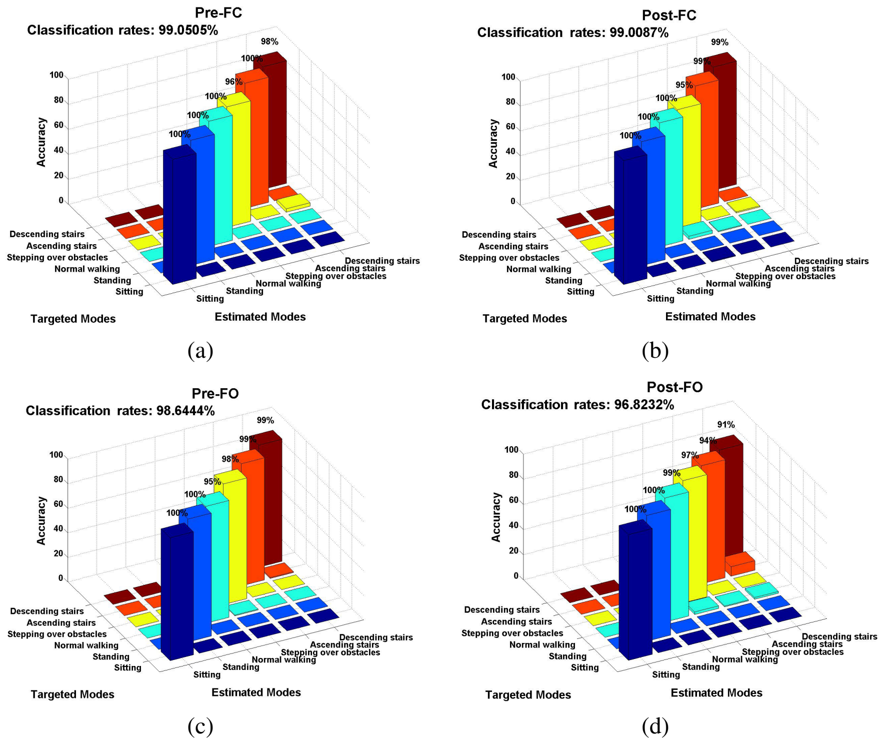

Fig. 5. Bar chart of confusion matrix indicating detailed recognition performance using plantar pressure signals in four phases. (a) Phase of Pre-FC (b) Phase of Post-FC (c) Phase of Pre-FO (d) Phase of Post-FO.

5 Conclusion and Future Work

In this paper, we have proposed a wearable plantar pressure measurement system to provide a new approach for locomotion mode recognition. The system showed competitive performances in recognition of daily locomotion modes for an amputee subject.

It was comparable to, if not better than, any other approach such as EMG based recognition [17].

In the future, continuous locomotion mode recognition based on plantar pressure analysis will be studied first. Control of powered prosthesis will be the following research core.

Acknowledgement. This work has been funded by the National Natural Science Foundation of China (No. 61005082, 61020106005), Doctoral Fund of Ministry of Education of China (No. 20100001120005) and the 985 Project of Peking University (No. 3J0865600).

References

1. Alexander, I.J., Chao, E.Y., Johnson, K.A.: The assessment of dynamic foot-to-ground contact forces and plantar pressure distribution: a review of the evolution of current techniques and clinical applications. Foot & Ankle 11(3), 152–167 (1990)
2. Cavanagh, P.R., Hewitt Jr, F.G., Perry, J.E.: In-shoe plantar pressure measurement: a review. The Foot 2(4), 185–194 (1992)
3. Orlin, M.N., McPoil, T.G.: Plantar pressure assessment. Phys. Ther. 80(4), 399–409 (2000)
4. Au, S.K., Weber, J., Herr, H.: Powered ankle-foot prosthesis improves walking metabolic economy. IEEE Trans. Robotics 25(1), 51–66 (2009)
5. Zhu, J., Wang, Q., Wang, L.: PANTOE 1: Biomechanical design of powered ankle-foot prosthesis with compliant joints and segmented foot. In: Proc. IEEE/ASME Int. Conf. Advanced Intelligent Mechatronics, pp. 31–36 (July 2010)
6. Zhu, J., Wang, Q., Huang, Y., Wang, L.: Adding compliant joints and segmented foot to bio-inspired below-knee exoskeleton. In: Proc. IEEE Int. Conf. Robotics and Automation, pp. 605–610 (2011)
7. Sato, T., Sakaino, S., Ohashi, E., Ohnishi, K.: Walking trajectory planning on stairs using virtual slope for biped robots. IEEE Trans. Ind. Electron. 58(4), 1385–1396 (2011)
8. Fan, R.E., Culjat, M.O., King, C., Franco, M.L., Boryk, R., Bisley, J.W., Dutson, E., Grundfest, W.S.: A haptic feedback system for lower-limb prostheses. IEEE Trans. Neural. Syst. Rehab. Eng. 16(3), 270–277 (2008)
9. Bamberg, S.J.M., Carson, R.J., Stoddard, G., Dyer, P.S., Webster, J.B.: The lower extremity ambulation feedback system for analysis of gait asymmetries: preliminary design and validation results. J. Prosthet. Orthot. 22(1), 31–36 (2010)
10. Chen, M., Huang, B., Xu, Y.: Intelligent shoes for abnormal gait detection. In: Proc. IEEE Int. Conf. Robotics and Automation, pp. 2019–2024 (May 2008)
11. Veltink, P.H., Liedtke, C., Droog, E., van der Kooij, H.: Ambulatory measurement of ground reaction forces. IEEE Trans. Neural Syst. Rehabil. Eng. 13(3), 423–427 (2005)
12. Yuan, K., Zhu, J., Wang, Q., Wang, L.: Finite-state control of powered below-knee prosthesis with ankle and toe. In: Proc. 18th IFAC World Congress, pp. 2865–2870 (August 2011)
13. Huang, B., Chen, M., Shi, X., Xu, Y.: Gait event detection with intelligent shoes. In: Proc. IEEE Int. Conf. Inf. Acquisition, pp. 579–584 (July 2007)

14. Shu, L., Hua, T., Wang, Y., Li, Q., Feng, D.D., Tao, X., Tao, X.: In-shoe plantar pressure measurement and analysis system based on fabric pressure sensing array. IEEE Trans. Inf. Technol. Biomed. 14(3), 767–775 (2010)
15. Kong, K., Tomizuka, M.: A gait monitoring system based on air pressure sensors embedded in a shoe. IEEE Trans. Mechatronics 14(3), 358–370 (2009)
16. Wen, J., Ding, Q., Yu, Z., Sun, W., Wang, Q., Wei, K.: Adaptive changes of foot pressure in hallux valgus patients. Gait Posture (in press, 2012), doi:10.1016/j.gaitpost.2012.03.030
17. Huang, H., Kuiken, T.A., Lipschutz, R.D.: A strategy for identifying locomotion modes using surface electromyography. IEEE Trans. Biomed. Eng. 56(1) (January 2009)

Human-Robot Interaction-Based Intention Sharing of Assistant Robot for Elderly People

Jeong-Yean Yang[1], Oh-Hun Kwon[2], Chan-Soon Lim[2], and Dong-Soo Kwon[2]

[1] Human-Robot Interaction Research Center
Korea Advanced Institute of Science and Technology
Daejeon, Korea
jyyang@robot.kaist.ac.kr
[2] Dept. of Mechanical Engineering
Korea Advanced Institute of Science and Technology
Daejeon, Korea
{kwonoh,limcs}@robot.kaist.ac.kr,
kwonds@kaist.ac.kr

Abstract. Intention reading has been considered as one of the essential issues in the field of human-robot interaction (HRI). Specifically, for the cooperation between human and robotic system a robot should be aware of a given situation and human intention, which necessarily requires high-level knowledge and balanced interaction. For the disabled and elderly peoples not familiar with manipulating robotic system, intention sharing between two different agents is preferable to accurate intention reading. In this paper, we focused on the intention sharing of human and robot assistant to improve the cooperation.

Keywords: component, Intention sharing, human-robot interaction, human-robot cooperation.

1 Introduction

Increasing the population ratio of elderly people, assistant robot that complements human's disability becomes the popular issue in robotics as an extension of rehabilitation robot. Considering premature development of robotic system, assistant robot has been focused on its functional purposes: robot-aided guiding for blind people, robot manipulator for disabled people, and so on.

In this paper, we focused on the robot aided vehicle for human walking. As described in Fig. 1, a walker is a common auxiliary device for elderly people who feel difficulty of walking by themselves. Its passive mechanical frame assists human in standing and walking. While the walking of a conventional walker device is human powered, the proposed system named Smart Walker has four motorized wheels and the active mechanism is controlled by force-feedback joystick and touch-based input command. The active actuation is designed for medical purpose of rehabilitation: lifting human from a bed and holding up human's weight during walking.

S. Lee et al. (Eds.): Intelligent Autonomous Systems 12, AISC 194, pp. 283–291.
springerlink.com

On the other hand, this robotic walker operates by human command and the uncertainty from human's hand becomes more important than typical passive typed devices. The misunderstanding of user intention and unnecessarily repetition of command changes are definitely more harmful with regarding to safety issues. In addition, elderly people are not familiar with informatics devices and the user group is physically handicapped persons. Thus, the robotic walker is a good example for an assistant robot through human-robot interaction (HRI) [1]. The robotic walker totally cooperates with human operation while it provides refined information considering the difficulty of user group.

In the proposed system, the feedback of a given command is divided into two areas. One is informative modalities such as visual, haptic, and auditory feedback, which are common in general robotic system. The other is physical movements of a robotic walker by controlling the motor driven wheels. With informative feedback, the cooperation in the robotic walker system enables an elderly people to reach where he wants to go.

Most elderly peoples who were born before 1950 feel difficulty of man-machine interface. They are not familiar with a computer-based operation and furthermore elderly people have less concentration for robot control owing to cognitive impairment. We assume that robot's intelligence and its smart behavior is absolutely preferable for elderly people. Moreover, human intention is not instantly observed. The human intention about where to go depends on the series of joystick commands. However, a robot only recognizes which direction a user wants to go. From the viewpoint of a robotic system, human's intention about where to go is not explicitly observed by joystick command and intention reading is achieved by understanding the relationships among a given situation. Furthermore, the interaction period is another issue. For instance, human feels surprise at sudden environmental changes while his happiness slowly changes during long term period.

Considering the cooperation between an elderly people and a robotic walker as described in Fig. 1, it is desirable that a robot system reads human's intention and automatically compensates human's control inputs in consistent way. This paper focused on intention reading by situation awareness and its sharing by extension of HRI method. Instead of autonomous locomotion problem [2], an assistant robot should understand which goal human heads, and it also estimates human intention properly. Thus, human preference about surrounding objects and rule-based user model are considered as landmarks for human's intention about where to go.

Reminding that the functionality of the robotic walker is the assistance of human locomotion, the frequent changes of human commands implies that two agents do not share the common intention. The control inputs from joystick correspond to local intention however an ultimate goal is not revealed in every instances. From the results of reasoning process during interaction, the robot system tries to estimate human intention. Additionally, assuming that elderly people are novices to visual feedback, the human friendly dialogs are designed to share the reasoning result by confirming human's intentional goal.

As a result, the goal of this approach is evaluated by the number of input commands that human changes his direction. The reduction of command changes implies that two agents cooperate with each other for moving toward equal goal positions by sharing intention respectively.

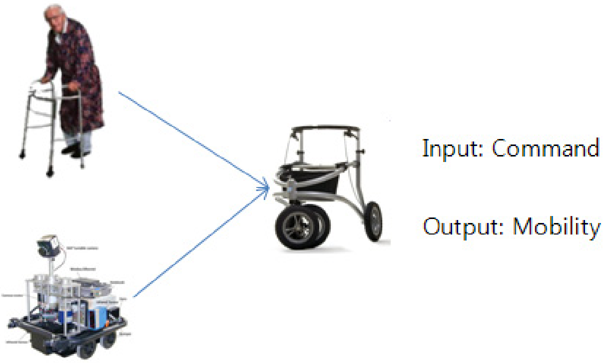

Fig. 1. Overview of the robotic walker

2 Intention Reading

The intention reading of the robotic walker is designed by rule-based reasoning model in the domain of locomotion behaviors [3~5]. An elderly people and a walker have several tasks such as approaching to other human or a specific position, going out of home, and doing exercise for rehabilitation. This domain covers the daily life of elderly peoples. In the Table 1, the keywords in the proposed domain are described. The keywords describe the symbolic representation that is possibly recognized by robot sensors with the help of position, emotion detection, touch sensors, and vision system-based object detection. For instance, going out task increases mental refreshment however also increases the possibility of getting cold. The objects at home include pet, cellphone, bed, and table of which each is related to other features. A cellphone induces more talking, which implicitly increases refreshment and reduces boring. A pet contributes to human's happiness while it requires laborious works that affects health. The network among keywords is directly or indirectly connected in complex manner and its effect for human's preferences is calculated by following connections. In this case, about one hundred rules are applied to describe the proposed domain.

Each rule increases or decreases designed factors such as emotion and preference. The exercise supports for better health however elderly people do not prefer it. In the proposed model, elderly people feel the highest preference from family keyword and the lowest from hunger. Every rules are defined for inducing other cases between [-1, 1], and minus one is the maximum negative value and one is the maximum positive value. While the direct relationship of keywords has the value between -1 and 1, the indirect relationship diminishes as in the manner of probabilistic network model. These rule sets are recursively calculated for estimating which and how much each keyword induces other keywords. In Fig. 2, the role of direct and indirect relationship is described. The health directly increases the preference and the exercise respectively while the exercise itself decreases the overall preference. In other words, the health is one of the preferable keywords for elderly people however the exercise decreases the preference even though the health increases the exercise. In our experiments, the left side of the table in Fig. 3 has a set of keywords and the right side corresponds to the queue for describing the current situation. For example, the keywords of home, pet, and friend indicates the preference over 4.

Table 1. Keywords defined in the proposed domain

Keywords
cellphone, talking, friend, pet, labor, dirt, touch, hit, friend, son, family, health, approach, collision, anger, hunger, boring, passenger, wallet, bed, sleep, table, wait, hunger, consumption, wealth, going out, refresh, satisfaction, tv, cold, home, happiness, exercise, fatigue, meal, noon, evening, supper, breakfast, lunch,

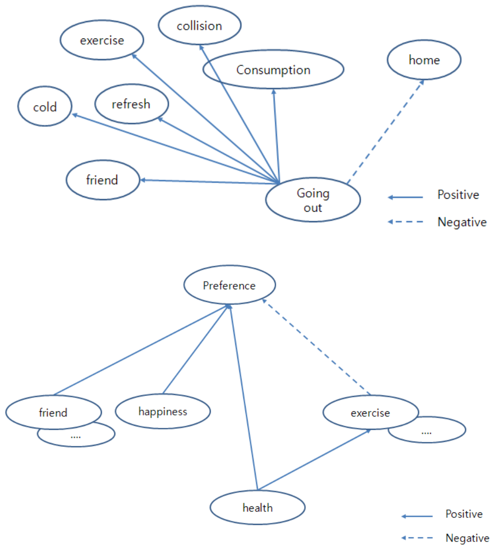

Fig. 2. Examples of rule sets about “going out” and “preference”

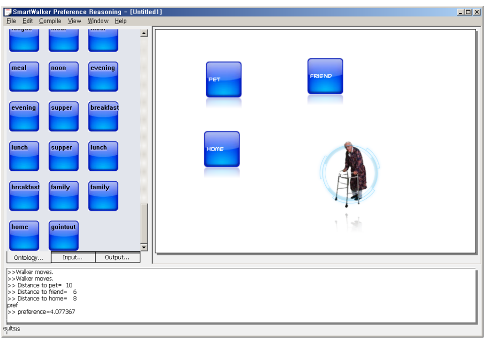

Fig. 3. Icon-based intention reading software environment

3 Intention Sharing

In the right part of Fig. 3, the robotic walker estimates the current intention of the user by observing surrounding situation. The observed keywords are stored into reasoning queue for estimating the current preference value. In an actual case, the effects of the symbolic keywords gradually diminish by passing away the given environment. While the robotic walker moves by keeping pace with a human, the roles of surrounding symbols are dependent on elapsed time and observation as they are forgotten at human brain.

The time constant has the maximum value when symbols are observed. As the robot walker moves, the observed symbols are added into the queue and their time dependent effects are also estimated by reasoning process. When the symbol disappears, its effect starts to decrease. The effect of time constant is multiplied by the positive and negative value of keywords. The lower time constant implies that the less effect of keywords stored in reasoning queue. Thus, the keyword meal has the longest time duration and it slowly increases hunger.

Assuming that the radius of observation is limited as described in Fig. 4, the surrounding symbols are related to the distance metric. The control inputs by joystick controls the moving direction of the robotic walker and the preference value from observed symbols are calculated for estimating the current human intention. As depicted in this example, the preference within observation bound indicates that the human intends to move toward pet by avoiding collision with the table. In this manner, the robot system estimates the user's current intention from the surrounding objects and situations, and finally the maximum value is estimated to be the user's intention.

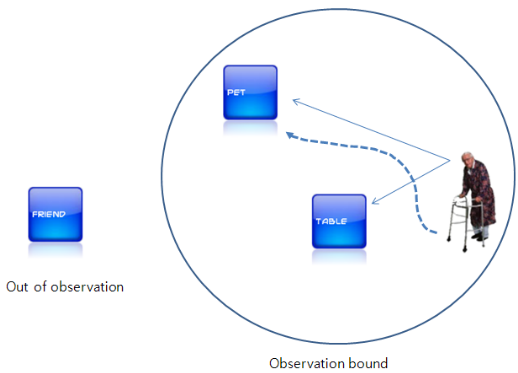

Fig. 4. Observation bound with respect to the relative distance from human to surrounding symbols

As a result, the user's command is affected by the results of intention reading estimated for maximizing preference. Our basic assumption implies that the frequent meaningless command can be reduced by intention sharing. When an obstacle is detected, the robotic walker determines to avoid it slowly by reasoning process. The abrupt changes of trajectory increase user's confusion so that the direction vector is gradually changed toward higher position. It is suitable condition because human and walker system are designed for slow locomotion. For the walking toward far position, the small effect of avoidance is being continuous before near the target positional symbol. However, it is the shortcoming that the intention reading is restricted within the observation bound. Our intention reading depends on the observation queue that stores the order of symbol appearance. It indicates that the intention within long-term operation cannot be estimated. For example, if the friend in Fig. 4 is the ultimate goal, the proposed intention reading does not explain the long-term locomotion.

On the other hands, intention sharing is designed for improving interactivity between both agents [6]. The vector difference between human's intentional direction and robot's estimated direction implies the disagreement of intention. When human starts going out task in order to meet his friend, the goal of the task cannot be exactly estimated owing to the limitation of unseen observation. Thus, the vector difference becomes larger when both agent's intention grows much disagreement. In the proposed rule-based model, the going out keyword induces the positivity of friend, exercise, health, and collision. Therefore, the reasoning model creates queries about what the real reason of the current task is. The candidates are chosen by user's additional input, and then its preference model is reconstructed by considering the friend in remote site and the objects in local site. The subtask that generates query of the hidden intention, contributes to reduce the difference of vector direction related to disagreement of intention. It is described in Fig. 5.

The reasoning of the long-term task is related to the history of the state transitions. Thus, in many cases the reasoning of symbolic queue in the proposed method is not sufficient for history-based reasoning. However, the superiority of reasoning in long-term period is still being questionable. Considering that the major purpose of the walker is not carrying people but assisting their walking, thus the interaction at the local site seems to be more desirable for practical purpose.

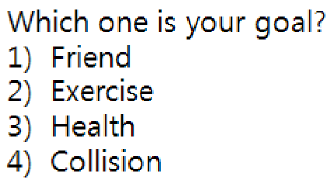

Fig. 5. Query example for sharing real intention. The current task "going out" induces the above four candidates.

4 Experimental Results

The experimental systems are composed of PC-based architecture for controlling the robotic system and reasoning a given environment. The movement of the robotic walker is controlled by touch-based joystick inputs. For convenience, the motion is changed by up, down, left and right command. In addition, Android-based small tablet that provides touch, display, and sound generation is used for displaying dialog and transferring user's command input. These two different types of systems are connected with USB cable and TCP/IP-based network connection is used with the help of bridge function.

The reasoning process about metaphysical features is estimated as described in Table. 2. In this case, the keyword family has the maximum preference. Among a hundred of rules, the keyword family is the most positive thing to induce happiness, talking reducing boring, and so on.

In table 3, many keywords for positive and negative preference are introduced. It is suitably matched with the people's common sense such that the keyword going out increases refreshment and possibility of meeting friend however it also increases diseases and consumption. In the rule set, the hunger induces the anger and decreases the health. Therefore, it has the lowest preference in this domain.

In table 4, the effect of intention sharing is testified. When the overall moving area is not so large and the area is nearly same with the observation area, the effect of intention sharing is not evidently shown. However, in the case of three times larger than the observation area, intention sharing shows better performance for estimating an ultimate goal. Considering that our test does not guarantee the global locomotion, the effect of querying the ultimate goal contributes to reduce the occurrences of disagreement.

Unfortunately, in this preliminary research the role of time elapsing is not clearly shown. In our guess, the working period with a given test space is too short for the time-based interaction to make sufficient effects for intention reading.

Table 2. Reasoning Result

Keywords	*Most Positive*	*Most Negative*
Preference	Family(3.1)	Hunger(-3.1)
Happiness	Home(7.8)	Dirt (-0.7) Consumption(-0.7)
Health	Meal(6.2)	Hunger(-2.0)
Exercise	Going out (3.0)	Sleep(0.4) Wait (0.4) Fatigue(0.4)
Boring	Home (5.2)	Goingout (0.5) Pet (0.5)
Hunger	Going Out (6.4)	Wealth(-1.0)
Talking	Home(5.6)	Sleep(0.4) Wait (0.4) Fatigue(0.4)

Table 3. Preference Result

Keywords	*Preference*
Friend	1.34
Goingout	-0.53
Exercise	-2.24
Talking	0.49
Pet	0.74
Family	3.06
Hunger	-3.1
Home	1.99

Table 4. Reasoning Result

	Average Number of Abrupt Input Changes In Local Area (Within Observation Bound)	*Average Number of Abrupt Input Changes in Wide Area*
Intention Reading w/o sharing	13/100	42/100
Intention Reading w/ sharing	9/100	19/100

5 Conclusion

In this paper, we focused on the effect of intention reading and sharing issues. The human intention is estimated by the typical rule-based reasoning process of the surrounding observed objects. The result of recognized situation is shared by query system in order to confirm walking direction. In many cases, intention reading is the proper solution for a robot to aware the current situation. Therefore, a robot is eager to understand human's real intention and a robot determines the better interaction way.

In the proposed experiment, we focused on the intention sharing and how it improves the interaction performance. The disagreement between two agents is evaluated by counting the abrupt command changes. The comparison between the human command and robot's estimated direction easily indicates the interaction failures. We tried to improve the interaction and focused on when both agents disagree to each other.

As expected, intention sharing is more efficient method for specifically cooperative behaviors. This system still has the possibility of amplifying the user's confusion caused by robot autonomy. Moreover, in further works, the intention sharing in multiple stages becomes the interesting issues for determining what questions will be more effective during overall interaction.

Acknowledgment. This project is financially supported by the Ministry of Knowledge and Economics through the research of "ADL support system for the elderly and disabled people" .

References

[1] Cao, Y.U., Fukunaga, A.S., Kahng, A.B.: Cooperative Mobile Robotics: Antecedents and Directions. Autonomous Robots 4, 1–13 (1997)

[2] Li, J., Pan, Q., Hong, B.: A New Approach of Multi-Robot Cooperative Pursuit Based on Association Rule Data Mining. International Journal of Advanced Robotic Systems, 329–336 (2010)

[3] de Barreto, G.A., Araujo, A.F.R., de Rosa, M.O.: A Reactive Rule –based System for Trajectory Planning of a Mobile Robot. In: Proc. of the IASTED/AAAI Conference on Artificial Intelligence and Soft Computing, pp. 419–422 (1998)

[4] Ciliz, M.K., Isik, C.: Fuzzy rule-based Motion Controller for an Autonomous Mobile Robot. Robotica 7, 37–42 (1989)

[5] Kim, D.J., Song, W.K., Han, J.S., Bien, Z.Z.: Soft Computing-based Intention Reading Technique as a Means of Human-Robot Interaction for Human Centered System, Soft Computing- A Fusion of Foundations, Methodologies, and Applications, vol. 7(3), pp. 160–166 (2003)

[6] Tomasello, M., Carpenter, M., Call, J., Behne, T., Moll, H.: Understanding and Sharing Intentions: The Origins of Cultural Cognition, vol. 28, pp. 675–735 (2005)

Human Tracking Using Improved Sample-Based Joint Probabilistic Data Association Filter

Nanyang Liu, Rong Xiong*, Qianshan Li, and Yue Wang

State Key Laboratory of Industrial Control Technology,
Zhejiang University,
Zheda Road 38, Hangzhou, 310027, China
rxiong@iipc.zju.edu.cn

Abstract. The human tracking problem is a hot issue in human-robot interaction, in which a conventional algorithm sample-based joint probabilistic data association filters (SJPDAF) is widely used. In this paper, the algorithm is first extended to the situation of multi-sensor fusion and then accelerated to promote the real-time performance. The simulation and experiments on robots both show good results, reflecting the robust and the accuracy of our improved SJPDAF.

Keywords: human tracking, multi-sensor fusion, SJPDAF.

1 Introduction

In the field of human-robot interaction, human tracking is a hot issue which has wide application in domestic service and military robots.

Human tracking mainly consists of human detection and tracking, both attracting the focus of the research. Schulz and Burgard proposed a sample-based joint probabilistic data association filters (SJPDAF) to realize the multi-targets tracking, which had been applied to human tracking successfully [1]. In [2], Gockley and Hemachandra achieved human detection by detecting legs of target human. To make the tracking behavior of a robot more like the human, Erwin Prasler presented a method to compute the trajectory by combing the motion ability of robot and predicted target location [3]. In [4], the trajectory was computed using artificial potential field. The sensors in these methods are all single laser scanner, which is vulnerable to objects with a similar geometric appearance with human, leading to tracking failure. The performance of human detection with laser scanner and camera are compared in [5], but the sensor information fusion is not investigated.

In this paper, the sensor detection models are added into SJPDAF to unify the measurement framework, realizing the multi-sensor fusion in human tracking. Besides, the efficiency of the multi-sensor SJPDAF is improved as well as the accuracy of tracking.

* Corresponding author.

S. Lee et al. (Eds.): Intelligent Autonomous Systems 12, AISC 194, pp. 293–302.
springerlink.com

The remainder of the paper is organized as follows: the SJPDAF algorithm is introduced in Section 2. The main contribution, multi-sensor fusion and efficiency improvement, is proposed in Section 3 and 4. In Section 5, the experimental on a domestic service robot is shown, followed by the conclusion in Section 6.

2 Background

In general, there may exist some disturbances besides the human, which should all be regarded as targets to track, in order to avoid confusion. To realize this goal, the joint probability density function (pdf) of all targets, i.e. disturbances and human, should be estimated. Based on the joint probabilistic data association filters (JPDAF), the SJPDAF was developed with its crucial step finding the association between measurements and targets [1], [7]. Here for fluent explanation, the JPDAF is first introduced.

Suppose there are n_t targets and m_t measurements at time t. The set of all targets is defined as $X(t)=\{x_1(t) \ldots x_{nt}(t)\}$, where $x_i(t)$ indicates the ith target at time t. $Z(t)=\{z_1(t) \ldots z_{mt}(t)\}$ denoted as the set of measurements from time 0 to t, where $z_j(t)$ is the jth measurement at time t. The association set is then defined as θ. In JPDAF, the association probability β_{ji} is computed as

$$\beta_{ji} = \sum_{\theta \in \Theta_{ji}} [\alpha \prod_{(j,i)\in\theta} \int p(z_j(t) \mid x_i(t)) p(x_i(t) \mid Z(t-1)) dx_i(t)] \tag{1}$$

where Θ_{ji} is the set of all possible events that associate the measurement j with the target i while α, the normalizer. Based on the association probability, the posterior pdf of target i can be estimated.

$$p(x_i(t) \mid Z(t)) = \alpha \sum_{j=0}^{m_t} \beta_{ji} p(z_j(t) \mid x_i(t)) p(x_i(t) \mid Z(t-1)) \tag{2}$$

In SJPDAF, the particle filter $S_i(t)$ is employed with K particles at time t for target i. A particle is denoted as $s_i^k(t)$ ($k = 1 \ldots K$). Then the algorithm is given with three steps as follows:

1) Predict the particles in previous time step.
2) Compute the association probability β_{ji} using (3).
3) Estimate the target at current time step using (2).

The sample-based association probability is computed as:

$$\beta_{ji} = \sum_{\theta \in \Theta_{ji}} [\alpha \prod_{(j,i)\in\theta} \frac{1}{K} \sum_{k=1}^{K} p(z_j(t) \mid x_i^k(t))] \tag{3}$$

At time t, the kth particle of target i has a weight $\omega_i^k(t)$ defined by:

$$\omega_i^k(t) = \alpha \sum_{j=0}^{m_t} \beta_{ji} p(z_j(t) \mid x_i^k(t)) \tag{4}$$

The SJPDAF shown above only considers the measurement model of the sensor $p(z_j(t) | x_i^k(t))$, while the detection model is not combined. In the case of multi-sensor, especially different kind of sensors, (3) is obviously inappropriate, inspiring us to build a unified framework for better modeling of the multi-sensor result fusion, extending the SJPDAF to a more general situation.

3 Sensors Detection Model and Fusion

For single sensor, conventional SJPDAF algorithm is enough, regardless of the detection model. When it comes to the multi-sensor situation, the detection cannot be ignored as they are not the same for different sensors. In this section, human detection with laser scanner and depth camera are first presented, followed by the analysis on detection model. The fusion method is given finally.

3.1 Human Detection Techniques

Detection with laser scanner is realized by detecting a part of the human body, such as legs and breast. Methods dealing with these problems mainly include baseline detection, curve fitting and machine learning [8]. We propose an arc fitting method as follows:

1) Sort the raw data from laser in the order of measurement angle and filter them by median filtering, acquiring a data set L.
2) Search the W-neighborhood of each data point: if a point $l(i)$ satisfy

a. there exists a point $l(j)$ such that $l(j) - l(i) > l_{sup}$
b. for any point $l(k)$ such that $l(j) - l(i) > l_{inf}$

then label it in L. Here l_{sup} and l_{inf} are thresholds while W, determined by the scale of human.

3) In L, search point sequences that are labeled continuously. It was considered as a human if the number of points in sequence $N(C)$ satisfy

$$N_{\text{sup}} > N(C) > N_{\text{inf}}$$

where N_{sup} and N_{inf} are thresholds. Generally, N_{sup} can be set to $2W$. An illustration of the method is shown in Figure 1.

To realize the detection with depth camera, we apply the face detection method based on AdaBoost proposed by Viola [6] to the head and shoulder detection of the target human.

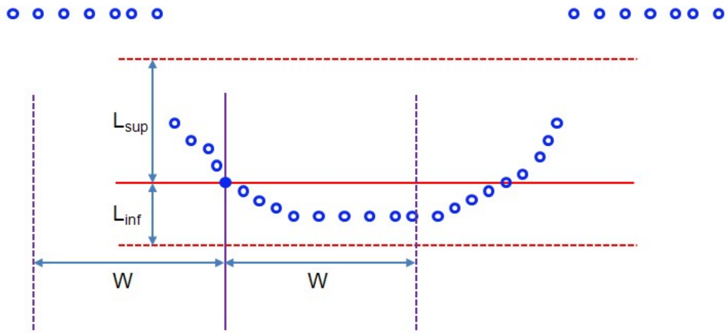

Fig. 1. Human detection with the laser scanner

3.2 Sensor Detection Model

It was shown in [9] that the detection probability is related to the intensity of the sensor signal. Denote the signal intensity at target $x_i(t)$ as I. The received signal of sensor α is then denoted as $I_\alpha(x_i(t))$. In practice, the intensity of the received should be $I_\alpha(x_i(t)) + \varepsilon_\alpha(t)$ where $\varepsilon_\alpha(t)$ is the noise in $N(0,\sigma^2_{t,a})$. Now the sensor detection model is defined as

$$D_a(t) = \begin{cases} 1 & if\, I_a(x_i(t)) + \varepsilon_a(t) > T_a \\ 0 & otherwise \end{cases} \tag{5}$$

where T_a is the threshold of the sensor. Define $E(x_i(t)) = I_\alpha(x_i(t)) - T_a$, the probability of successful detection can be evaluated as

$$\begin{aligned} p_a(x_i(t)) &= p(I_a(x_i(t)) + \varepsilon_a(t) \geq T_a) \\ &= 1 - \int_{-\infty}^{-E(x_i(t))} \frac{1}{\sigma_{t,a}\sqrt{2\pi}} \exp(-\frac{z^2}{2\sigma^2_{t,a}}) dz \end{aligned} \tag{6}$$

For target X_t, the likelihood of detection model is

$$\begin{aligned} L(D_a(t) = 0 \mid x_i(t)) &= 1 - p_a(x_i(t)) \\ &= 1 - \int_{-\infty}^{-E(x_i(t))} \frac{1}{\sigma_{t,a}\sqrt{2\pi}} \exp(-\frac{z^2}{2\sigma^2_{t,a}}) dz \end{aligned} \tag{7}$$

and

$$L(D_a(t) = 1 \mid x_i(t)) = p_a(x_i(t)) \tag{8}$$

In the case of laser scanner, the width of detected human $N(C)$ can be regarded as the intensity of signal, i.e. $I_\alpha(x_i(t))= N(C)$. Then, the difference between $N(C)$ and $2W$ is in Gaussian distribution, where $2W = k/L$ with L and k being the distance between robot and human and a constant. So the likelihood of laser scanner is

$$L(D_a(t)=1\,|\,x_i(t)) = \frac{1}{\sigma_{t,a}\sqrt{2\pi}}\exp(-\frac{(N(C)-2W)^2}{2\sigma_{t,a}^2}) \tag{9}$$

In the case of depth camera, the likelihood is defined as $L(D(t) = 1 \mid X_t) = 1$, since the probability of results given by each classifier in AdaBoost are all 1.

3.3 Multi-sensor Fusion

The sensor returns the measurement when a target is detected, i.e. $Da(t) = 1$. And the detection and measurement are independent. When no target is detected, the sensor returns $Da(t) = 0$. So the likelihood of the measurement returned by sensor a is

$$L(z_a(t)\,|\,x_i(t)) = p(z_a(t)\,|\,x_i(t)) \tag{10}$$

the likelihood of response returned by the sensor a can be defined as

$$L(D_a(t)=1, z_a(t)\,|\,x_i(t)) = p_a(x_i(t))\,p(z_a(t)\,|\,x_i(t)) \tag{11}$$

At time t, the detection results $D(t)=\{D_1(t) \ldots D_A(t)\}$ are returned by A sensors , their corresponding measurements are $z(t)=\{z_1(t) \ldots z_A(t)\}$. As the sensors are independent, the fusion likelihood can be computed by multiply all likelihoods together, shown as

$$L(D(t), z(t)\,|\,x_i(t)) = \prod_{a=1}^{A} L(D_a(t)\,|\,x_i(t)) \prod_{a=1}^{A} L(z_a(t)\,|\,x_i(t)) \tag{12}$$

Based on (12), (3) can then be modified to

$$\omega_i^k(t) = \alpha \sum_{j=0}^{m_t} \beta_{ji}\, p(L(D(t), z_j(t)\,|\,x_i^k(t))\,|\,x_i^k(t)) \tag{13}$$

which completes the derivation of the multi-sensor fusion based on the likelihood.

4 Algorithm Acceleration

The joint pdf computation in SJPDAF is relatively complex. For the sake of acceleration, we improved the methods to compute the association probability β_{ji}. Suppose the number of targets is H, a permutation matrix P with dimension $H!\times H$ is computed, of which each row is a combination of measurement and target. Then an association probability matrix B is introduced, defined as

$$B = \begin{bmatrix} b_{11} & \cdots & b_{n1} & b_{1in} \\ \vdots & \ddots & \vdots & \vdots \\ b_{1m} & \cdots & b_{nm} & b_{\min} \\ b_{1out} & \cdots & b_{nout} & b_{(m+1)(n+1)} \end{bmatrix} \tag{14}$$

where m and n are the abbreviation of m_t, the number of measurements in current time step, and n_{t-1}, the number in previous time step. b_{nm} is the association probability between measurement m and target n. b_{1out} … b_{nout} are the probability that a target is missing currently. b_{1in} … b_{min} are the probability that a new target occurs. Note that $b_{(m+1)(n+1)}$ is meaningless, need not to be computed. Based on the permutation matrix and association probability matrix, β_{ji} can be computed when multi-sensor are implemented by following steps:

1) Suppose there are two sensor a_1 and a_2 with number of measurements being n_{a1} and n_{a2}, the total number of combinations will be $n_{a1}\times n_{a2}\times(n_{a1}-n_{a2}+1)$. Denote the set of combination as Y, the likelihood of each combination y, $y\in Y$ can be computed by (9).

$$p_{P_{ji}i} = \prod_{a=1}^{A} L(D_a(t)\mid x_i(t)) \prod_{a=1}^{A} L(z_{P_{ji},a}(t)\mid x_i(t)) \tag{15}$$

2) For each combination, the corresponding target should be found. For P_{ji}, when $i \le n$ and $P_{ji} \le$ m, the corresponding probability in B is b_{Pjii}. When $i > n$ and $P_{ji} \le m$, the corresponding probability is b_{Pjiin}. And when $i \le n$ and $P_{ji} > m$, the corresponding probability is p_{iout}. Based on (12), a combination $p_{\max}$ with maximum probability can be obtained by comparing the product p_{Pj} of each row of P.

$$p_{P_j} = \prod_{i=1}^{H} p_{P_{ji}i} \tag{16}$$

3) An sensor combination with maximum probability $P_{max,y}$ can be found by comparing sensor combinations c and corresponding $p_{Pmax,y}$, determining the association between targets and measurements and combination of sensors.

By computing β_{ji}, the particle set of each target i is associated to a measurements, and can be updated by (11). The goal of the robot is to keep tracking the main target, which may disappear for a moment due to the occurrence of disturbances. So when the main target disappears, the corresponding set of particles is saved for future determination that whether a new target is the main target.

5 Experimental Results

5.1 Complexity Analysis

Suppose the maximum number of target to track is H. Computation of $p(z \mid x)$ takes time t_1, computation of product of each row of P takes time t_2 and searching the combination with maximum probability takes time t_3. Denote K as the number of particles. Then the conventional SJPDAF takes time T_1 to update the weight of particles, where T_1 is

$$T_1 = H! \times K \times t_1 + H^2 \times t_1 \tag{17}$$

Denote the time taken by the proposed SJPDAF as T_2

$$T_2 = H^2 \times t_1 + H! \times t_2 + (H! - 1) \times t_3 + H \times K \times t_1 \tag{18}$$

When $H > 1$

$$\begin{aligned} T_1 - T_2 &= H! \times K \times t_1 - H! \times t_2 - (H! - 1) \times t_3 - H \times K \times t_1 \\ &= H! \times (K \times t_1 - t_2 - t_3) > 0 \end{aligned} \tag{19}$$

$$\begin{aligned} \frac{T_1}{T_2} &= \frac{H! \times K \times t_1 + H^2 \times t_1}{H^2 \times t_1 + H! \times t_2 + (H! - 1) \times t_3 + H \times K \times t_1} \\ &\geq \frac{H! \times K \times t_1}{H! \times t_2 + (H! - 1) \times t_3} \approx K \end{aligned} \tag{20}$$

According to (19), in the situation of multi-target tracking, it can be found that the efficiency promotion is obvious when the number of targets (H) or the number of particles (K) is big. The time consumed by conventional SJPDAF is K times than that taken by proposed SJPDAF when the number of particles is K based on (20).

In the case of multi-sensor, take 2 sensors for example, the number of targets detected by the first sensor is denoted as H, while the second, H_1. Suppose that $H > H_1$, the total run time of conventional SJPDAF is

$$Td_1 \approx (H + H_1) \times (H + H_1 - 1) \times \cdots \times (H + 1) \times T_1$$

$$Td_2 = H \times (H - 1) \times \cdots \times (H - H_1 + 1) \times Td_2$$

Apparently, the proposed SJPDAF shows a better performance in efficiency according to (20).

5.2 Simulation

The simulation of conventional SJPDAF and improved SJPDAF are conduct on MATLAB. The indicator of comparison is RMS, which is defined as

$$RMS = \sqrt{\frac{1}{MT} \sum_{m=1}^{M} \sum_{t=1}^{T} (\hat{x}(m,t) - x(t))^2 + (\hat{y}(m,t) - y(t))^2} \tag{21}$$

where M is the number of simulations, T is the number of time steps, $\hat{x}(m,t)$ and $\hat{y}(m,t)$ are the least square estimation of target at time t in Mth simulation. $x(t)$, $y(t)$ are the true position of the target at time t. The configure of the simulation are $M = 50$, $T = 150$, $H = 6$ and $K = 20$. The sensing region of laser scanner is set as a semicircular region with a radius 10m cantering on the robot.

The results shown in Table 1 indicate that the SJPDAF combined with detection model is better than the conventional SJPDAF at all tested velocities. Especially when the human motion is slow, the improvement is obvious. As the human motion is usually random walking with velocity ranging from 0m/s to 1m/s, the improved SJDAPF is better. The simulations above are implemented on the single laser range finder. Here goes the simulation of fusion of laser scanners and depth camera. Compared to the former, the latter has a lower detection precision. The effective distance of the detection is set to 4m with perspective about 20 degree. Here a confidence parameter λ is added to represent the error detection. The confidence of laser scanner is $\lambda_l = 0.5\lambda_m$ while the depth camera, λ_m. And the error parameter is $\varepsilon_l = 0.5\varepsilon_m$ while the depth camera, ε_m.

Table 1. The average results of the experiment

	v=0.4m/s	v=0.4m/s	v=0.4m/s
With fusion model	29.2593	11.1841	3.0153
Without fusion model	6.4935	5.5135	2.8564

Fig. 2 shows the comparison between the case of single sensor and multi-sensor including the trajectories of the robot in tracking. The accuracy is lower due to the missing of the target when only laser scanner is used. The corresponding indicator, RMS = 10.9984. When for multi-sensor, the precision seems to be slightly bigger, but the accuracy is much better, leading to a smaller corresponding indicator, RMS = 5.2974.

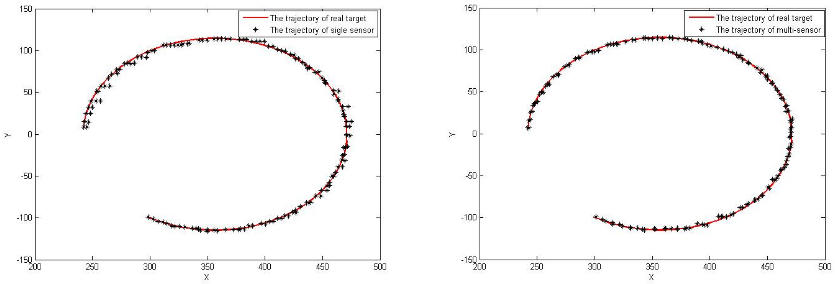

Fig. 2. Performance comparison among multi-sensor fusion and single sensor

5.3 Robot Experiments

The indoor human tracking system is implemented on our robot named ZJUPanda. The laser scanner and depth camera are both equipped as the input sensors. The laser scanner is HOKUYO UTM-30LX on the breast of the robot with an effective range of 30m and an angular resolution of 0.25 degree. The curve fitting method introduced in Section 3 is employed for human detection. The depth camera is MESA SR4000 on the head of the robot to realize the head shoulder detection of human. Besides, a laser scanner SICK-100 with an effective range of 8 and an angular resolution of 0.5 degree is employed for obstacle avoidance. As the data rate of depth camera is slower than that of the laser scanner, the fusion algorithm is triggered when a new frame of depth data comes. Otherwise, the target is detected only based on the range data.

The test is shown in the figures. The map of the environment is not built and there exists disturbances. Obstacles on the ground are chairs, desks and so on. The pillars in the environment have impact on the detection. When the target human walks near the pillar, it will fail with high probability. So the multi-sensor fusion is significant. The Fig. 3 shows the human tracking and obstacle avoidance. During the tracking, there are disturbances walking across the robot and target human, which is overcome with SJPDAF. The multisensory implementation improves the detection rate and robust to noise. As shown in figures, the robot can track a human in a narrow space. Because the depth camera is employed, the front and side of the human can both be tracked.

Fig. 3. Human following in populated environment by ZJUPanda robot

6 Conclusion

In this paper, the SJPDAF is investigated and extended to the situation of multi-sensor fusion. The laser scanner and depth camera are set as the example to show the feasibility of our improved scheme. Then an acceleration method is proposed to promote the efficiency by using the permutation matrix and association probability matrix. The simulation and robot experiments both show satisfactory results.

Acknowledgements. This work is supported by the National Nature Science Foundation of China (Grant No. NSFC: 61075078).

References

1. Schulz, D., Burgard, W., Fox, D.: People tracking with a mobile robot using joint probabilistic data association filters. International Journal of Robotics Research, IJRR (2003)
2. Gockley, R., Forlizzi, J., Simmons, R.: Natural person-following behavior for social robots. In: HRI (2007)
3. Prassler, E., Bank, D.: Boris Kluge. Motion coordination between a human and a mobile robot. In: Proc. of the International Conference on Intelligent Robots and Systems, IROS (2002)
4. Hoeller, F., Schulz, D., Moors, M., Shneider, F.E.: Accompanying persons with a mobile robot using motion prediction and probabilistic roadmaps. In: International Conference on Intelligent Robots and Systems, San Diego, USA (2007)
5. Kraubling, A., Schulz, D.: Data fusion for person identification in people tracking. In: International Conference on Information Fusion, Cologne, Germany (2008)
6. Viola, P., Jones, M.: Rapid object detection using a boosted cascade of simple features. In: International Conference on Information Fusion, Cologne, Germany (2008)
7. Bar-Shalom, Y., Fortmann, T.E.: Tracking and data association. Mathematics in Science and Engineering. Academic Press (1988)
8. Arras, K.O., Martinez Mozos, O., Burgard, W.: Using boosted features for the detection of people in 2d range data. In: Proc. of the IEEE Int. Conf. on Robotics and Automation, Rome, Italy (2008)
9. Yang, X., Pan, Q., Liang, Y., Wen, M.: Multi-sensor fusion tracking based on particle filtering and detection information. Control Theory and Applications 34(3) (2005)

Research on the Personalized Interaction Model Driven by User Behavior

Gu Xuejing[1,2], Wang Zhiliang[1], and Wang Chuanqi[2]

[1] School of Information Engineering
University of Science and Technology Beijing
Beijing, China
guxuejing@sina.com
[2] School of Electrical Engineering
Hebei United University
Tangshan, China

Abstract. An algorithm for extracting emotional drive parameters, as well as a prototype system for avatar which applied in the intelligent teaching based on user's interaction behavior have been posed, according to the multi-layer fuzzy comprehensive evaluation rule and Weber-Fechner law. It has been proved that the personalized emotional drive model would be beneficial to improve the user's experience in PAD Dimensions during the process of teaching interaction, by comparing the statistical score of PAD emotional scale in Chinese Express Edition.

Keywords: Human Computer Interaction, affective model, fuzzy comprehensive evaluation, Weber-Fechner law, PAD Dimensions.

1 Introduction

With the improvement of the computer, network, and multi-media technique, it enables that HCI shifts from the mode that human accommodates to machine to the mode that machine accommodates to human gradually, namely to provide the sufficient liberty to users. The requirement for the system should not only be suitable for the human's operation, but also meet the demands of human's aesthetic appreciation and cognition, as well as possessing the abilities such as listening, reading and speaking. Furthermore, the user should be able to communicate with the computer with the natural methods such as language, words, image, gesture and expression, like natually comminicating with another people. Therefore, the research on the avatar has been becoming the focus that has been paid more attention to by the researchers, various system based on HCI have been developed and been used in the domain of e-commerce, cyberchat, E-learning, games, tour conductor, online help, etc. One character of the avatar is that it is able to communicate with the real people via the humanlike natural style. However, one of key technologies of the natural interaction is the ability to supporting Affective-based HCI. It is well known that the comunication and interaction among the human is natual and rich in emotion, however, the computer does not have the ability of

S. Lee et al. (Eds.): Intelligent Autonomous Systems 12, AISC 194, pp. 303–310.
springerlink.com

emotion, and it hardly has the intelligence which is similar to the human's. Thus, HCI would hardly function in real harmonious and natural. Therefore, during the processing of HCI, it would be expected that the computer has the natual harmonious and emotional interaction abilities[1].

In the past 20 years, the various emotional or affective models that be used to support HCI such as A Control Model Based on Artificial Emotion for Anthropomorphic Robot[2], Formal Model of Emotional Agent[3], the comprehensive computable modeling method for virtual agents[4], modeling method forlearning system of the affective robort in multi mechanism[5], the autonomic Agent—Petra emotional model based on multi-layer Emotional process theory[6], etc, have been proposed by many researchers in various domains, such as cognitive science, artificial intelligence, HCI, robort, computer game, and so on. However, with the continuing research on the questions for emotional modeling, some 'confusions' have been emerged. Just as Eva Hudlicka said that the current questions for emotional modeling lacked of the fundamental clearness and the veracity, during the design processing, there was nearly no order could be followed. Meanwhile, she also mentioned that the artificial emotional model should care about 2 prime attributes, namely, the activation of emotion and the influence of emotion. By acknowledging and analyzing the multimode attribute of emotion objectively, she proposed to adopt the emotional psychology theory into artificial emotion modeling, among this, there should be quantity job be accomplished by the researchers in the domain of artificial affection. In addition, the relationship between the external stimuli and the activation emotion should be one of the major research contents[7].

In this paper, the related factors of the external stimuli signals which could influence the emotion driving have been discussed. Meanwhile, the mapping relation between stimuli and activation emotion has been expressed with HMM. according to the multi-layer fuzzy comprehensive evaluation rule and Weber-Fechner law, a kind of algorithm for extracting emotion activation parameter based on HCI character has been posed. The parameter would be used as the input for affective model in HMM, in order to generating affective feedback during interaction, and being adopted into avatar prototype system of the inteligent teaching. By the psychological physics experiment based on PAD (pleasure-displeasure, arousal-nonarousal, dominance-submissiveness), it is clear that the designed affective model in the paper enables to promote the user's positive emotion, arousal degree, and dominance during the process of intelligent teaching interaction.All these enable to provide a kind of design method in theoretical for humanizing HCI.

2 Extracing Parameter for Affective Drive

The humanizing HCI requires the machine is able to recognize the various kinds of natural behaviors initiatively, according to the context and the user's characteristics, as well as to figure out the user's interaction, further, to respond intelligently, since the affection is one of the major factors of the intelligence, the machine ought to possess the ability for affection interaction, in another word is that the machine must be able to extract the characteristic factors which would influence the interactive affection, from the natural behaviors of human. All these parameters would be accumulated, then to generate affective impress and affective response. The behavior factors that could effect the interactive affection are abundant. According to the different application, their range of values would be reduced from a certain extent; however, these are still sophisticated.

Fuzzy comprehensive evaluation is a kind of efficient decision-making method in multi-factor for comprehensively estimating object which influenced by different factors. The feature of this method is that the estimated result would be stated as a fuzzy set instead of providing the result in absolutely affirmative or absolutely negative. This is beneficial to describe the characteristic of imprecision of affection. Thus, the method for extracting parameter of affection drive based on fuzzy comprehensive evaluation rules has been proposed.

In the sophisticated HCI system, there are many influence factors of affection that need to be considered, and among the factors, there are some hierarchical layers. To avoid the problems that caused by the values of the evaluation matrix are in relatively less, such as less prominent of the key factors and the parametric equalization, the various factors would be classified into different layers according to their interdependences. Each layer would acquire an estimated result according to the fuzzy comprehensive evaluation method of the monolayer, then, the various results of different monolayers would be evaluated comprehensively, namely, to adopt the multi-layer fuzzy comprehensive evaluation. Firstly, it is neccessary to determine and partition the evaluation factors set and the comments set.

The evaluation factors set is consisted of all factors that could influence the interactional behavior attributes, which is expressed as $U=\{U_1,U_2\cdots,U_n\}$, U could be partitioned into k factors $U_1,\cdots,U_k$ $(i=1,2,\cdots,k)$ according to the attributes, and meet that$U_1\cup U_2\cup\cdots\cup U_k=U$; for the arbitrary $i\neq j$, $U_i\cap U_j=\Phi$, inter alia, $U_i=\{U_{i1}\cdots\cdots U_{ini}\}$, namely, each primary indicator is composed with various secondary indicators which are in same interdependence. According to the special application, the key factor of the dynamic user's behavior would be captured at all times via implicit way, and be used as the primary indicator or secondary indicator.

The comments set is formed by m kinds of comment levels which are used as evaluation criterions, and expressed as $V=\{V_1,V_2,\cdots,V_m\}$ .. The influence that the evaluation factor acted on interactional behavior attribute, would be embodied in its weight. The weight distribution of evaluation factor comes from the expert committee. The weight set contains the weight of each factor, then it forms the weight vector. The vector that is consisted of k sub-factors is $A=(a_1,\ldots,a_k)$, $\sum_{i=1}^{k}a_i=1$; The weight vector of sub-factor $U_i=\{U_{i1}\cdots\cdots U_{ini}\}$ could be indicated as $A_i=(a_{i1},a_{i2},\cdots\cdots,a_{ini})$,and $\sum_{j=1}^{n_i}a_{ij}=1,(i=1,2,\ldots,k)$. The top-level fuzzy evaluation matrix for the sub-factor U_i could be expressed as R_i

$$R_i = \begin{bmatrix} r_{11}^{(i)} & r_{12}^{(i)} & \cdots & r_{1m}^{(i)} \\ r_{21}^{(i)} & r_{22}^{(i)} & \cdots & r_{2n}^{(i)} \\ \cdots & \cdots & \cdots & \cdots \\ r_{n1}^{(i)} & r_{n2}^{(i)} & \cdots & r_{nm}^{(i)} \end{bmatrix} \quad (i = 1,2,\cdots,k) \tag{1}$$

r_{st} is the score relative to grade t that the interactional behavior attribute acquired under factor s . By adopting model $M(\circ,+)$, the top-level fuzzy comprehensive evaluation vector of the sub-factor U_i could be computed as

$$B_i = A_i \circ R_i = (b_{i1}, b_{i2}, \cdots, b_{im}) \qquad (i = 1,2,\cdots,k) \tag{2}$$

To treat sub-factor U_i as the single factor, and its top-level comprehensive evaluation vector B_i as its criteria, the secondary fuzzy evaluation matrix R could be gained. By adopting model $M(\circ,+)$ again, the secondary fuzzy evaluation vector could be worked out as

$$B = A \circ R = (b_1, b_2, \cdots, b_m) \tag{3}$$

The score of overall evaluation could be written as $W = B \circ V^T$, then the evaluation result of the user's behavior attribute could be calculated by fuzzy membership function. Furthermore, the value of evaluation result would used as the parameter of affection drive, which expressed as the stimulus intensity I . Since the functional relationship between quantity of human reaction and quantity of stimulation from objective environment has been described and quantitated from psychological perspective by Weber-Fechner law, while using will as the quantity of psychological stimulation, w_b as constant (set as 1/2), the relationship of the evaluation result between quantity of psychological stimulation and user's behavior attribute could be expressed as

$$Will = w_b \left(I_n / I_{n-1} \right) \tag{4}$$

The result would be adopted as the motivator for HMM affective model[8], then to drive the machine to generate affective response.

3 The Application of the Interactional Model Based on Behavior Driving Used in Intelligent Teaching

The English teaching prototype system of the affective avatar has been designed to express its intention and affective response via voice and expression, meanwhile, the interactional model based on behavior driving has been embedded into the system as well.

3.1 The Construction of the Interactional Teaching System in Multimoding and the Confirmation of the User's Behavior Attribute

The face modeling of the avatar has been achieved with the model CANDIDE-3 under MPEG-4 standard. The function of animation is based on FAP parameters. By adopting Speech SDK SAPI 5.1 provided by Microsoft, the TTS voice synthesis and phonetic recognition has been achieved, as well as the lip reading model based on 6 basic mouth shapes. This enables the function in lip synchronization during the avatar speaking. In addition, the system integrated eye tracking program, which is able to acquire the user's sight coordinates. To send the coordinates to avatar by using socket module, it could achieve the function with sight tracking. All these enable the HCI more naturally.

In the application, the user's behavior attributes could be classified into cognitive attribute and mood learning attribute, then the affective influence factor of interaction could be reduced according to the two attributes.

The primary indicator is

$$U = \{U_1, U_2 \cdots, U_n\} = \{studyfrequency\ ,\ knowledgegrasping\ ,\ initiative\} \tag{5}$$

The secondary indicator is

$$U_1 = \{U_{11}, U_{12}, U_{13}\} = \{times\ ,\ time\ ,\ weekfrequency\} \tag{6}$$

$$U_2 = \{U_{21}, U_{22}, U_{23}, U_{24}, U_{25}\} = \{word\ ,\ phrase\ ,\ grammar\ ,\ reading\ ,\ \mathrm{auralcomprehension}\} \tag{7}$$

$$U_3 = \{U_{31}, U_{32}, U_{33}\} = \{querytimes\ ,\ queryfrequency\ ,\ effectivelearningtime\ ,\ studyemotion\} \tag{8}$$

In order to facilitate processing, the value of the evaluation result in [0 , 1] would be defined as 1, then $R \in [1,100]$, $will \in [-1,1]$. By adopting the value of will as the initial stimulation type and intension criterion, to drive the psychological mode of the teacher based on HMM, the runtime interface of the system could be shown as Fig. 1.

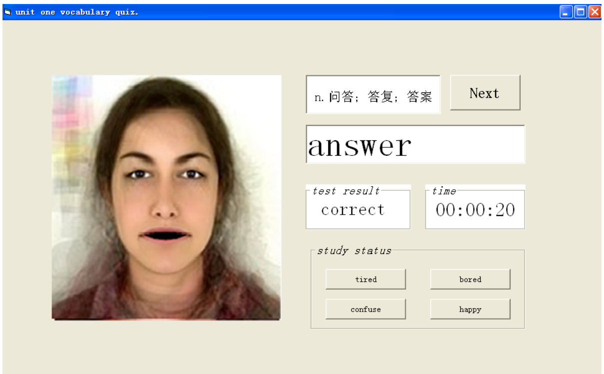

Fig. 1. Interface of affective model based on user's behavior driving

3.2 The Evaluation of Experience of Interactional Emotion with Affective Model that Used PAD Affection Scale

In the research, it is expected to gain the qualitative conclusion by quantitatively analyzing affective response. If the purpose of the task is just to compare the differences of emotional experiences while users using the various systems, the 'internal experience method' could be adopted merely. Since the concrete application does not require to measure the affection status in really precise, the disadvantages of 'internal experience method' could almost be cancelled out by comparing two sets of data that composed with a large number of samples, rather than considering the measurement of the physiological variable. Therefore, the research adopted the psychophysics method based on affection scale as the experimental method. Since the target user of the system is Chinese, PAD affection scale in Chinese Express Edition which is most suitable for estimating affection of Chinese has been adopted. The 3 dimensions in this PAD affection scale (pleasure-displeasure, arousal-nonarousal, dominance-submissiveness) would be measured in 4 items(totally in 12 items) individually. The scale is the 9 points semantic differential scale. Each item is composed with a pair of adjectives which stands different affection statuses. Furthermore, there are 9 points between the space of each pair of words, each value of the affection that expressed by each pair of words is different in its own dimension, however, is approximately same in the other 2 dimensions. The score range of each item is $[-4,4]$.

70 students in grade 7 (33 males and 37 females), who's mother language is Chinese, has been selected as the volunteers in this testing. They have been divided into two groups with 35 in each, and randomly experienced one of the two intelligent teaching prototype systems of avatar (affection edition, non-affection edition). The testing content was chapter 8, the testing term was two weeks. The PAD values have been recorded after using the testing system each time, and evaluation data of the two groups have been sorted after the entire testing. The scores of 4 items in each dimension P, A or D of each testee have been achieved, the average value of the 4 scores has been used to stand for the score in each value. Moreover, the statistical data of each group in dimension P or D have been computed with average value. However, while analyzing the score in dimension A, since the Chinese are normally not quite used to be evaluated in emotional activity, as well as the data volume that acquired in the test are not adequate enough, the skewed distribution is appeared in the score of dimension A. Therefore, by adopting median, the data for vocabulary testing in the intelligent teaching system based on both affection edition and non-affection edition in PAD are shown as Fig. 2.

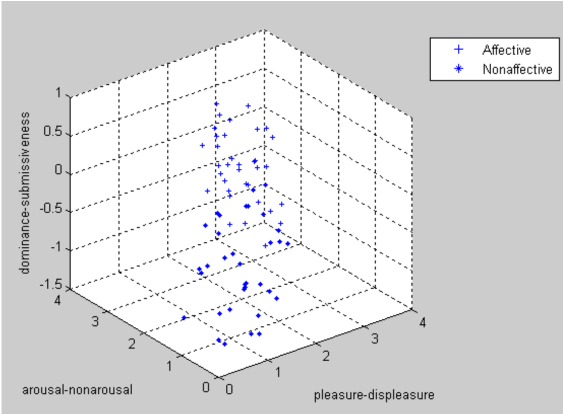

Fig. 2. Comparation of testing data in PAD in two groups

Thus, the difference of statistical data in dimension PAD between two groups could stated as

$$\mathbf{X}_D = (P_D \quad A_D \quad D_D) = (1.27 \quad 0.97 \quad 1.25) \tag{9}$$

The result revealed that the value in dimension P is obviously higher in affection edition than the one in non-affection edition, it proofed that the affection edition is beneficial to the user to acquire higher positive emotional status during interaction. The average values in dimension A and D in affection edition are all higher than the ones in non-affection edition. This show that the test process based on affective avatar could promote the user's interest, then it enables the user to accomplish the interactional test in relatively aware and concentrated status, which leads to the higher activities and stronger sense of control to the circumstance. Since during operating task, the interaction based on the avatar is user centered, during interaction the user would be respected in affection, therefore, the feeling that the user felt to be controlled is relatively weak, user has higher dominance. Therefore, the testing confirmed that the user would acquire higher pleasure and dominance while experiencing the system and the user could be attracted well during the teaching process.

4 Conclusion

During the process HCI, the affection play a significant role, however, how to acquire the stimulation factor of affection during interaction process is the key point in establishing affective interaction system. The paper proposed to adopt the quantitative description method of the affective factor attribute based on the user's behavior characteristics, to detect the user behavior signal, and to use these as the comprehensive evaluation factors. By adopting Weber-Fechner law, to generate the stimulus quantity of affection response in computer by using comprehensive evaluation result of the user behavior, this could be used as the drive parameter for HMM affective model. Moreover, HMM could also be used to reflect the corresponding relationship between stimulation from external user behavior and the affection expression. The influence that the personalized interaction model for behavior driving in the affective teaching system acted on the user's affection status in dimension P, A and D has been quantitatively described according to the experiment. The sensibility expression of the avatar system is presented in both linguistic way (the comprehension of natural language and voice synthesis) and non-linguistic way(facial expression and eye movement). The result of the test revealed that the model would be able to express affection in interactional teaching rationally and livelily, further to improve the level of the user's affective experience in the dimensions P, A and D.

With the rapid development in HCI, various HCI affective model for different applications has been emerging in endlessly, the personalized interaction model that been discussed in the paper would be able to provide a kind of theoretical design method for affective intelligent interaction.

References

[1] Picard, R.D.: Affective computing. MIT Press, Cambridge (1997)
[2] Song, Y., Jia, P.F.: A Control Architecture Based on Artificial Emotion for Anthropomorphic Robot. ROBOT 26(6), 491–495 (2004)
[3] Zhang, D., Shi, Z., Panyu: Formal Model of Emotional Agent. PR & AI 22(3), 381–387 (2009)
[4] Yang, H.: Study on Interactive Intelligent Virtual Agent and Its Emotion. Zhejiang University (2007)
[5] Wang, W.: Research of Robot Learning System Based on Affective Computing. Zhejiang University of Technology (2009)
[6] Lisetti, C.L., Marpaung, A.: Affective Cognitive Modeling for Autonomous Agents Based on Scherer's Emotion Theory. In: Freksa, C., Kohlhase, M., Schill, K. (eds.) KI 2006. LNCS (LNAI), vol. 4314, pp. 19–32. Springer, Heidelberg (2007)
[7] Hudlicka, E.: What are we modeling when we model emotion? In: Proceedings of the AAAI Spring Symposium - Emotion, Personality, and Social Behavior, Stanford University, CA, pp. 52–59 (2008)
[8] Gu, X.: Research on Modeling Artificial Emotion Based on HMM and Techniques Correlated with Avatar. University of Science and Technology, Beijing (2003)

A General Closed-Loop Framework for Multi-dimensional Sequence Processing

Qichuan Ding[1,2], Xingang Zhao[1], and Jianda Han[1]

[1] State Key Laboratory of Robotics, Shenyang Institute of Automation, Chinese Academy of Sciences, Shenyang 110016, China
[2] Graduate School, Chinese Academy of Sciences, Beijing 430081, China
{dingqichuan,zhaoxingang,jdhan}@sia.cn

Abstract. A novel closed-loop framework for multidimensional sequence processing is proposed in this paper. Traditional sequence-driven models are always forward, so no information is feedback to correct their outputs, which may deviate from the true values gradually due to the estimation error accumulating. To overcome the problem, the multidimensional vector in the input sequence is divided into two vectors based on its data attribute. One vector sequence generated from the original input sequence is considered as the new input sequence, and the other is considered as the measurement output sequence. The original output sequence is treated as the state sequence. Then, a closed-loop model in the state-space form is constructed, with which the states can be estimated online by filtering algorithms. The feasibility of the proposed framework has been verified by using the robot inverse kinematics.

Keywords: sequence processing, closed-loop framework, state-space model, robot inverse kinematics.

1 Introduction

The data with a sequential structure are common in a variety of applications, ranging from written or spoken language processing, to the production of continuous control signals, to multivariate time-series prediction [1, 11]. Sequence-driven models are usually used to describe the behavior of the dynamic systems, while their physical models are too complex to be built. The black-box models commonly used to analyze the input-output sequence include Neural Network (NN) [2], Support Vector Machine (SVM) [3], and Hidden Markov Model (HMM) [4]. Recurrent Neural Network (RNN) with a memory mechanism can retain past information in a flexible way, which is significant for sequence processing [5]. However, no information is included to correct the outputs of the RNN, which may deviate from the true values gradually due to the estimation error accumulating. HMM is an alternative modeling method to process sequence through taking context in a flexible manner. Many extended versions of HMM, such as Input Output HMM (IOHMM), Gaussian HMM, and Autoregressive HMM, have been studied to extend the applications of the standard HMM [6]. Unfortunately, HMM, which only has finite discrete hidden states, cannot describe the systems with continuous states [4].

S. Lee et al. (Eds.): Intelligent Autonomous Systems 12, AISC 194, pp. 311–321.
springerlink.com

For many applications, constructing closed-loop models in the form of continuous state-space equations will bring advantages for sequence processing [1]. By combining filtering algorithms with a state-space representation, the main computations can be divided into: 1) process update, i.e., predicting the states with state equation, and 2) measurement update, i.e., correcting the predicted states with the measurement equation [7, 8]. Therefore, the recursive estimated states can be utilized to control systems online.

In this paper, a framework based on modeling closed-loop models is proposed to process multidimensional sequence. The multidimensional sequence is preprocessed to be suitable for constructing state-space equation. The original output sequence is treated as the state sequence in the new framework. Every multidimensional vector in the original input sequence is divided into two vectors based on its data attribute, so two new sequences are generated from the original input sequence. One is considered as the new input sequence, while the other is considered as the measurement output sequence in the new framework. Therefore, a state equation and a measurement equation, which compose the complete state-space model, can be built with different modeling methods. The states, i.e. the outputs in the original sequence, can be estimated online, when the inputs is presented. The robot inverse kinematics is introduced to verify the feasibility of the proposed framework. The simulations show the improvement of the proposed modeling method comparing with the traditional numerical method.

2 Pre-knowledge

The models commonly used to process sequence are RNN and HMM, which take context into account in their model framework. Define $U=\left[u_1,u_2,\dots,u_n\right]$ to be an input sequence, and $X=\left[x_1,x_2,\dots,x_n\right]$ to be the corresponding output sequence. Each sample in U is a m-dimension vector, i.e., $u_k=\left[u_{1k},u_{2k,}\dots,u_{mk}\right]^T$. Correspondingly, the output is r-dimension vector, i.e., $x_k\in R^r$. The brief descriptions of RNN and HMM are presented below.

2.1 Recurrent Neural Network

Contrary to feedforward networks, recurrent networks can be sensitive, and be adapted to past inputs. A simple recurrent neural network with a time delay input is described in figure 1.

If we define the function of the RNN to be $g(\cdot)$, then we have,

$$x_{k+1}=g\left(x_k,u_k\right) \tag{1}$$

Formula (1) describes a recursive open-loop model, which can be used to estimate x_{k+1} according to a given input u_k online if it has been trained. However, the estimated values may deviate from the true values gradually, because no information is introduced to reduce the estimation error.

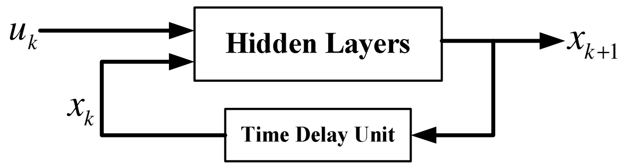

Fig. 1. The structure of Recurrent Neural Network

2.2 Hidden Markov Model

HMM can be viewed as a specific instance of the state space model, in which the latent variables (the states) are discrete. In figure 2, x_k is treated as the hidden state, and u_k is treated as the observation.

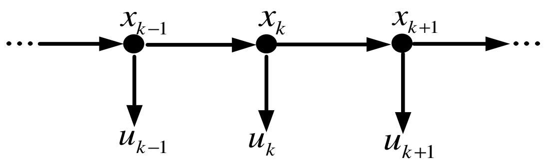

Fig. 2. Hidden Markov Model

The hidden state at every time takes its value in the finite set $Z = \{1, 2, \ldots, L\}$. HMM cannot describe the system with continuous states, so it is frequently used for sequence classification.

3 General Closed-Loop Framework

A general framework is proposed to overcome the problems existing in the traditional methods for sequence processing. With the novel framework, a continuous state-space model is constructed to process sequence.

3.1 Preprocessing

The multidimensional sequence needs to be preprocessed to be suitable for the closed-loop framework. The multidimensional vector u_k in U is divided into two parts based on its data attribute, i.e.,

$$u_k = \left[u_{1k}, u_{2k}, \ldots, u_{sk}, u_{(s+1)k}, \ldots, u_{mk}\right]^T = \begin{bmatrix} u_k^1 \\ u_k^2 \end{bmatrix}, \quad k = 1, 2, \ldots, n$$

where $u_k^1 = \left[u_{1k}, u_{2k,} \ldots, u_{sk}\right]^T$, $u_k^2 = \left[u_{(s+1)k}, u_{(s+2)k,} \ldots, u_{mk}\right]^T$, and $s < m$.

Then, two new vector sequences U^1 and U^2 are generated from the original input sequence, where $U^1 = \left[u_1^1, u_2^1, \ldots, u_n^1\right]$, $U^2 = \left[u_1^2, u_2^2, \ldots, u_n^2\right]$, and $U = \begin{bmatrix} U^1 \\ U^2 \end{bmatrix}$.

In the closed-loop framework, U^1 is treated as the new input sequence, while U^2 is treated as the measurement output sequence. The original output sequence X is treated as the state sequence.

3.2 Constructing the Closed-Loop Framework

After the sequence has been preprocessed, two models can be built to form the closed-loop framework. One is the state equation, which generates the state x_{k+1} with the input u_k^1 and the state x_k, i.e.,

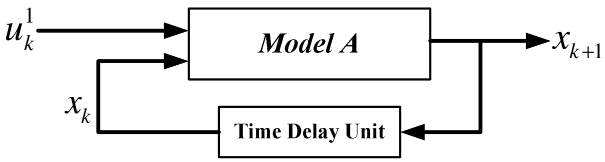

Model A can be constructed with arbitrary recursive model, such as RNN, Autoregressive Regression Model (AR). If we define the function of the *Model A* to be $f(\cdot)$, we can obtain,

$$x_{k+1} = f\left(x_k, u_k^1\right) \tag{2}$$

The other model is the measurement equation, which maps x_k in X to u_k^2 in U^2,

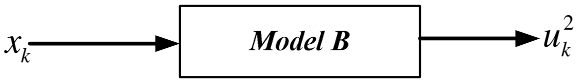

Model B can be constructed with black-box model (NN), or linear model. If we define the function of the *Model B* to be $h(\cdot)$, then we can have,

$$u_k^2 = h\left(x_k\right) \tag{3}$$

Combining *Model A* and *B* with the form of measurement feedback, we obtain the general closed-loop framework, as described in figure 3.

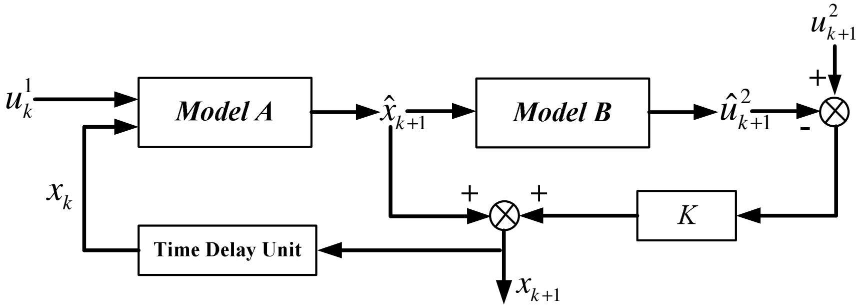

Fig. 3. The closed-loop framework

where K is the time variant gain. The final state estimated by the closed-loop model is concluded,

$$x_k = \hat{x}_k + K \cdot \left(u_k^2 - \hat{u}_k^2\right) \tag{4}$$

In formula (4), $\hat{x}_k$ is directly predicted by the *Model A*, and $K \cdot \left(u_k^2 - \hat{u}_k^2\right)$ is the correcting information obtained from the *Model B*. If $\hat{x}_k$ is inaccurate, the correcting information will pay an important role in the final x_k by setting K to be a larger value. Conversely, if $\hat{x}_k$ is accurate, the correcting information will pay a minor role in the final x_k by setting K to be a small value, or $K = 0$.

With the closed-loop framework, the estimated states cannot deviate from their true values, because the measurement is feedback to correct the estimated states real time.

Another advantage of the closed-loop framework may be unobvious, but also important. In many applications, the multidimensional vector u_k includes redundant information. The redundant information may increase the computation complexity and decrease the models' accuracy, while u_k has not been divided into two parts with traditional modeling methods. With the closed-loop framework, u_k is divided into two parts, and the redundant information u_k^2 is used as posterior knowledge to correct the predicted results, as in formula (4). Therefore, besides the computation burden is reduced, the redundant information can be utilized sufficiently.

3.3 Recursive Algorithms for State Estimation

In this section, we develop some recursive algorithms to calculate K, and estimate the state x_k online as well.

1) Minimum measurement error

The estimated state x_k by formula (4) can be input into the *model B*. Then K is iteratively updated to minimize the measurement error, i.e.,

$$\min_{K}\left\{u_k^2 - h\left(\hat{x}_k + K\cdot\left(u_k^2 - \hat{u}_k^2\right)\right)\right\} \tag{5}$$

where $h(\cdot)$ represents the function of the *model B*.

2) Filtering algorithms

In fact, the *model A* and *B*, i.e. formula (2) and (3), compose a state space model. We can express the model in a general form,

$$\begin{cases} x_{k+1} = f\left(x_k, u_k^1\right) \\ u_k^2 = h\left(x_k\right) \end{cases} \tag{6}$$

Thus, the filtering algorithm, such as the extend Kalman filter (EKF), unscented Kalman filter (UKF) [7], and particle filter (PF) [8], can be used to calculate K and estimate the state x_k online. Note that the *model A* and *B* are usually built with black-box models (NN), so $f(\cdot)$ and $h(\cdot)$ may not be expressed by explicit mathematics equations. Therefore, UKF and PF, which do not have to calculate Jacobian matrix, are more suitable for online estimation in the closed-loop framework.

4 Simulation

In this section, we verify the closed-loop framework with robot inverse kinematics. The robot inverse kinematics is to find the joint variables in term of the end-effector position and orientation. The closed form solution and the numerical solution are commonly found in the inverse kinematics problem. Robots only with special structure have the closed form solutions. Here, we only consider the numerical solution. The traditional numerical solution has been described detailed in previous work [9, 10].

4.1 The Closed-Loop Model of the Robot Inverse Kinematics

We construct the inverse kinematics model with the closed-loop framework. For a n-DOF robotic arm, we define T_i^{i-1} ($i = 1, 2, ..., n$) to be the homogeneous transformation of the coordinate frame $i-1$ respect to the coordinate frame i. In the inverse kinematics, the end-effector position and orientation are known, i.e., T_n^0 is known.

$$T_n^0 = T_1^0 \cdot T_2^1 \cdot \cdots \cdot T_n^{n-1} = \begin{bmatrix} r_{11} & r_{12} & r_{13} & r_{14} \\ r_{21} & r_{22} & r_{23} & r_{24} \\ r_{31} & r_{32} & r_{33} & r_{34} \\ 0 & 0 & 0 & 1 \end{bmatrix}$$

Given 12 numerical values for T_n^0 (the other four are trivial), we can obtain 12 equations, in which 3 equations relate to position, and 9 equations relate to orientation. There are only 3 orientation equations are independent.

If we define the vector of joint variables to be $\theta = [\theta_1, \theta_2, \ldots, \theta_n]^T$, we can obtain,

$$r_{ij} = \varphi_{ij}(\theta), \quad i = 1,2,3; j = 1,2,3,4 \tag{7}$$

$\varphi_{ij}(\cdot)$ can be obtained from the robot forward kinematics with D-H method.

In inverse kinematics, we use the known vector $r = [r_{11}, r_{21}, r_{31}, \ldots, r_{14}, r_{24}, r_{34}]^T$ to calculate the vector θ of joint variables.

With the proposed closed-loop framework, the input-output vectors have to be preprocessed. r is divided into two parts, $r^1 = [r_{11}, r_{21}, r_{23}]^T$ and $r^2 = [r_{33}, r_{14}, r_{24}, r_{34}]^T$ (Much redundant information exists in r, so only part of r is considered.) . Then, r^1 is treated as the input, and r^2 is treated as the measurement output. Besides, θ is treated as the state.

The state equation can be constructed by Newton-Raphson method,

$$\theta(k+1) = \theta(k) + J^{-1}(\theta(k)) \cdot (r^1 - \varphi^1(\theta(k))) \tag{8}$$

where $\varphi^1(\cdot) = [\varphi_{11}(\cdot), \varphi_{21}(\cdot), \varphi_{23}(\cdot)]^T$, $J = [\partial\varphi^1 / \partial\theta]$ is the Jacobi matrix, and J^{-1} is the inverse or pseudo-inverse matrix of J. k is the sample time.

The measurement equation is easily obtained, because the robot forward kinematics equation is primarily known.

$$r^2 = \varphi^2(\theta) \tag{9}$$

where $\varphi^2(\cdot) = [\varphi_{33}(\cdot), \varphi_{14}(\cdot), \varphi_{24}(\cdot), \varphi_{34}(\cdot)]^T$.

Combining formula (8) and (9), we build a state-space model of the robot inverse kinematics with the closed-loop framework,

$$\begin{cases} \theta(k+1) = \theta(k) + J^{-1}(\theta(k)) \cdot (r^1(k) - \varphi^1(\theta(k))) \\ r^2(k) = \varphi^2(\theta(k)) \end{cases} \tag{10}$$

4.2 Simulation Results

We verify the feasibility of our proposed closed-loop framework with the inverse kinematics of Puma560. Puma560 is a well known 6-DOF robot, and its six joints are all revolute joints. Table 1 lists the D-H parameters of Puma560 [10].

Table 1. The D-H parameters of Puma560

Link	α_i	a_i	d_i	θ_i
1	90	0	0	θ_1
2	0	0.432	0	θ_2
3	-90	0.02	0.15	θ_3
4	90	0	0.432	θ_4
5	-90	0	0	θ_5
6	0	0	0	θ_6

The robotics toolbox (robot8) for matlab [10] is used in our simulation. The traditional numerical method to solve the inverse kinematics problem has been included in the toolbox. In fact, the numerical method is an iterative algorithm based on gradient descent method. When we solve the inverse kinematics problem with the proposed closed-loop model, i.e. formula (10), UKF is used as the recursive algorithm to estimate the states in real time.

1) Generating simulation data

A trajectory of Puma560's joint variables, which starts at $\theta^{st} = [0,0,0,0,0,0]^T$ and ends at $\theta^{en} = [0.81,-1.82,-0.74,1.45,-0.58,0.66]^T$, is generated with the function $jtraj(\cdot)$ in robot8. The time step is 0.014*s*, and time length is 16*s*. The trajectory, i.e. the vector sequence of joint variables, is defined as Θ, which is input into the forward kinematics of Puma560 to generate the trajectory of the end-effector. We define the trajectory of the end-effector to be Γ, which includes the position and orientation information of the end-effector.

2) Verifying feasibility of the closed-loopframework

The trajectory Γ of the end-effector is used to calculate the trajectory Θ of joint variables. As discussed above, UKF is used to estimate the states in formula (10), which represent Θ in our proposed framework. Figure 4 depicts the estimation errors.

As can be seen from figure 4, the estimation errors of joint variables are convergent to zeros, which shows the feasibility of the proposed closed-loop framework.

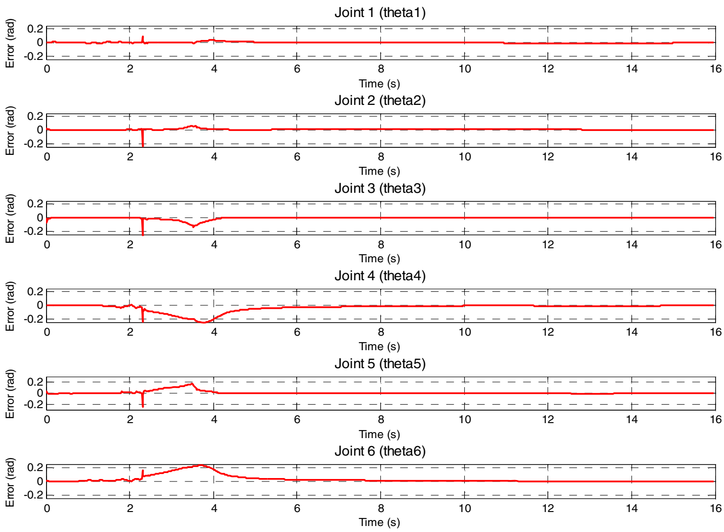

Fig. 4. The estimation errors of joint variables with the proposed method

3) Verifying improvement of the closed-loop framework for sequence with noise

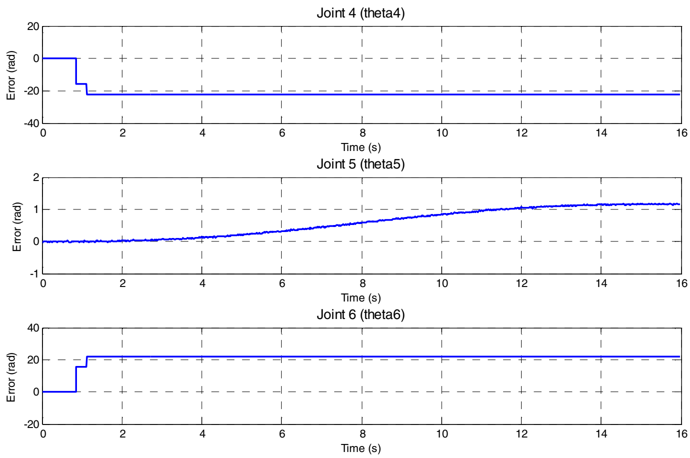

Fig. 5. The estimation errors of joint variables by using the traditional numerical method, with the sequence including Gaussian noise

In the second simulation, the input sequence, i.e. the trajectory Γ of the end-effector, is added Gaussian noise, whose mean is 0, and variance is 0.01. Then, the traditional numerical method and the proposed method are both used to estimate the joint variables with the input sequence, which includes Gaussian noise. The estimation errors are presented in figure 5 and 6, respectively.

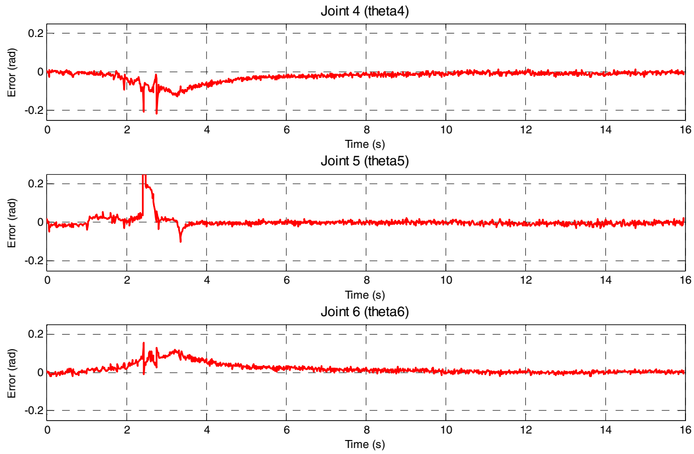

Fig. 6. The estimation errors of joint variables by using the proposed method, with the sequence including Gaussian noise

Because of the Gaussian noise, the estimation errors of joint variables ($\theta_4, \theta_5, \theta_6$) by using the classical numerical method are divergent, as shown in figure 5. However, the estimation errors by the proposed method are convergent to zeros, as shown in figure 6. The simulation shows that the measurement feedback in the closed-loop framework can improve the estimation accuracy.

5 Conclusion

In this paper, we propose a novel framework for multidimensional sequence processing. Based on the framework, a closed-loop model with the form of state-space representation can be built using the preprocessed input-output sequence. With the closed-loop model, the states can be estimated online by using recursive filtering algorithms. The estimated results cannot deviate from the true values because of measurement feedback. In additional, the redundant information included in the input sequence can be utilized sufficiently and properly with the proposed closed-loop framework.

The feasibility of the proposed framework has been verified with the robot inverse kinematics. The simulations show the novel modeling framework is effective, and can provide more accurate estimation when the sequence includes noise.

Acknowledgements. This research has been supported in part by National Natural Science Foundation of China under grant 60705028 and Natural Science Foundation of Liaoning Province, China.

References

1. Bengio, Y., Frasconi, P.: Input-Output HMM's for Sequence Processing. IEEE Trans. on Neural Networks 7(5), 1231–1249 (1996)
2. Guarneri, P., Rocca, G., Gobbi, M.: A Neural-Network-Based Model for the Dynamic Simulation of the Tire/Suspension System While Traversing Road Irregularities. IEEE Trans. on Neural Networks 19(9), 1549–1563 (2008)
3. Wan, V., Renals, S.: Speaker verification using sequence discriminant support vector machines. IEEE Trans. on Speech and Audio Processing 13(2), 203–210 (2005)
4. Li, Y.: Hidden Markov models with states depending on observations. Pattern Recognition Letters 26, 977–984 (2005)
5. Jaeger, H.: Tutorial on training recurrent neural networks, covering BPPT, RTRL, EKF and the 'echo state network' approach, GMD Report 159, German National Research Center for Information Technology, pp. 1–48 (2002)
6. Chamroukhi, F.: Hidden process regression for curve modeling, classification and tracking. Dissertation, Université de Technologie de Compiègne (2010)
7. Julier, S.J., Uhlmann, J.K.: Unscented filtering and nonlinear estimation. Proceedings of the IEEE 92(3), 401–422 (2004)
8. Arulampalam, M.S., Maskell, S., Gordon, N., Clapp, T.: A Tutorial on Particle Filters for online Nonlinear/Non-Gaussian Bayesian Tracking. IEEE Trans. on Signal Processing 50(2), 174–188 (2002)
9. Spong, M.W., Hutchinson, S., Vidyasagar, M.: Robot Dynamics and Control. John Wiley and Sons (2004)
10. Corke, P.I.: Robotics Toolbox for Matlab, `http://www.petercorke.com`
11. Aangenent, W., Kostic, D., Jager, B.D., Molengraft, R.V.D., Steinbuch, M.: Data-Based Optimal Control. In: American Control Conference, pp. 1460–1465 (2005)
12. Cortez, P., Embrechts, M.J.: Opening Black Box Data Mining Models Using Sensitivity Analysis. In: IEEE Symposium on Computational Intelligence and Data Mining (CIDM), pp. 341–348 (2011)
13. Frasconi, P., Gori, M., Sperduti, A.: A General Framework for Adaptive Processing of Data Structures. IEEE Trans. on Neural Networks 9(5), 768–786 (1998)
14. Westwick, D.T., Perreault, E.J.: Closed-Loop Identification: Application to the Estimation of Limb Impedance in a Compliant Environment. IEEE Trans. on Biomedical Engineering 58(3), 521–530 (2011)

Facial Expression Recognition from Infrared Thermal Videos

P. Shen, Shangfei Wang*, and Zhilei Liu

Key Lab of Computing and Communicating Software of Anhui Province
School of Computer Science and Technology,
University of Science and Technology of China, Hefei, Anhui, P.R. China, 230027
{speijia,leivo}@mail.ustc.edu.cn, sfwang@ustc.edu.cn

Abstract. In this paper, a spontaneous facial expression recognition method using infrared thermal videos is proposed. Firstly, the sequence features are extracted from the infrared thermal horizontal and vertical temperature difference sequences of different facial sub-regions. Secondly, a feature subset is selected according to their F-values. Thirdly, the Adaboost algorithm, with the weak classifiers of k-Nearest Neighbor, is used to classify facial expressions in arousal and valence dimensions. Finally, experiments on the Natural Visible and Infrared facial Expression (USTC-NVIE) database demonstrates the effectiveness of our approach.

1 Introduction

Facial expression recognition technology has a wide range of potential applications related to human-computer interaction and psychology. As a result, it has attracted more and more researchers' attentions in recent years. Among those, most researchers focus on the representation of visual information for facial expression. However, visible light may change with the location and time, which can cause significant influence on the image appearance and texture information. Infrared thermal images, recording the temperature distribution formed by face vein branches, are not sensitive to lighting conditions. Thus, thermal expression recognition is a crucial complementarity to visible expression recognition [1,2,3].

In this paper, we propose a facial expression recognition method using infrared thermal videos. Firstly, based on the feature points located by a semi-automatic algorithm, the thermal face of each frame is marked off and divided into four regions of interest (ROI), including the forehead, the nose, the left/right cheek (LC/RC), and the mouth. Secondly, in order to avoid the influence of both the temperature change of the environment and the temperature drift of the infrared thermal camera, the proposed horizontal and vertical difference data are calculated based on the original facial the temperature data of each frame. Thirdly, each ROI of the difference data is divided into several grids, and then four static statistic parameters (i.e. minimum, maximum, standard deviation, and mean) are extracted from each grid. For each statistic parameter vector constructed

* Corresponding author.

S. Lee et al. (Eds.): Intelligent Autonomous Systems 12, AISC 194, pp. 323–333.
springerlink.com

by the corresponding statistical parameter of the same grid in each difference data sequence, four dynamic parameters are further extracted, which are sequence mean, standard deviation, maximum variation, and maximum gradient. After that, the F-value feature selection method is used to obtain an optimal feature subset. Then the Adaboost algorithm, with the weak classifiers of k-Nearest Neighbor (KNN), is adopted as the classifier to distinguish facial expressions into arousal and valence dimensions. Finally, we experimentally evaluate the effectiveness of the proposed method on USTC-NVIE database. The experimental results show that our method is effective for classifying spontaneous expressions.

2 Related Work

Most present facial expression recognition research focuses on visible images. Recently, a few researchers have paid attention to the outer facial expression recognition or inner affective detection using infrared thermal images [3,4,5,6,7,8,9,10,11,12,13,14,15,16] Here, we only give a brief review of facial expression recognition from thermal images, listed in Table 1, together with features, classifiers and performance.

Table 1. Related work on facial expression recognition from thermal images/videos

Reference	features	classifiers	Performance				
			Expression (posed/ spontaneous)	Modality (image/ video)	category	Subject number	Accuracy rate
Masood Mehmood Khan[17][10]	Facial Thermal Feature Points (FTFPs)	linear discriminant (LDA)	posed	images	happiness,fear, sadness,disgust, neutral	16	66.3% - 83.8%
Masood Mehmood Khan [3]	FTFPs	LDA	spontaneous	images	happiness,anger, sadness,disgust, neutral	10	72%
Sophie Jarlier [12]	representative temperature maps	KNN	posed	videos	9 action units(AU)	4	56.4%
Leonardo Trujillo [18]	representative eigen-features	support vector machine(SVM)	posed	images	happiness,anger, Surprise	30	77%
Yasunari Yoshitomi [13][15]	2D-DCT on thermal difference images	neural network (NN)	posed	videos	anger, happiness, neutral, sadness, surprise	10	80.5%

From Table 1, we can see that most present research of facial expression from the infrared thermal spectrum focuses on posed expressions, which are captured by asking subjects to perform a series of emotional expressions in front of a camera. These posed expressions are usually exaggerated. Spontaneous expressions, on the other hand, may be subtle and differ from posed ones both in appearance and timing. Spontaneous expression recognition has very realistic and great significance for harmonious and natural human-machine interaction compared with posed expression recognition [1]. Although Masood Mehmood Khan et al. have studied the spontaneous facial expression recognition using thermal images and achieved good recognition rates, they did not consider the temporal information in thermal images, which is a very important cue for spontaneous expressions. Besides, the previous studies are all based on a small scale infrared thermal database, ranging from 4 to 30 subjects, so further research of facial expression recognition on a large scale database is very necessary. Thus, we propose a spontaneous facial expression recognition method using temporal thermal information and evaluate its effectiveness on a large scale database, which consists of a total of 177 subjects with three illuminations selected from USTC-NVIE database.

3 Method

The framework of our proposed facial expression recognition using infrared thermal videos is shown in Fig. 1, which consists of data preprocessing, feature extraction, feature selection and classification. Details of each module are described as follows.

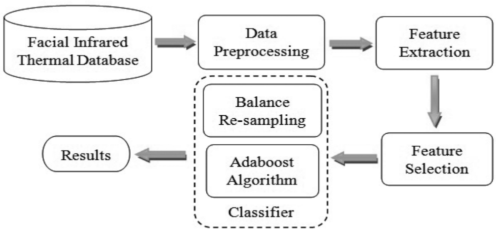

Fig. 1. Framework of facial expression recognition from infrared thermal videos

3.1 Data Preprocessing

Firstly, the feature point tracking method proposed by Ji [19] is adopted here to track points on an infrared facial image sequence based on the manually located feature points of the first frame. Secondly, four ROIs (i.e., the forehead, the nose, the left/ right cheek, and the mouth) are divided according to four tracked points, including the centers of two eyes, the tip of the nose and the tip of the jaw, as shown in Fig. 2. Thirdly, in order to reduce the computation complexity, each of the infrared image sequences is further re-sampled into a sequence with a constant length of n frames, in which the first frame is the onset expressional frame and the last frame is the apex expressional frame. Fourthly, each image is rotated and cropped according to Equations 1 and 2, and resized into $H \times W$ pixels using the bicubic interpolation method [20]:

$$angle = tan^{-1}(\frac{y_r - y_l}{x_r - x_l}) \tag{1}$$

$$\begin{cases} x_{Lu} = x_l - a(x_r - x_l) \\ y_{Lu} = y_l - b(y_n - y_l) \\ x_{Rl} = x_r + a(x_r - x_l) \\ y_{Rl} = y_j \end{cases} \tag{2}$$

where $angle$ is the angle of image rotation; (x_l, y_l), (x_r, y_r), (x_n, y_n) and (x_j, y_j) are the coordinates of the centers of the left and right pupils, the tip of the nose and the tip of the jaw, respectively; a determines the location of the left and right borders of this facial mask, and b determines the top border location of the facial mask; and (x_{Lu}, y_{Lu}) and (x_{Rl}, y_{Rl}) is the upper left and lower right vertex of the rectangle for image cropping, respectively.

Finally, considering the temperature change of the environment and the temperature shift of the infrared thermal camera, temperature difference data in both horizontal and vertical directions of the facial space is computed according to Equations 3 and 4:

$$\boldsymbol{D}_h(i,j) = \begin{cases} \boldsymbol{I}(i,j) - \boldsymbol{I}(i+1,j) & i = 1 \\ \boldsymbol{I}(i,j) - \boldsymbol{I}(i-1,j) & 2 \leq i \leq W \end{cases} \tag{3}$$

$$\boldsymbol{D}_v(i,j) = \begin{cases} \boldsymbol{I}(i,j) - \boldsymbol{I}(i,j+1) & j = 1 \\ \boldsymbol{I}(i,j) - \boldsymbol{I}(i,j-1) & 2 \leq j \leq H \end{cases} \tag{4}$$

where, $\boldsymbol{I}(i,j)$ is the temperature of pixel (i,j), $\boldsymbol{D}_h$ and $\boldsymbol{D}_v$ are the horizontal and the vertical temperature difference data respectively.

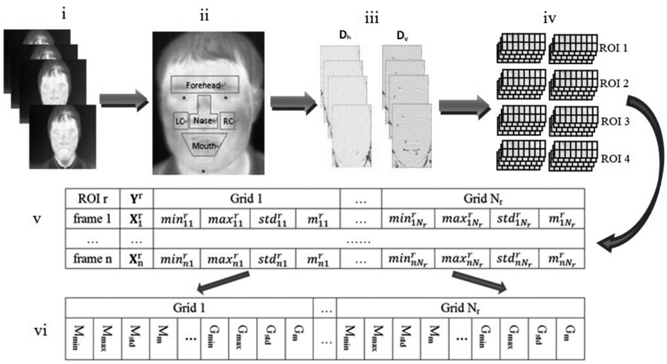

Fig. 2. Scheme of feature extraction: i. Original thermal image sequence; ii. The four ROIs; iii. The horizontal (left) and vertical (right) temperature difference data sequences; iv. The grid sequence of each ROI; v. The static parameter vector sequence of ROI r; vi. Final time-series features of ROI r.

3.2 Feature Extraction

Fig. 2 shows the scheme of our feature extraction method. Firstly, after the $\boldsymbol{D}_h$ and $\boldsymbol{D}_v$ have been calculated in step iii, for each ROI of each frame, the corresponding difference data ($\boldsymbol{D}_h$ and $\boldsymbol{D}_v$) are further divided into several grids with grid size of $w \times w$. Secondly, four static statistic parameters, including minimum min, maximum max, standard deviation std and mean m of each grid are computed. After that, the thermal information of ROI r in the frame i can be represented by these static parameters, and be denoted as $\boldsymbol{X}_i^r = \{min_{i1}^r, max_{i1}^r, std_{i1}^r, m_{i1}^r, min_{i2}^r, max_{i2}^r, std_{i2}^r, m_{i2}^r, \cdots, min_{iN_r}^r, max_{iN_r}^r, std_{iN_r}^r, m_{iN_r}^r\}$ as illustrated in step v, where N_r is the grid number of the ROI r, and $r = 1, 2, 3, 4$, representing the forehead, nose, cheek and mouth respectively.

Finally, the time-series features are computed based on each statistical parameter vector that consists of the according statistical parameter of the same grid in each frame of the difference data sequence, which is denoted as $\boldsymbol{Y}^r = \{\boldsymbol{X}_1^r, \boldsymbol{X}_2^r, \cdots, \boldsymbol{X}_n^r\}$ as illustrated in step vi of Fig. 2. Supposing x_{ik}^r is the k-th static parameter of $\boldsymbol{X}_i^r$, $k = 1, 2, \cdots, 4N_r$. Then, four dynamic parameters are defined as follows:

$$M_k^r = \frac{1}{n}\sum_{i=1}^{n} x_{ik}^r \tag{5}$$

$$S_k^r = \sqrt{\frac{1}{n}\sum_{i=1}^{n}(x_{ik}^r - M_k^r)^2} \tag{6}$$

$$V_k^r = max|x_{jk}^r - x_{ik}^r| \quad i, j \in 1, 2, \cdots, n \tag{7}$$

$$G_k^r = max\left|\frac{x_{jk}^r - x_{ik}^r}{j - i}\right| \quad i, j \in 1, 2, \cdots, n, i \neq j \tag{8}$$

Thus, for each grid sequence in the same location of the face space, four dynamic parameters (M, S, V and G) for each vector of four static statistic parameters (min, max, std and m.) are calculated. There are a total of 16 combination features in each grid, which could be named as M_{min}, M_{max}, M_{std}, M_m, S_{min}, S_{max}, $\cdots$, G_{min}, G_{max}, G_{std}, G_m.

3.3 Feature Selection

After the features have been extracted, a common used feature selection method, named analysis of variance (ANOVA), is used here. Supposing the facial expression states are given as $c(c_1, c_2, \cdots, c_l)$, where l is the number of expression states; and the group of thermal sequence feature k in expression states c_i is $\boldsymbol{C}_k^i = \{f_{1k}^i, f_{2k}^i, \cdots, f_{n_i k}^i\}$; f_{jk}^i is the k-th sequence feature of sample j in expression c_i; $j = 1, 2, \cdots, n_i$; and $n_i$is the number of samples in expression c_i. The formula for the one-way ANOVA F-test statistic for feature k is

$$F_k = \frac{\mathbf{S}_{\mathcal{B}}}{\mathbf{S}_{\mathcal{W}}} \tag{9}$$

where, F_k is called F-value. $\mathbf{S}_{\mathcal{B}}$ is "between-group variance", and is given as

$$\mathbf{S}_{\mathcal{B}} = \frac{\sum_{i=1}^{l} n_i(\bar{f}_k^i - \bar{f}_k)^2}{l - 1} \tag{10}$$

$\mathbf{S}_{\mathcal{W}}$ is ”within-group variance”, and is given as

$$\mathbf{S}_{\mathcal{W}} = \frac{\sum_{i=1}^{l} \sum_{j=1}^{n_i} (f_{jk}^{i} - \bar{f}_k^{i})^2}{n - l} \tag{11}$$

where n is the number of total samples, $\bar{f}_k^i$ is the mean of $\boldsymbol{C}_k^i$, and $\bar{f}_k$ is the mean of the k-th sequence feature of total samples.

The F-value is the ratio of the between-group variance to the within-group variance, which represents the classification capability of the feature. So we can select the features with large F-values in order to achieve more effective classification performance. In this step, final sequence features are sorted according to their F-values, and the top Z features with the highest F value are selected and used to classify the facial expressions in the next step.

3.4 Classification

The Adaboost algorithm can train several weak classifiers to be a strong classifier, and improve the overall classification performance, which has been widely used in visible facial expression recognition [21][22]. Here, we introduce the Adaboost algorithm into infrared thermal facial expression recognition. Considering KNN is the simplest classifier, which has been successfully used in some previous work [12], in this paper, we used KNN as weak classifiers of Adaboost. The cross-validation strategy is used to estimate its classification performance.

For each fold, the optimal features, which are obtained by the F-value feature selection method, are used to train the Adaboost classifier. In the training procedure, a sample subset is selected from the training data based on the weight distribution of all the training samples D_t , and used to train the weak classifier P_t , and this classifier with the minimum expression recognition error is selected in iteration t. The samples, which are predicted into the wrong class by using this weak classifier P_t, will be selected with greater probability into the next iteration. Thus, the weak classifier in the next iteration can only focus on processing these error classification samples. After that, we used the well trained Adaboost to classify expressions in the test set. The details of the Adaboost algorithm used in our approach are summarized as follows:

- Given a training set, where each sample i is (φ_i, y_i), $\varphi_i$is the sequence feature vector of sample i, and $y \in \{\pm 1\}$is the corresponding class label. The distribution of training samples is initialized to be $D_1 = \{1/n, 1/n, \cdots, 1/n\}$, n is the number of samples in training set.
- For $t = 1, \cdots, T$ iteration
  - Select a subset from the training data using the distribution D_t.
  - Train the weak classifier P_t in the selected subset.
  - Test the P_t in all training samples, and estimate the error rate ξ_t of P_t.
  - Compute the weight of P_t. $weights_t = log_{10} \frac{1-\xi_t}{\xi_t}$
  - Update the distribution D_{t+1} according to the following equations:

$$D_{t+1} = \begin{cases} \frac{\xi_t}{1-\xi_t} D_t & P_t(\varphi_i) = y_i \\ D_t & P_t(\varphi_i) \neq y_i \end{cases} \tag{12}$$

$$D_{t+1} = \frac{D_{t+1}}{sum(D_{t+1})} \tag{13}$$

– The final classifier, $H(\varphi_i)$, is a linear combination of these T weak classifiers.

$$H(\varphi_i) = sign(\sum_{t=1}^{T} P_t(\varphi_i) \times weights_t) \tag{14}$$

4 Experiments

4.1 Experimental Conditions

To evaluate the effectiveness of our method, experiments are implemented on the USTC-NVIE database, which contains both spontaneous and posed facial expression images of more than 100 subjects. The spontaneous sub-database of the USTC-NVIE database consists of image sequences from onset to apex, simultaneously collected by a visible and an infrared thermal camera under front, left, and right illumination respectively. All the visible apex images are labeled by 5 students with the intensity value of the six basic facial expressions (happiness, sadness, surprise, fear, anger, and disgust) on a three point scale (0, 1, and 2), as well as the arousal and valence on -1,0 and 1 [23].

The sample distribution of the spontaneous sub-database on valance and arousal is shown in Fig. 3. From Fig. 3 we can see that the intensity of samples' valence dimension ranges from -1 to 1, and the arousal dimension ranges from -0.7 to 1. Most samples' arousal intensity is positive, and their distribution is not balanced. In order to get a sub-database with the sample number of high level and low level expressions as balanced as possible, the samples with arousal and valence intensities equaling 1, or with arousal intensity less than 0 and valence intensity less than -0.7, are selected. Subsequently, the partitioned group with the arousal or valence intensity equaling 1 is labeled as high intensity expression and the arousal less than 0 or valence less than -0.7 is labeled as low intensity expression. For our experiments, each sequence sample must have $n - 1$ frames before the apex frame, and the samples that don't meet this condition shall be discarded. Finally, a total of 177 subjects (365 samples) from three illuminations are selected, which are grouped into 224 high arousal and 141 low arousal samples, as well as 125 high valence and 240 low valence samples. Although we try to get a balanced sub-database as best as we can, the numbers of high and low samples are still uneven here. To construct a further balanced training set, we randomly select the samples with the sample number U from these two classes respectively, in which U is the sample number in the smaller class group of valence or arousal.

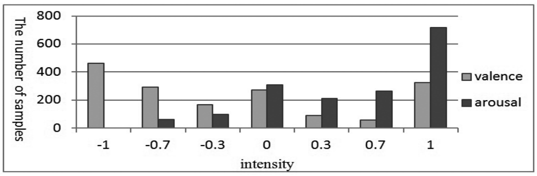

Fig. 3. The sample distribution on arousal and valence in USTC-NVIE database

Table 2. Experimental conditions of feature extraction

Parameters	a	b	n	w	N_1	N_2	N_3	N_4
Value	0.3	1.2	17	6	22	30	18	21

In our experiments, the resolution of the normalized facial image is set to be 84×80 pixels, and the parameters for feature extraction are shown in Table 2. A total of 2912 features are extracted from horizontal and vertical temperature difference data ($\boldsymbol{D}_h$ and $\boldsymbol{D}_v$) sequences, including 704 features in forehead ($16 \times N_1 \times 2$), 960 features in nose ($16 \times N_2 \times 2$), 576 features in cheek ($16 \times N_3 \times 2$), and 672 features in mouth ($16 \times N_4 \times 2$). As most of the subjects wore glasses, thereby masking the thermal features of the eye region, the eye region is not taken into account in our experiment. Finally, a 10-fold cross-validation is adopted, and the iteration number of the Adaboost is set to be 7 here.

4.2 Experimental Results and Analysis

Classification Performance. The average recognition rate curves for classification of high versus low level expressions with different numbers of selected features are shown in Fig. 4. From Fig. 4, we can observe that the highest recognition rates for classifying high versus low arousal and valence are 75.3% and 76.7% respectively. Here, the numbers of selected features are 122 and 264 respectively. From Table 1, we can see that Masood Mehmood Khan et al. have also done research on spontaneous expression recognition from thermal images, and achieved a recognition rate of 72% for classifying neutral and four basic spontaneous expressions [3] on a database of 10 subjects. Considering that the sample complexity of a large scale database is higher than that of a small one, the performance of our approach may be better.

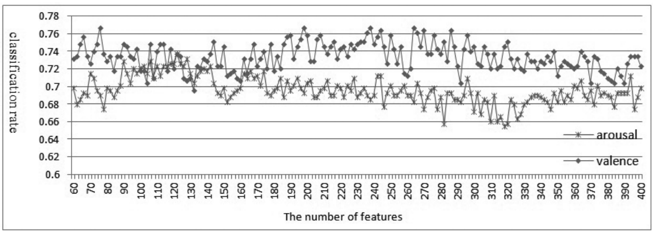

Fig. 4. The mean results for arousal and valence classification

Feature Distribution. Fig. 5 shows the distribution of selected features on four ROIs when the best recognition results on arousal and valence are achieved. From Fig. 5, we can see that most of the selected features, with the highest classification accuracy (in arousal or valence dimensions), are concentrated within the mouth and cheek regions, which may be explained as follows: People express different facial expressions

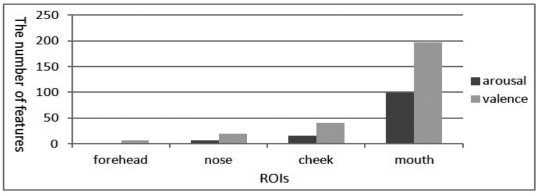

Fig. 5. The distribution of selected features on each ROIs when the best results are achieved

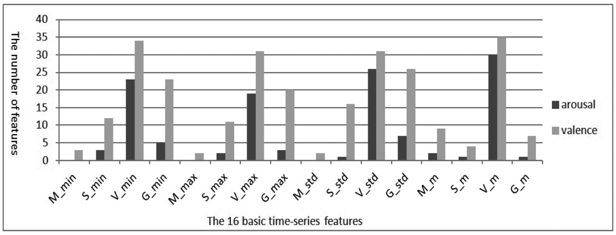

Fig. 6. Distribution of selected features on 16 kinds of basic sequence features when the best results were achieved

often with complex facial motions in the mouth and cheeks [23], which may cause the crumpling of the skin or changing of facial structures, for example, the opening and the closing of mouth, the movement of the zygomaticus in cheeks. These movements may cause a significant change of temperature in facial spatial dimension, and influence the pattern of the temperature difference data. The big change may yield large F-values of corresponding features according to equation 9. Thus, the features in these regions would be selected with high possibilities. For the nose, the temperature change caused by different expression states may be disturbed by the respiratory rate. Additionally, as reported by some previous studies, the temperature variance of the forehead region is very helpful for emotion analysis or expression recognition [8][9][24]. However, the features of the forehead region are not as useful as the features in the other facial sub-regions in this paper. The reason may be that the foreheads of some subjects used in our experiments are covered by their hair, which is an obstacle to feature extraction. The results of Fig. 5 indicate that the features in the mouth and cheek play an important role in classifying facial expressions in arousal and valence dimensions, which is consistent with some previous work [17][23].

On the other hand, as shown in Fig. 6, the selected features for the best classification results are mainly composed of seven basic sequence features: V_{min}, V_{max}, V_{std}, V_m, G_{min}, G_{max} and G_{std}. This shows that the maximum variation and gradient of temperature sequence, especially maximum variation, play a significant role in our expression recognition experiments, which is consistent with previous work [12]. On the contrary, the mean and standard deviation of temperature sequence are rarely selected, so these two may be independent from the expression states, or play a minor role in the classification task.

5 Conclusion

In this paper, the spontaneous expressions in arousal and valence dimensions are classified based on the Adaboost algorithm by using the thermal videos. Firstly, the horizontal and vertical temperature difference data are calculated from the semi-manually located facial regions of each frame, in which four ROIs are also marked out, named forehead, nose, mouth and cheeks. Secondly, for each grid in each ROI, four statistic parameters are extracted, and then four dynamic time-series features extracted from each static parameter vector are also obtained. Thirdly, the F-value feature selection method is used to obtain an optimal feature subset. Finally, the Adaboost algorithm with the weak classifier of KNN is used to classify expressions in arousal and valence dimensions. Experiments are implemented on USTC-NVIE database to validate the effectiveness of our method. The highest classification accuracies between high versus low arousal and valence are achieved with 75.3% and 76.7% respectively, which indicates that our method is effective for classifying expressions. Further analysis shows that the features of the mouth region play the most important role in classification arousal and valence compared with the features of some other facial regions.

Acknowledgment. This paper is supported by the NSFC (61175037), Special Innovation Project on Speech of Anhui Province (11010202192), project from Anhui Science and Technology Agency and Youth Creative Project of USTC.

References

1. Zeng, Z., Pantic, M., Roisman, G.I., Huang, T.S.: A survey of affect recognition methods: Audio, visual, and spontaneous expressions. IEEE Transactions on Pattern Analysis and Machine Intelligence 31(1), 39–58 (2009)
2. Fasel, B., Luettin, J.: Automatic facial expression analysis: a survey. Pattern Recognition 36(1), 259–275 (2003)
3. Khan, M.M., Ward, R.D., Ingleby, M.: Classifying pretended and evoked facial expressions of positive and negative affective states using infrared measurement of skin temperature. ACM Transactions on Applied Perception (TAP) 6(1), 1–22 (2009)
4. Jenkins, S., Brown, R., Rutterford, N.: Comparing thermographic, eeg, and subjective measures of affective experience during simulated product interactions. International Journal of Design 3(2), 53–65 (2009)
5. Levine, J.A., Pavlidis, I., Cooper, M.: The face of fear. The Lancet 357(9270), 1757 (2001)
6. Nozawa, A., Tacano, M.: Correlation analysis on alpha attenuation and nasal skin temperature. Journal of Statistical Mechanics: Theory and Experiment, P01007 (2009)
7. Nakanishi, R., Imai-Matsumura, K.: Facial skin temperature decreases in infants with joyful expression. Infant Behavior and Development 31(1), 137–144 (2008)
8. Pavlidis, I., Levine, J.: Thermal image analysis for polygraph testing. IEEE Engineering in Medicine and Biology Magazine 21(6), 56–64 (2002)
9. Puri, C., Olson, L., Pavlidis, I., Levine, J., Starren, J.: Stresscam: non-contact measurement of users' emotional states through thermal imaging. In: Extended Abstracts on Human Factors in Computing Systems, CHI 2005, pp. 1725–1728. ACM (2005)
10. Khan, M.M., Ward, R.D., Ingleby, M.: Infrared thermal sensing of positive and negative affective states. In: IEEE Conference on Robotics, Automation and Mechatronics, pp. 1–6. IEEE (2006)

11. Nhan, B.R., Chau, T.: Classifying affective states using thermal infrared imaging of the human face. IEEE Transactions on Biomedical Engineering 57(4), 979–987 (2010)
12. Jarlier, S., Grandjean, D., Delplanque, S., N'Diaye, K., Cayeux, I., Velazco, M., Sander, D., Vuilleumier, P., Scherer, K.: Thermal analysis of facial muscles contractions. IEEE Transactions on Affective Computing (99), 1 (2011)
13. Yoshitomi, Y.: Facial expression recognition for speaker using thermal image processing and speech recognition system. In: Proceedings of the 10th WSEAS International Conference on Applied Computer Science, pp. 182–186. World Scientific and Engineering Academy and Society, WSEAS (2010)
14. Krzywicki, A.T., He, G., O'Kane, B.L.: Analysis of facial thermal variations in response to emotion: eliciting film clips. Proceedings of SPIE 7343, 734312 (2009)
15. Koda, Y., Yoshitomi, Y., Nakano, M., Tabuse, M.: A facial expression recognition for a speaker of a phoneme of vowel using thermal image processing and a speech recognition system. In: The 18th IEEE International Symposium on Robot and Human Interactive Communication, RO-MAN 2009, pp. 955–960. IEEE (2009)
16. Hernández, B., Olague, G., Hammoud, R., Trujillo, L., Romero, E.: Visual learning of texture descriptors for facial expression recognition in thermal imagery. Computer Vision and Image Understanding 106(2-3), 258–269 (2007)
17. Khan, M.M., Ingleby, M., Ward, R.D.: Automated facial expression classification and affect interpretation using infrared measurement of facial skin temperature variations. ACM Transactions on Autonomous and Adaptive Systems (TAAS) 1(1), 91–113 (2006)
18. Trujillo, L., Olague, G., Hammoud, R., Hernandez, B.: Automatic feature localization in thermal images for facial expression recognition. In: IEEE Computer Society Conference on Computer Vision and Pattern Recognition-Workshops, CVPR Workshops, p. 14. IEEE (2005)
19. Wang, P., Ji, Q.: Multi-view face and eye detection using discriminant features. Computer Vision and Image Understanding 105(2), 99–111 (2007)
20. Keys, R.: Cubic convolution interpolation for digital image processing. IEEE Transactions on Acoustics, Speech and Signal Processing 29(6), 1153–1160 (1981)
21. Wang, Y., Ai, H., Wu, B., Huang, C.: Real time facial expression recognition with adaboost. In: Proceedings of the 17th International Conference on Pattern Recognition, ICPR 2004, vol. 3, pp. 926–929. IEEE (2004)
22. Bartlett, M.S., Littlewort, G., Frank, M., Lainscsek, C., Fasel, I., Movellan, J.: Recognizing facial expression: machine learning and application to spontaneous behavior. In: IEEE Computer Society Conference on Computer Vision and Pattern Recognition, CVPR 2005, vol. 2, pp. 568–573. IEEE (2005)
23. Wang, S., Liu, Z., Lv, S., Lv, Y., Wu, G., Peng, P., Chen, F., Wang, X.: A natural visible and infrared facial expression database for expression recognition and emotion inference. IEEE Transactions on Multimedia 12(7), 682–691 (2010)
24. Khan, M.M., Ward, R.D., Ingleby, M.: Automated classification and recognition of facial expressions using infrared thermal imaging. In: IEEE Conference on Cybernetics and Intelligent Systems, vol. 1, pp. 202–206. IEEE (2004)

Motion Planning of a Dual Manipulator System for Table Tennis

Guowei Zhang[1,2], Cong Wang[3], Bin Li[3], and Huaibing Zheng[3]

[1] Shenyang Institute of Automation,
Chinese Academy of Sciences, Shenyang, China
[2] Graduate School of the Chinese Academy of Sciences,
Beijing, China
zhgw@sia.cn
[3] Institute Shenyang Institute of Automation,
Chinese Academy of Sciences Shenyang, China
{cwang,libin,hbzheng}@sia.cn

Abstract. This paper describes the design and development of a novel dual manipulator system for table tennis as an application of Human-Robot Interaction (HRI). To hit table tennis quickly, a method to obtain time-constrained trajectory joining two way-points is developed and implemented. Because the quintic polynomial trajectory is a smooth curve and can reduce jerk, it appears to be excellent choice for hitting task. Five phase quintic polynomials are adopted to fit the smooth trajectory in joint space under the constraint of robotic kinematics parameters. The boundary conditions of five phase qunitic polynomials used to compute the trajectories are discussed under different initial kinematics conditions. Experimental results of actual robotic system with dual manipulators and vision system show that the proposed method works well.

1 Introduction

As one of the major effectors of a robot, HRI research is a multidisciplinary field with contributions from human-computer interaction, artificial intelligence, robotics, natural language understanding and social sciences. A robotic ping pong player system is a classic case of HRI, which involves the coordinated vision and arm movement to execute a task. In this paper, a new dual manipulator system is developed to hit ping pong ball, in which the vision system can predict the exact future trajectory of the ball through four-dimensional space-time, and provide the position, velocity of the ball and further direct the movement of the dual manipulator towards targets.

Andersson designed the first robot ping-pong player [1], which can play ping-pong against humans and machine, and meet the robot ping-pong rules proposed by Billingsley. The mechanical part of the robot is composed of a six degree of freedom (DOF) PUMA 260 manipulator with a paddle at the end of a 0.45m long stick. The 3D vision system consisted of four video cameras is charged with the task of predicting the exact future trajectory of the ball through four-dimensional space-time. Toshiba in Japan built a seven axis direct-drive (DD) articulated robot for the purpose of playing Ping-Pong [5]. The vision system consisted of two charged coupled device (CCD) cameras senses

S. Lee et al. (Eds.): Intelligent Autonomous Systems 12, AISC 194, pp. 335–344.
springerlink.com

the position and trajectory of the ball. The robot is prepared to play against a wall and is able to return the ball up to four consecutive times. Differing from the above studies, Matsushima et al. at Osaka University developed a robot system with the minimum number of degrees of freedom [9]. The robot is driven by four electric motors, two for the motion in a horizontal plane and other motors for paddle attitude. Further, a stereo vision system (Quick MAG System 3) extracts the ball's location from the image.

An important problem in this filed is motion planning, which deals with the robotic interception of moving objects with necessary velocity at a specific instant in time. Kober et al. studied the hitting and batting tasks using the seven DOF Barrett WAM robot [7]. Hujic et al. presented a novel active prediction planning and execution system for the robotic interception of moving objects with the ability to intercept the object anywhere along its predicted trajectory [6]. Buttazzo et al. described a real time control methodology for catching a fast moving object adapting the prediction technique to compensate the time delays introduced by visual processing and by the robot controller [3].

This paper is organized as follows. First, Section 2 describes the dual manipulator system for table tennis, mainly focusing on the humanoid manipulator design, table tennis serving equipment design. Section 3 illustrates the real time trajectory planning for hitting task with continuous movement. In Section 4, an experiment is presented to prove the motion planning method. Finally, in Section 5 the conclusion of this paper is given.

2 Dual Manipulator System

So far, the developed robotic ping pong players including single robotic arm, dual robotic arm or humanoid robot only take hitting and batting tasks, and can't serve table tennis ball using two arms, just as a human does. In this paper, a robotic ping pong player with two arms is developed. The left arm (named serving arm) is used for serving ball and right arm (named hitting arm) is used for hitting the ball. Fig. 1 illustrates the robotic ping pong player system developed by us.

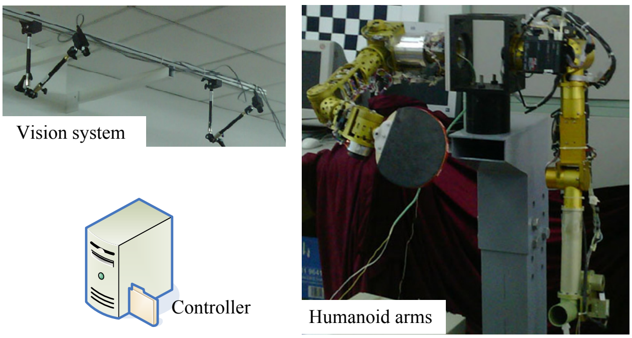

Fig. 1. Robotic ping pong player system

2.1 Humanoid Arm Design

For the purpose of playing table tennis, we need control the position of the paddle center and the normal vector of the paddle plane. Although Andersson stated that only five DOF are required for the paddle to execute the table tennis task. A six DOF manipulator was adopted to play table tennis [1]. Redundant manipulators with seven DOF were used in [9, 11, 12].

A novel humanoid arm (hitting arm) with six DOF is built as shown in Fig. 2. The three DOF in shoulder and one DOF in elbow control the position of the paddle, and two DOF in wrist adjust the normal of paddle plane. Because rotating the paddle about its normal vector can't change the flying trajectory of the ball after hitting. In this sense, we can see that the arm configuration is redundant. Moreover we can get the ideal joint velocity through varying the pose of the paddle in the condition of keeping the normal vector of the paddle unchanged. The serving arm has four DOF, which can adjust position and pose of serving equipment. In addition, the configuration of shoulder and elbow is same as the hitting arm.

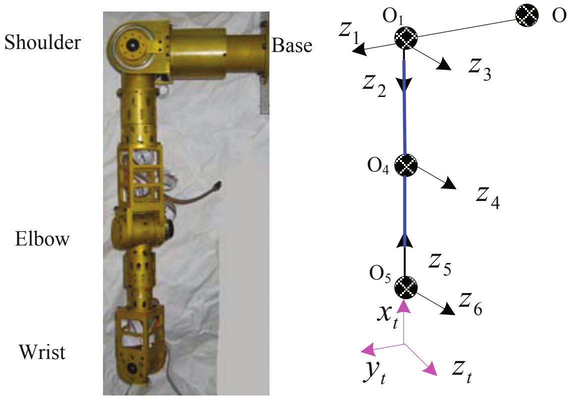

Fig. 2. Robotic ping pong player system

2.2 Table Tennis Serving Equipment

Fig.3 illustrates the table tennis serving equipment, which can serve five balls continuously. The cam is mounted on surface of the cam drive mechanism which is driven by a motor. When the cam turns, the cam follower moves down along the axis of the ejection mechanism. Then the ball in the delivering tube runs into the ejection guiding tube because of gravity. As the cam follower moves beyond the top point of the cam, the follower quickly moves up along ejection mechanism, and fires the ball. Then the ball flies out along the ejection guiding tube.

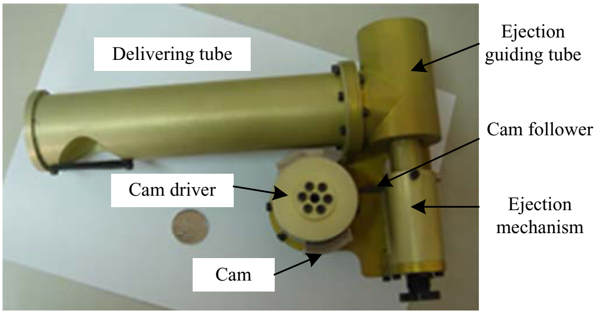

Fig. 3. Robotic ping pong player system

2.3 Control System

A multi-level distributed control architecture is put forward in the hardware design of the control system and a modular controller based on CANbus is designed to realize real-time control among multiple joints [4]. The real-time operation system VxWorks is adopted as the software platform of the control system.

2.4 Vision System

To track the ball, a vision system consisted of two CCD cameras (Point Grey) is built by Zhejiang University. The system can find the position of the ball at the end of each camera frame. After several frames, the observed trajectory fitted by the above data, is used to predict the future trajectory of the ball after it bounces on the table.

In this paper, the vision system predicts the ideal hitting position p_p, velocity v_i of the incoming ball and hitting time t_f to guide the hitting arm to hit the ball at a specified location in time.

3 Motion Planning

3.1 Table Tennis Task Description

In the human game play, the player serving the ball tosses the ball directly upward and strikes the ball with the racket on the ball's descent, then a play is commenced. Simulating the game like the human being, the table tennis task consists of two tasks including serving task and target-hitting task.

In the serving task, the left arm adjusts the position and pose of the table tennis serving equipment to keep the ball flying out of the ejection guiding tube in different direction. When the cam follower fires the ball, the ball is tossed upward without spin, and the right arm hits the ball against the opponent at an ideal point which can be estimated as a known parameter according to the position and pose of the serving equipment. Then the game begins.

The target-hitting task can be seen as a sense-plan-act cycle, in which the vision system data trigger the controller to plan the motion trajectory and drive the motors. The target-hitting task can be divided into three subtasks including waiting task, hitting task and returning task [9]. In the waiting task, the data provided by vision system are employed to estimate the normal vector a of the paddle and hitting velocity v_p associated with the trajectory to return the ball to the opponent, at the same time, smooth jerk-bounded trajectories in joint space are planned through the four way-points including initial position p_0, hitting position p_p, final position p_m, and position p_0. The hitting task is to return the incoming ball back at hitting position pp at the time t_f, in which time the velocity of the paddle gets hitting velocity v_p. The returning task is to return the paddle to the initial position p0 to prepare for the next hitting.

3.2 Motion Planning Algorithm

Several relevant trajectories were reviewed and compared in [1, 2, 10], such as trapezoidal velocity, quintic polynomials, cosine, and sinusoid on ramp. The advantage of the quintic polynomial is that the acceleration doesn't change to or from a finite value instantaneously. To eliminate the jerk partly caused by acceleration, it is clearly that the quintic polynomial approach appears to be an excellent choice for hitting task. However, when the initial and/or final speeds are non-zero, the resulting trajectory will be slower and may have a number of undesirable oscillations in position, velocity and acceleration among the way-points. For obtaining smooth jerk-bounded trajectories, a concatenation of the quintic polynomial is used to provide a smooth trajectory between two points [8].

Unlike Macfarlane's algorithm, we aim to solve the time-constrained motion planning problem. The desired motion trajectory of each joint is given as a quintic polynomial of time, and the basic equation is

$$p(t) = a_5t^5 + a_4t^4 + a_3t^3 + a_2t^2 + a_1t + a_0 \ , \tag{1}$$

Where a_0-a_5 are real coefficients. The boundary conditions are

$$\begin{aligned} p(0) = p_i, v(0) = v_i, a(0) = a_i \\ p(t_f) = p_f, v(t_f) = v_f, a(t_f) = a_f \end{aligned} \tag{2}$$

Where, variable p_i denotes the initial position; v_i denotes the initial velocity; a_i denote the initial acceleration. Similarly, variable p_f, v_f, a_f light up as the final position, velocity and acceleration respectively. t_f denotes the duration time.

In this paper, five phase quintic polynomials are adopted to fit a smooth trajectory joining two way-points for each joint, as shown in Fig. 4. The general boundary conditions corresponding to the five phase quintic polynomials are shown in Table 1. The acceleration ramp up and ramp down are symmetrical, and the speed ramp is also symmetrical about a straight line down from the start of the ramp to the end of the ramp [8]. The first phase is a acceleration trajectory and at the time t_1 the acceleration reaches the max value a_{max}. The second phase is also a acceleration trajectory, but the acceleration decreases from a_{max} to 0. After the acceleration trajectory, a constant speed trajectory

Table 1. Boundary conditions of five phase quintic polynomials

Node	Time	Position	Velocity	Acceleration
1	0	p_i	0	0
2	t_1	p_2	$0.5a_{max}t_1$	a_{max}
3	$2t_2$	p_3	$a_{max}t_1$	0
4	$t_f - 2t_2$	p_4	$a_{max}t_1$	0
5	$t_f - t_2$	p_5	$a_{max}t_1 - 0.5a_{max}t_2$	-a_{max}
6	t_f	p_f	v_f	0

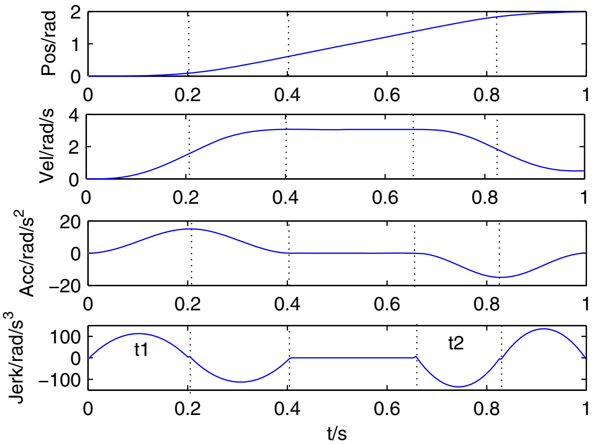

Fig. 4. Robotic ping pong player system

follows. It is similar to the acceleration trajectory, the deceleration trajectory is divided into two phases: in the forth phase the acceleration decreases form 0 to -a_{max} and the duration time is t_2; in the fifth phase the acceleration increases form -a_{max} to 0. In Table 1, the positions of the way-points are

$$\begin{aligned} p_2 &= p_i + a_{max}t_1^2(1/4 - 1/\pi^2) \\ p_3 &= p_i + a_{max}t_1^2 \\ p_4 &= p_i + a_{max}t_1^2 + a_{max}t_1(t_f - 2t_1 - 2t_2) \\ p_5 &= p_i + a_{max}t_1^2 + a_{max}t_1(t_f - 2t_1 - 2t_2) - a_{max}t_2^2(1/4 - 1/\pi^2) + a_{max}t_1t_2 \\ p_f &= p_i + a_{max}t_1^2 + a_{max}t_1(t_f - 2t_1 - 2_2) + a_{max}t_2^2 \end{aligned} \tag{3}$$

In the hitting task, the initial kinematics conditions of each joint are

$$v_i = 0, a_i = 0, a_f = 0 \,, \tag{4}$$

and the kinematics constraints are as following

$$-v_{max} \leq v_{lim} \leq v_{max}, -a_{max} \leq a_{lim} \leq a_{max} \,, \tag{5}$$

Where v_{max} is the joint's max velocity; v_{lim} denotes the extreme value of the joint's velocity; a_{lim} denotes the extreme value of the joint's acceleration.

When the initial parameters of each joint are

$$p_i \neq p_f, v_i = v_f = 0, a_i = a_f = 0\ , \tag{6}$$

One quintic polynomial can ideally draw the motion trajectory. But if the max velocity or acceleration is beyond its own limit under time constraint, the motion trajectory becomes unfeasible. Five phase quintic polynomials are used to represent the smooth trajectory and the acceleration time t_1 is equal to the deceleration time t_2. By applying the condition (6), we rewrite the equation (3) and obtain

$$\begin{aligned} p_f - p_i = 2a_{max}t_1^2 + a_{max}t_1(t_f - 4t_1) \\ a_{max} \geq 8(p_f - p_i)/t_f^2 \\ v_{max} \geq a_{max}t_1 \end{aligned} \tag{7}$$

When the initial parameters of each joint are

$$p_i \neq p_f, v_i = 0, v_f \neq 0, a_i = a_f = 0\ , \tag{8}$$

If the max velocity or acceleration is beyond its own limit, and $v_f/a_{max} \leq t_f - (p_f - p_i)/v_f$, the smooth trajectory is fitted by three phase quintic polynomials, and is constrained by the following conditions

$$\begin{aligned} p_f - p_i = at_1^2 + at_1(t_f - 2t_1) \\ v_f = at_1 \\ a \leq a_{max} \end{aligned} \tag{9}$$

If the max velocity or acceleration is beyond its own limit, and $v_f/a_{max} > t_f - (p_f - p_i)/v_f$, the smooth trajectory is fitted by five phase quintic polynomials, and is constrained by the following conditions

$$\begin{aligned} p_f - p_i = a_{max}t_1^2 + a_{max}t_1(t_f - 2t_1 - 2t_2) - a_{max}t_2^2 + 2v_ft_2 \\ v_f = a_{max}(t_1 - t_2) \\ v_{max} \geq a_{max}t_1 \end{aligned} \tag{10}$$

We can easily computer the time variable t_1 and t_2 and get the boundary conditions in Table 1 according to initial parameters. In our application, we can computer the joint positions j_0 and j_p corresponding to p_0 and p_p. Similarly, we can calculate the velocity v_i based on v_p. The final position p_m is unknown, but it can be computed by j_m in joint space. For any joint i, the boundary conditions are

$$\begin{aligned} p(t_f) = j_{pi}, v(t_f) = v_{ji}, a(t_f) = 0 \\ v(t_s) = 0, a(t_s) = 0 \end{aligned} \tag{11}$$

A straightforward attempt to compute the maximum acceleration as a function of an arbitrary j_{mi}, and then to minimize this maximum over j_{mi} turns out to be feasible. Applying the boundary conditions, we can obtain the final joint position

$$j_{mi} = j_{pi} + v_{ji}^2/a_{max}\ , \tag{12}$$

4 Experimental Result

To examine the method presented in Section 3, a series of smooth trajectory for all joints are planned. A set of data provided by vision system is

p_p=[55.990, 1545, 291.134]^{T}mm
v_i=[0.0475, 2.5412,-0.8327]^{T}m/s

In addition, the hitting motion's duration is 0.36s.

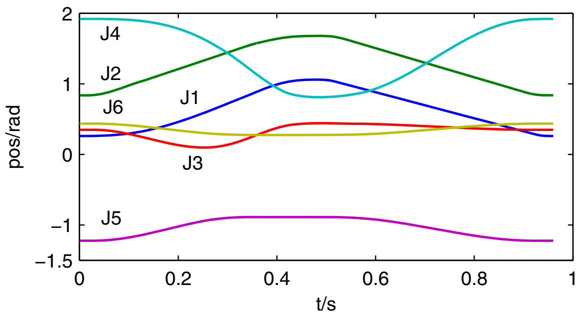

Fig. 5. Smooth trajectories of multiple joints

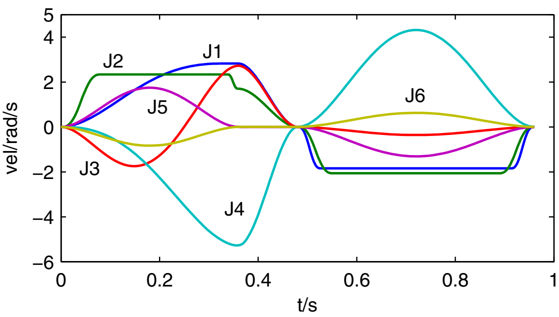

Fig. 6. Velocity curves of multiple joints

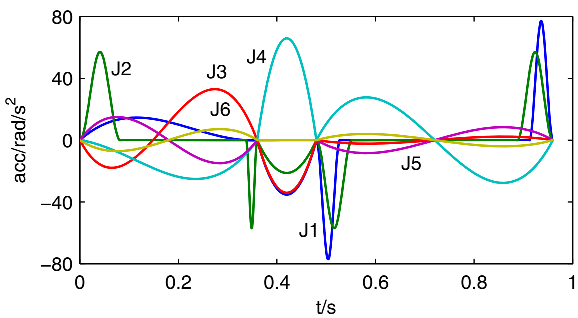

Fig. 7. Acceleration curves of multiple joints

Fig. 5 shows the smooth trajectories of each joint for one table tennis task cycle. Fig. 6 shows the continuous velocity curves of each joint. As shown in Fig. 7, the acceleration curves of each joint is continuous and at all interval points the acceleration doesn't change to or from a finite value instantaneously.

5 Conclusion

The paper addresses the design and build of a dual manipulator system for table tennis. For hitting task, we have described a method to plan a smooth trajectory with jerk limit. Five phase quintic polynomials are used to fit the joint trajectory according to initial kinematics conditions. Comparing with Macfarlane's work, we emphatically solve the time-constrained trajectory problem. Experimental results have shown that at all interval points the acceleration doesn't change to or from a finite value instantaneously, and doesn't excite vibrations in the dual manipulator system.

Acknowledgement. This work was supported by The National High Technology Research and Development Program of China (863 Program) (2008AA042602).

We would like to thank Rong Xiong and Yifeng Zhang from State Key Laboratory of Industrial Control Technology, Zhejiang University, for their help in vision system.

References

1. Andersson, R.L.: A robot ping-pong player: Experiment in real-time intelligent control. The MIT Press, Cambridge (1988)
2. Ata, A.A.: Optimal trajectory planning of manipulators: a review. Journal of Engineering Science and Technology 2(1), 32–54 (2007)
3. Buttazzo, G.C., Allotta, B., Fanizza, F.P.: Mousebuster: a robot system for catching fast moving objects by vision. In: The 1993 IEEE International Conference on Robotics and Automation, pp. 932–937 (1993)
4. Gong, H.L., Li, B., Zhang, G.W., et al.: Design of a modular control system for humanoid robot dexterous servo arm. Chinese Journal of Scientific Instrument 31(8), 106–110 (2010)
5. Hartley, J.: Toshiba progress towards sensory control in real time. Indust. Robot 14(1), 325–329 (1999)
6. Hujic, D., Croft, E.A., Zak, G., et al.: The robotic interception of moving objects in industrial settings: strategy development and experiment. IEEE/ASME Transactions on Mechatronics 3(3), 225–239 (1998)
7. Kober, J., Mlling, K., Kroemer, O., et al.: Movement templates for learning of hitting and batting. In: The 2010 IEEE International Conference on Robotics and Automation, pp. 853–858 (2010)
8. Macfarlane, S.: Online smooth trajectory planning for manipulators. Dissertation, The University of New Brunswick (1999)
9. Matsushima, M., Hashimoto, T., Miyazaki, F.: Learning to the robot table tennis task – Ball control & rally with a human. In: The 2003 IEEE International Conference on Systems Man and Cybernetics, vol. 3, pp. 2962–2969 (2003)

10. Rajan, R.: Motion Planning of Dynamic Systems. Dissertation, The University of Texas (2001)
11. Zhang, B., Xiong, R., Wu, J.: Kinematics analysis of a novel 7-DOF humanoid manipulator for table tennis. In: The 2011 International Conference on Electronics, Communications and Control (ICECC), pp. 1524–1528 (2011)
12. Zhang, Q., Xie, Z.W., Liu, Y.W., et al.: High Dynamic Humanoid Robot Arm for Ping-Pong Playing. Applied Mechanics and Materials 80-81, 1081–1085 (2011)

Integrated Balance Control on Uneven Terrain

Feng Xue[1], Xiaoping Chen[1], Jinsu Liu[1], and Daniele Nardi[2]

[1] Department of Computer Science and Technology,
University of Science and Technology of China,
Hefei, 230026, China
[2] Department of Compute and System Science,
Sapienza University of Roma,
Via Ariosto 25, Roma, Italy

Abstract. To reach competent Human-Robot Interaction, robots should be able to behave stably on uneven terrain in domestic environments. This paper addresses a technique, which integrates four balance control strategies and is used on Nao robot to realize walking on uneven terrain that is not modelled in advance. The most important two strategies are “Closed Loop Gait Pattern Generator” and “Posture Control”. The former one uses the filtered robot state based on Kalman filter. It helps to improve joint tracking, which is important for model based approaches. The latter one helps to make the trunk vertical to the ground. This strategy is very effective when walking on a slope. The other two strategies are “CoG (Center of Gravity) Height Control” and “Ankle Joint Control”, which are used to resist relatively large tilt and prevent potential falling over motion. *abstract* environment.

Keywords: Biped Walking, Balance Control, Uneven Terrain.

1 Introduction

The biped robots need the ability to maintain balance on uneven terrain in order to perform competent Human-Robot Interaction with human beings. However, it is not a trivial task due to high dimensional control space and complex dynamic model.

Recently, real time gait pattern modification techniques have been well studied. Tajima et al. [8] achieved a running motion by repeating compensation process at high frequency where the shifted CoG and foot location and the orientation are treated as initial conditions. Nishwaki et al. [7] made the robot be able to walk on piled tiles by using preview control to suppress ZMP fluctuation. Wieber [11] proposed a Linear Model Predictive Control (LMPC) scheme to compensate strong perturbations in simulation. In the work by Diedam el al. [3], an extended LMPC scheme considering foot step positions is employed. When the disturbance is not allowed by the support polygon, the Capture Region [4] should be computed to take a step to avoid a fall. However, it may lead the robot to undesirable behavior, especially when the terrain is uneven and

S. Lee et al. (Eds.): Intelligent Autonomous Systems 12, AISC 194, pp. 345–354.
springerlink.com

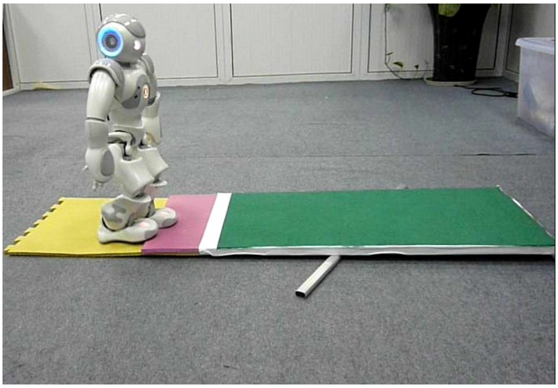

Fig. 1. The Uneven Terrains and Our Robot Named Nao

not modelled in advance as shown in Figure 1. Indeed on the path of the new trajectory, stronger disturbances may be waiting for the robot.

In our previous work [6] [5], we proposed a biped walking generator which is able to plan smooth and flexible walking motions on rough terrains. It works well in simulation environment, while in real case the robot fell over sometimes because of the modelling errors of environment and robot itself.

Yusuke et al. [12] proposed virtual compliance control and posture control strategies to realize a robot walking on slopes. In our work, the robot is not only able to walk forward on the slope, but also able to rotate or sidle on the slope. Moreover, the slope was not fixed but movable as shown in Figure 1.

The remainder of the paper is organized as follows. Section 2 will present the four strategies one by one in detail. Experiments are shown in Section 3. We draw our conclusions in Section 4.

2 Integrated Balance Control

2.1 Overview

This section describes the flow chart of the strategies to apply one by one in each control cycle. If it is in the first control cycle of a walking step, we invoke our gait pattern generator, which uses the latest robot state and simultaneously plans the desired CoG trajectory (a series of robot state) and ZMP trajectory for each control cycle of this walking step. Due to the delay of the joint sensors, we can not simply use them to compute the latest robot state. In consequence, a Kalman filter is introduced which is described in the next section. The following step is "CoG Height Control". It checks whether the tilt angle along lateral axis is large. And it will modify the CoG height to eliminate it. Then "Ankle Joint Control" is called to generate the compensations to the ankle joints, which will be added to the original desired foot trajectories. This will move the CoP which is at the foot edge to prevent potential falling over. All the joint trajectories are then computed via inverse kinematics. Before sending the joints trajectories to the actuators, “Posture Control” is called to make sure the trunk is vertical to the ground.

2.2 Real Time Closed Loop Gait Pattern Generator

In our previous work [2], we presented a gait pattern generator based on 3D-LIP model [9]. Its ZMP trajectories are represented as a cubic polynomial. Taking trajectory along X-Axis as an example, its function is : $P_x(t) = \sum_{i=0}^{3} a_i t^i$, where $P_x(t)$ is ZMP trajectories, a_i is the coefficient, and t is the time. Note that, in this paper, we set the sagittal direction (from the back to the front) as Y-Axis, and lateral direction (from the left to the right) as X-Axis.

The dynamics based on the 3D-LIP model is well known: (shown only X-Axis, Y-Axis is similar).

$$\ddot{X}(t) z_h = (X(t) - P_x(t))g \tag{1}$$

where $X(t)$ is the CoG trajectory along X-Axis, z_h is the height of the pendulum, and g is the acceleration of gravity.

Its analytical solution is:

$$\begin{bmatrix} X(t) \\ \dot{X}(t) \end{bmatrix} = A(t) \begin{bmatrix} x_i \\ \dot{x}_i \end{bmatrix} + [I - A(t)]C + B(t) \tag{2}$$

$$A(t) = \begin{bmatrix} cosh(qt) & \frac{1}{q} sinh(qt) \\ q sinh(qt) & cosh(qt) \end{bmatrix}$$

$$B(t) = \begin{bmatrix} \sum_{i=0}^{3} a_i t^i + 6a_3 t/q^2 - a_0 \\ 3a_3 t^2 + 2a_2 t \end{bmatrix}$$

$$C = \begin{bmatrix} a_0 + 2a_2/q^2 \\ a_1 + 6a_3/q^2 \end{bmatrix}, \quad q = \sqrt{\frac{g}{z_h}}$$

where $[x_i, \dot{x}_i]^T$ is the initial state, I is a 2×2 identity matrix and “$A(t)$, $B(t)$” are called *Time Matrices* which are determined by the time t. Note that the four coefficients $a_i, i = 0, .., 3$ have been solved by simultaneously planning as presented in our previous work [2].

Due to the delay of the joint sensors, we can not use the measured robot state computed from them as the initial state ($[x_i, \dot{x}_i]^T$). Thus, we treat it as a single-variable Kalman filter with no control component and no prediction algorithm. We use a single variable tuned by hand to plan the best weight between the desired robot state and the one measured from joint sensors. The measured CoG position is denoted as CoG_e and the desired one is treated as the guessed CoG denoted as CoG_g. So the filtered CoG position denoted as $CoG_f = [x_i, y_i, z_i]$ treated as the initial state is:

$$CoG_f = CoG_g + K_{CoG} * (CoG_e - CoG_g) \tag{3}$$

where K_{CoG} is the coefficient determined experimentally.

The filtered velocity of CoG is its first derivative. Together with the filtered position forms the filtered robot state (we also call it the planned robot state). Note that, when we use this filter to calculate the initial state ($[x_i, \dot{x}_i]^T$), the desired state is the one of the last control cycle. Moreover, we apply this filter also in the other control cycles which helps to avoid jitter problem.

As shown in Figure 2 where the gait pattern is closed-loop, the robot is pushed back at the very beginning. At the time of 850[s], the tilt angle was around 0.16[rad] and the measured CoG position is around -0.04[m]. The black line is the planned CoG position, filtered from the measured CoG position and the desired one (constantly 0[m]). The weight K_{CoG} used here is set to 0.3. After two double support phases (indicated as grey shadow), the robot managed to resist the tilt. And then the attitude sensor output is between -0.02[rad] and 0.02[rad].

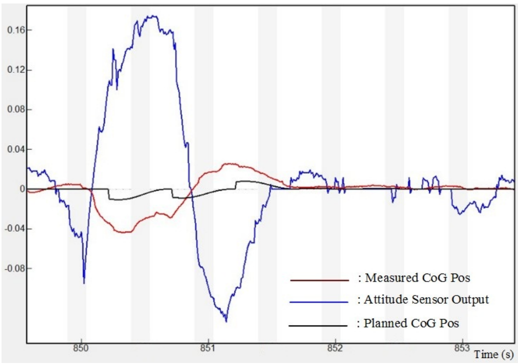

Fig. 2. The output of the attitude sensor around lateral axis, the planned and measured CoG position, when the gait pattern generator is closed-loop

2.3 Robot Posture Control

A PD controller is incorporated to filter the raw trunk angles denoted as θ_x and θ_y around X-Axis and Y-Axis respectively. The filtered trunk angle along X-Axis denoted as $TrunkRot_x$ is: (Y is similar)

$$TrunkRot_x = KTrunkP_x * \theta_x + KTrunkD_x * \dot{\theta}_x \tag{4}$$

where $KTrunkP_x$ and $KTrunkD_x$ are proportional gain and derivative gain respectively.

We can not simply add the angles to hip pitch joints even if they have been filtered. A large recovery value will make the robot jitter and a small one is not effective. The algorithm shown in Table 2.3 is for front-back posture control. The left-right one is similar. $Comp_i$ is denoted as the compensation to the two hip pitch joints in i-th cycle. K_{Gyro} and K_{Angle} are denoted as the gains used for gyrometer output $Gyro_x$ and trunk angle $TrunkRot_x$ respectively. Max is denoted as the threshold for the angle to be recovered in one control cycle.

Table 1. Pseudocode for posture recovery around lateral axis

```
POSTURE_RECOVERY
1  detGyro = K_Gyro * Gyro_x * 0.01
2  if (|detGyro| > Max) then
3     if (detGyro > 0) then detGyro = Max
4     else detGyro = -Max
5
6  detAngle = K_Angle * TrunkRot_x
7
8  Comp_i = Comp_{i-1} + detGyro + detAngle
```

This algorithm calculates the compensation angle to be set to the total hip pitch compensation of the control cycle. It first adds a certain percentage of the gyrometer output to it (see line 1 to line 4) which is able to adapt to the tilt speed. The faster the tilt, the larger compensation value or angle speed it will set to the hip joints. Moreover, it adds a certain percentage of the trunk rotation angle (line 6). This helps to gradually recover the posture. The two parameters K_{Gyro} and K_{Angle} are carefully tuned by hand to ensure an effective recovery and not causing jitter problem. As shown in Figure 3, the blue line is the compensation for hip pitch joints and the red line is the trunk angle. At the time around 112[s], the robot was pushed hard to the back, resulting in a large tilt angle around 0.2[rad] lasting 1[s]. Thanks to this algorithm the posture was recovered. In this case, K_{Angle} and K_{Gyro} were set to 0.01 and 0.008, respectively.

2.4 Robot CoG Height Control

When the robot is about to tip over, the planned "ZMP" where $M_x = 0$ and $M_y = 0$ is outside the support polygon (FZMP). Its moment generated by gravity and inertial force about the CoP equals to:

$$M = m\ddot{x}z\cos\theta - mg(x - p_{CoP}) \tag{5}$$

where θ is the angle that the robot tilts, p_{CoP} is the position of Center of Pressure. Note that, the height of CoG is controlled in a linear way, so it does not involve the term $\ddot{z}$.

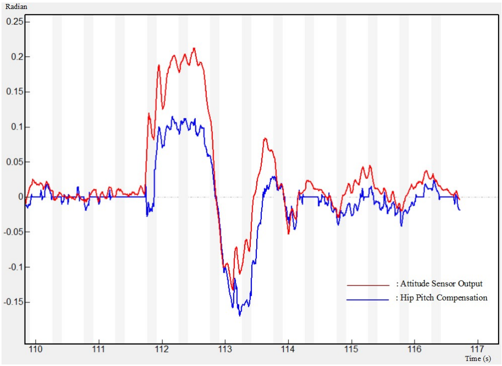

Fig. 3. Nao was pushed hard to the back. It shows the attitude sensor output and the compensation trajectory to the hip joint.

The CoG trajectory is generated according to the basic dynamic equation of LIP which is:

$$\ddot{x} z_h = g(x - p_x) \tag{6}$$

where z_h is the normal height of CoG. It is as the same as Equation 1. We rewrite it for convenience.

Thus we have:

$$M = mg(x - p_x) \cos\theta \frac{z}{z_h} - mg(x - p_{CoP}) \tag{7}$$

In this equation, $\cos\theta$ approximates to 1 and $(x - p_x)$ approximates to $(x - p_{CoP})$. Then, the sign of the moment M is governed by $(z - z_p)$. Therefore, the CoG height (or pendulum height) can be controlled to generate recovery moment which resists the robot from tilting over.

2.5 Ankle Joint Control

Many researches have employed ground reaction force control to generate a moment about the desired ZMP to compensate the disturbance [7] [10]. In our case, the FSR sensors are not accurate, not to mention the measured ZMP computed from them. The sensors only work when the CoP moves to the edge of the foot. Therefore, we use this strategy only in emergency situation. Table 2 is the algorithm for left foot recovery (right foot recovery is similar). Variable $LComp_i$ and $RComp_i$ are denoted as the compensation values of i-th cycle for left foot and right foot respectively. Note that both of them contain two elements since compensation is needed around X-Axis and Y-Axis.

The algorithm first sets the compensation of this cycle as equal as the last one (line 1). Two cases need to be considered to control the foot. The first one is that both of the feet are contacting the ground (in double support phase). The other one is that the left foot is the stance foot in single support phase. If the

Table 2. Pseudocode for CoP control of Left Foot

```
LEFT_FOOT_RECOVERY ( LComp_{i-1}, Det)
1   LComp_i = LComp_{i-1}
2
3   if ((in double support phase) OR (stance foot is left))
4   {
5      if (ZMP near the front edge) then LComp_i.y -= Det
6      else if (ZMP near the back edge) then LComp_i.y += Det
7
8      if (ZMP at the left edge) then LComp_i.x += Det
9      else if (ZMP at the right edge) then LComp_i.x -= Det
10  }
11  else
12  {
13     if (LComp_i.x > Det) then LComp_i.x -= Det
14     else (LComp_i.x < -Det) then LComp_i.x += Det
15     if (LComp_i.y > Det) then LComp_i.y -= Det
16     else (LComp_i.y < -Det) then LComp_i.y += Det
17  }
```

foot needs to be controlled, we check the measured zmp and try to rotate the foot both in X-Axis and Y-Axis in order to shift the ZMP back from the edge (see line 3 to line 8). The rotation speed is "Det" degree per cycle.

If the foot is not contacting the ground, then the compensation is gradually set to zero in the speed of "Det" degree per cycle (see line 9 to line 14).

3 Experiment

3.1 The Nao Robot

Robot Nao is manufactured by "Aldebaran-Robotics" [1] with its height of 0.57[m] and its weight about 4.5[kg]. It is equipped with two axis gyrometers, three accelerometers and four FSR (Force Sensitive Resistor) sensors. The torso orientation is computed by a built-in chip via those readings resulting a delay around 70[ms]. The joint sensors have a delay around 50[ms].

3.2 Walking on Uneven Terrain

We conducted experiments of walking on uneven terrains as depicted in Figure 1. The green one is a 2[cm] thick hard board (80[cm] in length) covered with a thin carpet. A 1.7[cm] height stick was put randomly under the board making it a movable slope with average slope around 2.43[degree]. The yellow object is 1[cm] thick plastic which is a little bit soft and the pink one piled on it has the same thickness and material. The robot was walking with step duration 0.5[s].

The time for double support phase was 0.14[s] (28% of the step duration). It was controlled via wireless to step across the two plastic layers and onto the movable slope where the robot would walk backward/forward, sidle and rotate left/right.

We first turned off all our balance strategies, the robot was not able to step across the plastics as shown in Figure 4. We also tried the walking engine provided by Aldebaran-Robotics (the standard walking engine coming with the robot) and the robot was not able to step across the plastics too.

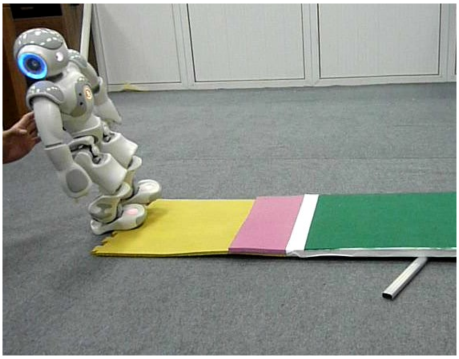

Fig. 4. The robot was unable to walk stably onto the steps when walking engine is open-loop

We switched back to our own walking engine and turned all of the strategies on and the robot accomplished the task successfully. It first walked onto the plastics with good looking walking style. Then it stepped on the slope and walked stably to the right. The tough part was when the robot was walking on the spot right above the stick. The movable slope tilted either left or right when the robot changed the support leg. Thanks to our new technique, the robot was able to perform omnidirectional and stable walking as hinted and shown in Figure 5. Video of these three experiments that available on line: *http://ai.ustc.edu.cn/en/demo/BalanceControlV2.php*.

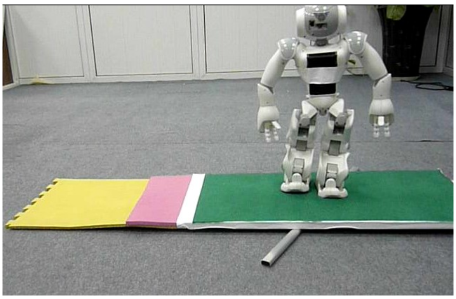

Fig. 5. The robot was able to walk stably onto the unstable board

4 Conclusion

The main contribution of this paper are the technique that integrates four balance strategies, and the realization of walking on uneven terrain on Nao robot.

The key contribution of our work is showing that a model based approach to omnidirectional humanoid walking can be effectively adapted by integrating different simple compensation strategies, that allow to effectively deal with different kind of disturbances. While at the current stage we have defined the parameters of the different strategies by hand, learning approaches can be applied to each of the strategies independently, thus enabling for a very flexible and effective development on different platforms.

Acknowledgments. This work is supported by the National Hi-Tech Project of China under grant 2008AA01Z150 and the Natural Science Foundations of China under grant 60745002 and 61175057.

References

1. Gouaillier, D., Hugel, V., Blazevic, P., Kilner, C., Monceaux, J., Lafourcade, P., Marnier, B., Serre, J., Maisonnier, B.: Mechatronic design of nao humanoid. In: IEEE International Conference on Robotics and Automation (2009)
2. Xue, F., Chen, X., Liu, J., Nardi, D.: Real Time Biped Walking Gait Pattern Generator for a Real Robot. In: Röfer, T., Mayer, N.M., Savage, J., Saranlı, U. (eds.) RoboCup 2011. LNCS, vol. 7416, pp. 210–221. Springer, Heidelberg (2012)
3. Diedam, H., Dimitrov, D., Wieber, P.-B., Mombaur, K., Diehl, M.: Online walking gait generation with adaptive foot positioning through linear model predictive control. In: IEEE/RSJ International Conference on Intelligent Robots and Systems (2008)
4. Pratt, J., Carff, J., Drakunov, S., Goswami, A.: Capture point: A step toward humanoid push recovery. In: Proceedings of IEEE International Conference on Humanoids (2006)
5. Liu, J., Xue, F., Chen, X.: A universal biped walking generator for complex environments with pattern feasibility checking. International Journal of Humanoid Robotics 08(2), 323 (2011)
6. Liu, J., Manuela, V.: Online zmp sampling search for biped walking planning. In: 2008 IEEE/RSJ International Conference on Intelligent Robots and Systems, IROS (2008)
7. Nishiwaki, K., Kagami, S.: Walking control on uneven terrain with short cycle pattern generation. In: Proceedings of IEEE International Conference on Humanoids (2007)
8. Tajima, R., Honda, D., Suga, K.: Fast running experiments involving a humanoid robot. In: IEEE International Conference on Robotics and Automation (2009)
9. Kajita, S., Kanehiro, F., Kanako, K., Yokoi, K., Hirukawa, H.: The 3D Linear Inverted Pendulum Model: A simple modeling for a biped walking pattern generation. In: IEEE/RSJ Int. Conf. on Intelligent Robots and System, IROS 2001, Hawaii, USA (2001)

10. Takenaka, T., Matsumoto, T., Yoshiike, T., Hasegawa, T., Shirokura, S., Kaneko, H., Orita, A.: Real time motion generation and control for biped robot - 4th report: Integrated balance control. In: The 2009 IEEE/RSJ International Conference on Intelligent Robots and Systems (2009)
11. Wieber, P.B.: Trajectory free linear model predictive control for stable walking in the presence of strong perturbations. In: Proceedings of IEEE International Conference on Humanoids (2006)
12. Sugahara, Y., Mikuriya, Y., Hashimoto, K., Hosobata, T., Sunazuka, H., Kawase, M., Lim, H.-O., Takanishi, A.: Walking control method of biped locomotors on inclined plane. In: Proceedings of the 2005 IEEE International Conference on Robotics and Automation (2005)

Towards Metareasoning for Human-Robot Interaction

Xiaoping Chen[1], Zhiqiang Sui[1], and Jianmin Ji[2]

[1] University of Science and Technology of China
Hefei, 230026, P.R. China
[2] The Hong Kong University of Science and Technology
Hong Kong
xpchen@ustc.edu.cn, {zqsui,jizheng}@mail.ustc.edu.cn

Abstract. This paper proposes a model of metareasoning for Human-Robot Interaction (HRI). Robots' basic abilities for HRI—planning, learning and dialogue—are characterized as three loops in the model, with each spanning ground, object and meta-level. The model provides a conceptualization of HRI and a framework for incremental development of large HRI systems such as service robots by building meta-level functions on top of existing ground/object level components. A case-study focusing on meta-level control shows that the approach is effective and efficient for some application domains. In particular, meta-level control suggests a new opportunity to speed up planning while preserving completeness without any change to object level planners. The experiments also show that, for some basic HRI tasks, there are simple meta-level strategies with performances better than the common strategy in previous work.

Keywords: HRI, metareasoning, modeling, meta-level scheduling.

1 Introduction

This paper concerns service robots that work together with humans (hereafter, service robots for short). It follows that human-robot interaction (HRI) is essential to these robots [15,9]. They should be able to understand users' requests and provide services for users accordingly by taking actions. The symbiosis of service robots and humans suggests new opportunities and challenges to Robotics and AI research. It has been observed that humans' and robots' abilities are complementary in many aspects and thus they should help each other in order to fulfill better services for humans [14,6,8]. One means to this end, which has drawn increasing interest recently, is to make robots capable of asking humans for help through human-robot dialogue [5,13,11].

Generally, service robots should possess three characteristics: autonomy, adaptability and sociality. Accordingly, these robots must be equipped with three basic abilities: planning, learning and dialogue (not necessarily through speech). For instance, a robot is not autonomous if it cannot by itself generate (and execute)

S. Lee et al. (Eds.): Intelligent Autonomous Systems 12, AISC 194, pp. 355–367.
springerlink.com

a plan of actions for a task. A further and crucial observation is that the coordination of all the three abilities is needed for robots with these characteristics. For example, to show its adaptability to a new task, a robot may need to plan its dialogue with humans, acquire knowledge/information through the dialogue, and achieve the task with the acquired knowledge/information. This process has to be realized by coordinating all the three abilities.

There have been a lot of research achievements regarding these abilities themselves. But their coordination has been less studied. This paper proposes a model as a conceptualization for analyzing the research issues and a framework of developing robots with the characteristics. The model consists of three levels —ground, object, and meta-level—as proposed in Metareasoning literature [7]. Each component of the robots is cast as a function at some level and each of the basic abilities, planning, learning and dialogue, is cast as a "loop" spanning the three levels. The main idea is to model the coordination of the three basic abilities as the interaction among the three loops at meta-level. This way, we introduce metareasoning into HRI and put forth an alternative approach against the HRI challenges. The planning loop extends the traditional perception-decision making-action loop with meta-level control and monitoring. The other two loops are similar extensions. Therefore, our model allows one to re-use various ground/object level components well developed in previous work, while strengthen and coordinate the basic abilities with new functions introduced at meta-level.

2 Issues of Metareasoning for HRI

2.1 Metareasoning

As proposed in [7] and well-accepted, metareasoning is captured by a three-level model as shown in Figure 1. The ground and object level in the model constitute the perception-decision making-action loop well known in AI. In this loop, an intelligent agent perceives some stimuli from the environment and behaves to achieve its goals according to the decisions it makes through reasoning. The result of these actions at the ground level is perceived and fed back to the object level, and the cycle continues. Metareasoning is defined as the process of reasoning about this reasoning cycle and thus constitutes the top level of the enlarged loop. In other words, reasoning controls actions at the ground level, whereas metareasoning controls the reasoning at the object level.

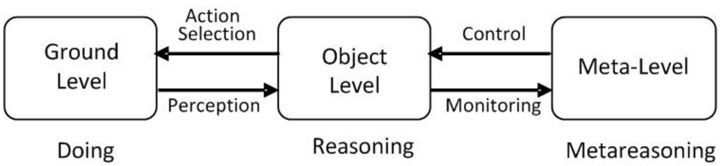

Fig. 1. General Metareasoning Model

Generally, metareasoning consists of the meta-level control and the introspective monitoring of reasoning. For a classical metareasoner, the goal of meta-level control is to improve the quality of its decisions by making some computational effort to decide what and how much reasoning to do as opposed to what actions to do. For example with an anytime algorithm that incrementally refines plans, an agent must choose between executing the current plan or further improving it in order to get a better one. Given that the passage of time itself has a cost, the metareasoner must judge which choice will lead to greater expected benefit and make the choice accordingly. On the other hand, the goal of introspective monitoring is to gather sufficient information with which to make effective meta-level control decisions. For instance, [4] maintains statistical profiles of past metareasoning choices and the associated performance, using them to mediate the subsequent control and dynamic composition of reasoning processes.

2.2 The Model of Metareasoning for HRI

The model of metareasoning for HRI (MM-HRI) proposed here is an extension of the General Metareasoning Model (GMM). The ground-level functions of MM-HRI include three types of actions: perception (like vision), physical actions (such as navigation and manipulation) and exchanging messages with users. Note that there is at least one human user in an HRI setting and thus human-robot communication is a necessary component of the robot. But the message function in the ground-level does not cover the full communication function. For example, ground level is not responsible for deciding what and when to say in human-robot dialogue.

The object level of MM-HRI includes three functions: planning, learning, and dialogue. A service robot that performs complex tasks must be able to plan its behaviors in advance by a planner. The generated plans, courses of ground level primitive actions (or, *atomic actions* for short), will be executed at the object level. In accordance with this object level function, there is a planning loop spanning three levels of MM-HRI, as shown in Figure 2 [7]. Both the plan generation and execution are controlled by metareasoning in order to meet following requirements: 1) computational efficiency, so as to generate (suboptimal) plans timely; 2) dynamic environment, which may cause replanning due to changes of the environment and/or users' intention; 3) incomplete knowledge, which brings about various object-level operations, eg, postponing the decision of what to do until the robot gains the information required for planning; 4) uncertainties, which may also result in replanning when the robot perceives that its actions did not reach the expected effects. Although some of these problems have been tackled at object level (eg, [3]), we argue that our three-level model provides a better framework for development of large-scale intelligent systems, particularly intelligent service robots described in Section 1.

The learner is responsible for acquiring knowledge from outside, which can be used by the robot later for problem-solving. Generally, the required knowledge includes: 1) information about the state of the environment and the robot that is necessary for planning and fulfilling the tasks at hand; 2) user models, e.g.,

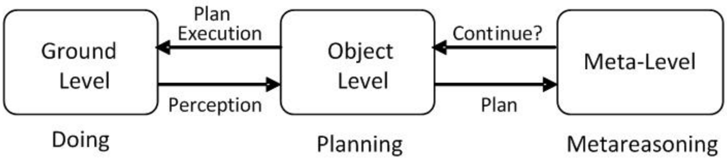

Fig. 2. Planning loop in MM-HRI

a model of the availability and accuracy of human observation providers with which the robot can get help more efficiently [14]; 3) domain knowledge required for the robot's missions but missing due to the unpredictability of real-world applications. Note that this kind of knowledge is usually expressed in natural languages. So we employ the term "material" to cover all the forms received at ground level. At object level, the robot extracts knowledge (learning results) or needs for further learning from the material. The latter is processed by metareasoner to produce new learning goals for the next circle of learning process [7]. At object level, the learning goals create some form of "learning evocator", such as questions to the user, and the cycle continues. The learning loop is shown in Figure 3.

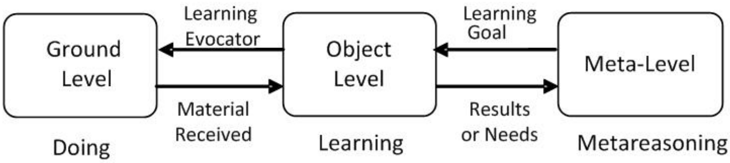

Fig. 3. Learning loop in MM-HRI

Generally, a service robot has a dialogue manager that is responsible for running the dialogue process of receiving users' service requests. This component is abstracted as a function in the object level of our model. In this paper, however, by "dialogue" we mean any information exchange between humans and robots, not limited to those through speech. The dialogue loop in our model is expected to produce human-robot dialogues not only for receiving service requests, but also for various kinds of "help" from users and other external sources. Whatever received from the human-robot communication at ground level is transformed into some internal representation called "expression" in figure 4. Then a component at object level tries to understand it and produce some "content" from it. The real meaning of the content depends on not only the dialogue itself but also what are going on in other MM-HRI loops. Anyway, the metareasoner will generate some "theme" for the next round of dialogue, with which some messages are generated at object level and sent to ground level.

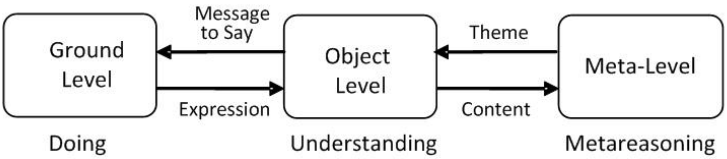

Fig. 4. Dialogue loop in MM-HRI

These three loops must coordinate and interleave their running in order to fulfill the overall performance of the robot. The interactions among the MM-HRI loops mainly occur at meta-level, which is the basic role of the robot's metareasoner. Figure 5 shows the sketch of the interaction and the entire MM-HRI. Note that Figure 2, 3, and 4 only show the internal nodes of each loop, respectively. Actually, either planning or learning loop includes both users and the environment as its external nodes, while dialogue loop includes users as the only external node of it.

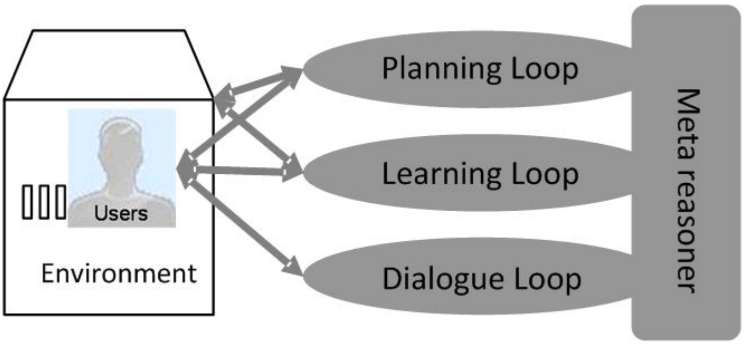

Fig. 5. Sketch of MM-HRI

2.3 Meta-level Interactions

Here we briefly describe meta-level interactions among MM-HRI loops, without specifying the interaction mechanisms formally.

(1) *Planning via Learning.* Lacking knowledge or information causes planning intractable or even infeasible. The difficulty can be reduced or even overcome when robots gain more information and/or knowledge. For example, a robot can observe its environment with its sensors or acquire relevant information/knowledge through dialogues with its users. Therefore, what is really needed is some mechanisms at meta-level with which the robot can coordinate its planning and learning loop. For instance, the metareasoner can identify missing information that is necessary for the robot's planner at object level and try to get the information before planning. When the robot is required to response to a task-stream,

i.e., a stream of tasks, it can plan for some of the tasks with complete information and execute the plan first. Meanwhile during the execution, it can observe the environment to collect information needed for other tasks. In this process, interleaving of planning and learning loop is launched and controlled by the metareasoner.

(2) *Learning via Dialogue.* There are various types of learning. In this paper, we focus on knowledge acquisition through human-robot dialogue. [13] demonstrates this kind of learning where the robot asks humans for help. In one of our previous case-studies, robot KeJia successfully solved a problem, which it had failed before, with knowledge it acquired through human-robot dialogue in a limited segment of English [5]. In these cases, the Understanding component also plays an essential role in learning. The basic topic in this type of learning is about how to ask users' help—what, when and where to ask [14], which requires the coordination of all the three loops. We will present some meta-level strategies of this type in Section 3.

(3) *Dialogue via Planning.* We have described some interactions between dialogue and planning loop above. Besides, there are other ways of interaction between them. Topics discussed a lot in the literature include dialogue generation by planning, understanding by virtue of planning, etc. These are also covered by our model. Moreover, our model covers some topics that are not so well studied yet. A key issue of human-robot collaboration is about how to collaborate on a common task jointly by humans and robots. The human and robot partners should form joint intention and then carry out joint actions for the task [2]. Therefore, a robot partner must coordinate its behavior involving dialogue and planning loop in the collaboration.

3 Case-Study: Meta-level Scheduling

The domain we chose, called eGPSR, is an enhanced variant of a test, called General-Purpose Service Robot, of RoboCup@Home [12]. In this test, a robot is given a set of tasks chosen randomly just before the test begins. These tasks involve a set of behaviors (e.g., following a person, finding a person, grasping and delivering objects), a set of portable objects (e.g., cans, cups and bottles) and a set of locations in a house. Moreover, concepts (e.g., "drink"), which represent classes of objects, are allowed to describe tasks. For simplicity, we identify any concept c with the class of objects it represents by abuse of notation. Any object in class c is called a c-object. When a concept c appears in the description of a task, it refers to any c-object. Therefore, tasks may be partially specified. For instance, the task *give me a drink* is understood as "give me anything to drink", without specifying which particular drink (an individual object) or its position in the environment. Moreover, tasks from one task set may be related to one another in a sense we will explain below.

We implemented a real robot KeJia [5,6]. In the case-study, three meta-level scheduling strategies were realized in one and the same high-layer subsystem of KeJia, called sub-KeJia. It only contains object-level and meta-level functions needed for the experiments, such as an object-level planner and a missing-information detector that detects what information is missing from the description of a task. The planner can generate a *plan* (a course of atomic actions) that achieves a task, only if the task is fully specified and there exists such a plan. For simplicity, the experiments were conducted on a software test-bed that simulates the domain, eGPSR, and KeJia's ground-level functions needed.

The strategies are evaluated with following criteria, which in turn reflect some prevalent requirements for HRI:

1. Cost of execution. A plan is of smaller cost of execution than another one for the same set of tasks, if the former contains the less number of atomic actions.
2. Efficiency of planning. Planning is time-consuming and service robots are required to provide real-time responses to its users, which depends on the efficiency of planning to a large extent.
3. Performance of asking. Previous experiments indicate that users would not like to be asked too many questions [14]. Asking more also makes a robot less autonomous. So *ceteris paribus*, asking less is better.
4. Completeness of resource-bounded deliberation. A resource-bounded metareasoner is *complete*, if it can solve all problems that can be solved under no resource limitation.

The meta-level scheduling strategies tested in this case-study are described informally below:

Eager-to-Ask strategy: For all input tasks, detect what information is missing; generate questions about the missing information; ask these questions of the users and complete the description of all the partially specified tasks with the information from the answers. Fulfill the completed tasks one by one in the input order by generating a plan for each completed task and executing the plan.

Lazy-to-Ask strategy: Fulfill the input tasks one by one in the input order. For each task, detect what information is missing; generate questions about the missing information if any; ask these questions of the users and complete the description of current task with the information from the answers; generate a plan for the current task; execute the plan.

Relevance-based-Ask strategy: Divide the set of input tasks into subsets, so that they are not related one another. Fulfill the subsets one by one using Lazy-to-Ask strategy, with each subset of tasks being taken as a (complex) task.

Each of these strategies contains operations at three levels. For instance, "generate a plan" is at object level and "execute a plan" ground level. Formal specification of such strategies demands a formal language with level tags of operators. Meanwhile, each strategy involves three loops. Asking is in dialogue loop, and extracting information to complete original tasks belongs to learning loop. So a meta-level scheduling strategy coordinates the three loops to achieve tasks. We illustrate how sub-KeJia works under Lazy-To-Ask Strategy with a small task set $T = \{$ *give Allen some drink; give Bill a bottle of coke*$\}$. Assume there are only one bottle of coke and one cup of coffee in the environment and the robot knows the facts but does not know the location of each drink in the beginning. Suppose after the first task is analyzed by the missing-information detector, KeJia allocates the cup of coffee to the concept "drink" (perhaps the robot should confirm this with question "how about coffee?" in real services. But we omit this here). Then it generates a question about the location of the coffee. After KeJia gets the missing information from user, it generates a plan of four atomic actions for the completed task with its object-level planner. Then KeJia executes the plan in the ground-level: *move to the location of coffee*, *grasp coffee*, *move to Allen and give the cup of coffee to Allen*. Assume the robot get the missing information of the second task, the location of coke, through its sensors during it executes above actions. Thus the knowledge of the second task is completed and the object-level planner generates a plan of it.

The main deference between the first two strategies is the time point when the robot asks questions of users. With Eager-to-Ask strategy, the robot asks questions before it plans for any task. It starts to plan only after it obtains all missing information in original tasks. This is the common strategy used in most of previous work [1]. One problem with it is that it fails to make use of concurrency of a robot's hardware and software components, as shown in above example. Lazy-to-Ask strategy improves in this aspect and thus got better performance of asking in the experiments (Section 4).

The first two strategies do little metareasoning except scheduling over lower-level operations. In particular, they do not consider the relevance among tasks and just try to fulfill them one by one in the input order. Consequently, the completeness is violated—some tasks cannot be achieved just due to the over-simplified meta-level strategies. Relevance-based-Ask strategy solves this problem with more metareasoning, mainly on the relevance among tasks.

The notion of "relevance" is technically complicated and defined as follows. Without loss of generality, we assume that planning problems are specified in PDDL [10] and each of them contains an initial state, a goal description (tasks), and a domain description which includes specifications of effects and preconditions of actions and other background knowledge.

Definition 1. *Given a domain description, an initial state, and two tasks t_1 and t_2. We say that t_2 is related to t_1 if there exists a plan P_1 that achieves t_1 and there does not exist a plan P_2 such that P_1 appended with P_2 could achieve both t_1 and t_2.*

If a task t_2 is related to another one t_1, then the tasks in the set $\{t_1, t_2\}$ should not be planned and executed separately in the order $\langle t_1, t_2\rangle$. As the robot may choose a plan P_1 to achieve t_1, but after the execution of P_1, t_2 can no longer be achieved without ruining t_1. For example, suppose a robot as a bar tender is given two tasks,

t_1: give Jim some drink; t_2: give Bob a can of Coke.

Assume there is only one can of Coke in the environment. Then t_2 is related to t_1, as after giving Jim the Coke, t_2 can no longer be achieved. On the other hand, if t_2 is not related to t_1, then a robot can solve $\{t_1, t_2\}$ separately in the order $\langle t_1, t_2 \rangle$. The notion of relevance between two tasks can be generalized to between two sets of tasks.

Definition 2. *Given a domain description, an initial state, and two sets of tasks T_1 and T_2. We say that T_2 is related to T_1 if there exists a plan P_1 that achieves all tasks in T_1 and there does not exist a plan P_2 such that P_1 appended with P_2 achieve all tasks in both T_1 and T_2.*

Proposition 1. *Given a domain description, an initial state, and a set of tasks $T = \{t_1, \ldots, t_n\}$. If for each $1 < i \leq n$, $\{t_i\}$ is not related to $\{t_1, \ldots, t_{i-1}\}$, then T can be achieved if and only if each task in the sequence $\langle t_1, \ldots, t_n \rangle$ can be achieved one after another.*

Proposition 2. *Given a domain description, an initial state, and a set of tasks $T = T_1 \cup \cdots \cup T_n$. If for each $1 < i \leq n$, T_i is not related to $T_1 \cup \cdots \cup T_{i-1}$, then T can be achieved if and only if each set of tasks in the sequence $\langle T_1, \ldots, T_n \rangle$ can be achieved one after another.*

Deciding whether a set of tasks is related to another is generally harder than deciding whether a set of tasks can be achieved by a plan. However, the problem can be greatly simplified in many domains, e.g., eGPSR. The relevance between tasks in this domain only results from "the limitation of resources".

Let $c \subset c'$ denote that c is a proper subset of c'. The set of all concepts appeared in eGPSR is denoted by C and the set of all portable objects in C by O. Then C under $\subset$ forms a hierarchy $(C, \subset)$. We assume that for any c and $c' \subset$ C, if c and c' do not disjoint, then it holds that $c \subset c'$ or $c' \subset c$. We also assume that the size of every concept $c \in C$, denoted by $|c|$, is fixed and known by the robot.

Given a task set T, we use $C(T)$ to denote the set of concepts appeared in T, $n(c, T)$ the number of occurrences of c in T (we do not consider any other requirements on resource in this paper). $C(T)$ can be created from T in linear time. In order to achieve all tasks in T, the planner must allocate to each concept $c \in C(T)$ a c-object; in other words, each occurrence of c in T demands an "occupation" of a c-object. A least efficient way of resource allocation for T_1 is to "run on" objects required by T_2. That is, when there are concepts $c \in C(T_2)$ and $c' \in C(T_1)$ such that $c \subset c'$, the robot allocates only c-objects to every c' in T_1, such that the c-objects may be used up unnecessarily for tasks in T_1, causing T_2 unsolvable. This is possible since a robot cannot consider the requirements by T_2 when it plans for T_1 before for T_2.

The basic idea of our heuristic algorithm (**Algorithm 1**) is to *test* if this least efficient way would cause T_2 unsolvable. In the algorithm, $o(c)$ records the number of c-objects occupied so far in the estimate process. The algorithm terminates in time $O(n^2)$, where n is the length of $C(T_1 \cup T_2)$.

Algorithm 1.

For each $c \in C(T_1 \cup T_2)$, $o(c) := 0$;
For each $c \in C(T_1)$ //occupation by T_1//
    $o(c) := o(c) + n(c, T_1)$;
    For each $c' \in C(T_1)$
        If $c \subset c'$ **then** $o(c') := o(c') + n(c, T_1)$;
    If $o(c) > |c|$ **then** return *false*; //T_1 is unsolvable//
For each $c \in C(T_2)$ //occupation by $T_1 \cup T_2$//
    $o(c) := o(c) + n(c, T_2)$;
    For each $c' \in C(T_1 \cup T_2)$
        If $c \subset c'$ **then** $o(c') := o(c') + n(c, T_2)$;
For each $c \in C(T_2)$ //run on objects by T_1//
    For each $c' \in C(T_1)$
        If $c \subset c'$ and $o(c) + n(c', T_1) > |c|$ **then** return *true*;
Return *false*.

Formally, an allocation of objects for a task set T is an assignment of objects to concepts in T, i.e., a mapping δ: $C(T) \rightarrow O$. Let $|c|_\delta$ denote the number of c-objects occupied by δ, for every $c \in C$. An assignment δ is called *feasible*, if $|c|_\delta \leq |c|$ for all $c \in C$. A domain is called *resource-determined* if for any task set T, there is a feasible assignment for T implies there is a plan for T. For example, eGPSR is a resource-determined domain. We have the following proposition.

Proposition 3. *Given any task sets T_1 and T_2 in a resource-determined domain. T_2 is not related to T_1 if Algorithm 1 returns 'false'.*

4 Experimental Results

The size of the environment is set as $10m \times 10m$ and there are about 20 objects including portable ones and furniture. Since a real robot's perception ability is limited, we simulate this feature approximately with "observation radius" (OR) in our test-bed. We assume the robot can perceive the information of all objects within the OR and no information of any object outside. The greater the OR is, the more (missing) information may be perceived.

We conducted two tests with OR taken as $1m$ and $2m$, respectively. Each test consists of three groups and each group 20 task sets. All task sets in one group contain the same number of tasks: there are 6 (8, 10) tasks in every task set in group 1 (2, 3, respectively). The tasks in any task set are chosen randomly under an additional restriction described later.

Table 1 shows the experimental results of test 1, where the observation radius is set as $1m$. Relevance-based-Ask strategy achieved all the tasks in each task set, while the other two do not since they cannot deal with relevance between tasks in the same task set. In particular, when two or more tasks in the same task set are related, both strategies may fail to generate plans for and thus fail to achieve some of these tasks, although they are not unsolvable in themselves.

Table 1. The results of test 1

OR=1m	Planning Time(s)	#Ask	#Atomic Actions	#Task Achieved
Group 1: 6 tasks in each task set				
Eager	1.01	8.70	22.55	5.55
Lazy	0.88	5.65	21.40	5.15
Relevance	1.21	5.70	23.50	6.00
Group 2: 8 tasks in each task set				
Eager	1.16	11.00	29.95	7.40
Lazy	1.01	5.90	29.15	7.10
Relevance	1.38	6.35	31.15	8.00
Group 3: 10 tasks in each task set				
Eager	1.68	13.45	37.40	9.25
Lazy	1.40	6.90	37.05	9.10
Relevance	1.82	7.45	38.55	10.00

The efficiency of planning among three strategies is of little difference in this test. The first two strategies produced on average 2 fewer atomic actions than the third strategy, because they achieved fewer tasks in some task sets. An obvious deference is that Eager-to-ask strategy always asks notably more number of questions than the other strategies, just because it obtains missing information only through asking questions, while the other two obtain some through the robot's sensors. Relevance-based-ask strategy asks a little more than lazy-to-ask strategy, as a tiny price for its completeness.

As the observation radius increases to $2m$, we can see from Table 2 that the ask times decreases about 40% with the second and the third strategy. The reason is that the robot can perceive more missing information without any additional effort or cost. This indicates that meta-level control affects the performance of asking remarkably when robots possess powerful perception.

Table 2. The results of test 2

OR=2m	Planning Time(s)	#Ask	#Atomic Actions	#Task Achieved
Group 1: 6 tasks in each task set				
Eager	0.96	8.70	22.85	5.65
Lazy	0.88	2.80	22.30	5.45
Relevance	1.38	3.90	23.75	6.00
Group 2: 8 tasks in each task set				
Eager	1.16	11.00	30.10	7.45
Lazy	1.06	3.05	29.30	7.15
Relevance	1.55	3.90	31.25	8.00
Group 3: 10 tasks in each task set				
Eager	1.58	13.45	37.25	9.20
Lazy	1.41	4.05	37.15	9.15
Relevance	1.94	4.90	38.65	10.00

In above tests, a task set may be divided into several sub-sets under the relevance-based strategy, where all tasks in each of these sub-sets are planned together. The additional restriction for selection of tasks is that any subset contains no more than two (related) tasks. It is well-known that the computation time of (object-level) planning will increase exponentially in the size of tasks (here the subsets of tasks) if all the tasks are planned together, no matter whether or not they are related. We did an additional test on planning for larger task sets with the same sub-KeJia. It showed that planning for a 6-task set frequently needs more than 1 hour. This provides strong evidence that it is necessary to reduce the size of subsets of tasks using some meta-level control techniques, such as relevance-based scheduling we used in the case-study.

5 Discussion and Conclusion

We draw following observations from this work, especially the case-study.

(1) Metareasoning provides an effective approach to HRI, particularly, the coordination of basic abilities of a service robot. This coordination is of most importance to HRI and reflected in our model as the coordination of planning, learning, and dialogue loop. This is the reason why we focus on the coordination in this paper while previous work on metareasoning focuses on internal process of individual loops.

(2) The model MM-HRI supplies a framework with which one can advance the performances of HRI by building meta-level functions on top of existing, well-developed ground/object level components. We implemented meta-level scheduling directly on previously developed low-level components and got new functions and better performances. Particularly, meta-level control suggests a new opportunity to speed up planning while preserving completeness with reasonable price for some application domains, without any change to the object level planner.

(3) The case-study shows that meta-level control affects the performances of HRI remarkably in at least three aspects: planning time, performance of asking, and completeness of resource-bounded deliberation. Compared to the common strategy in previous work, the two strategies we proposed in this paper got higher evaluation in the experiments. One important reason is that meta-level control can make better use of concurrency of a robot's hardware/software components.

One can draw more observations, e.g., asking is more desirable to acquire knowledge or information that cannot be perceived easily through robots' sensors. These observations suggest a lot of future work along this line of research.

Acknowledgments. This work is supported by the National Hi-Tech Project of China under grant 2008AA01Z150 and the Natural Science Foundation of China under grant 60745002 and 61175057. We thank Guoqiang Jin, Feng Wang, Jiongkun Xie, Hao Sun, Min Cheng, Xiang Ke and Kai Chen for their contributions to KeJia Project. The authors are also grateful to Shlomo Zilberstein for his help to this work.

References

1. Asoh, H., Motomura, Y., Asano, F., Hara, I., Hayamizu, S., Itou, K., Kurita, T., Matsui, T., Vlassis, N., Bunschoten, R., et al.: Jijo-2: An office robot that communicates and learns. IEEE Intelligent Systems 16(5), 46–55 (2001)
2. Bauer, A., Wollherr, D., Buss, M.: Human-robot collaboration: A survey. International Journal of Humanoid Robotics 5(1), 47–66 (2008)
3. Brenner, M., Nebel, B.: Continual planning and acting in dynamic multiagent environments. Autonomous Agents and Multi-Agent Systems 19(3), 297–331 (2009)
4. Carlin, A., Zilberstein, S.: Decentralized monitoring of distributed anytime algorithms. In: Proceedings of the 10th International Conference on Autonomous Agents and Multiagent Systems (AAMAS 2011), pp. 157–164 (2011)
5. Chen, X., Ji, J., Jiang, J., Jin, G., Wang, F., Xie, J.: Developing high-level cognitive functions for service robots. In: Proceedings of the 9th International Conference on Autonomous Agents and Multiagent Systems (AAMAS 2010), pp. 989–996 (2010)
6. Chen, X., Jiang, J., Ji, J., Jin, G., Wang, F.: Integrating nlp with reasoning about actions for autonomous agents communicating with humans. In: Proceedings of the 2009 IEEE/WIC/ACM International Joint Conference on Web Intelligence and Intelligent Agent Technology (IAT 2009), pp. 137–140 (2009)
7. Cox, M., Raja, A.: Metareasoning: A manifesto. Technical Memo 2028, BBN (2008)
8. Fong, T., Thorpe, C., Baur, C.: Robot, asker of questions. Robotics and Autonomous Systems 42(3-4), 235–243 (2003)
9. Fong, T.W., Thorpe, C., Baur, C.: Collaboration, dialogue, and human-robot interaction. In: Proceedings of the 10th International Symposium of Robotics Research, pp. 255–266. Springer (November 2001)
10. Ghallab, M., Howe, A., Christianson, D., McDermott, D., Ram, A., Veloso, M., Weld, D., Wilkins, D.: Pddl—the planning domain definition language. In: AIPS 1998 Planning Committee, vol. 78(4), pp. 1–27 (1998)
11. Kaupp, T., Makarenko, A., Durrant-Whyte, H.: Human-robot communication for collaborative decision making–a probabilistic approach. Robotics and Autonomous Systems 58(5), 444–456 (2010)
12. Nardi, D., Dessimoz, J., Dominey, P., Iocchi, L., Rybski, P., Savage, J., Schiffer, S., Wisspeintner, T., van der Zant, T., Yazdani, A.: Robocup@home: Rules and regulations (2008)
13. Rosenthal, S., Biswas, J., Veloso, M.: An effective personal mobile robot agent through symbiotic human-robot interaction. In: Proceedings of the 9th International Conference on Autonomous Agents and Multiagent Systems (AAMAS 2010), pp. 915–922 (2010)
14. Rosenthal, S., Veloso, M.M., Dey, A.K.: Learning accuracy and availability of humans who help mobile robots. In: Proceedings of the 25th AAAI Conference on Artificial Intelligence (AAAI 2011), pp. 1501–1506 (2011)
15. Thrun, S.: Toward a framework for human-robot interaction. Human–Computer Interaction 19(1-2), 9–24 (2004)

Learning Probabilistic Decision Making by a Service Robot with Generalization of User Demonstrations and Interactive Refinement

Sven R. Schmidt-Rohr, Fabian Romahn, Pascal Meissner, Rainer Jäkel, and Rüdiger Dillmann

Institute for Anthropomatics (IFA), Karlsruhe Institute of Technology, Germany
{srsr,romahn,meissner,jaekel,dillmann}@ira.uka.de

Abstract. When learning abstract probabilistic decision making models for multi-modal service robots from human demonstrations, alternative courses of events may be missed by human teachers during demonstrations. We present an active model space exploration approach with generalization of observed action effect knowledge leading to interactive requests of new demonstrations to verify generalizations.

At first, the robot observes several user demonstrations of interacting humans, including dialog, object poses and human body movement. Discretization and analysis then lead to a symbolic-causal model of a demonstrated task in the form of a preliminary *Partially observable Markov decision process*. Based on the transition model generated from demonstrations, new hypotheses of unobserved action effects, generalized transitions, can be derived along with a generalization confidence estimate. To validate generalized transitions which have a strong impact on a decision policy, a request generator proposes further demonstrations to human teachers, used in turn to implicitly verify hypotheses.

The system has been evaluated on a multi-modal service robot with realistic tasks, including furniture manipulation and execution-time interacting humans.

1 Introduction

Autonomous abstract decision making for multi-modal service robots needs models of environment causality to generate action policies. Real world environments are partially observable and not fully deterministic. Thus, *partially observable Markov decision processes* (POMDPs) are a suitable representation of an action model. However, efficient policy computation needs models which describe action and observation effects as well as mission goals explicitly.

Comfortable acquisition of these complex models is difficult. Different learning approaches exist: e.g. active learning by trial, interactive reinforcement learning or learning from demonstrations of human teachers. Compared to the first two, the latter approach is efficient as the human has extensive implicit and explicit domain knowledge while natural demonstrations are an efficient way of information transfer.

A disadvantage is the need for a human teachers time, thus imposing the use of a minimum number of demonstrations. Building on a simpler, previous system [1], we

S. Lee et al. (Eds.): Intelligent Autonomous Systems 12, AISC 194, pp. 369–382.
springerlink.com

present a methodology which tries to minimize demonstrations needed for the generation of probabilistic planning models by utilizing active model exploration and interactive refinement.

Model representation, the learning process, generalization and request generation are described in sec. 2. Evaluation of the method on a real robot is described in sec. 3, while sec. 4 compares related work and sec. 5 gives a conclusion.

2 Model Generation

The aim is to generate a POMDP [2], a tuple (S, A, M, T, R, O), for a specific robot service mission from a set of human demonstration sequences. Symbolic sets of states S, actions A, observations M and transition probabilities $p(s, a, s') \in T$ as well as observation probabilities $p(s, m) \in O$ and rewards $r(s, a) \in R$ have to be compiled. Based on a model, an execution-time policy can be computed by approximate value iteration, e.g. SARSOP [3].

Below, the relation between model symbols and real world is discussed in sec. 2.1 and a learning process overview given in sec. 2.2. Subsequently, generalization is presented in sec. 2.2 and request generation in sec. 2.4.

2.1 Service Robot Mission Model Representation

State symbols S are related to real world characteristics by robot perception and corresponding models, reflected by measurement symbols M. S and M are linked by O. Action symbols A are linked to actuator components.

A state s thus corresponds to a set of properties of the world p which can potentially be observed by a set of perception components. On a robot with several perception components, a state $s \in S$ is a class defined over a distinct combination of property sets. Each p results from a potential observation of a perception component, called modality D_l. A symbolic modality state $d_j^l \in D_l$ covers a set of similar potential observations $p_a, \ldots, p_z$.

$$s_i \in S : d^1_{x^i_1} \in D_1 \times \ldots \times d^n_{x^i_n} \in D_n \tag{1}$$

E.g.: $\{D_1, D_2, D_3\}$: *{robot position, human utterance, object poses}*, s_i : $robotAtTable \times bringTea \times teaOnTable$.

While related to a factored representation, because of modality interdependencies in T and O, it cannot be handled as such. An exemplary transition: $p(s_i, a_k, s'_j) \in T = 0.6$, a_k : $FetchTea$, s'_j : $robotAtHuman \times thankYou \times teaAtHuman$. The granularity of S, A is adjusted by discretization mode.

When learning models from demonstrations for both T and R, two main types of model aspects can be distinguished. In T these are *structural* stochastic transitions modeling agent independent characteristics of a mission on the one hand and *robot capability* stochastic transitions on the other.

E.g $p(robotAtHuman \times noTeaPresent, GotoTable, robotAtTable \times teaAtTable) = 0.4$, structurally modeling the chance to encounter tea at the table and $p(robotAtTable \times$

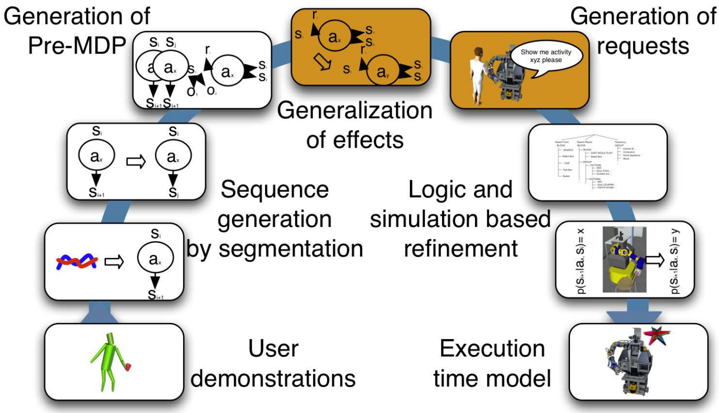

Fig. 1. The process for generating probabilistic decision making models by learning from human demonstrations (PMPM-PbD). Emphasis of this paper is highlighted.

$teaAtTable, PickTea, robotAtTable \times teaInRobotHand) = 0.8$, modeling motion planning and execution capabilities of the robot. In R, the types are *mission goal* positive rewards and *action cost* negative rewards.

2.2 Process Overview

Major stages of *Probabilistic mission planning model programming by demonstration* (PMPM-PbD) are depicted in fig. 1 with the focus of this paper highlighted.

Observation

Utilizes multiple sensors and perception processing components, either robot based - as in the setup, presented in sec. 3 - or parts of a smart room. One or several interacting humans perform natural demonstrations of a mission with differing courses of events. Data of all components, e.g. object localization, is recorded.

Abstraction

Derives mapping $P \to S$ followed by segmentation. As a result, each demonstration is represented as a state-action sequence $(\ldots, s_t, a_t, s_{t+1}, a_{t+1}, \ldots)$. Automatic discretization techniques as clustering in continuous property domains may be used.

Mapping

Generates a preliminary (PO)MDP model based on several demonstrations. All s, a in sequences are accounted for. Then, structural transitions T_D and goal rewards are generated by analysis of sequences. Probabilities $p(t_i)$ are derived from occurrence frequencies in demonstrations sets. More details about mapping can be found in [1].

Generalization

Derives transition hypotheses for unobserved transitions related to those appearing in demonstrations. The aim is to maximize information gathered from a limited set of demonstrations as described in sec. 2.3.

Request generation

Takes generalization confidence to rate transitions on necessity to be verified as presented in sec. 2.4. Relevant transitions are assembled into potential courses of events. Based on these sequences, human teachers are given requests to verify hypotheses. Together, generalization and requests perform hypotheses expansion and pruning.

Refinement

Several model aspects cannot be learned from demonstrations including observation model, action costs and robot capability transitions. PMPM-PbD uses background knowledge, geometric analysis and learning in dynamics simulation to compute these aspects, transforming a preliminary into a final model. Details are not further relevant for generalization and requests.

Autonomous execution

Policy computation generates a policy from this model by approximate value iteration. Finally, the policy is used for autonomous execution-time decision making of the robot performing the mission. An exemplary architecture is described in [4].

2.3 Generalization of Transitions

Determining new structural non-zero transition probabilities in a preliminary T can be interpreted as generating new hypotheses for causal effects, thus *generalizing* observed effects. On the abstract level, modalities D_i are the main structure suitable for generalization. *Modality states* $d_x^i \in D_i$, e.g. $teaAtTable, teaInRobotHand \in D_{obj} : (object poses)$ and corresponding *flat states* (see eqn. 1) reflect this structure. To estimate probabilities for $T(s_i, a_k, s'_j)$ with previously assigned $p(s_i, a_k, s'_j) = 0$ - thus unobserved - similarities within D_i and thus S have to be exploited. There are three types of generalization:

1. Generalize origin: $p(s_i, a_k, s'_j) \rightarrow p(s_g, a_k, s'_j)$
2. Generalize effect: $p(s_i, a_k, s'_j) \rightarrow p(s_i, a_k, s'_g)$
3. Generalize action: $p(s_i, a_k, s'_j) \rightarrow p(s_i, a_g, s'_j)$

The third type is not investigated further. The other two types imply that when observing transitions for several similar s_i (1) or s'_j (2), e.g when those states differ only in a single modality, chances are high that transitions may be non-zero for further similar states. To reflect respective transition similarities, a *transition mask* κ is defined:

$$A^* = A \cup \{*\}, A^*(a_i^*) = \begin{cases} A & \text{if } a_i^* = * \\ a_i & \text{else} \end{cases} \quad (2)$$

$$D_l^* = D \cup \{*\}, D_l^*(d_i^*) = \begin{cases} D_l & \text{if } d_i^* = * \\ d_i & \text{else} \end{cases} \quad (3)$$

$$S^* = D_1^* \times ... \times D_n^* \quad (4)$$

$$\kappa(s^*, a^*, s'^*) = \{s^* \in S^*, a^* \in A^*, s'^* \in S^*\} \quad (5)$$

E.g.: $\kappa_{example1} = \kappa(* \times bringTea, HandTea, robotAtHuman \times thankYou)$models from where the robot got tea is irrelevant for effect s'^*, thus a wildcard $*$ represents the robot location modality $D_{robotloc}$ in s^*. $\kappa_{example1}$ covers $|D_{robotloc}|$ transitions. Masks are used to define the scope of generalization κ_{scope} - e.g. type 1) has wildcards only in s^*, but not s'^* - and to describe the resulting, generalized hypotheses set κ_g.

Using masks, a set of hypotheses T_g for a set of transitions T_I, can be computed, given the following three elements:

1. A set of input transitions T_I, generating the hypothesis.
2. A transition mask $\kappa_{scope}(s^*, a^*, s'^*)$ defining the elements over which may be generalized.
3. A transition mask $T_g = \kappa_g(s^*, a^*, s'^*)$ containing the resulting generalized set of transitions.

Scope mask κ_{scope} is generated by analyzing onto which modalities actions have an effect in the set T_I in the types 1) and 2), as a is not generalized. For all $t(s, a, s') \in T_I, p(t) > 0$, each modality is checked for a change and in case $d_j^i \in s \neq d_k'^i \in s'$, a wildcard is inserted in κ_{scope} for the respective D_i in s^* (1) or s'^* (2).

The resulting set κ_g is derived by concept learning over T_I with mask κ_{scope}, whereby all $t \in T_I$ have to be considered as positive examples. Simply put, κ_g is the most specific mask which covers all of T_I with generalization (wildcards) only allowed, where defined by κ_{scope}.

Each $t_g \in \kappa_g(s^*, a^*, s'^*)$ is a contender for being non-zero, thus generalization confidence and estimated transition probability are calculated. Confidence is computed using distances between transitions, based on modality state distances. Probabilities can then be computed based on confidences and related transitions.

To compute distances between states $c(s_1, s_2)$, modality specific distance metrics $dc(d_1^i, d_2^i)$ are used, e.g. denoting geometric distance between regions or similarity between utterances or objects. If no specific metric is available, a simple, general metric $dc_{generic}$ can be used:

$$dc_{generic}(d_j^i, d_k^i) = \begin{cases} 1 & \text{if } d_j^i = d_k^i \\ 0 & \text{else} \end{cases} \quad (6)$$

$$c(s_1, s_2) = \frac{1}{n} \sum_{i=1}^{n} dc(s_1 : d_j^i, s_2 : d_k^i) \quad (7)$$

$$c(t_1, t_2) = c(s \in t_1, s \in t_2) \text{ type 1)}, c(s' \in t_1, s' \in t_2) \text{ type 2)} \quad (8)$$

For each generalized transition $t_g \in \kappa_g$, the nearest, observed transition, called *baseline* reference transition t_b is determined: $c(t_g, *) = c(t_g, t_b) = min(c(t_g, t_i), t_i \in T$. To

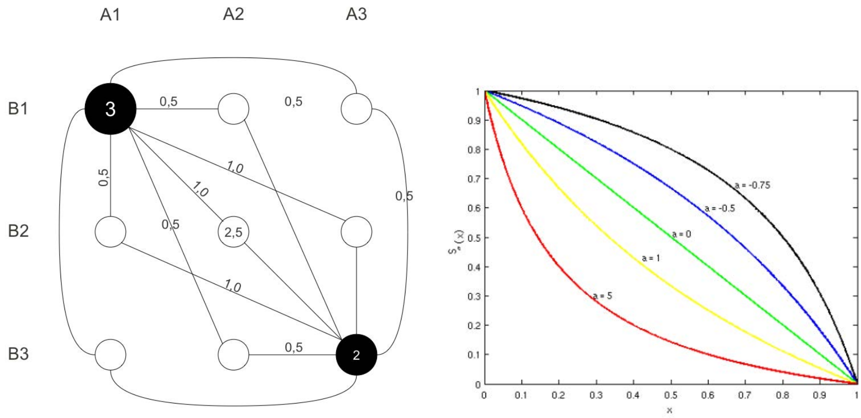

Fig. 2. Transition distance with two modalities A, B, each with three modality states and two observed transitions (black circles with observed frequency) on the left. Sugeno negation for some α parameters on the right.

compute basic generalization confidence $gc \in [0,1]$, $c(t_g,*)$ is coupled with a negation function, e.g. Sugeno-Negation $N_s(x) = \frac{1-x}{1+\alpha x}, \alpha \in (-1,\infty)$:

$$gc_{basic}(t_g) = \begin{cases} 1 & \text{if } t \text{ was observed} \\ N_s(c(t_g,*)) & \text{else} \end{cases} \tag{9}$$

Especially when using simple distance metrics, further aspects have to be considered when computing generalization confidence values. One such aspect, called *non-observation bias* (nob), reflects a derived transition t_g being less likely implied by a high number of observations of a reference transition t_b. Another aspect, called *certainty bias* (ceb) considers that an observed transition $t_{occ}(s_i,a_k,s'_j)$ with the same origin state and action as $t_g(s_i,a_k,s' \neq s'_j$, has its effect probability reduced by including t_g. However, observed transitions are always a better model estimate, thus including a bias against such t_g. This results in a refined generalization confidence $gc_T(t_g)$:

$$nob(t_g) = (1-\beta)^{occ(t_b)}, \beta \in [0,1] \tag{10}$$

$$t_g(s_i,a_k,s'_j), n = occ(t(s_i,a_k,s'_l)), ceb(t_g) = \begin{cases} 0 & \text{if } n = 0 \\ \sqrt[n]{\gamma} & \text{else} \end{cases} \tag{11}$$

$$gc_T(t_g) = gc_{basic}(t_g) * nob(t_g) * ceb(t_g) \tag{12}$$

Parameters α, β and γ determine the share of each aspect and have to be determined empirically for a setting.

While $gc_T(t_g)$ is also used directly in further processing steps (see sec. 2.4), its immediate purpose is to calculate transition probabilities $p_T(t_g)$ for hypotheses based on the most similar observed transition and its confidence:

$$\bar{p}_T(t_g(s_i,a_k,s'_j))) = gc_T(t_g) * p_T(t_b), t_b : \text{baseline} t \quad (13)$$

$$p_T(t_g) = \frac{\bar{p}_T(t_g)}{\sum_{s' \in S} p(s_i,a_k,s')} \quad (14)$$

Generalization assumes that estimated model knowledge, which hypotheses are, is better than always maintaining the zero assumption arising potentially from missing demonstrations. This is a Bayesian way of handling lack of information, yet not without pitfalls. Aggressively generalized transitions which do not reflect real world properties might in the worst case lead to an unusable policy. Therefore, a verification stage as described next is crucial.

2.4 Demonstration Request Generation for Verification

Request generation consists of two parts: relevance estimation of generalized transitions t_g and composition of demonstration requests. Relevance estimation ranks t_g so that requests are only generated to verify high impact t_g.

Relevance estimation is performed individually for t_g. Because evaluating all possible combinations of tuples $(t_g^1, \ldots, t_g^n)$ is infeasible, relevances arising only from multiple t_g added together, are not covered.

To evaluate a single t_g, the original model T_D generated from demonstrations without any generalization is taken and t_g added to form an evaluation model. For some further steps, an initial state s_{init} is needed, which can either be the most frequent initial state in demonstrations, be sampled from all initial states in demonstrations or defined by hand. Next, a policy is computed from the evaluation model and a number of simulation runs with that policy performed on the model. With these steps, all information has been gathered to calculate a set of relevance aspects $v_i(t_g)$. First, a subset, *state relevance* aspects $v_i(s_i)$ are computed:

$$\text{Freq. in demo. paths} : v_{demo}(s_i) = |s_i \in demo| / |demo| \quad (15)$$

$$\text{Freq. in sim. paths} : v_{sim}(s_i) = |s_i \in sim| / |sim| \quad (16)$$

$$\text{In T} : v_{in}(s_i) = \frac{|\{(\bar{s},a,s_i) | T(\bar{s},a,s_i) > 0, \bar{s} \in S, a \in A\}|}{|S| * |A|} \quad (17)$$

$$\text{Prob. in transitions} : v_{out}(s_i) = \frac{\sum_{\bar{s} \in S, a \in A} T(\bar{s},a,s_i)}{|S| * |A|} \quad (18)$$

$$\text{Rel. utility} : v_{util}(s_i) = \frac{u(b(p(s_i) = 1.0)) - min(u(s \in S))}{max(u(s \in S)) - min(u(s \in S))} \quad (19)$$

$$(20)$$

Total state relevance is empirically weighted:

$$\bar{w}_i, \{demo, sim, in, out, util\} : v(s_i) = \frac{\sum_{j=1}^{5} \bar{w}_j v_j(s_i)}{\sum_{j=1}^{5} \bar{w}_j} \quad (21)$$

Relevance for $t_g(s,a,s')$ can then be estimated:

$$\text{Origin state relevance} : v_s(s,a,s') = v_(s) \tag{22}$$

$$\text{Effect state relevance} : v_{s'}(s,a,s') = v_(s') \tag{23}$$

$$\text{Freq. in sim. paths} : v_{sim}(s,a,s') = |(s,a,s') \in sim|/|sim| \tag{24}$$

$$\text{Relative reward} : v_r(s,a,s') = \frac{r(s,a) - min(r(\tilde{s},\tilde{a}))}{max(r(\tilde{s},\tilde{a})) - min(r(\tilde{s},\tilde{a}))} \tag{25}$$

$$\text{Probability} : v_p(s,a,s') = p(s,a,s') \tag{26}$$

$$\text{Generalisation confidence} : v_{gc}(s,a,s') = gc_T(s,a,s') \tag{27}$$

$$\tag{28}$$

Total transition relevance is empirically weighted:

$$w_i, \{s,s',sim,r,p,gc\} : v(s,a,s') = \frac{\Sigma_{j=1}^{6} w_j v_j(s,a,s')}{\Sigma_{j=1}^{6} w_j} \tag{29}$$

Hypotheses t_g can then be ranked for inclusion in interactive demonstration requests which lead to verification of these t_g. Interactive requests have to be be understood by human teachers, should both include as many relevant t_g as possible and be suitable for a coherent demonstration sequence. First, suitable potential state-action chains have to be generated, each containing a maximum number of relevant transitions. Then, this chain has to be transformed into a request description which allows enough flexibility for the human to include deviations is necessary.

A greedy algorithm is used which performs a path search from an initially chosen generalized transition t_g^a via observed transitions t_i to a closest generalized transition t_g^b. The path search prefers likely transitions $p(t_i(s,\bar{a},s')) > p(t_j(s,a,s')), p(t_i(s,\bar{a},s')) > p(t_k(s,\bar{a},\bar{s}'))$ and short paths, using a breadth-first search. For t_g^a, a path from a start state s_{init} (as described above) to t_g^a is searched first. If that path cannot be found, t_g^a is temporarily discarded. Next, paths $t_r^a \rightarrow t_r^b, t_r^b \rightarrow t_r^c, \ldots$ to closest transitions are incrementally retrieved, added as long as one can be found.

A mechanism is necessary to detect t_g^{invalid} which do never occur in the mission. If the critical t_g^{invalid} in the path cannot be bypassed in the demonstration, the whole request is declined without the system getting to know where it failed. Hence, for each final state-action chain request, a binary tree is formed with each level splitting the set of remaining t_g^x in the path in two halves. In case a t_g^{invalid} is present in a segment, only the longest chains in the tree without t_g^{invalid} will be demonstrated. That way, the t_g^{invalid} can be identified after further demonstrations. Initially, the human teacher is only presented with the request representing the root path and then successively with sub-nodes if requests have to be declined because of t_g^{invalid} (see fig. 3).

Next, the internal representation has to be transformed into a natural request. Four techniques are suitable in principle:

1. State-action chains: unambiguous, but very complicated request descriptions and inflexible.
2. Action sequences: compact request descriptions, but effects cannot be controlled.

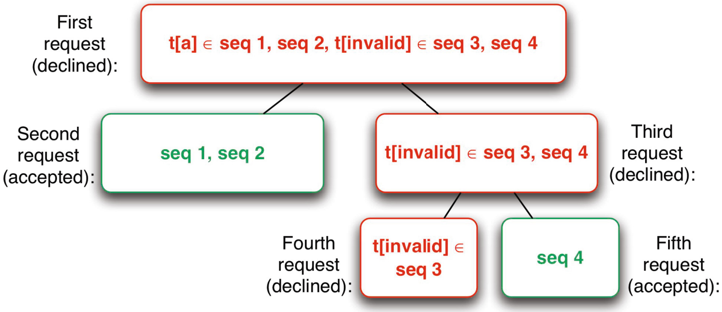

Fig. 3. Successive request generation for a path containing an invalid generalized transition which will never occur in a demonstrated mission

3. State sequences: complicated request descriptions, actions ambiguous, limited flexibility.
4. Sequences of modality changes: similar to state sequences, but compact request descriptions.

In practice, a combination of modality changes and action sequences balances advantages best. A sequence of modality changes is given with two special cases: a) in case a transition has $s = s'$, only the action is given, b) for t_g (but not other t_i), the action is given additionally to the modality change.

Then, the sequence is transformed into a graph visualization or natural speech, e.g. "Begin in state top/Pos1. Change the modality Pos from Pos1 to Pos2. Change the modality Lane from top to bottom and Pos from Pos2 to Pos3 by performing action switch." .

Finally, the resulting demonstrations are incorporated into the model generation process.

3 Experimental Setup and Results

The process as described in sec. 2.2 has been implemented on a multi-modal service robot including skills such as autonomous navigation, localization of small and large (furniture) objects, natural speech processing, classification of human body movements on top of NITE body tracking as well as autonomous motion planning (see fig. 4 and 5). The same skill components are used during both observation of demonstrations and autonomous execution. A Kinect sensor was utilized for visual perception components.

3.1 Demonstration Stage

During demonstrations, the robot observes one human, *robot actor* (roAc), representing the role of the robot and optionally a second human, representing an interacting human, *human actor* (huAc). Classification of human activities translates a body movement over time into symbolic activities *MovementType* as described in [5]. As a result, the following tuple of recording modalities $D_1, \ldots, D_n$ is used:

Fig. 4. Snapshot of a recording. Robot observing on the left, human actor in the center, robot actor on the right.

(roAc.Pose, huAc.Pose, huAc.MovementType, huAc.Utterance, Obj.Poses)
And action *a* modalities: *(roAc.MovementType, roAc.Utterance)*

The recording system performs abstraction as mentioned in sec. 2.2 for each modality. These modalities cover common aspects of multi-modal service robots, therefore, the utilized system is a typical representative. The robot follows a *roAc* actively with its head while the wide angled Kinect sensor allows to keep a large area around in the field of view to track objects and a *huAc* in the vicinity. In case of dialog, however, headsets are used for clear distinction between *roAc* and *huAc*. Several demonstrations of a pre-defined mission, representing differing courses of events and structural transition probability frequencies in that mission are recorded and segmented, leading to a set of sequences used for mapping and generalization.

3.2 Evaluation Missions

For evaluation of generalization and requests, a mission was chosen, serving a human a chair discretely and proactively without any spoken dialog. Basically, the goal was for the robot to learn which poses (distance and orientation) of the interacting human reflected a high likelihood of a desire to sit down and with which manipulation actions to pull a chair towards the human depending on the chair pose.

This mission contains several different types of uncertainties, present in the real world execution in a compact sized model, suitable for evaluation. Structural transitions representing human behavior and chair poses before pulling as well as the basic state and action sets can be generated from demonstrations.

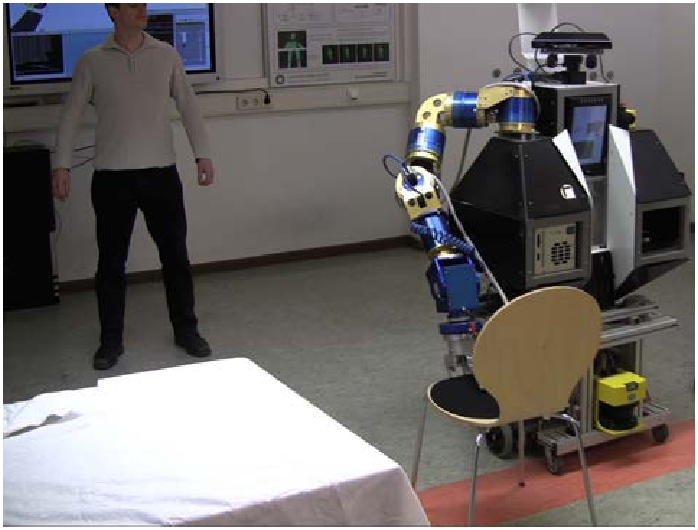

Fig. 5. Execution snapshot. Interacting human on the left, robot performing the robot role. Manipulation actions are executed using parameterized motion and grasp planning with online object localization.

3.3 Generation Stage

Two missions were demonstrated, A) with a focus on generalizing initial human pose (position and orientation) in respect to the likelihood of sitting down when presented with a chair (high reward). Mission B) had a focus on position and orientation of the chair and corresponding likelihoods of two different classes of motions (parameterizations of motion planning) being suitable for pulling the chair.

In mission A) the following modalities D_i were used: D_1^A: RobotPosition, D_2^A: ChairPosition, D_3^A: ChairOrientation, D_4^A: HumanPose and 3 different demonstration sequences performed, each a different number of times, to achieve non-uniformly distributed probabilities. The mapping lead to $|D_1^A| = 4, |D_2^A| = 4, |D_3^A| = 3, |D_4^A| = 9 \Rightarrow |S = 432, |A| = 8$. A total of 1157 generalizations of non-observed effects (t_g) were made, with 18 being considered crucial by a human expert analysis to scale to non-demonstrated aspects of the mission. Most non-crucial t_g affected the *idle* action. A total of 20 t_g were rated above the general threshold of which 7 had to be declined as invalid. The rest could be confirmed with demonstrations, again a different number of times to correct the estimated frequencies to the desired mission values. For mission B) the same modalities were used and 5 different demonstration sequences, again a different number of times performed. The mapping lead to $|D_1^A| = 4, |D_2^A| = 5, |D_3^A| = 5, |D_4^A| = 5 \Rightarrow |S = 400, |A| = 8$. A total of 1273 generalizations of non-observed effects (t_g) were made, with 14 being considered crucial by a human expert analysis. Most of the other t_g affected the *idle* action. A total of 22 t_g were rated above the general threshold and could be confirmed. These examples show the necessity of relevance estimation and the first one also the need for the binary tree request generation to decline false hypotheses.

3.4 Execution Stage

During execution of the mission by the robot, the computed policy was used by the online decision making system to autonomously select the next symbolic action when the previous terminated. Robot motion planning actions are represented by *manipulation strategies* (see [6] for details of the representation). All perception, processing and actuation was running solely on board (see fig. 5). In the real setting, deviations of perceived human and chair poses as well as in executed navigation and manipulations actions occur regularly as considered by observation model probabilities and error transition probabilities in the model. Deviations in real human poses and chair poses, as considered by structural transitions, were applied in the same manner as during demonstrations.

3.5 Evaluation Results

For evaluation, policies based on models generated from initial demonstrations and then further demonstrations after requests were pitted against a hand modeled finite state machine (FSM). To evaluate if the POMDP was able to consider the learned aspects sufficiently, the mission was performed (no matter if POMDP or FSM were controlling the robot) with human behavior and chair pose frequencies corresponding to the predefined mission concept (the "real" probabilities). Execution time (average duration of one main task performance within the mission) and failure frequency can be considered the primary performance criteria of the decision making system. Both missions were executed by the robot (and interacting human) and measured by a supervisor ten times for each controller. It included courses of events which were not present in the initial demonstrations, but only after generalization and request generation.

Mission	Avg. dur. POMDP	Fail. POMDP	Avg. dur. FSM	Fail. FSM
A	4:30 min	2/10	4:50 min	3/10
B	4:35 min	3/10	4:45 min	4/10

Failures included pulling the chair when the human had no interest and failing to pull the chair. Delays occurred when taking some time to interpret the human pose correctly, looking again for the chair or retrying to pull the chair.

The results show that the learned POMDP was able to match and even slightly surpass the performance of the hand-tailored FSM. The learned POMDP can achieve good performance from an efficient number of natural demonstrations of non-technical experts.

4 Related Work

There exists work related to several aspects presented here. Many approaches to learn symbolic task descriptions from human demonstrations are discussed in literature. Learning models for probabilistic decision making has been tackled mainly without using natural human demonstrations but still highlights important aspects for model generation. Generalizing task models for planning is also related. Finally, generation of interactive requests to improve models has been applied successfully to task model creation.

Popular low level imitation learning is quite distinct from the work presented here. On the symbolic level, several different categories can be distinguished, among them learning hierarchically organized sequences, learning finite state machines and learning planning models. A system to learn hierarchical representations of manipulation tasks was investigated by [7], yet neither multi-modality, nor flexibility by planning are covered. Learning finite state machines completely from the scratch, including basic structure and transitions was presented in [8] and tested in the robot soccer domain. Learning planning models, although not probabilistic ones, is discussed in [9].

Apart from using model-free policy learning, generating (PO)MDP models by means of learning is the obvious approach to the challenge how to retrieve the model. A technique which uses active learning with meta-distributions has been developed in [10], refining several aspects, e.g. transitions probabilities. Yet, it needs an initial state and action space and also an initial model. A theoretically even more powerful framework, BA-POMDPs, is explained in [11]. Because of complexity aspects, however, its planning horizon is very small in real settings, limiting its practicality. An imitation-learning related approach, generating properties of an MDP model for specific robot tasks is presented in [12].

There is a multitude of work concerning generalization of task knowledge for planning. In the scope of this work, those techniques, considering observations of humans are most relevant. A way to modify symbolic plans by analysis of observation of humans performing tasks was investigated in [13]. In that case, the application domain on a multi-modal service robot is also very similar to the PMPM-PbD application. The hierarchical PbD system in [7] was also extended by means of generalization over different, similar demonstrations, however, without further verification.

Interactive requests to a human by a robot to improve task models were used in a work [14] also using a kind of relevance measure to guide efficient selection of requests.

5 Conclusions and Future Work

We present a process to extend a POMDP model of a multi-modal robot mission when generated from a limited set of human demonstrations. It performs generalization of observed causal effects with subsequent verification by rating and then generation of requests for efficient further demonstrations. A strong emphasis was made on implementing the concept on a real, complex, multi-modal service robot, including both autonomous recording of demonstrations and execution to evaluate its suitability in realistic applications.

Future work has to include multi-mission spanning background knowledge for more fine grained generalization masks κ_{scope}, leading to even better selected hypotheses sets. Concerning request generation, empirical weighting parameters w_i could be learned over many missions.

This work has been conducted within the german SFB 588 “Humanoid Robots” granted by DFG.

References

1. Schmidt-Rohr, S.R., Lösch, M., Jäkel, R., Dillmann, R.: Programming by demonstration of probabilistic decision making on a multi-modal service robot. In: IEEE/RSJ International Conference on Intelligent Robots and Systems, Taipeh, Taiwan (2010)
2. Cassandra, A.R., Kaelbling, L.P., Littman, M.L.: Acting optimally in partially observable stochastic domains. In: Proceedings of the Twelfth National Conference on Artificial Intelligence (1994)
3. Kurniawati, H., Hsu, D., Lee, W.S.: SARSOP: Efficient point-based POMDP planning by approximating optimally reachable belief spaces. In: Proc. Robotics: Science and Systems (2008)
4. Schmidt-Rohr, S.R., Knoop, S., Lösch, M., Dillmann, R.: Bridging the gap of abstraction for probabilistic decision making on a multi-modal service robot. In: RSS, Zürich (2008)
5. Lösch, M., Schmidt-Rohr, S., Knoop, S., Vacek, S., Dillmann, R.: Feature set selection and optimal classifier for human activity recognition. In: RO-MAN (2007)
6. Jaekel, R., Schmidt-Rohr, S.R., Loesch, M., Dillmann, R.: Representation and constrained planning of manipulation strategies in the context of programming by demonstration. In: IEEE International Conference on Robotics and Automation, ICRA 2010 (2010)
7. Pardowitz, M., Knoop, S., Dillmann, R., Zollner, R.D.: Incremental learning of tasks from user demonstrations, past experiences, and vocal comments. IEEE Trans. on Systems, Man, and Cybernetics (2007)
8. Grollman, D., Jenkins, O.C.: Incremental learning of subtasks from unsegmented demonstration. In: IEEE/RSJ International Conference on Intelligent Robots and Systems (2010)
9. Veeraraghavan, H., Veloso, M.: Learning task specific plans through sound and visually interpretable demonstrations. In: IROS (2008)
10. Ross, S., Chaib-draa, B., Pineau, J.: Bayes-adaptive pomdps. In: NIPS. MIT Press (2007)
11. Jaulmes, R., Pineau, J., Precup, D.: A formal framework for robot learning and control under model uncertainty. In: 2007 IEEE International Conference on Robotics and Automation (April 2007)
12. Shon, A.P., Storz, J.J., Rao, R.P.N.: Towards a real-time bayesian imitation system for a humanoid robot. In: 2007 IEEE International Conference on Robotics and Automation, pp. 2847–2852 (2007)
13. Tenorth, M., Beetz, M.: Priming Transformational Planning with Observations of Human Activities.. In: IEEE International Conference on Robotics and Automation, ICRA (2010)
14. Chernova, S., Veloso, M.: Interactive policy learning through confidence-based autonomy. Journal of Artificial Intelligence Research 34 (2009)

A Topic Recognition System for Real World Human-Robot Conversations

Salvatore Maria Anzalone[1], Y. Yoshikawa[1], Hiroshi Ishiguro[1], Emanuele Menegatti[2], Enrico Pagello[2], and Rosario Sorbello[3]

[1] Intelligent Robotics Laboratory
Department of Systems Innovation
Graduate School of Engineering Science
Osaka University
[2] Intelligent Autonomous Systems Laboratory (IAS-Lab)
Department of Information Engineering
Faculty of Engineering
University of Padua
[3] Robotics Lab
Department of Computer Engineering
Faculty of Engineering
University of Palermo

Abstract. One of the main features of social robots is the ability to communicate and interact with people as partners in a natural way. However, achieving a good verbal interaction is a hard task due to the errors on speech recognition systems, and due to the understanting the natural language itself. This paper tries to overcome such kind of problems by presenting a system that enables social robots to get involved in conversation by recognizing its topic. Through the use of classical text mining approach, the presented system allows social robots to understand topics of conversation between human partners, enabling the customization of behaviours in their accordance. The system has been evaluated in different contexts, taking in account the quality and accuracy of the speech recognition syestem used by the social robot.

1 Introduction

Social robots are system able to communicate and interact as real partners with humans [1]. Communication between humans can be classified in two different kinds: verbal and non-verbal. While non-verbal communication is based on gazing, pointing, gesturing or changing of facial expressions, verbal communication is fully based on the speech [2]. Consequently, human speech is a natural and intuitive interface for communicating with robot. Despite of this, it is very difficult to achive good interaction with social robots using verbal communication because the nature of the auditive patterns and the nature of the human speech itself [3]. The auditive flow contains a lot of information that is hard to manage: environmental conditions with noise and echos, are the first problem to deal; a more complex matter to achieve is focusing the attention of the system on a single talker among a mix of several conversation and background noise, problem yet

S. Lee et al. (Eds.): Intelligent Autonomous Systems 12, AISC 194, pp. 383–391.
springerlink.com

Fig. 1. A sketch of the working environment of the system

described in literature as "cocktail party effect". At last, the human speech itself encodes several kind of information: who is the speaker, the speaker's identity; what the speaker is saying, the speaker's speech; how the speaker said it, the speaker's prosody.

Beyond these problems, that are all relative to the auditory recogition of the speech, another issue concerns the human natural language itself [4]: linguists do not have a complete understanding of the underlying rules of spoken languages because it seems impossible to describe them only in terms of syntax, semantics or phonetics rules, as it is possible to constructed language. The comprehension of the real meaning of the speech becomes a very hard task due to its incompleteness, ambiguity and semi structured or unstructured characterization.

Several studies tried to deal with these obstacles from both the speech recongition side and from the natural language processing point of view. Researchs tried to improve the accuracy of the speech recognition systems using a more detailed description of phonemes or through triphones [5] or using larger vocabulary or by providing additional constraints [6]. On the other side, researchs on natural language processing tried to achieve a deep understanding of the spoken utterances improving parsers, using stochastic models [7], context based ontologies or rich lexical databases that includes semantic information, such as Wordnet [8].

From the point of view of the researches on verbal communication for social robots many attempts have been performed. Simple command based based systems gave important results, but users should knows the commands or should be previously instructed about the behaviour of the robot [9]. Dialogue based systems have also been successfully used [10], but also in this case it is very difficult to achieve a free conversation speech, due to the dialogue system itself, that should be able to cover a wide spread of possible conversation paths. Some systems tried to use ontologies to retrieve a complete understanding of the conversation [11]. Other social robot systems tried to use customized algorithms, such as Latent Semantic Analysis, to extract from the speech some important characterizations, as well as the emotions [12] [13]. All these systems soffer from the problem of having errors on the input speech utterance, due to mistake of the speech recognition system[14].

The system presented in this paper allows social robots to get involved in conversation with humans as shown in Figure 1, by recognizing the topic of the current conversation. The system will try to overcome the low recognition rate on the accuracy of the speech recognition system by grounding conversation between people to its topic, using only the relevant words.

2 System Overview

The assumption made by this work is that it is difficult to obtain accurate and correct results from a speech recognition systems in real world applications. In order to avoid this problem, the system presented in this paper will recognize topics of the conversation in which a robot si involved by ignoring the details of the structure of each sentence, focusing only to the important words that will reveal what the the people is talking about.

The scenario considered by this system is a low-noise environment in which, as shown in Figure 1, two (or more) human partners talk in turn about a closed set of topics. The system has been supposed to be an efficent tool for several kind of application, such as to interact in a customized way as robotic companion, or to suggest information related to what people is talking about, as a robotic assistant, or as system able to profile human partners according to their favourite topics.

The system is composed by several reusable modules capable to cooperate and exchange information, as shown in Figure 2. The framework ROS allowed the development of these components to distribute the algorithms through several software units following a modular top-down approach. In particular, two main modules have been implemented: the speech recognition module and the topic classification module.

The speech recognition module is implemented through the use of Julius[15]. Julius is a state-of-art large vocabulary continuous speech recognition system that is able to perform in realtime. The system has been developed in a context of Japanese language users, then Julius has been traineed using a Japanese language model composed by 20k words from newspaper articles and an acustic model based on triphones to assure efficency and high performances.

The topic classification module carries out the recognition of the topic that emerges from the speech utterance decoded by using a slightly modified version of the "Term Frequency - Inverse Document Frequency" (TF-IDF) weighting, called "Term Frequency - Inverse Topic Frequency" (TF-ITF). The output of this system will be the set of probabilities related to each possible topic.

3 Topic Classification

The topic recognition system is based on a modified version of the TF-IDF ranking function, often used in text mining and information retrival. Given a corpus of documents, the TF-IDF weight is a statistical measure that evaluates how much a word is important to a document. The apporach chosen was to evaluate the TF-IDF weight for each word in a corpus of documents related to several topics by calculating how much a

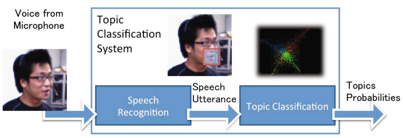

Fig. 2. A sketch of the ROS modules that compose the system

word is relevant to each topic, rather than each document, realizing a "Term Frequency - Inverse Topic Frequency" instead of the classical "Term Frequency - Inverse Document Frequency".

Given a corpus of documents labeled by their topic, the weight of the word W according to a topic T is calculated by the formula:

$$TF\text{-}ITF(W,T) = \frac{freq(W,T)}{\sum_w freq(w,T)} \times \log \frac{\sum_w \sum_{\substack{t \\ t \neq T}} freq(w,t)}{\sum_{\substack{t \\ t \neq T}} freq(W,t)}$$

The first part of the formula describe the term W using its frequency normalized by the number of the words of the topic T. The important property of the normalized frequency is that some words are more used in some contexts rather in others. Despite of this, the term frequency weight is not enough because many words, such as particles or auxiliar verbs, are used a lot in every context. The second part of the formula tries to overcome this limit, penalizing the terms that are used in the other topics.

According to this approach, it is possible to recognize and discard all the negligible terms by applying a simple thresholding to the TF-ITF: words with a higher TF-ITF weight in a cosidered topic will be taken in account as meaningful for that topic.

After a normalization of the TF-ITF weight of each word by its weight in all the topics, it is possible to analyze and classify complex sentences through the formula:

$$P(S,T) = 1 - \prod_{\forall w \in S} \left[1 - TF\text{-}ITF(w,T)\right]$$

Through a sequence of products the TF-ITF weight of each word inside a sentence is used to obtain the sentence probability to belong to a class T. For a given sentence, the topic classification system will in this way produce the probabilities for each trained topic.

4 Experimental Results

The system has been trained to recognize four different topics: "soccer", "ski", "baseball" and "swimming". For each topic, a folder of documents has been selected from the Japanese Wikipedia pages. Documents have been chosen in order to have about 20000 words for each category, equally distributed among the topics. The TF-IDF weight has been calculated for each word according to each of the four category, then, experimentally, a threshold for distinguish meaningless words, such as auxiliar verbs, particles, and stopwords, has been found.

Tests of the system have been performed in three kind of situation, as shown in Figure 3: using raw text from sport newspapers, without the use of the speech recognition system; using read speech in a controlled environment, through japanese television sport newscasts captured from YouTube; using spontaneous speech, captured in real conversation between people.

Experiments achieved have been evaluated in terms of accuracy, precision, sensitivity and specificity.

Fig. 3. Raw text, read text and free speech conversation

4.1 Raw Text

Raw text has been collected from japanese sport news websites. For each category a set of 10 documents have been chosen to evaluate their main topic. In this case the results obtained are free from the speech recogntion errors because the raw text is submitted directly to the topic classification system. Results shown the performances of the classification system in an ideal scenario using an errorless speech recognition system.

Table 1. The confusion matrices related to the newspapers raw text classification. Data is expressed in percentage

Actual class	Predicted class: Soccer	Baseball	Ski	Swim
Soccer	100	0	0	0
Baseball	0	100	0	0
Ski	0	0	100	0
Swim	0	10	10	80

Confusion matrix (see Table 1) and performances of the system shown an high reliability of topic classification system. In particular, experiments reported 98% of accuracy, 95% of precision, 97% of sensitivity, 98% of specificity, as shown in Table 4.

4.2 Read Text

For each category, five videos from YouTube have been collected. Videos of about one minute of length have been chosen from japanese television sport newscasts in order to evaluate the performances of the whole system, that now includes also the speech recognition system, in a controlled, noiseless, environment. Moreover, the use of newcasts videos allows the evaluation of the system in a best-case scenario because anchormen will talk using a formal diction.

Due to the use of the speech recognition system, a recognition rate performance has been added to the measures collected. As shown in the confusion matrix in Table 2, performances are still high, despite the recognition rate of the speech recognition system of 25%. Experiments shown 93% of accuracy, 90% of precision, 88% of sensitivity, 96% of specificity, as depicted in Table 4.

Table 2. The confusion matrices related to the read text classification. Data is expressed in percentage.

		Predicted class			
		Soccer	Baseball	Ski	Swim
Actual class	Soccer	60	0	20	20
	Baseball	0	100	0	0
	Ski	0	0	100	0
	Swim	0	0	0	100

4.3 Spontaneous Speech

To obtain spontaneous speech samples, six persons have been involved in an experiment. A video for each of the four categories has been shown to each person, then 3 couples have been formed. Each partecipant has been invited to describe and conversate in turn about a single video, for about one minute and half. Experiments have collected six audio samples for each of the four categories, a total of 24 audio samples of conversation. Spontaneous speech data set collected has been evaluated by the use of the whole system.

Table 3. The confusion matrices related to the spontaneous speech classification. Data is expressed in percentage.

		Predicted class			
		Soccer	Baseball	Ski	Swim
Actual class	Soccer	100	0	0	0
	Baseball	0	66	33	0
	Ski	16	0	66	16
	Swim	16	0	0	83

As it is possible to see in Table 3, the low recognition rate of the speech recognition system of 13% affects the performances of the whole system. However, despite of this, results are still very significative because their reliability. Experiments obtained 89% of accuracy, 79% of precision, 81% of sensitivity, 93% of specificity, as in Table 4.

4.4 Results Comparison and Limitations

The Table 4 shown a comparison between the different scenarios in which the system has been tested. Despite of the recognition rate of the speech recognition system, performances of the classification system are still high. This is a direct effect obtained by taking in account only some words classified as important in the considered contexts, while forgetting about the details: the speech recognition system does not need to be extremly accurate.

While achieving these performances, the system incur into several limitation. Independence of the topics to be recognized can affect the performances of the system, due

Table 4. Performances comparison in different scenarios. Data is expressed in percentage.

	Raw Text	Read Text	Spontaneous Speech
Recognized Speech	-	25	13
Accuracy	98	93	89
Precision	95	90	79
Sensitivity	97	88	81
Specificity	98	96	93

to the underlied naive independence assumption. While the system is able to distinguish highly uncorrelated, independent classes, such as "baseball" and "swimming", more errors may occour while trying to separate more related topics, such as "swimming" and "water polo". In this case, many words can be used in both the topic considered, such as "water" or "pool", reducing the reliability of the final results. At last, as shown in Figure 4, tests performed with chunks of conversation with different lenght shown that the system is able to assess the topic in the 80% of the experiments during their first 20 seconds.

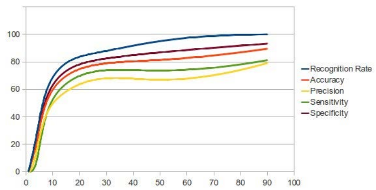

Fig. 4. Spontaneous speech performances among the time [sec]

5 Conclusion and Future Work

A natural language processing system for social robots involved in human conversations has been developed and tested. The system was based upon a slightly modified version of "Term Frequency - Inverse Document Frequency" weighting called "Term Frequency - Inverse Term Frequency", that allowed the system to forget about the details of the sentences, while recognizing the topic of the current conversation occurring between human partners. Experiments of the system performed in several scenarios shown the benefits and the limits of the presented approach.

Results shown encourage to pursuit on the experimentation of this approach in new, real, more complicated scenarios. While the presented system used Julius as state of the art speech recognition system, more experiments should be performed by using different and more efficent systems. Moreover, in order to assure better performances, a sound localization system will be used to try to deal with noisy environment and cocktail party effects. New experiments will try to capture relevant information from vocal interaction between robot's human partners in order to adapt its behaviours according to the occurring conversation, to profile them or to simply suggest them conversation related information.

Acknowledgments. Authors would like to thank Dr. S. Livieri, Dr. F. Dalla Libera, Prof. A. Chella, Prof. G. Vassallo for their support during the development of this project.

This work has been supported by a Grant-in-Aid for scientific research fellowships from Japan Society for the Promotion of Science (JSPS). This project was partially founded by Regione Veneto Cod. progetto: 2105/201/5/2215/2009 approved with DGR n. 2215, 21/07/2009.

References

1. Breazeal, C.: Toward sociable robots. Robotics and Autonomous Systems 42(3-4) (2003)
2. Breazeal, C.L.: Designing sociable robots. MIT Press (2004)
3. Benesty, J., Sondhi, M.M., Huang, Y., Greenberg, S.: Springer handbook of speech processing. The Journal of the Acoustical Society of America 126, 2130 (2009)
4. Jackson, P., Moulinier, I.: Natural language processing for online applications: Text retrieval, extraction and categorization, vol. 5. John Benjamins Pub. Co. (2007)
5. Darjaa, S., Cerňak, M., Trnka, M., Rusko, M., Sabo, R.: Effective triphone mapping for acoustic modeling in speech recognition. In: Proceedings of Interspeech 2011 Conference (2011)
6. Lee, A., Kawahara, T.: Recent development of open-source speech recognition engine julius. In: Proceedings: APSIPA ASC 2009: Asia-Pacific Signal and Information Processing Association, 2009 Annual Summit and Conference, pp. 131–137. International Organizing Committee (2009)
7. Teh, Y.W.: Bayesian tools for natural language learning. In: Proceedings of the Fifteenth Conference on Computational Natural Language Learning, p. 219. Association for Computational Linguistics (2011)
8. Fellbaum, C.: Wordnet. Theory and Applications of Ontology: Computer Applications (2010)
9. Shim, B.K., Cho, Y.K., Won, J.B., Han, S.H.: A study on real-time control of mobile robot with based on voice command. In: 11th International Conference on Control, Automation and Systems ICCAS 2011, pp. 1102–1103. IEEE (2011)
10. Toptsis, I., Li, S., Wrede, B., Fink, G.A.: A multi-modal dialog system for a mobile robot. In: Eighth International Conference on Spoken Language Processing (2004)
11. Kobayashi, S., Tamagawa, S., Morita, T., Yamaguchi, T.: Intelligent humanoid robot with japanese wikipedia ontology and robot action ontology. In: Proceedings of the 6th International Conference on Human-Robot Interaction, pp. 417–424. ACM (2011)
12. Anzalone, S.M., Cinquegrani, F., Sorbello, R., Chella, A.: An emotional humanoid partner. Linguistic and Cognitive Approaches To Dialog Agents (LaCATODA 2010) At AISB (2010)
13. Chella, A., Sorbello, R., Pilato, G., Vassallo, G., Balistreri, G., Giardina, M.: An Architecture with a Mobile Phone Interface for the Interaction of a Human with a Humanoid Robot Expressing Emotions and Personality. In: Pirrone, R., Sorbello, F. (eds.) AI*IA 2011. LNCS, vol. 6934, pp. 117–126. Springer, Heidelberg (2011)

14. Kraft, F., Kilgour, K., Saam, R., Stuker, S., Wolfel, M., Asfour, T., Waibel, A.: Towards social integration of humanoid robots by conversational concept learning. In: 2010 10th IEEE-RAS International Conference on Humanoid Robots (Humanoids), pp. 352–357. IEEE (2010)
15. Lee, A., Kawahara, T., Shikano, K.: Julius—an open source real-time large vocabulary recognition engine. In: Seventh European Conference on Speech Communication and Technology (2001)

Semi-autonomous Car Control Using Brain Computer Interfaces

Daniel Göhring, David Latotzky, Miao Wang, and Raúl Rojas

Artificial Intelligence Group
Institut für Informatik
Freie Universität Berlin, Germany

Abstract. In this paper we present an approach to control a real car with brain signals. To achieve this, we use a brain computer interface (BCI) which is connected to our autonomous car. The car is equipped with a variety of sensors and can be controlled by a computer. We implemented two scenarios to test the usability of the BCI for controlling our car. In the first scenario our car is completely brain controlled, using four different brain patterns for steering and throttle/brake. We will describe the control interface which is necessary for a smooth, brain controlled driving. In a second scenario, decisions for path selection at intersections and forkings are made using the BCI. Between these points, the remaining autonomous functions (e.g. path following and obstacle avoidance) are still active. We evaluated our approach in a variety of experiments on a closed airfield and will present results on accuracy, reaction times and usability.

1 Introduction

Autonomous cars play an important role in current robotics and A.I. research. The development of driverless cars started in the late '70s and '80s. Ernst Dickmann's Mercedes Benz achieved a travel velocity of 100 km/h on restricted highways without traffic [3]. In the DARPA Grand Challenge 2005, autonomous cars drove off-road on desert terrain, several of them reaching the finish line [9]. DARPA's Urban Challenge of 2007 demonstrated that intelligent cars are able to handle urban scenarios and situations with simulated traffic [10]. Lately, autonomous cars have been driving through real world traffic for testing purposes in urban and rural areas alike [8].

This research lead to the introduction of various driver assistance systems for street cars. One key aspect for driver assistance systems is how the interface between human and machine affects usability. This interface question is more important for people without full bodily control. Brain Computer Interfaces can be a solution here. Recently, BCI-systems have become relatively affordable and allow people to interact directly with their environment [5]. Another big field lies in human interaction within computer games, e.g. in the research game "Brain Basher" [1] or in [6]. As a sub-field of BCI research, BCI using motor imagination brain patterns has become popular, where the user has to think of a

S. Lee et al. (Eds.): Intelligent Autonomous Systems 12, AISC 194, pp. 393–408.
springerlink.com

motion instead of performing it physically [4]. In other work, users could control mechanical devices with EEG patterns [7]. In this paper we want to present a solution where a human controls a car just by using brain signals, i.e., without need for any physical interaction with the car.

In a first application, computer-aided free driving allows the passenger to claim steering- and speed-control in special areas. The car prevents traffic rule-violations and accidents by reclaiming control before they happen. The second application implements a semi-autonomous path-planning, where a car drives autonomously through a road-network until it arrives at so called decision points. Typically located at crossings, decision points require the passenger to choose which way to drive next.

The paper is structured as follows: Section 2 introduces the autonomous car "MadeInGermany" and the applied BCI hardware. In Section 3 we describe the training process and the classification approach used. Section 4 presents the developed usability interface which enables a human to easily and safely control the car[1] using brain patterns, followed by Section 5, which shows experimental results of the presented approach. Section 6 summarizes the paper and suggests future work.

2 Autonomous Car and BCI Hardware

2.1 Autonomous Car

Our autonomous car "MadeInGermany" served as a test platform c.f. Fig. 1: a modified Volkswagen Passat, equipped with a variety of different sensors and a drive by wire control via CAN bus. An introduction to these sensors is necessary at this stage, as they are used in the here-described semi-autonomous mode. The platform is equipped with six laser scanners, three at front and three at the back. Additionally, on top of the car a rotating laser scanner from Velodyne scans the near environment, c.f. Fig. 2. Further, the car has different radar sensors for obstacle detection and cameras, which are used for 3D feature extraction, lane and traffic light detection. The car actuators, i.e., gear shifting, motor and brake control are manipulated via CAN bus.

A modular architecture allows separate software-components for the different sensors and actuators on each car, while utilizing the same modules for decision-making and other higher level functions. Besides GPS and CAN data, the car relies on camera, lidar and radar sensors.

Besides, the authors want to mention, that the architecture described in this paper is also applied to a semi-autonomous wheelchair, c.f. Fig. 3, but in this paper we want to focus on the application to the semi-autonomous car.

2.2 Brain Computer Interface

The brain computer interface used in this approach is a commercial product, the Epoc cap from Emotive. It has 16 EEG sensors which measure potential

[1] BCI-car video here: http://www.youtube.com/watch?v=iDV_62QoHjY

Fig. 1. The autonomous car "MadeInGermany"

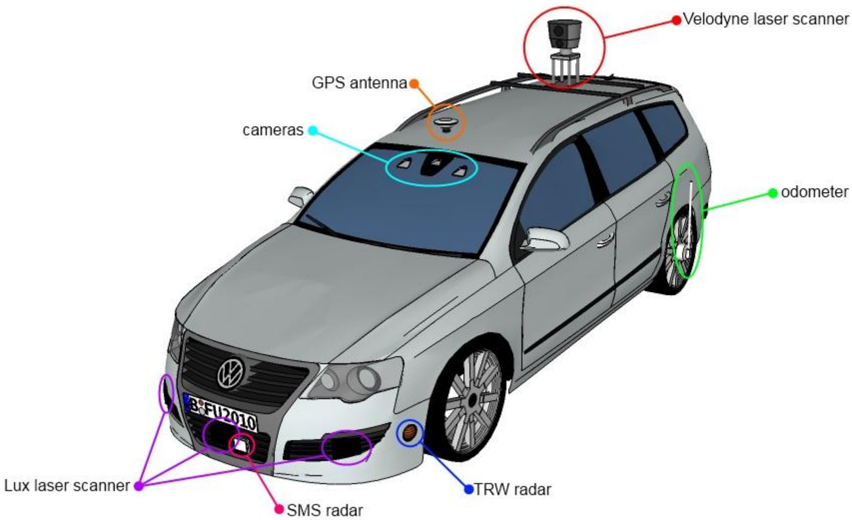

Fig. 2. Sensor configuration of "MadeInGermany"

Fig. 3. Autonomous wheelchair equipped with Kinect and lidar sensors

differences on the scalp. A contact fluid is necessary for good recognition. As a first step, the device has to be trained to the brain patterns of a user. The 16 sensor readings are mapped to four different direction classes or to the neutral class. Unfortunately we had no access to the sensor readings of the head sensors, thus, the first classification process was not transparent. The classification result is used by the controller module to generate throttle, brake and steering commands.

3 Training and Classification

In the training phase the user can decide whether to control the steering only (two classes) or to also control steering and velocity (four classes). The classification program then asks the user to sequentially think of the different direction schemes. Many users tend to think of different motions, i.e. they think of moving the right arm, without really performing those motions. Thus, certain motor images do activate different regions in the brain, but not necessarily the same regions as would be activated during real motions [2]. The corresponding electric brain patterns are measured by the BCI. Usually, this method is called "Motor Imagery".

The training process must be executed every time the user puts the cab on his head. After some time, a retraining can be necessary. After the training process, the user can estimate the quality of classification by performing an evaluation

Fig. 4. Epoc neuroheadset from Emotive. The cap is connected wirelessly to the computer

test. If classification is not sufficiently correct, a retraining is necessary; sometimes the user must choose other patterns, e.g. to think of other motions or images.

4 Interface Design

4.1 Requirements

With the free drive controller and BrainChooser alike, design of interface is essential for BCI usability. Important aspects we focused on were

- stability and smoothness of executed actions,
- robustness to falsely classified brain patterns,
- safety of executed maneuvers with respect to physical limitations and to the surrounding area,
- minimality of necessary actions for maneuvers.

Two solutions were developed and tested on the closed Tempelhof airfield, for which we designed a demonstration course, see Fig. 5.

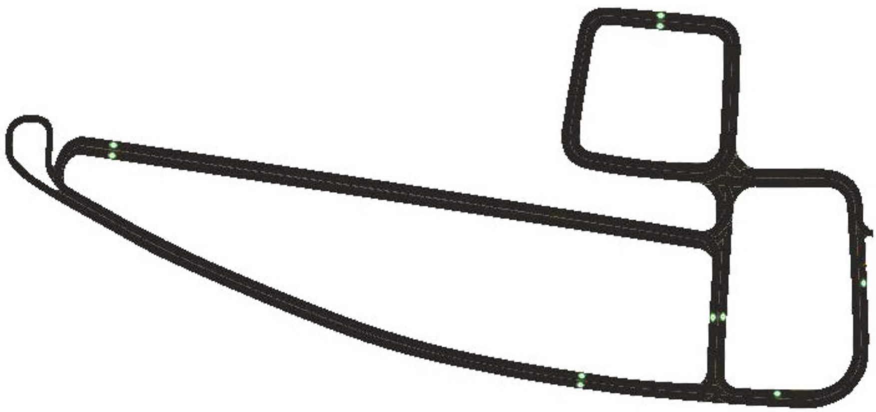

Fig. 5. Test parcours on closed Berlin-Tempelhof airfield

4.2 Free Drive

In free drive mode the operator has access to steering and speed control. Accidents are prevented by constantly monitoring the operator's decisions. If a collision is imminent or if the car is about to leave the free drive zone, the computer immediately stops the car. This application is interesting, because it demonstrates how well the system can be used in an environment, where decisions via BCI are time critical.

Control Actions. The four brain commands ("left", "right", "push", "pull") are mapped to steer and velocity commands as follows: Commands "left" and "right" increase or decrease the current steering wheel angle. Commands "push" and "pull" increase or decrease the desired velocity. This solution proved superior compared to giving direct throttle or brake commands, as it is easier to maintain a certain speed. When none of the four commands is detected, the velocity stays constant. The steering angle stays constant for one second, and then is reduced (or respectively increased) towards zero position, in which the car moves straight.

Control Frequency. Steering a car requires the driver to be able to execute steering motion with slow response times. To allow filtering of noisy brain signals, we allowed only one steering command per second in earlier tests. Then, a large steering angle was added to the current position. In this solution the driver had problems to execute small steering angles, the response times were shown to be too long. In further tests a control frequency of 5 Hz and a steer step of 0.6 rad proved to be a good solution, meaning that one revolution of the steering wheel takes about two seconds. The velocity can be increased or decreased by 0.15 m/s in each step. The steering angle is limited to $\pm 2.5\pi$. Velocities are cropped between 0 and 10 m/s.

Steering. When no "left" or "right" command is received for more than one second, the steering wheel returns to neutral position. At higher velocities (>2 m/s), the steering wheel turns more slowly and the steering angle limits are reduced. This prevents excessive centrifugal forces and allows the driver to stay on a desired trajectory without causing oscillations. The steering angle ω, depending on the velocity of the car v in m/s is limited to the following values (in rad):

$$\omega = 2.5\pi * \min(1.0, 2.0/v) \tag{1}$$

Accordingly, the steering angle change $\delta\omega$ within each time step is:

$$\delta\omega = 0.6\pi * \min(1.0, 2.0/v) \tag{2}$$

When the driver is accelerating or decelerating ("pull" or "push" commands), we also reduce the steering angle.

Steer Angle Smoother. Sending steering angle commands to the steering controller with 5 Hz only causes non-smooth steering maneuvers. The steer controller works with 100 Hz, therefore we implemented a steering angle smoother, which linearly extrapolates 20 desired angle values (one value for each 10 ms) for the controller. The result was a very soft turning steering wheel.

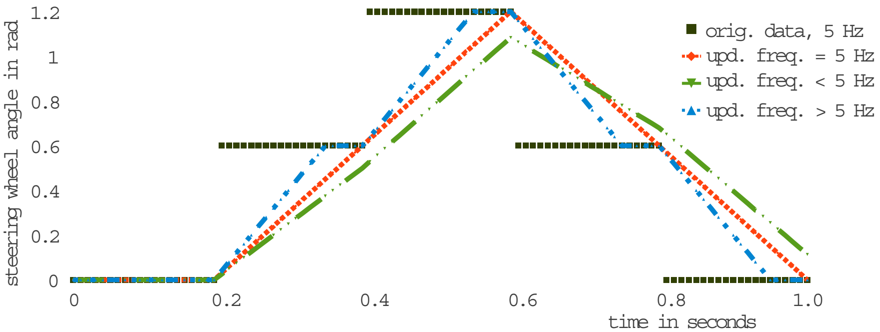

Fig. 6. Steer Angle Smoother, black dotted curve shows the raw angle values at 5 Hz; blue, red and green curves show interpolated values for interpolation frequencies higher, equal or lower than 5 Hz.

Velocity Controller. The desired velocity is input to a PID-controller. The PID-controller generates positive or negative output values. Positive outputs are weighted and mapped to throttle commands, negative outputs are similarly mapped to brake commands.

As experiments will show later, staying on a given trajectory can be hard at higher velocities, so an application on open traffic is far away. Therefore we implemented and tested another solution for the BCI, in which it assists the human in deciding which direction to take; all driving and safety relevant decisions are made by the car.

4.3 BrainChooser

While the autonomous car usually plans the best trajectory through the road network to reach its destination, the BrainChooser application allows the passenger, by using the BCI device, to modify the route at certain decision points, provided by the navigation module, e.g., at intersections.

The road network is presented as a directed graph of way-points which are connected by lanes. Curved lanes are approximated by spline interpolation over the way-points. Fig. 7 shows the spline interpolation of the road network graph with the car at a decision point for two possible directions.

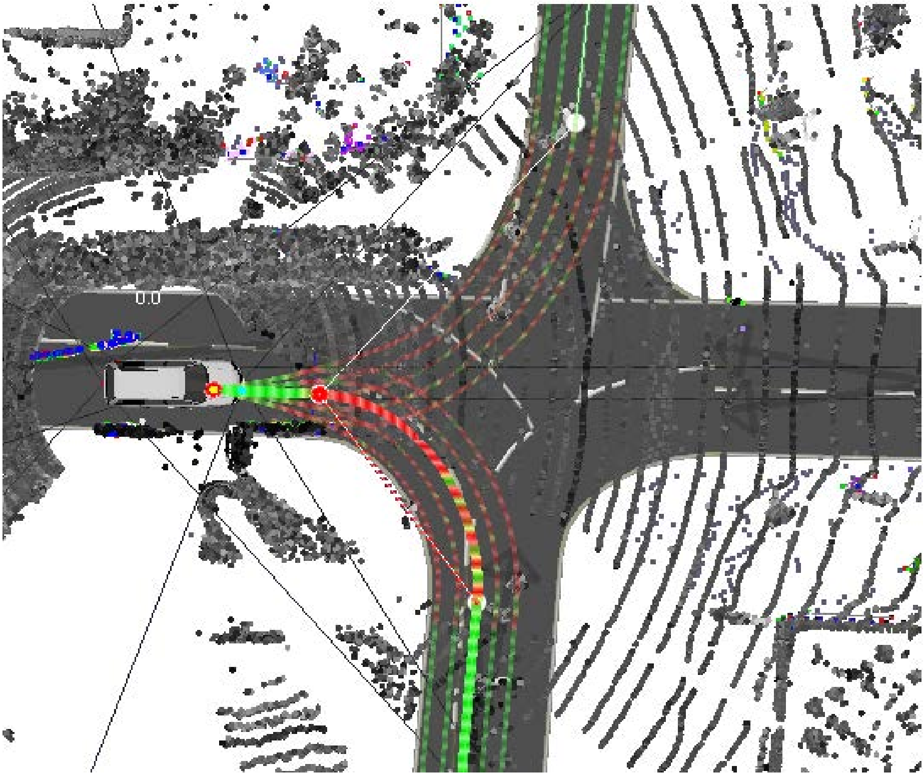

Fig. 7. A spline interpolation of the road network with a point cloud from the lidar-scanner for detecting obstacles. A path along the right lane has been chosen at the decision point in front of the crossroad, as indicated by the highlighted red-green line.

To find a desired trajectory in the road network, weights are assigned to lanes representing the distance, speed-limit and obstacles on the lanes, if necessary. When the car reaches a decision point where an operator's choice is required, e.g. an intersection, the operator is requested to choose a direction. The request is executed with the help of a synthetic voice recording. Once a choice was made, the chosen trajectory on the road network is processed and executed by the steering and velocity controller.

At decision points, the operator is requested by voice recording to input a direction with the BCI. Since it's usually not possible to hold a brain pattern steady over a long period of time, messages with detected patterns arrive at irregular intervals and include false positives. To robustly classify the brain pattern into one of the four categories, four variables (one for each possible pattern) accumulate the detection-probabilities. The variable which first passes a certain threshold defines the operator's decision. This method proved to be relatively robust to false detections. It also gives the operator the required time to enter the desired direction. To prevent distraction, no audio-feedback is given during the selection. However, a display presents the currently detected pattern, resulting in faster decisions.

5 Experiments

5.1 Benchmarks

We conducted different experiments on the former Tempelhof airport in Berlin.

Experiment 1. At first we measured the accuracy of control. The first task was to keep the car on an infield course, see Fig. 5, using "left" and "right" patterns for steering only. The velocity was set to 2 meters per second. The driver had to drive the track for three laps to see whether the accuracy remained constant over time. The resulting traces are depicted in Fig. 8; the errors are shown in Fig. 13.

Experiment 2. In the second experiment the driving person had to control throttle and brake in addition to the steering commands for left and right. The car was now able to accelerate from 0 to 3 meters per second. The resulting trace is shown in Fig. 11, the errors are shown in Fig. 13.

Experiment 3. To check the lateral error to the lane at higher speeds, we designed another track with long straight lanes and two sharp corners. The velocity was fixed to 5 meters per second and like in the first experiments, the driver had to steer left and right only, trying to stay at the reference lane. The resulting trajectory is shown in Fig. 12, the errors in Fig. 13.

Experiment 4. We checked the response time of the test person. The test person received different commands, such as "left", "right", "push" or "pull" from another person and had to generate the corresponding brain pattern - this had

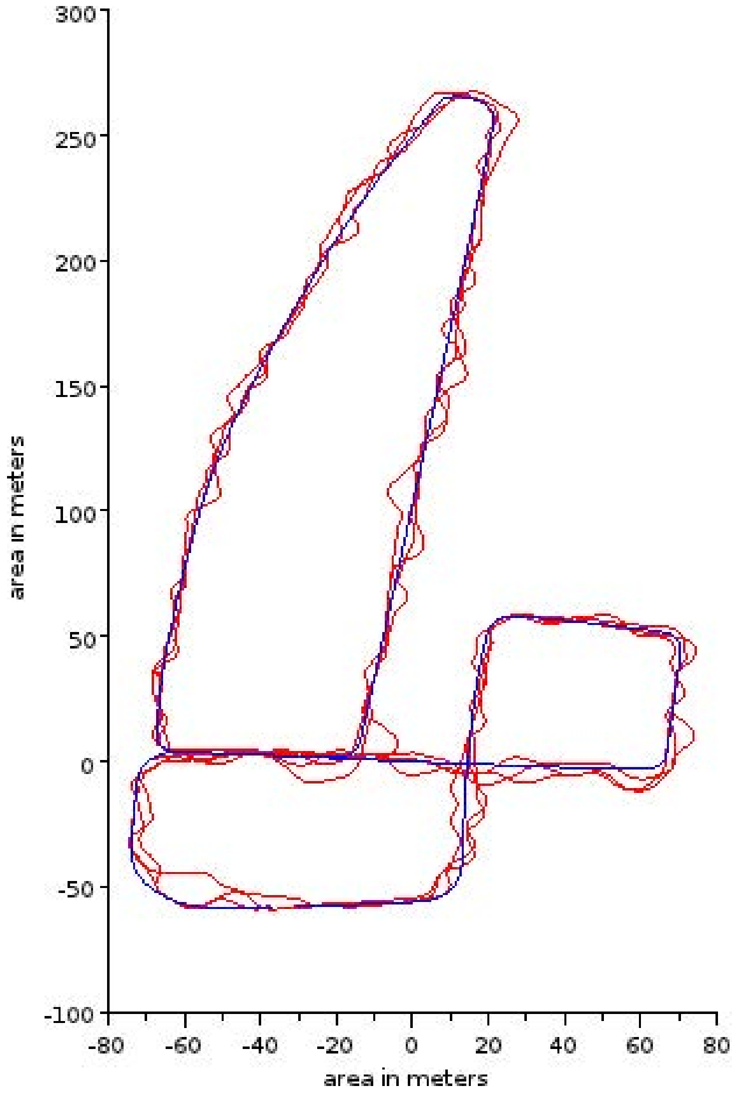

Fig. 8. Experiment 1: Infield test course. The test person had to control the car with two steering commands ("left" and "right"). Velocity was set to 2 meters per second. The traces of all three driven laps are depicted (red). Reference trace of the original track in blue.

to be recognized by the control computer. The time from the command until the recognition within the control computer was measured. We also measured falsely classified patterns.

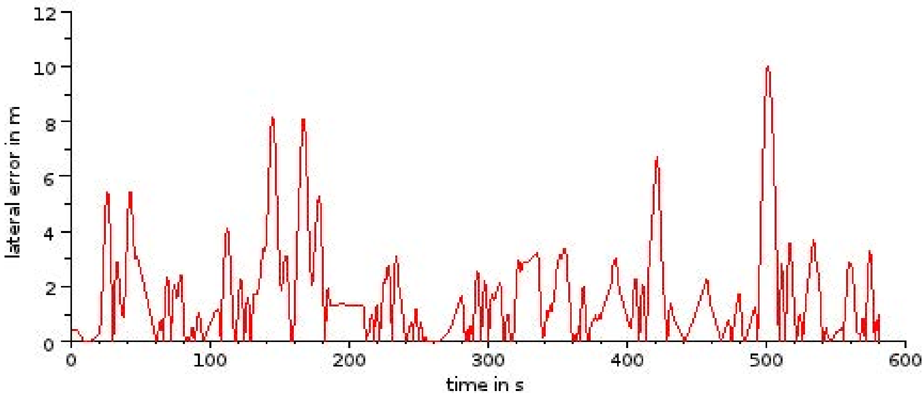

Fig. 9. Experiment 1: Lateral error of the car to the reference trajectory

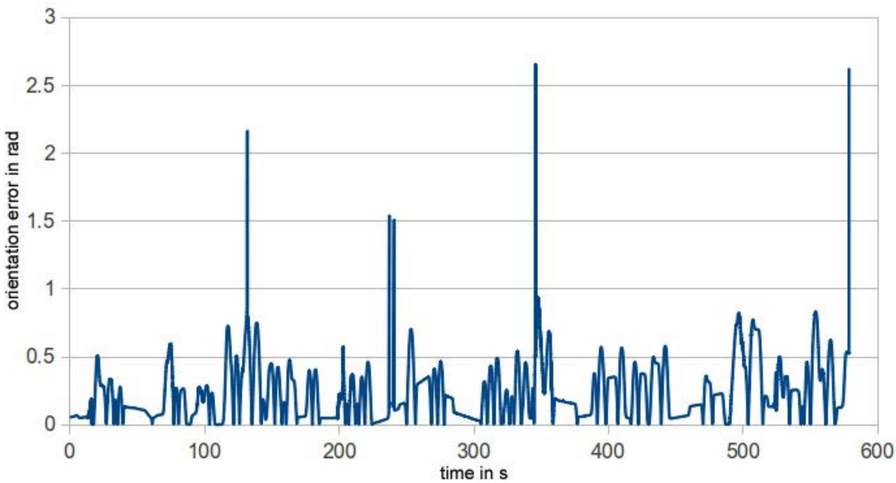

Fig. 10. Experiment 1: Orientation error of the car to the reference trajectory

Experiment 5. In this experiment, we tested the second module, the Brain-Chooser. Here, at intersections, the operator was asked to decide for the left or the right route. Then the test person had about ten seconds to decide for left or right direction. This long decision phase helps to filter out noise and ensures that the test person was generating the desired pattern over a longer time, reducing the risk of coincidentally generated patterns.

5.2 Experimental Results

Experiment 1. At the beginning of the first experiment we marked the desired lanes on the airfield. As we found, on a flat surface those lanes are hard to see

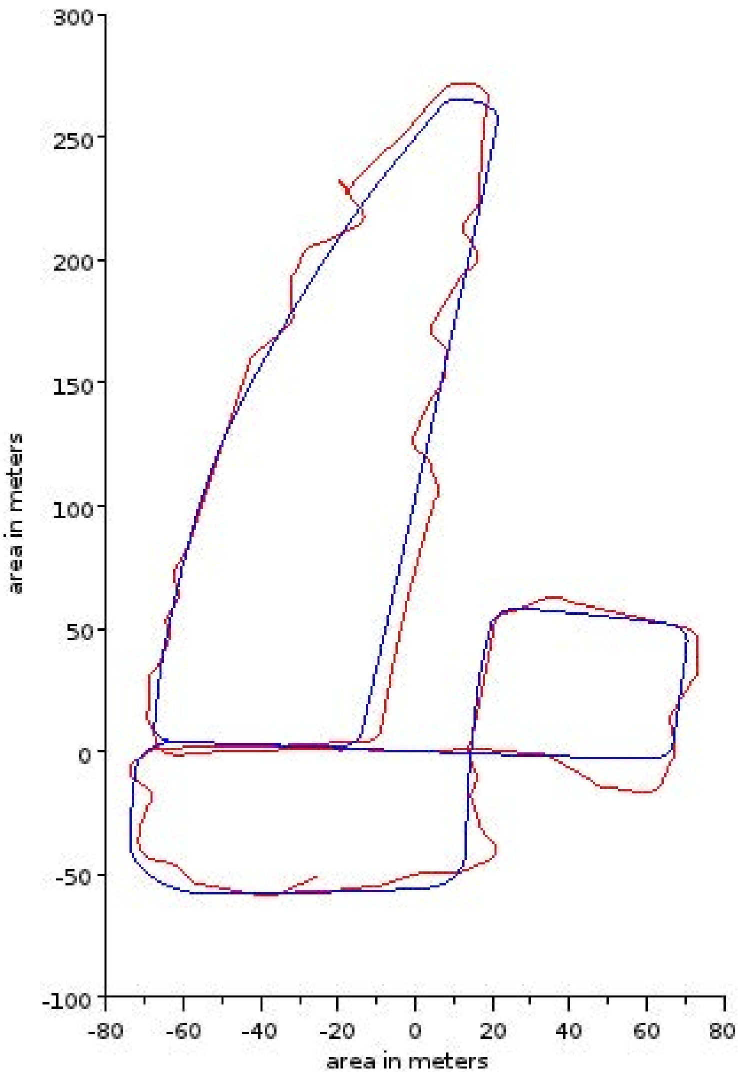

Fig. 11. Experiment 2: Infield test course. The test person had to control the car with four commands ("left", "right", "push", "pull") to steer the car and to adjust the velocity, 0-3 meters per second. The traces of the car (red) and of the original lap (blue) are depicted.

from greater distances. Moreover, it is difficult for a human driver to estimate his distance to the middle of the lane with centimeter accuracy. Therefore the test person had access to a computer monitor, which displayed a model of the car on the virtual track from bird's eye perspective. The test person succeeded in keeping a close distance to the desired trajectory, while only having to steer the car. We performed three tests to observe the variance between different laps.

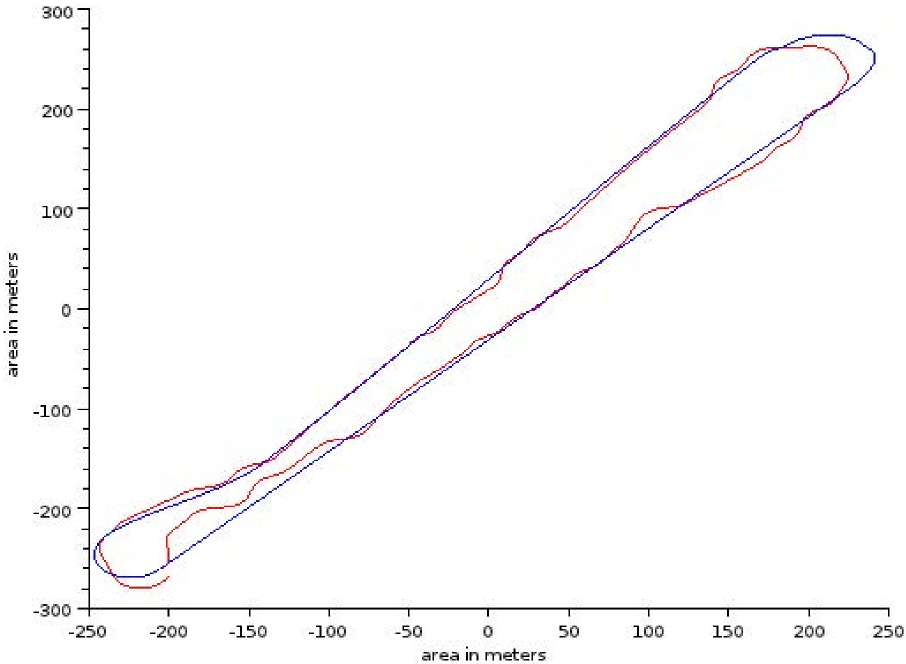

Fig. 12. Experiment 3: Speedway test course. As in the first experiment, the test person had to control the car with two steering commands. Velocity was set to 5 meters per second. The traces of the car (red) and of the original lap (blue) are depicted.

	σ_{lateral} [m]	σ_{angle} [rad]
Infield 2m/s, 2 DOF	1.875	0.200
Infield 3m/s, 4 DOF	2.765	0.410
Speedway 5m/s, 2 DOF	4.484	0.222

Fig. 13. Error measurements: Lateral distance to reference trajectory in meters and orientation error in rad. 2 or 4 DOF refer to the two or four patterns, the test person has to generate.

	2s or less	2 - 5 s	5 - 10 s	10 s or more	falsely class.
percent	26 %	36 %	10 %	9 %	20 %

Fig. 14. Experiment 4: Reaction times. The test subject is told to generate a certain pattern. A pattern counts as recognized, when the computer recognizes the correct class.

The standard deviation of the lateral error function over time was 1.875 meters for one lap, the error function is shown in Fig. 9. One lap lasted for about 10 minutes. In the following laps this error did not diverge by more than 0.2 m. The angular error standard deviation was 0.20 rad. The traces of the driven laps are shown in Fig. 8. Fig. 13 comprises the results of the first three experiments.

Experiment 2. The test person managed to control the car, controlling the velocity and the steering wheel. However, the accuracy of steering control was reduced, compared to Exp. 1, resulting in a larger standard deviation of the lateral error, which was 2.765 m. The standard deviation of the orientation was 0.410 rad and, thus, larger as well.

Experiment 3. The lateral error became even greater on the speedway. The speed was set to 5 meters per second and the test person tried to focus on heading in the right direction (keeping the orientation error small) rather than reducing the lateral distance. This is due to the fact that at higher speeds, the target point for orienting the car is displaced forwards. The standard deviation of the lateral error was 4.484, the standard deviation of the orientation error was 0.222 rad. The results are contained in 13.

Experiment 4. In this experiment we measured the time it takes to generate a pattern with the brain and to classify it. Results are shown in Fig. 14. Over 60 percent of the brain commands could be generated within 5 or less seconds, about 26 percent even within two seconds or less. In 20 percent of all cases the generated pattern was wrong. This was usually due to concentration problems of the test person. After a while, at latest after one hour a new training of the brain patterns is necessary. Further, after using the BCI for 90 minutes we experienced some tiredness of our test subject, which results in longer response times or higher inaccuracies.

Experiment 5. In this experiment for the BrainChooser the test person achieved correctly classified directions in more than 90 percent of cases.

6 Conclusion and Future Work

Brain-computer interfaces pose a great opportunity to interact with highly intelligent systems such as autonomous vehicles. While relying on the car as a smart assistance system, they allow a passenger to gain control of the very essential aspect of driving without the need to use arms or legs. Even while legal issues remain for public deployment, this could already enable a wide range of disabled people to command a vehicle in closed environments such as a parks, zoos, or inside buildings.

Free drive with the brain and BrainChooser give a glimpse of what is already possible with brain-computer interfaces for commanding autonomous cars. Modifying the route of a vehicle with a BCI is already an interesting option for applications that help disabled people to become more mobile. It has been proven that free driving with a BCI is possible, but the control is still too inaccurate for letting mind-controlled cars operate within open traffic. The semi-autonomous BrainChooser overcame this weakness, and decisions were performed with a high precision. Improvements of the BCI device could have multiple positive effects. One effect, of course, would be a more accurate control of the car, i.e., a more accurate steering and velocity control in free drive mode. Further, it is desirable to be able to distinguish more than four brain patterns in the future. This would enable the driver to give further commands, e.g., switching lights off and on, or setting the onboard navigation system to the desired location by thought alone.

More detailed experiments regarding this decline of concentration over time and within the context of car driving will be future work as well.

Acknowledgments. The authors wish to thank the German federal ministry of education and research (BMBF). Further, the authors would like to thank Henrik Matzke for his support as a test candidate in the experiments.

References

1. Bos, D.O., Reuderink, B.: Brainbasher: a bci game. In: Markopoulos, P., Hoonhout, J., Soute, I., Read, J. (eds.) Extended Abstracts of the International Conference on Fun and Games 2008, Eindhoven, Netherlands, pp. 36–39 (2008)
2. Decety, J.: Do executed and imagined movements share the same central structures? Cognitive Brain Research 3, 87–93 (1996)
3. Dickmanns, E.D., Behringer, R., Dickmanns, D., Hildebrandt, T., Maurer, M., Thomanek, F., Schiehlen, J.: The seeing passenger car 'vamors-p'. In: IVS 1994, pp. 68–73 (1994)
4. Laar, B.V.D., Bos, D.O., Reuderink, B., Heylen, D.: Actual and imagined movement in bci gaming. In: Adaptive and Emergent Behaviour and Complex Systems, AISB 2009 (2009)
5. Leeb, R., Lee, F., Keinrath, C., Scherer, R., Bischof, H., Pfurtscheller, G.: Brain-computer communication: Motivation, aim, and impact of exploring a virtual apartment. IEEE Transactions on Neur. Sys. and Rehab. Eng. 15, 473–482 (2007)
6. Nijholt, A., Tan, D., Allison, B., Milan, J., Graimann, a.B.: Braincomputer interfaces for hci and games. In: CHI 2008: Extended Abstracts on Human Factors in Computing Systems, pp. 3925–3928 (2008)
7. Pineda, J.A., Silverman, D.S., Vankov, A., Hestenes, J.: Learning to control brain rhythms: making a brain-computer interface possible. IEEE Transactions on Neural Systems and Rehabilitation Engineering 11(2), 181–184 (2003)
8. Thrun, S.: Official Google Blog: What we're driving at http://googleblog.blogspot.com/2010/10/what-were-driving-at.html (October 2010)

9. Thrun, S., Montemerlo, M., Dahlkamp, H., Stavens, D., Aron, A., Diebel, J., Fong, P., Gale, J., Halpenny, M., Hoffmann, G., Lau, K., Oakley, C., Palatucci, M., Pratt, V., Stang, P., Strohband, S., Dupont, C., Jendrossek, L.-E., Koelen, C., Markey, C., Rummel, C., van Niekerk, J., Jensen, E., Alessandrini, P., Bradski, G., Davies, B., Ettinger, S., Kaehler, A., Nefian, A., Mahoney, P.: Stanley: The robot that won the darpa grand challenge. Journal of Field Robotics 23(9), 661–692 (2006)
10. Urmson, C., Anhalt, J., Bagnell, D., Baker, C., Bittner, R., Dolan, J., Duggins, D., Ferguson, D., Galatali, T., Geyer, C., Gittleman, M., Harbaugh, S., Hebert, M., Howard, T., Kelly, A., Kohanbash, D., Likhachev, M., Miller, N., Peterson, K., Rajkumar, R., Rybski, P., Salesky, B., Scherer, S., Woo-Seo, Y., Simmons, R., Singh, S., Snider, J., Stentz, A., Whittaker, W., Ziglar, J., Bae, H., Litkouhi, B., Nickolaou, J., Sadekar, V., Zeng, S., Struble, J., Taylor, M., Darms, M.: Tartan racing: A multi-modal approach to the darpa urban challenge. Technical report, Tartan Racing (April 2007)

Perceptual Social Dimensions of Human - Humanoid Robot Interaction

Hiroshi Ishiguro[1,2], Shuichi Nishio[2], Antonio Chella[3], Rosario Sorbello[3], Giuseppe Balistreri[3], Marcello Giardina[3], and Carmelo Calí[4]

[1] Graduate School of Engineering Science, Osaka University, 1-3 Machikaneyama Toyonaka Osaka, Japan
[2] ATR Intelligent Robotics and Communication Laboratory, 2-2-2 Hikaridai seikacho sourakugun Kyoto, Japan
[3] DICGIM, RoboticsLab, Universitá di Palermo,V. delle Scienze, Palermo, Italy
rosario.sorbello@unipa.it
[4] Dipartimento FIERI-AGLAIA Universitá di Palermo, Palermo, Italy

Abstract. The present paper aims at a descriptive analysis of the main perceptual and social features of natural conditions of agent interaction, which can be specified by agent in human-humanoid robot interaction. A principled approach to human-robot interaction may be assumed to comply with the natural conditions of agents overt perceptual and social behaviour. To validate our research we used the minimalistic humanoid robot Telenoid. We have conducted human-robot interactions test with people with no prior interaction experience with robot. By administrating our questionnaire to subject after well defined experimental conditions, an analysis of significant variance correlation among dimensions in ordinary and goal guided contexts of interaction has been performed in order to prove that perception and believability are indicators of social interaction and increase the degree of interaction in human-humanoid interaction. The experimental results showed that Telenoid is seen from the users as an autonomous agent on its own rather than a teleoperated artificial agent and as a believable agent for its naturally acting in response to human agent actions.

1 Introduction

Since humanoid robots are going to be part of the lives of human beings, specific studies are oriented to investigating collaborative and social features related to human robot interaction. The present research aims at a descriptive analysis of the main perceptual and social features of natural conditions of agents interaction, which can be specified by agents in human-humanoid robot interaction. A principled approach to human-robot interaction may be assumed to comply with the natural conditions of agents overt perceptual and social behaviour. To conduct our research, in order to understanding areas of human cognition, which have not been tested or clarified until now, we used Telenoid (see.fig.1); a humanoid robot, designed to appear and behave like a minimalistic human.

S. Lee et al. (Eds.): Intelligent Autonomous Systems 12, AISC 194, pp. 409–421.
springerlink.com

Telenoid, as a minimalistic human, was created following processes to remove as many unnecessary features as possible choosing the necessary features for communication from humans and discarding the unrelated ones. The result is a robot endowed with some of perceptual and motor features of overt behaviour synchronized to speech, head and arms movement of a human agent through a Teleoperated system that allows us to study such perceptually accessible feateures as meaningful clues for social interaction. Our aim was : To understand how some features of perceptual behaviour work, such as distance and relative positions of agents, face regions spotted as highly informative about emotion or intention reading, the degree at which the space of the interaction appears to be a shared environment; To assess the degree of Believability of interaction along dimensions that can be reasonably taken as meaningful indicators of social interaction, both in free and task directed conditions. In order to prove our goals, we have conducted a human robots interactions test with people who did not have prior interaction experience with humanoid robots, though it was not excluded that they possessed informations or informal notions of IA and robotics. After every stage of interaction, each subject was asked to fill up a questionnaire whose questions were finalized to retrieve information about the salient perceptual and social dimensions of the interaction. Given the data analysis performed, we may claim only to have individuated two interaction dimensions, that is the Perceptual behaviour and Believability that can serve for either assess the perceptual and observable behaviour conditions of an humanoid agent, or to increase the natural-looking-like of interaction behaviour in human-humanoid interaction.

2 Telenoid

The Telenoid is a robot specifically designed for communication. It was designed to appear and behave like a minimalistic human. At first glance, is it possible to recognize the human features in the robot, but it can be interpreted as being either male or female, old or young. Due to this minimal design, the Telenoid allows people to feel as if a faraway acquaintance were close to them. The Telenoid has nine degrees of freedom. The provided DOF allow horizontal and vertical motion for the left and right eyes, opening and closing the mouth, yaw, pitch and roll rotations for the neck ,as well as motion for the right and left hand. The Telenoid length is approximately seventy centimeters, and its weight is around six kilograms. The skin is made of silicon, and the touch is similar to the human one. The Telenoid is a teleoperated robot. The operator's face directions, mouth movements and facial expressions are captured by a face recognition system. These face tracking results are used to create commands which are sent to a server via TCP/IP. The video stream for the face recognition system is obtained using a web camera attached to a laptop. Some spontaneous behaviors, such as 'bye-bye', 'happy' or 'hug' can be controlled by GUI buttons on the display. Some spontaneous behaviors, such as breathing, are generated automatically to create the sense that the robot is alive. The aim for the Telenoid was to create a minimalistic human's appearance, as such an appearance might allow any kind

Fig. 1. Telenoid robot

of person to transfer their own presence to distant locations. Telenoid, as a minimalistic human, was created following a strategy to remove as many unnecessary features as possible. Essential features that remained after this pruning process might be helpful to create efficient telecommunication media which can be used by all the types of people.

3 Related Work

The iCat, Poel et al.(2009)[1], is a user-interface robot able to exhibit a range of emotions through its facial features and it is generally controlled by predefined animations. ICub, Metta et al.(2008)[2], is a a child humanoid robot used in embodied cognition research. In contrast to these typical humanoid robots, Kanda et al.(2004)[3], Geminoid HI-1 is a humanoid robot with the external appearance of its ideator,Prof. Hiroshi Ishiguro and it is thought of being indistinguishable from real humans at first sight. Repliee R1 and Repliee Q2, Minato et al.(2004)[4] and Shimada et al.(2006)[5], are designed with the same aim of Geminoid, and the use of these kinds of robot points towards Android Science, Ishiguro(2007)[6].The uncanny sensation using android, as Shimada et al.(2006)[5] showed in their work, is reduced when their behaviors complexity is improved. A number of researches have investigated how human-robot interaction may be assumed to comply with the natural conditions of agents overt perceptual and social behavior. In this paper we use Telenoid as testbed for studying the social and perceptual abilities of robots copying with environment. In particular, much relevant literature appeared on the features of natural character of agents interaction.Since 1970, the research of Argyle at al.(1973)[7] and Argyle and Cook(1976),[8]was devoted to specify the different functions of gaze, and to highlight the proxemic indicators that contribute to the organization and to the dynamics of the interpersonal space that subserves social cognition and behavior (the so-called equilibrium theory of Argyle and Dean,1965[9]). Torres et al.(1997)[10] apply the empirical analysis of gaze behaviour in a dyadic-conversation paradigm to show a meaningful relationship between gaze and information retrieval of discourse content in the communicative humanoid agent proposed by Thorisson(1997)[11]. Vertegaal et al.(2001)[12] argue that evidence of gaze function in coordinative behaviour comes from research on gaze directional clues as reliable non-verbal predictors of conversations in multi-agent, multi-user environments. Mutlu et al.(2006)[13] study the extent at which gaze contact frequency between a storytelling robot and its human listeners is correlated with story understanding and recall. They argue that results highlight meaningful commonalities between human-human and human-robot communication. Jackson et al.(2004)[14] and Pietroni et al.(2008)[15] drew attention to other features of overt behavior that play an informative role in understanding other human agents purposive and intentional behavior.Furthermore neurophysiological research (Adolphs, 1999)[16] achieved consensus findings about the crucial link among the perception of emotional features, gaze of interacting agents, and the representation of emotional and social significance of salient stimuli by tracking the coordinated activation in specialized cortical and subcortical systems (Adolphs 2002[17]; Phan et al., 2001[18]; Phillips et al.,2003[19]).Therefore we reasoned that the emerging picture of natural interaction condition requires a general description of the environment, where cognitive and social interaction of agents with their surroundings obtains, which can be carved up at the level at which environment look somehow like to agents. Indeed since Koffka(2001)[20], Khler (1947)[21], Heider(1982)[22], and Lewin(1936)[23], cognition and behavior is proposed to be analyzed at the scale of what agents themselves take as meaningful units. Accordingly their environment can be decomposed in what they see as directly or indirectly accessible objects sense properties, affordances, scaffolds and proxies of other agents intentions and behaviors. Analytical treatment of the behavioral environment as it looks like from an agents standpoint allows to recover its qualitative structure that support cognition, agency and interaction with other agents. As Chrisley(2009) [24] pointed out, there is no hindrance to the definition of a synthetic phenomenology devoted to the research of perceptual qualities that carry out cognitive functions of an artifact such as a robot. Agents behaviour is to be explained as organized and regulated by the cognitive frames of reference that build up their environment.

4 Goal of the Experiments

From this theoretical framework and the relevant literature, we derived some features of overt behaviour that qualify as parameters for efficacious interaction given that they can work as perceptual and cognitive shared blocks of the environment where agents interact. We profited from Telenoid, a humanoid robot endowed with some of perceptual and motor features of overt behaviour tuned to speech and head movement of a human agent through a teleoperating system, to study such perceptually accessible features as meaningful clues for social interaction. A model of interaction was then set (1) to understand how some perceptual features work, such as distance and relative positions of agents, face regions spotted as highly informative about emotion or intention reading, the degree at which the space of the interaction appears to be a shared environment;(2)

to recover which perceptual features of overt behaviour among head movements, gaze and eye contact search, presence or absence of lips movement are held as salient by human agents to ascribe a meaningful conduct to the robot;(3) to assess the degree of believability of such an interaction along dimensions that can be reasonably taken as meaningful indicators of social interaction, both in free and task directed conditions. Hence, the interaction setting and the research methodology were modeled as followed.

5 Demonstration at Dinfo Department

5.1 Participants

Industrial Design Course students of the Faculty of Architecture (University of Palermo) were recruited who did not have prior interaction experience with humanoid robots, though it was not excluded that they possessed informations or informal notions of AI and robotics. There was no selection process. They were only informed of the possibility of taking part in a humanoids robot interaction experiment, and those who freely declared to have an interest whatsoever in joining it were selected. All participants (34 total, 12 male and 21 female with average age 20.27) were introduced to the Telenoid, to the interaction setting structure that required a two stage interaction with the robot and to fill up a questionnaire. Each participant was asked to choose a partner for the interaction and then to decide who will be interacting with the robot and who will be teleoperating it. A small number of couples of participants was allowed to switch their role in the two stages of interaction. Each couple was introduced to the setting and the control box by one of the researcher who was appointed also to tell the participants when each interaction stage was deemed to be over. All interactions were videotaped.

5.2 Design

A two stage interaction with Telenoid was prepared. A first free interaction stage, meant to allow subjects to adapt either to interact with the humanoid robot or to acquire as early as possible the skills for operating the robot through the control box. The subject that chose to teleoperate the robot entered a separate room where the control box was located in order to make him not visible to the other subject that interacted directly with to robot. A second interaction stage was instead task driven. Participants were allowed to choose an interactions scenario among a proposed range that spanned booking a hotel reservation, making a phone call to a mobile company to get a contract or services information, to matriculate or to enter his/her name or one of his/her fellows ones for a course examination by talking directly with the robot. Those who were to tele- operate the robot were asked to use all the knowledge acquired in one of these standardized contexts of interaction to act as formally as possible. This second stage was stopped as soon as the goal was attained. Before the first stage of interaction, each subject was asked to fill up a first part of the questionnaire whose questions range over general information about his/her own interest and hobbies, his/her interest in such fields as technology and robotics, his familiarity or knowledge of such fields, and the implicit degree of acceptability of robotic artifacts. After the first stage of interaction, each subject was given a free test that was assumed to serve as a distractor in order to avoid that expectations arisen after the adaptation interaction could distort the direct experience in the task driven second stage. The free test consisted of a random presentation of humanoid and not-humanoid robots pictures to whom each subject was asked to systematically couple an emotion name from a fixed set provided in a paper list. After the second task guided stage of the interaction, subjects were requested to fill up the second part of the questionnaire whose questions were about those very constructs built to recover information about the salient perceptual and social dimensions of the interaction. A few days later the interaction setting, a third part of the questionnaire was administered only to subjects who tele-operated the robot.

5.3 Methodology: Constructs and Item Analysis

The questionnaire was meant to cover two main constructs that according to our theoretical assumptions could recover some perceptual and social aspects of natural conditions of agents interaction, which were also hypothesized to rule the human-humanoid robot interaction. We reasoned that those aspects mirrored some salient ordinary cognitive abilities, which agents could specify in such cases to improve the efficacy of interaction. The first construct is intended to cover perceptual features of overt interactive behaviour. It is represented by items that add up to three different but convergent aspects: (1) the apparent distance of agents, and their sense of being sharing a common environment; (2) the perceptual attention to those parts of the robotic device that are perceived as more likely displaying meanings and intentions; (3) the reliability of robots observable behaviour given the degree of consistency among head and arms movements, gaze, utterance synchronization. Groups of items (1) and (2) are provided also with questions about the need to change some perceptual parameter in order to improve the interaction. Questions about the perception of distance were designed in order to cover in an ordinary and informal way findings about the multiple functions that space regions have when endowed with perceptual and motor interpretation to carry out or to detect meaningful action (neurobiological evidence about the motor-cognition integration systems that decompose interaction space in multiple phenomenal maps is summed in Gallese 2005[25]). For theoretical reasons, the perceptual awareness of sharing a common environment with the robot is assumed to be of momentous importance for the interacting subjects to ascribe intentions and actions to the robot itself and not to it only as an apparent proxy of the teleoperating subject. This aspect of interaction can prove to be the perceptual link with the second construct: believability. The concept is defined in Dautenhahn (1998)[26], and Poel et al. (2009)[1] operationalise it designing a construct whose aspects are represented by items grouped according to the indicators of personality, emotion, responsiveness, and self motivation. We chose to construe believability along the following dimensions: (4) valence, whose items cover the apparent robot capability to act due to internal or external (other agents, environment) causes; (5) motivation, whose items cover the apparent robot capability to display interest in other agents requests and goals; (6) value, whose items cover the coordination of robots behaviour with human agents; (7) communication, whose items cover the coupling between the robot overt behaviour and the intentions ascribed to it. These questionnaire parts were administered after the second task driven stage of interaction. Hence they are meant to represent the perceptual and social dimensions of the more complex interaction since the impressions that struck subjects eventually in the first free interaction had only an adapting subserving function for an efficacious interaction to obtain. These two parts were given together with a third part of the questionnaire was about the assessment of the overall interaction with the robot. The third questionnaire, which was administered a few days later only to those subjects who tele-operated the robot, was made up of questions that spanned the assessment of the technical design of the control box, its usability as regards the transmission of subjects own head movement, and of the delay between subjects utterances with respect to their perception by users interacting with the robots. Some eventual suggestions to improve usability were also included in order to make subjects operating intentions clear to those who interacted directly with the robot. Furthermore the technical features of the device were often traded off with perceptual and cognitive constraints that were presumed to constrain subjects task to drive the robot in such a way to interact effectively with other subjects and at the same time to have it appear as autonomous as possible.

5.4 Questions Structure

We describe now four questions that may serve as examples of structures we gave to items and of how they were expected to cover the different aspects of the dimensions we hypothesized. 1) At which distance do you think that the perception of Telenoid allows you to get a successful interaction? The answers were presented in a forced choice list as follows: a. near to the face; b. near to legs and knees; c. in the standard position(which was fixed for all subjects at 40 cm); d. it is indifferent; e. I dont know. This question was meant to reflect the hypothesis that space perception is codified in regions of interest and possible actions, that is in motor terms relative to different action range capabilities of ones own body parts. As Gallese (2005)[25] pointed out, space perception is decomposed in multiple regions that maps to visual, tactile and motor neuronal receptive fields, and the specialization of these regions subserves agents perceptual social understanding, that is the ability to directly sense other agents sensations, intentions, and actions. Hence, perceptual distances are to be taken as markers of multiple frames of reference that maps agents phenomenal space to object qualities and other agent intentions and actions. It is worth noticing that the following question required subjects to state whether they needed to actively modify the distance from the robot. 2) Does the coupling of robots utterances

Table 1. Pearson Coefficient for the 2 sections of the questionnary

	Believability section	Perceptual behavior section
Pearson Coefficient	0.94	0.98

with its head movements allow to understand its behaviour and effectually interact with it? Answers were to be given as ratings on a five points Likert scale. That question is designed to group with items that cover the integration among observable modules of robot behaviour. Since we assumed that meaningful descriptive units of behaviour must be picked up at the meso-scale level of what it is looking like to agents, we treated the perceptual features of interaction as sensory qualities that appear to have a meaning in themselves only when appropriately fit to one another rather than appearing as mere proxies of intentions or meanings to be retrieved beyond them (e.g. the robots supposed delivered mind by tele-operating). Similar questions were about eye positions, lips, gaze and their relationships with meaningful parts of the speech. 3) The following question is a further example of how we tried to cover the perceptual basis of the direct character of interaction with a robot that should appear endowed with a natural-like presence: At what extent do the following statements describe your perception of Telenoids behaviour during the interaction? Subjects were asked to rate their agreement on the suitability of the following statements on a Likert five points scale: - Telenoid looks like feeling the emotions it displays to have; - Telenoid looks like simulating the emotions it displays to have; - Telenoid looks like mimicking the emotions it displays to have; - Telenoid looks like playing the emotions it displays to have; - Telenoid looks like replicate the emotions it displays to have; - Telenoid looks like a screen on which some emotions are displayed. 4) As social features are concerned, items tried to represent them as directly observable as well such as in the following question with ratings on a five point Likert scale: - Telenoid acts depend on what he appear to like/dislike; - Telenoid acts depend on you appear to behave; - Telenoid acts depend on his appraisal of surrounding environment; - Telenoid acts depend on its taking care of my needs and requests. Please notice that how an agents tacit preferences, appraisals and judgments are highlighted along with the attention paid to an implicit sense of sharing a common environment where the interaction takes place.

6 The Experimental Results Evaluation

Items were formulated in the form of a single forced or multiple closed choice set, and as statements for which subjects were to rate agreement on a five-point Likert scale. We assumed that the perceptual and social dimensions can be reasonable represented as continua on a multiple items attitude scale. Standard item analysis has been performed on the codified data. Split-half Spearmann-Brown coefficient, Pearson Coefficient,and Cronbach alpha[27],showed in table1, were calculeted to test the reliability of the scales and the correlation among the multiple items of each single construct. We found significantly high values of reliability as regards the items correlation and the internal consistency of the scales measuring the perceptual and social dimensions.But given the substantive assumption the led to the design of our questionnaire and the high number of items per scale, high reliability value may depend on their number and their particular choice which fit the theoretical structure we wanted the interaction model to have.

Subjects responses are likely to converge upon the possibility of seeing in Telenoid an agent on its own only if some perceptual and social features of interaction are realized in the interaction setting. Subjects rate consistently as highly informative as possible gaze, head movement, utterances synchronization with motor behaviour, and are inclined to search for apparent qualities that perceptually contain the humanoid agent intentions profiting from their coordination and locating it in the appropriate space region for optimal interaction. It is worth noticing that all these observable aspects of interaction seem to comply with general conditions of social behaviour, and that it can be the reason why they fit well to the minimalist design of Telenoid that is reduced to essential traits. The high rating values of correlation among perceptual conditions of interaction seems to mirror an increase in the likelihood to see Telenoid as an autonomous agent on its own rather than perceiving him as a teleoperated artificial agent or as a screen for subjects feelings or thought to be simply conjured up on it. And that may justifies the sense of sharing a common environment wherein human and humanoid agents interact in that it is appropriate to modify ones own relative distances according to capabilities of motor behaviour in personal and peripersonal spaces, in order to have such essential features as the upper part of the face or the eyes appear in the right perceptual focus. The correlation with the perceived coordination of such observable features as head movement and gaze with speech parsing in meaningful units seems to indicate that perceptual features qualify the basis for understanding in a shared environment, which is not only physically defined but above all cognitively loaded. Responses to items covering the social dimension of interaction may confirm that:

Subjects inclined to see Telenoid as a believable agent mainly due to the way it appears to act in response to human agent actions, speech and request, the way it displays its motivations and care in essential observable features of its behaviour, the way it looks like to comply with emotions standardly supporting cooperative behaviour. Accordingly, believability degree seems to increase thanks to degree of internal consistency of the perception of behaviour, with the ability to display its purposive character in goal driven contexts. Further research is needed to assess whether this consistency is coherent as well, that is able to preserve itself across different contexts and changes happening to occur in the common surroundings.

Table 2. Contingency Table of the Questions:"At which distance do you think that the perception of Telenoid allows you to get a successful interaction?" and "What is it the description of the best situation in order to have a perfect interaction with the telenoid after you take him in your arms?"

	A1[a]	A2[b]	A3[c]	A4[d]	A5[e]
Near to the face	5	2	2	2	1
Near to legs and knees	2	0	2	0	0
At arm length	2	0	1	1	1
In the standard position	0	0	1	0	0
It is indifferent	0	0	0	0	1
I don't know	0	0	0	0	1

[a] I preferred to get closer to Telenoid with respect to initial position
[b] I preferred to push away the Telenoid with respect to its closer initial
[c] I chose the distance of the Telenoid according to moment of dialogue
[d] No preference about distance with the Telenoid
[e] I don't know

6.1 Contigency Tables

The tables 2, 3 and 4 show the contingency tables calculated for some of the questions of the questionnaire. Our goal is to search if there are correlation between the items of this questions that seem to be similar. In the first table there is a correlation between the answers (represented as rows) of the users for the Q1 question: At which distance do you think that the perception of Telenoid allows you to get a successful interaction? with the answers (represented as columns) of the users for the Q2 question: What is it the description of the best situation in order to have a perfect interaction with the telenoid robot after you take him in your arms ?. Every cell of the table2 is representative of the bivariate frequency distributions of the items. And it is used to record and analyze the relation between two questions. In particular it is possible to emphasize that 12 users answering Near to the face for the Q1 question they didnt give the same answer also for the Q2 question. Five users answered I preferred to get closer to Telenoid with respect to initial position, 2 answered I preferred to push away the Telenoid with respect to its closer initial , 2 answered I choose the distance of the Telenoid according to the moment and the topic of the current conversation, 2 answered No preference about distance with the Telenoid and only 1 didnt give any answer. The same key to the reading is possible to be applied for the comprehension of the value inside the other cells of the table.

Table 3. Contingency Table of the Questions:"What is it the description of the best situation in order to have a perfect interaction with the telenoid robot after you take him in your arms?" and the answers at Question: "At the start of the interaction on which part of the face deliberately have you turned your gaze to understand how to behave?"

	In the upper half of the face	In the lower half of the face	I don't know
A1 [a]	7	1	1
A2 [b]	2	0	0
A3 [c]	4	1	1
A4 [d]	1	1	1
A6 [e]	1	1	1

[a] I preferred to get closer to Telenoid with respect to initial position
[b] I preferred to push away the Telenoid with respect to its closer initial
[c] I chose the distance of the Telenoid according to moment of dialogue
[d] No preference about the distance with the Telenoid
[e] It is indifferent

Table 4. Contingency Table of the answers at the Questions:"At which distance do you think that the perception of Telenoid allows you to get a successful interaction?" and "At the start of the interaction on which part of the face deliberately have you turned your gaze to understand how to behave?"

	In the upper half of the face	In the lower half of the face	I don't know
Near to the face	8	2	2
Near to legs and knees	3	1	0
At arm length	3	1	1
In standard position	1	0	0
It is indifferent	0	0	1
I don't know	1	0	9

7 Conclusion and Future Works

The present research aims at a descriptive analysis of the main perceptual and social features of natural conditions of agent interaction, which can be specified by agent in human-humanoid robot interaction. We maintain that such a descriptive research can highlight dimensions that contribute to meaningful and natural-like interaction with humanoid robots. The main upshot of our research is the definition of two dimensions that can be taken to underlie human experience with interacting artifacts in ordinary and goal driven contexts. Those dimensions are specified as perceptual and social features according to theoretical assumptions on the level at which descriptive units of behaviour must be detected. We construed them as multiple items that can be taken as reliable indicators to retrieve some of those perceptual and social behaviour skills agents realize when faced with interaction contexts. As regards the current literature, we focus mainly to perceptual features of agents and multiple spaces for interaction behaviour, which can be perceptually specified in motor and action terms to an effectual interaction to obtain. As social dimension is concerned, we construed believability as more linked to some features of observable behaviour, which can prove momentous for agents disposition to social coordination, than as they are in the current literature, at least at the light of our current knowledge. Given the data analysis performed, we may claim only to have individuated two interaction dimensions that can serve for either assess the perceptual and observable behaviour conditions an humanoid agent is justifiably taken to comply with, or to increase the natural-looking-like of interaction behaviour in human-humanoid interaction.Further analysis and research are required in order to specify their single meaning, that is to quantify over the degree at which they represent a specification of unified conditions to which agents implicitly comply to find the extent at which these dimensions mutually reinforce each other and give a joint contribute for a successful and effectual interaction to obtain. By administrating our questionnaire to subject after well defined experimental conditions, an analysis of significant variance correlation among dimensions in ordinary and goal guided contexts of interaction may be performed. Furthermore, by coupling interaction setting conditions with brain imaging techniques, or ERP registration our descriptive analysis is likely to upgrade to a promising explanatory level.

References

1. Poel, M., Heylen, D., Nijholt, A., Meulemans, M., Van Breemen, A.: Gaze behaviour, believability, likability and the icat. AI Society 24(1), 61–73 (2009)
2. Metta, G., Natale, L., Nori, F., Sandini, G., Vernon, D., Fadiga, L., Von Hofsten, C., Rosander, K., Lopes, M., Santos-Victor, J., et al.: The icub humanoid robot: An open-systems platform for research in cognitive development. Neural Networks 23(8-9) (2010)
3. Kanda, T., Hirano, T., Eaton, D., Ishiguro, H.: Interactive robots as social partners and peer tutors for children: A field trial. Human-Computer Interaction 19(1), 61–84 (2004)
4. Minato, T., Shimada, M., Ishiguro, H., Itakura, S.: Development of an android robot for studying human-robot interaction. Innovations in Applied Artificial Intelligence, 424–434 (2004)
5. Shimada, M., Minato, T., Itakura, S., Ishiguro, H.: Evaluation of android using unconscious recognition. In: 6th IEEE-RAS International Conference on Humanoid Robots 2006, pp. 157–162. IEEE (2006)
6. Ishiguro, H.: Android science toward a new cross-interdisciplinary framework. Robotics Research 28, 118–127 (2007)
7. Argyle, M., Ingham, R., Alkema, F., McCallin, M.: The different functions of gaze. Semiotica 7(1), 19–32 (1973)
8. Argyle, M., Cook, M.: Gaze and mutual gaze (1976)
9. Argyle, M., Dean, J.: Eye-contact, distance and affiliation. Sociometry, 289–304 (1965)

10. Torres, O., Cassell, J., Prevost, S.: Modeling gaze behavior as a function of discourse structure. In: First International Workshop on Human-Computer Conversation, Citeseer (1997)
11. Thrisson, K.: Gandalf: an embodied humanoid capable of real-time multimodal dialogue with people. In: First ACM International Conference on Autonomous Agents, pp. 5–8 (1997)
12. Vertegaal, R., Slagter, R., van der Veer, G., Nijholt, A.: Eye gaze patterns in conversations: there is more to conversational agents than meets the eyes. In: Proceedings of the SIGCHI Conference on Human Factors in Computing Systems, pp. 301–308. ACM (2001)
13. Mutlu, B., Forlizzi, J., Hodgins, J.: A storytelling robot: Modeling and evaluation of human-like gaze behavior. In: 6th IEEE-RAS International Conference on Humanoid Robots 2006, pp. 518–523. IEEE (2006)
14. Jackson, P., Decety, J.: Motor cognition: a new paradigm to study self-other interactions. Current Opinion in Neurobiology (2004)
15. Pietroni, D., Van Kleef, G., De Dreu, C., Pagliaro, S.: Emotions as strategic information: Effects of other's emotional expressions on fixed-pie perception, demands, and integrative behavior in negotiation. Journal of Experimental Social Psychology (2008)
16. Anderson, S., Bechara, A., Damasio, H., Tranel, D., Damasio, A.; Adolphs, R.: Social cognition and the human brain. Trends in Cognitive Science 3, 469–479 (1999); Allen, C.: Behavioral and Brain Sciences (2004) (1991)
17. Adolphs, R.: Neural systems for recognizing emotion. Current Opinion in Neurobiology 12(2), 169–177 (2002)
18. Phan, K., Wager, T., Taylor, S., Liberzon, I.: Functionalneuroanatomy of emotion: a meta-analysis of emotion activation studies in pet and fmri. Neuroimage 16(2), 331–348 (2002)
19. Phillips, M., Drevets, W., Rauch, S., Lane, R.: Neurobiology of emotion perception: The neural basis of normal emotion perception. Biological Psychiatry 54(5), 504–514 (2003)
20. Koffka, K.: Principles of Gestalt psychology, New York (1955)
21. Kohler, W.: Gestalt psychology: An introduction to new concepts in modern psychology. Liveright Publishing Corporation (1992)
22. Heider, F.: The psychology of interpersonal relations. Lawrence Erlbaum (1982)
23. Lewin, K., Heider, F., Heider, G.: Principles of topological psychology (1936)
24. Chrisley, R.: Synthetic phenomenology. International Journal of Machine Consciousness 1(1), 53–70 (2009)
25. Gallese, V.: Embodied simulation: From neurons to phenomenal experience. Phenomenology and the Cognitive Sciences (2005)
26. Dautenhahn, K.: The art of designing socially intelligent agents: Science, fiction, and the human in the loop. Applied Artificial Intelligence 12, 7(8), 573–617 (1998)
27. Cronbach, L.: Coefficient alpha and the internal structure of tests. Psychometrika 16(3), 297–334 (1951)

Complex Emotional Regulation Process in Active Field State Space

Xin Liu[1] and Lun Xie[2]

[1] University of Science and Technology Beijing,
School of Automation and Electrical Engineering
liuxin87@yeah.net
[2] University of Science and Technology Beijing,
School of Computer and Communication Engineering
xielun@ustb.edu.cn

Abstract. Based on the emotional model described by 3-dimensional state space, a complex emotional regulation model is proposed and applied to real-time dynamic emotional regulation process. Emotional stimulus (single basic emotional state stimulus or complex emotional state stimulus) is converted into a field source in the space by the vector calculation. So the potential scalar function of each point can be calculated and normalized to a transferring probability matrix of basic emotional states. Finally, the complex emotional state is produced by hidden Markov stimulus transferring model and an auxiliary matrix. The result shows that a complex emotional regulation model in active field gets rid of the simple emotional control mode and generates a kind of complex emotion. It is more in line with the demand of emotional regulation in a complex interactive environment.

1 Introduction

The purpose of emotional model is to understand the objects emotional state via cognition and produces emotional state according to the changing external stimulus [1,2,3]. In the human-robot interactive process, the most important party is the analysis and regulation of human emotion, namely, cognitive-affective computing [4,5]. As the complexity and multiple correlation of human emotion, cognitive-affective computing is gradually developing with the deepening research.

Izzard, American well-known emotion psychologist, divides emotion into two categories: basic emotion and complex emotion. Basic emotion, which is congenital and preformed, has an unaided explicit expression, an internal experience, a physiology neural mechanism and a different adaptation function. It consists of 8-11 species of emotional states, including interest, surprise, pain, disgust, happiness, anger, fear, sadness, shyness, contempt, guilt. Complex emotion is divided into the following three categories (Table I shows some representative complex emotions): (1) 2-3 basic emotions mix to produce a complex emotion; (2) basic emotions and an inner impulse mix to produce a complex emotion; (3) basic emotions and an affective-cognitive structure mix to produce complex emotion [6].

In this paper, according to the spatial and temporal characteristics of the state space and the relations of field sources, an active field emotional regulation process model,

S. Lee et al. (Eds.): Intelligent Autonomous Systems 12, AISC 194, pp. 423–432.
springerlink.com

Table 1. Complex Emotion

Basic emotions mix	Emotion-impulse mix	Emotion-cognitive structure mix
Interest-happiness	Interest-sex drive	Pain-self abasement
Pain-anger	Fear-ache	Pain-distrust
Fear-shyness	Disgust-weariness	Quiet-shyness
Contempt-disgust-anger	Interest-sex drive-pleasure	Fear-guilt-distrust
Fear-guilt-pain-anger	Fear-anger-ache	Interest-anger-energy

which is combined the basic emotional state with the complex emotion state, is build on the basis of Izzard emotion classification. Here we see each basic emotional state as a field source; calculate the activation degree of it according to the species and intensity of stimulus; present the activation degree in the form of field intensity; normalize the activation degree as the state transferring probability matrix. The matrix assists the emotional transferring calculation in hidden Markov stimulus transferring model, and then complex emotional regulation process is implemented under the emotional stimulus.

2 Description of Emotional State Space in Active Field

As a classic emotional algorithm in human-robot interaction, the emotional model of MITs facial expression robot, Kismet, has three emotion characteristics (arousal, valence and stance) and they are mapped to the 3-dimensional emotional space [7]. Basic emotions include the following 14 species: accepting, content, alert, fear, sorrow, tired, unhappy, calm, soothed, anger, surprise, disgust, joy, stern.

Active field state space takes the impact of emotional change in the external environment. First, a robots input stimulus space$W = \{w_1, w_2, \cdots, w_n\}$is defined. n is the number of the afferent stimulus including the basic emotion stimulus and the complex emotion stimulus. The afferent state of interactive object changes in this space. We assume the robots own basic emotional state space is$S = \{s_1, s_2, \cdots, s_{14}\}$. S is the set of robots basic emotional states. Complex emotions in this paper is only involved with basic emotions mix, namely, 2-3 species of basic emotions mix to produce complex emotion. Robots emotional state transfers in the basic emotional set and the complex emotional set, and its initial state transferring probability is uniquely determined by the scalar potential function in the active field. Based on the above description, the robot dynamic emotional regulation process diagram is drawn, shown in Fig. 1.

3 Implementation of Complex Emotional Regulation Process

3.1 Attenuation Function and Threshold Function

Psychology emotion is instantaneous. The curve of emotion response is more similar to exponential image with time, so the exponential function is used as the attenuation factor of the emotional state [8]. The attenuation function of emotional state is shown in Fig. 2. Assumed that the emotional intensity begins to attenuate at t_0 and there is no new stimulus until t , the emotional attenuation function is:

$$E_t = \phi(E_0) = E_0 e^{-\beta(t-t_0)} \tag{1}$$

E_0 is the emotional intensity at t_0; E_t is the emotional intensity at t; β is emotional attenuation rate which controls the speed of emotional decline; $t - t_0$ is the time during the emotional attenuation.

For each basic emotional state, μ is defined as emotional activation threshold and ν is defined as emotional saturation threshold. If the intensity of stimulus is lower than μ, it has no effect on the robots behavior. If the intensity of stimulus is higher than μ, this emotional state is activated. When the emotional intensity reaches the saturation threshold ν, the emotional intensity reaches the maximum. ν ensures that the emotional intensity cant overflow the boundary.

Depending on the personality, the threshold function of emotional activation is introduced [9]. The image is shown in Fig. 3.

$$\mu(x) = \begin{cases} 0 & a < a_0 \\ \frac{1}{2} + \frac{1}{2} \cdot \sin\left[\pi\left(\frac{x-a_0}{a_1-a_0} - \frac{1}{2}\right)\right] & a_0 < a < a_1 \\ 0.5 & a > a_1 \end{cases} \tag{2}$$

3.2 Transferring Probability of Active Field Emotional State

According to the concept of the active field in physics, a specific stimulus is defined as a field source in the emotional state space, and the strength of stimulus determines the

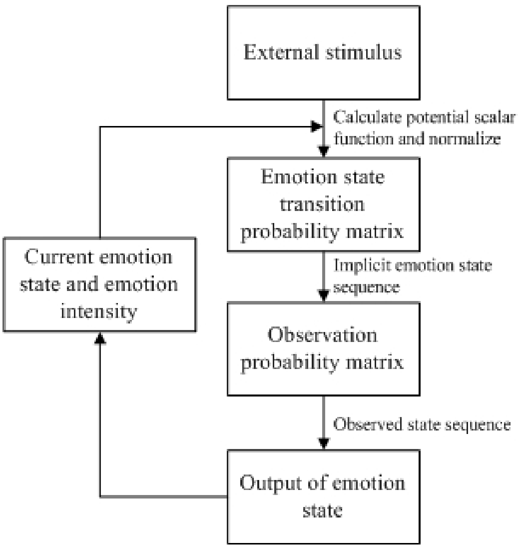

Fig. 1. The robot dynamic emotional regulation process diagram

intensity of active field. In the emotional state space, the potential of the basic emotional state is proportional to the intensity of the active field, and is inversely proportional to the distance. When the stimulus is a complex emotion, the source is more than one active field. On the basis of the stimulus type, model can be divided into the following two situations:

3.2.1 Stimulus is a Single Basic Emotional State

When the only active field E exists in the emotional space, the potential at any point $M(x,y,z)$ is:

$$U(M) = \mu \cdot E_t \cdot |\vec{E} - \vec{M}| \tag{3}$$

$\vec{E}$ is the vector from the origin of coordinate to the field source E; $\vec{M}$ is the vector form the origin of coordinate to point M; E_t is the emotional attenuation function; μ is an impact factor.

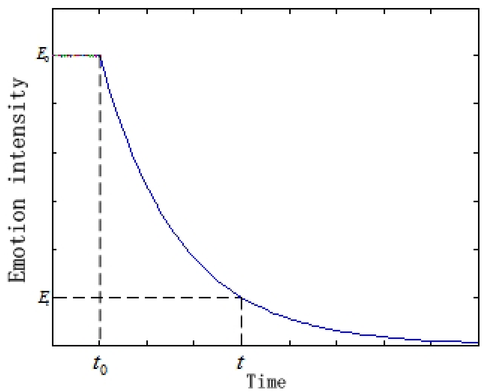

Fig. 2. The image of emotional attenuation function

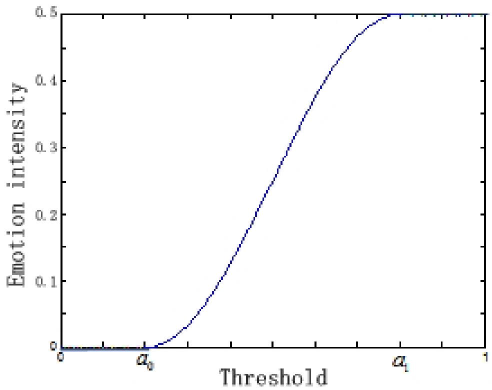

Fig. 3. The image of emotional activative threshold function

According to the intensity of the field, the potential surface can be calculated, shown in Fig. 4.

3.2.2 Stimulus is a Complex Emotional State

When there are several field sources in the emotional space, namely the stimulus is a complex emotional state, the potential at any point in the space is determined by the sum of the each source potential.

When the active fields $E_i(i = 1, 2, \cdots, 14)$ exist in the emotional space, the potential at any point $M(x, y, z)$ is:

$$U(M) = \sum_{i=1}^{N_E} \mu_i \cdot E_{it} \cdot (\vec{E} - \vec{M}) \tag{4}$$

Multiple active fields can be transformed into a single one by vector calculation, and then we could get the potential surface, shown in Fig. 5. Here each field source expresses a basic emotional state. The sum of multiple active fields indicates that the stimulus is complex emotion. This will be able to enrich the species of stimulus, and more close to the real interactive environment.

Based on the stimulus, the potential scalar function of each basic emotion can be calculated, and it can form the initial probability matrix of emotional state via the normalization.

Random variable X represents the set of emotional states. $p_{ij}(k)$ is the step transferring probability from the state $X(k) = s_i$ at time k to the state $X(k+1) = s_j$ at time $k+1$ and $\sum_{j=1}^{N} p_{ij}(k) = 1$, $0 \le p_{ij}(k) \le 1 (i, j = 1, 2, \cdots, N)$, N is the number of emotion states. The proof is as follows:

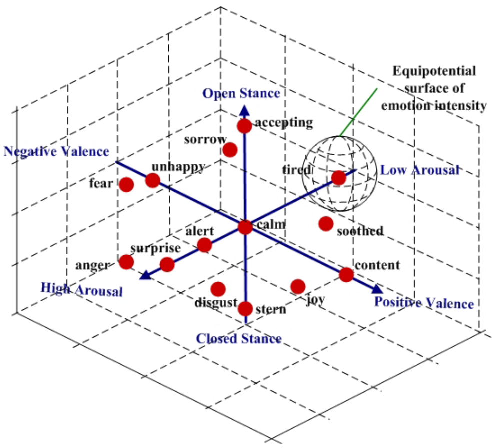

Fig. 4. The potential surface of a single stimulus in the emotional space

$$\begin{aligned}
&\sum_{j=1}^{N} p_{ij}(k) = \sum_{j=1}^{N} P\{X(k+1)=s_j|X(k)=s_i\} \\
&= \tfrac{1}{P\{X(k)=s_i\}} \sum_{j=1}^{N} P\{X(k+1)=s_j, X(k)=s_i\} \\
&= \tfrac{1}{P\{X(k)=s_i\}} P\left\{ \bigcup_{s_j \in X} (\{X(k+1)=s_j, X(k)=s_i\}) \right\} \\
&= \tfrac{1}{P\{X(k)=s_i\}} P\left\{ (\bigcup_{s_j \in X} \{X(k+1)=s_j\}) \cap \{X(k)=s_i\} \right\} \\
&= \tfrac{1}{P\{X(k)=s_i\}} P(ineviable\ event \cap \{X(k)=s_i\}) \\
&= \tfrac{P\{X(k)=s_i\}}{P\{X(k)=s_i\}} = 1
\end{aligned} \tag{5}$$

The step transferring probability from state $X(k) = s_i$ to state S_j is: $p_{ij}^{(1)}(k) = P\{X(k+1) = s_j|X(k) = s_i\} = p_{ij}(m)$.

Similarly, the n-step transferring probability from state $X(k) = s_i$ at time k to state S_j is: $p_{ij}^{(n)}(k) = P\{X(k+n) = s_j|X(k) = s_i\}$, and $\sum_{j=1}^{N} p_{ij}^{(n)}(k) = 1$, $0 \leq p_{ij}^{(n)}(k) \leq 1 (i, j = 1, 2, \cdots, N)$, N is the number of emotional states.

As time goes by, emotional state continuously tends to stability in the case of no other stimulus. Namely, the transferring probability $p_{ij}^{(n)}$ has a limitation $\lim_{n\to\infty} p_{ij}^{(n)} = \pi_j$ $i, j = 1, 2, \cdots N$, when $n \to \infty$.

3.3 Transferring Process of Emotional Stimulus in HMM

Hidden Markov emotional state stimulus transferring process can be described by $\lambda = (N, M, A, B, \Pi)$ in the probability space. N is the number of emotional states, M is the total number of stimulus species, Π is the distribution of initial emotional state probability, A is the state transferring probability matrix, and B is the stimulus matrix [10,11].

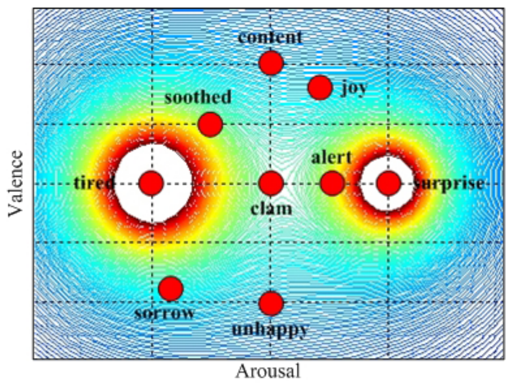

Fig. 5. The potential surface of a complex external stimulus in the emotional space

$$B_{M\times N} = \begin{bmatrix} B_1 \\ B_2 \\ \vdots \\ B_M \end{bmatrix} = \begin{bmatrix} b_1(1) & b_2(1) & \cdots & b_N(1) \\ b_1(2) & b_2(2) & \cdots & b_N(2) \\ \vdots & \vdots & \cdots & \vdots \\ b_1(M) & b_2(M) & \cdots & b_N(M) \end{bmatrix} \tag{6}$$

When the stimulus is a basic emotion, $M = N$. When the stimulus is a complex emotion, which is consist of basic emotions i, j, k , auxiliary matrix $F_{N\times N}$ is introduced.

$$F_{N\times N} = \begin{bmatrix} F_{1\bullet} \\ F_{2\bullet} \\ \vdots \\ F_{N\bullet} \end{bmatrix} = \begin{bmatrix} f_1(1) & f_2(1) & \cdots & f_N(1) \\ f_1(2) & f_2(2) & \cdots & f_N(2) \\ \vdots & \vdots & \cdots & \vdots \\ f_1(N) & f_2(N) & \cdots & f_N(N) \end{bmatrix} \tag{7}$$

Row vector $F_{j\bullet}(1 \le j \le N)$ corresponds to the stimulus of the basic emotion j. The species of the stimulus can be determined by the row vector, and the constraint condition is:

$$\sum_{j=1}^{N} f_i(j) = 1, (1 \le i \le N) \tag{8}$$

Assuming $f_i(j) = \begin{cases} \varsigma, \ if \ i = j \\ \sigma, \ if \ i \ne j \end{cases}$, and $\varsigma \ge \sigma$, $\tau = \frac{\varsigma}{\sigma}$, $\tau > 1$,we can put them into (7) and get $\begin{cases} \varsigma = \tau/(N-1+\tau) \\ \sigma = 1/(N-1+\tau) \end{cases}$, $\tau > 1$, thereby the auxiliary matrix F is obtained.

$$\begin{aligned} B_{M\times N} &= [B_{1\bullet}\ B_{2\bullet} \cdots B_{i\bullet} \cdots B_{N\bullet}]^T_{(N-2)\times N} \\ &= \begin{bmatrix} F_{1\bullet}\ F_{2\bullet} \cdots \underset{\substack{m\ne i\\ m\ne j\\ m\ne k}}{F_{m\bullet}} \cdots (F_{i\bullet} + F_{j\bullet} + F_{k\bullet}) \cdots F_{N\bullet} \end{bmatrix}^T_{(N-2)\times N} \end{aligned} \tag{9}$$

Row vector $B_{i\bullet}$ is the complex emotional stimulus vector.

Because $\sum_{m=1}^{M} b_i(m) = \sum_{j=1}^{N} f_i(j) = 1, (1 \le i \le N)$, the matrix B is still content with the demand of HMM. Thus, we can get the value of emotional state in the stimulus transferring process by $\lambda = (N,M,A,B,\Pi)$

4 Simulation Experiment

4.1 A Single Stimulus

Based on the OCC cognitive-affective model, a field source with the emotional attenuation function (1) and the threshold function (2) is set as a stimulus of content emotional state at time 0. And at time 3 the stimulus disappears.The result is shown in Fig.6. The experiment shows that when the robot receives a stimulus of content, the emotion of content is activated within a short time, and the content leads to other emotions like joy and soothed. Thus, the content, joy and soothed quickly reach a certain intensity. And without other new stimulus they gradually decrease, and tend to calm. This result corresponds to the mechanism of human emotional regulation.

4.2 A Complex Stimulus

Based on the OCC cognitive-affective model, two sources with the emotional attenuation function (1) and the threshold function (2) are set as an content-joy-mixed stimulus at time 0. And at time 3 the stimulus disappears. The result is shown in Fig.7. The experiment shows that when the robot receives a complex emotional stimulus of content and joy, the content and joy emotional states are activated within a short time, and they lead to other emotions like stern and soothed. Thus, the emotional states of content, joy, stern and soothed quickly reaches a certain intensity. Then, in the case of no new stimulus, the emotional intensity gradually decreases, and tends to calm. This result corresponds to the mechanism of human emotional regulation.

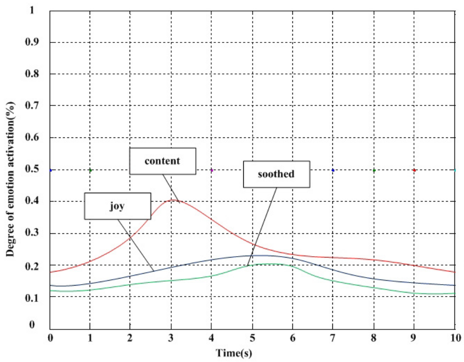

Fig. 6. Emotional activation curves with a single content stimulus

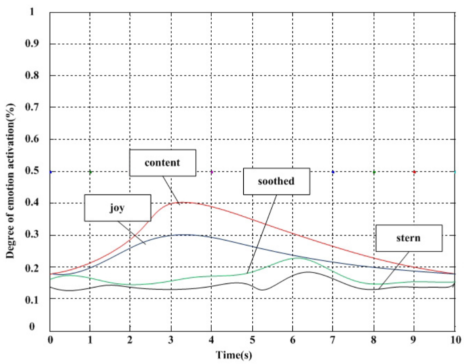

Fig. 7. Emotional activation curves with the complex emotion stimulus

5 Conclusion

On the basis of the affective computing model of facial robot Kismet, this paper proposes an emotional state model with the description of the active field, which transforms several field sources into a single one via the vector calculation of the potential energy gradient, and analyzes the potential surface in the emotional space for determining the transferring probability matrix. Then, we introduce the auxiliary matrix into HMM for implementing the dynamic regulation process of robots emotion. This model has the following characteristics: (1) under the premise of psychological significance, it enriches the species of the external stimulus and the emotional output and it reflects the complexity of human emotional regulation; (2) personality caused by individuality is reflected in the common of human emotional regulation by the active threshold function; (3) the saturation threshold ensures that the emotional regulation is effective in stimulus of any intensity and species, and reflects the whole stability of human emotion in flux.

Human emotional regulation process is very complex, so it demands many kinds of impact factors including the internal factors and the external environmental conditions in the interaction. Thus, it is difficult to fully consider. This paper only considers some typical impact factors and basic-emotions-mixed states, but how to research the multiple complex emotional regulation in more multiplex environment still needs further study.

Acknowledgement. This work is supported by National Natural Science Foundation of China (No.61170115 & No.61105120) and the Open Research Project Funds for Key Laboratory of Complex Systems and Intelligence Science (No. 20110108).

References

1. Wang, G., Teng, S., Fu, K.: Artificial Emotion Medel Based on Random Process. In: 2010 2nd International Workshop on Intelligent Systems and Applications (ISA), May 22-23, pp. 1–4 (2010)
2. Xu, Q.L., Zhou, F., Jiao, J.: Design for User Experience: an Affective-Cognitive Modeling Perspective. In: 2010 IEEE International Conference on Management of Innovation and Technolog (ICMIT), June 2-5, pp. 1019–1024 (2010)
3. Yu, D., Fang, J., Zhou, Y., Zhao, P.: A Model of Emotional Interactions Based on Affective Cognitive Algorithm. In: 11th International Conference on Advanced Communication Technology, ICACT 2009, Febuary 15-16, pp. 2149–2154 (2009)
4. Leon, E., Montalban, I., Schlatter, S., Dorronsoro, I.: Changes Using Non-Parametric Cumulative Sum. In: 2010 Annual International Conference of the IEEE Engineering in Medicine and Biology Society (EMBC), August 31-September 4, pp. 1109–1112 (2010)
5. Liu, X., Xie, L., Yang, W., Wang, Z., Fu, S.: Dynamic Regulation Process of Facial Expression Robot. Control Theory & Applications 28(7), 936–946 (2011)
6. Burgstaller, W., Lang, R., Porscht, P., Velik, R.: Technical Model for Basicc and Complex Emotions. In: 2007 5th IEEE International Conference on Industrial Informatics, June 23-27, pp. 1007–1012 (2007)
7. Breazeal, C.: Function Meets Style: Insights From Emotion Theory Applied to HRI. IEEE Transactions on Systems, Man, and Cybernetics-Part C: Applications and Reviews 34(2), 187–194 (2004)

8. Mstsumaru, T.: Discrimination of Emotion From movement and Addition of Emotion in Movement to Improve Human-Coexistence Robots Personal Affinity. In: Mstsumaru, T. (ed.) The 18th IEEE International Symposium on Robot and Human Interactive Communication, RO-MAN 2009, September 27-October 2, pp. 387–394 (2009)
9. EI-Nasr, M.S., Yen, Y.: Flame Fuzzy Logic Adaptive Model of Emotions. Autonomoius Agents and Muli-Agent Systems 3, 219–257 (2000)
10. Ji, S., Watson, L.T., Carin, L.: Flame Fuzzy Logic Adaptive Model of Emotions. Semisupervised Learning of Hidden Markov Models via a Homotopy Method 31(2), 275–287 (2009)
11. Wang, W., Wang, Z., Zheng, S., Gu, X.: Individual Differnence of Artificial Emotion Applied to a Service Robot. Frontiers of Computer Science in China 5(2), 216–226 (2011)

A Development of Art Robot System for Representation of Brightness of Image*,**

Sangwook Kim, Myeongjin Song, Paul Kim, Geunjoo Lee,
Nyamsuren Ganbold, and Jiamei Tang

School of Electrical Engineering and Computer Science
Kyungpook National University, Daegu, Korea
kimsw@knu.ac.kr
{mjsong,paulkim,gjlee,suren,jmtang}@media.knu.ac.kr

Abstract. Existing drawing robots draw pictures using robot-arm based on coordinates extracted from image processing. However, they draws pictures by presenting contours and brightness, they lacked the technique of stepped representation of brightness and due to that, resulting pictures differed a lot compared to its original version. This paper proposes art robot system that is capable of detection and extraction of brightness in images, along with dynamic representation of brightness lines that change with accordance to the value of brightness level. Proposed robot system analyzes and classifies the brightness by its density and based on this brightness levels, brightness and shade is drawn by repeated reproducing of overlapped lines. This representation of brightness method can draw pictures with various types of brightness by adjusting the number of brightness lines and leveling of brightness.

Keywords: Brightness, Art Robot, Robot Arm.

1 Introduction

Art robot in professional robotic field is getting much attention lately, and various image processing and robot controlling techniques are emerging. In humanoid robotics, there are numerous of human portrait drawing robots that utilize arms. However, existing robots draw portraits using contours extracted from input face images. Moreover, those robots cannot represent the brightness and shade in various types of images.

Therefore, this study designs and develops the art robot system that can represent brightness in images. In order to represent brightness and shade of images, proposed art robot manages fine controlling of arm, adjusts intervals between brightness lines for it. Also, addition of contours makes it possible to draw more real and solid looking images.

---

* Following are results of a study on the "Human Resource Development Center for Economic Region Leading Industry" Project, supported by the Ministry of Education, Science & Technology(MEST) and the National Research Foundation of Korea(NRF).
** This work was supported by the second stage of the Brain Korea 21 Project in 2012.

S. Lee et al. (Eds.): Intelligent Autonomous Systems 12, AISC 194, pp. 433–441.
springerlink.com

In order to achieve this, this study proposes methods to represent brightness and shade. Proposed method defines the levels according to density of brightness from input image and based on those levels, sets of coordinates extracted for each pixel by equalizing brightness density levels with neighboring pixels. Brightness is represented by using effective drawing technique, along with analysis and validation of the trajectories from coordinate values to create robot arm's moving paths.

The rest of the paper is organized as follows. Section 2 discusses about the related works and section 3 describes the design of art this robot system. The next section proposes and describes the methods to represent brightness and shade for in this art robot system, and next one describes about the robot arm controlling algorithm for drawing in art robot system. Finally, section 6 draws the conclusion.

2 Related Works

The work of F. Yao and G. Shao on Chinese Painting Robot used real brush as drawing tool to represent width of the lines [1]. As an ink-painting robot, this research represents facets and lines by ink density and line thickness. However, it lacks the ability to draw pictures other than ink-painting, for its limitations on representing contours separately and it is not compatible with drawing shades.

P. Tresset et al., conducted Aikon robot project. This robot draws the portrait using the professional painter's technique [2, 3]. But, drawing speed was slow and contour representation of human face was not accurate.

The robot Hektor, developed by J. Lehni and U. Franke, used spray as drawing tool to represent thickness [4, 5]. Hektor draws by the Script algorithm that calculates the drawing paths from illustrator extracted vector values. Although, it draws relatively accurately with simple architecture, it has drawbacks of scattered and flowed paints on the image, caused by mediocre controlling of amount of spray being sprayed.

Thus, to overcome above mentioned problems in related literatures, this study proposes an art robot system that can represent brightness and shade of an image. This research develops an art robot system that can produce more solid and real-feeling drawing results by using leveling of brightness in steps and adjustments of gap between brightness lines.

3 Architecture of Art Robot System

This system draws more realistic pictures by adjusting line width and fine movement of robot arm, after identifying and classifying shade and shadows by step by step from the input image.

The heuristic arm controlling techniques for picturing brightness and shade divided in to two, image processing and robot arm controlling. Figure 1 shows the diagram of data flow between each module in different development scenarios.

After getting the image file as input through the vision system, like camera and smartphone, it analyzes the image file to detect and extract the brightness and shade. By extracting brightness data, brightness density is digitized and extracted based on given coordinate sets.

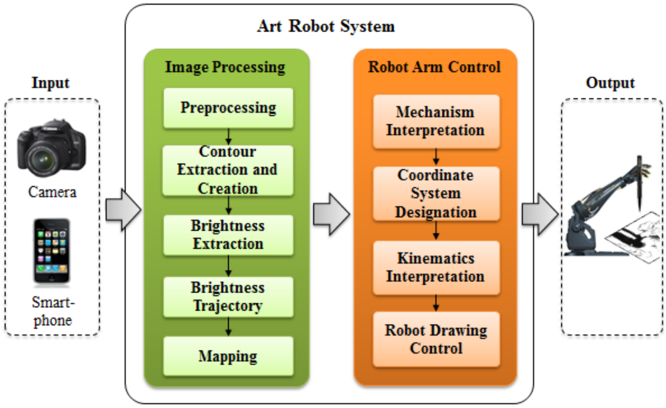

Fig. 1. System Architecture of Art Robot

In order to draw, contour is extracted with adjusted line width and sets of coordinates are extracted. Then drawing is performed based on this extracted coordinates sets.

After drawing contour lines, brightness and shade are drawn in detail. During the stage of brightness representation, fine adjustment of intervals between drawing lines, results in more real and natural feeling picture. After finishing of the drawing, it notifies the user about completion.

4 Image Processing

Existing portrait drawing robots considered contour lines and brightness for drawing. It was difficult to depict special features of the real image. Representation of brightness line produces more realistic looking images [7].

4.1 Classification of Brightness and Shade

Input images received from vision system are analyzed and as a result, contours, brightness and shade are classified. Each pixel of image is digitized with values and those values are clustered, step by step [8].

However, it takes longer for robot arm to draw if we classify brightness in too many steps, and too much overlapping of lines results in unclear-looking image. So that, it uses 5-step classification of brightness to represent brightness density as shown in Figure 3.

Since, the extraction of trajectory using these kinds of values is difficult, images are converted to grayscale and each pixel's brightness density is leveled depending on the level of light and dark shades. For instance, every pixel has values between 0 ~ 255 according to brightness, and if there are 5 levels of brightness, all the possible pixel values are divided into 5 levels by its density of brightness contrast and each level's

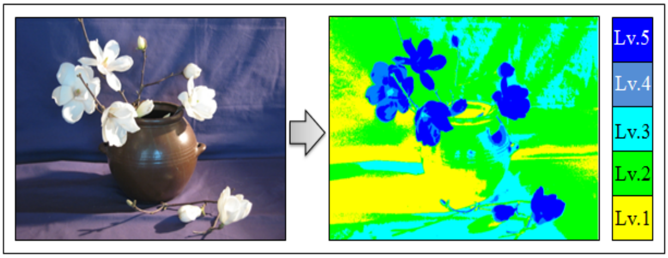

Fig. 2. 5-Step Representation of Brightness

value range is defined. Step 1 level's brightness density defined by values between 1 and 50 and values ranging 51 to 102 is for step 2. These level values get each pixel to take its level value in range of 1-5. That is, the bigger the level value, the darker it gets and the smaller it is, the brighter it gets when it is drawn. Robot arm trajectory is extracted using the pixels and presented by above proposed method.

4.2 Trajectory Creation and Extraction

The input image received through earlier mentioned processes is represented in two-dimensional array by its level values as shown in Figure 3 and, array indexes represent the coordinates of the image and each dimension's size of the array indicates the vertical and horizontal size of image respectively. With those level valued coordinates, brightness and shade are represented by extracting brightness lines as orange and purple straight lines depicted in Figure 3. First, directions of brightness lines are defined by setting different directions for each line.

For example, as shown in Figure 3, horizontal direction is for step 1, vertical for step 2 and direction and angle for next steps are adjusted respectively to represent the brightness and shade in image. There are two major factors in representation of brightness and first one is overlapping of brightness lines. Step 5 is represented without the brightness line as it has the highest brightness density, step 4 and lower are drawn with brightness lines of 4-step leveling directions. Then, in step 3, brightness line with the level-3 direction is drawn overlapping on stage-4 brightness lines.

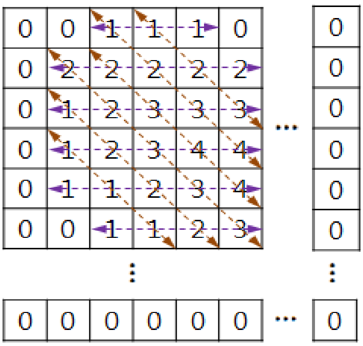

Fig. 3. Brightness Density Leveling

In this way, step 1 shows the highest density of brightness and shade as it has lines drawn with 4 different directions in overlapped manner to increase the density of lines, and next steps show the lower brightness and shade degree as it gets smaller number of overlapping lines. Second main factor to represent brightness and shade is the number of lines to be drawn. Increasing the number of brightness lines to draw gives brightness and shade, a lot more denser and compact brightness lines and so that, completeness of the drawn picture enhances. However, drawing speed of robot arm become slower, since drawing trajectories created are a lot more in number. When extracting brightness lines from the simple leveled coordinates, there are lines those are too short and lines those are impossible for actual robot arm to draw or even some of those valid lines can take too long for robot arm to draw. Therefore, too short lines and in-valid lines are pruned as shown in Figure 4 below.

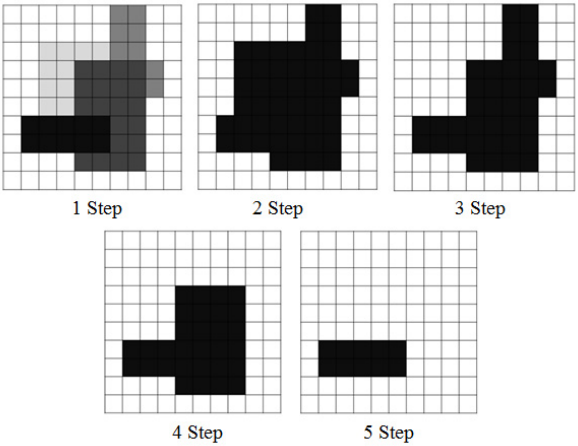

Fig. 4. Steps in Brightness Representation

$$L_{shade} = \{L_{11}, L_{12}, \dots, L_{21}, \dots, L_{S_w S_h}\} \tag{1}$$

$$\text{if} \left(term < \sum_{i=cur-term}^{cur+term} \left(\frac{L_i}{term \times 2} \right) \right)$$

$$L_{cur} = 0$$

$$\text{if} \left(term \geq \sum_{i=cur-term}^{cur+term} \left(\frac{L_i}{term \times 2} \right) \right)$$

$$L_{cur} = 1$$

Where S_w in Equation (1) denotes the width of image, S_h denotes the height of image, L_{shade} denotes the set of brightness levels. L_{cur} presents the level value for current coordinate and term is the variable holds the validity of brightness line. Lines are examined one-by-one and examination in one line starting from L_{cur} to left and right sides for value of term and calculates the sum and mean of those values. If the mean value is less than value of term, it is considered as invalid and if the mean value is greater than the term, it is considered as valid level value and as a result, invalid brightness lines are discarded.

In Figure 4, (a) illustrates the classified level of brightness density in 5-steps and in (b), it shows the representation of step-1 being all the brightness lines are drawn except the brightest parts, in (c), it shows all except brightest and second to brightest, and in (d), (e), it illustrates the state of each level's appropriate brightness lines drawn.

View of the resulting image differs greatly, depending on the change in brightness density level and number of brightness lines used, and this characteristic is illustrated in Figure 5 with various settings of brightness density level and in Figure 5 with different numbers of brightness lines.

From Figure 5 that depicts the comparison of different step methods, it can be inferred that steps more than 5 gives no big difference to the quality and smaller steps are inadequate for brightness representation. From the Figure 6, it can be concluded that number of lines greater than 50 shows no difference compared to number of lines being 50. Also values lower than 50 lines are inadequate for reasonable separation of brightness density and it shows that the most appropriate values for number of lines to be drawn ranges from 40 to 50 depending on size of input image.

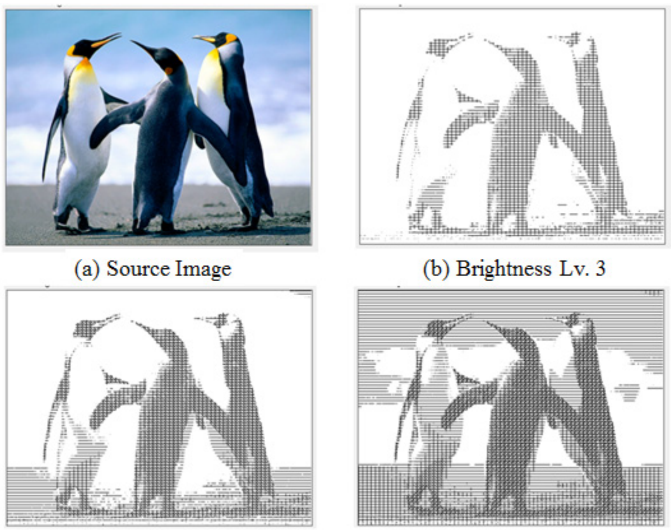

(a) Source Image (b) Brightness Lv. 3

(c) Brightness Lv. 4 (d) Brightness Lv. 5

Fig. 5. Brightness Step according to Level

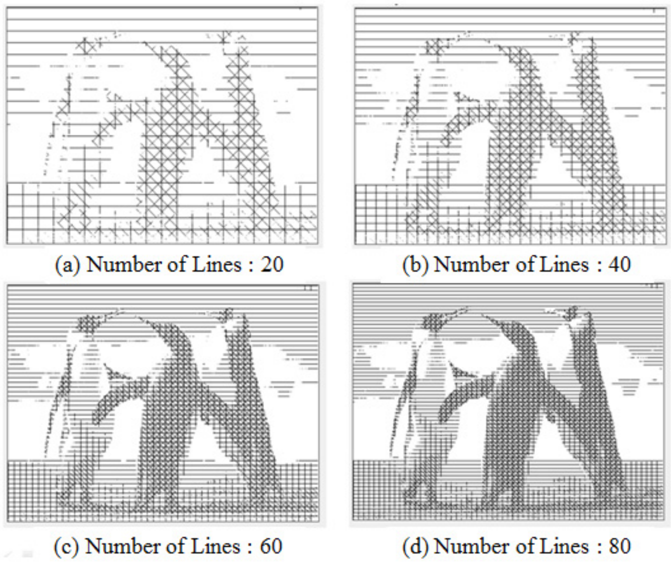

Fig. 6. The number of Brightness Lines

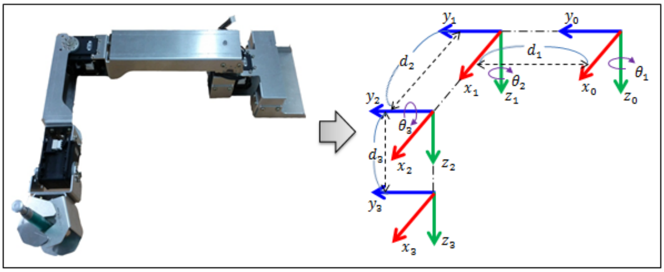

Fig. 7. Coordinate Transformation of Art Robot Arm

5 Robot Arm Controlling

Drawing is performed by controlling robot arm according to brightness trajectory extracted. Art robot for drawing has easy to understand structures that even for the user who sees the robot for the first time could understand it.

Robot controlling parts in art robot system is selected as human arm type robot, as it maximizes the ability of suppressing and controlling of vibration of robot arm during movement through z-axis. Making the movement of z-axis by shoulder-joint results in larger inertia in lower parts and at the same time vibration becomes stronger. Thus, robot in this system is structured as it used joints in arm to minimize the inertia. In

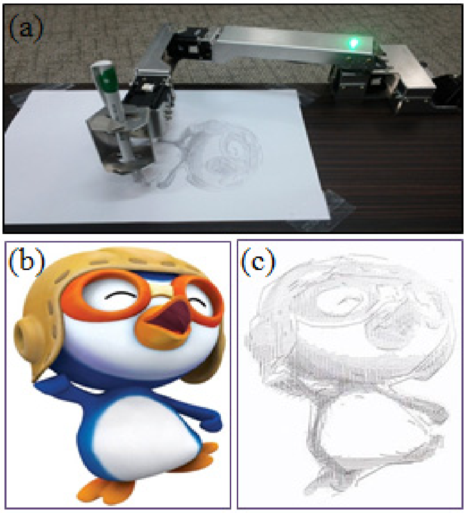

Fig. 8. (a) Drawing of Robot Arm, (b) Source Image, (c) Drawing Result

addition, portability and durability has been increased as it is manufactured using aluminum that is lightweight and corrosion resistant. Robot is composed of total of three DYNAMIXEL MX-28 and one XEL device for moving Z-axis and two XEL devices for movement through two-dimensional plane. DYNAMIXEL MX-28's features unlike any other product with PID control and the minimum of as fine as 0.088° angle is controlled to increase the accuracy and ensured the communication speed up to 3Mbps and makes high-speed controlling possible.

Method of arm controlling is that it produced and stored in one package. This package is then composed of parameters such as speed of arm, strength, and timing. The package stored in this way makes faster robot arm controlling possible. In addition, because of the use of three XELs, Sync packet is created and synchronized with each XEL.

6 Conclusions

In this paper, it proposed the system that can draw more accurate and realistic pictures, which can not only picture the contour width, but also brightness and shade. When brightness is represented, it calculates the shortest trajectory to decrease the drawing time and designs brightness representation method that is valid for various types of image with the right style of brightness representation.

For the future work, this research is planning to develop android application that can draw picture when user touches screen and also working on the developments of different kinds of robot controlling methods. This can be used in various effective ways in the age of smart devices and intelligent robotics.

References

[1] Yao, F., Shao, G.: Painting Brush Control Techniques in Chinese Painting Robot. In: IEEE International Workshop on Robot and Human Interactive Communication (2005)

[2] Tresset, P., Leymarie, F.F., Khaorapapong, N.: SKEDIOMATA: Guinea Pig and Performer. In: The 17th International Symposium Electronic Art, ISEA (2011)

[3] Tresset, P., Leymarie, F.F.: `http://sites.google.com/site/aikonproject`

[4] Hooi, I., et al.: PICARSO Programmable Interface Controller With Autonomous Robotic Spraying Operation. In: Proceedings of the Australasian Conference on Robotics and Automation, ACRA (2010)

[5] Franke, U., Lehni, J.: "Hektor", `http://hektor.ch/Book/Hektor.pdf/`

[6] Benedettelli, D.: LEGO Mindstorms NXT Portrayer Robot (September 2008), `http://robotics.benedettelli.com/portrayer.htm/`

[7] Calinon, S., Epiney, J., Billard, A.: A Humanoid Robot Drawing Human Portraits. In: The 5th IEEE-RAS International Conference on Humanoid Robots (2005)

[8] Bassiou, N., Kotropoulos, C.: Color image histogram equalization by absolute discounting back-off. Computer Vision and Image Under Standing 107(1-2), 108–122 (2007)

IV: Autonomous Multi-agent Systems and Life Engineering

Hyungsuck Cho

Autonomous systems require a variety of autonomy in order to carry out tasks given to them in known or unknown environments. To take some examples, task analysis to identify type of works to be done, task recognition based upon the analysis, modalities and methodologies to solve problem associated with the tasks, formulation of system configurations suitable to achieve the tasks, strategies for manipulation of the systems, motion planning, control and sensing for dynamic motion of the systems for the manipulation and so on. The papers presented here in this chapter treat all of the important issues related to the topics mentioned above. The chapter is composed of five segments of different topics which cover broad spectrum of topics related to autonomous systems such as life engineering, adaptive behavior of biological systems and robots (mobilgence), multi-agent robots, and design of autonomous system's components including robotic manipulators and walkers and finally robotic mechanism and design associated with autonomy of the robotic systems.

Living entities have a capability of adapting themselves to changing environment with intelligent sensory-motor functions. The intelligence of generating such adaptive functions is a consequence of the interaction of the body, brain, and environment, called "mobilgence" has been the subject of research in recent years, which makes effort to embed such functions into robotic systems. The following five papers treat various kinds of subjects related to the above mentioned issues.

1) Effect of Mediolateral Knee Displacement on Ligaments and Muscles around Knee Joint: Quantitative Analysis with Three-dimensional Musculoskeletal Ligament Knee Model
2) Robot Colony Mobility in a Thermodynamics Frame
3) Throwing Darts Training Support System based on Analysis of Human Motor Skill
4) Muscle activities Changing Model by difference in sensory inputs on human posture control
5) Minimalist CPG Model for Inter- and Intra-limb Coordination in Bipedal Locomotion

Multi-agent systems approach that can carry out tasks difficult–to-solve solve for an individual agent utilizes intelligence of multiple agent within an environment. This problem-solving behavior is the result of coordination of the agents from their intelligent interaction.

The following thirteen papers discuss cooperation strategy in various situations, multi-robot formation and its control methods, information retrieval systems, task allocation for spatially and temporally distributed tasks and so on.

1) Dynamic Partition of Collaborative Multiagent based on Coordination Trees
2) A distributed kinodynamic collision avoidance system under ROS
3) Authentication using shared knowledge. Learning agents.
4) Cooperative Particle Swarm Optimization-based Predictive Controller for Multi-Robot Formation
6) Modeling pedestrians in an airport scenario with a time-augmented Petri net
7) Cooperation without exploitation between self-interested agents
8) Controlling Formations of Robots with Graph Theory
9) Information Gathering Multi Agent Framework System
10)Study of Query Translation Dictionary Automatic Construction in Cross-Language Information Retrieval
11) A Multi-Agent Information Retrieval System Based on Ontology
12) Task allocation for spatially and temporally distributed tasks
13) Learning Task Performance in Market-Based Task Allocation

Autonomous manipulation of robots in known or unknown environments requires high performance of motion, accurate path planning under unknown environments, relevant sensors and actuators motion guiding device. The topics related to this category that are included here deal with robotic manipulators and autonomous systems with rigorous treatment on their mechanism and design The following ten papers present methodologies and analyses to solve these problems

1) A Framework for Unknown Environment Manipulator Motion Planning via Model Based Realtime Rehearsal
2) Embedded Joint Torque Sensor with Reduced Torque Ripple of Harmonic Drive
3) Design and Analysis of Variable Yielding-torque Spring-Clutch (VSC) for the Safety of Operating Robot Arm
4) Vibrotactile Cues for Motion Guidance
5) Driving and Turning Control of a Single-Wheel Mobile Robot
6) Modeling and Dynamics of Extended Elastic Actuator Applied to Robot
7) Towards Long-Term Collective Experiments
8) Control of a Trident Steering Walker - Design of Motion Parameters Based on a Propulsion Transfer Function -
9) Real-Time 3D Model Reconstruction with a Dual-Laser Triangulation System for Assembly Line Completeness Inspection
10) An Evolution strategy based autonomous algorithm for roll-to-roll web control system

The four papers presented in Poster Session discuss typical subjects important and essential to the development of autonomous functions for the autonomous systems

1) Mechanism Design and Locomotion of Snake Robot
2) Expression Intensity Recognition Based on Multilayer Hybrid Classifier
3) Cooperative Multi-Robot Searching Algorithm
4) Analysis of affective effects on steady-state visual evoked potential responses

A life engineering that refers to promote activities of living creatures and artifacts in certain environments deals with a variety of autonomous systems and their characteristic properties. Fourteen papers belong to this category and they are listed as,

1) Effect of Potential Model on Monte-Carlo Go
2 Acquisition of Ground Behavior on the Locust Model under the Virtual Physical Environment
3) Behavior of ships after the Great East Japan Earthquake
4) Target Enclosure for Multiple Targets
5) A Study on Acquisition Method of Nonverbal Cues for Intelligent Agents: A Case Study on Facial Expression Analysis
6) Study on Twining of Virtual Seaweed in Fluid Environment
7) Visualization of spatial expression ability using a 3-D expression system
8) Application of Flocking Algorithm to Attitude Control of Humanoid Robot
9) Velocity Correlation in Swarm Robots with Directional Neighborhood
10) Feedback Control of Traffic Signal Network of Less Traffic Sensors by Help of Machine Learning
11) Composite Artificial Neural Network for Controlling Artificial Flying Creature
12) Polycentric Framework for Robotic Kinematics
13) Cluster Analysis of Collective Behavior for a Robotic Swarm
14) Detection of Breast Cancer based on Texture Analysis from Digital Mammograms

In the years to come a great number of machines and systems themselves are expected to operate with their own autonomous function with and without interaction of human beings while adapting to spatially and temporally varying environments. To enable this functionality it is prerequisite for them to have capability of perception, reasoning, decision making and action with high level of autonomy. This chapter in a sense highlights some of this perspective and therefore I hope that all the papers contained here will contribute to the future technological trend.

Effect of Mediolateral Knee Displacement on Ligaments and Muscles around Knee Joint: Quantitative Analysis with Three-Dimensional Musculoskeletal Ligament Knee Model

Yuki Ishikawa[1], Qi An[1], Yusuke Tamura[2], Atsushi Yamashita[1], Hiroyuki Oka[3], and Hajime Asama[1]

[1] Department of Precision Engineering, Graduated School of Engineering, The University of Tokyo, Tokyo, Japan
ishikawa@robot.t.u-tokyo.ac.jp
[2] Department of Precision Mechanics, Faculty of Science and Engineering, Chuo University, Tokyo, Japan
[3] The 22nd Century Medical and Research Center, Graduated School of Medicine, The University of Tokyo, Tokyo, Japan

Abstract. Knee osteoarthritis (OA) becomes a major public issue, but a strategy to prevent the disease has not established yet due to lack of an accurate method to measure an internal motion of the knee of individual patients. Therefore mechanical engineering model and a standard of evaluation of the disease is needed to improve the situation. Currently, there are a few studies to develop the model including allowance of joint movement and ligaments. Thus this study shows the model accuracy by forward dynamics and discusses the result of inverse dynamics of various gait patterns. As a result, it can be confirmed that ligaments are more effective than muscles around knee joint with our various models. In addition we propose the important factor of knee OA from gait pattern and models.

1 Introduction

Knee osteoarthritis (OA) is thought to be a major public health issue causing chronic disability [1]. Clinical research has suggested that the instability of a knee joint causes the changing structure of joint and gait disorder. Therefore it is important to research an effect of gait patterns on the knee joint. Although, many efforts have been made to identify an optimal diagnostic tool for this disease, no definitive tools have been reported until now. The most reason is due to lack of objective or accurate method for measurement of the motion. Therefore mechanical engineering knee model and a standard of evaluation method of the disease is needed to achieve prevention of the disease.

One of the important features of the knee joint is that bony limitation of movement is a little. Therefore it is necessary to consider allowance of joint movement such as slide with rolling, soft tissues such as a ligament, a cartilage and a meniscus. Especially a ligament is an important factor to decide the movement of the knee joint; ligaments

S. Lee et al. (Eds.): Intelligent Autonomous Systems 12, AISC 194, pp. 447–456.
springerlink.com

make an axis of the joint, and decide a degree of freedom and the range of knee joint movement, which is related with the disease (OA).

Although recently knee joint models have been developed, there are few models that consider allowance of joint movement, three-dimensional movement and functions of ligaments. Moreover they do not test accuracy of their developed model. Almost all studies made their models just from previous mechanical property data. Therefore they tend to ignore an effect of whole model dynamics. Therefore this study uses a verification methodology by forward dynamics which gives the developed knee joint model some loads and sees its displacement caused by the loads. This displacement can be compared with a past cadaver study or a partial living body experiment [2]. In this study, anterior-posterior displacement and tibial rotation are considered to be important and focused; from clinical study anterior cruciate ligament is known to control anterior-posterior movement and to cause cartilage damage [3] [4] and tibial rotation is also proposed to be a possible cause for the disease [5].

Therefore our objective is to develop the knee model including ligaments and to test its accuracy with forward dynamics calculation. In addition, the effect of mediolateral knee displacement on ligaments and muscles is clarified to elucidate factors of knee OA from our developed model.

2 Knee joint

2.1 Bones and Joints

A knee is made up of four bones; a femur, a patella, a tibia and a fibula. The patella floats over the front of the knee joint. The tibia and the fibula are the two parallel bones in the lower leg. These bones compose three joints; the medical femur-tibia joint, the lateral femur-tibia joint and the femur-patella joint. Where the bones meet they are covered with articular cartilage and the femur-tibia joint has a medial meniscus and a lateral meniscus. These structures work as ”cushions” or ”shock absorbers”. They also provide stability to the knee. Articular capsule covers a whole joint and gives a limitation of vertical knee movement.

2.2 Muscles

There are mainly eleven muscles attached to a knee joint; the medial vastus muscle, the intermediate vastus muscle, the lateral vastus muscle, the rectus femoris muscle, the long head of biceps femoris muscle, the short head of biceps femoris muscle, the semimembranosus muscle, the semitendinous muscle, the sartorius muscle, the gracilis muscle and the gastrocnemius muscle. The former four muscles work as knee extension and latter seven muscles work as knee flexion.

2.3 Ligaments

Ligaments are like strong ropes that connect bones and provide stability to joints. In the knee, there are four main ligaments; the anterior cruciate ligament (ACL), the posterior cruciate ligament (PCL), the medial collateral ligament (MCL), and the lateral collateral ligament (LCL). Ligaments are composed with some bundles and they are attached to the knee bones to make facets. The ligaments work like a spring which exerts tension force if the length of ligaments is longer than its neutral length.

3 Model

3.1 Simulation Method

SIMM (Corp. MusculoGraphics) is employed to develop and verify the three-dimensional musculoskeletal right leg knee ligament model. This software can calculate the muscle force from a specified musculoskeletal model with body trajectory and floor reaction force data (inverse dynamics calculation)

It can also calculate the displacement from the musculoskeletal model with external forces (forward dynamics calculation).

3.2 Detail

In our suggested model, 6 degrees of freedom movement is allowed and also liga-ments and cartilage are included. In order to consider irregular slide and rolling of the knee joint, 6 degrees of freedom movement is needed. Our developed knee model is designed as Fig. 1 (a). The overall model is shown in Fig. 1 (b). The positions of ligaments are shown in Fig. 1 (c). These positions are decided by anatomical structure. The number of bundles and their stiffness are determined from the previous studies of Shelburne *et al.* and Blankevoort *et al.* [6] [7]. Their strain is determined from trial and error. The length of neutral ligament (L_0) is calculated by equation (1) with the length of ligament when knee is extended (L_e) (Table 1). L_0, L_e and ε represent ligament neutral length, ligament length in knee extended and strain in knee extended. An articular capsule is also given as a function of ligaments. To represent cartilage and meniscus, there are ten

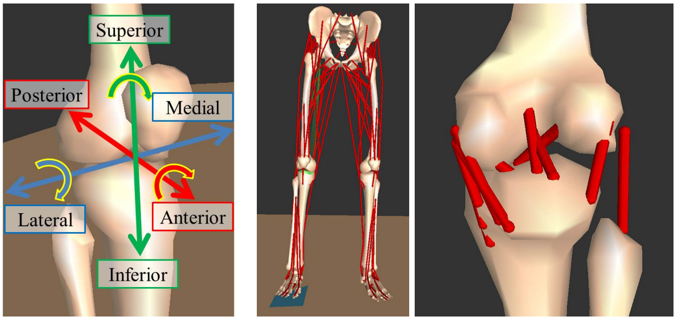

(a) (b) (c)

Fig. 1. Knee model. (a) Coordination. (b) Overall view. (c) Ligaments position.

Table 1. Bundle of ligaments, stiffness and strain

Bundle of ligaments	Stiffness [N/strain][a]	Strain [-]
aACL	1000	0.069
pACL	1500	-0.017
aPCL	2600	-0.087
pPCL	1900	-0.090
aMCL	2500	-0.209
cMCL	3000	-0.006
pMCL	2500	0.016
aCM[b]	2000	-0.299
pCM[b]	4500	-0.087
LCL	4000	-0.020
Mcap[c]	2500	-0.028
Lcap[c]	1000	0.018

[a] Shelburne *et al.* [6]

[b] A deeper part of MCL

[c] An articular capsule

spring points on the surface of femur. These points generate reaction force depending on a distance from bone surface. These mechanical properties are determined from the study of Neptune *et al.* [8].

$$L_0 = \frac{L_e}{1+\varepsilon}. \tag{1}$$

4 Verification of Model

The model is verified by comparing results of either a cadaver study or a living body experiment with the result of forward dynamics simulation. In the forward dynamics simulation, displacement of the knee joint can be observed by giving some load on the developed knee model. This displacement is comparable to the cadaver study or the living body experiment.

4.1 Anterior-Posterior Displacement

Firstly, anterior-posterior displacement is focused. In the past studies, researchers examined tibia displacement with femur by external voluntary load set on the knee joint in vivo and in vitro [9-13]. Since in this paper, range of knee joint movement is 0-30 degrees, this movement range is employed in the model. Then the knee joint of our model is given 100 N loads on anterior or posterior when the knee joint flexion angle is fixed as 0 or 30 degrees.

Table 2 shows results of knee displacement of our dynamics simulation and past studies. When 100 N is given to knee joint at flexion of 0 degree, our simulation result shows 4.17 mm anterior displacement. Almost all other studies indicate about 5 mm in the same situation. Therefore this model can be confirmed to be correct to represent anterior displacement of the knee joint. At knee joint flexion of 30 degree, knee displacement is larger than the one at 0 degree. Also other studies suggest change of knee displacement at 0 degree should be larger than the one of 30 degrees. From this result, this model can be confirmed to be correct to represent mechanism of the knee joint.

Table 2. Anterior-posterior displacement

Searcher	Status (Vivo/Vitro/ /Simulation)	Force [N]	Flexion angle [degree]	Displacement [mm] Anterior	Posterior
The current study	Simulation	100	0	4.17	3.22
		100	30	9.90	6.23
Fukubayashi *et al.* [9]	Vitro	100	0	5.2	3.9
		100	30	7.1	6.0
Daniel *et al.* [10]	Vivo	89	20	5.6	2.8
Shoemaker and Markolf [11]	Vitro	100	0	2.3	3.1
		200	0	3.4	4.7
		100	30	5.7	3.6
		200	30	7.0	5.0
Lim *et al.* [12]	Vivo	134	20	4.9	3.4
LaPrade *et al.* [13]	Vitro	88	0	3.4	5.1
		88	20	3.9	6.4
		88	30	3.8	5.5

4.2 Tibial Rotation

Secondary, tibial rotation is examined to verify the developed model. In the past studies, researchers examined tibial rotation with femur by generating external voluntary torque on knee in vitro [13-15]. The displacement of tibial rotation is analyzed when 5 or 10 Nm torque is exerted on the developed knee joint model when its flexion angle is fixed to 0 or 30 degrees.

Table 3 shows results of our simulation and past cadaver studies. At the knee joint flexion of 0 degree, our simulation result is 18.7 degree internal angle by 10 Nm torque. On the other hand, almost all other studies indicate approximately 10 degrees or slight higher. Therefore this model can be confirmed to be correct to represent internal rotation of the knee joint. Our simulation result is 29.0 degree external angle by 5 Nm torque. On the other hand, almost all other studies indicate smaller than 20 degrees. Therefore this model is more soft than those studies in external rotation of the knee joint.

At knee joint flexion of 30 degree, knee rotation is larger than that at 0 degree. Also other studies suggest change of knee rotation at 0 degree should be larger than the one of 30 degrees. From this result, this model can be confirmed to be correct to represent mechanism of the knee joint.

Table 3. Tibial rotation (Internal-external)

Searcher	Status (Vivo/Vitro/ /Simulation)	Torque [Nm]	Flexion angle [degree]	Rotation [degree] Internal	angle External
The current study	Simulation	5	0	13.2	29.0
		10	0	18.7	42.5
		5	30	22.6	27.9
		10	30	26.7	39.9
LaPrade *et al.* [13]	Vitro	5	0	7.7	8.8
		5	20	15.3	17.1
		5	30	17.0	17.7
Ahrens *et al.* [14]	Vitro	12.8	0	10.3	-
		14.8	0	-	12.3
		11.1	30	12.2	-
		13.9	30	-	12.6
Coobs *et al.* [15]	Vitro	10	0	11.1	11.8
		10	15	15.0	14.8
		10	30	17.5	14.8

5 Simulation

5.1 Gait Patterns

SIMM has normal gait pattern data (body trajectory and reaction force data) which is obtained by motion capture camera and floor reaction force sensor. To make mediolateral gait patterns we change the data of knee marker in mediolateral axis.

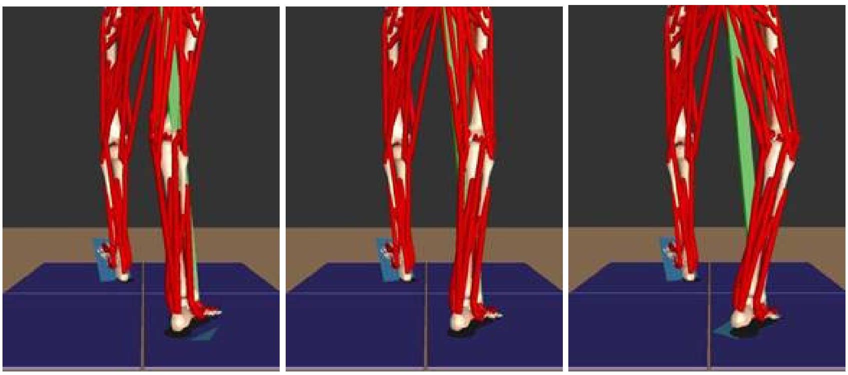

(a) Med50 (b) Normal (c) Lat50

Fig. 2. Gait patterns. (a), (b) and (c) represent the situation of walking with medial, normal and lateral knee displacement.

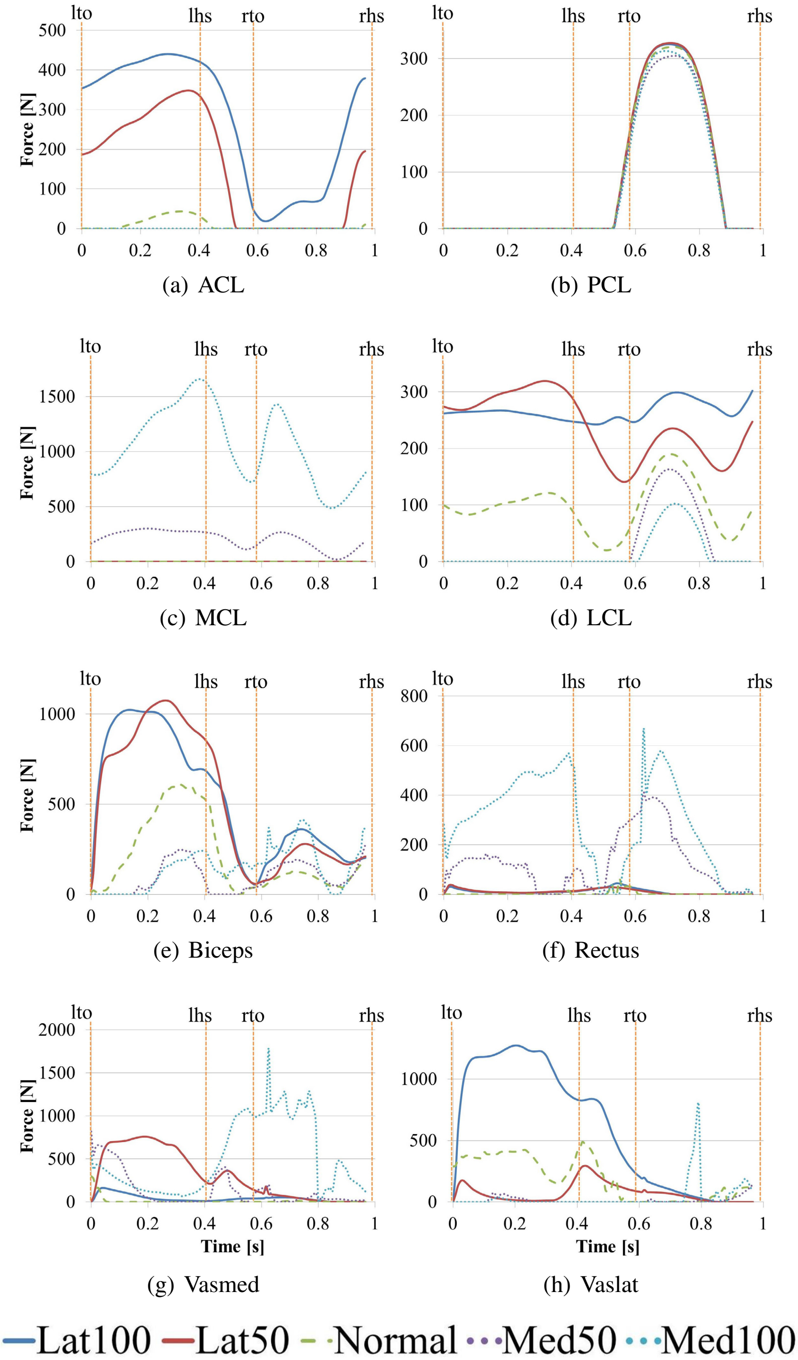

(a) ACL (b) PCL

(c) MCL (d) LCL

(e) Biceps (f) Rectus

(g) Vasmed (h) Vaslat

Fig. 3. Ligaments and muscles force. rto, rhs, lto and lhs represent right toe off, heel strike, left leg toe off and heel strike

Then five different gait patterns are tested including a normal walking (Normal); walking with 100 mm medial (Med100), 50 mm (Med50), 50 mm lateral (Lat50), and 100 mm lateral (Lat100) right knee displacement. Walking with medial knee displacement means baker-legged walking and walking with lateral knee displacement means bandy-legged walking. A knee position in each gait patterns at the same point during a walking phase is shown in Fig. 2. Figure 2(a) shows Med50, center (b) shows Normal and (c) shows Lat50. Gait data is cropped from left heel strike to right heel strike.

5.2 Force of Ligaments and Muscle

We input the former five gait patterns to our model and calculate the force of ligaments and muscles by inverse dynamics. Force of ACL, PCL, MCL and LCL is obtained. Also force of the biceps femoris muscle (Biceps), the rectus femoris muscle (Rectus), the medial vastus muscle (Vasmed) and the lateral vastus muscle (Vaslat) is obtained.

6 Result and Discussion

Figure 3 shows gait simulated results of ligaments and muscles force. Force of ACL rises with increased lateral displacement. Shelburne *et al.* showed that maximum force of ACL is about 200 N and force-time curve has two peaks in normal walking [2]. This feature can be found in our result. Therefore the function of ACL is thought to be correct though the result of anterior-posterior displacement is different. Force of PCL has mostly the same curve shape in all case. In a left leg stance phase, force of PCL has a peak. This reason is thought that the length of PCL is stretched by a swing leg movement of knee in right leg extension. Force of MCL rises with increased medial displacement. This reason is thought that the length of MCL is stretched by a medial movement of knee in right leg extension. Force of LCL rises with increased lateral displacement. Shelburne *et al.* showed that maximum force of LCL is about 100 N in normal walking [2]. Therefore our result is thought to be correct.

Force of Biceps rises with increased lateral displacement. This reason is thought that Biceps is antagonistic to Vasmed and Vaslat which have the same peak. Force of Rectus totally rises with increased medial displacement. This reason is thought that LCL alternately generates a moment of valgus in lateral displacement. Force of Vasmed in Med100 has a large peak in left leg stance phase. This reason is thought that Vasmed generates a moment of varus to suspend right leg. Force of Vaslat rises with increased lateral displacement and has a peak in right leg stance phase. This peak is thought that Vaslat lifts right leg. Generally Vaslat of patients of knee OA is weaker than one of healthy people. In such a case, it is difficult to support a lateral knee movement by Vaslat. Our result indicates that LCL and Vaslat, which are also generating a moment of valgus, raise a burden on lateral displacement. Therefore it can be suggested that lateral displacement is one of the factors of medial knee OA.

7 Conclusion and Future Works

Three-dimensional musculoskeletal knee model with ligaments is developed. Validity of the model could be tested with our suggested forward and inverse dynamics simulation. Also the effect of gait patterns on ligaments and muscles around a knee joint is discussed during considering knee OA.

For the future study, more sets of parameters, such as mechanical property and attachment position of ligaments, will be tested to improve accuracy of the model for individuals. Then we will make the system of diagnosis of the knee joint.

Acknowledgement. This presentation is supported by NEC C&C Foundation. This work was in part supported by KAKENHI, Grant-in-Aid for Scientific Research (B) (24300198). The authors thank Mr. Yoshihiko Fujita (Corp. nac Image Technology) for supporting making the model.

References

1. March, L.M., Bachmeier, C.J.M.: Economics of Osteoarthritis a Global Perspective. Bail. Clin. Rheumatol. 11(4), 817–834 (1997)
2. Shelburene, K.B., Pandy, M.G., Torry, M.R.: Comparison of Shear Forces and Ligament Loading in the Healthy and ACL-deficient Knee during Gait. Journal of Biomechanics 37(3), 313–319 (2004)
3. Yeow, C.H., Cheong, C.H., Ng, K.S., Sin Lee, P.V., Hong Goh, J.C.: Anterior Cruciate Ligament Failure and Cartilage Damage during Knee Joint Compression: a Preliminary Study Based on the Porcine Model. The American Journal of Sports Medicine 36(5), 934–942 (2008)
4. Shin, C.S., Chaudhari, A.M., Andriacchi, T.P.: The Influence of Deceleration Forces on ACL Strain during Single-leg Landing: A Simulation Study. Journal of Biomechanics 40(5), 1145–1152 (2007)
5. Foroughi, N., Smith, R., Vanwanseele, B.: The Association of External Knee Adduction Moment with Biomechanical Variables in Osteoarthritis: A Systematic Review. Knee 16(5), 303–309 (2009)
6. Shelburne, K.B., Kim, H.J., Sterett, W.I., Pandy, M.G.: Effect of Posterior Tibial Slope on Knee Biomechanics during Functional Activity. Journal of Orthopaedic Research 29(2), 223–231 (2011)
7. Blankevoort, L., Huiskes, R.: Ligament-Bone Interaction in a Three-Dimensional Model of the Knee. Journal of Biomechanical Engineering 113(3), 263–269 (1991)
8. Neptune, R.R., Wright, I.C., Van Den Bogert, A.J.: A Method for Numerical Simulation of Single Limb Ground Contact Events: Application to Heel-Toe Running. Computer Methods in Biomechanics and Biomedical Engineering 3(4), 321–334 (2000)
9. Fukubayashi, T., Torzilli, P.A., Sherman, M.F., Warren, R.F.: An in Vitro Biomechanical Evaluation of Anterior-posterior Motion of the Knee. Tibial Displacement, Rotation, and Torque. The Journal of Bone & Joint Surgery 64A(2), 960–968 (1982)
10. Daniel, D.M., Malcom, L.L., Losse, G., Stone, M.L., Sachs, R., Burks, R.: Instrumented Measurement of Anterior Laxity of the Knee. The Journal of Bone & Joint Surgery 67A(5), 720–726 (1985)
11. Shoemaker, S.C., Markolf, K.I.: Effect of Joint Load on the Stiffness and Laxity of Ligament-Deficient Knees. Journal of Bone & Joint Surgery 67A(1), 136–146 (1985)
12. Lim, H., Lee, Y., Wang, J., Park, J., Suh, D., Kim, Y., Bae, J.: Anterior and Posterior Knee Laxity in a Young Adult Korean Population. Knee Surgery Sports Traumatology Arthroscopy 19(11), 1890–1894 (2011)

13. LaPrade, R.F., Wozniczka, J.K., Stellmaker, M.P., Wijdicks, C.A.: Analysis of the Static Function of the Popliteus Tendon and Evaluation of an Anatomic Reconstruction: The Fifth Ligament of the Knee. The American Journal of Sports Medicine 38(3), 543–549 (2010)
14. Ahrens, P., Kirchhoff, C., Fischer, F., Heinrich, P., Eisenhart-Rothe, R., Hinterwimmer, S., Kirchhoff, S., Imhoff, A., Lorenz, S.: A Novel Tool for Objective Assessment of Femorotibial Rotation: a Cadaver Study. International Orthopaedics 35(11), 1611–1620 (2011)
15. Coobs, B., LaPrade, R., Griffith, C., Nelson, B.: Biomechanical Analysis of an Isolated Fibular (Lateral) Collateral Ligament Reconstruction using an Autogenous Semitendinosus Graft. The American Journal of Sports Medicine 35(9), 1521–1527 (2007)

Robot Colony Mobility in a Thermodynamics Frame

Antonio D'Angelo[1] and Enrico Pagello[2]

[1] Dept. of Mathematics and Computer Science, Univ. of Udine, I-33100, Italy
antonio.dangelo@dimi.uniud.it
[2] IAS-Lab, Dept. of Information Engineering, Univ. of Padua, I-35100, Italy
epv@dei.unipd.it

Abstract. In the last decade the development of multirobot systems has come to maturation providing a lot of important results in many applicative domains. Many paradigms and approaches have been devised to this aim but one of them seems very promising for future applications: dense colony of robots where the large numbers of individuals is combined with a very small dimension for each of them. Here, the key point is a behavior-based paradigm embedded in the mobiligence framework as it appears particularly suitable to deal with the sensing activity where the physics of the interaction is made explicit to take advantage from it. Within this point of view the paper explores a design method to deal with sensor information which, avoiding any symbolic representation, is maintained at a somewhat physical level as a metaphor of the events observed in the environment. The idea of *substratum* is introduced as a convenient representation of the physical level currently in use. The key properties of the thermal metaphor are considered and implemented to trigger appropriately a colony of robots to execute a collective task. The *temperature distribution*, *heat flux*, *diffusivity* and *dispersion* are all discussed as different aspects of the stigmergy included as a key feature of the swarm which forces each individual to behave collectively.

Keywords: roboticle, mobiligence, robot coordination, stigmergy, thermal metaphor.

1 Introduction

Humans, animals and even insects show adaptive behaviors as a key feature of being living systems. To an external observer such individual and social behaviors appear like intelligent sensory-motor coordinations, most of them essential for their survival, where the coordination mechanism implements the adaptation to the environment in form of *pre-cognition* and *anticipatory behavior*.

Hence, the adaptive behavior is an emergent property of living systems which stems from the interaction of their bodies, brain included, and the environment itself whose information are acquired dynamically through locomotion, object grasping and manipulation, etc... Starting from these considerations, Asama [2], has coined the term **mobiligence** referring to the intelligence which emerges through the interaction between an agent and its environment because of its mobility.

In its seminal paper Asama supposes that such an intelligence stems from the distinguishing properties of *embodied plasticity*, *abduction* and *co-embodiment* with the

S. Lee et al. (Eds.): Intelligent Autonomous Systems 12, AISC 194, pp. 457–468.
springerlink.com

environment. Within this approach he suggests to take into account both the behavior generated by perception and also the behavior generating knowledge which becomes the external and internal processing of flow of information through which agents can reason about. So we have location information, dynamical information and also experience, which refers more properly to the cognitive structure of the agent. From a different perspective, biological studies address physiological models useful to make hypotheses which can be integrated into engineered technologies and methodologies to grow up implementable dynamical systems. This approach is especially useful when a large number of robots must be coordinated to execute collective tasks where the interference for limited resource acquisition is critical.

To overcome this problem, instead of generating a specific model of the environment using local information, and considering that the model is only needed to deliver proper motor commands, one could claim the presence of a substratum which underlies both perception and action activities driving the flow of information accordingly.

For example, let us consider a colony of robot individuals performing the collective task of maintaining the group formation. Here, the main role of sensors is monitoring the task execution by suppling the control parameters with the right values to adjust the relative positions of individuals. The observed behavior can be interpreted as *gas diffusion process*, the substratum, where a number of robots move towards a region in the same fashion as a spreading gas.

Jantz et al.[13] and Kerr et al.[15] have used the kinetic theory of gases for analysing collision and realising sweep motion in a bounded region, Also, Kinoshita et al.[11] have defined and monitored suitable thermodynamic parameters of a robot group to identify its *macroscopic state*: random motion, periodic motion and deadlock. In both cases the substratum is more properly the *kinetic theory of gas*.

D'Angelo et al.[3] have used a thermodynamic approach to formulate the relationship between the effect of the behaviour of a single robot and both its diffusion and merging in a swarm, as it appears at macroscopic level. Each robot is interpreted as a gas particle, and the energy exchange is considered through thermodynamic equations. More recently, the fluid-dynamic-based model of roboticles [5] has been augmented with the convective motion [7] of the fluid driven by a temperature distribution which acts as stigmergic information and whose properties are discussed hereafter. The rest of the paper is organized as follow: Sect. 2 summarizes the key features of the roboticle model especially pointing out the autopoietic loop; Sect. 3 extends the model to a multirobot system whereas Sect. 4 discusses an example.

2 The Fluid Dynamic Metaphor

The behavior-based approach, including the roboticle model itself, is grounded on the so called *sensorimotor coordination* for the close connection between sensing and acting which drives the acquisition from the environment of all the relevant information to carry out robot tasks. Normally, data are processed at reactive level and only a small number of them cross the *deliberative fence* which converts the signal nature of sensing into an appropriate symbolic representation.

In fact, the role of sensor information is that of monitoring the physical objects through their relevant properties for the task execution. For example, the electrical metaphor is very popular and it is commonly used in many motion planning applications, i.e. Latombe [10]. Also Arkin [1] has used this metaphor to implement behaviors as a couple of perceptual and motor schemas.

Subsymbolic approaches [12], [9] are faced with processing a huge number of data [14], which come from many sources and which must deliver motor commands with a short latency time. Sensor information don't need to be converted into any symbolic representation but they can be maintained at physical level as a metaphor of observed events in the environment, depending on the physics of the interaction.

With this respect, the roboticle model suggests the *metaphor for the navigation task* by interpreting the motion as *it comes from the particle streaming in a fluid*. In this sense the roboticle model creates a substratum by fulfilling the operating environment with a fluid which flows from the source position to the target position and the robot follows one of its streamlines since they lap the obstacles without entering their contours.

Roboticle Model

The fluid dynamic metaphor ([4], [5], [6], [8]) implements the substratum as if sensor signals were coming from a really observed fluid. So, the substratum is the velocity field $\mathbf{V}$ of a fluid whose streaming is generated by the scalar potential F and the vector potential $\mathbf{M}$ termed, respectively, *dissipative function* and *internal momentum*, accordingly to the following equation

$$\mathbf{V} = -grad\ F - rot\ \mathbf{M} \tag{1}$$

where the vector potential $\mathbf{M} = M\hat{\mathbf{k}}$ has only one component, M, normal to the plain surface. Thus, roboticles are point-reduced robots whose dynamical model is based on the property to explore the environment where they are moving around. Their functioning stems from a simple and well-sound mechanism which triggers acquired information towards effectors and forces them along preset trajectories. Their behavior is completely described in terms of scalar and cross products between the current velocity $\mathbf{V}$ and the short arc $d\mathbf{r}$.

In fact, the scalar product, termed *effort*, can be understood as the *elementary work* made by the vector field $\mathbf{V}$ along the elementary trajectory arc $d\mathbf{r}$ whereas the not null component of the cross product, termed *percept*, provides the rate of trajectory change when roboticle drives away from its nominal trajectory. If we express them in a cartesian frame of reference through the cartesian components u and v of the velocity $\mathbf{V}$ and the cartesian components dx and dy of the short arc $d\mathbf{r}$, it yields to

$$\begin{aligned} \mathbf{V} \cdot d\mathbf{r} &= udx + vdy = Vds \\ \hat{\mathbf{k}} \cdot (d\mathbf{r} \wedge \mathbf{V}) &= vdx - udy = \delta P \end{aligned} \tag{2}$$

where δP accounts for the sensor information of the percept. If we make explicit the contributions of both potentials, we obtain

$$\begin{aligned} \delta P &= \delta L + dM & \qquad \delta L &= g_{11} dM - g_{12} dF \\ Vds &= \delta Q - dF & \qquad \delta Q &= g_{21} dM - g_{22} dF \end{aligned} \tag{3}$$

where δL and δQ are two auxiliar quantities called *committing effort* and *committed perception*, respectively. The parameters g_{ij} describe, at abstract level, how the roboticle governor's unit really works.

Autopoietic Loop
The previous relations establishes the key feature of the roboticle model, known as *autopoietic loop*. In fact, by simple substitutions, we can easily obtain

$$\begin{aligned} \delta P &= (1+g_{11})dM - g_{12}dF \\ Vds &= g_{21}dM - (1+g_{22})dF \end{aligned} \tag{4}$$

and, then, by introducing the quantities

$$\mathbf{K}_f = \frac{g_{21}}{1+g_{11}} \qquad \mathbf{K}_b = -\frac{g_{12}}{1+g_{22}} \tag{5}$$

called, respectively, *direct* and *reverse gains*, we can write the following more meaningful relations

$$\begin{aligned} \delta E_{ff} &= \mathbf{K}_b \left[\delta P + \delta P_{erc}\right] \\ \delta P_{erc} &= \mathbf{K}_f \left[Vds - \delta E_{ff}\right] \end{aligned} \tag{6}$$

where the quantities $\delta P_{erc} = g_{12}dF$ and $\delta E_{ff} = g_{21}dM$ have been introduced for reason of compactness. The graphical representation of the *autopoietic loop* is depicted in fig. 1 which stems directly from equations (6): all useful perceptual information enter the "black box" labelled $\mathbf{K}_f$ where they are coherently amplified to feed effectors so that the "black box" labelled $\mathbf{K}_b$ provides the necessary input information about effector functioning to be summed up with the sensor information coming from environment.

We conclude this short discussion by observing that the parameters g_{ij} are dimensionless because they are the ratio between quantities of the same type and, more important, they are only partially indipendent. In fact, the following identities hold

$$g_{11}g_{22} - g_{12}g_{21} = 1 \qquad g_{21} = g_{12} \tag{7}$$

and they justify that the autopoietic loop is completely described by assigning only the direct and reverse gains. Every instantiation of roboticle functioning requires a specific relation between these gains. For example, let us consider a robot moving around to detect meaningful beacons. We can design its control unit so that, if such a beacon is recognized, its behavior is regulated by the relation

$$\mathbf{K}_f = \frac{m\mathbf{K}_b}{\sqrt{1+(1-m^2)\mathbf{K}_b^2}} \tag{8}$$

and the observed behavior is depicted in fig. 2 where the highlighted robot trajectory is compared with the isothermal distribution detected around the obstacle. This topic will be discussed in some detail in the next sections.

3 The Thermodynamical Metaphor

If you look upon a colony of robots placed on a arena densely enough of individuals, you can regard the outermost robots as colony boundary and the internal dynamics shows each individual is moving in a *brownian motion* fashion. Within this model we can regard the individuals of the colony as **gas particles** moving around in a 2-dimensional space where each robot has no active sensor and its motion is driven by direction changing due to the contact with other robots.

The fluid dynamical metaphor, depicted by eqns. (3) and presented in Sect. 2, can be also interpreted in term of the first law of thermodynamics: the roboticle formulation [8] suggests to understand δP as the *thermal* unordered energy entering the robot's governor unit in the form of *perceptual flow* whereas Vds is the *mechanical* ordered work driving effectors as *effort*. Really speaking, the roboticle model makes use of two such equations, the former referred to its sensors and the latter to its effectors. With the same respect, the *committing effort* δL and the *committed perception* δQ are a kind of internal work and internal heat, respectively.

Heat Diffusion

But the collisions among individuals can be also interpreted as the *temperature* of the colony so that it can be used to trigger its purely reactive group behaviour which stems from a number of individuals immersed in a fluid with well-specified thermal properties. The *motion engine* is the result of the fluid dynamic metaphor augmented with a suitable temperature distribution. It animates the hypothetical fluid by introducing a *convective motion* inside the fluid by the well-known formula

$$\mathbf{H} = -\rho \; grad \; T \tag{9}$$

where **H** is the *heat flux* due to a given *temperature gradient* inside the fluid. Its *diffusivity* ρ takes different values in different positions since it contrasts selectively heat diffusion. Thus, *grad* T acts as thermomotive force which maintains the *heat flux* **H** whereas ρ can be assimilated to the environmental response to the applied gradient and it takes into account the agent distribution inside the colony which is assumed dense in the environment.

From the point of view of a robot colony the interpretation of the thermomotive force *grad* T yields to a model of interaction among individuals where the *diffusivity* ρ provides the necessary regulation of the heat flux **H**. Because this mechanism works globally, namely, it is triggered by the collective task, the motion engine for each individual acts locally on each roboticle[1] through an appropriate velocity field which implements the fluid dynamic metaphor for the individual.

Thermomotive Force

The fluid dynamic extension to the convective streaming metaphor is a different way to implement the stigmergic coordination on colony behavior[2]. The temperature level, which is a scalar quantity, can be interpreted as a *generalized pheromone* which stimulates the social behavior of the colony. For the aim of this paper we restrict the analysis to those behaviors which reduce interference among individuals.

If we review eqn. (9) from this point view, the interaction among individuals requires the thermomotive force to be bound to the dynamical sources of the fluid, namely, the dissipative function F and the internal momentum M. In our metaphor, the stationary

[1] The model we shall use for each individual of the robot colony.

[2] Namely, the implicit control of the collective task.

state of the convective motion should be responsible of the *maintainance property* of the behavior. This circumstance takes the form

$$\oint_{\mathscr{L}} \mathbf{H} \cdot d\mathbf{l} + \int_{\mathscr{S}} \mathbf{M} \cdot \hat{\mathbf{n}}\, dS = 0 \tag{10}$$

where the *heat flux* **H** is selected as it were the *magnetic field* generated by the *current* **M**. This assumption ensures that **H** is fully compatible with the possibly steady state of the fluid dynamic of the roboticle velocity field.

A further property of the *heat flux* **H** relates the convective motion of the fluid to its attractors and repulsors. To this aim we start from the well-known principle of *heat flux conservation* by augmenting it with the *source density* F[3] to brings into equilibrium unbalanced gradient diffusion with the accumulated heat

$$\oint_{\mathscr{S}} \mathbf{H} \cdot \hat{\mathbf{n}}\, dS + \frac{d}{dt} \int_{\mathscr{V}} k_e T\, dV = \int_{\mathscr{V}} F\, dV \tag{11}$$

Now, let us transform the preceding integral relations into a more usable derivative form. To this aim we apply well-known mathematical theorems (such as Stokes) yielding to

$$\mathbf{M} = -rot\ \mathbf{H} \qquad\qquad F = div\ \mathbf{H} + k_e \frac{\partial T}{\partial t} \tag{12}$$

which bind the thermal flux to the internal momentum **M** and the dissipative function F. The latter generalizes the thermal energy balancing by equating the sum of heat flux exiting a close region and its accumulation over the time (right side) with possible sources or sinks dislocated in the region itself (left side). Thus, the dissipative function F is just the mechanism which dissipates the thermal energy provided by the temperature gradient of the fluid inside the region.

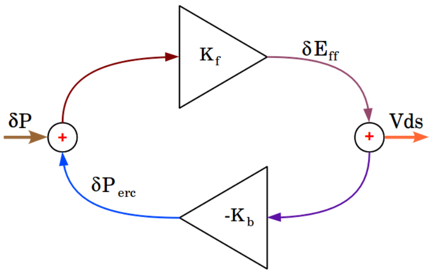

Fig. 1. How the autopoietic loop controls a moving roboticle

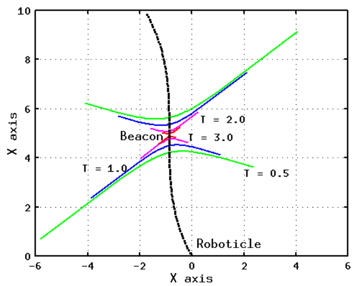

Fig. 2. Temperature-based representation of a beacon driving a roboticle

[3] The dissipative function previously discussed.

4 Stigmergic Heat Equation

Heat diffusion is central in the definition of the convective motion of roboticles. More precisely, in the following we shall show that **H** obeys the non-homogenous heat equation. This statement comes easily from eqns. (1) and (12), using well-known vectorial identities, which yield to the non-homogenous heat equation

$$\nabla^2 \mathbf{H} - \frac{k_e}{\rho}\frac{\partial \mathbf{H}}{\partial t} = -\mathbf{V} \tag{13}$$

also by substituting the involved quantities appearing in (9). The time derivative term includes the scalar function ρ which only depends on coordinates since it characterizes the environment response to the heat flux. A similar equation can be obtained for the temperature T as it will be explained in the next subsection.

Diffusivity
The coordination of a dense colony of robots takes advantage of the thermal properties of the fluid[4] in what it provides the designer with the explicit implementation of the stigmergic response of the robot colony. In fact, the temperature distribution triggers the streamline distribution within the fluid and this property strongly depends on the diffusivity ρ, namely, a scalar quantity which defines how the environment reacts to the convective motion.

Because the fluid dynamic motion of roboticles depends on the internal momentum and the dissipative function, let us make explicit such a relation. So, if we start from the internal momentum, we have

$$\mathbf{M} = -rot\mathbf{H} = rot(\rho \nabla T) = \nabla \rho \wedge \nabla T \tag{14}$$

namely, remembering that **M** has only one component directed normal to the plain and multiplying both sides by ρ and rearrange the terms, we obtain

$$\rho M = H_1 \frac{\partial \rho}{\partial y} - H_2 \frac{\partial \rho}{\partial x} \tag{15}$$

where also eqn. (9) has been considered. With the same respect, starting from the latter equation appearing in (12), we can write

$$F = div(-\rho \nabla T) + k_e \frac{\partial T}{\partial t} = -\rho G - \nabla T \cdot \nabla \rho \tag{16}$$

where we have introduced the new scalar quantity G defining the non-homogenous heat equation for the temperature T,

$$\nabla^2 T - \frac{k_e}{\rho}\frac{\partial T}{\partial t} = G \tag{17}$$

Now, if we multiply both sides of the preceding relations by the diffusivity ρ and rearrange the terms, we obtain

$$\rho(F + \rho G) = H_1 \frac{\partial \rho}{\partial x} + H_2 \frac{\partial \rho}{\partial y} \tag{18}$$

[4] Which hypothetically laps roboticles.

also remembering the heat flux definition given by eqn. (9). Thus, eqns. (15) and (18) show how the diffusivity influences the heat flux making evident the dependency of the internal momentum and the dissipative function of roboticles.

Temperature Distribution

The thermal properties of the fluid dynamic metaphor are really noteworthy. However, we are not interested to deal with the convective motion of the fluid in general but we want to find out temperature distributions which can solve easily the *problem of the stigmergic control* inside a group of robots. To this aim, let us review eqn. (9) by introducing the polar coordinates to compute the differential form. We have

$$-\rho dT = (H_1x + H_2y)\frac{dr}{r} + (H_2x - H_1y)d\varphi \tag{19}$$

so that, if we take the diffusivity in a given environmental point as the scalar product of the heat flux in that point and its distance $\mathbf{r}$ from the origin of the stigmergy, namely, $\rho = \mathbf{H} \cdot \mathbf{r} = H_1x + H_2y$, the preceding equation yields to

$$-dT = \frac{dr}{r} + \frac{tan\Psi - \tan\varphi}{1 + tan\Psi\, tan\varphi}d\varphi \qquad tan\Psi = \frac{H_2}{H_1} \tag{20}$$

having introduced the angle Ψ for the cartesian components of the heat flux. Now, the integration of the differential form expressing the temperature T is straightforward; let us rewrite it into a more compact form

$$-dT = \frac{dr}{r} + tan(\Psi - \varphi)d\varphi \tag{21}$$

and the temperature distribution is determined by the only directional component. This is a very interesting property because we want the convective motion of the fluid be interpreted as a suggestion for the roboticles to move on useful trajectories. To this aim we shall consider the temperature distributions built as follow.

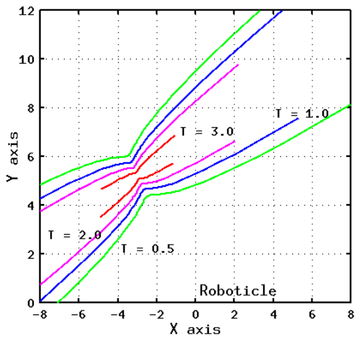

Fig. 3. The obstacle representation as it is detected by a roboticle

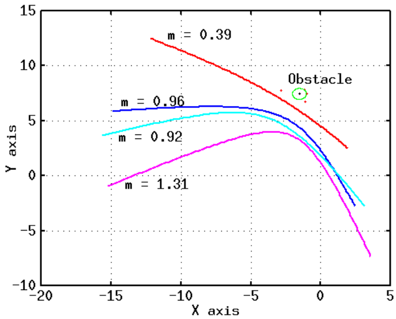

Fig. 4. A group of roboticles forced by an obstacle to turn left

First of all we define the direction Ψ of the heat flux by the sum of the *basic directions* Ψ_i with i ranging form 1 to N and each Ψ_i bound to the radius direction φ with the simple relation

$$tan\Psi_i = k_i \, tan\varphi \qquad tan\Psi_i = \frac{1}{k_i \, tan\varphi} \qquad i = 1,..,N \tag{22}$$

so that the heat direction can be easily computed using the composition rule for the tangent, namely, $tan\Psi = tan(\Psi_1 + \Psi_2 + ... + \Psi_N)$. We shall term this kind of temperature allocation *direction driven distribution* because it highlights the response of a roboticle to the obstacle with the respect of assigned driving directions. For simplicity, we have positioned the obstacle on the center of the frame of reference.

This property provides some degree of assimetry for the roboticle motion approaching the obstacle. In such a way the environment around the obstacle appears anisotropic and Ψ_i is termed the *i-th driving direction*. In the following we shall consider the case of two driving directions at most. In fact, in all the simulations we have found that the stigmergy originating the isotropical, monopolar and dipolar temperature distributions can cover the most cases of interest.

Monopolar Source – When a monopolar source is assumed, only one driving direction is considered. In that case it is more convenient to take the constant k_1 with the form $k_1 = \frac{1-p}{1+p}$ so that the heat direction $tan\Psi$ is either $\frac{1-p}{1+p}s$ or $\frac{1+p}{1-p}\,\frac{1}{s}$ where, for convenience and compactness, we have introduced the auxiliar variable $s = tan\varphi$. In the former case the temperature distribution for an obstacle put on the center of the frame of reference, takes the form

$$a^2 \exp(-2T) = r^2(1 + p\cos 2\varphi) \tag{23}$$

An example of this distribution appears in fig. 2 where the obstacle is used as beacon by a roboticle whose autopoietic loop is triggered with the dissipative component greater than the conservative one ($m < 1$).

Dipolar Source – A more interesting situation stems from a dipolar source of stigmergy. For the following discussion we shell assume $tan\Psi_1 = \frac{1-n}{f}s$ and $tan\Psi_2 = -\frac{1-n}{f+n}s$ yielding to the direction component of the temperature appearing below

$$tan\Psi = \frac{ns}{p + (1-n)s^2} \qquad p = \frac{f+n}{1-n}f \tag{24}$$

where the auxiliar quantity p has been introduced for convenience. In this case, the temperature distribution takes the form

$$a^2 \exp(-2T) = x^{2(1-n)} \left(px^2 + y^2\right)^n \tag{25}$$

with the obstacle centered in the origin of the frame of reference. An example of a roboticle observing such an obstacle is shown in fig. 3.

Dispersion

Up to now we have considered only the temperature distribution designed to track actively the objects in the environment. Their recognition and interpretation is made on the basis of the stigmergic information associated with them. However, the collective behavior of a colony depends on both the single behavior of each individual and how each robot reacts to the behavior of the nearby individuals. The thermal metaphor deals with this key feature by factorizing the contribution of the diffusivity ρ by introducing a new scalar quantity W, termed *dispersion*, such that

$$\rho = W \exp(-kT) \tag{26}$$

where k is an auxiliar parameter useful to describe the relative weight of the temperature, namely, the stigmergic factor, with the respect to how the colony influences each robot individual.

In many cases we can assume $k = 2$ but in the avoiding obstacle example, briefly discussed, we shall take $k = \frac{2}{n}$ where n is a measure of the regulating parameter q which controls the autopoietic loop of each roboticle, reported below

$$\mathbf{K}_f = \frac{q\mathbf{K}_b}{q + \sqrt{1 + \mathbf{K}_b^2}} \qquad q = \frac{1-n}{1+n} \tag{27}$$

When a roboticle detects the obstacle, the autopoietic loop adapts its behavior by trying to match the parameter n with the same describing the obstacle as temperature distribution (see fig. 3). Now the obstacle acts as a cue with suggests the most appropriate trajectory for the roboticle. Such a situation is depicted in fig. 4 where a few roboticles show their motion around the obstacle. Each of them has modified its autopoietic loop choosing a different value[5] for m, with $m = \sqrt{n}$.

However, as it appears from fig. 4, different roboticles provide different positions for the same obstacle; its real position is depicted by the green circle. The dispersion function used by this example allows roboticles to approach the obstacle uniformly except for a specified direction. It is the watershed which delimits the area beyond which roboticles cannot access. In this case the dispersion function W can be approximated by $W_0 r^4(1 + \cos 2\varphi)$ where the distance r and the direction φ are referred to a frame of reference centered on the obstacle and the y-axis is taken as watershed. As it is not directly accessible from the colony, this fact motivates the different positions of the same obstacle detected by the roboticles.

5 Conclusion

In the paper we have presented a methodology design aimed to provide a colony of robots with a coherent collective behavior. The guideline has been the behavior-based paradigm of roboticles embedded in the more general framework of mobiligence in what sensor information, maintained at subsymbolic level, balance the behavior generated by perception with the behavior generating knowledge about the environment. This activity is carried out by the so called autopoietic loop which controls individual robots without a real interpretation of sensing at symbolic level.

By relating the autopoietic loop of each individual with the emergent collective behavior of the colony we have shown that its role can be fully understood through the

[5] i.e., m=0.96 for the blue trajectory, m=0.39 for the red one.

stigmergic properties of the temperature distribution of the colony. In fact, this paradigm has been devised to extend coherently the roboticle model to a multirobot system: the information exchanging amomg individuals occur without considering explicitly the group because the perceptual interpretation is made from the point of view of the colony itself.

This kind of stigmergy has been obtained by assuming that each individual robot is acting under the influence of a thermomotive force, namely, a temperature gradient generated accordingly to the obstacles encountered during the roboticle motion. It defines indirectly the collective task of the group, provides an effective interpretation of the obstacles and motivates their presence. Moreover, we have argued some properties about the relationship between the diffusivity ρ, the temperature T and the dispersion W. A short example of a colony which encounters a meaningful obstacle, suggesting a change of direction, has been discussed. Simple simulations have shown that each individual robot provides approximatively the same interpretation of the thermal field and, moreover, intuitive properties of the diffusivity can be established. With the respect to the previous work we have found a general method to assign a thermal distribution to obstacles which, coherently to the required collective task, depends on their functional anisotropy.

Acknowledgements. This work was partially supported by a grant of the University of Padua's Special Project on *Mobility, Perception, and Coordination for a Team of Autonomous Robots*.

References

1. Arkin, R.: Behavior-Based Robotics. The MIT Press (1998)
2. Asama, H., Yano, M., Tsuchiya, K., Ito, K., Yuasa, H., Ota, J., Ishiguro, A., Kondo, T.: System principle on emergence of mobiligence and its engineering realization. In: IROS 2003, Las Vegas, NV, pp. 1715–1720 (2003)
3. D'Angelo, A., Funato, T., Pagello, E.: Motion control of dense robot colony using thermodynamics. In: DARS 2008, pp. 85–96. Springer, Tsukuba (2008)
4. D'Angelo, A., Ota, J., Pagello, E.: How intelligent behavior can emerge from a group of roboticles moving around. In: IROS 2003, Las Vegas, NV, pp. 1733–1738 (2003)
5. D'Angelo, A., Pagello, E.: Making collective behaviours to work through implicit communication. In: Casals, A., Dillmann, R., Giralt, G. (eds.) ICRA 2005, Barcelona, pp. 81–87 (2005)
6. D'Angelo, A., Pagello, E.: From mobility to autopoiesis: acquiring environmental information to deliver commands to the effectors. In: IAS 2009, pp. 640–647. IOS Press, Tokyo (2006)
7. D'Angelo, A., Pagello, E.: A thermodynamic framework for robot colony control. In: IAS 2011, pp. 259–270. IOS Press, Ottawa (2010)
8. D'Angelo, A., Pagello, E., Yuasa, H.: Issues on autonomous agents from a roboticle perspective. Journal of Intelligent and Robotic Systems, 389–416 (2008)
9. Kohonen, T.: Self-Organizing Maps, Information Sciences, vol. 30. Springer (2001)
10. Latombe, J.C.: Robot Motion Planning. Springer (1991)
11. Kinoshita, M., Watanabe, M., Kawakami, T., Yokoi, H., Kakazu, Y.: Macroscopic quantitative observation of multi-robot behavior. In: Computational Intelligence and Multimedia Applications, Yokosuka, Japan, pp. 190–194 (2001)

12. Pisokas, J., Nehmzow, U.: Subsymbolic action planning for robots: Generalised representations of experience. In: Groen, F., Amato, N., Bonarini, A., Yoshida, E., Krose, B. (ed.) 8th Conference on Intelligent Autonomous Systems, pp. 666–673. IOS Press (2004)
13. Jantz, S.D., Doty, K.L., Bagnell, J.A., Zapata, I.R.: Kinetics of robotics: The development of universal metrics in robotic swarms. In: Florida Conference on Recent Advances in Robotics, Miami, USA (1997)
14. Weser, M., Jockel, S., Zhang, J.: Fuzzy multisensor fusion for autonomous proactive robot perception. In: IEEE International Conference on Fuzzy Systems, pp. 2262–2267 (2008)
15. Kerr, W., Spears, D., Spears, W., Thayer, D.: Two Formal Gas Models for Multi-agent Sweeping and Obstacle Avoidance. In: Hinchey, M.G., Rash, J.L., Truszkowski, W.F., Rouff, C.A. (eds.) FAABS 2004. LNCS (LNAI), vol. 3228, pp. 111–130. Springer, Heidelberg (2004)

Throwing Darts Training Support System Based on Analysis of Human Motor Skill

Hiroshi Yamaguchi and Toshiyuki Kondo

Tokyo University of Agriculture and Technology, 2-24-16 Naka-cho, Koganei, Tokyo 183-8588, Japan
yamaguchi@livingsys.lab.tuat.ac.jp, t_kondo@cc.tuat.ac.jp

Abstract. Measurement, analysis, and modeling of human motor functions have been intensively studied because human motor skills are useful for various applications, such as digital archiving, sports training, rehabilitation, etc. Targeting the sport training support application, in the paper, we focus on a throwing darts movement that requires sophisticated control of the upper arm to realize precise throwing, and we investigate the relationship among motion trajectories, muscle activities, and throwing accuracy, from the viewpoint of release timing. Experimental results showed that skilled subjects demonstrated small temporal variance and a fixed timing of release; it was just before the moment their elbow angular velocity became maximum. Based on the findings, we developed a training support system for throwing darts. To evaluate validity of the proposed system, we executed training experiments of beginners.

1 Introduction

Recently, measurement, analysis, and modeling of human motor functions have been intensively studied (e.g., [1, 2, 3]), because knowledge about human skilled motion and its extraction techniques are valuable for various applications, such as digital archiving of skilled technicians, sports training support system for beginners, or developing a novel rehabilitation procedure for the aged or disabled people. Targeting these practical applications, we had focused on the investigation of human motor skills, such as basketball dribbling[4] and throwing darts movement[5].

Especially in the throwing darts study[5], we investigated the relationship among motion trajectories, muscle activities, and throwing accuracy. The previous study suggested that a fixed throwing trajectories was obtained first, and muscle activities were subsequently optimized, in the throwing skill acquisition process. Moreover, a resultant dart position on a dartboard would be a function of the position and speed (i.e., direction) of the dart at a release timing, although there is a report referring to the timing is not a limiting factor[6]. In the previous work, however, we could not explicitly consider release timing, because a precise release timing was difficult to measure by using a vision-based motion capture system, even if we used a high-speed camera for the purpose.

In the paper, we especially focus on measuring a precise release timing for further analysis of the throwing darts skill. For this aim, we develop an apparatus for measuring a precise release timing by using a force sensitive resistor (FSR). Using the device,

S. Lee et al. (Eds.): Intelligent Autonomous Systems 12, AISC 194, pp. 469–478.
springerlink.com

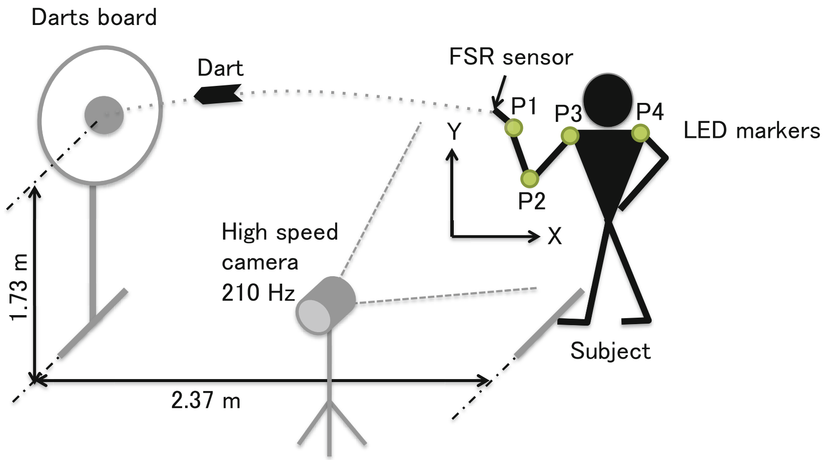

Fig. 1. Measurement system for off-line analysis

we can simultaneously record release timing, motion trajectories, and surface EMG signals to investigate the relationship among motion trajectories, muscle activities, and throwing precision, from the viewpoint of release timing.

Based on the findings, we develop a training support system for throwing darts, and we execute training experiments to evaluate the validity of the proposed system.

2 Analysis of Throwing Movement

To be clear the relationship among motion trajectories, muscle activities, release timing, and throwing precision, we investigate off-line analysis of throwing movements.

2.1 Method

2.1.1 Subjects

For the purpose of the throwing movement analysis, four healthy young right-handed male subjects (22.0±1.0 years old, height: 1.73±0.03 m, weight: 63.0±5.0 kg) participated in the experiments as volunteers. Two were experts (subject A and B), and two had less than one year of experience (subject C and D).

2.1.2 Procedure

Each subject threw darts aiming at the center of the dartboard (i.e., the bull) three times in one trial. The trial was repeated 16 times, for a total of 48 throws per subject. The throwing conditions were based on the rules of the World Darts Federation (Fig. 1) [7]. The height of the bull was set to 1.73 m, and the distance between the dartboard and the throwing line was 2.37 m.

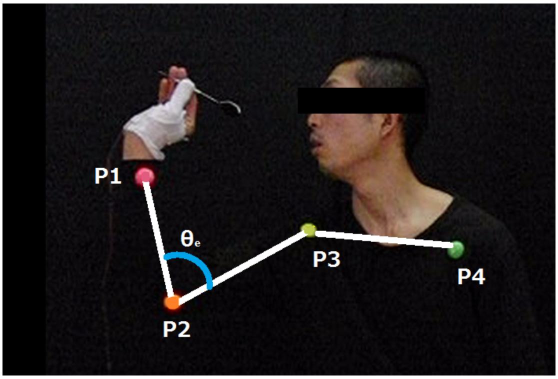

Fig. 2. Position of markers

For convenience, we decompose the throwing darts movement into four phases by defining three distinct timings. The first timing, *take back*, corresponds to the first point at which the wrist (P1) comes to rest after starting the motion. The second timing, *release* corresponds to the moment the darts is freed from the hand, and the third timing, *completion of throwing*, is defined as the first moment when the horizontal velocity of the wrist (P1) reduces to zero after the *take back*.

During the trials, we captured motion data at 210 Hz using a high-speed camera (CASIO, EX-FH20). To retrieve the upper limb movement from the video, we used LED markers, which were attached to four positions; wrist, elbow, right and left shoulder (Fig.2, P1, P2, P3, and P4), respectively. The video was analyzed by using a motion analysis software (PV-STUDIO 2D, L.A.B. Inc.). According to the motion data, the elbow joint angle (θ_e) was calculated as shown in the figure.

The EMG data were sampled at 1.0 kHz from four target muscles, the *deltoid muscle*, *triceps brachii muscle*, *biceps brachii muscle*, and *extensor carpi ulnaris muscle*, the same muscles as in our previous study [5].

To measure a release timing precisely, we developed a measuring apparatus by using a force sensitive resistor (FSR) sensor, which detects the changes of pressure between thumb and index finger. To eliminate the effect of unpleasantness resulting from the use of the FSR sensor device, all data measured in the first three trials were discarded from the analysis.

After the experiments, we took out the region of interest, i.e., before and after 0.5 seconds at the *take back* from the measured data. The captured motion trajectories were smoothed by the moving average for each of the five points. The motion trajectories were normalized by the relative coordinates centered on the right shoulder position at the *take back*. Furthermore, the EMG data were band-pass filtered (cutoff frequency of 10–500 Hz) and smoothed by the moving average for each of the 10 points. The final dart destinations were recorded in a coordinate system centered on the board.

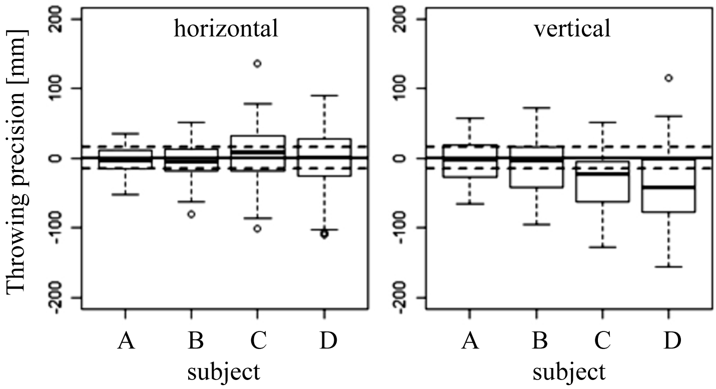

Fig. 3. Throwing precision (A, B:experts, C, D:beginners)

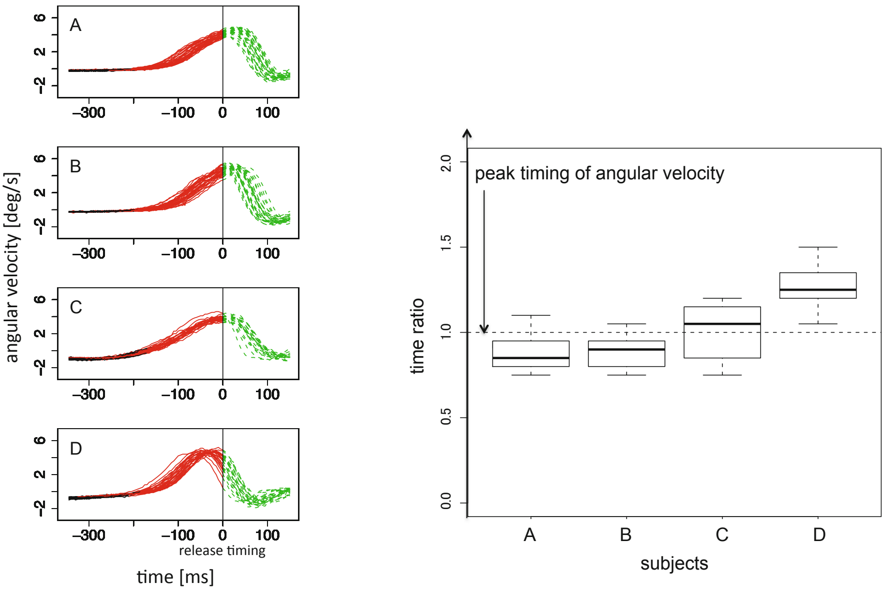

Fig. 4. Left: Elbow joint angular velocities ($\dot{\theta}_{elbow}$) aligned at release timing. Right: Distribution of release timings aligned at peak of elbow joint angular velocity.

2.2 Results

2.2.1 Precision

Fig.3 shows the statistical distribution of the final destinations of the darts. The left graph corresponds to the horizontal distribution and the right graph corresponds to the

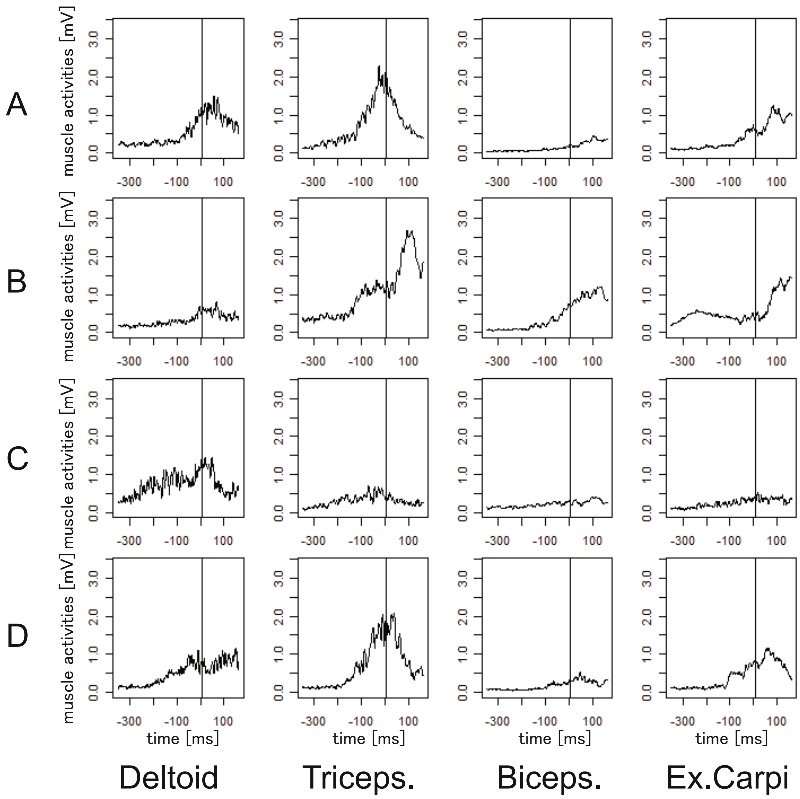

Fig. 5. Muscle activities (EMG) aligned at release timing

vertical distribution. The horizontal dashed lines represent the bull area (approx. 16 mm). As can be seen from the figure, the resultant distribution appears to be related to experience. We can observe that the beginners tend to be downward in the vertical result. This tendency is consistent with Bazzucchi's findings, that beginners' throwing tends to be collected below and spread from side to side [1].

2.2.2 Release Timing

Fig.4 left shows elbow joint angular velocities across the trials aligned at the release timing. From the result, it seems that the skilled subjects (i.e., subject A and B) demonstrated small temporal variance and maintained a fixed release timing; it was just before the peak moment the elbow joint angular velocity became maximum. On the contrary, we can see that beginner's release timing (especially subject D) showed large variance and delay.

This is clearly confirmed in Fig.4 right graph, which represents the distribution of the resultant release timing across the trials aligned at the peak of the elbow joint angular velocity (here, the time ratio 0.0 and 1.0 correspond to the *take back* and the peak, respectively).

2.2.3 Muscle Activities

Fig.5 demonstrates rectified and averaged time series of EMG signals during the throwing period aligned at the release timing (left to right: the *deltoid muscle*, *triceps brachii muscle*, *biceps brachii muscle*, and *extensor carpi ulnaris muscle*). The vertical line in each graph indicates the release timing.

As shown in the figure, we cannot confirm a distinct relationship between the muscle activities and throwing precision, because the result of subject D (beginner) resembles that of subject A (expert). However, the muscle activities measured from subject A perfectly represent ideal features, i.e., the agonist (*triceps brachii muscle*) is activated just before the release timing, and the antagonist (*biceps brachii muscle*) is relaxed during the throwing period. Therefore it seems that subject D has good potential to be an expert because he has already optimized muscle activities for throwing darts.

On the other hand, we confirm a co-contraction of antagonist muscle in subject B. It implies that his muscle activities have not yet been optimized. In the case of subject C, we cannot confirm the peak of agonist activity since his release timing was varied at the every trials.

3 Training Support System

Based on the findings explained in the previous section, we hypothesized that optimizing the release timing would improve throwing precision, especially in vertical direction. To clarify this hypothesis, we developed a throwing darts training support system (Fig.6), and executed training experiments of beginners to evaluate the validity of the system.

3.1 Method

3.1.1 System

As shown in Fig.6, we used a 3D motion capture system (Radish/3D, Library Inc.) with high speed camera (150 Hz). For this aim, subjects wore a black T-shirts with color markers (see Fig.2). This enables online measurement of the elbow joint angular velocity. Subjects also put a FSR sensor on their thumb to detect the precise release timing.

After each throwing, subjects can review the relationship between the release timing and the elbow joint angular velocity through a visual feedback displayed on a monitor besides them (Fig.7). In the visual feedback, subjects can also confirm the difference from an ideal release timing that of subject A explained in the previous section.

3.1.2 Subjects

To evaluate the proposed system, four healthy young right-handed male subjects (height: 1.76$\pm$0.06 m) participated in the experiment as volunteers (subject a, b, c, and d). They had no experience of playing darts.

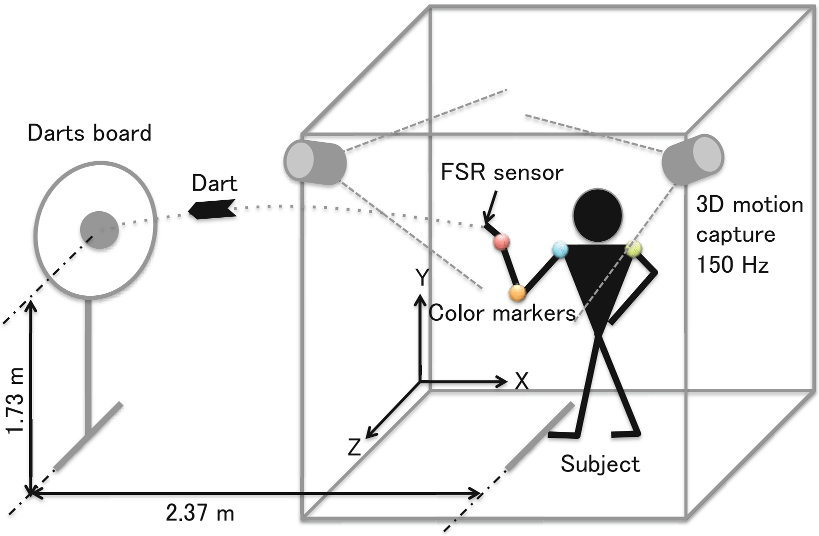

Fig. 6. Overview of training support system for throwing darts

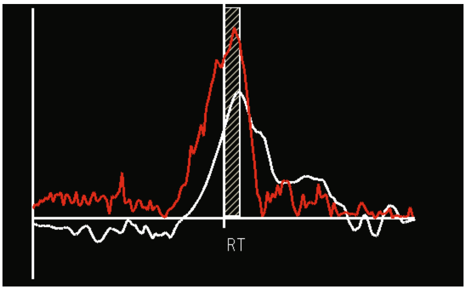

Fig. 7. Visual feedback used for throwing darts training includes elbow joint angular velocity and ideal release timing. Online result (red) and the expert result for reference (white) were displayed together.

3.1.3 Procedure

Before training, all subjects executed eight trials (i.e., 24 throws) to confirm their baseline throwing precision. After the *pre-test*, each subject executed training sessions using the proposed training system. Each training session includes 108 throws, subject a experienced one session, subject b–d experienced three sessions. After the training, *post-test* was executed likewise the pre-test.

3.2 Results

Fig.8 shows distributions of horizontal and vertical throwing precision before and after training sessions (i.e., pre and post-tests). From the result, we can see that subject b

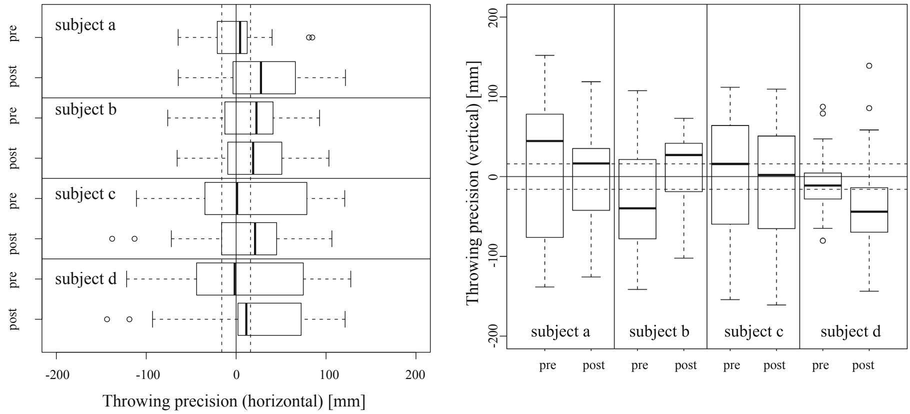

Fig. 8. Change of the throwing precision in horizontal (left) and vertical (right) directions

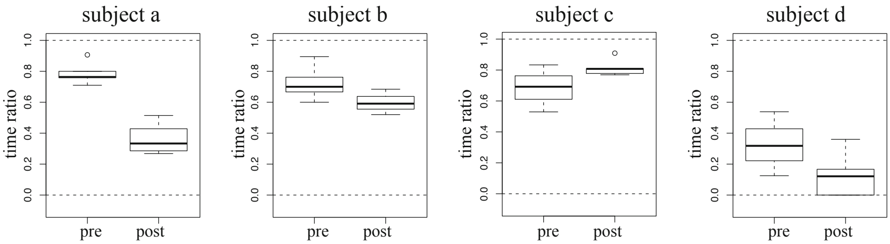

Fig. 9. Change of the release timing aligned at the peak of elbow joint angular velocity

and c indicate a tendency of improvement or maintaining in both directions; on the contrary subject a and c show degradation of the precision either in horizontal or vertical direction. In addition, Fig.9 shows change of the release timing aligned at the peak of elbow joint angular velocity. This figure demonstrates that the release timing of subject b and c converged into a fixed timing with small variance, likewise subject A in Fig.4. Based on these results, we have considered that our hypothesis — optimizing release timing improves throwing precision — would be correct.

Meanwhile, we have suspected the reason subject a or d got worse is as follows. In subject a case, it is probably caused by shortage of training sessions, because his vertical precision seemed to be improving. On the other hand, one of the reasons why the result of subject d got worse is that the throwing trajectory (elbow joint) shown in Fig.10 was quite different with that of the target (subject A). Since the subject had a different throwing strategy, the visual feedback given by the proposed training support system might confuse his motor learning process.

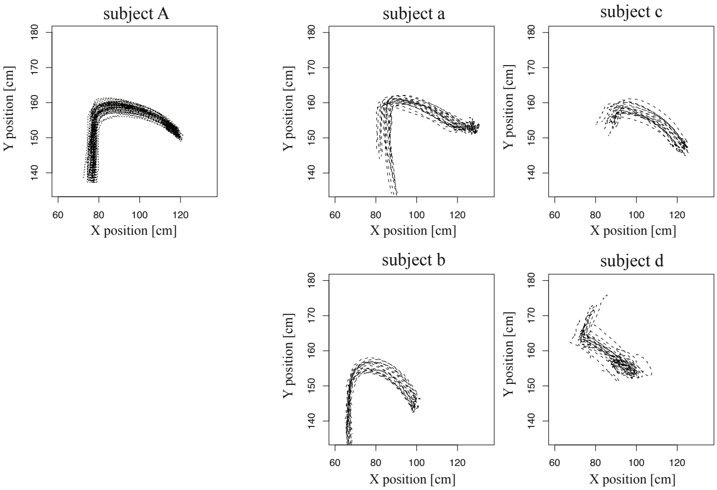

Fig. 10. Trajectories of wrist (P1); target trajectory (left, subject A) and resultant trajectories in post-test (right, subject a-d)

4 Conclusion

In the paper, we have presented a relationship among motion trajectories, muscle activities, and throwing precision, from the viewpoint of release timing. Experimental results show that skilled subjects demonstrate small temporal variance and a fixed release timing that is just before the moment the elbow angular velocity becomes maximum. Based on the feature, we developed a training support system for throwing darts. Through training experiments of four beginners, we can confirm that the validity of the proposed training support system.

Acknowledgements. This research has been partially supported by a Grant-in-Aid for Scientific Research (B) (21360201, 23300216) from MEXT.

References

1. Bazzucchi, I., Riccio, M.E., Felici, F.: Tennis Players show a lower coactivation of the elbow antagonist muscles during isokinetic exercises. Journal of Electromyography and Kinesiology, 752–759 (2008)
2. Hung, Y.-C., Kaminski, T.R., Fineman, J., Monroe, J., Gentile, A.M.: Kaminski, Julie Fineman, Jane Monroe, A.M.Gentile: Leaning a multi-joint throwing task: a morphometric analysis of skill development. Experimental Brain Research, 197–208 (2008)
3. Sakurai, S., Ohtsuki, T.: Muscle activity and accuracy of performance of the smash stroke in badminton with reference to skill and practice. Journal of Sports Sciences 18, 901–914 (2000)

4. Abe, S., Nozawa, T., Kondo, T.: A Proposal of EMG-Based Training Support System for Basketball Dribbling. In: Smith, M.J., Salvendy, G. (eds.) HCI International 2009, Part I. LNCS, vol. 5617, pp. 459–465. Springer, Heidelberg (2009)
5. Yamaguchi, H., Kondo, T.: Analysis of Motor Skill for Throwing Darts: Measurement of Release Timing. In: Proceedings of SICE Annual Conference (2011)
6. Smeets, J.B.J., Frens, M.A., Brenner, E.: Throwing darts: timing is not the limiting factor. Experimental Brain Research 144, 268–274 (2002)
7. W.D.F.: http://www.dartswdf.com/aa_darts/

Muscle Activities Changing Model by Difference in Sensory Inputs on Human Posture Control

Ryosuke Chiba[1], Hiroaki Ogawa[2], Kaoru Takakusaki[3], Hajime Asama[4], and Jun Ota[2]

[1] Graduate School of System Design, Tokyo Metropolitan University
6-6 Asahigaoka, Hino-shi, Tokyo 191-0065, Japan
rchiba@sd.tmu.ac.jp
[2] Research into Artifacts, Center for Engineering (RACE), The University of Tokyo, Chiba, Japan
{ogawa,ota}@race.u-tokyo.ac.jp
[3] Research Center for Brain Function and Medical Engineering, Asahikawa Medical University, Asahikawa, Japan
kusaki@asahikawa-med.ac.jp
[4] Department of Precision Engineering, The University of Tokyo, Tokyo, Japan
asama@robot.t.u-tokyo.ac.jp

Abstract. For understanding of human posture control, changes in muscular activity caused by changes in sensory inputs are very important because the control mechanism is complicated with integrating multi-inputs and outputting various and simultaneous muscular activity. In this research, we aim to obtain quantitative changes in muscular activity caused by changes in sensory inputs. For this purpose, we propose a method to be founded on the idea that muscle activity is divided into external force elements and internal elements. With this method, we can show the existence of internal muscular activity as well as external muscular activity. And it is considered that new model of human posture control with the difference of sensory inputs might be obtained.

Keywords: mobiligence, human posture control, multi modality, muscle activity.

1 Introduction

Humans control their posture well by controlling the muscle activity of the whole body with the cranial nervous system using multi-sensory inputs. The construction of sensory inputs and muscular activity model has a significant meaning medically and biologically because this model leads us to understand how the brain functions. Thus, it is important to examine the relationship between senses and muscular activity as the first steps in constructing this model.

In former studies, the human posture control was researched by Nashner[1] and Bottaro[2]. In these studies, however, changes in muscular activity that resulted from changes with sensory inputs integration were not discussed clearly.

In other some resources, the posture controls with the different sensory inputs are modeled in focus on torque controls at each joint. Peterka[3] propose the posture

S. Lee et al. (Eds.): Intelligent Autonomous Systems 12, AISC 194, pp. 479–491.
springerlink.com

control model with PID control for understanding of influences between the sensory inputs and torque outputs (see Fig.1). In this paper, the influences of sensory inputs are just summed with certain weights at an integrator. Therefore they consider the influences of sensory inputs independently. Kooij[4] propose the posture control model with Kalman filter for the estimation of sensory noise and human state based on their previous work[5].

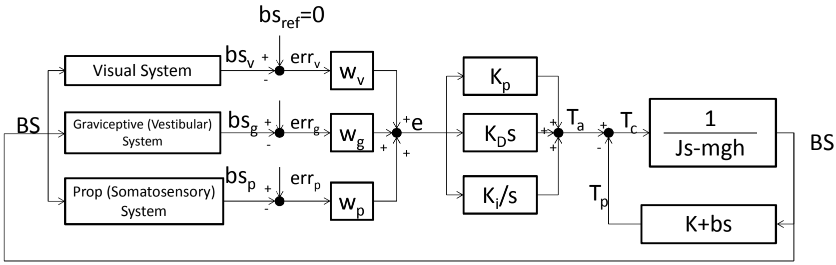

Fig. 1. "Independent channel" model of sensory integration in postural control showing a weighted addition of contributions from visual, proprioceptive, and graviceptive systems to the generation of an active corrective torque, T_a, as well as a passive torque contribution, T_p, related to body movement relative to the feet[3].

In these previous researches, the outputs are considered as torque of each joint. However, it is considered that human control not torque but muscular activity connected to neurons in spinal cord. The posture might be controlled from sensory inputs to muscular activity through many neurons. The muscular activities are various in the same torque because of the existence of flexor and extensor muscles. In other words, torque at each joint makes "external force" for the human posture directly, and the muscular activity makes not only "external force" but also "internal force" such as stiffness at each joint. In the same posture, the outputs of the posture control may be different because of the existence of the "internal force" with the difference of sensory inputs.

For example, a person with Parkinson's disease makes action with high muscle tonus but the changes of their posture is very small with very low torque. It can be considered that they make "very high internal force" and "very low external force".

Therefore, this paper proposes a method to obtain quantitative changes in muscular activity caused by changes in sensory inputs. From the understandings of quantitative changes in muscular activity, the internal force by the changes of sensory inputs may be found.

To achieve this purpose two challenging points exist:

i) How to change sensory inputs with the changes of muscular outputs

ii) How to obtain the quantitative "internal" muscular activity without "external" muscular activity

Regarding the changes of the sensory inputs, we propose the method of changing sensory inputs by inhibiting or stimulating three senses (visual sense, vestibular sense and somatosensory sense) which are considered closely related to posture control[3],[4]. Regarding the internal muscular activity, muscle activity changes seem to occur when an external force is applied to the body causing posture changes. Thus, we propose a method to estimate changes in muscular activity by external force and exclude them.

In this study, maintaining a standing posture is targeted due to measuring changes in muscular activity by sensory inputs because it is a simple movement limited to changes in muscular activity. In addition, physically-healthy persons are targeted because the how the brain functions may differ from that of those who are physically-challenged.

2 Proposed Method

It is assumed that the muscular activity of posture control is expressed in elements changed by external forces and elements as indicated by the sensory inputs as the internal force, making the following formula applicable:

$$g_i(Condition_j) = Activity_{ij} - f_i(CoP_j) \qquad (1)$$
$$i = 1, \dots, n \qquad j = 1, \dots, m$$

where $Activity_{ij}$ is scalar of the ith muscular activity in the condition j and $f_i(CoP_j)$ are the ith muscular activity with “normal sensory input” in the condition j. The condition is the variety of the changes of the sensory inputs mentioned later.

CoP_j is a variable to indicate the center of pressure of human body instead of the human posture. Therefore, $f_i(CoP_j)$ can be considered as the muscular activity for “external force” to maintain the posture. From the above formula, $g_i(Condition_j)$ can be considered as muscular activity for “internal force”. $Condition_j$ is vector meaning the sensory inputs in the jth condition. If any sense is normal, with no inhibition and stimulation, $g_i(Condition_j)$ will be 0 because $Activity_{ij}$ equals to $f_i(CoP_j)$. The n is the number of muscles to be measured and the m is the number of conditions with the changes of sensory inputs.

The method for obtaining $g_i(Condition_j)$ is described. $f_i(CoP_j)$ is calculated from the model constructed by measuring EMG of subject's muscles in various postures with the normal sensory inputs. $Activity_{ij}$ is obtained by measuring EMG of subject's muscles when subject's senses are inhibited and/or stimulated. $g_i(Condition_j)$ is calculated as the difference between measured Activityij and modeled $f_i(CoP_j)$. Figure 2 shows the outline of this method (see chart in next page).

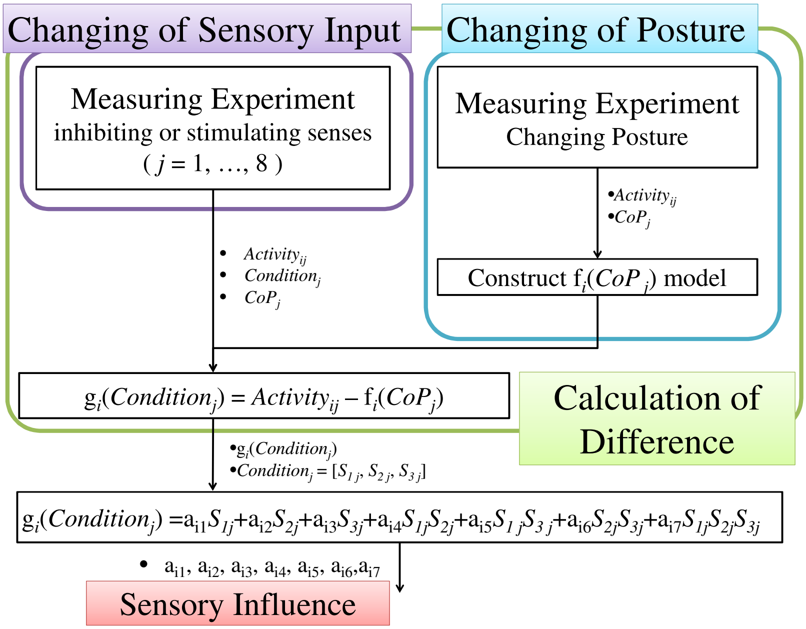

Fig. 2. Outline of proposed method

2.1 Calculation of Muscular Activity for External Force

In maintaining a standing posture, posture and external forces are considered uniquely decided provided the Center of Pressure (CoP) position is uniquely decided. In this study, CoP_j is defined as vector meaning CoP position and it is considered that the external force is $f_i(CoP_j)$.

Experiments were performed to measure CoP_j and $Activity_{ij}$ when any subject's sense is uninhibited or not stimulated; that is, $g_i(Condition_j) = 0$, and subject leans to the front or back, to the left or right, and any combination thereof. CoP is measured by four scales and calculated. $Activity_{ij}$ is measured as EMG of each muscle and calculated. The model of f( ) is constructed with measured CoP and $Activity_{ij}$.

In concrete, for the construction of this model, the subjects are measured the muscular activities at 9 points to change their posture. And then, the muscular activities of 16 points are estimated with the average of the neighbor activities. Finally, we make meshes based on the measured points and estimated points. Figure 3 shows these points where x is right side and y is front side. The measured points may need to increase for the precise estimation. However, the number of the points is set 9 of the minimal value because we consider the subjects' exhaustion.

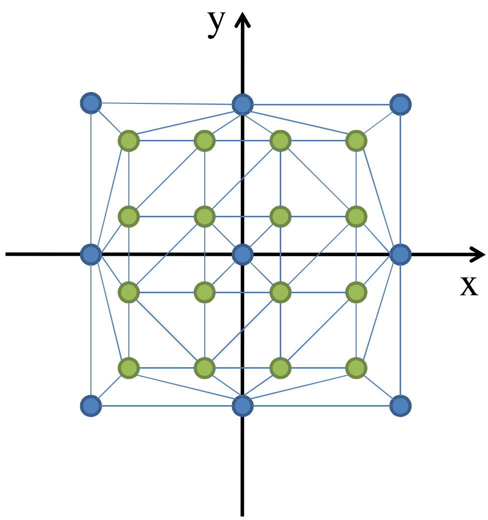

Fig. 3. Measured and estimation points for $f_i(CoP_j)$ model. Blue points indicate the measured points and green points indicate the estimated points.

2.2 Calculation of Muscular Activity for Internal Force

The internal force elements $g_i(Condition_j)$ can be obtained from muscular activities and external force elements mentioned above.

And for the estimation of influence of sensory inputs, we calculate the coefficients of the input factors. As mentioned later, we set 8 conditions corresponding to 3 sensory inputs. Each sensor is inhibited or stimulated and combined them in our experiments.

Therefore, the influence of each sensory input and these combinations can be obtained with the below formula.

$$g_i(Condition_j) = a_{i1}S_{1j}+a_{i2}S_{2j}+a_{i3}S_{3j}+a_{i4}S_{1j}S_{2j}+ a_{i5}S_{1j}S_{3j}+a_{i6}S_{2j}S_{3j}+a_{i7}S_{1j}S_{2j}S_{3j} \quad (2)$$

where S_{1j} indicate the sensory condition j in sensor1 (visual). S_{2j} indicate the sensory condition j in sensor2 (vestibular). S_{3j} indicate the sensory condition j in sensor3 (somatosensory).

So, we can obtain the a_1, a_2, a_3, a_4, a_5, a_6 and a_7 from the value of $g_i(Condition_j)$ with 8 kinds of conditions.

2.3 Method for Inhibiting or Stimulating Senses

Sensory inputs from visual, vestibular, and somatosensory systems are considered: the visual sense is inhibited by closed eyes, the vestibular sense is inhibited by a caloric test that upset the vestibular system by pouring cold water into the ear cavity, and the somatosensory sense is stimulated by touching a part of the body. If these senses are inhibited or stimulated, subjects tend to change their posture.

- If only the vestibular sense is inhibited, subject can maintain the standing posture (Fig. 4(a)).
- If both visual and vestibular senses are inhibited simultaneously, subject leans to the same side of inhibited ear (Fig. 4(b)).
- If both visual and vestibular senses are inhibited and somatosensory sense is stimulated simultaneously, subject recovers its standing posture (Fig. 4(c)).

The interesting thing is that the side of the leaning depends on the side of inhibited vestibular sense, but the touching point for the stimulated somatosensory sense is independent to recover their posture. Now, we have not verified and made the consideration the reasons. We will try to model this fact in the future work.

From these changes of the posture with the changes of sensory inputs, we can provide 8 conditions with different sensory inputs. $Condition_1$ is the normal posture and $Condition_{2\text{-}7}$ are the inhibitions and/or stimulation of the 3 sensory inputs. Table 1 shows the combinations of these sensory inputs as conditions. Table 2 shows the S_{1j}, S_{2j}, S_{3j} values in each condition. The $g_i(Condition_j)$ can be obtained from these 8 conditions experiments and $a_{1\text{-}7}$ can be obtained the $g_i(Condition_j)$ and the S_{1j}, S_{2j}, S_{3j} values in each conditions.

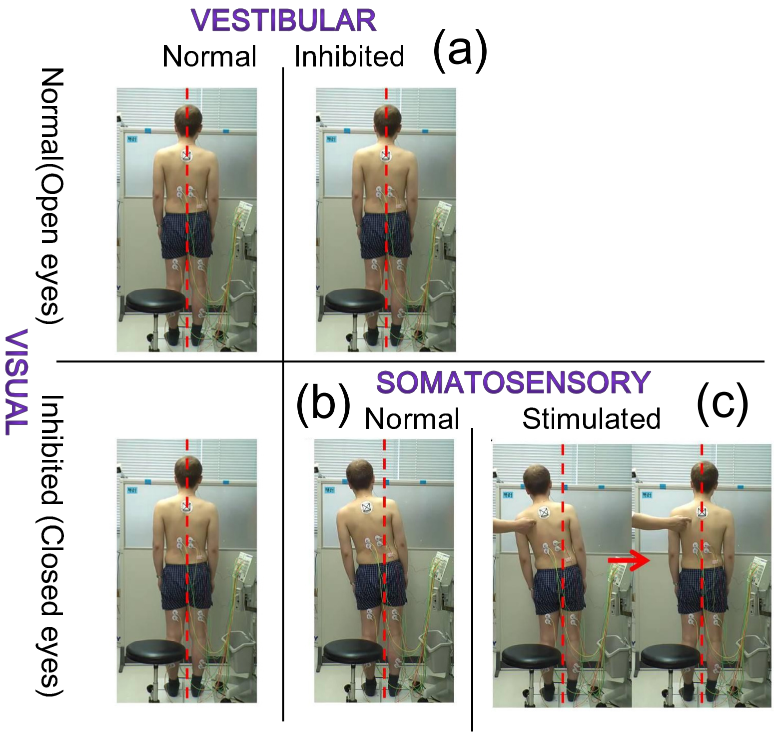

Fig. 4. Posture Change

Table 1. Conditions of sensor changings

(n : normal, i : inhibited, s : stimulated)

Conditions	1	2	3	4	5	6	7	8
Visual (S1)	n	i	n	i	n	i	n	i
Vestibular (S2)	n	n	n	n	i	i	i	i
Somatosensory (S3)	n	n	s	s	n	n	s	s

Table 2. Values of S_{1j}, S_{2j}, S_{3j}

Condition	1	2	3	4	5	6	7	8
S_{1j}	0	1	0	1	0	1	0	1
S_{2j}	0	0	0	0	1	1	1	1
S_{3j}	0	0	1	1	0	0	1	1

3 Experiment

3.1 Experimental Conditions

Subjects are 12 males in their twenties. Figure 5 shows muscles measured in experiments. We carry out the measurements of these muscles in the experiment for external for elements ($f_i(CoP_j)$) and in every 8 conditions. And then, we calculate the internal force element ($g_i(Condition_j)$) from muscular activities in 8conditions and the external force elements.

The visual inhibitions are achieved with “close eyes” and the vestibular inhibitions are achieved with pouring cold water “to left ear”. The somatosensory stimulations are achieved with touching at “any point on the surface of his body”.

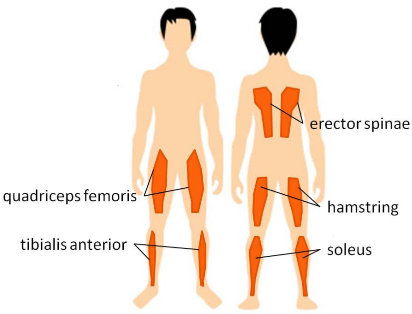

Fig. 5. Measured muscles

3.2 Experimental Results and Discussion

3.2.1 External Force Elements Model

At first, we show the results of the model for the representation of relationship between muscular activity and the center of pressure in order to model the external force elements.

For these models, we carry out the experiments in which subject change his posture to be 9 points of center of pressure. Those are front, front-right, front-left, center, center-right, center-left, back, back-right and back-left.

Figure 6 shows the model of each muscle. (l.) means the left side of body and (r.) means the right side. In these graphs, x axis indicates the right and left side (x plus is right), and y axis indicates the front and back side (y plus is front). And z axis indicates the muscular activity. In these graphs, it can be seen that circle points which

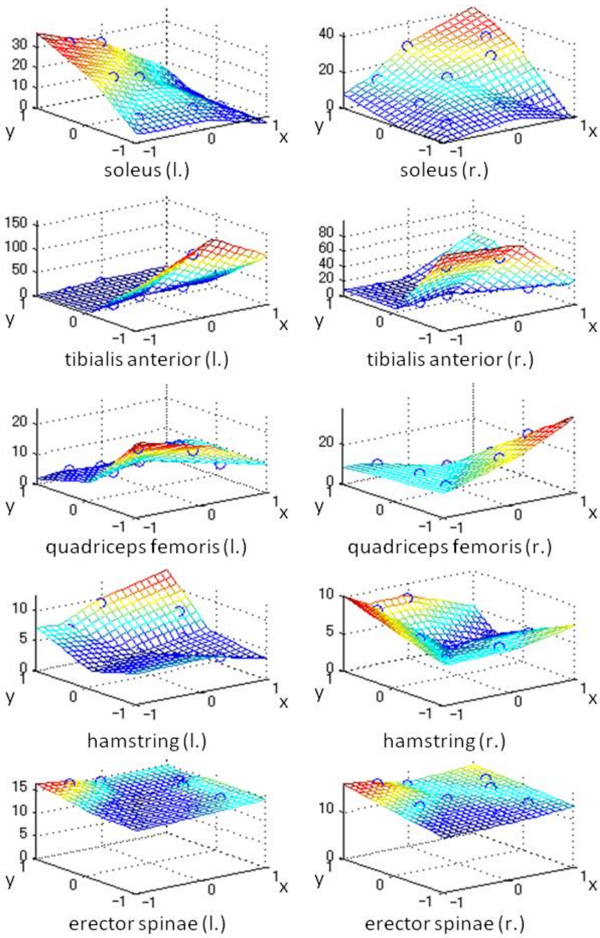

Fig. 6. Modeled external force element activity for each muscle

are the measured points. And then, we construct the model based on these measured muscular activities.

As the results, it can be seen that the activity of left side soleus increases when the CoP is front-left. On the other hand, the activity of right side soleus increases when the CoP is front-right. It is considered that these are very natural because soleus should work when human bends his body to front and keep the posture.

3.2.2 Internal Force Element Calculation

From the model of external force element mentioned above, the $f_i(CoP_j)$ can be obtained. In concrete, the experiments of 8 conditions might make the human posture change and the CoP might be changed. Therefore, using the CoP data, the external force element remove from the muscular activities. The result should be the muscular activities of the internal force elements by the changes of sensory inputs.

Table 3 shows the results of muscular activities of each muscle i in each condition j. Condition_1 is normal condition that is no inhibition and no stimulation. Therefore, the muscular activities are all 1.0 as the control data. The other activities are normalized based on this control data.

Table 4 shows the results of muscular activities for "internal force elements" of each muscle i in each condition j. These values are calculated based on the formula (1). Figure 7 shows the difference of the center of pressure in each condition. It can be seen that the CoP are various because the postures are various in the experiments. Therefore, for obtaining the "internal force element", $f_i(CoP_j)$ plays very important role.

In both tables, high values are painted red and low values are painted blue. It can be seen that both $Activity_{ij}$ and $g_i(Condition_j)$ are very high from condition5 to condition8. This result is very natural because human makes his body "hard" when sensory inputs, especially vestibular, are inhibited and not stimulated. In condition6, subjects lean their body and their all muscular activities are also high.

Table 3. Muscular activities in 8 conditions ($Activity_{ij}$)

conditions	1	2	3	4	5	6	7	8
soleus (left)	1.00	1.19	1.18	1.34	1.38	1.71	1.40	1.84
soleus (right)	1.00	1.12	1.11	1.21	1.29	1.48	1.32	1.60
tibialis anterior(l)	1.00	1.26	1.40	1.33	2.29	4.51	2.47	4.41
tibialis anterior(r)	1.00	1.29	1.25	1.23	2.35	4.44	2.15	4.33
quadriceps femoris(l)	1.00	1.16	1.21	1.20	1.64	3.61	1.91	4.49
quadriceps femoris(r)	1.00	0.91	0.90	1.10	1.88	2.81	1.93	3.35
hamstring(l)	1.00	1.44	1.64	1.68	1.44	1.75	1.62	1.94
hamstring(r)	1.00	1.38	1.39	1.60	1.38	1.64	1.47	1.64
erector spinae(l)	1.00	1.03	1.04	1.05	1.12	1.16	1.14	1.23
erector spinae(r)	1.00	1.02	1.01	1.04	1.15	1.21	1.15	1.26

Table 4. Muscular activities of internal force elements in 8 conditions ($g_i(Condition_j)$)

conditions	1	2	3	4	5	6	7	8
soleus (left)	-0.04	0.01	-0.01	-0.01	0.21	0.47	0.17	0.51
soleus (right)	-0.06	-0.11	-0.06	-0.03	0.17	0.42	0.13	0.40
tibialis anterior(l)	-0.31	-0.39	-0.18	-0.21	0.64	2.63	0.78	2.72
tibialis anterior(r)	-0.37	-0.49	-0.49	-0.5	0.68	2.67	0.54	2.67
quadriceps femoris(l)	-0.24	-0.33	-0.21	-0.18	0.19	1.94	0.48	2.96
quadriceps femoris(r)	-0.2	-0.54	-0.51	-0.23	0.44	1.18	0.43	1.82
hamstring(l)	-0.23	0.005	0.184	0.15	0.13	0.41	0.17	0.54
hamstring(r)	-0.15	0.053	0.096	0.213	0.02	0.27	-0.03	0.20
erector spinae(l)	-0.04	-0.08	-0.13	-0.13	-0.06	0.02	-0.02	0.06
erector spinae(r)	-0.04	-0.09	-0.18	-0.15	-0.06	0.03	-0.03	0.07

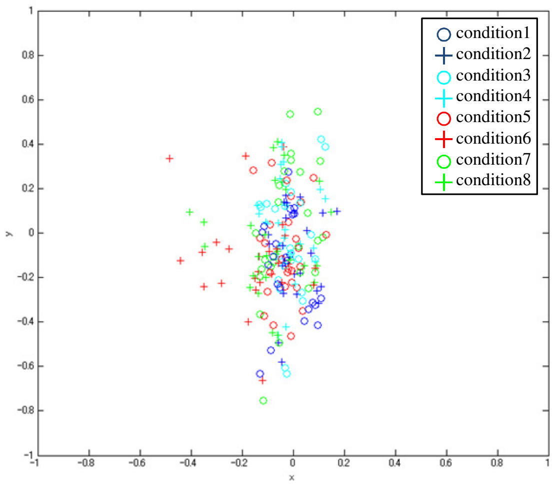

Fig. 7. Center of pressure in each condition

3.2.3 Influence of Sensory Inputs

From the calculation of $g_i(Condition_j)$ mentioned above, the influences of the sensory inputs to the internal force element activities can be obtained based on the formula (2).

Figure 8 shows the results of $a_{1\text{-}7}$. The coefficients has the meanings that a_1 is only visual influence, a_2 is only vestibular influence, a_3 is only somatosensory influence, a_4 is the combination influence of visual and vestibular, a_5 is the combination influence of visual and somatosensory, a_6 is the combination influence of vestibular and somatosensory and a_7 is the combination influence of visual, vestibular and somatosensory.

Form the result of Fig.8, it is clear that a_4 is significantly high regarding the error. That is to say, human makes their body "hard" in the situation that both visual and vestibular systems are inhibited(a_4). However, in such a situation, with the stimulation of the somatosensory system, their posture control works well.

From this result, it can be considered that "internal force elements" exist on the human posture control by the changes of sensory inputs. Moreover, we can find that the sensory inputs are integrated and utilized in human posture control. The sensory inputs cannot be considered independently. Therefore, we think that multi-modality should be more considered.

These results are the average of subjects in which there are several individual differences. However, there are obvious means statistically. Therefore, we think these results are general.

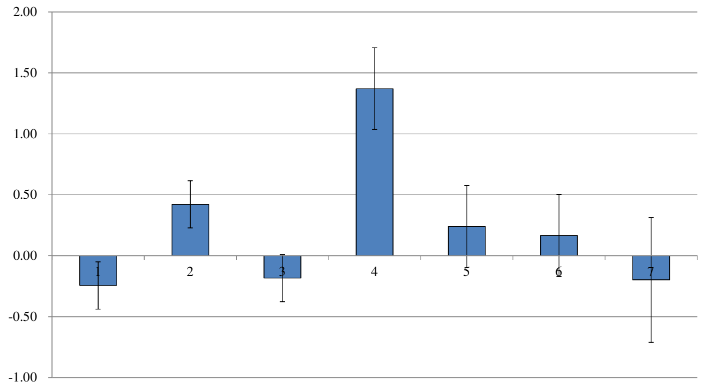

Fig. 8. Influence of each sensory input and these combinations ($a_{1\text{-}7}$)

3.3 Discussion of Model

From the results in this paper, we may be able to consider a new model of human posture control.

In the torque based human posture control, both flexor and extensor muscles make only "external force (torque)" on the joint (Fig.9). However, in this paper, we suggest that the existence of "internal force ($g_i(Condition_j)$)" by the difference of the sensory inputs. At the same time, the sensory inputs do not independently work but work with the integration.

Therefore, we extend the posture control model the previous work. Figure 10 shows the new posture control model. In this model, the flexor and extensor muscles are controlled by both external output and internal output. About the external output, Peterka's model[3] can be applied. Internal elements should be driven by sensory integrator. However, that is not still understood well how to control the internal force elements.

In the dangerous situation such as 2 or more sensory inputs inhibition, it is very natural to make the high body stiffness. It is very importance that the existence is found. In previous studies, only torque calculation is focused on. Our contribution is the findings of the fact that not only torque but also joint stiffness and viscosity should be considered in the modal.

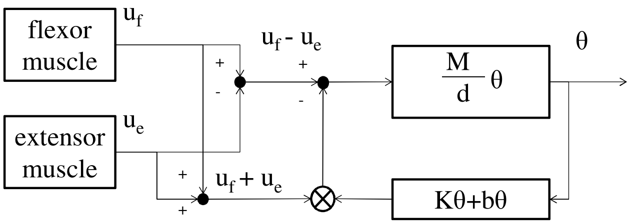

Fig. 9. Model of previous work (Torque based) [6]

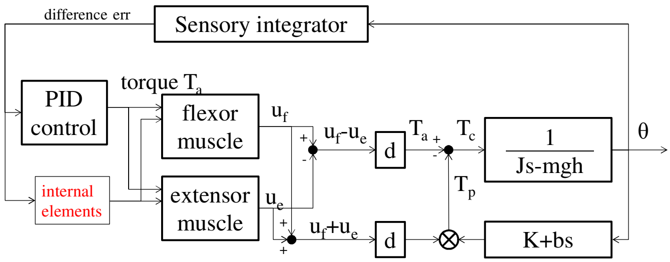

Fig. 10. Model of this work (Muscular Activity based)

4 Conclusion

This paper proposed a method to obtain quantitative changes in muscle activity caused by changes in sensory input conditions. With this method, we can show the existence of internal force elements as well as external force elements. The sensory inputs are integrated in human posture control as multi-modality.

Form the results, the new model of human posture control is suggested. The internal elements are driven by the sensory integrator and these make the human body stiffness.

As the future work, we firstly consider the control model of internal force element. And the sensory inputs integrator is also important for the understandings of human posture control. For these works, we will carry out more experiments and to measure how to work the brain in the experiments with NIRS.

In this study, the posture can be measured by the center of pressure. However, we can measure more certain posture with motion capture systems.

References

1. Nashner, L.M., et al.: Stance posture control in select groups of children with cerebral palsy: Deficits in sensory organization and muscular coordination. Exp. Brain. Res. 49, 393–409 (1983)
2. Bottaro, A., Yasutake, Y., Nomura, T., et al.: Bounded stability of the quiet standing posture: an intermittent control model. Human Movement Science 27, 473–495 (2008)
3. Peterka, R.J.: Sensorimotor Integration in Human Postural Control. Journal of Neurophysiol. 88, 1097–1118 (2002)
4. van der Kooij, H., Jacobs, R., Koopman, B., van der Helm, F.: An adaptive model of sensory integration in a dynamic environment applied to human stance control. Biological Cybernetics 84, 103–115 (2001)
5. van der Kooij, H., Jacobs, R., Koopman, B., Grootenboer, H.: A multisensory integration model of human stance control. Biological Cybernetics 80, 299–308 (1999)
6. Ito, K.: Physical Intelligent System Theory. Kyoritsu-shuppan (2005) (in Japanese)

Minimalist CPG Model for Inter- and Intra-limb Coordination in Bipedal Locomotion

Dai Owaki[1], Takeshi Kano[1], Atsushi Tero[2], Masakazu Akiyama[2], and Akio Ishiguro[1,3]

[1] Research Institute of Electrical Communication, Tohoku University
2-2-1 Katahira, Aoba-ku, Sendai 980-8577, Japan
{owaki,tkano,ishiguro}@riec.tohoku.ac.jp
[2] Institute of Mathematics for Industry, Kyushu University,
744 Motooka, Nishi-ku, Fukuoka 819-0395, Japan
{tero.atsushi,masakazu.akiyam}@gmail.com
[3] CREST (Core Research for Evolutional Science), Japan Science and Technology Agency,
7 Goban-cho, Chiyoda-ku, Tokyo 102-0057, Japan

Abstract. Inter- and intra-limb coordination for bipedal locomotion were numerically investigated using a "minimalist" bipedal robot model and an unconventional central pattern generator (CPG)-based control scheme that exploits local sensory feedback generated from the discrepancy between the control system, mechanical system, and environment. The simulation results showed that a bipedal robot controlled by the proposed controller exhibits walking and running gaits dependent only on one parameter: the angular velocity of the oscillators. Interestingly, spontaneous inter- and intra-limb coordination were found to be inherent to the proposed design scheme for stable bipedal locomotion. These findings are expected to lead to a useful methodology for robots to generate stable and adaptive locomotion.

Keywords: bipedal locomotion, inter- and intra-limb coordination, discrepancy.

1 Introduction

Animals exhibit astoundingly adaptive, supple, and versatile locomotion under real-world constraints. Robot bodies must have a significantly higher number of degrees of freedom relative to that of animals than they have at present in order to realize similar capabilities. *Autonomous decentralized control* plays a pivotal role in successfully coordinating movement with many degrees of freedom in response to various circumstances and it has attracted considerable attention. In fact, animals deftly coordinate the many degrees of freedom in their bodies through the use of intraspinal neural networks called *central pattern generators* (CPGs), which are responsible for generating rhythmic movements, particularly those related to locomotion [1, 2].

Based on this biological finding, various studies have been conducted thus far to incorporate artificial CPGs into legged robots with the aim of generating highly adaptive locomotion [3]—[6]. In these studies, neural network topologies in CPGs

S. Lee et al. (Eds.): Intelligent Autonomous Systems 12, AISC 194, pp. 493–502.
springerlink.com

and local sensory feedback mechanisms have been discussed in an attempt to elucidate the generation mechanisms of situation-dependent locomotion patterns. Nevertheless, the proposed mechanisms could not fully reproduce the innate behaviors of real animals. One of the reasons is that these studies have mainly focused on the inter-limb coordination mechanism. Although the intra-limb coordination mechanism should also play a pivotal role in generating adaptive locomotion, they have been designed completely on an ad-hoc basis.

Thus, the objective of this study is to propose a minimalist CPG model for inter- and intra-limb coordination in bipedal locomotion. An extremely simplified biped robot was modeled in this study using the minimalist approach, as shown in Fig. 1, and an conventional CPG-based control scheme was designed, which exploits local sensory feedback generated from the discrepancy between the control system, mechanical system, and environment. In this work, the validity of our proposed control scheme was verified in the simulations. The results indicate that the proposed control scheme allows the robot to perform *walking* and *running*, which depend only on one parameter, the intrinsic angular velocity, ω, of the oscillators. This fact supports our control scheme feature that can explain the inter- and intra-limb coordination mechanism used for bipedal locomotion generation. Bipedal locomotion is generated via inter- and intra-limb coordination [7], so these results are expected to shed new light on bipedal locomotion generation mechanism.

2 Model

2.1 Mechanical Structure

Figure 1 shows the biped model. In this figure, the black mass points (1 and 2) represent the upper body and the hip, while the blue mass points represent the right knee and foot masses (3 and 4), and the green mass points represent the left knee and foot masses (5 and 6), respectively. Motion is expressed through the motion of these six mass centers. The trunk link (link 1-2) and thigh links (link 2-3, link 2-5) are modeled as rigid links. Springs with a large stiffness constant are implemented at the knee joints (joints 2-3-4, joint 2-5-6), which results in a compass-like biped model [8, 9]. In our model, simple spring-like actuators known as *real-time tunable springs* (RTSs) [10] are implemented at the hip joints θ_i (joint 1-2-3, joint 1-2-5) and in the shank segments l_i (link 3-4, link 5-6) in order to generate bipedal locomotion. This control model is based on the physiological findings [11] on cat gait, in which the limb axis length (like $\tilde{l}_i$) and orientation (like $\tilde{\theta}_i$) coordinates are independently represented at the lowest sensory processing levels in the spinal cord.

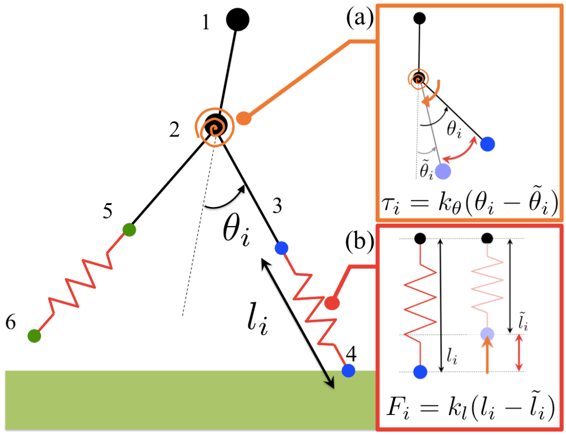

Fig. 1. Simple biped model employed. Spring-like actuators known as *real-time tunable springs* (RTSs) [10] are implemented at the hip joints θ_i and in the shank segments l_i. Schematic representations of (a) rotational spring type RTS and (b) linear spring type RTS.

2.2 Actuator and Sensor

An RTS can actively alter its resting length (*i.e.*, the zero force length (or angle) of the spring). As shown in Fig. 1, a linear spring type RTS was implemented for the shank segments and a rotational spring type RTS was implemented for the hip joints. They are described by the following equations:

$$F_i = k_l(l_i - \tilde{l}_i), \tag{1a}$$

$$\tau_i = k_\theta(\theta_i - \tilde{\theta}_i), \tag{1b}$$

where F_i and τ_i represent the force and torque applied by each RTS (left: *i=0*, right: *i=1*). k_l and k_θ represent the spring constants. l_i and θ_i represent the actual length of the shank segment and the actual angle of the hip joint. $\tilde{l}_i$ and $\tilde{\theta}_i$ represent the resting length and resting angle, which vary according to the oscillator phases in order to generate rhythmic locomotion.

It is noteworthy that the RTS is able to perform not only as an actuator but also as a passive mechanical element. For this reason, the force (or torque) stemming from the interaction between the body and the environment can be measured as a discrepancy between the controlled value $\tilde{l}_i$ or $\tilde{\theta}_i$ and the actual value l_i or θ_i by sensing the force (or torque) on the RTS. Therefore, RTSs play an essential role in sensing important sensory information for adaptive locomotion generation.

2.3 Discrepancy Function

Each RTS drives the legs according to the motor command from the corresponding oscillator. However, owing to the elasticity of the RTSs, the behavior of the robot does not completely follow the motor command from the control system, but is somewhat influenced by the surrounding environment and the physical constraints of the body. Consequently, the actual length l_i of the shank segments and the joint angle θ_i of the hip joints deviate from $\tilde{l}_i$ and $\tilde{\theta}_i$.

The discrepancy function I is defined on the basis of the magnitude of the deviation. As shown by previous studies [10, 12, 13], the discrepancy function has to be able to characterize the magnitude of the discrepancy detected between the control system, the mechanical system, and the environment. I is designed as follows:

$$I = \frac{1}{2}\sum_i \left\{ \sigma_l (F_i)^2 + \sigma_\theta (\tau_i)^2 \right\}, \tag{2}$$

where σ_l and σ_θ, respectively, are the parameters characterizing the effect of F_i and τ_i on I. In fact, F_i and τ_i contain information about the discrepancy because these forces are determined as a result of the interaction between the mechanical system and the environment.

2.4 Control Scheme

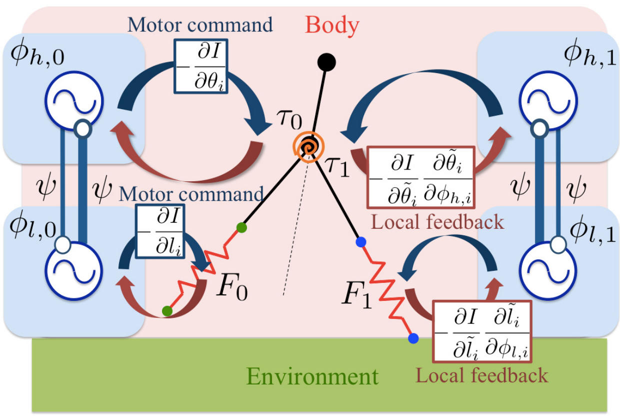

Fig. 2. Schematic of body and control systems of proposed biped model

Our minimalist CPG is modeled by *phase oscillators* and two phase oscillators described in (3a) and (3b) are implemented in each leg for RTS controls:

$$\dot{\phi}_{h,i} = \omega + g_{h,i} + f_{h,i}, \tag{3a}$$

$$\dot{\phi}_{l,i} = \omega + g_{l,i} + f_{l,i}, \tag{3b}$$

where $\phi_{h,i}$ and $\phi_{l,i}$ are the oscillator phases of hip joints and leg segments, respectively, and ω represents the angular velocity of the oscillators (left: $i=0$, right: $i=1$). The third terms on the right hand side in (3) denote the local sensory feedbacks from the mechanical system to the hip joint and leg segment oscillators, respectively.

The target angle $\tilde{\theta}_i$ and target length $\tilde{l}_i$ of the RTSs given by the phases $\phi_{h,i}$ and $\phi_{l,i}$ of the oscillators are as follows:

$$\tilde{\theta}_i = \theta_0 - A_\theta \cos\phi_{h,i} \tag{4a}$$

$$\tilde{l}_i = l_0 - A_l \sin\phi_{l,i} \tag{4b}$$

where A_θ and A_l denote the amplitudes of the target angle and length, respectively. θ_0 and l_0 denote the offset angle and length of the target, respectively.

The second terms on the right hand side in (3) expresses the coupling between the oscillators, *i.e.*, neural connections:

$$g_{h,i} = \varepsilon_\theta \sin(\phi_{l,i} - \phi_{h,i} - \psi) \tag{5a}$$

$$g_{l,i} = \varepsilon_l \sin(\phi_{h,i} - \phi_{l,i} + \psi) \tag{5b}$$

where ε_θ and ε_l are the coupling strengths. When the local sensory feedback is absent, the phase difference between hip joint and leg segment oscillators in the same leg is entrained into ψ; the phase difference helps to determine the target pattern of one leg's motion, as shown in Fig. 3. The actuators, *i.e.*, RTSs, at the hip joints and in the shank segments drive the legs according to the target $\tilde{\theta}_i$ and $\tilde{l}_i$ to generate locomotion.

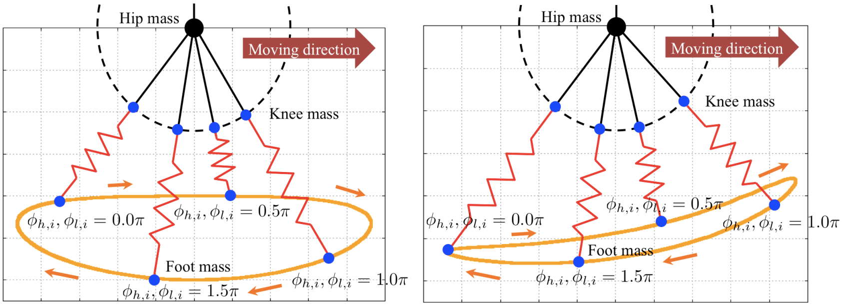

Fig. 3. Foot trajectory according to oscillator phases. (a) $\psi = 0.0\pi$ and (b) $\psi = 0.4\pi$.

Then, the local sensory feedback terms, $f_{h,i}$ and $f_{l,i}$, are set as follows,

$$f_{h,i} = -\frac{\partial I}{\partial \phi_{h,i}} = -\frac{\partial I}{\partial \tilde{\theta}_i}\frac{\partial \tilde{\theta}_i}{\partial \phi_{h,i}} = \gamma_\theta \tau_i \sin\phi_{h,i} \tag{6a}$$

$$f_{l,i} = -\frac{\partial I}{\partial \phi_{l,i}} = -\frac{\partial I}{\partial \tilde{l}_i}\frac{\partial \tilde{l}_i}{\partial \phi_{l,i}} = -\gamma_l F_i \cos\phi_{l,i} \tag{6b}$$

where $\gamma_\theta = \sigma_\theta A_\theta k_\theta$ and $\gamma_l = \sigma_l A_l k_l$. Note that this phase modification is calculated only with locally available sensory information from the RTSs, namely, τ_i and F_i. The phases are modified to reduce the total discrepancy I because of these feedback terms, which lead to the inter- and intra-limb coordination for stable locomotion.

The following equations are considered:

$$h_{\theta,i} = -\frac{\partial I}{\partial \theta_i} = -\sigma_\theta (k_\theta)^2 (\theta_i - \tilde{\theta}_i) = -\alpha_\theta \tau_i \tag{7a}$$

$$h_{l,i} = -\frac{\partial I}{\partial l_i} = -\sigma_l (k_l)^2 (l_i - \tilde{l}_i) = -\alpha_l F_i \tag{7b}$$

where $\alpha_\theta = \sigma_\theta k_\theta$ and $\alpha_l = \sigma_l k_l$. As these equations show, $h_{\theta,i}$ and $h_{l,i}$ help to reduce the discrepancy I through θ_i and l_i. Note that these equations correspond to the models having linear and rotational type RTSs in Eqs. (1a) and (1b). These facts strongly suggest that our proposed actuator models (RTSs) also behave such that they reduce the total discrepancy I by using locally available variables, which yields a "good" coupling between the control and mechanical systems for adaptive locomotion.

Furthermore, the key consideration in the present model is that the RTSs are strategically placed at joints and in the segments. The discrepancy I detected between the control and the mechanical systems provides significant information about the way in which the robot interacts with the environment because such elastic materials deform according to the current motion. In conclusion, this compliant mechanism allows the robot to exploit the *active perception* or *sensory-motor coordination* [14].

3 Simulation Results

The validity of the design scheme proposed was verified using the biped robot. To this end, simulations were conducted using various parameter settings and various initial conditions. The robot's parameters and the initial conditions were selected by trial and error during these simulations. The conditions used for the simulation are shown in Table 1.

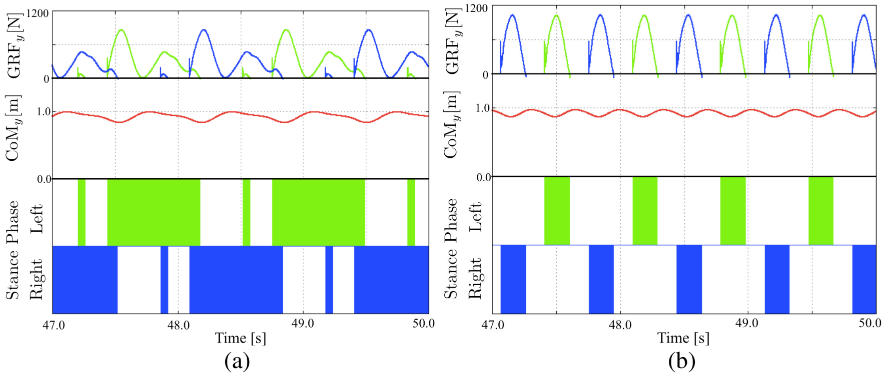

Fig. 4. (a) Walking gait. ω = 5.4 rad/s. (b) Running gait. ω = 10.0 rad/s.

Figure 4 compares gait patterns of bipeds with different intrinsic oscillator angular velocities, ω. The top portions of the graphs in the Figs. 4 (a) and (b) show GRFs perpendicular to the ground (blue: right leg, green: left leg). The graphs in the middle of these figures represent the y-position of the hip mass during walking and running. The graphs in the bottom show the gait diagrams, in which blue and green indicate the stance phases of the right and left legs, respectively. Note that bipeds have different gait patterns that depend only on one parameter, *i.e.*, the angular velocity ω of the oscillators, which determines locomotion velocity. Moreover, various gait patterns can be observed according to the change in the intrinsic oscillator angular velocities, *e.g.*, a category of *walking* for 3.0 to 6.6 rad/s and a category of *running* for 6.7 to 10.0 rad/s. Human walking and running movements are distinguished by a set of basic characteristics that are generally agreed upon in biomechanics [15]—[17]. They are as follows:

- Vertical GRF
- Vertical body excursion
- Duty factor: the stance period of one foot, as a percentage of the gait cycle, *etc*.

In this paper, we distinguish between gait patterns by employing (i) the vertical GRF, (ii) the vertical body excursion, and (iii) the gait diagram, as shown in Fig. 4.

Table 1. Body and control parameters

Parameters	Value	Unit
Body Parameters		
Body mass	10.0	[kg]
Hip mass	10.0	[kg]
Knee mass	7.5	[kg]
Foot mass	1.0	[kg]
Trunk length	0.5	[m]
Thigh length	0.5	[m]
Shank length	0.5	[m]
Leg spring k_l	20000.0	[N/m]
Leg damper c_l	25.0	[Ns/m]
Hip spring k_θ	12000.0	[Nm/rad]
Hip damper c_θ	0.0	[Nms/rad]
Control parameters		
RTS target angle amplitude; A_θ	0.15π	[rad]
RTS target length amplitude; A_l	0.07	[m]
Average RTS resting angle; θ_0	0.0	[rad]
Average RTS resting length; l_0	0.50	[m]
Phase difference between $\tilde{l}_i$ and $\tilde{\theta}_i$; ψ	0.40π	[rad]
Coupling strength; ε_θ	17.0	[rad/s]
Coupling strength; ε_l	1.7	[rad/s]
Local feedback magnitude; σ_θ	0.5e-06	[rad/N^{2}s]
Local feedback magnitude; σ_l	4.0e-06	[rad/N^{2}m^{2}s]

3.1 Walking

There are three reasons for which the gait for ω = 5.4 rad/s is regarded as *walking*: (i) this biped demonstrates a “two peak” GRF curve perpendicular to the ground during one period [16]; (ii) the vertical body excursion increases toward the middle of the stance phase [17]; and (iii) the biped has a *double-stance phase* period.

Interestingly, these profiles agree well with those of a walking human [15].

3.2 Running

There are three reasons for which the gait for ω = 10.0 rad/s is regarded as *running*: (i) the "one peak" GRF curve perpendicular to the ground during one period [16], which is different from that shown in Fig. 4 (a); (ii) the vertical body excursion that decreases toward the middle of the stance phase [17]; and (iii) the biped's performance during the *flight phase* period. Interestingly, these profiles also agree well with those of a running human [15].

4 Discussions and Conclusions

A control scheme that exploits the local sensory feedback generated from the detected discrepancy between the control system, the mechanical system, and the environment is proposed in this study. Simulation results indicate that our robot exhibits stable walking and running motions by exploiting the sensory information provided by "soft and deformable" actuators known as RTSs.

It is interesting to note that our model exhibits stable walking and running motions via inter- and intra-limb coordination. One plausible explanation for these results is that the proposed local sensory feedback allows each leg to recognize the positional relationship between legs, *i.e.*, how the legs support the body at that moment, without having to perform calculations that lead to a high computation cost. This mechanism allows appropriate physical communication between individual components via the robot body.

In our model, intra-limb coordination is partly governed by neural connections between hip joint and leg segment oscillators in Eqs. (5a) and (5b): The parameter ψ denotes the phase difference between $\tilde{l}_i$ and $\tilde{\theta}_i$. However, the effect of the local sensory feedback based on the detected discrepancy, which stems from the actual motion, enables the phase relationship between l_i and θ_i to be appropriately modified in a way that is related to the current s motion, resulting in the generation of gait patterns suited to the situation encountered. Additional work is required for detailed verification of the inter- and intra-limb coordination for adaptive bipedal locomotion, *e.g.*, how to achieve the autonomous generation of inter- and intra-limb coordination. This study constitutes the first step toward understanding the inter- and intra-limb coordination mechanism for the adaptive bipedal locomotion.

In the future, we intend to clarify the effect of stiffness adjustment mechanism on inter- and intra-limb coordination. Furthermore, we intend to verify the validity of our scheme for control of a quadruped robot, a hexapod robot, or a bipedal robot with many degrees of freedom. We expect the subsequent findings to contribute to a useful methodology that enables robots to generate adaptive locomotion.

Acknowledgements. This work was partly supported by a Grant-in-Aid for Young Scientists (B) No. 23760381 from the Ministry of Education, Culture, Sports, Science, and Technology (MEXT), Japan.

References

1. Shik, M.L., Severin, F.V., Orlovskii, G.N.: Control of Walking and Running by Means of Electrical Stimulation of the Midbrain. Biophysics 11, 756–765 (1966)
2. Grillner, S.: Neurobiological Bases of Rhythmic Motor Acts in Vertebrates. Science 228, 143–149 (1985)
3. Taga, G., Yamaguchi, Y., Shimizu, H.: Self-organized Control of Bipedal Locomotion by Neural Oscillators. Biological Cybernetics 65, 147–159 (1991)
4. Fukuoka, Y., Kimura, H., Cohen, A.H.: Adaptive Dynamic Walking of a Quadruped Robot on Irregular Terrain Based on Biological Concepts. Int. J. Robotics Res. 22, 187–202 (2003)
5. Aoi, S., Tsuchiya, K.: Stability Analysis of a Simple Walking Model Driven by an Oscillator with a Phase Reset Using Sensory Feedback. IEEE Transactions on Robotics 22, 391–397 (2006)
6. Righetti, L., Ijspeert, A.J.: Pattern Generators with Sensory Feedback for the Control of Quadruped Locomotion. In: Proc. of ICRA 2008, pp. 819–824 (2008)
7. Diedrich, F.J., Warren, W.H.: Why Change Gaits? Dynamics of the Walk-Run Transition. Journal of Experimental Psychology 21, 183–202 (1995)
8. McGeer, T.: Passive bipedal running. Proc. of the Royal Society of London, Series B, Biological Science 240, 107–134 (1990)
9. Owaki, D., Osuka, K., Ishiguro, A.: On the embodiment that enables passive dynamic bipedal running. In: Proc. of ICRA 2008, pp. 341–346 (2008)
10. Umedachi, T., Takeda, K., Nakagaki, T., Kobayashi, R., Ishiguro, A.: Fully Decentralized Control of a Soft-bodied Robot Inspired by True Slime Mold. Biological Cybernetics (2010), doi:10.1007/s00422-010-0367-9
11. Poppele, R.E., Bosco, G., Rankin, A.M.: Independent Representations of Limb Axis Length and Orientation in Spinocerebellar Response Components. J. Neurophysiol. 87, 409–422 (2002)
12. Sato, T., Kano, T., Ishiguro, A.: On the Applicability of the Decentralized Control Mechanism Extracted from the True Slime Mold: A Robotic Case Study with a Serpentine Robot. Bioinspiration and Biomimetics 6 (2010), doi:10.1088/1748-3182
13. Kano, T., Nagasawa, K., Owaki, D., Tero, A., Ishiguro, A.: A CPG-based Decentralized Control of a Quadruped Robot Inspired by True Slime Mold. In: Proc. of IROS 2010, pp. 4928–4933 (2010)
14. Pfeifer, R., Bongard, J.: How the Body Shapes the Way We Think: A New View of Intelligence. MIT Press (2006)
15. Alexander, R.M.: Walking and Running. American Scientist 72, 348–354 (1984)
16. Keller, T.S., Weisberger, A.M., Ray, J.L., Hasan, S.S., Shiavi, R.G., Spengler, D.M.: Relationship between Vertical Ground Reaction Force and Speed during Walking, Slow Jogging, and Running. Clinical Biomechanics 11, 253–259 (1996)
17. Pandy, M.G.: Simple and Complex Models for Studying Muscle Function in Walking. Philosophical Transactions of the Royal Society of London Series B 358, 1501–1509 (2003)

Dynamic Partition of Collaborative Multiagent Based on Coordination Trees*

Fang Min[1], Frans C.A. Groen[2], and Li Hao[1]

[1] Institute of Computer Science
Xidian University, China
mfang@mail.xidian.edu.cn
[2] Informatics Institute
University of Amsterdam, The Netherlands
F.C.A.Groen@uva.nl

Abstract. In team Markov games research, it is difficult for an individual agent to calculate the reward of collaborative agents dynamically. We present a coordination tree structure whose nodes are agent subsets or an agent. Two kinds of weights of a tree are defined which describe the cost of an agent collaborating with an agent subset. We can calculate a collaborative agent subset and its minimal cost for collaboration using these coordination trees. Some experiments of a Markov game have been done by using this novel algorithm. The results of the experiments prove that this method outperforms related multi-agent reinforcement-learning methods based on alterable collaborative teams.

Keywords: reinforcement learning, multi-agent, coordination tree, Markov games.

1 Introduction

A Markov game, also known as a stochastic game, is generally considered as the combination of a Markov decision process and a matrix game[1]. When multiple agents deal with a Markov game, there are a number of relative independent actions or action series that can be taken[2][3]. For example in a pursuit game, predators need to explore their objects and then to hunt evaders together. In multi-robot team coordination, the robots need to form teams and coordinate other actions dynamically. So, we need an approach to judge the cooperative relationship among agents.

The learning of multiple agents is a complex problem. The collaborative multi-agent Markov decision process[4][5][6]model is often used in research. Hyper-Q learning[7] learns mixed strategies in stochastic games, using observations of other agents' play. The states in Hyper-Q consist of observations or estimates of opponents' strategies. By learning a value function of state-action pairs, the Hyper-Q algorithm obtains its mixed strategies. Another solution technique is based on the

* This work was supported by the national natural science funds in China with No.61070143 and the science project of Shaanxi with No. 2011K09-28.

S. Lee et al. (Eds.): Intelligent Autonomous Systems 12, AISC 194, pp. 503–510.
springerlink.com

framework of coordination graphs (CGs)[8]. In a CG each node represents an agent and connected agents indicate a local coordination dependency. Each dependency corresponds to a local payoff function which assigns a value to every possible action combination of the involved agents. The Max-Plus algorithm and Variable Elimination(VE)[8] based on coordination graphs are used to find the optimal joint action. These algorithms demand that the structure of the CG used is determined beforehand. It is difficult for agents to calculate dynamic neighbors and to select an optimal action. If the neighbors of an agent have a tree structure, the Max-Plus algorithm based on coordination graphs can optimize the global reward. When the neighbors of an agent have a graph structure, Max-Plus algorithm can not cope with the complexity of the underlying graph structure[9].

In summary, an optimal joint action selection method is needed to copy with the complicated relation of agents. Therefore, we present a dynamic distributed selection algorithm of a joint action based on coordination trees. Using this method, the multi-agent reinforcement algorithm of team Markov games could be applied.

2 Coordination Trees for Describing the Collaborative Relationship among Agents

Suppose n agents are present in two fighting sides. The number of cooperative agents in one side is Nb, the number of opposite agents is Nr. One of the opposing sides need k agents to collaborate $(k \le \min(Nb, Nr))$ and take care of an agent of the other side. A key problem is how to obtain the cooperative agents of one agent.

We define a coordination graph which describes a global cooperative relation between agents. In a coordination graph, there are two kinds of nodes. The first one is a node for the agent Ag_i, and the second one is a set node B_j which don't include the agent Ag_i. The tree structure is shown in fig. 1.

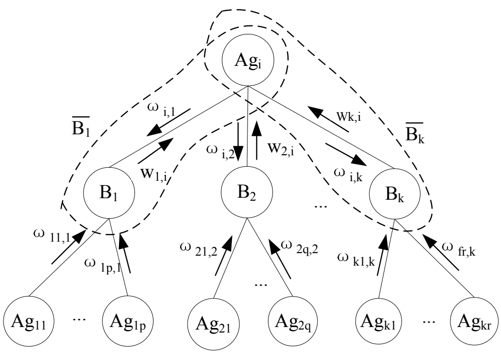

Fig. 1. The coordination tree of Ag_i

Define: Suppose that we have a coordination tree $Tr=(V,E)$ with |V| vertices and |E| edges, where $V=\{B\_Set, Ag\_Set\}$, $Ag\_Set=\{Ag_i, i=1,2,...,Nb\}$, and $Set\_B=\{B_j, j\in[1,...,C_{\mathrm{CoN}}^{k-1}]\}$.

There are not edges between two agents or two set nodes. An agent node can only link set nodes, and a set node has only sides with agent nodes. The side between node Ag_i and B_j denotes that the agent Ag_i cooperates with the agents in the set B_j. All coordination trees of agents are defined based on a coordination graph. For an agent Ag_i, a tree with root Ag_i is defined, which has three layers of nodes and describes the relation of the collaborative agents. The tree structure is shown in fig. 1.

(1) A root node, Ag_i, is an agent, which need to select an agent set B_j to collaborate with.

(2) Each child node of the root is an agent subset $B_j, j\in[1,...,C_{\mathrm{CoN}}^{k-1}]$. B_j is an agent subset which may collaborate with Ag_i. $\mathrm{CoN}(\mathrm{CoN}\le Nb)$ is the number of the agents in the view of the agent Ag_i. C_{CoN}^{k-1} is the number of potential subsets collaborating with the agent Ag_i. For example, there are n agent sets collaborating with B_j in figure 1,in which n is equal to C_{CoN}^{k-1}.

$$B_j=\{Ag_{ji} \mid Ag_{ji}\in Ag\_Set\ and\ Ag_{ji}\ne Ag_i, i=1,2,...,k-1\} \tag{1}$$

Where the set Ag_Set is an agent set. An agent Ag_i needs to select $k-1$ agents to collaborate with. A tree with a root Ag_i is built and has sub nodes B_j, and $Ag_i\notin B_j$.

(2) A team $\overline{B}_j$ is formed with Ag_i and B_j.

$$\overline{B}_j=B_j+\{Ag_i\} \tag{2}$$

(3) Each node of tree in the third layer is an agent which may collaborate with agents in B_j.

An agent Ag_{jl} might collaborate with subset B_j ,where $Ag_{jl}\notin B_j \cap Ag_{jl}\ne Ag_i$.

(4) Two kinds of weights are present.

The weight ω on the edge of a tree denotes the minimal collaborative cost of an agent with a subset. The weight w is the minimal collaborative cost of a subset collaborating with another agent than Ag_i. For node B_j in the second layer, the weight $\omega_{i,j}$ denotes the collaborative cost of B_j with Ag_i. The weight $w_{j,i}$ is the collaborative cost of B_j collaborating with an agent Ag_{jl} ($Ag_{jl}\ne Ag_i$). We need now to select an optimal collaborative subset for Ag_i based on coordination trees.

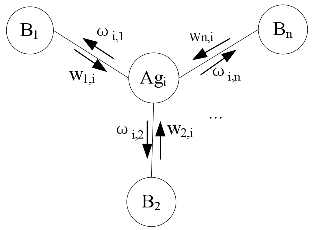

Fig. 2a. Communication model of the agent Ag_i

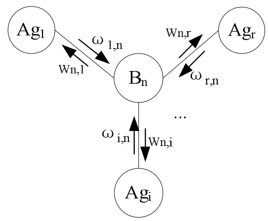

Fig. 2b. Communication model of the agent subset B_k

(5) Communication modes between an agent and agent subsets.

The communication model of the agent Ag_i is showed in fig.2a, and the communication model of the subset B_k is showed in fig.2b. Each agent Ag_i sends collaborative cost or a payoff $\omega_{i,j}$ to the subset $B_j\,(Ag_i \notin B_j)$ which connect to Ag_i by a edge .The subset B_j will return a minimal collaborative cost or a maximal payoff $w_{j,i}$ to Ag_i collaborating with one other agent except the agent Ag_i.

3 Calculating a Collaboration for an Agent

3.1 Dynamic Partition of Collaborative Subsets

We present an algorithm for an agent based on this coordination tree structure. An agent Ag_i can select its collaborating agent subset according to the algorithm CSCT below.

Algorithm: CSCT- calculating **C**ollaborative **S**ubset based on **C**oordination **T**ree

(1) The agent Ag_i sends a cost $\omega_{i,j}$ to each agent in B_j, which denotes the collaborative cost with $k-1$ agents in subset B_j.

(2) When B_j receives a cost $\omega_{i,j}$, it returns a message $w_{j,i}$ to Ag_i which is the cost of B_j collaborating with another agent. For example, the subset B_j on the second layer in fig.1 selects a potential collaborative agent Ag_{jm} instead of Ag_i at the cost:

$$w_{j,i} = \min_{Ag_{jm}}(\{\omega_{m,j}\}) \tag{3}$$

Where Ag_{jm} is one child node of B_j, and the $\omega_{m,j}$ is the weight between the node B_j and the node Ag_{jm}.

(3) The agent Ag_i selects the optimal collaborative subset B_j.

Because each agent learns joint actions rationally, it makes decision for a maximal reward of all agents. Each agent can estimate the possible actions of other agents based on a coordination tree. The rate $\omega_{i,j} / w_{j,i}$ is a probability measure that denotes B_j collaborating with Ag_i. The B_j with minimal $\omega_{i,j} / w_{j,i}$ value is the appropriate subset to collaborate with Ag_i.

$$B_j = \arg\min_{B_j} (\omega_{i,j} / w_{j,i}) \tag{4}$$

3.2 Policy of Joint Actions

After calculating collaborative subset based on coordination tree, joint action in a team $\overline{B}_j$ should be decided. In multi-agent's learning procedure, the system's state switching is determined by the actions of the learning agent and other agents together. In most cases, the agent's action in a certain state is a random behavior which obeys some probability distribution[10][11][13]. Thus the learning agent can model the beliefs of other relevant agents by observing their behavior histories. Other agents' strategies obey certain probability distributions, which can be partially determined by prior knowledge and observations, thus their strategies can be estimated. Therefore, through observation and statistic analysis in the learning process, one agent can learn the strategies of other agents and understand their influence on the environment[12] [14]. Through making use of the estimated probabilities of other agents' actions to ensure the selection of optimal joint actions, members in teams take the best response actions according to other agent's actions in the same environment[15]. Every cooperative team learns independently, multiple cooperative teams can prevent the problem of dimensionality to some extent. Single agent is able to learn in a multi-agent framework. The joint action in a team $\overline{B}_j$ is determined by using the behavior probability estimation and joint action statistic.

4 Experiment Setup and Simulation

4.1 Environment and Agent Setting

There are n agents for the red side and the blue side fighting each other. Nb is the number of agents in the blue side, and Nr is the number of agents in red side. Only surrounded by k opposite agents simultaneously an agent can be destroyed. We use a two-dimensional plane as the experimental environment. Each agent has a view field $vision\_v$. Blue side agents perform according to a reinforcement learning method, the agents of red side act according to specific policy and they know nothing about the action policy of each other. For a blue side agent, the threat distance of a red side agent is d ,where $d \le vision\_v$, which means that the distance between two opposite agents is larger than the threat distance d in the view, there is no threat each other.

4.2 Parameter Setting

We design two experiments and analyze the performance of the above methods. The first experiment has a 15×15 grid, with four red side agents versus four blue ones. The second experiment has a 20×20 grid, with four red side agents versus five blue ones. When a red side agent was destroyed by the blue side team, a reward r is given. When a blue side agent is destroyed by the red side team, a reward -r is given as punishment. The exploration rate is denoted as ε. In order to prove the suitability of the algorithm presented in this paper, we compare our method to a nearest neighbor approach. In that approach teams of collaborative agents are formed with the closest other agent.

In our experiments, the parameters reward, the discount γ, the exploring rate ε are set to 1000, 0.9, 0.3 respectively, and the number of collaborative agent is all set to 2. The attenuation factor is set to 0.6. The action set is {stop, up, down, left, right}. The current state s is the agent's location. At the beginning of each simulation, agents start from different positions, and the game ends when all opposite agents are caught successfully. The h-step back method is used to redistribute the reward. That means the reward $\beta^h r$ of the final state is regarded as the reward of the h-step back, where β is an attenuation factor. The number of back states should less than the size of view, therefore, $vision\_v \geq h$.

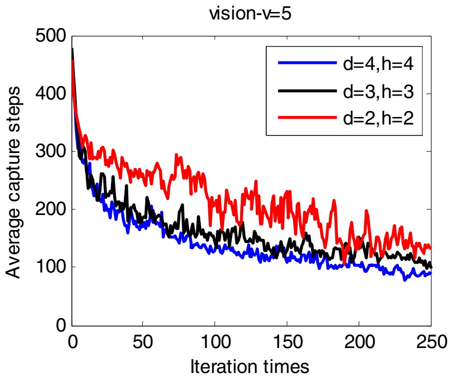

Fig. 3. Comparison of 4 versus 4 agents in a 15×15 grid

In fig.3, the horizontal axis shows the number of learning iterations, the vertical axis shows the number of steps needed at each capture. For showing and analyzing the experimental result conveniently, we draw the average value per 4 time steps in the learning periods. Each experiment is repeated 20 times. From the first experimental result in fig.3, the Q-learning of team Markov games based on coordination trees could converge to the optimal value finally. It is observed that, the closer d and h are to $vision\_v$, the better results we get. When d is close to $vision\_v$, blue side agents can easily sense the threat from the red side agent in a larger view. The bigger h is, the more previous states the rewards feed back through the Q-table, thus accelerating the convergence.

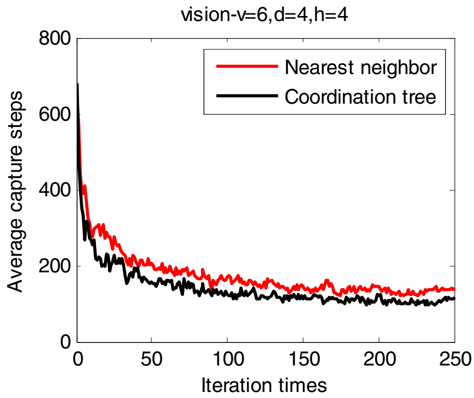

Fig. 4. Comparison of different learning algorithms in a 20×20 grid

From the second experiment results in fig. 4, we find that the policy based on coordination trees is better than the method of selecting the nearest neighbors. When using the coordination tree method, Ag_i calculates the probability of collaborating with other agents based on communication, the agent subset with a maximum probability was selected as its cooperation object. So each agent can select its cooperation object freely according to observations on the environment and the behavior probability estimation and the nearest agents of Ag_i don't necessarily select Ag_i as its cooperation object.

5 Conclusion

In the study of Markov game, it is difficult to form the team of cooperating agents dynamically and to decide on the joint action of agents. On the basis of multi-agent reinforcement learning with agent teams in Markov games, we present a cooperation tree-structure by using the subset of cooperation agents as the nodes of a tree. Two kind of weights are defined which describe the cost of an agent collaborating with or without an agent subset respectively. Each agent calculates its collaborative agent subset with a minimal cost based on coordination trees. From the results of our experiments in a simulation environment, the collaborative team calculating and joint action learning of multi-agent based belief model can all improve the algorithm performance.

Acknowledgements. Many thanks are given to Prof. Shimon Whiteson in Amsterdam University who gives some helpful suggestions for this paper.

References

1. Boeling, M.: Multiagent Learning in the Presence of Agents with Limitations. CMU 4, 1–172 (2003)
2. Parker, L.E.: Distributed algorithms for multi-robot observation of multiple moving targets. Autonomous Robots 12(3), 231–255 (2002)
3. Pynadath, D.V., Tambe, M.: The communicative multiagent team decision problem: Analyzing teamwork theories and models. Journal of Artificial Intelligence Research 16, 389–423 (2002)
4. Guestrin, C.: Planning under uncertainty in complex structured environments. PhD thesis, Computer Science Department, Stanford University (August 2003)
5. Groen, F.C.A., Spaan, M.T.J., Kok, J.R., Pavlin, G.: Real World Multi-agent Systems: Information Sharing, Coordination and Planning. In: ten Cate, B.D., Zeevat, H.W. (eds.) TbiLLC 2005. LNCS (LNAI), vol. 4363, pp. 154–165. Springer, Heidelberg (2007)
6. Kok, J.R., Spaan, M.T.J., Vlassis, N.: Non-communicative multi-robot coordination in dynamic environments. Robotics and Autonomous Systems 50(2-3), 99–114 (2005)
7. Tesauro, G.: Extending Q-learning to general adaptive multi-agent systems. In: Advances in Neural Information Processing Systems, vol. 16 (2004)
8. Guestrin, C., Koller, D., Parr, R.: Multiagent planning with factored MDPs. In: Advances in Neural Information Processing Systems (NIPS) 14. MIT Press (2002a)
9. Kok, J.R., Vlassis, N.: Collaborative Multiagent Reinforcement Learning by Payoff Propagation. Journal of Machine Learning Research, 1789–1828 (2006)
10. Christopher Gifford, M., Agah, A.: Sharing in Teams of Heterogeneous,Collaborative Learning Agents. International Journal of Intelligent Systems 24(2), 173–200 (2009)
11. Zhang, C., Lesser, V.R., Abdallah, S.: Self-organization for coordinating decentralized reinforcement learning. In: Proceedings of AAMAS, pp. 739–746 (2010)
12. Hoen, P.J.'., de Jong, E.D.: Evolutionary Multi-agent Systems. In: Yao, X., Burke, E.K., Lozano, J.A., Smith, J., Merelo-Guervós, J.J., Bullinaria, J.A., Rowe, J.E., Tiňo, P., Kabán, A., Schwefel, H.-P. (eds.) PPSN 2004. LNCS, vol. 3242, pp. 872–881. Springer, Heidelberg (2004)
13. Kapetanakis, S., Kudenko, D.: Reinforcement learning of coordination in heterogeneous cooperative multi-agent systems. In: Proceedings of the Third Autonomous Agents and Multi-Agent Systems Conference (2004)
14. Panait, L., Luke, S.: Cooperative Multi-Agent Learning: The State of the Art. Autonomous Agents and Multi-Agent Systems 11(3), 387–434 (2005)
15. Li, J., Pan, Q., Hong, B.: A new multi-agent reinforcement learning approach. In: 2010 IEEE International Conference on Information and Automation (ICIA), vol. 6, pp. 1667–1671 (2010)

A Distributed Kinodynamic Collision Avoidance System under ROS

Nicoló Boscolo[1,⋆], Riccardo De Battisti[1,⋆], Matteo Munaro[1], Alessandro Farinelli[2], and Enrico Pagello[1]

[1] Department of Information Engineering
University of Padova, via Gradenigo, 6B 35131 Padova, Italy
{debattis,boscolo2,munaro,epv}@dei.unipd.it
[2] Department of Computer Science
University of Verona, Strada Le Grazie, 15 37134 Verona, Italy
alessandro.farinelli@univr.it

Abstract. This paper focuses on decentralized coordination for small or medium groups of heterogeneous mobile robots with relatively low computational resources. Specifically, we consider coordinated obstacle avoidance techniques for mobile platforms performing high level tasks, such as patrolling or exploration. In more details, we propose the use of a greedy kinodynamic collision avoidance approach for the single robots and the use of the the Max-sum algorithm for multi-robot coordination. The system implementation and its testing are based on the popular robot middleware ROS and the gazebo simulation environment. Obtained results show that our distributed collision avoidance approach is able to achieve safe navigation in real-time with a very low overhead in terms of computation and communication.

1 Introduction

The ability to safely navigate in crowded environments is a key element for most applications involving mobile robots, and collision avoidance is a crucial component of any navigation systems. Here we focus on coordinating robots' maneuvers to achieve collision avoidance for a group of mobile platforms with limited computational capabilities. The *collision avoidance problem* in a known static environment with multiple robots has a wide literature, but we can identify two approaches: the *reactive (myopic)* and the *predictive* one. The former is a class of methods that permits robots to avoid collisions on a dynamic environment without explicit communication. Such methods include the *Dynamic Window Approach* [4] and *Velocity Obstacles* [8]. The latter has his most recent extension on the *Optimal Reciprocal Collision Avoidance* (ORCA) [16]. This can be used to simulate thousands of moving agents without collisions and achieve this objective without communication. Among myopic methods, path deformation techniques compute a flexible path that is adapted on-line so as to avoid

⋆ Nicoló Boscolo and Riccardo De Battisti contributed equally to this work.

S. Lee et al. (Eds.): Intelligent Autonomous Systems 12, AISC 194, pp. 511–521.
springerlink.com

moving obstacles [18]. These approaches are very efficient in simulations with a high number of agents as shown with *Reciprocal Velocity Obstacles* (RVO) [3]. However, that approach only works well if the only moving obstacles are other robots with the same behavior, furthermore some deadlocks can arise, e.g. the *dancing behavior*, and it can not deal with the *Inevitable Collision State* (ICS)[1] issue [10]. The predictive approaches can be addressed either with coupled or decoupled approaches. *Coupled* approaches guarantee completeness but generate an exponential dependence on the number of robots and use a centralized computation [7]. Decoupled approaches allow robots to compute their own paths and then resolve conflicts, so that feasible solutions are usually incomplete, but computed faster and in a decentralized way. For instance, in prioritized planners, where low priority robots have to adapt their path plans upon the decisions of high priority robots, this decoupled approach could have a heavy impact on finding a feasible real-time solution. The solution to the path-planning problem for robots with second-order dynamics, i.e. the kind of robots proposed in this work, can be achieved by using a sampling-based tree planner [15,2] and, even if all robots decide a feasible plan, maybe its end state is an ICS [10]. The literature on contingency planning to avoid ICS in static environments shows that braking maneuvers are sufficient to provide safety if used within a control-based scheme [17] or in sampling-based replanning [5], as well as with learning-based approximations of ICS sets [13] or approximations for computing space×time obstacles [6].

This work uses a not prioritized, decoupled approach and is inspired by the safety rules proposed in [2] about how to avoid ICS and collisions between robots. This system is based on the computation of a set of plans concatenated with the robot's contingency plan and the exchange of this information among robots. This permits the choice of a safe trajectory for every robot. Here, we propose the same kind of decoupled approach but with some key differences: the *factor graph* [14] as communication network, the *max-sum algorithm* [1] for the distributed coordination. The system still provide safety and good performance even without real-time design communication protocols such as in ROS. The paper is organized as follows. Section 2 outlines the problem statement. Section 3 presents the description of the collision avoidance system, first focusing on its single components, then explaining some algorithm contributions to the problem and finally illustrating the implementation within the ROS system. Section 4 explains the experiments conducted and the results obtained. Finally, conclusions and future works are discussed in Section 5.

2 Problem Statement

Let R be a set of n independent robots, i.e. $R = \{R_1, R_2, \ldots, R_n\}$ and let each robot R_i, $1 \leq i \leq n$ have second order dynamics ruled by the time constraint

$$\dot{x}_i\,(t) = f\,(x_i\,(t)\,, u_i)\,,\ g\,(x_i\,(t)\,, \dot{x}_i\,(t)) \leq 0,\ \forall t \in \mathbb{R},$$

[1] A state is an ICS if every next state involves a collision.

where $x_i(t)$ represents a system state, u_i a robot control and function f and g are both smooth. Let $E \subseteq \mathbb{R}^2$ be the *environment* where the robot operates and $FE \subseteq E$ the *free environment*, the free space of that environment. Given a point $p \in \mathbb{R}^2$, for each robot R_i, $f_P(R_i, p)$ is called the *footprint* on the point p, i.e. the subset of FE occupied by the robot, while $c(R_i) \subseteq \mathbb{R}^2$ is the center of that footprint. The 2D local subspace of FE where robot R_i can perceive and move, i.e. every $c(R_i)$ such that $f_P(R_i, c(R_i)) \subseteq FE$, is called the *safe environment* and is represented by SE_i.

Let robot R_i be the owner of a *local goal* list GL_i filled with 2D space points $(x, y) \in SE_i$, the problem to be solved is the following: every robot R_i have to reach its *global goal* G_i passing through a sequence of local goals, where a local goal can be reached by choosing a linear trajectory and maintaining a speed v_i selected from V_i, a discrete set of velocities. In particular, when a local goal is reached, R_i has to compute a new GL_i and select both a new local goal $gl_i \in GL_i$ and a velocity $v_i \in V_i$ such that, until R_i does not reach gl_i, $\forall t$

$$\begin{cases} f_P(R_i, v_i \cdot t) \in SE_i \\ f_P(R_i, v_i \cdot t) \cap f_P(R_i, v_j \cdot t) \neq \emptyset \quad \forall i \neq j \end{cases}.$$

3 System Description

The planning cycle is executed by performing the following steps on the system represented in Figure 1:

1. The *Environment Model Builder* retrieves sensor and odometry data and computes a *costmap*, i.e. a discrete grid inflated with costs obtained from the environment sensor data;
2. Given the global goal and the SE, the *Local Goals Generator* computes a set of feasible[2] goals around the robot position. Next the robots start the coordination step which ends with the selection of such goals that maximize the distances between all robots.
3. Given a local goal and by using the A^* algorithm [12], the *Motion Planne*r computes a path whose distance is covered with the dynamic window approach[9].
4. The *Controller* receives the path and starts to send the motion commands to the real robot in sense-react loop until it does not reach the local goal.

Let *SD* be the *safe distance* (e.g. 0.5 meters) equals to the space needed by the robot to safely carry out one of its ICS escape maneuverers. The ICS is avoided using a simple policy: each robot has to cover at least a distance of SD, such that if the path has a length $L \geq SD$ the robot will move for that length L minus the safe distance SD, i.e. $L - SD$.

Our escape action is divided into two steps: first the robot tries to rotate slowly with the purpose of updating the costmap with some moving obstacles, then, if after two rotations obstacles still blocks its path the robot stops and looks for another path.

[2] Feasible means that for sure there is a path between robot position and the goal.

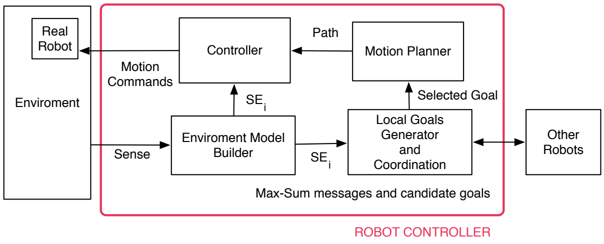

Fig. 1. Block schema of the collision avoidance system

3.1 Local Goal Generator and Coordination

In this section we outline the theoretical and mathematical frameworks used for developing our collision avoidance algorithm *(Local Goal Generator and Coordination* on Figure 1).

3.1.1 Navigation Algorithm

Our navigation algorithm is detailed in Figure 2. Specifically we use a set structure called *geostructure,* where we keep all the computed goals. Geostructure is able to return the goals directly reachable from the current robot position (*neighbourhood*). Next, when we call c*ompute_goals_from* function, we select the safe[3] goals around the robot position that are not near to the useless goals in geostructure. Finally, if at least a goal is found, we select the local goal that minimizes the distance to the global goal, otherwise recovery actions are taken.

3.1.2 Factor Graph

We use the *factor graph* [14] framework to perform our coordination problem. Specifically, given a real valued function $g(x_1, x_2, \dots, x_n) = \sum_{i=1}^{m} f_i(\mathbf{x_i})$, where $\mathbf{x_i} \subseteq \{x_1, x_2, \dots x_r\}$, $r \leq n$, a factor graph is defined as a bipartite graph that shows the structure of this summation. In particular the factor graph $FG = \{\mathbf{x}, \mathbf{f}\}$ consists of *variable nodes* $\mathbf{x} = \{x_1, x_2, \dots, x_n\}$ and *function nodes* $\mathbf{f} = \{f_1, f_2, \dots f_m\}$ where a variable node x_i is connected to the function node f_j if and only if the variable is an argument of the function, i.e. $x_i \in \mathbf{x}_j$.

3.1.3 Max-sum Algorithm

The max-sum algorithm belongs to the family of iterative *message passing* algorithms called *Generalized Distributive Law* (GDL) [1], which can be combined with factor graphs to efficiently compute functions like $g(\cdot)$. Given a set of robots, i.e. $R_1, R_2, \dots, R_n$, and a factor graph $FG = (\mathbf{x}, \mathbf{F})$ (see an example in Figure 4) where each robot R_i owns a function F_i and a subset $\mathbf{x_i} \subseteq \mathbf{x}$ of variables,

[3] A goal is defined as *safe* when the trajectory towards it does not make robot collide.

```
geostructure gs;
position global_goal;
while(global_goal is not reached){
    curr_pos = get_current_position();
    gs.add(curr_pos);
    gs.find(curr_pos).type = GOOD;
    local_goals = compute_goals_from(curr_pos);
    if(local_goals.size() > 0){
        new_local_goal = select_best(local_goals);
        gs.add(new_local_goal);
        move_to(new_local_goal);
    }else{
        gs.find(curr_pos).type = USELESS;
        recovery_goal = gs.find_good_neighbour(curr_pos);
        if(not set recovery_goal)
            contingency_plan();
        else
            move_to(recovery_goal);
    }
}
```

Fig. 2. High level navigation procedure

the max-sum algorithm computes $\mathbf{x}^* = \arg\max_{\mathbf{x}} \sum_{i=1}^{n} F_i(\mathbf{x_i})$ by repeatedly passing *variable-to-function* q-messages and *function-to-variable* r-messages. Let $\mathbf{x}_i$ be a set of paths to candidate local goals, $F_i(\mathbf{x}_i)$ represents the minimum distance between all possible local goals, logarithmically weighted with the distance to the global goal G_i (see Figure 3). In case $\mathbf{x}_i$ would lead to a collision, $F_i(\mathbf{x}_i)$ is set to an arbitrarily small positive quantity ϵ. Hence $\mathbf{x}^*$ represents the local goals that maximize the system utility $\sum_{i=1}^{n} F_i(\mathbf{x_i})$, i.e. the local goals whose relative trajectories allow each robot to avoid collisions and to get closer to its global goal at the same time. A similar coordination problem in [2] is modeled with coordination graphs [11] and it is solved using the message passing algorithm max-plus [11], but that method does not consider *n-ary* functions. In our approach such functions are very important because they allow us to simultaneously consider, if necessary, not only collisions between couples of robots, but collision between a group of n robots. In particular in our approach each robot owns only its local part of the factor graph, hence a minimal factor graph can be computed even without a real distributed computation. Indeed as Table 1 shows, the Max-sum computational time increases exponentially with the number of graph connections, so in order to keep low the time to reach a solution we communicate with just the two nearest neighbors. As in Algorithm 1 the robot computes the main cycle, where in step 2b we consider neighbors just the robots which are less than

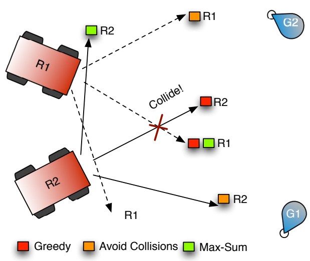

Fig. 3. Comparison between 3 motion planning methods in choosing the local goals with $|GL_i| = 3$

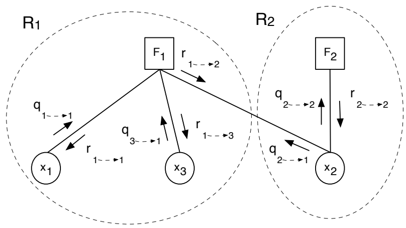

Fig. 4. Example of a simple factor graph, the robots R_1, R_2, the function nodes F_1, F_2, the variables nodes x_1, x_2, x_3

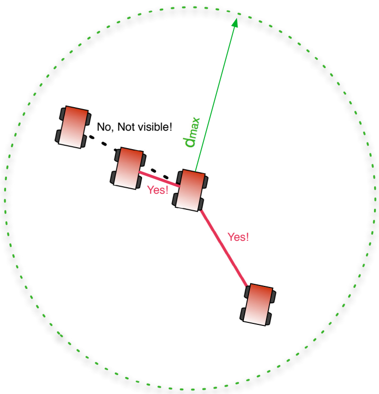

Fig. 5. Line of sight neighbor selection

Algorithm 1. Sense-plan-act cycle

1. *Sense*;
2. *Plan*:
   (a) Compute some possible local goals and their relative trajectories;
   (b) if there are not neighbors which can collide with myself go to 3, else continue;
   (c) if all neighbors do not want to perform the Max-sum algorithm go to 2b, else continue;
   (d) Create the local variables and the local function;
   (e) Create the factor graph with its neighborhood;
   (f) Perform Max-sum and choose the best trajectory;
3. *Act*
   (a) Bring the robot to the trajectory velocity;
   (b) Keep moving until the local or the global goal is reached.

a d_{max} far from the robot. Such distance is that a robot could cross if it moves at the maximum velocity for T_{act}, i.e. the time of the *act* step, and it is so defined

$$d_{max} = v_{max} \cdot T_{act}.$$

In 2e entry, the connection are created after the local graph is computed and it is not rare that two agents are not symmetrically situated in the neighbors set. Indeed the factor graph is a not oriented graph so we check locally the graph consistency. For instance, let the robot R_i be the owner of the variable TR_i *locally connected* with an external function F_j, whose owner is robot R_j, hence if for some reasons in the factor graph of R_j there is not connection between F_j and TR_i, the R_i local edge will be deleted. As stated before, when the Max-sum uses complete factor graphs the communication times grow exponentially (see Table 1) with the number of nodes. We use a *graph pruning* policy where an agent is connected with two nodes at most.

Table 1. Complete factor graph communication times

Variable nodes	Function nodes	Communication Times (secs)
2	2	0.3
3	3	2.7
4	4	23

3.2 System Design under ROS

The middleware ROS (*Robot Operating System*) makes available libraries and tools to help software developers to create robot applications, e.g. hardware abstraction, device drivers, visualizers, message-passing and package management. ROS is organized in software packages with binary nodes that can communicate with other ones even if they are in different packages thanks to asynchronous recipients called *topic* and *service*. Nodes are connected to each other by a peer-to-peer connection but all the nodes have to communicate with the *Master service*[4] to enable the connection. This kind of network architecture highly favors a distributed arrangement. In our developed package the executable node, called *pioneer3AT* node, has three main tasks:

- communicate with other "max-sum" robots;
- compute the new node goal;
- strictly collaborate with *move_base*, the other ROS node used in this system.

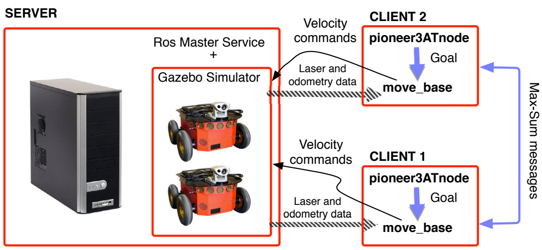

Fig. 6. System setup for our ROS implementation

Given the footprint of the robot, environmental data from on-board sensors (e.g. laser, stereoscopic camera) and the odometry, the *move_base* node has the objective to compute the velocities and the steering angles of the robot in order to reach a goal communicated by the pioneer3AT node. *Move_base* is tuned for avoid the static obstacles by using the Dynamic Window Algorithm. This node also publishes a costmap of the local environment built from the sensor data, which is used to compute the path toward the local goal by using the A^* algorithm. Moreover, we do our test using virtual worlds builded for the *gazebo simulator* [5]. Its APIs permit the modeling and the developing of a virtual pioneer3AT, which can read the velocity command computed by the move_base node. The strength of this modular approach is the reusability of the code and its portability. In fact, the pioneer3AT node source code can be easily adapted and executed on a group of real robots even different from the pioneer3AT.

4 Experiments and Results

The tests on our collision avoidance approach have been focused on the scalability of the planning cycle times. The workbench was a workstation[6] where we

[4] Master service only provides lookup information in some way like a DNS server.
[5] This tool is directly available in ROS.
[6] This machine is equipped with an Xeon 3.10 GHz quad-core processor and 3.8 GiB DDR3 RAM memory.

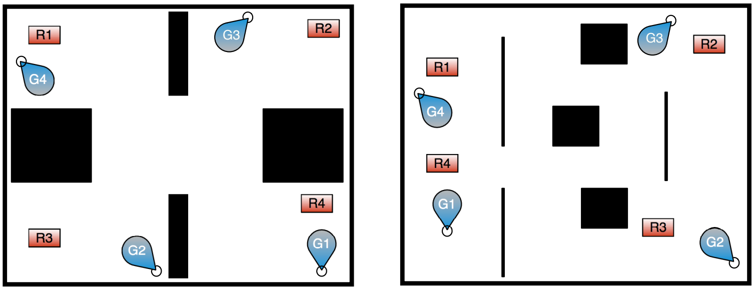

(a) Crossroads (b) Labyrinth

Fig. 7. Scenarios with robots R_1 , R_2 , R_3 , R_4 and global goals G_1 , G_2 , G_3 , G_4

Table 2. Mean algorithm execution times (s) in the crossroads scenario with different number of robots and different $|GL_i|$, $*$: outlier data due to RAM memory swapping

Robots	**Number of local goals**				**Resources per robot**
Units	**4**	**6**	**8**	**12**	**RAM, CPU #**
2	0.15	0.28	0.37	0.43	1.5 GiB, 2
3	0.48	1.32	107.49*	65.89	1.0 GiB, 1
4	2.02	29.52	-	-	0.7 GiB, 1

simulated the robots as different ROS nodes. We used two different scenarios created for the Gazebo environment. In the first one (see Figure 7(a)), robots have to reach their global goals respectively placed on their opposite corner. In the second scenario (see Figure 7(b)) the placement of walls, blocks and goals has been changed for creating a labyrinth. All the simulations involved on the tests have a key topic: all the nodes share the machine memory and its processors, hence increasing the number of robots results in a reduction of resources that they can own. In Table 2 we report the mean execution times for a full round of our algorithm (message exchanges and convergence to a local goal choice) and in the last column we show the estimated RAM and number of CPUs available for each node: we can consider these resources like a virtual on board robot computer with low resources. Moreover, we consider also the worst communication case, where factor graphs are complete[7] so every robot has to exchange messages with all other robots. This case could happen for example, in the first scenario, when all the robots are closed on the center of the environment and they need to share their own paths with all other players. Our tests showed the important role played by the number of candidate goals computed in each planning cycle: we noticed that if this number decreases under the 6 units, collisions happen on almost the 100% of the tests. As shown on Table 2, we can deduce that a real-time onboard robot computer needs 1 CPU with 1 GiB RAM at least.

[7] In a complete factor graph every node function has all the node variables as neighbors, in other words the functions have all the variables as arguments.

5 Conclusions

We built a decoupled and distributed coordination approach with low computational overhead using the Max-Sum and a greedy algorithm with the aim of using it on robots with low computational resources. Since the first results look promising, we envision to try it on a real low cost robots group. As a future work, we also plan to implement a reactive collision avoidance system able to avoid unknown objects, like people.

References

1. Aji, S.M., McEliece, R.J.: The generalized distributive law. IEEE Transactions on Information Theory 46(2), 325–343 (2000), doi:10.1109/18.825794
2. Bekris, K.E., Tsianos, K., Kavraki, L.E.: Safe and distributed kinodynamic replanning for vehicular networks. Mobile Networks and Applications 14(3) (2009)
3. Van den Berg, J., Lin, M., Manocha, D.: Reciprocal velocity obstacles for real-time multi-agent navigation. In: IEEE International Conference on Robotics and Automation 2008, pp. 1928–1935. IEEE (2008)
4. Brock, O., Khatib, O.: High-speed navigation using the global dynamic window approach. In: IEEE International Conference on Robotics and Automation 1999, vol. 1, pp. 341–346. IEEE (1999)
5. Bruce, J., Veloso, M.: Safe multi-robot navigation within dynamics constraints. In: Proceedings of the IEEE, Special Issue on Multi-Robot Systems (2006)
6. Chan, N., Kuffner, J., Zucker, M.: Improved motion planning speed and safety using regions of inevitable collision. In: 17th CISM-IFToMM Symposium on Robot Design, Dynamics, and Control, RoManSy 2008 (2008)
7. Clark, C., Rock, S.M., Latombe, J.-C.: Motion planning for multiple mobile robot systems using dynamic networks. In: IEEE Int. Conference on Robotics and Automation, pp. 4222–4227 (2003)
8. Fiorini, P., Shiller, Z.: Motion planning in dynamic environments using velocity obstacles. The International Journal of Robotics Research 17(7), 760–772 (1998)
9. Fox, D., Burgard, W., Thrun, S.: The dynamic window approach to collision avoidance. IEEE Robotics & Automation Magazine 4(1), 23–33 (1997)
10. Fraichard, T., Asama, H.: Inevitable collision states. a step towards safer robots? In: Intelligent Robots and Systems 2003, vol. 1, pp. 388–393 (2003), doi:10.1109/IROS.2003.1250659
11. Guestrin, C., Koller, D., Parr, R.: Multiagent planning with factored MDPs (2001)
12. Hart, P., Nilsson, N., Raphael, B.: A Formal Basis for the Heuristic Determination of Minimum Cost Paths. IEEE Transactions on Systems Science and Cybernetics 4(2), 100–107 (1968), doi:10.1109/TSSC.1968.300136
13. Kalisiak, M., van de Panne, M.: Faster motion planning using learned local viability models. In: ICRA 2007, pp. 2700–2705 (2007)
14. Kschischang, F.R., Frey, B.J., Loeliger, H.-A.: Factor graphs and the sum-product algorithm. IEEE Transactions on Information Theory 47, 498–519 (1998)

15. LaValle, S.M., Kuffner Jr., J.J.: Randomized kinodynamic planning (1999)
16. Van Den Berg, J., Guy, S., Lin, M., Manocha, D.: Reciprocal n-body collision avoidance. Robotics Research, 3–19 (2011)
17. Wikman, T.S., Branicky, M.S., Newman, W.S.: Reflexive collision avoidance: A generalized approach. In: ICRA (3), pp. 31–36 (1993)
18. Yang, Y., Brock, O.: Elastic roadmaps–motion generation for autonomous mobile manipulation. Auton. Robots 28, 113–130 (2010), doi: http://dx.doi.org/10.1007/s10514-009-9151-x

Authentication Using Shared Knowledge: Learning Agents

Vadim Kimlaychuk

Dept. of Computer Control, Tallinn University of Technology
Ehitajate tee 5, Tallinn 19086, Estonia
vadim@dcc.ttu.ee

Abstract. The way to identify user in existing computer systems has for a long time been simple. It is enough to provide correct password (or identity token) and the majority of the systems will "recognize" you as legal user of given username if any. There is no difference for such a system if there is one person behind this username or many. Authentication of the user for many years has been reduced to the problem of the username validation and is not answering question "Is the user really who he/she represents himself to be?" This problem was identified from the very beginning and there were many attempts to solve it, but without success. General idea to overcome this mismatch is to know more about personality of the user. The key concept here is shared information knowledge (between user and the system) that must be unique. This knowledge can be gathered by intelligent software agents. Article describes JADE [1] agents for shared knowledge multi-agent system that can dynamically learn new concepts and perform learned actions.

Keywords: shared knowledge authentication, learning software agents, JADE.

1 Problem Background

It is natural for the human to recognize other human by voice, appearance, gait, gestures, etc. You probably never ask your mother to say password in order to let her in. There can be mistakes to identify who is your opponent for instance if we talk about twins who want to cheat teacher and appearance, voice and gesture is not enough to be sure who is in front of you. Even though for the mother and other close relatives this is usually not the case. The main reason for this is the unique information that is shared between the parties during their life. The more people communicate with each other, the more they share experience from the common events the better and more precise they can identify each other. We claim to say that for the human there is no problem to identify other human he knows if it is possible to talk to the opponent personally.

Unfortunately in our modern life personal contacts become less frequent because of wide range of communication services that are offered. People tend to communicate through e-mails, messenger services, phones, etc. more often than personal meetings. This contributes to the success of social engineering [2] [3] techniques where intruder

S. Lee et al. (Eds.): Intelligent Autonomous Systems 12, AISC 194, pp. 523–531.
springerlink.com

uses open information in order to pretend to be some person to get sensitive information.

For the computer systems situation is even worse. Computers cannot recognize human face, voice and gestures as efficient as people do. There are number of reliable systems with very high probability of identifying person by fingerprint, iris of the eye, voice and, of course password, but all these properties nowadays can be easily copied and re-produced. That is why more sophisticated systems check not only physical parameters of the user but also try to be more intelligent to ask some specific questions. As we will show later – asking the question from the user is only half a problem. The more difficult is to get and construe answer from the user especially when we expect it in a form of clear text input[1].

In general all the systems that try to get more information about personality of the user are built on 3 main principles: creating the question, asking the question, parsing the answer. Each of these steps can be done in a numerous number of ways and can be automated with different level of the success.

Here we have the major difference between common authentication systems and knowledge based – the success rate and its measurement. The prevalent approach is deterministic. Either user knows password (has key) or not and thus – authenticated or not. Overall result is binary AND of authentication functions if they are many.

The other approach is probabilistic. Biometric authentication systems already work with probability, because object they inspect (voice, face, eye, etc.) tends to deviate from the constant.

For the shared knowledge systems we assume that the user is who he pretends to be if he knows shared secret with some probability. Overall result is the sum of series of authentication functions with a limit = 1. Here we also assume that we make many iterations to reach appropriate level of trust towards the user, because single authentication function cannot give us appropriate level of authentication.

The first type of the system is in fact special case of the second one. If we rise up trust level for authentication function till 100% then we have binary answer to the question if user is authenticated or not.

2 Recent Situation

There are still only 3 ways to authenticate the user in modern computer systems [5] [6] [7]. They are:

- knowledge-based authentication (passwords and passphrases, PINs, graphical passwords)
- token-based authentication (physical tokens such as smartcards or badges)
- biometric-based authentication (using user's physical characteristics such as fingerprint, hand geometry, iris pattern or face)

[1] One of the successful implementation of the human identification is CAPTCHA [4]. It works quite well in their domain where there is a need to separate human answer from the machine generated one. Unfortunately it is not a way to separate one human from another.

Ultimate systems use all 3 at the same time to diminish risk of wrong person to access valuable resource. Unfortunately, as we mentioned above, all 3 types of the resources can be copied. That is why people continue to evaluate computer systems that will be smart enough to identify human by something very personal that cannot be reproduced or guessed by someone else. There are number of papers published in this area [7] [8] [9]. Probably the closest one to this article that can be found in the public resources is "Access control by testing for shared knowledge" [10]. It underlines the problem of user's identification in social networks and shows how private information can be used to increase the level of trust from the system towards the user. Major problems for implementing shared knowledge authentication are:

1. static set of pre-defined questions that needs to be maintained by human
2. problem to identify the correct answer (in case of direct user input)
3. intra-word deviations and spelling errors (like: behavior vs behaviour)
4. alternative words (abbreviations, acronyms, and synonyms)
5. perception/feeling (violet/dark blue, dark/light, far/close)
6. extra or missing words (like "and", "or", "the", "a", etc.)
7. problems identifying user if the input is organized as a set of pre-defined answers, high probability of "guesses"
8. extra-time for the user to answer and type-in text and as a result - low satisfaction of such a system that asks questions not related to its main tasks
9. probabilistic user access control instead of deterministic

It is seeing that complexity of such a system is nearly equal to machine that must recognize natural human languages and be able to ask questions like people do.

3 Requirements for Authentication System

From all the points mentioned above there are certain demands for the system that will allow identifying user in addition to username and password combination.

System should not ask questions. Thus we eliminate problem number 4 and 2.

System should observe user's behavior and transform it into knowledge that can be shared with other parts of the system and can be analyzed for the purpose of getting user's identity. This behavior can include and is not bounded to the speed the user types in words, speed user clicks on the mouse button, URLs he is visiting in Internet, items he is searching in search-engines, favorite software to run, working time, etc. Everything depends on the sensors we have to observe the user.

This knowledge we get cannot be reduced to the number of static parameters – otherwise we cannot evolve our system and need to stick to specific data structure. We see that efficient way of holding information is ontology. Ontology can always be extended with new meanings, actions and behaviors. Possibility to study new ontological concepts allows us to teach agents that operate in terms of this ontology like humans. That is why especially software agents and multi-agent systems (MAS) were chosen to fulfill our task. Focus must be shift towards social-oriented MAS with certain rules similar to human society. We cannot operate with different releases of the software because it is hard from any point to measure version of the knowledge that may grow on all the agents in parallel.

System should evaluate the level of trust towards the user based on observation and for that we have defined *trust function.*

4 Trust Function

Let us define the "trust function" as in (1). Codomain of this function is between 0 and 1, where 1 means the user is authenticated and 0 – is not. For the deterministic authentication we have very simple function as superposition of all the single results for the authentication function (f_n). If at least one of them failed the result of the authentication is 0. It can be described with the formula:

$$y = \bigcap_{1}^{\infty} f_n, y = \{1 | 0\}, f_n = \{1 | 0\} \tag{1}$$

For probabilistic approach the result of summary for all authentication functions lies between 0 and 1. Probability of that user is authenticated cannot be negative and at the same time depending on the results of the authentication functions it can be increased or decreased. It can be described with formula:

$$\begin{cases} y_0 = & p_0 \\ y_n = y_{n=1} + p_n(y_{n-1}) \end{cases}, \quad y = (0;1), p = (-1;1)$$

We have to define initial probability of the user to be authenticated (p_0). Initial probability is a probability of the user to be authenticated without applying any authentication function. In the simplest case it can be equal to 1/u where u is total number of users in the system.

Probabilistic authentication function (p_n) depends on the result on the previous step (y_{n-1}). Thus one single authentication step may have different impact on the result depending on current value of probability. Immediate value of the *trust function* on step n is yn evaluated as in (2).

At the moment it is not clear how to describe function p_n more precisely. It is proposed to use set of weighted coefficients based on expert's estimation. Ultimately probabilistic function should be evaluated by the system dynamically, based on the feedback from the users or monitoring tools at the runtime.

5 Difficulties to Design Such a System

Observation of user's behavior initially is not bounded. But information we get as a result may be considered as private. This is true especially if we observe user's communications. Gathering any kind of information in observation mode is always question of privacy and hence – needs to be legally accepted.

Legacy is not probably the main problem in designing such a system. There is still no good theoretical and practical background of how intelligent systems should be designed in order to be human-like. Multi-agent system theory is probably the closest one because it encompasses sensors, behaviors, agents, social activities – everything we need to fulfill the task. Another strong side of MAS is its natural ability to process information in parallel without unconditional centralization.

Implementation and usage is another weak point. It can take some time for the system to make assumption about user identity if we want agents to act insensibly. By all means this kind of system will be more complex and slower than system that is operating with traditional authentication methods. The main difficulty to build shared knowledge authentication system is knowledge itself. What to represent, how to represent, how to share this knowledge and how to evolve it. That is why the initial task we tried to accomplish is to create simple MAS with minimal number of agents that can demonstrate how knowledge can be transferred and used.

6 Software Agents

6.1 Roles and Properties

For this task it was defined three types of the agents. First type is agent under test called “student”. Initially it knows nothing, but can accept messages from other agents and ether adopt new knowledge or demonstrate the result of known actions.

Second type of the agent is “teacher”. It knows initially something. In our case it knows mathematical operation add on two elements – ether integer or fractional numbers. Teacher can also send this knowledge during communication act. Teacher is also able to find any students before communication act happens because only students are able to learn.

There is also third type of the agent. It is called “examiner”. Examiner knows the same terms teacher does, but it searches for the student agents in order to inspect their knowledge by sending them special type of requests. In our case examiner sends to student two integers expecting student to answer with the result of summary operation.

6.2 Ontology

Initially “student” agent knows only *studentOntology* that is empty and both “teacher” and “examiner” share the same *teacherOntology*. “Examiner” must operate with terms that teacher trains and thus have a feedback from other agents. It is important that “teacher” agent does not perform actions it trains other agents, but “examiner” does and can control that result of the action is correct from the reply of examinee.

For the “student” should be defined general response action in order to create any kind of responses for the request from other agents.

For the “teacher” and “examiner” ontology is static (does not change over the time), but for the “student” ontology is dynamically extendable – agent adds new notions and actions by the set of communication acts. All the initial elements are described in Table 1.

Table 1. Ontologies in knowledge sharing experiment

Ontology name	Action	Arguments	Agent
teacherOntology	add	double, double	teacher, examiner
teacherOntology	add	int, int	teacher, examiner
teacherOntology	add	long, long	teacher, examiner
studentOntology	Response	string[]	student

There are certain ACL messages that agent will react to. They are described in Table 2.

Table 2. Message types in agent communications

Message	Source	Target	Description
teacherOntology	add	double, double	teacher, examiner
teacherOntology	add	int, int	teacher, examiner
teacherOntology	add	long, long	teacher, examiner

Ontologies are programmed in JADE using internal framework class – *BeanOntology*. Advantage of this method is fast ontology generation and ontology class serialization/deserialization.

6.3 Results of Simulation in JADE

Agents are programmed in JAVA using JADE platform. Interactions between agents (i.e. messages and their context) user can trace using JADE build-in agents: Sniffer and Dummy Agents. Sniffer agent GUI screenshots are shown at Fig. 1 and Fig. 2.

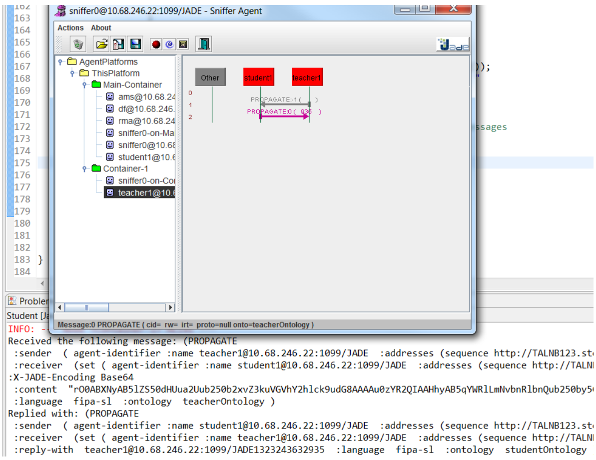

Fig. 1. Student obtains new knowledge from the teacher

There are two main phases shown at figures:

1. Student gets new knowledge from the teacher (Fig 1.)
2. Student demonstrates the result of the operation to examiner (Fig 2.)

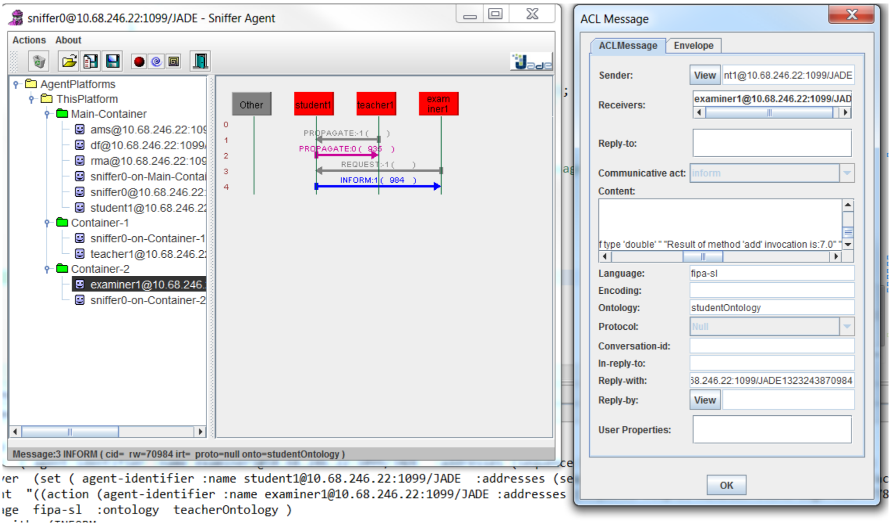

Fig. 2. Student answers to examiner with a result of addition operation

JAVA reflection [11] is used to interpret class methods of the ontological element at the runtime. The main advantage of the described method is ability to train agents without MAS or single agent being re-started or re-initialized.

7 Further Work

This prototype shows how agents can obtain knowledge and use actions to execute required functionality. Yet this is a first step to build MAS that will be able to calculate trust function and make assumption about user identity.

Trust function does not define which particular parameters we need to measure in order to calculate authentication function (f_n). These parameters are application specific and depend on operational domain. For the working authentication system application domain must be defined, notwithstanding that designing principles are general; ontology elements are domain-specific.

Probabilistic function (p_n) is another critical part of the system that needs to be investigated. Since it is correlated with authentication function it also depends on application domain.

It is hard for us to find real application to implement MAS authentication having enough users being using it actively. The main problem is proprietary software owned by private companies. Simulating users activity in laboratory does not give us real output and can’t be used for research.

8 Conclusion

Some of the user identity algorithms are realized in the software that tracks behavior of the customers in web-shops, search engines and media-players. The main goal for this is to help user find information he searches and promote new goods that may be interesting for potential purchaser. Without knowing user's profile it is almost impossible to guess what he/she prefers. Unfortunately recent methods are quite straight-forward and based on very simple tasks like filling in the questionnaire and passing some tests. Information update is done in most cases annually by the same methods. This kind of information is not enough to make assumptions about real identity of the user. On the other hand this type of information is provided by user. He knows what kind of information being asked for and answers on his free will.

Taking all above in consideration we don't see shared knowledge authentication as primary way for authenticating users. The main reason for that is speed. User cannot spend much time to communicate with the system just to be able to log-in. Nevertheless after log-in procedure we have enough time to judge who is working behind this account and may restrict access to critical resources if there is doubt regarding user identity. Strong side of such a system is that it knows the user and more the user works with the system the better system recognizes the user. Authentication is not bounded to initial log-in procedure but lasts during all the period of work.

Another function that shared knowledge can carry on is system usability. If we know user's preferences we can serve his needs faster. Good example is user profile in operating system. It holds all customizations that user has made to desktop, applications, system components, etc. manually. Instead system will adapt to user's needs automatically. Traditional application areas like online shopping, information search and gaming can also get benefit from knowing real user's profile.

References

1. Fabio, B., Giovanni, C., Greenwood, D.: Developing multi-agent systems with JADE. John Wiley & Sons (2007)
2. Mitnick, K., Simon, W., Wozniak, S.: The art of deception. John Wiley & Sons (2002)
3. Long, J., Wiles, J.: No Tech Hacking: A Guide to Social Engineering Dumpster Diving and Shoulder Surfing, pp. 101–121. Syngress (2008)
4. Yan, J.,, A.: A A Low-cost Attack on a Microsoft CAPTCHA. School of Computing Science, Newcastle University, UK (2008)
5. Magno, M.B.: Survey of user authentication mechanisms. Naval Postgraduate School, Monterey (1996)
6. Sasse, A.: Usability and trust in information systems. CiteSeerX (2008)
7. Schneier, B.: Applied cryptography, pp. 52–68. John Wiley & Sons (1996)
8. Nosseir, A., Connor, R., Dunlop, M.: Internet Authentication Based on Personal History - A Feasibility Test. CiteSeerX (2005)

9. Nosseir, A., Connor, R., Revie, C., Terzis, S.: Question-based authentication using context data. In: Nordic Conference on Human-Computer Interaction, vol. 189, pp. 429–432 (2006)
10. Zviran, M., Haga, W.G.: User authentication by cognitive passwords: an empirical assessment. In: Proceedings of the Fifth Jerusalem Conference on Information Technology, pp. 137–144 (1990)
11. Toomim, M., Zhang, X., Fogarty, J., Landay, J.A.: Access Control by Testing for Shared Knowledge. In: Conference on Human Factors in Computing Systems (2008)
12. Forman, I., Forman, N.: Java reflection in action. Manning Publications (2004)

Cooperative Particle Swarm Optimization-Based Predictive Controller for Multi-robot Formation

Seung-Mok Lee and Hyun Myung

KAIST, 291 Daehak-ro, Yuseong-gu, Daejeon 305-701, Republic of Korea
seungmok@kaist.ac.kr, hmyung@kaist.ac.kr

Abstract. In this paper, cooperative particle swarm optimization (CPSO)-based model predictive control (MPC) scheme is proposed to deal with the formation control problem of multiple nonholonomic mobile robots. In distributed MPC framework, control input of each robot needs to be optimized over a finite prediction interval considering control inputs of the other robots, where the objective function is coupled by the state variables of the neighboring robots. To solve the optimization problem on a prediction interval, we present a modified CPSO algorithm which finds a Nash equilibrium between multiple robots. Simulations are performed on a group of nonholonomic mobile robots to demonstrate the effectiveness of the proposed MPC scheme incorporating CPSO.

1 Introduction

Model predictive control (MPC) has been successfully applied to control complex systems in industry as one of the most popular optimal control techniques. The control technique is derived on the basis of the prediction of the future behavior estimated by the explicit model of the system. Thus, the application to nonlinear system is not easy because the nonlinear optimization process should be completed within a limited time.

Recently, some researchers have studied the possibility of applying evolutionary algorithms (EAs) to solve the optimization problem in MPC. Onnen et al. [1] suggested a genetic algorithm (GA) in order to optimize a control sequence, and they showed the effectiveness of the GA comparing to a branch-and-bound discrete search algorithm. Similar algorithms applying GA to MPC were presented in [2,3,4]. More recently, modified particle swarm optimization (PSO) algorithms have been combined with MPC as presented in [5,6,7,8] due to the fact that PSO algorithms provide quick results even with multiple objectives and constraints [6]. In particular, the PSO-based nonlinear MPC controller developed in [7] showed its better performance compared to a MPC controller using quadratic programming.

Cooperative particle swarm optimization (CPSO) algorithm is a variant of PSO, employing multiple swarms to optimize different variables of the solution in a cooperative coevolution (CC) framework. An early attempt to apply the CC framework to PSO was made by Bergh and Engelbrecht [9], resulting in two CPSO algorithms, namely CPSO-S_K and CPSO-H_K. Recent studies by Li and Yao [10,11] suggest cooperative coevolving PSO (CCPSO) and CCPSO2 incorporating *random grouping* and *adaptive weighting* schemes, and their performance was validated on benchmark functions of up to 1,000 dimensions.

S. Lee et al. (Eds.): Intelligent Autonomous Systems 12, AISC 194, pp. 533–541.
springerlink.com

The problem of interest here is cooperative control between subsystems in MPC framework by including coupling terms in the objective function. Subsystems which are coupled in the objective function are referred as neighbors. In this paper, a distributed MPC scheme incorporating CPSO algorithm is presented where each subsystem is assigned its own optimization problem and communicates information only with neighboring subsystems. Thus, each subsystem has a particle swarm to optimize its objective function value, and the optimization problem is solved according to a Nash equilibrium strategy, i.e., in the optimization process, the swarms coevolve to reach a Nash equilibrium state by exchanging the best particles between the subsystems. In general, it has been found that finding the Nash equilibrium is very difficult given that the system is nonlinear [12]. In [13], a receding horizon Nash controller was developed for multi-agent systems, but it has been limited to linear systems. Thus, this paper proposes a distributed MPC incorporating CPSO having multiple swarms. The proposed MPC scheme is simulated for a formation control problem of multiple nonholonomic robots.

2 Modified CPSO for Distributed MPC

A Nash equilibrium strategy is a collection of strategies of all subsystems, and each strategy is the best response regarding the others' strategies. When the system reaches a Nash equilibrium, no subsystem can further improve their cost by changing its strategy given that all the others keep their strategies fixed or stationary. A Nash equilibrium strategy $(u_1^*, u_2^*, ..., u_M^*)$ is defined by the condition

$$J_i(u_1^*, u_2^*, ..., u_{i-1}^*, u_i^*, u_{i+1}^*, ..., u_M^*) \le J_i(u_1^*, u_2^*, ..., u_{i-1}^*, u_i, u_{i+1}^*, ..., u_M^*) \quad (1)$$

for $i = 1, ..., M$ where J_i is the objective function of the i-th subsystem and u_i is an arbitrary control input.

In order to reach the Nash equilibrium, each subsystem needs first to know what the others' strategies are. However, the others' strategies are not available at the time when a subsystem computes its strategy since the state variables and control inputs of the multiple subsystems are coupled together in the objective functions, which results in a chicken and egg problem.

To deal with the problem, the concept of cooperative particle swarms is adapted such that all subsystems reach a Nash equilibrium at the same time in a distributed way. Since CPSO coevolves the multiple particle swarms by exchanging the global best particles with neighboring swarms, we have selected CPSO as the optimizer for multiple subsystems.

2.1 Cooperative Particle Swarms for Nash Equilibrium

For each subsystem, an objective function defined as a coupled form by the state variables and control inputs of the neighboring subsystems is given, and a particle swarm is assigned to each subsystem in order to optimize the given objective function. To reach the Nash equilibrium, each subsystem evolves its particle swarm with respect to its objective function by exchanging the global best particle with its neighboring swarms, while the neighboring swarms are also evolving.

The proposed cooperative PSO algorithm incorporates two new schemes to improve its performance. First, we put the best particle from the neighboring swarms together into the particle swarm to be optimized at the initialization step. Second, the best particles to be used to evaluate the objective function are updated at every generation. The details are given below.

2.1.1 Particle Initialization

At every update time step, particles of each swarm should be initialized in order to research optimal control input. When initializing the particles of i-th swarm, the global best particles from j-th swarm are used where $j \in \mathcal{N}_i$ and $\mathcal{N}_i$ is the set of the swarms neighboring with j-th swarm. The fact that the optimization process starts with the best particles from itself and neighboring swarms leads to improved convergence performance.

2.1.2 Objective Evaluation

Let $P_j.\mathbf{x}^i_{l-1}$ be the current position of the i-th particle of the j-th swarm at generation $l-1$, $P_j.\mathbf{y}^i_{l-1}$ the personal best of the i-th particle of the j-th swarm, and $P_j.\hat{\mathbf{y}}_{l-1}$ the global best particle of the j-th swarm. For M subsystems, at generation l, j-th subsystem optimizes its objective function J_j using the j-th swarm $P_{j,l-1}$ and the global best particles $P_i.\hat{\mathbf{y}}_{l-1}$ from $\mathcal{N}_j$ where $i \in \mathcal{N}_j$, and then the same process iterates through all swarms from $j = 1$ to M at the same time. After the optimization process of a generation, each subsystem sends the global best particle to neighboring subsystems. In order to evaluate the objective, each particle $P_j.\mathbf{x}_i$ constructs a context vector $\hat{\mathbf{s}}_{\mathcal{N}_j}(P_j.\mathbf{x}_i)$ consisting of the particle $P_j.\mathbf{x}^i_l$ and the received best particles from its neighbor $\mathcal{N}_j$. For example, in three-subsystem case where their objective functions are coupled with each other, i.e., $\mathcal{N}_1 = \{2,3\}$, $\mathcal{N}_2 = \{1,3\}$, and $\mathcal{N}_3 = \{1,2\}$, the context vectors can be constructed as $\hat{\mathbf{s}}_{\mathcal{N}_1}(P_1.\mathbf{x}_i) = (P_1.\mathbf{x}^i_l, P_2.\hat{\mathbf{y}}_l, P_3.\hat{\mathbf{y}}_l)$, $\hat{\mathbf{s}}_{\mathcal{N}_2}(P_2.\mathbf{x}_i) = (P_1.\hat{\mathbf{y}}_l, P_2.\mathbf{x}^i_l, P_3.\hat{\mathbf{y}}_l)$, and $\hat{\mathbf{s}}_{\mathcal{N}_3}(P_3.\mathbf{x}_i) = (P_1.\hat{\mathbf{y}}_l, P_2.\hat{\mathbf{y}}_l, P_3.\mathbf{x}^i_l)$, at generation l. The subsystems reach a Nash equilibrium when there are no subsystems which can further improve their objective evaluation.

2.1.3 Update Rule

The update rule for the i-th particle in the j-th swarm is given by

$$P_j.\mathbf{x}^i_{l+1} = P_j.\mathbf{x}^i_l + P_j.\mathbf{v}^i_{l+1}, \tag{2}$$

$$P_j.\mathbf{v}^i_{l+1} = w_l P_j.\mathbf{v}^i_l + c_1 r_1 (P_j.\mathbf{y}^i_l - P_j.\mathbf{x}^i_l) + c_2 r_2 (P_j.\hat{\mathbf{y}}_l - P_j.\mathbf{x}^i_l), \tag{3}$$

where w_l is the inertia coefficient, which decrease linearly to maintain a balance between exploration and exploitation, c_1 and c_2 are acceleration coefficients, and r_1 and r_2 are random values uniformly and independently generated at every generations within $[0,1]$.

2.2 Nash Equilibrium-Based Predictive Control

The Nash equilibrium-based predictive control is based on the proposed CPSO as shown in Algorithm 1. There are two main loops, inner and outer, in order to perform Nash equilibrium-based predictive control. The outer loop is for the process of MPC, and the inner loop is for the optimization over a finite prediction interval through the CPSO at each control time step t. In the inner loop, for $P_j.\mathbf{x}_l^i$, its personal best $P_j.\mathbf{y}_l^i$ is checked, and then the global best $P_j.\hat{\mathbf{y}}_l$ is checked for update. When the subsystems reach a Nash equilibrium, the states of the subsystems are updated using $P_j.\hat{\mathbf{y}}_l$ in the time interval $[t, t+\delta t)$ where $\delta t < T$. These procedures are repeated until a termination condition is satisfied.

Algorithm 1. The pseudocode of the Nash equilibrium-based MPC incorporating CPSO algorithm. In this psudocode, the j-th subsystem is considered.

Create and initialize swarm;
repeat
  for each particle $i \in [1, ..., \texttt{swarmSize}]$ **do**
    Initialize particle;
  end for
  repeat
    for each particle $i \in [1, ..., \texttt{swarmSize}]$ **do**
      if $J_j(\hat{\mathbf{s}}_{\mathcal{N}_j}(S_j.\mathbf{x}_l^i)) < J_j(\hat{\mathbf{s}}_{\mathcal{N}_j}(S_j.\mathbf{y}_{l-1}^i))$ **then**
        $S_j.\mathbf{y}_l^i \leftarrow S_j.\mathbf{x}_l^i$
      else
        $S_j.\mathbf{y}_l^i \leftarrow S_j.\mathbf{y}_{l-1}^i$
      end if
      if $J_j(\hat{\mathbf{s}}_{\mathcal{N}_j}(S_j.\mathbf{y}_l^i)) < J_j(\hat{\mathbf{s}}_{\mathcal{N}_j}(S_j.\hat{\mathbf{y}}_{l-1}))$ **then**
        $S_j.\hat{\mathbf{y}}_l \leftarrow S_j.\mathbf{y}_l^i$
      else
        $S_j.\hat{\mathbf{y}}_l \leftarrow S_j.\hat{\mathbf{y}}_{l-1}$
      end if
    end for
    Update position and velocity of each particle in P_j using (2) and (3);
    Send $P_j.\hat{\mathbf{y}}_l$ to neighboring robots;
    Receive $P_i.\hat{\mathbf{y}}_l$ from neighboring robots where $i \in \mathcal{N}_j$;
    $l \leftarrow l+1$;
  until Termination condition is satisfied;
  Perform state update of plant j using $P_j.\hat{\mathbf{y}}_l$ in the time interval $[t, t+\delta t)$;
  $t \leftarrow t+\delta t$;
until Termination condition is satisfied;

3 Application to Multi-Robot Formation Control

3.1 Multi-Robot Formation Control Problem

Consider a group of M identical differential drive mobile robots. The motion state of j-th robot defined by $X_j = [x_j, y_j, \theta_j]^T$ can be described by

$$\begin{bmatrix} x_j(k+1) \\ y_j(k+1) \\ \theta_j(k+1) \end{bmatrix} = \begin{bmatrix} x_j(k) + \Delta T \cos\theta_j(k) v_j(k) \\ y_j(k) + \Delta T \sin\theta_j(k) v_j(k) \\ \theta_j(k) + \Delta T \omega_j(k) \end{bmatrix} \quad (4)$$

where X_j is described by its position (x_j, y_j) and orientation θ_j; v_j and ω_j are the linear and angular velocities of each robot, respectively, k is a discrete time step, and ΔT is a sample time.

A desired formation pattern $\mathscr{P}$ consisting of M vertices satisfies the relationships, $\sum_{i=1}^{M} p_{ix} = 0$ and $\sum_{i=1}^{M} p_{iy} = 0$, where p_{ix} and p_{iy} are defined by orthogonal coordinate such that the center of the formation pattern $\mathscr{P}$ is placed at the origin of the orthogonal coordinate.

Now, we define the multi-robot formation control problem in a similar way to [14] as follows:

Problem Definition 1. *Consider a group of nonholonomic mobile robots, given a reference path X_r and a desired formation patterns $\mathscr{P}$. For each robot j, using its own state $[x_j, y_j, \theta_j]^T$, its neighbors' state $[x_i, y_i, \theta_i]^T$ for $i \in \mathscr{N}_j$, the reference path X_r, and the desired formation pattern $\mathscr{P}$, find a predictive controller such that*

$$\lim_{t\to\infty} \begin{bmatrix} x_j - x_i \\ y_j - y_i \end{bmatrix} = \begin{bmatrix} p_{jx} - p_{ix} \\ p_{jy} - p_{iy} \end{bmatrix}, 1 \le j \ne i \le M, \tag{5}$$

$$\lim_{t\to\infty} \begin{bmatrix} \sum_{j=1}^{M} (x_r - \frac{x_j}{M}) \\ \sum_{j=1}^{M} (y_r - \frac{y_j}{M}) \\ \sum_{j=1}^{M} (\theta_r - \frac{\theta_j}{M}) \end{bmatrix} = \begin{bmatrix} 0 \\ 0 \\ 0 \end{bmatrix}. \tag{6}$$

Equations (5) and (6) mean that the formation and tracking error converge to zero as $t \to \infty$, i.e., the center of the group of robots tracks the reference path while maintaining the desired formation pattern $\mathscr{P}$.

3.2 State Description

The global best particle $P_j.\hat{\mathbf{y}}$ represents the predicted control input of subsystem j, $u_j(t) = [v_j(t), \omega_j(t)]^T$, over a prediction interval T as a sequence, i.e.,

$$P_j.\hat{\mathbf{y}} = [v_j(1), v_j(2), ..., v_j(N-1), \omega_j(1), \omega_j(2), ..., \omega_j(N-1)] \tag{7}$$

subject to $|v_j(k)| \le V_{max}$ and $|\omega_j(k)| \le \Omega_{max}$, for $j = 1, 2, ..., M$ and $k = 1, 2, ..., N-1$ where N is a number of prediction steps. Based on v_j and ω_j, the robot state can be produced from the current pose $X_j(1) = [x_j(1),\ y_j(1),\ \theta_j(1)]$ at update time t using (4) as $x_j(k+1) = x_j(1) + \sum_{m=1}^{k} \cos\theta_j(m) v_j(m) \Delta T$, $y_j(k+1) = y_j(1) + \sum_{m=1}^{k} \sin\theta_j(m) v_j(m) \Delta T$, and $\theta_j(k+1) = \theta_j(1) + \sum_{m=1}^{k} \omega(m) \Delta T$.

3.3 Objective Function

The control objective is to achieve two goals: tracking a reference path and maintaining a desired formation in a cooperative and distributed way. Considering system (4) with its neighbors $\mathscr{N}_j$, the objective function J_j, for robot j over a number of finite prediction interval step N can be expressed as follows:

$$J_j = \sum_{k=1}^{N} ||\tilde{X}_j(k)||_P^2 + \sum_{i \in \mathscr{N}_j} \sum_{k=1}^{N} ||\tilde{X}_j(k) - \tilde{X}_i(k)||_Q^2 \tag{8}$$

where $\tilde{X}_j = [\tilde{x}_j \; \tilde{y}_j \; \tilde{\theta}_j]^T$, $\tilde{x}_j = x_r + p_{xj} - x_j$, $\tilde{y}_j = y_r + p_{yj} - y_j$, and $\tilde{\theta}_j = \theta_r - \theta_j$. Also, $P = P^T > 0$, $Q = Q^T > 0$, and $||x||_P^2$ represents $x^T Px$.

Since the multi-robot formation control problem can be considered to be a nonseparable problem (i.e., there are coupling terms in the objective functions), it can be optimized by the proposed CPSO algorithm.

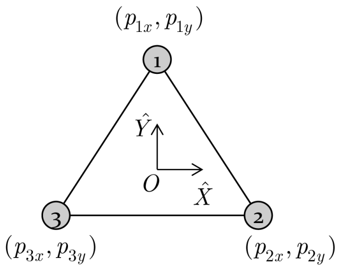

Fig. 1. Desired formation pattern of robots. In simulation, $(p_{x1}, p_{y1}) = (0, \frac{0.1}{\sqrt{3}})$, $(p_{x2}, p_{y2}) = (0.05, -\frac{0.05}{\sqrt{3}})$, and $(p_{x3}, p_{y3}) = (-0.05, -\frac{0.05}{\sqrt{3}})$.

3.4 Simulation Results

The number of prediction horizon steps is selected as $N = 10$, while the control time interval and prediction time interval are selected to be $\delta t = 0.1$s and $\Delta T = 0.1$s. Thus, the prediction horizon is 1s. Since the controller has high computational burden as the prediction interval increase, a long prediction length is not feasible. The weight matrices P and Q are set to be diagonal where $P = \mathtt{diag}[0.1,\ 0.1,\ 0.1]$ and $Q = \mathtt{diag}[0.1,\ 0.1,\ 0.1]$.

For the optimization process by the modified CPSO, each swarm has a population size of 100, and the maximum number of generations is 100. The inertia weight w_l starts with 0.9 and linearly decrease to 0.4. The search space is limited to real-valued variables within $[-V_{max}, V_{max}]$ and $[-\Omega_{max}, \Omega_{max}]$ for v_j and ω_j, respectively, where $V_{max} = 10$m/s and $\Omega_{max} = \pi$rad/s. The acceleration coefficients are $c_1 = 2.0$ and $c_2 = 2.0$.

Three mobile robots are used with the network graph described in Fig. 1. The reference path is a sinusoidal path given by $x_r(t) = 0.1t$, $y_r(t) = 0.8\sin(t/10)$, and $\theta_r(t) = \arctan 2(\dot{y}_r, \dot{x}_r)$. Initially, the robots are located at $X_1 = [0.0, 0.0, \pi/2]^T$, $X_2 = [0.0, -0.05, \pi/2]^T$, and $X_3 = [0.0, 0.05, \pi/2]^T$, respectively. The desired formation pattern $\mathscr{P}$ is an equilateral triangle formation in which the desired separation between the robots is 0.1m, i.e., $p_{x1} = 0$, $p_{y1} = 0.1/\sqrt{3}$, $p_{x2} = 0.05$, $p_{y2} = -0.05/\sqrt{3}$, $p_{x3} = -0.05$, and $p_{y3} = -0.05/\sqrt{3}$ as shown in Fig. 1. To validate the performance, the tracking error e_T and the formation error e_F are defined by $e_T = \sqrt{(x_r - x_c)^2 + (y_r - y_c)^2}$ and $e_F = \sqrt{||\tilde{X}_1 - \tilde{X}_2||^2 + ||\tilde{X}_2 - \tilde{X}_3||^2 + ||\tilde{X}_3 - \tilde{X}_1||^2}$, respectively.

The resulting trajectories of the group of the robots are shown in Fig. 2. It is shown that the three robots maintain a triangular formation while the center of the

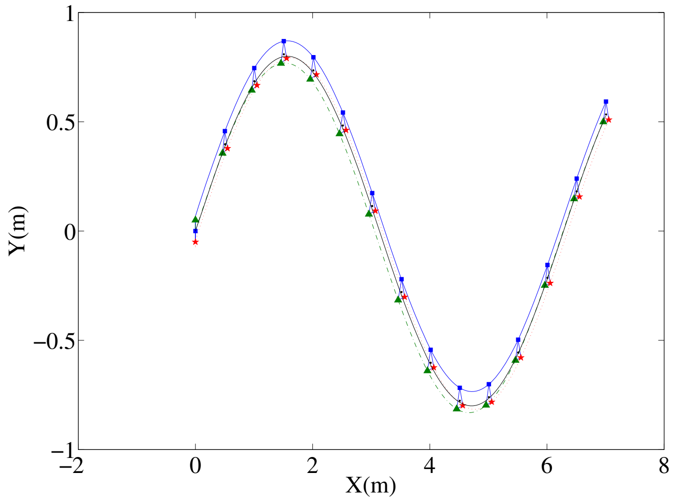

Fig. 2. Triangular formation tracking a sinusoidal reference path. The robot locations sampled at every 5s are indicated by squares, stars, and triangles for $j = 1,2,3$ and the black dots denote the center of the formation. The headings are tangential to the robot's path.

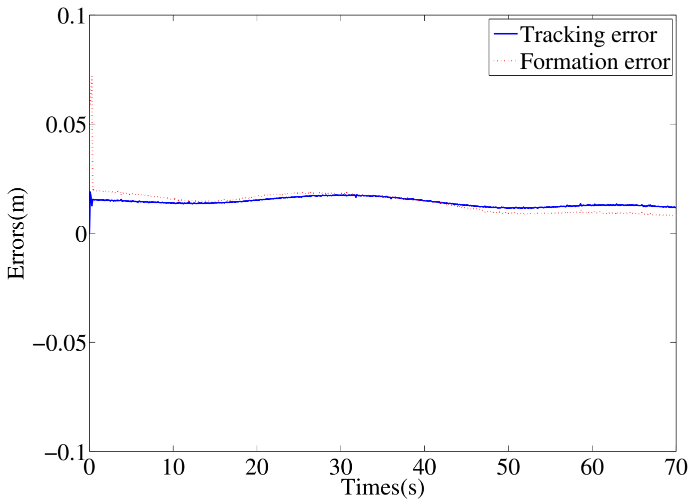

Fig. 3. The tracking error e_T and formation error e_F during tracking a sinusoidal reference path

formation tracks the given reference path using the transmitted information from neighboring robots. Fig. 3 shows the tracking error and formation error which are stable during maneuvering.

4 Conclusion and Future Works

In this paper, a distributed MPC scheme incorporating CPSO was proposed for multi-robot formation control problem. For the optimization process in MPC, a Nash equilibrium strategy was used to solve the optimization problem by exchanging particle information which has the best experience among neighboring subsystems. In the simulation, using the proposed MPC scheme, it was found that the robots moved to track a given reference path, while maintaining a desired formation pattern successfully.

Future works may include investigations of the stability, robustness, improvement of convergence speed, and comparative studies between the proposed method and conventional MPC schemes. The final goal of this research is the development of real-time cooperative MPC scheme according to the Nash equilibrium strategy.

Acknowledgements. This research was supported by the MKE(The Ministry of Knowledge Economy), Korea, under the Human Resources Development Program for Convergence Robot Specialists support program supervised by the NIPA(National IT Industry Promotion Agency) (NIPA-2011-C7000-1001-0001). It was also supported by Basic Science Research Program through the National Research Foundation of Korea (NRF) funded by the Ministry of Education, Science and Technology (grant number 2012-0003897).

References

1. Onnen, C., Babuska, R., Kaymak, U., Sousa, J.M., Verbruggen, H.B., Iserman, R.: Genetic algorithms for optimization in predictive control. Contr. Eng. Practice 5(10), 1363–1372 (1997)
2. Fravolini, M.L., Ficola, A., Cava, M.L.: Real-time evolutionary algorithms for constrained predictive control: Frontiers in Evolutionary Robotics, pp. 139–184. InTech (2008)
3. Martinez, M., Senent, J.S., Blasco, X.: Generalized predictive control using genetic algorithms. Eng. Appl. Artif. Intell. 11(3), 355–367 (1997)
4. Shin, S.C., Park, S.B.: GA based predictive control for nonlinear processes. Electron. Lett. 34(20), 1980–1981 (1998)
5. Newman, A.J., Martin, S.R., DeSena, J.T., Clarke, J.C., McDerment, J.W., Preissler, W.O., Peterson, C.K.: Receding horizon controller using particle swarm optimization for closed-loop ground target surveillance and tracking. In: Proc. SPIE 2009, vol. 7336 (2009)
6. Yousuf, M.S.: Nonlinear predictive control using particle swarm optimization: application to power systems. VDM Verlag Dr. Müller (2010)
7. Mercieca, J., Fabri, S.G.: Particle swarm optimization for nonlinear model predictive control. In: Proc. ADVCOMP, pp. 88–93 (2011)
8. Sedraoui, M., Abdelmalek, S.: Multivariable generalized predictive control using an improved particle swarm optimization algorithm. Informatica 35(3), 363–374 (2011)

9. van den Bergh, F., Engelbrecht, A.: A cooperative approach to particle swarm optimization. IEEE Trans. Evol. Comput. 8(3), 225–239 (2004)
10. Li, X., Yao, X.: Tackling high dimensional nonseparable optimization problems by cooperatively coevolving particle swarms. In: Proc. IEEE CEC, pp. 1546–1553 (2009)
11. Li, X., Yao, X.: Cooperatively coevolving particle swarms for large scale optimization. IEEE Trans. Evol. Comput. 16(2), 210–224 (2012)
12. Sefrioui, M., Periaux, J.: Nash genetic algorithms: examples and applications. In: Proc. IEEE CEC, pp. 509–516 (2000)
13. Gu, D.: A differential game approach to formation control. IEEE Trans. Control Syst. Technol. 16(1), 85–93 (2008)
14. Dong, W.: Flocking of multiple mobile robots based on backstepping. IEEE Trans. Syst. Man Cybern. Part B-Cybern. 41(2), 414–424 (2011)

Modeling Pedestrians in an Airport Scenario with a Time-Augmented Petri Net

Djura Smits, Arnoud Visser, and Frans C.A. Groen

Intelligent Systems Lab Amsterdam, Universiteit van Amsterdam
P.O. Box 94323, 1090 GH Amsterdam, The Netherlands

Abstract. In this paper time-augmented Petri nets are used to model people in the transit hall of an airport. Their behavior is strongly influenced by an event with a clear deadline (their flight), but typically there is so much time left that they linger and can be tempted to show random other behaviors, often induced by the location (encountering a coffee corner or a toilet). All behaviors are stochastic, but the firing rate is made a function of both location and time. This framework allows to show a rich set of behaviors; the diversity of the emergent behaviors is initiated with probabilities from observations in an actual transit hall of an airport.

1 Introduction

Simulation of pedestrians is a widely studied topic. Simulation could predict the emergent patterns in the movements of people, for instance when monitoring them in public places [1]. The local interactions of multiple people generate regular patterns of motion, although less frequent interactions could be interpreted as suspicious behavior. The detection of this suspicious behavior would be the reason why the pedestrians are monitored in the first place, yet it could be easily confused with less frequent but normal behavior as for instance a patrolling police officer or somebody waiting on another. By enriching the behaviors of pedestrians, the addition of suspicious behavior can be made less obvious, which allows to easily create artificial testing data for suspicious behavior detection algorithms and such. In this paper the enrichment of the behaviors is made possible by initiating the interaction of the environment.

Another way to look at the behavior of groups of pedestrians is to explicitly specify how they behave when they enter a certain type of situation [3]. In our approach, we would like to be able to specify behavior by drawing situations on an environment. For example, when a food stand is present in the area, we would like to be able to indicate that the agents that are placed in the neighborhood of that stand are able to perform a certain food-buying behavior, and by doing so, inject this behavior into the pedestrians nearby.

An additional requirement is that we would like to indicate a certain deadline for an agent which is the time at which its goal is not reachable any more. This approach results in roughly two types of behavior, hurried and relaxed. When

S. Lee et al. (Eds.): Intelligent Autonomous Systems 12, AISC 194, pp. 543–551.
springerlink.com

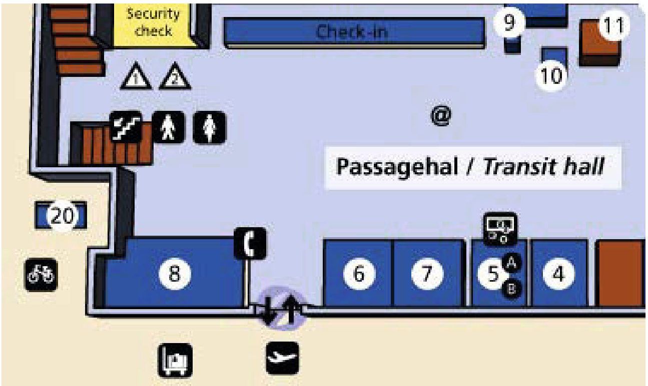

Fig. 1. A snapshot of the map of Rotterdam Airport. The numbers on the map indicate a luggage locker (9), meeting point (10), elevator (11), smoking shelter (20), shops (4,5,7) and information desks (6,8). Courtesy Rotterdam The Hague Airport.

the deadline approaches, less and less actions are likely to be done, since actions that take much time would result in not reaching the goal in time.

We validated our model by mimicking certain behaviors found on Rotterdam airport. We chose Rotterdam airport because time restrictions are very prevalent in a transit hall like the one on Rotterdam airport (see Fig. 1).

2 Related Work

As previously mentioned, most studies focus on aggregated crowd behavior or the behavior of an individual in such crowd [3]. In such cases the interaction with the environment is mainly reduced to collision detection. This greatly limits the applicability of the simulation. In many situations there is not a crowd with many people doing the same, but a situation where individuals could be distinguished, each individual doing something different. The obvious solution is to extend the knowledge of the pedestrians with instructions about how to interact with each other or with objects in the environment. This has been successfully done for instance by Shao and Terzopoulos [4]. They used an extensive psychological model to determine the behavior of the individuals. This led to a simulation in which the behavior looks very realistic, even when one person is followed for a long time. The downside to this method is that the behavioral model for the pedestrians has to be specifically crafted for the environment, which will be very time consuming. It would be easier to generate the virtual human agents if the environment would automatically decide for the agents what interactions are possible and appropriate. The first step towards this focus was made by Kallmann and Thalmann who introduced the principle of smart objects [5].

Their agents' behavior is determined by both their current condition (e.g. hungry or tired) and the available objects placed in the environment. In the most basic approach, these smart objects take complete control of the agents for a short period of time and let them interact with the object. The big advantage of this method is that the information for interacting with a specific object does not need to be stored in the pedestrians, but is stored in the objects themselves. This way, additional behavior can be added to a pedestrian by simply placing a new object in the environment. The object also keeps track about how many agents can interact with it at the same time and if the interaction should be the same for all agents. For instance, an elevator modeled as a smart object will make the first agent interacting with it press the button, but not the next agents that approach this object. By using smart objects, the internal model of the pedestrians can be kept very simple, because they do not need to remember specific information about how to interact with the objects. Furthermore, this means that the pedestrians do not have to be specifically designed for the current simulation environment, because the environment will tell them how to act. In the most basic approach to smart objects, the agents lose all their autonomy when they approach a smart object.

The challenge approached in this paper is to combine the smart object approach with time-driven behaviors; the pedestrians are typically on a location with a goal and have to perform a number of behaviors before a deadline. To model the time-aspect we have chosen to use Petri nets, as described in the next section.

3 Method

Petri nets are a mathematical modeling language used for the description of distributed systems [7]. A Petri net is a bipartite graph consisting of two types of nodes: places and transitions. These nodes are connected by directed arcs. An arc can run from either a place to a transition, or from a transition node to a place, but never from a place to a place, or between two transitions. Activity in a Petri net is expressed by the movement of tokens from place to place, through transitions. Input arcs (from place to transition) denote which places need to contain tokens in order to enable the transition. When a transition is enabled, it consumes the tokens from the input places, and produces tokens in the place indicated by the output arc. Basic Petri nets can be described by a five-tuple:

$$PN = (P, T, I, O, M_0) \tag{1}$$

which comprises of

- a set of places $P = (p_1, p_2, ..., p_m)$,
- a set of transitions $T = (t_1, t_2, ..., o_m)$,
- a set of input arcs $I \subset P \times T$,
- a set of output arcs $O \subset T \times P$,
- an initial marking $M_0 = (m_{01}.m_{02}, \ldots, m_{0m})$.

There are several reasons why we chose Petri nets over other behavior models. First of all, many toolkits are available to easily construct these networks. Moreover, Petri nets can more easily be extended to incorporate useful functionality such as dealing with time. Lastly, there are many tools out there to create new petri nets that can be incorporated into a system in a modular fashion.

Petri nets have been extended in many ways in order to accommodate many different functionalities. The extension that attracts our attention the most is *generalized stochastic Petri nets* [8]. In this extension, there are two types of transitions: *immediate* and *timed* transitions. The generalized stochastic Petri net (GSPN) model can be described as a six-tuple:

$$GSPN = (P, T, I, O, M_0, \Lambda) \tag{2}$$

where (P, T, I, O, M_0) is the marked untimed PN underlying the SPN, and $\Lambda = (\lambda_1, \lambda_2, \ldots, \lambda_n)$ is an array of (possibly marking dependent) firing rates associated with transitions.

Immediate transitions always have priority over timed transitions, and the likelihood of firing a timed transition is dependent on a parameter called the *firing rate* of the transition. This rate indicates the firing delay of the timed transition. This firing rate may be marking-dependent, so it should be written as $\lambda_i(M_j)$. The average firing delay of a transition t_i in marking M_j is $[\lambda_i(M_j)]_{-1}$.

3.1 Deadlines

The essential extension to the situations framework that is proposed in this paper adds an element of time to the system. This is needed to enable the system to deal with daily motion patterns. An important element without which the system cannot succeed is knowledge about how long actions are going to take. Only when this information is known to the agent (or system) it can be decided whether taking a certain action will result exceeding the deadline for the goal.

Central in our design is path planning to a *base place*, where a check is made if it is still possible to reach the (time constrained) goal. Then, we will compute for every transition that will not take the pedestrian to its goal, how much time it takes to get back to the base state. Then we can check whether the goal place is still accessible from the base state when a certain transition has been taken. We use this information to modify the timed transition rate, so pedestrians are more likely to choose the actions that leave them more time to reach their goal. This modification implies that the Petri net is no longer non-stationary.

3.2 Assumptions

The method we propose is based on various assumptions which have to be clarified. An important assumption is that the environment of the pedestrians is designed in such a way that it helps creating realistic behavior. This means that situations have to be defined in such a way that a pedestrian will walk into them and act in the appropriate way. In many cases, intuitively designed environments will cause the right behavior. For instance, in most train stations, the eating stands are placed in such a way that pedestrians will have to walk close to them in order to get to their destination.

Another assumption we make is that the pedestrians have to be at a certain place at a certain time. This makes the system more suitable for daily routine type situations rather than cases in which pedestrians are walking around without a proper goal. However, most situations can be described as having a deadline (e.g. eventually, most people have to go to bed), so this assumption is not necessarily very restrictive.

3.3 Path Planning

To initiate the stochastic Petri net, it has to be known how long an action will take. However, in many cases the duration of action is depended on the travelled distance. It is possible to do perform path-planning between often used places and store them before running the simulation. The travel distance can easily be computed using the *Dijkstra shortest path algorithm* [13]. In our system we can use this to compute the time from any place to the goal place (the source). This can be very useful when we would like to compute an estimate of how long a pedestrian will be busy with executing a behavior in a certain situation. But since the Petri nets are probabilistic, it will never be possible to give an exact prediction of the time it takes to execute a certain behavior.

In our implementation, we used the MASON multiagent simulation toolkit to create a 2 dimensional environment for our pedestrian agents.

4 Results

4.1 Quantitative Experiment

It is very difficult to quantitatively establish whether lifelike behavior has been modeled. However, it is possible to check whether the mechanics of time planning work as predicted. In order to do this, we log the pedestrian's relative time when they arrive at their goal to check how much time they had left until their deadline. If the model works correctly, this time should roughly correlate to how the time probability function has been chosen. We will discuss the various functions we have used to model the probabilities over time.

4.2 Qualitative Experiment

Apart from quantitative analysis, we will also qualitatively judge the pedestrians' behavior. We will do this by comparing our modeled behavior with real-life behavior from recordings of Rotterdam airport. We have picked a couple of specific behaviors that we have modeled with our system.

The Behaviors

Going to the toilet: In the videos, we observed that a typical behavior that manifests itself multiple times in the video material is that one person goes to the toilet, and another one waits until this person has come back. The Petri net used for this can be found in figure 2.

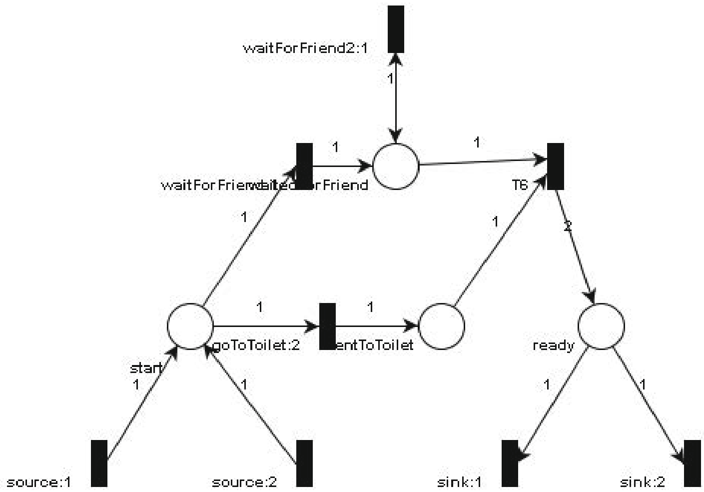

Fig. 2. Behavior model for the toilet situation. Transitions are given with black rectangles, places with white circles.

- **Standing in the queue for the check-in desk:** One constant factor in the video material seemed to be the people lining up in front of the check-in desk. There are many ways to model this behavior with our framework. The situation area is chosen such that the pedestrians in it will together form an orderly line.
- **Checking in:** When the pedestrians reach the end of the queue situation, they will enter the check-in situation, in which they will stand in front of the check-in desk for a little while, after which they are free to go again.
- **Lean Against Pillar:** Another recurring behavior we saw is that people lean against the pillars in the hall. This is a type of idle behavior, a variation on the standing still behavior.

The Petri nets of those four situations are stationary; the firing rate is not a function of time. The duration of the behaviors for each situation is variable, which is stochastically decided. The four situations could be combined with a base state (see Fig. 4), where the decision is made which behavior model is activated. The probabilities of those transitions are a function of time. The probability for GoToGoal increases when the time approaches the departure time, while the probability of a transition to the behavior models ToiletSituation, StandInQueue and LeaningAgainstPillar decreases.

Figure 5 shows how those behaviors are combined in an environment which resembles the transit hall of Rotterdam airport. At the lower left a revolving door is visible, which is the place where agents enter the simulation. The upper right a number of check-in counters, at the upper left the security checkpoints towards the departure hall. The toilets are at the left, at the bottom a number of shops are present. This layout resembles the map as given in Fig. 1.

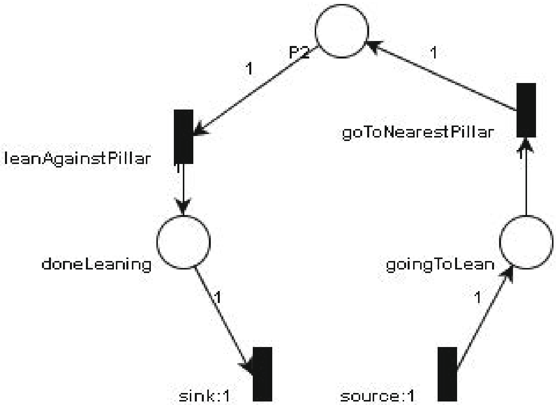

Fig. 3. Behavior model for the pillar situation

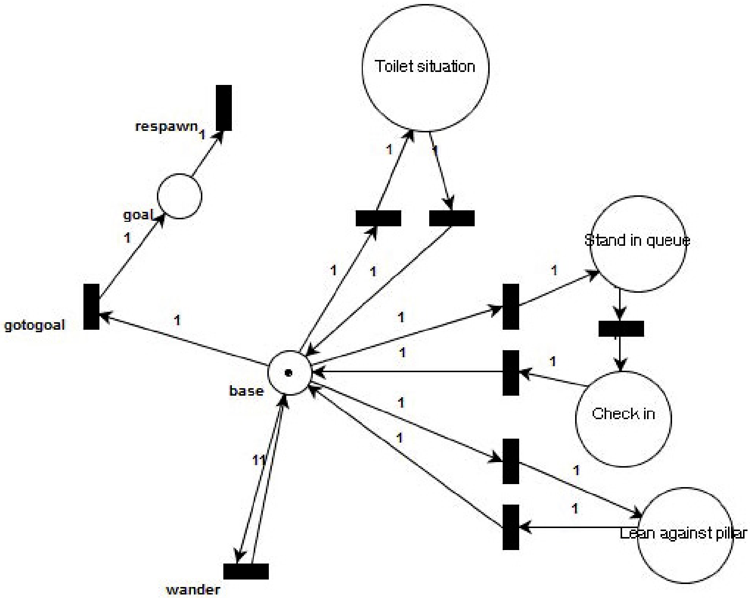

Fig. 4. Complete behavior model of a human in a transit hall

Figure 6 shows how the remaining time towards the security check is distributed when a large fraction of the pedestrians have decided to go the toilet (45% of the simulated agents). Detailed analysis of the logs showed that some pedestrians waited on each other and went to the security check in pairs. Furthermore, this shows that by specifying the probabilities for going to the pedestrians' goal, the probabilities for other actions are also affected.

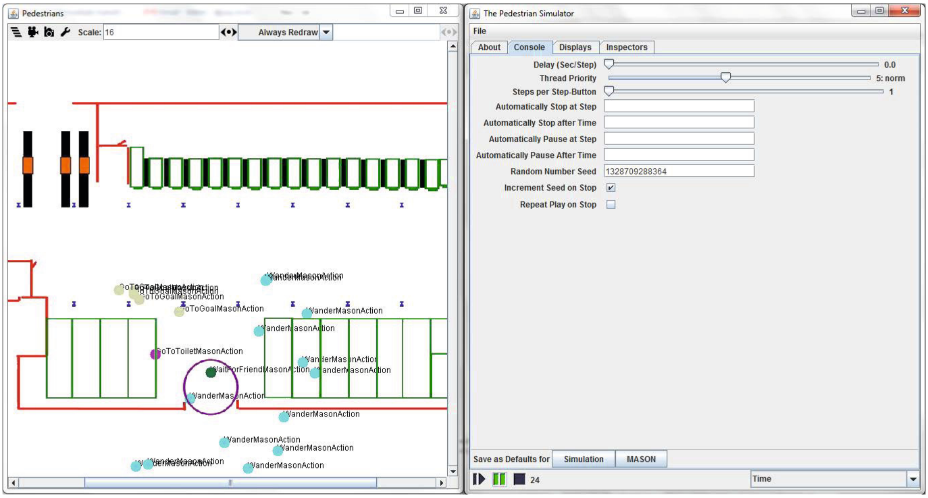

Fig. 5. Screenshot of the simulation environment with four different behaviors (Wander, GoToGoal, GoToToilet, WaitForFriend)

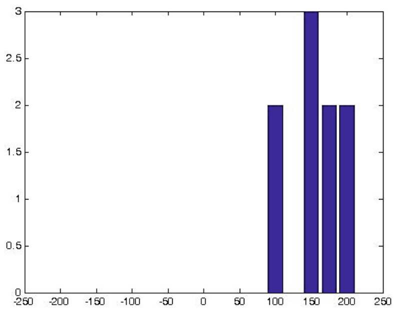

Fig. 6. Distribution of the remaining time towards the security check for pedestrians which went to the toilet

5 Conclusion

In this paper an innovative method to model pedestrian behavior is presented. A time-augmented Petri net is used to make the behavior stochastic. The probability of starting a behavior is made a function of both the location and the time left. This framework is demonstrated on a departure hall scenario, where the time left is the departure time (in this case of an airplane). The conclusion can be made that this framework allows to generate a rich set of emergent motions, which makes it applicable to generate artificial testing data for suspicious behavior detection algorithms.

Acknowledgment. The authors would like to thank Philip Kerbusch for his input.

References

[1] Moore, B.E., Ali, S., Mehran, R., Shah, M.: Visual crowd surveillance through a hydrodynamics lens. Commun. ACM 54(12), 64–73 (2011)

[2] Ritter, F.E., Shadbolt, N.R., Elliman, D., Young, R.M., Gobet, F., Baxter, G.D.: Techniques for modeling human performance in synthetic environments: A supplementary review. Human Systems Information Analysis Center, Wright-Patterson Air Force Base, Ohio, State of the Art Report HSIAC SOAR 02-02 (June 2002)

[3] Giordano, J.C., Reynolds Jr., P.F., Brogan, D.C.: Exploring the constraints of human behavior representation. In: Proceedings of the 36th Conference on Winter Simulation, WSC 2004 Winter Simulation Conference, pp. 912–920 (2004)

[4] Shao, W., Terzopoulos, D.: Autonomous pedestrians. In: Proceedings of the 2005 ACM SIGGRAPH/Eurographics Symposium on Computer Animation, SCA 2005, pp. 19–28. ACM, New York (2005)

[5] Kallmann, M., Thalmann, D.: Modeling objects for interaction tasks. In: Proc. Eurographics Workshop on Animation and Simulation, pp. 73–86 (1998)

[6] Sung, M., Gleicher, M., Chenney, S.: Scalable behaviors for crowd simulation. Comput. Graph. Forum 23(3), 519–528 (2004)

[7] Petri, C.A.: Kommunikation mit automaten. Ph.D. dissertation, Universität Bonn, 1962, translated by C F Greene Jr, Applied Data Research Inc, Technical Report RADC-TR-65-377, vol. 1 (supl. 1) (January 1966)

[8] Bause, F., Kritzinger, P.S.: Stochastic Petri nets - an introduction to the theory. Vieweg (2002)

[9] Bonet, R.P.P., Llado, C.M., Knottenbelt, W.: Pipe v2.5: A petri net tool for performance modelling. In: Proc. 23rd Latin American Conference on Informatics, CLEI 2007 (October 2007)

[10] Billington, J., Christensen, S., van Hee, K., Kindler, E., Kummer, O., Petrucci, L., Post, R., Stehno, C., Weber, M.: The Petri Net Markup Language: Concepts, Technology, and Tools. In: van der Aalst, W.M.P., Best, E. (eds.) ICATPN 2003. LNCS, vol. 2679, pp. 483–505. Springer, Heidelberg (2003)

[11] Peterson, J.: Petri Nets and the Modelling of Systems. Series in Computer Science. MIT Press (1981)

[12] Ajmone-Marsan, M., Balbo, G., Conte, G., Donatelli, S., Franceschinis, G.: Modelling with Generalized Stochastic Petri Nets. Series in Parallel Computing. John Wiley and Sons (1995)

[13] Dijkstra, E.W.: A note on two problems in connexion with graphs. Numerische Mathematik 1, 269–271 (1959)

Cooperation without Exploitation between Self-interested Agents

Steven Damer and Maria Gini

Department of Computer Science and Engineering,
University of Minnesota,
200 Union St SE, Minneapolis, MN 55455, USA
{damer,gini}@cs.umn.edu

Abstract. We study how two self-interested agents that play a sequence of randomly generated normal form games, each game played once, can achieve cooperation without being exploited. The agent learns if the opponent is willing to cooperate by tracking the attitude of its opponent, which tells how much the opponent values its own payoff relative to the agent's payoff. We present experimental results obtained against different types of non-stationary opponents. The results show that a small number of games is sufficient to achieve cooperation.

1 Introduction

We study cooperation between two self-interested agents, where an agent may be hostile but may also be willing to give up part of its expected payoff to provide a benefit to its opponent. Following game theory an agent should select the action that provides its own highest expected payoff, without regard for the opponent's outcome. However, many forms of cooperation are observed in evolution [13], and in iterated games [2]. Social Value Orientation theory [11] recognizes that people's behaviors depend on their personalities, and that people with a prosocial orientation highly regard the payoffs of others they interact with.

We study agents that play a sequence of non-zero-sum normal form games, each game played only once by the same two players. Playing against the same opponent enables the agents to observe each other, but since the game changes each time, it is harder to detect if the opponent is cooperative. Our setting is similar to stochastic games [15], but to simplify the learning process the payoff distribution is known to both players and each game is independent of the previous state and agents actions.

The main contributions of this paper are the use of a regularized particle filter to learn the willingness of the opponent to cooperate and experimental results against different types of non-stationary opponents. We show that an agent can predict the behavior of its opponent within the limits implied by the rate at which the opponent changes, and achieve a cooperative outcome without risking significant exploitation.

2 Background on Cooperation Model

We use the model presented in [6] and extend the work in [7] to non-stationary opponents. In this model an agent adopts an *attitude* towards its opponent, which determines

S. Lee et al. (Eds.): Intelligent Autonomous Systems 12, AISC 194, pp. 553–562.
springerlink.com

how much weight it attaches to its opponent's payoff relative to its own payoff. An attitude is a real number in the range [-1, 1]. An attitude of 1 means that the player wants to maximize social welfare, 0 that the agent is indifferent to the opponent's payoff, and -1 that the agent is spiteful. The attitude of the opponent is private information and must be learned. This model is functionally equivalent to Social Value Orientation theory [11] with a different parametrization, using attitude values instead of an angle representing the ratio of utility of the agent's payoff and the opponent's payoff.

Let's call the agents x and y, and their attitudes A^x and A^y respectively. To select its action, each agent computes a modified game. In the modified game agent x has a new payoff function P'^x defined as $P'^x_{ij} = P^x_{ij} + A^x \times P^y_{ij}$, where P^x_{ij} is the payoff in the original game for player x and P^y_{ij} is the payoff for the opponent when they choose respectively actions i and j. Similarly agent y computes a modified payoff function using its attitude A^y. Each agent selects an action which maximizes its score in the modified game, but receives its payoff from the original game.

An agent acting according to this model uses three parameters, the agent's *attitude*, an estimate of the opponent's attitude, which we call *belief*, and a *method* of choosing an action in the modified game. For simplicity we assume that agents play a strategy which is part of a Nash equilibrium. This is not the only choice, but it is convenient since it limits the method to a discrete set. In this context, method is simply the choice of which Nash equilibrium is used.

To indicate its willingness to cooperate, an agent first has to learn the attitude used by the opponent and then sets its own attitude to be higher than the estimated attitude of the opponent by a *reciprocation* value. Specifically, a reciprocating agent x sets its own attitude A^x to be equal to B^x, its estimate of the opponent's attitude, plus a reciprocation

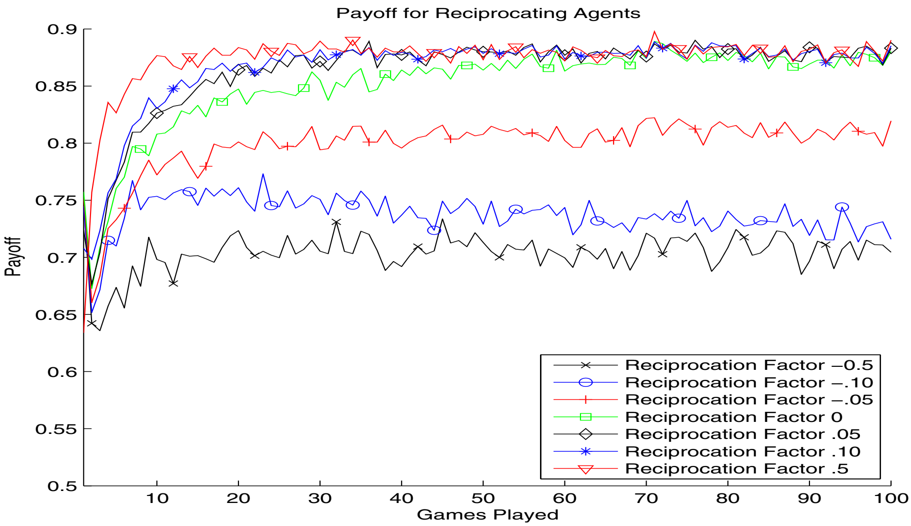

Fig. 1. Payoffs for various choices of R when two reciprocating agents play each other

level R, $A^x = B^x + R$. If this results in a value below 0 or above 1, the value is set to 0 or 1. The value is not allowed to drop below 0 because attempting to take revenge on an opponent will reduce the agent's score. The value is not allowed to increase beyond 1 because two agents with attitudes higher than one can result in inefficiencies as each agent attempts to force its opponent to take a higher share of the payoff.

Figure 1 shows how different reciprocation levels affect the payoffs. We can see that any non negative reciprocation level produces cooperation and higher payoffs. The reciprocation level we use in our experiments is .1, since it limits the potential loss but is sufficient to lead to full cooperation.

3 Learning

In every round the agent observes the payoff matrix of the game, chooses its own action, and observes the action chosen by its opponent. From that information, it needs to learn a probability distribution over the attitude, belief, and method of the opponent. Due to the complex interactions between those parameters and the game being played, it is not possible to do this analytically.

Instead we use a particle filter, which represents a probability distribution with a number of samples drawn from it (see Algorithm 1). The distribution represented by the particles is a discrete distribution with probability of each particle proportional to its weight. When an observation is made, each particle's weight is updated by multiplying it by the probability assigned to the observation by that particle.

We use a regularized particle filter [12], which resamples from a continuous instead of a discrete distribution. As observations are made, the relative probability of the particles changes. At the extreme, if one particle has all the weight, the distribution is effectively represented by a single particle. To avoid this, when the effective number of particles drops below a threshold, a new set of particles is drawn by sampling from the existing distribution and adding noise.

Noise is drawn from a Gaussian distribution with 0 mean and standard deviation equal to $N^{-1/6}$ times the standard deviation of the particle set, where N is the number of particles. This is an improvement over the approach in [6] because it doesn't require knowledge of the distribution from which games are drawn and increases accuracy. Method is a discrete value, so it cannot be perturbed with Gaussian noise. Instead, with some probability we change it to a random new method. The optimal probability is found using a technique called Leave-One-Out, where we select the probability that gives the highest likelihood of resampling the current distribution from a distribution created by removing one particle from the current set.

We use 400 particles with attitude and belief drawn from a Gaussian distribution centered at 0 with the identity matrix as a covariance matrix, and method drawn from a uniform distribution over the list of methods under consideration. We assign each particle a weight of .0025 and resample if the effective number of particles goes below 200.

Algorithm 1. *RegularizedParticleFilter*

Generate initial set P of N particles
for particle $p \in$ P **do**
Assign attitude att_p, belief bel_p, and method $method_p$ of particle p from prior
Assign weight $weight_p = 1/N$
end for
while presented with data **do**
Observe opponent's action M in game G
Compute effective number of particles $N_{eff} = 1/[\sum_{p \in P} weight_p{}^2]$
if $N_{eff} >$ threshold **then**
for particle $p \in$ P **do**
Compute probability of opponent's action M in game G, $prob_p$, given att_p, bel_p, and $method_p$
Update $weight_p$=$weight_p \times prob_p$
end for
else
Compute standard deviation Std_{att} of att_p and standard deviation Std_{bel} of bel_p
$h = N^{-1/6}$
Compute perturbation probability pp for $method_p$
while accepted particles < total particles **do**
Select particle p from P with probability proportional to $weight_p$ and create new particle p'
Assign attitude and belief adding Gaussian noise $att_{p'} = att_p + h \times N(0, Std_{att})$; $bel_{p'} = bel_p + h \times N(0, Std_{bel})$
With probability pp, $method_{p'}$ = random method else $method_{p'} = method_p$
Compute $prob_{p'}$= probability of opponent's action M in G given $att_{p'}$, $bel_{p'}$, and $method_{p'}$
Accept p' with probability $prob_{p'}$
end while
end if
end while

4 Experimental Results

We now present experimental results obtained against several classes of non-stationary opponents. Experiments against a stationary opponent and in self-play have been reported in [7]. We measure *model accuracy*, i.e. the Euclidean distance between the estimate of attitude and belief of the opponent and their true values, and *prediction accuracy*, i.e. the Jensen/Shannon divergence between the prediction and the actual probability distribution used by the opponent.

We use randomly generated normal form games with 16 actions per player, and payoffs uniformly distributed between 0 and 1, as in [6]. We have found experimentally that 16 actions provide a good balance between model and prediction accuracy. Model accuracy increases with the number of actions, since each action is more informative as more alternatives are rejected, but prediction accuracy decreases because the space of the predicted distribution increases.

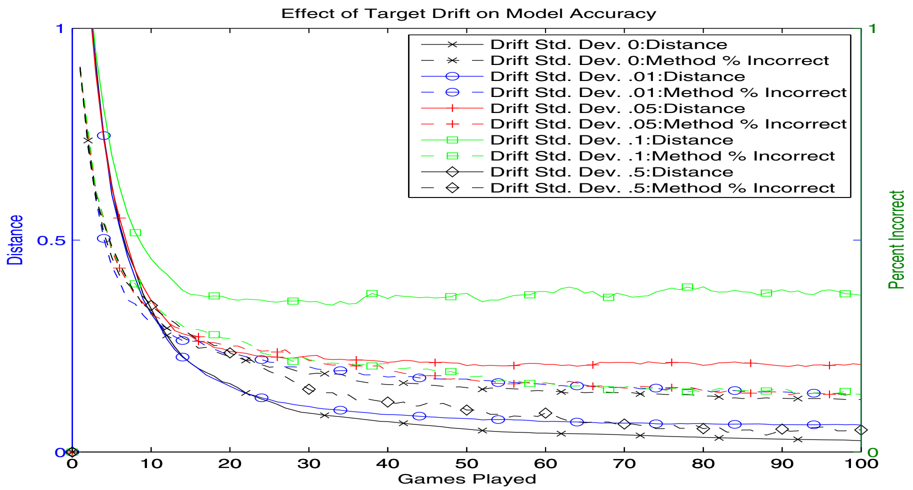

Fig. 2. Model accuracy when learning a randomly drifting target. Results aggregated over 100 sequences of games. Learning targets drawn from a 0 mean Gaussian.

We have explored two types of non-stationary opponents, both separately and in combination. The first type changes its values for attitude and belief according to *random drift* with a Gaussian distribution. This models an agent which gradually adjusts its strategy. The second type changes by *redrawing* values from the prior with a fixed probability. This models an agent which changes according to some threshold, or which may be replaced without notice. The third type combines *random drift and redrawing*.

Figure 2 and Figure 3 show the effect of various levels of drift on model and prediction accuracy. Unsurprisingly, as drift increases, accuracy decreases. An odd effect is that the accuracy for the method increases for a high drift. This occurs because there are regions in the model space in which method does not affect the agent's actions. With a high drift rate, the opportunity to get out of those regions outweighs the difficulty caused by the rapid change in values. The model error increases as drift increases, but still provides a reasonable estimate of the opponent's intentions. With a .5 drift, the prediction accuracy is equivalent to being able to correctly identify one action out of sixteen 55% of the time.

Figure 4 shows the payoffs, which remain high even with a large drift. Omniscient payoff is the expected payoff when the agent knows the opponent's attitude, belief, and method. Payoff without learning is the expected payoff when the agent best responds to the prior over the opponent's attitude, belief, and method. Both values were found empirically.

Figure 5 shows the effect of randomly redrawing the target from the prior. Random resets make learning considerably more difficult. No learning is possible with a reset probability greater than .05. This is because the agent does not have sufficient time to

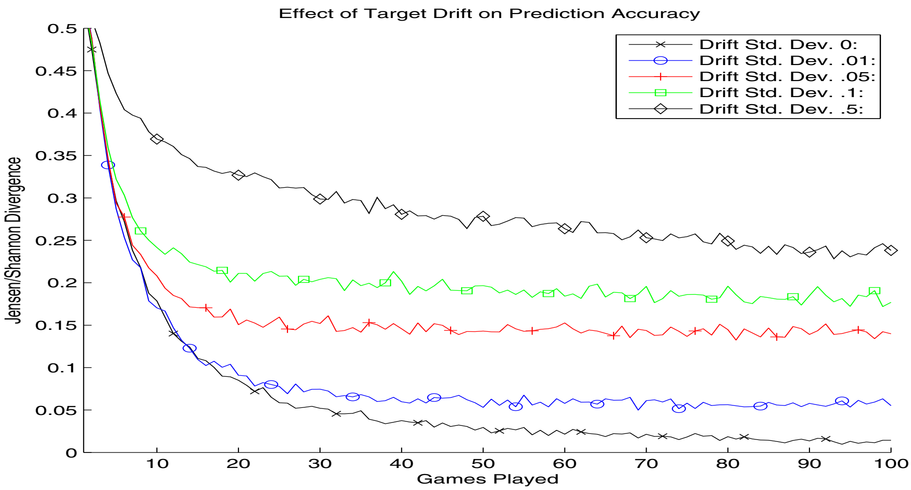

Fig. 3. Prediction accuracy when learning a randomly drifting target. Results aggregated over 100 sequences of games. Learning targets drawn from a 0 mean Gaussian.

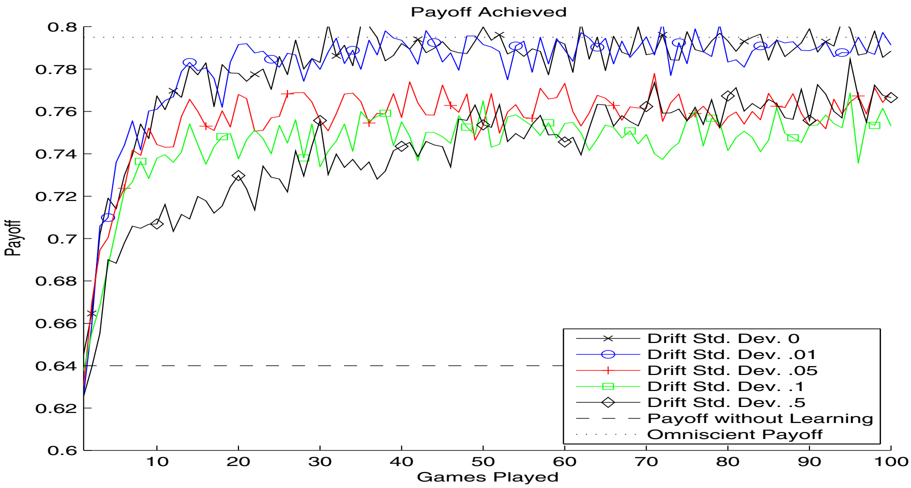

Fig. 4. Payoffs of agent against a randomly drifting target

learn between resets. For example, with a reset probability of .25, on average there are 4 games between resets, which is not sufficient to fully learn the target. Figure 6 shows the corresponding payoffs. As expected, higher reset probabilities result in lower payoffs.

Figure 7 shows the effect of combining both types of nonstationarity. Unsurprisingly, it is much harder to learn when the parameters are changing slightly in every game, and occasionally radically. However, it still possible to make reasonable predictions.

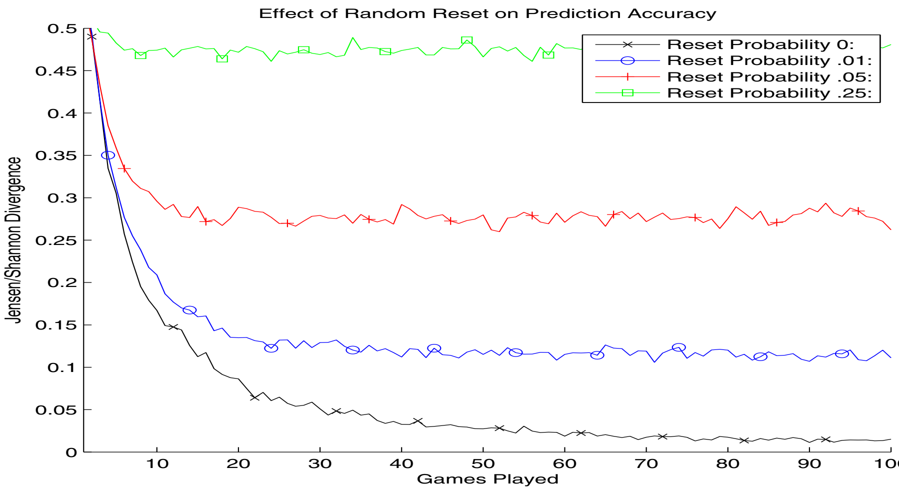

Fig. 5. Prediction accuracy when learning a randomly resetting target. Results aggregated over 100 sequences of games.

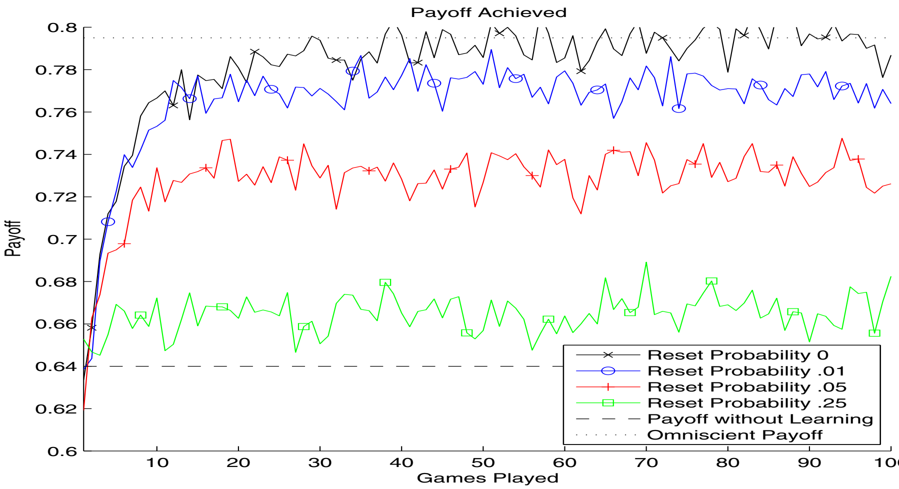

Fig. 6. Payoffs of agent against a randomly resetting target

This is particularly valuable because it implies the ability to track the behavior of much more sophisticated agents by modelling their changes in attitude and belief as random behavior. Figure 8 shows the corresponding payoffs. Despite the large prediction error, the payoffs of the agents are higher than if no learning had occurred.

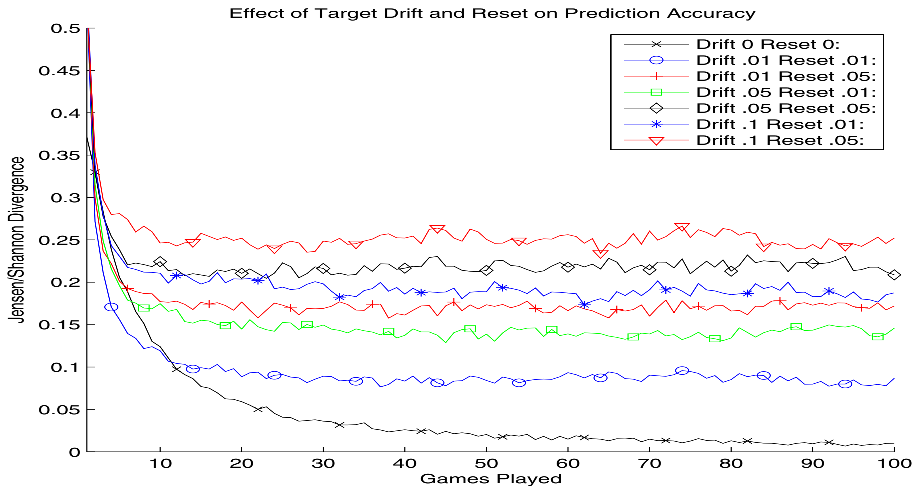

Fig. 7. Prediction accuracy when learning a randomly drifting and resetting target. Results aggregated over 50 sequences of games.

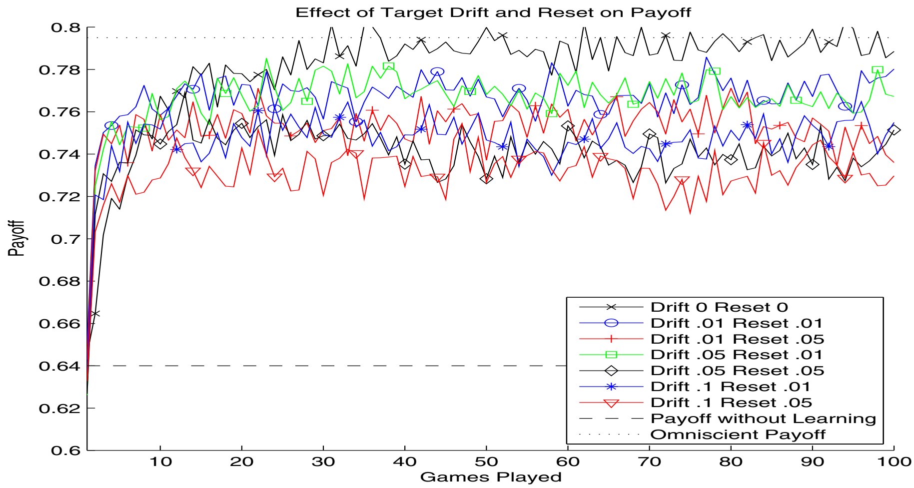

Fig. 8. Payoffs against a randomly drifting and resetting target

5 Related Work

Our model of cooperation is based on models developed to explain human cooperation in normal form games. Valavanis [16] proposed a modification of a normal form game to reflect an agent's preferences over its opponent's utility. Frohlich [9] pointed out that this can lead to an ill-defined utility function, and proposed restricting an agent's preferences to its opponent's consumption instead of utility. Fitzgerald [8] introduced a utility which is linear in the opponent's payoff, and pointed out that positive attitudes will not necessarily reduce the level of contention between agents. An overview of some of the many different models which have been used to explain human behavior can be found in [3]

Reciprocation is recognized as an effective way to motivate an opponent to cooperate, as demonstrated in the Tit-for-Tat strategy for iterated prisoner's dilemma [2]. However, Tit-for-Tat does not perform well in noisy environments. One way to handle that [1] is to track deviations from a learned opponent policy, resetting when it becomes apparent that the learned policy is inaccurate. This problem is similar to the one we deal with, where the environment is the source of noise in the observations, instead of nonstationarity of the opponent.

Most research on learning for agents which play normal form games has focused on repeated play of a single game against a stationary opponent with the goal of finding either an equilibrium or a Pareto-optimal outcome in self-play. Fudenberg [10] provides a good overview of fictitious play, which explores the effects when agents attempt to learn their opponents actions and then choose the best response. Reinforcement learning is a popular technique for dealing with normal form games. Unlike the techniques presented in this paper, it does not require a complete description of the game, however it requires repeated interactions within a single game in order to learn the optimal actions. M-Qube [5] is a reinforcement learning algorithm which balances best response, cautious learning to bound losses, and optimistic learning by looking for strategies with potentially high returns even if risky. The algorithm provably bounds losses in repeated games but it requires playing thousands of times.

AWESOME [4] is the first algorithm guaranteed to learn to play optimally against stationary opponents and to converge to a Nash equilibrium in self play. It also learns to play optimally against opponents that eventually become stationary. To guarantee convergence in self-play, it assumes all agents play the same Nash equilibrium. By limiting the history the opponent can use, the algorithm described in [14] learns against non-stationary opponents by playing thousands of repeated games. We are interested in methods that learn much more rapidly.

6 Conclusions and Future Work

We have described a regularized particle filter to learn model parameters and we have evaluated the performance of the learning algorithm against non-stationary opponents. The model is effective for achieving cooperation in situations where cooperative actions are not obvious.

This paper shows results for random non-stationary opponents. It would be interesting and useful to examine the performance of this model when applied to other types of non-stationary opponents. Another point to investigate is a method to compute appropriate reciprocation levels from the game and from the probability distribution over the model parameters of the opponent, instead of using a preset level.

References

1. Au, T.C., Kraus, S., Nau, D.: Symbolic noise detection in the noisy iterated chicken game and the noisy iterated battle of the sexes. In: Proceeding of the First International Conference on Computational Cultural Dynamics, ICCCD 2007 (2007)
2. Axelrod, R.M.: The evolution of cooperation. Basic Books (1984)
3. Camerer, C.F.: Progress in behavioral game theory. The Journal of Economic Perspectives 11(4), 167–188 (1997)
4. Conitzer, V., Sandholm, T.: AWESOME: A general multiagent learning algorithm that converges in self-play and learns a best response against stationary opponents. Machine Learning 67(1-2), 23–43 (2007)
5. Crandall, J.W., Goodrich, M.A.: Learning to compete, cooperate, and compromise using reinforcement learning. Machine Learning (2010)
6. Damer, S., Gini, M.: Achieving cooperation in a minimally constrained environment. In: Proc. of the Nat'l Conf. on Artificial Intelligence, pp. 57–62 (2008)
7. Damer, S., Gini, M.: Extended abstract: Friend or foe? detecting an opponent's attitude in normal form games. In: Proc. Int'l Conf. on Autonomous Agents and Multi-Agent Systems (2011)
8. Fitzgerald, B.D.: Self-interest or altruism. Journal of Conflict Resolution 19, 462–479 (1975)
9. Frohlich, N.: Self-Interest or Altruism, What Difference? Journal of Conflict Resolution 18(1), 55–73 (1974)
10. Fudenberg, D., Levine, D.K.: The Theory of Learning in Games. MIT Press (1998)
11. McClintock, C.G., Allison, S.T.: Social value orientation and helping behavior. Journal of Applied Social Psychology 19(4), 353–362 (1989)
12. Musso, C., Oudjane, N., Legland, F.: Improving regularized particle filters. In: Doucet, A., de Freitas, N., Gordon, N. (eds.) Sequential Monte Carlo Methods in Practice, pp. 247–271. Springer, New York (2001), citeseer.ist.psu.edu/musso01improving.html
13. Nowak, M.A.: Five rules for the evolution of cooperation. Science 314, 1560–1563 (2006)
14. Powers, R., Shoham, Y., Vu, T.: A general criterion and an algorithmic framework for learning in multi-agent systems. Machine Learning 67(1-2), 45–76 (2007)
15. Shapley, L.S.: Stochastic games. Proceedings of the NAS 39, 1095–1100 (1953)
16. Valavanis, S.: The resolution of conflict when utilities interact. The Journal of Conflict Resolution 2(2), 156–169 (1958), http://www.jstor.org/stable/172973

Controlling Formations of Robots with Graph Theory

Jan Carlo Barca, A. Sekercioglu, and A. Ford

Department of Electrical and Computer Systems Engineering,
Monash University, Melbourne, Australia
research@jancarlobarca.com,
ahmet.sekercioglu@eng.monash.edu.au,
adam.ford.eng@gmail.com

Abstract. A number of techniques that allow autonomous multi-robot systems to be held within formation-like structures exist but they are limited by a high communication load, high energy usage and a lack of robustness. This research improves on state-of-the-art formation control schemes for leader-follower type multi-robot systems by employing mechanisms that enable groups of robots to move in two-dimensional formations without the need for inter robot communication. We also incorporate techniques that enable the robots to move back into formation in a precise manner when external interferences have caused the formation shape to deteriorate. The control system is derived through the use of graph theory and has been tested rigorously in a realistic simulator to prove its applicability to multi-robot control.

1 Introduction

A multi-robot (MR) system consists of a group of robots that act autonomously and is designed to solve problems that would be impossible for a single robot. In single robot systems, there is a huge responsibility put onto one robot which, in turn causes a single point of failure. MR systems address this issue by creating redundancies and expanding responsibilities, therefore providing a decreased system fail rate. As the field of robotics progresses, there is a need to focus research efforts more towards distributed-type robotic systems [1].

Formations in robotics can be defined as the inter-relational physical structure where the MR system is kept in tightly pre-defined restricted patterns. It allows the ability to move large objects [2] compared to just one robot, and decreases the overall time and effort required for large area exploration and mapping. The applications of formations within MR systems are extensive, they can range from military Unmanned Aerial Vehicle surveillance, mapping and surveying of environments and exploration of unpredictable territory to mobile sensory networks and satellite high-resolution imagery [3,2,4]. As the world becomes more dangerous and conflicting, there arises a need to produce systems, such as those that incorporate formations that enhance the safety of human beings.

One of the advantages of having a MR system maintaining formation is that all robots can depart from and arrive at a waypoint at the same time. There is also a psychological effect if used within a military application that if a huge group of objects is

S. Lee et al. (Eds.): Intelligent Autonomous Systems 12, AISC 194, pp. 563–574.
springerlink.com

moving towards a group of enemies, it can have a detrimental effect on morale. In our work we focus on triangular and diamond formations due to the benefits associated with these particular formations. A triangular formation allows the system of robots to be gradually exposed to an area, and offers formation leniency because no entity follows directly behind another. While diamond formations allow forward, side and back protection to the group when used within a military scenario and entering environments where being ambushed is a possibility [2,5].

There are some areas of formation control that can be improved on. High computational usage can, for example, prevent formation control algorithms from running to their full potential [6]. In our work, which builds upon the techniques presented in [2,4] we reduced this problem by using graph theory and minimal constraints to enable formation control without the need for inter robot communication, thus reducing energy consumption. Other variables that come into play when MR systems are deployed in dynamic real world environments are the disturbances caused by the interactions between different robots in the system and the interferences from obstacles in the environment [4,6], which can make it hard for the system to retain a precise formation structure. This problem can be observed in several well established formation control techniques for MR systems such as the morphogenesis based techniques presented by [7-9] and the potential fields based technique presented by [10]. None of these techniques can ensure that the exact formation shape is regained if the system is affected by external disturbances. To address this issue we incorporate a gradient decent function that enables the robots to move back to their exact positions in the formation after they have been forced away by external interference. A difference between other formation control techniques that use minimally rigid graphs and our work is that our technique does not rely on Global Positioning Systems (GPS) to correct the positions of robots in the formation. This is advantageous as it opens up for using the technique in areas where GPS is unavailable, such as indoors, underground, in the ocean or in space. Relevant definitions from graph theory are introduced in the following section.

2 Theory – Definitions and Preliminary Remarks

Leader-follower type MR systems usually have one *main leader (ML)* that guides the movement of the followers by means of *sub-leaders (SL).* These *SL* are located at intersection points of branched graphs, which are rooted in the *ML,* and guide the movement of robots further down in the graph hierarchy. Followers can therefore have more than one leader guiding their movement even if only one *ML* exists.

To define the physical relations between the individual robots, the use of graph theory is seen to be greatly beneficial because of its algorithms and definitions that have been developed to find rigid and minimally-constrained structures. Therefore to gather a total understanding on the theories behind this research, a broad knowledge of graph theory is required. A series of relevant definitions and concepts from graph theory are therefore described in this section.

Directed edges are represented by the constraints that are defined within a graph. For example, if two vertices (***a***) and (***b***) exist and they are connected by an edge, then the edge is directed if ***a*** connects to ***b***, but ***b*** is not connected to ***a***. If ***a*** connects to ***b***, and ***b*** also connects to ***a***, then the edge is undirected. It is often desirable to use directed edges in MR systems as only one robot in a pair is responsible for maintaining a particular inter robot constraint. This is beneficial as the energy consumption associated with maintaining the constraint can be kept at a minimum. A graph with only directed edges is referred to as a digraph.

To devise a graph that is structured and rigid, it is required that all constraints are able to be followed and the distances between each vertex must remain constant at any time. For a two-dimensional graph to be defined as minimally rigid the graph must be in a state that if any edge was to be removed it would cause the graph to be no longer rigid [11]. One can check if a graph with (v) number of vertices is minimally rigid by testing if the number of edges (e) satisfies '$|e| = 2\ |v| - 3$' [11]. It is beneficial to use minimally rigid graphs in MR systems as no unnecessary constraints are used to uphold desired formations, which in turn ensures that particular formation shapes can be maintained in an energy efficient manner.

For a rigid graph to become persistent, it must have its undirected edges replaced by directed edges [12]. This can be done by replacing each of the undirected edges with directed edges in a way that retains the rule that a digraph is persistent only if any two vertices in the graph can preserve their relative distance constraints during any motion [12]. Fig. 1 illustrates a persistent and a non-persistent graph. Next section describes how constraints that have been defined with graph theory can be maintained by an MR system.

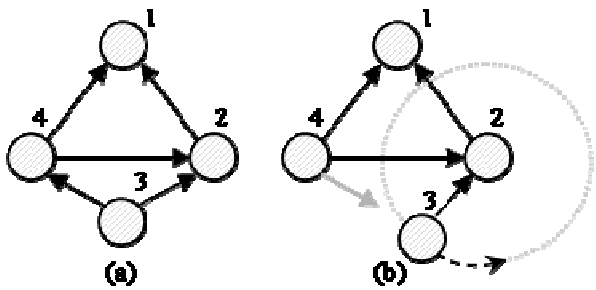

Fig. 1. Persistent and non-persisten graphs: (a) is persistent as all vertices can maintain their relative distance during any motion, and (b) is non-persistent as vertex 4 is unable to satisfy all its distance constraints when vertext 3 moves along the dotted circle

3 Dual Leader Averaging Follower Algorithm

An overview of how the followers operate is given in Fig. 2. All robots in the MR system make use of this control method with the exception of the *ML*, which is controlled by a human operator. (The *ML* can also alternatively follow pre-defined paths.) One can observe that the control method enables the robots to take relative distance and angle measurements to one or two leaders into account during the control process. How these measurements are captured with a distance measuring device and flow through the control system can also be observed. Any distance measuring device can be used to support the control process as long as the device makes it possible to determine relative distances and angles to other robots. Each component of the control method is discussed in the following subsections.

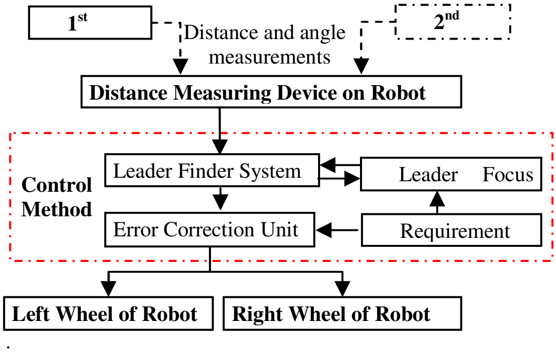

Fig. 2. Overview of how followers operate

3.1 Leader Focus Unit

The Leader Focus Unit (LFU) assists the Leader Finder System (LFS) with "locking" onto allocated leader/s. The LFU offers this support by transmitting the expected relative angle/s between the robot at hand and its associated leader/s to the LFS at startup. The LFU obtains this information from the Requirement Unit (RU) which contains all necessary constraints for maintaining a particular formation shape. After startup the LFU continues to assist the LFS by transmitting the previous relative angle/s between the robot and its leader/s. The purpose behind the LFU is to reduce the processing load associated with iterating through data from the distance measuring device when searching for leader/s.

3.2 Leader Finder System

The LFS checks if a robot is located at the relative angle/s provided by the LFU. If a robot is not detected at an expected angle, then the search arc is expanded horizontally with one resolution in left and right directions along the horizontal axis. This expansion of the search arc is repeated incrementally until a robot is detected (Fig. 3). Empirical results show that this approach works when the robots are distributed according to desired formation patterns from the outset. (Refer to [5] for a technique that can be used to generate desired formation patterns.) Once a robot is detected the actual relative angle and distance to the robot are passed over to the Error Correction Unit (ECU). If the LFU transmitted two angles to the LFS, then the search is repeated for the second angle to find a second leader. Feedback is also sent to the LFU if there is a discrepancy between the angle/s transmitted to the LFS and the actual angle/s to the leader/s.

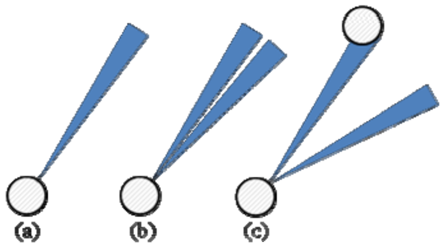

Fig. 3. Search for a leader: (a) the search is initiated in the angle provided by the LFU, b) the search arc is expanded in left and right directions along the horizontal axis if no robot is detected in the initial region, and c) the search arc is expanded incrementally until a robot is found

3.3 Error Correction Unit

The ECU enables robots to reduce the discrepancy between their desired and their actual relative position with respect to their leader/s so that relevant formations can be maintained. A mechanism that is employed when a robot has two leaders will be discussed first as most robots in our formations have two leaders.

3.4 Error Correction with Two Leaders

This mechanism compares the measurements provided by the LFS with desired distance and angle measurements obtained from the RU, in order to calculate an error vector that pushes the robot at hand towards a desired relative pose with respect to two leaders. The idea is illustrated in Fig. 4, where one can observe how follower (*F1*) moves according to the $e_{x,ave}$ and $e_{y,ave}$ vectors to reduce the discrepancy between the actual and the desired relative pose with respect to leaders (*L1*) and (*L2*).

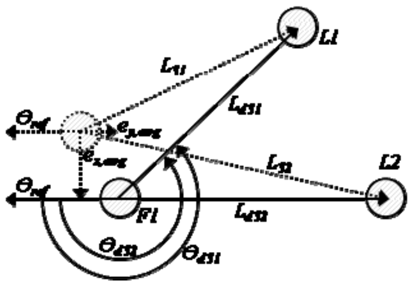

Fig. 4. Reducing discrepancy between desired and actual relative pose of follower *F1*

The mechanism initiates by calculating two separate sets of error vectors with respect to *L1* and *L2*. Corresponding vectors are then synthesized to produce average error vectors, which *F1* acts upon while attempting to mirror the two leader velocities. The preliminary error vectors are calculated according to (1) to (4) and synthesized using (5) and (6).

$$e_{x,31} = (L_{31}\cos(\theta_{31}) - L_{d31}\cos(\theta_{d31})) \quad (1)$$

$$e_{y,31} = (L_{31}\sin(\theta_{31}) - L_{d31}\sin(\theta_{d31})) \quad (2)$$

$$e_{x,32} = (L_{32}\cos(\theta_{32}) - L_{d32}\cos(\theta_{d32})) \quad (3)$$

$$e_{y,32} = (L_{32}\sin(\theta_{32}) - L_{d32}\sin(\theta_{d32})) \quad (4)$$

where:

$e_{x,31}$	: *x*-coordinate for error displacement vector between *F1* and *L1*
$e_{y,31}$	: *y*-coordinate for error displacement vector between *F1* and *L1*
L_{31}	: Actual distance between *F1* and *L1*
L_{d31}	: Required distance between *F1* and *L1*
θ_{31}	: Actual angle between *F1* and *L1* with respect to θ_{ref}
θ_{d31}	: Required angle between *F1* and *L1* with respect to θ_{ref}

$$x = e_{x,ave} = (e_{x,32} + e_{x,31})/2 \quad (5)$$

$$y = e_{y,ave} = (e_{y,32} + e_{y,31})/2 \quad (6)$$

where:

$e_{x,ave}$	: *x*-coordinate average error displacement vector
$e_{y,ave}$	: *y*-coordinate average error displacement vector

To control the forward velocity of *F1* a proportional derivative controller acts upon changes in the *y* variable with respect to *F1*'s required position as in (8). The velocity is only computed for the *y* axis as forward velocities are specified in a local coordinate system where the positive *y* axis always point directly in front of the robot.

$$\Delta y = \frac{y(t) - y(t-T)}{T} \quad (7)$$

$$V_{control} = \begin{cases} K_v.\Delta y + K_{dist}.\log(y(t)+1) - K_{dist}.1.05.\log(y(t-T)+1) + V_1, & y(t) \geq 0 \\ K_v.\Delta y - K_{dist}.\log(-y(t)-1) + K_{dist}.1.05.\log(-y(t-T)-1) + V_1, & y(t) < 0 \end{cases} \quad (8)$$

where:

Δy	: Change in $e_{y,ave}$ over two sequential samples
$y(t)$	: *y*-coordinate average error as a function of time
T	: Sample rate of distance measuring device
V_1	: Current velocity of *F1* in millimeters per second
V_{contro}	: Required velocity of *F1* in millimeters per second
K_{dist}	: Distance constant for velocity control
K_v	: Velocity constant for velocity control

While the *y*-coordinate changes a velocity control mechanism takes into account the rate at which this value changes and compensates to mirror the formation speed while still maintaining the displacement required. The angular velocity of *F1* is controlled using a proportional transparent dead-zone controller. The average angle of the error vector is calculated first (9). Then the magnitude of the average error vector is calculated (10) for use within the angular speed's dead-zone proportional controller (12). A secondary heading is also calculated (11) from the original readings and constraints for use within the controller. The heading result from (11) begins to influence the controller when *F1* enters a dead zone (magnitude of the error vector is less than d).

$$e_{\theta,ave} = \tan^{-1}\frac{x}{y}; x<0$$

$$\tan^{-1}\frac{x}{y}+\pi; x\geq 0, y>0 \tag{9}$$

$$\tan^{-1}\frac{x}{y}-\pi; x\geq 0, y<0$$

$$|e_{average}| = \sqrt{e_{x,ave}^{2}+e_{y,ave}^{2}} \tag{10}$$

$$e_{direction} = \frac{(\theta_{31}-\theta_{d31})+(\theta_{32}-\theta_{d32})}{2} \tag{11}$$

$$\omega_{control} = \begin{cases} K_{ang}.e_{\theta,ave}, |e_{average}|>d \\ K_{ang}.(e_{direction}-(e_{direction}-e_{\theta,ave})\frac{|e_{average}|}{d}), |e_{average}|\leq d \end{cases} \tag{12}$$

where:

$e_{\theta,ave}$	: Average angle of error vector
$\omega_{control}$	: Correction angle for *F1* in degrees per second
K_{ang}	: Constant for angular control system
d	: Dead-zone constant

3.5 Error Correction with One Leader

If *F1* only has one leader then distance and angle constraints are retained using (13) to (16). Equation (13) is used to calculate the distance error between the desired and the actual position of *F1*, whilst (15) is used to determine the heading error. The idea is illustrated in Fig. 5 where one can observe how *F1* moves according to the $e_{x,31}$ and $e_{y,31}$ vectors to reduce the discrepancy between the desired and actual relative pose with respect to *L1*.

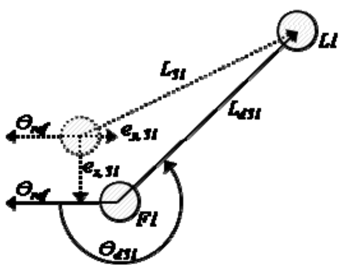

Fig. 5. Reducing discrepancy between desired and actual relative pose of follower *F1*

$$e_{distance} = L_{31} - L_{d31} \tag{13}$$

$$V_{control} = K_{dist}.\log(e_{distance}) \tag{14}$$

$$e_{direction} = (\theta_{31} - \theta_{d31}) \tag{15}$$

$$\omega_{control} = K_{ang}.e_{direction} \tag{16}$$

4 Simulation Design and Results

Two types of simulations that have been carried out to test the robustness of the proposed control method towards interferences that causes formation shapes to deteriorate are presented in this section. The interferences are introduced in the form of various accelerations and changes in the heading direction of the *ML*. Both simulation types were carried out with the Microsoft Robotics Developer Studio simulator suite and varying numbers of simulated robots equipped with a differential drive and a Laser Range Finder (LRF). The LRF has a viewing angle of 360°, a resolution of 1° and an update rate of 4 Hertz. The parameters that were used for implementation specific variables throughout the simulations are presented in Table 1.

Table 1. Parameters for implementation specific variables

T	0.25 seconds	K_v	0.168 millimeters
K_{dist}	60.057 millimeters	d	500 millimeters
K_{ang}	0.75 degrees	-	-

An overview of the constraints that were used in the triangular and diamond shaped formations that were employed throughout the simulations is provided in Fig. 6. One can observe that four different types of constraints were employed. The exact parameters associated with each constraint type are provided in Table 2.

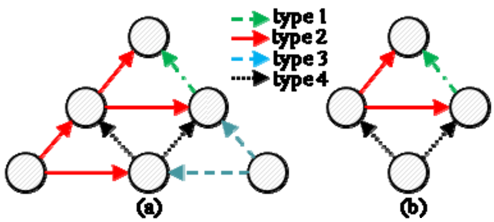

Fig. 6. (a) triangular and (b) diamond formations that were employed throughout the simulations

Table 2. Parameters for each constraint type

Type	Distance in millimeters	Angle 1 in degrees	Angle 2 in degrees
1	2000	210	-
2	2000	90	150
3	2000	210	270
4	2000	150	210

4.1 Robustness toward Increasing Leader Robot Acceleration

Simulations that investigated how robust the control method is towards accelerations of the *ML* are described in this section. It is important to investigate this issue as the *ML* will vary its velocity frequently in our future research as we intend to use the control method to operate MR systems in unpredictable and cluttered environments. Two sets of simulations were carried out to investigate the issue.

In the first set of simulations the velocity of the *ML* was increased from zero to 320 millimeters per second (mm/sec) before the average time it took for the robots to regain the formation was recorded. The outcome of this process is presented in Fig. 7. One can observe that it takes about two seconds for the followers to mirror the velocity of the *ML*. After this initial period the followers start to converge into their required positions. After 18.5 seconds the robots in the diamond formation converge. The robots then begin to oscillate in and out of the desired positions. Empirical results show that this behavior is a result of the relatively slow update rate of our LRF. We therefore expect that this behavior can be reduced by employing a distance measuring device with a faster update rate. Robots in the triangular formation converge and start to oscillate 7.1 seconds later, which shows that the control method enables both formations to converge to their desired shape.

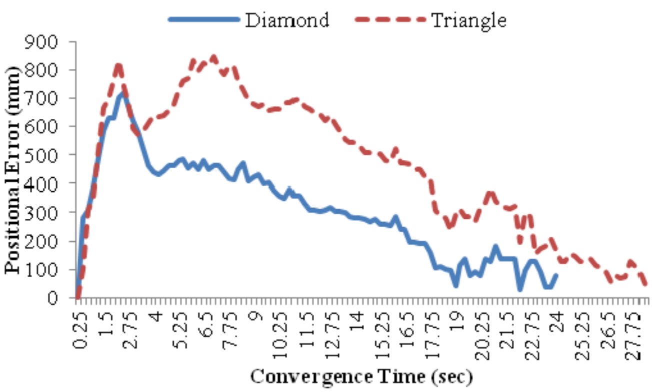

Fig. 7. Difference between desired and actual positions for followers as velocity of *ML* increased

In the second set of simulations the velocity of the *ML* was first increased from zero to 25.36 mm/sec before the average convergence time was recorded. This process was then repeated 30 times while incrementally increasing the velocity of the *ML* with 25.36 mm/sec per run. The results from this process are presented in Fig. 8. One can observe that the convergence time is close to zero for both formations until the velocity of the *ML* reaches 150 mm/sec. However, one can also observe that the convergence time increases exponentially when the velocity of the *ML* is increased beyond this point. By studying the two graphs in Fig. 8 it furthermore becomes clear that the triangular formation has a tendency to convergence later than the diamond shaped formation. Empirical results show that this is due to the relatively larger size of the triangular formation.

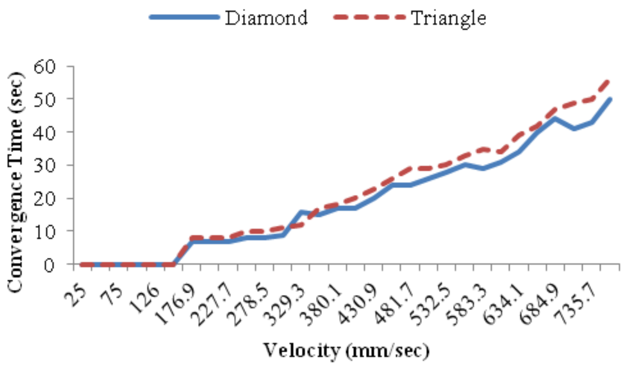

Fig. 8. Average convergence time of followers when target velocity of *ML* is increased

4.2 Robustness toward Increasing Curvature in Travel Path

This section describes simulations that were carried out to investigate how robust the control method is towards changes in the heading direction of the *ML*. It is important to investigate this issue as we intend to deploy our MR system into environments with obstacles in the future, and it is therefore expected that the *ML* will have to change heading direction frequently to avoid collisions. To investigate the issue we initially set the velocity of both wheels on the *ML* to 328 mm/sec and measured the average convergence time. The speed of the left wheel was then increased in intervals of 6.1 mm/sec until the control method failed to uphold the desired formation. Results from these simulations are depicted in Fig. 9. One can observe that the convergence time increases linearly as the turning curvature increases, and that the control method fails to uphold the formations when the left wheel has a speed of 540 and 556 mm/sec. Empirical analysis show that the control method fails at these speeds because the formations become so deteriorated at certain parts of the travelling path that the followers lock onto wrong leaders.

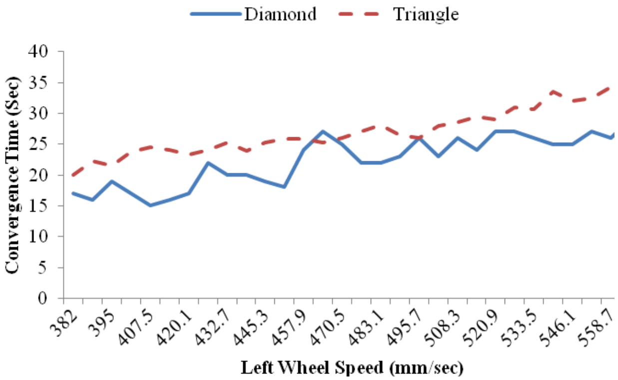

Fig. 9. Convergence time as turning curvature of *ML* is increased

5 Conclusions

A control method that enable groups of robots to move in formations without the need for inter robot communication has been presented. Simulations carried out to investigate how robust the control method is towards changes to the velocity and the heading direction of the *ML* was also described. Results from these simulations show that both triangular and diamond formations converge to their desired shapes when the control method is employed. However, results also show that the robots have a tendency to oscillate around their ideal positions after they have converged due to the relatively slow update rate of our LRF. In addition, it was found that the control method can fail to preserve formation shapes when the turning curvature of the *ML* is large as our robots easily lock onto wrong leaders in these situations. Our current research investigates how: i) robots can converge efficiently to their ideal positions with higher sensor update rates, ii) to preserve formations when follower robots lose sight of their leaders due to external disturbances such as obstacles, and iii) to make the control method more scalable. We also perform tests on real robots.

Acknowledgments. This research was supported in part by Lise and Arnfinn Hejes Grant for Education and Research. We would like to thank Adv. Harald Røer for the way he administered the grant. We would also like to thank Dr Dale Ford and Ashleigh Garling for their comments and insightful suggestions for improving the paper.

References

1. Parker, L.E.: Current Research in multirobot systems. Artif Life Robotics 7, 1–5 (2003)
2. Chen DS, J., Yang, J., Chen, H.: Leader-Follower Formation Control of Multiple Non-Holonomic Mobile Robots Incorporating a Receding-Horizon Scheme. The International Journal of Robotics Research 29(6), 727–747 (2010)
3. Florian Durfler, B.F.: Geometric Analysis of the Formation Problem for Autonomous Robots. IEEE Transactions on Automatic Control 55(10), 2379–2384 (2010)

4. Castro, R., Alvarez, J., Martinez, J.: Robot Formation Control using Backstepping and Sliding Mode Techniques. Paper presented at the Electrical Engineering, Computing Science and Automatic Control, 6th International Conference, Toluca (January 2009)
5. Barca, C., Sekercioglu, A.: Generating Formations with a Template based Multi-Robot System. In: Australasian Conference on Robotics and Automation, Melbourne, pp. 1–9 (2011)
6. Yuqing He, J.H.: Multiple Robots Formation Control Based on Receding Horizon Optimization. Paper presented at the IEEE International Conference on Information and Automation, June 22-25 (2009)
7. Guo, H., Meng, Y., Jin, Y.: Analysis of local communication oad in shape formation of a distributed morphogenetic swarm robotic system. In: IEEE Congress on Evolutionary Computation, Barcelona, pp. 1–8 (2010)
8. Mamei, M., Vasirani, M., Zambonelli, F.: Experiments of Morphogenesis in Swarms of Simple Mobile Robots. Applied Artificial Intelligence 18(9-10), 903–919 (2004)
9. Jin, Y., Meng, Y., Guo, H.: A morphogenetic self-organization algorithm for swarm robotic systems using relative position information. Paper Presented at the UK Workshop on Computational Intelligence, Colchester (2010)
10. Barnes, L., Valavanis, M.K.: Swarm Formation Control Utilizing Elliptical Surfaces and Limiting Functions. IEEE TRansactions on Systems, Man and Cybernetics 39(6), 1434–1445 (2009)
11. Anderson, B., Yu, C., Fidan, B., Hendrickx, J.: Rigid Graph Control Architectures for Autonomous Formations. IEEE Control Systems Magazine (2008)
12. Luo, X.-Y., Li, S.-B., Guan, X.-P.: Automatic generation of min-weighted persistent formations. Chinese Physics B 18(8), 3104–3114 (2009)

Information Gathering Multi Agent Framework System

Young-Im Cho

Dept. of Computer Science, The University of Suwon
San 2-2, Wau-ri, Bongdam-eup, Hwaseong, Gyeonggi-do, 445-743, Korea
ycho@suwon.ac.kr

Abstract. In this paper, I propose an information gathering system by multi agent platform. For the purpose of that, I build the information relevance network. Also, I propose a new multi agent platform. The proposed system is compared with that of the conventional information search system by surveying the satisfaction of the users for both systems. Also, the searching speed is faster than the conventional method.

Keywords: Multi-Agent, Ontology, Collaborative Information Gathering, Agent Framework.

1 Introduction

Many studies have been actively carried out in a distributed processing environment by using agent systems for efficient network management. Multi agent systems promote the efficiency in solving problems by cooperating among agents. Also, each agent independently manages its own tasks by dividing a whole work into smaller units and assigning them to each agent. There are many application areas in the real world, using the multi agent systems. One of these areas is the digital library system. The personalization is done by analyzing the topic of papers. In this case, the papers whose topic is not relevant to the queried keywords request by a user but contents are relevant to them are not recommend. In order to solve the problem, I consider the abstracts in the papers for providing a personalized paper search list according to the user's behavior on the papers and the relevance among keywords in the abstracts.

Also, another problem the multi agent-based digital library systems have is that users themselves should visit all possible search servers one by one. To overcome the problem, I propose a new platform of multi agent digital library system which is mobile search system. Users do not need to visit all possible search servers with the same query by using the new platform. My system automatically visits to all possible search servers when user requests a query. In this case, the scheduling of visiting the search servers is needed. Also, the negotiation for the results searched from the servers needs to be made for complicated situations such as the duplicated search results from multiple servers. Also, the personalized paper search algorithm builds user's individual relevance network from analyzing the appearance frequencies of keywords in the searched papers. The relevance network is personalized by providing weights to the appearance frequencies of keywords according to users' behaviors on the searched list, such as "downloading," "opening," and "no-action." Also, I enable interaction among multi agents by developing an artificial negotiation algorithm.

S. Lee et al. (Eds.): Intelligent Autonomous Systems 12, AISC 194, pp. 575–584.
springerlink.com

In the experimental section, I demonstrate the proposed method using 100 faculties' search information employed in the University of Suwon. Also, the performance of the proposed method is compared with that of the conventional paper search system by surveying the satisfaction of users for both systems. In addition, I analyze the searching speed of the system to show both the advantage and disadvantage of my mobile-based searching system.

Distributed Environment-Centered Agent Framework (DECAF) has been used for the framework to design various intelligent multi agent-based systems [1] such as BIG (Bounded Information Gathering System) [2, 3]. DECAF is a kind of operating system including various modules such as Agent Initialization, Dispatcher, Planner, Scheduler, and Executor. Agent Initialization defines tasks and provides task templates in the format of hash table to Planner. Dispatcher analyzes incoming KQML (Knowledge Query Manipulation Language) messages in the queue from agents and pending action and places on the objectives queue for Planner. Then, Planner monitors the objectives queue and matches new goals to an existing task template as stored in task template hash table. Scheduler selects actions in action results queues sent from Executer at runtime according to users' requirement. Then, Executor checks the agenda queue if any further work to be done. Also, Executor produces Action modules of the agents, sends KQML messages, searches other agents, and interacts between agents. Agent systems have been developed using various languages and platforms, and they can be classified into internet agent, intranet agent, and desktop agent by purpose.

In DECAF, tasks of the agents are usually assigned by GPGP (Generalized Partial Global Planning) [2, 4] and TAEMS (Task Analysis Environment Modeling and Simulation) [5]. GPGP was developed from PGP (Partial Global Planning) [6], which acts as a coordination algorithm of multi agents. GPGP has two main advantages over PGP. One is that it reduces the overhead of systems, which occurs by overlapping interaction among agents. The other is that it is independent from some specific domain areas. Therefore, GPGP can make heterogeneous multi agent systems having different functions. User's requirements can be decomposed by GPGP and structured by TAEMS. The root task in TAEMS can be decomposed into subtasks which can be decomposed into methods, too. The leaf node acts as a method which means acted elements.

2 Information Gathering Multi Agent Framework

A digital library serves a lot of information on-line. The advantages of digital libraries over conventional libraries are user friendly, on-site service, and accessibility. However, in case of not having standardized platform, the search of heterogeneous information from digital libraries may be hard, or impossible in some cases. To solve the problem, I develop a mobile multi agent-based digital library system using DECAF. The 'mobile' means that agents autonomously move a server to a server without user's interference. The mobile multi agent-based digital library system can eliminate unnecessary and duplicate information stored in Internet or DB. Also, existing digital libraries do not have or learn about the user's information. It causes unnecessary or useless information for the user to appear in the searched results. To solve the problem, I propose a mobile multi agent-based personalized digital library system (MAPS). MAPS provide the personalized search list from users' usage history.

2.1 System Overview

Fig. 1 shows the overall architecture of MAPS consisting of three main parts such as Information Gathering Multi Agent Framework using DECAF, Personalization Agent, and Digital Library Server. Information gathering is a method for implementation of user's personalized strategy. Therefore in this paper, I use information gathering instead of information search or filtering.

Once a user requests a query with keywords, Agent Manger (AM) in DMMAF receives the query through the Matchmaker Agent and prepares the user's profile because the search results are obtained by the user's profile. Scheduling Agent determines the order of the agents' visit to the digital library server. The documents are collected from an agent's visit to web servers (DBMS) according to the scheduled order. Digital Library Server (sub host) accepts the agents by defined port, agents approach the DBMS of web servers. During the agent visiting, Negotiation Agent customizes the collection at each web server by eliminating duplicate documents with its previously visited web servers via a network. Each visit is done in company with the Mobile Multi Agent (MMA). The attributes of MMA includes the plan code, agent ID, host URL, and resources (user's profile). The plan code is the agent's task generated by Scheduling Agent. The agent ID is the unique number of each agent, which is generated by Matchmaking Agent. The host URL is the address to return. The resource is the user's profile. Personalization Agent provides the user a personalized search list from the negotiated documents according to the user's profile. Then, Information Collection Agent shows the final searched results to user through the user interface.

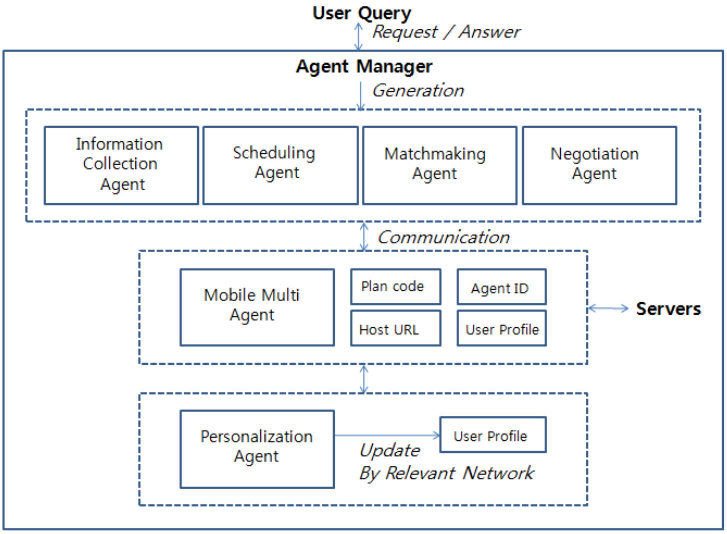

Fig. 1. The basic structure of information gathering multi agent framework

2.2 Module Functions and Algorithms

DMMAF is a proposed agent framework for distributed environment in this paper. DMMAF has five components such as Agent Manager, Plan Editor, ANS, MMA, \Transfer Protocol.

Agent Manager receives a user's query, creates agents, and controls the agents' operations. Matchmaker Agent communicates between Matchmaker Agent and UI. Also, Matchmaker Agent creates agents according to the schedule generated by Scheduling Agent. Scheduling Agent searches the optimal path to visit servers and informs it to the plan editor in DECAF. The plan editor creates the plan codes. Information Collection Agent sends the final searched results to the user through UI. Negotiation Agent removes the duplicated results through KQML communication language among MMAs. Agent Name Server creates the MMA and saves the multi agents' record about creation and deletion information of each MMA. The transfer protocol of the MMA is to encrypt and decrypt the agent byte code, plan code, user profile, and resources. Byte codes which are sent through network are doing the parsing process. MMA visits the host having user keyword and user profile. MMA negotiates with other agents using negotiation algorithm and search the DB.

Agent task Group assigns Task_1, Task_2, and Task_3 to Agent 1, Agent 2, and Agent 3 respectively. The tasks are automatically decomposed into methods, and the agents execute the assigned tasks by the methods. There are five types of relationships among methods. *Add_R* is the add relationship, i.e., adding the result of a method to that of other methods. *Activate_R* is the relationship making the running method keep running continuously. *Compensate_R* is the relationship that compensates the results of methods if needed. *Replace_R* replaces the results of receiving methods with those of sending methods. *Contradict_R* ignores the results of receiving methods. Also, there are lots of relationships between methods and tasks and between methods and resources, such as *Enable, Facilitate, Produce, Consume,* and *Limits*. In the negotiation algorithm, if the agents in the same level take different actions, then *max* operation operates to produce the output of the agents. Otherwise, *min* operation is operated.

The information about MMA moving is transferred in byte stream type surrounded by the defined tag of the KQML protocol. The byte stream is parsed according to the defined tag and the clone byte of the byte stream is transferred to the next web server.

2.3 Modeling Keyword Relevance Network

From abstracts in the papers retrieved by a user's query with a keyword, I measure the relevance between nouns in the abstracts and the keyword. For example, if a user requests a query with a keyword through a search engine then the search engine retrieves every relevant paper with the keyword. Also, I can extract the abstracts from the retrieved papers by parsing them. From the extracted abstracts, I can compute the frequency of the appearance of each noun as in Eq (1).

$$freq(keyword, noun_i) = \sum_{a=1} n_{i,a} \quad (1)$$

where $n_{i,a}$ is the appearance number of noun i from the a^{th} retrieved Also, $freq(keyword, noun_i)$ implies the strength of the relevance of the retrieved noun i with respect to a keyword over all abstracts

As seen in Eq (1), the strength of the relevance between the keyword and a noun depends on the appearance frequency in the abstracts. If the number of the appearance of a noun is large, it can be considered the noun is very relevant with the keyword. In the same way, each noun also can be a possible keyword queried by the user. However, if I take an account of keywords for the nouns appeared even a single frequency over all abstracts then the number of keywords for the user can increase exponentially as time passes. It causes the relevance network complicated. To avoid this situation, it is needed to decide the threshold of the frequency of the appearance for each noun as the qualification of being a keyword. The value of the threshold can be determined from the empirical experience in the experimental section later. Following the previous process, the generalized keyword relevance network among the keywords can be viewed as in Fig.2.

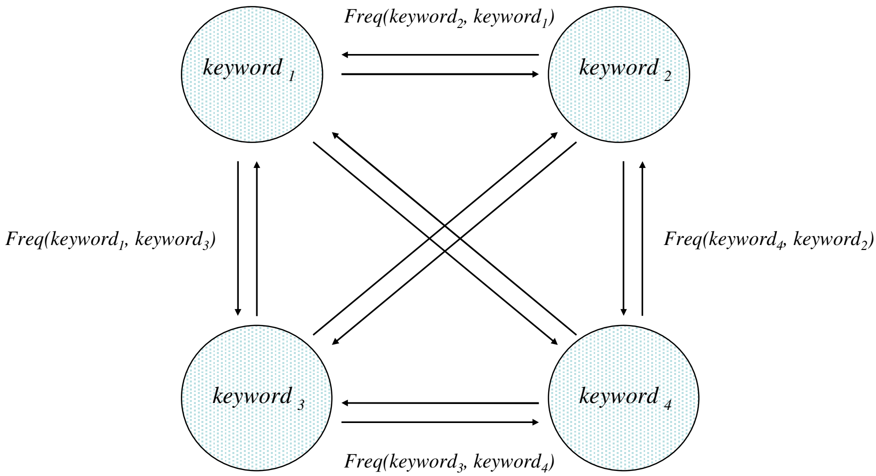

Fig. 2. The fully connected relevance network of keywords in the information gathering multi agent framework

From the keyword relevance network, I can't provide the personalized search list of papers because an identical list is showed for all users with the same queried keywords. In order to solve the problem, I modify Eq (1) by giving weights to the computation of the frequency of appearance of keywords according to the user's behaviors (actions) on the searched list, such as downloading, opening, and no-action.

$$freq(keyword_i, keyword_j) = \sum_{a=1} w_a n_{i,j,a} \quad (2)$$

where w_a is the weight of the user's behavior for paper a and $n_{i,j,a}$ is the appearance number of keyword j from the a^{th} retrieved paper by the query of keyword i. In general, the action of downloading papers from the searched list is understood that the user is very interested in the paper. From this point of view, the keywords in the paper can be considered more preferred than the other two actions, opening and no-action. In order to take this into the consideration, I give relatively large value of the weight w_a for the action of downloading, compared to the other two actions. In the same concept, opening papers implies that the papers are more preferred than taking no-action for the papers. Therefore, the order of the values of the weight for the three actions is downloading > opening > no-action. The value of the weight for each action is also determined by the empirical experiment.

Eq (2) shows the relevance between two keywords. However, users often request a query with more than one keyword (called a set of keywords in this paper). The generalization of Eq (2) for various numbers of keywords can be expressed in Eq (3) which implies the strength of the relevance of keyword j for the set of keywords.

$$freq(Set\_keyword, keyword_j) = \sum_{k=1}^{s} freq(keyword_k, keyword_j) \quad (3)$$

where *Set_keyword* is a set of queried keywords and s is the number of the queried keywords. For the convenience, Eq (3) can be expressed in the normalized form as in Eq (4).

$$Nfreq(Set\_keyword, keyword_j) = \frac{freq(Set\_keyword, keyword_j)}{\sum_{j=1}^{J} freq(Set\_keyword, keyword_j)} \quad (4)$$

where $Nfreq(Set\_keyword, keyword_j)$ is the normalized strength of the relevance of keyword j for the set of keywords. According to the value of the normalized strength of keyword relevance, the order of the searched papers in the list is determined. For instance, from the searched papers using queried keywords, the papers having high normalized relevance with respect to the queried keywords place on top position and front pages in the searched list.

3 Evaluation

3.1 Optimal Threshold

I implemented my system using the JAVA web server in the Window NT environment. In the server, I used the JSDK which is Java servlet developer kit 1.4 to run my system. MS SQL server 2000 was used as the relational database. Also, JDBC (Java Database Connectivity) was used in order to connect database with servlet.

I obtained the optimal threshold of the frequency of the appearance of each noun for determining whether it is suitable for a keyword. The optimal threshold can be estimated by recall and precision [7] using Eq (5).

$$\mathrm{Re}\,call = \frac{|R_a|}{|R|},\quad \mathrm{Pr}\,ecision = \frac{|R_a|}{|A|} \tag{5}$$

Recall is $|R_a|$, the ratio of the number of target papers among retrieved result papers, to $|R|$, whole desired target papers. Precision is $|R_a|$ to $|A|$, retrieved result papers. The collection means the collected sample papers for my experiment, where 96 sample papers were collected. The process to estimate the optimal threshold is as follows. I classified the sample papers into 12 groups by the similarity of their content. The 8 papers are contained in each group. So, $|R|$=8. It is the best scenario that all 8 papers in the group are listed with no paper in the other groups when I request a query with a keyword existing in the group. Fig. 3 shows the mean precision, computed using Eq (5), of each group for 5 times repeated experiment by varying the requested keywords. Fig.3 (b) is for the recall by threshold.

It is also done by varying the value of the threshold, denoted as *t*, from 1 to 4. For *t* = 1, all target papers were retrieved, i.e., $|R_a|$=8. In this case, the recall becomes 1. However, the mean retrieved paper number is 31, i.e.,$|A|$=31 in which too many undesired papers were included. By Eq (5), the precision equals 25.81% which means that the efficiency is too low even though all target papers were retrieved. As mentioned in Section 3, it is because too many related keywords for each keyword exist in the user's relevance network by considering even a single appeared noun as a keyword. For *t* = 2, the mean number of the retrieved target papers is$|R_a|$=7 out of the whole retrieved paper number $|A|$=12. The recall decreases to 87.5%, compared to *t* = 1. However, the precision increased to 58.3%. For *t* = 3, the mean number of the retrieved target papers is$|R_a|$=2 out of the whole retrieved paper number $|A|$=3. The recall reduces to 25%. The precision increased to 66.7%. The three times appearance for each noun is the strong condition for becoming related keywords for each keyword. In other words, small number of related keywords for each keyword exists in the user's relevance network. It causes the precision to increase and the recall decreases at the same time. For *t* = 4, the mean number of the retrieved target papers is$|R_a|$=0 out of the whole retrieved paper number $|A|$=0. From the experimental results, I found that *t* = 2 provide the optimal performance by the trade-off relationship between the recall and the precision. Thus, I used two time appearance as the threshold of the keywords for evaluating the performance of my personalized paper search system shown in the next section.

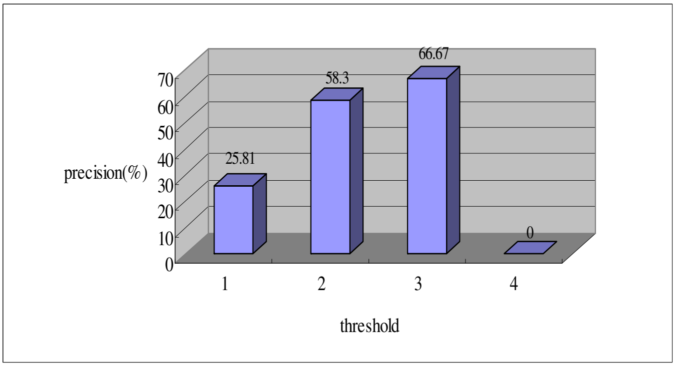

(a) Precision by threshold

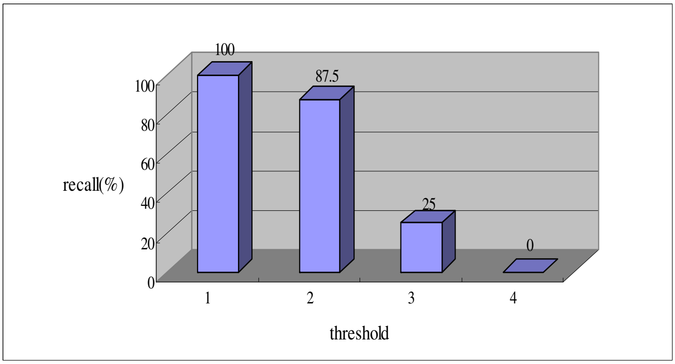

(b) Recall by threshold

Fig. 3. Optimal threshold

3.2 Searching Speed

In this section, I analyzed the searching speed of my system to show both the advantage and disadvantage of my mobile-based searching system. To evaluate MAPS searching speed, I simulated my system in the environment with one main host and 3 sub hosts. I compared the searching speed of my system with the traditional remote data access (RDA) searching method, according to the number of duplicated papers retrieved from the servers.

As seen in Fig.4, the initial searching times of MAPS system (0.18 seconds) takes longer than the conventional system (0.11 seconds). It is because my searching system is operated by cooperation between multi-agents. The searching time of my system increases by about 0.001 seconds per one duplicate paper, while about 0.007 seconds for the conventional system. Thus, as the number of the duplicate papers retrieved from the multiple severs increases, the searching time of the conventional method increases more drastically than my method. When the duplicate papers are around 15 per server, the speed of my system begins to outperform the conventional system.

From the simulation, it can be concluded that my system is efficient when a lot of duplicated papers exist in many DBMS.

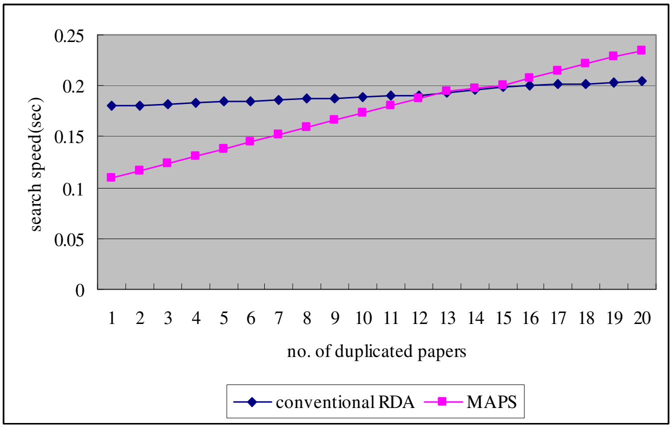

Fig. 4. Searching speed between MAPS and RDA

3.3 Experimental Results

For the experiment, I chose the values of weight of users' behavior for paper a, as in Eq (2), $w_a = 5$ for downloading, $w_a = 2$ for opening, and $w_a = 1$ for no-action, respectively. Those values were determined by exhaustively empirical experience using 100 faculties in the University of Suwon, Korea. The information of the users' paper search behaviors had been collected during one month. When those values of weights were used, the satisfaction of my system for the faculties reached to the maximum point.

In ACM PORTAL for the queried keyword '*network*' by a faculty, the 64,493 papers were found. It is a huge number of papers the user needed to look up for finding the most relevant papers of what the user was looking for.

For the same keyword used in the ACM PORTAL, the normalized strength of the relevance for keyword "neural" is 0.47 which is the biggest relevant keyword to the 'network'. It means that the user had been interested in the papers with keywords 'network' and 'neural' during the period so he/she had acted the downloading or opening for those papers. For the user, my system placed the papers with the keywords having 'network' and 'neural' in their abstracts on the top positions in the searched list. By placing a user's possibly preferred papers on the early pages in the searched list, it can save time to surf the list and reduce the user's effort to find his/her preferred papers.

Also, I evaluated the performances of my system and the conventional search system by comparing the satisfaction of both systems for the 100 faculties. As a result, 98% (27 for "very satisfactory", 71 for "satisfactory") out of 100 expressed their satisfaction for my system, while only 5% for the conventional system.

4 Conclusion

In this paper, I proposed a framework for mobile-based personalized paper search system. By using the proposed system, users do not need to visit all possible search servers with the same query by using the new platform. Also, the system provides users' personalized search list by building user's individual relevance network from analyzing the appearance frequencies of keywords in the searched papers. As seen in the previous experimental section, I showed that users can save paper search time and reduce an effort to find their preferred paper when many duplicate papers exist in DBMS, which are retrieved from multiple search servers.

However, the values of the weights for users' behaviors, i.e., $w_a = 5$ for downloading, $w_a = 2$ for opening, and $w_a = 1$ for no-action was obtained from the exhaustively empirical experiment. The values might not be optimal for all users. For the further work of this paper, I need to develop an automatic algorithm for determining the values according to each individual user.

References

1. Birmingham, W.P., Durfee, E.H., Mullen, T.: The Distributed Agent Architecture of the University of Michigan Digital Library. In: AAAI Spring Symposium on Information Gathering form Heterogeneous, Distributed Environments. AAAI Press
2. Graham, J.R., Decker, K.S.: Towards Distributed, Environment Centered Agent Framework. In: Appearing in Intelligent Agents IV, Agent Theories, Architectures, and Languages
3. Lesser, V., Horling, B., Klassner, F., Raja, A., Wagner, T., Zhang, S.: BIG: An Agent for Resource-Bounded Information Gathering and Decision Making. Artificial Intelligence Journal, Special Issue on Internet Information Agents 118(1-2), 197–244 (2000)
4. Graham, J., Windley, V., McHugh, D., McGeary, F., Cleaver, D., Decker, K.: Tools for Developing and Monitoring Agents in Distributed Multi Agent Systems. In: Workshop on Agents in Industry at the Fourth International Conference on Autonomous Agents, Barcelona, Spain (2000)
5. Logoze, C., Fielding, D.: Defining Collections in Distributed Digital Libraries. D-Lib Magazine 4(11) (1998), `http://www.dlib.org/dlib/november98/lagoze/11lagoze.html`
6. `http://www.greenstone.org/cgi-bin/library`
7. Baeza-Yates, Ribeiro-Neto: Modern Information Retrieval. Addison-Wesley(1992)

Study of Query Translation Dictionary Automatic Construction in Cross-Language Information Retrieval

Su-Mei Xi[1] and Young-Im Cho[2]

[1] College of Information,
Shandong Polytechnic University
3501 University-ro, Changqing-gu, Jinan 250-353, China
xsm@ suwon.ac.kr

[2] College of Information Technology,
University of Suwon
San 2-2, Bongdam-eup, Hwaseong-si, 445-743, Korea
ycho@suwon.ac.kr

Abstract. The bilingual machine-readable dictionary is the commonly-used resources for query and translation based on the cross-language information retrieval; however, the traditional method of constructing the bilingual dictionary manually wastes time and energy. This paper uses the method of statistics to automatically obtain the translation dictionary from the English-Chinese parallel corpus for query and translation.

Keywords: cross-language, information retrieval translation dictionary.

1 Introduction

Cross-language information retrieval (CLIR) tries to identify relevant documents in a language different from that of the query. Its main problem is matching between query and documents of different languages. At present the main approach is to add language conversion mechanism (query translation or document translation) on the basis of monolingual information retrieval system [1].

2 Principle of Automatic Construction of Query Translation Dictionary

Based on the existing ambiguity problem-solving approach, we follow the following principles in constructing a query translation dictionary.

- Part of speech information term marked. There are many words which have more than one part of speech in natural language, and different part of speech generally means different meaning [2]. Polysemy problem can be solved to some degree by combining part of speech information to translate query.

S. Lee et al. (Eds.): Intelligent Autonomous Systems 12, AISC 194, pp. 585–592.
springerlink.com

- Provide phrase-level translation. Average precision can be increased 25% when translating query using phrase unit compared to the word unit, but the quality of phrase translation will largely affect the retrieval results
- Provide translation of named entities as detailed as possible [3].
- Provide the using information of words [4].

3 Query Translation Dictionaries Automatically Construction Based on Statistics

The method of translation dictionary automatically construction based on sentence aligned parallel corpus can be divided into five steps, specific process shown in Figure 1. The core issue what will be solved during the translation dictionary construction is acquisition of the candidate translation unit (including words unit and phrases) and generation of the translation equivalent pairs.

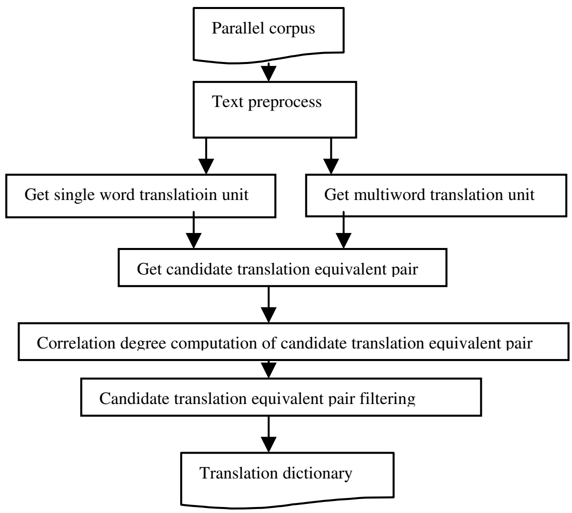

Fig. 1. Flowchart of translation dictionary automatically construction

3.1 Preprocess

The main task of preprocess is to process sentence aligned English-Chinese parallel corpora, including word segmentation and part of speech tagging of Chinese corpora and part of speech tagging of English corpora. The tools of word segmentation and part of speech tagging both are open-source toolkit developed by Stanford University [5]. Here is a sentence pair after the above processing.

English: Making _VBG sure_RB the_DT column_NN is_VBZ used_VBN for_IN unique_JJ identification_NN ._.

Chinese: 请_VV 确保_VV 唯一_JJ 标识_NN 列_NN 。_PU

Among them the identification after "_" is part of speech, here we use the Penn Treebank Tag Set.

3.2 Obtain the Candidate Translation Unit

Considering the roles of part of speech and phrase identification in word sense disambiguation and affecting query translation, nouns and verbs will be obtained separately when obtaining the candidate translation units and noun phrases will be identified.

1) Single word. Firstly, Single word translation unit of noun and verb can be obtained using the results of word segmentation and part of speech tagging. The reason which selects these two parts of speech as candidate translation unit is that these two parts of speech ratio are high among the queries and they also determine the main meaning of queries. Secondly, we can filter stop words to generated verb candidate translation unit and delete those unmeaning translation units such as ”可以”、”应该”、”能够”、”be”、” have、has、had、s、re、ve” and so on.

2) Noun phrase. Recognizing the noun phrase by using part of speech pattern constraint method, generating candidate noun phrase, calculating the correlation degree of all of the adjacent word pairs of candidate noun phrase by combining statistic information, if the adjacent words’ correlation degree is lower than a given threshold value in this noun phrase, this phrase will be deleted and the final noun phrase translation unit will be obtained.

Firstly, defining some noun phrase part of speech patterns using linguistic knowledge, combining result of text part of speech tagging, the candidate noun phrase will be extracted. The part of speech patterns in this paper includes the followings:

AN, NN, AAN, ANN, NNN, NAN, ANNN, AANN, AAAN, NNNN.

Where A is adjective, N is noun, the longest length of noun phrase is 4 and the shortest is 2.

We can use statistic information to filter the candidate noun phrase. The detailed process is as follows: assuming one candidate binary noun phrase includes two words N_1,N_2, counting the frequency of phrases N_1N_2 and single word N_1 and N_2 appearing in corpora, and then calculate the correlation degree of N_1,N_2 using formula Log Likelihood Ratio(LLR). The reason of selecting LLR coefficient is that this formula can process the correlation strength of low-frequency pair, the correlation degree calculation formula is as follows:

$$LLR(N_1,N_2) = 2[\log L(p_1,a,a+b) + \log L(p_2,c,c+d) - \log L(p,a,a+b) - \log L(p,c,c+d)] \quad (1)$$

Where a= freq(N_1, N_2), denotes the frequency of binary noun phrase N_1N_2 in the corpora, b= freq(N_1)-freq(N_1, N_2),denotes the number of sentence of N_1 appearing but N_2 disappearing, c=freq(N_2)-freq(N_1, N_2), denotes the number of sentence of N_2 appearing but N_1 disappearing, d=N-a-b-c, denotes the number of sentence of N_1 and N_2 both disappearing, and N denotes is total number of sentence of corpora. $\log L(p,k,n) = k\log(p) + (n-k)\log(1-p)$, $p_1 = a/(a+b)$, $p_2 = c/(c+d)$, $p = (a+c)/(a+b+c+d)$, $\log(0)=0$.

According to the calculated LLR value, for each noun phrase $N_1,\ldots,N_k$ ($2 <= k <= 4$), if the LLR value of all binary phrases $N_{i-1}N_i$ included in this noun phrase are greater than threshold value α, this phrase will be regarded as a multi-word units, otherwise, if existing $N_{i-1}N_i$, whose LLR value is lower than threshold value α, this phrase will be deleted from candidate phrase list. And then stemming for all obtained English translation units by using Porter Stemmer, the final candidate translation unit will be generated. Table 1 is a candidate translation unit from two example sentence of 3.1.

Table 1. case of candidate translation unit extraction

	English candidate translation unit	***Chinese candidate translation unit***
Noun	Column, ident Unique ident	标识列，唯一标识 唯一标识列
verb	Make us	确保

3.3 Generate Translation Equivalent Pairs

In this section we obtain candidate translation equivalent pairs according to English-Chinese translation unit, calculate the correlation degree of translation equivalent pairs, filter the expect value and English-Chinese Chinese-English dictionaries, and generate the final translation dictionary.

1) Obtain Candidate Translation Equivalent Pairs

We omit the length of candidate translation unit when generating noun candidate translation equivalent pairs. Only if pair of noun or noun and noun phrase appears in a pair of bilingual sentence they will be regarded as candidate translation equivalent pairs. The process of verb candidate translation equivalent pairs uses same approach.

2) Correlation Degree Calculation

Firstly count appearing frequency of all candidate translation equivalent pairs and each candidate translation unit, delete the candidate translation equivalent pairs whose co-occurrence frequency is less than 5, and then calculate the correlation degree of each translation equivalent pair.

There are four common formulas about calculating translation equivalent pair correlation degree, including LLR, Dice coefficient mentioned above, also including MI andΦ^2 coefficient. We use these four methods to calculate candidate translation equivalent pair correlation degree in order to comparing them in this paper. The detailed formulas are as follows:

$$MI= \log[a/(a+b)\ (a+c)] \quad (2)$$

$$Dice(cp,ep) = 2a\ /(2a+b+c) \quad (3)$$

$$\Phi^2 = (ad-bc)^2 / \ [(a+b)\ (a+c)\ (b+d)\ (c+d)] \quad (4)$$

Where a= freq(cp, ep), denotes the number of sentence pairs which including Chinese candidate translation unit cp and English candidate translation unit ep, b=freq(cp)-freq(cp,ep),denotes the number of sentence pairs which only including cp but not including ep, c= freq(ep)-freq(cp, ep), denotes the number of sentence pairs which only including ep but not including cp,, d= N-a-b-c, denotes the number of sentence pairs which not including cp and ep, and N denotes is total number of sentence pairs of corpora.

3) Filtering

We descending sort all English translation items of each Chinese candidate translation unit according to its correlation degree of Chinese translation unit, generating Chinese-English bilingual dictionary and English-Chinese bilingual dictionary. Final translation dictionary can be obtained through expect value filtering, Chinese-English English-Chinese dictionary combining filtering, deleting some translation equivalent pairs.

4 Experimental Result and Analysis

The corpora of experiment is English-Chinese parallel corpora of computer field, which come from web sites and has been processed by sentence aligned, and it includes 300000 sentence pairs. The total number of bytes is 87 612 118.

According to above method, translation equivalent pairs can be extracted automatically from corpora and then two translation dictionaries about English-Chinese dictionary and Chinese-English dictionary will be generated. The detailed information about dictionaries is shown as table 2.

It can be seen from table 2 that generally not only total tokens but also number of equivalent pairs are the least, which generated by LLR coefficient, but they are the most which generated by MI coefficient. Furthermore, the number of noun tokens and equivalent pairs are similar whatever it generated by each of four coefficients. However, the case of verb is very different.

Table 2. Statistic result of generated dictionary

	coefficient	*Total noun tokens*	*Noun phrase tokens*	*Total noun equivalent pairs*	*Verb tokens*	*Verb equivalent pairs*
Chinese-English dictionary	LLR	6015	2831	8195	1413	1906
	Φ^2	6431	3015	8844	2148	3231
	Dice	7501	3328	13345	3251	10380
	MI	8424	4338	12417	4314	11113
English -Chinese dictionary	LLR	5734	3032	8195	1161	1853
	Φ^2	6215	3414	8844	1707	3130
	Dice	7070	3828	13345	2129	10129
	MI	7576	4484	12417	2480	10878

150 tokens have been selected randomly from the dictionary, including 50 noun phrase tokens and 50 verb tokens. The translation equivalent pairs that come from four statistic formulas based on co-occurrence have been evaluated separately. For calculation of precision of translation dictionary, the following method is used in this paper.

Precision=(number of equivalent pairs of correct translation in dictionary+ 0.5×number of equivalent pairs of partly correct translation in dictionary)/the total number of translation equivalent pairs.

According to above method, we can obtain noun word unit, verb and noun phrase evaluation results, shown as table 3, table 4 and table 5.

Through analyzing table 3, table 4 and table 5, the following conclusions can be drawn.

1) Generally speaking under the corpora environment this paper used, the statistical property of LLR coefficient is better than the other three coefficients, and Φ^2 is better than LLR only for English-Chinese noun phrase equivalent pairs. The reason is that the correct number (43) of English-Chinese noun phrase equivalent pairs is less than Φ^2 (45), but the wrong number (2) is greater than Φ^2 (1).

Table 3. Evaluation result of noun word unit equivalent pair

		Correct equivalent pairs	*Partly correct equivalent pairs*	*Total equivalent pairs*	*precision*
Chinese-English	LLR	143	61	206	0.8792
	Φ^2	144	71	215	0.8758
	Dice	154	92	284	0.7042
	MI	142	100	258	0.8235
English -Chinese	LLR	149	41	206	0.8228
	Φ^2	150	40	214	0.7943
	Dice	165	64	261	0.7548
	MI	155	70	270	0.7037

Table 4. Evaluation result of verb equivalent pair

		Correct equivalent pairs	*Total equivalent pairs*	*precision*
Chinese-English	LLR	50	68	0.7353
	Φ^2	57	79	0.7216
	Dice	83	147	0.5646
	MI	87	147	0.5918
English -Chinese	LLR	61	77	0.7922
	Φ^2	76	107	0.7103
	Dice	116	222	0.5225
	MI	118	231	0.5108

2) For noun dictionary, the main factor which affects dictionary precision is indirectly related problems, i.e. some idiomatic and phrases may make some bilingual words that not responds directly having high co-occurrence frequency. For example, in generated noun dictionary, “系统“ has two translations, one is “system” and the other is “oper”, among which “oper” means ”Operating”. Because ” Operating System” is a fixed phrase in computer field ”系统” and ” Oper” will be extracted as translation equivalent pair.

Table 5. Evaluation result of np equivalent pair

	coefficient	*Correct equivalent pairs*	*Partly correct equivalen t pairs*	*Wrong equivalent pairs*	*Precision of multiword unit*
Chinese-English	LLR	45	35	0	0.7813
	Φ^2	45	37	0	0.7743
	Dice	49	46	1	0.7500
	MI	48	43	2	0.7473
English -Chinese	LLR	43	26	2	0.7887
	Φ^2	45	27	1	0.8013
	Dice	48	34	3	0.7647
	MI	49	36	3	0.7614

Although it will be regarded as wrong translation equivalent pair when evaluating dictionary, during CLIR process if "System" and "Oper" are submitted to the system as translation of "系统", the final retrieval effect may be high for it equivalent to the query expansion, increasing retrieval contextual information.

3) All equivalent pairs that partly correct translation in noun dictionary can play a query expansion role in CLIR.

4) The main reason about the number of verb token equivalent pairs of MI and Dice is much larger than LLR andΦ^2 is that the filtering is more loose of MI and Dice coefficient, which reserving lots of wrong translation items. The detailed analysis is as follows:

In the sample set of Chinese-English verb dictionary generated by MI and LLR coefficient, correct translation equivalent pairs are 87 and 50, ratio is 87 /50 =1.74. Wrong translation equivalent pairs are 60 and 18, ratio is 60/18= 3.33. The total equivalent pairs are 147 and 68, ratio is 147/68= 2. 16. 3.33> 2.16> 1.74, i.e. the ratio of wrong translation equivalent pairs > the ratio of total equivalent pairs > the ratio of correct translation equivalent pairs. The result is same about English-Chinese verb dictionary.

5 Conclusions

This paper mainly explores how to construct translation dictionary which suit for cross-language information retrieval query translation, summarizing the characteristics of translation dictionary which suit for CLIR query translation, automatically constructing a query translation according these characteristics, comparing their performance of four common statistic models based on co-occurrence. By analyzing experimental result, we find that the ambiguity problem which CLIR faced can be solved in some degree by editing query translation based on corpora.

References

1. Chen, A., Kishidak, Jiang, H.: Automatic construction of a Japanese-English lexicon and its application in cross-language information retrieval (2008), http://www.clis.umd.edu/conferences/midas/papers/chen.ps.
2. Davism, D.: A trec evaluat ion of query translation methods for multi-lingual text retrieval (September 15, 2008), http://trec.nist.gov/pubs/trec4/papers/nmsu.psgz
3. Lin, C.-H., Chen, H.: An automatic indexing and neural network approach to concept retrieval and classification of multilingual (Chinese-English) Documents (December 15, 2008), http://dlist.sir.arizona.edu/526/01/lin.pdf
4. Davism: New experiments in cross-language text retrieval at NM SU's computing research lab. In: Proceedings of TREC-5. Gaithersburg, pp.447–453 (1997)
5. Bdksterosl, C.W.B.: Dictionary-based methods for cross-lingual in formation retrieval. In: Proceedings the 7th International DEXA Conference on Database and Expert Systems Applications, Zurich, Switzerland, pp. 791–801 (1996)
6. Ballesterosl, Croft, W.B.: Phrasal translation and query expansion techniques for cross-language information retrieval. In: Proceedings of the 20th Annual International ACM SIGIR Conference on Research and Develpment in Information Retrieval (SIGIR 1997), USA, Philadelphia, pp. 84–91 (1997)
7. Demner-Fushmand, O.: The effect of bilingual term list size on dictionary-based cross-language information retrieval (May 30, 2007), http://ieeexplore.ieee.org/iel5/8360/26341/01174250.pd?ftp=&isnumber=&arnumber=117425
8. http://nlp.stanford.edu/software/index.shtml

A Multi-Agent Information Retrieval System Based on Ontology

Qian Gao[1] and Young-Im Cho[2]

[1] School of information, Shandong Polytechnic University
3501 University-ro, Changqing-gu, Jinan 250-353, China
[2] College of Information Technology, University of Suwon
San 2-2, Bongdam-eup, Hwaseong-si, 445-743, Korea
gq@spu.edu.cn, ycho@suwon.ac.kr

Abstract. Traditional information retrieval systems are lack of semantic comprehension, and also have inherent ambiguity of short keyword queries. To solve this problem, this paper proposed a Multi-Agent Information Retrieval System based on Ontology. Introducing ontology to information retrieval system can realize knowledge domain-expression in order to provide users with the increment of information service and refine the initial query. Furthermore, group agent use improved collaborative information filtering algorithm to construct the group preference base equal to the compilations of all the term preference sets of the similar users served by personal agent, so as to accomplish the personalized information retrieval according to users' interest of the group preference base and rank the retrieval results by comprehensively considering of the users' preference about a certain theme and the frequency of the keywords of the retrieved document that appear in the relevant domain.

Keywords: agent, query refinement, ontology, collaborative information filtering.

1 Introduction

In this era, the information stored by internet is increased exponentially. People can hardly acquire what they really want from web quickly since the web information is open, dynamic and isomeric. The information content is updated continuously, and coverage of the web by individual search engines only come to 30%-50%[3] of all Internet information resources. To solve this problem, people have designed many information retrial systems to locate and manage web document. However, when we retrieve the words specified by users, normally the information retrieval technology either adopts the classification catalogues retrieval methods which realize the retrieval according to the subject properties of the resources or adopts the full text retrieval technology which needs to set up the inverted index from documents to tokens[1]. Generally, the performance of these methods depends on the identification method of the field and users' understanding, so that the above methods have a poor capability of supporting semantic matching as well as some other limitations.

S. Lee et al. (Eds.): Intelligent Autonomous Systems 12, AISC 194, pp. 593–602.
springerlink.com

In order to solve these problems, this paper proposed a Multi-Agent Information Retrieval System based on Ontology. Firstly, from the personal requirement of information retrieval, we use ontology as a means of knowledge domain-expression to form terminology ontology so as to refine the initial query and classify the documents stored in the location information database; then we use information retrieval agent to establish preference base for each user, and carry on the classified management for them. On this basis, the retrieval agent intelligently realizes the information retrieval from the local information database automatically according to users' preference.

The information retrieval agent is composed of personal agents, and group agent whose preference base is equal to the compilations of all the term preference sets of the similar users. We adopt the improved multi-agent collaborative information filtering technology to realize the searching of the personal agent with the similar user preference, so as to accomplish the personalized information retrieval according to the user's interest of the group preference base and rank the retrieval results by comprehensive considering of the users' preference about a certain theme and the frequency of the keywords of the retrieved document that appear in the relevant domain.

2 Structural Model of the Multi-agent Information Retrieval System Based on Ontology

The traditional search engine technology can not provide personalized retrieval information according to users' interest or preference. The retrieval mechanism based on keywords or theme can not meet the query requirements of the users, and has shortcomings of poor real-time and poor ability of information navigation[4].

To solve this problem, we introduced ontology into the information retrieval system to realize the expression of the information need and the relationship between concepts of different domains with the formalized terms, so as to provide users with increment of information service.

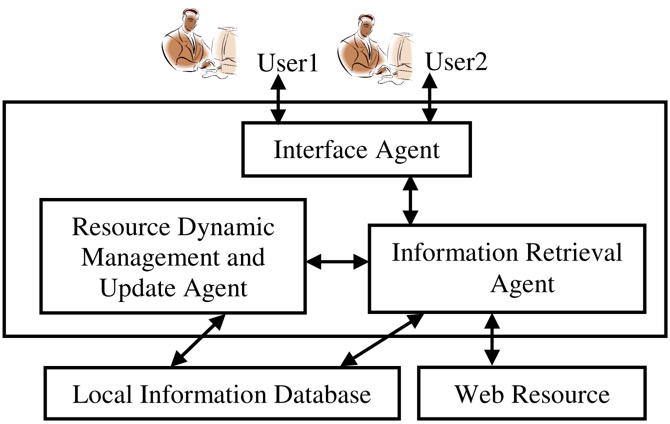

Fig. 1. System Framework

Therefore, in this paper, there are two mainly designed ideas: the query refinement and documents classification based on the ontology; the personalized information retrieval services based on multi-agent technology and improved collaborative information filtering algorithm.

As shown in Fig.1, our proposed information retrieval system is composed of 3 agents, whose function will be introduced below in order.

2.1 Interface Agent

There are two main functions of interface agent: first, it interacts with users and accepts the users' retrieval query and returns the retrieval results back to users; second, it analyses and reformulates the received user's query, returns the estimated proposals (and its estimations) back to the user for choosing the best one and finally sends the refined query to the Information Retrieval Agent. The specific structure of the Interface Agent is shown in Fig.2

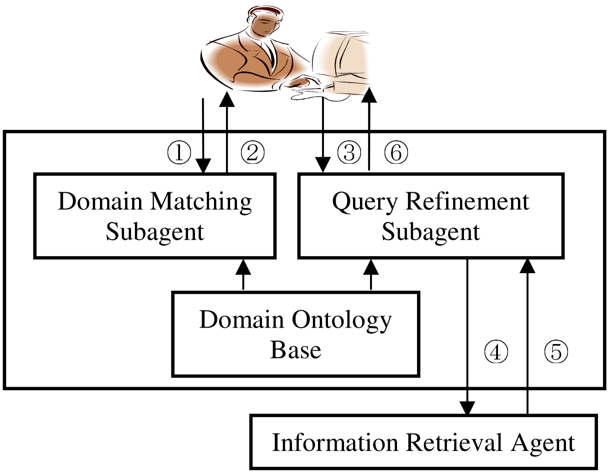

Fig. 2. The Specific Structure of the Interface Agent

In the Interface Agent, we construct two subagents: one is Domain Matching Subagent, and the other one is Query Refinement Subagent. First, user sends the initial query to the Domain Matching Subagent(DMSA, as shown on Fig.2, road ①), and then the DMSA analyses the user's query according to the Domain Ontology Base to find the domains the query may belong to, and submit its proposals composed of the initial query and the belonged domains to the user(as shown on Fig.2, road ②). Second, the user chooses the exact domain the query belongs to, and sends the selection to the Query Refinement Subagent (QRSA, as shown on Fig.2, road ③), then the QRSA expands the feedback query with hypernym (kind-of relationship), hyponym (part-of relationship) and allomorph (instance-of relationship) according to the ontology tree, and finally sends the refined query to the Information Retrieval Agent (IRA, as shown on Fig.2, road ④). Finally, after the retrieval, the IRA and QRSA submits the retrieved results back to the user(as shown on Fig.2, road ⑤,⑥).

2.1.1 Domain Matching Subagent

Thus, Assume O_1 , O_2, O_3, …, O_n are the ontologies of the domain D_1 , D_2, …, D_n respectively and $T_{i=}\{t_{i1},t_{i2},\ldots\}$, $i\in(1,n)$ are the terms set worked out from the ontology O_i. Assume Q= $\{q_1, q_2,\ldots,q_m\}$ is the initial query of the user. If $Q\cap T_i=\emptyset, 1\leqslant i\leqslant n$, it means that the query has no relevance to this certain domain. Thus we can get all the domains D_{f1}, D_{f2},…, D_{fk} (Here the $Q\cap T_{fj}\neq\emptyset$, $f1\leqslant fj\leqslant fk$) relevant. Then add the name of the relevant domain D_{f1}, D_{f2},…, D_{fk} as additional feature of the initial query and send back to the users.

Assume the suggested query set by the Domain Matching Subagent are ((Q, D_{f1}), (Q, D_{f2}),……, (Q, D_{fs})). If some different users input the same query, then after their selection, the query fed back by the users are ((Q, D_{fi1}), (Q, D_{fi2}),……,(Q, D_{fis})). Finally, after the feedback of the different users, the modified query set will be (α_1(Q, D_{f1}), α_2(Q, D_{f2}),……, α_s(Q, D_{fs})), where the α_i is the weight of the query in a certain domain. Since the more attention the users receive, the bigger the α_i value is, the value α_i can effectively reflect the needs of users. Therefore, after a period of modification, the weight of the modified query smaller than a set value will be discarded. Normally, we consider these domains the deviation of the definition about the query, so in the latter, when a certain user inputs the same initial query, the Domain Matching Subagent will not consider the discarded domain.

With this method, the system can know the domain that most users concern about, so as to provide more accurate information for the retrieval.

2.1.2 Query Refinement Subagent

For a certain user, the query fed back must be in an exact domain, and in form of (Q, D_{fi}). Considering the initial query as provided by the user may be an inadequate representation of the user's information needs, we use Query Refinement Subagent to expand the query fed back with hypernym (kind-of relationship), hyponym (part-of relationship) and allomorph (instance-of relationship) according to the ontology tree.

2.2 Resource Dynamic Management and UpdateAgent

The main function of the Resource Dynamic Management and Update Agent can be classified into three aspects:

The first function is to classify the documents stored in the local information database into their own domains, so as to narrow the retrieval scope and improve the retrieval speed.

Generally, most documents list the keywords and the abstract, especially for the academic papers. The keywords given by any document should embody the most core content of the document, which we can use as the main information to judge which domain the documents belong to and classify the documents in combination with the content of the documents and under the assistance of the ontology knowledge. Assume KW= $\{k_1, k_2,\ldots,k_m\}$ are the keywords set of a certain document in the local information database. If $KW\cap T_i=\emptyset$, $1\leq i\leq n$, it means that the keywords set of the document has no relevance to this document. Thus we can get all the domains D_{f1}, D_{f2},…, D_{fk} (Here the $KW\cap T_{fj}\neq\emptyset$, $f1\leq fj\leq fk$) relevant.

Through this method, we can classify each document stored in the local information database into their own domains, and a certain document can be classified into several domains. Hence in the future, when the Information Retrieval Agent retrieves documents in the local information database, only the documents belonging to the same domain with the query can be retrieved.

The second function is to monitor whether the retrieved documents were stored in the local information database. If not, store the documents into the local information database and analyze the new document according to the knowledge of the ontology base and classify the new documents into their own domains.

The third function is to monitor whether the content of the page in the local information base has any change or not. If there is, reclassify the changed documents.

2.3 Information Retrieval Agent

Information retrieval agent is the core part of the multi-agent information retrieval system based on ontology, which performs the automatic acquisition and information retrieval service of the local resources and web resources according to users' preference.

Information retrieval agent is composed of user-oriented personal agents and group agent. A personal agent can acquire the information about users' browsing interest from the users it serves directly or indirectly. A group agent first acquires the interest of every user from the personal agents, and then adopts the improved multi-agent collaborative information filtering technology to find the users with common interest, so as to find the pages that can reflect the common interest of the users and monitor these pages constantly to adapt to the changing needs of the user groups. The simple framework of the information retrieval agent is shown in Fig.3.

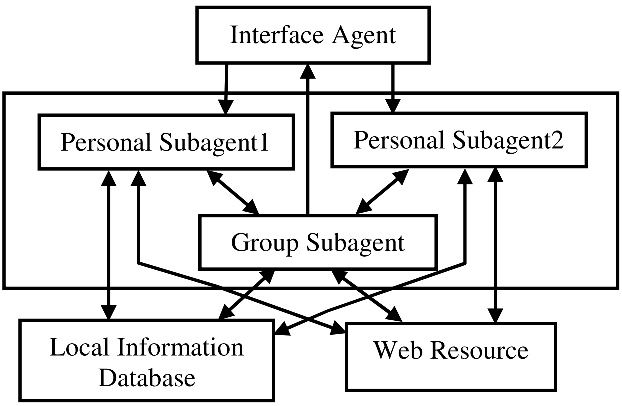

Fig. 3. Simple Framework of the Information Retrieval Agent

The personal subagents and group subagent are all composed of several modules with every module serving for a specific personal agent or group agent, independently shouldering part of the job belonging to subagents. The detailed framework of the information retrieval agent is shown in Fig.4.

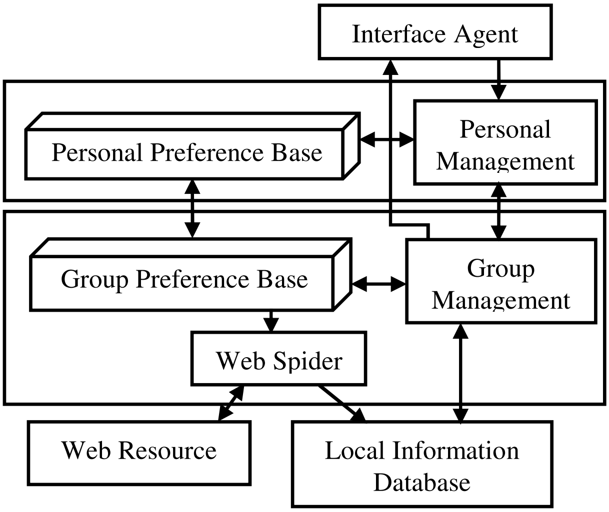

Fig. 4. Detailed Framework of the Information Retrieval Agent

2.3.1 Personal Preference Base

Personal preference base is used for storing users' personal interest or preference. It has been found that, if the users only have interest in part themes, then what they will browse must be the web page set relevant to these themes. Thus we can use the theme or directly use the web pages to describe users' interest. Web preference vector can express users' interest more directly than theme preference vector, but there are thousands of web pages in the internet, while users just click a small part of them, hence it is very difficult and impractical to learn Web preference vector. So we use theme preference vector to express the users' interest.

The users' theme preference vector can be expressed as $T=[T(1),\cdots,T(m)]$, where m stands for the number of the theme considered, T(i) indicates the interest degree of the users to the ith theme, and the vector T satisfies $\sum_{i=1}^{m} T(i) = 1$

2.3.2 Group Preference Base

The users who have the similar Personal Preference Base can be put in a group, and their personal interest or preference will be stored in the Group Preference Base. The theme preference vector of a group preference base can be expressed as $n \times m$ evaluation vector R, where n is the number of the users with similar interest, m is the number of the relevant themes and R_{ij} is the evaluation value of interest of jth terms given by user i. (It can reflect the preference).

2.3.3 Personal Management

Personal management agent obtains the theme preference of the users from their browsing history and stores the theme preference by means of vector T in the personal preference base.

The proposed paper adopts the topic sensitive PageRank algorithm[2] put forward by Taher H. Haveliwala of Stanford University to calculate the quality score of the web page A about theme t, so as to deduce the relationship between the browsing probability vector V and the theme preference vector T, where the browsing probability vector V=[V(1),···,V(n)], n is the number of the web pages, V(i) indicates the probability of web page i browsed by users, which satisfies $\sum_{i=1}^{m} V(i) = 1$. I will not introduce the algorithm in my paper.

2.3.4 Group Management Agent

Group management agent adopts the improved collaborative information filtering technology to realize searching of the personal agents with similar user interest and to copy the theme preference of the corresponding personal preference base to the group preference base. The improved algorithm is as follows:

Step 1: Calculate the similarity of interest between user i and user j served by personal agent

We adopt a sn×sm evaluation vector R' to store the degree of interest of all the users to all the themes, where sn is the number of the users served by personal agent, sm is the number of all the themes, and R'_{ij} is the evaluation value of interest of jth term given by users i. If the value of R'_{ij} is NULL, it means that the ith user hasn't made the assessment for the jth term. The similarity function S(i,j) is defined as (1):

$$S(i,j) = \alpha \bullet \frac{NS_i}{NS_{ij}} + \beta \bullet \frac{NS_j}{NS_{ij}} + \gamma \bullet \frac{\sum_{k \in ss_{ij}} \left(R_{ik} - \bar{R}_i \right) \bullet \left(R_{jk} - \bar{R}_j \right)}{\sqrt{\sum_{k \in SS_{ij}} \left(R_{ik} - \bar{R}_i \right)^2} \sqrt{\sum_{k \in ss_{ij}} \left(R_{jk} - \bar{R}_j \right)^2}} \tag{1}$$

S_i is the personal preference term set of user i, S_j is the personal preference term set of user j, $S_{ij}=S_i \cup S_j$. NS_i is the number of theme in the personal preference term set S_i, NS_j is the number of theme in the personal preference term set S_j, NS_{ij} is the number of theme in the preference term set S_{ij}. $\bar{R}_i$ and $\bar{R}_j$ are the average evaluation value that equals to the total theme value of S_i or the total theme value S_j to the total theme value of S_{ij} respectively. SS_{ij} is the theme subset, in which personal user i and user j have evaluation value in item set S_{ij}, α β γ are all constants, where α+β+γ=1.

Step 2: Rank the personal preference term set of user i and user j according to the value of S(i,j). If the value of S(i,j) is lager than the pre-set similarity threshold S, the users i and j have the similar interest and preference. Hence the users with the similar interest and preference are served by a group agent, and the term set among the preference base equal to the compilations of all the term preference sets of the similar users.

Step 3: For all the terms in the group preference base, predict the degree of interest I_{ik} of user i in item k. The function I_{ik} is defined as (2):

$$I_{ik=} \bar{R}_i + u \sum_{t \in group} (S(i,t) \bullet (R_{ik} - \bar{R}_t)) \qquad (2)$$

Where the $1/u = \sum_{t \in group} s(i,t)$

Step 4: Rank the documents retrieved from the location information database by comprehensively considering the I_{ik} and the frequency 'fre_{fk}' of the keywords of the retrieved document that appear in the relevant domain D_f which reflects the semantic approximate matching degree of the terms of the document and the ontology O_f.

2.3.5 Web Spider

Web spider analyzes the user's preferences of the group preference base it belongs to, on the basis of which, it searches the web pages that fit the group preferences, and puts the searched web pages into the local information database.

Web Spider is a program that can capture webpage from the web. Given a URL set, spider utilizes the links between HTML documents, according to the depth first or width first strategy to "climb" from one webpage to another. In order to avoid the spider sinking into deep search chain or endless loop so as to be far away from the search target, generally we need to designate the width and depth of the search in advance.

3 Simulation

3.1 Experiment Method

The simulation experiments are executed to investigate the recall ration and the precision ration of the Multi-Agent Information Retrieval System based on Ontology. We use Java as programming language and adopt Eclipse integrated development environment by using open source framework "Jena" to analyze and operate the ontology files.

In order to evaluate the performance of our proposed System, we use Each-movie database containing the evaluation of 1628 movies by 72916 users in 18 months.

We calculate 20 users' retrieval results by means of the traditional information retrieval system and our proposed system respectively with each retrieval system for 5 times.

3.2 Experimental Results

The results were analyzed by general appraising method which has two indications: recall ration and precision ration. The simulation results exhibit that, for the same number of documents and queries, different threshold S will lead to different results, shown as fig.5 and fig.6 respectively.

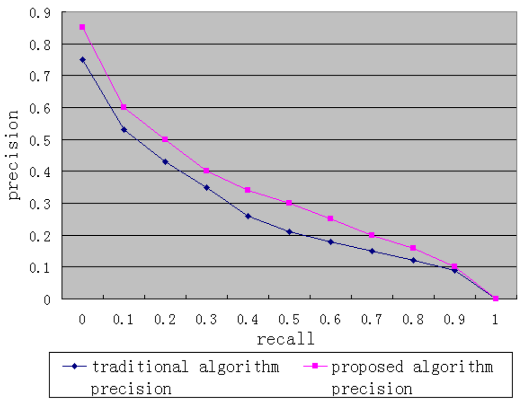

Fig. 5. Averaged 11-point precision/recall graph with S of 0.5

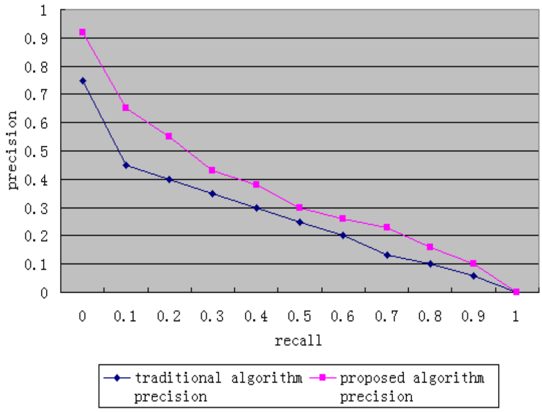

Fig. 6. Averaged 11-point precision/recall graph with S of 0.6

4 Conclusion

This paper proposed a Multi-Agent Information Retrieval System by combining the ontology, multi-agent technology and improved collaborative information filtering technology. The structural model of the system has been introduced and the solution has been suggested to provide personalized retrieval information according to users' interest or preference.

Through making use of ontology, the information retrieval system can realize expressing the information need and the relationship between the concepts of different domains with the assistance of the formalized terms, so as to provide users with increment of information service. Through multi-agent, it is easier to cooperate and interact with each other to accomplish some complex tasks or targets. Each agent has its own function.

The simulation results reveal that for the appropriate threshold S, the proposed system can achieve better result than traditional ones.

References

1. Guarino, N., Masolo, C., Vetere, G.: OntoSeek: Content-Based Access to the Web. IEEE Intelligent Systems 14(3), 70–80 (1999)
2. Haveliwala, T.H.: Topic-Sensitive PageRank: A Context-Sensitive Ranking Algorithm for Web Search. IEEE Transactions on Knowledge and Data Engineering 15(4), 784–796 (2003)
3. Spink, A., Jansen, B.J.: A study of results overlap and uniqueness among major Web search engines. In: Information Processing and Management, pp. 1379–1391 (2006)
4. Kechid, S., Tamine-Lechani, L., Boughanem, M., Drias, H.: Personalizing Information Retrieval in a Distributed Environment. International Review on Computers and Software (IRECO.S.) 2(3), 98–107 (2007)

Task Allocation for Spatially and Temporally Distributed Tasks

Julio Godoy and Maria Gini

Department of Computer Science and Engineering, University of Minnesota,
200 Union St SE, Minneapolis, MN 55455, USA
godoy@cs.umn.edu,gini@cs.umn.edu

Abstract. In multi robot task allocation, a set of tasks has to be allocated to a group of robots while optimizing some measure (for example, fuel or time). In order to find the optimal allocation, an exponential number of possibilities must be explored. In this work, we extend the Consensus Based Bundle Algorithm, to improve its support for tasks with time constraints. The modified algorithm is compared with the original one in order to show how strategic modifications to the algorithm increase the number of tasks successfully completed.

1 Description of Problem

Multi robot task allocation addresses the problem of matching tasks to robots in a way that satisfies a certain criterion or optimization function. The criterion is usually to minimize the distance traveled, or to minimize the time to complete all the tasks, or maximize the number of completed tasks. Real problems often have additional constraints. For example, in a post-disaster scenario, tasks location and their magnitude may be initially unknown, so robots should first explore the environment and dynamically allocate tasks as they find them. Also, the amount of time to reach tasks might be limited, after which some of them may no longer be available (for example, a wounded civilian may have died), or may be too complex to complete (for example, a fire may be too big to put off). There might be obstacles in the predicted path to a task, and some tasks may need a minimum number of robots allocated in order to be completed.

We build upon a decentralized auction algorithm, the Consensus Based Bundle Algorithm [1], and modify it in order to incorporate stronger temporal constraints. This is useful for scenarios where, for example, the lives of wounded civilians depend on how fast ambulances can reach them.

2 Related Work

The area of multi robot task allocation has seen many contributions over the last decade. In this work, we focus on allocation methods based on auctions. A comparison of auction-based methods and token-based approaches [11] shows that auctions produce higher rewards but require more communications. However, Kalra et al. [4] compared both approaches and concluded that, when the task information is accurate, auction based methods achieve better performance.

S. Lee et al. (Eds.): Intelligent Autonomous Systems 12, AISC 194, pp. 603–612.
springerlink.com

When using auctions to allocate tasks, agents submit bids for the desired tasks. The amount of each bid is the value of the task for the agent, or is related to an objective metric, such as the distance. The auctioneer selects the agent which submitted the best bid for each task, and assigns it to that particular agent. Since we assume the agents are cooperative, social welfare increases when the most valuable combination of tasks is assigned to each agent.

Sandholm [9] proposes an algorithm for combinatorial auctions, a method that returns the optimal solution, but of exponential complexity, which makes it unfeasible for use in multi robot domains. Dias et al, [2] first discussed the use of auctions in the context of task allocation in a multi robot system, while Koenig et al. [5] proposed an efficient auction based algorithm which allows robots to account for already assigned tasks in their subsequent bids.

Auctions are distributed methods, but require communication among all the robots. To avoid the complete communication requirement, several approaches use consensus based algorithms [12,1], where each robot determines independently its tasks and an equilibrium is reached by iteratively sharing information with its local neighbors.

When tasks have time constraints, the allocation algorithms have to handle scheduling in addition to cost. In [3] sequential auctions are used for situations where the reward for completing tasks decreases over time. In this case, time windows are not allowed to overlap. Similarly in [6] each task has a specific time window but again with no overlap. Overlapping time windows are not allowed as they would violate the constraint that there is a strict total order of the tasks. Finally, Ponda et al. [7] proposed a modification of the CBBA algorithm that deals with soft time constraints: agents have to arrive to a task before its deadline, without considering the time it takes the agent to complete the task. Ramchurn et al. [8] uses mixed integer programming to solve the problem of finding coalitions to do tasks, considering distance (allocating tasks to closer agents) and time (to allocate tasks with deadlines to agents that can reach them and execute them before the deadline).

In this work we consider tasks that have overlapping time windows and whose duration can be shorter than the time window. In our approach, time windows are considered hard constraints, so each task has to be completed within its time window.

3 Tasks with Time Windows

In many real world scenarios, tasks are not always available. For example, in rescue scenarios, there might be wounded civilians that could perish if not assisted on time. They might also be buried under semi collapsed buildings, that may collapse completely after some time, preventing them from being rescued afterwards. Fires might appear, and they might become un-extinguishable if they grow loo large.

These urgent tasks may appear anytime, or may all appear at the same time. It becomes critical that an agent not only reaches a task, but also that it reaches it in a specific time period, where the task is doable. This time period is called *time window*. Due to these extra constraints, tasks now have time related properties associated with them, specifically:

- *Start time* is the time from when the task can be done, the beginning of its time window. Before this time, the task does not exist.
- *End time* is the last time point an agent can work on the task. It marks the end of the time window of the task. After this time, the task does no longer exist.
- *Duration* is the time it takes an agent to do the task, once it is in the task location. Its length is at most the length of the task's time window.

A task is doable if the agent can reach it no later than $(Endtime - Duration)$, as otherwise it cannot complete it before its end time. For simplicity, we consider only tasks that are done by a single agent, so duration is a fixed number for each task. We also assume that task locations are known, and that there are no obstacles in the paths.

4 Extensions to CBBA

Our work extends the CBBA algorithm [1] and its modification in [7] where each task has an associated time window. We start by summarizing CBBA. The CBBA algorithm follows a two phase design:

Phase 1: Bundle Construction

Each agent assigns a score to each task (based on time or spatial criterion) and one by one selects the task with the maximum score, amongst the unassigned ones. This is repeated until all tasks have been assigned or the maximum bundle size has been reached. This is different from traditional bundle algorithms [9], where all possible bundle combinations are tested.

An agent has two lists of tasks, the bundle itself (b_i) and the path (p_i), which contains the same tasks as the bundle, but in the order they will be visited. Let L_t be the maximum bundle size and $S_i{}^{p_i}$ the total reward agent i receives by doing the tasks on path p_i. Each task is inserted in a position in the agent's path p_i where it maximizes the score improvement. $\oplus_n$ is the operation of inserting the second list after the nth element of the first list, while $\bigoplus_{end}$ appends the second list to the first.

Algorithm 1 [1] summarizes the first phase of CBBA, where y_i is the winning bid list, z_i the winning agent list, and b_i and p_i respectively the bundle and path lists. J is the set of all possible combinations of tasks, of which each bundle is an instance. $\mathbb{I}(.)$ is the indicator function ($= 1$ if argument is true and 0 otherwise),

Phase 2: Conflict Resolution

After each agent has a bundle of pre allocated tasks, the agents communicate with each other, comparing their bids for the tasks in their bundles with other agent's bids for the same tasks. When an agent is outbid by another for a task, not only it has to release that task, but also all others it was planning to visit after that, as the score associated with them is no longer valid. In order to reach consensus, three lists are shared amongst the agents: the winning bids list y_i, the winning agent list z_i and a vector of time stamps of thelast information update from other agents, s_i.

Algorithm 1. CBBA Phase 1 for agent i at iteration t (from [1])

procedure Build Bundle($z_i(t\text{-}1)$,$y_i(t\text{-}1)$, $b_i(t\text{-}1)$)
$y_i(t)$=$y_i(t\text{-}1)$; $z_i(t)$=$z_i(t\text{-}1)$; $b_i(t)$=$b_i(t\text{-}1)$; $p_i(t)$=$p_i(t\text{-}1)$
while $|b_i| < L_t$ **do**
$c_{ij} = \max_{n \le |p_i|} S_i^{p_i \oplus_n \{j\}} - S_i^{p_i}, \forall j \in J / \ b_i$
$h_{ij} = \mathbb{I}\ (c_{ij} > y_{ij}), \forall j \in J$
$J_i = \arg\max_j c_{ij} \cdot h_{ij}$
$n_{i,J_i} = \arg\max_n S_i^{p_i \oplus_n J_i}$
$b_i = b_i \bigoplus_{end} J_i$
$p_i = p_i \bigoplus_{n_i,J_i} J_i$
$y_{i,J_i}(t) = c_{i,J_i}$
$z_{i,J_i}(t) = i$
end while
end procedure

At the time agent i receives a message from another agent k, using the information of lists z_i and s_i, it can take one of three actions [1] on task j:

1. update: $y_i j = y_k j, z_i j = z_k j$
2. reset: $y_i j = 0, z_i j = \emptyset$
3. leave: $y_i j = y_i j, z_i j = z_i j$

For example, an update action is taken when a better bid is found, a reset action is performed when both agents i and k believe that each other is the winner of task j and, in case both agents agree on the winner, no action is performed. An interesting feature of this phase is that the agents don't need to communicate directly with each other to reach consensus, but only to form a connected graph. This puts less constraints on the communication, and makes the algorithm suitable for environment conditions where communication is restricted. Detailed cases and the respective actions can be found in [1].

4.1 Maximizing the Number of Completed Tasks

In the implementation of CBBA the task start and end times, agents, and tasks positions are randomly generated. The task duration is equal to the length of its time window. The implementation leaves room for improvement. First, it doesn't consider the ending time of tasks in the score function that assigns a value for each agent to perform a task. Hence, two tasks with the same starting time but different ending time (one more urgent than the other), are considered equal in terms of value for the agent. Second, a task is considered completed even if the task duration exceeds its ending time.

We modified the score function and evaluation mechanism to maximize the number of completed tasks, creating a variant of CBBA that we call MOD, and compared the results to the normal CBBA implementation. We consider an agent able to complete a task only if it can reach the task in a time that allows for its total completion (the duration of the task) before its time window ends.

Specifically, we consider both starting and ending times of tasks when computing the scores. Also, we added a sub algorithm to CBBA in order to test the feasibility of adding a task in the time before other already assigned tasks. This situation may arise when, after allocating the most valuable tasks, the algorithm finds that it can add another task (which previously was not very valuable), but because of time constraints, the new task has to be done before other tasks already allocated. This may create a situation where a previously assigned task is no longer doable in its time window, or needs to be shifted inside its time window.

We implemented a two way check to ensure that when a task is inserted before another, no time constraint is violated. The first check is via a value called *MinAlloTime*, which keeps track of the task with the smallest difference between the ending time and the current completion time in the temporal allocation. This way, if the new task has a duration longer than *MinAlloTime*, it is discarded and the insertion is aborted. The second check is via a procedure shown in Algorithm 2, in which the time added for inserting a new task m in position j is compared with the time constraints of all tasks that would be done after it in the agent bundle. If the arrival time of the agent to task $j+1$ after doing m is altered, then a check is done to ensure that task in position $j+1$ can still be done before the end of its time window. If not, the insertion is not feasible in position j and the next position $j+1$ is checked. Otherwise, the task is inserted in position j and the starting time for task in position $j+1$ is updated (i.e. the task is shifted) to reflect this insertion. In this case, all consecutive tasks must also be checked in case they also need to be shifted inside their time windows.

In Algorithm 2, a task is added before others if (1) the agent has empty slots in its bundle, (2) the task is the most valuable amongst the remaining ones; and (3) tasks already allocated can still be done in their respective time windows.

The difference is noticeable in the simple examples in Figure 1 and Figure 2. CBBA doesn't allocate task 2 to the agent (there is a single agent in this example), even though there is enough time to complete it. Due to the way the score function is designed, the agent just performs task 1 and 3.

Algorithm 2. Feasibility determination for agent i to do task m in position j of path p_i

$AddedT = start_m + duration_m + TravelT(m, Task_{j+1})$
if $AddedT < start_{Task_{j+1}}$ **then**
  return False
else
  if $AddedT > start_{Task_{j+1}}$ **then**
    if $AddedT + duration_{Task_{j+1}} < end_{Task_{j+1}}$ **then**
      $start_{Task_{j+1}} = AddedT$
      return True /* Task m feasible at position j */
    else
      return False /* Task m unfeasible at position j */
    end if
  end if
end if

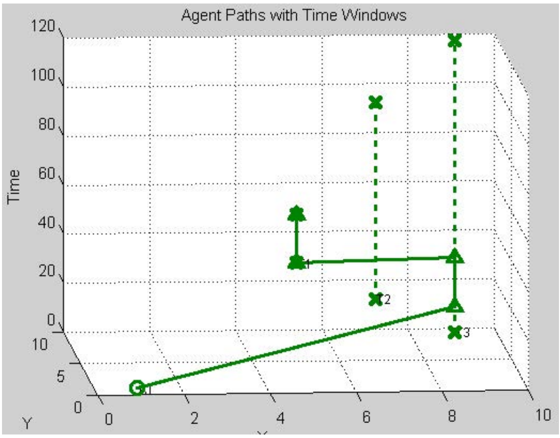

Fig. 1. Solution produced by CBBA

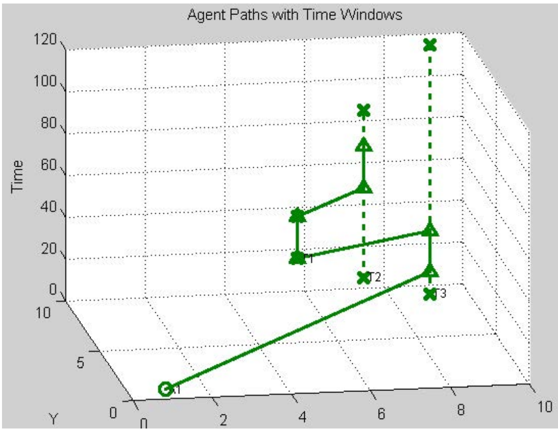

Fig. 2. Solution produced by MOD

5 Experimental Results

To test the impact of our modifications on the number of completed tasks, we tested MOD against the original CBBA in different settings, where the number of agents and tasks varied, as so did the tasks duration, length, start and ending time of their time windows. Finally, we also varied the size of the grid where the agents and tasks were placed. Because the grid is not made of discrete cells but of continuous X,Y coordinates, the increase of the size is the same as having the same grid but with the agents moving slower or faster.

The experiments considered using from two to ten agents, and from 10 to 100 tasks in different combinations, in order to evaluate specific scenarios. Each experimental setting was run 30 times, the resulting values are an average over the total set of results. The statistical significance of each experiment was tested with $p \leq 0.05$.

To start, we compare the number of tasks completed out of 10 in a scenario with two agents, with different task duration times. Table 1 summarizes the results.

Table 1. Two agents and 10 tasks with different task durations (TD)

Total number of tasks	TD=5	TD=10	TD=20	TD=40
CBBA	9.3333	8.3333	6.5333	4.3667
MOD	9.7333	9.3333	8.1667	5.7667

The differences in the results in Table 1 are statistically significant, except when task duration is 5. As task duration increases, the proportional difference in the average number of completed tasks between CBBA and MOD increases, favorably to MOD. At the same time, the average number of completed tasks decreases for all approaches, due to the higher chance of having short overlapping time windows.

The next experiment involves three agents and 50 tasks. Table 2 shows average number of tasks completed, total time to completion and total distance traveled by the agents. The values in Table 2 reflect the number of completed tasks. The approaches that complete more tasks also have a higher average path cost and larger average time needed to complete the tasks.

Table 3 shows the results for a larger scenario. This is useful to analyze the scalability of the proposed approach to longer distances. 10 agents are placed in a grid 10 times larger than the one used in previous experiments, with 100 tasks. In this case, MOD completes in average 50% more tasks than CBBA.

In order to analyze how both approaches perform under specific time window configurations, we include two additional scenarios: (a) the task duration is equal to its time window, and (b) the time window is four times the length of the task duration. For the first scenario, the difference between the two approaches is not statistically significant, mainly because the agents have fewer chances to vist the tasks, due to their constrained time windows.

Table 4 shows the number of completed tasks for scenario (b). In this case, because the agents have more room to decide when to complete a certain task, the modifications to CBBA improve performance.

Table 5 shows the number of completed tasks for different agent-task configurations that have the same early start time, emulating a real-world scenario where a disaster occurs and suddenly many tasks appear that differ in both time duration and end time. It can be seen that MOD performs much better than the original CBBA, due to the change in the constraints and the task shifting in order to maximize the completion rate. In both cases, low values indicate overlapping time windows.

Table 2. Three agents and 50 tasks, using multiple metrics with different task durations (TD)

Total number of tasks	TD=5	TD=10	TD=20	TD=40
CBBA	31.5333	21.5	13.3667	7.8667
MOD	30.3	24.3	16.6	10.3667

Total time	TD=5	TD=10	TD=20	TD=40
CBBA	114.8018	123.7246	136.1574	156.6719
MOD	153.0252	169.5668	186.7175	206.6135

Total distance	TD=5	TD=10	TD=20	TD=40
CBBA	95.4677	59.5234	33.5156	14.2594
MOD	86.693	63.1454	42.0853	23.3113

Table 3. Ten agents and 100 tasks, in a scenario ten times larger than the scenario used for the other experuments

Total number of tasks	TD=5	TD=10	TD=20	TD=40
CBBA	39.0333	32.8	25.4	18.5667
MOD	52.3667	48.1	38.0333	27.5667

Table 4. Three agents and 20 tasks, with time windows four times the task duration (TD)

Total number of tasks	TD=5	TD=10	TD=20	TD=40
CBBA	18.4	16.2	11.5333	7.1667
MOD	15.6667	16.6667	15.2667	12.9333

Table 5. Number of tasks completed when all tasks have the same start time

Total number of tasks	2A10T	3A20T	3A50T	10A100T
CBBA	2.8667	4.333	4.8	12.9333
MOD	6.2333	11.0714	17	31.5

Finally, the number of iterations of the algorithm before reaching consensus was also tested, in experiments performed with different numbers of agents and tasks. The total number of iterations required by MOD is just 35% of the ones required by CBBA.

The modifications made to CBBA increase the number of completed tasks. Although with small tasks duration times the performance is in many cases similar to CBBA, as this time increases the enhancements start to show off, enhancing performance differences (in terms of number of completed tasks) that are most visible in the case where all tasks have the same start time. Increasing the number of completed tasks is not trivial, as it requires to find a tradeoff between space and time, and a detailed analysis of how each of these dimensions affects the possibility of completing more tasks is something that goes beyond the scope of this paper.

Another interesting improvement is in the number of iterations required to reach convergence, which is less than half as normal CBBA. This implies that by using MOD, the algorithm is less vulnerable to communication errors, and hence it is more adequate for use in communication constrained environments.

6 Conclusions and Future Work

We presented our modifications to CBBA in order to improve its performance with tasks that have time windows. We have presented how the tradeoff between space, time, and communication affects the number of tasks completed. Some results matched our initial intuition while others showed us some interesting and unforeseen correlations, that give light to future enhancements. The number of tasks completed increases to different degrees depending on the specific setting. The number of communication rounds required to reach consensus is also greatly reduced, opening new possible applications to the algorithm.

As future work, we will perform a theoretical analysis of our approach and aim at improving specific performance metrics while, at the same time, keeping an appropriate overall performance balance. For instance, we will consider adding levels of criticality to the tasks, so when not all the tasks can be done, the agents could work on the most critical tasks first. Another line of future research is related to inter-task constraints, similar to the approach developed in [10]. Specifically, we will analyze how precedence constraints between tasks and their decomposition affects performance and convergence time of the multi-robot system.

References

1. Choi, H.L., Brunet, L., How, J.P.: Consensus-based decentralized auctions for robust task allocation. IEEE Trans. on Robotics 25, 912–926 (2009), http://dl.acm.org/citation.cfm?id=1653147.1653161, doi:10.1109/TRO.2009.2022423
2. Dias, M.: Traderbots: A new paradigm for robust and efficient multirobot coordination in dynamic environments. Ph.D. thesis, Carnegie Mellon, Pittsburgh, Pennsylvania (2004)
3. Ekici, A., Keskinocak, P., Koenig, S.: Multi-robot routing with linear decreasing rewards over time. In: Proc. Int'l Conf. on Robotics and Automation, pp. 3944–3949 (2009), http://dl.acm.org/citation.cfm?id=1703775.1704082
4. Kalra, N., Martinoli, A.: Comparative study of market-based and threshold-based task allocation. In: Gini, M., Voyles, R. (eds.) Distributed Autonomous Robotic Systems 7, pp. 91–101. Springer, Japan (2006)

5. Koenig, S., Tovey, C., Lagoudakis, M., Markakis, V., Kempe, D., Keskinocak, P., Kleywegt, A., Meyerson, A., Jain, S.: The power of sequential single-item auctions for agent coordination. In: American Association of Artificial Intelligence, pp. 1625–1629 (2006), http://dl.acm.org/citation.cfm?id=1597348.1597457
6. Melvin, J., Keskinocak, P., Koenig, S., Tovey, C.A., Ozkaya, B.Y.: Multi-robot routing with rewards and disjoint time windows. In: Proc. IEEE/RSJ Int. Conf. on Intelligent Robots and Systems, pp. 2332–2337 (2007)
7. Ponda, S.J., Redding, J., Choi, H.L., How, J.P., Vavrina, M.A., Vian, J.: Decentralized planning for complex missions with dynamic communication constraints. In: American Control Conference (2010)
8. Ramchurn, S.D., Polukarov, M., Farinelli, A., Truong, C., Jennings, N.R.: Coalition formation with spatial and temporal constraints. In: Int'l Conf. on Autonomous Agents and Multi-Agent Systems, pp. 1181–1188 (2010)
9. Sandholm, T.: Algorithm for optimal winner determination in combinatorial auctions. Artif. Intell. 135, 1–54 (2002), doi:10.1016/S0004-3702(01)00159-X
10. Whitten, A.K., Choi, H.L., Johnson, L.B., How, J.P.: Decentralized Task Allocation with Coupled Constraints in Complex Missions, pp. 1642–1649. IEEE (2011)
11. Xu, Y., Scerri, P., Sycara, K., Lewis, M.: Comparing market and token-based coordination. In: Int'l Conf. on Autonomous Agents and Multi-Agent Systems, pp. 1113–1115. ACM, New York (2006)
12. Zavlanos, M.M., Spesivtsev, L., Pappas, G.J.: A distributed auction algorithm for the assignment problem. In: Proc. 47th IEEE Conference on Decision and Control, pp. 1212–1217 (2008)

Learning Task Performance in Market-Based Task Allocation

Charles E. Pippin[1] and Henrik Christensen[2]

[1] Georgia Tech Research Institute,
Georgia Institute of Technology, Atlanta, Georgia 30332
pippin@gatech.edu
[2] Center for Robotics and Intelligent Machines,
Georgia Institute of Technology, Atlanta, Georgia 30332
hic@gatech.edu

Abstract. Auction based algorithms offer effective methods for de-centralized task assignment in multi-agent teams. Typically there is an implicit assumption that agents can be trusted to effectively perform assigned tasks. However, reliable performance of team members may not always be a valid assumption. An approach to learning team member performance is presented, which enables more efficient task assignment. A policy gradient reinforcement learning algorithm is used to learn a cost factor that can be applied individually to auction bids. Experimental results demonstrate that agents that model team member performance using this approach can more efficiently distribute tasks in multi-agent auctions.

1 Introduction

The area of multi-agent systems has been an active area of research for many years, due in no small part to the ability for a team of robots to operate more efficiently and be more robust to failure than a single robot. However, there are still many challenges related to the interaction between the robots themselves. In traditional multi-agent systems approaches, each team member explicitly operates as part of a team and has the team's goals either explicitly or implicitly encoded. However, future robotic teams may have different internal goals as well as performance capabilities, costs, and owners. As such, robots may need to learn which team members reliably estimate and perform tasks as part of a team.

This work describes approaches for learning task performance of team members as applied to the multi-agent auction domain. A reinforcement learning algorithm is used to learn a cost factor for adjusting each agent's bids, based on the observed performance of that agent in completing tasks as estimated.

Market-based auction methods are a class of decentralized algorithms that solve the multi-robot task allocation problem by splitting computation across multiple nodes and iteratively performing task assignments [1]. The basic auction approaches to the task allocation problem assume that team members can be trusted and have the goal of the team in mind (to reduce the overall cost) [2]. These algorithms serve as a mechanism for distributed task allocation and generally do not explicitly consider each individual team member's performance characteristics. However, there are situations in which

S. Lee et al. (Eds.): Intelligent Autonomous Systems 12, AISC 194, pp. 613–621.
springerlink.com

teams may be formed dynamically, and the individual players within the team may have varying levels of performance and task estimation accuracy. In order for tasks to be allocated efficiently, it is important to be able to reliably trust that robots will perform their assigned tasks with costs that closely approximate their estimated costs. If a robot regularly exceeds its estimated cost for performing a task, the auction algorithm should be able to adjust the estimate to reflect the robot's true expected performance.

This paper will present an approach for learning which team members perform tasks at costs that accurately reflect the estimated costs. This approach can be used to more effectively perform auction based task allocation by using a reinforcement learning algorithm to adjust a cost factor that is applied to each team member's bid estimates.

The rest of this paper is organized as follows. In Section 2, we present the background and related work for learning in multi-agent auctions. In Section 3, we discuss the use of the reinforcement learning algorithm within an auction framework. In Section 4, we present results of simulated experiments using this approach. Finally, in Section 5, we conclude and present future work.

2 Related Work

The ability to determine when a robot is not performing or functioning as expected can be used to re-assign tasks or call attention to an operator. An analysis of approaches to robot performance based metrics are presented by Parker in [3].

Pippin and Christensen considered allocating tasks to robots with different sensors characteristics in [4]. Given the probabilities of detection for each sensor, the expected utility is calculated and applied to each agent's cost bid. In that work, the sensor performance characteristics were known in advance.

An example of learning opportunity costs in auctions was performed in simulation of Martian rovers [5]. The appropriate opportunity costs allow for the specialized robots to avoid becoming underutilized. Over multiple simulations, the different types of robots adjusted their opportunity costs such that neither was underutilized.

Agents learned what valuation to bid by direct observations of similar other agents in [6]. The approach in that work is for the agent to learn to adapt its valuation (and the resulting bid) to market conditions in a simulated, electronic market, using a reinforcement learning algorithm. The market domain was inspired by real world electronic commerce applications in which physical resources, such as trucks, and workers, competed to win tasks. The related problem of learning whether an agent should submit a bid is useful in domains in which computing a bid can be expensive because communication and computation costs can be considerable [7].

Jones, Dias and Stentz investigated techniques for learning proper task cost estimates in oversubscribed domains, using auction algorithms [8]. In that work, each robot attempted to learn its own bid estimates, and had full knowledge of its own state vectors, including its own schedule. In this paper, we are interested in learning whether bids accurately match the estimated values, but from the viewpoint of the auctioneer. The auctioneer has less visibility into the state features that can be used to estimate a bid and relies on the estimated vs. actual cost to apply a cost adjustment to future bids.

This paper uses a learning approach that is very similar to that used in Kohl and Stone for learning fast gaits on quadrupedal robots [9]. They applied a policy gradient reinforcement learning algorithm to learn control parameters for leg motions. The policy gradient algorithm was also applied by Mitsunaga, et al. to adapt robot behaviors to human partners [10]. This paper will apply the policy gradient learner to the task of learning a cost factor for other robots' cost estimates in market-based auction algorithms.

3 Approach

Robots may fail to perform tasks according to their initial estimate for a number of reasons. For instance, in complex domains, the cost function may be expensive to calculate and the task estimate might be based on a heuristic function. Perhaps, over time a robot's performance might have degraded due to hardware failure or wear. Finally, the robot's internal state may not reflect the true state of the robot, causing errors in estimation.

For this paper, we will assume that a subset of the team members regularly misestimate task costs by an unknown factor, due to errors in the robot's internal state model. Therefore, the task is to learn the true cost factor for those robots. A learning algorithm will be used to approximate the cost factor and apply it to the task assignment function used by a market based auction algorithm.

3.1 Auction Approach

In the basic multi-agent auction algorithm, the problem is to assign tasks to agents. The tasks in this case are to visit a target location and perform an observation. In the auction framework, each robot is a *bidder* and the items to be auctioned are the tasks. Each of the agents in the system also participates as an *auctioneer* and periodically auctions new task requests (it is assumed that the task requests are periodically provided to the agent by an external process, such as a human operator or other event). This approach can easily be used on teams with different robot characteristics: each robot knows their own location and cost function and submits cost based bids to the auctioneer. While costs and rewards use the same basis for calculation, no revenue is actually exchanged. Rather, an agent awards itself a utility value when one of its own tasks is completed.

In this work, the agents each maintain a current task list and locally compute their bid to complete the proposed task. The bid consists of the time-based cost to perform the task. A potential source of error in task estimation is in the use of an insertion heuristic for calculating the marginal cost to perform a task, in addition to those tasks already assigned. In this paper, each robot plans to visit the targets in the order in which they were assigned (using the $O1$ assignment rule from [11]). For each auction announcement received, each robot calculates its bid as the amount of time required to complete the task in addition to those on the current task list. When the winning *bidder* is assigned a new task, the task is appended to the robot's assigned task list.

3.2 Learning the Cost Factor

The learning method used in this work is the *policy gradient reinforcement learning* (PGRL) algorithm. This is a reinforcement learning method that is used to estimate the policy gradient when the true value function is not known. The PGRL algorithm is presented in detail by Baxter and Bartlett in [12], and it is shown that this approach converges towards a local optimum.

3.2.1 The PGRL Algorithm

The pseudocode for the PGRL algorithm, adapted from [9] and [10], is shown in Figure 1. At the beginning of the algorithm, the policy vector, Θ, is initialized. In this paper, we are using the algorithm to learn a single parameter, θ, which is the cost factor to apply to a robot's task estimation. Therefore, we initialize $\theta = 1$, reflecting the belief that each robot perfectly estimates tasks that they will perform. In the main loop, the algorithm generates a set of random permutations for the policy by adding either $+\varepsilon$, 0 or $-\varepsilon$ to the policy.

Next, each of these permutations is evaluated by the system and the resulting reward is received. Averages of the rewards are maintained for the permutations of each type. After all of the permutations have been evaluated, the gradient is approximated by calculating the adjustment, a_j, related to each parameter in the policy. Each parameter's step distance, ε_j, and the global step distance, η, are applied to a_j and the values are normalized. Finally, the policy is updated with the adjustment.

An example of learning a cost factor, θ, using the PGRL algorithm is shown in Figure 4(a). In this example, the unknown cost factor is 2, and θ is initialized to 1. After about 100 evaluations, the learned policy begins to converge near the true value.

3.2.2 Learning in Auctions

The PGRL is applied to multi-robot auctions by applying the learned cost factor to each robot's bid, as shown in Figure 2. Each auctioneer maintains a PGRL learner for each known team member. After auctioning a task, the auctioneer will receive a set of bids from team members, where each bid represents the time-based cost for the bidder to complete that task. The auctioneer then queries the learner to get the cost factor, θ, related to that agent. This cost factor is multiplied by the original bid in line 3 to get an updated estimate for the agent to perform the task. The resulting bid in the set with the minimum cost is then awarded the task.

When a task is completed by an agent, the auctioneer that assigned the task is sent a message with the completed task information. The auctioneer can then compare the updated estimated cost for the task with the actual cost for completion, as shown in Figure 3. The ratio of these costs is used to determine the reward signal used by the reinforcement learner. The PGRL reward function, shown in Figure 4(b), calculates the scalar reward signal from this value. The reward is used by the PGRL algorithm, as described above, to calculate adjustments to the cost factor.

4 Experimental Results

4.1 Experimental Setup

A set of experiments were performed in simulation to test the cost factor learning approach in a multi-agent auction environment. In these experiments, each robot has 50

```
Θ ← initial policy vector of size N
while NOT done do
    Θ^T ← t random permutations of Θ
    for t = 1 → T do
        Run system using parameter set Θ^t
        Evaluate reward
    end for
    for n = 1 → N do
        Avg_{+ε,n} ← average reward for all Θ^t that have a positive perturbation in dimension n.
        Avg_{0,n} ← average reward for all Θ^t that have zero perturbation in dimension n.
        Avg_{−ε,n} ← average reward for all Θ^t that have a negative perturbation in dimension n.
        if (Avg_{0,n} > Avg_{+ε,n} AND Avg_{0,n} > Avg_{−ε,n}) then
            a_j ← 0
        else
            a_j ← (Avg_{+ε,n} − Avg_{−ε,n})
        end if
    end for
    A ← A/|A| ∗ η
    a_j ← a_j ∗ ε_j, ∀j
    Θ ← Θ + A
end while
```

Fig. 1. The Policy gradient reinforcement learning algorithm pseudocode, with N policy parameters. During each iteration, t random policies are sampled near the current policy for evaluation. The resulting reward from each sample is used to estimate the gradient and move by a small amount in the correct direction.

Input: The set of posted bids, B.
Input: The set of bidders, A.

```
for all a : A do
    θ ← GetTheta(Learner_a)
    B*_a ← θ ∗ B_a
    EstCost_{B_a} ← Cost_{B*_a}
end for
winner ← Min(B*_a)
AnnounceWinner(winner, a)
```

Fig. 2. HandleBids() pseudocode. The policy gradient reinforcement learning method learns the cost parameter, θ, for each team member. This cost factor is applied to future bids for that agent.

```
ActualCost ← (CompleteTime − StartTime)
CostFactor_task ← ActualCost / EstCost_{B_a}
UpdateRL(Learner_a, CostFactor_task)
```

Fig. 3. TaskComplete() pseudocode. The estimated vs. actual task completion time is used to evaluate the value of θ in the reinforcement learning algorithm.

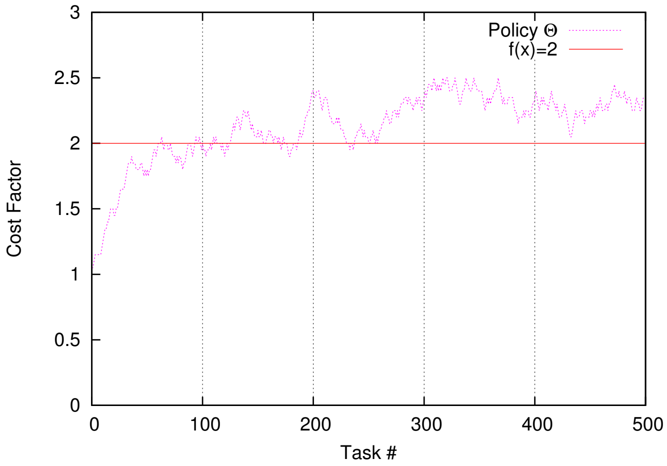

(a) Learning the Cost Factor

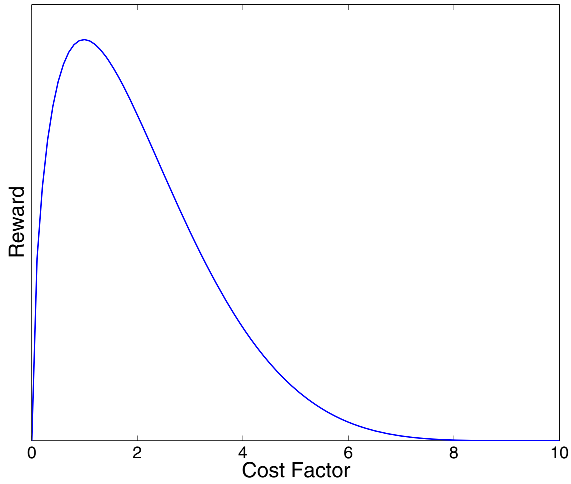

(b) Cost Factor Reward Function

Fig. 4. The PGRL approach to learning the cost factor: (a) The policy gradient reinforcement learning method learns the cost parameter, θ. In this example, the agent's unknown true cost factor is 2. (b) The reward function used by the PGRL algorithm converts an observed cost factor to a reward value.

tasks that arrive at regular intervals and are sequentially auctioned by that robot's auctioneer. As part of the auction process, they also bid on their own tasks. The robots in the simulation have a limited communications range and can therefore only perform auctions with a subset of the other team members at a given time.

Rewards are given for task completion to the robot that originated the task. Each robot submits bids that represent the time-based cost for completing a task. Specifically, the bid represents the number of time steps until the task could be completed. Once a robot finishes all tasks in its list, it no longer accumulates costs in the simulation. The initial locations of the robots and the tasks are randomly chosen for each iteration.

4.1.1 Task Estimation

In this paper, the source for estimation error is assumed to be due to poor performing robot having an incorrect model of its own performance capabilities. To simulate robots that bid poorly, a percentage of robots on the team are modeled as *poor performers* by randomly assigning a cost factor at the start of the experiment, using a normal distribution with $\mu = 2$ or $\mu = 3$ and $\sigma = 0.1$. When a *poor performer* bids on a task, the unknown cost factor is drawn from this distribution and is applied to the robot's task performance to simulate error in estimation and execution.

4.1.2 Learning and Applying the Policy

During the learning phase, 1000 auctions were performed with the PGRL algorithm running with a varying number of poor performers on the team in order to learn the cost factors. These experiments used a centralized learner to share the results across each agent's auctioneer.

After the cost factors were learned, they were loaded and a set of experiments were performed to perform auctions using the learned cost factor as the PGRL initial policy. The algorithm continued to learn online, but the step distance, ε_j was reduced to minimize exploration. This *policy learner* method is compared against a *naive* auction method which does not consider performance; a *known state* method that has access to the true cost factor for each team member; and a *no cooperation* method in which each team member performs all of its tasks without the benefits of cooperation. For each experiment, the average global score represents the score (*average task reward / average cost*) for the team. For each set of experiments, results were averaged over 100 runs.

4.2 Results and Discussion

The results of these experiments are shown in Figure 5. The average global score using each strategy is plotted against teams with 2, 3 and 4 *poor performers* on a team of 6 robots. The error bars represent 1 standard deviation.

The *known state* strategy represents the best score on average that a team could achieve given the number of *poor performers* on the team. This strategy has access to an oracle with knowledge of each team member's hidden state and can calculate the true cost factor to apply to each bid. The scores for the *policy learner* strategy approach the scores of the *known state* strategy. The *policy learner* also scores better than the *naive* strategy which only uses a basic auction and does not consider bid estimation accuracy of each team member. Finally, the *no cooperation* strategy scores the worst, demonstrating that it is better to have poor performers on the team than to work on tasks in isolation.

The results indicate that the *policy learner* strategy can result in up to a 10% improvement in team performance than over the basic auction approach alone. Intuitively, we expected that the gap between the *policy learner* and the *naive* approaches would be larger. However, the auction method distributes task effectively as the *poor performers* get behind. That is, as the number of tasks begins to back up for the *poor performers*, the costs to add a task to the end of their schedule increases, and they win fewer auction assignments. This occurs even though their costs are underestimated. We intend to explore additional bidding and task insertion heuristics using this technique in future work. Nevertheless, these experiments demonstrate that the application of a learner to the cost estimates can be more effective than methods that do not consider estimation accuracy.

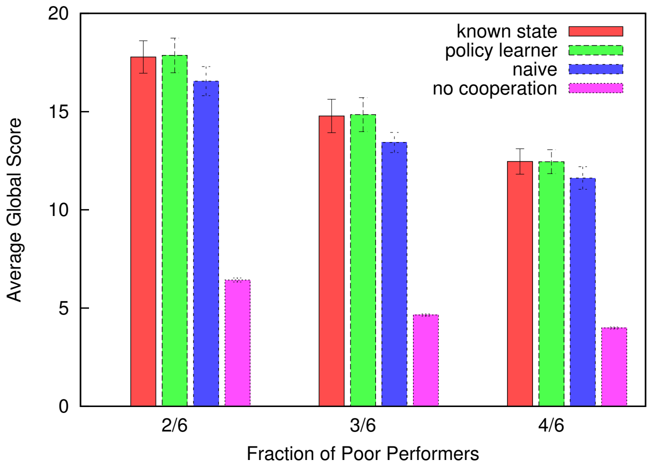

Fig. 5. Task Performance: The learning method is compared with a method that knows the state of each agent in advance, a naive auction method that doesn't consider performance and with the case of no cooperation.

5 Conclusion

This paper presents a reinforcement learning method for recognizing which agents are more likely to submit bids that accurately reflect the true cost for performing tasks. The above experiments showed that a learning mechanism can be effective for detecting poorly-performing team members in auctions, when compared to the naive approach. This may prove useful in situations in which auction based teams are dynamically formed and not all team members are likely to estimate costs correctly. The algorithm learned the cost factor to apply to each team member's bid estimate in a multi-robot auction. The results show that by learning the performance characteristics of individual robots, tasks can be allocated more efficiently.

Future work will consider additional learning mechanisms relevant to task performance. This is related to the problem of determining how to recognize when tasks that were assigned to another agent were not only completed according to the initial cost estimate, but completed within stated quality parameters. In addition, we would like to determine how well this method performs with the use of additional bidding and task insertion heuristics. Finally, we hope to validate this approach with a set of experiments using a team of indoor mobile robots.

Acknowledgment. This work was funded internally by the Georgia Tech Research Institute. We wish to thank the anonymous reviewers for their helpful comments.

References

1. Bertsekas, D.P.: The auction algorithm for assignment and other network flow problems: A tutorial. Interfaces 20(4), 133–149 (1990)
2. Koenig, S., Keskinocak, P., Tovey, C.: Progress on agent coordination with cooperative auctions. In: AAAI Conference on Artificial Intelligence (2010)
3. Parker, L.E.: Reliability and fault tolerance in collective robot systems. In: Kernbach, S. (ed.) Handbook on Collective Robotics, Pan Stanford Publishing (2012)
4. Pippin, C., Christensen, H.: A Bayesian formulation for auction-based task allocation in heterogeneous multi-agent teams. In: Proceedings of the SPIE, vol. 8047, p. 804710 (2011)
5. Schneider, J., Apfelbaum, D., Bagnell, D., Simmons, R.: Learning opportunity costs in multi-robot market based planners. In: Proceedings of the IEEE International Conference on Robotics and Automation, ICRA (2005)
6. Oliveira, E., Fonseca, J.M., Manuel, J., Nicholas, F., Jennings, N.R.: Learning to be competitive in the market. In: Proceedings of the AAAI Workshop on Negotiation: Settling Conflicts and Identifying Opportunities (1999)
7. Busquets, D., Simmons, R.: Learning when to auction and when to bid. In: Gini, M., Voyles, R. (eds.) Distributed Autonomous Robotic Systems, vol. 7, pp. 21–30. Springer (2006)
8. Jones, E., Dias, M.B., Stentz, A.T.: Learning-enhanced market-based task allocation for disaster response. In: Intelligent Robots and Systems (IROS) (October 2007)
9. Kohl, N., Stone, P.: Policy gradient reinforcement learning for fast quadrupedal locomotion. In: Proceedings of the IEEE International Conference on Robotics and Automation (May 2004)
10. Mitsunaga, N., Smith, C., Kanda, T., Ishiguro, H., Hagita, N.: Robot behavior adaptation for human-robot interaction based on policy gradient reinforcement learning. In: Intelligent Robots and Systems (IROS), pp. 218–225 (August 2005)
11. Ekici, A., Keskinocak, P., Koenig, S.: Multi-robot routing with linear decreasing rewards over time. In: Proceedings of the 2009 IEEE International Conference on Robotics and Automation, ICRA (2009)
12. Baxter, J., Bartlett, P.L.: Infinite-horizon policy-gradient estimation. Journal of Artificial Intelligence Research (2001)

A Framework for Unknown Environment Manipulator Motion Planning via Model Based Realtime Rehearsal

Dugan Um, Dongseok Ryu, and Sungchul Kang

Mechanical Engineering, Texas A&M University-CC
6300 Ocean Driver, Corpus Christi, TX 78412, USA
Dugan.um@tamucc.edu,
dongseok.ryu@tamucc.edu,
kasch804@gmail.com

Abstract. In this paper, we propose a novel framework for an unknown environment path planning of manipulator type robots. Unknown environment motion planning, by its nature, requires a sensor based planning approach. The problem domain of unknown environment planning is notoriously hard, especially for difficult cases. The framework we propose herein is a sensor based planner composed of a sequence of multiple MBPs (Model Based Planners) in the notion of cognitive planning using realtime rehearsal. That is, by the proposed framework, one can use a combination of model based planners as tactical tools to resolve location specific problems in overall planning endeavor. The enabling technology for the realtime rehearsal is a sensitive skin type sensor introduced in the paper. We describe the developed sensor and demonstrate the feasibility of solving a difficult unknown environment problem using the introduced sensor based planning framework up to 3 DOF linked manipulator.

Keywords: sensor based planning, randomized sampling, unknown environment motion planning, collision avoidance, cognitive planning.

1 Introduction

Unknown environment motion planning is one of the most daunting tasks in path planning study. Sensor based approaches have been the dominant trends in the study of unknown environment planning for decades. When it comes to unknown environment planning, a planner calls for continuous perception and planning, thereby closing the loop between sensation and actuation.

In manipulator planning especially for unknown environments, similar notion is applicable. For instance, In [1], Lee and Choset promoted the GVG concept to HGVG to solve higher order unknown environment planning problems. The main point of study is to introduce a new roadmap (HGVG) construction method by which a systematic roadmap of free configuration spaces can be incrementally constructed using line-of-sight sensor data.

S. Lee et al. (Eds.): Intelligent Autonomous Systems 12, AISC 194, pp. 623–631.
springerlink.com

Another example is introduced in [2], where simultaneous path planning with free space exploration is proposed using a skin type sensor. In their approach, a robot is assumed to be equipped with a sensitive skin.

The roadmap approach proposed by Yu and Gupta [3] solves sensor-based planning problems for articulated robots in unknown environments. They incrementally build a roadmap that represents the connectivity of free C-spaces. The usefulness of a collision sensor attached on the end-effector is demonstrated in their recent work [12].

Sensitive skin [4] proposed by Lumelsky and innovated thereafter by Chung and Um [6] poses itself as a tool to bridge the gap between the model based planning and unknown environment planning domains. It is unique in that it can either report impending collision with any part of the body at any moment or impart a realtime environment mapping capability during the course of planning operations. Endowed with such uniqueness, sensitive skin will result in a SLAM capability for many degrees of freedom robotic manipulators. In terms of unknown environment planning, sensitive skin is unique in that many advanced strategies studied in the model based planning problem domain can be utilized to solve unknown environment planning problems, including problems with local minima.

To that end, we propose a novel framework of sensor based planner constituting the totality with a sequence of model based planners using a sensitive skin type sensory device and a realtime rehearsal based cognitive planning algorithm. In each step of sequences in the framework, one can use a particular model based planer tailored to attack location specific problems perceived by the realtime sensing capability of a skin type sensor. The notion of cognitive sense of planner imparts the decision capability so that the planner can select the best strategy case by case in each local area to expedite the search process as well as to increase the probability of overall convergence (See Figure 1).

Perception objective:

Obtain environmental affordance.

Action objective:

In crowded area, increase traversability.
In less crowded area, increase manipulability and observability.

2 RRT-CABOMBA Planner

The planner we propose to implement the concept in Figure 1 and to maximize the usefulness of the IPA sensitive skin is a RRT variant, namely RRT-CABOMBA planner in which the framework introduced in Figure 1 is realized in full. The planner resembles how a natural aquatic cabomba stretches underwater.

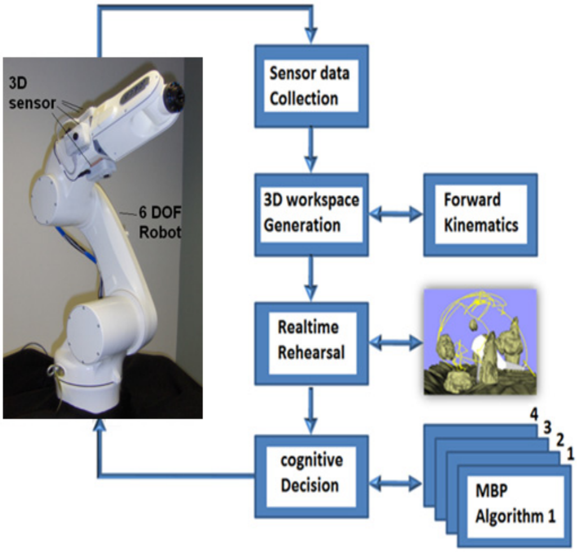

Fig. 1. Concept of the framework of the sensor based path planner

RRT-CABOMBA searches an unknown space based on local probing data via the IPA skin and develops a local map in a virtual workspace. In each local workspace, the RRT-CABOMBA grows a local RRT in matching C-space to examine spatial distribution. Depending on the spatial distribution value, the RRT-CABOMBA will determine which MBP is the most suitable for the sensed local area. Search completeness in local area will be granted as long as each MBP used is a complete planner, but the global search completeness is assured by the space filling completeness of the algorithm.

The RRT-CABOMBA is a planner as manifested in Figure 1 with the following logic.

RRT-CABOMBA

1. Sensor data collection
Sense a local workspace with a skin type sensor.

2. Virtual workspace generation
Generate a local virtual work space with measured 3D depth information.

3. Realtime rehearsal
Grow an RRT in C-space based on local virtual environment established in step 2.

4. Cognitive decision
Measure the spatial distribution of the grown local tree. Determine which MBP is the most suitable for the sensed area.

5. *Advance the robot*

Move the robot to the next position depending on the MBP strategy chosen at step 4.

6. *Convergence check*

Check if the goal position is reached. If not, loop back to step 1.

In step 1, we apply a global algorithm such that the cabomba tree is steered toward the goal position by controlling the sensing direction biased toward the goal position. Steering toward a goal yields faster convergence to the goal at the cost of being entrapped at local minima often. Space filling completeness of the algorithm, however, resolves local minima issue in the overall search endeavor.

In step 2, piecewise information from each sensor is put together to form a complete virtual environment for sensed areas. We utilize *nth* order standard distance distribution as a measure of spatial distribution in step 4. That is,

$$\sigma_N = \sqrt{\frac{1}{N}\sum_{i=1}^{N}(\theta_i - \theta_{mean})^2},$$

where θ_i is the sampled nodes of i_{th} joint and θ_{mean} is the mean value of θ_i. σ_N, if larger than $\sigma_{threshold}$, signals an open c-space, or crowded space otherwise. The value of $\sigma_{threshold}$ is determined empirically. In our case, 0.3 yields reasonable performance (maximum value is 0.5). In step 4, depending on the value of σ_N, the algorithm switches the local strategy. For step 5, in our simulation, we only use following two MBPs for open and crowded cases.

MBP #1 (Open c-space): Move to a node closest to the mean values of sampled nodes

MBP #2 (Crowded c-space): Use Bug algorithm

For *MBP #1*, as mentioned earlier, moving to a mean value of θ_i offers probabilistically best location for next move in terms of maneuverability for each joint, thus may increase reachability as well. The Bug algorithm in *MBP #2* is chosen for reasonable traversability, but can be replaced with variety of other MBP algorithms feasible for specific needs in each local area.

The bug algorithm in MBP #2 proposed originally by Dr. Lumelsky [0] has a unique property of global convergence in 2D and 3D unknown environments. For higher order manipulator path problems, one can utilize algorithms introduced in [8][9][10]. These algorithms deal with difficult cases in higher order path problems.

3 Manipulator Path Planning Simulation

In order to verify the usefulness of the proposed RRT-CABOMBA planner for a 2 DOF manipulator in a unknown environment, a simulation setup has been proposed. Below is the RRT-CABOMBA algorithm with the mechanism to ensure the resolution-completeness of the RRT-CABOMBA.

$i = 1$; $C_1 = q_o$;
$\Lambda_1 = \{C_1\}$; $q_1 = q_o$;
do while $SDD(\Lambda_i) > \delta$
    if ($\min_{l \in R} d(q_\bullet, \Lambda_i) = 0$)
      return /* A path has been found!
      else
      $W_i = S_{free}$ /* Sensed free work space by IPA sensor
      $C_i \leftarrow T_{RRT}$ *grown from* q_i *until node no.>N*
      $\Lambda_i = \Lambda_{i-1} \cup \{C_i\}$
    $i = i + 1$
  endif
  SWITCH $SDD(C_i)$
    Case 1: $q_i \leftarrow mean(C_i)$
    Case 2: $q_i \leftarrow$ *Bug_Algorithm*
    Case 3: $q_i \leftarrow rand\_conf(\Lambda_i)$
  end SWITCH
enddo
return (ε) /* No path!

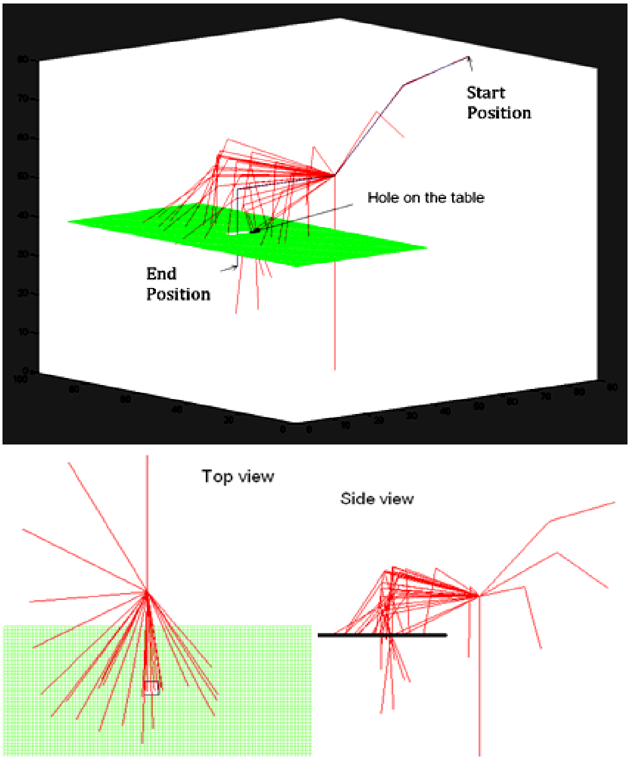

Fig. 2. 3 DOF Manipulator (RRR) planning with RRT-CABOMBA planner

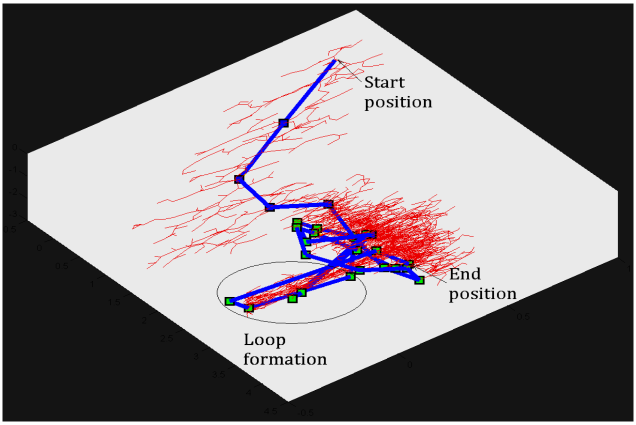

Fig. 3. Corresponding C-space with planning trajectory

One example of a 3DOF manipulator planning by the RRT-CABOMBA algorithm is shown in Figure 2 (work space) and Figure 3 (corresponding c-space). As shown in Figure 4, the proposed planner converges to the goal rapidly within 100sec in average with a dual core, 3 GHz, 3G RAM PC. Compared in the same chart is the original RRT for two performance indices. Notice that the number of collision-free nodes by RRT-CABOMBA is almost five times less than that of original RRT and search period is only a fraction compared to that of the original RRT.

4 Experiments

A series of experiments is carried out to test the performance of the IPA sensitive skin for implementation in the planning framework we proposed. Shown in Figure 5 is the software architecture for simultaneous operation of a 6 DOF manipulator and multiple 3D sensors.

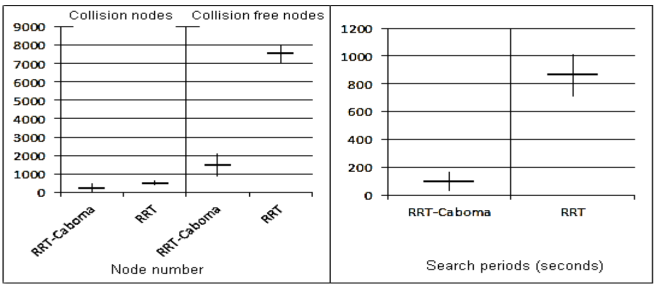

Fig. 4. Performance indices for 3DOF RRT-CABOMBA

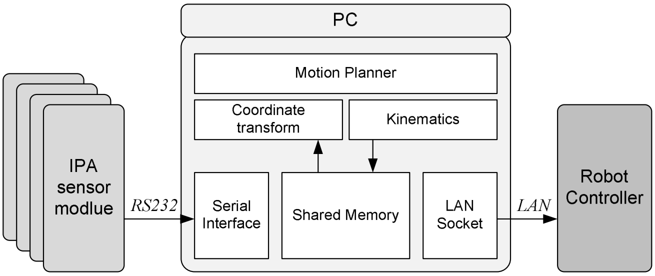

Fig. 5. Software architecture

As shown in Figure 6, four IPA sensitive skin sensors are installed for demonstration. Collision shield by the 3D sensors attached on the manipulator allows Simultaneous Planning and Mapping (SPAM) for unknown environment motion planning in realtime.

In Figure 7, a testbed of the proposed algorithm is in place with Styrofoam based arbitrary shaped obstacles in the robot's workspace. First three joints are used for testing purpose. Since the developed 3D sensor captures 21 frames per second with 30cm of hemispheric sensing range, robot can move up to 10cm/sec safely. Currently, for the given configuration in Figure 7, the robot can move from an arbitrary starting point to another arbitrary point within about a minute range in average if a path exists. As mentioned earlier, the tendency of the robot moving to the open c-space for the best manipulability helps the robot converge faster to the goal position probabilistically. In Figure 7, however, as the robot detects an object that blocks the global path to the destination, it switches its planner to the Bug algorithm to follow the object's surface. Parallelism in planning and mapping in a cloud computing environment is an objective to improve the planning performance.

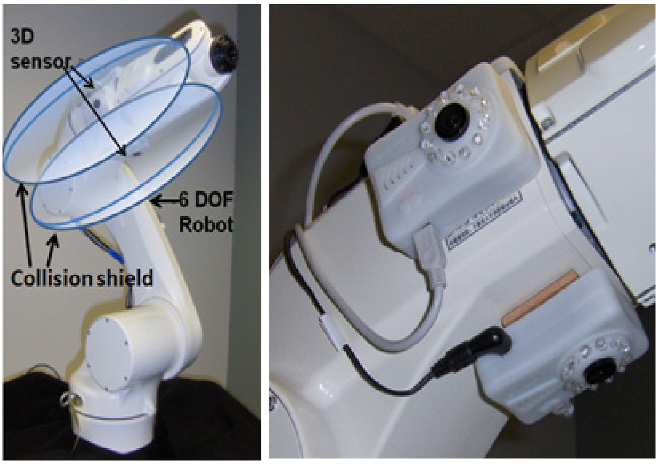

Fig. 6. IPA sensitive skin sensor installation

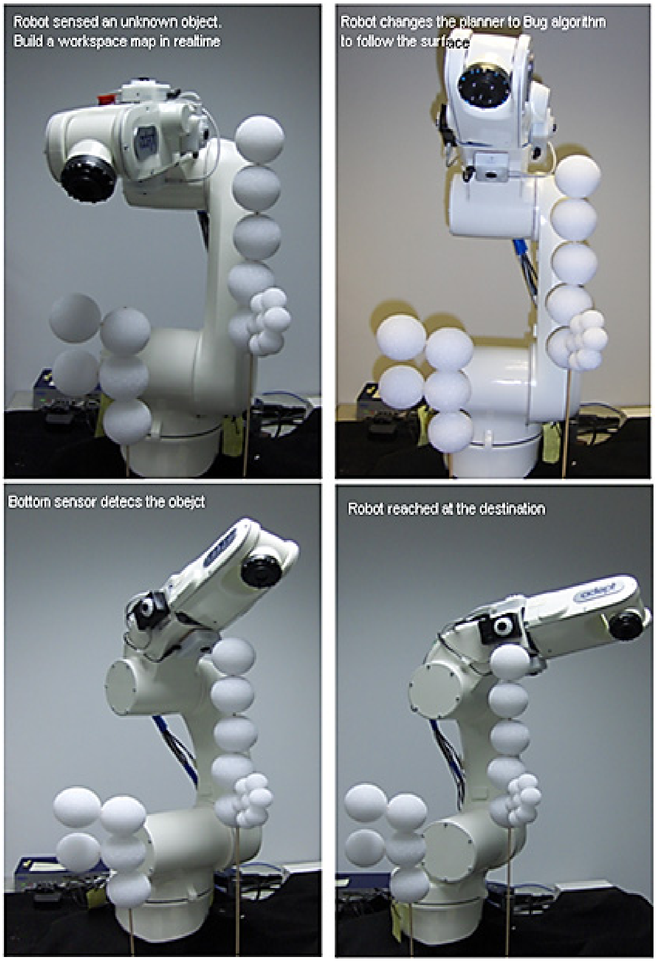

Fig. 7. Motion planning test in an unknown environment

5 Conclusion

A novel manipulator path search framework with a sensitive skin type sensor for a completely unknown environment planning has been investigated. To that end, a novel IPA sensitive skin has been developed and introduced in the paper. The proposed algorithm, RRT-CABOMBA planner, provides a unique solution for difficult unknown environment planning problems by merging sensor based planners and model based planners in cognitive sense.

In RRT-CABOMBA, multiple MBPs can be used to tackle local-area specific planning problems. Cognitive decision making has been studied with realtime rehearsal for each step motion to eclectically select the best possible local strategy in each step. For the feasibility test of the proposed algorithm, a series of simulations has been performed and the results are shared in the paper.

Although the time-lag in realtime workspace mapping is a bottleneck for a real world implementation, for the proof of the usefulness, the concept of realtime distributed execution of the proposed algorithm in cloud computing environment is under investigation.

References

[1] Lee, J.Y., Choset, H.: Sensor-based Planning for a Rod-shaped Robot in Three Dimensions: Piecewise Retracts of R^3 x S^2. International Journal of Robotics Research 24(5), 343–383 (2005)
[2] Mehrandezh, M., Gupta, K.K.: Simultaneous path planning and free space exploration with skin sensor. In: Proc. of the IEEE Int. Conf. on Robotics & Automation, Washington DC, pp. 3838–3843 (May 2002)
[3] Yu, Y., Gupta, K.: Sensor-based probabilistic roadmaps: Experiments with and eye-in-hand system. Journal of Advanced Robotics, 515–536 (2000)
[4] Cheung, E., Lumelsky, V.: A sensitive skin system for motion control of robot arm manipulators. Jour. of Robotics and Autonomous Systems 10, 9–32 (1992)
[5] Kavraki, L., Latombe, J.-C.: Randomized preprocessing of configuration space for fast path planning. In: Proc. Int. Conf. on Robotics & Automation, San Diego, pp. 2138–2145 (May 1994)
[6] Um, D.: Sensor Based Randomized Lattice Diffusion Planner for Unknown Environment Manipulation. In: Proc. Of the IEEE Int. Conf. on Intelligent Robots and Systems, Beijing, China, pp. 5382–5387 (2006)
[7] LaValle, S.M., Kuffner, J.J.: Rapidly-exploring random trees: Progress and prospects. In: Proc. of Workshop on the Algorithmic Foundations of Robotics (2000)
[8] Kurniawati, H., Hsu, D.: Workspace importance sampling for probabilistic roadmap planning. In: Proc. of IEEE/RSJ International Conference on Intelligent Robots and Systems, Sendai, Japan, vol. 2, pp. 1618–1623 (September 2004)
[9] Zheng, S., Hsu, D., Reif, J.H.: Narrow passage sampling for probabilistic roadmap planning. IEEE Transactions on Robotics 21, 1105–1115 (2005)
[10] Lumelsky, V.: Algorithmic and complexity issues of robot motion in an uncertain environment. Journal of Complexity, 146–182 (1987)
[11] Amato, N.M., Wu, Y.: A randomized roadmap method for path and manipulation planning. In: IEEE Int. Conf. on Robotics & Automation, pp. 113–120 (1996)
[12] Torabi, L., Gupta, K.: Integrated View and Path Planning for an Autonomous six-DOF Eye-in-hand Object Modeling System. In: IEEE Int. Conf. on Intelligent Robots and Systems, Taiwan (October 2010)

Embedded Joint Torque Sensor with Reduced Torque Ripple of Harmonic Drive

In-Moon Kim, Hwi-Su Kim, and Jae-Bok Song

School of Mechanical Engineering, Korea University
5-1, Anam-dong, Seongbuk-gu, Seoul 136-713, Korea
{mydook,fight704,jbsong}@korea.ac.kr

Abstract. Joint torque sensors are widely used in service robots for force control and collision detection. However, since torque sensors are often directly connected to a harmonic drive, it must be insensitive to torque ripple, the noise from the harmonic drive due to its unique structure. The magnitude of torque ripple is several times higher than electrical noise, and it significantly decreases robot's force control and collision detection performances. In this study, we propose the torque ripple reduction method through the change of the installation position of Wheatstone bridges, and the structure design of torque sensor for service robot arms through FEM analysis. The performance of the proposed reduction method was verified through experiments.

Keywords: joint torque sensor, torque ripple, harmonic drive, service robot arm.

1 Introduction

Six-axis force/torque (F/T) sensors are often installed at the end-effector of a robot arm for force control. However, F/T sensors are too expensive to be widely used in industrial or service robots. Furthermore, this F/T sensor mounted at the wrist of a robot arm can detect only contacts at the end-effector since it cannot measure external forces applied to links other than the end-effector. However, if joint torque sensors are installed at each joint of a manipulator to directly measure torques [2], manipulators can detect collision occurring not only at the end-effector but also at each link. Moreover, the external force applied to the end-effector can be estimated without the use of an expensive 6-axis F/T sensor [3].

To effectively measure joint torques, joint torque sensors are often placed between the output plate of a harmonic drive and the following link of the robot arm. However, such a configuration tends to add noise from the harmonic drive, called torque ripple, to the torque sensor output. This torque ripple is characterized by periodic oscillation whose frequency varies depending on the angular velocity of the harmonic drive and whose magnitude is several times higher than that of ordinary electrical noise. Because of this varying frequency, it is difficult to apply a normal software filter (e.g., low-pass filter or band-pass filter) to remove this ripple. Therefore, such torque ripple significantly deteriorates the performances of force control and collision detection of a manipulator. To deal with these problems, a torque ripple reduction method should be applied to the joint torque sensor. Several methods were proposed to reduce torque

S. Lee et al. (Eds.): Intelligent Autonomous Systems 12, AISC 194, pp. 633–640.
springerlink.com

ripple: modeling the mechanical properties of the harmonic drive [4], applying a Kalman filter [5], attaching strain gauges on the flexspline of the harmonic drive [5-6], and applying a switching notch filter [7].

However, these previous approaches were not effective in successfully eliminating torque ripple. A harmonic drive is difficult to model because of its complex structure. The parameters have to be identified regularly since the characteristics of a harmonic drive change with the lubrication condition. A Kalman filter, on the other hand, may induce a time delay, and requires an appropriate error model. Placing strain gauges on the flexspline can be a useful solution, but strain gauges must be placed at exact positions and in exact orientations. The switching notch filter also induces a time delay, which is not desirable.

In this paper, we propose a novel torque ripple reduction method that uses two Wheatstone bridge circuits to effectively eliminate torque ripple. The proposed reduction method does not induce any time delay unlike software filtering which requires computational burden. Furthermore, compact joint torque sensor for a service robot arm and an embedded amplifier are proposed.

This paper is organized as follows. Section 2 presents the structure of the proposed joint torque sensor and Wheatstone bridge. Section 3 describes the cause of torque ripple and the reduction method. The effectiveness of the proposed torque ripple reduction method is evaluated in Section 4. Finally, Section 5 presents our conclusions.

2 Embedded Joint Torque Sensor

The structure of a joint torque sensor shown in Fig. 1(a) should deform linearly in response to an external torque. This deformation $\delta\theta$ is measured by the strain gauges attached to the joint torque sensor, and the measured deformation is then converted to the torque according to the following equation.

$$\tau = k_t \cdot \delta\theta \tag{1}$$

where k_t is the rotational stiffness of the joint torque sensor. As shown in Fig. 1(a), the joint torque sensor is usually installed between the speed reducer and the output link, so that only joint torque is measured without joint friction.

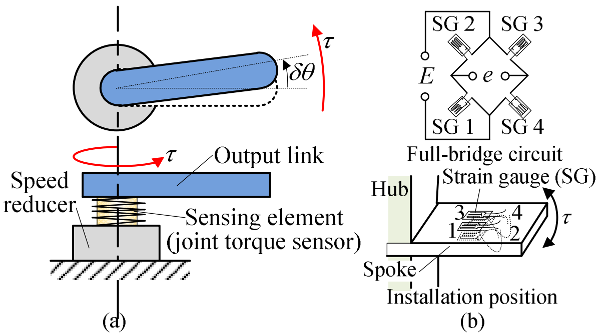

Fig. 1. (a) Deformation of the joint torque sensor, and (b) Wheatstone bridge (installation position and full-bridge circuit)

The structure of the joint torque sensor is designed to consider the maximum size, capacity and safety factor of a typical service robot arm. This structure shown in Fig. 2(a) has a unique hub-spoke shape with slits, which makes the sensor more sensitive to an external torque [8]. The optimum locations to attach strain gauges can be found through FEM analysis shown in Fig. 2(b). In general, the maximum strain of the optimum location is between 800 and 1000 μm/m. The structure was designed such that the maximum allowable torque of 80 Nm and the rotational stiffness of 2.5 kNm/° was achieved with a safety factor of 2.5. The values were chosen in consideration of the specifications of a typical service robot arm.

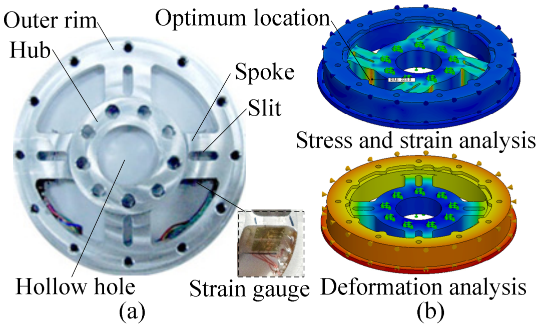

Fig. 2. Embedded joint torque sensor: (a) structure, and (b) amplifier

A Wheatstone bridge circuit shown in Fig. 1(b) is used to measure the deformation of the joint torque sensor. A Wheatstone bridge, which is also known as a full-bridge circuit, is composed of four strain gauges (SG), attached to the spokes at which maximum strains occur. A full-bridge circuit amplifies the output of a strain gauge by four times by summing up all the resistance changes of the strain gauges. Also, it compensates for the deformations of the spokes due to a temperature change.

3 Torque Ripple Reduction

The torque ripple induced by the unique structure of a harmonic drive is a periodical noise which adversely affects the force control and collision detection of a manipulator. Its frequency depends on the angular velocity of the harmonic drive, so a simple filter is not sufficient to completely remove this torque ripple. In this section, the cause of torque ripple will be analyzed in detail and an effective method of its reduction will be also presented.

3.1 Cause of Torque Ripple

A harmonic drive is composed of a wave generator, a flexspline and a circular spline as shown in Fig. 3. It is widely used in manipulators due to its light weight, high precision, and high gear reduction.

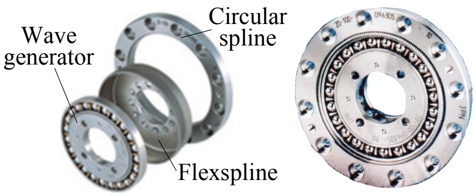

Fig. 3. Components of harmonic drive [9]

A harmonic drive reduces joint speed through its unique structure. When a wave generator (i.e., the input of the harmonic drive) rotates, it deforms the flexspline (i.e., the output of the harmonic drive) into an elliptic shape. This deformation shown in Fig. 4(a) induces the deformation of the hub of the joint torque sensor, which is connected to the flexspline. It leads to twists of the spokes, and these twists affect the strain gauges of the Wheatstone bridge. Therefore, each strain gauge is subjected to the two strains, one caused by the applied torque and the other by the twist of the spoke [5].

When the wave generator rotates at a constant speed in no load, as shown in Fig. 4(b), torque ripple can be expressed as a sinusoidal wave of 3 Nm amplitude (peak-to-peak). Note that its amplitude is several times higher than amplitude of the electrical noise. Therefore, torque ripple disturbs a torque sensor's ability to accurately measure external torques and consequently, degrades a robot's performance in force control and collision detection. Therefore, torque ripple should be eliminated or suppressed.

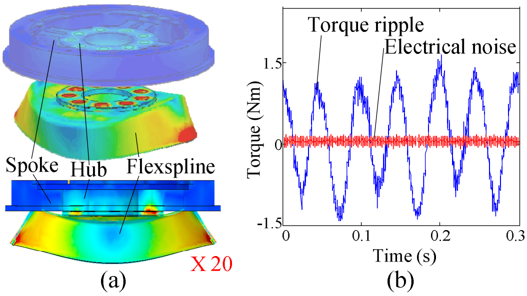

Fig. 4. (a) Effect of deformation of flexspline on joint torque sensor, and (b) torque ripple

3.2 Torque Ripple Reduction Method

The frequency of torque ripple is proportional to the angular velocity ω_w(°/s) of the wave generator because each turn of a wave generator generates two deformations of the flexspline, which correspondingly leads to two periods of torque ripple. In other words, as shown Fig. 5, a half turn of the wave generator generates a period of torque ripple. Therefore, the frequency f (Hz) of torque ripple is expressed by

$$f = \frac{\omega_w}{180} = \frac{r\omega_f}{180} \tag{2}$$

where ω_f (°/s) is the angular velocity of the flexspline, which is the output of the harmonic drive, and r is the speed reduction ratio of the harmonic drive. Also, the value of 180 was used to convert degrees into radians. As described above, torque ripple is periodic, proportional to the rotational velocity of the flexspline. Therefore, it is difficult to eliminate torque ripple when the rotational velocity is changing.

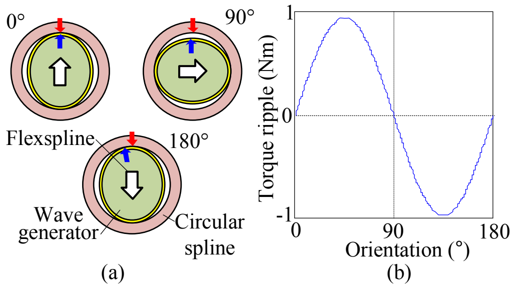

Fig. 5. Relation between orientation of wave generator and period of torque ripple: (a) orientation of wave generator, and (b) torque ripple

One of the most effective methods to eliminate torque ripple would be to measure two ripples of the same magnitude and opposite phases and take an average of the two. As shown in Fig. 5, since the period of torque ripple is 180°, 90° rotation of the wave generator will generate torque ripple with the opposite phase. Therefore, installing two Wheatstone bridges placed 90° apart, as shown in Fig. 6(a), will enable simultaneous measurements of two torque ripples of opposite phases.

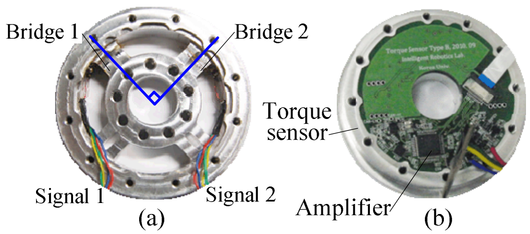

Fig. 6. (a) Two Wheatstone bridges arranged perpendicular to one another, and (b) amplifier embedded into the joint torque sensor

The two signals are proportional to the external torque, but the torque ripples have opposite phases. The measured signals can be expressed by

$$\begin{aligned} \tau_{B1} &= \tau + A\sin(2\pi f t) \\ \tau_{B2} &= \tau + A\sin(2\pi f t + 2\phi) \\ \tau &= \frac{(\tau_{B1} + \tau_{B2})}{2} \end{aligned} \tag{3}$$

where τ_{B1} and τ_{B2} are signals 1 and 2 from bridges 1 and 2, respectively, τ (Nm) is the external torque applied to the joint, A (Nm) is the amplitude of the torque ripple, and f (Hz) is the frequency of the torque ripple, and ϕ (= 90°) is the phase difference between the two signals. As shown in Eq. (3), the two measured signals contain the same external torque and the torque ripples of opposite phases. Taking the average of those two signals yields the external torque of interest without torque ripple.

To measure two torque ripples of opposite phases at the same time, a dual-channel embedded amplifier shown in Fig. 6(b) was developed. A microprocessor (ARM Cortex-M3) embedded into the amplifier is used taking an average of two torque signals to minimize torque ripple. Furthermore, an additional software filter (e.g., low-pass filter or band-pass filter) can be applied through the embedded processor, if needed.

The proposed method does not involve complex computation or the use of a filter. This hardware compensation method does not induce any time delay since no software filtering is involved.

4 Experiments and Discussion

The experimental setup shown in Fig. 7 was constructed to evaluate the performance of the proposed torque ripple reduction method. The joint module consists of a harmonic drive, a joint torque sensor, a cross-roller bearing and a hollow shaft. A component-type harmonic drive with a reduction ratio of 160 was used for this experiment. The joint torque sensor with two Wheatstone bridges was directly connected on the flexspline of the harmonic drive. A cross-roller bearing was used to support the moment load applied to the joint torque sensor (i.e., the moments in directions other than the direction of interest) so that only the rotational torque could be applied to the joint torque sensor. The constructed robot arm was operated through a motor and a belt-pulley connection, and thus, the motor torque was transmitted to the link via the joint module including the joint torque sensor. To verify the torque ripple reduction method, experiment was conducted at constant velocity.

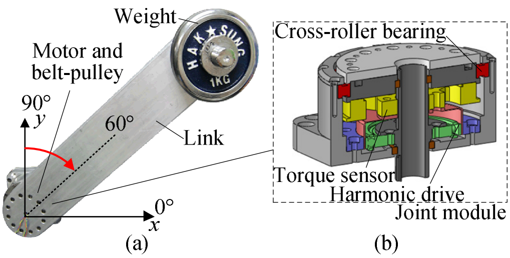

Fig. 7. (a) Experimental setup for torque ripple reduction, and (b) cross sectional view of joint module

A torque signal was recorded when the robot arm was rotated from 90° to 60° at a constant angular velocity of 20°/s, and the results are presented in Fig. 8(a). Torque signals 1 and 2 were measured from the Wheatstone bridges, respectively, installed at the joint torque sensor as shown in Fig. 6, and the filtered signal was also plotted. As shown in Fig. 8(b), the amplitude of the torque ripple was clearly reduced.

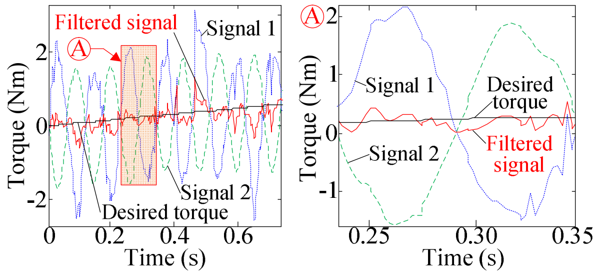

Fig. 8. Experimental results of constant angular velocity of robot joint: (a) general view, and (b) expanded view

Furthermore, as the reduction ratio was 160 and the angular velocity of the robot joint was 20°/s, according to Eq. (2), the frequency of the torque ripple should be 17.8 Hz. This was verified on Fig. 9. Figure 9(a) shows the FFT plot of both torque signals; there is a large peak at 17.8 Hz, which corresponds to the torque ripple. Figure 9(b) shows the FFT plot of the filtered signal, with no peak at 17.8 Hz. This shows that taking the average of the two torque signals from the two Wheatstone bridges successfully reduces torque ripple. This method does not require any additional complex software filter algorithms, which induce an undesirable time delay.

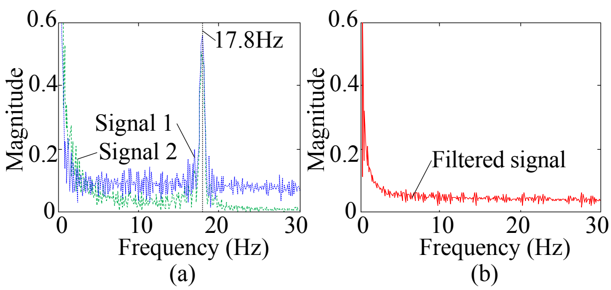

Fig. 9. FFT plots: (a) before torque ripple reduction, and (b) after torque ripple reduction

5 Conclusion

This paper proposed a torque ripple reduction method using two Wheatstone bridges. With the proposed reduction method, torque ripple can be minimized without any undesirable time delay. Furthermore, a compact joint torque sensor for a service robot arm and an embedded amplifier are proposed. Based on our analysis and experimental result, the following conclusions are drawn.

1. Torque ripple was greatly reduced by taking the average of the torque signals from the two Wheatstone bridges installed perpendicular to one another. This method did not require the use of any software filter to prevent any time delay.
2. The developed joint torque sensor, compact in size, could be easily installed at each joint of a service robot. The dual-channel amplifier was embedded into the sensor module, so that two torque signals can be obtained from the two bridges to effectively remove torque ripple.

Acknowledgements. This work was supported by the Center for Autonomous Intelligent Manipulation under Human Resources Development Program for Convergence Robot Specialists (Ministry of Knowledge Economy) (NIPA-2011-C7000-1001-0003) and by Basic Science Research Program through the National Research Foundation of Korea (NRF) funded by the Ministry of Education, Science and Technology (No. 2011-0001150).

References

1. Gravel, P.D., Newman, S.W.: Flexible robotic assembly efforts at Ford Motor Company. In: Proceedings of the IEEE International Symposium on Intelligent Control, pp. 173–182 (2001)
2. Hirzinger, G., Sporer, N., Albu-Schaffer, A., Hahnle, M., Krenn, R., Pascucci, A., Schedl, M.: DLR's torque-controlled light weight robot III – are we reaching the technological limits now? In: Proceedings of the IEEE International Conference on Robotics and Automation, pp. 1710–1716 (2002)
3. DLR, "Institute of Robotics and Mechatronics, Status Report 1997-2004," Part 1, pp. 35–42(2004)
4. Timothy, D.T., Warren, P.S.: A Nonlinear Model of Harmonic Drive Gear Transmission. In: IEEE Int. Conf. on Robotics and Automation, vol. 12(3), pp. 368–374 (1996)
5. Hamid, D.T., Belanger, P.R.: Torque Ripple and Misalignment Torque Compensation for the Built-In Torque Sensor of Harmonic Drive Systems. IEEE Trans. on Instrumentation and Measurement 47(1), 309–315 (1998)
6. Jonathon, W.S., Richard, F.: Improved Torque Fidelity in Harmonic Drive Sensors Through the Union of Two Existing Strategies. IEEE/ASME Trans. on Mechatronics 11(4), 457–461 (2006)
7. Kim, J.H., Kim, Y.L., Song, J.B.: A Switching Notch Filter for Reducing the Torque Ripple Caused by a Harmonic Drive in a Joint Torque Sensor. Trans. of the KSME (A) 35(7), 701–833 (2011)
8. Aghili, F., Buehler, M., Hollerbach, J.M.: Design of a Hollow Hexaform Torque Sensor for Robot Joints. The International Journal of Robotics Research 20(12), 967–976 (2001)
9. `http://www.shds.co.kr`

Design and Analysis of Variable Yielding-Torque Spring Clutch (VSC) for the Safety of Operating Robot Arm

MyungOok Hyun, Junho Choi, and Sungchul Kang

Bionics Center,
Korea Institute of Science and Technology
Hwarangno 14 gil 5, Seungbuk-gu, Seoul 136-791, Korea
Operator43@naver.com,
{junhochoi,kasch}@kist.re.kr

Abstract. Joint stiffness control for safety is widely investigated and many devices are invented both active and passive control of joint stiffness. However, none of them are satisfied both larger torque endurance and active control. The variable yielding torque spring-clutch (VSC) can guarantee both active control and large torque endurance. This paper explains about initial motivation and detail procedures from design objective to making prototype and testing.

Keywords: Variable Stiffness, Spring-Clutch, Safety Robot.

1 Introduction

Safety problem during robot operation is already concerned a little before using robot at human life, especially at automation device of factory or exploring device of dangerous environments. However, as nowadays, safety is more considered than before because robots are used in human life more closely. Therefore, many devices of increasing safety of robot at interaction with human have been invented until now, and variable yielding torque spring-clutch (VSC) is one of these devices.

VSC is attached at robot arm joint, and eliminates joint stiffness instantly by releasing joint lock when limit torque enters from arm link due to unexpected crash or contact between human. Additionally, changing joint stiffness with electric motor and lever-mechanism, VSC can endure both the weight of robot arm and operating torque.

Concept of safety joint applying stiffness/compliance control begins from variable stiffness actuator (VSA) of A. Bicchi, Pisa Univ.[1]. From then, many devices of joint stiffness control are invented, including QA joint[2], FSJ[3] of German DLR team, HDAU[4] of Korea Univ., VSJ[5,6], spring-clutch[7] of KIST. However, though many inventions, there is no device which satisfies both enough large joint torque and active joint stiffness control. Spring-clutch have enough large torque for heavy robot arm, but are passive devices so that these cannot control joint stiffness actively. Similarly, HDAU, VSJ, QA joint and FSJ have active joint stiffness control, but also have small joint torque comparing with spring-clutch so that they can't be endure large input torque from heavy robot arm. For conquering this problem, VSC is designed for both the ability of active joint stiffness control and large torque endurance.

S. Lee et al. (Eds.): Intelligent Autonomous Systems 12, AISC 194, pp. 641–649.
springerlink.com

2 Design of VSC

2.1 Necessity of VSC

Service robot sharing work space with human operators is exposed to possibility of unexpected collision. In order to prevent damage to human operator, it is important to have small stiffness at the joints of the manipulator. However, for a manipulation tasks that require accuracy of the manipulator, it is necessary for the joint to remain rigid. The spring-clutch introduced in [7] is capable of changing the stiffness depending on the torque exerted. The spring-clutch is released when external torque is beyond the threshold torque and remains rigid when the external torque is less than the threshold.

However, when the spring-clutch is installed in a multi degree-of-freedom manipulator, it is difficult to design a constant threshold since the torque due to the gravity changes as the pose of the manipulator changes. To cope with torque due to gravity, which varies as pose of the manipulator changes, it is necessary to change the threshold torque.

The proposed VSC changes the threshold torque, acts as a rigid joint when the external torque is less than the threshold torque, and is released if the external torque is greater than the threshold torque. At figure.1 and equation (1), the yielding torque of VSC is determined by threshold angle and spring preload.

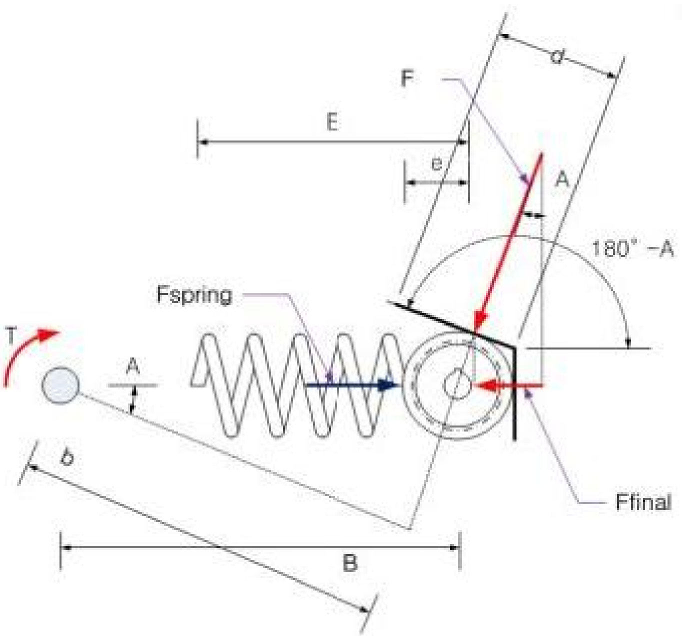

Fig. 1. Theory of yielding torque at VSC

$$F = \frac{T}{b} = \frac{T}{B \cdot \cos(\alpha)} \tag{1}$$

$$F_a = F \cdot \sin(\alpha) = \frac{T}{B \cdot \cos(\alpha)} \cdot \sin(\alpha) = \frac{T}{B} \cdot \tan(\alpha)$$

$$F_{spring\ comp} = F_a = K \cdot e,\ T = \frac{F_a}{\tan(\alpha)} \cdot B = \frac{K \cdot e}{\tan(\alpha)} \cdot B$$

2.2 Objective Function of VSC and Sensitivity Analysis

Rearranging characteristics of VSC for robot arm, we can construct objective function as in (2).

$$\begin{aligned} &Minimum\ \ Output\ \ Torque < 5\ Nm \\ &Maximum\ \ Output\ \ Torque > 15\ Nm \\ &\quad subject\ \ to \\ &\qquad torque\ \ changing\ \ speed > 10\ Nm/s \\ &\qquad total\ \ diameter \le 120\ mm \\ &\qquad total\ \ height \le 25\ mm \\ &\qquad torque\ \ resolution < 0.5\ Nm \end{aligned} \tag{2}$$

Maximum torque of invented spring-clutch is about 15Nm (increasing spring coefficient of spring-clutch device at a range of durability), therefore VSC should have larger range of changing torque for substitution. With this consideration, we choose yielding torque range from 5 to 15Nm. Constraints are composed with conditions of satisfying active joint stiffness control and avoiding dimension/weight increase.

Firstly, we should have decided one parameter for controlling joint stiffness. Therefore, for choosing design parameter, as you can see at table.1 and figure.2, we have proceed sensitivity analysis about yielding torque change due to changing two parameter, threshold angle and spring preload, with Minitab ver.14 program and Taguchi method for multi-level and 2-parameter.

Table 1. Parameter Matrix using Taguchi Method

Threshold Angle (Degree)	Spring Preload (Newton)	Measured Torque (N*m)
60	36.9	4.86
60	78.4	7.24
70	36.9	8.68
70	78.4	12.14
80	36.9	19.89
80	78.4	26.35

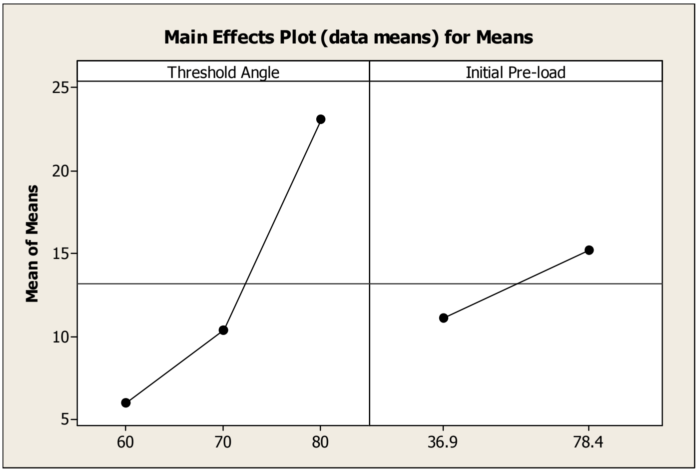

Fig. 2. Parameter sensitivity about yielding torque

As in figure.2, yielding torque is more sensitive for changing threshold angle than changing spring preload, therefore threshold angle is more efficient than spring preload for increasing yielding torque range of SCA. Nevertheless, through design process, we have many obstacles for realizing mechanism of threshold angle changing, for example, instability problem. For this reason, we change design parameter as spring preload instead of threshold angle for changing yielding torque because of system robustness.

3 Detail Design Ideation and Selection

After changing design parameter of VSC as spring preload, we proceeded detail mechanism design which operators can change spring preload real-time so that they can control joint stiffness as operating conditions. With many design trials and motor selection due to proper mechanism, including 4-bar linkage, slider mechanism, cam-follower, we finally designed VSC as figure.3, linear actuator for linear compressing motion and lever mechanism for generating larger compressing force. Comparing with initial spring-clutch, the total diameter of VSC is increase by 20mm and its height is increased by 7mm, but also is able to install at our robot arm.

As you can see at figure.4(a), when linear motor is actuated by upward direction, lever mechanism moves counter- clockwise and spring of pusher bearing is compressed. Pusher bearing is contacted with threshold cam of rotor, therefore, by compressing spring with linear motor, spring preload is increased and threshold yielding torque is also increased corresponding to spring preload as in figure.4(b).

Similarly, when linear motor is actuated by downward, spring is decompressed and yielding torque is also decreased as in figure.5(a) and (b).

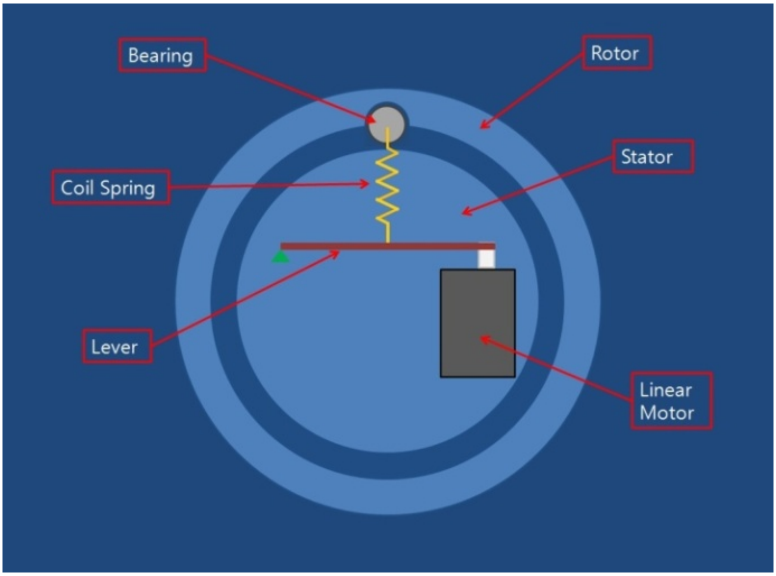

Fig. 3. Concept of VSC using linear motor and lever mechanism

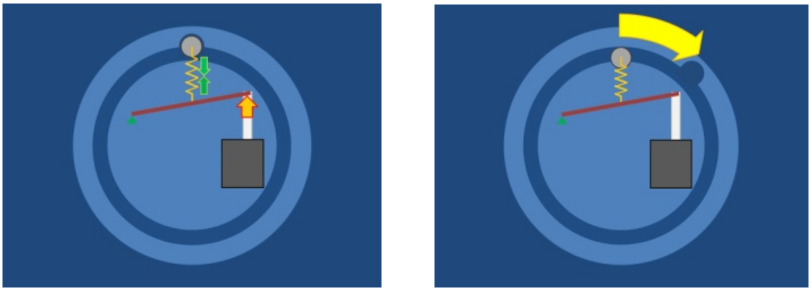

(a) (b)

Fig. 4. Increasing yielding torque procedures; (a) upward moving of linear motor for spring compression, (b) increased yielding torque is applied at VSC

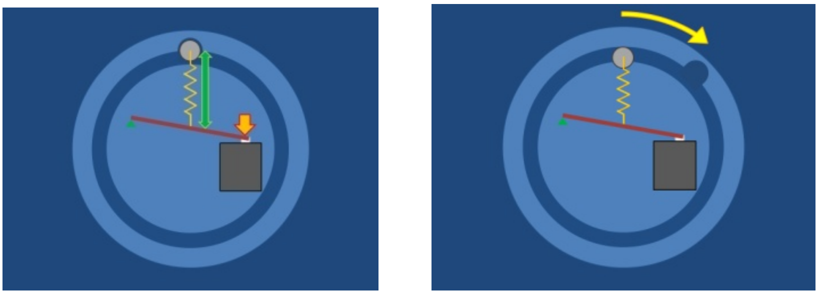

(a) (b)

Fig. 5. Decreasing yielding torque procedures; (a) downward moving of linear motor for spring compression, (b) decreased yielding torque is applied at VSC

Lever mechanism is necessary at VSC, because spring force due to compressing and yielding is very large, about 100N, and there is no linear actuator satisfying both dimension constraints and objective function. Overcoming this obstacle, we arrange lever mechanism between linear motor and pusher bearing as figure.4, which gives larger force and shorter stroke at the spring, and we can find proper linear motor.

Next step, searching linear motor of high-force generation and small size, we find two candidates, L12 of Firgelli Co. and LSA-3024SD/SDF of Potenit Co., as table.2. Comparing parameters, L12 has larger generating force and smaller width than LSA-3024SD/SDF, but also there is no feedback device inside of L12 so it is only controlled by open-loop and cannot guarantee its position. On the contrary, LSA-3024SD has smaller force and larger width but also has feedback device inside, potentiometer, so that we can control linear motor with closed-loop and guarantee its position by potentiometer. Considering motor control and torque resolution, we finally choose LSA-3024SDF - changing motor and reduction gear of LSA-3024SD - which generates larger force than L12 an LSA-3024SD but has slower motor speed.

Table 2. Parameter Comparison of Three motors

Parameters	Firgelli L12	Potenit LSA3024SD	Potenit LSA3024SDF
Dimension (mm)	15*18*70	15*28*75	15*28*75
Gear Ratio	1:210	1:150	1:450
Generating Force (N)	45	20	60
Speed (mm/s)	5	9	3
Input Voltage (V)	6~12	5~12	5~12
Feedback	X	O	O

At last, we designed detail mechanism and selected linear motor as in figure.6, and we also made prototype VSC and constructed experimental procedures of VSC.

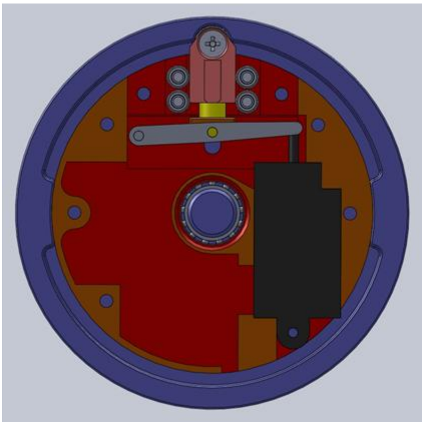

Fig. 6. Design Layout of VSC using Solidworks 2011 version

4 Prototype Manufacture and Test

4.1 Experiment Method

Prototype VSC is made as you can see at figure.7 and comparison data with spring-clutch is arranged at table.3.

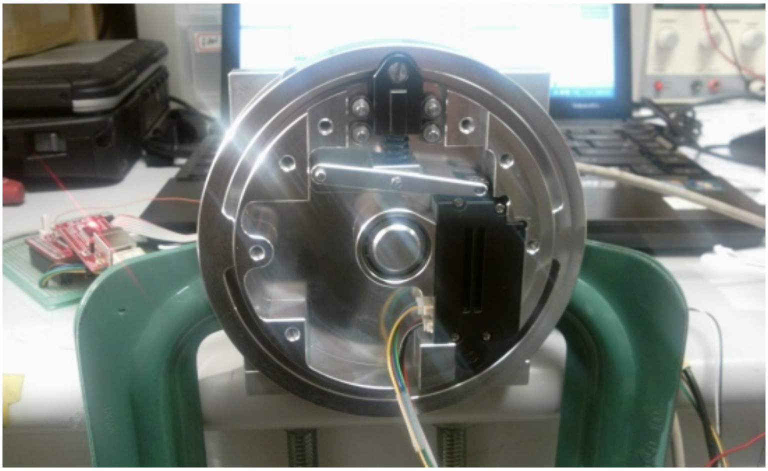

Fig. 7. Prototype VSC with lever mechanism

Table 3. Comparison Data with Spring Clutch

Dimension & Performance	Spring Clutch	VSC
Outer Diameter	100mm	120mm
Assembly Height	15mm	22mm
Total Weight	250g	400g
Threshold Depth	3.5mm	4.0mm
Spring Coefficient	12.3N/mm	12.3N/mm
Spring Compression	3mm	1~4mm
Yielding Torque	7Nm	4~17Nm

MCU for controlling linear actuator is ATmega128 of Atmel with pulse width modulation (PWM), and coil spring of pusher bearing is SWL-8-20 of Misumi Co. (spring coeff. : 12.3N/mm, initial spring preload and torque : 12.3N / 4Nm). Yielding torque is measured by torque wrench DB25N-S of Tohnichi Co., and 10 times with clockwise and counter- clockwise for confirming repeatability. Measuring yielding torque with changing spring preload, we can find the linearity of yielding torque as figure.8.

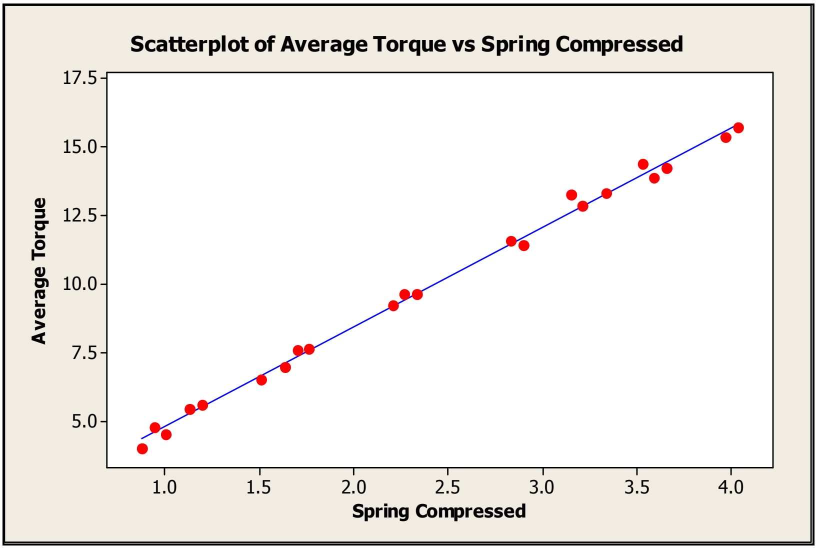

Fig. 8. Torque Measurement Data due to Spring Compression

As torque test results shows, we confirm that we can change yielding torque with real-time. Furthermore, torque changing speed is about 9Nm/s which is calculated with speed of linear motor, 6mm/s, reduction ratio of lever, and torque difference per spring compression 4.33Nm/mm. And torque resolution calculated by linear motor resolution is 0.13Nm, which satisfies our design constraints. Dimension constraints are also satisfied our requirement though its total diameter and assembly height is increased comparing with initial spring-clutch.

5 Conclusion

The designed VSC is capable of changing threshold torque on-line. Since the torque due to the gravity changes in a multi DOF manipulator as the configuration of the manipulator changes, it is necessary to have VSC at the joint of the manipulator in order to guarantee safety during interaction with human, enduring both operating torque and gravity effect of robot arm. Therefore, VSC can be used in similar devices which operate in human life. In this paper, the method to determine model parameters was presented. Experimental result shows that the threshold torque changes on-line as the compression by the spring changes.

Acknowledgements. This paper is supported by 21 Century Frontier Project of KIST cognitive intelligence robot center.

References

1. Tonietti, G., Schiavi, R., Bicchi, A.: Design and Control of a Variable Stiffness Actuator for Safe and Fast Physical Human/Robot Interaction. In: Proceeding of IEEE International Conference on Robotics and Automation (2005)
2. Albu-Schaffer, A., Wolf, S., Eiberger, O., Haddadin, S., Petit, F., Chalon, M.: Dynamic Modelling and Control of Variable Stiffness Actuators. In: IEEE International Conference on Robotics and Automation (2010)
3. Wolf, S., Eiberger, O., Hirzinger, G.: The DLR FSJ: Energy based design of a variable stiffness joint. In: IEEE International Conference on Robotics and Automation (2011)
4. Kim, B.S., Song, J.B.: Hybrid Dual Actuator Unit: A Design of a Variable Stiffness Actuator based on an Adjustable Moment Arm Mechanism. In: IEEE International Conference on Robotics and Automation (2010)
5. Choi, J.H., Park, S.C., Lee, W.S., Kang, S.C.: Design of a Robot Joint with Variable Stiffness. In: IEEE International Conference on Robotics and Automation (2008)
6. Choi, J.H., Hong, S.H., Lee, W.S., Kang, S.C.: A Variable Stiffness Joint using Leaf Springs for Robot Manipulators. In: IEEE International Conference on Robotics and Automation (2009)
7. Lee, W.S., Choi, J.H., Kang, S.C.: Spring-Clutch: A Safe Torque Limiter based on a Spring and CAM Mechanism with the Ability to Reinitialize its Position. In: IEEE/RSJ International Conference on Intelligent Robots and Systems (2009)

Vibrotactile Cues for Motion Guidance

Yeonsub Jin[1], Changmok Chun[1], Yeonhwa Cha[1],
Gi-Hun Yang[2], and Sungchul Kang[1]

[1] Bionics Center, Korea Institute of Science and Technology
Hwarangno 14 gil 5, Seungbuk-gu, Seoul 136-791, Korea
jeyong3@naver.com, changmook@kist.re.kr,
{yh.chacha,kasch804}@gmail.com
[2] Underwater Robot Research Group, Korea Institute of Industrial Technology
1271-18, Sa 1-dong, Sangrok-gu, Ansan-si, Gyeonggi-do, Korea
yanggh@kitech.re.kr

Abstract. In this paper, we have developed motion guiding device with utilizing Kinect of Microsoft Inc. for motion capturing sensor and phantom sensation which is famous tactile illusion effect generating space and direction induced vibrational information. The system detects real time motion of arm and its designated path. Then it guides arm motion along with the detected path with directional vibration information. The directional information of upper arm and lower arm was generated in order for the motion guidance by vibrations with the consideration of the pose of the arm. Instead of the discrete vibration in the vicinity of the vibrating motor, we could express continuous vibration for generating locational feedback along the arm with tactile illusion effect which induces the intentional motion. In order to evaluate the vibrational algorithm, the tactile illusion effect was implemented in the motion guidance experiments of the extension and flexion motion of the elbow joint.

Keywords: tactile motion guidance, vibrotactile, phantom sensation, haptic.

1 Introduction

Recently, tactile feedback device with vibrotactile was developed in various fields; medical robots, entertainment, hand-held device, and so on. Even though there is no organized and standardized way of tactile expression, the tactile stimulus travels 5 times faster than visual stimulus, 20m/s, and the surface area of skin is almost $2m^2$ which is the largest tissue of the whole body. With these benefits of tactile feedback, there have been lots of researches involved in these fields. The tactile feedback technology is now getting considered as the interfacial technology of the information recognition and expression between the user and machine. Researchers who study haptic fields, investigated body motion guidance with the tactile feedback device. These devices capture the motion and pose of the user in real-time, and generate visual, tactile, auditory feedback for guiding user to follow given motion. It possesses the potential applicability into the sports rehabilitations like yoga, golf, and so on.

S. Lee et al. (Eds.): Intelligent Autonomous Systems 12, AISC 194, pp. 651–659.
springerlink.com

In this study, we introduced the arm motion guiding vibrotactile feedback device. The vibrotactile feedback technology conveys not only the spatial information but also directional information. We have applied the phantom sensation, the famous tactile illusion effect, for generating the directional tactile feedback according to the error between the location of the arm and its targeting location so as to guide the arm into the target path and position. The recognition of the current position of the arm causes the attention to visual information and helps detect the exact location of the arm. It induces the intentional motion, which eventually helps rehabilitation process.

This paper explains the previous works related to tactile motion guidance, and introduces the suggested tactile device and the evaluation of the motion guidance algorithm with tactile illusion effects.

Fig. 1. Two vibrotactile bands are worn on the right arm. Eight actuators are mounted in the vibrotactile band. KINECT sensor for motion capture is attached to ceiling. User motion and desired motion displayed on the monitor.

2 Background

2.1 Related Works

As a relatively new focus of haptics research, many vibrotatile motion guidance systems have been developed. In [5], while subjects played the violin, vibrotactile feedback was provided for posture error, bowing hand movement, and violin placement. Other applications using similar methodologies include dance training [6], stroke rehabilitation [7,8], rowing [9,11], gait retraining [10], and snowboarding [12].Each application of vibrotactile feedback algorithm provides directional information but it does not provide feedback of the current motion. Vibrotactile

Feedback of the current motion induces intentional motion. It is more effective in learning and rehabilitation than conventional motion guidance devices. As long as using a simple motor, vibrotactile feedback guidance is difficult to transmit spatial information and directional information because vibration is typically not uni-directional but omni-directional and consists of various frequencies and amplitudes. To overcome this limitation, researchers have been trying to use multi-actuators by utilizing an illusory effect of tactile sensation. The forearm, including the wrist, is one of the preferred parts of the body to stimulate the vibrotactile cues using an array-type vibrotactile display. Oakley et al. [2] applied their multi-element, forearm-mounted vibrotactile display to the forearm and investigated the feasibility of the device. Piateski and Jones [1] had compared the performance of the arm and torso mounted vibrotactile display by testing the ability of subjects to identify patterns of vibrotactile stimulation, their results indicated that the torso was superior as compared to the forearm in identification of vibrotactile patterns. Phantom sensation could be applied to the vibrotactile rendering method. Phantom sensation is also called funneling illusion and related to apparent movement phenomenon [3], which is time varying effect of phantom sensation. Under some conditions, the two stimuli are experienced as a single point somewhere between the exact location depending upon the relative intensity of the stimulation, the relative timing of onsets, and the sensitivity of the skin. Phantom sensation is also associated with the cutaneous rabbit. It can provide directional information. As several pulses are delivered in rapid succession, illusory sensations are felt at discrete and evenly spaced locations between two stimulators.[4] By utilizing above sensory illusions, we can display both spatial and directional information together through the vibrotactile motion guidance system for motion feedback and guidance.

3 Vibrotactile Feedback and Guidance System

We are developing a prototype of vibrotactile motion guidance system using Phantom sensation to provide current motion feedback for universal arm motion as fig 1. The component of our current system includes a KINECT for motion capture, two vibrotactile bands with motor controller and desktop PC for graphic. We named this system VT-WARE because it could be used in variety applications though it developed as device for rehabilitation in early. This system developed to use a cheap sensor and vibrotactile motor for personal user. And it is much more convenient for user to wear and use the device for motion guidance system, because the device contains no connected wire

3.1 Motion Capture

Kinect of Microsoft Inc. was used as arm motion detecting sensor. Kinect is a motion sensing input device by Microsoft for the Xbox 360 video game console and Windows PCs. We have acquired 3D coordinates of skeleton joints using windows SDK for KINECT. The targeting motion of upper arm and forearm were estimated as following equation with the shoulder position Pd,s = {xd,s , yd,s , zd,s}, elbow position Pd,e = {xd,e, yd,e, zd,e}, and wrist position Pd,w = {xd,w , yd,w , zd,w}. In order for the system to enable to save various motions, the sequential poses were captured. User loaded the saved motion and was able to learn targeting motion along with tactile and visual guidance. Since the arm length of user and saved motion are different, each joint coordinates of desired pose were calibrated as eq.1.

$$\begin{aligned} l_{u,u} &= \overline{P_{u,s}P_{u,e}} \\ l_{u,f} &= \overline{P_{u,e}P_{u,w}} \\ P_{d,e} &= P_{d,s} + l_{u,u}u_{u,u} \\ P_{d.w} &= P_{d,e} + l_{u,f}u_{u,f} \end{aligned} \quad , \qquad (1)$$

where lu,u stands for length of upper arm, lu,f is the length of forearm, uu,u means unit vector of user`s upper arm, and uu,f means unit vector of user's forearm. The desired motion and motion of user can be displayed on monitor as in fig 2.

We are researching of the sensor fusion between IMU and KINECT because the motion capture through KINECT cannot identify the shoulder roll, forearm pronation, and supination.

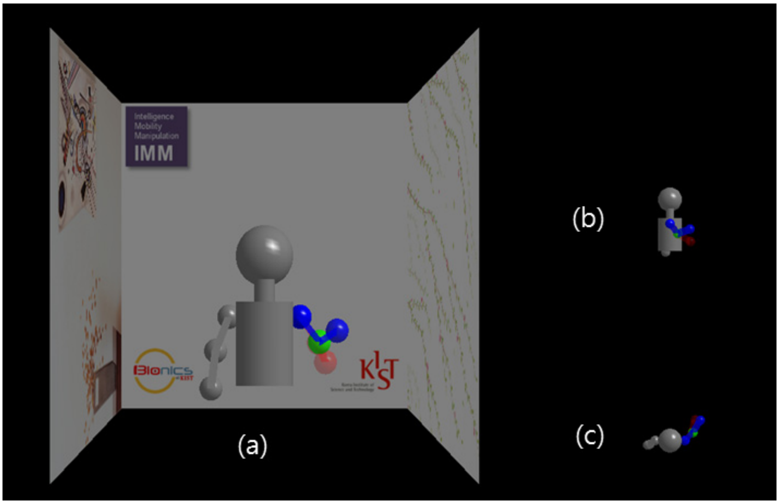

Fig. 2. Desired motion (Red color) and motion of user (Blue color) are displayed on the monitor. When joints of user are reached the correct position, the color at the joint turns green color. (a) Front view, (b) Side view, (c) Top view.

3.2 Vibrotactile Band

We have customized the vibrotactile band for guiding the upper arm and forearm. Each band is consist of four bar-type eccentric motor (CMS motor, CMS-V0610), ATMEGA128 for motor control, XBEE for wireless communication to control PC, and small size battery as in fig3. We have chosen the eccentric motor which vibrates tangential direction on the contacting skin so as to express the tactile illusion effect. [4] For the vibrating motor, the RMS voltage is 3.0V and rate speed is about 10,000 rpm. We have fabricated the assembled piece in order to diminish heating and maximizing the contacting surface area. Four pieces are installed at 0º, 90º, 180º, and 270º around the band. Motor controller and the battery also inserted inside of the band. In order to minimize the size of motor controller, we have designed custom control circuit board integrating ATmega128 and XBee. Flexible band with a zipper is convenient for user to wear as in Fig. 4(a)

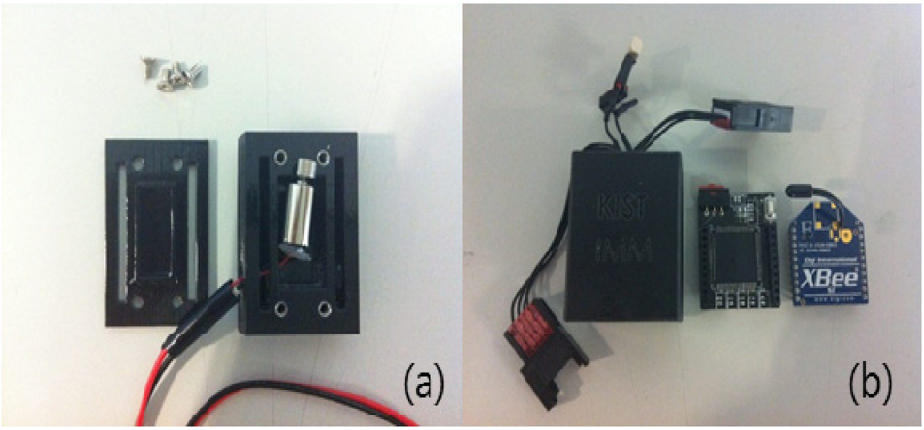

Fig. 3. (a) Vibration piece: bar-type eccentric motor and assembled piece (b) custom control circuit : assembled piece for control circuit (left), ATMEGA128(middle), XBee(right)

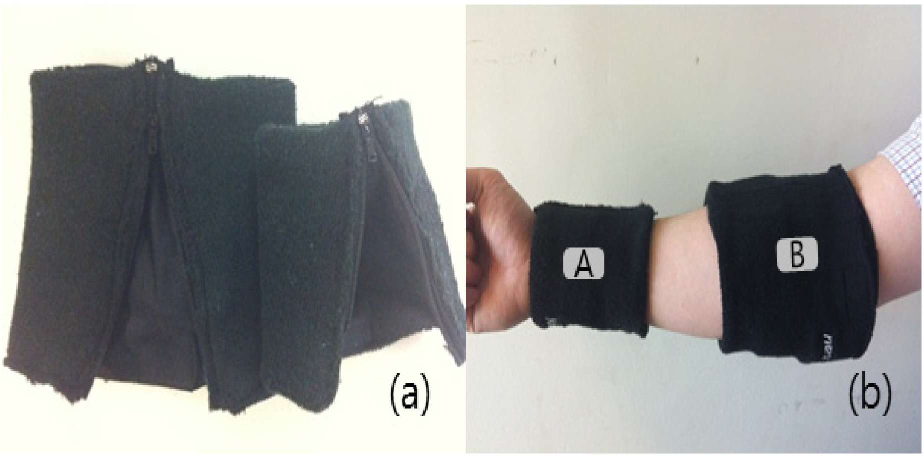

Fig. 4. (a) VT-Band: Flexible band with a zipper (b) VT-Band is worn right arm, A and B are actuator position

3.3 Vibrotactile Feedback Algorithm

We provide the tactile feedback for user to follow the desired arm pose as pre-assigned motion of upper arm and forearm. Motion feedback algorithm uses the spatial information which phantom sensation generates. The motion guiding algorithm utilizes the directional information with tactile illusion effect which can generate continuous spatial stimulus. Vibrotactile guides the direction of arm pose into desired arm pose. This paper only includes the motion of elbow extension and flexion.

3.3.1 Motion Feedback

At first, we estimated the angle of upper arm and forearm for displaying the current position of elbow motion.

$$\theta_u = \cos^{-1}\frac{v_{fore} \cdot v_{upper}}{\|v_{fore}\|\|v_{upper}\|}, \tag{2}$$

where Vfore and Vupper represent directional vector of forearm and upper arm, respectively. We have matched the estimated angle and the vibration of the phantom sensation. User wears two sets of band at wrist and upper arm. Through the one actuator on each band produce the phantom sensation. The displacement between two actuators A and B is around 8 inches as in fig 4(b). The location of the vibration on forearm is matched with the measured angle of the arm and the vibration moves according to the extension and flexion motion of elbow. Therefore, user can monitor his arm movement as in fig 5. Our motion feedback algorithm enables the intentional movement comparing to other conventional motion guidance researches. The signal generation of the phantom sensation can be found in [13].

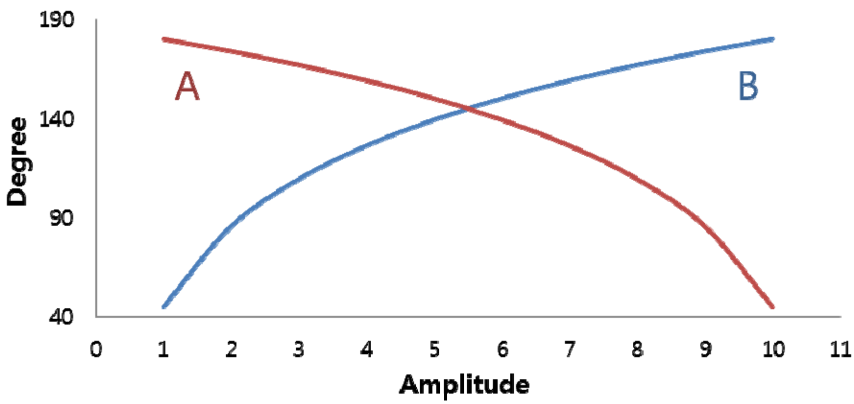

Fig. 5. Motion feedback algorithm: x-axis is angle between upper arm and forearm, y-axis is amplitude of actuator

3.3.2 Motion Guidance

In order to guide into desired pose, elbow extension and flexion motion generates continuous vibration towards wrist and elbow, respectively. The direction of arm movement can be explained through the direction of vibrational signal. Vibration repeats as 1 Hz and it changes for letting user know if the desired pose is obtained as in fig. 6.

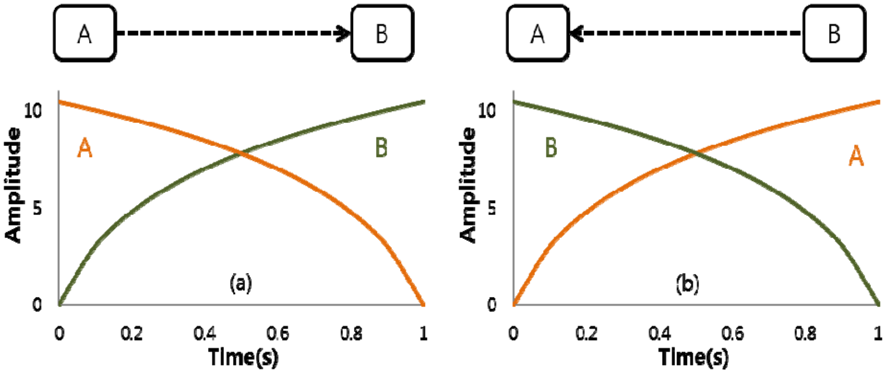

Fig. 6. Motion guidance algorithm: (a) Direction from A to B, (b) Direction from B to A, Vibration is generated by controlling amplitude of actuator

4 Evaluation

4.1 Experiment Method

The main purpose in this experiment was recognition of directional information using motion guidance algorithm. Prior to starting experiment, each subject experienced phantom sensation using motion feedback for about 5 minutes. During motion feedback, subject was explained the purpose of experiment. They had a motion guidance session order of FV, FVT and FT mode using motion guidance algorithm described in Section 3.C.2.each mode was repeated 3 times. Motion of subjects was recorded automatically in desktop PC. Subjects were able to rest at any point. After finishing the experiment, each subject was requested quality of motion feedback, efficiency of motion guidance recognition and preference for FV and FT feedback.

4.2 Experimental Results

Fig 7 shows the average elbow angle value in terms of time for desired motion and feedback motion for each mode, FV, FVT, and FT. The average errors of angle from the desired motion were 1.105 and 1.538 for FVT mode and FV mode, respectively. FT mode generates 4.4675 degree for mean error. Every feedback session shows the possibility for motion guidance. It seemed easy to guide motion since the experiments have been carried out in 1DOF coordination environment. Almost every subject could recognize the vibrational direction explicitly and commented that it is more absorbing and interesting than visual guidance mode.

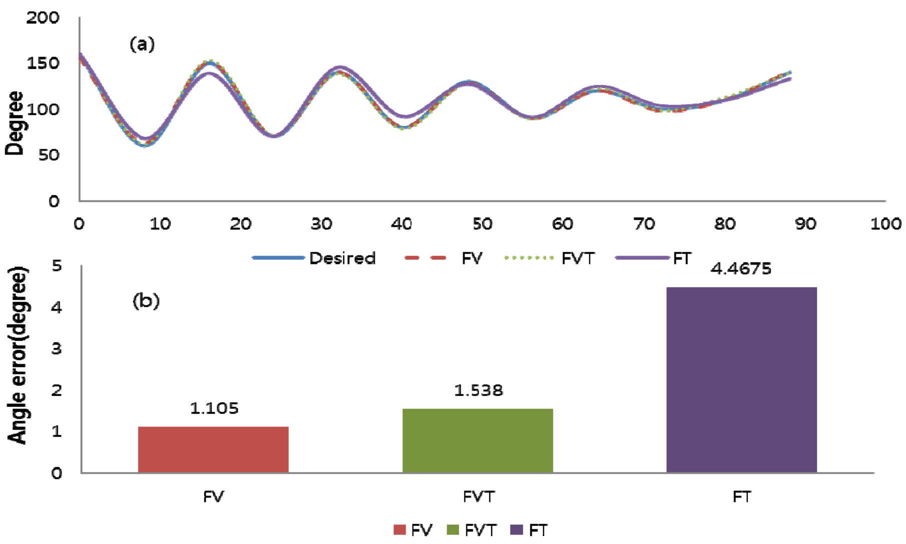

Fig. 7. (a) The average elbow angle of FV, FVT, FT session, and desired motion (i.e. the motion profiles of FV and FVT were almost equivalent with the desired motion.) (b) The average angular error of FV, FVT and FT session

5 Conclusion

We developed vibrotactile motion guidance device implementing tactile illusion effect, 'phantom sensation'. Our motion guidance system consists of motion capture system, VT-Band, and desktop PC. The coordinates of joints are acquired with Kinect and the arm motion was estimated. Two sets of VT-band are consists of four bar-type actuators, motor controller, and XBee for wireless communication. Flexible material and wireless harness of VT-Band makes it easier and more convenient for user use the device. The vibrotactile feedback algorithm using phantom sensation displays the current angle of the elbow with spatial information along the arm. The device guides the arm towards the targeting direction according to the direction of tactile feedback. The estimation if the device is efficient for guiding the elbow motion with tactile illusion effect was carried out. Most of subjects were able to recognize the directional information. The motion guidance with only vibrotactile feedback requires more intentions comparing to the motion guidance with visual information. For the future, the motion detection of the shoulder roll, forearm pronation, and supination will be studied and implement the suggested algorithm into muti-DOF environments.

References

1. Piateski, E., Jones, L.A.: Vibrotactile Pattern Recognition on the Arm and Torso. In: Proceedings of Worldhaptics (March 2005)
2. Oakley, I., Kim, Y., Lee, J., Ryu, J.: Determining the Feasibility of Forearm Mounted Vibrotactile Displays. In: IEEE Proceedings of Symposium on Haptic Interfaces for Virtual Environment and Teleoperator System, Alexandria, pp. 27–32 (March)
3. Rahal, L., Kammerl, J., Cha, J., Steinbach, E., Saddik, A.E.: Investigating the Influence of Temporal Intensity Changes on Apparent Movement Phenomenon. In: IEEE International Conference on Virtual Environments, Human-Computer Interfaces and Measurement Systems (VECIMS), Hong Kong, China, May 11-13, pp. 310–313 (2009)
4. Alles, D.S.: Ingormation transmission by phantom sensations. IEEE Transactions on Man-machine Systems, 85–91 (March 1970)
5. van der Linden, J., Schoonderwaldt, E., Bird, J., Johnson, R.: Musicjacket—combining motion capture and vibrotactile feedback to teach violin bowing. IEEE Transactions on Instrumentation and Measurement 60(1), 104–113 (2011)
6. Drobny, D., Borchers, J.: Learning basic dance choreographies with different augmented feedback modalities. In: Proc. ACM Conference on Human Factors in Computing System (CHI), New York, NY, USA, pp. 3793–3798 (2010)
7. Kapur, S., Premakumar, S.A., Jax, L.J., Buxbaum, A.M.: Vibrotactile feedback system for intuitive upper-limb rehabilitation. In: Proc. IEEE World Haptics Conference, pp. 621–622 (2010)
8. Lieberman, J., Breazeal, C.: TIKL: Development of a wearable vibrotactile feedback suit for improved human motor learning. IEEE Transactions on Robotics 23(5), 919–926 (2007)
9. Ruffaldi, E., Filippeschi, A., Frisoli, A., Sandoval, O., Avizzano, C., Bergamasco, M.: Vibrotactile perception assessment for a rowing training system. In: Proc. IEEE World Haptics Conference, pp. 350–355 (2009)
10. Shull, P., Lurie, K., Shin, M., Besier, T., Cutkosky, M.: Haptic gait retraining for knee osteoarthritis treatment. In: Proc. IEEE Haptics Symposium, pp. 409–416 (2010)
11. van Erp, J.B.F., Saturday, I., Jansen, C.: Application of tactile displays in sports: where to, how and when to move. In: Proc. Eurohaptics, pp. 105–109 (March 2006)
12. Spelmezan, D., Schanowski, A., Borchers, J.: Wearable automatic feedback devices for physical activities. In: Proc. of the Fourth International Conference on Body Area Networks, pp. 1:1–1:8. ICST, Brussels (2009)
13. Yang, G., Jin, M., Jin, Y., Kang, S.: T-Mobile: Vibrotactile Display Pad with Spatial and Directional Information for Hand-held Device. In: The 2010 IEEE/RSJ International Conference on Intelligent Robots and Systems, Taipei, Taiwan, October 18-22, pp. 5245–5250 (2010)

Driving and Turning Control of a Single-Wheel Mobile Robot

Junehyung Park and Seul Jung

Dept. of Mechatronics Engineering, Chungnam National University
220 Gung-dong, Yuseong-gu, Daejeon 305-764, Korea
vij232@hotmail.com, jungs@cnu.ac.kr

Abstract. This paper presents driving and balancing control of a single-wheel mobile robot system called the name of GYROBO. GYROBO utilizes a gyro effect to stabilize itself. Three actuators are used to perform driving and balancing tasks. After modification of hardware and relocation of materials inside the wheel housing of the previous GYROBO model, performances of trajectory following control as well as balancing control are improved. Linear controllers are used for both roll, pitch and yaw angle control. GYROBO is required to follow the specified trajectories commanded by a remote operator. Trajectories include a straight line and curved trajectories. Experimental studies of driving and turning control are conducted and its performances are demonstrated.

Keywords: single-wheel mobile robot, gyro effect, balancing, driving and turning control.

1 Introduction

Research on mobile robots has been dominant in the field of robotic areas due to the increasing utilities of service robots. To function as a service robot, mobility is a fundamental capability for a robot to perform tasks.

Mobility of mobile robots becomes a challenging problem as the number of wheels is decreasing. The number of wheels determines three categories of mobile robots, a plane contact, a line contact and a point contact robot.

Surely, the majority of mobile robots having four wheels belong to the plane contact category. Mobile robots of the plane contact category have stable driving performance but have kinematics constraints as a nonholonomic system. One disadvantage is the limited maneuverability that allows wide turning so that applications in narrow space are not feasible.

Three-wheel mechanism can be used for the narrow space application since the robot forms a holonomic system structure of generating omnidirectional movements. Omni directional mobile robots are of use in indoor environment that does not require fast driving, but good maneuverability.

Two-wheel mobile robots are the category of a line contact that explores challenging mobility since balancing by two-wheel is difficulty and should be

S. Lee et al. (Eds.): Intelligent Autonomous Systems 12, AISC 194, pp. 661–670.
springerlink.com

guaranteed. To maintain balancing in the heading direction, pitch angle control becomes important. Segway is one of successful commercialized two-wheel mobile robots [1]. Research on two-wheel mobile robots has been enormously increased and demonstrated challenging control performances [2-6].

The last category is a single-wheel robot that makes a point contact on the ground. Control of a single-wheel mobile robot is quite challenging because it can fall down in any directions with ease. Thus, control of a single-wheel robot is the most difficult among aforementioned categories.

A single-wheel robot balances itself by gyro effects induced from a fast rotating flywheel as shown in Fig.1 [7]. Gyrover has been a dominant model to present a single-wheel mobile robot for many years with several models [8-10]. A single sphere type mobile robot has been presented to demonstrate balancing and navigation [11].

In the previous research, GYROBO I has been presented and demonstrated its balancing performance, but an oscillatory behavior has been observed [12]. To suppress the oscillation, several design modifications of GYROBO I have been made to improve balancing performances.

All of hardware should be packed within a single wheel to make the center of mass be located on the horizontal and vertical axis of the wheel. Locating materials to make the system be symmetrical in horizontal axis becomes an important factor for successful balancing. Therefore, modification of a body structure has been done by relocating materials inside the wheel.

In this paper, experimental studies of following straight and curved trajectories are performed. The trajectories are given for GYROBO to follow through wireless communication from a remote operator.

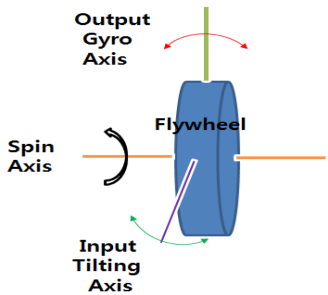

Fig. 1. Concept of gyro effect of a flywheel

2 GYROBO Modeling

The structure of GYROBO is a disc-typed mobile robot. Fig. 2 shows the kinematic configuration of GYROBO. Variables are listed in Table 1.

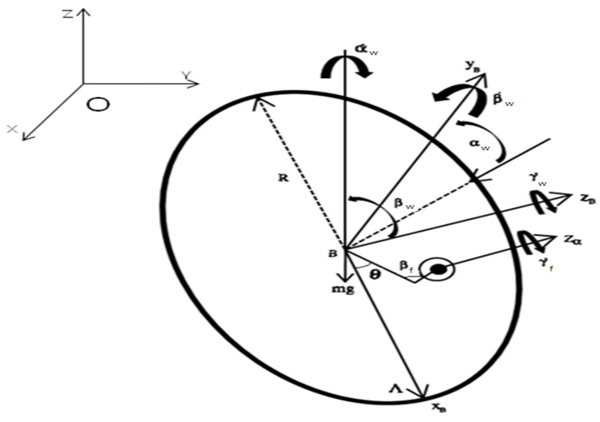

Fig. 2. Model of GYROBO

Table 1. Definition of Variables

X, Y, Z	Position coordinate frame
α_w, β_w, γ_w	Precession, Lean, Rolling Angle of the wheel
β_f, γ_f	Tilt angle and spin angle of the flywheel
R	Radius of the wheel
m	Total mass
u_d, u_t	Torque of drive motor and tilt motor
μ_α	Friction coefficient in yaw direction
I_x, I_y, I_z	Moment of Inertia of Body
I_{xf}, I_{yf}, I_{zf}	Moment of Inertia of Flywheel
S_x, C_x	Sin(x), Cos(x)
$S_{x,y}$, $C_{x,y}$	Sin(x+y), Cos(x+y)

There are two wheels to be controlled. One is a system body that rolls and another is the flywheel to generate gyro motions. Rotation variables or the body are $\alpha_w, \beta_w, \gamma_w$ which are roll, yaw, and pitch angle, respectively. Variables for the flywheel are β_f, γ_f which are tilt and spin angles, respectively. Therefore, controlling the tilt angle of the flywheel regulates α_w, β_w of the GYROBO.

Since GYROBO moves on the plane, the Cartesian velocity can be described as below.

$$\begin{cases} \dot{X} = R(\dot{\gamma}_g C_\alpha + \dot{\alpha} C_\alpha C_\beta - \dot{\beta} S_\alpha S_\beta) \\ \dot{Y} = R(\dot{\gamma}_g S_\alpha + \dot{\alpha} S_\alpha C_\beta + \dot{\beta} C_\alpha S_\beta) \end{cases} \quad (1)$$

The dynamic equation can be represented as below in [10].

$$M(q)\ddot{q} = F(q,\dot{q}) + Bu \tag{2}$$

where M is the inertia matrix, B is the input transformation matrix, u is the control input vector, $q = [\alpha_w, \beta_w, \gamma_w]^T$, and $F = [F_1, F_2, F_3]^T$. The closed loop feedback control input is $u = [u_d u_t]^T$.

Although the detailed dynamic equation is given in [10], here we use a non-model based control method. It is true that modelling a single wheeled system is quite difficult and modelled parameters do not often match with those of a real system.

3 Control Scheme

Here we assume that the flywheel rotates at the high constant speed. Then the tilting angle β_f of the flywheel is a key variable to generate control input for GYROBO to balance as in Fig. 1. Angles of GYROBO are a precession (yaw) angle, α_w , a lean (roll) angle, β_w , and a rolling (pitch) angle, γ_w . The rolling angle is simply controlled by a driving DC motor. The precession and lean angles are controlled by the force induced from the cross product of rotational forces of the spin axis and the titling axis of the flywheel. Thus, the control input variable of GYROBO is the tilt angle, β_f of the flywheel.

Control inputs for the roll and yaw angle control are designed separately as a PD control method.

$$u_\beta = k_{p\beta}(\beta_{dw} - \beta_w) + k_{d\beta}(\dot{\beta}_{dw} - \dot{\beta}_w) \tag{3}$$

$$u_\alpha = k_{p\beta}(\alpha_{dw} - \alpha_w) + k_{d\alpha}(\dot{\alpha}_{dw} - \dot{\alpha}_w) \tag{4}$$

where $k_{p\beta}, k_{d\beta}$ are PD controller gains for the roll angle control and $k_{p\alpha}, k_{d\alpha}$ are PD controller gains for the yaw angle control.

The control input to the tilt angle of the flywheel is the sum of two control output signals given in (3) and (4).

$$u_t = u_\beta + u_\alpha \tag{5}$$

Fig. 3 shows the control block diagram for controlling angles of GYROBO. There are other control input signals to GYROBO, the driving torque u_d to the wheel and the spin torque u_γ to the flywheel which form open loop control.

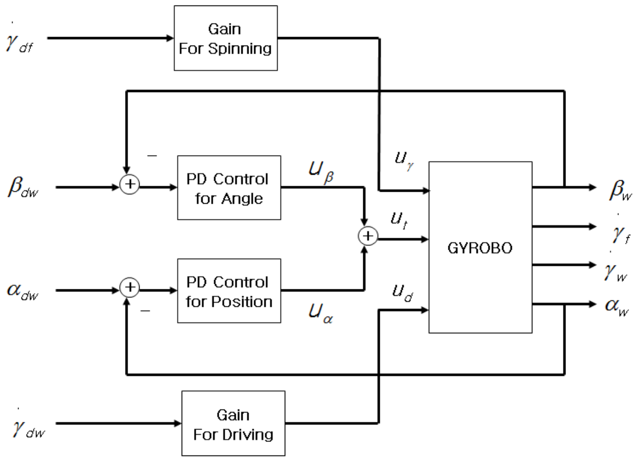

Fig. 3. Control block diagram of driving control

4 GYROBO System

4.1 GYROBO Design

Real implementation of GYROBO is shown in Fig. 4. Three actuators, a drive motor, a spin motor, and a tilt motor are used to generate three angular motions. A drive motor generates the motion of a pitch angle, and combination of a tilt motor and a spin motor generates roll and yaw motions. A drive motor actuates the wheel and a tilt and a spin motors actuates the flywheel. Sensors and control hardware are located on the center of the top. A battery is located at the bottom to lower the center of the gravity.

It has an outer and an inner wheel structure as shown in Fig. 4. The outer wheel is made of rubber and the inner wheel contains all hardware. The outer and the inner wheel are connected by several rollers.

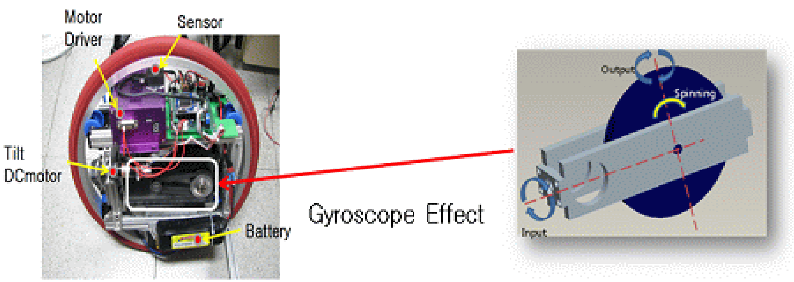

Fig. 4. Overall system structure of GYROBO

All of materials are packed inside the wheel which is the inner wheel. The diameter and the mass of the wheel are 0.45*m* and 11.2*kg,* respectively. The diameter and the mass of the flywheel are 0.15*m* and 2.1*kg,* respectively.

The most important concern for the design is the flywheel part which generates the gyro effects by rotating at high speed. High speed rotation of the flywheel produces vibration due to many reasons such as asymmetry of a flywheel body, nonlinearity from a timing belt, a loose spin axis, and loosely coupled parts. Vibration causes inaccurate sensing measurement which results in poor control performance and unstable balancing.

The drive motor rotates the wheel itself by friction force. At initial driving, slip may occur to drive the wheel. Since the drive motor generates driving motion, open loop control is applied.

The current system has three different sensors, a gyro, and an encoder. The gyro sensor can measure 3 axes angular motions.

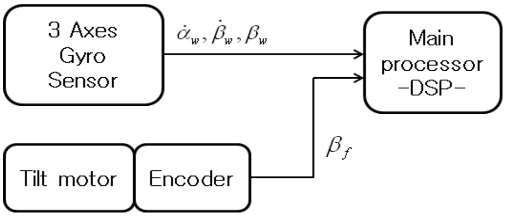

Fig. 5. Estimation of angle data

Fig. 5 shows the block diagram of obtaining data from the gyro sensor. Although the gyro sensor provides three axes data, two axes data are used since the yaw angle data are not reliable.

4.2 Hardware Design

An overall control hardware structure is constructed as shown in Fig. 6. A DSP chip is used as a main controller for managing sensor signal processing, calculation of control algorithm, and PWM generation to motor drivers. Three sensors are used to detect motion of GYROBO. A three axes gyro sensor, a tilt sensor, and an encoder are used to detect the posture of the system. The gyro sensor is used for measuring a lean (roll) angle of the wheel and the tilt sensor is used for tilting the flywheel.

An operator uses a joystick to command the desired signals S_f, S_d to GYROBO through wireless communication remotely where the desired spin velocity is $S_f = \dot{\gamma}_{df}$ and the desired driving velocity $S_d = \dot{\gamma}_g$ as shown in Fig. 3.

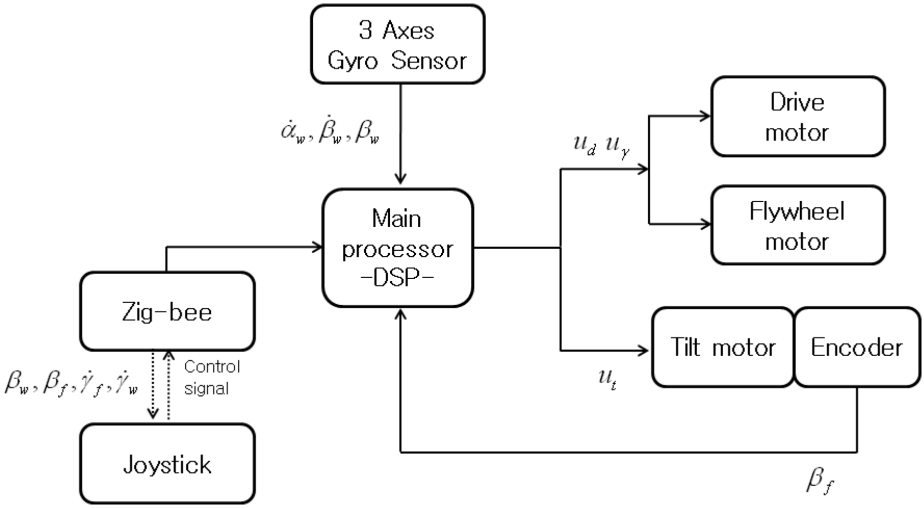

Fig. 6. Hardware structure

5 Experimental Results

5.1 Balancing Control

Firstly, balancing control has been tested. Balancing control at one point of a single-wheel robot is more difficult than when it is moving forward. In this experiment, a roll angle is controlled only. At the beginning, GYROBO seems to make balancing, but it goes unstable. We notice that the tilting angle of the flywheel of GYROBO keeps increasing in one direction. This makes the system unstable.

In order to make the tilt angle converge, the angle should be maintained at around zero degree. Control inputs for the flywheel spin and the drive wheel are considered as open loop control. The tilting of the flywheel is only a closed loop control input. Therefore, leaning against one direction results in unstable balancing performance.

To remedy this problem, a yaw angle control loop is added as shown on the control block of Fig. 3. PD gains of roll and yaw angle control for experimental studies. PD gains are selected by trial and error experimental procedure for the better performances. The proportional gain of yaw control is set to zero because yaw angle data measured from the 3-axes gyro sensor are so noisy that they are not suitable to be used.

After adding the yaw angle control loop, balancing performances are much improved as shown in Fig. 7. Images are taken during the balancing control task from 0 to 12 seconds. Although there are small oscillatory movements in the yaw angle direction, GYROBO maintains balance well.

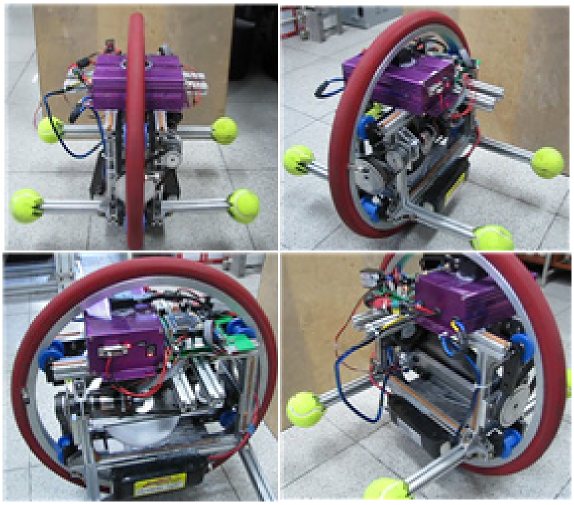

Fig. 7. Balancing demonstration of using roll and yaw angle control

5.2 Turning Control

The next experiment is to turn the direction while balancing at one point. The desired roll command is given for GYROBO to make turn.

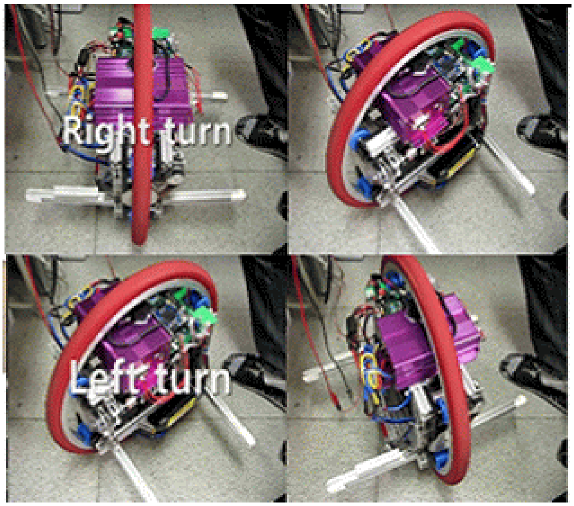

Fig. 8. Turning control demonstration

Fig. 8 shows the real demonstration of turning in the right and left direction. At the beginning, GYROBO tries to make balancing for some time. Then GYROBO turns right and makes a left turn at one point contact with floor. It is unfortunate that a 360 degrees turning task is impossible with current design of GYROBO. The reason is that control of the tilting angle of the flywheel is difficult due to the mechanical design. In order for GYROBO to make a 360 degrees turn, the flywheel has to be tilted in one direction. This configuration is not allowed with the current version due to limited space inside the inner wheel.

5.3 Straight Line Following Control

Final experiment is for GYROBO to move the straight line inside the building. The straight line trajectory is given by an operator through wireless communication.

Initially, an operator holds GYROBO by hands to make the system stable balancing. After releasing, GYROBO tries to balance itself by tilting a little bit on the right hand side due to the slip of the wheel with the floor. Then GYROBO moves forward as commanded. Fig. 9 demonstrates tracking control of the straight line trajectory. Speed of GYROBO is about 0.25m/sec, which is considered as a slow movement.

Fig. 9. Straight line trajectory control

6 Conclusion

A single-wheel mobile robot is tested for balancing and driving control performances. Linear controllers enable GYROBO to be stabilized after several modifications of the mechanical design of GYROBO. Locating the center of mass of the system at the center to make symmetrical system is one of important factors for a successful balancing task. The second important design is to reduce rotational vibration of the high speed flywheel. After fixing mechanical problems, sensor filtering and fusing methods with other sensors are considered.

GYROBO successfully follows the specified trajectories in the plane given by a remote operator. Linear controllers for both roll and yaw angles are used and perform well although sensor signal in yaw direction is not available.

In the future, an additional sensor can be added to the current hardware for more accurate measurement. Then aggressive maneuvering control tasks such as moving backward, turning 360 degrees, climbing over an obstacle will be investigated through experimental studies.

Acknowledgements. This work was supported by the 2011 Basic Research Program from Korea Research Fund and AIM under Human Resources Development Program for Convergence Robot Specialists (Ministry of Knowledge Economy)**,** Korea.

References

[1] Segway, `http://www.segway.com`
[2] Pathak, K., Franch, J., Agrawal, S.: Velocity and position control of a wheeled inverted pendulum by partial feedback linearization. IEEE Trans. on Robotics 21, 505–513 (2005)
[3] Jeong, S.H., Takayuki, T.: Wheeled Inverted Pendulum Type Assistant Robot: Design Concept and Mobile Control". In: IEEE IROS, pp. 1932–1937 (2007)
[4] Kim, S.S., Jung, S.: Control experiment of a wheel-driven mobile inverted pendulum using neural network. IEEE Trans. on Control Systems Technology 16(2), 297–303 (2008)
[5] Noh, J.S., Lee, G.H., Jung, S.: Position control of a mobile inverted pendulum system using radial basis function network. International Journal of Control, Automation, and Systems Engineering 8(1), 157–162 (2010)
[6] Noh, J.S., Lee, G.H., Choi, H.J., Jung, S.: Robust control of a mobile inverted pendulum system using RBF neural network controller. In: IEEE ROBIO, pp. 1932–1937 (2008)
[7] Rui, C.L., McClamroch, N.H.: Stabilization and Asymptotic Path Tracking of a Rolling Disk". In: IEEE Conf. on Decision & Control, pp. 4294–4299 (1995)
[8] Xu, Y., Au, K.W.: Stabilization and Path Following of a Single Wheel Robot. IEEE/ASME Transactions on Mechatronics 9(2), 407–419 (2004)
[9] Nandy, G.C., Xu, Y.S.: Dynamic Model of A Gyroscopic Wheel. In: Proc. IEEE Int. Conf. on Robotics and Automation, pp. 2683–2688 (1998)
[10] Xu, Y.S., Oh, Y.S.: Control of single wheel robots. Springer (2005)
[11] Lauwers, T.B., Kantor, G.A., Hollis, R.L.: A dynamically stable Single-Wheeled Mobile Robot with Inverse Mouse-Ball Drive. In: IEEE Conference on Robotics and Automations, pp. 2884–2889 (2006)
[12] Kim, P.K., Park, J.H., Jung, S.: Experimental Studies of Balancing Control for a Disc-Typed Mobile Robot Using a Neural Controller: GYROBO. In: ISIC2010, Multi-Conference on Systems and Control, pp. 1499–1503 (2010)

Modeling, Dynamics and Control of an Extended Elastic Actuator in Musculoskeletal Robot System

Fuben He[1], Yande Liang[1], Haohan Zhang[1], and Enrico Pagello[2]

[1] School of Mechanical Engineering, Dalian University of Technology
No.2 Linggong Road, Ganjingzi District, Dalian 116024, China
hefuben@mail.dlut.edu.cn, lydjx@dlut.edu.cn,
hhzhang1988@gmail.com

[2] IAS-Lab, Dept. of Information Engineering, University of Padua
Via Ognissanti 72, Padua 35129, Italy
epv@dei.unipd.it

Abstract. The conventional actuator of robot needs to be improved since the bandwidth of motor is limited and it cannot provide enough flexibility to perform the compliance in robot locomotion interacted with environment. In this paper, we present a novel elastic actuator so as to enhance the range of robot activities for adaptability. Considering the characteristics of elasticity and the demands in reality, a feasible study model is developed and constructed. According to the theory of Newton-Euler dynamics equations, the dynamics of model is mathematically described. To avoid unpredictable errors and manage joint oscillation in advance, we also employ a feedforward controller to operate the actuator. Moreover, the actuator can be regarded as the robotic "muscle-tendon" for its function is similar to the muscle-tendon model in human body. Therefore, we apply this actuation to a virtual robot arm based on the Musculoskeletal Robot System (MRS) to evaluate the performances of elastic actuators. The results of experiments indicate that this actuation is effective and contributed to realize the compliant locomotion.

Keywords: modeling, dynamics, elastic actuator, musculoskeletal mechanism, feedforward control.

1 Introduction

Usually we put more attention on electronic motor drives since they are widely used in various robots like industrial manipulators, humanoids, robotic vacuums, etc. The main benefits of such drive mode are convenient assembling, simple control and fast response [1], [2]. Thus, it is reasonable and appropriate to apply the motors as the actuators to drive robot directly. In traditional opinions on design of robot joints, when it refers to the form of mechanical connection between motor and link, "the stiffer the better" is considered as the premise [3]. Although the techniques of stiff actuator have been deeply developed and improved, there are still some drawbacks in robot locomotion such as compliant interactions, force contacts, low-cost energy movements and other advanced behaviors [1], [4]. Because of limited bandwidth of

S. Lee et al. (Eds.): Intelligent Autonomous Systems 12, AISC 194, pp. 671–681.
springerlink.com

motor and high stiffness, the capacities of actuator are often confined which leads robot to lose efficacy and performs badly in some cases. To make up for the shortcomings, currently a number of studies and designs like spring-tendon mechanisms [5], biological robot arm [6] and elastic biped robot [4] have been exploited. In addition, some researchers have also successfully put forward several feasible issues which apply elastic elements to the actuators [8], [9]. Their studies indicate that the elastic actuators offer positive advantages which can minimize peak torques, store and release energy efficiently in the movements and even guarantee the safety during the human-robot interaction [10].

Actually elastic actuators may have a few deviations when the desired positions of robot joints are commanded. Because of the elasticity, when there are external forces or torques applied, the parts linked to joints will be oscillating and damping until they reach the equilibrium positions. This can really influence the accuracy of whole robot system which results in the complexity of control structure. However, introducing more redundant actuators can solve this problem effectively which enhances the operability in elastic motions [10]. Besides, the disadvantage can be also improved by applying sensors to detect the positions of joint and motor rotation in real time so that control policy can be changed promptly by feedback data [11]. Moreover, contrary to the stiff actuators, the elastic ones can provide excellent compliance for the diversity of robot locomotion during the operation process. Certainly they are able to enhance the properties of robot and expand the abilities of motors immensely. Therefore, it is valuable and necessary to apply these elastic actuators to robot studies. Moreover, in some studies, the elastic actuators are regarded as the form of robotic "muscle-tendon" which refers to the biological model of muscle-tendon in human body [5], [11]. These approaches combine the robot actuations with bionics in order to construct a bio-inspired elastic robot towards the human-like movements.

Towards the purposes of compliance and energy efficiency in robot locomotion, we develop a novel and feasible elastic actuator. The design philosophy is derived from original elastic actuators and model of human muscle-tendon. Some dynamics equations are given out for describing actuated movements and constructing the control policies. Adopting this actuator, we also set up a musculoskeletal robot arm to evaluate the elastic drive mode. Finally, the experimental results show that the type of actuator is applicable and effective especially in MRS.

2 Elastic Actuator Model

In elastically actuated robot system, stiffness is an important parameter which should be adjustable and controllable during the operation. Thus, we need to develop a model with variable stiffness to satisfy the demands. Series Elastic Actuator (SEA) is a typical and widely known actuator with sufficient elasticity [8]. However, the compliance of SEA is fixed and cannot be changed in the activities for its capabilities extremely depend on the characteristics of elastic elements like extension springs or torsion springs. In order to extend its application, we focus on bionics for seeking new ways to implement the elastic actuation. When human body executes a motion or gait task, muscles are excited by Central Nervous System (CNS) to develop forces which are transmitted by tendons to musculoskeletal system for performances. Naturally, muscle-tendon is considered as a type of actuator which generates forces by muscle contraction. The total muscle force is the sum of passive force and active force in parallel according to Hill-type model [13]. Since the SEA has limitations in stiffness compliance, we develop an extended elastic actuator integrated with the concepts of SEA drive mode and muscle-tendon model. The schematic diagram of extended elastic actuator is depicted in figure 1.

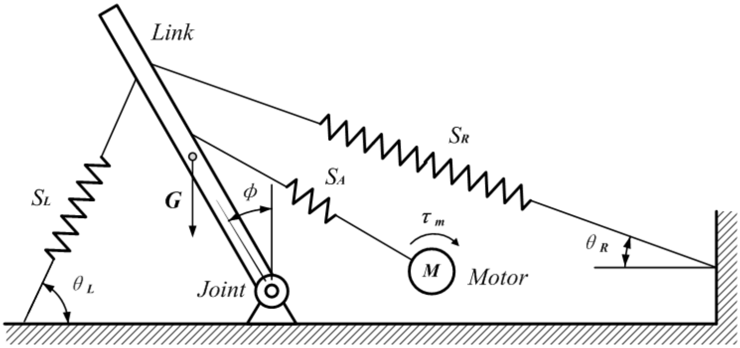

Fig. 1. Schematic diagram of extended elastic actuator

In the figure, S_L and S_R denote two extension springs effecting passive forces to keep the equilibrium positions of joint, while θ_L and θ_R are their angular positions in the system. S_A is an active spring which connects the motor and the link. ϕ is the angular position of link. τ_m is the output torque of motor and G represents the gravity which locates at the mass center. The link can move only in single direction, because the position of joint is restricted by the maximum elongations of active spring. This design can avoid the link from falling into uncontrollable positions and guarantee the accuracy of joint movements.

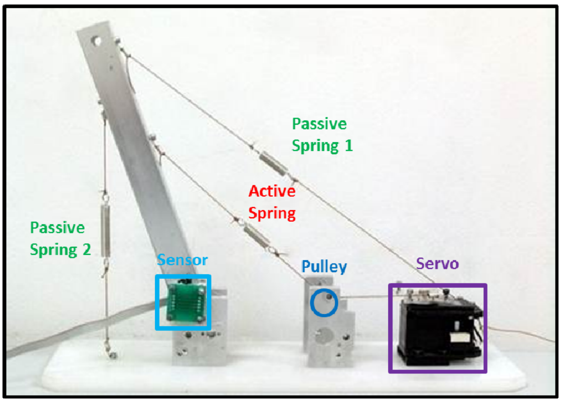

Fig. 2. Mechanism of extended elastic actuator

We also set up a real experimental platform for the extended elastic actuator as depicted in figure 2. It contains one active spring and two passive springs corresponding to the schematic diagram above. Different from other motors, servo has its own feedback controller to insure accurate motions to operate the motor rotations in real time. Moreover, in order to detect movements of link, we apply a magnetic position sensor which is mounted in the joint construction. If detected positions of motor and joint can be considered as system feedback data in control, the dynamic oscillation and elastic shakes of link can be monitored, so that the system stiffness is able to be adjusted during the movements. With the real model of extended elastic actuator, we can carry out a lot of significant experiments.

3 Dynamics Description

As control policy and robot construction are determined by dynamics of the extended elastic actuator, it demands to analyze the system dynamic locomotion primarily in order to obtain the properties. Based on the Newton-Euler equations, assuming that the friction can be ignored and the conditions are ideal, we can describe the dynamics of actuator by mathematics equations.

3.1 Decomposed Models

Due to the complexity of actuator model, we decide to decompose the system into two functional models based on the spring characteristics and the actuation approaches, which are mass-passive-model and mass-active-model depicted in figure 3.

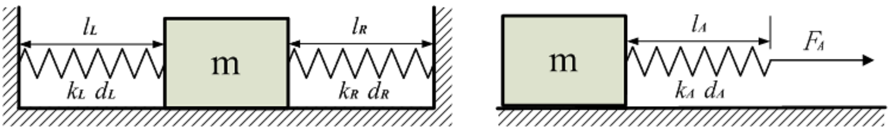

Fig. 3. Mass-passive-model (*left*), Mass-active-model (*right*)

The mass-passive-model (*left*) includes two passive springs at both sides of the mass. Actually this model is an oscillator which describes the stiffness of the elastic actuator during movements. Since passive springs play the roles of impedance, the mass finally stops at the initial position after the horizontal vibration caused by internal forces. In the mass-active-model (*right*), the external force F_A is applied to the mass by the active spring. It indicates that the movements of mass are determined by the force driving and spring drawing. Although the movements of mass models depicted in figure 3 are translational in the planes, they can be transformed to joint rotational motions similar to the model in figure 1, so that the decomposed models can be applied to describe the activities of the extended elastic actuator in dynamics.

3.2 Dynamics Equations

In the generalized coordinate system, the vector $\boldsymbol{q}$ is defined to represent the joint angular positions. Then the corresponding joint angular velocities can be expressed by the vector $\dot{\boldsymbol{q}}$. Similarly, $\ddot{\boldsymbol{q}}$ represents the vector of angular accelerations.

According to Newton-Euler Equations, the state of the general system or stiff actuator can be formulated as following equation.

$$\boldsymbol{M}(\boldsymbol{q})\ddot{\boldsymbol{q}} + \boldsymbol{C}(\boldsymbol{q},\dot{\boldsymbol{q}})\dot{\boldsymbol{q}} + \boldsymbol{G}(\boldsymbol{q}) = \boldsymbol{\tau}_m \tag{1}$$

$\boldsymbol{M}(\boldsymbol{q})$ is the mass matrix containing $\boldsymbol{q}$, $\boldsymbol{C}(\boldsymbol{q},\dot{\boldsymbol{q}})$ represents the coriolis and centripetal effects, $\boldsymbol{G}(\boldsymbol{q})$ is the gravity force, $\boldsymbol{\tau}_m$ represents the torque of motor.

For reinforcing the learning of elasticity in mass-models, we present an equation to express the force effects of springs during the oscillating movements. Based on Hooke Theory, this equation owns a damping item $\boldsymbol{D}(\dot{\boldsymbol{q}})$ and a stiffness item $\boldsymbol{K}(\boldsymbol{q})$. Here $\boldsymbol{D}$ and $\boldsymbol{K}$ are the damping coefficient matrix and stiffness coefficient matrix separately. So the elasticity of system can be determined:

$$\boldsymbol{E}(\boldsymbol{q},\dot{\boldsymbol{q}}) = \boldsymbol{D}(\dot{\boldsymbol{q}}) + \boldsymbol{K}(\boldsymbol{q}) \tag{2}$$

In the mass-passive-model, the coriolis, centripetal and gravity forces can be ignored for the movements of mass are placed on the horizontal plane. In addition, there is no external force applied, so the total torque of system equal zero. Combining the definitions of general dynamics in (1) and elasticity expression in (2), the states of model can be determined by equation (3) and $\boldsymbol{s}_p$ is the vector of mass positions.

$$\boldsymbol{M}_p(\boldsymbol{s}_p)\ddot{\boldsymbol{s}}_p + \boldsymbol{E}_P(\boldsymbol{s}_p,\dot{\boldsymbol{s}}_p)\boldsymbol{s}_p = 0 \tag{3}$$

Similarly, the states of mass-active-model are determined by equation (4) where $\boldsymbol{s}_a$ represents the vector of mass positions and $\boldsymbol{\tau}_a$ is the external torque.

$$\boldsymbol{M}_a(\boldsymbol{s}_a)\ddot{\boldsymbol{s}}_a + \boldsymbol{E}_a(\boldsymbol{s}_a,\dot{\boldsymbol{s}}_a)\boldsymbol{s}_a = \boldsymbol{\tau}_a \tag{4}$$

To describe the states of elastic actuator model in figure 1, the coriolis, centripetal and gravity forces need to be taken in account as the movements of joint are rotational. Combining (1), (3) and (4), the dynamics of model is described by equation (5) where $\boldsymbol{E}(\boldsymbol{q},\dot{\boldsymbol{q}})$ represents passive and active elastic efforts in mass-spring models.

$$\boldsymbol{M}(\boldsymbol{q})\ddot{\boldsymbol{q}} + \boldsymbol{C}(\boldsymbol{q},\dot{\boldsymbol{q}}) + \boldsymbol{E}(\boldsymbol{q},\dot{\boldsymbol{q}})\boldsymbol{q} + \boldsymbol{G}(\boldsymbol{q}) = \boldsymbol{\tau}_m \tag{5}$$

Introducing triangle functions to the differential equation (5), the position vector $\boldsymbol{q}$ can be expressed by a cosine function in time domain [15]. In the equation (6), A is the amplitude of system oscillation and α is the early phase i.e. the initial position of joint. d is the damping coefficient and k is the stiffness coefficient. ω_1 represents the circular frequency which involves the inherent frequency ω_0 and the index p which is determined by $p=d/2m$.

$$q(t) = Ae^{-pt}\cos(\omega_1 t - \alpha) \tag{6}$$

The performances of the elastic actuator depend on the values of damping d and stiffness k. In the movements, k determines the amplitude and frequency while d mainly represents the extent of oscillation and time of reaching equilibriums. Both of them can be adjusted to adapt the dynamic changes.

Comparing (1) and (5), we can discover that the elastic actuator owns an additional elastic item $\boldsymbol{E}(\boldsymbol{q},\dot{\boldsymbol{q}})$ which does not exist in the stiff actuator. In the case that the system input $\boldsymbol{\tau}_m$ is the same, it indicates that the elasticity has the effects of storing and releasing energy in the movements. In other words, the dynamics equations can principally explain the phenomenon of oscillating and damping in theory.

4 Control System

To control the elastic actuator seems to be a hard work since there is not sufficient joint stiffness in the model which leads the link to unexpected movements. And few control law can be proposed to satisfy the demands of smooth and exact trajectories in locomotion. Although the joint stiffness of our actuator is very low for tracking high compliance, the actuation can be operated by applying emulated spring stiffness as feedforward controller to correct the input signals [16]. Assuming that the spring deployed in the actuator has a linear characteristic and the input signals are transformed into Fourier series as sine functions, the system responses can be described by desired stiffness:

$$\boldsymbol{\sigma}_{max} = \frac{\boldsymbol{\rho}_{max}}{2} + \frac{\boldsymbol{\rho}_{min}}{2} + \frac{k_d\left|\boldsymbol{\rho}_{max} - \boldsymbol{\rho}_{min}\right|}{2k}, \boldsymbol{\sigma}_{min} = \frac{\boldsymbol{\rho}_{max}}{2} + \frac{\boldsymbol{\rho}_{min}}{2} - \frac{k_d\left|\boldsymbol{\rho}_{max} - \boldsymbol{\rho}_{min}\right|}{2k} \quad (7)$$

In this equation, k_d represents the desired virtual spring stiffness. Considering the model in figure 1 as 1-DOF pendulum applied with rotary actuator, the link oscillates between limit angles $\boldsymbol{\rho}_{max}$ and $\boldsymbol{\rho}_{min}$ whereas the angles can be extended to $\boldsymbol{\sigma}_{max}$ and $\boldsymbol{\sigma}_{min}$ due to the adjusted spring stiffness.

To operate the system by inputting the desired movements $q(t)$, according to the equation (7), the trajectory of link can be corrected by feedforward controller applied with the desired virtual stiffness technique. Then, the desired motor rotations $\boldsymbol{\delta}_d$ and the desired joint positions $\boldsymbol{q}_d$ can be obtained from the adjusted trajectory. However, in dynamic movements, some unexpected deviations are produced due to unpredictable reasons. Thus, the offsets of positions need to be derived from the feedback outputs which are $\hat{\boldsymbol{\delta}} = \boldsymbol{\delta}_d - \boldsymbol{\delta}$ and $\hat{\boldsymbol{q}} = \boldsymbol{q}_d - \boldsymbol{q}$. Defining the spring torques $\boldsymbol{\tau}_s$ and damping torques $\boldsymbol{\tau}_d$ in the elastic actuation, the control torque $\boldsymbol{\tau}$ can be determined:

$$\boldsymbol{\tau} = k(\hat{\boldsymbol{\delta}} - \hat{\boldsymbol{q}}) - d\dot{\boldsymbol{q}} + \boldsymbol{g}(\boldsymbol{q}) = \boldsymbol{\tau}_s - \boldsymbol{\tau}_d + \boldsymbol{g}(\boldsymbol{q}) \quad (8)$$

From equation (8), a simple control structure of the extended elastic actuator can be obtained as depicted in figure 4.

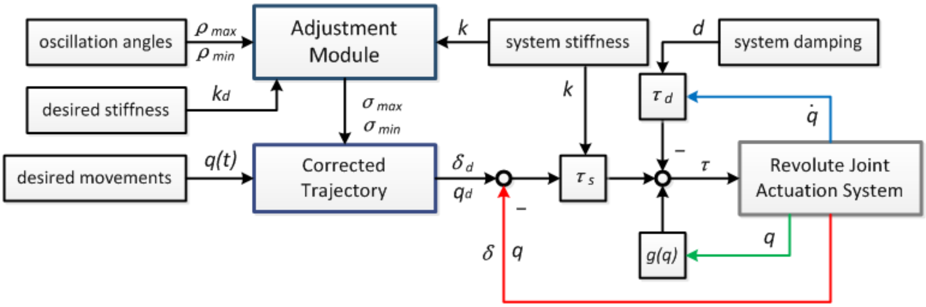

Fig. 4. Schematic of control structure

5 Experiments

5.1 Evaluation of Actuator Model

In order to evaluate the system capacities, we have developed some simulations. After setting up the initial conditions, we apply four different input signals imitating the torques of motor to drive the mechanical structure. Two sine inputs are applied to evaluate the performances of elasticity in time domain while two pulse inputs are expected to provide the opportunities to explore the extra properties of the extended elastic actuator. According to output data gained from the simulations, some plots of experimental results are depicted in figure 5.

In the simulations, the end time is set to *2s* and the peak value of torque is limited under *2.5N·m* according to the inherent characteristics of springs. As illustrated in the figure 5, when the model is driven by the continuous sine torque input, the curves of position and angular velocity appear smooth with high compliance. When the continuous pulse torque input is applied, the positions of joint change smoothly and regularly, though there are some tiny periodical peaks emerging in the plots of angular velocity. Furthermore, when the motor acts the periodical damping motions, the joint starts to oscillate promptly until to the equilibrium positions. It indicates that there are no distinct differences in the results of damping sine input and damping pulse input. However, it is significant to note that the frequencies of system movements are greatly decreased comparing with the frequencies of input signals. These consequences demonstrate that our elastic actuator has excellent performances in buffering and absorbing peak shocks independent of the types of input signals.

5.2 Simulation of Robot Arm

In addition, applying with the extended elastic actuator developed in this paper, we introduce the musculoskeletal structure to construct a 2-segmented robot arm based on the principals of MRS. In the mechanism, the *shoulder* and *elbow* joints are actuated by motors deployed with torsion springs. Passive extension springs are applied to restrict the movement ranges of each segment. These springs can be

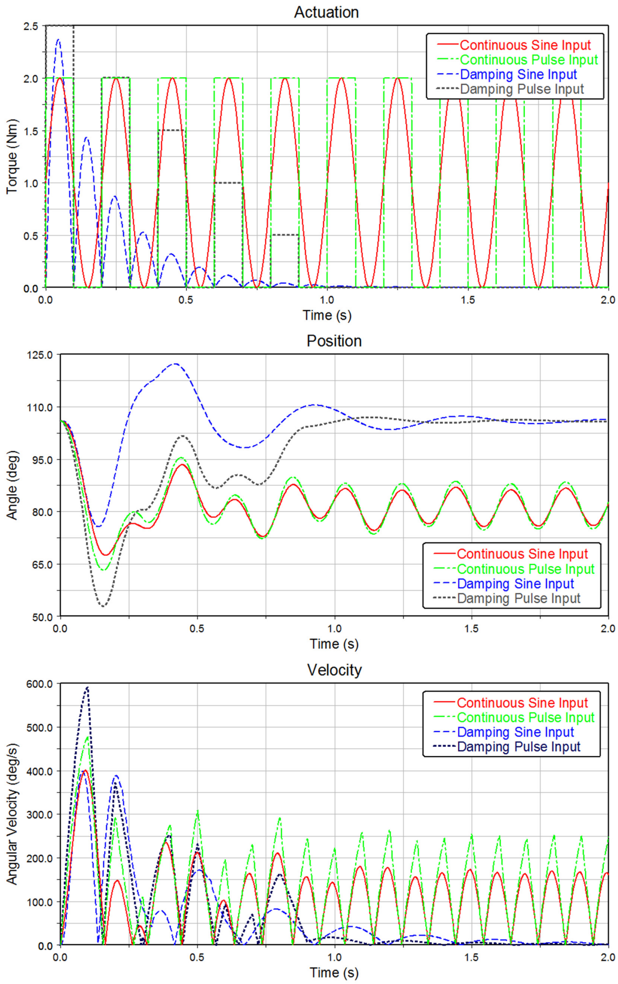

Fig. 5. Result plots of applied torque inputs (*top*), joint angular positions (*center*) and angular velocities (*bottom*)

regarded as a series of muscles including mono-articular muscles as *brachialis* and *deltoid*, bi-articular muscles as *biceps* and *triceps* muscles of arm. This bionic robot is expected to act compliant movements and human-like behaviors based on the design of muscle-tendon system. To estimate the capabilities of MRS, we prepare and manage a simulation to command the arm to follow the desired movements which contain the trajectory of pushing a door as illustrated in figure 6.

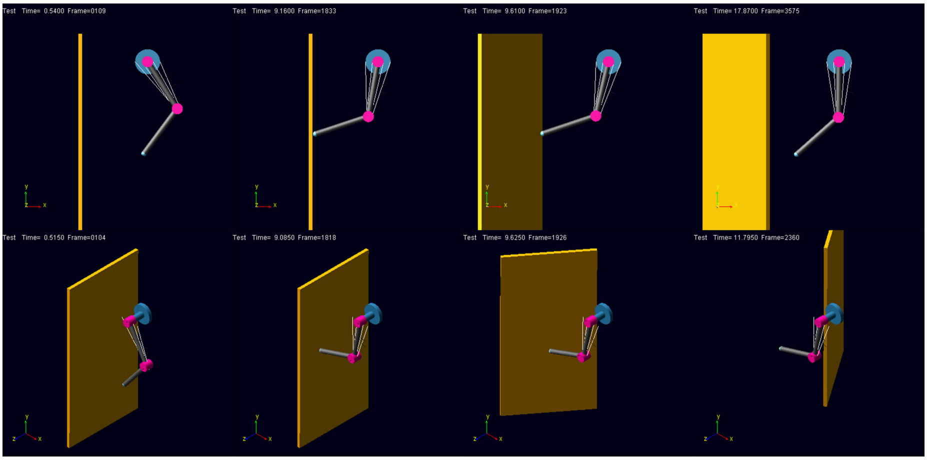

Fig. 6. Sequence pictures of operation in side view (*top*) and isometric view (*bottom*)

Some preparations are considered before the experiment acts. The stiffness and damping coefficients of the torsion springs mounted on motors and the passive extension springs attached to the arm are determined from the practice. The duration time of experiment is defined in *30s* while the steps of simulating computation are set to *6000*. By utilizing the control structure depicted in figure 4, inputting the desired trajectories of two joints to the system, the actual positions of *shoulder* and *elbow* can be detected and plotted as depicted in figure 7. The sequence pictures of operation are generalized in figure 6. The operation of robot arm performs an obvious compliant locomotion and flexibility to decrease the impacts. However, there are still some deviations in dynamic movements especially in the effects of interacting forces between the end-effector and door. As this nonlinear elastic MRS is difficult to execute, further related studies will be promoted and discussed.

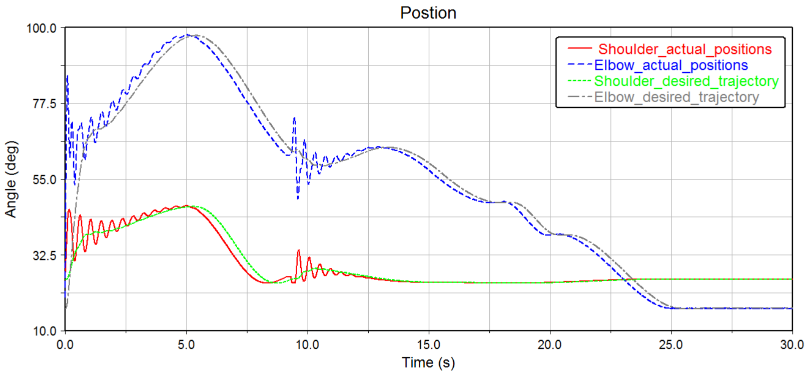

Fig. 7. Desired joint trajectories and plots of variable positions during operation

6 Conclusion

Since elastic actuators have the benefits on enhancing the compliance in locomotion and avoiding the damages forced to motors, in this paper, we successfully develop an extended elastic actuator based on the principals of original SEA and muscle-tendon model. The model is feasible and applicative in constructing the robot in reality. For the description of elastic actuation and the methods of control policy, the dynamics equations are presented so that elasticity applied in the system can be expressed and calculated mathematically. In the case that low stiffness in joint results in undesirable behaviors, a feedforward controller is promoted to decrease the influences. Through the experiments, the results provide sufficient evidences to prove the practicality and feasibility of our extended elastic actuator.

Although this type of elastic actuator is very suitable for MRS, control problem is still existed to cause variety of errors during the operation. MRS is an extremely nonlinear system which determines the complex control structure design. Hence the studies on reducing the complication of control method remain the most important directions in the future. We expect to go further in the research area of elastic mechanism in robots and follow the developments of bionics to improve the compliance of robot locomotion. And more robots in MRS like bipedal robots can be promoted to apply the extended elastic actuator for expected performances.

Acknowledgements. This study has been supported in part by Engineering Training Center in Dalian University of Technology and IT+Robotics Spin-off Company of University of Padua.

References

1. Klug, S., Lens, T., von Stryk, O., Möhl, B., Karguth, A.: Biologically Inspired Robot Manipulator for New Applications in Automation Engineering. In: Proc. of Robotik 2008, Nr. 2012, VDI Wissensforum GmbH (June 2008)
2. Hayward, V.: Design of a Hydraulic Robot Shoulder Based on a Combinatorial Mechanism. In: Yoshikawa, T., Miyazaki, F. (eds.) Experimental Robotics III. LNCIS, vol. 200, pp. 295–309. Springer, Heidelberg (1994)
3. Salisbury, K., Eberman, B., Levin, M., Townsend, W.: The Design and Control of an Experimental Whole-Arm Manipulator. In: Proc. 5th Int. Symp. on Robotics Research, pp. 233–241 (February 1991)
4. Förg, D., Ulbirch, H., Seyfarth, A.: Study of a Bipedal Robot with Elastic Elements. In: 41st Int. Symp. on Robotics/6th German Conf. on Robotics, pp. 689–695 (June 2010)
5. Hollander, K., Ilg, R., Sugar, T., Herring, D.: An Efficient Robotic Tendon for Gait Assistance. Journal of Biomechanical Engineering 128(5), 788–791 (2006)
6. Lens, T., Kunz, J., Trommer, C., Karguth, A., von Stryk, O.: BioRob-Arm: A Quickly Deployable and Intrinsically Safe, Light-Weight Robot Arm for Service Robotics Applications. In: 41st Int. Symp. on Robotics/6th German Conf. on Robotics, pp. 905–910 (June 2010)
7. Tomei, P.: A Simple PD Controller for Robots with Elastic Joints. IEEE Transactions on Automatic Control 36, 1208–1213 (1991)

8. Pratt, G., Williamson, M.: Series Elastic Actuators. In: IEEE/RSJ Int. Conf. on Intelligent Robots and Systems, vol. 1, pp. 399–406 (1995)
9. Robinson, D., Pratt, J., Paluska, D., Pratt, G.: Series Elastic Actuator Development for a Biomimetic Walking Robot. In: IEEE/ASME Int. Conf. on Advanced Intelligent Mechatronics, pp. 561–568 (1999)
10. Van Ham, R., Sugar, T., Vanderborght, B., Hollander, K., Lefeber, D.: Review of Actuators with Passive Adjustable Compliance/Controllable Stiffness for Robotic Applications. IEEE Robotics and Automation Magazine 16(3), 81–94 (2009)
11. Radkhah, K., Lens, T., Seyfarth, A., von Stryk, O.: On the Influence of Elastic Actuation and Monoarticular Structures in Biologically Inspired Bipedal Robots. In: Proc. 2010 IEEE Int. Conf. on Biomedical Robotics and Biomechatronics, pp. 389–394 (2010)
12. Vanderborght, B., Van Ham, R., Lefeber, D., Sugar, T., Hollander, K.: Comparison of Mechanical Design and Energy Consumption of Adaptable, Passive-compliant Actuators. The Int. Journal of Robotics Research 28, 90–103 (2009)
13. Zajac, F.: Muscle and Tendon Properties Models Scaling and Application to Biomechanics and Motor Control. Critical Reviews in Biomedical Engineering 17(4), 359–410 (1989)
14. Spong, M.: Modeling and Control of Elastic Joint Robots. ASME Journal of Dynamic Systems, Measurement and Control 109, 310–319 (1987)
15. Edwards, C., Penney, D.: Differential Equations and Boundary Value Problems Computing and Modeling, 4th edn. Pearson Prentice Hall (2007)
16. Radkhah, K., Kurowski, S., Lens, T., von Stryk, O.: Compliant Robot Actuation by Feedforward Controlled Emulated Spring Stiffness. In: Ando, N., Balakirsky, S., Hemker, T., Reggiani, M., von Stryk, O. (eds.) SIMPAR 2010. LNCS, vol. 6472, pp. 497–508. Springer, Heidelberg (2010)

Towards Long-Term Collective Experiments

Florian Vaussard, Philippe Rétornaz, Steven Roelofsen, Michael Bonani,
François Rey, and Francesco Mondada

EPFL – STI – LSRO, Station 9,
1015 Lausanne, Switzerland
florian.vaussard@epfl.ch

Abstract. It is often challenging to manage the battery supply when dealing with a fleet of mobile robots during long experiments. If one uses classical recharge stations, then agents are immobilized during the whole recharge process. In this study, we present a novel approach that employs a battery pack swapping station. Batteries are charged in a rotating barrel, and the robots dock only for the time of the hot-swap process. We attained an unavailability time of only 40 seconds, with a success rate of 100 % on a total of 46 trials. Experiments above 8 hours are performed in three arenas with different configurations, which proves the relevance of our approach.

1 Introduction

Collective robotics is a field generating a high academic interest. Using several robots has been proposed as an elegant way to solve complex problems, that are impossible for only one entity. We can cite, for example, experiments in collective gap crossing [8], collective construction [13], or cooperative localization and grasping of objects [3].

In practice, the main heel of collective robotics is the dependency on electric power, each autonomous entity usually having its own battery. The realisation of complex experiments often requires runs of several hours or even days. A classic solution is to use a charging station, which requires a downtime of the agents during the corresponding period. Often, to avoid this downtime, one person constantly maintains the setup. Otherwise, some laboratories have heavy installations consisting of a floor powering system, which is very expensive to build and to maintain. A new solution is needed to maintain an availability close to 100 %.

In this study, we will demonstrate a novel solution for autonomous robots in the form of automatic hot-swapping of batteries. The design relevance is validated through a simulation, and the final prototype is tested under experimental conditions, totalling more than 24 hours of work with 3 robots operating simultaneously.

2 Prior Works

Batteries and other storage devices have always limited mobile devices. The problem of autonomously recharging a robot, or a fleet of robots, has already been extensively

S. Lee et al. (Eds.): Intelligent Autonomous Systems 12, AISC 194, pp. 683–692.
springerlink.com

studied. Several designs have been considered and tested [2,5,9,10,11,12]. The problem was also studied using *Unmanned Aerial Vehicles* (UAV) [4,16]. However, with such an approach, the robots are unusable during the whole recharge process.

In the literature, battery swapping is often mentioned as a way to get rid of the charging time [17,19]. But practically speaking, few working implementations exist. To the best of our knowledge, authors of [18] are the first to realise a proof of concept using an autonomous robot. Their robot is able to enter the charging dock by following a magnetic tape, and the exchange process takes 45 seconds. However, the design is complex and is limited to two charging units. No other data is provided.

The work of [15] introduced the first prototype of a swapping system for an autonomous helicopter. It is able to recharge up to 8 batteries in parallel using related health management algorithms. No experiment yet proves the viability of the solution. Finally, several modules were developed and discussed in [14] for another UAV system, but no complete prototype is currently available.

Finally, some researchers used an arena with a conductive floor to provide a continuous power supply [6]. This is a big investment in terms of time and money, and requires hardware adaptations. Moreover, the floor has to be flat, which limits the relevance to a subset of experiments.

3 Simulation

We first modelled the battery swapping system to assess the relevance of our approach. Let us take N_r robots, each one having an autonomy of T_r seconds. We aim to build a charger capable of recharging N_c batteries in parallel, each battery taking T_c seconds to charge. At the equilibrium, the maximum number of robots we can sustain is approximated by the conservation law:

$$N_r = N_c \cdot \frac{T_c}{T_r} \quad . \tag{1}$$

However, this is an idealization and does not account for the worst case scenario. To identify the requirements for the charger, we modelled T_r and T_c as Gaussian distributions. Parameters are given in Table 1 and are used to match the figures encountered in practice. A discrete time simulation is performed under Matlab and computes, at each time step, the maximum number of batteries simultaneously in charge. The result is shown in Fig. 1.

For our first design, the target is fixed at 15 slots, due to the physical space constraints imposed by the size of the battery packs. According to this simulation, this choice allows up to 5 robots to run simultaneously.

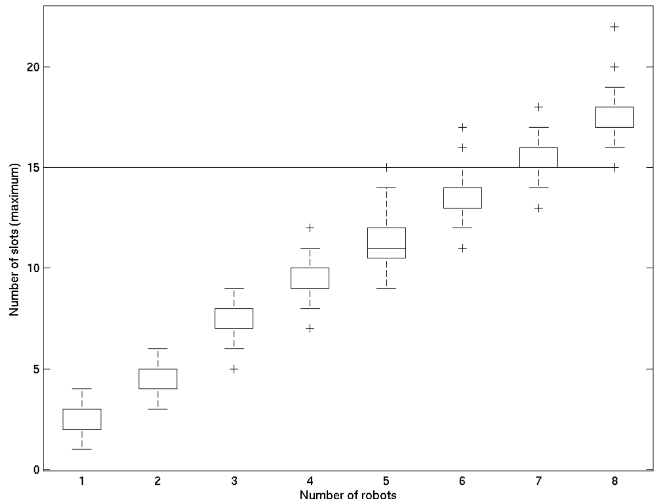

Fig. 1. Number of charging slots needed, with respect to the number of robots used during the experiment. The horizontal line is the targeted design (15 slots).

Table 1. Simulation parameters, modelled as Gaussian distributions

		Time	
		$\hat{T}$ (s)	σ (s)
Autonomy	T_r	10800	3600
Recharge time	T_c	19800	1800

4 Hardware Design

4.1 Mobile Robotic Platform

The robotic platform was designed with battery hot-swapping as a key feature from the beginning. We identified three requirements to ease long-term robotic swarm experiments: 1) online battery hot-swap, 2) automated battery exchange, and 3) compact design.

The first requirement is motivated as follows. If the robot must be switched off to swap its battery, then long-term experiments will be difficult. In most of the experiments, a wireless link to a supervision computer must be kept for logging or management purposes. The embedded computer must thus stay online for the whole experiment, keeping its state and all network connections opened.

The second requirement is of practical interest. If the experiments are run for several hours, or even days, then it is not efficient to manually swap the battery. Moreover, since we want to swap the battery while the system is running, we need a high level of

(a) (b) (c)

Fig. 2. Hardware design. (a) The marXbot robot. (b) The swappable battery pack (inside view). (c) The charging station with a docked marXbot.

determinism. A human is not able to achieve such reliability, especially in an experiment that lasts for several hours.

The third requirement seems obvious but is critical in small mobile robots. We cannot afford to have a big and bulky system, as it would increase the size and the weight of the robot. For collective experiments, it is a critical point, as many robots are used concurrently in a limited space.

The marXbot robot, pictured in Fig. 2(a), was designed with these requirements in mind [1]. Both specific mechanical and electronic designs are needed to enable battery hot-swapping.

4.1.1 Mechanical Design

The battery is located at the centre of the robot and is easily accessible from the backside. Moreover, the battery has a specific grabbing artefact that enables mechanical grasping. The battery is placed as low as possible, enhancing the stability by bringing down the centre of mass. The electrical contact is performed through lateral sliding contacts. When the battery is fully inserted, the contact is automatically established without requiring any specific connection mechanism.

4.1.2 Electronic Design

The electronics need to cope with the battery suddenly disappearing while running. This was resolved by using a backup supply. In our case, two 2.5 V / 10 F serially connected super-capacitors are embedded in the marXbot. They can power the vital subsystems, including the embedded computer, for 15 seconds. Two power buses are implemented throughout the robot. The first one is directly connected to the battery, typically for the motors and other non-critical electronics. The second bus is dynamically switched between the battery and the super-capacitor's supply.

A series of dedicated electronics are in charge of the switching by using an infrared sensor to detect the battery's removal. These electronics ensure a deterministic switching time, which provides a reliable power source. The system is fully autonomous and does not require any supervision.

The battery is a single cell 10 Ah lithium-polymer battery, as shown in Fig. 2(b). The protection circuit is embedded in the plastic housing and the electrical connection is made using two gold-plated sideways printed circuit boards.

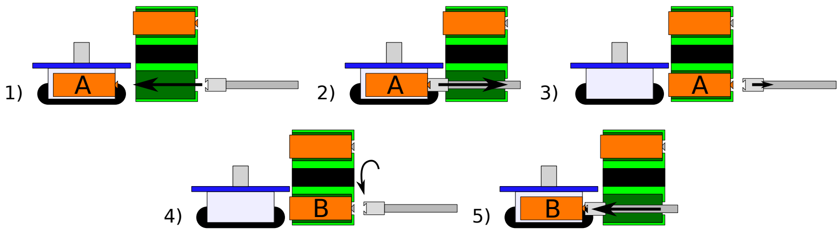

Fig. 3. Working principle of the battery exchanger

4.2 Robotic Charger

The robotic charger is wheel-shaped, with the charging slots distributed around the barrel. The main design goal was to fit as many batteries as possible in one station in order to sustain the operation of several robots at the same time. In order to let the experiment run unattended, the reliability was also an important driving criterion. The final station is shown in Fig. 2(c).

4.2.1 Mechanical Design

The mechanical design is quite straightforward. A rotating barrel can hold and recharge 15 batteries in parallel. Two linear arms are placed on each side of the docking bay. When the robot arrives in front of the charger, the arms centre the robot and hold it firmly in place. A motorized gripper grasps the battery inside the robot, pulls it out of the mobile robot and brings it in the barrel. It then lets the barrel rotate, and then pushes back a freshly charged battery. There are a total of 5 degrees of freedom. A diagram of the complete sequence is shown in Fig. 3.

4.2.2 Electronic Design

The 5 motors are controlled by several microcontrollers. The swapping state machine is entirely executed on the microcontrollers. The synchronization among the microcontrollers is performed through a CAN bus using the Aseba event-based framework [7]. Each slot has independent charging and monitoring electronics, ensuring a safe operation. Each battery is charged at 2.5 A under 4.2 V. The total peak power consumption is about 160 W.

4.3 High Level Design

The swapping station is connected to a supervision computer. Each robot taking part in the experiment is also connected to the computer through a Wi-Fi connection.

When a robot needs to get a fresh battery, it asks the supervision computer to get a lock on the charger. If no other robot is using the charger, then the computer grants the permission and the robot starts searching for the charger. If the charger is already in use, then the robot is put on a waiting list and has to wait until the supervisor gives it the lock.

As the arena used in this experiment is quite small, a search based on a wall-following method is used to find the swapping station. The method is able to detect loops, like isolated obstacles, as shown in Fig. 5(a). This method proved to be robust in our case. The location of the charging bay is marked with an ISO-15693 RFID tag on the ground, so the robot can detect when it has to start the docking sequence.

Other methods should be envisioned in more complex environments, such as visual feature detection or range-based *Simultaneous Localization And Mapping* (SLAM). The marXbot has the necessary sensors and is directly suitable for both approaches.

5 Results

We conducted two sets of experiments. The first one assesses the reliability and performance of the swapping mechanism. For this purpose, several consecutive swaps are conducted with the robot starting next to the station.

The second experiment is used to simulate a longer experiment, where several robots are covering the arena using a random walk. They autonomously go to the swapping station when the available energy reaches a low threshold.

Both experiments were run without any human interaction, except to start and stop the experiments.

5.1 Battery Replacement

In this experiment, we ran 24 battery swaps. The success rate was 100 %. The time required by each step of the process is shown in Fig. 4. The first step is the alignment and grasping of the robot by the station. During the second step, the robot runs without its battery on the backup supply. The charging station needs only 10 to 11 seconds to swap the battery. The entire process takes less than the 15 seconds provided by the embedded backup supply. The third step is the release of the robot, which is considerably faster than the others steps.

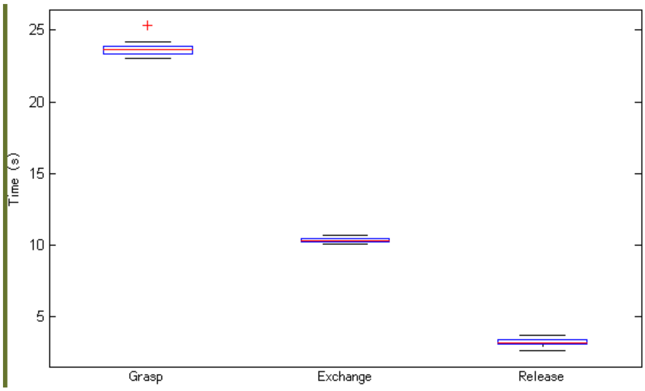

Fig. 4. Validation experiment: break down of the time required by each step of the battery replacement process

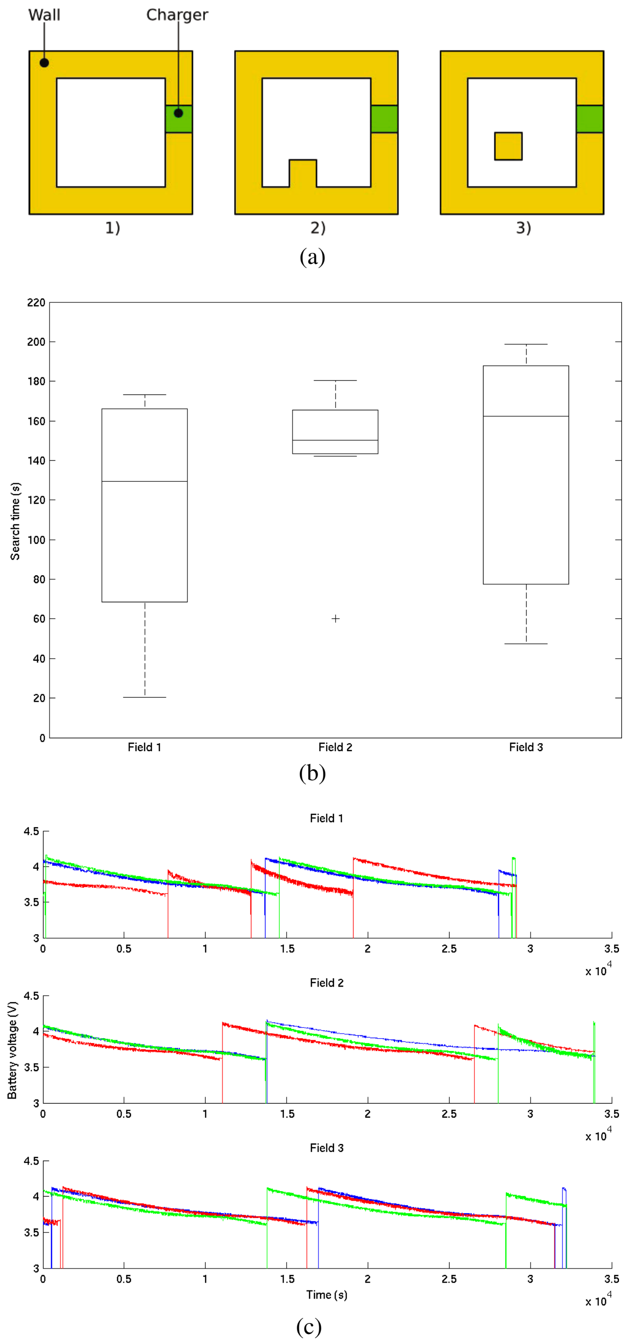

Fig. 5. The long-term experiments: (a) The three test fields. (b) Time to find and reach the charger on each field. (c) Voltage for each robot, as a function of the time and for each field.

We can already draw a positive conclusion based on these results. The battery swap is indeed reliable and robust. The total time needed to change the battery is less than 40 seconds, while the robot runs only 10 seconds on the super-capacitors. This is fast enough to keep the ARM processor running and the Wi-Fi connection alive.

5.2 Long Experiment

We ran 3 long experiments, each one lasting more than 8 hours. During these experiments, three robots were moving randomly in a 2x2 m arena. The configuration of the arena was changed between each experiment, as shown in Fig. 5(a). In order to maximize the number of battery swaps, we decided to artificially limit the cut-off voltage to 3.6 V.

We recorded the time needed to find the charger based on our naive wall-following approach (Fig. 5(b)). This method takes a considerable amount of time, in the order of several minutes. However, since the robots have an uptime of about 2-3 hours per battery, the 200 seconds needed to reach the charger are negligible. Thus, the wall-following method is perfectly justified in this situation, as it is robust and does not need any powerful computing resources.

Fig. 5(c) shows the results of the experiments. Each line corresponds to the voltage of individual robots. The robots successfully shared the same charger and were able to run for more than 8 hours without any failure. Each robot had its battery swapped several times and no power outages were experienced. In total, 22 successful swaps were performed.

6 Conclusion

We showed the possibility of autonomously hot-swapping the batteries of a small mobile robot. The achieved performance and reliability enables the use of small mobile robots during long term experiments. This opens the possibility of potential new research avenues on collective experiments.

This study shows that it is possible to have virtually infinite autonomy with only a minimal impact on the performed experiment. This is achieved through the careful design of the marXbot robot and the charger.

The next step is to use several chargers and a swarm of robots in a larger area. This would require better algorithms to share the resource and localize the charger. However, the proposed hardware remains perfectly valid.

Acknowledgement. This research was supported by the Swiss National Science Foundation through the National Centre of Competence in Research Robotics. This work was also supported by the Swarmanoid and Ascens projects, both funded by the Future and Emerging Technologies programme (IST-FET) of the European Community, respectively under grants 022888 and 257414. The information provided is the sole responsibility of the authors and does not reflect the Community's opinion. The Community is not responsible for any use that might be made of data appearing in this publication.

References

1. Bonani, M., Longchamp, V., Magnenat, S., Rétornaz, P., Burnier, D., Roulet, G., Vaussard, F., Bleuler, H., Mondada, F.: The marXbot, a miniature mobile robot opening new perspectives for the collective-robotic research. In: IROS, pp. 4187–4193. IEEE (2010)
2. Cassinis, R., Tampalini, F., Bartolini, P., Fedrigotti, R.: Docking and charging system for autonomous mobile robots. Department of Electronics for Automation, University of Brescia, Italy (2005)
3. Dorigo, M., Floreano, D., Gambardella, L., Mondada, F., Nolfi, S., Baaboura, T., Birattari, M., Bonani, M., Brambilla, M., Brutschy, A., et al.: Swarmanoid: a novel concept for the study of heterogeneous robotic swarms. Tech. rep., Technical Report TR/IRIDIA/2011-014, IRIDIA, Université Libre de Bruxelles, Brussels, Belgium (2011)
4. Kemper, F.P., Suzuki, K.A.O., Morrison, J.R.: UAV Consumable Replenishment: Design Concepts for Automated Service Stations. Journal of Intelligent and Robotic Systems 61(1-4), 369–397 (2011)
5. Kim, K., Choi, H., Yoon, S., Lee, K., Ryu, H., Woo, C., Kwak, Y.: Development of docking system for mobile robots using cheap infrared sensors. In: 1st International Conference on Sensing Technology, Palmerston North, New Zealand (2005)
6. Krieger, M.J.B., Billeter, J.B.: The call of duty: Self-organised task allocation in a population of up to twelve mobile robots. Robotics and Autonomous Systems 30(1-2), 65–84 (2000)
7. Magnenat, S., Rétornaz, P., Bonani, M., Longchamp, V., Mondada, F.: ASEBA: A Modular Architecture for Event-Based Control of Complex Robots. IEEE/ASME Transactions on Mechatronics (2010)
8. Mondada, F., Pettinaro, G., Guignard, A., Kwee, I., Floreano, D., Deneubourg, J., Nolfi, S., Gambardella, L., Dorigo, M.: SWARM-BOT: A new distributed robotic concept. Autonomous Robots 17(2), 193–221 (2004)
9. Parker, G., Georgescu, R., Northcutt, K.: Continuous power supply for a robot colony. In: Proceedings of World Automation Congress 2004, vol. 15, pp. 279–286. IEEE (2004)
10. Parker, G.B., Zbeda, R.S.: Controlled use of a robot colony power supply. In: 2005 IEEE International Conference on Systems, Man and Cybernetics, vol. 4, pp. 3491–3496. IEEE (2005)
11. Silverman, M., Jung, B., Nies, D., Sukhatme, G.: Staying alive longer: Autonomous robot recharging put to the test. Center for Robotics and Embedded Systems (CRES) Technical Report CRES 3, 015 (2003)
12. Silverman, M.C., Nies, D., Jung, B., Sukhatme, G.S.: Staying Alive: A Docking Station for Autonomous Robot Recharging.. In: ICRA, pp. 1050–1055. IEEE (2002)
13. Stroupe, A.W., Okon, A., Robinson, M.L., Huntsberger, T., Aghazarian, H., Baumgartner, E.T.: Sustainable cooperative robotic technologies for human and robotic outpost infrastructure construction and maintenance. Auton. Robots 20(2), 113–123 (2006)
14. Suzuki, K.A.O., Filho, P.K., Morrison, J.R.: Automatic Battery Replacement System for UAVs: Analysis and Design. Journal of Intelligent and Robotic Systems 65(1-4), 563–586 (2012)
15. Swieringa, K.A., Hanson, C.B., Richardson, J.R., White, J.D., Hasan, Z., Qian, E., Girard, A.: Autonomous battery swapping system for small-scale helicopters. In: ICRA, pp. 3335–3340. IEEE (2010)
16. Valenti, M., Bethke, B., Dale, D., Frank, A.A., McGrew, J.S., Ahrens, S., How, J.P., Vian, J.: The MIT Indoor Multi-Vehicle Flight Testbed. In: ICRA, pp. 2758–2759. IEEE (2007)

17. Wang, H., Xu, H., Jones, A.: Crucial Issues in Logistic Planning for Electric Vehicle Battery Application Service. In: 2010 International Conference on Optoelectronics and Image Processing (ICOIP), vol. 1, pp. 362–366. IEEE (2010)
18. Wu, Y., Teng, M., Tsai, Y.: Robot docking station for automatic battery exchanging and charging. In: IEEE International Conference on Robotics and Biomimetics, ROBIO 2008, pp. 1043–1046. IEEE (2009)
19. Yang, Y., Ding, X., Zhu, J.: Discuss Charging-Discharging and Sale Technology of the Electric Vehicle. Advanced Materials Research 347, 3908–3914 (2012)

Control of a Trident Steering Walker - Design of Motion Parameters Based on a Propulsion Transfer Function

Hiroaki Yamaguchi, Toshiyuki Takeda, and Atsushi Kawakami

5-10-1 Fuchinobe, Chuo-ku, Sagamihara-shi, Kanagawa 252-5258, Japan
{yamaguchi,takeda,kawakami}@robotics.it.aoyama.ac.jp

Abstract. This paper introduces and describes a novel design methodology of the motion parameters for an undulatory locomotor: a trident steering walker based on a performance index: a propulsion transfer function. The undulatory locomotor transforms its periodic changes of shape into its movement, and it has a singular attitude in which it cannot perform such transformation. In order to prevent the locomotor from having the singular attitude, we propose to design the motion parameters based on the propulsion transfer function which is a metric of the attitude from the singular attitude. The propulsion transfer function is defined in kinematics although the motion of the locomotor should be evaluated in dynamics, so that we propose to measure the propulsion force of the locomotor in a dynamics simulator and to analyze the relationship between the propulsion transfer function defined in kinematics and the propulsion force measured in dynamics. We demonstrate that it is effective to design the motion parameters based on the propulsion transfer function.

1 Introduction

The design of mobile mechanisms and the establishment of methods for their control are important issues of research in mechanical engineering. This paper introduces and describes a novel design methodology of the motion parameters for an undulatory locomotor: a trident steering walker [8] [9] [10] based on a performance index: a propulsion transfer function. Undulatory locomotion is transformation of periodic changes in shape into movement. Heretofore, there have been proposed mobile mechanisms which move by undulatory locomotion, such as a snake-like robot [3], a roller walker [4], a snake board [7], a roller racer [6], a rollerblading robot [1] and a RoboTrikke [2]. In order to achieve stable operation of these undulatory locomotors, a closed loop control method such as a feedback control method for causing them to follow desired paths is thought to be necessary.

The trident steering walker is an undulatory locomotor designed so that its kinematical equation can be converted into a chained form, which is a canonical form. Based on this chained form, a feedback control method [9] [10] is proposed by one of the authors which enables the locomotor to follow any path whose curvature is two times differentiable by transforming the periodic driving of its three joints into its movement through the periodic operation of its four steering systems whose wheels are all passive. One particular problem is that the trident steering walker has a singular attitude in which the locomotor cannot transform driving its three joints into its movement, i.e., in which

S. Lee et al. (Eds.): Intelligent Autonomous Systems 12, AISC 194, pp. 693–705.
springerlink.com

the locomotor cannot be propelled. Kinematics of the trident steering walker specifically describes the singular attitude. There is a singular attitude in which all the steering wheels of the locomotor are parallel to each other. Also, there is a singular attitude in which all the steering wheels have the same revolution center in a two-dimensional plane. However, dynamics of the locomotor is required to describe how the locomotor having the singular attitude decelerates by resistance, e.g., rolling resistance of wheels.

In order to evaluate the motion of the locomotor dynamically, we measure the resultant force of the projections of the forces working on the base of the locomotor in its moving direction which indicates the propulsion force in a commercial multibody dynamics simulator, LMS Virtual. Lab Motion where mass, moment of inertia of each part, virtical stiffness of each wheel, its damping constant, rolling resistance, cornering stiffness and a friction coefficient between each wheel and the ground are totally considered. It is necessary to design the motion parameters of the trident steering walker in such a manner as to prevent the locomotor from having the singular attitude. To this end, one of the authors has defined a metric of the attitude from the singular attitude in kinematics [8] and, in this paper, we use this metric as a performance index: a propulsion transfer function on designing the motion parameters of the locomotor. Especially, we analyze the relationship between the propulsion transfer function defined in kinematics and the propulsion force measured in dynamics, and we demonstrate that it is effective to design the motion parameters based on the propulsion transfer function.

2 Structure of Trident Steering Walker

The trident steering walker in Fig.1 has an equilateral triangular base on which objects to be carried can be loaded. A steering system is attached at the barycenter of the base. Links are connected throuth joints at each corner of the base, and a steering system is attached at the midpoint of each link. Each of the wheels on these four steering systems is passive. The trident steering walker can transform the periodic driving of its three joints into (a) the movement or (b) the rotation of the base through the periodic operation of its four steering systems.

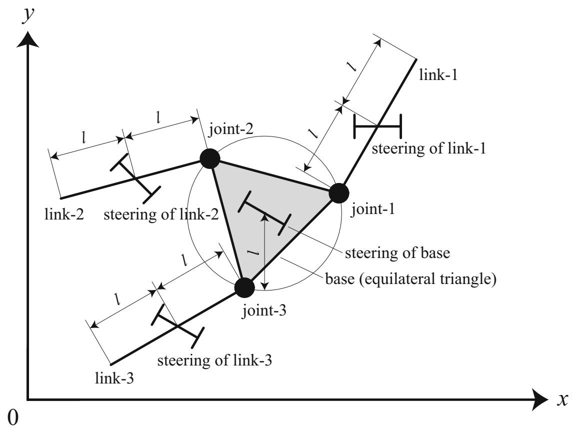

Fig. 1. A Trident Steering Walker

3 Trident Steering Walker with Virtual Mechanical Elements

As shown in Fig.2, a virtual axle, a virtual link attached to the virtual axle and a virtual steering system attached at the end of the virutal link are defined. Another virtual steering system attached at the midpoint between the steering axis of the steering system at the barycenter of the base and the rotational axis of the first joint is defined. Consequently, the kinematical equation can be converted into a five-chain, single-generator chained form [9] [10].

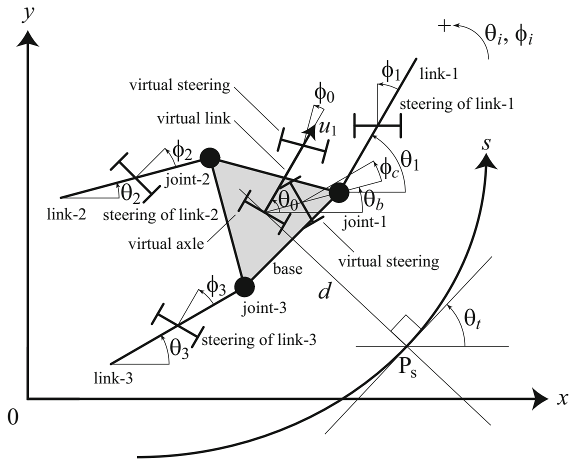

Fig. 2. A Trident Steering Walker with Virtual Mechanical Elements

4 Path Following Motion

The path-following motion is motion of causing the barycenter of the equilateral triangular base to move along the path while controlling the orientation of the base relative to the orientation of the tangent of the path at the barycenter [9] [10]. When the barycenter of the base deviates from the path, a point $\mathbf{P_s}$ on the path that gives the position of the barycenter of the base relative to the path is determined as described below [9] [10]. The "tangent of the path at the point $\mathbf{P_s}$" and the "straight line connecting the point $\mathbf{P_s}$ and the barycenter of the base" are always orthogonal. The position of the point $\mathbf{P_s}$ is taken to be s on the coordinate axis defined along the path. The position of the barycenter of the base is taken to be d on the other coordinate axis which is the straight line orthogonal to the tangent of the path at the point $\mathbf{P_s}$ (see Fig.2). The orientation with respect to the x-axis of the tangent of the path at the point $\mathbf{P_s}$ is represented as an angle θ_t. At this time, an orientation θ_{p0} of the virtual link relative to the orientation of the tangent of the path at the point $\mathbf{P_s}$, a relative orientation θ_{pb} of the base, and relative orientations θ_{p1}, θ_{p2} and θ_{p3} of the links 1-3 are given as: $\theta_{p0} = \theta_0 - \theta_t$, $\theta_{pb} = \theta_b - \theta_t$, $\theta_{pi} = \theta_i - \theta_t$, $i = 1,2,3$. A derivative $c(s)(=d\theta_t/ds)$ with respect to s of the angle θ_t which represents the orientation of the tangent of the path at the point $\mathbf{P_s}$ is the curvature of the path. In this control method, the position d of the barycenter of the base relative to the point

$\mathbf{P_s}$ on the path and the orientation θ_{p0} of the virtual link relative to the orientation of the tangent of the path at the point $\mathbf{P_s}$ both are converged into zero, and the relative orientation θ_{pb} of the base is converged into a desired value θ_{pbd}.

5 Kinematical Equation

5.1 Kinematical Equation of Trident Steering Walker

This subsection describes the kinematical equation in a Cartesian coordinate system of the trident steering walker shown in Fig.1. The kinematical equation is derived in Eqs.(1) and (2) as:

[A] $\|\cos(\theta_b + \phi_b)\| \geq \frac{1}{\sqrt{2}}$:

$$\hat{A}\begin{pmatrix} \dot{x}_b \\ \dot{\theta}_b \end{pmatrix} = \hat{B}\begin{pmatrix} \dot{\psi}_1 \\ \dot{\psi}_2 \\ \dot{\psi}_3 \end{pmatrix}, \tag{1}$$

$$\dot{y}_b = \tan(\theta_b + \phi_b)\dot{x}_b,$$

$$\hat{A} = \begin{pmatrix} \hat{a}_{11} & \hat{a}_{12} \\ \hat{a}_{21} & \hat{a}_{22} \\ \hat{a}_{31} & \hat{a}_{32} \end{pmatrix}, \quad \hat{B} = \mathrm{diag}\,(\hat{b}_{11} \quad \hat{b}_{22} \quad \hat{b}_{33}),$$

$$\begin{aligned} \hat{a}_{11} &= \sin(\theta_1 + \phi_1) - \cos(\theta_1 + \phi_1)\tan(\theta_b + \phi_b), \quad \hat{a}_{12} = -l\cos(\theta_1 + \phi_1 - \theta_b) - l\cos\phi_1, \\ \hat{a}_{21} &= \sin(\theta_2 + \phi_2) - \cos(\theta_2 + \phi_2)\tan(\theta_b + \phi_b), \quad \hat{a}_{22} = l\cos(\theta_2 + \phi_2 - \theta_b + \tfrac{1}{3}\pi) + l\cos\phi_2, \\ \hat{a}_{31} &= \sin(\theta_3 + \phi_3) - \cos(\theta_3 + \phi_3)\tan(\theta_b + \phi_b), \quad \hat{a}_{32} = l\cos(\theta_3 + \phi_3 - \theta_b - \tfrac{1}{3}\pi) + l\cos\phi_3, \end{aligned}$$

$$\hat{b}_{11} = l\cos\phi_1,\ \hat{b}_{22} = -l\cos\phi_2,\ \hat{b}_{33} = -l\cos\phi_3.$$

[B] $\|\sin(\theta_b + \phi_b)\| > \frac{1}{\sqrt{2}}$:

$$\check{A}\begin{pmatrix} \dot{y}_b \\ \dot{\theta}_b \end{pmatrix} = \check{B}\begin{pmatrix} \dot{\psi}_1 \\ \dot{\psi}_2 \\ \dot{\psi}_3 \end{pmatrix}, \tag{2}$$

$$\dot{x}_b = \tan(\theta_b + \phi_b)^{-1}\dot{y}_b,$$

$$\check{A} = \begin{pmatrix} \check{a}_{11} & \check{a}_{12} \\ \check{a}_{21} & \check{a}_{22} \\ \check{a}_{31} & \check{a}_{32} \end{pmatrix}, \quad \check{B} = \mathrm{diag}\,(\check{b}_{11} \quad \check{b}_{22} \quad \check{b}_{33}),$$

$$\begin{aligned} \check{a}_{11} &= \sin(\theta_1 + \phi_1)\tan(\theta_b + \phi_b)^{-1} - \cos(\theta_1 + \phi_1), \quad \check{a}_{12} = -l\cos(\theta_1 + \phi_1 - \theta_b) - l\cos\phi_1, \\ \check{a}_{21} &= \sin(\theta_2 + \phi_2)\tan(\theta_b + \phi_b)^{-1} - \cos(\theta_2 + \phi_2), \quad \check{a}_{22} = l\cos(\theta_2 + \phi_2 - \theta_b + \tfrac{1}{3}\pi) + l\cos\phi_2, \\ \check{a}_{31} &= \sin(\theta_3 + \phi_3)\tan(\theta_b + \phi_b)^{-1} - \cos(\theta_3 + \phi_3), \quad \check{a}_{32} = l\cos(\theta_3 + \phi_3 - \theta_b - \tfrac{1}{3}\pi) + l\cos\phi_3, \end{aligned}$$

$$\check{b}_{11} = l\cos\phi_1,\ \check{b}_{22} = -l\cos\phi_2,\ \check{b}_{33} = -l\cos\phi_3.$$

$$\dot{\psi}_i = \dot{\theta}_i - \dot{\theta}_b, \quad i = 1,2,3. \tag{3}$$

A vector $(x_b, y_b)^T$ represents the position of the barycenter of the equilateral triangular base. Angles θ_1, θ_2, θ_3 and θ_b respectively represent the orientations of the links 1-3 and the base. Angles ϕ_1, ϕ_2, ϕ_3 and ϕ_b respectively represent the steering angles of the steering systems on the links 1-3 and on the base. Angular velocities $\dot{\psi}_1$, $\dot{\psi}_2$ and $\dot{\psi}_3$ are the angular velocities of driving the joints 1-3 respectively. It is understood from Eqs.(1) and (2), that there is a singular attitude on performing undulatory locomotion of the trident steering walker shown in Fig.1 as follows.

<<Singular Attitude>>
"The attitude of rank$\hat{A} < 2$ in Eq.(1) or rank$\check{A} < 2$ in Eq.(2) is a singular attitude in which the moving velocity $(\dot{x}_b, \dot{y}_b)^T$ and the rotational angular velocity $\dot{\theta}_b$ of the equilateral triangular base cannot be uniquely determined from the angular velocities $\dot{\psi}_1$, $\dot{\psi}_2$ and $\dot{\psi}_3$ of driving the joints 1-3, i.e., in which the trident steering walker cannot be controlled."

5.2 Kinematical Equation of Trident Steering Walker with Virtual Mechanical Elements

This subsection describes the kinematical equation in the *s*-*d* coordinate system of the trident steering walker with the virtual mechanical elements shown in Fig.2. A vector x shown below is defined as a state variable vector.

$$x = \left(s, d, \phi_0, \theta_{p0}, \phi_c, \theta_{pb}, \phi_1, \theta_{p1}, \phi_2, \theta_{p2}, \phi_3, \theta_{p3}\right)^T. \quad (4)$$

A vector $(s,d)^T$ represents the position of the barycenter of the equilateral triangular base in the *s*-*d* coordinate system. Angles θ_{p0}, θ_{pb}, θ_{p1}, θ_{p2} and θ_{p3} respectively represent the orientations of the virtual link, the base and the links 1-3 relative to the orientation of the tangent of the path at the point $\mathbf{P_s}$. Angles ϕ_0, ϕ_c, ϕ_1, ϕ_2 and ϕ_3 respectively represent the virtual steering angle of the virtual link, the virtual steering angle of the base, and the steering angles of the links 1-3.

When we take the velocity of the virtual link to be u_1, the kinematical equation which is the time derivative $\dot{x}$ of the state variable vector x is derived as:

$$\dot{x} = \Sigma_{i=1}^{6} g_i(x) u_i. \quad (5)$$

Components of $g_i(x)$, $i = 1, 2, \cdots, 6$ in Eq.(5) are given in the paper [9]. Five control inputs u_2, u_3, u_4, u_5 and u_6 in Eq.(5) are the virtual steering angular velocity of the virtual link, the virtual steering angular velocity of the base, and the steering angular velocities of the links 1-3, respectively. Obviously, the velocity u_1 of the virtual link is not a control input. This u_1 is determined so that Eq.(6) is satisfied when the angular velocities $\dot{\psi}_1$, $\dot{\psi}_2$ and $\dot{\psi}_3$ that drive the joints 1-3 are taken to be angular velocity inputs v_1, v_2 and v_3.

$$\dot{\psi}_i = \dot{\theta}_{pi} - \dot{\theta}_{pb} = \gamma_i u_1 = v_i, \quad i = 1, 2, 3. \quad (6)$$

Scalars γ_i, $i = 1, 2, 3$ are given in the paper [9]. An angular velocity $\dot{\psi}_0$ that drives the virtual joint, that is, an angular velocity input v_0, is calculated from u_1 so that Eq.(7) is satisfied as:

$$\dot{\psi}_0 = \dot{\theta}_{p0} - \dot{\theta}_{pb} = \gamma_0 u_1 = v_0. \quad (7)$$

A scalar γ_0 is given in the paper [9].

6 Propulsion Transfer Function

This section describes the definition of a propulsion transfer function [8] which is a metric of the attitude of the trident steering walker from the singular attitude. As we have described in Subsection 5.1, the singular attitude is an attitude in which the moving velocity $(\dot{x}_b, \dot{y}_b)^T$ and the rotational angular velocity $\dot{\theta}_b$ of the equilateral triangular base cannot be uniquely determined from the angular velocities $\dot{\psi}_1$, $\dot{\psi}_2$ and $\dot{\psi}_3$ of driving the joints 1-3. This physically means that the singular attitude is an attitude in which the trident steering walker cannot be propelled. There is a singular attitude in which all the steering wheels are parallel to each other. Also, there is a singular attitude in which all the steering wheels have the same revolution center in a two-dimensional plane. When an experimental vehicle of the trident steering walker has the singular attitude, it decelerates because of resistance, e.g., rolling resistance of wheels. In order to cause the trident steering walker to move against such resistance, it is necessary to prevent the locomotor from having the singular attitude as much as possible. To this end, we define a metric of the attitude of the locomotor from the singular attitude, a propulsion transfer function as:

[A] $\|\cos(\theta_b + \phi_b)\| \geq \frac{1}{\sqrt{2}}$:

$$\hat{P} = \hat{P}_1 + \hat{P}_2 + \hat{P}_3, \tag{8}$$

$$\hat{P}_1 = \left\|\det \hat{M}_1\right\|, \ \hat{P}_2 = \left\|\det \hat{M}_2\right\|, \ \hat{P}_3 = \left\|\det \hat{M}_3\right\|,$$

$$\hat{M}_1 = \begin{pmatrix} \hat{a}_{11} & \hat{a}_{12} \\ \hat{a}_{21} & \hat{a}_{22} \end{pmatrix}, \ \hat{M}_2 = \begin{pmatrix} \hat{a}_{21} & \hat{a}_{22} \\ \hat{a}_{31} & \hat{a}_{32} \end{pmatrix}, \ \hat{M}_3 = \begin{pmatrix} \hat{a}_{11} & \hat{a}_{12} \\ \hat{a}_{31} & \hat{a}_{32} \end{pmatrix}.$$

[B] $\|\sin(\theta_b + \phi_b)\| > \frac{1}{\sqrt{2}}$:

$$\check{P} = \check{P}_1 + \check{P}_2 + \check{P}_3, \tag{9}$$

$$\check{P}_1 = \left\|\det \check{M}_1\right\|, \ \check{P}_2 = \left\|\det \check{M}_2\right\|, \ \check{P}_3 = \left\|\det \check{M}_3\right\|,$$

$$\check{M}_1 = \begin{pmatrix} \check{a}_{11} & \check{a}_{12} \\ \check{a}_{21} & \check{a}_{22} \end{pmatrix}, \ \check{M}_2 = \begin{pmatrix} \check{a}_{21} & \check{a}_{22} \\ \check{a}_{31} & \check{a}_{32} \end{pmatrix}, \ \check{M}_3 = \begin{pmatrix} \check{a}_{11} & \check{a}_{12} \\ \check{a}_{31} & \check{a}_{32} \end{pmatrix}.$$

When the trident steering walker has the singular attitudes, the propulsion transfer function $\hat{P}$ in Eq.(8) or $\check{P}$ in Eq.(9) is zero. Therefore, we design the motion parameters of the locomotor in such a manner as to make $\hat{P}$ in Eq.(8) or $\check{P}$ in Eq.(9) as high as possible.

7 Conversion into Chained Form

This section describes the conversion [9] [10] of the kinematical equation of the trident steering walker with the virtual mechanical elements shown in Fig.2 into a five-chain, single-generator chained form based on differential geometry [5]. First, the six vector fields $g_i(x)$, $i = 1, 2, \cdots, 6$, of Eq.(5) are converted as:

$$\begin{cases} f_1(x) = g_1(x)\,(1 - dc(s))\,/\cos\theta_{p0} \\ f_i(x) = g_i(x), \quad i = 2, 3, \cdots, 6. \end{cases} \tag{10}$$

Next, the six values u_i, $i = 1,2,\cdots,6$, are converted as:

$$\begin{cases} \tilde{u}_1 = u_1 \cos\theta_{p0}/(1-dc(s)) \\ \tilde{u}_i = u_i, \quad i = 2,3,\cdots,6. \end{cases} \tag{11}$$

Thus, the kinematical equation of Eq.(5) is rewritten as:

$$\dot{x} = \Sigma_{i=1}^{6} f_i(x)\tilde{u}_i. \tag{12}$$

Using the six vector fields $f_i(x)$, $i = 1,2,\cdots,6$, the state variables in the kinematical equation of Eq.(5) are converted as:

$$\begin{cases} z_{11} = h_1 = s & z_{31} = L_{f_1}h_3 & z_{51} = L_{f_1}h_5 \\ z_{21} = L_{f_1}^2 h_2 & z_{32} = h_3 = \theta_{p0} - \theta_{pb} & z_{52} = h_5 = \theta_{p2} - \theta_{pb} \\ z_{22} = L_{f_1}h_2 & z_{41} = L_{f_1}h_4 & z_{61} = L_{f_1}h_6 \\ z_{23} = h_2 = d & z_{42} = h_4 = \theta_{p1} - \theta_{pb} & z_{62} = h_6 = \theta_{p3} - \theta_{pb}, \end{cases} \tag{13}$$

where $L_p q = \frac{\partial q}{\partial x_1}p_1 + \frac{\partial q}{\partial x_2}p_2 + \cdots + \frac{\partial q}{\partial x_n}p_n$, $p = (p_1, p_2, \cdots, \ p_n)^T$. The time derivative of Eq.(13) becomes the five-chain, single-generator chained form shown in Eq.(14).

$$\begin{array}{lll} \dot{z}_{11} = w_1 & \dot{z}_{21} = w_2 & \dot{z}_{i1} = w_i \\ & \dot{z}_{22} = z_{21}w_1 & \dot{z}_{i2} = z_{i1}w_1 \\ & \dot{z}_{23} = z_{22}w_1 & i = 3,4,5,6, \end{array} \tag{14}$$

$$\begin{array}{l} w_1 = \tilde{u}_1 \\ w_i = \Sigma_{j=1}^{6} L_{f_j} L_{f_1}^2 h_i \tilde{u}_j, \quad i = 3,4,5,6. \end{array}$$

8 Control Inputs for Path Following Motion

This section describes the path following feedback control method [9] [10]. Based on the five-chain, single-generator chained form of Eq.(14), the control inputs w_i, $i = 1,2,\cdots,6$, are designed as below. The control input w_1 is designed as:

$$w_1 = a_0 \neq 0. \tag{15}$$

The value a_0 of Eq.(15) is a non-zero constant. It physically means the moving velocity $\tilde{u}_1$ of the barycenter of the equilateral triangular base along the path. The moving velocity $u_1 (= \tilde{u}_1(1-dc(s))/\cos\theta_{p0})$ of the virtual link is not zero either. The angular velocities $\dot{\psi}_1$, $\dot{\psi}_2$ and $\dot{\psi}_3$ for driving the joints 1-3, i.e., the angular velocity inputs v_1, v_2 and v_3, are determined uniquely by Eq.(6). The angular velocity $\dot{\psi}_0$ for driving the virtual joint, i.e., the angular velocity input v_0, is also determined uniquely by Eq.(7).

The control input w_2 is designed as:

$$w_2 = p_{21}z_{21} + p_{22}\frac{z_{22}}{a_0} + p_{23}\frac{z_{23}}{a_0^2}. \tag{16}$$

The coefficients p_{21}, p_{22} and p_{23} are designed so that the variable $z_{23} (= d)$ converges into zero exponentially.

The control input w_3 is designed as:

$$w_3 = p_{31}z_{31} + p_{32}\frac{z_{32} + \theta_{pbd}}{a_0}. \tag{17}$$

The coefficients p_{31} and p_{32} are designed so that the orientation θ_{pb} of the equilateral triangular base relative to the orientation of the tangent of the path at the point $\mathbf{P_s}$ converges into a desired relative orientation θ_{pbd} exponentially.

Of course, it is necessary that the trident steering walker following the path keeps moving. In other words, at least one of the joints 1-3 must be driven to satisfy the condition of $w_1 = a_0 \neq 0$ in Eq.(15). Thus, the angles ψ_1 ($=z_{42}$), ψ_2 ($=z_{52}$) and ψ_3 ($=x_{62}$) of the joints 1-3 must be changed periodically while the trident steering walker avoids the singular attitude, so that the control inputs w_i, $i = 4,5,6$, are designed as:

$$w_i = p_{i1} z_{i1} + p_{i2} \frac{z_{i2}}{a_0} + A_i \sin(\omega_i t + \varphi_i), \quad i = 4,5,6. \tag{18}$$

The coefficients p_{i1}, p_{i2}, $i = 4,5,6$, are designed so that the variables z_{i2}, $i = 4,5,6$, that represent the angles of the joints 1-3 converge into periodic functions r_i, $i = 4,5,6$, as shown in Eq.(19).

$$z_{i2} = r_i = \hat{A}_i \sin(\hat{\omega}_i t + \hat{\varphi}_i), \quad i = 4,5,6, \tag{19}$$

where $\hat{\omega}_i = \omega_i$, $i = 4,5,6$. The amplitudes $\hat{A}_i$ and phases $\hat{\varphi}_i$ of the periodic functions r_i, $i = 4,5,6$, in Eq.(19) are functions of the amplitudes A_i and phases φ_i of the oscillatory terms $A_i \sin(\omega_i t + \varphi_i)$, $i = 4,5,6$, in Eq.(18). By adjusting A_i, ω_i and φ_i, $i = 4,5,6$, in Eq.(18), therefore, $\hat{A}_i$, $\hat{\omega}_i$ and $\hat{\varphi}_i$, $i = 4,5,6$, in Eq.(19) are designed to keep the trident steering walker moving while avoiding the singular attitude of rank$\hat{A} < 2$ in Eq.(1) or rank$\check{A} < 2$ in Eq.(2).

9 Simulation Results

A 10th-order Bezier curve is set to be the path as shown in Fig.3. Its control points are indicated by black dots.

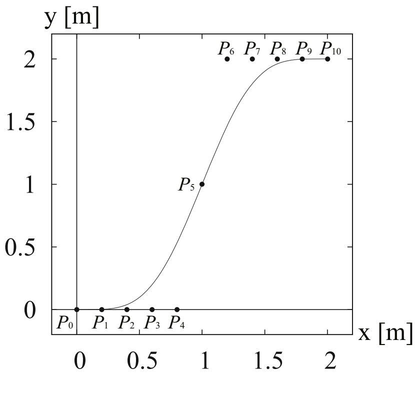

Fig. 3. A 10th-order Bezier Curve

In order to cause the point $\mathbf{P_s}$ which represents the position of the barycenter of the base on the path to move the distance L(=3.123816[m]) from the start point $\mathbf{P_0}$ to the end point $\mathbf{P_{10}}$ in the time T(=60.0[s]), the moving velocity w_1 of the point $\mathbf{P_s}$ on the path is given as:

$$\dot{s} = \tilde{u}_1 = w_1 = a_0 = L/T = 3.123816/60.0 = 0.052064[\mathrm{m/s}].$$

The desired value θ_{pbd} of the orientation θ_{pb} of the base relative to the orientation of the tangent of the path at the point $\mathbf{P_s}$ is given as:

$$\theta_{pbd} = 0.0[\text{rad}].$$

The coefficients of Eqs.(16), (17) and (18) which are the control inputs are given as:

$$p_{21} = -0.9,\ p_{22} = -0.27,\ p_{23} = -0.027,$$
$$p_{i1} = -0.6,\ \ p_{i2} = -0.09,\ \ i = 3,4,5,6.$$

Then, the amplitudes $\hat{A}_i$, the angular frequencies $\hat{\omega}_i$, and the phases $\hat{\varphi}_i$ of the periodic functions r_i, $i = 4,5,6$, of Eq.(19) into which the angles $\psi_1(=z_{42})$, $\psi_2(=z_{52})$, $\psi_3(=z_{62})$ of the joints 1-3 converge respectively, are given as:

$$\hat{A}_4 = \pi/12[\text{rad}],\ \hat{\omega}_4 = \pi/5[\text{rad/sec}],\ \hat{\varphi}_4 = \pi/3[\text{rad}],$$
$$\hat{A}_5 = \pi/12[\text{rad}],\ \hat{\omega}_5 = \pi/5[\text{rad/sec}],\ \hat{\varphi}_5 = \pi/6[\text{rad}],$$
$$\hat{A}_6 = \pi/12[\text{rad}],\ \hat{\omega}_6 = \pi/5[\text{rad/sec}],\ \hat{\varphi}_6 = 0.0[\text{rad}].$$

At this time, the amplitudes A_i, the angular frequencies ω_i, and the phases φ_i of the oscillatory terms $A_i \sin(\omega_i t + \varphi_i)$, $i = 4,5,6$, in the control input of Eq.(18) are given as:

$$A_i = \hat{A}_i \frac{4\hat{\omega}_i^2 + p_{i1}^2}{4a_0} \omega_i = \hat{\omega}_i \varphi_i = \hat{\varphi}_i - \text{atan2}(4\hat{\omega}_i p_{i1}, -4\hat{\omega}_i^2 + p_{i1}^2),$$
$$i = 4,5,6.$$

The initial conditions are given as:

$$(s,d)^T\,|_{t=0} = (0.0[\text{m}], 0.0[\text{m}])^T\,,$$
$$\phi_0|_{t=0} = 0.0[\text{rad}], \qquad \theta_{p0}|_{t=0} = 0.0[\text{rad}],$$
$$\phi_c|_{t=0} = 0.0[\text{rad}], \qquad \theta_{pb}|_{t=0} = 0.0[\text{rad}],$$
$$\phi_1|_{t=0} = 0.097162[\text{rad}], \quad \theta_{p1}|_{t=0} = 0.228690[\text{rad}],$$
$$\phi_2|_{t=0} = -0.602318[\text{rad}], \ \theta_{p2}|_{t=0} = 0.129428[\text{rad}],$$
$$\phi_3|_{t=0} = -0.564380[\text{rad}], \ \theta_{p3}|_{t=0} = -0.002479[\text{rad}].$$

A model of the trident steering walker in a commercial multibody dynamics simulator, LMS Virtual. Lab Motion, is shown in Fig.4. The parameter that determines its size is l=0.20[m]. The weight of the equilateral triangular base is 14.411[kg] and its moment of inertia at its barycenter around an axis perpendicular to the x-y plane is 0.223[kgm^2]. The weight of each of the links 1-3 is 2.405[kg] and its moment of inertia at its barycenter around an axis perpendicular to the x-y plane is 0.013[kgm^2]. The radius of each of the steering wheels is 0.04[m] and its width is 0.003[m]. The weight of the wheel is 0.042[kg]. The moment of inertia of the wheel at its barycenter around its rolling axis is 3.036×10^{-5}[kgm^2] and that around an axis perpendicular to the x-y plane is 1.538×10^{-5}[kgm^2]. The weight of each of the forks holding the steering wheels is 0.061[kg] and the moment of inertia of the fork at its barycenter around an axis perpendicular to the x-y plane is 9.915×10^{-6}[kgm^2]. The vertical stiffness of the steering wheel is 10000[N/m] and its damping constant is 1000[kg/s]. The rolling resistance of the steering wheel is 0.002. The friction coefficient between the steering wheel and the ground is 1.0. The cornering stiffness of the steering wheel is 200535.288[mkg/rads^2]. In order to evaluate the motion, we measure the resultant force $f_p(=f_{p1} + f_{p2} + f_{p3})$ of the projections of the forces working on the base at its three corners in the direction from the barycenter of the base to the joint 1 as shown in Fig.5.

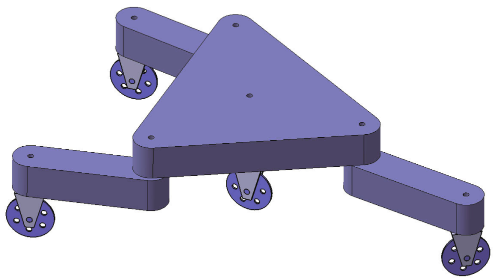

Fig. 4. A Model of the Trident Steering Walker in a Commercial Multibody Dynamics Simulator, LMS Virtual. Lab Motion

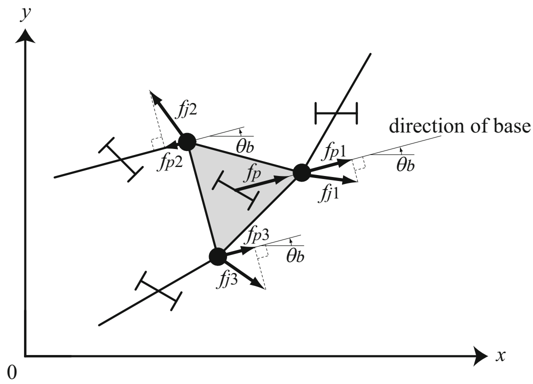

Fig. 5. A Resultant Force $f_p(=f_{p1}+f_{p2}+f_{p3})$ of the Projections of the Forces Working on the Base at its Three Corners in the Direction from its Barycenter to the Joint 1

A simulation result is shown in Figs.6 and 7. As can be understood from Fig.6, the trident steering walker achieved the motion following the path which is the 10th-order Bezier curve, however, it took 65.73[s] which is 5.73[s] more than $T(=60.0[\text{s}])$ for the locomotor to reach the end point $\mathbf{P_{10}}$. This is because there is the rolling resistance of the steering wheels. This is also because, as Fig.7(a) shows, the trident steering walker has an attitude which is close to the singular attitude in which the propulsion transfer function $\hat{P}(\check{P})$ is zero at an interval 10.0[s], so that the locomotor decelerates by the rolling resistance significantly in the interval. As Fig.7(b) shows, the resultant force f_p is low when the propulsion transfer function $\hat{P}(\check{P})$ is low.

Another simulation result is shown in Figs.8 and 9. The phases φ_i, $i=4,5,6$, of the periodic functions r_i, $i=4,5,6$, of Eq.(19) are given as: $\hat{\varphi}_4$=$4\pi/3$[rad], $\hat{\varphi}_5$=$2\pi/3$[rad], $\hat{\varphi}_6$=0.0[rad]. The initial conditions are given as:

$$
\begin{aligned}
&(s,d)^T\,|_{t=0} = (0.0[\mathrm{m}], 0.0[\mathrm{m}])^T\,, \\
&\phi_0|_{t=0} = 0.0[\mathrm{rad}], \qquad \theta_{p0}|_{t=0} = 0.0[\mathrm{rad}], \\
&\phi_c|_{t=0} = 0.0[\mathrm{rad}], \qquad \theta_{pb}|_{t=0} = 0.0[\mathrm{rad}], \\
&\phi_1|_{t=0} = -0.6388041[\mathrm{rad}],\ \theta_{p1}|_{t=0} = -0.1538821[\mathrm{rad}], \\
&\phi_2|_{t=0} = -0.1467246[\mathrm{rad}],\ \theta_{p2}|_{t=0} = 0.2603651[\mathrm{rad}], \\
&\phi_3|_{t=0} = -0.7331629[\mathrm{rad}],\ \theta_{p3}|_{t=0} = -0.1065828[\mathrm{rad}].
\end{aligned}
$$

The other conditions remain the same. As can be understood from Fig.8, it took 61.17[s] which is 1.17[s] more than $T(=60.0[\mathrm{s}])$ for the locomotor to reach the end point $\mathbf{P_{10}}$, i.e., the locomotor could move faster compared with the case of Fig.6. This is because, as Fig.9(a) shows, the trident steering walker never has the attitude which is close to the singular attitude in which the propulsion transfer function $\hat{P}(\check{P})$ is zero. As Fig.9(b)

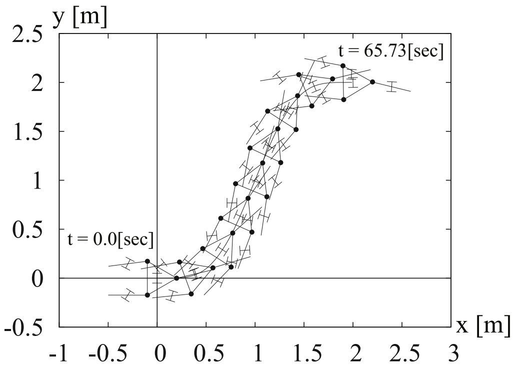

Fig. 6. A Simulation Result

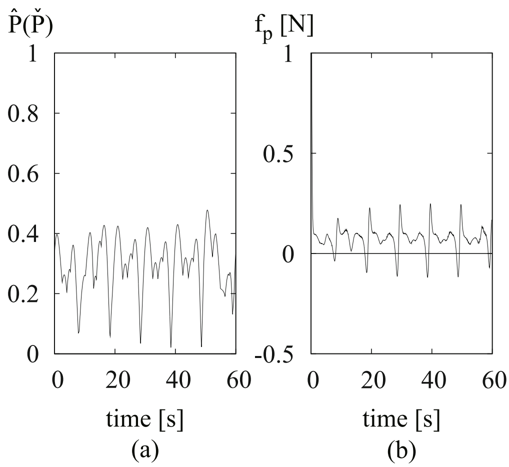

Fig. 7. (a) An Evolution of the Propulsion Transfer Function $\hat{P}(\check{P})$ and (b) an Evolution of the Resultant Force f_p of the Projections of the Forces Working on the Base at its Three Corners in the Direction from its Barycenter to the Joint 1

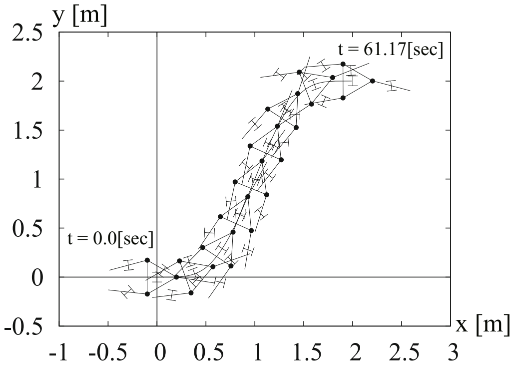

Fig. 8. A Simulation Result

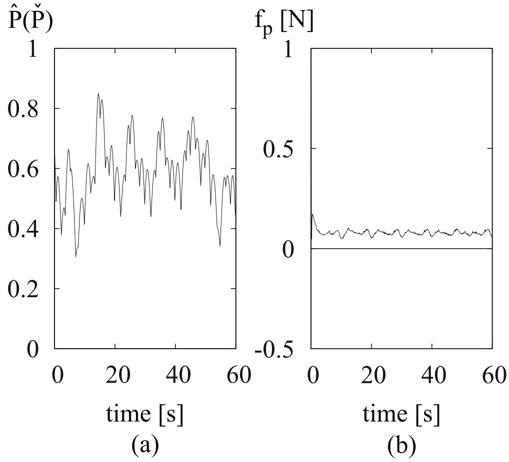

Fig. 9. (a) An Evolution of the Propulsion Transfer Function $\hat{P}(\check{P})$ and (b) an Evolution of the Resultant Force f_p of the Projections of the Forces Working on the Base at its Three Corners in the Direction from its Barycenter to the Joint 1

shows, the resultant force f_p is more stable compared with that in Fig.7(b), so that the base is moved faster against the resistance force working on the base at its barycenter which is due to the rolling resistance of the steering wheel on the base. As these simulation results show, the trident steering walker produces the propulsion force which is more stable when the propulsion transfer function is higher, which means that it is effective to design the motion parameters based on the propulsion transfer function.

10 Conclusion

We have proposed a novel design methodology of the motion parameters of an undulatory locomotor: a trident steering walker based on a performance index: a propulsion transfer function. The trident steering walker transforms the periodic driving of its three joints into its movement by the periodic operation of its four steering systems, and the locomotor has a singular attitude in which it cannot perform such transformation. In order to prevent the locomotor from having the singular attitude, we have proposed to design the motion parameters based on the propulsion transfer function which is a metric of the attitude from the singular attitude. Especially, we have analyzed the relationship between the propulsion transfer function defined in kinematics and the propulsion force measured in a dynamics simulator, and we have demonstrated that it is effective to design the motion parameters based on the propulsion transfer function.

Acknowledgment. This research was supported by a Grant-in-Aid for Scientific Research(C) (No. 22560230) from the Ministry of Education, Culture, Sports, Science and Technology (MEXT) (Japan Society for the Promotion of Science (JSPS)), for which the authors would like to express their deep gratitude.

References

1. Chitta, S., Heger, F.W., Kumar, V.: Design and Gait Control of a Rollerblading Robot. In: Proceedings of the 2004 IEEE International Conference on Robotics and Automation, New Orleans, LA, USA, pp. 3944–3949 (April 2004)
2. Chitta, S., Cheng, P., Frazzoli, E., Kumar, V.: RoboTrikke: A Novel Undulatory Locomotion System. In: Proceedings of the 2005 IEEE International Conference on Robotics and Automation, Barcelona, Spain, pp. 1597–1602 (2005)
3. Hirose, S.: Biologically Inspired Robots (Snake-like Locomotors and Manipulators). Oxford University Press (1993)
4. Hirose, S., Takeuchi, H.: Study on Roller-Walk (Basic Characteristics and Its Control). In: Proceedings of the 1996 IEEE International Conference on Robotics and Automation, Minneapolis, MN, USA, pp. 3265–3270 (April 1996)
5. Isidori, A.: Nonlinear Control Systems, 2nd edn. Springer (1989)
6. Krishnaprasad, P.S., Tsakiris, D.P.: Oscillations, SE(2)-Snakes and Motion Control: A Study of the Roller Racer. Dynamical Systems 16(4), 347–397 (2001)
7. Ostrowski, J.P., Burdick, J.W.: The Geometric Mechanics of Undulatory Robotic Locomotion. International Journal of Robotics Research 17(7), 683–701 (1998)
8. Yamaguchi, H.: Control of a New Type of Undulatory Wheeled Locomotor: a Trident Steering Walker Based on Chained Form. Journal of Robotics and Mechatronics 21(4), 541–553 (2009)
9. Yamaguchi, H.: A Path Following Feedback Control Law for a New Type of Undulatory Locomotor: a Trident Steering Walker. In: Proceedings of the 14th International Conference on Advanced Robotics (ICAR 2009), Munich, Germany (June 2009)
10. Yamaguchi, H., Morinaga, T., Kawakami, A.: A Path-following Feedback Control Law with a Variable Velocity for a Trident Steering Walker and its Experimental Verification. In: Proceedings of the 8th IFAC Symposium on Nonlinear Control Systems (NOLCOS 2010), Bologna, Italy, pp. 1187–1192 (August 2010)

Real-Time 3D Model Reconstruction with a Dual-Laser Triangulation System for Assembly Line Completeness Inspection

Edmond Wai Yan So, Matteo Munaro, Stefano Michieletto,
Mauro Antonello, and Emanuele Menegatti

Intelligent Autonomous Systems Laboratory
Department of Information Engineering, University of Padua
via Ognissanti, 72, Padua PD 35129, Italy
{edmond.so,matteo.munaro,stefano.michieletto}@dei.unipd.it,
{antonelm,emg}@dei.unipd.it

Abstract. In this paper, we present an improved version of our Dual Laser Triangulation System, a low-cost color 3D model acquisition system built with commonly available machine vision products. The system produces a color point cloud model of scanned objects that can be used to perform completeness inspection tasks on assembly lines. In particular, we show that model acquisition and reconstruction can be achieved in real-time using such a low-cost solution. Our results demonstrate that 3D-based inspection can be achieved readily and economically in a real industrial production environment.

1 Introduction

Machine vision is widely used for quality control tasks in industrial environments. In the past, such systems have relied mainly on 2D-based image analysis [4]. Without depth information, difficulties often arise when dealing with non-rigid objects such as hoses and cables, and when the contrast between the background and the part to be inspected is low. As a result, there is a high interest in using 3D model acquisition technologies to overcome these problems.

Although commercial 3D scanner products are becoming more readily available [2], their proprietary nature and limited configurations make it difficult to adapt them to different needs in an industrial environment. Some of them only produce range images with only depth information, making it difficult to perform certain inspection tasks that can be easily performed with color information. On the other hand, devices that produce both color and depth information usually have a prohibitively high cost. Our current research is focused on developing a low-cost color 3D model acquisition system that can be highly configurable for a variety of completeness inspection tasks (presence/absences of parts, correct type/position/orientation). The reconstructed model will include both depth and color data so that both type of information can be readily exploited for the inspection task at hand. To this end, we have developed a prototype using commercially available machine vision products. We have previously introduced our Dual Laser Triangulation System (DLTS) in [5]. In this paper, we present improvements to this system. In particular, we have integrated our DLTS with a conveyor belt

S. Lee et al. (Eds.): Intelligent Autonomous Systems 12, AISC 194, pp. 707–716.
springerlink.com

system, and substantially improved the processing software to perform in real-time, making our system readily deployable in a real industrial production environment.

2 System Configuration

2.1 Dual Laser Triangulation System

In a laser triangulation system, if the plane of the a laser line with respect to a camera is known, the 3D position of laser points observed on the image plane can be recovered through triangulation. When a laser triangulation system is used in an assembly line operation where the sensor assembly is scanning from a fixed direction, occlusions are bound to occur due to object geometry. Although it is possible to use two cameras to observe a single laser line to mitigate this problem, as we have previously argued in [5], using dual lasers with one camera is more advantageous due to the lower cost and the lower data processing. Our Dual Laser Triangulation System (DLTS) consists of a downward-looking camera and two line lasers at a fixed orientation with respect to the camera (Fig. 1). A line light provides illumination to part of the scene so that color texture in addition to depth information can be obtained. Fig. 2 illustrates how our DLTS is able to alleviate the occlusion problem on one of our sample inspection parts.

2.2 Hardware Prototype

In our first prototype, our DLTS was mounted on a robot arm (Fig. 3a), which is moved over the object to be scanned and inspected. While this setup makes it flexible to position the camera and lasers at arbitrary angles to obtain the scan, the large workspace of

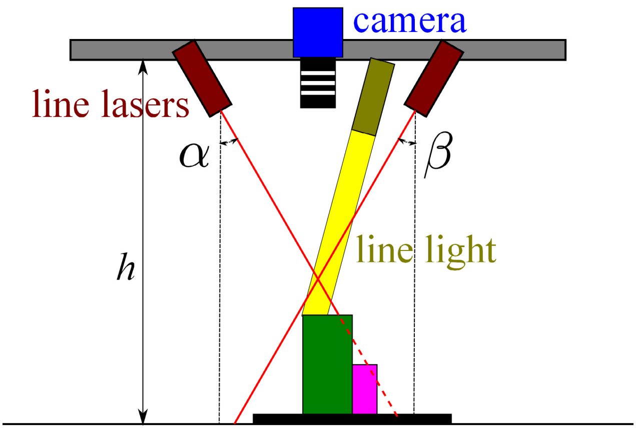

Fig. 1. Configuration of our Dual Laser Triangulation System (DLTS). Here, the pink object cannot be observed by the left laser due to occlusion from the taller green object. Using dual lasers alleviates this problem.

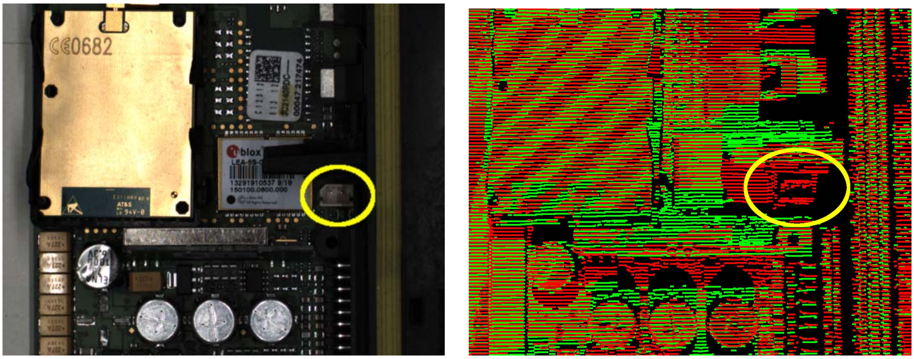

(a) (b)

Fig. 2. A practical example of the advantage of our DLTS over a single laser system. (a) Image of the sample part being inspected. (b) Using dual lasers, the white connector being inspected (circled in yellow) is occluded in the scan of one laser (green dots) while visible in other laser (red dots).

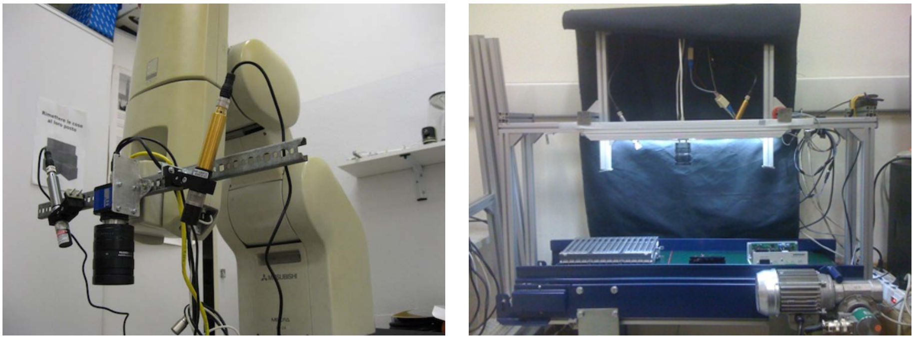

(a) (b)

Fig. 3. (a) Our first prototype with the DLTS mounted on a robot arm. (b) Our current prototype with the DLTS integrated into a conveyor belt system.

the robot arm makes it difficult to construct a compact enclosure to control the lighting. We have constructed another prototype system incorporating a conveyor belt (Fig. 3b) that simulates more realistically a typical assembly line environment. In this system, an enclosure made with black curtains draped over the sensor assembly allows us to create a controlled lighting environment, so that laser line detection can be performed easily. The distance between the sensor assembly and the conveyor belt (h in Fig. 1), as well as the orientation of the laser lines with respect to the camera (angles α and β in Fig. 1) can be easily adjusted to adapt to different inspection requirements, as will be elaborated in §2.4.

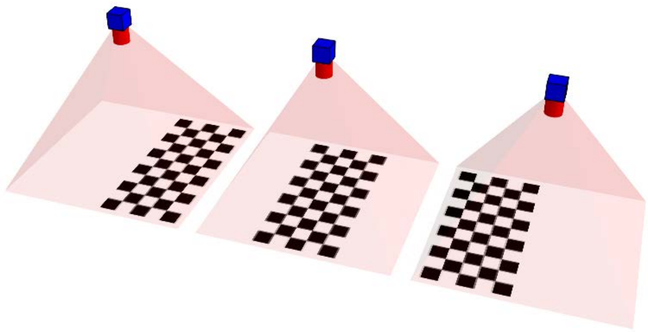

Fig. 4. Camera to conveyor-belt calibration using multiple rigidly connected checkerboard patterns (i.e., printed on a same sheet of paper)

2.3 Sensor Calibration

As before, our system is calibrated using a three step process as described below.

Camera Calibration

The intrinsic parameters of our camera is recovered using the widely used plane-based technique by Zhang [6].

Camera to Laser Calibration

The plane of the laser lines with respect to the camera is recovered by observing the projection of the laser lines on a checkerboard placed at various arbitrary orientations. After the pose of the checkerboard is recovered, the 3D location of the observed laser points can be triangulated. Repeating this at various checkerboard orientations results in a collection of 3D points spanning the plane of the laser lines. The parameters of the laser planes are then determined using principal component analysis.

Camera to Conveyor Belt Calibration

To combine the triangulated points obtained across different frames into a single model, the motion of the scanned object on the conveyor belt relative to the camera coordinate frame needs to be known. To recover this translation, we place a calibration board on the conveyor belt and acquire images of it after commanding the conveyor belt to different positions. Instead of a single checkerboard pattern, the calibration board has three separate patterns printed on the same sheet of paper, so that the separation distances between them are precisely known (Fig. 4). This is done so that the range of the motion is not limited by the need to maintain the same checkerboard pattern within view of the camera at all the different positions.

In addition to being a pure translation, the motion of an object on a conveyor belt is further constrained because the translation should lie in the same plane as the conveyor belt itself. Thus, we formulate the calibration problem as a constrained pose estimation problem [3]. Instead of estimating n general poses $\{R_i \in SO(3), T_i \in \mathbb{R}^3\}$ (rotation and

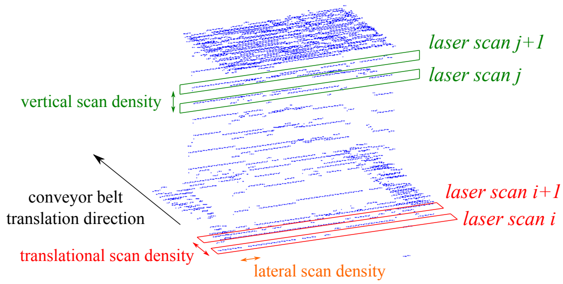

Fig. 5. Definition of terms used to characterize point cloud density

translation from the camera to the checkerboard at position $i = 1 \ldots n$) with $6n$ DOF, we impose the following constraints. First, because the motion between the checkerboard poses should be pure translations, all of the rotations should be the same, $R_1 = R_i = \ldots = R_n$, so we estimate a single rotation R for all of the poses. Second, the translations between all of the poses should be collinear, so we estimate a single direction vector $\hat{t} \in S^2$ such that $T_i = T_1 + \mu_i \hat{t}$, where μ_i is the magnitude of the translation from the first checkerboard pose to the i-th pose. Third, because the translation should lie in the plane of the checkerboards, $\hat{t}$ is characterized using a single parameter θ such that $\hat{t} = \cos\theta\hat{i} + \sin\theta\hat{j}$, where $\hat{i}$ and $\hat{j}$ are unit vectors along the X and Y axes in the checkerboard coordinate frame. Hence, the objective function for our pose estimation problem is:

$$\underset{R,\theta,\mu_i}{\operatorname{argmin}} \|x_j - K \cdot [R|T_i] \cdot X_j\|^2 \tag{1}$$

This equation involves $6 + n$ independent variables (3 for R, 3 for T_1, θ, and μ_i for $i = 2 \ldots n$). Here, K refers to the camera calibration matrix, x_j are the observed image coordinates of the checkerboard corners, and X_j are the 3D coordinates of the checkerboard corners.

2.4 Point Cloud Density and Resolution

The point density of the reconstructed 3D model is determined by a number of interdependent factors, including the camera frame rate, the speed of the conveyor belt, and the orientation of the laser lines. As illustrated in Fig. 5, we define the translation scan density as the distance between laser scan lines on a surface parallel to the translation direction, the vertical scan density as the distance between laser scan lines on a surface perpendicular to the conveyor belt, and the lateral scan density as the distance between adjacent points in the same scan line.

The translational scan density is simply a function of the conveyor belt speed v and the camera frame rate fps: $density_{tranlational} = \frac{v}{fps}$. The vertical scan density is additionally dependent on the laser line orientation α: $density_{vertical} = density_{translational} \cdot \tan(\pi - \alpha)$. The lateral scan density is dependent on the camera focal length f, the

Table 1. Reconstruction density and resolution

Parameter	Value
Translation Scan Density	0.75 *mm*
Vertical Scan Density	1.61 *mm*
Lateral Scan Density	0.09 *mm*
Vertical Resolution	0.17 *mm*

pixel size s_{px}, and the actual scene distance h: $density_{lateral} = s_{px} \cdot \frac{h}{f}$. Assuming unit pixel resolution (i.e., no subpixel localization of the laser points), the lasers can be oriented so that the their imaged points span half of the image over the range of the height of the scanned object. Thus, the vertical resolution of our DLTS is $res_{vertical} = \frac{\text{maximum scanned object height}}{0.5 \cdot \text{image height}}$.

Table 1 shows the reconstruction density and resolution for our current setup, with $v = 15mm/s$, $fps = 20$, $\alpha = 25°$, $h = 350mm$, $f = 17mm$, and $s_{px} = 4.4\mu m$. The camera has a resolution of $1600x1200$ pixels.

3 3D Model Acquisition Pipeline

Our 3D model acquisition pipeline follows a standard approach [1]. Previously, our system is configured in a two-pass operation, with the lasers on and the lights off during the forward pass to acquire range information, and with the lasers off and the lights on during the backward pass to obtain texture information. By integrating a collimated line light as shown in Fig. 1, a single-pass operation is made possible. Also, we believe that a colorized point cloud (§3.4) along with a stitched texture image (§3.5) is sufficient for most inspection tasks, so we have omitted the time-consuming step of surface mesh reconstruction.

3.1 Laser Detection

The two lasers are positioned carefully such that their line of intersection is well above the height of the object to be inspected, so their reflectance are restricted to separate halves of an image. Each column in each half of an image is scanned for the location of the respective laser line. Although the line lasers we are using are red, simply searching for the peak value in the red channel along each column in the image is not very robust, as the laser line often saturates the CCD sensor, and spurious reflections of the laser line onto neighboring surfaces can result in multiple peaks, as shown in Fig. 6. Instead, we scan for the peak of the sum of the pixel values across the RGB channels. This laser detection method effectively results in unit pixel localization accuracy.

3.2 Point Cloud Generation

The detected laser points are triangulated as described in [5]. To combine scans from multiple frames into a single point cloud mode, the triangulated 3D points from each

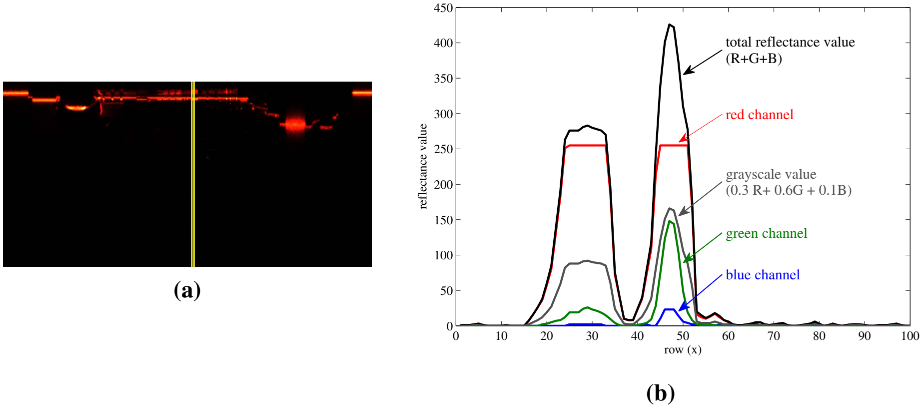

Fig. 6. Laser detection. (a) Single frame showing laser line reflectance across the sample part. (b) Laser reflectance profile across the single column highlighted in yellow in (a).

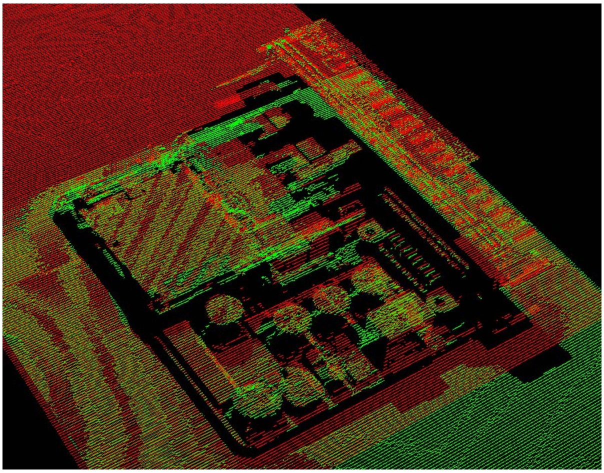

Fig. 7. Point cloud generated by combining the laser points observed by both lasers and referencing them to a common coordinate frame

frame i are translated along the conveyor belt direction by a distance d_i as given by the conveyor belt encoder (Fig. 7). The laser points from each frame are triangulated and integrated into the point cloud in real time.

3.3 Range Image

Range image generation is a one-time process performed after the entire point cloud has been constructed. It is generated by simply projecting the point cloud onto the image

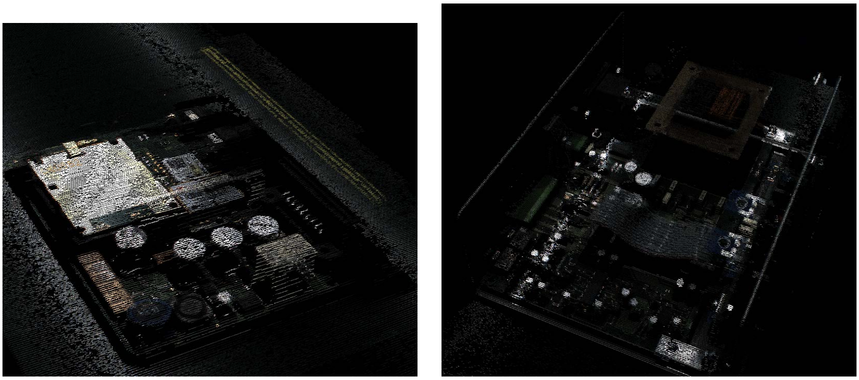

(a) (b)

Fig. 8. Colored point cloud for two sample parts

plane at a user-specified resolution, and can be completed extremely fast in the order of milliseconds. Example images can be found in [5].

3.4 Point Cloud Coloring

For each texture image, the camera is positioned over the point cloud at the position where the image was acquired, and the points are projected onto the image plane. The projected points that lie within the image are assigned the color of their corresponding pixels. Fig. 8 shows the results of this process on two sample parts.

Because successive images overlap, to minimize processing time, the point cloud is partitioned evenly between the images so that each point is only colorized using a single image. Thus, each point is texturized using the view whose image center is closest to the point. To produce better results, each point could be texturized using the view where the viewing angle and the surface normal is minimized. However, this would require estimating a surface normal for each point, thereby increasing the processing time.

3.5 Texture Stitching

For some inspection tasks, traditional 2D image analysis may still be the best approach. We accommodate for this by generating a texture image stitched together from successive frames using the known conveyor belt motion. We follow a similar procedure as described in [5], with modifications that discards overlapping regions between successive frames to minimize processing time, as we have done in the point cloud coloring process. Furthermore, instead of using nearest-neighbor interpolation, which produces sharp discontinuities (Fig. 9a), we have used bilinear interpolation along with blending of pixel values between successive images to improve the results (Fig. 9b).

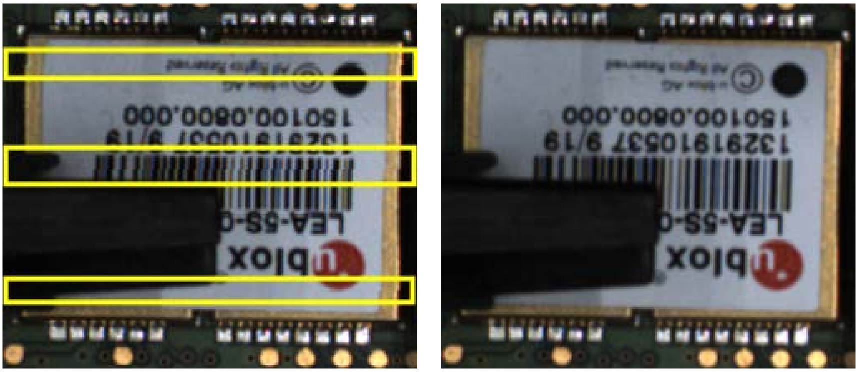

(a) (b)

Fig. 9. Texture stitching. (a) Using nearest neighbor interpolation. Some of the sharp discontinuities are highlighted in yellow. (b) Using bilinear interpolation and pixel blending across successive frames.

4 Experiments and Results

Table 2 shows some performance statistics of our color 3D model acquisition pipeline over a typical scan using a standard workstation (Intel Xeon E3-1225 quad-core @ 3.1GHz). The acquisition consists of 380 laser frames and texture frames (19 seconds), producing a point cloud with 473,192 points (Fig. 8a). The total execution time of 18.5ms is well under the 50ms frame acquisition interval (for 20 fps).

Table 2. Performance Statistics

Process	Time per Frame	Total Time
Laser Detection and Triangulation	15.835 *ms*	5,589 *ms*
Range Image	N/A	76 *ms*
Texture Stitching	0.725 *ms*	250 *ms*
Point Cloud Coloring	1.896 *ms*	654 *ms*
Total	18.456 *ms*	6.84 *s*

5 Conclusions and Future Work

We have demonstrated a color 3D model acquisition system that can perform in real-time, making our system suitable for deployment in a real industrial production environment. We are currently building a generic library of inspection algorithms that can be applied to the colorized point cloud and stitched texture images, and we plan to demonstrate a complete low-cost 3D inspection system soon.

Acknowledgement. This research has received funding from IT+Robotics (http://www.it-robotics.it) and the European Union's Seventh Framework Programme for Research and Technological Development (http://ec.europa.eu/research/fp7/) under grant agreement No. 262009.

References

1. Bernardini, F., Rushmeier, H.: The 3D model acquisition pipeline. Computer Graphics Forum 21(2), 149–172 (2002)
2. Bi, Z., Wang, L.: Advances in 3D data acquisition and processing for industrial applications. Robotics and Computer-Integrated Manufacturing 26(5), 403–413 (2010)
3. Haralick, R., Joo, H., Lee, C., Zhuang, X., Vaidya, V., Kim, M.: Pose estimation from corresponding point data. IEEE Transactions on Systems, Man and Cybernetics 19(6), 1426–1446 (1989)
4. Malamas, E.N., Petrakis, E.G.M., Zervakis, M., Petit, L., Legat, J.: A survey on industrial vision systems, applications and tools. Image and Vision Computing 21(2), 171–188 (2003)
5. Munaro, M., Michieletto, S., So, E., Alberton, D., Menegatti, E.: Fast 2.5D model reconstruction of assembled parts with high occlusion for completeness inspection. In: International Conference on Machine Vision, Image Processing, and Pattern Analysis (2011)
6. Zhang, Z.: A flexible new technique for camera calibration. IEEE Transactions on Pattern Analysis and Machine Intelligence 22(11), 1330–1334 (2000)

An Evolution Strategy Based Autonomous Algorithm for Roll-to-Roll Web Control System

Thanh T. Tran, Ganeshthangaraj P. Muhammad Zubair, and Kyung-Hyun Choi

Dept. of Mechatronics, Jeju National University
66 Jejudaehakre, Jejusi-jejudo, 690-756, Korea
{thanhtt,khchoi}@jejunu.ac.kr,
{ganeshthangaraj,zubairaw}@hotmail.com

Abstract. Roll-to-roll based manufacturing technology play an important role in making printed electronics possible at high speed and low cost. In order to increase the adaptability and flexibility to detect effectively the external and internal disturbances, several algorithms for roll-to-roll web control system are proposed in recent years. However, almost all proposals are employed without taking attention in the change in time of radii of unwinder and rewinder. In this paper, a control system design is proposed firstly for non-linear roll-to-roll web control system using the uni-directional crossfeed two-channel design approach. Secondly, an evolution strategy based autonomous algorithm is developed to detect the errors and automatically recover the errors at every time interval in the presence of the varying radii. The numerical simulations validate the stability and reliability of the proposed approach.

Keywords: web tension, evolution strategy, feedback, roll-to-roll, uni-directional crossfeed.

1 Introduction

With the rapid development of digital computer in recent years, the genetic algorithm (GA) and Evolution Strategy (ES) design are considered as a key role in developing the modern automation systems and the other fields that have the ability of detecting the system errors due to the external and internal disturbances and automatically recovering the errors in order to make system stable and improve the precision. Until now, some modifications of GA are proposed and applied to automation systems (Aytekin Bagis, 2007; H. Madadi Kojabadi and Q. Cao, 2005; Jin-Sung Kim, Jin-Hwan Kim, Ji-Mo Park, Sung-Man Park, Won-Yong Choe and Hoon Heo, 2008 ;Y.P. Wang, H.H. Chung, N.R. Watson, and S.S. Matair, 2000). To achieve more effective search, the optimization algorithm (Aytekin Bagis, 2007) is based on the integration of classical genetic algorithm structure and systematic neighborhood structure. The simulation results show that the proposed algorithm is applied only on the limit range such SISO linear system. The analytical procedures (M. Zhunang and D. P. Atherton, 1993) for obtaining optimum PID controller settings for minimization of time weighted integral performance criteria is employed for the dead time plant model. A method to design an

S. Lee et al. (Eds.): Intelligent Autonomous Systems 12, AISC 194, pp. 717–729.
springerlink.com

optimal disturbance rejection PID controller is proposed by (Renato A. Kronhling and Joost P. Rey, 2001) based on optimization of the disturbance rejection constraints. The simulation outcomes prove the slow response in time. An optimization algorithm is proposed for designing PID controllers (H. Madadi Kojabadi and Q. Cao, 2005; Chen-Huei Hsieh and Jyh-Hong Chou (2007)), which minimizes the asymptotic open-loop gain of a system with uncertainty using the quantitative feedback theory. Hung-Cheng Chen and Sheng-Hsiung Chang (2006) suggested a PID controller design for an active magnetic bearing using the genetic algorithm. The results show that the proposals are convenient for control system with fixed parameters and with no high accuracy requirement. In reality, there are many plants with the changing parameters in time in operating progress such as roll-to-roll web system and under the effect of disturbances in operating process. Therefore, detecting the system errors and automatically recovering the errors are necessary and are has been given attention by researchers in recent years. In this paper, an algorithm is proposed for the non-linear roll-to-roll web control systems with the changing of radii in time and due to the impact of disturbances. The contributions of the proposed algorithm are the following:

1. A control system design is proposed firstly for non-linear roll-to-roll web control system using the uni-directional crossfeed two-channel design approach.
2. An evolution strategy based autonomous algorithm is developed to detect the errors and automatically recover the errors at every time interval in the presence of the varying radii.

2 Design of Uni-directional Crossfeed Two Channel System

Consider a linear state space model given below

$$\dot{x}(t) = Ax(t) + Bu(t) \tag{1}$$

$$y(t) = Cx(t) + Du(t) \tag{2}$$

where the Jacobian matrices A, B, C, and D are constant and distinct for each operating point.

The Evans and Cavicchi gain and phase root migration design procedures exist in the Laplace domain. Therefore, the Laplace transformation must be applied to the linear model in Equation (1) and (2).Laplace transformation leads to algebraic equations in the Laplace domain instead of differential equations in the time domain, which are appropriate for root locus usage. Taking the Laplace transformation of Equation (1) and (2) yields

$$y(s) = C((sI - A)^{-1}B + D)u(s) \tag{3}$$

where I is an identity matrix of the same dimensions as A, G(s) denotes the transfer function matrix, and s denotes complex frequency. G(s) can be further written as

$$G(s) = \frac{Cadj(sI - A)B + Ddet(sI - A)}{\det(sI - A)} \tag{4}$$

Equation (4) indicates G(s) is a rational polynomial matrix where each element has a common denominator polynomial, the system characteristic polynomial det (sI - A). Roots of the denominator polynomial coincide with the eigenvalues of A.

Suppose the output and input vectors are expanded to show the individual scalar signals, or

$$y(s) = [y_1(t)\ y_2(t)\ y_3(t)\ \dots y_m(t)] \tag{5}$$

$$u(s) = [u_1(t)\ u_2(t)\ u_3(t)\ \dots u_n(t)] \tag{6}$$

The following is designing steps for the systems of two-inputs and two outputs.

2.1 Loop Closure 1

There Consider a 2×2 system which is to be modified by a control system, such as an aircraft and roll-to-roll web control system with unsatisfactory handling characteristics

$$\begin{bmatrix} y_1 \\ y_2 \end{bmatrix} = \begin{bmatrix} g_{11} & g_{12} \\ g_{21} & g_{22} \end{bmatrix} \begin{bmatrix} u_1 \\ u_2 \end{bmatrix} \tag{7}$$

Explicit dependency upon s has been deleted in Equation (7) for conciseness. Figure 1 illustrates the block diagram of this open-loop system. In this development, the input and output signals are generic. However, in a R2R web control application, y1(s) and y2(s) could represent web velocity and tension, respectively, while u1(s) and u2(s) may represent torques at unwinder and rewinder. From Figure 1, four transfer functions exist: y1(s)/u1(s) and y2(s)/u2(s) which are the main channels, and y1(s)/u2(s) and y2(s)/u1(s) which are the cross channels

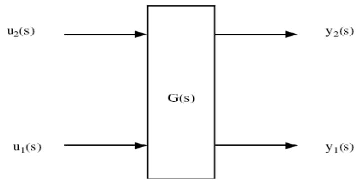

Fig. 1. Open-loop system

The $y_1(s)$ to $u_1(s)$ loop is closed first. The control law loop is

$$u_1 = k_{11}(y'_{1c} - y_1) \tag{8}$$

where k_{11} (s) denotes the compensator transfer function and y'_{1c} denotes the intermediate command signal entering the loop, as shown in Figure 2. The purpose of this loop might be to augment damping or quicken the response of a mode strongly associated with the $u_1(s)$ to $y_1(s)$ channel. Another basic role this loop may serve in is to stabilize inherent airframe instability.

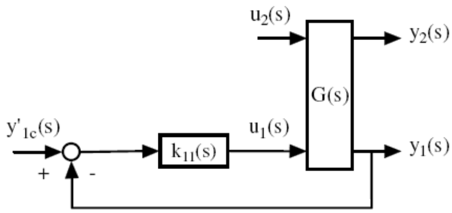

Fig. 2. Loop Closure 1

Combining the equations (7) and (8) yields

$$y_1 = g_{11}k_{11}(y_{1c}^{'} - y_1) + g_{12}u_2 \tag{9}$$

$$y_2 = g_{21}k_{11}(y_{1c}^{'} - y_1) + g_{22}u_2 \tag{10}$$

Using the first of these equations, $y_1(s)$ can be solved for in terms of $y_{1c}^{'}(s)$ and $u_2(s)$. After substituting this result for y1 (s) , the second of the two equations can be solved for y_2 (s) in terms of $y_{1c}^{'}(s)$and $u_2(s)$. The intermediate augmented system after closing the first loop is thus

$$y_1 = \frac{k_{11}g_{11}}{1+k_{11}g_{11}} y_{1c}^{'} + \frac{g_{12}}{1+k_{11}g_{11}} u_2 \tag{10}$$

$$y_1 = \frac{k_{11}g_{21}}{1+k_{11}g_{11}} y_{1c}^{'} + \frac{g_{22}+k_{11}\tilde{g}}{1+k_{11}g_{11}} u_2 \tag{11}$$

In Equation (11), the plant coupling factor $\tilde{g}$(s) is defined as

$$\tilde{g} = g_{11}g_{22} - g_{12}g_{21} \tag{12}$$

Equation (12) is closely related to the plant transmission zero polynomial. The denominator from equations (10) and (11) is used for the gain and phase root locus design, or

$$1 + k_{11}g_{11} = 0 \tag{13}$$

In the gain root locus, k_{11} is used to place the poles with $\theta_{11} = 0$ rad, while in the phase root locus, θ_{11} is used to migrate the poles with the nominal design value for k_{11}. These various gain and phase root loci would be used to design the nominal stability and performance levels and their robustness after the first loop closure.

2.2 Crossfeed Insertion

Various In the case that zeros of the modified $y_2(s)/u_2(s)$ channel are not conducive for closing the second loop, a $u_2(s)$ to y'1c(s) crossfeed is often considered. The crossfeed control law is

$$y_{1c}^{\prime} = y_{1c} + k_{cf}u_2 \tag{14}$$

where $k_{cf}(s)$ is the crossfeed compensator and $y_{1c}(s)$ is the final command signal exciting the initial loop. Figure 3 shows the block diagram for this second design step.

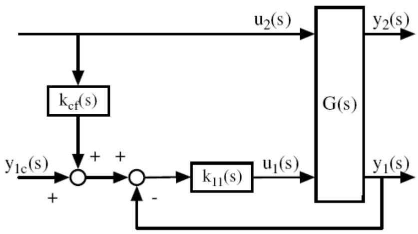

Fig. 3. Crossfeed Insertion

Combing the equations (11), (12) and (13) yields:

$$y_1 = \frac{k_{11}g_{11}}{1+k_{11}g_{11}}(y_{1c} + k_{cf}u_2) + \frac{g_{12}}{1+k_{11}g_{11}}u_2 \quad (15)$$

$$y_1 = \frac{k_{11}g_{21}}{1+k_{11}g_{11}}(y_{1c} + k_{cf}u_2) + \frac{g_{22}+k_{11}\tilde{g}}{1+k_{11}g_{11}}u_2 \quad (16)$$

After manipulating Eqs (15) and (16), these two equations become

$$y_1 = \frac{k_{11}g_{11}}{1+k_{11}g_{11}}y_{1c} + \frac{g_{12}+k_{cf}k_{11}g_{11}}{1+k_{11}g_{11}}u_2 \quad (17)$$

$$y_2 = \frac{k_{11}g_{21}}{1+k_{11}g_{11}}y_{1c} + \frac{g_{22}+k_{11}\tilde{g}+k_{cf}k_{11}g_{21}}{1+k_{11}g_{11}}u_2 \quad (18)$$

Equation (17) and (18) is the math model for the intermediate augmented system after crossfeed insertion. From Equations, observe that crossfeed gain appears in both the $y_1(s)/u_1(s)$ and $y_2(s)/u_2(s)$ channel numerators. The implication is that $k_{cf}(s)$ can be used for manipulation of transfer function zeros. The governing gain and phase root migration equation for the $y_2(s)/u_2(s)$ channel zeros is

$$1 + k_{cf}\frac{k_{11}g_{21}}{1+k_{11}\tilde{g}} = 0 \quad (19)$$

Comparing Equation (19) with Equation (13) shows that the zeros originate from the numerator roots of $g_{22}(s) + k_{11}(s)\tilde{g}$ (s) for small values of k_{cf} and terminate on the numerator roots of $k_{11}(s)g_{12}(s)$ for large values of k_{cf} . The objective here might be to leverage the root loci features in the second loop closure, yet to be considered, by relocating the zeros to more favorable regions in the complex plane. In the phase root locus, k_{cf} is used to assess performance robustness through zero movements with the nominal design value for k_{cf} fixed.

The governing gain-phase root locus relation for the $y_1(s)/u_2(s)$ channel zeros is

$$1 + k_{cf}\frac{k_{11}g_{11}}{g_{12}} = 0 \quad (20)$$

In Equation (20), the crossfeed compensator could be employed to render the response $y_1(s)$, or an undesirable modal contribution to $y_1(s)$, unexcitable from input $u_2(s)$ by tailoring the zero locations in the gain root locus to cancel the critical poles. Robustness of the performance can also be evaluated with both the gain and phase root locus. Finally note in Equation (18), the closed-loop poles are not affected by the crossfeed compensator, as well as the remaining channel numerators in $y_1(s)/y_{1c}$ (s) and $y_2(s)/y_{1c}(s)$.

2.3 Loop Closure 2

The $y_2(s)/u_2(s)$ loop closure utilizes the following control law

$$u_1 = k_{11}(y_{1c}' - y_1) \tag{21}$$

where $k_{22}(s)$ denotes another compensator and $y_{2c}(s)$ denotes the command signal for the second feedback loop. Augmentation of damping or response speed could be the primary function in this loop. Other possible functions are to simply stabilize the air-frame, or eliminate steady state errors. Figure 4 illustrates the corresponding block diagram

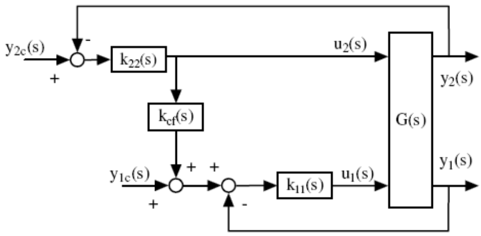

Fig. 4. Loop Closure 2

The output $y_2(s)$ is computed first from the second expression in Equation (21).Clearing the denominator and collecting the $y_2(s)$ terms results in an expression for $y_2(s)$ as a function of $y_{1c}(s)$ and $y_{2c}(s)$. Using the $y_2(s)$ result in the first expression in Equation (21) gives the corresponding expression for $y_1(s)$. The final closed-loop system resulting from this derivation is

$$y_1 = \frac{k_{11}(g_{11}+k_{22}\tilde{g})}{\Delta} y_{1c} + \frac{k_{22}(g_{12}+k_{cf}k_{11}g_{11})}{\Delta} y_{2c} \tag{22}$$

$$y_1 = \frac{k_{11}g_{21}}{\Delta} y_{1c} + \frac{k_{22}(g_{22}+k_{11}\tilde{g}+k_{cf}k_{11}g_{21})}{\Delta} y_{2c} \tag{23}$$

In Eqs (22) and (23), the final overall denominator term $\Delta(s)$ is defined as

$$\Delta = 1 + k_{11}g_{11} + k_{22}(g_{22} + k_{11}\tilde{g} + k_{cf}k_{11}g_{21}) \tag{24}$$

From the denominator of Equation (23), the gain and phase root locus can be introduced based on the following relationship.

$$1 + k_{22}\frac{g_{22}+k_{11}\tilde{g}+k_{cf}k_{11}g_{21}}{1+k_{11}g_{11}} = 0 \tag{25}$$

This design step would set the closed-loop poles at their final locations in the s-plane with resulting nominal stability and performance levels. The root loci can then be used to assess stability robustness (gain and phase margins).

3 Evolution Strategy Based Autonomous Algorithm for R2R Web System

3.1 A Brief Overview of Evolution Strategy

Evolution strategies (ES), piloted by Rechenberg in the 1960s and further explored by Schwefel, are then based on the concept of *the evolution of evolution*. While ESs considers both genotypic and phenotypic evolution, the emphasis is toward the phenotypic behavior of individuals. Each individual is represented by its genetic building blocks and a set of strategy parameters that models the behavior of that individual in its environment. Evolution then consists of evolving both the genetic characteristics and the strategy parameters, where the evolution of the genetic characteristics is controlled by the strategy parameters. The following is a brief of the proposed ES

```
Initiate the strategy parameters
Evaluate the objective function J
Evaluate the constraints
Calculate the maximum value of objective function
Calculate the fitness function value of each population
   Select the best population
   While stopping condition(s) not true do
        For i =1, n do
          Choose i ≥ 2,
          Constraint handling using the Deb's method
          Calculate and select the population
          End
          Tournament selection
          Create offspring through Local, Intermediate recombination operator
             Mutation with anisotropic self-adaption of mutation strength
End
Prepare new population to apply using the (μ + λ) − ES
Check the boundary violence
End
```

3.2 Mathematical Model of Roll-to-roll Web System

Figure 5 shows the two-span roll-to-roll web that consists of unwinder, winder, infeed unit, and two loadcells, rollers, lateral control unit and dancer system. The idle rollers guide the moving web around the load cell in a fixed angle. In order to operate web, unwinder and rewinder motors are used with control torques τ_u and τ_r respectively. There are two dancers on unwind and rewind sides to take up the slack during start-up and shutdown

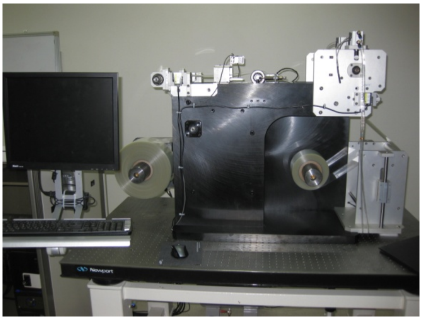

Fig. 5. The roll-to-roll web control system

It is assumed that no web slippage occurs, the web has no permanent deformation due to applied tension, and the load cell and dancer dynamics is ignored. By using Newton's law and the principle of mass conservation with aforementioned assumptions, the non-linear dynamic equations of single-span roll-to-roll web control system can be written as follows:

$$\dot{\omega}_u = \frac{B_u}{J_u}\omega_u + \frac{R_u}{J_u}T - \frac{1}{J_u}\tau_u \tag{26}$$

$$\dot{T} = -KR_u\omega_u - \frac{R_r}{L}T\omega_r + KR_r\omega_r \tag{27}$$

$$\dot{\omega}_r = \frac{R_r}{J_r}T - \frac{B_r}{J_r}\omega_r + \frac{1}{J_r}\tau_r \tag{28}$$

The inertia change satisfies the following equations:

$$R_u = R_{u0} - \frac{h\theta_u}{2\pi} \tag{29}$$

$$R_r = R_{r0} + \frac{h\theta_r}{2\pi} \tag{30}$$

where J_{u0} = total moment of inertia of the unwind roll and motor at start-up time, J_{r0} = total moment of initial inertia of the rewind roll and motor at start-up time, J_u = total moment of inertia of the unwind roll and motor, J_r = total moment of inertia of the rewind roll and motor, ω_u = angular velocity of the unwind roll, θ_u = rotational angular of the unwind roll, ω_r = angular velocity of the rewind roll, θ_r = rotational angular of the rewind roll, R_{r0} = initial radius of the rewind roll, R_{u0} = initial radius of the unwind roll, R_u = operating radius of the unwind roll, R_r = radius of the rewind roll, w = the width of web. The given problem is to design the controller that is required to keep web tension and web velocity at prescribed reference values, satisfy the performance specifications and obtain the high precision and stability.

3.3 Evolution Strategy Based Autonomous Proposal for Roll to Roll Web Control System

In this proposal, digital computers are considered as controllers. The use of sensors is to determine the output values of system. Depending on the reference values, output values and the objective function, the proposed algorithm calculates the convenient gains of controllers and automatically updates the gains after certain time intervals.

Due to the change of parameters and disturbances in operating process, the initial gains are not suitable any more. Thus, a gain tuning scheme needs to be employed at every time interval to make system stable and reliable. The second one has a function that will adjust automatically the gains by using the information about the difference between the output and reference and the value of objective function. The following is the algorithm diagram for the ES based control system design scheme.

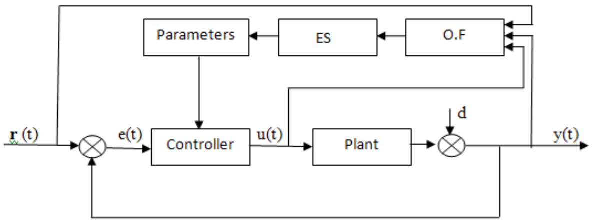

Fig. 6. Evolution strategy base control system design algorithm

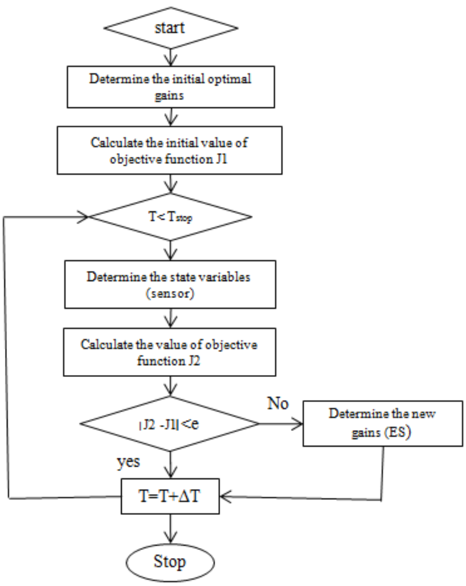

Fig. 7. The algorithm diagram of automatically tuning controller scheme

4 Numerical Simulation

4.1 Simulation Data

By applying the proposed design of PI controllers in chapter 2 and using the root locus design method shown in Fig. 1, Fig. 2, Fig. 3 and Fig. 4, the design parameters are shown in table I, II, and III. The radii of the R2R web system is changing in time, thus, an automatically tuning scheme of web control system is represented in Fig. 6 and Fig. 7, the simulation results are employed with the parameters in two cases. Firstly, a tension command of 0.5 (kgf) is employed in 10 seconds to show the effect of the proposed design in chapter 2. Secondly, a tension command of 0.5 kgf is employed in 50 seconds to show the effect of the online gain tuning scheme using the ES.

Table 1. Parameters of ES

Parameters	Values
A number of generation	N=100
Size of population	S=10
The probability of mutation	p_m=0.5
The probability of crossover	P_c=0.5
Evolution strategy parameters	τ=0.5;τ'=0.25

Table 2. Simulation Parameters of Web Control System

Parameters	values	units
Radius of the unwind roll	0.04	(m)
Radius of the rewind roll	0.015	(m)
Total moment of inertia of unwind roll and motor	0.0000195	(kg/m/s)
Total moment of inertia of rewind roll and motor	0.0000195	(kg/m/s)
Total length of web	0.3	(m)
Spring constant of web	200	(kg/m)
Coefficient of vicious friction of unwinder	0.00002533	(kgms/rad)
Coefficient of vicious friction of unwinder	0.00002533	(kgms/rad)
The thickness of web	0.00002	(m)
The width of web	0.02	(m)

Table 3. Design Parameters in Chapter 2

Parameters	values	units
k_{cf}	0.03	[]
Tension controller: k_p	4.30	[]
Tension controller: k_i	0.11	[]
Web velocity controller: k_p	0.50	[]
Web velocity controller: k_i	0.13	[]

4.2 Experimental Results

Case 1: Step command for web tension

The simulation condition is set up with the zero initial conditions and the desired web tension $T_{ref} = 0.5$ (Kgf) and web velocity of 3.5 (m/s). The following is simulation results;

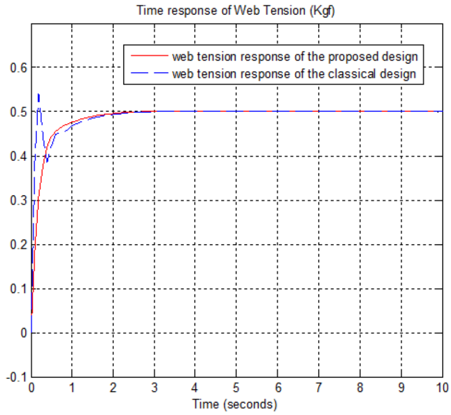

Fig. 8. Step command of 0.5 (kgf) in 10 seconds

From the simulation result, the time response of web tension of the proposed design eliminates the overshoot as compared to the classical design method

Case 2: Affect of the change of radii

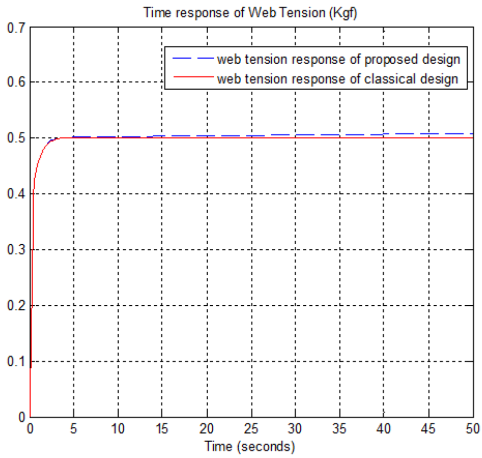

Fig. 9. Step command of 0.5 (kgf) in 50 seconds

From the above simulation result, the web tension response of the classical design goes away from the reference tension due the change of radii of unwinder and rewinder shown with the dashed line in Figure 9. With the online gain tuning scheme of using the ES, the web tension response of the classical design is improved well shown on the solid line in Figure 9

5 Conclusion

In this paper, firstly, 2 inputs and 2 outputs control system design is proposed for nonlinear control system using the uni-directional crossfeed two-channel design approach. Secondly, a scheme for designing the control system with automatic gain tuning in the presence of disturbance and changing parameters in time of using the Evolution Strategy. Finally, single-span roll to roll web control system is applied. The simulation results employed in Matlab/Simulink give the feasibility of proposed algorithm. The following conclusions are made:

1. The web tension response of single-span roll to roll web system with proposed algorithm eliminates overshoot, shorter settling time and also gives high precision when compared to the classical approaches.
2. The online gain tuning scheme of using the ES keeps web tension at reference tension in the presence of the changing radii.

With the rapid development of sensors and electronic devices, the proposed control algorithm results in a control system with high precision and are useful for applications with digital computational system.

Acknowledgements. This study is supported by Ministry of Knowledge Economy through project "Materials and Components Development", Korea.

References

1. Choi, K.-H., Tran, T.T., Kim, D.-S.: Back-Stepping Controller Based Web Tension Control for Roll-to-Roll Web Printed Electronics System. Journal of Advanced Mechanical Design, Systems, and Manufacturing 5(1), 7–21 (2011)
2. Tran, T.T., Choi, K.-H., Chang, D.-E., Kim, D.-S.: Web Tension and velocity control of two-span roll-to-roll system for printed electronics. Journal of Advanced Mechanical Design, Systems, and Manufacturing 5(4), 329–346 (2011)
3. Choi, K.-H., Tran, T.T., Kim, D.-S.: An new approach for intelligent control system design using the modified genetic algorithm. Int. J. Intelligent Systems Technologies and Applications 9(3/4) (2010)
4. Choi, K.-H., Tran, T.T., Su, Y.B., Kim, D.-S.: Printing Pressure Control Algorithm of Roll-to-Roll Web System for Printed Electronics. In: Frontiers of Assembly and Manufacturing, pp. 187–209. Springer (2010)
5. Choi, K.H., Thanh, T.T., Kim, D.S.: A control system design of automatically tuning controller for roll to roll web system using the modified genetic algorithm. In: Proceedings of the 7th Asian Control Conference, Hong Kong, China, August 27-29 (2009)

6. Kang, C.-G., Lee, B.-J.: Stability analysis for design parameters of a roll-to-roll printing machine. In: International Conference on Control, Automation and Systems 2007, COEX, Seoul, Korea (2007)
7. Song, S.-H., Sul, S.-K.: A new tension controller for continuous strip processing line. IEEE Transactions on Control Systems Technology 11(1), 2225–2230 (1998)
8. Zolotas, A.C., Halikias, G.D.: Optimal design of PID controllers using the QFT method. IEE Proc. Control Theory Applications 46(6), 585–589 (1999)
9. Kim, J.-S., Kim, J.-H., Park, J.-M., Park, S.-M., Choe, W.-Y., Heo, H.: Auto tuning PID controller based on improved genetic algorithm for reverse osmosis plant. Proceedings of World Academy of Science Engineering and Technology 30, 1001–1007 (2008)
10. Lee, B.-J., Kim, S.-H., Kang, C.-G.: Analysis of a nonlinear web-tension control system of a high-speed gravure printing machine. In: SICE-ICASE International Joint Conference, Bexco, Busan, Korea, October 18-21 (2006)
11. Lin, K.C.: Observer – based tension feedback control with friction and inertia compensation. IEEE Transactions on Control Systems Technology 11(1), 109–118 (2003)
12. Lin, K.C., Tsai, M.-C., Chen, K.-Y.: Web tension control of a start-up process using observer techniques with friction and inertia compensation. In: The 27th Annual Conference of the IEEE Industrial Electronics Society (2001)
13. Shin, K.-H., Kwon, S.-O., Kim, S.-H., Song, S.-H.: Feedforward control of the lateral position of a moving web using system identification. IEEE Transactions on Industry and Applications, 345–351 (2003)

Mechanism Design and Locomotion of a Snake Robot

Qin Gao[1], Zhelong Wang[1,2], Hong Shang[3,⋆], Weijian Hu[3], and Ming Jiang[1]

[1] School of Control Science and Engineering, Dalian University of Technology, Dalian, China
[2] State Key Laboratory of Robotics, Shenyang Institute of Automation, Chinese Academy of Sciences, Shenyang, China
[3] Technical Division, National Earthquake Response Support Service, Beijing, China
shong660@163.com

Abstract. As a high redundancy system with high stability and adaptability, disaster rescue robot is widely used in collapsed buildings for search and rescue work. In the paper, a snake-like robot based on cylinder module is developed. The robot prototype consists of eleven modules that are connected by revolute joints. Each joint has two degrees of freedom and allows bending in two mutually orthogonal planes. The serpenoid curve is considered as the control law and control parameters of snake curve are chosen by simulation and adjusted after experiment. Experimental results of snake robot show that the gait based on serpentine curve is reasonable and controlled easily.

1 Introduction

Snake robots have the potential to make substantial contributions in areas such as rescue missions, firefighting, and maintenance where it may either is too narrow or too dangerous for personnel to operate [1]. It has proven that the snake-like robots are more flexible and adaptable in difficult environments than conventional wheeled or legged mobile mechanisms.

Snake robots with many degrees of freedom have been studied in the past decades. The important characteristic of limbless locomotion was investigated and the mechanism of snake robot was also analyzed by many researchers. The early research on snake robots can be dated as far back as the robot made by Shigeo Hirose in 1972 which has 20 revolute joints with one degree of freedom called the Active Cord Mechanism model ACM II [2]. After his snake robot more and more prototypes and locomotion methods related to snake-like robot has been reported. A serpentine robot named GMD was realized by driving wheel as the scales [3]. Recently, the paper [4] presented a novel joint mechanism with spherical module for a snake robot aimed at enabling the robot to demonstrate obstacle-aided locomotion in cluttered and irregular environments. Furthermore, research has been aimed at mathematical formulation of snake motion, kinematics [4] and dynamics [5], using robotic snakes with wheels [6], crawler tracks [7] or only the snake body itself [8]. The work in [9] offered a Gibbs-Appell method analyzing the dynamic dynamic model in detail. The work [10] explained the method of non-smooth to build the dynamic model of the snake robot.

⋆ Corresponding author.

S. Lee et al. (Eds.): Intelligent Autonomous Systems 12, AISC 194, pp. 731–738.
springerlink.com

Although much work related to snake robot was analyzed in the published literature, there are still many challenges to face both on the modeling and control of snake robot due to its high number of degrees of freedom and how to achieve an easily controlled gait for practical use of snakelike robot movement is worthwhile to consider. Most work was done on the creeping propulsion since lateral locomotion is the most frequently and efficient form of snakes. To achieve creeping locomotion on a supporting plane, a snake robot with different friction coefficients in the tangential and the normal directions with respect to the body is designed in the paper. Up to now most of the snake robot employ wheels to realize the directional friction, which are also utilized in our robot. To establish an easily controlled gait for practical use of snakelike robot movement, a crawl locomotion gait model based on a serpenoid curve is presented in the paper. The efficiency of the gait is given. Parameters of the criterions and their influence on the efficiency of the gait are discussed by simulations and experiments.

2 Mechanical Designs and Control System

As a biological machine, snake robot is always designed to connect in series joint units which can bend in an animated manner. In the section, the mechanism design and control system of our robot will be introduced.

2.1 Mechanism Design

In our design, the cylinder module of snake robot is capable of becoming extended or removed easily. The whole mechanical snake consists of eleven links which are connected through active joints that allow bending in two mutually orthogonal planes. The joint module of snake robot, as shown in Fig. 1, mainly consists of two small dc motors, two motor housings, two bevel gear set, passive wheels and an active ring. Each revolute joint with two degrees of freedom is directly actuated by two motors. One motor is used to control the angle between one link and the next link on the horizontal plane and the other is used to control the angle between the link and the next on the vertical plane.

To show the diversity of our snake robot, we will discuss the mechanism compared to Anna Konda which is designed as a firefighter robot with joints operated by a water

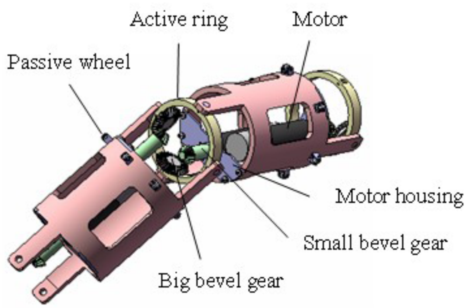

Fig. 1. The structure of one joint of our snake robot

hydraulic actuation system[12]. In our design, A small geared dc motor is chosen to actuate the joint due to its great torque and compact size that make it possible to realize small module to increases flexibility in ruins environment. The joints with two degrees of freedom make it possible for snake robot to be capable of locomotion in complex three-dimensional environment.

The dimension of the module of our snake robot is much smaller than that of Anna Konda. The head link of our robot is special where it does not contain the same internals as the body links, but rather makes room for infrared sensor, power and controllers. This gives the head segment a length 20cm, and a radius 8cm while the body segments a length 16cm and a radius 8cm. The maximum angle in yaw and pitch direction with respect to each module are both $\pm 45°$ which are limited by the position and shape of the bevel gear set.

In the published paper [10], Anna Konda achieves sidewinding motion successfully but the lateral locomotion without the aid of external obstacles is not mentioned and it is a apparent challenge since its mechanism design does not meeting the character of diversity of friction force in normal and tangential direction which is essential to the special gait of serpentine locomotion. Wheels are a simple and efficient tool to help achieve the locomotion. In our design, six passive wheels are fixed on the cylinder body in the uniform distribution. With the modified construction, the flexibility and adaptability of our snake robot will be enhanced.

2.2 Control System of Snake Robot

Our snake robot consists of 11 links and has 20 degrees of freedom. The robot control system mainly comprises of a computer, dual serial motor controllers, position feedback sensors and power supply, and is shown in Fig. 2.

The main computer, as a centralized controller, is responsible for the high level control such as parameters setting, motion shape selection and dealing with the feedback information from position sensors. The microcontroller based on Atmel Atmega1280 is employed to detect the voltage change signal of position sensor and offers feedback to the computer. The dual serial motor controller Qik 2s9v1 produced by Pololu company, as Fig. 3, is employed as a motor controller. Each joint is equipped with such a

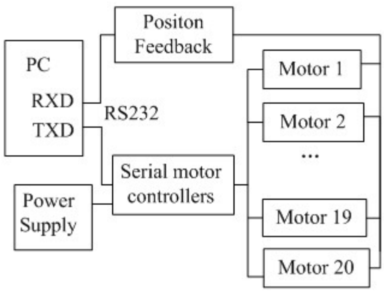

Fig. 2. The general control architecture of the snake robot

controller. Once the motor controller receives control data from computer via RS232 transmitted in the scheduled protocol format defined by the motor controllers' manufacturer, it drives to control the joints' pitch and yaw.

3 Gaits for Snake Robot and Kinetics Model

The snake robots achieve all forms of movement mainly through controlling the shape of the body. We control the shape appropriately, and then the snake robot will achieve the desired locomotion. Here, inchworm locomotion based on serpentine curve is the elective movement for our robot. The inchworm locomotion is based on traveling waves of mechanism deformation on the plane. We simplify the snakelike robot as a multilink system consisting of N identical links. The number of links that form the traveling wave is $n = 4$ and the number of whole snake robot is $N = 11$. Fig. 4 shows general steps of the inchworm locomotion of snake robot. At the beginning all the links stay in a straight line. The propulsion step of a traveling wave is from state b to state d. After one entire cycle of movements, the snake robot advances along the desired direction for a distance d_{step}. In the paper, we assume the robot move in low speed, so its dynamistic effect can be not considered in this case and its kinematical analysis of serpentine locomotion is presented in the following paper. The traveling wave model is shown as Fig. 5, and the relative angles of the joint are derived from serpenoid curve.

Serpenoid curve first introduced by Shigeo Hirose is efficient [11]. According to his studies, the tangential angles of this path must be a sinusoidal function, the snake curvature satisfies

$$\rho = -ab\sin(bs) \tag{1}$$

where α represents the amplitude of an angle, b represents constant ratio and s represents the snake curve arc length, respectively. The curve angle can be derived from integration of the curvature function as follows

$$\theta(s) = \alpha cos(bs) \tag{2}$$

Then we find the relative joint angle as

$$\varphi = \theta(s+l) - \theta(s-l) = 2\alpha sin(bl)sin(bs) \tag{3}$$

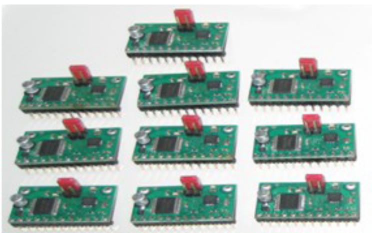

Fig. 3. A dual serial motor controller Qik 2s9v1 used in the snake robot

where l is half the length of one body link of snake robot. Now we can get the relative angle of each joint which is time function as follow

$$\varphi_i = A sin(-\omega t + (i-1)\beta) \tag{4}$$

where $A = -2sin(bl)$, $\omega t = bs$, $\beta = 2bl$, for $i = 1, \cdots, N-1$. In the work [12], it presents that A, β are the parameters that determine the shape of the serpenoid curve realized by the snake robot and ω specifies how fast the serpentine wave propagates along the body, the simulation results based on different control parameters are shown as Fig. 6.

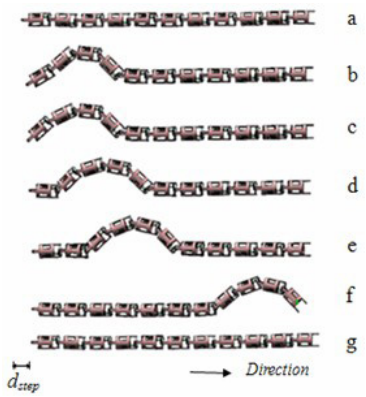

Fig. 4. The movement steps of the inchworm gait based on traveling wave

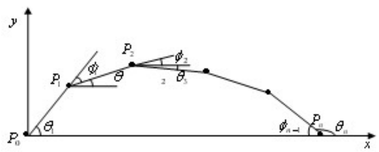

Fig. 5. The link model of snake robot

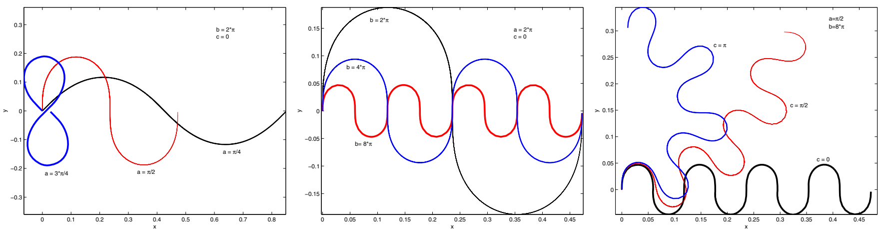

Fig. 6. The various serpentine curves when the parameter a varies(left),b varies(middle),and c varies(right)

In the paper, we assume the number of links forming the traveling wave $n = 4$. The initial relative angle of the motion curve at $t = 0$ is obtained as

$$\varphi_i^0 = Asin(i\beta) \tag{5}$$

for $i = 1, 2, 3$. Then the forward distance after one entire cycle of movements is obtained by

$$d_{step} = l(n - \sum_{i=0}^{n} cos(\varphi_{i+1} - \varphi_i)) \tag{6}$$

We assume that the initial shape of snake robot is in a straight line state, and thus there is a transition step of movement from static state to creeping state. For starting the locomotion, the initial winding angle is increased gradually from zero to a required value. The change is transmitted from the front joint to the end joint in order and the snake robot move forward at a distance of d_{step} after one entire cycle of the traveling wave formed by n joints.

4 Experience

In this section, we present the experimental results. All the small motors are actuated at the same time, so the body of snake robot can be curled up into sine curve in a moment. Then we will carry on control all segment rotating in the same regulation, but just under a time space. The reference relative joint angles are dependent on the parameters $\alpha = \pi/6$ rad, $\beta = \pi/3$ rad, $\omega = 1.5$ rad, which control the shape of the traveling wave and the speed of the wave. The experimental motion is shown in Fig. 7.

From the Fig. 7, we find that the traveling wave seems smooth since the relative joint angels are based on the classical serpentine curve. The inchworm locomotion is

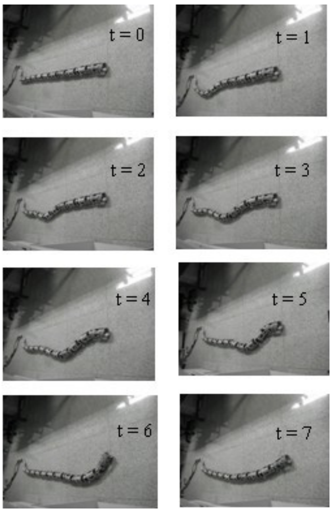

Fig. 7. The experimental result of inchworm locomotion

often applied on the vertical plane, but it does not mean the similar traveling wave is impossible to realize on the horizontal plane. The experimental results for the motion prove that the inchworm locomotion is a useful method for snake robot. The robot moves forward at a distance 9cm approximately within 10 seconds after one entire cycle of the sine wave traveled from the end joint to the front joint in order.

However, there are some problems needed to notice. The shape of the whole snake robot was not able to recover a straight line as an initial straight line state when one cycle motion ends. Many reasons might account for the problem. Firstly, although snake robot moves slowly to avoid the sideslip, it is not valid that the contact force between a snake-like robot and the ground surface is not considered totally. So the pure kinematical model built in the paper may contribute to the final arc state of the snake robot. Secondly, the snake robot designed in the paper has a noticeable free play in the joints of about $3 - 5°$. This results in that the control of the joint angles is not completely accurate and a joint angle might not be able to reach its desired angle.

5 Conclusion

In the paper we design a snake robot with joint of two degrees of freedom and realize its inchworm gait which is a practical motion and controlled easily. Experimental results of the snake robot show that the gait based on serpentine curve is reasonable and the snake robot moves forward smoothly. However, there are still a lot of work that need to solve. The speed of the motion is not enough efficient in order to avoid sideslip. The contact force between snake robot and the ground surface is necessary to consider and a new model is needed to build badly.

Acknowledgment. This work is partially supported by the China Postdoctoral Science Foundation (20080441102), China Earthquake Sector Research Funds (200808075), National Science and Technology Major Project Grant (2010ZX04007-011-5) and National Natural Science Foundation of China (61174027).

References

1. Transeth, A.A., Pettersen, K.Y.: Developments in snake robot modeling and locomotion. In: 9th IEEE International Conference on Control, Automation, Robotics and Vision, ICARCV 2006, pp. 1–8 (2006)
2. Hirose, S.: Biologically inspired robots: Snake-like locomotors and manipulators (1993)
3. Klaassen, B., Paap, K.L.: Gmd-snake2: a snake-like robot driven by wheels and a method for motion control. In: Proceedings of 1999 IEEE International Conference on Robotics and Automation, vol. 4, pp. 3014–3019. IEEE (1999)
4. Liljeback, P., Fjerdingen, S., Pettersen, K.Y., Stavdahl, O.: A snake robot joint mechanism with a contact force measurement system. In: IEEE International Conference on Robotics and Automation, ICRA 2009, pp. 3815–3820. IEEE (2009)
5. Nilsson, M.: Serpentine locomotion on surfaces with uniform friction. In: Proceedings of IEEE/RSJ International Conference on Intelligent Robots and Systems (IROS 2004), vol. 2, pp. 1451–1455. IEEE (2004)

6. Liljeback, P., Stavdahl, O., Pettersen, K.: Modular pneumatic snake robot: 3d modelling, implementation and control. Modeling, Identification and Control 29(1), 21–28 (2008)
7. Yamada, H., Chigisaki, S., Mori, M., Takita, K., Ogami, K., Hirose, S.: Development of amphibious snake-like robot acm-r5. In: Proc. ISR 2005 (2005)
8. Miyanaka, H., Wada, N., Kamegawa, T., Sato, N., Tsukui, S., Igarashi, H., Matsuno, F.: Development of an unit type robot kohga2 with stuck avoidance ability. In: 2007 IEEE International Conference on Robotics and Automation, pp. 3877–3882. IEEE (2007)
9. Vossoughi, G., Pendar, H., Heidari, Z., Mohammadi, S.: Assisted passive snake-like robots: conception and dynamic modeling using gibbs–appell method. Robotica 26(3), 267–276 (2008)
10. Transeth, A.A., Leine, R.I., Glocker, C., Pettersen, K.Y.: Non-smooth 3d modeling of a snake robot with frictional unilateral constraints. In: IEEE International Conference on Robotics and Biomimetics, ROBIO 2006, pp. 1181–1188. IEEE (2006)
11. Liljeback, P., Stavdahl, O., Beitnes, A.: Snakefighter-development of a water hydraulic fire fighting snake robot. In: 9th International Conference on Control, Automation, Robotics and Vision, ICARCV 2006, pp. 1–6. IEEE (2006)
12. Sato, M., Fukaya, M., Iwasaki, T.: Serpentine locomotion with robotic snakes. IEEE Control Systems Magazine 22(1), 64–81 (2002)

Expression Intensity Recognition Based on Multilayer Hybrid Classifier

Xia Mao, Chongping Wang, and Yuli Xue

School of electronic and information engineering, BeiHang University
P.O.Box 206, Beihang University, Beijing, China
moukyou@buaa.edu.cn, chongpingwang@126.com

Abstract. In this paper, an automatic system for recognizing expression intensity is proposed. Modified Active Appearance Model (MAAM) is utilized to extract facial feature points (FFPs), and then, according to the FFPs' position, the sequence is preprocessed. Coarse-to-fine pyramid algorithm is employed to track FFPs for extracting 23 optical flow vectors, and eliminating the error caused by rigid movement of head. Expression intensity is recognized by multilayer hybrid classifier. Support Vector Machine (SVM) classifies the expression in the form of optical flow vectors, and KNN classifier recognizes the intensity. We conduct the experiments on Cohn-Kanade expression database and the result shows good effect.

Keywords: Expression intensity recognition, MAAM, optical flow vector, SVM, KNN.

1 Introduction

Facial expression, an important form for communication, has rich emotion information. Automatic expression understanding can increase the emotional dimension for human-computer interaction (HCI). Since the 1990s, the research of expression recognition is increasingly active and has attracted many institutes [1-4].

The static and dynamic expression recognition under controlled condition has reached a high level. However most of them only recognize six basic expressions: happy, sad, fear, disgust, surprise and angry. Psychology research indicates that only six basic expressions cannot understand human emotion perfectly. Actually human emotion may vary with intensity of identical expression, so recognizing different intensity is significant and can serve in HCI for perceiving human emotion precisely. Now, researchers have studied subtle expression recognition: James and Kanade used the method combining sparse optical flow, dense optical flow and the high gradient for subtle expression recognition [5]; Park and Kim recognized subtle expression by amplifying facial optical flow feature vector [6]. Expression intensity recognition attracts no comprehensive attention, as it is more difficult than subtle expression recognition. For expression intensity recognition: Essa and Pentland used optical flow representing the variety of the expression intensity [7]; Amin and Yan measured expression intensity from facial images by self-organizing maps [8].

S. Lee et al. (Eds.): Intelligent Autonomous Systems 12, AISC 194, pp. 739–748.
springerlink.com

Expression intensity recognition is still developing; further effort is required to promote the expression recognition. This paper proposes expression intensity automatic recognition system as shown in Fig.1: It consists of two main parts: (1) feature extraction and (2) expression intensity recognition. Feature extraction consists of three steps: First, Modified-AAM fitting extracts 40 facial feature points. Second, the input sequence is preprocessed. Finally, the motion vectors of 23 feature points are extracted. After feature extracted, expression intensity is recognized: Using SVM recognize expression and then corresponding K-NN classifier is selected to classify expression intensity into less, middle and very.

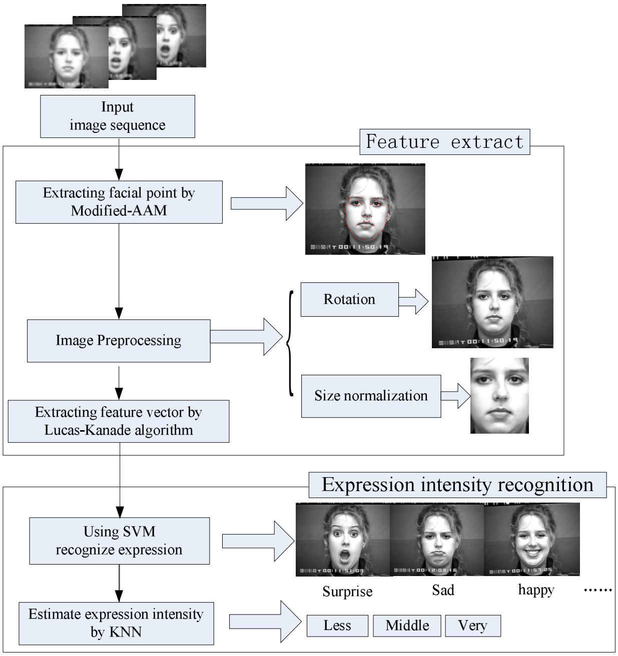

Fig. 1. Expression intensity automatic recognition system

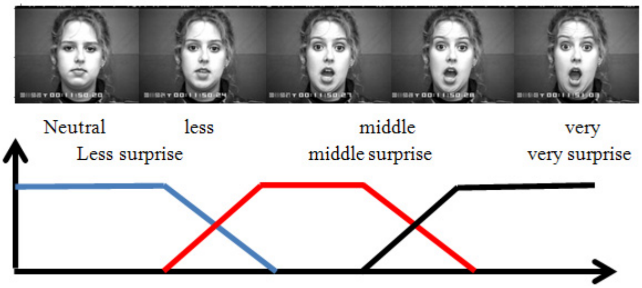

Fig. 2. An expression sequence and its classification

Expression intensity is divided into three classes, which is corresponding to a part of the time sequence of expression, which is shown in Fig.2.

The remainder of this paper is as follows. In Section 2, we introduce how to extract optical flow vectors. In Section 3, multilayer hybrid classifier is presented to recognize expression intensity. Section 4 discusses experimental results on CMU Expression Database showing that our approach is effective for expression intensity recognition. Conclusions are stated in Section 5.

2 Feature Extraction

Automatic expression recognition can not be achieved by manually marking FFPs, so we extract facial feature points (FFPs) automatically with modified active appearance model.

2.1 Modified Active Appearance Model (MAAM)

In 1998, Cootes first proposed AAM based on ASM [9]. AAM establishes models for both object shape and texture, and than combining shape and texture model to establish appearance model, which reflects change of object shape in company with texture, so the accuracy is higher than the ASM. But it fails to align object in large scale motion. In order to improve the nonlinear alignment performance of AAM, we apply a variant of the nonlinear manifold learning algorithm, Local Linear Embedded, to model shape-texture manifold [10]. Experiments show that our method maintains a lower alignment residual to some small scale movements compared to traditional AAM based on Principal Component Analysis (PCA) and makes a successful alignment to large scale motions when PCA-AAM failed.

After AAM model is established, target matching is realized by adjusting the parameters of the model to make the gray difference between synthetized image and searched image minimum, namely minimizing the error showing in (1).

$$\Delta = \|\delta g\|^2 = \|g_s - g_m\|^2 \tag{1}$$

Where g_s is the normalized sampling values of actual image texture, and g_m is image texture, which can be calculated by texture model.

With a larger number of FFPs to build appearance model, the result is more accurate at the expense of computational complexity. So we use 40 feature points representing the facial shape. We extract FFPs in the Cohn-Kanade database by MAAM, shown in Fig.3.

2.2 Image Preprocess

Recognition accuracy can be improved by preprocessing, including angle and size normalization.

Fig. 3. 40 FFPs on the face

Angle normalization: the quality of extracted feature vectors will be affected by tilted facial images. So facial images need to be rotated ensure uniformity of the face geometrical position. Firstly we calculate the angle between horizontal line and two eyes, and then, image is reverse rotated by this angle. Bilinear quadratic interpolation is used to calculate pixel gray value of the new coordinates produced by rotation, and rotated image is clipped to match the original.

Size normalization: clipping image to reduce the factor has nothing to do with the expression intensity recognition after image rotated. Suppose horizontal distance of eyes is D, clipping approach and clipped image are illustrated in Fig.4.

Fig. 4. Rotated and clipped image

2.3 Feature Extraction

AAM can be applied to video tracking directly, which is suitable for small motion, but fails to make use of similarity between frames. So we use LK algorithm to track FFPs. Barron compared various optical flow algorithms [11], and the result indicates that LK algorithm is more accurate, stability, fast, and easy to implement.

The principle of LK algorithm tracking FFPs is based on three hypotheses: the first one is brightness constant which can be expressed as:

$$f(t) \equiv I(x, y, t) = I(x + \Delta x, y + \Delta y, t + \Delta t) \tag{2}$$

Where $I(x, y, t)$ is the gray of (x, y) at time t, $I(x+\Delta x, y+\Delta y, t+\Delta t)$ is gray of $(x+\Delta x, y+\Delta y)$ at time $t+\Delta t$.

The second is time continuous and Equation (2) can be converted to Taylor formula at $I(x, y, t)$.

$$\frac{\partial I}{\partial x}u+\frac{\partial I}{\partial y}v+\frac{\partial I}{\partial t}=0 \tag{3}$$

Where $u=\frac{dx}{dt}$, $v=\frac{dy}{dt}$ is velocity in x and y axis of (x, y) at time interval $\Delta t=t_k-t_{k-1}$ respectively. There are two variable in (3). It has no definitely solution without constraint added.

The last hypothesis is spatial consistent, in other words, pixels in a small area have the same optical flow. This can be established as follows.

$$\begin{bmatrix} I_x(p_1) & I_y(p_1) \\ I_x(p_2) & I_y(p_2) \\ \vdots & \vdots \\ I_x(p_{n\times n}) & I_y(p_{n\times n}) \end{bmatrix}\begin{bmatrix} u \\ v \end{bmatrix}=\begin{bmatrix} I_t(p_1) \\ I_t(p_2) \\ \vdots \\ I_t(p_{n\times n}) \end{bmatrix} \tag{4}$$

u, v motion weight can be calculated from (4).

We select 23 FFPs most relevant to expression, of which 6 in eyebrows, 8 in eyes, 3 in nose and 6 in mouth. LK algorithm is utilized to track FFPs for obtaining optical flow vectors. Fig.5 illustrates the changing process of disgust sequence FFPs' position. Expression characteristics are: the eyebrows curl, lips down, the nose drive up, and eyes closed slightly reveal an expression of disgust.

(a) (b) (c) (d) (e)

Fig. 5. The changing process of disgust sequence FFPs' position

Rigid motion of head is inevitable in the process of tracking FFPs. There is large error in optical flow vectors as illustrated in Fig.6.

Fig. 6. Fixed optical flow vectors are achieved

In order to eliminate it, optical flow vectors are fixed by affine transform to current frame: firstly, angle rotation; secondly, align with the first frame. Then using the current FFPs' position minus the first frame, fixed optical flow vectors will be achieved as Fig.6 shows.

3 Expression Intensity Classify

Six basic facial expressions and each have three kinds of intensity; the classes need to be recognized up to 18. For samples near the hyperplane constructed by SVM, it is not easy to discriminate them. But, KNN classifier can use the information of samples to classify them, so multilayer hybrid classifier is used to recognize expression intensity. Firstly, SVM classifies the expression in the form of optical flow vectors into six basic expressions, and then recognizing intensity by corresponding KNN classifier.

3.1 SVM Recognize Expression

SVM can solve problems of small samples, nonlinear and high dimensional, widely applied in pattern recognition. The basic idea can summary as follows: converting input space into a higher dimension by non-linear transform, then constructing optimal linear plane in new space. Nonlinear transform is achieved by kernel function, so the key issue of SVM classifier design is to choose the kernel function. There are four kernel functions: linear kernel, polynomial kernel function, radial basis kernel function and Gaussian kernel function. The kernel function is selected by experiment based on classification accuracy, and finally we choose radial basis kernel function.

For training samples, 23 feature vectors are used to train SVM classifier. The trained SVM is used to classify 23 feature vectors of test sample into six basic expressions, and then the KNN classifier is selected to classify expression intensity into three kinds.

3.2 KNN Classify Intensity

Edward proposed K-Nearest Neighbor (KNN) on the basis of Nearest Neighbor (NN) [12]. It classifies test sample to the class who appears most time among the k nearest neighbors' sample. This non-parametric classification algorithm is very effective, and its basic principles are summarized as follows:

$L=\{(x_i, y_i), x_i \in \mathbf{R}^d, i=1,2,\ldots,N\}$ are labeled data sets, x_i is train data, y_i is its label, and $y_i \in \{\omega_1, \omega_2, \ldots, \omega_c\}$. x_t is the test sample and y_t is its label, Euclidean distance between x_i and x_t is:

$$d(x_t, x_i) = \left(\sum_{j=1}^{d} \left| x_{tj} - x_{ij} \right|^2 \right)^{1/2} \tag{5}$$

Suppose k_i represents sample number of class ω_i among k nearest sample of x_t .

$$\sum_{i=1}^{c} k_i = k \tag{6}$$

The class of x_t is the label corresponding to maximum of k_i

$$y_t = \max_i (k_i) \tag{7}$$

Then we label the expression sequence and then extract the optical flow vectors of different intensity. Optical flow vectors of different intensity are added to training set. There are training set for six basic expressions respectively and six KNN classifiers are constructed to classify expression intensity.

4 Result

The expression databases used in our experiments are Cohn-Kanade Expression Database [13]. As we know, expression intensity varies from neutral to apex in sequence. 40 sequences are randomly selected from the database for each basic expression. 15 students to label the sequence; 1, 2, 3 represent less, middle and very respectively. According to the statistical results, we label each of the sequence with the class which most of the students have agreed on. Fig.7 is a labeled sequence.

Neutral 1 2 3

Fig. 7. The labeled sequence

Firstly expression of last frame is recognized, the selected 40 sequences are divided into quarters. The feature vectors are extracted by our approach and SVM is used to classify the feature vectors. The leave-one cross-validation approach is used to make maximal use of the available data. Table I presents confusion matrix, contrast to the result without image sequences preprocessed and rigid motion error eliminated, our method is better.

Table 1. Confusion matrix for expression recognition

Expression	happy	sad	fear	disgust	surprise	angry
happy	40	0	0	0	0	0
sad	0	37	1	0	0	2
fear	3	0	35	1	1	0
disgust	0	0	1	39	0	0
surprise	0	0	1	0	39	0
angry	0	2	0	3	1	34

For expression intensity recognition, 10 sequences are picked out of 40 labeled sequences as test set and the rest as training set. Sample of less, middle and very intensity is selected from a sequence respectively. So each basic expression includes 30 test samples and 90 training samples. For training samples, totally 540 of six basic expressions are used to train SVM and 90 of each expression includes three kinds of intensity are employed to train KNN classifier. For test samples, SVM classifies them into six basic expressions. According to the result of expression recognition, corresponding KNN classifier is selected to recognize expression intensity. Table II is the recognition result of expression with different intensity by SVM and Table III is expression intensity recognition result by KNN classifier.

Table 2. Expression with different intensity recognition result

Expression	happy	sad	fear	disgust	surprise	angry
happy	26	1	2	1	0	0
sad	1	21	3	2	1	2
fear	6	1	20	1	2	0
disgust	1	0	3	22	0	4
surprise	2	0	2	1	25	0
angry	1	5	1	3	0	21

Table 3. Expression intensity recognition result by KNN classifier

Expression	happy			sad			fear		
intensity	1	2	3	1	2	3	1	2	3
accuracy	7	9	10	5	6	8	5	7	8
Expression	**disgust**			**surprise**			**angry**		
intensity	1	2	3	1	2	3	1	2	3
accuracy	5	7	10	6	8	10	5	6	9

The above three experiments indicates that recognition accuracy of last frame in sequence can reach 95.5% by image sequences preprocessing and error eliminating. While recognition accuracy of expression including different intensity is 75.5%, for the discrimination of less intensity is low. Even though, expression intensity recognition accuracy of this approach is far better than [8] and accuracy obtained by a single classifier (SVM or KNN).

5 Conclusion

This paper presents an automatic intensity recognition system, which can recognize different expression intensity. MAAM is used to promote the accuracy of FFPs mark, as the foundation for the system. Then we use pyramid LK algorithm to track FFPs and obtain optical flow vectors with error eliminated. Expression intensity is recognized by multi-level hybrid classifier and classification capacity is better than a single classifier (SVM or KNN). It can be used in intelligent machine to understand human emotion precisely.

Good result for expression intensity recognition is achieved with the average accuracy 75.5%. But now, the accuracy is still low and there are no more effective approaches for expression intensity recognition, so further research is needed to improve the expression intensity recognition accuracy.

Acknowledgements. This work is supported by International Science and Technology Cooperation Program of China and Japan (No.2010DFA11990), National Nature Science Foundation of China (No.61103097). The authors wish to thank J. F. Cohn for supplying us the Cohn-Kanade Facial Expression database.

References

1. Donato, G.: Classifying facial actions. IEEE Transactions on Pattern Analysis and Machine Intelligence 21(10), 974–989 (1999)
2. Ma, L., Khorasani, K.: Facial expression recognition using constructive feedforward neural networks. IEEE Transactions on Systems, Man, and Cybernetics, Part B: Cybernetics 34(3), 1588–1595 (2004)
3. Wu, Y., Liu, H., Zha, H.: Modeling facial expression space for recognition. In: IEEE/RSJ International Conference on Intelligent Robots and Systems, pp. 1968–1973 (2005)
4. Jung, S.U., An, K.H., Chung, M.J.: Efficient rectangle feature extraction for real-time facial expression recognition based on AdaBoost. In: IEEE/RSJ International Conference on Intelligent Robots and Systems, pp. 1941–1946 (2005)
5. Lien, J.J.J.: Subtly different facial expression recognition and expression intensity estimation. In: IEEE Computer Society Conference on Computer Vision and Pattern Recognition, pp. 853–859 (1998)
6. Park, S., Kim, D.: Subtle facial expression recognition using motion magnification. Pattern Recognition Letters 30(7), 708–716 (2009)
7. Essa, Pentland: Coding, analysis, interpretation, and recognition of facial expressions. IEEE Transactions on Pattern Analysis and Machine Intelligence 19(7), 757–763 (1997)
8. Amin, M.A., Yan, H.: Expression intensity measurement from facial images by self-organizing maps. In: IEEE International Conference on Machine Learning and Cybernetics, vol. 6, pp. 3490–3496 (2008)
9. Cootes, T., Edwards, G.J.F., Taylor, C.J.: Active appearance models. IEEE Transactions on Pattern Analysis and Machine Intelligence 23(6), 681–685 (2001)
10. Wang, X.K., Mao, X., Caleanu, C.D.: Nonlinear Shape-Texture Manifold Learning. IEICE Transactions on Information and Systems 93(7), 2016–2019 (2010)

11. Barron, J.L., Fleet, D.J., Beauchemin, S.S.: Performance of optical flow techniques. International Journal of Computer Vision 12(1), 43–77 (1994)
12. Patrick, E.A., Fischer III, F.P.: A generalized k-nearest neighbor rule. Information and Control 16(2), 128–152 (1970)
13. Lucey, P., et al.: The Extended Cohn-Kanade Dataset (CK+): A complete dataset for action unit and emotion-specified expression. In: IEEE Computer Society Conference on Computer Vision and Pattern Recognition Workshops (CVPRW), pp. 94–101 (2010)
14. Ertekin, S., Huang, J., Giles, C.L.: Active learning for class imbalance problem. In: Proceedings of the 30th Annual International ACM SIGIR Conference on Research and Development in Information Retrieval, pp. 823–824 (2007)

Cooperative Multi-robot Searching Algorithm

Seohyun Jeon, Minsu Jang, Daeha Lee, and Young-Jo Cho

ETRI, 218 Gajeongro, Yuseonggu, Daejeon, 305-700 Korea
{happyseohyun,minsu,bigsum,youngjo}@etri.re.kr

Abstract. The problem of multi-robot for searching mission with fully communicative known environment is considered in this paper. Robots are required to maneuver every part of the given environment repeatedly until they find a target object. In order to increase the effectiveness of deploying the mult-robot, they need to be spread out sufficiently, not overlapping the searching area with other robots. To achieve this, we proposed an algorithm about deploying the multi-robot with maximizing the on-line coverage of the searching area. A shared dynamic map and its updating algorithm is proposed. Robots find next exploration area autonomously while updating the shared dynamic map. The algorithm is tested by simulation and the result is presented.

Keywords: multi-robot, coverage, searching, cooperative searching.

1 Introduction

A multi-robot system is well suited for searching and exploration of robotic mission, especially when the mission is time consuming or dangerous. Searching a target with multiple mobile robots is practical for such applications as building maintenance or environmental monitoring. The multi-robot system can locate the fire ignition point [1], clean or find an intruder of a building [2] or search source of radiation, mines [3], victims [4], and the odor of waste [5], regarding its attached sensor and manipulator.
To find a target with multi-robot, rather than visiting the searching area once, robots are required to maneuver continuously until they find a target object or terminated by user. The purpose of multi-robot searching algorithm is therefore different with multi-robot coverage or exploration problem.[6][7] Robots have to continuously visit every part of the map, by maximizing the multi-robot coverage at the same time. In order to increase the effectiveness of deploying the multi-robot, they need to be spread out sufficiently, while not overlapping the searching area with other robot. We proposed a multi-robot searching algorithm satisfying these requirements by deploying the multi-robot which autonomously finds the next exploration area. Since all robots have own goal, they move simultaneously to maximize overall spatial coverage, this problem is the matter of cooperative distributed intelligence problem.[8] This paper is organized as follows. Section II contains background knowledge about assumptions and dynamic map. Section III introduces the proposed algorithm with virtual goal selection. Section IV presents experimental results of the proposed searching algorithm. Finally, section V briefly discusses conclusion and future work.

S. Lee et al. (Eds.): Intelligent Autonomous Systems 12, AISC 194, pp. 749–756.
springerlink.com

2 Background

2.1 Premise

The cooperative searching algorithm is performed on the basis of following premise.

1. Robots are performed in known environment and able to localize.
2. Robots can fully communicate.
3. When target object is within the sensor range, the robot is able to detect it.

Robots are deployed on the known environment with location sensor, thus, the robot knows where itself and other robots are. Since the main pupose of the algorithm is to find an object on an empty area, such as finding a fire point, or finding an intruder in a building, no dynamic obstacle is assumed. The fully communicative infrastructure enables robots know locations of other robots and share the same topological map. Robots have their sensor to recognize the target object. The sensor can vary for its application, for example, a camera for finding a human intruder, or a thermometer for finding a fire point. When the target object is within the sensor range, we assumed that the robot is always able to detect it. Once the target is found, the mission is terminated.

2.2 Dynamic Map

The global map in [6] is used to represent the area that has been explored, and further plan the paths and coordinate actions. In addition to the property of the global map, following two mechanisms are applied to change the values of the grid cells. The dynamic map is expressed with *decrement* and *reset* mechanism.

Decrement. The dynamic map automatically changes the overall value of the grid cells on each time step either ascending or descending order, the opposite of the reset value.

Reset. The value of the grid cells within sensor range are the reset value.

The dynamic map is similar to the occupancy grid map, however, the only difference is that it automatically changes the value of grid cell after certain amount of time step. For convenience we assumed descending order. The decremental cells refers the open space of the dynamic map. The minumuim value is limited to 1 to prevent from confusion of the wall value 0.
Cells covered by sensor are the checked area by the robot meaning no object of interest was found. The value of the grid cells in such area is set to 255, the white color when expressed in bitmap. The *reset* and *decrement* value of the cell C_{ij} of dynamic map can be expressed respectively as in the Eq.1.

$$C_{ij} = \begin{cases} 255, & \text{if } C_{ij} \text{ is within the sensor range} \\ C_{ij} - 1, & \text{otherwise } (C_{ij} \geq 1) \end{cases} \quad (1)$$

The updating algorithm of the dynamic map using two mechanism is summarized in **Algorithm1**.

Step	**Algorithm 1** Dynamic map updating algorithm
1:	Initialize dynamic map to 1.
2:	**While** Moving to the virtual goal **do**
	(a) **If** grid cells are within sensor range: $C_{ij} = 255$;
	(b) **Else**: $C_{ij} = C_{ij} - 1 (C_{ij} \geq 1)$;

The dynamic map after few steps a robot has moved is depicted in the Fig.1. All cells of dynamic map are initialized to one. (Fig.1 (a)) Then, cells are updated to 255 if they are within sensor range. Otherwise, rest of the cells in dynamic map is decreased by one.(Fig.1 (b)) Fig.1 (c) and (d) shows the dynamicmap after robot's first and tenth move, repectively.

Having cells updated, other robots should know which cells have been *reset* because this information is further used to select virtual goal. Therefore, coordinates of the *reset* cells are broadcasted to other robots. Rather than sending the checked cells'coordinates directly every time, the robot collects the cells for certain amount of time and broadcast them to other robot at once to reduce communication load. Only coordinates of reset cells are necessary because others will be automatically degraded every time step. This way, all robots can share one dynamic map.

2.3 Virtual Goal

To keep robots continuously wandering the given area, robots are required to select own virtual goal, and move toward it. From the initial arbitrarily positions, robots select own virtual goal from the dynamic map. When selecting the virtual goal, the lowest value among frontier cells is chosen as in the Fig.2. Frontier cell is the boundary cell of the sensor distance. Since the dynamic map is descending order, it can be inferred that lowest value means it has not been discovered for a long time. If there are frontier cells with same value, the one closest to the robot's front orientation is selected.

2.4 Cooperative Searching Algorithm

When moving toward the virtual goal, the robot updates the dynamic map regarding the method in section **2.2**. In this operation, the robot checks the cells within the sensor distance whether target object exists or not. If target object does not appear, the values of the cells are set to *reset* value. (In this case, 255) And, these cell's coordinates are collected and broadcasted to other robots so that the other robots also recognize the area has been discovered. Robot itself also updates own dynamic map if coordinates of other robot are received. Thus, all robots can maintain one dynamic map. When a robot reaches to the virtual goal, it automatically selects new virtual goal using the method in section **2.3** again to explore new area until the user commands termination.

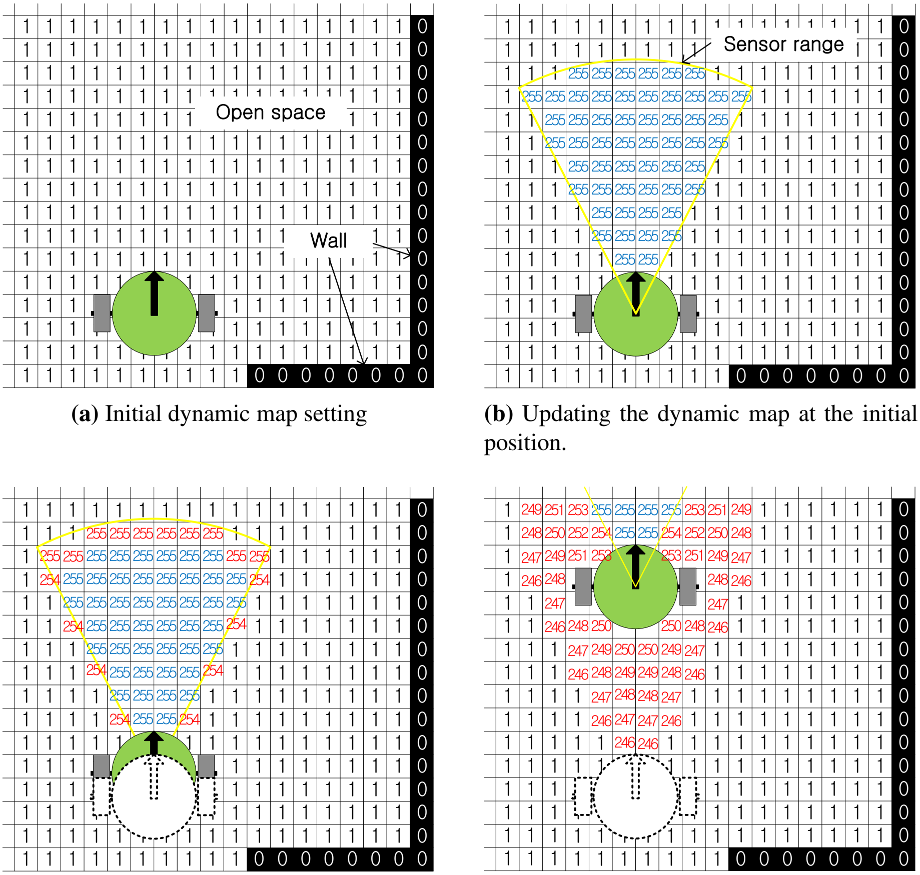

(a) Initial dynamic map setting

(b) Updating the dynamic map at the initial position.

(c) Updating the dynamic map after first step.

(d) Updating the dynamic map after tenth step.

Fig. 1. Updating the dynamic map after several time step

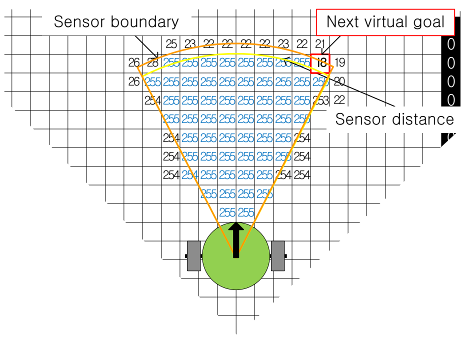

Fig. 2. The virtual goal is selected as the lowest cell among boundary cells of the sensor distance

As a result, robots can move all regions continuously until they find the object. The proposed algorithm can be summarized as follows.

Step	**Algorithm 2** Coordinated multi-robot searching algorithm
1:	Initialize the dynamic map.
2:	Find the lowest value of boundary cell for the virtual goal.
3:	**If** there are several candidates for the virtual goal from step **2**, select one that closest to the robot's orientation.
4:	**While** moving to the virtual goal **do** **If** cells are within sensor distance: $C_{ij} = 255$; **Else** $C_{ij} = C_{ij} - 1, \qquad (C_{ij} \geq 1)$;
5:	**If** the robot has arrived to the virtual goal, go to step **2**.
6:	**If** the target object is found, the algorithm is terminated.

3 Experimental Results

We tested the algorithm on $9 \times 12m$ office-like map as in Fig.3. The map is simply composed of wall and open space. Robot's sensor range is assumed to be $1.5m$ and 180 degree. Five differential drive robots are used. The dynamic map is shared among robots instantaneously. New virtual goal is selected when the robot approaches the target within $1m$.

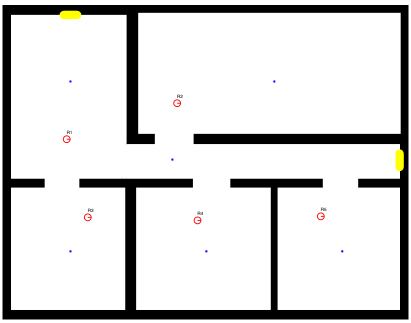

Fig. 3. Five robots are depicted in red. For experiment, six spots are selected in the middle of the room and the corridor in blue dots to measure how often robots visit the point.

To measure the passing rate of robot, six blue spots are selected from the middle of four rooms and corridor as in the Fig.3. From the lower left fiducial point of the map, points are located as in the Table 1.

The simulation result is depicted in Fig.4. It represents overall dynamic map after several time step. Fig.4.(a) shows the bitmap image of the dynamic map that initially unexplored except the front side of robot. It can be seen from the Fig.4.(b),(c) and (d),

Table 1. Coordinates of the selected spots

Points	1	2	3	4	5	6
x:	2	6	10	5	2	8
y:	2	2	2	4.7	7	7

after 7, 30 and 150 time step, respectively, that as the robot moves toward the dark area of the map, the past passage correspondingly become darker. The bright area is the sensor range of five robots, meaning the region has currently being discovered. And the dark area means the area has not been detected for a while.

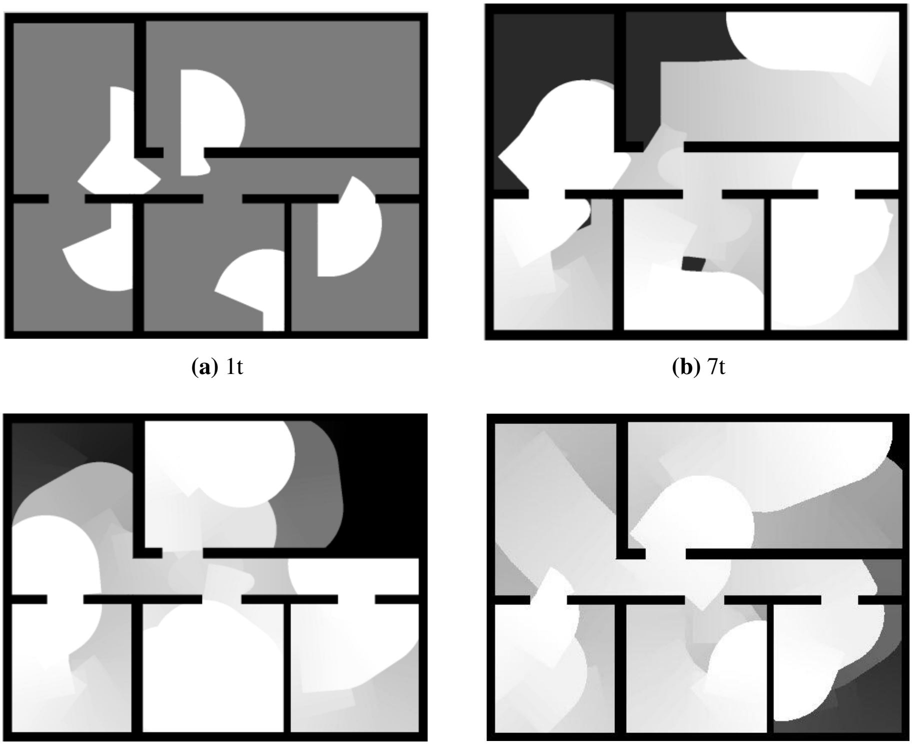

(a) 1t **(b)** 7t **(c)** 30t **(d)** 150t

Fig. 4. Image file of the dynamic map after 1t(a), 7t(b), 30t(c), 150t(d)

During simulation it has been observed that since the robot selects virtual goal autonomously, the algorithm helps robot being scattered to different region, even though more than one robots are gathered to near position once.

Figure 5 shows the passing time of the corresponding six points after 2000 seconds. As can be seen in the Fig. 4 and 5, the frequency of the robot passing through the points

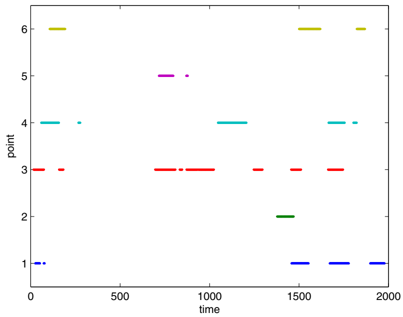

Fig. 5. Five robots are depicted in red. For experiment, six spots are selected in the middle of the room and the corridor in blue dots to measure how often robots visit the point.

can possibly be non-uniform; however, the all points receives almost equal chance being detected by robot as time passes.

4 Conclusion

The problem we consider is that robots are required to repeatedly visit every part of the map in order to detect the object of interest. Thus, we proposed a multi-robot searching algorithm using dynamic map and virtual goal selection method. The simulation result proves that the proposed algorithm is considerably effective and relatively simple for searching mission in a known environment of multi-robot system. To reinforce the algorithm, physical test should be followed. This algorithm can be used in surveillance and monitoring of robotic mission.

Acknowledgements. This research was supported by MKE under collaborative intelligence project.(10037352)

References

1. Marjovi, A., Nunes, J.G., Marques, L., de Almeida, A.: Multi-robot exploration and fire searching. In: IROS, October 10-15, pp. 1929–1934 (2009)
2. Ahmadi, M., Stone, P.: A multi-robot system for continuous area sweeping tasks. In: ICRA, May 15-19, pp. 1724–1729 (2006)
3. Acar, E.U., Choset, H., Yangang, Z., Schervish, M.: Path Planning for Robotic Demining: Robust Sensor-based Coverage of Unstructured Environments and Probabilistic Methods. International Journal of Robotics Research 22(7-8), 441–466 (2003)
4. Kantor, G., Singh, S., Peterson, R., Rus, D., Das, A., Kumar, V., Pereira, G., Spletzer, J.: Distributed search and rescue with robot and sensor teams. In: Proc. of the 4th Intl. Conf. on Field and Service Robotics, pp. 327–332 (2003)
5. Lu, Q., Han, Q.: On Designing a Cooperative Control System for Multiple Mobile Robots to Locate the Source of Odor. In: Proc. of 18th IFAC World Congress, pp. 9446–9451 (2011)

6. Burgard, W., Moorsy, M., Stachniss, C., Schneidery, F.: Coordinated multi robot exploration. IEEE Transactions on Robotics 21, 376–386 (2005)
7. Gonzalez, E., Alarcon, M., Aristizabal, P., Parra, C.: BSA: A Coverage Algorithm. In: Proc. International Conf. on Intelligent Robots and Systems, vol. 2, pp. 1679–1684 (2003)
8. Parker, L.E.: Distributed intelligence: Overview of the field and its application in multi-robot systems. Journal of Physical Agents, 2(1) (March 2008)

Analysis of Affective Effects on Steady-State Visual Evoked Potential Responses

Shangfei Wang, Guobing Wu, and Yachen Zhu

Key Lab of Computing and Communicating Software of Anhui Province
School of Computer Science and Technology,
University of Science and Technology of China, Hefei, Anhui, P.R. China, 230027
sfwang@ustc.edu.cn, {guobing,zhuyc}@mail.ustc.edu.cn

Abstract. This paper aims to investigate the effect of different emotional states on healthy subjects' steady-state visual evoked potential responses. First, affective steady-state visual evoked response experiments are designed and implemented. Emotion eliciting pictures selected from the International Affective Picture System are flickered on the four directions of the screen at the frequency of 10Hz, 11Hz, 12Hz and 15Hz respectively. Subjects' EEG signals are recorded by a Quik-cap simultaneously. After that, spectral density analysis and canonical correlation analysis are conducted across trials respectively to extract features. Then a one-way analysis of variance is performed to evaluate the effect of different emotional states on subjects' steady-state visual evoked potential responses. Results show that there exist significant differences between steady-state visual potential response under different emotional states. Both positive and negative emotions enhance subjects' steady-state visual evoked potential responses. Thus it is easier to detect subjects response under positive and negative emotional states than that under neutral state.

Keywords: affective, steady-state visual evoked potential responses, canonical correlation analysis.

1 Introduction

The essence of Brain Computer Interface (BCI) is to infer human's mind by brain activities [1]. It not only broadens the range of human-computer interfaces, but also offers a new development method to study the human brain. Steady-state visual evoked potentials (SSVEPs) are subjects' natural responses to visual stimulation at specific frequencies. When the retina is excited by a visual stimulus ranging from 1 Hz to 100 Hz, the brain generates electrical activity at the same or multiples of frequency of the visual stimulus. SSVEP has several superiorities such as higher signal-to-noise ratio, higher accuracy rate, better information transfer rate as well as little training compared with other sources, such as slow cortical potentials and cortical rhythms, therefor it has been one of the most commonly used noninvasive electrophysiological sources in EEG-based BCI systems [2][3]. Although considerable progress has been made in the field of SSVEP-based BCI, and several related systems have already been proposed

S. Lee et al. (Eds.): Intelligent Autonomous Systems 12, AISC 194, pp. 757–766.
springerlink.com

[2][4][5][6][7][8], only a few researchers have considered the affective effects on subjects' SSVEP responses. Affect is a psycho-physiological phenomena, which may influence subjects' SSVEP brain responses [9][10].

A. H. Kemp et al. [11] were the first to investigate affective effects on subjects' SSVEP responses. Seventy-five pictures from the International Affective Picture System (IAPS) , categorized as pleasant, neutral, and unpleasant, were selected according to the Self-Assessment Manikin (SAM) ratings. Each emotion eliciting picture was presented in a flickering paradigm at 13Hz for a period of 6s. Steady-state probe topography was used to evaluate the SSVEP associated with the processing of pleasant and unpleasant images low in arousal content. After that, analysis was conducted by the subtraction between the activity when viewing neutral pictures and the activity when viewing pleasant as well as unpleasant pictures. Results revealed that both pleasant and unpleasant valence was related to transient, widespread, and bilateral frontal SSVEP latency reductions.

Andreas Keil et al. [12] conducted a similar experiment. They chose sixty pictures from IAPS to present in a flickering paradigm at 10Hz and analyzed the visual perceptional differences among six categories, i.e. threat and mutilation (unpleasant), families and erotica (pleasant), and household objects and persons (neutral). Phase and amplitude of the 10Hz SSVEP were extracted by FFT, and the analysis of variance (ANOVA) was conducted. The experimental results showed that the amplitude of the 10Hz SSVEP was boosted up during viewing of pleasant and unpleasant pictures, in contrast to neutral pictures at parieto-occipital recording sites.

Instead of using IAPS pictures, Hovagim Bakardjian et al. [13] adopted eight emotion eliciting video clips of facial expression image sequences. Each emotion eliciting video clip was associated with an independent command and flashed on the different locations of the monitor simultaneously at different frequencies, i.e. 5.0Hz, 5.4Hz, 6.0Hz, 6.67Hz, 7.5Hz, 8.55Hz, 10.0Hz, and 12.0Hz. The participants were asked to focus on a fixed video stimulus during a period of 4s to . The evoked SSVEP was translated to control a robotic arm. Signal energy measures were conducted for the BCI analysis. At last, a two-way ANOVA was carried out, showing that the SSVEP activity was significantly dependent on the affective type of video clips.

In this paper, we aim to investigate the effect of different emotional states on healthy subjects' SSVEP at four commonly used frequencies, including 10Hz, 11Hz, 12Hz and 15Hz. The framework of our work is illustrated in Figure 1. First, an affective SSVEP experiment is designed and implemented. Eighty-four pictures, consisting of twenty-eight positive, twenty-eight neutral and twenty-eight negative ones, are selected from IAPS. Since the brightness and contrast of stimuli are associated with SSVEP brain responses[8][14], a one-way ANOVA is performed to evaluate whether there are significant differences in brightness or contrast between three kinds of emotion eliciting images. The analysis results show that there are no significant differences in brightness or contrast among three groups.

Then each emotion eliciting picture is flickered on the four locations of the screen at a frequency of 10Hz, 11Hz, 12Hz and 15Hz respectively. Subjects' EEG signals are recorded by a Quik-cap simultaneously. During the interval of two trials, subjects are required to report their induced emotions in valence and arousal with the help of SAM.

These self-reported data are used to evaluate the effect of emotion eliciting pictures . After data collection, spectral density analysis (SDA) and canonical correlation analysis (CCA) are conducted across trials respectively to extract features. Then, a one-way ANOVA is performed to evaluate the effect of different emotional states on subjects' SSVEP responses. Experimental results show that there exists significant differences between SSVEP responses under different emotional states. Both positive and negative emotions enhance subjects' SSVEP responses. Last, classification is conducted according to the two kinds of features respectively. Better performance is obtained when subjects are under positive or negative states, which indicates that it is easier to detect subjects' responses under positive and negative emotional states than under neutral state.

The rest of this paper is organized as follows. Section 2 describes the affective SSVEP experiment. Section 3 elaborates on data analysis. Experimental results and discussions are given in Section 4. Section 5 summarizes the paper.

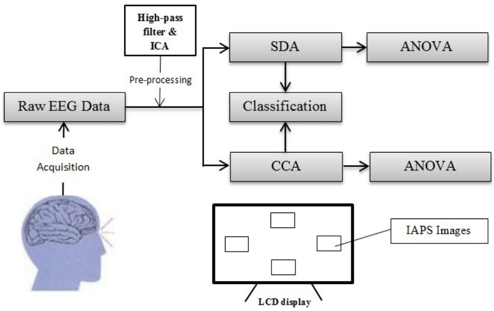

Fig. 1. Framework of the proposed method

2 Affective SSVEP Experiments

2.1 Subjects

Six healthy participants (three males and three females, from 18 to 23 years old) participated in the experiments. All of them were ensured in normal corrected vision. Before the experiment, an informed consent form was signed by each subject and we paid a certain amount of money for his/her participation after the experiment.

2.2 Stimuli

Eighty-four emotion eliciting pictures, were chosen as stimuli from the IAPS [8], including 28 positive pictures whose valence ranges from 7.02 to 8.34, 28 neutral pictures with valence from 4.46 to 5.46, and 28 negative pictures with valence from 1.8 to 3.47 [5].

2.3 Experiment Procedure

First, a detailed description was given to the participants about the arrangement of the experiments, the meaning and the measurement scale of arousal and valence and matters needing attention during the experiment. Second, he/she was asked to sit on a sofa in the isolate room and wear the Quick-cap and an earphone. Third, the experiment was performed according to the experimental protocol illustrated in Figure 2. For each experiment, there were four blocks, representing 10Hz, 11Hz, 12Hz and 15Hz, respectively. Participants were required to focus on one of four locations in each block continuously, which consist of the following steps:

Step 1. A fixation cross was displayed for 3s.

Step 2. Four rectangles in four directions (up, down, left and right) with one in yellow were shown to remind the subject which rectangle to gaze at in the following BCI task for 2s.

Step 3. One emotion eliciting picture flickered with frequencies of 10Hz, 11Hz, 12Hz and 15Hz for 10s respectively. Then the experiment procedure went to step 2. This loop continued 21 times, displaying seven positive, seven neutral and seven negative pictures. The order of emotion category of pictures was random, in order to reduce the order effect.

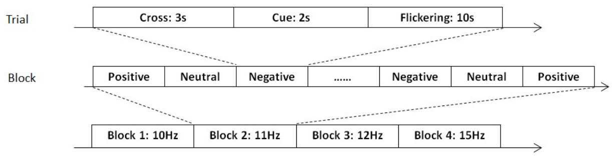

Fig. 2. Experiment protocol

During the interval of the trials, subjects were asked to report their real induced emotion using valence and arousal, ranging from -2 to 2, with the help of the SAM.

EEG signals were acquired via a Quik-cap (Neuro Inc., EI Paso, TX) with 32 Ag-AgCl electrodes arranged in an extended 10-20 system montage. Neuroscan Synamps2 bio amplifiers were used, and EEG signals were recorded using Neuroscan Scan software (v4.3.1). The sampling rate for all channels was 500Hz. For presentation, E-prime (v2.0 beta) was used [16].

3 Data Analyses

After the affective SSVEP experiments, data analyses are performed on the collected EEG signals, including data preprocessing, feature extraction of SDA and CCA, a one-way ANOVA and classification.

3.1 Preprocessing

First, bad channels of raw EEG data are removed. Second, the remaining EEG data are filtered by a high-pass filter with a cut-off frequency of 1Hz to remove the direct current (DC) noise. Finally, Independent Component Analysis (ICA) is performed to remove blink, eye movement and muscle artifacts. One subject's EEG data was deleted due to its invalid collection. Thus, for each kind of frequency, there are 105 samples. Since the SSVEP response can be effectively detected in the occipital region [2][17][18], EEG signals of five electronica nodes, O1, O2, Oz, P3 and P4, are taken for further analysis, among which, O1,O2 and Oz are in the center of the occipital region, and P3 and P4 are in the edge of the occipital region.

3.2 Feature Extraction

Two kinds of commonly used features are extracted from the preprocessed EEG signals. One is SDA, and the other is CCA. To successfully detect harmonic frequencies from SSVEP, SDA requires more EEG data to achieve the same performance as that of CCA. Thus, 9s and 5s EEG data are used to extract features of SDA and CCA respectively.

SDA is a method to calculate a function of frequency related to a deterministic function of time or a stationary stochastic process. FFT is performed on a period of 9s EEG data, and the sums of fourier coefficients at fundamental frequency and its corresponding second harmonics for four frequencies are extracted as features [19].

CCA method is a statistical method, measuring the linear relationship between two sets of variables. It finds a set of basis vectors for each set of variables so that the correlation between the two canonical variables, and the projections of the variables onto these basis vectors, are maximized [2][6][20][21].

Here, $X(t) = (X_1(t), X_2(t), ...X_5(t))$ represents five channels of preprocessed EEG signals. The other variable $Y_f(t)$, represents repetitive visual stimuli,

$$Y_f(t) = \begin{bmatrix} sin(2\pi ft) \\ cos(2\pi ft) \\ sin(4\pi ft) \\ cos(4\pi ft) \\ sin(6\pi ft) \\ cos(6\pi ft) \end{bmatrix} t = \frac{1}{T}, \frac{2}{T}, ..., \frac{N}{T}; f = 10, 11, 12, 15. \quad (1)$$

where f is the base frequency, T is the sampling period, and N is the number of sampling points.

Let W_x and W_x denote two sets of basis vectors. Then a pair of combinations $\{U = X^T W_x, V = Y^T W_y\}$, are the projection of X and Y onto U and V respectively. The linear relationship between X and Y, now can be obtained by computing the maximum value of correlation coefficient between U and V in terms of the selection of W_x and W_x [19][20], which can be computed by the following formula:

$$\begin{aligned} \underset{W_x, W_x}{max}\ \rho(U, V) &= \frac{E\left[U^T V\right]}{\sqrt{E\left[U^T U\right] E\left[V^T V\right]}} \\ &= \frac{E\left[W_x^T X Y^T W_y\right]}{\sqrt{E\left[W_x^T X X^T W_x\right] E\left[W_y^T Y Y^T W_y\right]}} \end{aligned} \tag{2}$$

Thus, four coefficients are obtained.

3.3 Affective Effect Analyses Using ANOVA

After feature extraction, a one-way ANOVA is performed to investigate whether there exists significant difference between SSVEP response under three kinds of emotions for each frequency.

3.4 Classification

Classification is performed using SDA features and CCA features respectively. The command is recognized as the frequency whose corresponding feature is the largest among four kinds of frequencies.

4 Experimental Results and Discussion

4.1 Analyses of the Stimuli

Since the brightness and contrast of stimuli are associated with SSVEP brain responses [8][14], the brightness and contrast of difference emotion eliciting pictures should be similar in our experiments, since we only investigate affective effects on SSVEP responses. We first extract the mean and variance of the gray value of each picture as the features of brightness and contrast respectively. Then, a one-way ANOVA was performed to evaluate whether there are significant differences in brightness and contrast between three kinds of emotion eliciting pictures respectively. For brightness, $F(2, 81) = 0.629$ and $p = 0.536$, and for contrast, $F(2,81) = 0.099$ and $p = 0.906$. The results showed that there are no significant differences in brightness and contrast among three emotional images.

Although the chosen eighty-four pictures are well evaluated by 100 college students according to [15], subjects in our experiments may have different feelings about these pictures, since their racial and cultural backgrounds are different. Thus, subjects are required to give their evaluation to the stimuli during the experiments. Then, a one-way ANOVA is conducted on self-report data of the three groups to investigate whether there are significant differences among them. The result of [$F = 216.76$, $p<0.001$] shows there exist significant differences among three kinds of emotion eliciting pictures. After that, three groups of t-test are performed, and results showed that there exist significant differences between the self-reported data of positive and negative pictures, positive and neutral pictures, and neutral and negative pictures. It demonstrated that the chosen pictures achieved the eliciting purpose of emotions.

4.2 Experimental Results and Analyses of Affective Effect on SSVEP Responses

The mean of five channels' SDA and CCA are used for analysis of ANOVA. Table 1 and Table 2 list the results.

Table 1. Significance differences of SSVEP responses under three emotional states at a 0.05 level(with *) by using SDA

Emotions	10Hz	11Hz	12Hz	15Hz
Overall	0.003*	0.005*	0.012*	0.005*
Neutral vs. Negative	0.001*	0.001*	0.004*	0.002*
Neutral vs. Positive	0.008*	0.027*	0.023*	0.031*
Negative vs. Positive	0.445	0.243	0.461	0.508

Table 2. Significance differences of SSVEP responses under three emotional states at a 0.05 level (with *) by using CCA

Emotions	**10Hz**	**11Hz**	**12Hz**	**15Hz**
Overall	0.009*	0.000*	0.007*	0.001*
Neutral vs. Negative	0.003*	0.000*	0.000*	0.000*
Neutral vs. Positive	0.017*	0.001*	0.006*	0.005*
Negative vs. Positive	0.49	0.36	0.632	0.296

From the two tables, we can see that overall significant differences of SSVEP responses under three emotions in four frequencies are discovered by using both SDA and CCA features, which may reveal that emotion eliciting pictures induce human emotions successfully and have effects on SSVEP responses. Furthermore, significant differences ($p < 0.05$) between SSVEP responses under neutral states and those under negative states as well as positive states are found by using both SDA and CCA features. It also shows that no significant difference between SSVEP responses under negative states and those under positive states are found by using either SDA or CCA features, which may display that both positive and negative states have similar effects on SSVEP responses.

Figure 3 and Figure 4 present the Mean Amplitude of SDA and CCA under three emotions in four frequencies. From the two Figures, we can see that the means of features are larger in the negative and the positive states than in the neutral state, which also demonstrates that emotion eliciting pictures can boost up the SSVEP responses. Negative pictures enhanced SSVEP amplitude slightly higher than positive ones, which may reflect that negative content is better stimuli to elicit SSVEP. However, a long-time negative state would reduce subjects' comfort level and increase fatigue. Considering the reliability as well as participants' comfort level, positive pictures would be the best choice as stimuli. All the results shown in the tables and figures support that brain activity of SSVEP can be enhanced by positive or negative pictures compared with neutral pictures in four kinds of frequencies, which are consistent with previous

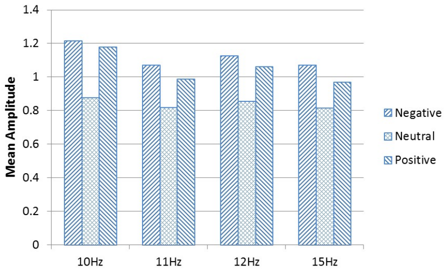

Fig. 3. Mean Amplitude of SDA of 10Hz, 11Hz, 12Hz and 15Hz for three emotions

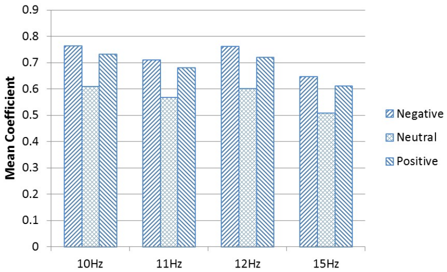

Fig. 4. Mean Coefficient of CCA of 10Hz, 11Hz, 12Hz and 15Hz for three emotions

research [11][13][18]. The reason may be that as a consequence of overt visual attention for SSVEP response, positive or negative stimuli may be more attractive than neutral stimuli [22].

4.3 Classification

The classification rates are presented in Table 3, which shows that better performance is achieved in the negative and positive states than in the neutral state. It could be explained from the perspective of the enhancement of signal-noise-ratio, since stronger SSVEP is elicited by the negative or the positive state compared with the neutral state. In addition, negative pictures enhanced SSVEP amplitude slightly higher than positive ones do. Thus, the classification performance under negative states is a little better than that under positive states. The classifier using SDA is slightly more effective than that using CCA. However CCA requires less EEG data than SDA does.

Table 3. classification performance

	Accuracy rate using SDA	**Accuracy rate using CCA**
Neutral	82.05%	74.36%
Negative	83.92%	82.52%
Positive	83.75%	81.25%

5 Conclusions and Future Works

This study aims to investigate the effect of different emotional states on SSVEP responses at four kinds of frequencies. First, we design the affective SSVEP experiment, in which emotion eliciting pictures from IAPS are adopted to induce subjects' emotions and SSVEP responses. Second, SDA and CCA features are extracted from the EEG data. A one-way ANOVA is performed to evaluate the effects of different emotional states on SSVEP responses. Then, classification is conducted according to two kinds of features respectively. The experimental results show that the brain activity of SSVEP can be enhanced by positive or negative pictures compared with neutral pictures, and negative pictures enhance SSVEP amplitude slightly higher than positive ones do.

Compared with others' work, our contribution can be concluded as follows: first, we investigate affective effects on SSVEP responses at four kinds of frequencies (10Hz, 11Hz, 12Hz, 15Hz) simultaneously and independently, while Andreas Keil et al. [12] and A. H. Kemp et al. [11] only focused on one frequency. Our research shows the potential of affective SSVEP response in the application of multi-command BCI. Second, we have considered not only SDA but also CCA. Both features are proper to distinguish different SSVEP response. The classification performance of SDA is slightly better than that of CCA, while CCA requires less data than SDA.

This work does not consider gender difference in affective SSVEP responses. We plan to recruit more subjects and conduct further experiments on the gender effect on affective SSVEP responses. Our study may provide potential new directions in BCI research.

Acknowledgment. This paper is supported by the NSFC (61175037), Special Innovation Project on Speech of Anhui Province (11010202192), project from Anhui Science and Technology Agency and Youth Creative Project of USTC.

References

1. Nijholt, A., Tan, D.: Brain-Computer Interfacing for Intelligent Systems. IEEE Intelligent Systems 23(3), 72–79 (2008)
2. Bin, G., Gao, X., Yan, Z., Hong, B., Gao, S.: An online multi-channel SSVEP-based brain Ccomputer interface using a canonical correlation analysis method. Journal of Neural Engineering 6(4), 046002 (2009)
3. Pastor, M.A., Artieda, J., Arbizu, J., Valencia, M., Masdeu, J.C.: Human Cerebral Activation during Steady-State Visual-Evoked Responses. The Journal of Neuroscience 23(37), 11621–11627 (2003)
4. Lalor, E.C., Kelly, S.P., Finucane, C., Burke, R., Smith, R., Reilly, R.B., McDarby, G.: Steady-state VEP-based brain-computer interface control in an immersive 3D gaming environment. EURASIP J. Appl. Signal Process., 3156–3164 (2005)
5. Wang, Y.-T., Wang, Y., Jung, T.-P.: A cell-phone-based brain Ccomputer interface for communication in daily life. Journal of Neural Engineering 8(2), 025018 (2011)
6. Lin, Z., Zhang, C., Wu, W., Gao, X.: Frequency Recognition Based on Canonical Correlation Analysis for SSVEP-Based BCIs. IEEE Transactions on Biomedical Engineering 53(12), 2610–2614 (2006)

7. Gollee, H., Volosyak, I., McLachlan, A.J., Hunt, K.J., Graser, A.: An SSVEP-Based Brain CComputer Interface for the Control of Functional Electrical Stimulation. IEEE Transactions on Biomedical Engineering 57(8), 1847–1855 (2010)
8. Zhu, D., Bieger, J., Molina, G.G., Aarts, R.M.: A survey of stimulation methods used in SSVEP-based BCIs. Intell. Neuroscience, 1–12 (2010)
9. Molina, G.G., Tsoneva, T., Nijholt, A.: Emotional brain-computer interfaces. In: 3rd International Conference on Affective Computing and Intelligent Interaction and Workshops, ACII 2009 (2009)
10. Nijboer, F., Carmien, S.P., Leon, E., Morin, F.O., Koene, R.A., Hoffmann, U.: Affective brain-computer interfaces: Psychophysiological markers of emotion in healthy persons and in persons with amyotrophic lateral sclerosis. IEEE (2009)
11. Kemp, A.H., Gray, M.A., Eide, P., Silberstein, R.B., Nathan, P.J.: Steady-state visually evoked potential topography during processing of emotional valence in healthy subjects. Neuroimage 17(4), 1684–1692 (2002)
12. Keil, A., Gruber, T., Mller, M.M., Moratti, S., Stolarova, M., Bradley, M.M., Lang, P.J.: Early modulation of visual perception by emotional arousal: evidence from steady-state visual evoked brain potentials. Cognitive, Affective, & Behavioral Neuroscience 3(3), 195–206 (2003)
13. Bakardjian, H., Tanaka, T., Cichocki, A.: Emotional faces boost up steady-state visual responsesforbrain Ccomputer interface. NeuroReport 22(3), 121–125 (2011), doi:10.1097/WNR.0b013e32834308b0
14. Vernon Odom, J., Bach, M., Barber, C., Brigell, M., Marmor, M.F., Tormene, A.P., Holder, G.E.: Vaegan, Visual evoked potentials standard. Documenta Ophthalmologica 108(2), 115–123 (2004)
15. Lang, P.J., Bradley, M.M., Cuthbert, B.N.: International affective picture system (IAPS): Technical manual and affective ratings. The Center for Research in Psychophysiology, University of Florida, Gainesville, FL (1999)
16. Schneider, W., Eschman, A., Zuccolotto, A.: E-Prime reference guide, Psychology Software Tools, Inc. (2002)
17. Friman, O., Volosyak, I., Graser, A.: Multiple Channel Detection of Steady-State Visual Evoked Potentials for Brain-Computer Interfaces. IEEE Transactions on Biomedical Engineering 54(4), 742–750 (2007)
18. Hakvoort, G., Reuderink, B., Obbink, M.: Comparison of PSDA and CCA detection methods in a SSVEP-based BCI-system. Enschede, Centre for Telematics and Information Technology, University of Twente (2011)
19. Cheng, M., Gao, X., Gao, S., Xu, D.: Design and implementation of a brain-computer interface with high transfer rates. IEEE Transactions on Biomedical Engineering 49(10), 1181–1186 (2002)
20. Borga, M.: Canonical Correlation: a Tutorial (January 2001)
21. Hardoon, D.R., Szedmak, S., Shawe-Taylor, J.: Canonical correlation analysis: An overview with application to learning methods. Neural Computation 16(12), 26 (2004)
22. Lauri, N., Jukka, H., Calvo Manuel, G.: Eye movement assessment of selective attentional capture by emotional pictures. Emotion 6(2), 257 (2006)

Effect of Potential Model on Monte-Carlo Go

Pruning the *igo* Game Tree Using Potential and Potential Gradient

Makoto Oshima, Koji Yamada, and Satoshi Endo

Graduate School of Engineering and Science, University of the Ryukyus
1 Sembaru, Nishihara, Okinawa 903-0213, Japan
mako10@eva.ie.u-ryukyu.ac.jp

Abstract. In this study, we tackled the reduction of computational complexity by pruning the *igo* game tree using the potential model based on the knowledge expression of *igo*. The potential model considers *go* stones as potentials. Specific potential distributions on the *go* board result from each arrangement of the stones on the *go* board. Pruning, using the potential model, categorizes the legal moves into effective and ineffective moves in accordance with the threshold of the potential. In this experiment, 4 kinds of pruning strategies using the potential and 5 kinds of pruning strategies using the potential gradients were evaluated. The reduction rates differed according to how the potential and potential gradients were set. The best pruning strategy resulted in a 20% reduction of the computational complexity. In this research we have successfully demonstrated pruning using the potential model for reducing computational complexity of the *go* game.

Keywords: Monte-Carlo Go, potential, potential gradient, pruning.

1 Introduction

Monte-Carlo Go [1] is computer *igo* which satisfies strength without the knowledge expressions of *igo*. Monte-Carlo Go is very computationally intensive. However, reducing computational complexity is possible by properly pruning the *igo* game tree. In this study, we tackled the reduction of computational complexity by pruning the *igo* game tree using the potential and the potential gradient.

2 Proposed Method

The proposed method in this research consists of Monte-Carlo Go and the potential model.

2.1 Monte-Carlo Go

Monte-Carlo Go evaluates legal moves at each phase to choose the next move by simulation based on the Monte-Carlo search. Monte-Carlo search consists of many

S. Lee et al. (Eds.): Intelligent Autonomous Systems 12, AISC 194, pp. 767–774.
springerlink.com

moves of a simulation. This simulation is called "Play Out". Play Out involves both sides constantly choosing the next move alternately and randomly from the current phase to the end game. Play Out calculates an estimation ($\overline{X_i}$) for each legal move (i). Variable number (S_i) is the number of times of Play Out. Variable number (X_i) is the total considerations of Play Out. In Play Out, if an offensive move wins, the consideration is (+1), and if it loses, the consideration is (+0). As a result, the move which has the best estimation is selected as the next move.

$$\overline{X_i} = X_i / S_i \tag{1}$$

2.2 Potential Model

Stones influence the possibility that surrounding intersections become their territory. The potential model quantifies these influences by assuming *go* stones as potentials following earlier studies [2–4].

2.2.1 Definition of Potential Model

The definition of potential in this experiment is shown in (2–4) and Table 1. The plus or minus of (3) is switched by the setting of the proposed method. The potential gradient *PG(X, Y)* is calculated by Geographical Information Systems [5] with potential value.

$$r = \sqrt{(X - x_i)^2 + (Y - y_i)^2} \tag{2}$$

$$P_i(X, Y) = \pm 1 / m^r \tag{3}$$

$$P_{all}(X, Y) = \sum_{k=1}^{n} P_k(X, Y) \tag{4}$$

Table 1. Mathematical Expression

Symbol	Definition
r	Euclidean distance
m	Attenuation rate of potential. $m > 1$.
x_i, y_i	Intersection of $stone_i$
$P_k(X, Y)$	Potential to intersection (X, Y) from $stone_k$
n	Total number of stones on the *go* board
$P_{all}(X, Y)$	Total potential to intersection (X, Y) from $stone_{1\text{–}n}$
$PG(X, Y)$	A potential gradient at an intersection (X, Y)

2.2.2 Pruning Using Potential Model

Potential Filters: Potential Filters are pruning instruments in this experiment. At each phase to choose the next move, these Filters pruned legal moves according to the following procedures:

I. Calculate potential distribution result from arrangement of *go* stones on the *go* board.
II. Rank legal moves by each magnitude of potential (or potential gradient.)
III. Categorize the ranked legal moves into effective and ineffective moves in accordance with thresholds for the ranking. (Each Potential Filter has unique threshold levels.)
IV. Eliminate the ineffective moves from candidates for the next move. (Run Monte-Carlo search only on effective moves.)

In accordance with the number of eliminated legal moves, the computational load of Monte-Carlo search is reduced, i.e., these Potential Filters reduce the range of search spaces on the *go* board.

Configurations of Potential Filters: Table 2 shows the threshold conditions of 5 Filters. Each Potential Filter ranked legal moves in descending order of potential values (except for Random Filter), and categorized them in accordance with each threshold condition for the ranking. All Filters mutually reduced by half the number of legal moves. Thus all Filters reduced by half the computational load at each phase to choose the next move.

Table 3 shows the threshold conditions of another 5 Filters. Each Potential Filter ranked legal moves in descending order of potential gradient values and categorized them in accordance with each threshold condition for the ranking. In these Potential Filters, the attenuation rate (*m*) critically involved their filtering functions. According to the magnitude of (*m*), potential gradients of surrounding intersections of each stone became higher. In contrast, the lower (*m*) became, there were higher potential gradients of intersections between black stones and white stones. For example in Table 3, Potential Filter 5, variable (*m*) is 4 and the intersection marked with an x between a black stone and a white stone is ranked 41^{st} in order of magnitude of potential gradient. In the case of Potential Filter 6, the intersection marked with an x is ranked 23^{rd}. In the case of Potential Filter 7, the intersection marked with an x is ranked 9^{th}. In the case of Potential Filter 8, the intersection marked with an x is ranked 3^{rd}. In the case of Potential Filter 9, the intersection marked with an x is ranked 1^{st}.

On and Off Switch of Potential Filter: Potential Filters had a switching point, which switched their states on and off. This switching point was within a range of legal intersection numbers on the *go* board. A switching point was selectable from 2 to 169 when the board size was 13 x 13 (= 169).

During the course of a game, in the case a remaining legal move number on the *go* board was above a switching point, the Potential Filters were on. If a remaining legal move number was under a switching point, the Potential Filters were off. In this

Table 2. Types of Potential Filters (Random Filter and Potential Filter 1–4)

Method	Random Filter	Potential Filter 1	Potential Filter 2	Potential Filter 3	Potential Filter 4
Ranking	-	Potential	Potential	Potential	Potential
m	-	2	2	2	2
Black/ White	-	+/–	+/–	+/–	+/+
Filtering	Random	Low 50%	Top 50%	Above 25% and below 75%	Low 50%
Overhead	-	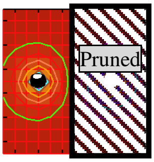	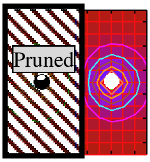	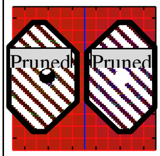	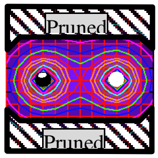
Landscape	-	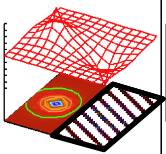	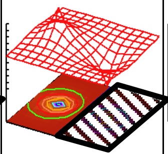	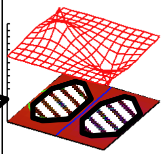	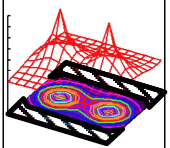

Table 3. Types of Potential Filters (Potential Filter 5–9)

Method	Potential Filter 5	Potential Filter 6	Potential Filter 7	Potential Filter 8	Potential Filter 9
Ranking	Potential Gradient	Potential Gradient	Potential Gradient	Potential Gradient	Potential Gradient
m	4	2	1.5	1.25	1.15
Black/ White	+/–	+/–	+/–	+/–	+/–
Filtering	Low 50%	Low 50%	Low 50%	Low 50%	Low 50%
Overhead	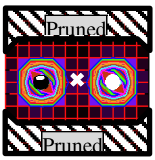	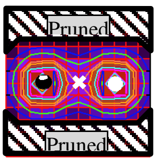	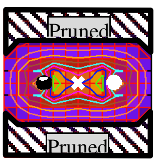	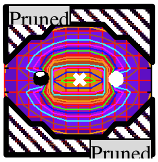	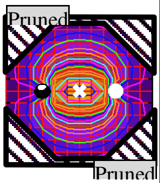
Landscape	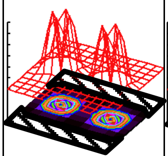	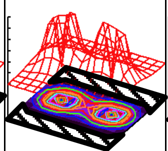	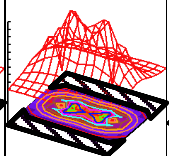	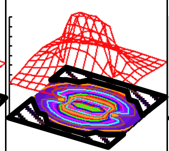	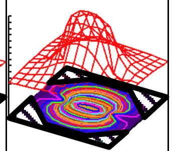

experiment, boundaries where Potential Filters became ineffective from effective were measured by changing the switching point. The boundaries were the points where winning percentages crossed an average winning percentage between two normal Monte-Carlo Go.

Monte-Carlo search has higher performance when a game tree is small. In contrast, Monte-Carlo search has low performance when a game tree is large. Thus, pruning is effective in the opening game. However, afterwards, pruning gradually becomes ineffective.

3 Strength of Monte-Carlo Go with Potential Filters

Monte-Carlo Go with Potential Filters used the initiative move while normal Monte-Carlo Go used the passive move. In a match-up between two normal Monte-Carlo Go, the winning percentage of the initiative move was 51% when board size was 13 x 13. (The winning percentage of the initiative move exceeded 50% because the initiative move was advantageous.) Therefore, 51% is considered the average level of normal strength.

4 Results and Observation

The strength of Monte-Carlo Go with Potential Filters is shown in Fig. 1, upper (Random Filter and Potential Filter 1–4) and lower (Potential Filter 5–9) graphs, left axis. Strength transitioned with Filters and switching points. A winning percentage of 51% and calculating the results of the Random Filter were important for comparing and evaluating the effects and tendency of Potential Filters. Total Play Out numbers needed in one game are shown in Fig. 1, upper and lower graphs, right scale. Total Play Out numbers transitioned with these Filters and switching points.

In theory, when the Random Filter was used, the next move became the best move by Monte-Carlo search 50% of the time and the second or several moves thereafter by Monte-Carlo search the other 50% of the time. When the number of legal moves was large, Monte-Carlo search had low precision. Thus, strength did not decrease very much because there was no defining difference between the best move and the second or several moves thereafter by Monte-Carlo search. The precision of Monte-Carlo search increased with a decrease in the number of legal moves. The strength of the Random Filter decreased gradually with a decrease in the number of legal moves.

Potential Filter 1 became the bias around which black stones gathered. In the opening game, these collective black stones effectively strengthened initiative territory. However, in the middle game, the initiative move could not expand its territory. As a result, the passive move acquired more territory than the initiative move on the *go* board. When strength exceeded average (51%), Potential Filter 1 properly pruned ineffective moves that Monte-Carlo search was unable to do. Thereafter, the strength of the Potential Filter 1 decreased gradually with a decrease in the number of legal moves and an increase in the precision of Monte-Carlo search. In fact, the pruning of Potential Filter 1 hampered the precision of Monte-Carlo search.

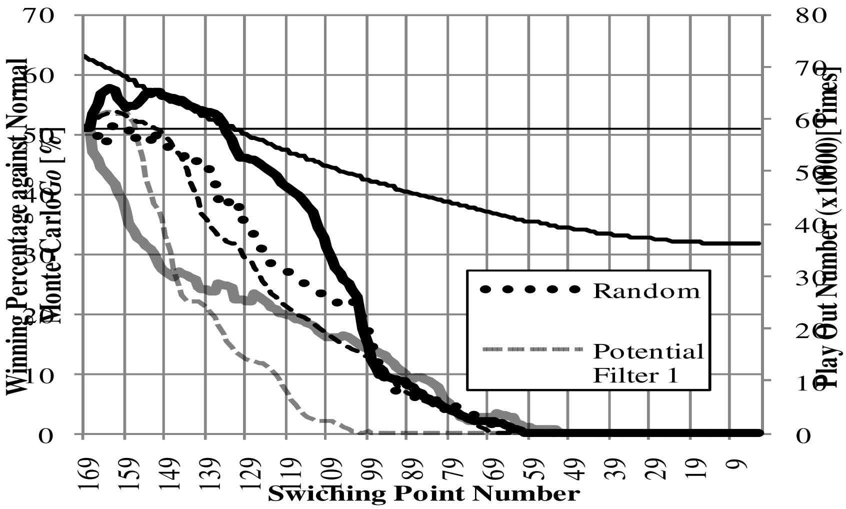

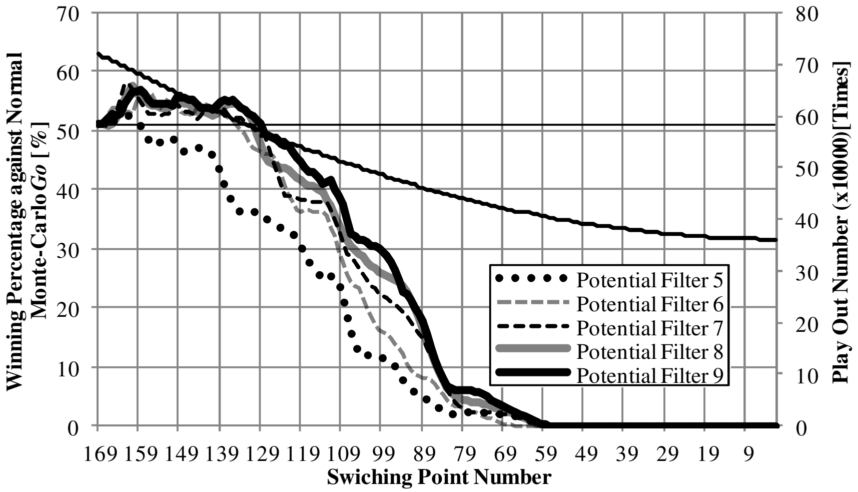

Method	Border	Play Out Number	Reduction Rate	Method	Border	Play Out Number	Reduction Rate
Random	-	722400	0.00	Potential Filter 5	160	681150	05.7
Potential Filter 1	157	673200	06.8	Potential Filter 6	135	592350	18.0
Potential Filter 2	152	649950	10.2	Potential Filter 7	132	578950	19.9
Potential Filter 3	-	722400	00.0	Potential Filter 8	132	578950	19.9
Potential Filter 4	135	592350	18.0	Potential Filter 9	129	572400	20.1

Fig. 1. Strengths of Monte-Carlo Go with Potential Filters

Potential Filter 2 became the bias where black stones were attracted around white stones. In the opening game, black stones effectively suppressed white stones. However, in the middle game, black stones were removed easily by collective white stones. As a result, the passive move acquired more territory than the initiative move on the *go* board. When strength exceeded average (51%), Potential Filter 2 properly pruned ineffective moves.

Potential Filter 3 became the bias where black stones were scattered on the *go* board. These black stones were removed easily by collective white stones. As a result, the passive move acquired more territory than the initiative move on the *go* board. In the opening game, Potential Filter 3 barely pruned ineffective moves. However, Potential Filter 3 gradually decreased in strength compared with other Filters.

Potential Filter 4 became the bias where stones were attracted around black and white stones. Potential Filter 4 could prune more properly than the other Filters, but drastically decreased in strength compared with other Filters in the middle game.

Potential Filter 5–9 became the bias where black stones were attracted around black and white stones, and areas between black and white stones were closed. This is important in *igo*. Potential Filter 5–9 could prune more properly than the other Filters but drastically decreased in strength compared with other Filters in the middle game. Each Potential Filter had a specific value (m). The lower (m) became, the stronger their bias and effect of pruning became. However, this experiment showed that the effects of pruning converge at a constant level even when (m) became lower considerably.

5 Summary

In this study, we tackled the reduction of computational complexity by pruning the *igo* game tree using the potential model based on the knowledge expression of *igo*. In our experiments, 9 pruning strategies (Potential Filters) were evaluated for their pruning effect. Maintaining normal strength of Monte-Carlo Go, Potential Filter 4, based on homopolarity potential distribution, could reduce up to 18% of total Play Out numbers needed in one game. Homopolarity potential could identify important areas around black and white stones. Potential gradient could identify important areas around black and white stones that were in closer proximity. Potential Filters 5–9, based on potential gradient distribution, could reduce up to 5.7–20.1% of total Play Out numbers needed in one game. Potential gradient could identify important areas around black and white stones that were in closer proximity, In addition, identified areas and their pruning effect changed according to attenuation rate (m).

In this research we successfully demonstrated pruning using the potential model for reducing computational complexity of the *go* game. However, our experiments were limited as the Play Out number was set at 100 and the board size was set at 13 x 13. For our future research, we will expand the proposed strategy to tackle more complex games with larger Play Out numbers and *go* board size. We will analyse the effect on game developments in more detail, both numerically and analytically.

References

[1] Brügmann, B.: Monte Carlo Go. Technical report, Physics Department, Syracuse University (1993)
[2] Zobrist, A.L.: A model of visual organization for the game of GO. In: Proceedings of the Spring Joint Computer Conference, AFIPS 1969, May 14–16, pp. 103–112 (Spring 1969)
[3] Nakamura, K., Syuhei, K.: Analyzing Go Board Patterns Based on Numerical Features. IPSJ Journal (The Information Processing Society of Japan) 43(10), 3021–3029 (2002)
[4] Yajima, T.: Effect of Stone and Effect of Table. SIG Technical Reports, Surugadai, Kanda, Chiyoda: The Information Processing Society of Japan, pp. 41–46 (2009)
[5] Burrough, P., McDonnell, R.: Principles of Geographical Information Systems, p. 190. Oxford University Press (1998)

Acquisition of Ground Behavior on the Locust Model under the Virtual Physical Environment

Yuta Umemura, Masahito Yamamoto, Ikuo Suzuki, and Masashi Furukawa

Graduate School of Information and Technology, Japan
{stttt,masahito,mack}@complex.ist.hokudai.ac.jp, ikuo@mail.kitami-it.ac.jp

Abstract. We have studied about ground behavior on the locust model under the virtual physical environment. In the previous study, the locust model acquires jumping behavior by use of neuro-evolution. However, a real locust often uses the jumping and walking behavior more flexibility. In this study, we realize the jumping and walking behavior for the same locust model. Both of those behavior are trained by use of neuro-evolution which is composed of artificial neural network(ANN) and real-coded genetic algorithm(RCGA). We analyze the obtained jumping and walking behavior and show the possibility to acquire flexible behavior.

1 Introduction

The creature often uses walking, running, and jumping behavior as ground behavior. They realize effective and flexible locomotion to select appropriate behavior from them which is suitable for surroundings and purpose. As for an artificial creature, most of studies focus on only one ground behavior[1][2][3]. However, in order to realize effective and flexible locomotion, it needs to acquire multiple ground behavior and composite behavior composed of multiple optimized behavior on the same model .

Such a model and composite behavior have been applied to various fields such as robotics [4], biological analysis[5] and CG animation[6]. In this paper, we use the locust model as a locomotion model under the virtual physical environment. Neuro-evolution is applied to optimize the locomotion of the given locust model and the jumping and if is proved that the model acquires walking behavior.

2 The Locust Model

We prepare the virtual physical environment by use of PhysX for the model. PhysX is a physics motion calculating engine developed by NVIDIA. PhysX reproduces a physical phenomenon such as gravity, collision and friction by integrating physical equations. By use of PhysX, we can model rigid body with joints between some rigid body.

We model the locust elements composed of some rigid body with joints. The model is composed of three parts, body, fore legs and back legs as shown in Fig.1.

S. Lee et al. (Eds.): Intelligent Autonomous Systems 12, AISC 194, pp. 775–783.
springerlink.com

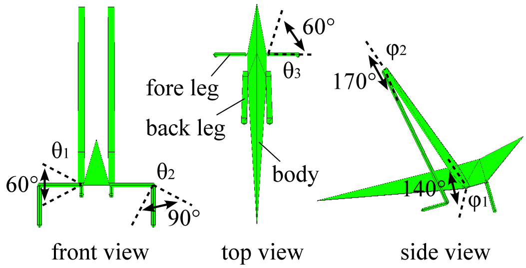

Fig. 1. The locust model

Eight actuators are implemented to joints between a body and a femur and between a femur and a tibia at both sides of fore legs and back legs. The model is controlled by eight actuators and the active leg angle ranges are shown in Fig.1 where $\theta_1, \theta_2, \theta_3, \phi_1 and \phi_2$ represent their angles. θ_{xR}, ϕ_{xR} represents each angle at right legs and θ_{xL}, ϕ_{xL} represents each angle at left legs.

3 Neuro-evolution

Neuro-evolution is one of learning methods to optimize Artificial Neural Network(ANN) by Genetic Algorithm(GA). We adopt Real-Coded Genetic Algorithm(RCGA) where genes in GA are represented by the real number.

3.1 ANN

ANN is a learning model on human train. The human brain learns by evolving the synaptic connection. ANN realizes learning by changing synaptic weights. We adopt three layer ANN because it has sufficient learning ability and a simple complex structure(Fig.2).

3.2 RCGA

GA is one of Evolutionary Computation(EC). GA adopts some operations for evolution of creature such as reproduction, natural selection and mutation. In GA, a group of solution candidates corresponds to considered population. The value calculated by evaluation function corresponds to fitness of each individual in the given environment. GA reaches the optimum solution by advancing evolution of a group of solution candidates with their evaluation values.

RCGA has genes as real number. Genes correspond to synaptic weights of ANN. RCGA optimizes ANN by evolving a group of genes. The following represents a flow of RCGA.

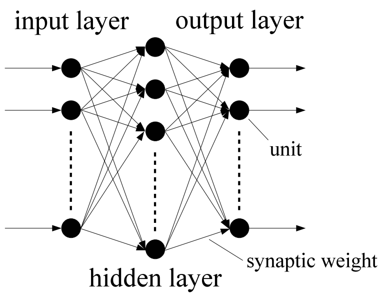

Fig. 2. ANN

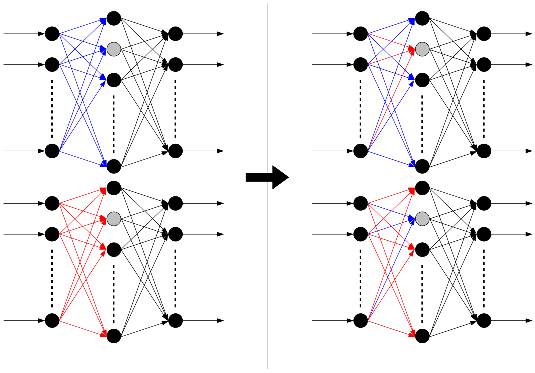

Fig. 3. -Neuro- crossover

1. Generate which have random numbers[-1.0,1.0]
2. Evaluate the genes by calculating fitness function
3. Apply "selection", "crossover" and "mutation" operation
4. Preserve a new group of genes as the next generation
5. Repeat 2)∼4) till a terminating condition is satisfied
6. Extract a best solution in the last generation

"selection", "crossover" and "mutation" are used as the genetic operation.

An elite preserving strategy is adopted as "selection" which preserves the best individual to the next generation.

"Crossover" adopts the two-point crossover(Fig.3).

"Mutation" changes one of genes. It avoids to fall into local solutions.

4 Acquiring Jumping Behavior

The model acquires jumping behavior by optimizing angles of actuators at back legs by use of neuro-evolution. The output of ANN controls actuators at the back legs. We suppose that a locust mainly jumps by use of the back legs so that the fore legs are fixed in this experiment.

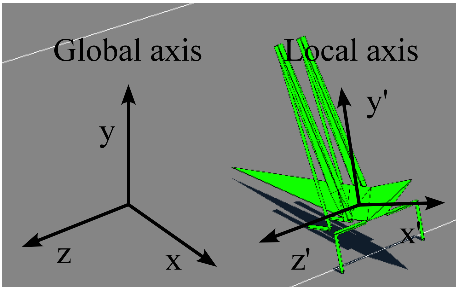

Fig. 4. The global axis and the local axis

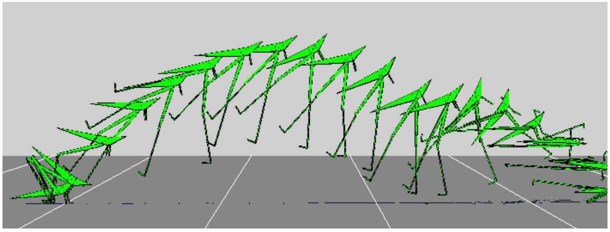

Fig. 5. Locomotion of the locust model trained for jumping

4.1 Setting Neuro-evolution

In this experiment, the ANN has 10 units in the input layer, 20 units in hidden layer and four units in output layer. The following variables represent 10 inputs.

- four angles at the back legs
  $\phi_{1R}, \phi_{1L} \in [0, 7\pi/9]$,$\phi_{2R}, \phi_{2L} \in [0, 17\pi/18]$
- inclination of the model $ic_1, ic_2, ic_3 \in [-1, 1]$
- touch sensors of the back legs and the ground
  $s_{1R}, s_{1L} \in (1 or - 1)$
- equation about height of the model $1/(H + 1) \in [0, 1]$

The inclination of the model represents the inner product of the local axis and the global axis(Fig.4).

Right and left back legs have touch sensors s at their lower edge. The touch sensor gives 1 if the back leg touches the ground and the touch sensor gives -1 if the back leg does not touch the ground.

We give the height of the model $1/(H + 1)$ to the input as the equation in order to restrict the range.

Four outputs, $O_1, O_2, O_3, O_4 \in [-1, 1]$ are scaled up to $O'_1, O'_2, O'_3, O'_4 \in [-10°, 10°]$. $O'_1 \sim O'_4$ represent displacement angles every $1/120[s]$ for each actuators. Each actuators at back legs are operated according to $O'_1 \sim O'_4$.

In RCGA, we have 50 individuals as a population. RCGA is terminated when the generation number becomes 1000. The elite preserving strategy, crossover and mutation rate are implemented with 10%, 30% and 0.1% respectively.

The fitness function is set as expressed in (1). D represents the forward distance that the model has jumped. H represents the hight the model has jumped. Maximizing E leads to acquire jumping behavior far and higher.

$$E = D * H \tag{1}$$

4.2 Results and Discussion

Acquired jumping behavior is shown in Fig.5. The model jumps forward by kicking back legs.

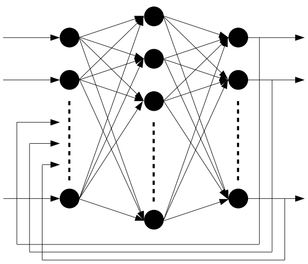

Fig. 6. Recurrent ANN

5 Acquiring Walking Behavior

The model acquires the walking behavior by optimizing angles of actuators at fore legs by use of neuro-evolution as well. The output of ANN controls actuators at fore legs. We suppose that a locust mainly walks by use of fore legs so that the back legs are fixed in this experiment.

5.1 Setting of Neuro-evolution

In this experiment, the ANN has 17 units in the input layer, 20 units in the hidden layer and six units in the output layer. The following variables represent 17 inputs.

- six angles at fore legs
  $\theta_{1R}, \theta_{1L} \in [-\pi/6, \pi/6]$, $\theta_{2R}\theta_{2L} \in [-\pi/6, \pi/3]$
  $\theta_{3R}, \theta_{3L} \in [0, \pi/3]$
- inclination of the model $ic_1, ic_2, ic_3 \in [-1, 1]$
- touch sensors of fore legs $s_{2R}, s_{2L} \in (1 \ or \ -1)$
- outputs of ANN $O_5, O_6, O_7, O_8, O_9, O_{10} \in [-1, 1]$

We consider that walking behavior is realized by repeating the movement of legs periodically. Six outputs ANN are set. The recurrent ANN is used. The recurrent ANN has an advantage to acquire the walking behavior easily.

Six outputs $O_5, O_6, O_7, O_8, O_9, O_{10}$ are also scaled up to $O'_5, O'_6, O'_7, O'_8, O'_9, O'_{10} \in [-2°, 2°]$. Each actuator at fore legs is operated according to $O'_5 \sim O'_{10}$ as displacement angles every $1/120[s]$.

Setting RCGA is same as experiment in acquiring the jumping behavior. The 50 individuals are given and RCGA is terminated when the the generation number reaches 1000. The elite preserving strategy, cross over and mutation rate are implemented with 10%, 30% and 0.1%.

The fitness function is set as expressed in (2). Maximizing E leads to acquiring a forward behavior further.

$$E = D \tag{2}$$

5.2 Results and Discussion

Acquired walking behavior is shown in Fig.7. The model walks by controlling fore legs periodically.

Fig.8∼10 represent displacement of the output at each actuator. Some outputs take the form of waveform. The model realizes periodical leg locomotion behavior by use of this feature.

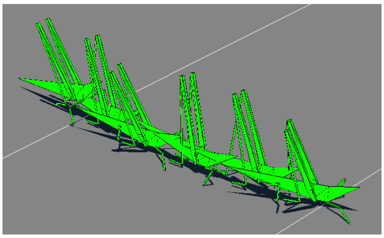

Fig. 7. Locomotion of the locust model trained for walking

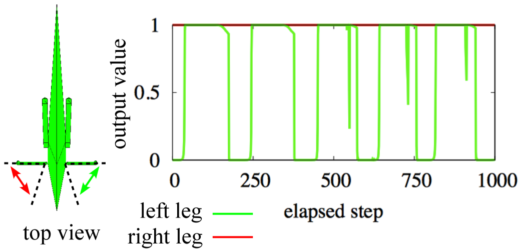

Fig. 8. Displacement of the output correspond to θ_3 and θ'_3

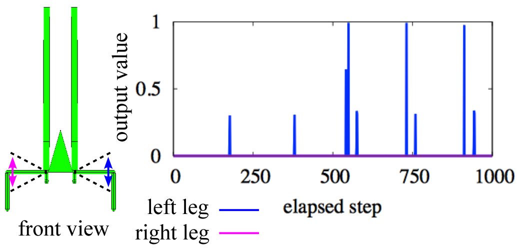

Fig. 9. Displacement of the output corresponding to θ_3 and θ'_3

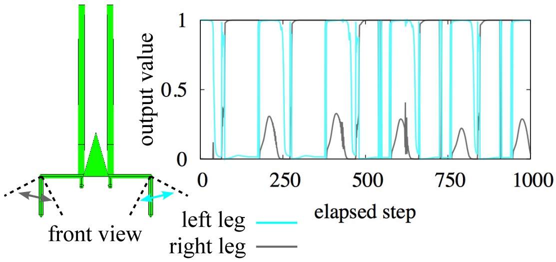

Fig. 10. Displacement of the output corresponding to θ_3 and θ'_3

6 Acquiring Walking Behavior By Four Legs

The model acquires walking behavior by use of two fore legs. In this experiment, we add the middle legs on the model and analyze whether the model also acquires the walking behavior on four legs.

6.1 The Locust Model

We add the middle legs to the model as shown in Fig.11. $\sigma_1, \sigma_2, \sigma_3$ represent angles of each actuator. Angle ranges of σ_1 and σ_2 are the same as θ_1 and θ_2. The angle range of σ_3 is set as shown in Fig.11.

6.2 Setting of Neuro-evolution

In this experiment, the ANN has 31 units in the input layer, 35 units in the hidden layer and 12 units in the output layer. The following variables represent 31 inputs.

- six angles at fore legs
  $\theta_{1R}, \theta_{1L} \in [-\pi/6, \pi/6]$, $\theta_{2R}\theta_{2L} \in [-\pi/6, \pi/3]$
  $\theta_{3R}, \theta_{3L} \in [0, \pi/3]$

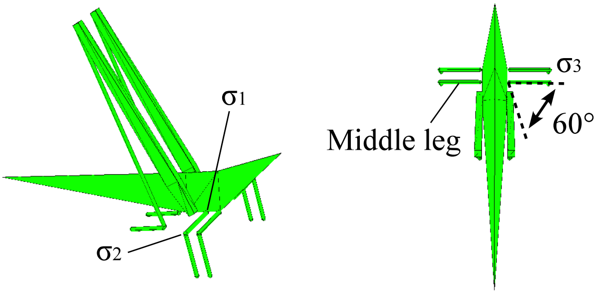

Fig. 11. The locust model with middle legs

- six angles at middle legs
  $\sigma_{1R}, \sigma_{1L} \in [-\pi/6, \pi/6]$, $\sigma_{2R}\sigma_{2L} \in [-\pi/6, \pi/3]$
  $\sigma_{3R}, \sigma_{3L} \in [-\pi/3, 0]$
- inclination of the model $ic_1, ic_2, ic_3 \in [-1, 1]$
- touch sensors of fore legs $s_{2R}, s_{2L} \in (1\ or\ -1)$
- touch sensors of middle legs $s_{3R}, s_{3L} \in (1\ or\ -1)$
- outputs of ANN $O_{11} \sim O_{22} \in [-1, 1]$

We also adopt the recurrent ANN in this experiment. 12 outputs $O_{11} \sim O_{22}$ are scaled up to $O'_{11} \sim O'_{22} \in [-2°, 2°]$. Each actuators at fore legs and middle legs are operated according to $O'_{11} \sim O'_{22}$ as displacement angles every $1/120[s]$.

Setting RCGA is the same as the experiment of acquiring the jumping behavior and acquiring walking behavior on fore legs. The elite preserving strategy, cross over and mutation rate are implemented with 10%, 30% and 0.1% in 50 individuals and 1000 generation.In this experiment, we also use (2) as the fitness function.

6.3 Results and Discussion

Acquired walking behavior is shown in Fig.12. The model walks by controlling fore legs and middle legs.

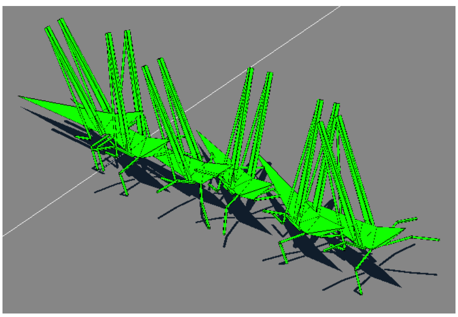

Fig. 12. Locomotion of the locust model with middle legs trained for walking

However, the model only use two legs to walk. It fixes other two legs not to be obstacles for walking. The reason why such behavior are obtained is synchronizing legs' control are not taken consideration. If we consider about the stability of posture of the model in the fitness function, the model may use four legs for walking and acquire stable walking.

7 Conclusion

The locust model acquires the jumping and walking behavior by use of neuro-evolution. A functional difference between that back legs take charge of the jumping behavior and that fore legs take charge of the walking behavior leads to acquire different behavior on the same model.

In a future work, we plan to acquire more flexible and efficient behavior by combining both jumping and walking behavior.

References

[1] McKinley, P.A., Smith, J.L., Gregor, R.J.: Responses of elbow extensors to landing forces during jump downs in cats. Experimental Brain Research 49 (1983)
[2] Yong, C.: Jumping mechanism and simulation of the locust-like robot. In: 2010 2nd International Conference on Education Technology and Computer (ICETC), vol. 1, pp. V1 (2010)
[3] Kikuchi, F., Ota, Y., Hirose, S.: Basic performance experiments for jumping quadruped. In: Intelligent Robots and Systems(IROS 2003), vol. 4, pp. 3378–3383 (2003)
[4] Kovac, M., Schlegel, M., Zufferey, J.C., Floreano, D.: A miniature jumping robot with self-recovery capabilities. In: Intelligent Robots and Systems(IROS 2009), pp. 583–588 (2009)
[5] Gronenberg, W.: Fast actions in small animals: springs and click mech- anisms. Journal of Comparative Physiology A: Neuroethology, Sensory, Neural, and Behavioral Physiology 178(6), 727–734 (1996)
[6] Liu, C.K., Popovic, Z.: Synthesis of complex dynamic character motion from simple animations. ACM Transactions on Graphics (TOG) 21(3), 408–416 (2002)
[7] Furukawa, M., Morinaga, M., Ooe, R., Watanabe, M., Suzuki, I., Yamamoto, M.: Behavior Composed for Artificial Flying Creature. In: Joint 5th International Conference on Soft Computing and Intelligent Systems and 11th International Symposium on Advanced Intelligent System, pp. 861–867 (2010)

Behavior of Ships after the Great East Japan Earthquake

Saori Iwanaga and Yoshinori Matsuura

Dept. of Maritime Safety Technology, Japan Coast Guard Academy
Kure, Hiroshima, Japan
{s-iwanaga,matsuura}@jcga.ac.jp

Abstract. The Great East Japan Earthquake occurred at 14:46 on Friday, 11 March 2011. It was the most powerful known earthquake to have hit Japan, and one of the five most powerful earthquakes in the world since modern record-keeping began in 1900. The earthquake triggered extremely destructive TSUNAMI waves of up to 40.5 meters. In this study, we study about damage of ships and urgent evacuation to pick new actual explication and various lessons out. We focus on the evacuation from TSUNAMI. Then, we analyze about ships evacuation from TSUNAMI using multi-agent simulation and we want to prepare for a coming earthquake. Then, we investigate the evacuation to shelter from TSUNAMI of evacuee and perform the own mission of staffs.

Keywords: The Great East Japan Earthquake, TSUNAMI, evacuation, multi-agent simulation.

1 Introduction

The earthquake off the Pacific coast of Tohoku, also known as the 2011 Tohoku earthquake, or the Great East Japan Earthquake, was a magnitude 9.0 undersea megathrust earthquake off the coast of Japan that occurred at 14:46 on Friday, 11 March 2011. It was the most powerful known earthquake to have hit Japan, and one of the five most powerful earthquakes in the world overall since modern record-keeping began in 1900. The earthquake triggered extremely destructive tsunami waves of up to 40.5 meters. In some cases it traveled up to 10 km inland.

Over 20,000 people dead and the missed and over 125,000 buildings damaged or destroyed by the earthquake. The earthquake and tsunami caused extensive and severe structural damage in Japan, including heavy damage to roads and railways as well as fires in many areas, and a dam collapse. Around 4.4 million households in northeastern Japan were left without electricity and 1.5 million without water.

In our viewpoint, we focus on the evacuation from TSUNAMI. Then, we analyze about evacuation of ships from TSUNAMI using multi-agent simulation and we want to prepare for a coming earthquake. When considering evacuation, we often stick to only evacuation to a hill and a shelter to get it. But, as seen on TV news, some ships rode on land, capsized or sink by TSUNAMI. And staffs of local public bodies lead evacuation or staffs of peace or rescue organization go to the office urgently. Then, there occur very traffic jam and it is difficult to reach the destination. We investigate the evacuation to shelter from TSUNAMI of evacuee and perform the own mission of staffs.

S. Lee et al. (Eds.): Intelligent Autonomous Systems 12, AISC 194, pp. 785–793.
springerlink.com

2 Behavior of Ships after the Earthquake

We can review the behavior of ships by AIS data in Japan immediately after the earthquake, because AIS data of ships were recorded. AIS is abbreviation of Automatic Identification System [1].

With the AIS installed, ships are able to monitor the movement of a multiple number of ships simultaneously regardless of visibility, thereby dramatically reducing the ship collision. Furthermore, ground facilities can obtain the ship-specific information necessary for automatic, real-time maritime traffic control. AIS will play an important role in ensuring navigational and operational efficiency in congested waterways [1].

In Japan, passenger ships of less than 300 tons of gross tonnage and all ships of more than 300 tons of gross tonnage for international sailing, and all ships of more than 500 tons of gross tonnage for non-international sailing have to be equipped AIS [2]. It was described by Table 1.

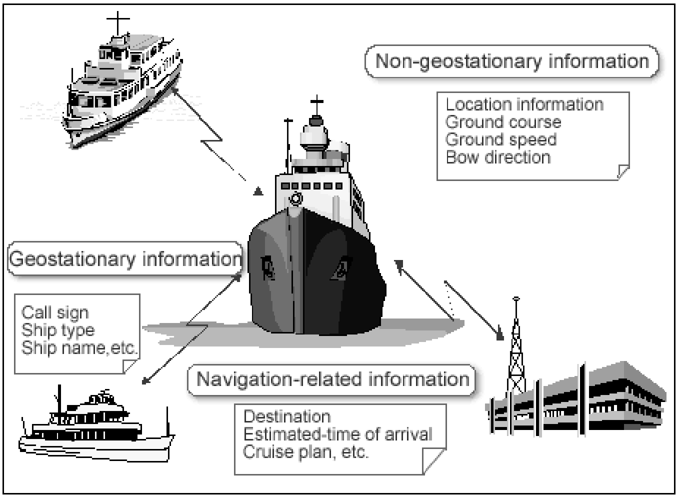

Fig. 1. Functions of AIS [1]

Table 1. Obligation of AIS equipment on ship in Japan[2]

Gross Tonnage	International Voyage	
	Engage in	Not Engage
Under 300 tons	Passenger Liner	No
Above 300 tons	All Ships	No
Above 500 tons	All Ships	All Ships

2.1 Hachinohe Port

Figure 2 is figure of the real AIS data of ships at Hachinohe Port in Aomori. Figure 2 (a) shows that six ships with active AIS berthed at the earthquake. An isosceles triangle is the symbol of ship and the heading is shown by the top. Speed and the heading of the ship are described by a bar, that is, length of the bar means the speed and the direction of bar means the heading of ship. And light lines mean the tracks of ships.

In this area, TSUNAMI warning announced at 14:49 and big TSUNAMI warning announced at 15:14. Then, TSUNAMI attacked Hachinohe Port at 15:51 and it was up to 6.2 meters. Figure 2 (b) shows the behavior of ships when TSUNAMI attacked. Four ships left the wharf, which is wall of bank, to offshore in 30 minutes after the earthquake and they could get over TUSNAMI. Ship A (1 k tons), which anchored off the wharf urgently, was tossed about by TSUNAMI, but it could get over TSUNAMI. As shown in Figure 2 (c), ship A could go offshore. Figure 2 (c) shows the behavior of ships at 1.5 hour after the earthquake, there was another ship B in the port. It left the wharf urgently and anchored 200 meter off wharf, but, it was pushed by TSUNAMI and hit the wharf. Moreover, about 350 fishing ships are flowed out or damaged. Gross tonnage of ship B is 56 k tons.

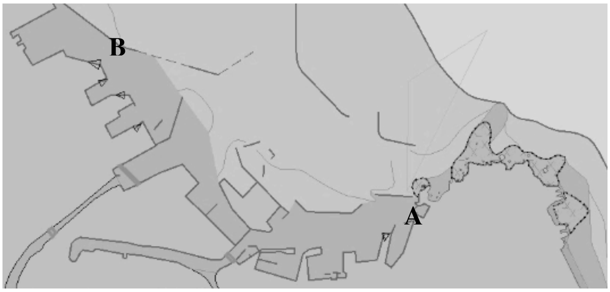

(a) Immediately after the earthquake

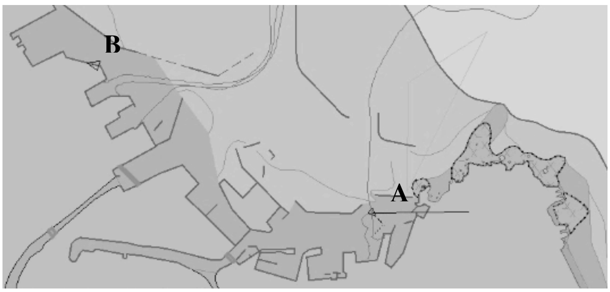

(b) When TSUNAMI attacked

Fig. 2. Tracks of ships in Hachinohe port

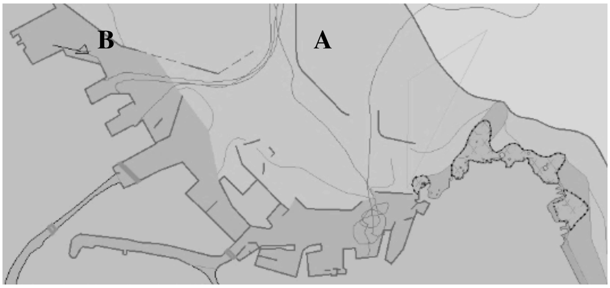

(c) At 1.5 hour after one hour

Fig. 2. (*continued*)

2.2 Kamaishi Port

Figure 3 is figure of the real AIS data of ships at Kamaishi Port in Iwate. In Figure 3 (a) shows that a ship with active AIS berthed at the earthquake. In this area, big TSUNAMI warning announced at 14:49. TSUNAMI attacked Kamaishi Port at 15:21 and it was up to 4.1 meter. Figure 3 (b) shows the behavior of ships when TSUNAMI attacked. The ship C was loading and unloading at that time. And it was pushed by TSUNAMI and the mooring rope was cut. Figure 3 (c) shows the behavior of ships at 2 hour after the earthquake, the ship floated and rode on land. 546 fishing ships are also flowed out or damaged. Gross tonnage of ship C is 4 k tons.

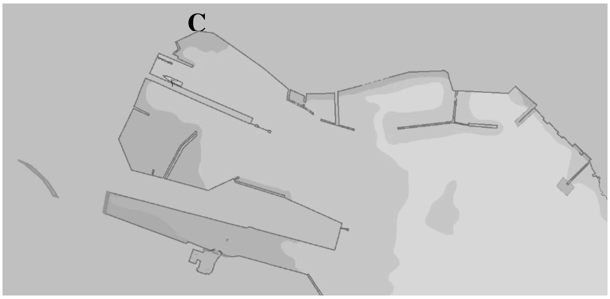

(a) Immediately after the earthquake

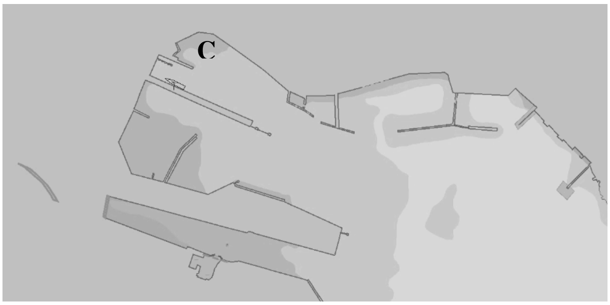

(b) When TSUNAMI attacked

Fig. 3. Tracks of ships in Kamaishi port

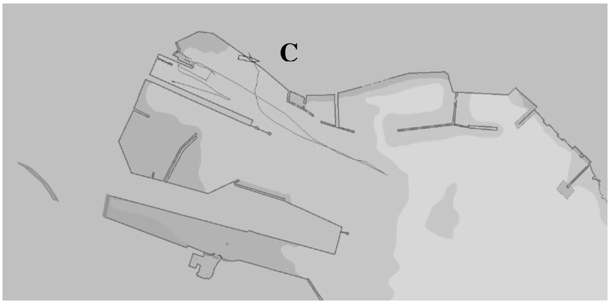

(c) At 2 hour after one hour

Fig. 3. (*continued*)

2.3 Sendai-Shiogama Port

Figure 4 is figure of the real AIS data of ships at Sendai-Shiogama Port in Miyagi. Figure 4 Figure 4 (a) shows that 14 ships with active AIS berthed at the earthquake. In this area, big TSUNAMI warning announced at 14:49. TSUNAMI attacked Sendai-Shiogama Port at 15:49. Figure 4 (b) shows the behavior of ships when TSUNAMI attacked. Nine ships left the wharf to offshore in 30 minutes after the earthquake and they could manage to escape from TUSNAMI. Ship D left the wharf about 40 minutes after the earthquake, then it was tossed about by TSUNAMI, but it could to escape from TUSNAMI. Figure 4 (c) shows the behavior of ships at 1.5 hour after the earthquake, there were five ships in the bay. Ship E left the wharf about 1 hour after the earthquake and it dodged other ships and could escape from TUSNAMI. Ship F, G and H were said to be loading and unloading at that time and gross tonnage of each ship is 6 k, 154 k, 5 k tons. Ship F left the wharf and anchoring urgently and it was tossed about by TSUNAMI. And the rope was get round, then it could not sail lat last. Ship G also left the wharf and anchoring urgently and it was tossed about by TSUNAMI. But, it could escape from the port though it hit another ship F. And ship H started to leave the wharf, but, it was too late. Rope was cut by TSUNAMI and it floated and rode on land.

(a) Immediately after the earthquake

Fig. 4. Tracks of ships in Sendai-Shiogama port

(b) When TSUNAMI attacked

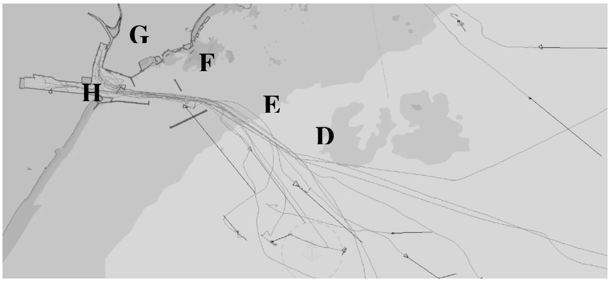

(c) At 1.5 hour after one hour

Fig. 4. (*continued*)

Then, we found that going offshore early for ship, about in 30 minutes, could escape the TSUNAMI. But, indeed many ships were loading or unloading at the earthquake. And ships anchored off the wharf, but, whether it is safety or not depend on the circumstance. In case of TSUNAMI, Japan Coast Guard also advises to go leave the port for safety, which is the cope with the TSUNAMI. Table 2. shows cope with TSUNAMI when TSUNAMI warning alarmed in the port, which is settled in "TSUNAMI measure of Japan Coast Guard" [3]. In the action plan for disaster of Japan Coast Guard provide the emergency measure for disaster. And it include ensure the traffic safety on the sea and safety action for dangerous object. The damage of ship is not only loss of property. If large ships hit the wharf, go down or ride on land, it causes the delay of restoration or transport. Otherwise, the accident of ship loaded dangerous object happens to be environmental damage. Therefore, the evacuation of ships is important.

Table 2. Cope with TSUNAMI when TSUNAMI warning alarmed in the port (current version)[3]

TSUNAMI Warning	Time to Spare	Ships Getting Shore		
		Large or middle ship		Small ship
		Ship Leaden Dangerous Object	General Ship	Pleasure Boat, small fishing boat
3m, 4m, 6m, 8m, Above 10m	No	SL, SW, EP in principle	SL, EL	EL
	Middle	SL, SW, EP in principle	SL, EP or EL	LT or EL (EP in some cases)
	Yes	SL, SW, EP	SL, EP	LT (EP in some cases)
1m, 2m	No	SL, SW, EP in principle	SL, EL or SM	EL
	Middle	SL, SW, EP in principle	SL, EP or EL or SM	LT or EL (EP in some cases)
	Yes	SL, SW, EP	SL, EP or SM	LT (EP in some cases)

SL: Stop Loading or unloading SW: Stop Working
EP: Evacuation from the Port EL: Evacuation for Land
LT: Landing and Tie the ship SM: Strengthen Mooring

3 Model

When ship berths, that is stays in the port, the sailors are not always on the ship and many sailors are on the ground. So, to go offshore the ship, the sailors must rerun the ship quickly. But, the roads to the port are crowded because many people evacuate from TSUNAMI for the shelters or hills. Then, sailors will confront the crowded for the port.

After the earthquake, almost people will evacuate for shelters or hills. But, there are other people. Indeed, Staffs of local public bodies or city worker have to lead evacuation or broadcast for going away to hills. Policemen went to the traffic accident point. Firemen extinguish a fire. And some fire brigades went to shut the floodgate. Staffs of Japan Coast Guard went to work, which is the port, immediately.

At the beginning, we only focus on evacuation of ships. But, ships could not launch because the sailor could not gather the ship in time. So, we expand the research area not only on the sea but also on the land. Generally speaking, when we think about disaster, we tend to focus on the evacuation of people. But, there are many people to support the evacuee. And they want to complete the mission, safety. But, there occur very traffic jam and it is difficult to arrive at the destination. Then, we investigate the evacuation to shelter from TSUNAMI of evacuee and action to perform the own mission using multi-agent simulation.

Then, we have an idea of simulation of earthquake offshore of Japan and TSUNAMI. We denote briefly as follows.

3.1 Space

We deal with land and ocean. The sample is shown Figure 5 using Google Map (http://www.google.co.jp). In land, there are many roads and almost people move on the roads to get away. And people want to get away in time to survive. So, behavior of people is restricted by space and time. But, there might be traffic jam or the road might cut by earthquake. On the other hand, sailors gather to port to launch the ship to offshore. If sailor is in town, he will be done to confront the crowded for the port to go back to port. Then, when the sailors gather to the ship, the ship will launch to offshore. On the sea, ship can move freely because there are not specified road. But, if ship move freely, ships can corrupt each other or ship can go aground. Then, it becomes difficult for ships to go away. Especially after earthquake, almost all are in hurry. Then, we design the sea route for simplify the simulation.

Fig. 5. Image of simulation

3.2 Agents

We define the agents as Table 3. Evacuee agent evacuate from TSUNAMI shelter or hill immediately. City worker agent of local public bodies broadcasts the information about TSUNAMI and leads evacuation or patrol the town immediately. And policeman agent goes to point of traffic jam or traffic accident immediately. Fireman agent leads evacuation. Sailor agent in town goes to the port. If sailors of ship are gathered, the ship agent leaves the port t to offshore.

Table 3. Agents in Simulation

	Behavior	**Destination**	**Start time**
Evacuee	Move	Hills	Immediately
City worker	Stay building		Immediately
	Patrol		Immediately
Policeman	Move	Traffic jam point	Immediately
Fireman	Patrol		Immediately
Sailor	Move	Port	Immediately
Ship	Move	Offshore	When sailors gather

3.3 Simulation

We are now programming using multi-agent simulator Artisoc [4]. Artisoc allows us to help easily and quickly reproduced on a computer interactions between humans, is a multi-agent simulator to analyze social phenomena alive dynamically changing.

Artisoc, the five-year plan implemented in fiscal 2003 Scientific Creation Project "social order change research by the multi-agent simulator," which was developed as part of copyright, Ltd. Kozo Keikaku belong to both the Graduate School of Arts and Sciences, Professor, University of Tokyo Susumu Yamakage. Using this simulator, some disasters or accidents are dealt with such as TSUNAMI in Okushiri in 1993, accident on Akashi footbridge in 2001.

4 Conclusion

Now, we are discussing and programming the simulation. We analyze about ships evacuation from TSUNAMI using multi-agent simulation and we want to prepare for a coming earthquake. By AIS data, we found that going offshore early for ships effective to escape the TSUNAMI. When considering evacuation, we often stick to only evacuation to a hill and a shelter to get it. And staffs of local public bodies lead evacuation or staffs of peace or rescue organization go to the office urgently. Then, there occur very traffic jam and it is difficult to reach the destination. Then, we expand the research area not only on the sea but also on the land. We investigate the evacuation to shelter from TSUNAMI of evacuee and perform the own mission of staffs.

References

1. Ministry of Internal Affairs and Communications for Equipment of Ships (2002), `http://www.tele.soumu.go.jp/e/adm/system/satellit/ais/index.htmRegulations` (in Japanese)
2. `http://law.e-gov.go.jp/htmldata/S09/S09F01401000006.html`
3. Japan Cost Guard, TSUNAMI measure of Japan Coast Guard (2005) (in Japanese) `http://www.kaiho.mlit.go.jp/info/tsunami/tsunami-shiryo.pdf`
4. Aritisoc, `http://mas.kke.co.jp/index.php`

Target Enclosure for Multiple Targets

Masao Kubo[1], Hiroshi Sato[1], Akihiro Yamaguchi[2], and Tatsuro Yoshimura[3]

[1] National Defense Academy of Japan, Yokosuka
{masaok,hsato}@nda.ac.jp
[2] Fukuoka Institute of Technology, fukuoka, Japan
aki@fit.ac.jp
[3] Japan Ground Self-Defense Force, Tokyo

Abstract. Target enclosure by autonomous robots is useful for many practical applications, for example, surveillance of disaster sites. Scalability is important for autonomous robots because a larger group is more robust against breakdown, accidents, and failure. However, traditional models only discussed cases in which minimum number of robots enclose a single target so that there is no way to utilize the redundant number of robots. In this paper, to achieve a highly scalable target enclosure model about the number of target to enclose, we introduce swarm based task assignment capability to Takayama et al.'s enclosure model. Our robots can enclose without any global predefined position assignments for each target,, for example, a Hamiltonian cycle, a chain structure etc.. The behavior is shown by computer simulations.

1 Introduction

In this paper, we propose a robotic swarm model that can allocate robots to an unspecified number of targets. In this model, each robot moves according to Takayama's target enclosure model but a new reference rule is introduced. By this reference rule, the robots do not need to keep the predefined assigned position of circular formation, so that it is possible for each robot to switch its target. Additionally, density based target selection rule is adopted to achieve stable target enclosure. The performance is verified by computer simulation.

Target enclosure, which is useful for monitoring disaster sites and unknown vehicles, has recently become an important goal for multiple robots. Robots can operate in dangerous circumstances, replacing human presence.

Disaster sites are usually far from an operator. In this case, it is uncertain for a group of robots to examine the exact number of sites to be observed. Therefore, it is desirable that more robots than necessary are employed, which enables them to accept a larger number of targets . For this purpose, the tasks of target allocation and target enclosure must be performed simultaneously.

However, it seems difficult for most target enclosure models proposed so far to realize this requirement.

There are 2 reasons as follows. Firstly, there is no researches which discuss multiple target to enclose environments. Secondly, except for the study of Kobayashi et al.[4], all other studies require that a particular physical arrangement of the robots be maintained in order to build a target enclosure.

S. Lee et al. (Eds.): Intelligent Autonomous Systems 12, AISC 194, pp. 795–803.
springerlink.com

For example, Yamaguchi[11] discussed a target capturing task in which the robots must maintain a chain structure. Kim et al.[3] discussed the target enclosure problem; in their solution, each robot needs information on the relative speed of one robot and relative geographical relation to its target to determine its behavior. If the relationship between a robot and its reference robot is considered as a link in graph theory, the graph of the group of robots must follow a Hamiltonian cycle.

When a robot changes the target to be enclosed, the following two events should be considered: withdrawal and accedence of the robot. In the former, the remaining robots in the group must maintain the constraint of the Hamiltonian cycle without the removed robot. In the latter, a group that satisfies the Hamiltonian cycle condition and the new member must form a new Hamiltonian cycle. As far as we know, discussion of these events is inadequate when there are no restrictions on the timing of withdrawal and accedence of robots.

Therefore, at first, we propose a new reference rule which makes this condition of maintaining a Hamiltonian cycle to achieve target enclosure relax. We focused on the study of Takayama et al.[10]. In their model, each robot needs information of one neighbor and its target. As in other studies, this model also requires the Hamiltonian cycle constraint. However, in this paper, we show that this model can realize target enclosure without this constraint when each robot bases its behavior on information from its nearest neighboring robot [6]. Therefore, in this model, robots can change targets without considering the above two events.

Target assignment function for a group of robots is achieved also by distributed manner. Robots can change their target by themselves. However, they fail to enclose multiple targets when too many robots change their target simultaneously. Therefore, we introduce density based target change rule which is inspired by the task allocation mechanism of swarm robotics research [12].

This paper is organized as follows. First, Takayama et al.'s model is introduced. Next the proposed method based on using the nearest neighbor as a reference is presented. Then, computer simulations are also used to demonstrate the multiple targets allocation capability of this model.

2 Takayama's Target Enclosure Model

Firstly, Takayama's target enclosure model is explainedD

2.1 Takayama's Target Enclosure Model

In this section, we assume that all robots choose the same target. We assume that on a two-dimensional (2D) plane, there is only one target O at the origin and n robots. Fig.1 illustrates the case of $n = 5$. Robots are numbered counterclockwise as $P_1, \ldots, P_n$, and r_i is the position vector of the robot P_i. In the target enclosure task, each robot moves to the corresponding white marker.

To achieve this task, Takayama et al.[10] proposed the following model. Each robot determines its control input, speed v_i, and angular velocity ω_i using two aspects of angular information: relative angles with respect to the target and an anterior neighboring

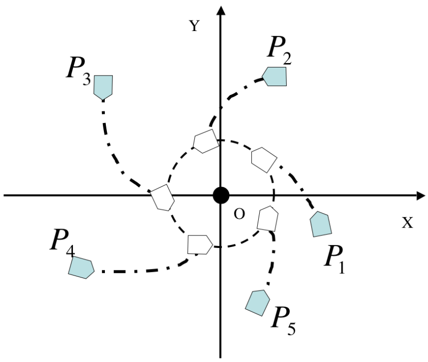

Fig. 1. Process of target enclosure using five robots

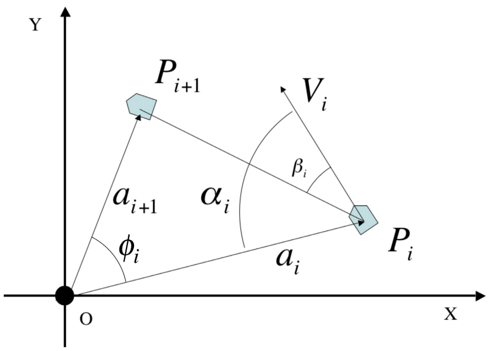

Fig. 2. Model of Takyama's target enclosure: α, β

robot,denoted as α_i and β_i, respectively. As a result, rotational movement occurs with a central focus on the target.

$$v_i = f\beta_i \tag{1}$$

$$\omega_i = v_i/\bar{r} - k\cos\alpha_i, \tag{2}$$

where the parameters $\bar{r}, k$, and $f > 0$ specified beforehand. P_{i+1} is the robot to which P_i refers, and $\bar{r}$ is the expected distance to the target. In Takayama et al.'s model, the i-th robot refers to the $i+1$-th robot, and the n-th robot refers to the first robot P_1. That is, if the relationship between a robot and its reference robot is considered as a link in graph theory, the graph of the group of robots must be a Hamiltonian cycle. The authors proved the convergence to the goal state of the target enclosure under this constraint.

Takayama et al. reported the following three characteristics of their model. (E1) The distance between the target and each robot converges to $\bar{r}$. (E2) The speed vector V_i and the vector $(O - P_i)$ are orthogonal. (E3) The gaps between a robot and its neighbors are equalized, i.e., $\phi_i = \frac{2\pi}{n}$.

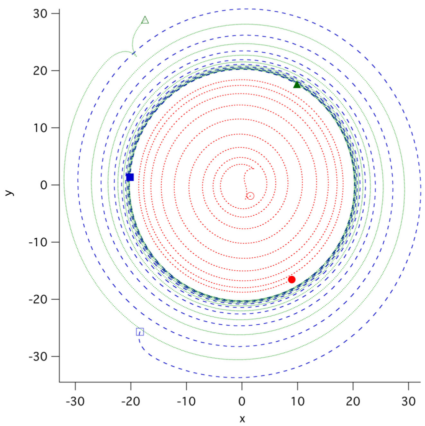

Fig. 3. Verification of Takayama et al.'s model for a three-robot group. Open markers indicate start points, and filled markers indicate final locations. This figure visualizes each robot approaching the target along a circular orbit.

2.2 An Example of Enclosure Process

A set of computer simulations was conducted to verify characteristics (E1)-(E3).

The simulation conditions were as follows. The target was at the origin of a 100 $\times$ 100 2D plane field. The initial positions of three robots were randomly specified, and it was assumed that $\bar{r} = 20m$. The robots' trajectories are shown in Fig.3. Their initial positions are indicated by open markers, and their final positions are noted by filled markers. One robot started its motion near the origin; the other two were at least 20 units away from the origin. This figure shows that each robot converged to a circle having a diameter $\bar{r}$ of 20 units. The gaps between these robots also became equal, i.e., $\phi_i = 2\pi/n = 2\pi/3$.

3 The Proposed Algorithm for Multple Targets Enclosure

3.1 Nearest Neighboring Robot as the Reference

In this paper, the robots observed by the i-th robot are considered to be its reference robots. In the original Takayama et al.'s model, the i-th robot P_i's reference robot is the $i+1$-th robot P_{i+1}. This relationship forms a Hamiltonian cycle. As mentioned above, this constraint makes target allocation behavior difficult. It also causes the scalability problem. Furthermore, each robot must identify its reference robot from the group of robots. This typically becomes difficult as the group size increases.

Therefore, we examine a new reference robot scheme in which each robot considers its anterior neighboring robot as its reference robot. Each robot controls itself as described in equations 1 and 2, but it chooses its nearest neighbor as its reference robot. If possible, the robots can change their target during the target allocation task. Such a system also has higher scalability because individual robots need not be identified to observe the nearest robot.

Algorithm 1. Multiple Targets Enclosure Agent

if $mode_i$ attribute of agent i is $Enclosure\,mode$ **then**
  Keep enclosing its nearest target with its nearest agent in $Enclosure\,mode$.
  if $|r_i - r_{i,neighbor}| < r_m$ **then**
    Set its $mode_i$ attribute to $Target\,selecting\,mode$ with probability p_{et}
  end if
else if its $mode_i$ attribute is $Target\,selecting\,mode$ **then**
  Choose a target to go, except for the nearest.
  repeat
    Go to the target.
  until the target is not its nearest target.
  Set its $mode_i$ attribute to $Enclosure\,mode$.
end if

3.2 Enclosure of the Unspecified Number of Targets

In this section, a new robotic swarm of which agents adopt the proposed nearest neighbor reference is proposed. Task assignment technique and information transmission of swarm robotics fashion [12] are adopted for the target selection. An agent of this model gives up its current target and shifts another when it is congested.

To achieve swarm for multiple targets, we introduce new parameter and terminology. Firstly, a new attribute we call $mode_i$ is introduced to represent current state of each agent. 2 modes are used, namely, $Enclosure\,mode$ and $Target\,selecting\,mode$. The first mode indicates that an agent engages in the aforementioned target enclosure task. On the other hand, $Target\,selecting\,mode$ means that a robot tries to be changing its target. Also, we suppose each agent can sense mode of its neighbor agents.

Algorithm 1 denotes operations at agent i. When it is in $Enclosure\,mode$, agent i encloses its nearest target while it is referring to its nearest agent . However, if the distance between the referring agent is too short, namely $|r_i - r_{i,neighbor}| < r_m$, agent i changes its mode to $Target\,selecting\,mode$ with probability p_{et} per unit time.

When agent i is in $Target\,selecting\,mode$, this agent goes to one of new targets directly. It does not enclose any targets during this mode. Agent i changes its mode to $Enclosure\,mode$ when the target is its nearest target and it starts to enclose the target.

4 Verification of the Proposed Nearest Neighbor Reference Model

4.1 Evaluation of Enclosure Task

In this paper, the target enclosure task for an n-robot group is defined as follows. The task consists of determining the distance to the target and equalizing the gap angle.

The distance task is

$$E_d = \sum_{i=1}^{n} (r_i - \bar{r})^2. \tag{3}$$

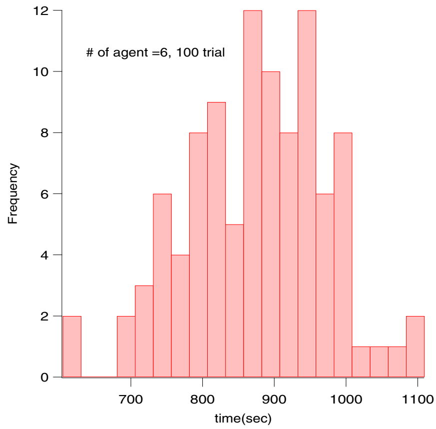

Fig. 4. Time to achieve enclosure for 6-robot group

The angle equalization task is

$$E_a = \sum_{i=1}^{n} (\phi_i - \frac{2\pi}{n})^2. \tag{4}$$

Because of these two requirements, the robots are deployed evenly on a circle having a radius of $\bar{r}$.

4.2 Verification of Target Enclosure Task for Larger Groups

The above discussion shows that the proposed model can achieve angle equalization for a small group. However, we did not provide the proof of the distance task represented by equation 3. In addition, we did not verify the performance for groups of more than four robots. Therefore, in this section, we discuss the ability to achieve target enclosure by using computer simulations.

We examined 3-, 4-, 6-, and 12-robot groups. There was only one target at the origin, and it was assumed that $\bar{r} = 20$. The initial position of a robot was specified inside a 100×100 rectangular region by a 2D uniform random number generator. We counted the time to achieve target enclosure as the time until $E_d + E_a < 0.5$ in equations 3 and 4. This simulation was repeated 100 times for each group size.

Fig.4 show the results for the 6-robot groups. The x-axis of each graph indicates the time required to achieve enclosure, and the y-axis denotes the frequency. For the three-robot system, the average time required for enclosure is 813.123, and the standard deviation is 125.737. For the four-robot system, the average time is 847.660 and the standard deviation is 102.825. For the six-robot system, the average time is 874.143 and the standard deviation is 96.921. For the 12-robot system, the average time is 1044.371 and the standard deviation is 115.408.

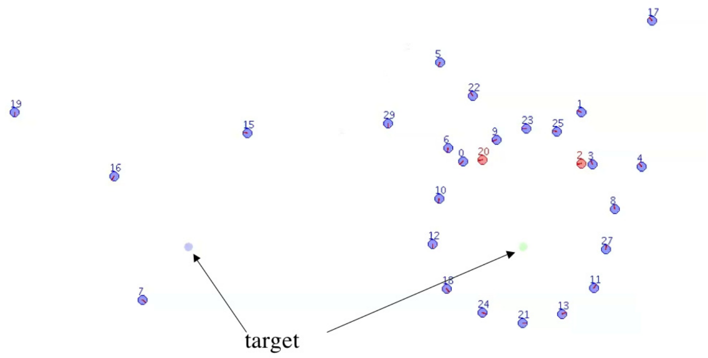

Fig. 5. A scene in the middle of a run(n=30)

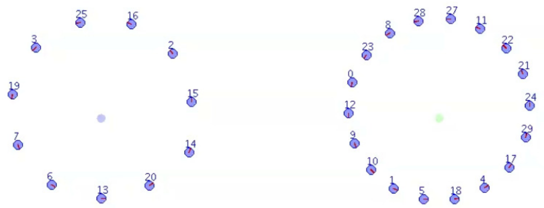

Fig. 6. A scene in the end of a run(n=30)

Thus, as the number of robots increases, the time required to achieve target enclosure increases. However, in all the simulations, groups of any size can achieve this task. Therefore, we conclude that any group of fewer than 13 robots can achieve target enclosure.

4.3 Computer Simulation

The result of computer simulation is shown in this section. Fig.5 and 6 illustrate a run with 2 targets. The number of agent n is 30. $\bar{r} = 4$, $r_m = 0.5$, $p_{et} = 0.01$. There 2 targets are 15 away.

Fig.5 shows a scene of middle of this run. On the other hand,Fig.6 illustrates a snapshot of end of this run. Initially, all of the 30 robots are deployed at random around right hand side region of the field. Therefore, at the beginning, most of the all agents enclose the right hand side target. This overconcentration causes congestion.Therefore, No.2 and No.20 agents in Fig.5 change their mode to *Target selecting mode*. These agents are depicted by red filled circle. Right after this scene, these agents went to the left side target and the number of agents who enclose the left target increased. Finally, in this run, the number of agents of the left and the right hand side target were 11 and 19, respectively. The balance seems to be influenced by r_m. This result is reasonable so that we confirm that the proposed agents can enclose multiple targets.

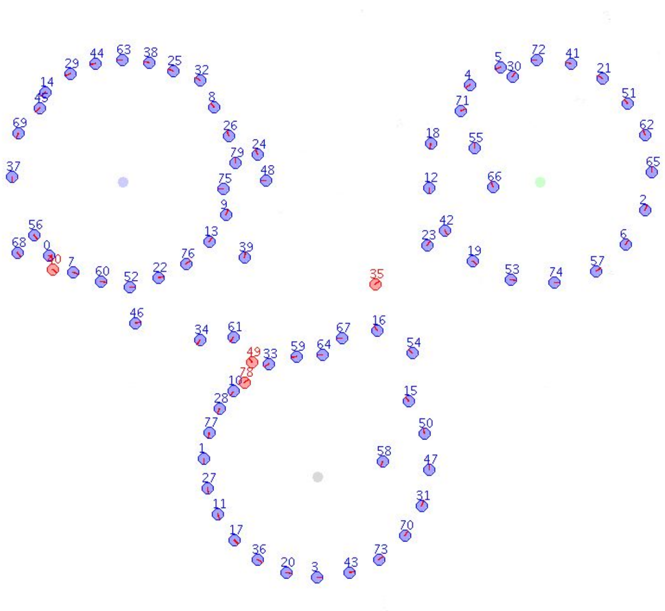

Fig. 7. A scene in a run(n=80)

Fig.7 shows a snapshot of a 80 robots group for 3 targets. As you see, the proposed robots can enclose more than 2 targets.

5 Conclusion

In this paper, algorithm for agents to enclose multiple targets has been discussed. Agents do not know the exact number of targets beforehand. Traditional target enclosure models have to keep some predefined structures at every moment so that it is difficult to adopt the difference of the number of targets. Therefore, firstly, a new condition of Takayama's target enclosure algorithm is discussed. In this condition, each agent encloses target with referring to its nearest neighbor and they do not have such predefined constraints. This new condition is confirmed by the series of computer simulation. Finally, the new target enclosure algorithm is proposed which includes target selection behavior based on swarm robots fashion. The total behavior is confirmed by the computer simulation.

References

1. Eppstein, D., Paterson, M.S., Yao, F.F.: On Nearest-Neighbor Graphs. Discrete & Computational Geometry 17(3), 263–282 (1997)
2. Jackson, E.A.: Perspectives of Nonlinear Dynamics 1. Cambridge University Press, New York (1995)

3. Kim, T.H., Sugie, T.: Cooperative control for target capturing task based on a cyclic pursuit strategy. Automatica 43, 1426–1431 (2007)
4. Kobayashi, Y., Otsubo, K., Hosoe, S.: Autonomous Decentralized Control of Capturing Behavior by Multiple Mobile Robots. Transactions of the Society of Instrument and Control Engineers 43(8), 663–671 (2007)
5. Kawakami, H., Numerikawa, T.: Network-topology Independent Cooperative Target-enclosing Behavior by Swarms of Vehicle. Transactions of the Society of Instrument and Control Engineers 5(12), 688–695 (2009)
6. Kubo, M., Yoshimura, T., Yamaguchi, A., Sato, H.: Individual Recognition-Free Target Enclosure Model. In: The Proceedings of the 17th Artificial Life and Robotics, pp. 608–613 (2012)
7. Marshall, J.A., Brouvke, M.E., Francis, B.A.: Formations of Vehicles in Cyclic Pursuit. IEEE Transactions on Automatic Control 49(11), 1963–1974 (2004)
8. Olfati-Saber, R.: Flocking for Multi-Agent Dynamic Systems: Algorithms and Theory. IEEE Trans. on Automatic Control 51(3), 401–420 (2006)
9. Olfati-Saber, R., Fax, J.A., Murray, R.M.: Consensus and Cooperation in Networked Multi-Agent Systems. Proceedings of the IEEE 95(1), 215–233 (2007)
10. Takayama, Y., Yamamoto, S., Takimoto, T.: Distributed Formation Control of a Nonholonomic Multi-agent System for Target-enclosing Operations. In: Proceedings of 9th SICE System Integration Division Annual Conference, pp. 697–680 (2008)
11. Yamaguchi, H.: A Cooperative Hunting Behavior by Nonholonomic Mobile Robot Troops. Transactions of the Japan Society of Mechanical Engineers. C 69(688), 3285–3292 (2003)
12. Ducatelle, F., Förster, A., Caro, G.D., Gambardella, L.: New task allocation methods for robotic swarms. In: 9th IEEE/RAS Conference on Autonomous Robot Systems and Competitions (2009)

A Study on Acquisition Method of Nonverbal Cues for Intelligent Agents: A Case Study on Facial Expression Analysis

Jun Hakura, Masaki Kurematsu, and Hamido Fujita

Graduate School of Software and Information Science, Iwate Prefectural University
152-52 Sugo, Takizawa, Iwate 020-0193, Japan
hakura at iwate-pu.ac.jp

Abstract. The paper proposes a method to acquire nonverbal cues for an intelligent agent that can be used in communications with human partner. A framework to extract the information that affords a key to understand intension, mental state, affect, or signs evoked by a person through nonverbal communication between the person and an intelligent agent. The aim of the framework is to make intelligent agents to be able to extract the nonverbal cues through trial-and-error style learning. A limited functionality of the framework is implemented and applied to a facial expression analysis as a case study. The main advantage of the method is that it would acquire the cues as some time-series information inherent to particular facial expressions. Thus the agent Result in a preliminary experiment shows that this implemented method have potential to extract nonverbal cues concerning with fake and real smiles.

Keywords: nonverbal cue, facial expression analysis, intelligent agent, time-series data.

1 Introduction

This paper proposes a method to extract the information that affords a key to understand intension, mental state, affect, or signs evoked by a person through nonverbal communication between the person and an intelligent agent.

Recent progresses on intelligent agents have triggered demands for artificial creatures to behave much like human. Those demands include nonverbal communication. According to Argyle [1], nonverbal communication is a key to understand human social behavior. Psychological studies suggests that nonverbal cues convey information about attitudes, personality traits, intelligence, intentions, mental and physical states, physical characteristics, identity, deception, and roles [2]. Nonverbal communication is deeply related with nonverbal cues from human behaviors such as facial expression, gaze, gestures, postures, and so on [1].

There are a lot of psychological studies that try to analyze the relations between nonverbal cues and their meanings. It is natural that they rely on the human cognitive abilities of feature extraction in movements, because their targets are the interaction

S. Lee et al. (Eds.): Intelligent Autonomous Systems 12, AISC 194, pp. 805–813.
springerlink.com

between humans. Therefore, we should give such abilities to the intelligent agents so that they are able to interact with humans through nonverbal communication.

This study, therefore, tries to introduce a mechanism with which the agent itself can extract the valid signals that can be considered as nonverbal cues, through interactions with human. Meanings of nonverbal signals vary variously depending on the culture, situation, sender, receiver, environment, and so forth. Moreover, it is hard to have clear definition concerning with which parts of the nonverbal cues should be taking into account. It must be very important for the agent to have clear definition of the nonverbal cues to be able to achieve thoughtful interaction with the partner. The definition might include meaning of a nonverbal cue, which part of the body is related to the cue, how the particular body part is moving, and which part of the movement is equivalent to the cue. The meaning of a nonverbal cue should be connected with behavior of the agents. This means that the agent should perceive the nonverbal cues as its possible behaviors with expected reactions by the partner as discussed in the next subsection. However, only an outline of the whole framework is described in the paper because this is an ongoing study and only some parts of the whole framework are implemented.

This paper, therefore, concentrates on how to extract nonverbal cues when series of sensory inputs representing the cues with some meaning is provided. A perceptual mechanism of the nonverbal cues is also introduced. An implementation of the limited version of an invariant extraction method is described in detail from the perspective of mental state estimation through facial expressions obtained by a vision system [3]. A preliminary experiment shows the mental state estimation methods with the invariant have a potential to distinguish sequences of facial expression of voluntary smile from those of involuntary smile and voluntary disgust.

2 Basic Framework of Agents with Perceptual Ability of Nonverbal Cues

The intelligent agent assumed in this study consists of set of sensors, set of behaviors, actuators, and a decision-making module with the perceptual ability of nonverbal cues. Functions assigned to these components might differ depending on the role of the agent. The sensors are expected to sense information on targets assigned to the sensor. Namely, a tracking mechanism is expected to the sensors. The set of behaviors is also given earlier according to the role of the agents, and actuators realize the behavior in the environment of the agent.

The set of sensors consists of various kinds of sensors. The sampling rate of each sensor, therefore, might be different according to the specification of the sensor. Therefore, temporal data with asynchronous observations by the sensors are obtained. The main task assigned to the perceptual mechanism in the decision-making module is to extract the patterns in the sequences of these temporal data that correlate highly with behavior of the agent. The patterns can be regarded as the nonverbal cues. Although a single sensor could obtain the patterns, combinations of these patterns obtained by several sensors might imply different nonverbal cues. The decision-making module will provide the perceptual ability of the agent as described in the next paragraph.

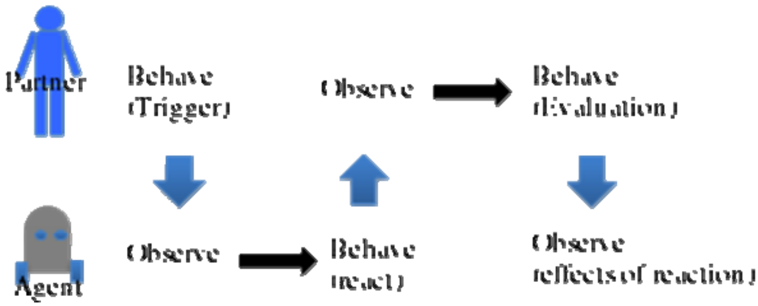

Fig. 1. Interaction between Human Partner and Agent

The perceptual ability of the cues is acquired through interaction with the partner person. Therefore, the perceptual ability of the agent is a function of the set of sensors, set of behaviors, actuators of the agents, environment, and the partner. Fig. 1 illustrates basic idea of the acquisition of perceptual ability. The agent is assumed to be facing with a person with whom the agent interacts (we will refer the person as a partner). The agent observes movements of the partner through its sensors. The agent cannot interpret the movements as nonverbal cues at the beginning of the interaction. Then, the agent records the movement of the partner as a sequence of sensory inputs so that it can afterward extract the nonverbal cues from the accumulated set of the sequences. At this moment, the agent somehow selects a behavior from the given set of behaviors. The behavior selection is done at random at the beginning and gradually learned to select purpose-oriented behavior for achieving the role of the agent. The partner, then, is expected to observe the behavior of the agent and would react to it. This reactive behavior of the partner can be considered as an evaluation, or it provides a meaning of the previous behavior of the partner, because it reflects the behavior of the agent, and accordingly the perception of the previous behavior of the partner by the agent. Finally, the agent could notice the meanings by observing the reaction of the partner. Iterating this process provides relations between observed sequences of sensory inputs, selected behavior, and the reaction of the partner. When a particular behavior results in the same reaction of the partner, there might exist some invariants in the input sequences. This study assumes that the invariants can be considered as the nonverbal cues. The agent can use the nonverbal cues to expect the reaction of the partner when it reacts to the partner with certain behavior.

One of the main points in the framework is how to extract nonverbal cues from sequences of the sensory input. This paper, therefore, will tackles with this point of the framework using a case study in the domain of facial expression analysis, and the other points are remained as future works. To make the problem much clearer, we would settle some limitations, i.e., we use a single vision sensor that senses facial expressions of a partner, and the sequences of the sensory inputs are labeled not with the behavior of the agent but by human observer, to the framework.

3 Acquisition of Nonverbal Cues on Facial Expression Analysis

There are many studies that aim to extract information from facial expression of a person, e.g. [4], [5], [6]. Most studies in this domain rely on shapes of the facial parts, i.e., mouth, eyes, eyebrows and etc., which change as facial expression evoked. This paper tries to implement limited functionalities of proposed framework as a first step of the whole framework. As an example of what nonverbal cues imply, mental states of a person are considered.

When we see facial expressions of other person, we are able to estimate mental states of the person. Moreover we can guess the facial expression is whether voluntary or spontaneous. This ability seems inherent to our perceptual ability and automatically achieved without forcing us to concentrate on the observation of the facial expressions. However, accuracy of the guessing grows higher when we are familiar with the person. What this circumstance implies can be inferred that we are able to acquire some key features in the movement of the facial expressions that expresses a particular mental state. The key features are extracted as a temporal sequence of sensory input and referred as the nonverbal cues in this paper.

The overview of the whole mechanism is depicted in Fig. 2. The system roughly composed of a vision system, data collection process, data labeling process, the facial expression analyzer, the nonverbal cue extractor, nonverbal cue database, and mental state estimator. While the data collection processes and data labeling process are the tasks to be done by the agent itself in the framework, we would entrust the work to a person in this paper. The mechanism has two phases, i.e., extraction phase and estimation phase. The modules to be used in both phase is different: the extraction phase does not use mental state estimator and estimation phase does not require the data collection, labeling, and extractor. The rest of the section describes an implementation of each phase and its component in detail, respectively.

3.1 Extraction Phase of Nonverbal Cues

The goal of this phase is to construct a database of the nonverbal cues. The extraction phase starts from collections of the facial expressions as a set of dynamic images. Each dynamic image is collected in the duration when a person is naturally interacting with the partner. We will call this person as a target person. The camera of the vision system is set near the eye position of the target person.

The target person is required to watch the collected raw dynamic images to judge what types of the mental states of the partner are observed during the interactions. This judgment is completely done in a subjective manner. Namely, the target person freely judges the mental states of the partner depend only on the knowledge, experience, or feeling of his/her own. The results of judgment are recorded as a couple of a sequence of the images and a label of the judgment. The labeling process is a selection of starting and ending point of the facial expressions that considered to be including particular signs of mental states. As results of the labeling process, we will obtain a set of dynamical images with a limited number of the labels. Each label is associated with nonverbal cues of mental states.

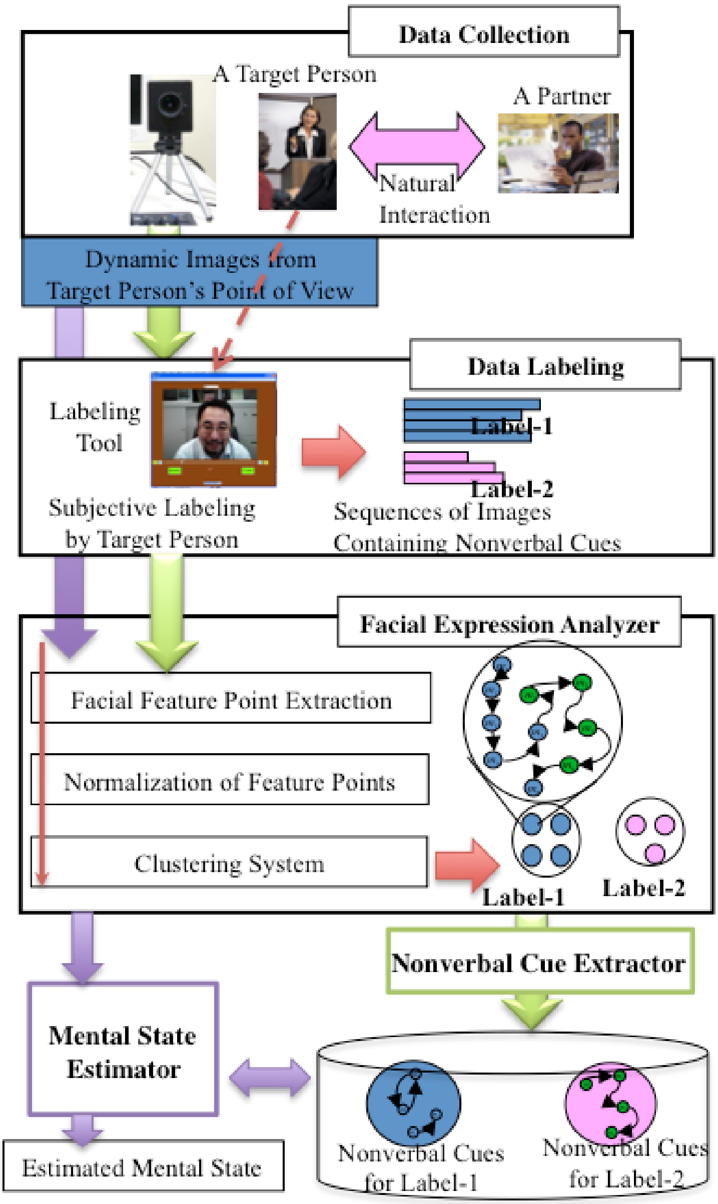

Fig. 2. Outline of Proposed Mechanism in Case Study

The dynamic images are the input to the facial expression analyzer. The analyzer consists of a facial feature point extraction, a normalization of the feature points, and the clustering system. Each dynamical image contains the developmental process of the facial expressions. To capture the developmental process, we adopt the facial feature point to make the too rich information of the visual data simpler. The movements of the facial feature points are assumed to represent the developmental process of the facial expressions. By tracking the feature points during the whole developmental process of the facial expression, we can identify facial expressions. To achieve the tasks, we have adopted the Face Sensing Engine (FSE) developed by OKI Electric Industry Co. Ltd. [7]. The FSE achieves a robust real time search of face and feature points for every frame of a dynamic image provided by the vision system compared to the Active Appearance Models (AAM) [8]. Because the vision system is affected by a variety of noises from ambient lights, this characteristic is important for the task. The FSE can detect up to fifty-six feature points. Among these points, we have empirically selected the twenty-six points to capture the facial expressions.

By using FSE, we can translate the segmented raw dynamic images into sequences of the position vectors whose components are the positions of the feature points in the image coordinate system. The position vectors, however, are not representing the pure movements of the facial expressions derived only from the facial expressions. The distance between camera and the partner and movements of the head of the partner affect the vectors. To cancel these factors, we have to align the feature points by adjusting the center, the scale, and the angles of the vectors. For this aim, we use the point detected as the nose head as the center point, the distance between the points at the tail of the eyes as a unit distance, and rotate the vector so that the angle of the line linking the points is to be zero.

The data still contain a lot of noises caused by the rapid movement of the person, change of facial contours, and the drawbacks of using the camera. Moreover, the movement of the face seldom occurs in the same way, and the subjective way of interpreting the mental state results in a variety of the facial expressions to be interpreted as the same meanings. One way to overcome the difficulties is treating the similar movements as the same movement. The clustering system serves as an implementation method of this role. The Self-Organizing Map (SOM) [9] can serve as the clustering system. The output layer in this paper has a lattice structure so that every output unit has the same number of the neighbor units. It can map not only the similar vectors into the same cluster, but the neighbor clusters have the similar input vectors as input. The output of the SOM is a state constituting the facial expression that the target person is interpreted as representing a mental state.

The nonverbal cue extractor analyses the state transitions generated by the clustering system. The state transitions have following characteristics: a) the durations of the transitions are not uniform, b) The states that has labeled as the near number represent the similar movements, c) the state transitions with the same label can be interpreted as the same mental state but is not guaranteed to contain the same movement because of ambiguities of the human judgment, and d) states in a state transition might contain some states generated from the noise caused by the miss sensing of the facial feature point extraction process.

The nonverbal cue extractor, firstly, tries to find common structure in the state transitions with the same label. This process is done in as follows. When we have N_l state transitions with the same label l, we denote the set of state transitions with label l as $\mathbf{S}^l$, where $|\mathbf{S}^l| = N_l$. Each state transition labeled as l then can be denoted as

$S_j^l = < s_0^{jl}, s_1^{jl}, \cdots, s_{n_j}^{jl} >, s_i^{jl} = \{0, 1, \cdots Nc\}$, where n_j is the duration of the transition and Nc is number of states, i.e., the output units in the SOM, to be allowed to use. $s_i^{jl} \in S_j^l$ is a candidate of the invariant, if and only if there exist $s_{m_k}^{kl}$ in $\forall S_k^l \in \mathbf{S}^l$, $| s_i^{jl} - s_{m_k}^{kl} | \leq N$, where N is the distance between the state to be allowed to treat the different states as the same state, and m_k is the state number of state transition k that should be minimum and never used before. Note that m_k proceeds when it is used as matched with previous s_i^{jl}. After examining all state transitions in the above manner, the nonverbal cues are defined as $I^l = \{ < \{ \min(C_i^{jl}), \cdots, \max(C_i^{jl}) \} > \}$, where C_i^{jl} is a set of states that are selected as the i th candidate of the nonverbal cue.

The second task of the nonverbal cue extractor is eliminating the common sequences observed among the different invariants. This elimination process is done by a simple manner. Namely, we just remove all element of the C_i^{jl}, C_k^{jl}, until $C_i^{jl} \cap C_k^{jl} = \{\varphi\}$. This would allow the nonverbal cues to be exclusive with each other.

3.2 Mental State Estimation Phase Using Nonverbal Cues

The mental state estimation phase uses the same clustering system, mental state estimator, and the database of the nonverbal cues. The partner in this time is facing with the agent. The dynamic images obtained in the same manner are categorized by the same clustering system, because the movement of the feature points must be categorized in the same cluster to compare it with the nonverbal cues. The categorized movement is also treated as a state in this phase. Every time the vision system captured a frame of image, the movement is calculated by subtracting the positions previous feature points from that of current feature points. The acquired movement is, then, translated into a state by the clustering system.

The function of the mental state estimator is quite simple, i.e., it just receives the state from the clustering system and asks the database whether there exist nonverbal cues that contain corresponding state. When there are some cues, they are the candidates until there is an exception or the whole invariants are matched with state transitions temporally observed. In the latter case, the estimator concludes that the mental state is observed. The estimator always observes the possibility of the occurrence of any mental state corresponding to the nonverbal cues in the database in parallel.

The rest of the paper is devoted to show the potential of the proposed method by showing the result of a brief preliminary experiment.

4 Preliminary Experiment on Facial Expression

To show the extraction ability of the nonverbal cue by of the proposed method, a simple preliminary experiment is carried out. The situation of the experiment is as follows: A student is facing with a professor in a room and asked to act smile for seven times, and disgust for two times. After that the student chat with the professor. The whole situation was recorded through CCD camera from the professor's point of view. After the sessions ended, the professor judged and labeled the facial expressions of the student as "fake smile", "fake disgust", and "real smile". As a result, we have seven sequence of the "fake smile", two of "fake disgust", and two of "real smile". The proposed mechanism extracts the nonverbal cues for "fake smile" using four sequences of "fake smile" and a "real smile". The facial features constituting the facial expressions are categorized into thirty categories with the SOM.

The only nonverbal cue "fake smile" extracted by the proposed mechanism consists of just one state transition between two states. This transition, however, could act as a nonverbal cue, because the method could identify the rest of the seven sequences of "fake smile" and distinguished them from the other nonverbal cues, i.e., "real smile" and "fake disgust". The extracted nonverbal cue might consist of noise, because detected feature points often contain noise. The noises, however, themselves contain meaningful information that is derived from the combination of the environment, sensing device, and facial expressions.

5 Conclusion

This paper proposes a framework to extract the information that affords a key to understand intension, mental state, affect, or signs evoked by a person through nonverbal communication between the person and an intelligent agent. A limited functionality of the framework is implemented and applied to a facial expression analysis as a case study. The proposed method has potential to detect true mental state under a certain situation. However, verifications on the extracted invariants are remained as future works that includes applying more stable feature points detector, test in variety of environment with more subjects. Implementation of the whole framework is also remained as a future work.

References

1. Argyle, M.: Bodily communication, 2nd edn., Methuen (1988)
2. Hall, J.A.: Nonverbal communication. In: Sander, D., Scherer, K.R. (eds.) The Oxford Companion to Emotion and The Affective Sciences, pp. 282–283. Oxford University Press, Oxford (2009)
3. Hakura, J., Kurematsu, M., Fujita, H.: Facial Expression Invariants for Estimating Mental States of Person. In: Proceedings of the 2009 Conference on New Trends in Software Methodologies, Tools and Techniques: Proceedings of the Eighth Somet 2009, pp. 518‐530 (2009)
4. Fasel, B., Luettin, J.: Automatic facial expression analysis: a survey. Pattern Recognition 36, 259–276 (2003)
5. Pantic, M., Rothkrantz, L.J.M.: Toward an affect-sensitive multimodal human-computer interaction. Proceedings of the IEEE 91, 1370–1390 (2003)
6. Tian, Y., Kanade, T., Cohn, J.F.: Recognizing action units for facial expression analysis. IEEE Transactions on Pattern Analysis and Machine Intelligence 23, 97–115 (2001)

7. Oki Electronic Industry, Face Sensing Engine Version 4 Application Development Guide: FSE Feature Point Detector Edition (FP) (2008)
8. Cootes, T.F., Edwards, G.J., Taylor, C.J.: Active Appearance Models. IEEE Transactions on Pattern Analysis and Machine Intelligence 23(6), 681–685 (2001)
9. Kohonen, T.: Self-organization and associative memory. Springer, Berlin (1989)

Study on Twining of Virtual Seaweed in Fluid Environment

Jun Ogawa[1], Masahito Yamamoto[2], Ikuo Suzuki[2], and Masashi Furukawa[2]

[1] School of Engineering, Hokkaido University
Hokkaido, Japan 060-0814
ogawa@complex.ist.hokudai.ac.jp
[2] Graduate School of Information Science and Technology
Hokkaido University
Hokkaido, Japan 060-0814
{masahito,ikuo,mack}@complex.ist.hokudai.ac.jp

Abstract. This paper describes the twining of seaweed in fluid environment by computer simulation of virtual seaweed. The morphology of virtual seaweed is modeled by Lindenmayer system. Then, two physical properties, which are adhesiveness and tear, are artificially introduced into this model. Physics engine is adopted to realize its physical motion. A fluid environment is constructed by the Lattice Boltzmann method. The method calculates time evolution of particle distribution to simulate fluid motion. The motion of virtual seaweed is acquired by moving in the environment. In order to find the twining conditions and the way of avoiding it, the simulation is executed by altering the environment. We ascertained that the virtual seaweed behavior has the close relationship with the water flow.

Keywords: Seaweed cultivation, Twining of seaweed, Physics modeling, Lindenmayer system, Lattice Boltzmann Method.

1 Introduction

In recent years, fossil fuel depletion is caused by growing world population and expanding the globalization of industry, which is a serious problem. Seaweed cultivation has been attracted as a means of new energy production [1][2]. Seaweed can be grown ten times faster than most terrestrial plants, because it has high photosynthesis efficiency. It consumes greenhouse gasses such as carbon dioxide and methane in growing. These grown seaweed produce fine oil. Seaweed oil has a potential as an alternative to petroleum oil. This oil can be applied to car fuel. Therefore, the seaweed cultivation contributes as a realization of a material circulating society. However, there are large number of challenges in the seaweed cultivation. One of the major challenges is the realization of more large and more efficient environment for cultivating seaweed. It is beneficial to maximize the advantage of photosynthesis for seaweed. General seaweed cultivation tank usually circulates water to prevent the seaweed from sinking. This kind of tank can be enhanced the absorption of carbon dioxide for the seaweed by moving the entire underwater. However, the water circulation causes the seaweed to twine and tear, which interfere with growth.

S. Lee et al. (Eds.): Intelligent Autonomous Systems 12, AISC 194, pp. 815–824.
springerlink.com

In this paper, we study the twining of virtual seaweed in fluid environment from computer simulation. This study aims at discovering the conditions which cause the seaweed twining and the water circulation avoiding twinings. First, seaweed and fluid environment are modeled by Lindenmayer system and fluid dynamics. Then, the behavior of the virtual seaweed can be controlled in the fluid environment and verifies its physical motion from simulation.

2 Modeling Seaweed and Environment

We introduce the model of virtual seaweed and fluid environment. In order to mimic real seaweeds, the morphology of the seaweed model is determined by Lindenmayer system. The physical model of virtual seaweed is consisted of the connections of the small rigid spheres. In order to model soft motions as marine plants of this model, virtual seaweed has three degrees of freedom. Two physical properties (adhesiveness and tear) are modeled into the seaweed model, which can be reflected real seaweed properties.

In this study, physics engine is employed for simulating seaweed and fluid motions. The physical model of fluid environment has constructed by NVIDIA PhysX which is the physics engine provided by NVIDIA Corporation [3]. PhysX can be dynamically simulated the basic physical law. However, applied functions are not supported in the PhysX. Therefore, two fluid forces (buoyancy and drag force) are calculated in the environment. The fluid motions are simulated by Lattice Boltzmann method.

2.1 Virtual Seaweed

Physics Model. The Lindenmayer system is an algorithm that can represent the growth processes of natural objects [4][5]. This algorithm is proposed by Hungarian theoretical biologist and botanist, Aristid Lindenmayer. Seaweed is grown by iterating cell divisions and the cell growth. By applying the Lindenmayer system, the growth process of virtual seaweed represents the natural form for most plants. Our proposed Lindenmayer system is adopted as the modeling of seaweed. Its growth process shows in Fig.1. This model consists of three hundred forty rigid bodies. One rigid body is the sphere of 0.50 meters in radius. The virtual seaweed model is shown in Fig.2.

Physical Property. The virtual seaweed mimics real seaweeds by modeling of two physical properties. One property is an adhesiveness. This property represents epiphytic property for seaweeds. The virtual seaweeds are worked weakly attractive force when they colide each other in underwater. This property is defined as the adhesiveness and it shows in Fig.3. The simulated coulomb force works to two rigid bodies as the adhesiveness, when the distance of two rigid bodies are less than a certain threshold r_t. The strength of the force are defined in the following 1.

$$F_A = k_a \frac{1}{r^2} \quad \text{for} \quad r < r_t \tag{1}$$

where k_a is the adhesive coefficientCr is the distance between two rigid bodies, and r_t is the threshold of distance between two rigid bodies.

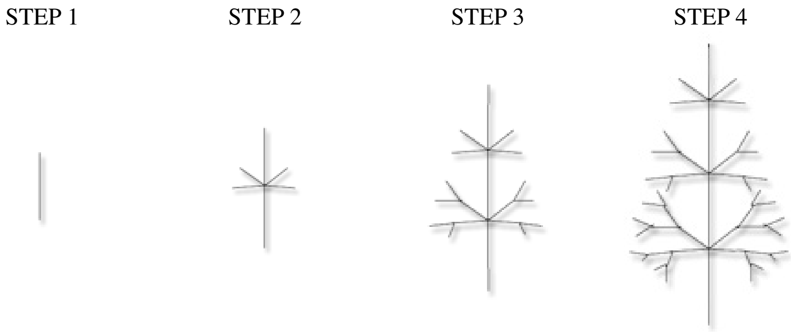

Fig. 1. Growth process of virtual seaweed

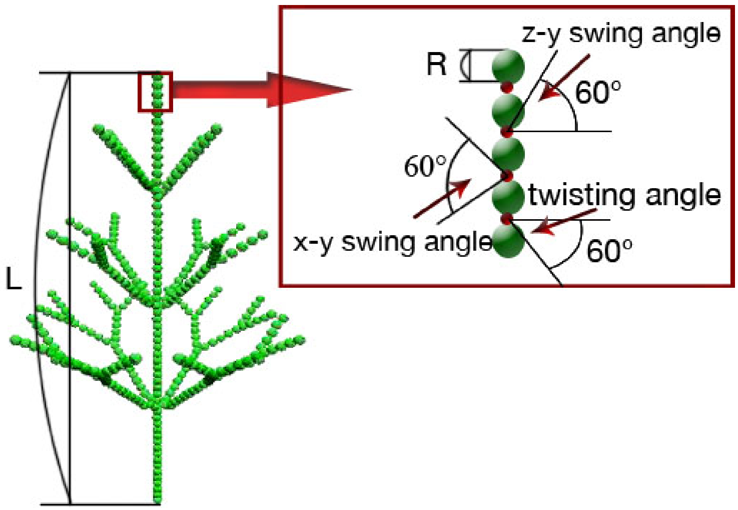

Fig. 2. Virtual seaweed model

The other is a tearing, this property is shown in Fig.4. Seaweed may be torn into some parts by the twining and water flow. Its phenomenon are modelled by adding strong force into seaweed. The connection between two rigid bodies for virtual model is broken by adding the force F_A above 10^6[N]. The torn connection by tear phenomenon cannot be reproduced.

2.2 Fluid Environment

Fluid Forces. The fluid environment is developed by modeling two fluid forces. These forces are buoyancy and drag force based on fluid dynamics.

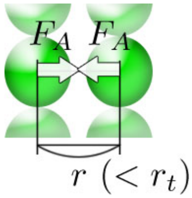

Fig. 3. Adhesiveness of virtual seaweed

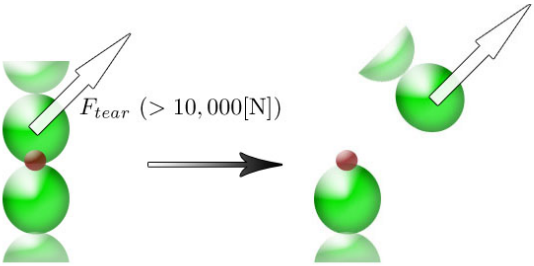

Fig. 4. Tear phenomenon of virtual seaweed

In a fluid environment, the vertical upward force that called buoyancy F_B works to objects by Archimedes' principle shown in Fig.5(a). The force is calculated by the following (2).

$$F_B = \rho V g \tag{2}$$

where ρ is the water density, V is a volume of rigid body, g is the gravity acceleration.

The drag force strength is given by (3). F_D works the rigid body in fluid environment shown in Fig.5(b). The drag force that is proportional to square of the relative velocity with a fluid. Its direction is inverse movement vector.

$$F_D = \frac{1}{2}\rho A C_D v^2 \tag{3}$$

ρ is water density, A is a projected area, C_D is the substance-specific drag coefficient, v is relative velocity with fluid.

Fluid Motion. In order to develop realistic water flow, the flow is modeled by Lattice Boltzmann method that is one of analysis techniques for computational fluid dynamics [6]. The Lattice Boltzmann method numerically simulates the fluid motion by calculating time evolution of particle distribution based on the idea of cellular automata. This method can represent the high-precision flow without noise. The fluid environment is discretized into unit lattices at the method. The continuous motion of fluid is determined by the particle movements in the lattice. Functions for particle distribution is obtained by calculating the ensemble average of number of particles in the lattice. It is easy to compute the fluid density and velocity from the particle distribution. These particles

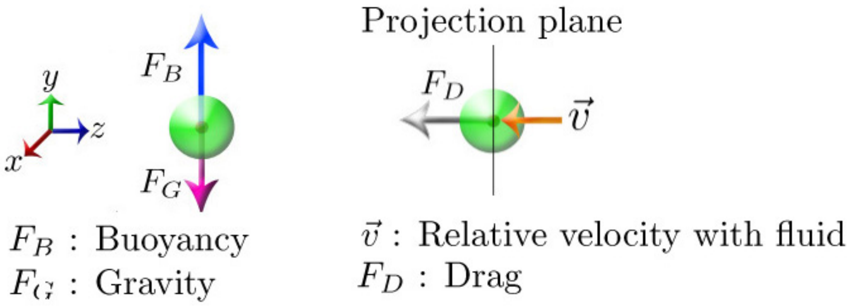

(a)Buoyancy (b)Drag force

Fig. 5. Buoyancy and drag force

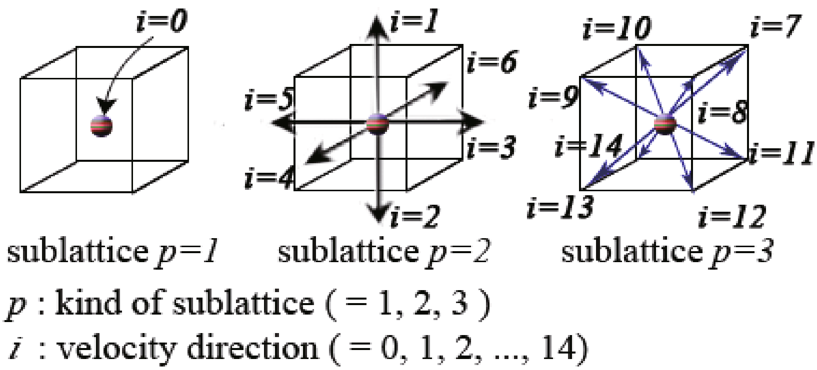

Fig. 6. 3D15V Model

iterate these processes of translation and collision for simulation. The particle movements such as translation and collision is the important factors at the Lattice Boltzmann method [7]. Water is a fluid and its density is not changed by pressure. Therefore, water flow can be treated as a incompressible fluid.

Water is a fluid and its density is not changed by pressure. We employ D3Q15 model as a particle distribution model. The D3Q15 is suitable for treating a incompressible fluid. Its particles have fifteen velocities shown in Fig.6. The lattice Boltzmann equation shown in (4) is employed for calculating time evolution of particle distribution [8].

$$f_i\left(x + e_i \Delta t, t + \Delta t\right) = \left(\frac{\lambda - 1}{\lambda}\right) f_i\left(x, t\right) + \frac{1}{\lambda} f_i^{eq}\left(x, t\right) \tag{4}$$

where λ is the relaxation frequency, f_i is the particle distribution function, i is kind of particle velocity.

(a)Before (b)After

Fig. 7. This figure gives an overview of the translate and collide processes for a fluid cell next to an obstacle

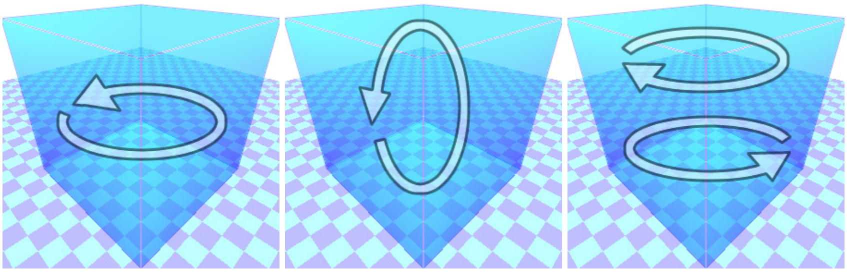

(a)Transverse circulation (b)Vertical circulation (c)Convection circulation

Fig. 8. Three fluid environment

These particles move repeating a collision. They transit from movement state to equilibrium one by constant rate. The following (5) represents the particle equilibrium distribution [8].

$$f_i^{eq}(x,t) = \omega_i \rho \left(1 - \frac{3}{2}\boldsymbol{u}^2 + 3(\boldsymbol{e_i} \cdot \boldsymbol{u}) + \frac{9}{2}(\boldsymbol{e_i} \cdot \boldsymbol{u})^2\right) \tag{5}$$

where f_i^{eq} is local equilibrium distribution, ω_i is the weight coefficient, ρ is the fluid density, $\boldsymbol{u}$ is the fluid velocity, $\boldsymbol{e_i}$ is the particle velocity.

The particles distribution of the lattice including obstacles cannot be calculated. Therefore, *bounce-back* is employed as boundary condition. This condition rebounds particles into the 180 degrees of direction from the obstacle shown in Fig.7.

3 Twining Experiment

In order to observe the twining of virtual seaweed in fluid environment, we examine the motions of the seaweed in three environments with different fluid velocity.

3.1 Objective

The motions of seaweeds are strongly influenced by the flow patterns and fluid velocities. Therefore, the objective of this experiment is to find the condition by altering the fluid velocities and water flow patterns so as to avoid the twining of seaweeds.

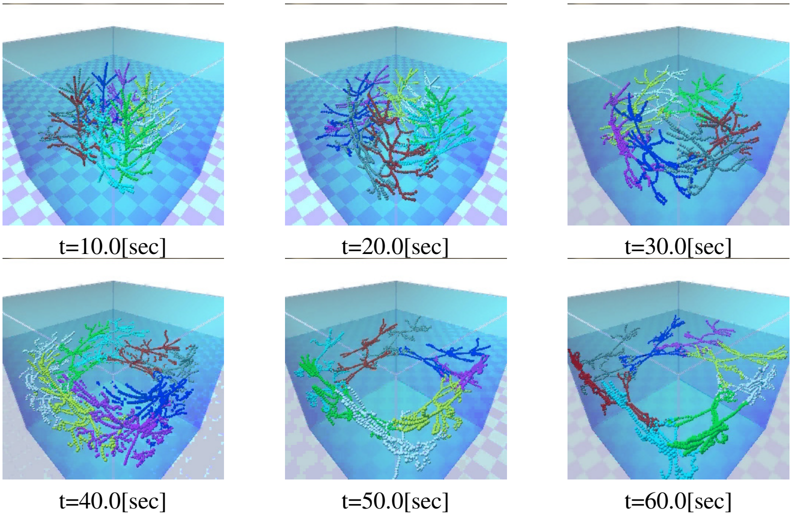

Fig. 9. Alteration of virtual seaweed's motion

3.2 Experimental Conditions

In this experiment, the control environment is the virtual environment with transversely circulate water. The fluid velocity is 1.4[m/s] for this environment and it is treated as the control velocity. Its environment is shown in Fig.8(a). These environments for the experiment consist of 80^3 lattices. There are two types of experiments as follows.

- Comparing seaweed motion by three kinds of fluid velocities
- Comparing seaweed motion by three kinds of flow patterns

First, these fluid velocity are twice and half of the control velocity. The twice velocity is 2.8[m/s] and half one is 0.7[m/s]. Then, three kinds of flow patterns are shown in Fig.8. However, fluid velocity comparison is only conducted by Fig.8(a). Virtual seaweed density ρ_r = 998.2[kg/m^3], adhesive coeffcient k_a=10^3, water density ρ = 998.2[kg/m^3], drag coefficient C_D = 1.0, the project area A = $0.25^2\pi$.

3.3 Results

Different Fluid Velocity. The alteration of seaweed motion in control environment shows in Fig.9. Then, the number of collisions between two rigid bodies for virtual seaweeds shows in Fig.10. From the results, it is easy to develop the twining phenomenon when decelerating the fluid velocity. The seaweed twining for twice control velocity is rapidly resolved for circulation.

Different Flow Pattern. The number of collisions for virtual seaweeds by three kinds of flow patterns are shown in Fig.11. At the convection circulation, parts of leng stem are twined by water flow. Then, the other flow patterns twines the seaweed from parts of short branch.

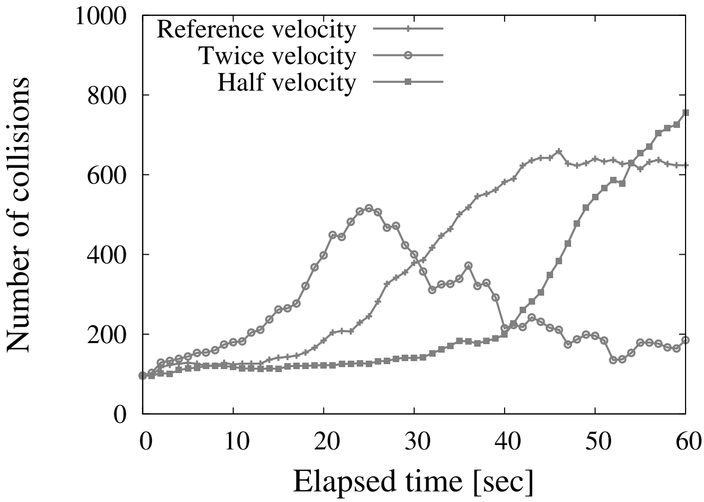

Fig. 10. Comparison of seaweed motion for different fluid velocities

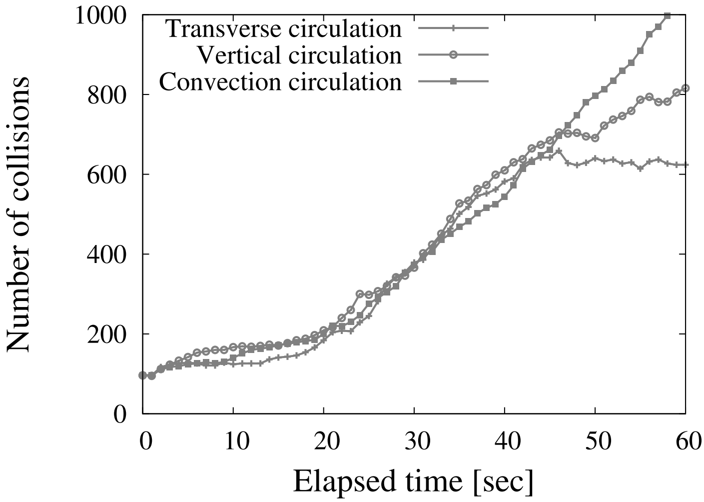

Fig. 11. Comparison of seaweed motion for different flow patterns

3.4 Discussion

From the comparison for different velocity, seaweed motion is differently changed by altering the fluid force strength. The high fluid velocity can be extended these seaweeds toward the outside of tank by employing centrifugal force. Therefore, the contacted parts of seaweed is peeled when adding the force larger than attractive one to these seaweeds.

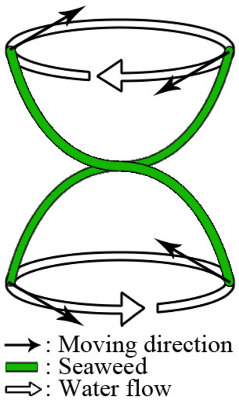

(a) Hourglass twining

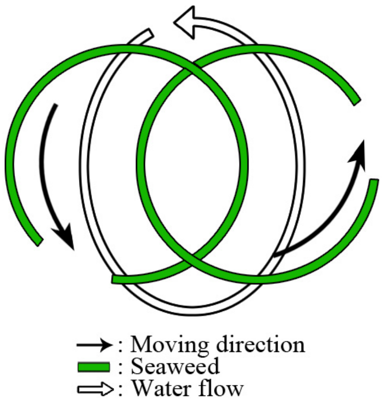

(b) Looped twining

Fig. 12. Twining conditions

There are two kinds of the seaweed twining, which shows in Fig.12. One is a hourglass twining shown in Fig.12(a). At the Fig.8(c), water flow moves these seaweeds in a hourglass motion. The hourglass motion surely develops the seaweed twining, because it cannot avoid the cross contact of seaweeds. Then, the other is a looped twining shown in Fig.12(b). This type of twining is easily developed in most fluid flow. In the Fig.12(b), the looped twining is also caused to seaweeds when one flow direction is inverse.

4 Conclusion

In order to study the twining seaweed by computer simulations, we modeled virtual seaweed with physical properties and fluid environment. This study shows about the twining as follows.

- The twining can be avoided by high fluid velocity
- The low velocity cannot peel the contacted parts of seaweed.
- To generate the force strengh lager than attractive one is needed to resolve the twining
- There are two types of the twining seaweed
- The hourglass motion surely develops the twining phenomenon (Fig.12(a))
- The most twining type is the looped one (Fig.12(b))

In the future work, we will approach the control method of water flow for avoiding twining seaweed. Analysis of motion from different seaweed models is also important matter. Then, it is needed to compare this model with real seaweed and cultivation tank, for improving reproducibility of this computer simulation.

References

1. Watanabe, M.M.: Future perspective of technology for algal biomass energy. Jpn. Soc. Mechanical Engineers 113(1098), 32–35 (2010)
2. Yokoyama, S., Jonouchi, K., Imou, K.: Energy Production from Marine Biomass: Fuel Cell Power Generation Driven by Methane Produced from Seaweed (2007)
3. NVIDIA PhysX, http://www.nvidia.com/object/physx_new.html
4. Sen, S.I., Day, A.M.: Modelling trees and their interaction with the environment: A survey. Comput. Graphics 29, 805–815 (2005)
5. Corbit, J.D., Garbary, D.J.: Computer simulation of the morphology and development of several species of seaweed using Lindenmayer systems. Comput. Graphics 17, 85–88 (1993)
6. Hou, S., Zou, Q., Chen, S., Doolen, G., Allen, C.: Cogley Simulation of Cavity Flow by the Lattice Boltzmann Method. Journal of Computational Physics 118, 329–347 (1985)
7. Chen, S., Doolen, G.D.: Lattice Boltzmann Method for Fluid Flows. Annu. Rev. Fluid Mech. 30, 329–364 (1998)
8. McNamara, G., Zanetti, G.: Use of the Bolzmann equation to simulate lattice-gas automata. Phys. Rev. Lett. 61(11), 2332–2335 (1988)

Visualization of Spatial Expression Ability Using a 3-D Expression System

Akihiro Suzuki, Masayuki Wajima, Takashi Kawakami, and Tetsuo Okazaki

Engineering Research Department,
Hokkaido Institute of Technology
7-15 Maeda, Teine-ku, Sapporo, Hokkaido, Japan
{r09301,wajima,kawakami,okazaki}@hit.ac.jp

Abstract. The objective of this paper is to analyze how children develop their spatial expression ability in 3-D space. We prepared a 3-D expression system that has "Translation-test", "Rotation-test" and "Paper-lay-out-test". As an experiment, we collected data by using our 3-D expression system for children between the ages of 4 and 6 in a pre-school in August 2009, January 2010, and August 2010. We conducted a survey on correlation between the system and WPPSI: WPPSI is an IQ test. At these experiments, we conducted 5 performance tests with WPPSI. The results are summarized as follows: 1) Children are able to recognize virtual 3-D space of the system, and are able to express images in virtual 3-D space; 2) The data shows the trend that spatial expression ability in space becomes better with advancing ages; 3) We obtained correlations between the system and WPPSI. The system can analyze some abilities that are difficult for WPPSI.

1 Introduction

Various articles have been published on the process of how children in Japan develop their spatial perception. For example, these articles try to understand it by means of studying paintings[1], using toy blocks[2] and having conversations [3][4]. However, paintings depends on 2-D expression. And with toy blocks, children are highly likely to have space with different parameters. Children likely to have a different sense of gravity and children's space likely to have a different coordinate axis from our adult's space. And children's conversational ability needs a long period for development. The Wechsler Preschool and Primary Scale of Intelligence test (WPPSI)[5], one of the standardized IQ tests, has subtests to analyze spatial perception ability. But the WPPSI analyzes ability using 2-D space. Moreover, test examiners need to understand the WPPSI test, and children need to endure a test period of longer than 2 hours.

So, we feel that our approach, which uses a computer, is more effective. We prepared a 3-D expression system to measure the developmental growth of spatial expression ability in 3-D space. As far as we know, this is the first approach that studies children's spatial development using a computer. We conducted a series of experiments with 4 to 6 years old children in a pre-school, as the first step

S. Lee et al. (Eds.): Intelligent Autonomous Systems 12, AISC 194, pp. 825–834.
springerlink.com

in studying the development of spatial growth. The aim of the experiment is to measure how children develop their spatial expression ability over a period of time.

2 Prepared System

2.1 3-D Expression System

We define some basic spatial expression abilities as follows:

- Operation abilities in defined 3-D space
  - ability to cognize and understand a limited 3 dimensional area
  - ability to move something to a target position in a space, or ability to draw a figure in a 3 dimensional area
- Expression abilities of relations
  - ability to cognize relations of distances, directions, and dimensions between one thing and the other
  - ability to decide distances, directions, and dimensions for the target relations

Our 3-D expression system needs functions for understanding those abilities, and needs methods of spatial expressions for understanding that childrenfs immanent 3-D space. So, we formulated the following methods of spatial expressions in a computer, and employed those methods on our 3-D expression system. Fig.1 is a mock picture showing the stage of expression of complex perspective (4 to 7 years old) according to Higashiyama[1]. The picture has a road and a railway track from an overhead view and a house and a train from lateral view. A 3-D image can be expressed by dividing Fig.1 into various parts and to lay out the parts in a 3-D image as Fig.2. Similarly, we applied this method to the system. The system has a function that a user to lay out illustrated papers in a virtual 3-D program. We also equipped the system with other functions by means of operating cubes for understanding the operation abilities.

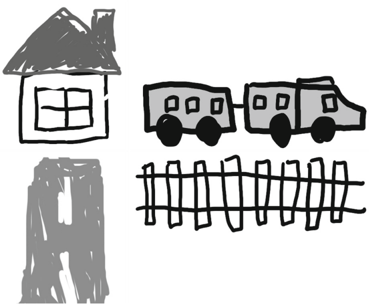

Fig. 1. A child's drawing

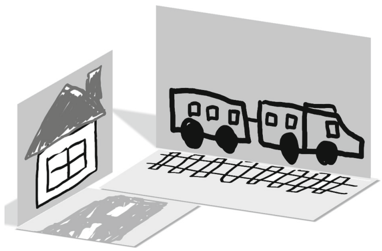

Fig. 2. Lay out in 3-D space

2.2 Overview of the System

We prepared a 3-D expression system which meets the requirements in section 2.1. We developed the system using the C++ programming language, the system works on Windows. Fig. 3 shows the execution screen of the system. The function buttons are located at the top of the screen. Located at the left of the screen are a color palette, undo button and redo button, and the button that can be used to create a paper. The rest of the area is space to express 3-D images. We applied Nintendo's Wii Remote[6] as an operation device for the system. The operation device for the system requires acceleration sensors and gyroscope sensors to rotate the papers, and optical sensors and buttons to translate and choose the papers. Because, to use a mouse and a manipulator, which are commonly used in computer graphics, is hard for children who have limited or no computer experiences. So, we adopted Wii Remote for the system.

The system has functions of creating new papers, drawing on papers, displaying cubes for experiments, translating and rotating papers and cubes, and translating and rotating a view. And the system has functions of Translation-test, Rotation-test, Paper-lay-out-test for experiments. The Translation-test and the Rotation-test are tests for analyzing the operation abilities in 3-D space. The Paper-lay-out-test is a test for analyzing the expression abilities of relations.

Fig. 3. 3-D expression system

3 Experiment Overview

We conducted the experimental tests in August 2009, January 2010, and August 2010 in a pre-school as shown Fig.4. The examinees were 14 children 4-years-old, 17 children 5-years-old, and 11 children 6-years-old, 26 boys and 16 girls. 15 children took the experiments twice in the first experiment and also in the second experiment. We tested Translation-test, Rotation-test, and Paper-lay-out-test for children in every experiment. In August 2010, we used the WPPSI IQ test. These experiments were conducted in individual room. We explained to them the method of operation, and tests before tests. The required time of experiments was about 20 minutes. Fig.5 shows the process of the tests.

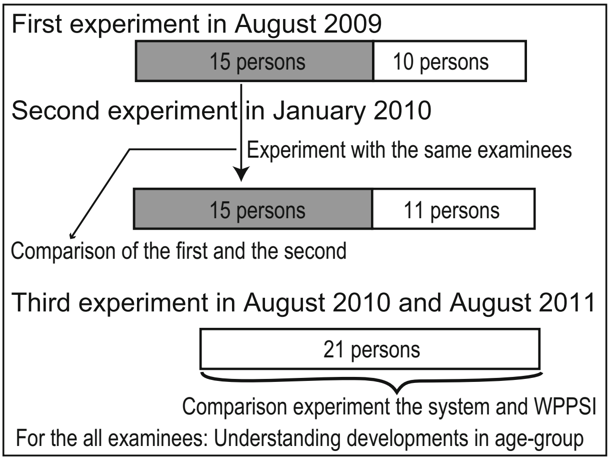

Fig. 4. Experiment plan

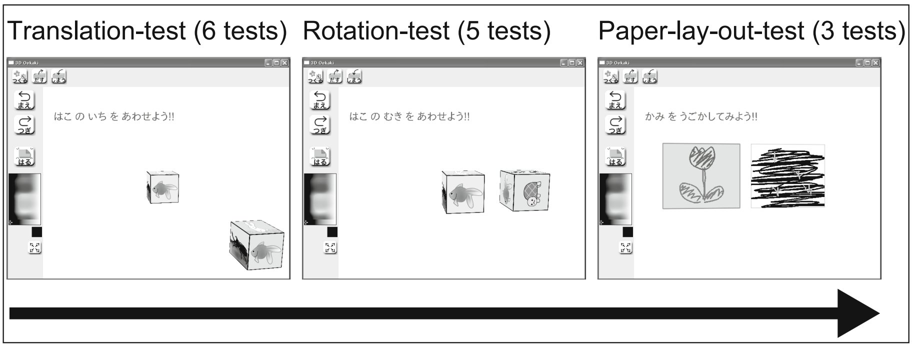

Fig. 5. Process of tests

4 Difference of Operation Ability in Space in Half a Year

4.1 Experiment Methods

We describe Translation-test and Rotation-test as follows:

– Translation-Test: Two cubes of the same size but different colors are arranged at different positions in advance. An examinee translates the highlighted cube at the center to another cube. There are 6 different tests as shown Fig.6.
– Rotation-test: Two cubes of the same size but different colors are arranged in different directions in advance. An examinee rotates the highlighted cube until the same direction is obtained as the other one. There are 5 different tests as shown in Fig.7.

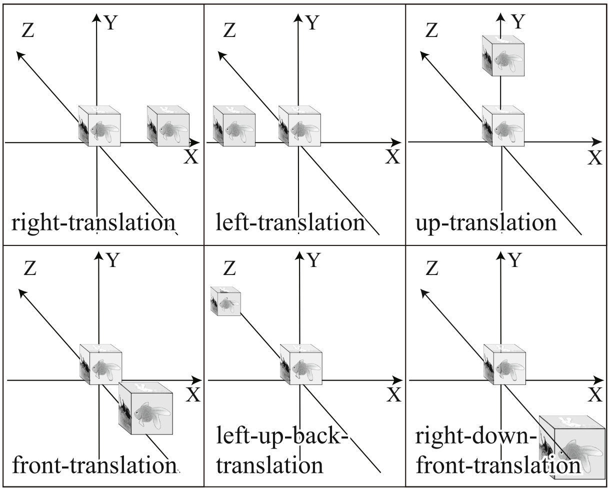

Fig. 6. Translation-test

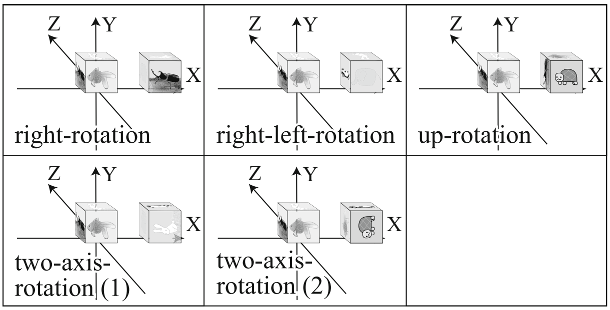

Fig. 7. Rotation-test

4.2 Experimental Result

Fig.8 shows the average times and the standard deviations of time required to complete a test, and the rates of completion. In the second experiment, most of the average times of the Translation-test and the Rotation-test are shorter than the first experiment. And in the second experiment, most rates of completion of the Translation-test and the Rotation-test are greater than the first experiment. By t-test, the average times of right-rotation, right-left-rotation, and two-axis-rotation(2) are significantly different between the first experiment and the second experiment (p¡.05). By F-test, the average times of right-translation, up-translation, right-rotation, right-left-rotation, and up-rotation are significantly different between the first experiment and the second experiment. This result

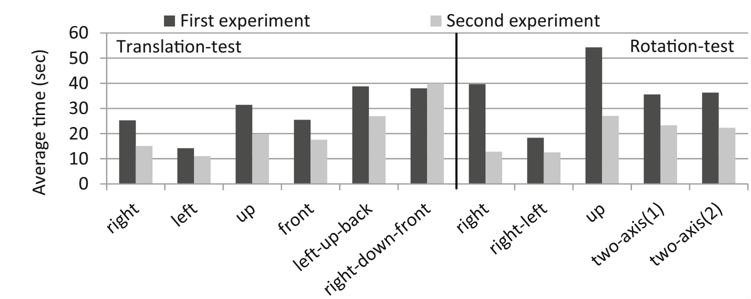

		right	left	up	front	left-up-back	right-down-front	right	right-left	up	two-axis(1)	two-axis(2)
first experiment	average time	25.3	14.2	31.5	25.5	44.5	41.3	39.7	18.3	54.3	35.6	36.3
	standard deviation	26.6	11.6	40.4	15.1	25.3	26.3	43.4	23.8	38.7	22.1	17.5
	completed rate	1.00	1.00	0.87	0.93	0.73	0.60	1.00	1.00	1.00	1.00	0.80
second experiment	average time	15.1	11.1	19.7	17.6	29.9	43.1	12.8	12.6	27.1	23.3	22.3
	standard deviation	13.5	7.5	16.5	19.0	17.1	52.9	16.2	11.7	19.3	16.4	18.0
	completed rate	1.00	1.00	1.00	0.93	0.73	0.73	1.00	0.93	1.00	0.87	1.00

Fig. 8. Average time and standard deviation in 6 month

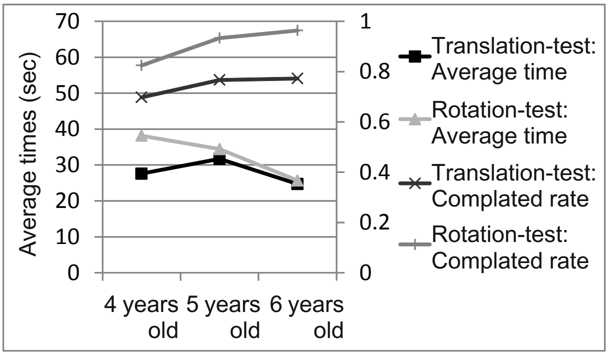

Fig. 9. Average time and rate of completion

provides evidence that shows the difference of children's development of operation ability in space. Moreover, the result provides evidence that children can recognize the virtual space.

Fig. 9 shows the average times and the rates of completion of all the examinees of the Translation-test and the Rotation-test in their age-group. The average times decrease with the rates of completion increasing with advancing age. However, the average time of 5-year-old children for the Translation-test is longer than for the 4-year-old children. Because the rates of completion increase from 5-year-old, the examinees of 5-year-old that could complete the tests with longer time increased. This result shows that we can measure development of operation ability in space using the system.

5 Correlation of the System and a IQ Test

5.1 Experiment Methods

In our experiment in August 2010 and August 2011, we used this system and the Japanese version of the WPSSI for the 14 children. The aim of this experiment was to validate the evidence that the system is an effective tool to measure a developmental stage of spatial expression ability.

The Japanese version of the WPPSI is an intelligence test designed for children ages 3 years 10 months to 7 years 1 months. The WPPSI provides subtests with 6 verbal tests and 5 performance tests. And it provides Verbal and Performance IQ scores, and a Full Scale IQ score. However, the WPPSI is not specialized in understanding the spatial expression ability. We conducted all 5 performance subtests of Animal House, Picture Completion, Mazes, Geometric Design, and Block Design.

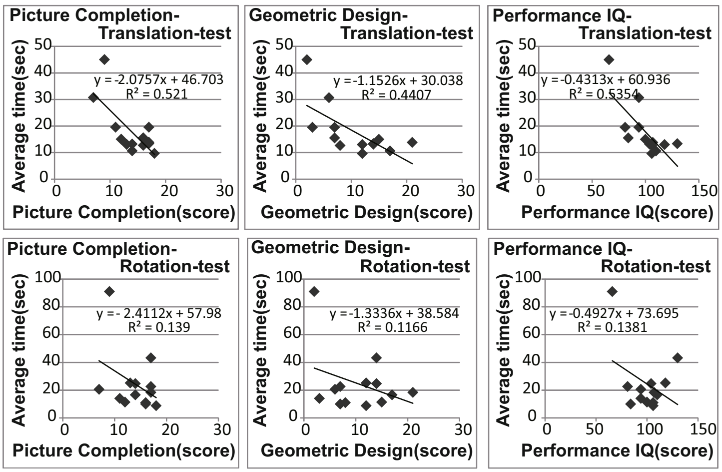

Fig. 10. Correlation between the system and WPPSI

5.2 Experimental Result

Fig.10 shows the examples of correlation between the required times of the system and the scores of the WPPSI. The upper graphs show correlations between average times of the Translation-test and the WPPSI, and the lower graphs show correlations between average times of the Rotation-test and the WPPSI.

In the Translation-test and the WPPSI, the average time increases with the score of WPPSI increasing. This result is the same in other all Translation-tests. By test of no correlation, Picture Completion and Geometric Design correlate significantly with the Translation-test (p¡.05). Moreover, the sum of raw score correlates significantly with the Translation-test. This result shows that children have an ability of systematizing a way to reach a goal in Mazes, or an ability of painting by comparing an original with their own picture in Geometric Design effect in virtual space. But, we found no correlation between the Rotation-test and the WPPSI. However, this result shows that the system can analyze abilities that are hard for the WPPSI to measure because the results of the Rotation-test improve with advancing age in section 4.2.

That is, the system obtained an equal result to the WPPSI for analyzing spatial expression ability. And the system can analyze spatial expression abilities that are hard to understand with the WPPSI.

6 Visualization of Expression Abilities of Relations

6.1 Experimental Method

Paper-lay-out-test is an experiment to test the ability to express the positional relation between two papers. Two illustrated papers are arranged in virtual 3-D space of the system in advance. In real space, the test examiner shows a relation to the child using the two illustrated papers. And in the virtual 3-D

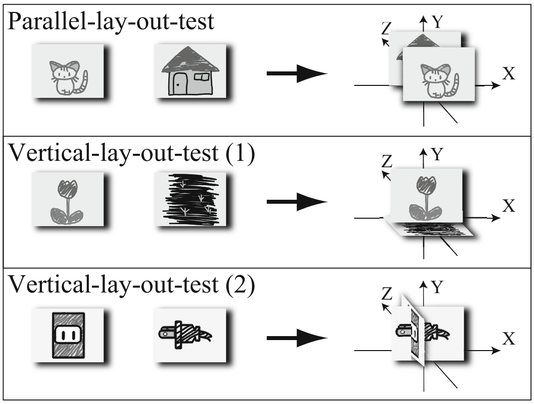

Fig. 11. Paper-lay-out-test

space of the system, the child will arrange the papers similar to the relation. The Paper-lay-out-test consists of Parallel-lay-out-test, Vertical-lay-out-test(1), and Vertical-lay-out-test(2) as in Fig.11. We added vertical-lay-out-test(2) from January 2010.

6.2 Experimental Result

Fig.12 shows the 9 typical expression patterns that we obtained from the examinees. Table 1 shows the frequencies of expression patterns of all examinees and the frequencies of examinees of the first experiment and the second experiment, the underlined data shows the correct expression pattern.

In the pattern 0, two papers are arranged at the same position, is highest frequency in all the tests except the Vertical-lay-out-test(2). This result is caused by a lack of understanding the experimental descriptions, a confusion of the Translation-test, or undeveloped spatial expression ability.

In the Parallel-lay-out-test, 8 examinees expressed the correct expression for the pattern 1. The rest of children expressed the pattern 2 or 5. We could not obtain significant differences between the first experiment and the second

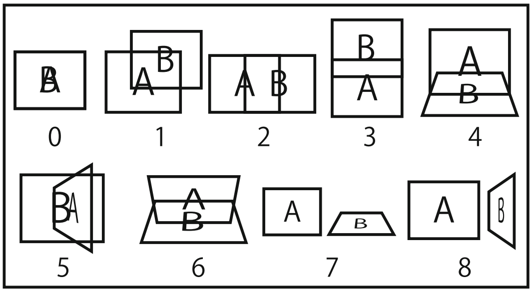

Fig. 12. Expression patterns

Table 1. Result of Paper-lay-out-test

		Parallel			**Vertical(1)**		**Vertical(2)**
patterns	*all*	*first*	*second*	*all*	*first*	*second*	*all*
0	36	10	8	24	6	4	14
1	**8**	**2**	**1**	9	4	1	1
2	5	2	2	1	0	0	5
3	1	0	1	3	0	2	0
4	0	0	0	**14**	**3**	**5**	0
5	7	1	3	2	0	2	**16**
6	1	0	0	2	1	1	0
7	2	0	0	3	1	0	0
8	1	0	0	1	0	0	1

experiment. This result is caused by the following reasons: it was hard for examinees to understand whether they should arrange the papers with opening a gap or arrange the papers to the same position such as the pattern 0; or undeveloped spatial expression abilities.

In the Vertical-lay-out-test(1), 14 examinees expressed the correct expression for the pattern 4. We see that the number of the pattern 4 increases, the number of the pattern 3 and 5 as nearly correct expression increases, the number of the pattern 0 and 1 decreasing in half a year. In the Vertical-lay-out-test(2), the highest number of 16 examinees expressed the correct expression for the pattern 5.

This result shows that we are able to obtain spatial expression in 3-D space, and the system obtained data showing childrenfs development of the expression abilities of relations with advancing age.

7 Conclusion

We prepared a 3-D expression system to understand the developmental stage of spatial expression ability, and conducted evaluation experiments using the system in a pre-school. The results are summarized as follows:

- Children are able to recognize virtual 3-D space of the system, and are able to express images in virtual 3-D space.
- The data shows the trend that spatial expression ability in space becomes better with advancing age.
- We obtained correlations between the system and WPPSI. The system can analyze some abilities that are difficult for WPPSI.

In future studies, we will continue to conduct experiments in a pre-school, and make an evaluation method to understand developmental stages of spatial expression ability from the acquired data.

References

1. Higashiyama, A.: Children's Space Recognition and It's Expression, vol. 83, pp. 71–81. Kobe University (1989)
2. Wechsler, D.: Wechsler Intelligence Scale for Children-III. Pearson (1991)
3. Takeuchi, Y.: Can Children Understand Aerial Photographs as Map-like Representations? Aichi University of Education 6, 43–48 (2003)
4. Ogawa, A.: Young Children's Spatial Perspective Taking Ability: The Relationship between Children's Understanding and Production of Drawings in Two Conditions, Kyoto University, vol. 52, pp. 412–426 (2006)
5. Wechsler, D.: Wechsler Preschool and Primary Scale of Intelligence. Pearson (1967)
6. Ito, K., Fukuda, T.: Wii Remote. Transactions of the Japan Society of Mechanical Engineers 110, 908–909 (2007)

Application of Flocking Algorithm to Attitude Control of Humanoid Robot

Sho Yamauchi, Hidenori Kawamura, and Keiji Suzuki

Hokkaido University
{sho-yamauchi,kawamura,suzuki}@complex.ist.hokudai.ac.jp

Abstract. Flocking algorithm of multi agent system is robust and disaster tolerant even though agents face obstacles or destructed. In this paper, we focus on applying these mechanism to single humanoid robot by assuming that the robot is the set of agents. We extend flocking algorithm to be capable of using in single robot and apply it to humanoid robot to maintain standing posture.

1 Introduction

In multi agent system, several distributed algorithms such as the work of Reynolds[1] are known to have agents flock. Systems using these techniques are robust and disaster tolerant even though some of them are destructed.These are known as swarm intelligence and there exists multi-agent robot system applied these techniques.

Also, hexapod robot OSCAR[2] is designed to be fault tolerant by applying boids algorithm.

However, for single robot there is no particular way to apply these techniques to generate homeostasis in robot. In this paper, we introduce the way to apply flocking algorithm for multi agent system to single humanoid robot for stabilizing its attitude.

We expect that these techniques make robot robust and be capable of dealing with unexpected situation.

We assume that each sensor and servo motor of humanoid robot is an agent of multi agent system to apply distributed algorithms.

2 Flocking Algorithm

Without theoretical framework, it is hard to extend algorithm so we adopt distributed flocking algorithm presented by Olfati Saber[3]. In his work, a theoretical framework for design and analysis of distributed flocking algorithms are proposed as follows.

Now we consider the agent set V. Let $q_i \in \mathbb{R}^m$ denote the position of agent i for all $i \in V$. Each agent has dynamics

$$\begin{cases} \dot{q}_i = p_i \\ \dot{p}_i = u_i \end{cases} \tag{1}$$

where $q_i, p_i, u_i \in \mathbb{R}^m$.

S. Lee et al. (Eds.): Intelligent Autonomous Systems 12, AISC 194, pp. 835–842.
springerlink.com

The set of neighbors of agent i is denoted by

$$N_i = \{i \in V : \|q_j - q_i\| < r\} \tag{2}$$

where $r > 0$ is the interaction range.

Agents are designed to maintain identical distance with other agents denoted as follows.

$$\|q_j - q_i\| = d, \forall j \in N_i(q) \tag{3}$$

Then, the input u_i for the agent i is determined

$$u_i = u_i^\alpha + u_i^\gamma \tag{4}$$

where u_i^α is a gradient-based and consensus term, u_i^γ is a navigational feedback.

By using σ-norm such as

$$\|z\|_\sigma = \frac{1}{\varepsilon}[\sqrt{1+\varepsilon\|z\|^2} - 1] \tag{5}$$

and bump function $\rho_h(z)$,

$$\rho_h(z) = \begin{cases} 1 & z \in [0,h) \\ \frac{1}{2}[1+\cos\pi\frac{(z-h)}{(1-h)}] & z \in [h,1] \\ 0 & otherwise \end{cases} \tag{6}$$

elements a_{ij} of adjacency matrix $A(q)$ is defined

$$a_{ij}(q) = \rho_h(\|q_j - q_i\|_\sigma / r_\alpha) \in [0,1], j \neq i \tag{7}$$

where $r_\alpha = \|r\|_\sigma$.

Also, gradient $\sigma_\varepsilon(z)$ is given by

$$\sigma_\varepsilon(z) = \frac{z}{\sqrt{1+\varepsilon\|z\|^2}} = \frac{z}{1+\varepsilon\|z\|_\sigma} \tag{8}$$

Then, define an action function $\phi_\alpha(z)$ as

$$\phi_\alpha(z) = \rho_h(z/r_\alpha)\phi(z - d_\alpha) \tag{9}$$

$$\phi(z) = \frac{1}{2}[(a+b)\sigma_1(z+c) + (a-b)] \tag{10}$$

where $d_\alpha = \|d\|_\sigma$.

Now define $\mathbf{n_{ij}}$ as

$$\mathbf{n_{ij}} = \sigma_\varepsilon(q_j - q_i) = \frac{q_j - q_i}{\sqrt{1+\varepsilon\|q_j - q_i\|^2}} \tag{11}$$

Then,

$$u_i{}^\alpha = \sum_{j\in N_i} \phi_\alpha(\|q_j - q_i\|_\sigma)\mathbf{n_{ij}} + \sum_{j \in N_i} a_{ij}(q)(p_j - p_i) \tag{12}$$

$$u_i{}^\gamma = -c_1(q_i - q_r) - c_2(p_i - p_r) \tag{13}$$

where q_r,p_r are the state of ideal agent.

3 Extended Flocking Algorithm

This algorithm is to have agents configure uniform lattice satisfies (3). However, to apply this algorithm to single humanoid robot,we extend this algorithm to be capable of configuring arbitrary lattice. We introduce the extended distributed flocking algorithm which can make any lattice. We consider a matrix D.This matrix D has elements given by the distance d in (3) among each agent. The distance between agent i and j is denoted as d_{ij}.Now we assume that there exists n agents.

$$D = \begin{bmatrix} d_{11} & d_{12} & \cdots & d_{1n} \\ d_{21} & \ddots & & \vdots \\ \vdots & & \ddots & \vdots \\ d_{n1} & \cdots & \cdots & d_{nn} \end{bmatrix} \tag{14}$$

where $d_{ii} = 0, (i = 1,2,...,n)$,$d_{ij} = d_{ji}, (i, j = 1,2,...,n)$.

Also, we assume that each agent has own destination. The destination means the ideal agent. It is allowed that some destinations are shared among some agents. Now we consider that s destinations exist. The distance among destinations are denoted by matrix R as

$$R = \begin{bmatrix} r_{11} & r_{12} & \cdots & r_{1s} \\ r_{21} & \ddots & & \vdots \\ \vdots & & \ddots & \vdots \\ r_{s1} & \cdots & \cdots & r_{s} \end{bmatrix} \tag{15}$$

where $r_{ii} = 0, r_{ij} = r_{ji}, (i, j = 0,1,...,s)$.

Then we define r in (2) for each agent. r_i, r for agent i which has destination k, is given by

$$r_i = \min\{r_{kj}, j = 1,2,...,s, (k \neq j)\} \tag{16}$$

Therefore, (2),(7),(9) are changed as follows.

$$N_i = \{i \in V : \|q_j - q_i\| < r_i\} \tag{17}$$

$$a_{ij}(q) = \rho_h(\|q_j - q_i\|_\sigma / r_{i\alpha}) \in [0,1], j \neq i \tag{18}$$

$$\phi_\alpha(z) = \rho_h(z/r_\alpha)\phi(z - d_{ij_\alpha}) \tag{19}$$

Also, if agent i has a destination k,(20) is given by

$$u_i^\gamma = -c_1(q_i - q_{rk}) - c_2(p_i - p_{rk}) \tag{20}$$

where q_{rk} and p_{rk} are the state of ideal agent which indicates destination k.

Fig.2 shows the example of flocking configured by this extended algorithm. In Fig.2, three circles indicate destination. Agents are represented as small triangle. The destination for each agent is the circle which is the same color. In this experiment, the distance d_{ij} is determined as

$$d_{ij} = \begin{cases} const & s_i = s_j \\ r_{ij} & s_i \neq s_j \end{cases} \tag{21}$$

where s_i is the destination of agent i and s_j is that of agent j.

Fig.2 shows the sequential results of the blue and red circle's move.

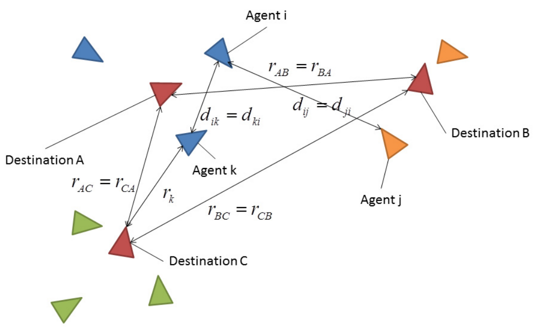

Fig. 1. The relationship among agents

4 1-Dimensional Flocking Algorithm and Probabilistic Fluctuation

To apply this algorithm to humanoid robot, we consider the state of agent as scalar. Each agent represents the value of angle of servo motor or specific sensor value. We also apply probabilistic fluctuation to agents in order to avoid stagnation. We consider a robot model which have constraints below,

1. There are 6 agents. Each agent represent a part of robot body.
2. Agent 4 is uncontrollable. The state of this agent is determined by the equation

$$q_4 = p_3 - 0.3p_5 + 0.01u_{random} \tag{22}$$

   where $u_{random} \in (-0.5, 0.5)$. this value is given randomly from this range.
3. The task of agents is to reduce error value of Agent 4 from Agent 4's destination. Agents destinations are $\{0, 0.2, 0.4, 0.6, 0.8, 1.0\}$ respectively. Error value ε is given by

$$\varepsilon = \sqrt{(q_4 - q_{r4})^2} \tag{23}$$

4. Agent 4 represents a sensor of robot and input value has model of environment.

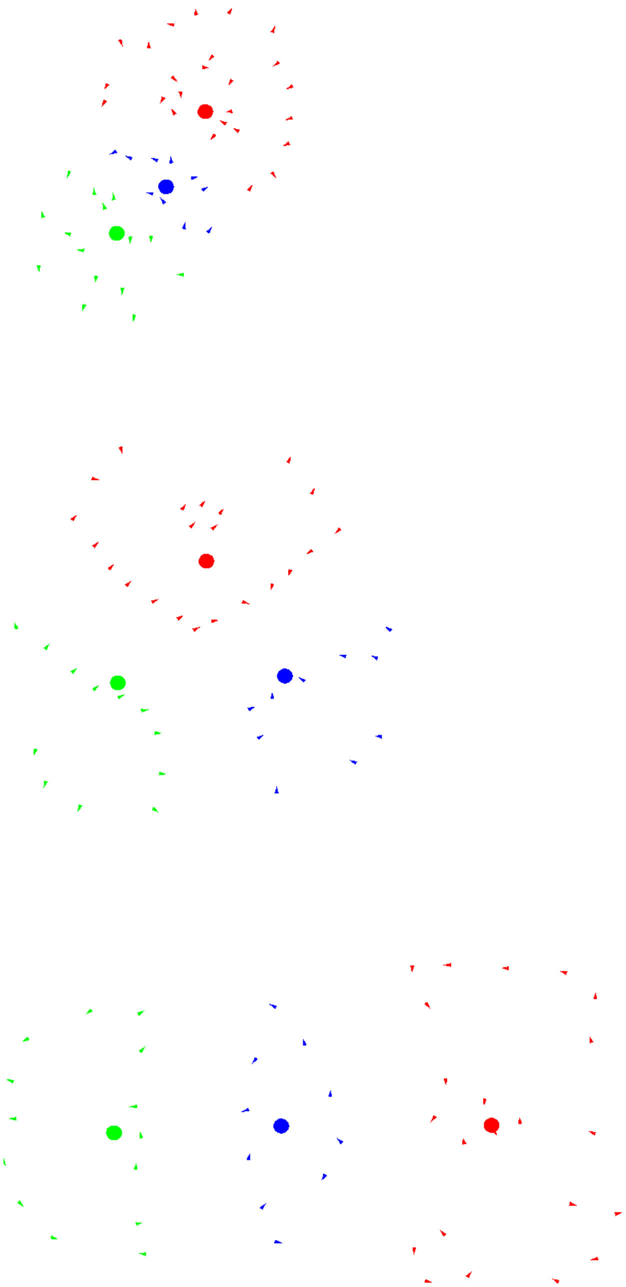

Fig. 2. 2 dimensional flocking experiment

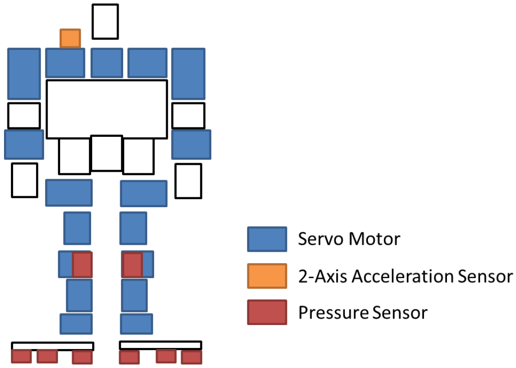

Fig. 3. Servos and Sensors of KHR-3HV

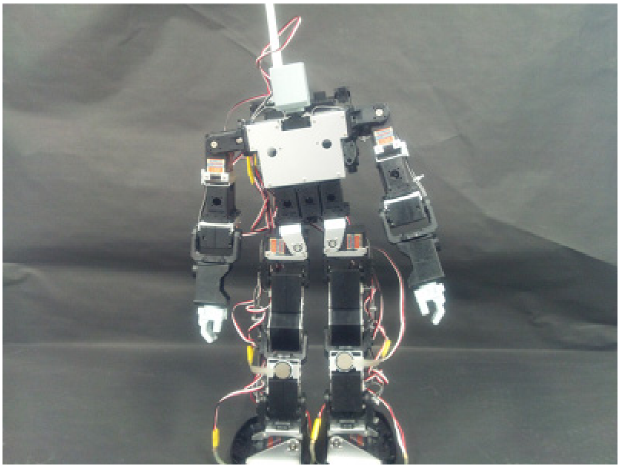

Fig. 4. KHR-3HV

In this situation, without any changes, agents except agent 4 are bound for their destination and wouldn't move to adjust agent 4's state. To deal with this problem, we introduce probabilistic fluctuation term to input value u_i. Now we change (4) as

$$u_i = u_i^{\alpha} + u_i^{\gamma} + u_i^{prob} \tag{24}$$

$$u_i^{prob} = 0.01\varepsilon v_{random} \tag{25}$$

where $v_{random} \in (-0.5, 0.5)$.

We experimented in this situation. Each trial consists of 10000 steps. Table 1 shows that the average ε value of 10000 trial of both with probabilistic fluctuation term and without it.

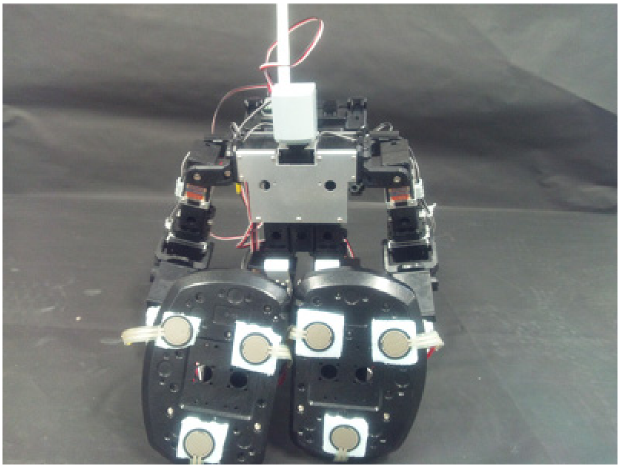

Fig. 5. FSR402 Sensors

Table 1. Experimental results of Average ε values

	Average ε value
With fluctuation term	295.61
Without fluctuation term	354.77

This result indicates that agent's movement caused by the probabilistic fluctuation term reduce the error value of Agent 4, sensor agent. This mechanism is useful to adjust sensor values by moving servo motors of single humanoid robot in environment which has unknown model.

5 Applying Algorithm to Humanoid Robot

We apply this algorithm to single humanoid robot. In this experiment, we use humanoid robot, Kondo KHR-3HV. This robot has 10 sensors. 8 sensors are force sensing resistor FSR402 as pressure sensor. Other 2 sensors are acceleration sensors. Also this consists of 17 servo motors.

We consider each servo and sensor to be an agent which have scalar state value. Servo agents have angle value, and sensors have own specific value. We give the humanoid robot the task to maintain standing posture. Before the experiment, we have to make robot stand and record its specific value of each agent. These ideal values of standing posture is the destinations for each agent. Through experiment, we succeeded in having robot maintain standing posture by applying flocking algorithm.

Fig.6 shows the result of this experiment. In Fig.6, x-axis and y-axis shows time steps and ε values respectively. When this experiment start, posture of this humanoid robot is ideal, so ε value is almost zero. However, small move causes great increase of ε value (step 0-10). After that, we can see the decrease and suppression of ε value.

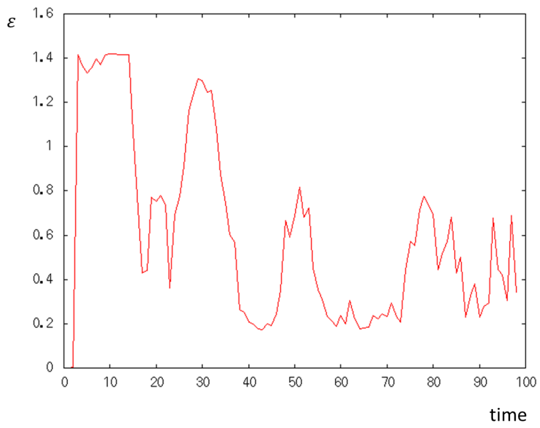

Fig. 6. Result of ε value

6 Conclusion

We extended flocking algorithm to be capable of making arbitrary lattice of agents. Also we introduced probabilistic fluctuation term to the algorithm to adjust sensor values by moving servo motors. And we applied these algorithm to single humanoid robot to have maintain standing posture.

References

1. Reynolds, C.W.: Flocks, herds, and schools: a distributed behavioral model. In: Computer Graphics (ACM SIGGRAPH 1987 Conference Proceedings), vol. 21(4), pp. 25–34 (July 1987)
2. Jakimovski, B., Meyer, B., Maehle, E.: Self-reconfiguring hexapod robot OSCAR using organically inspired approaches and innovative robot leg amputation mechanism. In: International Conference on Automation, Robotics and Control Systems, ARCS 2009, USA, July 13-16 (2009)
3. Olfati Saber, R.: Flocking for multi-agent dynamic systems: Algorithms and theory. IEEE Transactions on Automatic Control 51(3), 401–420 (2006)

Velocity Correlation in Swarm Robtos with Directional Neighborhood

Keitaro Naruse

School of Computer Science and Engineering, University of Aizu
Tsuruga, Ikki-machi, Aizu-Wakamatsu 965-8580, Japan
naruse@u-aizu.ac.jp

Abstract. Most of robotic systems introduce a directionless neighborhood area, such as a circle or sphere, for robot communication and interaction because it reflects a natural property of some physical sensors and devices. On the other hand, it has reported that some of natural birds employ directional neighborhood for neighbor observation. In this paper, we introduce the directional neighbor to a robotic swarm system, and we investigate how it affects to the connectivity and stability of the system.

Keywords: flocking, directional neighborhood, velocity correlation.

1 Introduction

The objective of this paper is to investigate the effect of directional neighborhoods in flocking in swarms. In the conventional flocking algorithms, a shape of neighborhoods of agents or robots is not considered significantly. For example, most of multiple agent systems introduce a circular neighborhood for the neighborhoods, because it is the simplest shape and it reflects a neighborhood of physical devices such as omnidirectional cameras and radio communication devices.

However, recent research activities have shown that starling birds seem to observe other ones topologically, not by a metric distance [1]. They shoot a video of a flock of the starling birds, reconstruct a 3D model of the flock, and generated a 3D position and velocity of the birds. The results show that the birds are not placed isotropic: The placement of the nearest neighborhood birds changed by a heading angle, such that more birds are distributed in left and right sides but less ones are found in front and back sides. Furthermore, it has reported that behavioral correlations in the swarm are scale free: The motion change of a single bird affects to and is affected by that of all other birds in the swarm, no matter how large the swarm is. The scale-free correlations provide each bird with an effective perception range much larger than the direct inter-individual interaction range, thus enhancing global response to perturbations. The results suggest that flocks behave as critical systems, poised to respond maximally to environmental perturbations [2].

From those evidences, it can have an advantage if we introduce a directional neighborhood to a robotic swarm system, particularly when we have a very large number of robots such as thousands of them.

S. Lee et al. (Eds.): Intelligent Autonomous Systems 12, AISC 194, pp. 843–851.
springerlink.com

On the other hand, if we introduce it, a flock can be fragile, which means easy to be fragmented, because a neighborhood shape is affected sensitively by a heading angle. Therefore, it is important to know how much the robotic swarm is maintained and fragmented if we introduce the directional neighborhood.

At this point, let us review briefly about flocking. In the field of the swarm robotics [3], the formation and the stability of a swarm are of the central issues. The first research on an artificial swarm is called Boid model proposed by Reynolds in 1987 [4]. Each of the robots can know the relative speed and position of neighboring robots and decides its motion using them. Reynolds showed that a natural looking swarm can be emerged only by the three simple local interaction rules of separation, cohesion, and alignment. However, Boid model is a rule based system and the mathematical properties such as the stability of the swarm were not discussed.

Olfati-saber gave a mathematical framework to the swarm formation [5]. He formalized the motion of the robots as a dynamical system of particles, and showed several stability theorem of a swarm. For example, he proved that a swarm made by Boid model is easy to be fragmented, and that a swarm is stable if all of the robots know a destination. Su et al. investigated the relation between the swarm stability and the number of robots which knows the destination [6]. They showed numerically that a small number of the robots can navigate a swarm to the destination. Furthermore, many models based on the local interaction are proposed [7] [8].

All the above models assume an isotropic neighbor or abstract neighbor model, in which they have not considered a specific shape of neighborhoods.

In this paper, we develop the dynamical system for the directional neighborhood, and show how it affects to the flocking. More concretely, we introduce an angle affected norm to the distance measurement in the dynamical system, and develop a linear system for the flocking. Then we investigate the velocity correlation among agents. The numerical experiments show that a different velocity correlation patterns are found in flocking of the directional neighborhood from the conventional undirectional one, which can give us a new notion of flocking.

The outline of the paper is organized as follows: Section 2 presents the directional neighborhood and the dynamics of flocking. We show numerical experiments of the proposed model in Section 3. Conclusion is given in Section 4.

2 Directional Neighborhood and Flocking

In the proposed swarm model, each of the robots is assumed to communicate with other robots in a directional neighborhood area as shown in Fig.1, in which a shape of the neighborhood area is a bow tie shape, spreading widely in left and right sides. If the other robots are in the area, they are regarded as neighborhood robots. As shown in Fig. 2, the configuration of the robot is a position of x and y, and a heading angle of θ. Since the neighborhood area is angle sensitive, the neighborhood network becomes an asymmetric one. For example, in Fig. 2, the robot r_1 observes r_2 and r_3, but r_2 cannot observe r_1.

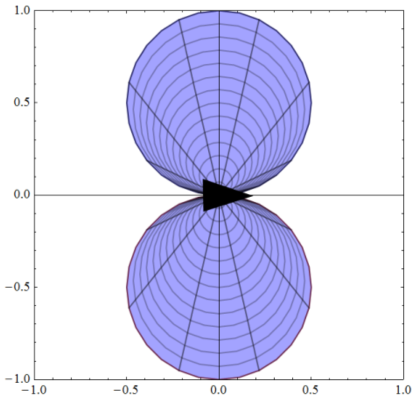

Fig. 1. Directional neighborhood area

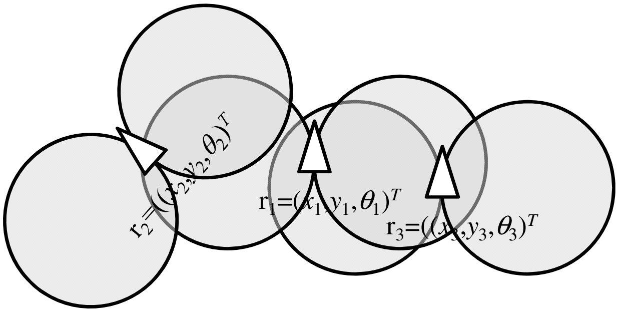

Fig. 2. Robots and directional neighborhood area. The neighborhood relations form an asymmetric observation graph.

Then, let us define the anisotropic neighbor as

$$nb\left(\mathbf{p} = (x, y, \theta)^T\right) = \sqrt{x^2 + y^2}\cos(k\theta + \phi). \tag{1}$$

In the following, we use k=1 and $\phi=\pi/2$, which make the neighbor as in Fig. 2. If we introduce k=0 and $\phi=\pi/2$, it becomes a circular neighborhood. Therefore, the above anisotropic neighbor can be considered as a generalized neighborhood function.

Next, let us represent a set of neighboring robots of a robot i as N_i. If a robot i

$$N_i = \{\, j \mid nb(\mathbf{p}_j - \mathbf{p}_i) < r \},\tag{2}$$

where $\mathbf{p}_i$ and $\mathbf{p}_j$ is a position vector of a robot i and j, respectively.

We represent motion of the robots by an attractive and repulsive force of each pair of the robots, and the force interaction is limited in the neighborhood range. Therefore, if a robot is out of the range of all the other robots, it is isolated, and it cannot be controlled by the target anymore. We call the situation as fragmentation, and we consider a swarm is stable if the fragmentation is never occurred. The basic idea of flocking is shown in Fig. 3. Each of the robots generates a translational and rotational acceleration so that it remains in a fixed distance *d*, aligns a heading angle, then coincides a translational and rotational velocity to other robots in neighborhood.

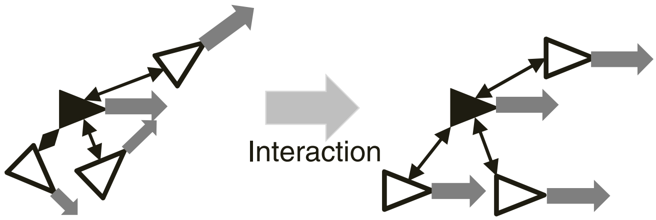

Fig. 3. Flocking force. Each of the robots generates a force so as maintaining a fixed distance d, aligning a heading angle, and coinciding a translational and rotational velocity.

Now, let us represent the dynamics of a robot *i*. In this paper, all of the robots are assumed to be a point mass and the motion of the robots is represented by a force.

$$\mathbf{p}_i(t) = (x_i(t), y_i(t), \theta_i(t))^T, \tag{3}$$

$$\begin{cases} \dot{\mathbf{p}}_i(t) = \mathbf{v}_i(t), \\ \dot{\mathbf{v}}_i(t) = \mathbf{u}_i(t), \end{cases} \tag{4}$$

where $\boldsymbol{p}_{\mathrm{i}}$, $\boldsymbol{v}_{\mathrm{i}}$, and $\boldsymbol{u}_{\mathrm{i}}$ is the position or configuration, velocity, and acceleration as a control input of *i*-th robot, respectively.

Then, let us represent the acceleration for flocking. We introduce a potential force on the distance so that we can represent the robot motion of keeping a distance d to the others. Furthermore, we introduce a consensus force on the velocity for the equal velocity to the others.

$$\mathbf{u}_i(t) = \sum_{j \in N_i} \mathbf{u}_{ij}^p(t) + \sum_{j \in N_i} \mathbf{u}_{ij}^v(t), \tag{5}$$

$$\mathbf{u}_{ij}^p(t) = \left(\left(k_p^t \left\| \mathbf{p}_j - \mathbf{p}_i \right\| - d\right) \frac{\mathbf{p}_j - \mathbf{p}_i}{\left\| \mathbf{p}_j - \mathbf{p}_i \right\|}, k_p^r (\theta_j - \theta_i) \right), \tag{6}$$

$$\mathbf{u}_{ij}^v(t) = \left(k_v^t (\dot{\mathbf{v}}_j - \dot{\mathbf{v}}_i), k_v^r (\dot{\theta}_j - \dot{\theta}_i)\right), \tag{7}$$

where *k* related terms represent a control gain, in which the subscripts *p* and *v* shows a position and velocity, respectively, and the superscripts *t* and *r* do a translational and rotational motion, respectively. Eq (6) expresses position related acceleration such as an attraction and repulsion, while Eq (7) does velocity matching one. By summing those two accelerations, flocking can be done.

3 Numerical Experiments on Flocking

First, let us see the very simple instance of flocking by two robots. Figure 4 shows a sequence of snapshots of the two robots, moving from left to right. They are placed in a stable distance with a same orientation and a same translational velocity, but they have different rotational speed in an initial condition. Then, they move to left, rotating counter clockwise direction. During the motion, a relative distance between the two robots is almost same, but a neighborhood is changing: They observe each other in earlier time period, but they go out of the neighborhood in later time period.

The above instance shows a typical phenomenon of the directional neighborhood: Even if they are stayed in a close area, they may not observe each other. The neighborhood graph can be changed easily just by changing an orientation of robots a little amount. On the other hand, if we apply directionless neighborhood such as a simple circle, the above phenomenon never occurs, because a distance between robots is related to the neighborhood area directly, once a robot goes out of a neighborhood area of other robots, there is no chance to come back to it.

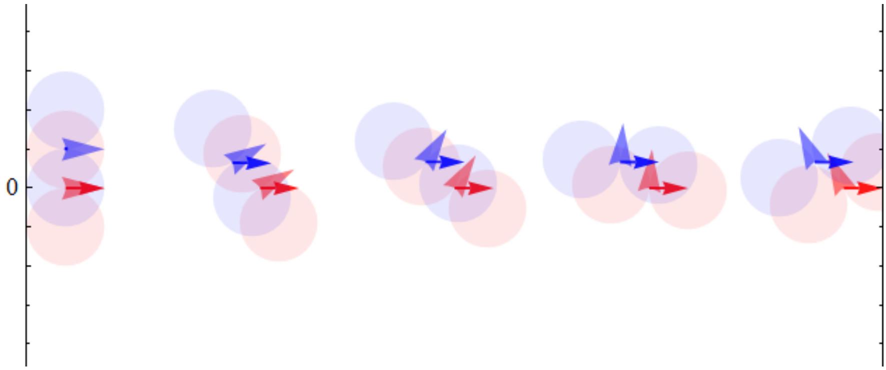

Fig. 4. Flocking force. Each of the robots generates a force so as maintaining a fixed distance *d*, aligning a heading angle, and coinciding a translational and rotational velocity.

The, let us investigate with a larger number of robots of a hundred, comparing the directional neighborhood robots with the directionless ones. Figure 5 shows a sequence of snapshots of a hundred of robots by the directional neighborhood with one second intervals. Each of the dots represents a robot, and the dot with a circle shows a reference robot, which moves with a fixed constant velocity, but all the other robots are influenced by the reference robot if it is in a neighborhood area. The reference robot is introduced for giving a fixed point to a swarm for measurement, because a swarm always changes positions and velocities, and it is difficult to analyze in a static frame. In this case, the reference robot moves left to right, horizontally. Similarly, Fig. 6 shows a sequence of snapshots of a same number of robots with the directionless neighborhood. Same control parameters and initial conditions are given to both of the cases.

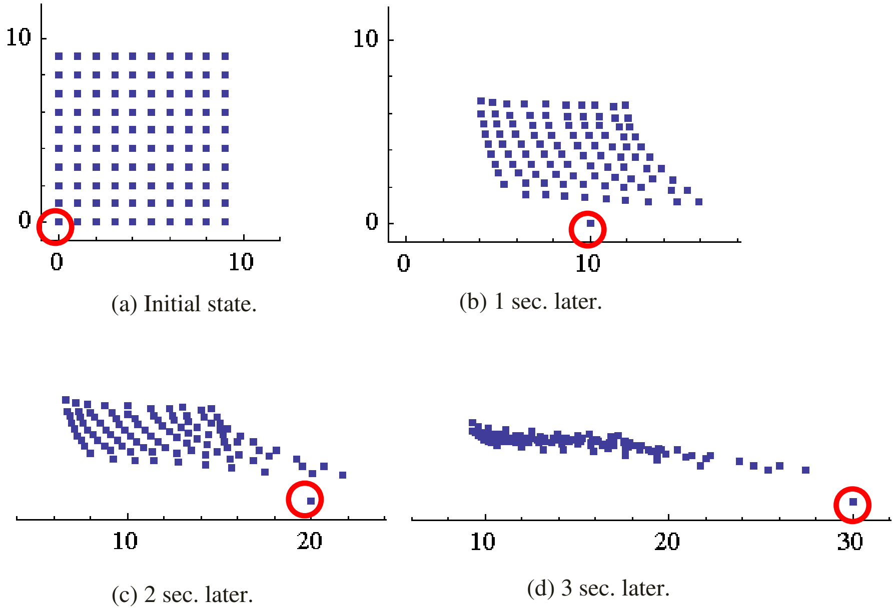

Fig. 5. Swarm of directional neighborhood robots

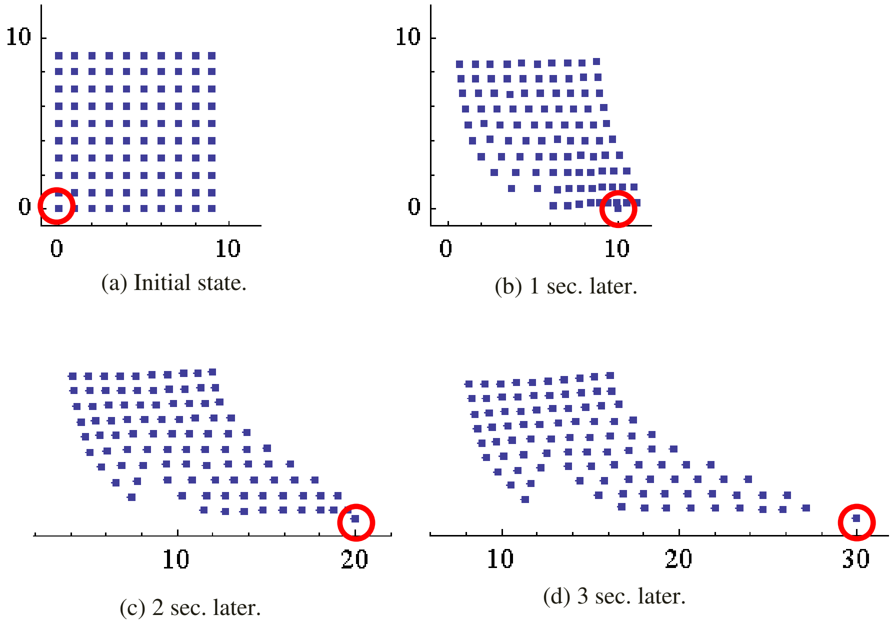

Fig. 6. Swarm of un-directional neighborhood robots

Observing Fig. 5, a swarm of the directional neighborhood changes itself largely to a longer and narrower shape. On the other hand, in a swarm of the directionless neighborhood case, most of the robots far from the reference robot stay in almost same position as in initial ones, and only some of the robots close to the reference robot change their position. Therefore, a part of the swarm changes its shape. Just glancing the two figures, the directional neighborhood robots give us an impression more similar to a natural swarm.

Then, let us see inside the swarm. Figure 7 is a velocity correlation to the reference robot for a distance from it with a time interval of one second in the case of the directional neighborhood robots. And Fig. 8 shows a same one for the directionless neighborhood robots case.

Figure 7(a) and 8(a) shows an initial state, in which velocity of all of the robots are initialized with random values, a correlation value of all of the robots are distributed around zero values.

In the case of the directionless neighborhood robots, shown in Fig. 8, as times goes, robots near the reference robot interact with it, and their velocity becomes close to it due to the mechanism of flocking, yielding a velocity correlation close to one in a short distance to the reference robot. On the other hand, robots far from the reference

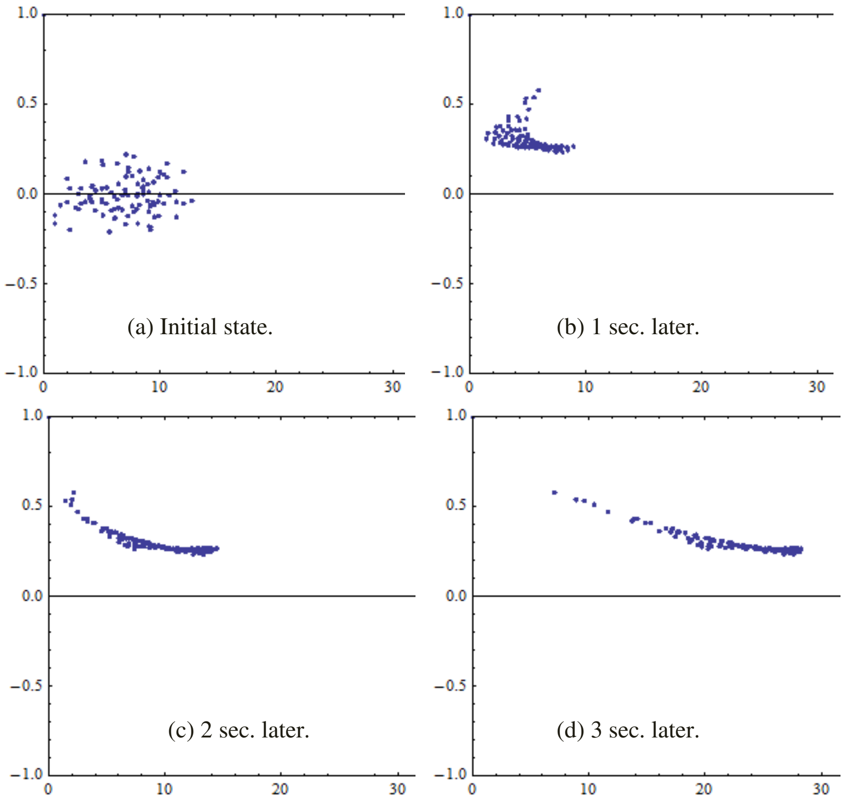

Fig. 7. Velocity correlation of directional neighborhood robots

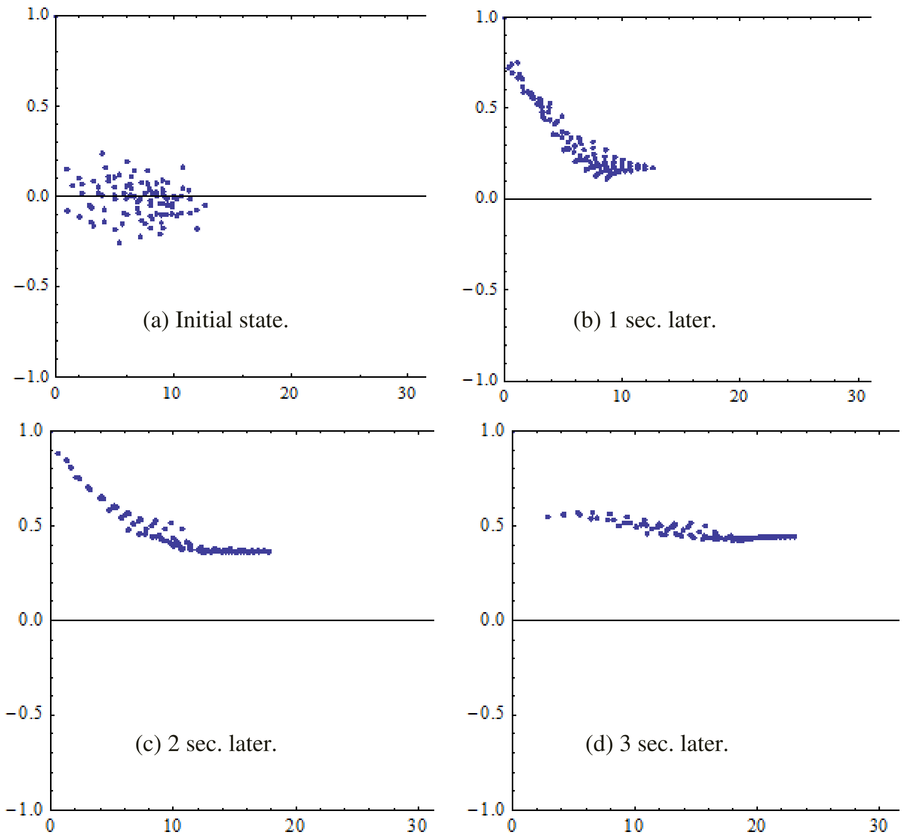

Fig. 8. Velocity correlation of un-directional neighborhood robots

robot have no opportunity to interact with it directly, and a velocity correlation gets close to zero in a long distance to the reference. Therefore, the relation between the distance to the reference robot and the velocity correlation to it shows a gradual decrease from one to zero, which is shown in Fig. 8(b) and (c). If time passes furthermore, the reference robot moves away from the swarm, the swarm has no direct interaction with it. Eventually, the velocity correlation to the reference robot stays in a certain value, not changing by a distance to it, which is shown in Fig. 8(d).

Then, in the case of the directional neighborhood robots, they show almost same changes in later stages such as in Fig, 7(c) and (d). However, in a transient stage of Fig. 7(b), it shows an interesting velocity correlation, in which there exist two robot groups with a different velocity correlation even they are located at a same distance to the reference robot. In other words, the swarm involves a large velocity fluctuation between robots, which can be observed in an natural flock [1]. We conclude that naturally looking flocking can be emerged from the directional neighborhood robots.

4 Conclusion

In this paper, we developed the dynamical system for the swarm robotic system with the directional neighborhood. We showed that the directional neighborhood can make more naturally looking flocking than the directionless neighborhood robots.

The proposed directional neighborhood robots show interesting characteristic when giving a perturbation to a stable or static swarm, which can be some basis for developing a faster converging flocking.

References

1. Ballerini, M., et al.: Interaction ruling animal collective behavior depends on topological rather than metric distance: Evidence from a field study. PNAS 105(4), 1232–1237 (2008)
2. Cavagnaa, A., et al.: Scale-free correlations in starling flocks. PNAS 107(26), 11865–11870 (2010)
3. Ren, W., Beard, R.W., Atkins, E.M.: A Survey of Consensus Problems in Multi-agent Coordination. In: Proceedings of the 2005 in American Control Conference, vol. 3, pp. 1859–1864 (2005)
4. Reynolds, C.W.: Flocks, herds, and schools: A distributed behavioral model, Proceedings of Computer Graphics. ACM SIGGRAPH 1987 Conference 21(4), 25–34 (1987)
5. Olfati-Saber, R.: Flocking for multi-agent dynamic systems: Algorithms and theory. IEEE Transactions on Automatic Control 51(3), 401–420 (2006)
6. Su, H., Wang, X., Lin, Z.: Flocking of Multi-Agents With a Virtual Leader. IEEE Transactions on Automatic Control 54(2) (2009)
7. Kurabayashi, D., Osagawa, K.: Formation Transition based on Geometrical Features for Multiple Autonomous Mobile Robots. Journal of the Robotics Society of Japan 23(3), 376–382 (2005)
8. Tanner, H.G., Jadbabaie, A., Pappas, G.J.: Stable flocking of mobile agents, part I: Fixed topology. In: Proceedings of 42nd IEEE Conference on Decision and Control, pp. 2010–2015 (2003)

Feedback Control of Traffic Signal Network of Less Traffic Sensors by Help of Machine Learning

Takumi Wakahara[1] and Sadayoshi Mikami[2]

[1] Graduate School of System Information Science, Future University Hakodate
Hakodate, Japan
g3107007@fun.ac.jp

[2] Depertment of Complex and Intelligent Systems, FutureUniversity Hakodate
Hakodate, Japan
s_mikami@fun.ac.jp

Abstract. As a way of resolving vehicle congestion, there is a feedback control approach which models a traffic network as a discrete dynamical system and derives feedback gain for controlling green light times of each junction. Since the input is the sensory observed traffic flow of each link, and since the state equation models both the topology and the parameters of the network, it is effective for adaptive control of a wide area traffic in real-time. One of the essential factors in a state equation is the vehicles' turning ratio at each junction. However, in a normal traffic sensor layout, it is impossible to directly measure this value in real-time, and values from traffic census are used. This paper is to propose a method that predicts this value in real-time through machine learning and gives more appropriate feedback control. Out idea is to find the turning ratio through probabilistic search by Reinforcement Learning referring to the degree of improvement of the entire traffic flow. At this moment we have finished formulation of the scheme and the verification for the performance by a traffic simulator is on the way.

Keywords: Reinforcement Learning, Traffic light Control, Feedback Control, Discrete Dynamical System, Split.

1 Introduction

It is desired for modern urban transport to control traffic lights in a wide area in real-time according to sensory observed parameters such as traffic flows and queue lengths [3]-[5]. However, the number and the variations of traffic sensors are usually very limited in an urban road network, and it is also difficult to put many new sensors in a network by the reasons of cost and construction problems etc.

Our approach is to apply Machine Learning to estimate values of current traffic properties that are important but are not being able to measure by current sensor layouts. The approach is linked with a feedback based traffic network control [1][2].

From the next chapter, firstly we describe the background of the current traffic light control methods and why we focus on the feedback approaches. Secondly, we

S. Lee et al. (Eds.): Intelligent Autonomous Systems 12, AISC 194, pp. 853–861.
springerlink.com

describe the formulation of the feedback based traffic control method which we rely on. Finally, we show the scheme of the Reinforcement Learning based approach to estimate the missing traffic properties and improve the entire traffic flow based on a current traffic flow measurements.

2 Traffic Lights Control for Urban Traffic Network

The traffic control problem is highly complex. There are many reasons for this complexity such as: (1) Controllable factors, such as split, cycle, and offset, are limited and influence multiple roads at a time; (2) Dynamics is complex. One junction's traffic is affected by the traffic of many other areas, and delay time is large; (3) Immeasurable human factors exist. Driver's hidden intention affects the flow. But this is not measured in advance; (4) Sensors are costly and limited. A vehicle detector is usually used. But it measures only current flow at a pinpoint location.

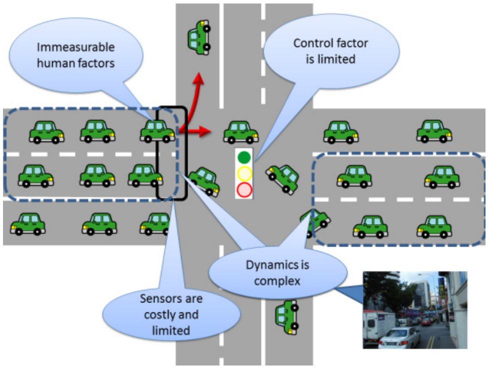

Fig. 1. Reasons of traffic light control problem complexity

One of the key points to deal with these is to realize adaptive light control. SCOOT [3], SCATS [4], and MODERATO [5] systems are well known. These are based on an idea of measuring a degree of traffic flow passing through a junction and controlling light parameters accordingly. Although these are effective and practically used in many cities, some parameters are relying on human design. More importantly, coordinated adaptive controls between multiple traffic lights are not considered. Only considered is an offset, which is a time shift of light phases between two adjacent junctions. But major control factors such as split (green time ratio) and cycle time (one cycle of traffic lights for a junction) are not well considered.

Recently, some approaches from control theory sides are taking attention [1][2]. Applying the notion of optimization and stability gives rigid control. Also the approach provides control scheme over multiple junctions.

The method is based on a "store and forward" method [9], which models traffic network as a discrete time dynamical system in terms of inflow and outflow. Characteristics of traffic flow at each junction are represented by some factors such as a rate of cars turning to each direction. By formulating the traffic as a discrete dynamical system, the approach applies feedback control to control split by the flow rate of each road. In the papers [1] [2], they derive feedback control gain directly by using optimal control methods such as the LQ optimization methodology.

This approach is both theoretically and practically useful and is used in some cities. But there are still some parameters that human should carefully predetermine.

One of the biggest parameters that are essential for modeling but is difficult to measure is a turning ratio. This is the rate of cars that turns to each direction, and thus contains human factors, which is not able to measure by sensors. Since the rate describes the key structure of a junction, its accuracy affects the feedback performance.

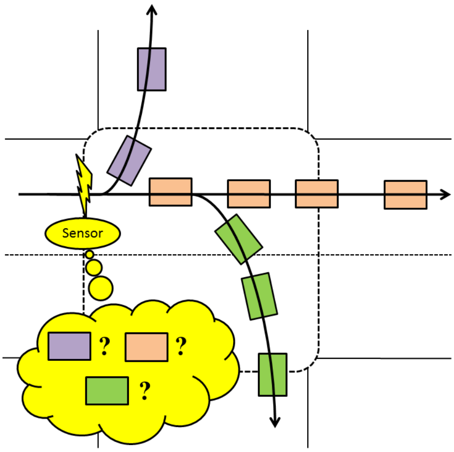

Fig. 2. Situations where turning rate is not measured by vehicle sensors

However, this factor is difficult to monitor in real time. One reason is that, as in Fig.2., a traffic sensors allocated at the inward of the junction cannot separate either the coming car is from left or right. Another is that, although a sensor is allocated at a turning lane, the lane is often used both right turn and straight traffic, and cannot derive pure right turning traffic. Also in a near saturated situation, where queue is reaching to the next junction, potential demand for turning is not measured because of the blockage, and model parameters are wrongly estimated.

This paper aims at providing a machine learning approach to estimate turning ratio from observation of traffic flow, by which traffic lights control that properly reflects the current situation will be realized.

Because exact turning ratio is not measurable in real-time, any methods that needs training data are not applicable. However, it is said that the traffic flow will be improved if the feedback controller uses more exact model, that is, more exact turning ratio values. It results in a combinatorial search for a set of turning ratios that will improve the traffic flow, and this is done by Reinforcement Learning (RL) [6].

In this paper, the notion of feedback control of traffic lights by discrete dynamical systems modeling is first introduced, and the design of learning systems to predict the parameters of the model is described in detail.

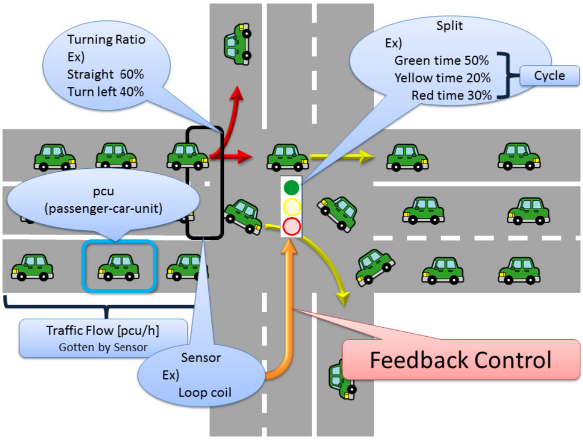

Fig. 3. Road network configuration

3 Traffic Model

3.1 Road Network Configuration [1]

A condition of traffic in a lane is described by a *traffic flow* [pcu/h], where pcu is a passenger-car-unit which is intended to count the number of cars in terms of standard car size. For example, a bus would be counted as 2 or 3 pcu. A maximum flow rate that is able to pass through a road (lane) is called a saturated flow [pcu/h].

Traffic network is represented as a directed graph. Fig.4. shows an example of simple two-junctions-one-way configuration. Each road is described as a link L_i with it traffic flow l_i. At a junction, link L_i is connected to the other links $\{L_n | n \in O_i\}$ where O_i is a set of indexes of outgoing links. Also $\{L_m | m \in I_i\}$ are a set of links from incoming direction and I_i is its indexes. Each car arriving at a junction will go to the next link at a certain probability. We call it as a turning ratio t_{ij}, which denotes a rate of flow from link *i* to *j*. denotes a saturated flow for the link *i*.

Traffic lights at a junction controls flow from one link to the other. A type of traffic light is called a *phase*. For major 4 roads junction there are usually 4 phases: allowing all forwarding traffic (phase 1 and 3), and right turn and straight through only (2 and 4), where phases 1 and 2 are for horizontal traffic in Fig.4. These phases rotate cyclically, and the duration is called a cycle time. A ratio of green light for phase i at junction m is called a split g_mi. Difference of cycle start time between two adjacent intersections is called an offset. It plays a role to allow vehicles departing from one junction not to be stopped by another junction.

3.2 Discrete Dynamical Systems Model of Traffic Flow [1][2]

Assume that all the lights in consideration are controlled by the same cycle time *T*, and that the offset is set to zero. Traffic flow for a link *i* is formulated by the difference of incoming flow and outgoing flow, which is written as:

$$l_i(k+1) = l_i(k) + q_i(k) - r_i(k) \tag{1}$$

Where $q_i(k)$ is an inflow and $r_i(k)$ is an outflow, and k denotes that the values are at k-th cycle. Outflow is affected by traffic lights. In a near saturated situation, the outflow $r_i(k)$ is proportional to the cumulative green times of the lights that controls outward traffic of the link i. Therefore, the outflow is described as $r_i(k) = s_i \sum_{j \in O_i} g_{nj}$. Note that sideways without traffic light control are omitted.

Inflow is also affected by green time of the traffic lights located at an incoming junction. For each link $\{L_m | m \in I_i\}$, traffic flow going to the link i is proportional to the turning ratio from m to i. By considering the green time for the flow from m to i, the inflow $q_i(k)$ is described as:

$$q_i(k) = \sum_{j \in I_i} s_j t_{ji} g_{j v_{ji}^m} \tag{2}$$

where v_{ji}^m gives a phase number for the junction m that affects flow from the link j to i.

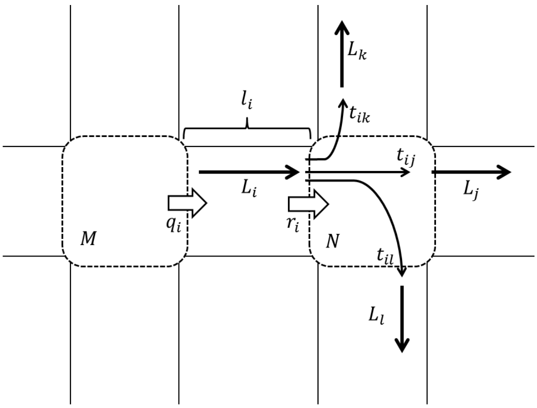

Fig. 4. Description of a traffic network

4 Feedback Control of Traffic Lights

The above linear discrete dynamical system of traffic flow allows the application of feedback control of the traffic lights. To begin with, the targeting traffic flow should be specified. We assume that the traffic flow l_i will be balanced under a steady traffic demand by an appropriate traffic light control. We denote this equilibrium flow as l_i^N. The nominal green time g_i^N should also be assumed. By describing $x_i(k) = l_i(k) - l_i^N$ and $u_{ij}(k) = g_{ij}(k) - g_{ij}^N$, a state equation for traffic is derived as:

$$x(k+1) = x(k) + Bu(k) \tag{3}$$

where x, u are the vector representations of x_i, u_{ji} and B is a matrix which includes traffic network configuration factors such as saturated flow and turning ratio.

For this state equation, the LQ-optimal control problem is able to be applied, which derives the feedback gain K for the following feedback scheme [1]:

$$g(k) = -Kx(k) \tag{4}$$

This is also used as a feedback scheme without explicitly using the nominal green time g^N and the flow l^N such that:

$$g(k) = g(k-1) - K\big(l(k) - l(k-1)\big) \tag{5}$$

By this, a split for a phase of a junction is modified in real time according to the current flow of the links in a network.

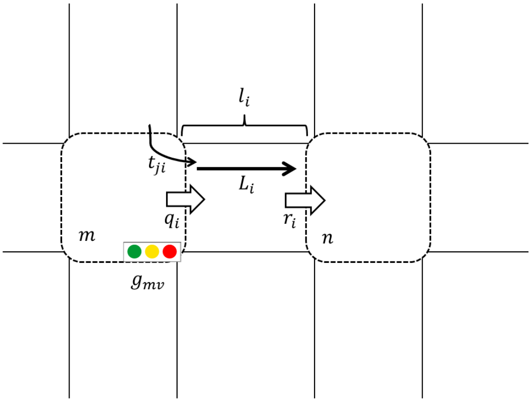

Fig. 5. Description of inflow

5 Learning to Estimate Turning Ratio

5.1 Application of Unsupervised Learning

The feedback gain K depends mainly on the saturated traffic flows, road network configuration, and the turning ratios. The former two factors do not change in a short period. But the turning ratios are the most changeable factors and it is necessary to know its latest value in real time. As described in section 1 and Fig.2, the turning ratio is usually difficult to measure, and the values which are collected by such as traffic survey are often used. Our idea is to estimate the value through observations by using machine learning method.

Since the true values for the turning ratio are not known, it is not possible to apply supervised learning methods. Instead, it is expected that the total traffic flow will be improved if the feedback controller uses more exact model parameters. This means that we can use an unsupervised learning method that searches for a set of turning ratios that will improve the traffic flow.

5.2 Design of the Learning System

To this end, we employ a Reinforcement Learning (RL) method [6]. The design of the learner is as follows:

1) State Space

Appropriate state space design is important for both the time to the convergence and the specificity of the acquired knowledge. Urban transportation is a daily event and the profile of the flow in a day is mostly the same on the day of the week. Also there are seasonal changes and the weather condition factors. About a day flow profile, a peak period traffic usually lasts for an hour or around. Thus, the granularity of the turning ratio parameter would be at least one hour. By these, one idea of the state space is to split every 30 minutes, 7 days, and 12 months plus public holidays. This results in around 4000 states.

2) Learner allocation and actions

The learning system's output is the set of turning ratios for every direction. A link i is connecting to other links $\{L_n | n \in O_i\}$, and each connecting link n is associated with a turning ratio t_{in}. By this, we allocate one RL at each link. An RL has an action set $a_w = \{t_{in}^w | n \in O_i\}, w = 1 \dots W$ where W is a number of actions. A candidate turning ratio t_{in}^w should be initialized by using appropriate value such as the one being fluctuated a small amount from a value collected by traffic survey data. Too much number of actions leads to insufficient learning experiences, and the appropriate value should be five (larger, a bit larger, normal, a bit smaller, and smaller) for one ratio. Thus, in case of 3 directions, the action should be 15 in total.

In RL, a state-action value function *Q(s,a)* is learned, and one action that has probabilistically highest Q value is selected. Since the Q value represents a flow of corresponding links, it means that the parameter set that improves nearby flow will be chosen.

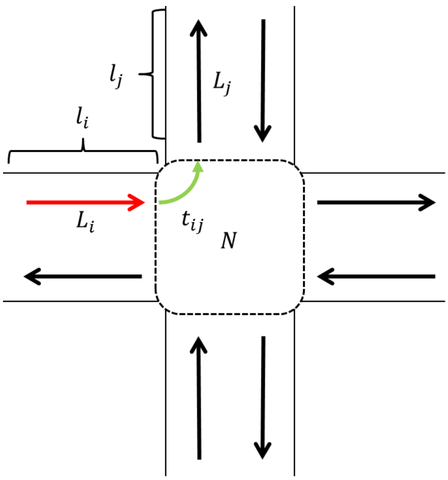

Fig. 6. Links corresponding to a turn rate

3) Reward (exaluations)

Reward is a sum of flow. Traffic lights allocated at a junction at the outward of a link affects all the links $\{L_i | n \in O_i\}$ that are connecting to the outward of the link. Therefore, the performance function (reward) should be set to $\sum_{n \in O_i} L_n$.

Although the evaluation is local, the adjacent RL learner shares part of the flows for their performance evaluation, which will effect for acquiring global optimal values in a long run.

4) Timing of learning invocation and learning frequency

Feedback control is done at each cycle, which is usually ranging from half to a few minutes. Therefore, the timing of invocation of learning and action selection should be the same as the cycle time. By this, the learning frequency in a year should be the product of 30 [cycles/30min] and 4 [days/month] equals to 120 times per state. If the number of actions is 15, one state-action pair will experience about 8 times of trials. This seems relatively small but if we choose an initial action sets (i.e. candidates of turning ratios) close enough to the real situations, it should be practically feasible even for a small number of trials.

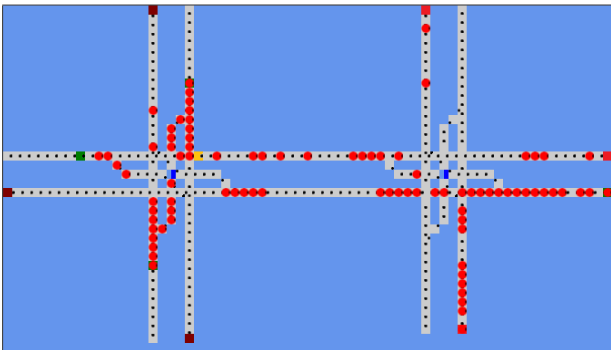

Fig. 7. Traffic simulator

6 Discussions

Currently, we are preparing to verify for the performance of the proposed scheme by using a traffic simulator. Fig.4 shows a screen shot of the simulator under construction. This is a simple cellular automata model with right turn lane. But it is expected to exhibit some important properties of traffic congestions such as a blocked phenomenon by a right turn traffic.

There are some user-defined non-trivial parameters in this method, and the sensitivity of the performance to these parameters should be investigated. Most influential parameters will be the set of actions. How much the degree of fluctuation should be is a rather intuitive factor. However, there is no way to explicitly know the true value of the turning ratio, unless tracking every vehicle's travelling route at every junction, which is too much costly. Therefore, this method provides at least one of the ways to estimate the values by observation.

7 Conclusions

This paper proposed a machine learning approach to improve the model parameters of the feedback control of an urban transit network. The proposed method is to provide estimation of turning ratio that is not obtained from real-time sensor measurement. An estimation method by RL is suitable for this purpose since the result of choosing a candidate of the parameter is measurable in real time. We will continue to verify the performance of the proposed method through simulations.

The feedback method on which this paper is relying is not considering cycle time and offset control. Including these controls will be highly complex problem, and a stochastic combinatorial approach like this paper seems to be one of the promising ways for further investigation.

References

1. Diakaki, C., Papageorgiou, M., Aboudolas, K.: A multivariable regulator approach to traffic-responsive network-wide signal control. Control Engineering Practice 10(2), 183–195 (2002)
2. Wakasa, Y., Iwaoka, K., Hanaoka, K., Tanaka, K.: A Control Engineering Approach to Real-Time and Network-Wide Traffic Signal Control. Transactions of the Society of Instrument and Control Engineers 42(9), 1076–1082 (2006) (in Japanese)
3. Hunt, P.B., Robertson, D.I., Bretherton, R.D., Royle, M.C.: The SCOOT on-line Traffic Signal Optimisation Technique. Traffic Engineering and Control 23(4), 190–192 (1982)
4. Lowrie, P.R.: SCATS: The Sydney Co-ordinated Adaptive Traffic System – Principles, Methodology, Algorithms. In: Proceedings of the IEE International Conference on Road Traffic Signalling, pp. 67–70 (1982)
5. Sugiyama, Y.: Physics of Traffic Flow. Nagare: The Japan Society of Fluid Mechanics 22(2), 95–108 (2003) (in Japanese)
6. Sutton, R.S., Barto, A.G.: Reinforcement Learning: An Introduction. The MIT Press (1998)
7. Bando, M., Hasebe, K., Nakayama, A., Shibata, A., Sugiyama, Y.: Dynamical model of traffic congestion and numerical simulation. Physical Review E 51(2), 1035–1042 (1995)
8. Bando, M., Hasebe, K., Nakanishi, K., Nakayama, A., Shibata, A., Sugiyama, Y.: Phenomenological Study of Dynamical Model of Traffic Flow. Journal de Physique I 5(11), 1389–1399 (1995)
9. Lämmer, S., Helbing, D.: Self-control of traffic lights and vehicle flows in urban road networks. Journal of Statistical Mechanics: Theory and Experiment 2008(4), P04019 (2008)
10. Mimura, S., Hisai, M.: Construction of Real-Time Control Logic for Signalized Network Under Over-Saturated Condition. Memoirs of the Faculty of Engineering Yamaguchi University 57(1), 15–19 (2006) (in Japanese)
11. Ishikawa, H., Shimizu, H., Sobata, Y., Kobayashi, M.: Congestion Length Control for a Traffic Network. IPSJ Journal 45(4), 1154–1162 (2004) (in Japanese)

Composite Artificial Neural Network for Controlling Artificial Flying Creature

Ryosuke Ooe, Ikuo Suzuki, Masahito Yamamoto, and Masashi Furukawa

School of Information Science and Technology
Hokkaido University
Sapporo, Japan
{ooe,ikuo,masahito,mack}@complex.ist.hokudai.ac.jp

Abstract. This paper proposes a composite artificial neural network (CANN). The CANN is a method that contains concepts of an evolutionary artificial neural network, a neural network ensemble and subsumption architecture, and designed for efficient robot control. In the CANN, while low-level ANNs work as actual controllers for calculating outputs, a high-level work as a selector. The high-level ANN works up some optimized ANNs, which output real values, into a controller. In order to verify performance of the CANN, numerical experiments are carried out. An artificial flying creature (AFC) is controlled by the CANN for flying to a target point. Motions of the AFC is calculated by a virtual physics environment, which consists of functions of a physical engine PhysX and a simple drag force calculation. Experimental results show that performance of the CANN is higher than that of a simple ANN.

Keywords: artificial life, evolutionary artificial neural network, particle swarm optimization, neural network ensemble.

1 Introduction

As robots used by human become complex, their control methods also become complex. Although many researchers have built up the knowledge to control the complex robots, it is not often sufficient. If a control strategy looks like the best, there are sometimes better strategies that no one has discovered yet. An evolutionary artificial neural network (EANN [2]) is one of the methods that have a potential for discovering unknown but better control strategies.

The EANN is the method that uses an artificial neural network (ANN) as a controller and optimizes parameters of ANNs by using an evolutionary computation (EC). The EC is an efficient algorithm but trial and error to search unknown solutions. Therefore, there can exist both the case of discovering the best solution and the case of missing the best. In spite of this uncertainty, the EANN has been used in a field of robot control, such as virtual creatures [1] and bipedal robots [3], and successfully realized the control for complex behaviors.

While the EANN has the advantage that only little knowledge is required for controlling robots, there is a weakness in the EANN that optimization by the EC

S. Lee et al. (Eds.): Intelligent Autonomous Systems 12, AISC 194, pp. 863–871.
springerlink.com

depends on a probability. An initial convergence of solutions, that is, the phenomenon that solutions stay at a local minimum value in early search steps, especially prevents the EANN from searching better solutions. To avoid this phenomenon, methods of keeping diversity of genes or behaviors in search groups have been studied by researchers [4]~[5]. A difficulty of additional learning is also a factor that prevents the EANN from realizing better controls.

In fields of pattern recognition and classification, neural network ensembles [6] have been introduced. The neural network ensemble is a method that an average value or a major decision of many ANNs that are learned enough is used as an output of the ensemble group for improving ability of ANNs. The neural network ensemble seems to be not efficient for controlling robots, because output values of the EANN are real numbers in robot control, which are different from binary values in the pattern recognition.

To solve this problem, we propose a composite ANN (CANN) for robot control. The CANN is the control method based on the EANN, to which concepts of the neural network ensemble and subsumption architecture [7] are applied. The CANN uses the ANN selected from many ANNs by a selector ANN to calculate output values. Since the CANN as a whole works as an ANN, a CANN can use another CANN as a part of itself.

In order to verify performance of the CANN, experiments of numerical calculation for controlling an artificial flying creature (AFC) are carried out. A flight behavior is a complex movement in three-dimensional space and requires complex control. Motions of the AFC are calculated by a virtual physics environment, which is based on a physics engine, PhysX, for expressing real motions following the physical law.

The computational method of the virtual physics environment is described in Section Two. Particle swarm optimization (PSO) is adopted as an EC method in our study. Algorithms of the CANN and the PSO are explained in Section Three. Details of experiments, such as a structure of the AFC and experimental conditions, are written in Section Four. Results of the experiments are described in Section Five. Finally, our study is summarized in Section Six as a conclusion.

2 Virtual Physics Environment

2.1 Summary of Function

The virtual physics environment is the software that can automatically calculate the multi-body dynamics in fluid. It fundamentally uses PhysX functions for calculating rigid body dynamics. Although PhysX supports a kind of fluid simulation, its computational costs is so high that it is not suitable for real time simulation. Therefore, we have additionally implemented a simple drag force calculation, which has low computational costs, to develop the virtual physics environment. The virtual physics environment can carried out simulation in fluid very fast. However, it cannot calculate simulation of fluid itself, because no change of fluid is took account of in the environment.

2.2 Physical Engine

A most common purpose of a physical engine, such as PhysX, is to improve reality of motions in three dimensional computer graphics (3DCG). It is mainly used in fields of 3DCG animation and game. In addition to reality, the physical engine can simulate easily various types of physical objects, such as a cloth, an elastic object and a vehicle, in recent years. So it is often used for research on robotics, artificial life and other application.

The physical engine can calculate motions of many types of objects. The function of joint constraints is especially useful for modeling complex robots. Not only joint constraints, but also effects of collision and friction are considered by the physical engine to calculate motions. Since complex calculations are automatically performed, the physical engine can be regarded as a black box for physical motion calculation.

2.3 Drag Force

An object in fluid is affected via surfaces of the object by the fluid, and then a motion of the object is changed. If a state of fluid changes little, it is considered that an effect from fluid to the object depends on its velocity and angular velocity relative to the constant flow. Therefore, this effect is roughly expressed by a drag force, which is known in fluid dynamics.

Suppose that an object is moving in fluid as shown in Fig. 1. The drag force ΔD, which acts on a divided small surface of the object, is given by

$$\Delta D = \frac{1}{2} \Delta A \, \rho \, C_d \, \boldsymbol{v}^2 \cos\theta \tag{1}$$

where ΔA, ρ, C_d, $\boldsymbol{v}$, and θ are the area of the divided small surface, the density of fluid, a drag coefficient, the velocity of the small surface, and an angle between a normal of the surface and a direction of $\boldsymbol{v}$.

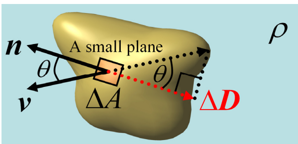

Fig. 1. An object moving in fluid

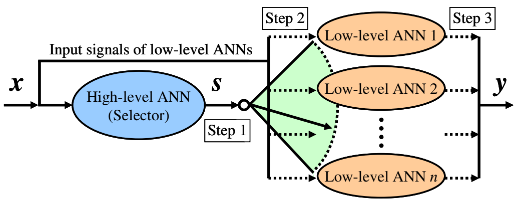

Fig. 2. The artificial flying creature

Applying the equation (1) to all divided surfaces of the object leads to the drag force that acts on the object. Although this drag force is a kind of the quasi-steady fluid force and a rough approximation for the real fluid force, it is processed fast and easily combined with a physical engine.

3 Composite Artificial Neural Network

3.1 Calculation Algorithm

The CANN is one of methods applying the neural network ensemble to robot control. Although there can be many methods for working up ANNs which output real numbers into the neural network ensemble, the CANN simply uses an ANN as a selector.

Fig. 2 shows a concept of the CANN. A CANN has a selector ANN and a group of ANNs, which actually output signals for controlling a robot. In a CANN, the selector ANN is referred to as the high-level ANN and an ANN in the group is referred to as a low-level ANN. When an input vector $\boldsymbol{x}$ is given, the CANN can calculate an output vector $\boldsymbol{y}$ by following three steps which are demonstrated below.

1) *Calculation in the high-level ANN: The high-level ANN calculates the output vector* $\mathbf{s}$ *from the input vector* $\mathbf{x}$*. The dimension of* $\mathbf{s}$ *is the same as the number of low-level ANNs.*
2) *Selection of the activated low-level ANN: Each element in the vector* $\mathbf{s}$ *represents a priority of each low-level ANN. The low-level ANN that has the maximum value of the priority is selected.*
3) *Calculation in the low-level ANN: The selected low-level ANN calculates the output vector* $\mathbf{y}$*, which is the output of the CANN, from the input vector* $\mathbf{x}$*.*

3.2 Particle Swarm Optimization

A high-level ANN and low-level ANNs in the CANN are optimized by using an evolutionary computation (EC) the same as the EANN. Particle swarm optimization (PSO [8]) is adopted as the EC in the CANN, because the PSO has a highly convergent feature and has shown a higher performance than real-coded genetic algorithm (RCGA) in preliminary examinations.

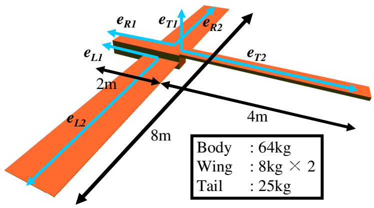

Fig. 3. The artificial flying creature

The PSO is the optimization method that many particles move about in hyperspace for searching the optimal solution. A position of a particle represents the parameters of an ANN. The position of the particle i at search step k+1, $\boldsymbol{p}^i_{k+1}$, is calculated by

$$\boldsymbol{v}^i_{k+1} = w\boldsymbol{v}^i_k + c_1 r_1(\boldsymbol{p_d}^i_k - \boldsymbol{p}^i_k) + c_2 r_2(\boldsymbol{p}_{gk} - \boldsymbol{p}^i_k). \quad (2)$$

and

$$\boldsymbol{p}^i_{k+1} = \boldsymbol{p}^i_k + \boldsymbol{v}^i_{k+1}. \quad (3)$$

where w, c_1 and c_2 are coefficients. r_1 and r_2 are uniform random numbers from 0 to 1. $\boldsymbol{p_d}$ is the best position of the particle i. $\boldsymbol{p_g}$ is the best of all particles.

4 Experimental Setup

4.1 Artificial Flying Creature

An artificial flying creature (AFC) is a virtual robot realized in silicon by the virtual physics environment. The AFC shown in Fig. 3 consists of four parts: a body, a tail and two wings. The tail and two wings can rotate on each axis. When a value is given as a relative rotation angle, the AFC rotates each part to correspond its relative angle with the given angle. To simplify control of the AFC, rotations of two wings are perfectly symmetrical. Therefore, there are four control parameters for controlling the AFC.

The AFC has a virtual sensory system and a controller, which is a simple three-layered ANN or a CANN. The sensory system can measure states of the AFC, and perceive cognitive information about the target that the AFC has to go. The sensory system gives the following eight values: pitch and roll angles of the AFC, a forward velocity, relative angles on the axes $\boldsymbol{e}_{L1}$ and $\boldsymbol{e}_{L2}$, an angular velocity on the axis $\boldsymbol{e}_{L1}$, and vertical and horizontal angles relative to the target point. A controller of the AFC receives these values as inputs from the sensory system to calculate four values as outputs, and then the AFC moves each part according to the outputs.

4.2 Controller

To compare performances of a CANN and a simple ANN, two types of controllers are designed for controlling the AFC. One is the CANN that has a high-level ANN and three low-level ANNs. The number of inputs in all ANNs is eight values shown above. The number of neurons in the middle layer is twenty for all ANNs. The number of outputs is three for the high-level ANN, and four for the low-level ANNs. The other is the ANN that has eight, twenty and four neurons in the input, middle and output layer. It is completely the same as the low-level ANN in the CANN.

4.3 Experimental Conditions

The AFC is initially placed on the point of (0, 100, 0) in a state of rest. The direction of z axis is the same as an initial forward direction of the AFC. After the initial setup, the AFC starts flying to the target point of (100, 150, 100) by using its own controller.

The time step of numerical integration in PhysX is set up as 1/100 seconds. The AFC is moving by its controller for twenty seconds, in other words, for two thousand steps. The AFC is also been evaluated for the flight. The evaluation of the AFC is calculated by

$$\sum_{t=0}^{2000} f(t), \quad f(t)=\begin{cases} \dfrac{10}{r+10} & : t < T \\ 1 & : t \geq T \end{cases} \tag{4}$$

where t, r, and T are a time step, a distance from the center of the AFC to the target point of (100, 150, 100), and the time that the AFC arrives at a position within one meter from the target for the first time in its flight.

All ANNs are optimized by PSO, in which coefficients w, c_1 and c_2 are set up as 0.4, 2.0 and 2.0, and in which the number of particles is set up as twenty. In the case of the CANN, learning of a high-level ANN is carried out after independent learning of each low-level ANN. Learning of a low-level ANN is done for two hundred search steps independently three times. After three learned low-level ANNs have been given, a high-level ANN in the CANN is done for four hundred search steps. So the total search step of the CANN is one thousand.

On the other hand, learning of a simple ANN, which is the same way as learning of a low-level ANN in the CANN, is done simply for one thousand. Since computational costs for physical simulation by PhysX is much higher than that for calculation of an ANN or a CANN, computational costs for evaluating a flight of the AFC controlled by the simple ANN is almost the same as that by the CANN.

5 Result and Analysis

5.1 Result for Thirty Trials

The learning experiments of the simple ANN and the CANN ware carried out thirty times. Fig. 4 shows each change of the averaged evaluation for thirty trials given by PSO. In the case of the CANN, each evaluation given by three independent learning for low-level ANNs is put in order before six hundred search steps, and then the evaluation for a high-level ANN is shown from six hundred to a thousand search steps.

Fig. 4 shows that the average evaluation of the CANN at six hundred search steps, when the learning of a high-level ANN in the CANN starts, is higher than the average evaluation for three low-level ANNs. This result means that the best low-level ANN among three is selected as a base for control at the first step in the learning of a high-level ANN. The average evaluation of the CANN at a thousand search steps, when the learning is finished, is 5.04 percent higher than that of the simple ANN.

Fig. 5 shows the rate of increase in comparing six hundred search steps and a thousand search steps for thirty trials. Although the rate is lower than 50 percent in most cases, there are four cases that the rate is higher than 100 percent. The average rate of increase is 40.00 percent. This result shows that the CANN, which simply selects a low-level ANN by a high-level ANN to calculate outputs, can have higher

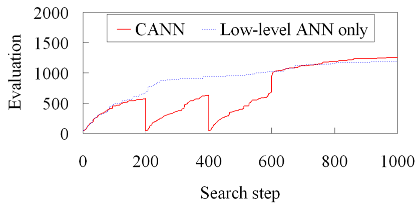

Fig. 4. The average evaluations for thirty trials

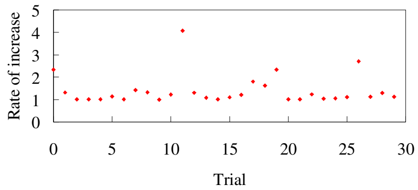

Fig. 5. The rates of increase

performance than each performance of low-level ANNs. If the concept of selection by a high-level ANN results in high performance, replacing low-level ANNs in the CANN with various types of controllers will be one of future works and lead to higher performance.

5.2 The Best Example

The highest rate of increase in comparing six hundred and a thousand search steps is 307.25 percent. In the best case, the evaluations of three low-level ANNs that have finished learning are no more than 295.35, 386.70 and 303.11. The AFC can arrive at a position within one meter from the target in less than twenty seconds by using none of the three low-level ANNs. After the learning of a high-level ANN, however, the AFC can do in no more than 4.96 seconds by using the low-level ANN 0 and 1.

Fig. 6 shows the change of selection for low-level ANNs. Although the low-level ANN 2 is not selected at all, the CANN selects the low-level ANN 0 and 1 well for better flight. Red, green and blue lines in Fig. 7 are flight trajectories for flight of the low-level ANN 0, 1 and the CANN. In the flight of the low-level ANN 0, the movement of the AFC is very slow but stable. In that of the low-level ANN 1, the AFC is moving relatively fast but unstably. On the other hand, in the flight of the CANN, the movement of the AFC is very fast and stable. The flight of the CANN is much faster than that of the low-level ANN 0 and 1. This result shows a feature that the CANN can realize high performance, which is quite different from performance of each low-level ANN.

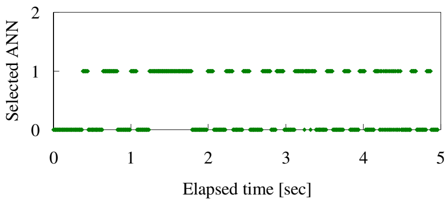

Fig. 6. The numbers of selected low-level ANNs

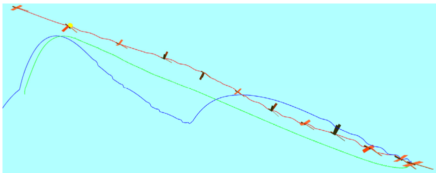

Fig. 7. The trajectories of the AFC

6 Conclution

This paper describes the CANN, which contains concepts of the EANN, the neural network ensemble and the subsumption architecture. In addition, numerical experiments for controlling the AFC by using the CANN are carried out, and then the following are demonstrated.

1) The CANN uses the best low-level ANN as a base controller.
2) The CANN has higher performance than that of a simple ANN for the same computational costs.
3) The CANN changes the selected low-level ANN at various timing of intervals to realize higher performance that is quite different from performance of each low-level ANN.

In this paper, the CANN uses the low-level ANNs that learned in the same experimental conditions, such as an evaluation. Examination for performance in the case that the CANN uses the low-level ANNs, which learned in different experimental conditions, is one of future works.

References

[1] Sims, K.: Evolving virtual creatures. In: Proc. 21st Annual Conference on Computer Graphics and Interactive Techniques, pp. 15–22 (1994)
[2] Yao, X.: Evolving Artificial Neural Networks. Proc. of the IEEE 87(9), 1423–1447 (1999)
[3] Allen, B., Faloutsos, P.: Complex networks of simple neurons for bipedal locomotion. In: IROS 2009, Proc. of 2009 IEEE/RSJ International Conference on Intelligent Robots and Systems, pp. 4457–4462 (2009)
[4] Sareni, B., Krahenbuhl, L.: Fitness sharing and niching methods revisited. IEEE Transactions on Evolutionary Computation (1998)

[5] Gomez, F.: Sustaining diversity using behavioral information distance. In: GECCO 2009, Proc. of the 11th Annual Conference on Genetic and Evolutionary Computation (2009)
[6] Hansen, L.K., Salamon, P.: Neural network ensembles. IEEE Transactions on Pattern Analysis and Machine Intelligence 12, 993–1001 (1990)
[7] Brooks, R.A.: A Robot that Walks; Emergent Behaviors from a Carefully Evolved Network. Neural Computation 1(2), 253–262 (1989)
[8] Kennedy, J., Eberhart, R.: Particle swarm optimization. IEEE International Conference on Neural Networks 4, 1942–1948 (1995)

Polycentric Framework for Robotic Kinematics

Akihiro Hayashi[1], Toshifumi Satake[2], and Shinya Haramaki[3]

[1] Mechanical Information Sceience and Technology, Kyushu Institute of Technology
680-4 Kawazu Iizuka, Fukuoka 820-8502, Japan
hayashi@mse.kyutech.ac.jp
[2] Information Systems Engineering, Asahikawa National College of Technology
2-2 Shunkoudai Asahikawa, Hokkaido 071-8142, Japan
satake@asahikawa-nct.ac.jp
[3] Mechanical Engineering, Ariake National College of Technology
150 Higashi-hagio Ohmuta, Fukuoka 836-8585, Japan
haramaki@ariake-nct.ac.jp

Abstract. This paper proposes an generic framework of kinematics process for improving the operability of robotic systems. In the framework, metaphysical subsystems and connection rules are defined, and kinematics process is composed of a set of subsystems assembled by their connection rules in which input/output relation of subsystems are associated with each other. Kinematics of generic robotic systems is solved by cooperating the localized calculation embedded in subsystems. The framework is applied to case studies of the forward and the inverse kinematics problems of seven d.o.f. robot manipulator.

Keywords: robotics system, kinematics, polycentric.

1 Introduction

Robot technologies have been cultivated in so far as practical industrial applications. Indeed, many types of robot are widely used into mass manufacturers as an indispensable facilities. This success has brought about the expectation that is practical use of robotic technologies of late, not only for industrial fields but also for human life support problems. That is, however, not easy and not always in the case of human life support robots because of the complicated versatility to be concerned on tasks, users, and environments.

The circumstances of human life ought to be not tailored for robots much still less than for robot works. The works and the surroundings would be in complicated and versatile situations. The situations can not be anticipated in the most cases. In addition to this, typical robot users, who are rarely distinguished for one's knowledge of robotic technologies, have to be required to make plan and operation about robot motion and control. More sophisticated operability is especially desirable to embody human life support robotic systems.

The operability of robotic system is closely related to the robot motion control because of the manipulation of robot users to be almost concerned to motion control. Then kinematics technique is also indispensable basis in robotic motion control.

S. Lee et al. (Eds.): Intelligent Autonomous Systems 12, AISC 194, pp. 873–881.
springerlink.com

So, the first thing to be addressed in this study investigates a generic kinematics framework.

In the kinematics of robotic systems, mathematical analysis had been investigated [1][2][3], and the techniques based on the analysis is still used for formularizing the kinematics models. Hence the technique of kinematics in robotic systems is rarely discussed in so far as recently. The conventional techniques are, however, often the rigid principles in the least meaning of that the technique is regarded as the way to make a formula for individual robots, and of that a singularity problem can not be disregarded by its mathematical rigors.

For improving the operability in robotic systems, this study introduces the concept of polycentric systems[4] in developing of a generic kinematics framework. Polycentric system is generally designed by subdividing a complicated large-scale system into several subsystems. It does not have any central control elements, and each subsystem may play as a prime mover on the circumstances. This paper presents a polycentric kinematics framework and the possible impact of the improved robotic systems is confirmed through the case studies.

2 Polycentric Kinematics Framework

2.1 Preliminary Design Concept

When it is generally said "operability", it tends to suppose human/machine interface problems. The term of "operability" in this study refers to enable the robotic system to permit the insufficient manipulation of robot users and the changing situation in the current of robot motion as a normal condition, and to compensate for the insufficiency and the uncertainties. The matters must be also provided in a generic and potential ability, because the matters referred here are related to an intelligent, and an intelligent is a generic framework possible to induce an appropriate situation for the various circumstances. This study applies the concept of polycentric system as a practical prescription to represent intelligent in artificial systems into developing a kinematics framework.

Polycentric systems approach in robotic systems is not ever brand-new, and several activities have been conventionally studied as a modeling method of kinematics process[5][6]. Robotic systems are composed of the mechanical parts such as prismatic or rotational joints, links, effectors, and so on. Especially, the relation between a pair of joints and their adjacent links is well known as a basis of the description of kinematics properties[1]. Many approaches, therefore, are often treated as an object oriented approach in which the kinematics role of mechanical parts such as joints and links are formulated as a processing part for modeling kinematics process.

On the other hand, a polycentric system is defined as the system in which system objectives is emerged by the interaction through the individual action of distributed subsystems[7]. The feature is an inherent instability provoked by the closed information/data network structure so as to be shown in for example a social system, ecological system, biological system, and so on[4] and it becomes a source of

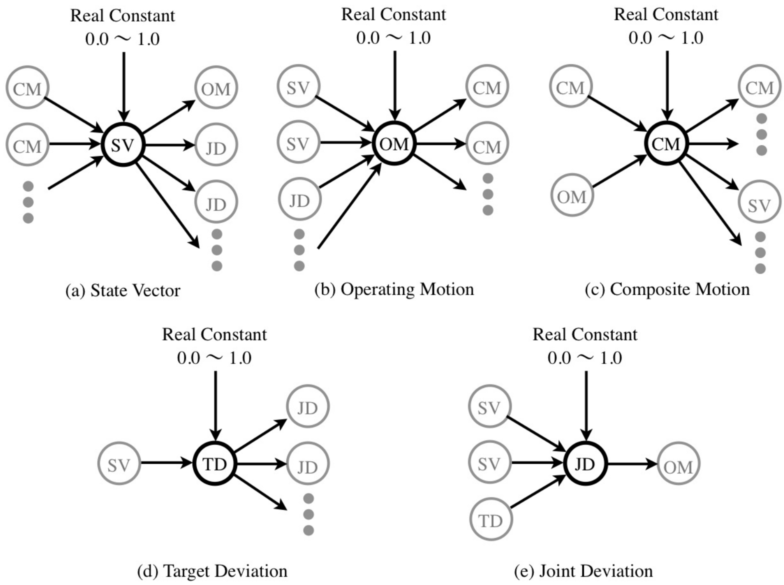

Fig. 1. Subsystems and connection rules prepared in this kinematics framework

versatility in an artificial system. For utilizing the feature, the kinematic role of mechanical parts are subdivided into metaphysical subsystems, and some rules to connect the I/O relation of subsystems are defined as it possible to draw out more elaborate polycentric efficiency.

2.2 Subsystem Definitions

Five types of subsystems and their connection rules, as shown in Fig.1, are defined for constituting a polycentric kinematics framework. A subsystem is a software entity which consists of data objects and their processing, and leads themselves to their interaction through the delivery of data objects with each other. They are called by the names of State Vector (**SV** in short), Operating Motion (**OM** in short), Composite Motion (**CM** in short), Target Deviation (**TD** in short), and Joint Deviation (**JD** in short), respectively.

SV consists of a vector object and its transformation process. The vector object is used to represent the part of geometry in robotic systems such as the point of actions, the pose of joints, the position of end effecters, fingertips, and so on. All geometric information needed for modeling of robotic systems are represented by using of a set of **SV**s. Transformation process transforms vector object for the data of composite motion delivered from **CM** described in the below.

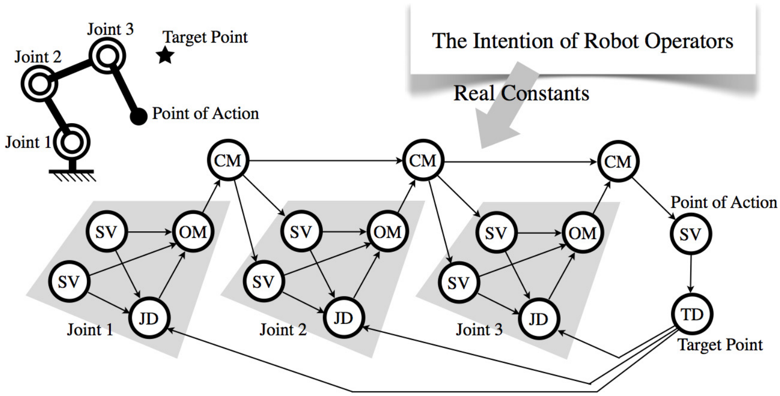

Fig. 2. Kinematics process model of typical manipulator

TD calculates the position deviation between the point of action and its target point. The point of action here refers to the point of tasks, such as fingertips, end effecter, and so on, to be remarked for the kinematics process and it is represented by **SV**. Target point is assigned from the outside of system as a manipulation of robot operators. The generated deviation provokes subsystem **JD** to be transformed into joint deviation. **JD** is one-to-one correspondence with **TD**, and it transforms target deviation into joint deviation. The geometry data of joint are represented by two **SV**s associated with itself. The joint deviation transformed by **JD** is the solution of inverse kinematics process locally conducted at the joint and that is succession from {**TD**} to {**JD**}.

OM generates operating motion for the joint deviation transformed by **JD**. Operating motion depends upon the pose of joint. The pose of joint is taken from two **SV**s associated with itself. As shown in Fig.1, **OM** is connected to **CM**, and the generated operating motion are passed to subsystems located at the tip side of robotic systems via **CM**. **CM** makes a composite motion by combining two operating motion transmitted from **OM** and **CM**. **CM** plays the role of the link in a practical robotic mechanism. The succession from{**OM**} to {**SV**} via {**CM**} represents forward kinematics process conducted locally at each joint.

In addition to this, real constants that take the values in zero to one can be also set on each subsystem for controlling the activity of subsystems based on an intention of robot operators. The constants work to control the start and stop of subsystems, or to multiplier factors of the output of each subsystem.

2.3 Kinematics Process Modeling

Kinematics process is composed of subsystems assembled according to the mechanism of robotic systems. Figure 2 shows the kinematics process of typical three degree of freedom manipulator. Arrows in Fig.2 explain the input/output relation of each subsystem as well as the data object feed.

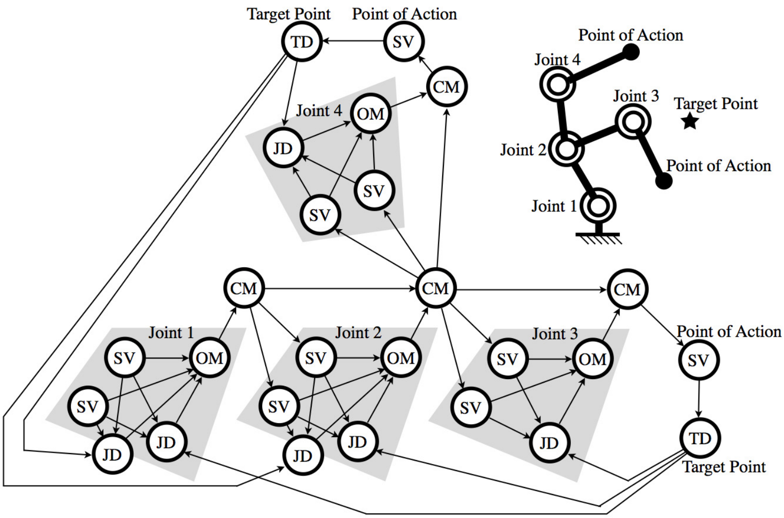

Fig. 3. Extension example of kinematics process model

A set of {**SV**,**SV**,**OM**,**JD**} enclosed by hatching, {**SV**,**TD**}, and {**CM**}in Fig.2 correspond to joints, the point of action, and links, respectively. The succession from {**SV**,**SV**} to {**OM**}, then successively performed from {**CM**}, {**SV**,**SV**},…,{**CM**}, to {**SV**} represents the robot mechanism from the base to the fingertip. The succession also describes the flow of process to obtain forward kinematics solution. The succession from {**TD**} to {**JD**} corresponds to inverse kinematics process performed locally on the each of joints. The process of forward and inverse kinematics is closed via {**OM**}, so a closed system is formed as shown in Fig.2.

The framework can easily applied for the kinematics process model of various type of mechanism in robotic systems. Figure 3 shows kinematics process of the extended robot mechanism. The extension can be done by connecting input/output of subsystems newly added for the extension.

3 Principle of Kinematics Process

3.1 Forward Kinematics Process

The feature of this framework is to be the instability that is the inherent feature of closed system in which the dynamic of behavior is emerged by the change of circumstances. The instability is provoked by the manipulation of robot users. For instance, when output of all subsystems is maintained in a specified state, the entire system can be considered under a stable situation. In the case, if the output of a certain subsystem shifts a different value, the chain reaction of all subsystems would be invoked by this small change. Every subsystem plays this leading role, and the system is polycentric.

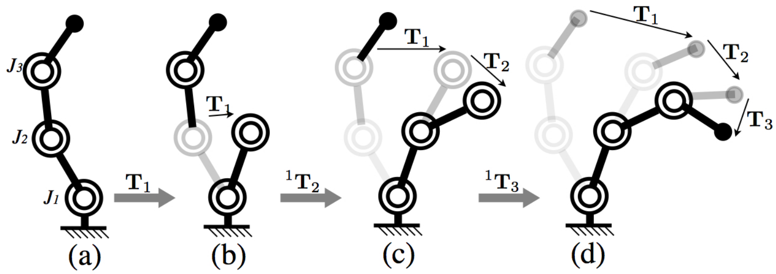

Fig. 4. The sequence of forward kinematics process

Suppose in the case that the entire system is stable state as shown in Fig.4 (a). In the situation, the rotation of joint located at the most base side induces **OM** to generate operating motion $\mathbf{T}_1$ that consists of rotation and translation. The operating motion is transmitted to next two **SV**s via **CM**, as the result of this, the pose of joint is transformed as shown in Fig.4 (b). If this joint also rotates, operating motion $\mathbf{T}_2$ is generated in the same manner. Both of operating motions are compounded into ${}^1\mathbf{T}_2$, then the composite motion ${}^1\mathbf{T}_2$ is transmitted toward the tip side of manipulator via **CM**. Each operating motion is correctly transmitted toward tip side of manipulator with their composition in Fig.4 (c) to (d). Kinematics properties, therefore, are satisfied for the overall robots. In finally, the operating motion ${}^1\mathbf{T}_3$ is transformed to the point of action located at the tip end of manipulator.

3.2 Inverse Kinematics Process

Inverse kinematics process is invoked by the successive approximations of **JD**s for the deviation obtained by **TD**. In the case that the pose of manipulator is in a stable state, if a target point was assigned to **TD**, then **TD** calculates the target deviation between the point of action and the target point. The target deviation provokes **JD** to transform the target deviation into joint deviation. Joint deviation is the projection of target deviation for the pose of joint. The joint deviation of each joint is transformed to the operating motion by **OM**. According to the manner of forward kinematics process, The operating motion transforms the pose of robots, as the result of this, the target deviation is also changed, and then new action of **JD** is provoked for the different target deviation. The sequences described in the above are repeated until that the entire system becomes a next stable situation. When this next stable situation is appropriate for the circumstances, it would be considered that the sequence can be regarded as a sort of adaptation. The geometric data of joints and the point of action are internal knowledge in terms of the pose of robot recognized by robotic system itself. The operating motion of each joint also expresses the solution of inverse kinematics problem.

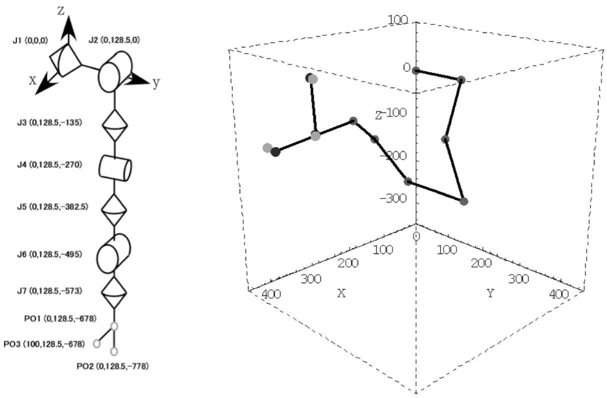

(a) Initial pose (b) The detected pose

Fig. 5. The obtained pose of manipulator

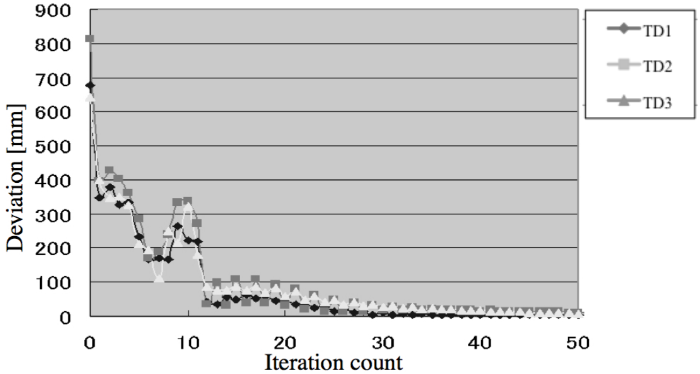

Fig. 6. The transition of target point deviations

4 Case Studies

The inverse kinematics process of seven d.o.f. manipulator has been executed to confirm the potential impact of this framework. The initial pose of manipulator is shown in Fig.5 (a). Three points of action are set at the fingertip of manipulator. Three target points are assigned on the points of action respectively, staying the relation about their location. This corresponds to a typical inverse kinematics problem for the pose of fingertip.

Figure 5 (b) is the pose of manipulator to be obtained by this numerical experiment. The numerical result is shown in Fig.6 that explains the transition of deviation between three points of action and their target points in iteration process.

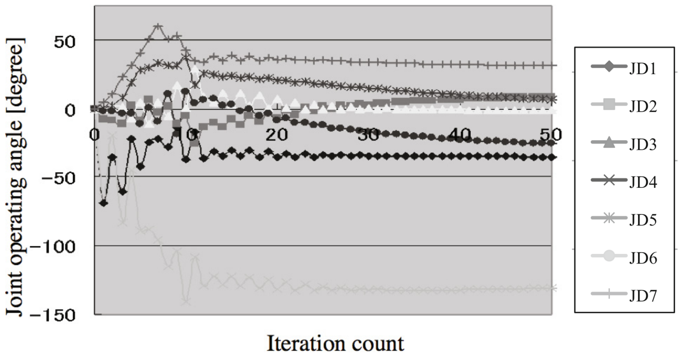

Fig. 7. The transition of joint operating angles

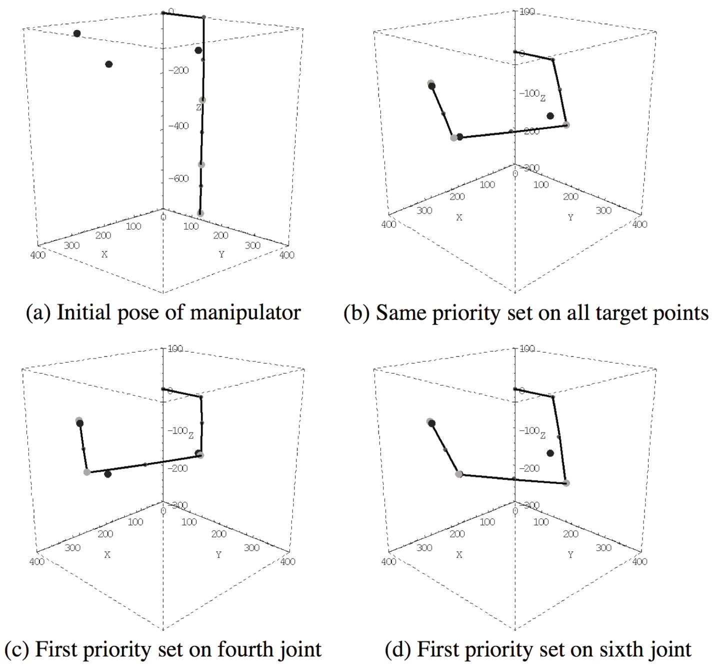

Fig. 8. The pose detect problem for three target points

The deviations gradually converge toward zero so that means to obtain the desired pose for the fingertip. Figure 7 is the transition of operating angle in each joint. Figure indicates that instability of operating angles are provoked first, and then they are converged to next stable situation.

Three points of action are reset at the fingertip, fourth joint, and sixth joint, respectively. The pose of middle part of fingertip position. The joints located at the base side, such as the first joint, second joint, and third joint, affect the motion of all points of action. The extent of influence can be preferred by real constants set on **JD**s.

The results are showed in Fig.8. Black circles of the figure are three target points which are set for a parts of fingertip, sixth joint, and fourth joint. The pose (a) is the initial pose. The pose (b) is the result in the same value of real constants to be set on all **JD**s. The pose (c) is preferred with the fourth joint. The pose (d) is preferred with the sixth joint. These results indicates to be able to obtain a preferred pose of robots by changing the value of real constants to be set on **JD**s.

In mathematical rigorous technique, solvable target points must be desired in the inverse kinematics problems without the singularity problem. This local inverse technique is to find operating angle for minimizing the deviation from the point of action to the target point, therefore, the solvable is not required for target points. Indeed, the configuration of manipulator does not exist to satisfy three target points in this case study, hence the pose of robots depends upon the value of real constants.

5 Conclusion Remarks

This paper proposes a polycentric kinematic framework for the basis to improve the operability of robotic systems by means of a polycentric system concept. In the framework, metaphysical subsystems and their connection rules are defined as elements to construct kinematic process in robotic systems. Subsystem is a software entity consisting of data objects and their operation. Kinematics model is composed of a set of the subsystems. It represents the mechanism as well as the forward and the inverse kinematics process of robotic systems. The inverse kinematics problems have been performed for typical seven d.o.f. manipulator. The feasibility and the possible impact of the improved robotic systems is confirmed through the case studies.

References

[1] Denavit, J., Hartenberg, R.S.: A kinematic Notation for Lower-Pair Mechanisms Based on Matrices. J. of Applied Mechanics, 215–221 (1955)
[2] Balestrino, R., Maria, G.D., Scivvicco, L.: Robust Control of Robotic Manipulators. In: The 9th IFAC World Congress, pp. 410–425 (1984)
[3] Chiacchio, P., Chiverini, S., et al.: Closed-Loop Inverse Kinematics Schemas for Constrained Redundant Manippulators with Task Space Augumentation and Task Priority Strategy. The Int. J. of Robotic Research 10(4), 410–425 (1991)
[4] Urich, H.: Self-Organization and Management of Social System. Springer (1984)
[5] Ning, K.: Rearch on Embedded MAS based Manipulator Contrrol. Industrial Robot An International Journal 33(2), 97–105 (2006) (unpublished)
[6] Mori, A., Naya, F., et al.: Multiagent-based Distributed Manipulator Control. In: Proc. of the IEEE/SCICE/RSF Int. Conf. on Multisensor Fusion and Integration for Intelligent System, pp. 289–296 (1996)
[7] Itoh, M.: Problems to be Solved on Decentralized Autonomous System Study. J.of SICE 32(10), 789 (1993)

Cluster Analysis of Collective Behavior for a Robotic Swarm

Kazuhiro Ohkura[1], Toshiyuki Yasuda[1],
Chikara Morishita[1], and Yoshiyuki Matsumura[2]

[1] Hiroshima University, 1-4-1, Kagamiyama, Higashi-Hiroshima, 739-8527, Japan
{kohkura,yasu}@hiroshima-u.ac.jp,
[2] Shinshu University, Ueda, Nagano, 386-8567, Japan
matsumu@shinshu-u.ac.jp

Abstract. Swarm robotics is a new research field of multi-robot systems which generally consists of many homogeneous autonomous robots without a global controller. Since a robotic swarm is controlled by an emergent way of many interactions with the other robots or an environment, such as a result of self-organization, robot learning or artificial evolution, no method has been known to grasp the macroscopic collective behavior in a practical sense, according to the best of our knowledge. In this paper, based on this situation, a novel method for analyzing the macroscopic collective behavior inspired by a technique in the field of complex network is proposed. The effectiveness of the proposed method is demonstrated on a robotic swarm behavior for the cooperative transport problem by extracting the community structure based on the modularity optimization.

1 Introduction

Swarm Robotics (SR) [5], [8], [7], [13], is a new research field that deals with many homogeneous autonomous robots without a global controller. The main inspirations come from the observation of social insects like termites or bees. Therefore, SR expects the emergence of sophisticated global behavior as a result of self-organization through many local interactions among autonomous robots and between autonomous robots and their environment.

So far, it has been pointed out that the design methodology of robot controllers can mainly be classified into the following two approaches [13]. The one is so-called the ad-hoc approach or the behavior-based approach [1]. This approach implies that behaviors of individual robots are designed manually beforehand to achieve a desired collective behavior. The other is called the principled approach [4], [10], [11], [13]. Instead of programming each robot's behaviors manually, a certain general methodology is adopted for developing appropriate collective behavior. In either case, since a robotic swarm is controlled by a way of emergent synthesis, no methods have been known for grasping the collective behavior in a macroscopic manner so far, according to the best of our knowledge. This would be caused by the intrinsic characteristic that a robotic swarm has

S. Lee et al. (Eds.): Intelligent Autonomous Systems 12, AISC 194, pp. 883–891.
springerlink.com

a too much redundancy for controlling by a conventional method. No one can identify which robots are useful and which robots are useless in a robotic swarm, particularly in a changing situation.

In this paper, based on this recognition, a novel method for grasping the macroscopic collective behavior is proposed based on the techniques in complex networks. The effectiveness of the proposed method is demonstrated with a series of computer simulations that deals with the cooperative transport problem by 40 autonomous robots.

2 Cooperative Transport

Figure 1(a) shows the cooperative transport problem at the initial condition. The size of the square field is 3500×4000. A robotic swarm composed of 40 autonomous mobile robots is randomly placed on the upper-left of the field. Three objects, L, M and S, whose bodies are painted in green, violet and white, respectively, are placed on the field. On the other hand, a fixed obstacle painted in red is also placed on the field. The objective of the robotic swarm is to push three objects to their goals each of which is painted in the same color as the object, respectively. The three objects are assumed to be so heavy that a single robot cannot move. For instance, L needs five robots to move. Of course, these robots have to cooperate with each other to push the object to the same direction to combine their forces. Similarly, it is also assumed that two objects, M and S, need three and two robots to move, respectively.

All the robots are assumed to have the same specifications as shown in Figure 1(b). A robot has six IR sensors at its front and two IR sensors at its back. An omni-vision camera is equipped on the center of its body. A robot has the ability of detecting the nearest robot, the second nearest robot and the nearest object through the image processing from the camera. The information about the observing robot is composed of the nearest distance, the direction to it, the direction of the robot's front and the color represented as the set of R, G and B. Note that each direction is shown by a pair of *sin* function and *cos* function. A robot detects an object as the information of the nearest distance and the direction. It is also assumed that a robot has a compass for finding its own global direction and two motors for right and left wheels, respectively. However, since we assume here that a robot cannot detect any information about the goals, they have to find the goal positions through artificial evolution. Therefore, the information obtained by these types of sensors forms the input layer of a robot controller composed of 32 neurons and the output layer composed of two neurons. All the robots are assumed to have the same ANN controllers.

3 Associated Network

In the field of swarm robotics, some big projects, such as [3] and [9], have been discussing the methodologies of how to develop useful collective behaviors by means of artificial evolution. The cooperative transport problem is one of the

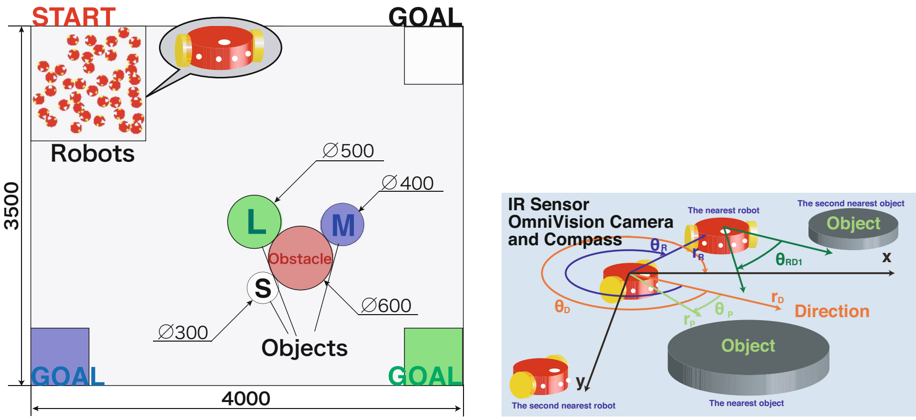

(a) Initial condition (b) Specifications of a robot

Fig. 1. Cooperative transport problem

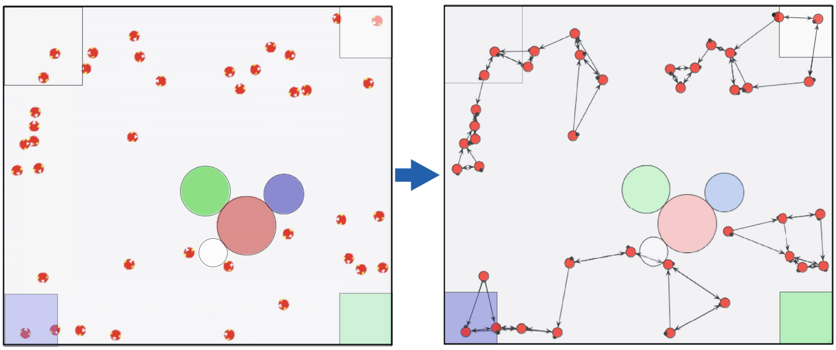

Fig. 2. Network associated with a SRS

representatives in this problem domain. Some results for this problem have been obtained by Dorigo's group [11], [14]. However, to the best of our knowledge, no methods have widely been known for how to analyze the evolving collective behavior from a macroscopic viewpoint.

Therefore, in this paper, a novel method of analyzing macroscopic collective behavior of a robotic swarm is proposed. Suppose that a robotic swarm is mapped onto a complex network comprised of nodes as robots and links as informational connections between them. Then, various tools in the field of complex networks is applicable to the network. For instance, suppose that 40 robots are scattered as shown in the left side of Figure 2. Then, a complex network can be built as shown in the right side. For instance, let us discuss how to divide a robotic swarm into subgroups each of which may have a certain functional role. Then, we can think about applying various clustering techniques of complex networks. Assume that we take the GN method [2] [6] to detect the community structure.

The output of the GN method may be drawn in the form of a dendrogram, which represents an entire nested hierarchy of possible community divisions for the network as shown in the left side of Figure 3. In order to determine the best clustering result for a given network, a measure called modularity [6] is introduced. The modularity measure Q is calculated as follows:

$$Q = \sum_i (e_{ii} - a_i^2) = \mathrm{Tr}(\boldsymbol{e}) - ||\boldsymbol{e}||^2 \tag{1}$$

where the matrix $\boldsymbol{e}$ is the symmetric matrix $k \times k$ where k is the number of divisions, the element e_{ij} of $\boldsymbol{e}$ is the fraction of links that connects the node in the cluster i and the node in the cluster j, $a_i = \sum_j e_{ij}$, $\mathrm{Tr}(\boldsymbol{e}) = \sum_i e_{ii}$ gives the fraction of edges in the network that connect vertices in the same community. $||\boldsymbol{e}||$ indicates the sum of the matrix elements. If the number of within-community edges is no better than random, $Q = 0$. A value approaching the maximum $Q = 1$ implies a strong community structure. Then, we can obtain the best community structure on a dendrogram at the condition that Q shows the maximal value. Based on this discussion, a robotic swarm can be divided into subgroups at the condition that the associated network shows the best community structure.

4 Computer Simulations

4.1 Experimental Settings

The evolving swarm has to solve the initial condition as shown in Figure 1(a). This layout is called the basic pattern (BP) below. If the robotic swarm can solve BP successfully, then five additional patterns called the random patterns (RPs) in which three objects and one obstacle are placed randomly in the field are examined. For each run, the swarm collects the points described on Table 1. Therefore, the fitness f of the swarm is calculated as:

$$f = \begin{cases} P_{BP} & \text{if it fails in BP,} \\ P_{BP} + \frac{1}{5}\sum_{n=1}^{5} P_{RP_n} & \text{otherwise.} \end{cases} \tag{2}$$

where P_{BP} is the sum of points collected while solving in the case of BP. Similarly, P_{RP_n} is the sum of points while solving in the case of the n-th RP. This form of fitness calculation is for the purpose of avoiding the overfitting to BP. Objects are removed from the field when they reach their goal corners, respectively.

The ANN controller is evolved by means of MBEANN with the parameter set in Table 2. The details of MBEANN are described in elsewhere [12].

4.2 Simulated Results

The robotic swarm has achieved appropriate behavior by artificial evolution with MBEANN. The details of evolving process are not described here, because artificial evolution is not the main part of this paper. Let us focus on checking

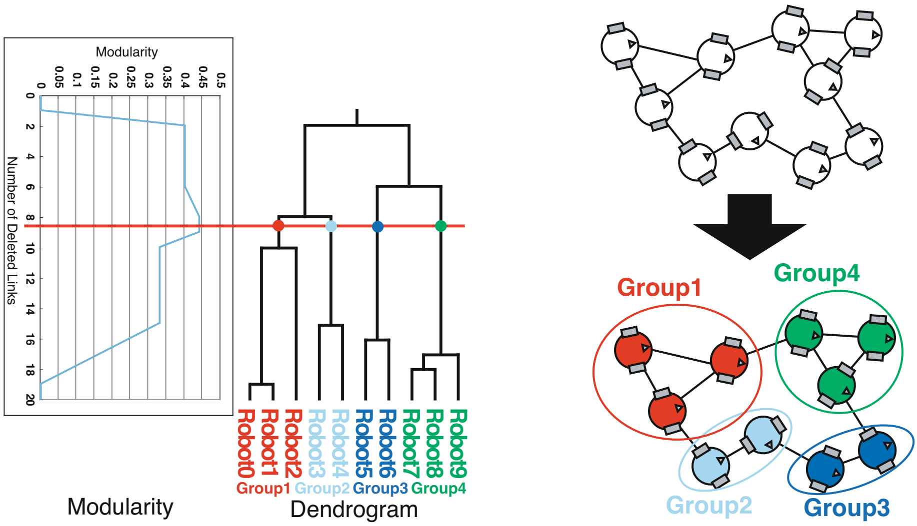

(a) Dendrogram and modularity (b) Network clustering

Fig. 3. Illustrating the subgroup detection by clustering for a group of 10 robots

Table 1. Points for object L (Points for M and S are calculated in the same way as L and then multiplied by 0.6 and 0.4, respectively)

Successful transport	+3000(/object)
Unsuccessful Transport	+Dist(last pos., goal pos.)
Touching an object	+0.05(/step)

Table 2. Parameters for MBEANN

Population size	100
Maximal generation	500
Add-node rate	0.01
Add-connection rate	0.1
Weight mutation rate	1.0

the usefulness of the proposed method for analyzing the macroscopic collective behavior.

Figures 4 and 5 show the snapshots of simulated experiments in the case of BP. Note that robots belonging to the same subgroup are painted in the same color, but color itself does not have a particular meaning.

Figure 4(a) shows the initial positions of the swarm. They are placed at randomly at the square upper-left corner divided into nine subgroups. Graph placed at the right side shows the nine dots each of which shows the resultant velocity of the robots in the subgroup. Since the dots are gathering at the center of the graph, they are not actively moving at the beginning.

Figure 4(b) shows the snapshot that all subgroups are approaching to objects. The right graph shows that the subgroup 7 is approaching to the objects the fastest of all the subgroups.

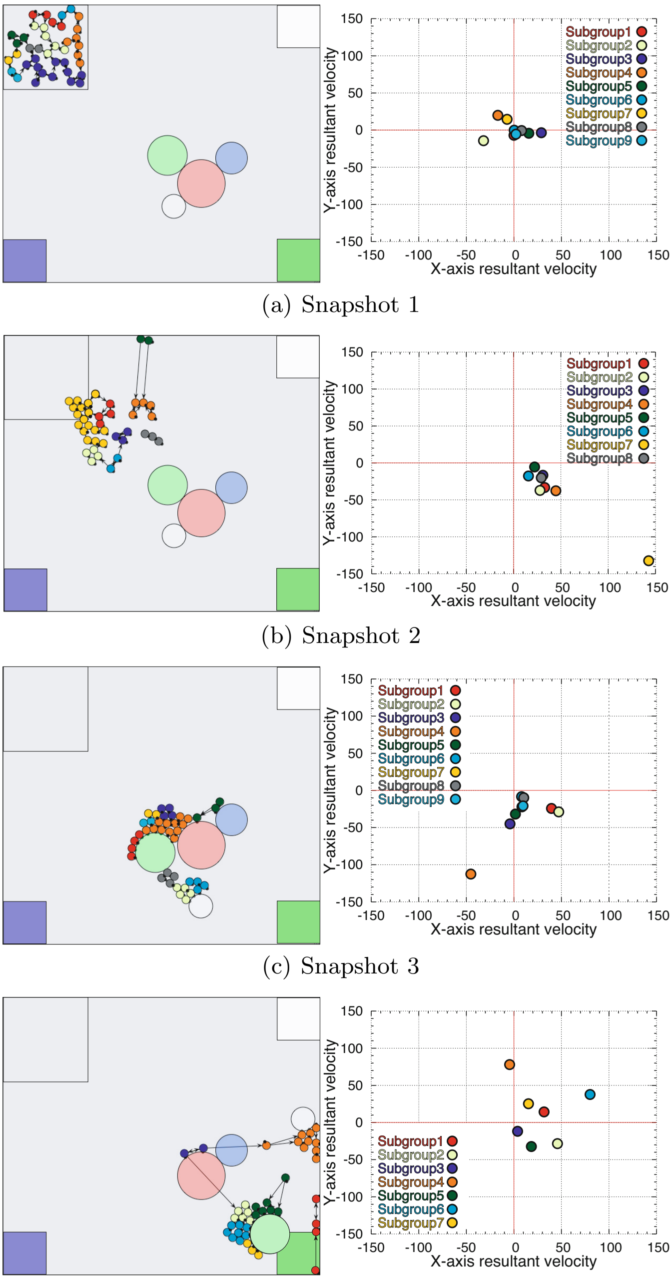

(a) Snapshot 1

(b) Snapshot 2

(c) Snapshot 3

(d) Snapshot 4

Fig. 4. Results of clustering for several snapshots and the resultant velocities of the subgroups

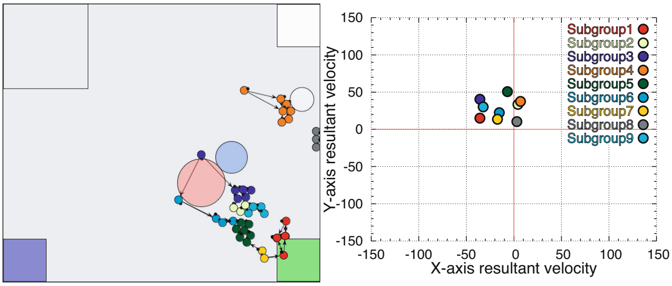

(a) Snapshot 5

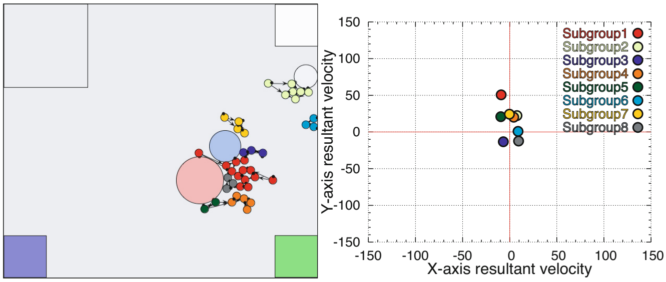

(b) Snapshot 6

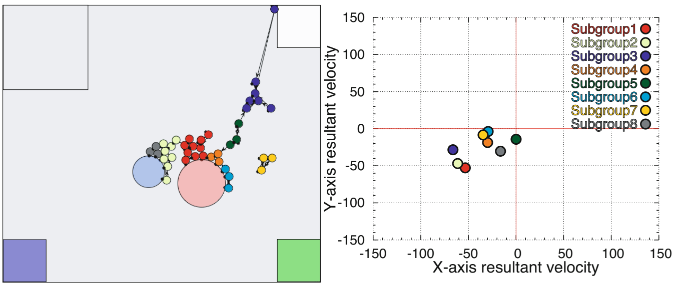

(c) Snapshot 7

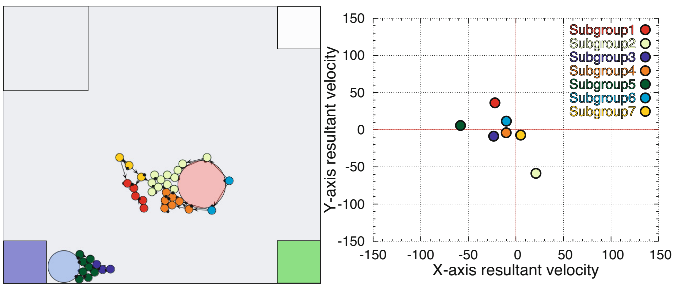

(d) Snapshot 8

Fig. 5. Results of clustering for several snapshots and the resultant velocities of the subgroups

Figure 4(c) shows the snapshot that L and S are pushing by the robots. S is pushed by the subgroups 2 and 6 moving to the lower right side. On the other hand, L is mainly pushed by the subgroup 4 to the lower left side and subsidiarily is pushed by the subgroup 1 to the right side. Thanks to the balance between the two subgroups, L is moving to the lower side to avoid the obstacle.

Figure 4(d) shows the snapshot that L is almost reaching the goal. L is pushed to the lower side by the subgroup 5, to the lower right by the subgroup 2, to the upper right by the subgroup 6 and to the upper side by the subgroup 7, then L is moving to the right side. On the other hand, S is moved by the subgroup 4 to the upper side. The subgroups 1 and 3 are doing nothing.

Figure 5(a) shows the snapshot just after L reaches its goal. The subgroup 4 still continues pushing S, while almost all the others are moving to the upper left. From Figure 5(b), we can understand that the subgroup 1 starts pushing M to the upper side, while the subgroup, labeled 2 in this snapshot, is continuously but slowly pushing S to the upper side. Similarly, from Figure 5(c) showing the snapshot just after finishing pushing S to its goal, M is pushed by the subgroups 2 and 8 to the lower left. The last one, Figure 5(g), shows the snapshot just before reaching M to its goal. The subgroup 5 mainly pushes M to the left side while the subgroup 3 is supporting the subgroup 5. The others are wandering around the unmovable object.

As explained above, the usefulness of the proposed method has been verified.

5 Conclusions

In this paper, a novel method of analyzing the collective behavior of a robotic swarm based on clustering was proposed. The method was evaluated with the cooperative transport problem in which three objects to move and a fixed obstacle were placed on the field. It was found that the proposed method is useful for grasping the functional roles of the subgroups. In the near future, we are planning to generalize the associated network not only as an indirected graph but also as a weighted directed graph so that the associated network can include more information about the robotic swarm.

References

1. Arkin, R.: Behavior-Based Robotics. The MIT Press (1998)
2. Girvan, M., Newman, M.E.J.: Community Structure in Social and Biological Networks. Proceedings of the National Academy of Sciences of the United States of America 99, 7821–7826 (2002)
3. http://www.swarm-bots.org/
4. Baldassarre, G., Nolfi, S., Parisi, D.: Evolution of Collective Behavior in a Team of Physically Linked Robots. In: Raidl, G.R., Cagnoni, S., Cardalda, J.J.R., Corne, D.W., Gottlieb, J., Guillot, A., Hart, E., Johnson, C.G., Marchiori, E., Meyer, J.-A., Middendorf, M. (eds.) EvoWorkshops 2003. LNCS, vol. 2611, pp. 581–592. Springer, Heidelberg (2003)

5. Dorigo, M., Trianni, V., Sahin, E., Groß, R., Labella, T.H., Baldassarre, G., Nolfi, S., Deneubourg, J.-L., Mondada, F., Floreano, D., Gambardella, L.M.: Evolving Self-Organizing Behaviors for a Swarm-bot. Autonomous Robots 17(2-3), 223–245 (2004)
6. Newman, M.E.J., Girvan, M.: Finding and Evaluating Community Structure in Networks. Physical Review E 69, 26113 (2004)
7. Şahin, E.: Swarm Robotics: From Sources of Inspiration to Domains of Application. In: Şahin, E., Spears, W.M. (eds.) Swarm Robotics WS 2004. LNCS, vol. 3342, pp. 10–20. Springer, Heidelberg (2005)
8. Dorigo, M., Tuci, E., Groß, R., Trianni, V., Labella, T.H., Nouyan, S., Ampatzis, C., Deneubourg, J.-L., Baldassarre, G., Nolfi, S., Mondada, F., Floreano, D., Gambardella, L.M.: The SWARM-BOTS Project. In: Şahin, E., Spears, W.M. (eds.) Swarm Robotics WS 2004. LNCS, vol. 3342, pp. 31–44. Springer, Heidelberg (2005)
9. http://www.swarmanoid.org/
10. Tuci, E., Ampatzis, C., Vicentini, F., Dorigo, M.: Evolved Homogeneous Neuro-controllers for Robots with Different Sensory Capabilities: Coordinated Motion and Cooperation. In: Nolfi, S., Baldassarre, G., Calabretta, R., Hallam, J.C.T., Marocco, D., Meyer, J.-A., Miglino, O., Parisi, D. (eds.) SAB 2006. LNCS (LNAI), vol. 4095, pp. 679–690. Springer, Heidelberg (2006)
11. Groß, R., Tuci, E., Dorigo, M., Bonani, M., Mondada, F.: Object Transport by Modular Robots that Self-assemble. In: Proc. of the 2006 IEEE International Conference on Robotics and Automation, ICRA 2006, pp. 2558–2564 (2006)
12. Ohkura, K., Yasuda, T., Kawamatsu, Y., Matsumura, Y., Ueda, K.: MBEANN: Mutation-Based Evolving Artificial Neural Networks. In: Almeida e Costa, F., Rocha, L.M., Costa, E., Harvey, I., Coutinho, A. (eds.) ECAL 2007. LNCS (LNAI), vol. 4648, pp. 936–945. Springer, Heidelberg (2007)
13. Sahin, E., Girgin, S., Bayindir, L., Turgut, A.E.: Swarm Robotics. In: Blum, C., Merkle, D., (eds.) Swarm Intelligence - Introduction and Applications, pp. 87–100. Springer (2008)
14. Groß, R., Dorigo, M.: Towards Group Transport by Swarms of Robots. International Journal of Bio-Inspired Computation 1(1-2), 1–13 (2009)

Detection of Breast Cancer Based on Texture Analysis from Digital Mammograms

Eun-Byeol Jo, Ju-Hwan Lee, Jun-Young Park, and Sung-Min Kim

Dept. of Medical Bio Technology, Dongguk University-Seoul
26 Pil-dong 3-ga, Jung-gu, Seoul 120-749, Korea
{eunbyeol27,tupac1969}@gmail.com, pipen@nate.com,
smkim@dongguk.edu

Abstract. In this study, we propose a novel breast cancer detection algorithm based on texture properties of mass area. Proposed method extracts the midpoint of mass area by using AHE (Adaptive Histogram Equalization), and selects the ROI (Region of Interest) in the original image. L1-norm based smoothing filter is then employed to stabilize the mass area, and the form of the mass is determined. Additionally, we measured homogeneity and Ranklet using SVM (Support Vector Machine) to analyze texture properties of the selected mass area. As a result, we observed that the proposed method shows the more stable and outstanding performance for Korean women compared with the existing methods.

Keywords: mammogram, breast cancer, SVM (Support Vector Machine), Ranklet, homogeneity.

1 Introduction

Recently, an early diagnosis of breast cancer has been shown to be an important research as the death rate of breast cancer increases [1,2]. Mass is one of the most essential factor to diagnose breast cancer among the existing parameters. Although numerous studies have performed to detect malignant areas based on the mass properties, the detection rate is still remained as about 80% [3,4]. Asian females including Korean women typically show the characteristics of dense breast. In general, it is difficult to detect the malignant tissues on dense breast, since dense breast have much larger mammary glandular tissues compared with the normal [5]. The existing diagnostic algorithms therefore present the low detection accuracy for mass type breast cancer in Korean women.

To cope with these limitations, a number of studies were done to improve the detection rate for mass type breast cancer. Karseemeijer detected the malignant tissues in the original image based on the directivity of texture to improve the detection rate [6]. As similar with [6], Mudigonda et al. extracted the directivity of each pixel from the original image, and analyzed texture properties [7]. Brake et al. improved the detection accuracy for breast cancer by employing Karseemeijer's method as multi focusing way [8]. Huang et al. translated mass properties into 1

S. Lee et al. (Eds.): Intelligent Autonomous Systems 12, AISC 194, pp. 893–900.
springerlink.com

dimensional profile, and diagnosed the cancer based on their peak and bottom points [9]. In addition, Petrick et al. applied the adaptive enhancement filter to obtain the increased detection rate for the breast cancer [10]. On the other hand, Zheng presented the high true positive rate (TP) of 90% for the breast cancer based on Gabor cancer detection (GCD) algorithm [11]. Despite these efforts, the existing methods revealed some fatal limitations. Firstly, the previous methods failed to determine the directivity of the pixel gradient due to the minor variances of the original image. Secondly, the malignant tissues were not separated from the normal tissues in dense breast image.

In this study, we propose a novel breast cancer detection technique based on texture properties of mass area to cope with the above limitations. The proposed algorithm extracts the midpoint of mass area by using AHE (Adaptive Histogram Equalization), and selects the ROI (Region of Interest) from the original mammogram image. Next, L1-norm based smoothing filter is employed to stabilize the mass area, and then the form of the mass is determined. In addition, in order to analyze texture properties of the selected mass area, we measured homogeneity and Ranklet by using SVM (Support Vector Machine). The rest of the paper is organized as follows: Section 2 introduces the details of the proposed detection algorithm. Section 3 gives the experimental results. Lastly we conclude our findings in Section 4.

2 Methods

2.1 Extraction of Mass Area Using AHE (Adaptive Histogram Equalization)

Generally, malignant tissues are brighter than normal tissues. We therefore applied AHE algorithm iteratively to separate the mass type cancer area from the original image. AHE separates the midpoint of the mass area from the background as the contrast of the image increases locally [12]. In particular, the brightness between the midpoint and background shows clear differences. We thus determined the threshold value (T_c) adaptively for all test images (Figure 1). Figure 2 presents the extraction procedure of the midpoint from the original mammogram image by using iterative AHE. We performed AHE 18 times iteratively, and obtained midpoints of mass area.

In the digital mammogram, it is required to determine the midpoint of mass as well as mass area to extract cancer tissues. To do this, we computed the radius of mass area based on the mean brightness of the neighboring pixels regarding midpoint. Generally, mass area is brighter than the background area, and the brightness is diminished, when the pixel recedes from the center of mass. In other words, the mean brightness decreases as the radius from the midpoint increases, whereas the value converges to a certain level as the radius breaks away from the mass. We therefore

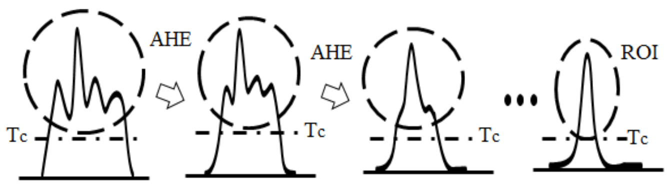

Fig. 1. Extraction procedure of mass area

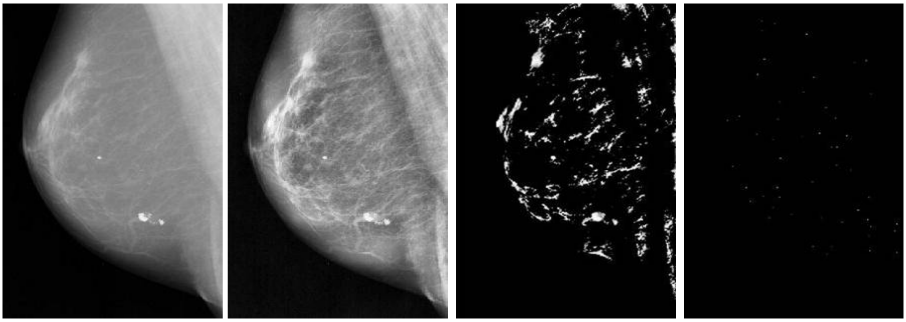

(a) Original image (b) AHE 1 time (c) AHE 18 time (d) Centers of masses

Fig. 2. Extraction procedure of the midpoint based on AHE (Adaptive Histogram Equalization)

considered that the pixel belongs to a different mass area, only when the mean brightness increases three consecutive times. Namely, we classified the ROIs as malignant tissues, when the mean brightness converges to a certain value.

Mean brightness of the pixels that located within the radius r from the center of mass can be calculated by equation (1):

$$C(\gamma) = \frac{1}{N_\gamma} \sum_{(i,\, j) \in C_r} I(i,\ j),\ r = 1,2,\cdots \tag{1}$$

where the I(i, j) indicates the brightness corresponding to the midpoint, γ means the radius of mass area, and C_r means coordinates of each pixel located within radius r.

$$\begin{aligned} \gamma^1 &= \underset{\gamma}{\operatorname{argmin}} \left\{ \gamma \left| \frac{C(r-i-1) - C(r-i)}{C(r-i-1)} \right| < \varepsilon \right\} \\ \gamma^2 &= \underset{\gamma}{\operatorname{argmin}} \{ \gamma \left| C(r-i) - C(r-i-1) \right| < 0 \} \end{aligned} \tag{2}$$

The radius of mass area is derived by equation (2) for i=0, 1, and 2, and we finally obtained radius of mass area by $\gamma = \min(r^1, r^2)$.

2.2 Extraction of the Form of Mass Using Smoothing Filter

As mentioned above, mass area is relatively brighter than normal tissues. It is however difficult to detect the mass area specifically due to the large variation of pixels within the mass area. We therefore employed an L1-norm based smoothing filter to stabilize the unstable image signals. We also determined the form of mass by using the line connection method.

Nevertheless, mass area generally showed discontinuity in the boundary lines, as we detected all image signals without any residues based on the employed smoothing filter. The condition for determining the boundary lines in the mass area is shown in equation (3) with a co-occurrence matrix p for i=0, 1, and 2. In other words, we

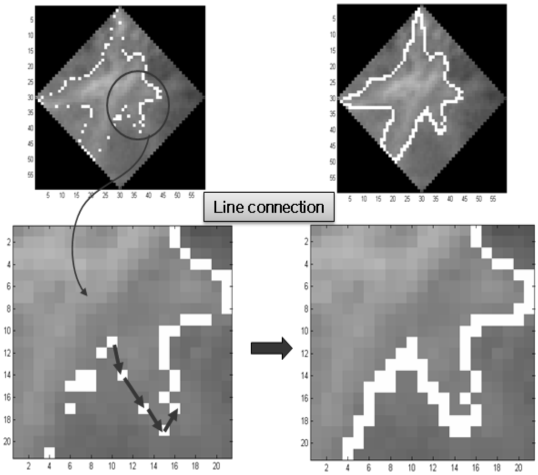

Fig. 3. Determination of the mass from based on line connection method

selected the contour lines of mass area, when the brightness converges to a certain value or suddenly increases or increases after some reduction. We then computed the included angle for each location by utilizing location information. In addition, we produced the boundary lines after supplementing directivity properties (Figure 3).

$$\begin{aligned}
\gamma_\theta^1 &= \operatorname{argmin}\left\{\gamma \left| \frac{P_\theta(r-i+1) - P_\theta(r-i)}{P_\theta(r-i+1)} \right| < \varepsilon_1 \right\} \\
\gamma_\theta^2 &= \operatorname{argmin}\left\{\gamma \left| \frac{P_\theta(r-i+1) - P_\theta(r-i)}{P_\theta(r-i+1)} \right| < \varepsilon_2 \right\} \\
\gamma_\theta^3 &= \operatorname{argmin}\left\{\gamma \left| \frac{P_\theta(r-i+1) - P_\theta(r-i)}{P_\theta(r-i+1)} \right| < 0 \right\}
\end{aligned} \tag{3}$$

2.3 Texture Analysis Based on the Homogeneity and Ranklet

The central area of mass shows uniform texture form, since mass type breast cancer usually spreads from the center section to the surrounding tissues [13]. It is therefore possible to separate the malignant tissues from the normal tissues in the dense breast image by using a homogeneity coefficient. The homogeneity coefficient (H) can be calculated by equation (4):

$$H = \sum_{i \le M} \sum_{j \le M} \frac{P(i,\ j)}{1 + |i - j|} \tag{4}$$

where p(i,j) means a co-occurrence matrix with a vertical and horizontal distance of 1. M indicates the size of the central area to measure the uniformity of texture. We adjusted M as 20% of the total size of mass, and the size of the co-occurrence matrix was designated as 5x5.

Additionally, we extracted the directivity coefficients for vertical, horizontal and diagonal directions by employing Ranklet approach. Based on these directivities, the malignant tissues were differentiated from the background image. Ranklet vectors corresponding to each direction are computed by equation (5):

$$R = \frac{2W_{YX}^{i}}{N^2/4} - 1, \ i = v, h, d \tag{5}$$

where W_{YX} presents the coefficient of the relative brightness grade, R_i indicates Ranklet Vectors for each direction, and N is the number of total pixels.

2.4 Optimization of the experimental parameters by SVM (Support Vector Machine)

SVM method minimizes the general errors due to the utilization of SRM (Structural Risk Minimization). We therefore employed SVM classifier to optimize the homogeneity coefficient and Ranklet vector. Discriminating equation for SVM classifier is shown in equation (6):

$$f(x) = \mathrm{sgn}(\sum_{i=1}^{N} \alpha_i y_i (x_i^T x) + b) \tag{6}$$

where α_i and y_i indicates the weight vector and class level, respectively. N and x means the number of support vector and the number of input vector, respectively.

We set each of the fifty mammograms to perform SVM training for optimization of the Homogeneity and Ranklet. The optimum threshold value was selected as 0.37, since the missing rate of mass detection was revealed less than 5%. We then produced the specific Ranklet model, which showed 115 support vectors, 1.7857 of weight vector value, and bias of 1.9451.

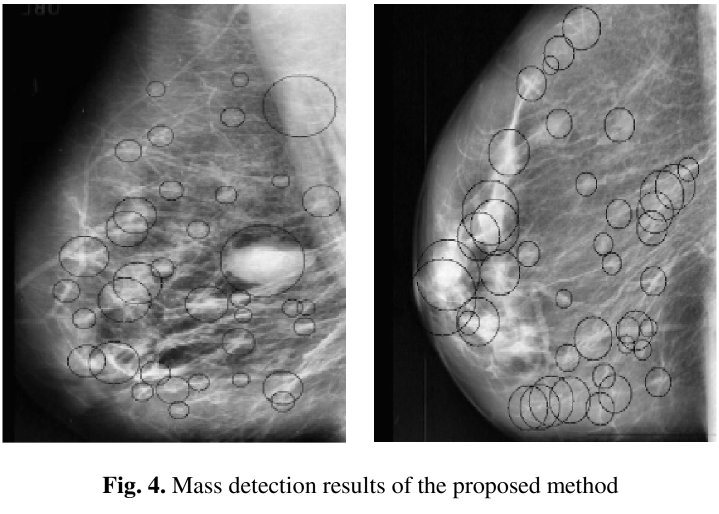

Fig. 4. Mass detection results of the proposed method

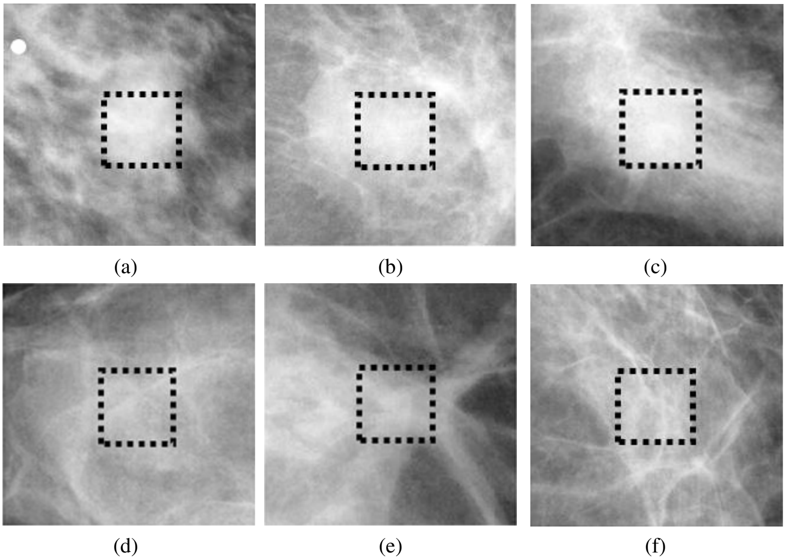

Fig. 5. Cancer (a,b,c) and normal regions (d,e,f) for measuring Homogeneity and Ranklet

Table 1. Results of texture analysis by SVM (Support Vector Machine)

	(a)	(b)	(c)	(d)	(e)	(f)
H[a]	0.4934	0.5354	0.5250	0.3533	0.3776	0.3667
RV[b]	0.17	0.12	0.04	0.51	0.61	0.66
RH[c]	0.25	0.20	0.25	0.07	0.22	0.14
RD[d]	0.26	0.35	0.18	0.66	0.18	0.12

a. Homogeneity, b. Vertical Ranklet, c. Horizontal Ranklet, d. Diagonal Ranklet

3 Results

The existing methods need advanced information to detect the mass, whereas our method detected the size of mass adaptively even without any information about mass properties. The proposed method therefore revealed a high detection rate of mass over 98% for pre-diagnosed breast cancer tissues by clinician (Figure 4). In addition, our method produced an 85.4% of true pulse rate for a total of 82 mass-type breast cancer cases, and the number of false alarms was shown as 2.6 per image. Moreover, we succeeded to reduce the computational load compared to the gradient-orientation based approach due to the utilization of the variation of pixel brightness.

On the analysis of texture by homogeneity and Ranklet, our method also revealed reasonable results. The proposed approach presented clear differences of the homogeneity between normal tissues and cancer tissues. Figure 5 and Table 1 indicate the results of texture analysis based on homogeneity and Ranklet vectors. Moreover, the differences of the Ranklets were also significant. Namely, Ranklet vectors were shown to be small in cancer tissues, whereas the large values were revealed in the normal tissues. Consequently, we confirmed that the cancer tissues show no directivity due to the dispersive diffusion of the cancer.

4 Conclusions

In this study, we proposed a novel cancer detection algorithm based on texture properties of tissues. Proposed algorithm extracted the midpoint of mass area using AHE, and selected the ROI from the original image. In addition, L1-norm based smoothing filter was employed to stabilize the mass area, and the form of the mass was determined. In order to analyze the texture properties of mass area, we measured homogeneity and Ranklet by using SVM. As a result, it was observed that the proposed method shows the more stable and outstanding detection performance for Korean women compared with the existing algorithms.

In future study, we will focus on the minimization of the false alarm of mass detection by employing the weight function for each texture property. Through this implementations, we will develop the fully automated CAD system to provide an early diagnosis of breast cancer.

Acknowledgements. This work was supported by the Dongguk University Research Fund.

References

1. Zhang, L., Ren, Y., Huang, C., Lin, F.: “A novel automatic tumor detection for breast cancer ultrasound images. In: International Conference on Fuzzy Systems and Knowledge Discovery (FSKD), pp. 401–404 (2011)
2. Nadvoretskiy, V., Ermilov, S., Brecht, H.P., Su, R., Oraevsky, A.: Image processing and analysis in a dual-modality optoacoustic/ultrasonic system for breast cancer diagnosis. Photons Plus Ultrasound: Imaging and Sensing (2011)
3. Liu, B., Cheng, H.D., Huang, J., Tian, J., Tang, X., Liu, J.: Fully automatic and segmentation-robust classification of breast tumors based on local texture analysis of ultrasound images. Pattern Recognit. 43(1), 280–298 (2010)
4. Phipps, A.I., Li, C.I., Kerlikowske, K., Barlow, W.E., Buist, D.S.: Risk factors for ductal, lobular, and mixed ductal-lobular breast cancer in a screening population. Cancer Epidemiol. Biomarkers Prev. 19(6), 1643–1654 (2010)
5. Jane, D., Ruth, W., Anne, G., Deborah, T.: Mammographic density, estrogen receptor status and other breast cancer tumor characteristics. Breast J. 16(3), 279–289 (2010)
6. Karssemeijer, N.: Detection of masses in mammograms. In: Image-Processing Techniques for Tumor Detection, pp. 187–212. Marcel Dekker, Inc., New York (2002)
7. Mudigonda, N.R., Rangayyan, R.M., Leo Desautels, J.E.: Detection of breast masses in mammograms by density slicing and texture flow-field analysis. IEEE Trans. Med. Imaging 20(12), 1215–1227 (2001)

8. Brake, G.M., Karssemeijer, N.: Single and multiscale detection of masses in digital mammograms. IEEE Trans. Med. Imaging 18(7), 628–639 (1999)
9. Huang, S.F., Chang, R.F., Chen, D.R., Moon, W.K.: Characterization of speculation on ultrasound lesions. IEEE Trans. Med. Imaging 23(1), 111–121 (2004)
10. Petrick, N., Sahiner, B., Chan, H.P., Helvie, M.A., Paquerault, S., Hadjiiski, L.M.: Breast cancer detection: evaluation of a mass-detection algorithm for computer-aided diagnosis-experiencein 263 patients. Radiology 224(1), 217–224 (2002)
11. Zheng, Y.: Breast cancer detection with Gabor features from digital mammograms. Algorithm 3(1), 44–62 (2010)
12. Moayedi, F., Azimifar, Z., Boostani, R., Katebi, S.: Contourlet-based mammography mass classification using the SVM family. Comput. Biol. Med. 40(4), 373–383 (2010)
13. Cheng, H.D., Shan, J., Ju, W., Gou, Y., Zhang, L.: Automated breast cancer detection and classification using ultrasound images: A survey. Pattern Recognit. 43(1), 299–317 (2010)

Author Index